Green Energy and Technology

Fethi Aloui
Ibrahim Dincer *Editors*

Exergy for A Better Environment and Improved Sustainability 2

Applications

Springer

Green Energy and Technology

More information about this series at http://www.springer.com/series/8059

Fethi Aloui • Ibrahim Dincer
Editors

Exergy for A Better Environment and Improved Sustainability 2

Applications

Springer

Editors
Fethi Aloui
LAMIH UMR CNRS 8201
Department of Mechanical Engineering
University of Valenciennes (UVHC)
High Engineering School (ENSIAME)
Valenciennes Cedex, France

Ibrahim Dincer
Faculty of Engineering and Applied Science
University of Ontario Institute of Technology
Oshawa, ON, Canada

ISSN 1865-3529 ISSN 1865-3537 (electronic)
Green Energy and Technology
ISBN 978-3-319-62574-4 ISBN 978-3-319-62575-1 (eBook)
https://doi.org/10.1007/978-3-319-62575-1

Library of Congress Control Number: 2017955058

© Springer International Publishing AG, part of Springer Nature 2018
This work is subject to copyright. All rights are reserved by the Publisher, whether the whole or part of the material is concerned, specifically the rights of translation, reprinting, reuse of illustrations, recitation, broadcasting, reproduction on microfilms or in any other physical way, and transmission or information storage and retrieval, electronic adaptation, computer software, or by similar or dissimilar methodology now known or hereafter developed.
The use of general descriptive names, registered names, trademarks, service marks, etc. in this publication does not imply, even in the absence of a specific statement, that such names are exempt from the relevant protective laws and regulations and therefore free for general use.
The publisher, the authors and the editors are safe to assume that the advice and information in this book are believed to be true and accurate at the date of publication. Neither the publisher nor the authors or the editors give a warranty, express or implied, with respect to the material contained herein or for any errors or omissions that may have been made. The publisher remains neutral with regard to jurisdictional claims in published maps and institutional affiliations.

Printed on acid-free paper

This Springer imprint is published by the registered company Springer Nature Switzerland AG
The registered company address is: Gewerbestrasse 11, 6330 Cham, Switzerland

Preface

During the past two decades, we have witnessed many drastic changes in science, technology and engineering. One of these drastic changes is the revitalization of exergy concepts, methods, approaches, etc. Exergy now appears to be a well-established and distinct discipline which has come out of the second law of thermodynamics and gone beyond thermodynamics to be used in many other disciplines, such as chemical, biotechnology, civil, environmental, architectural, industrial, system, electrical, geology, topography, etc. in engineering and chemistry, biology, physics, mathematics, business, informational technology, economy, medicine, etc. in non-engineering areas.

As a result of these recent changes and advances, exergy has gone beyond thermodynamics and become a new distinct discipline because of its interdisciplinary character as the confluence of energy and environment. It was a prime motive to initiate a conference series on Exergy, Energy and Environment in 2003. The conference, since then, has been running successfully under the title of "International Exergy, Energy and Environment Symposium (IEEES)". The conference has a multidisciplinary nature, covering three main areas of exergy, energy and environment, and aims to provide a forum for researchers, scientists, engineers and practitioners from all over the world to exchange information; to present high-quality research results and new developments in the wide domain covered by exergy, energy and the environment; and to discuss the future direction and priorities in the field.

This edited book, which is a multidisciplinary reference, will serve as a comprehensive source for researchers, scientists, engineers, undergraduate students and professionals on the recent advances in exergy, energy and environmental issues. It discusses current problems, future needs and prospects in the area of energy and environment. This unique book contains, in addition to some invited contributions, the selected papers from the latest Seventh International Exergy, Energy and Environment Symposium (IEEES-7) which was held in the University of Valenciennes in Valenciennes, France. It covers a broad range of topics on energy conservation and analysis; entropy and exergy analyses; entropy generation minimization;

exergy, energy and environmental modelling; exoeconomics and thermoeconomics; hydrogen generation and technology; fuels and alternatives; heat and mass transfer; renewable energy; new and clean energy technologies; refrigeration and heat pump systems; combustion technology; thermal systems and applications; air-conditioning systems; thermodynamics optimization; modelling of energy systems; combustion/gasification; process optimization; sectoral energy and exergy utilization; waste exergy emissions; etc.

In closing, the editors gratefully acknowledge the assistance provided by numerous individuals, especially for reviewing and revising several chapters, checking for consistency and finalizing them for publication. The editors also register their sincere appreciation to the authors for their contributions which have made this unique edited book possible.

Valenciennes Cedex 9, France — Fethi Aloui
Oshawa, ON, Canada — Ibrahim Dincer

Contents

About the Editors

Fethi Aloui was appointed as Professor of Mechanical Engineering and Energy at the University of Valenciennes (UVHC), France (at the Engineering School ENSIAME), Laboratory LAMIH (UMR CNRS 8201), in September 2011 after working more than 14 years as Associate Professor in Process Engineering, Energy and Fluid Mechanics at the University of Nantes, France. His speciality field is transfer and transport phenomena in fluid mechanics and engineering processes. He has published over 200 journal and conference papers so far. He serves as Associate Editor of the *Journal of Applied Fluid Mechanics* and the *International Journal of Energy Research*. He is also the co-organizer (each year since 2010) of the ASME-FEDSM "Symposium on Transport Phenomena in Energy Conversion from Clean and Sustainable Resources". He regularly reviews for *Journal of Applied Fluid Mechanics*, *Applied Energy*, *International Journal of Energy Research*, *International Journal of Heat and Fluid Flow*, *International Journal of Coal Science and Technology, Fuel* and many other journals.

Ibrahim Dincer is a full Professor of Mechanical Engineering in the Faculty of Engineering and Applied Science at UOIT. He is Vice President for Strategy in International Association for Hydrogen Energy (IAHE) and Vice-President for World Society of Sustainable Energy Technologies (WSSET). Renowned for his pioneering works in the area of sustainable energy technologies, he has authored and co-authored numerous books and book chapters, more than 1000 refereed journal and conference papers, and many technical reports. He has chaired many national and international conferences, symposia, workshops and technical meetings. He has delivered more than 250 keynote and invited lectures. He is an active member of various international scientific organizations and societies and serves as editor-in-chief, associate editor, regional editor and editorial board member on various prestigious international journals. He is a recipient of several research, teaching and service awards, including the Premier's Research Excellence Award in Ontario, Canada, in 2004. He has made innovative contributions to the understanding and development of sustainable energy technologies and their implementation. He has actively been working in the areas of hydrogen and fuel cell technologies, and his group has developed various novel technologies/methods/etc.

Part I
Environment Impact Assessment and Potential Solutions

Wastes of Oil Drilling: Treatment Techniques and Their Effectiveness

Abbas Hadj Abbas, Hacini Messaoud, and Aiad Lahcen

1 Introduction

The development of the oil industry has created many environmental problems that contribute in the degradation of some natural ecosystems, especially sheets of groundwater. The environmental laws require adequate treatment of these wastes in order to avoid any degradation. The oil industry in the region of Hassi Messaoud is very developed which produces industrial waste with dangerous elements. During the drilling a large quantity of solid and liquid industrial wastes are generated. These releases contain toxic chemicals such as heavy metals and organic pollutants (Lefebrre 1978). These elements cause problems for the humans, animals (Cranford et al. 1999), and plants (Atlas 1984). Additional information can be given by Scriban (1999). So, what are the treatment methods and their effectiveness?

The study area is in the field of Hassi Messaoud, which is about 850 km in the south of Algiers and 350 km from the Tunisian border (Askri et al. 2003).

The aim of this work is to find solutions that can reduce or stop the influence of these toxic elements. For this purpose we adopted a method of work, beginning with a literature search for oil drilling, drilling fluids, and waste products used (Yaiche 2006). We made site visits to recognize nearby the identity of these wastes, their

A.H. Abbas (✉)
Department de forage et MCP, Laboratoire de géologie de Sahara, Université de Kasdi Merbah Ouargla, Rouissat Ouargla, Ouargla 30130, Algeria
e-mail: abbashadjabbas@gmail.com

H. Messaoud
Department de forage et MCP, Laboratoire de géologie de Sahara, de Kasdi Merbah Ouargla, Rouissat Ouargla, Ouargla 30130, Algeria

A. Lahcen
la société de National Oil Well Varco, Hassi Messaoud, Rouissat Ouargla, Ouargla 30130, Algeria

© Springer International Publishing AG, part of Springer Nature 2018

F. Aloui, I. Dincer (eds.), *Exergy for A Better Environment and Improved Sustainability 2*, Green Energy and Technology,
https://doi.org/10.1007/978-3-319-62575-1_1

chemical components, and their influence on the environment, and we have seen the appropriate means to treat these wastes and to a make limit concerning their negative influence. It was found that there are two methods of treatment which are chemical and thermal (Khodja 2008). These methods are based on the utilization of cement inerting and utilization of high temperatures to trap toxic elements (Damou 2007). More details on this process can be given by Cherifi (2006).

This fieldwork is made to diagnose the treatment methods of these wastes and make the neutralizing of these toxic products effective. Sampling of waste is done according to conventional methods. Samples before and after treatment during several phases of drilling to make a homogeneous mixture, the latter are of the oil drilling waste of Hassi Messaoud area before and after each method of treatment and then transported these samples to the laboratory for analysis and retrieve results that can improve the use of these methods (use of equipment catalog of heavy metals, CRD (2010)).

2 Results and Discussion

2.1 Results of Analysis of the Crude Wastes (Before Treatment)

The results of analysis of nine samples showed that the toxic components are the hydrocarbon and heavy metals (Pb, Cu, Cr, Cd, Zn, Mn). The concentrations of hydrocarbon exceed the conventional norms in Algeria or the variation of between 1.98% and 9.61%; the maximum value was recorded in the sample 5 (9.61%) and the minimum value in the sample 4 (1.98). The norms of the concentrations of heavy metals are from 14.1 mg/l (sample 4) and 46.5 mg/l (sample 2) for the lead, between 0.1 mg/l (sample1) and 0.2 mg/l (sample 4) for cadmium, from 5.3 mg/l (sample 4) and 12.6 mg/l (sample 2) for the zinc, and between 1.2 mg/l (sample 4) and 1.8 mg/l (sample 1) for manganese, while the norms of lead, copper, chromium, cadmium, zinc, and manganese are 01, 03, 0.1, 0.2, 05, and 01 in succession. These norms are indicated in the Official Gazette of the Republic of Algeria (1993) and some environmental laws in the Official Gazette 2005 version (2005) and 2007 version (2007).

After comparing the results of the previous elements, their norms and standards, which are indicated in the reference (Official Gazette of the Republic of Algeria 1993), we can say that there are values that exceed the maximum limits, for example, in (sample 1) the value of lead is equal to 32.6 mg/l, so it exceeds the norm of lead that is equal to 0.1 mg/l, and the same value for the zinc in the (sample 2) is equal to 12.6 which exceeds the maximum value (0.5 mg/l) and the same for manganese.

Table 1 Results of the test of hydrocarbon and heavy metals for the crude wastes (before treatment)

Samples	Heavy metals concentration in mg/l						Content of oils (%)
	Lead (pb)	Copper (Cu)	Chromium (Cr)	Cadmium (Cd)	Zinc (Zn)	Manganese (Mn)	
1	32.6	00	00	0.1	8.5	1.8	4.40
2	46.5	00	00	0.1	12.6	2.1	4.00
3	15.8	00	00	00	7.4	1.7	4.65
4	14.1	00	00	0.2	5.3	1.2	1.98
5	/	/	/	/	/	/	9.61
6	/	/	/	/	/	/	6.56
7	/	/	/	/	/	/	9.40
8	/	/	/	/	/	/	3.2
9	/	/	/	/	/	/	2.2

For oil tenures there are two values that exceed the norms in the 5 and 6 samples ($9.61\% > 5\%$). According to the above table, the hydrocarbon and heavy metals are harmful elements conventionally (Table 1).

2.2 *Results of Analyses Before and After Solidification/ Stabilization*

According to the results shown in Table 2 (last page), it was found that the concentrations are generally less than the maximum limit indicated by the Algerian state and Sonatrach. But we record a value that exceeds the maximum values, for example, the value of lead in (sample 1) is equal to 1.8 mg/l $>$ 1 mg/l; to justify this result, we suppose that the amount of cement added is not sufficient to trap the metal.

On the other hand, we record the content of chromium in the treated samples which is equal to 0.23 mg/l which is higher than those of untreated samples 00 mg/l; thus the presence of this metal in the cement used for solidification is the origin of this augmentation.

2.2.1 Optimization of the Method of Solidification/Stabilization (Chemical Method)

Optimization of Cement

From the figure, it was found that the content of hydrocarbons in the presence of a fixed concentration of sodium silicate is inversely proportional to the concentration of added cement, but it can also be noticed that between the values of the

Table 2 Concentrations of heavy metals

Samples	Heavy metals concentration in mg/l						Hydrocarbon concentration (%)
	Lead (Pb)	Copper (Cu)	Chromium (Cr)	Cadmium (Cd)	Zinc (Zn)	Manganese (Mn)	
Sample 1 before treatment	32.6	00	00	0.1	8.5	1.8	4.40
Sample 1 after treatment	8.1	00	00	0.1	0.56	0.1	1.40
Sample 2 before treatment	46.5	00	00	0.1	12.6	2.1	4.00
Sample 2 after treatment	00	00	00	0.1	00	00	1.30
Sample 3 before treatment	15.8	00	00	00	7.4	1.7	/
Sample 3 after treatment	00	00	0.23	00	00	00	0.53
Sample 4 before treatment	14.1	00	00	0.2	5.3	1.2	1.98
Sample 4 after treatment	00	00	0.34	0.1	00	00	1.51

concentration of cement between (200 and 300 kg/m^3), the reduction is not very important (from 5.08 to 4.28% for almost double the amount of cement added). This can be justified by the fact that cement creates a solid matrix which protects the film formed by the sodium silicate and enhances encapsulation. The content of hydrocarbons decreases as we add cement, but by reaching a certain value of the quantity of cement added, the content of hydrocarbons continues to decrease but at a slower manner. The effect of the cement is more interesting at high hydrocarbon levels.

For economic reasons (the cost of cement), we have an optimal concentration of cement equal to 200 kg/m^3 and try to improve the solidification with sand (Fig. 1).

Optimization of Sand (Fig. 2)

According to the shape of the curve, we can say that the result obtained above is improving as we add sand. The hydrocarbon content is decreased by 6.56% (the

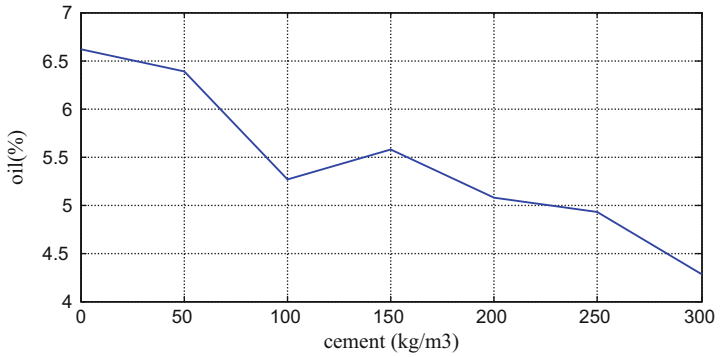

Fig. 1 Changes in the content of hydrocarbons according to the concentration of CPA425 cement

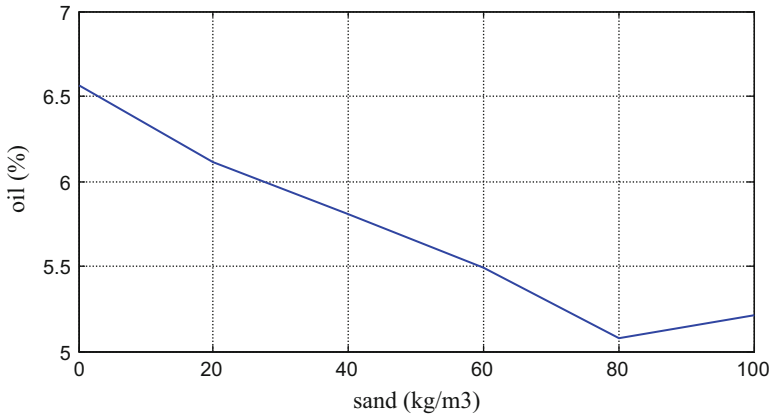

Fig. 2 Changes in the content of hydrocarbons according to the concentration of sand

sand concentration is zero) to 5.21% after addition of 100 kg of sand; this is logical because the latter strengthens the matrix formed by the cement (solidifying).

We stopped at a concentration of sand equal to 100 kg/m^3 (we will consider the following as optimal) for two reasons:

- The decrease in the hydrocarbon content is very low, almost 1–100 kg/m^3 of sand.
- The particle size of the sand can increase the permeability of our treated waste, thus making it less resistant to the infiltration liquids inside the matrix.

Optimization of Sodium Silicates

On this curve, it is found that the percentage of hydrocarbons decreases to a value equal to 6.25%, which corresponds to a concentration of sodium silicate of 10 l/m^3.

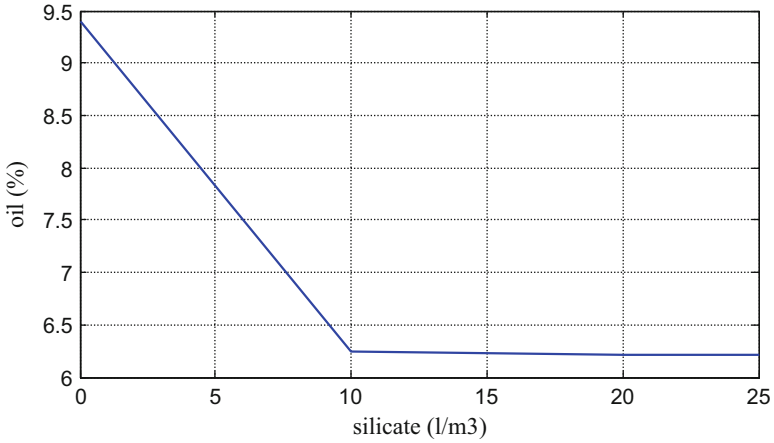

Fig. 3 Changes in the content of hydrocarbons according to the concentration of sodium silicates

After this value, it is obtained practically a bearing (or a very small decrease) in silicate form a covering around the contaminant and attracts Ca++ (from the cement). The latter in turn attracts other molecule silicates. This force of attraction becomes weak gradually as the silicate covering is superimposed on each other, and this is what explains the shape of the graph. The retention of hydrocarbons is stagnant, once when it exceeded a certain concentration of sodium silicate; in our case, the concentration is 10 l/m3 (when it is considered as optimal) (Fig. 3).

Optimization of Activated Carbon

From the presented curve, it is found that the content of hydrocarbons decreases to a value equal to 5.88% which corresponds to a concentration of the activated carbon equal to 30 kg/m^3; after this value the hydrocarbon content rises.

We notice again that our graph has an optimum, which is moving toward a concentration not to exceed, to avoid the contaminant immigration (Fig. 4).

Test Result of Solidification of the Matrix: Resistance of Free Compression

According to the graph above, we see that the resistance of free compression for our sample treated increases as we add cement.

We have two things: firstly making concrete from the treated waste requires the addition of large quantities of cement; secondly, the pretreatment sample was very brittle (Fig. 5).

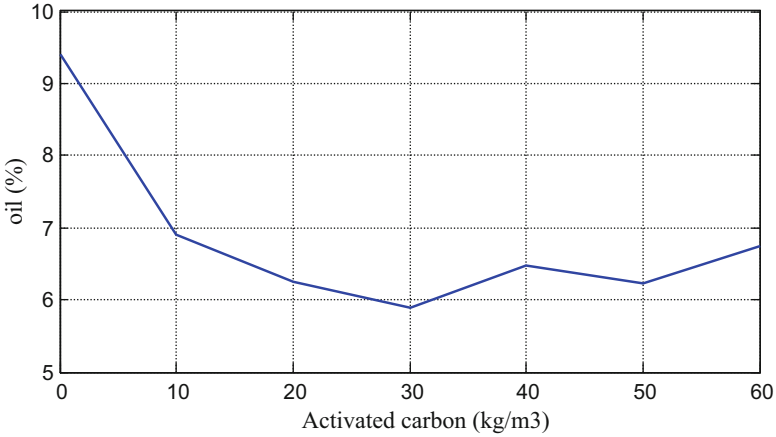

Fig. 4 Changes in the content of hydrocarbons according to the concentration of the activated carbon

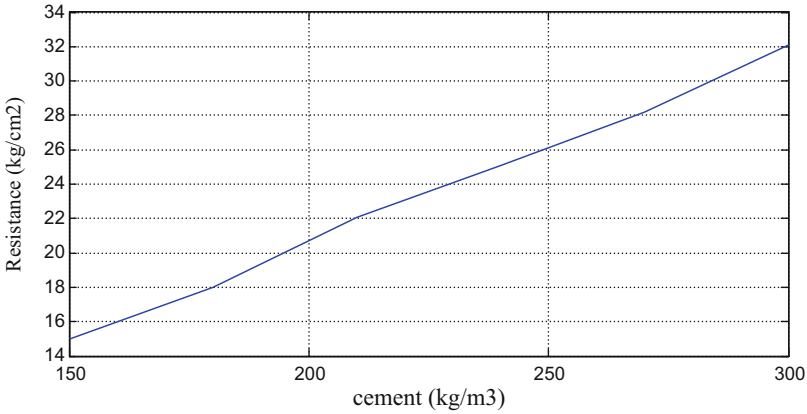

Fig. 5 Variation of the mechanical resistance as a function of the concentration of CPJ425 cement

2.2.2 The Content of the Oil Before and After the Heat Treatment (TDU or TPS)

From the results recorded in the previous table, it was found that our treatment (thermal treatment) is very effective for the hydrocarbon; besides the results of the analysis of the sample after treatment respond fully to the norms (lower to the maximum-tolerated values). But heavy metals retain the same concentration before and after treatment. So, this method is effective for hydrocarbon and its inverse for heavy metals.

Table 3 Results before and after treatment

Samples	Mass of oil expressed in (g)	Test sample expressed in (g)	Hydrocarbon concentration (%)
Before treatment	3.20	100	3.20
After treatment	Traces	100	Traces

3 Conclusion

Based on the results obtained at the end of this study, we argue that oil discharges present risks to the environment because of their compositions which exceed the maximum limits conventional by the Algerian state (degree of contamination of discharges of approximately 9.61% of the oil, so this value exceeded the 5% crud waste).

According to the application of the methods of treatment, it is found that the method of solidification is effective for the trap of heavy metals, so the optimum concentrations are 200 kg/m^3 for the cement, 100 kg/m^3 for the sand, 10 l/m^3 for the silicate, and 30 kg/m^3 for the activated carbon.

On the other side, the thermal treatment is effective for the pollution of hydrocarbons (some traces).

From the results shown in Table 3, it is found that the method of solidification is not a final solution (according to the forces of free compression and moisture that can liberate of toxic elements), so this is the filtration of these toxic elements into the water table.

For a good result of treatment, it is necessary to apply a combination of solidification and heat treatment.

References

Askri, H., Belmecheri, A., Benrabah, B., Boudjema, A., Boumendjel, K., Daoudi, M., Drid, M., Ghalem, T., Docca, A. M., Ghandriche, H., Ghomari, A., Guellati, N., Khennous, M., Lounici, R., Naili, H., Takherist, D. et Terkmani, M. Geology of Algeria. WEC Algeries Algeria (2003)

Atlas, R.M.: Petroleum Microbiology, p. 685. Macmillan Publishing Company, New York (1984)

Cherifi, M.: Drilling waste management for environmental protection in Hassi Messaoud Field, Faculty Design and Technology, School Engineering, the Robert Gordon University, Aberdeen, June 2006.

Cranford, P.J., Gordon Jr, D.C., Lee, K., Armsworthy, S.L., Tremblay, G.-H.: Chronic toxicity and physical disturbance effects of water and oil-based drilling fluids and some constituents on adult sea Scallops (Placopecten magellaniccus). Mar. Environ. Res. **48**, 225–256 (1999)

CRD: (Use of equipment catalog of heavy metals). Hassi Messaoud (2010)

Damou, F.: The adaptability study for the use of thermal desorption and solidification/stabilization processes for the treatment of drill cuttings in HASSI MESSAOUD Field, Faculty of Design and Technology, School of Engineering, The Robert Gordon University, Aberdeen, September 2007

Khodja, M.: Study of the Performance and Environmental Consideration. University Louis Pasteur, Strasburg (2008)

Lefebrre, G.: Chemistry of Petroleum Corporation Editions Technip. Publication I.F.P (1978)

Official Gazette of the Republic of Algeria (10/07/1993)

Official Gazette of the Republic of Algeria (11/09/2005)

Official Gazette of the Republic of Algeria (22/05/2007)

Scriban, R.: Biotechnologie, 5ème édition edn. Tec. et Doc. Lavoisier, Paris (1999)

Yacine, A.: Environmental impact assesment of the drilling activities in the Hassi Messaoud Field, Faculty of Design and Technology, School of Engineering, The Robert Gordon University, Aberdeen, June 2006

Comparative Study of the Adsorption of Nickel on Natural Bentonite and on *Streptomyces rimosus* Dead Biomass

Faroudja Mohellebi and Radia Yous

1 Introduction

Pollution from heavy metals has become a serious problem for human health and for the environment. Heavy metals are not biodegradable and tend to accumulate in organisms, causing various diseases (Inglezakis et al. 2003). The existence of heavy metals, such as copper (Cu), nickel (Ni), zinc (Zn), lead (Pb), mercury (Hg), chromium (Cr), and cadmium (Cd) in wastewater, is the consequence of several activities like chemical manufacturing, paint pigments, plastics, metallurgy, and nuclear industry (Quintelas et al. 2009). Among the various diseases associated with the presence of these toxic elements in the human body are neurotoxicity, severe gastrointestinal irritation, and lung cancer (Jiang et al. 2009, Agouborde and Navia 2009).

For the removal of these metals from wastewater, there are a series of processes currently used for this object: chemical precipitation (Matlock et al. 2001), membrane filtration (Molinari et al. 2004), electrolytic reduction (Beauchesne et al. 2005), solvent extraction (Silva et al. 2005), ionic exchange (Pehlivan and Altun 2007), and adsorption (Ajmal et al. 1998). Most of these methods may not be suitable at industrial scale, due to low efficiency or expensive applicability to a wide range of pollutants, generation of residues, and difficulty in locating optimal operating conditions when different heavy metals are present in a solution, and need a pretreatment. Adsorption of various materials, such as activated carbon (Chen and

F. Mohellebi (✉)
Ecole Nationale Polytechnique, Département Génie Chimique, 10,
Avenue Hassen BADI, El-Harrach, Alger 16200, Algeria
e-mail: ferroudja.iddir@g.enp.edu.dz

R. Yous
Université Hassiba Ben Bouali, Département de Technologie, BP 151, Chlef, Algeria

© Springer International Publishing AG, part of Springer Nature 2018

F. Aloui, I. Dincer (eds.), *Exergy for A Better Environment and Improved Sustainability 2*, Green Energy and Technology,
https://doi.org/10.1007/978-3-319-62575-1_2

Wu 2004), biomaterials (Han et al. 2006), and clay minerals (Sharma 2008), is now recognized as an efficient and economic method to remove metal ions from aqueous solutions.

In recent years, many porous materials found increasing interest as adsorbents due to their abundance in nature, low cost, good cation adsorptive properties, and large surface area.

Mineral materials used to remove heavy metals include bentonite, zeolite, and montmorillonite. Low-cost biosorbents such as the dead biomass wastes from the pharmaceutical industry have been intensively studied for the removal of metallic ions from industrial effluents.

The aim of the present work is to examine the possibility of using natural bentonite and dead biomass of *Streptomyces rimosus* to remove nickel from aqueous solutions. The bentonite was obtained from SIG (western Algeria). The *Streptomyces rimosus* biomass was obtained from the pharmaceutical industry.

The applicability of theoretical models, such as Langmuir and Freundlich, for the equilibrium data fitting was tested. The values of global diffusion coefficients and rate constants were calculated.

Nomenclature

B	Adsorption equilibrium constant ($L.mg^{-1}$)
C_e	Equilibrium concentration of metal ion in solution ($mg.L^{-1}$)
C_0	Initial concentration of metal ion in solution ($mg.L^{-1}$)
C_s	Concentration of the metal ion at the particle surface ($mg.L^{-1}$)
C_t	Concentration of metal ion in solution at t time ($mg.L^{-1}$)
C_B	Adsorbent concentration in the solution ($g.m^3$)
CEC	Cation exchange capacity (meq/100 g)
D_u	Diffusion coefficient in the solid ($m^2.min^{-1}$) according to Urano and Tachikawa model
D_w	Diffusion coefficient in the solid ($m^2.min^{-1}$) according to Weber and Morris model
d_P	Particle size diameter (m)
K_1	Adsorption rate constant for the first-order adsorption (min^{-1})
K_2	Adsorption rate constant for the second-order adsorption (min^{-1})
k_f, n_f	Freundlich's adsorption constants
K_W	Diffusion coefficient in the solid ($mg.g^{-1}.min^{-1/2}$)
m	Mass of adsorbent (g)
q_e	Amount of adsorbed heavy metal per unit adsorbent mass at equilibrium ($mg.g^{-1}$)
q_m	Maximum adsorption capacity ($mg.g^{-1}$)
q_t	Amount of adsorbed heavy metal per unit adsorbent mass at t time ($mg.g^{-1}$)
S	Surface area of the clay per unit solution volume (m^{-1})
v	Volume of the metal solution (mL)
Greek letters	
β	External mass transfer coefficient ($m.min^{-1}$)
ρ_{app}	Apparent volume mass of the clay ($g.m^{-3}$)

2 Diffusion Models

Various models of diffusion have been examined, including single steps of diffusion in external or intraparticle or combined phenomena (Van Vliet et al. 1980; Mathews and Weber 1984).

2.1 External Mass Transfer Diffusion Model

This model, which is an application of Fick's law, describes the evolution of the solute concentration in the solution C_t (mg.L^{-1}), as a function of the difference in the concentrations of the metal ion in the solution, C_t, and at the particle surface C_S (mg.L^{-1}) according to Eq. (1)

$$\frac{\partial\, C_t}{\partial\, t} = -\beta S\,(C_t - C_S) \tag{1}$$

The coefficient is determined after making some assumptions such as a surface concentration C_S negligible at $t = 0$, a concentration in solution tending to the initial concentration C_0, and also negligible intraparticle diffusion. So, the previous equation can be simplified to

$$\left[\frac{dC_t}{dt}\right]_{t\to 0} = -\beta\, S\, C_0 \tag{2}$$

The initial rate of sorption, $-\beta S$ (min^{-1}), is obtained by polynomial linearization of C_t/C_0 and subsequent derivation at $t = 0$.

The surface area is approximated as the external surface area. Moreover, the particles are supposedly spherical and S is calculated as the external surface compared to the solid/liquid ratio in the solution; thus,

$$S = \frac{6C_B}{d_P \rho_{app}} \tag{3}$$

2.2 Intraparticle Mass Transfer Diffusion Model

The models chosen refer to theories developed by Weber and Morris (1962) and Urano and Tachikawa (1991).

According to the intraparticle diffusion model proposed by Weber and Morris (1962), the initial rate of intraparticle diffusion was calculated by linearization of the curve $q_t = f\,(t^{\,0.5})$ and using Eq. (4)

$$q_t = K_w t^{0.5} \tag{4}$$

where K_w is the diffusion coefficient in the solid (mg.g^{-1}.min$^{-1/2}$) (Eq. (5)).

$$K_w = \left(\frac{12 q_e}{d_p}\right)\left(\frac{D_w}{\pi}\right)^{0,5} \tag{5}$$

Another kind of intraparticle diffusion model was proposed by Urano and Tachikawa (1991). The sorption kinetic data were modeled by the following equation:

$$-\mathrm{Log}_{10}\left[1 - \left(\frac{q_t}{q_e}\right)^2\right] = \frac{4\pi^2 D_u t}{2.3\ d_p^2} \tag{6}$$

3 Kinetics of Adsorption

Adsorption kinetics is used in order to explain the adsorption mechanism and adsorption characteristics.

3.1 Pseudo-First-Order Reaction Kinetics

The adsorption rate constant proposed by Lagergren (1898) and Ho (2004) using first-order reaction kinetics is shown below:

$$\frac{dq_t}{dt} = k_1(q_e - q_t) \tag{7}$$

The integration of Eq. (7) gives the following expression:

$$\log(q_e - q_t) = \log q_e - \frac{k_1}{2.303} t \tag{8}$$

3.2 Pseudo-Second-Order Reaction Kinetics

Adsorption data were also evaluated according to the pseudo-second-order reaction kinetics proposed by Ho and McKay (1998).

$$\frac{dq_t}{dt} = k_2(q_e - q_t)^2 \tag{9}$$

If Eq. (9) is integrated, the following expression is obtained:

$$\frac{t}{q_t} = \frac{1}{k_2 q_e^2} + \frac{t}{q_e} \tag{10}$$

4 Adsorption Isotherm Models

In this work, adsorption isotherms of bentonite and treated biomass for nickel ion were expressed mathematically in terms of the Langmuir and Freundlich models.

The Langmuir equation, in the linear form, is written as:

$$\frac{C_e}{q_e} = \frac{1}{q_m.b} + \frac{C_e}{q_m} \tag{11}$$

For the Freundlich equation, the linear form is written as:

$$\text{Log}\, q_e = \text{Log}\, K_f + \frac{1}{n_f}\text{Log}\, C_e \tag{12}$$

5 Materials and Methods

5.1 Adsorbent Characterization

The clay used in this study was collected from Maghnia bentonite deposit, 500 km northwest of Algiers.

This bentonite sample, white in color, was cleaned, dried, and sieved into sizes of 100 μm. Chemical and physical properties of the bentonite used for adsorption experiments are presented in Tables 1 and 2, respectively. This adsorbent was used directly for the experiments without any treatment.

For the divalent cations, magnesium is the element most dominating (46.0 meq/100 g), that is, to about four times the quantity of calcium (11.0 meq/100 g). For monovalents cations, the most dominating element is sodium (36.7 meq/100 g).

S. rimosus biomass produced during oxytetracyclin antibiotic production was collected after fermentation. The biomass was washed with distilled water and dried at 50 °C for 24 h. It was then crushed and sieved in order to select a fraction with particle diameters ranging between 50 and 160 μm. The biomass was then treated with 0.1 M NaOH for 30 min and, once again, washed, dried at 50 °C for 24 h, and sieved to retain the particle size fraction between 50 and 160 μm. In these conditions, the solid particles can be considered as spheres with an average diameter of

Table 1 Chemical composition of bentonite (%)

SiO_2	66.00
Al_2O_3	14.20
CaO	3.86
MgO	3.00
Fe_2O_3	2.42
Na_2O	1.42
K_2O	1.30
TiO_2	0.34
MnO	0.03
P_2O_5	0.07
S	<0.1
L.O.I*	7.01

*Loss on ignition

Table 2 Physical composition of bentonite

Color	White
pH	8
SG ($g.cm^{-3}$)	1.90
Size $<10^{-3}$ mm	49%

Table 3 Physical and chemical characteristics of the biomass

Properties	Untreated biomass	NaOH-treated biomass
Particle size (μm)	50–160	50–160
Humidity (%)	3.2	4.4
Density (g/cm^3)	0.43	0.41
Specific area (m^2/g)	0.13	0.14
Zeta potential (V)	*−0.06*	*−0.07*

105 μm, which is the average of the 50–160-μm fraction. The obtained physical and chemical characteristics of the biomass are reproduced in Table 3.

All experimental results were generally expressed as adsorption capacity "q" which we define as follows:

$$q = \frac{(C_0 - C_t)}{m} \times V \tag{13}$$

6 Results and Discussion

6.1 Adsorption Kinetics

Adsorption kinetics is used in order to explain the adsorption mechanism and adsorption characteristics.

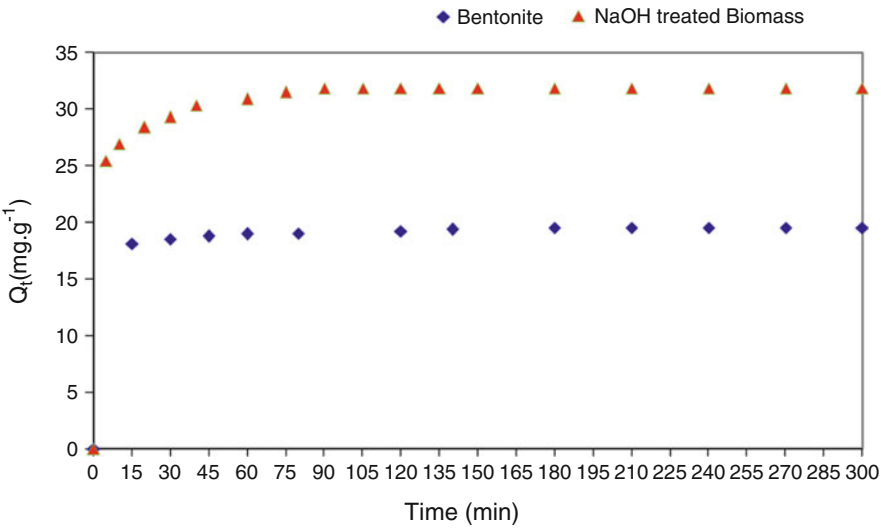

Fig. 1 Adsorption kinetics of nickel on bentonite clay and on NaOH-treated biomass. Initial metal concentration 100 mg.L^{-1}, adsorbent dosage 1 g/200 mL and pH = 7

Table 4 Values of Ni^{2+} biosorption and adsorption constant rates

	First-order reaction		Second-order reaction	
	K_1 (min^{-1})	R^2	K_2 (g. mg^{-1}.min^{-1})	R^2
Bentonite	0.026	0.677	0.07	0.999
Treated biomass	0.028	0.629	0.05	0.966

The kinetics of removing nickel by dead biomass and untreated bentonite clay is presented in Fig. 1.

The treated biomass adsorbent gave better adsorption capacity than the bentonite as the contact time increased. It was observed that the bentonite consistently had a constant adsorption capacity (18 mg.g^{-1}) for nickel all throughout the contact times used which meant equilibrium was rapidly reached, and as quickly as 15 min, the adsorption sites were already saturated to maximum uptake capacity. For biomass, there was an initial increase in adsorption capacity, but after 60-min contact time, the adsorption capacity remained constant (30 mg.g^{-1}).

The kinetic studies of adsorption of Ni (II) onto treated biomass and bentonite were carried out using the first-order and second-order models on experimental data, and the values obtained are given in Table 4.

The regression coefficients obtained from the pseudo-first-order kinetic graph were low. The second-order kinetic model kinetics gave high values of regression correlation coefficient as seen in Table 4. This implied that the mechanism of adsorption of nickel on bentonite and treated biomass followed second-order kinetics.

6.2 Diffusion Models

Table 5 shows the values of the internal diffusion coefficients D_w and D_u, and of the external mass transfer coefficients β.

The above values show that resistance to external mass transfer is negligible compared to internal distribution. Nonetheless, we must compare the experimental results with those calculated by the kinetic and diffusional models. This comparison is illustrated in Figs. 2 and 3.

From these figures, we find that the kinetic model is closer to experimental results.

Table 5 Parameters of diffusion models

	β (m.min^{-1}) external mass transfer coefficient	D_w (m^2.min^{-1}) according to Weber and Morris model	D_u (m^2.min^{-1}) according to Urano and Tachikawa model
Bentonite	3.54. 10^{-5}	1.5. 10^{-10}	0.8. 10^{-10}
Treated biomass	1.2. 10^{-4}	7.12. 10^{-12}	3.43. 10^{-12}

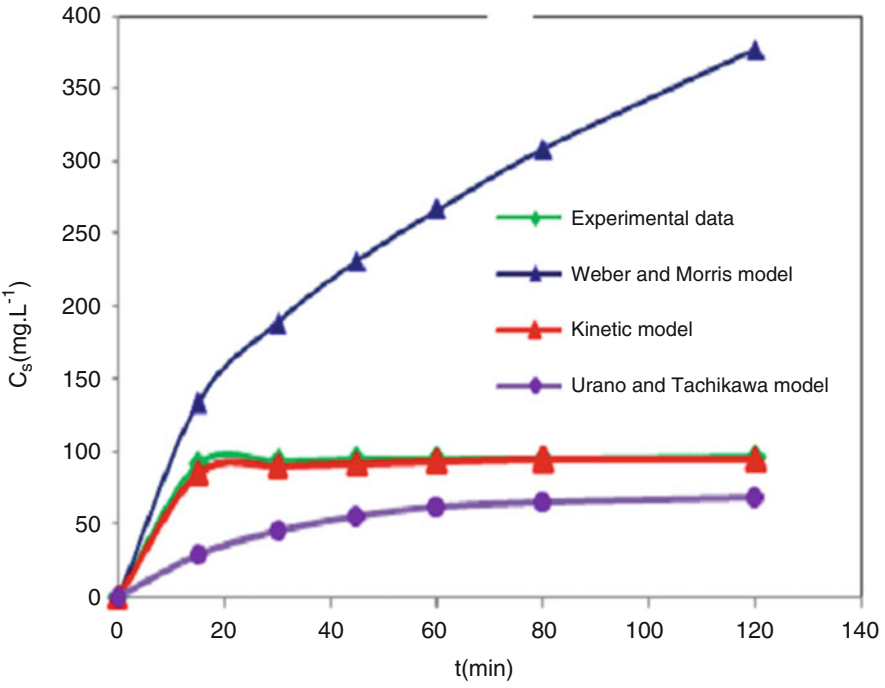

Fig. 2 Comparison of the experimental results with the diffusion models (adsorbent: bentonite)

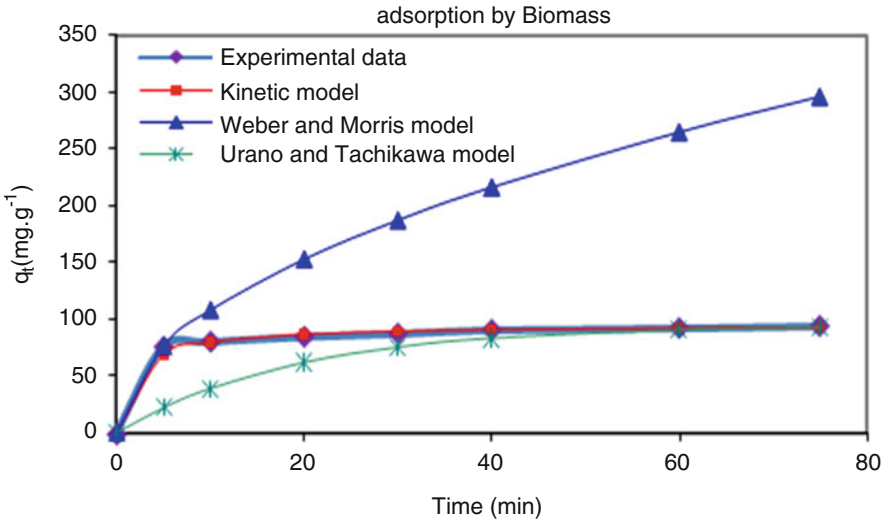

Fig. 3 Comparison of the experimental results with the diffusion models (adsorbent: treated biomass)

Table 6 The parameters for Langmuir and Freundlich isotherms

	Langmuir			Freundlich		
	b	q_m(mg.g^{-1})	R^2	K_f	n_f	R^2
Bentonite	0.45	20	1	46.55	3.62	0.900
Treated biomass	0.08	32.5	0.998	7.84	4.44	0.885

6.3 Adsorption Isotherms

The best estimated values of all the equation parameters are summarized in Table 6.

The adsorption isotherm data well fitted with the linearized Langmuir equation and provided $R^2 = 1$ for bentonite and $R^2 = 0.998$ for biomass.

7 Conclusion

A comparison of two low-cost adsorbents (bentonite and NaOH-treated biomass) showed that NaOH-treated biomass as an adsorbent was more efficient in metal ion removal from solution when compared with bentonite.

These results show that bentonite and biomass can be used effectively for the removal of Ni(II).

Considering the abundance and low price of these adsorbents and their physical and chemical characteristics, they are materials to be efficiently applied in the environmental industry. They can be used in the treatment of mining and/or industrial effluents with metallic contents above the standard values considered by the corresponding legislation.

References

Agouborde, L., Navia, R.: Heavy metals retention capacity of a non-conventional sorbent developed from a mixture of industrial and agricultural wastes. J. Hazard. Mater. **167**, 536–544 (2009)

Ajmal, M., Khan, H., Ahmad, S., Ahmad, A.: Role of sawdust in the removal of copper(II) from industrial wastes. Water Res. **32**, 3085–3091 (1998)

Beauchesne, I., Meunier, N., Drogui, P., Hausler, R., Mercier, G., Blais, J.F.: Electrolytic recovery of lead in used lime leachate rom municipal waste incinerator. J. Hazard. Mater. **120**, 201–211 (2005)

Chen, J.P., Wu, S.: Acid/base-treated activated carbons: characterization of functional groups and metal adsorptive properties. Langmuir. **20**, 2233–2242 (2004)

Han, R., Zhang, J., Zou, W., Xiao, H., Shi, J., Liu, H.: Biosorption of copper(II) and lead(II) from aqueous solution by chaff in a fixed-bed column. J. Hazard. Mater. **B133**, 262–268 (2006)

Ho, Y.S.: Citation review of Lagergren kinetic rate equation on adsorption reaction. Scientometrics. **59**, 171–177 (2004)

Ho, Y.S., McKay, G.: Sorption of dye from aqueous solution by peat. Chem. Eng. J. **70**(2), 115–124 (1998)

Inglezakis, V.J., Loizidou, M.D., Grigoropoulou, H.P.: Ion exchange of Pb^{2+}, Cu^{2+}, Fe^{3+}, and Cr^{3+} on natural clinoptilolite: selectivity determination and influence of acidity on metal uptake. J. Colloid. Interface. Sci. **261**, 49–54 (2003)

Jiang, Y., Pang, H., Liao, B.: Removal of copper (II) ions from aqueous solution by modified bagasse. J. Hazard. Mater. **164**, 1–9 (2009)

Lagergren, S.: Zur theorie der sogenannten adsorption gelöster stoffe. K. Sven. Vetenskapsakad. Handl. **24**(4), 1–39 (1898)

Mathews, A.R., Weber Jr., A.W.J.: Modeling and parameter evaluation for adsorption in slurry reactors. Chem. Eng. Commun. **25**(1–6), 157–171 (1984)

Matlock, M.M., Howerton, B.S., Atwood, D.A.: Irreversible precipitation of mercury and lead. J. Hazard. Mater. **84**, 73–82 (2001)

Molinari, R., Gallo, S., Argurio, P.: Metal ions removal from wastewater or washing water from contaminated soil by ultrafiltration–complexation. Water Res. **38**, 593–600 (2004)

Pehlivan, E., Altun, T.: Ion-exchange of Pb^{2+}, Cu^{2+}, Zn^{2+}, Cd^{2+}, and Ni^{2+} ions from aqueous solution by Lewatit CNP 80. J. Hazard. Mater. **140**, 299–307 (2007)

Quintelas, C., Rocha, Z., Silva, B., Fonseca, B., Figueiredo, H., Tavares, T.: Removal of Cd(II), Cr (VI), Fe(III) and Ni(II) from aqueous solutions by an *E. coli* biofilm supported on kaolin. Chem. Eng. J. **149**, 319–324 (2009)

Sharma, Y.C.: Thermodynamics of removal of cadmium by adsorption on an indigenous clay. Chem. Eng. J. **145**, 64–68 (2008)

Silva, J.E., Paiva, A.P., Soares, D., Labrincha, A., Castro, F.: Solvent extraction applied to the recovery of heavy metals from galvanic sludge. J. Hazard. Mater. **120**, 113–118 (2005)

Urano, K., Tachikawa, H.: Process development for removal and recovery of phosphorus from wastewater by a new adsorbent.2. Adsorption rates and breakthrough curves. Industrial & Engineering Chemistry Research. **30**(8), 1879–1899 (1991)

Van Vliet, B.M., Weber Jr., W.J., Hozumi, H.: Modeling and prediction of specific compound adsorption by activated carbon and synthetic adsorbents. Water Res. **14**(12), 1719–1728 (1980)
Weber, W.J., Morris, J.C.: Removal of biologically resistant pollutants from waste waters by adsorption. In: Advances in Water Pollution Research, pp. 231–266. Pergamon Press, Oxford (1962)

Process Simulation and Energy Consumption Analysis for CO_2 Capture with Different Solvents

Boyang Xue, Yanmei Yu, and Jian Chen

1 Introduction

Carbon dioxide capture and storage (CCS) technology is considered to be the most effective technology to reduce greenhouse gas emissions in the future (Jones and Wigley 1990). The cost of CCS technology applied in fossil fuel power plant is about 40–60 \$/t CO_2 (Fei et al. 2005). And the electricity price will increase by 45% when coupled with CCS (Le Moullec and Kanniche 2011b). Among all the parts of the cost, the CO_2 capture process plays a major role (Fei et al. 2005). Thus, the most crucial problem CCS faces now is that the energy consumption of capture and separation process is tremendous. The absorption with amine solutions is the most reliable and efficient method of CO_2 capture, which is widely applied in fossil fuel power plants at present. Several studies are found in the literature that discuss the two main paths to reduce energy consumption in CO_2 capture process, developing new solvents and optimization of the process configurations (Oyenekan and Rochelle 2007; Aroonwilas and Veawab 2007; Le Moullec and Kanniche 2011a; Cousins et al. 2011).

Many kinds of amine have been studied in CO_2 capture process, such as monoethanolamine (primary amine, MEA), diethanoamine (secondary amine, DEA) (Diab et al. 2013), methyldiethanoamine (tertiary amine, MDEA) (Zhang and Chen 2010) and aminomethylpropanol (sterically hindered primary amine, AMP) (Li et al. 2013), piperazine (heterocyclic amine, PZ) (Li et al. 2014), and so on.

But at present MEA is still considered to be the main solvent in aqueous alkanolamine-based capture processes because of its high absorption rate and low

B. Xue • Y. Yu • J. Chen (✉)
State Key Laboratory of Chemical Engineering, Tsinghua University, Beijing 100084, China
e-mail: cj-dce@tsinghua.edu.cn

© Springer International Publishing AG, part of Springer Nature 2018

F. Aloui, I. Dincer (eds.), *Exergy for A Better Environment and Improved Sustainability 2*, Green Energy and Technology,
https://doi.org/10.1007/978-3-319-62575-1_3

solvent cost, as well as the fact that MEA is easy to regenerate (Aaron and Tsouris 2005).

As the heat of reaction with CO_2 in MEA is quite high (around 85 kJ/mol CO_2), it leads to a high energy requirement for stripping. DEA is also suitable for low-pressure operations and has a lower heat of reaction with CO_2 (around 70 kJ/mol CO_2). Secondary amines, like DEA, are much less reactive to sulfur components and their reaction products are not particularly corrosive. All these factors make DEA an attractive option for CO_2 capture. However, a disadvantage of DEA is that it exhibits slow kinetics (Kohl and Nielsen 1997; Carson et al. 2000; Gabrielsen et al. 2005; Galindo et al. 2012; Warudkar et al. 2013).

Le Moullec et al. (2014) reviewed 20 different process modifications, which are almost exhaustive, for numerous publications so far. However, most studies evaluate process modification for MEA solvent only and the interaction between solvent and process is ignored. Therefore, it is worth investigating the energy consumption of different amine solvents in different process.

As a result, this work proposes a comparative study on CO_2 capture process flow sheet modifications between MEA and DEA to decrease their energy consumptions. Including the conventional capture process, 10 process flow sheet modifications are evaluated at first step, which are inspired by the work of Le Moullec et al. (2014). The simulations are carried out with commercial software to calculate energy consumption for different process flow sheets for a power plant and with a CO_2 compression process. For further study and discussion, a detailed analysis is presented to study the effect of some significant parameters in capture process and the total energy consumptions of each condition are evaluated and compared.

2 Simulation Hypothesis

As many commercial simulation softwares perform well in process simulation such as Aspen Plus, ProMax, PRO/II, CO2SIM, and so on, PRO/II (version 9.0) is selected to be the simulation software in this work due to the simplicity and usability that fulfill the purpose of this study. With the amine packages in PRO/II, results obtained for MEA and DEA are accurate enough for use in final design work, because the parameters have been regressed from a large number of sources for MEA and DEA systems, resulting in good prediction of phase equilibrium. The accuracy of the simulations using PRO/II can also be validated in the following part. In the simulation, the property system uses the amine packages, which were already implemented in PRO/II, and electrolyte algorithm is calculated in both vapor and liquid phases. An equilibrium stage is assumed in absorber and stripper of all the processes. Although equilibrium models are known to give qualitatively different results from rate-based models, equilibrium models are less complex to solve than rate-based models. On the other hand, the reaction rates of amines like MEA and DEA are fast enough when large theoretical stages or packed height were implemented. Kinetics has little effect and the deviations between simulation and

experiment are acceptable. Thus, the first step of approximation to study the optimization strategy in capture process is equilibrium models and proposed methodology will be then extended to rate-based models (Rodriguez et al. 2011).

2.1 Chemical Equilibrium of Amine System

The chemistry of aqueous primary and secondary amines scrubbing CO_2, like MEA and DEA, behave similarly in thermodynamics. In aqueous solutions, CO_2 reacts in an acid–base buffer mechanism with alkanolamines. The acid–base equilibrium reactions in PRO/II are written as chemical dissociations following the approach taken by Kent and Eisenberg (1976):

$$H_2O \leftrightarrow H^+ + OH^- \tag{1}$$

$$CO_2 + H_2O \leftrightarrow HCO_3^- + H^+ \tag{2}$$

$$HCO_3^- \leftrightarrow CO_3^{2-} + H^+ \tag{3}$$

$$REACOO^- + H_2O \leftrightarrow REAH + HCO_3^- \tag{4}$$

$$REAH + H^+ \leftrightarrow REAH_2^+ \tag{5}$$

where R represents an alkyl group, and here REA equals to MEA, DEA. The chemical equilibrium constants for the dissociation reactions are represented by polynomials in temperature as follows:

$$\ln K_i = A + \frac{B}{T} + \frac{C}{T^2} + \frac{D}{T^3} \tag{6}$$

2.2 Conventional CO_2 Capture Process Simulation Validation

A typical CO_2 capture process, shown in Fig. 1, mainly consists of absorber, stripper, and heat exchanger. As the figure shows, the flue gas enters into the bottom of absorber and contacts with the countercurrent lean CO_2 loading solvent flow introduced from the top of the column. After CO_2 absorption, amine solvent becomes a rich CO_2 loading flow, which then exits absorber from the bottom and is pumped to stripper to desorb CO_2. Before being injected into stripper, the cold rich solvent will be preheated by hot, lean solvent exiting from the bottom of stripper. Heated rich solvent enters into stripper to release CO_2 and then becomes lean solvent again. Pure CO_2 flow can be collected from the top of stripper for further processing and the amine solvent is cycled in two columns to capture CO_2 continuously.

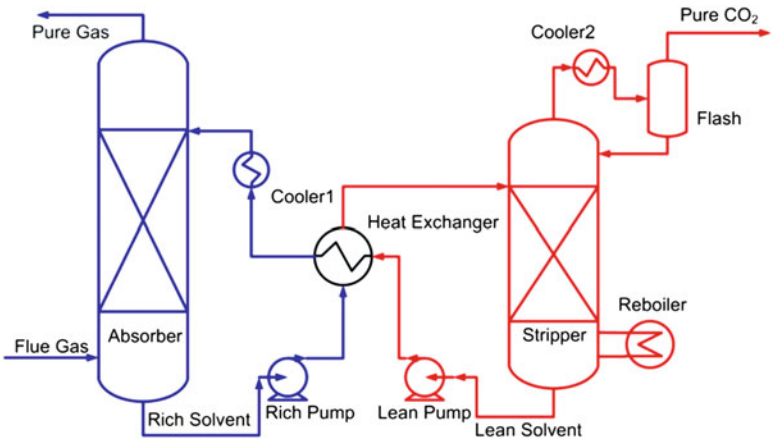

Fig. 1 Conventional CO_2 capture process

The work of Cousins et al. (2012) presented a lot of experimental data on CO_2 capture pilot plant. This work selected the pilot plant data of 1/02/2011, 24/03/2011, 31/03/2011 to validate the simulation process, and the comparison of simulation and experiment is shown in Table 1. As all the parameters were kept the same as in the literature, good agreements on rich loading and reboiler temperature are obtained. Because of the neglect of kinetics, around 10% of deviation on CO_2 capture ratio and reboiler duty is acceptable. These results can validate the accuracy of process simulation to some extent.

In process simulation of this work, the flue gas is made up of 10% CO_2, 6% H_2O, and 84% N_2 in volume, and the flue gas enters at 40 °C, 1.2 bar. As mentioned before, ideal equilibrium stages are used in simulating both absorber and stripper, and the stage number is 10, which is a feasible amount of stages proved in previous work (Warudkar et al. 2013). The operating pressure of absorber is 1 bar, stripper is 1.5 bar, and 0.1 bar pressure drops in the two column. The temperature pinch of heat exchanger is 10 °C. For reference simulation, 30 wt% MEA and 40 wt% DEA aqueous amine are used to capture 90% CO_2 of flue gas, and the CO_2 lean loading is set at 0.25 mol CO_2/mol MEA and 0.1 mol CO_2/mol DEA, which are all at their typical concentrations in various literatures and practice. All of these parameters are kept constant in the simulation of following process modifications in order to make effective comparison in energy consumption and optimization strategy. For further study and discussion in this work, parameter changes will be highlighted individually.

Table 1 Comparison of pilot plant results with the simulation results for MEA

Date	Rich loading (mol CO_2/mol MEA)	$T_{reboiler}$ (GJ/t CO_2)	CO_2 capture (%)	Q_{reb} (GJ/t CO_2)
1/02/2011				
Literature	*0.466*	*116.9*	*75.5*	*4.0*
Pro/ii	*0.477*	*116.1*	*80.1*	*3.6*
24/03/2011				
Literature	*0.486*	*117.1*	*77.7*	*4.2*
Pro/ii	*0.481*	*116.2*	*79.7*	*3.6*
31/03/2011				
Literature	*0.472*	*116.5*	*72.2*	*3.9*
Pro/ii	*0.475*	*115.8*	*75.1*	*3.4*

3 Process Modifications Description

Some studies and reviews of process modification have already been published in open literatures (Oyenekan and Rochelle 2007; Le Moullec and Kanniche 2011a; Cousins et al. 2011; Ahn et al. 2013; Le Moullec et al. 2014), which contain a variety of amine-based capture process modifications for the purpose of energy consumption reduction. Le Moullec et al. (2014) reviewed 20 different process modifications, which are almost exhaustive, for numerous publications so far. However, most studies evaluate process modification for MEA solvent only and the interaction between solvent and process needs to be considered. Therefore, it is worth investigating the energy consumption of different amine solvents in different processes. In this work, nine different process modifications are simulated using MEA and DEA solvent to study the energy consumption, and comparing them with the reference process.

3.1 Intercooled Absorber (ICA)

Intercooled absorber is a widely studied and used modification (Aroonwilas and Veawab 2007; Karimi et al. 2011). Absorption of CO_2 is an exothermic process that will lead to the temperature rise in the absorber. This has a negative effect on thermodynamic driving force for absorption and it results in lowering the solvent absorption capacity. Figure 2 illustrates that this modification is to remove a part or all of the liquid flow from the absorber at one of its stages, cooling it, and then injecting it back at the same part. Intercooled absorber is efficient in control of the temperature in the absorber column, which can increase the carrying capacity of the solvent and hence reduce the required amount of recycling solvent as well as the

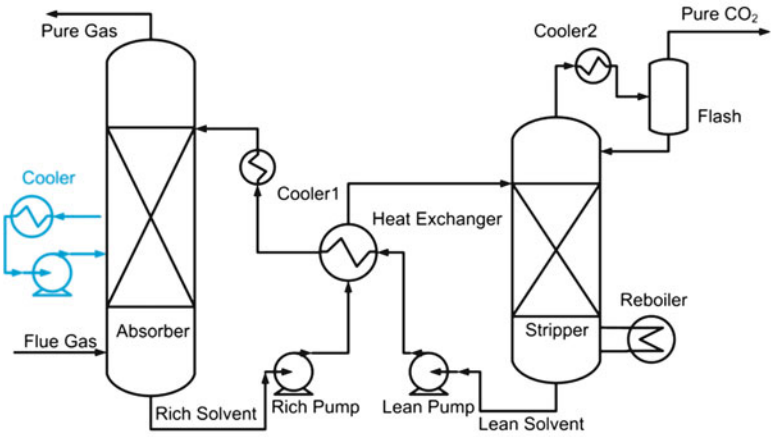

Fig. 2 Intercooled absorber (ICA)

size of equipment. In simulation work, the fifth stageis cooled to the temperature of 45 °C for MEA and DEA. As a result, the rich CO_2 loading reaches 0.492 mol CO_2/mol MEA, which is 0.465 mol CO_2/mol MEA in conventional process. For DEA, 0.468 mol CO_2/mol DEA obtained as only 0.447 mol CO_2/mol DEA in reference. It is found that the recycled lean amine solvent is reduced by 11.5% for MEA and 4.7% for DEA. Thus, 7.1% of reboiler duty is saved by MEA, and DEA gains 2.8%. ICA is more efficient for MEA than DEA because the heat of reaction with CO_2 is higher for MEA. In such favorable process in thermodynamics, MEA gains more benefits by cooling in absorber.

3.2 Flue Gas Precooling (FGP)

Flue gas precooling is a simple modification discussed in the work of Tobiesen et al. (2007) and Le Moullec and Kanniche (2011a). As Fig. 3 shows, flue gas is cooled to a lower temperature before being introduced to absorber. The principle of flue gas precooled is similar to that of the intercooled absorber to some extent, which also lowers the temperature of vapor–liquid mixture in absorber and enhances CO_2 absorption in thermodynamic aspect. Thus, higher rich loading solvent and less reboiler duty are foreseeable. Flue gas is cooled to 30 °C in our simulation, and around 5% reduction in reboiler duty is achieved with MEA, compared with a 2% saving with the DEA case.

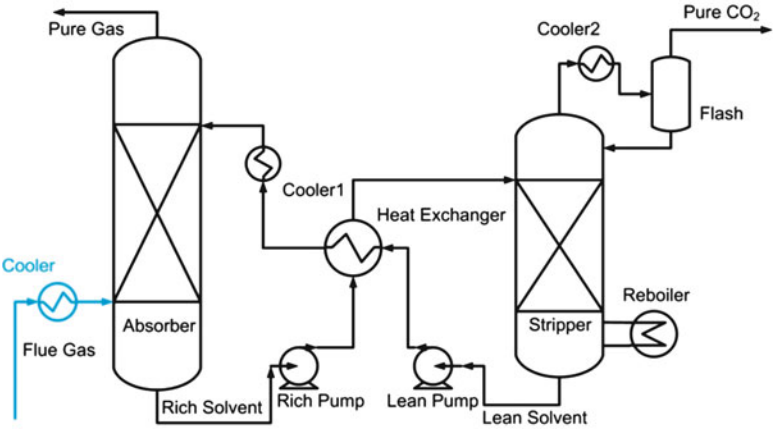

Fig. 3 Flue gas precooling (FGP)

3.3 Rich Solvent Split (RSS)

This process modification was suggested way back by Eisenberg and Johnson (1979). In Fig. 4, it splits the cold rich loaded solvent into two flows, and the split one remains unheated when it enters the top of stripper, while the other one is heated in the lean/rich heat exchanger and it is injected at lower stage. With the rich split modification, the heated rich solvent can reach a higher temperature at which CO_2 can desorb more easily. Meanwhile, the vapor released from the rich solvent meets with the cold solvent injected above, which is able to strip a little CO_2 from it. Thus, there is a reduction in reboiler duty. At first, 10% of the rich solvent unheated is split to the top of stripper in our study. There is a saving in reboiler duty of 7.7% from reference in MEA and 7% in DEA. RSS has neutral effect on rich loading and solvent required as the absorption process remains the same.

In published literatures, rich solvent split often combines with other modifications such as rich solvent preheating and split flow, which is discussed in the following. All these process modification combinations have similar principle and reduce energy consumption in the same way.

3.4 Rich Solvent Pre-heating (RSP)

As Herrin (1989) proposed, the cold rich solvent can be heated by the hot vapor exiting the stripper, as Fig. 5 shows, which can make use of the latent heat and reduce the cooling water required in stripper condenser. It seems to be efficient because the rich solvent can be heated twice. However, due to the temperature of the hot vapor is exactly similar with the rich solvent temperature after heated by hot lean solvent, even a little lower, the heat transfer cannot exist if all rich solvent is

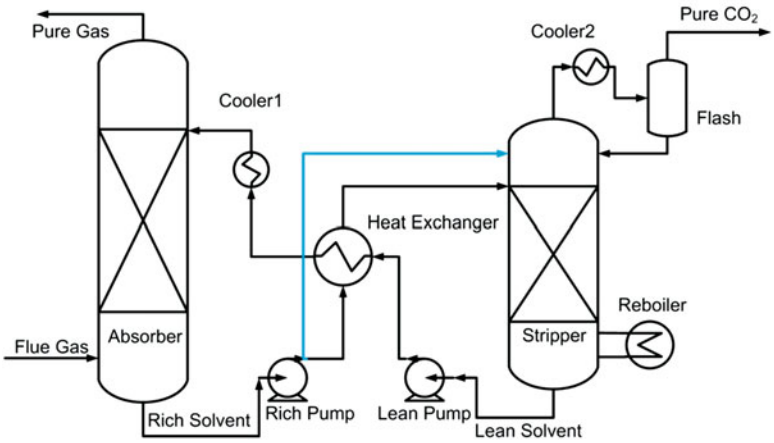

Fig. 4 Rich solvent split (RSS)

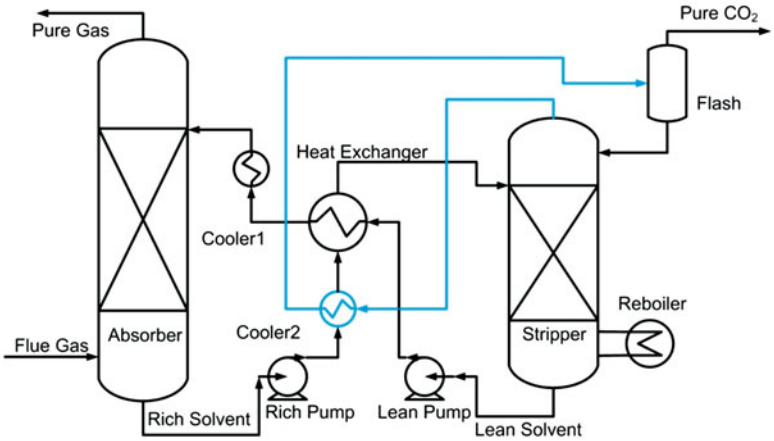

Fig. 5 Rich solvent preheating (RSP)

heated. No energy reduction is obtained in the simulation of MEA or DEA. But obvious benefits are gained if combining rich solvent preheating with rich solvent split (Ahn et al. 2013); contact with a fraction of cold rich solvent can break the heat transfer limit. Then the wasted heat can be used and other principles of energy saving are the same with rich solvent split – no more tautology or simulation here.

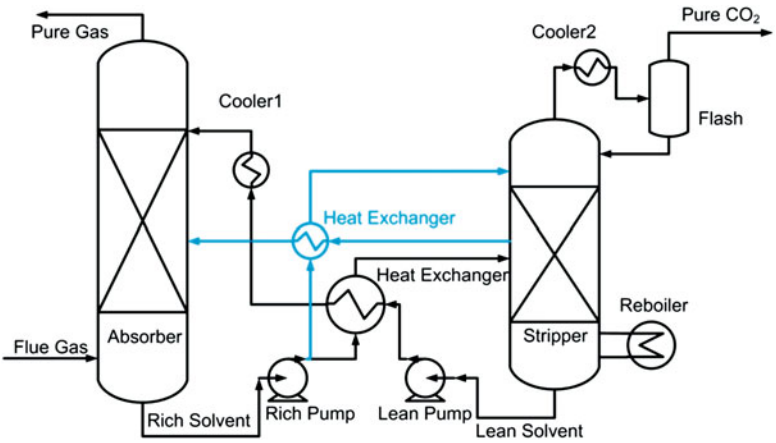

Fig. 6 Solvent split flow (SSF)

3.5 Solvent Split Flow (SSF)

The modification of split flow was first proposed by Shoeld (1934), consisting of a partial regeneration cycle of lean solvent. A flow of semi-lean solvent is taken from the middle of the stripper, having heat exchange with the cold rich solvent and is injected to the middle of absorber. Among all the variants of split flow modifications, the most common one is described by Leites et al. (2003) and Aroonwilas and Veawab (2007), as shown in Fig. 6. It is a combination of two modifications: simple split flow and rich solvent split. Furthermore, as the semi-lean solvent is cooled down before entering absorber, it also takes a little bit advantage of ICA. Many parameters need to be taken into account to reach a minimal energy consumption; for example, the stages to draw off semi-lean solvent from stripper and inject into absorber, the flow rate of cold rich solvent split fraction and semi-lean solvent, and the introduced stage of hot rich solvent. In principle and simulation, the semi-lean stream is drawn off from the middle of stripper to provide the cold rich solvent split with more heat. Since less rich solvent contacts with the hot lean solvent leaving stripper, hot inlet stream reaches higher temperature, and then if it is injected at lower part of stripper, energy saving is further allowed. Optimal energy savings are found in simulation when taking all these factors into account. As a result, simulation shows that SSF can lead to a 7.6% cut in reboiler duty in MEA case, correspondingly 7.8% in DEA case.

It is worth mentioning that the required amount of circulating solvent becomes larger in the solvent split flow modification than in the conventional process because the average solvent working capacity is lowered. Bigger equipments such as columns and pumps are required to match with the flow rate.

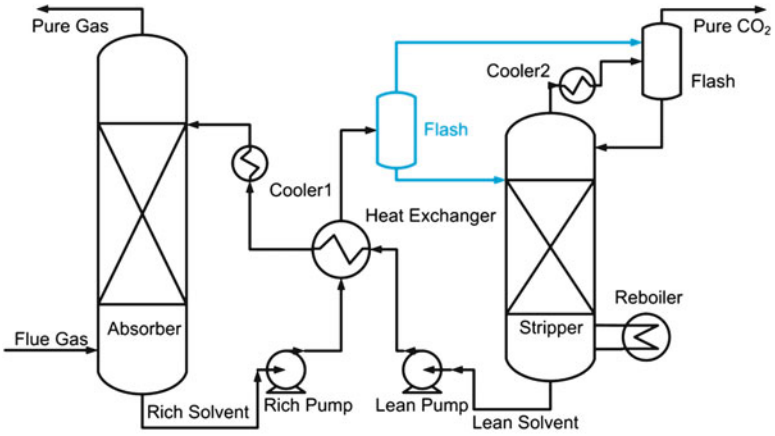

Fig. 7 Rich solvent flashing (RSF)

3.6 Rich Solvent Flashing (RSF)

The principle of the modification of rich solvent flashing is to flash the inlet stream of stripper before entering, as Fig. 7 illustrates. By flashing the hot rich solvent, a little more CO_2 is gained, whereas vaporization lowers the temperature of liquid phase. In fact, this flashing process is just like completing separation process once at an ideal stage, so the phenomenon in which occurs happens in the top stage in stripper. As a result, this modification does not obviously reduce energy consumption except providing one more stripping stage. Simulation result in this work is the same as what Le Moullec and Kanniche (2011a) claimed.

3.7 Stripper Condensate Bypass (SCB)

In the modification of stripper condensate bypass, the condensate liquid is not fed back to the top of stripper. Instead, this stream is directly injected to the absorber. This modification is used in the work of Oexmann and Kaher (2009) as Fig. 8. The simulation of this work provide a 0.6% reboiler duty saving with MEA and 0.4% with DEA, that is, stripper condensate bypass almost makes no difference in limiting energy consumption. Because of the small flow rate of condensate, the duty saving for heating it in stripper is restricted.

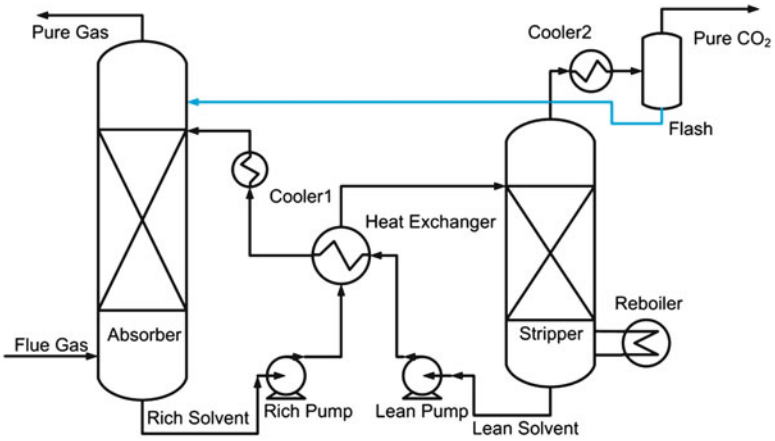

Fig. 8 Stripper condensate bypass (SCB)

3.8 Stripper Condensate Heating (SCH)

The modification of stripper condensate heating is proposed and studied in Aroonwilas and Veawab (2007) and Ahn et al. (2013) as Fig. 9. As vapor temperature in the top of the stripper is high, stripper condensate heating is to make use of this to heat the stripper condensate, and then feeding the hot condensate back to the bottom of stripper to provide a little heat recovery. Nevertheless, it has been proved by theoretical analysis and simulation in this work that there is insignificant gain in energy consumption. Only 1% of reboiler duty is reduced both for MEA and DEA.

3.9 Lean Vapor Compression (LVC)

Lean vapor compression is one of the most widely suggested modifications in a variety of literatures and patents, such as Batteux and Godard (1983), Reddy et al. (2007), and Woodhouse and Rushfeldt (2008). As Fig. 10 shows, the principle is to flash the hot lean solvent at a lower pressure, then compress the hot vapor generated and reinject it into the bottom of stripper. As the vapor benefits from the sensible heat of hot lean solvent as well as recompression, it can reach a very high pressure and temperature, which can provide additional steam and heat in the column for stripping. In the simulation, the hot lean solvent is flashed to the atmospheric pressure and this modification shows significant savings in reboiler duty. With MEA, a 12.8% of reduction is obtained, and as for DEA, LVC allows a gain of 11.9% of reduction in reboiler duty. However, it should be noted that as a compressor is introduced here, it leads to the additional electricity consumption that cannot be neglected. The adiabatic efficiency of the compressor is 80% in

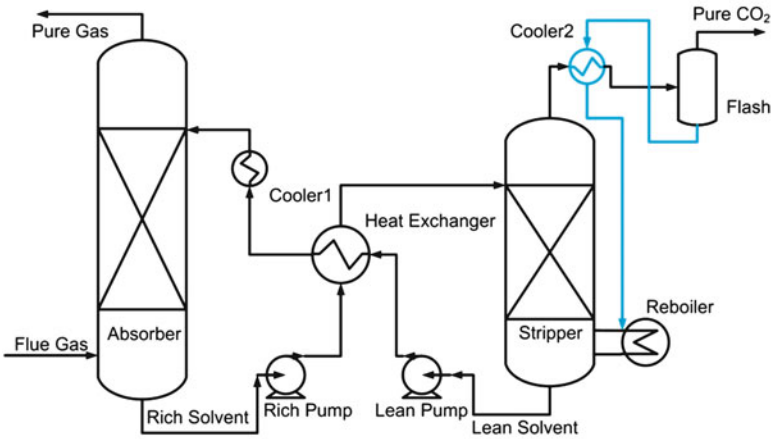

Fig. 9 Stripper condensate heating (SCH)

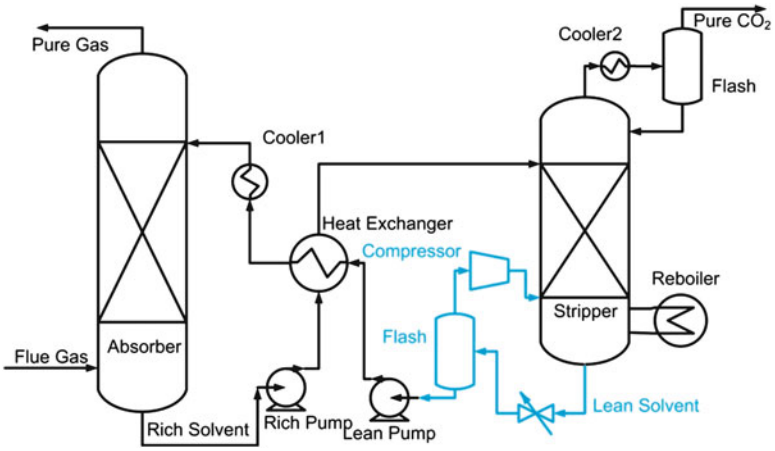

Fig. 10 Lean vapor compression (LVC)

simulation, and the performance of total energy saving compared with the conventional process will be discussed in detain in the following.

4 Results and Discussions

Preliminary simulation results have been presented in the previous part; process modifications description, and detailed simulation results and further discussion will be demonstrated in the following paragraphs, including process operating parameter adjustments, and total energy consumption is calculated for comparison.

4.1 Total Work Calculation

As mentioned before, the process modification of LVC introduces a compressor to generate vapor with high pressure and temperature, and the electricity consumption should not be neglected. Therefore, it is essential to investigate the total energy consumption to make a global comparison with the conventional process.

The equivalent work (W_{eq}) is commonly used to evaluate the process configuration performance to unify the thermal and electrical energy consumptions. As there are a variety of expressions in calculating the total equivalent work, such as Le Moullec and Kanniche (2011a), Ahn et al. (2013), and Van Wagener et al. (2013), we finally calculate the total equivalent work for this work by the following equation from Van Wagener and Rochelle (2011) and Liang et al. (2015):

$$W_{eq} = 0.75 \times Q_{reb}\left(\frac{T_i + 10\text{K} - T_{sink}}{T_i + 10\text{K}}\right) + W_{comp} + W_{add} \tag{7}$$

It uses a Carnot efficiency term that accounts for the increasing value of steam at high temperature. Additionally, 75% efficiency is applied to account for nonideal expansion in the steam turbines. T_i is the reboiler temperature (K); 10 K means the temperature of steam in the reboiler is 10 K higher than T_i; Q_{reb} is the reboiler duty (GJ/t CO_2); T_{sink} is the cold end temperature of Carnot engine, and set at 313 K here; W_{comp} is the compression work (GJ/t CO_2); W_{add} is the additional equipment work such as the compressor in LVC (GJ/t CO_2).

As for calculating the compression work, the simple following correlation can be used:

$$W_{comp} = 8.3673 + 22.216 \ln P_F - (27.118 + 0.0256 P_F) \ln P_S \tag{8}$$

where W_{comp} is the compression work (kWh/t CO_2); P_F is the final delivery pressure, and P_F is set here as 110 bar; P_S is the initial pressure of compression, which equals to the stripper pressure.

The total equivalent work of each of the process modifications described previously is shown in Table 2 for MEA and Table 3 for DEA. All the process modifications apart from RSF and RSP exhibit lower energy consumption for MEA. As for DEA, only RSF has negative effect.

4.2 Effect of Amine Concentration and Lean Solvent Loading

The loading of the lean amine solution is a significant factor in reducing the energy consumption. More solvent is required to be circulated when the lean loading is high in order to capture the same amount of CO_2. The reboiler heat duty is rather sensitive to the solvent flow rate as the vaporization of water for CO_2 stripping

Table 2 Total equivalent work of process using MEA

Modifications	Rich Loading (mol CO_2/mol MEA)	Q_{reb} (GJ/t CO_2)	W_{add} (GJ/t CO_2)	W_{eq} (GJ/t CO_2)	Total Energy Savings (%)
Conventional	*0.465*	*3.460*	*0*	*0.911*	
ICA	*0.492*	*3.216*	*0*	*0.873*	*4.20*
FGP	*0.485*	*3.278*	*0*	*0.883*	*3.17*
RSS	*0.465*	*3.192*	*0*	*0.869*	*4.61*
RSP	*0.465*	*3.461*	*0*	*0.912*	*−0.02*
SSF	*0.463*	*3.196*	*0*	*0.870*	*4.54*
RSF	*0.465*	*3.634*	*0*	*0.939*	*−3.03*
SCB	*0.465*	*3.432*	*0*	*0.908*	*0.38*
SCH	*0.465*	*3.411*	*0*	*0.904*	*0.80*
LVC	*0.465*	*3.018*	*0.039*	*0.876*	*3.87*

Table 3 Total equivalent work of process using MEA

Modifications	Rich Loading (mol CO_2/mol DEA)	Q_{reb} (GJ/t CO_2)	W_{add} (GJ/t CO_2)	W_{eq} (GJ/t CO_2)	Total Energy Savings (%)
Conventional	*0.447*	*3.168*	*0*	*0.856*	
ICA	*0.468*	*3.078*	*0*	*0.842*	*1.64*
FGP	*0.468*	*3.080*	*0*	*0.842*	*1.60*
RSS	*0.447*	*2.945*	*0*	*0.821*	*4.06*
RSP	*0.447*	*3.153*	*0*	*0.854*	*0.27*
SSF	*0.440*	*2.921*	*0*	*0.818*	*4.50*
RSF	*0.447*	*3.302*	*0*	*0.877*	*−2.44*
SCB	*0.447*	*3.131*	*0*	*0.850*	*0.73*
SCH	*0.447*	*3.136*	*0*	*0.851*	*0.58*
LVC	*0.447*	*2.791*	*0.0368*	*0.833*	*2.70*

contributes most to the reboiler duty at low solvent flow rate values. If lean loading is extremely low, more heat is provided by the reboiler duty as the heat of reaction between amines and CO_2 accounts for the majority. As for amine concentration, it will affect the solvent capture capacity because low rich loading will be obtained if a more concentrated solution is used. And the proportion of water increases when diluted solution is implemented. These will all lead to a further reduction of reboiler duty. It can be observed in Figs. 11 and 12 that the optimal lean loading increases with MEA concentration rising. The minimum of reboiler duty occurs at approximately 0.17 mol CO_2/mol MEA in 30 wt% MEA. When DEA was used, it was noticed that irrespective of the concentration used, the optimal lean loading is obtained around 0.05 mol CO_2/mol DEA. It also can be concluded that the reboiler duty is more sensitive to lean loading in process using MEA. And these curves reveal furthermore that at higher amine concentrations, the flexibility of process increases because change in the lean loading will have a minor effect. Galindo et al. (2012) and Dinca (2013) also claimed the same point of view.

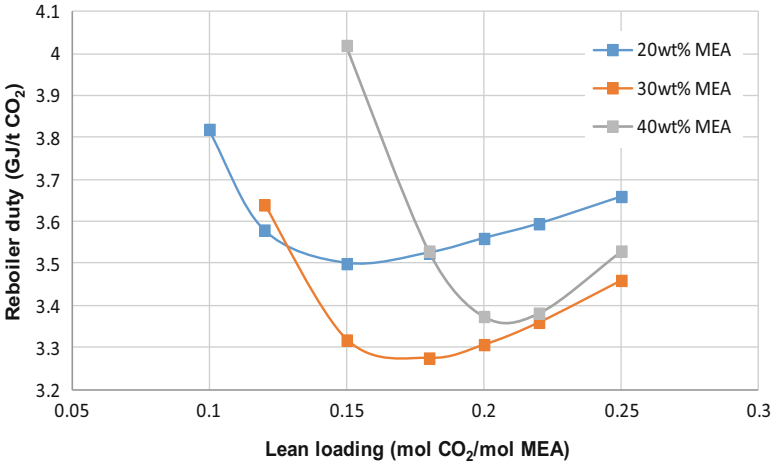

Fig. 11 Effect of MEA concentration and CO_2 loading of lean solvent on reboiler duty

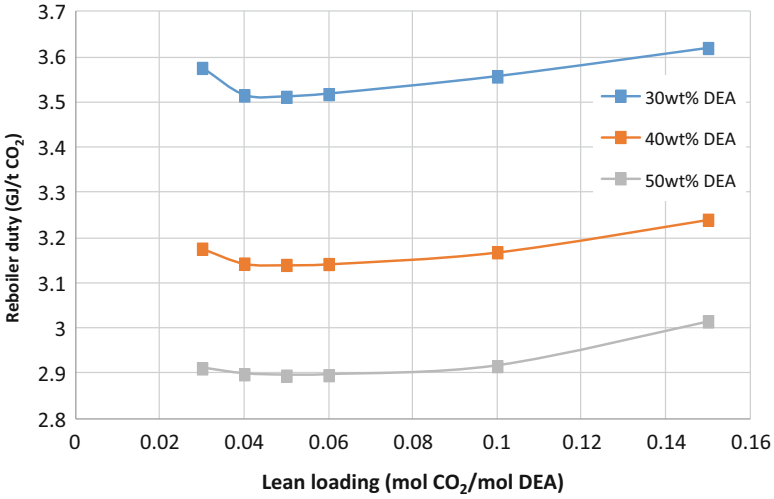

Fig. 12 Effect of DEA concentration and CO_2 loading of lean solvent on reboiler duty

4.3 Effect of CO_2 Concentration in the Flue Gas

The CO_2 content in the flue gas of typical coal-fired power plants lies in the range of 12–15 vol% (wet), and in natural gas combined cycle power plant, the CO_2 concentration will drop to below 5 vol%. It will be of value to explore how CO_2 concentration affects the energy consumption in two different amines. Figure 13

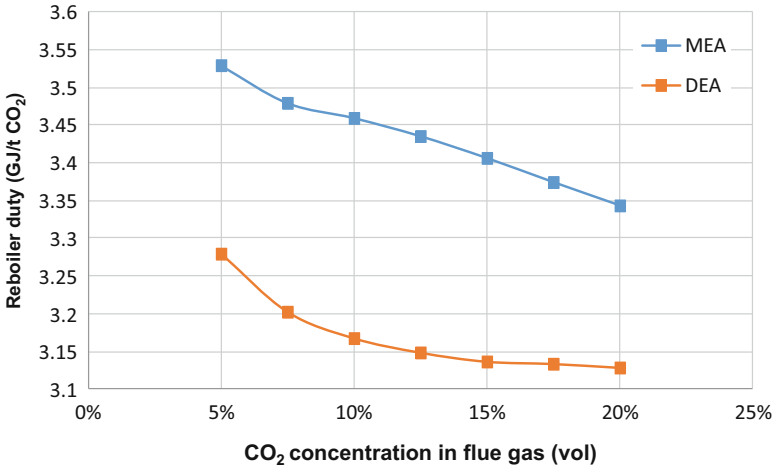

Fig. 13 Effect of CO_2 concentration in the flue gas on reboiler duty

illustrates the simulation results in conventional process when varying CO_2 concentration from 5 to 20 vol%. As expected, the reboiler duty decreases with CO_2 concentration rising up correspondingly both for MEA and DEA. A noticeable change in reboiler duty is observed when using MEA. In contrast, there is no significant difference for DEA when CO_2 is more than 10 vol%. These results are caused by the difference from the heat of reaction.

4.4 Effect of Stripper Pressure

It is a common view that the operating pressure of the stripper is a key parameter of reboiler duty reduction, which has been reported in many publications such as Oyenekan and Rochelle (2007). There is also a process modification proposed by Oyenekan and Rochelle (2006) and Le Moullec and Kanniche (2011a), which is to operate the stripper at vacuum/subambient pressure. CO_2 desorption becomes easier as stripper pressure is high. From another perspective, if stripper pressure is lower, lower pressure steam is required for solvent regeneration because the reboiler temperature goes down. Therefore, the influence of stripper pressure should be evaluated in total equivalent work to search for the optimal strategy. Figure 14 illustrates the results of simulation for conventional process, and it indicates that both for MEA and DEA, higher pressure is beneficial to reducing total energy consumption.

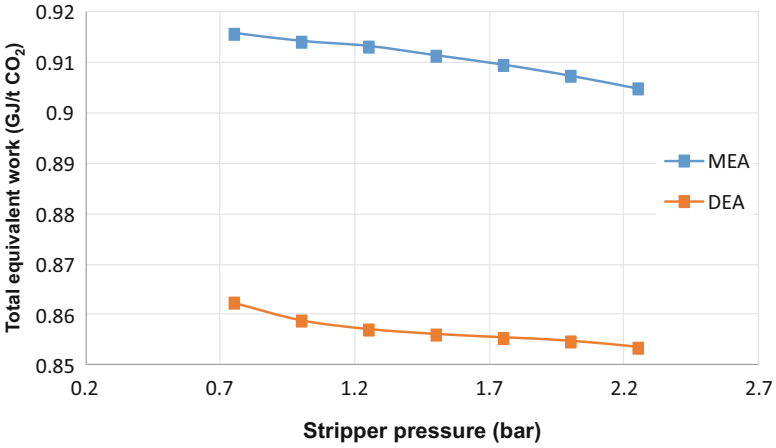

Fig. 14 Effect of stripper pressure on total equivalent work in the conventional process

4.5 Effect of Lean Solvent Loading for Process Modifications

As the principle and simulation results mentioned previously, the loading of the lean amine solution is of great significance in the reducing of energy consumption. And the simulation results indicated that the reboiler heat duty is rather sensitive to the lean loading. Thus, it is essential to simulate all the processes to come up with the optimal energy saving strategies. The process modification of ICA, RSS, SCH, LVC, SSF are selected to make comparison with the conventional process according to previous simulation results and discussion, as these configurations present better performance in terms of reducing energy consumption. The result shows in Fig. 15 for MEA and Fig. 16 for DEA. As for MEA, all the total equivalent work of these processes has a minimum point as the lean loading is increasing. In conventional process, ICA, and SCH, the minimums occur at approximately 0.18 mol CO_2/mol MEA, and it rises to 0.22 mol CO_2/mol MEA for RSS and SSF. In contrast, minimum of LVC appears at around 0.16 mol CO_2/mol MEA because the heat provided by compressed vapor is quite effective. At lower lean CO_2 loading, the total equivalent work of RSS, SCH, and SSF is higher than conventional process due to a larger amount of circulating solution. As a whole, the total equivalent works of these configurations for MEA are in the following order: LVC < ICA < RSS < SSF < SCH < conventional process.

On the other hand, the results of processes using DEA appear somewhat different from MEA. The trends of conventional process, SCH, LVC are quite the same, as all of them have a minimum point at the lean CO_2 loading of about 0.15 mol CO_2/mol DEA. ICA raises this point to 0.2 mol CO_2/mol DEA while SSF lowers it to 0.1 mol CO_2/mol DEA. The total equivalent work of RSS has an obvious change as the minimum point occurs at 0.15 mol CO_2/mol DEA. The energy consumption of

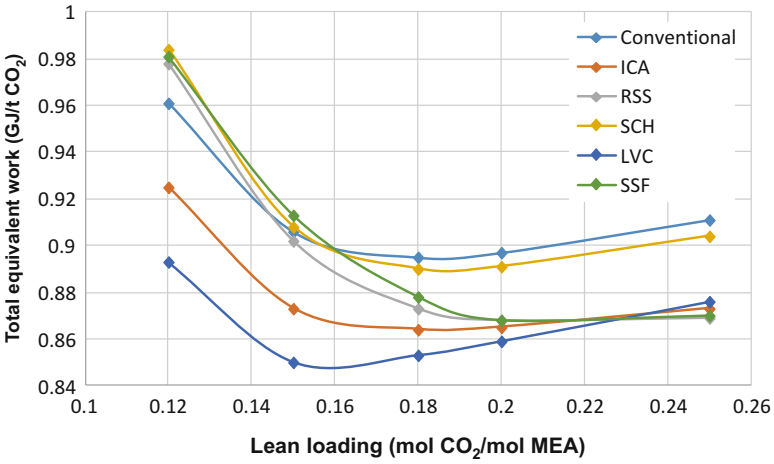

Fig. 15 Compare total equivalent work between different process configurations at different lean loading of MEA

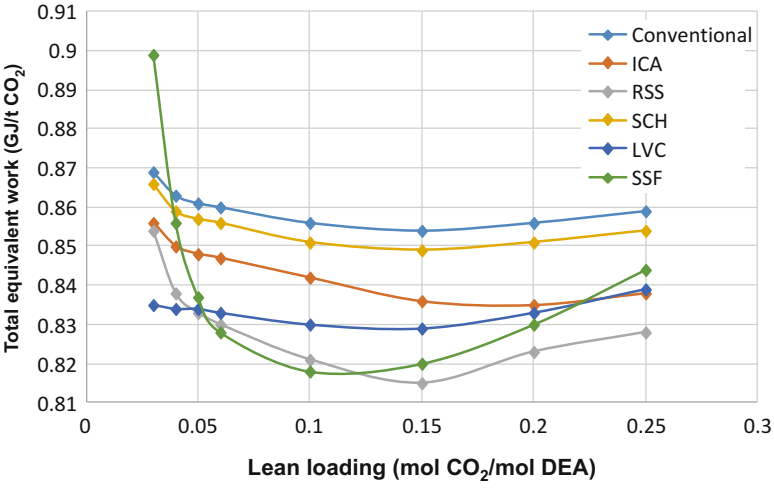

Fig. 16 Compare total equivalent work between different process configurations at different lean loading of DEA

SSF is higher than the conventional process due to lower working capacity of amine and a larger amount of circulating solution. In general, the total equivalent works of these configurations for DEA are in the following order: RSS ~ SSF < LVC < ICA < SCH < conventional process. Compared with MEA, it can be concluded that RSS or the variant of RSS is more efficient than DEA, because CO_2 is easier released from DEA solution in thermodynamics. And ICA is more favorable to MEA, which is also the reason from the difference of absorption heat. LVC gains benefits both for MEA and DEA.

5 Conclusions

In this work, including the conventional process, ten different process configurations have been simulated both for MEA and DEA on the same operating conditions, such as flue gas composition, CO_2 loading of lean amine solution, amine concentration, CO_2 capture ratio, and so on. To make a more valuable and comprehensive evaluation on energy consumption reduction, the performance is presented in terms of the total equivalent work as well as reboiler duty. It is worth mentioning that all simulations are restrained to maintain the temperature of amine solution below 120 °C, to avoid the degradation of MEA and DEA. As a result, process modifications are proved to be an efficient way to optimize the energy consumption in CO_2 capture process using MEA and DEA. It has been shown that ICA, RSS, SSF, LVC are favorable in MEA, as from 3.87% to 4.61% of total equivalent work is reduced, respectively, in preliminary simulation; and for DEA, RSS, SSF, LVC have better performance, as from 2.70% to 4.50% is reduced.

Meanwhile, this work presents the influence of four operating parameters in energy savings, namely, amine concentration, loading of lean amine solvent, CO_2 concentration in the flue gas, and stripper pressure. All these factors vary in both conventional process and process modifications with MEA and DEA. The study of amine concentration and lean loading shows that the optimal lean loading increases with MEA concentration rising, but it basically keeps constant in DEA. Moreover, reboiler duty is more sensitive to lean loading in process using MEA than DEA. When changing the CO_2 concentration in the flue gas, a more significant change in reboiler duty is observed when using MEA and less for DEA when CO_2 is more than 10 vol%. The effect of lean solvent loading on process modifications for MEA and DEA is quite different, and the minimum point of total equivalent work also depends on amine type and process. But, for both MEA and DEA, higher pressure is beneficial to reducing total energy consumption in all of the processes. Approximately, 10% reduction can be obtained in process modifications using MEA and 8% in DEA. LVC has the best performance when implement higher stripper pressure is used, and 9% of reboiler duty reduction is obtained in MEA and 8% in DEA.

The comparative study and evaluation of process modifications between MEA and DEA are proposed in this work, which present the influence of the interaction between solvent and process. It is essential in post-combustion process design to make optimization strategy. Further work will be continued with different solvents, such as MDEA, AMP, PZ, or amine blends in different processes.

Acknowledgments This work was supported by China Natural Science Foundation (key project No.51134017), EU FP7 Marie Curie International Research Staff Exchange Scheme (Ref: PIRSES-GA-2013-612230), and China State Key Laboratory of Chemical Engineering (key project No. SKL-ChE-12Z01).

References

Aaron, D., Tsouris, C.: Separation of CO2 from flue gas: a review. Sep. Sci. Technol. **40**(1-3), 321–348 (2005)

Ahn, H., Luberti, M., Liu, Z., et al.: Process configuration studies of the amine capture process for coal-fired power plants. Int. J. Greenhouse Gas Control. **16**, 29–40 (2013)

Aroonwilas, A., Veawab, A.: Heat recovery gas absorption process. Patent No. WO 2007/107004 A1 (2007)

Batteux, J., Godard, A.: Process and installation for regenerating an absorbent solution containing gaseous compounds. Patent No. US 4384875 A1 (1983)

Carson, J.K., Marsh, K.N., Mather, A.E.: Enthalpy of solution of carbon dioxide in (water + monoethanolamine, or diethanolamine, or N-methyldiethanolamine) and (water + monoethanolamine+ N-methyldiethanolamine) at T = 298.15 K. J. Chem. Thermodyn. **32** (9), 1285–1296 (2000)

Cousins, A., Wardhaugh, L.T., Feron, P.H.M.: Preliminary analysis of process flow sheet modifications for energy efficient CO_2 capture from flue gases using chemical absorption. Chem. Eng. Res. Des. **89**(8), 1237–1251 (2011)

Cousins, A., Cottrell, A., Lawson, A., Huang, S., Feron, P.H.M.: Model verification and evaluation of the rich-split process modification at an Australian-based post combustion CO_2 capture pilot plant. Greenhouse Gas Sci. Technol. **2**, 329–345 (2012)

Diab, F., Provost, E., Laloué, N., et al.: Effect of the incorporation of speciation data in the modeling of CO_2–DEA–H_2O system. Fluid Phase Equilib. **353**, 22–30 (2013)

Dinca, C.: Comparative analyses of primary and secondary amines for CO_2 chemical process capture in a CFBC pilot installation. J. Clean Energ. Technol. **1**(3), 228–233 (2013)

Eisenberg, B., Johnson R.R.: Amine regeneration process. No. US 4152217 (1979)

Fei, W.Y., Ai, N., Chen, J.: Capture and separation of greenhouse gas CO2 - the challenge and opportunity for separation technology. Chem. Ind. Eng. Process. **24**(6), 1–4 (2005) (in Chinese).

Gabrielsen, J., Michelsen, M.L., Stenby, E.H., et al.: A model for estimating CO_2 solubility in aqueous alkanolamines. Ind. Eng. Chem. Res. **44**(9), 3348–3354 (2005)

Galindo, P., Schäffer, A., Brechtel, K., et al.: Experimental research on the performance of CO_2-loaded solutions of MEA and DEA at regeneration conditions. Fuel. **101**, 2–8 (2012)

Herrin, J.P.: Process sequencing for amine regeneration: U.S. Patent 4,798,910 (1989)

Jones, P.D., Wigley, T.M.L.: Global warming trends. Sci. Am. **263**(2), 84–91 (1990)

Karimi, M., Hillestad, M., Svendsen, H.F.: Investigation of intercooling effect in CO_2 capture energy consumption. Energy Procedia. **4**, 1601–1607 (2011)

Kent, R.L., Eisenberg, B.: Better data for amine treating. Hydrocarb. Process. **55**(2), 87–90 (1976)

Kohl, A.L., Nielsen, R.: Gas Purification. Gulf Professional Publishing, Houston (1997)

Le Moullec, Y., Kanniche, M.: Screening of flowsheet modifications for an efficient monoethanolamine (MEA) based post-combustion CO_2 capture. Int. J. Greenhouse Gas Control. **5**(4), 727–740 (2011a)

Le Moullec, Y., Kanniche, M.: Optimization of MEA based post combustion CO_2 capture process: flowsheeting and energetic integration. Energy Procedia. **4**, 1303–1309 (2011b)

Le Moullec, Y., Neveux, T., Al Azki, A., et al.: Process modifications for solvent-based post-combustion CO_2 capture. Int. J. Greenhouse Gas Control. **31**, 96–112 (2014)

Leites, I.L., Sama, D.A., Lior, N.: The theory and practice of energy saving in the chemical industry: some methods for reducing thermodynamic irreversibility in chemical technology processes. Energy. **28**(1), 55–97 (2003)

Li, H., Li, L., Nguyen, T., et al.: Characterization of piperazine /2-aminomethylpropanol for carbon dioxide capture. Energy Procedia. **37**, 340–352 (2013)

Li, H., Frailie, P.T., Rochelle, G.T., et al.: Thermodynamic modeling of piperazine /2-aminomethylpropanol /CO2 /water. Chem. Eng. Sci. **117**, 331–341 (2014)

Liang, Z., Gao, H., Rongwong, W., et al.: Comparative studies of stripper overhead vapor integration-based configurations for post-combustion CO_2 capture. Int. J. Greenhouse Gas Control. **34**, 75–84 (2015)

Oexmann, J., Kather, A.: Post-combustion CO_2 capture in coal-fired power plants: comparison of integrated chemical absorption processes with piperazine promoted potassium carbonate and MEA. Energy Procedia. **1**(1), 799–806 (2009)

Oyenekan, B.A., Rochelle, G.T.: Energy performance of stripper configurations for CO_2 capture by aqueous amines. Ind. Eng. Chem. Res. **45**(8), 2457–2464 (2006)

Oyenekan, B.A., Rochelle, G.T.: Alternative stripper configurations for CO_2 capture by aqueous amines. AICHE J. **53**(12), 3144–3154 (2007)

Reddy, S., Gilmartin, J., Francuz, V.: Integrated compressor /stripper configurations and methods. Patent No. WO /2007 /075466. Fluor Technologies Corporation Fluor Technologies Corporation (2007)

Rodríguez, N., Mussati, S., Scenna, N.: Optimization of post-combustion CO_2 process using DEA–MDEA mixtures. Chem. Eng. Res. Des. **89**(9), 1763–1773 (2011)

Shoeld, M.: Purification and separation of gaseous mixtures. Patent No. US 1971798 (1934)

Tobiesen, F.A., Svendsen, H.F., Mejdell, T.: Modeling of blast furnace CO_2 capture using amine absorbents. Ind. Eng. Chem. Res. **46**(23), 7811–7819 (2007)

Van Wagener, D.H., Rochelle, G.T.: Stripper configurations for CO_2 capture by aqueous monoethanolamine. Chem. Eng. Res. Des. **89**(9), 1639–1646 (2011)

Van Wagener, D.H., Rochelle, G.T., Chen, E.: Modeling of pilot stripper results for CO_2 capture by aqueous piperazine. Int. J. Greenhouse Gas Control. **12**, 280–287 (2013)

Warudkar, S.S., Cox, K.R., Wong, M.S., et al.: Influence of stripper operating parameters on the performance of amine absorption systems for post-combustion carbon capture: part I. High pressure strippers. Int. J. Greenhouse Gas Control. **16**, 342–350 (2013)

Woodhouse, S., Rushfeldt, P.: Improved absorbent regeneration. Patent No. WO, 2008, 63079: A2 (2008)

Zhang, Y., Chen, C.C.: Thermodynamic modeling for CO_2 absorption in aqueous MDEA solution with electrolyte NRTL model. Ind. Eng. Chem. Res. **50**(1), 163–175 (2010)

Experimental Investigation of n-Butanol/Diesel Fuel Blends and n-Butanol Fumigation: Evaluation of Engine Performance, Exhaust Emissions, and Heat Release

Zehra Şahin, Orhan Durgun, and Orhan N. Aksu

1 Introduction

In diesel engine, various alternative fuels and fuel additives such as alcohols (Chen et al. 2012a; Goldsworthy 2013), biodiesel (Mohsin et al. 2014), dimethyl ether (Park and Lee 2014), and natural gas (Lounici et al. 2014) can be easily used. Among them, oxygenated fuels have drawn more attentions as they have the capability to dramatically reduce particulate matter emissions, without causing serious penalties on unburned hydrocarbon (HC), NO_x, and engine performance parameters (Chen et al. 2013; Rakopoulos et al. 2014). Also, many oxygenated fuels, such as biodiesel, ethanol, and n-butanol, can be produced from plants. Since plants absorb CO_2 during growth (Tutak 2014), the combustion of those fuels does not lead to additional carbon dioxide emission, and this feature consists one of the key solutions of the global warming gas emissions. Moreover, oxygenated fuels being biologically renewable, using them as alternative fuels or fuel additives, can reduce the dependence on un-renewable fossil fuels (Chen et al. 2012a), support local agricultural industries, and enhance farming incomes (Tutak 2014). Because of these advantages, much effort has been devoted to investigate the effects of

Z. Şahin (✉)
Karadeniz Technical University, Faculty of Engineering, Mechanical Engineering Department, Trabzon, Turkey
e-mail: zsahin@ktu.edu.tr

O. Durgun
Avrasya University, Faculty of Engineering and Architecture, Mechanical Engineering Department, Trabzon, Turkey
e-mail: odurgun@ktu.edu.tr

O.N. Aksu
Karadeniz Technical University, Sürmene Abdullah Kanca High School, Trabzon, Turkey
e-mail: onaksu@ktu.edu.tr

© Springer International Publishing AG, part of Springer Nature 2018

F. Aloui, I. Dincer (eds.), *Exergy for A Better Environment and Improved Sustainability 2*, Green Energy and Technology,
https://doi.org/10.1007/978-3-319-62575-1_4

various oxygenated fuels especially alcohols on the performance and emissions of diesel engines by applying different techniques (Chen et al. 2012a, 2013; Tutak 2014).

Blending and fumigation techniques are the most preferred methods for using different alcohols in diesel engines (Tutak 2014).The first technique is the simplest method and here any suitable alcohol is mixed with diesel fuel. This mixture is used by typical fuel supply system and the engine mainly operates due to diesel principle. However, it is well known that limited amount of alcohol (up to 10% v/v) can be used in the blends because of the miscibility problems of alcohol in diesel fuel. For this reason solubility additives are also required (Tutak 2014; Ferreira et al. 2013). The second technique is various alcohol fumigation methods. In this technique various alcohols are introduced into intake air by using a simple carburetor or a low-pressure injection system. Here, minor modifications are required for intake system.

In the relevant literature, alcohol, especially ethanol and methanol, blends and fumigation applications can be found (Goldsworthy 2013; Tutak 2014; Abu-Qudais et al. 2000; Zhang et al. 2011; Chauhan et al. 2011; Sahin et al. 2015). All those studies revealed promising results for exhaust emissions and engine performance parameters.

From this brief evaluation of literature, it can be said that n-butanol is a very competitive biomass-based renewable fuel, and it has more advantages as automotive fuel compared to methanol and ethanol. The main advantages of n-butanol as engine fuel can be summarized as follows: n-butanol has larger lower heating value, a higher cetane number, lower volatility, larger viscosity, better lubricity, and a higher flashpoint. In addition, butanol can be mixed with diesel fuel without serious phase separation. Owing to these advantages, n-butanol/diesel fuel blend studies began to increase in the recent years (Chen et al. 2012a, 2014; Yao et al. 2010; Dogan 2011; Siwale et al. 2013). Even so, n-butanol fumigation studies are very limited (Chen et al. 2013). For this reason, in the present study, both using of n-butanol/diesel fuel blends and applying of n-butanol fumigation have been investigated experimentally, and the obtained results for two methods are compared to neat diesel fuel (NDF).

2 Experimental System and Test Procedure

2.1 Engine and Experimental Setup

Experiments for NDF, nBDFBs, and nBF were conducted in a DI automotive diesel engine. Main technical specifications of the engine are given in Table 1, and schematic diagram of the test system used was presented in Fig. 1. The test bed was produced by Cussons. Here, loading was done by a water brake and the brake moment was measured electronically.

Table 1 Main technical specifications of the test engine

Engine	Renault K9K 700 turbocharged automotive diesel engine
Displacement	1.461 l
Number of cylinder	4
Bore and stroke	76 & 80.5 mm
Compression ratio	18.25:1
Maximum power	48 kW at 4000 rpm
Maximum torque	160 Nm at 1750 rpm
Connecting rot length Injection system Number of nozzle holes Nozzle hole diameter	130 mm Common rail injection system[a] 5 0.12 mm

[a]High pressures up to 2000 bar

In-cylinder gas pressure was measured by using of an air-cooled quartz pressure sensor (type GH13P, AVL). This sensor has a measuring range of 0–250 bar and linearity of ±0.3% for full-scale output, and it was mounted on the head of the first cylinder of the engine in place of the hot plug. The signal outputs of the pressure sensor were amplified by an electronic indicating system (type P4411, Cussons). TDC signal of the engine which was used for injection timing was also used to determine TDC position. The signals of pressure and crank angle (CA) were synchronized and recorded by a data acquisition system (NI PCI-6221 type, National Instruments). The average in-cylinder pressure profile over 100 complete cycles was used to calculate the rate of heat release.

NO_x emission was measured by using a NO_x gas analyzer (MEXA-720, Horiba). Accuracy of NO_x is within ± 3–5% ppm. Smoke was determined by a smoke opacimeter (MGA-1500, Sun). The readings values are provided as smoke opacity in % Hartridge units and the accuracy of smoke measurement is within 0.1%.

2.2 Operating Conditions

In this study, the effects of nBDFBs and nBF on engine performance, combustion, and exhaust emissions were experimentally studied and compared for two different loads and speeds. Here, experiments were conducted at two different engine speeds of 2000 rpm (i.e., the max-torque condition) and 4000 rpm (i.e., the rated-power condition) for three different low n-butanol ratios (2, 4, and 6%, by vol.). Here, engine loads of 145 and 132 Nm at 2000 rpm and 110 and 96 Nm at 4000 rpm were selected. Tests were firstly carried out for NDF to obtain a database for comparison of the results of three n-butanol ratios. Then, during nBDFB tests, blends of nB2 (e.g., nB2 contains 2% n-butanol and 98% diesel fuel in volume basis), nB4, and nB6 were prepared and used in the tests under the same conditions.

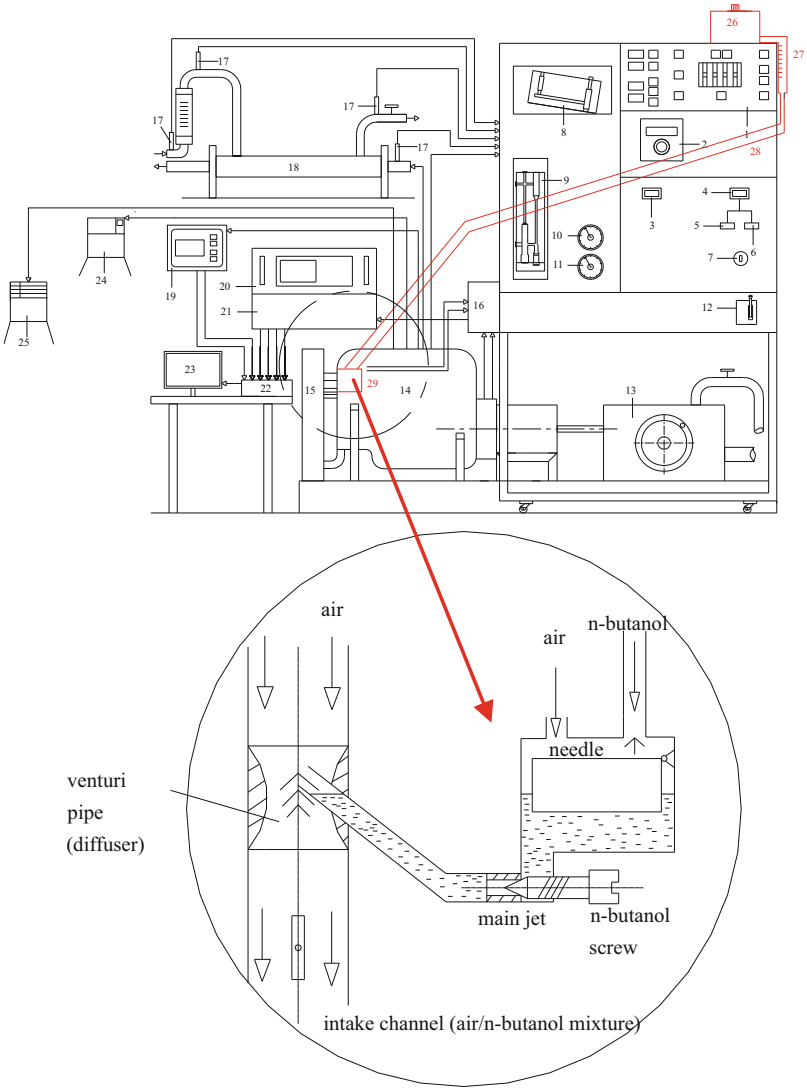

Fig. 1 Schematic view of the test system. (*1*) Fuel measurement unit; (*2*) digital display for temperatures; (*3*) speed; (*4*) force; (*5*, *6*) loading unit; (*7*) start switch; (*8*) inclined manometer; (*9*) coolant flow meter; (*10*) oil temperature; (*11*) inlet manifold pressure; (*12*) gas throttle; (*13*) hydraulic dynamometer; (*14*) engine; (*15*) coaling package; (*16*) inference unit for gas pressure, fuel line pressure, and crank angle pickup sensors; (*17*) thermocouples; (*18*) exhaust gas calorimeter; (*19*) gas analyzer (NO_x analyzer); (*20*) oscilloscope; (*21*) electronic indicating system; (*22*) data acquisition card; (*23*) computer; (*24*) smoke analyzer; (*25*) gas analyzer (HC and CO_2 emissions); (*26*) n-butanol tank; (*27*) scaled glass bulb; (*28*) flexible hose; (*29*) carburetor

After completed n-butanol blend experiments, n-butanol fumigation tests were performed. In the fumigation method, n-butanol was introduced into intake air by using a simple carburetor. This carburetor was mounted on the inlet manifold, and gas and air throttles and the other auxiliary equipment of the carburetor are dismantled, and orifice diameter is chosen sufficiently large. By this way, it was aimed to eliminate probable effects of carburetor orifice restriction on the intake air flow and volumetric efficiency. As usual, air inlet was connected to the air consumption measuring box by a flexible hose. On the other hand, n-butanol flow rate is controlled by a fine threaded adjustment screw which can change the carburetor main fuel jet section. Technical view of this adapted carburetor was presented in Fig. 1. Here, for fumigation tests, to obtain three different n-butanol ratios of ~2 (nBF2), 4 (nBF4), and 6 (nBF6)%, by vol., carburetor main jet opening was adjusted at three different positions.

At the beginning of the experiments, the engine was run for approximately 30 min, and at the end by reaching its steady-state conditions, cooling water temperature becomes 70 ± 5 °C. For example, at 2000 rpm for NDF tests, firstly the load of the engine was adjusted as 145 Nm (506 N loading force). Then, tests were performed for loading moments 145 and 132 Nm. Here, constant 2000 rpm speed is retained by adjusting fuel delivery rate suitable. Thus, tests for NDF at 2000 rpm were carried out at two different engine loads. Similar experiments were repeated at engine speeds of 4000 rpms for NDF. After completing of the NDF tests, nBDFB tests have been carried out. Here, nBDFBs have been prepared just the before beginning of blend experiments to obtain as possible as homogeneous mixtures for tests. However, it was observed that n-butanol blended easily with reference diesel fuel and any homogeneity problem did not occur for selected fuel blends. Then, firstly tests for nB2 have been performed under two different loads at 2000 and 4000 rpm. Similar tests have been performed for nB4 and nB6 blends.

In the fumigation tests, the adapted carburetor was mounted on to intake manifold of the engine. Also, as shown in Fig. 1, a small n-butanol tank, a scaled glass bulb, and suitable pipe connections were added to intake system for injecting and measuring n-butanol flow rate. Any other modification on the engine and experimental system was not done and the engine mainly operates due to diesel principle. At 2000 rpm, firstly the load of the engine was adjusted as 149 Nm. Then, carburetor main jet opening was adjusted to the first opening and it was fixed. This opening gives approximately 2% n-butanol ratio. Thus, tests for nBF2% at 2000 rpm were carried out at 145 and 132 Nm engine loads. The engine speed retains at 2000 rpm by adjusting suitable fuel delivery rate. After that, carburetor main jet opening was adjusted to the second opening, and it was again retained fixed at the same 2000 rpm engine speed. This opening gives approximately nBF4 and tests for this n-butanol ratio were performed at 145 and 132 Nm engine loads. Similar experiments for nBF6 were carried out. At 4000 rpm, the same test procedure was applied for nBF2, nBF4, and BF6. Actual n-butanol ratios for various carburetor main jet openings were computed by using test measurement values related to fuel consumption.

2.3 Calculation of Engine Characteristics

In this section, the principles of the calculation of engine performance parameters and determination of blended fuel properties for NDF, nBDFB, and nBF are summarized. The details of the calculation process can be found in various references such as Durgun (1990) and Durgun and Ayvaz (1996). Here, fuel consumption of the engine was determined by using a calibrated glass burette, and consumption duration of 100 mL of diesel fuel or n-butanol/diesel fuel mixture was measured. By this way, effective power output, total fuel consumption, brake specific fuel consumption (bsfc), and effective efficiency have been calculated by using the following relations:

$$N_e(\text{kW}) = 0,1013\frac{T_b\omega}{p_0}\sqrt{T_0/293}X_{\text{hum}} \tag{1}$$

$$B[\text{kg/h}] = \frac{\Delta m_f}{\Delta t} = \frac{\Delta V\,\rho_f 3600}{\Delta t 10^6}, \text{nBDFB} \tag{2a}$$

$$B[\text{kg/h}] = \frac{\Delta m_f}{\Delta t} = \frac{(100\,\rho_d + V_{nB}\rho_{nB})3600}{\Delta t 10^6}, \text{nBF} \tag{2b}$$

$$b_e[\text{kg/kWh}] = \frac{B}{N_e}\ ,\eta_e = \frac{3600}{Q_{\text{LHV}}b_e} \tag{3a, b}$$

In Eq. (1), T_b (Nm) is brake torque, ω is angular velocity of the crankshaft, and p_0 (MPa) and T_0 (K) are pressure and temperatures of ambient air, respectively. X_{hum} is the humidity correction factor and it is determined depending on dry and wet thermometer temperatures. In Eqs. (2a) and (3a), ΔV is the volume of consumed fuel, Δt (s) is the duration of consumption of ΔV volume (100 mL) of fuel, ρ_f is the density of diesel fuel or blended fuel, and Q_{LHV} is the lower heating value of diesel fuel or blended fuel. Here, lower heating values of diesel fuel and n-butanol have been calculated by using well-known Mendeleyev formula (Kolchin and Demidov 1984).

In the present study, to see clearly the effects of nBDFBs and nBF on engine performance and exhaust emissions, variation ratios of engine characteristics and exhaust emissions in respect of NDF were calculated. For example, variation ratio of bsfc was computed as follows:

$$\frac{\Delta b_e}{b_e} \times 100[\%] = ((b_{e,bf} - b_{e,d})/b_{e,d})100 \tag{4}$$

where $b_{e,bf}$ and $b_{e,d}$ are bsfc for blended fuel (or fumigated fuel) and diesel fuel, respectively.

2.4 Cost Analysis

Cost analysis has also been done by using the practical relationship, which was proposed originally by Durgun (Durgun 1990; Durgun and Ayvaz 1996).

2.5 Estimation of Heat Release Rate (HRR)

HRR was calculated by applying the method given by Heywood (1988). Here, in the heat release analysis, HRR was computed by using cylinder pressure data, sampled at a resolution of 0.4 crank angle degrees. By applying the first law of thermodynamics, the HRR can be modeled as follows given by Heywood (1988):

$$\frac{\mathrm{d}Q}{\mathrm{d}\theta} = \frac{\gamma}{\gamma - 1} p \frac{\mathrm{d}V}{\mathrm{d}\theta} + \frac{1}{\gamma - 1} V \frac{\mathrm{d}p}{\mathrm{d}\theta} \tag{5}$$

where $\mathrm{d}Q/\mathrm{d}\theta$ is the rate of the heat release (J/deg.), γ is the ratio of specific heats, p is the in-cylinder gas pressure, and V is in-cylinder volume. Here to calculate HRR, it is assumed that the cylinder gas content consists of a homogeneous mixture of air and combustion products. It is further assumed that pressure waves, large temperature gradients, fuel vaporization, and leakage through the piston rings do not occur. Thus, HRR analysis calculations have been performed along the crank angles during the interval of inlet valve closure and exhaust valve opening.

2.6 Error Analysis and Uncertainties

Error analysis was also applied to the measured values and uncertainties were determined by using Kline and McClintock's method (Holman 2001). Here, each value has been measured three times and for this reason Student's t-distribution has been applied to the experimental data. By the evaluation of measured data, the determined uncertainty intervals of torque, effective power, and bsfc values are found at the levels of 0.1–0.5%, 0.04–0.5%, and 0.1–6.5%, respectively. From these results, it can be stated that the probable uncertainties in the measuring of the principle values and in the derived values would not affect significantly the uncertainties of the numerical results.

3 Results and Discussion

3.1 HRR, In-cylinder Pressure and Temperature

The effects of nBDFB and nBF on HRR, in-cylinder pressure, and temperature are evaluated separately in the following paragraph. As can be seen in Figs. 2, 3, and 4, the applied two methods influence combustion and mixing process in different ways, for example, HRR diagram shapes and in-cylinder gas pressure curves are slightly different and systematically changed by n-butanol percentages. For this reason, here the effects of two methods on HHR, in-cylinder pressure, and temperature are presented separately.

n-Butanol/diesel fuel blends: HRR and crank angle for different nBDFB at 2000 and 4000 rpms are given in Figs. 2a and 3a, respectively. As can be seen from Figs. 2a and 3a, the tendencies of HRR variations are fairly similar and follow the same typical characteristics for different nBDFBs and NDFs. It can be also

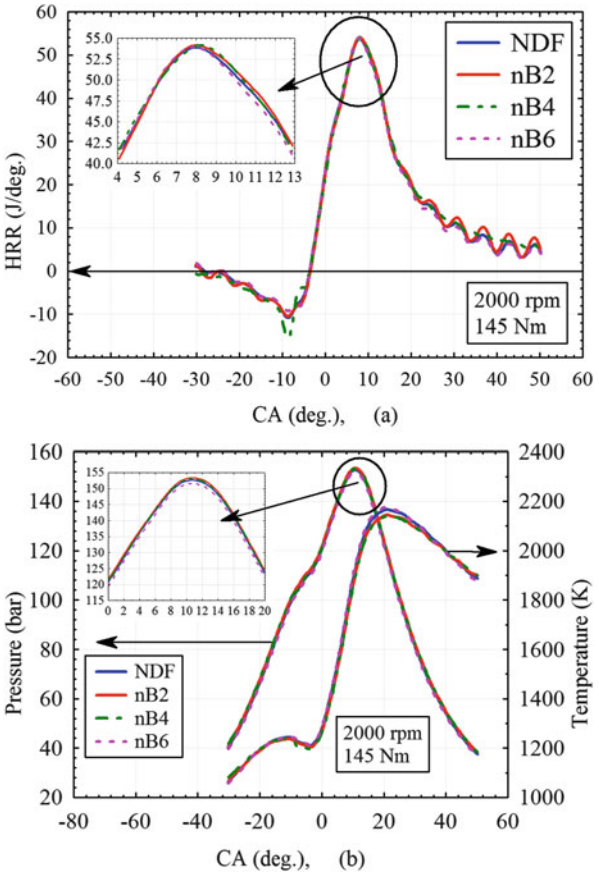

Fig. 2 (**a**, **b**) HRR, in-cylinder pressure and temperature versus CA for NDF and different nBDFBs at 2000 rpm

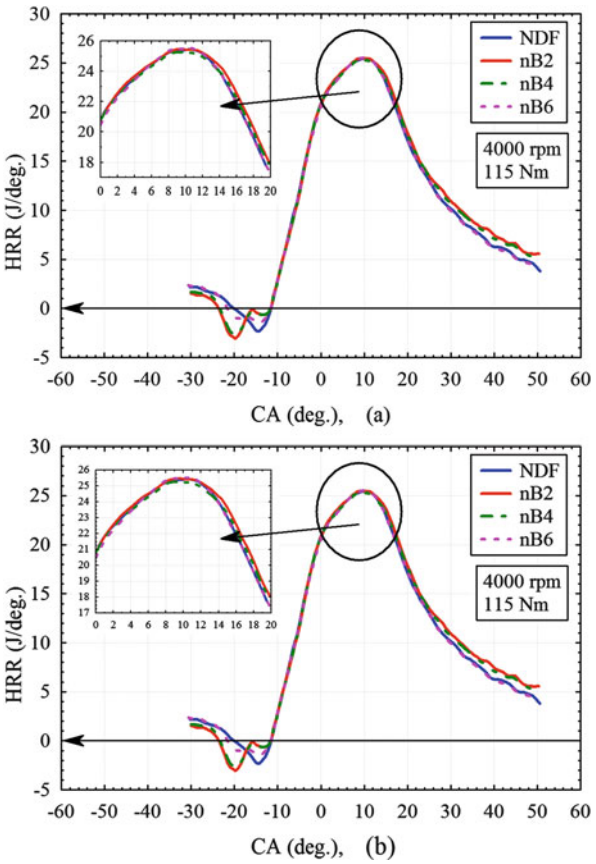

Fig. 3 (**a**, **b**) HRR, in-cylinder pressure and temperature versus CA for NDF and different nBDFBs at 4000 rpm

observed in these figures that the effect of nBDFB on the maximum value of HRR is small. For nB2, HRR values during diffusion-controlled combustion phase and also the maximum value of HRR are slightly higher than that of NDF at 2000 and 4000 rpms. This is also confirmed by the bsfc and effective efficiency trends as will be inspected in Figs. 8a, b and 9a, b. These figures show that effective efficiency increases and bsfc decreases at two engine speeds for nB2. At 2000 rpm, for nB4, the maximum HRR is also higher than that of NDF, but it is lower than that of nB2. For this reason, effective efficiency and bsfc are also improved slightly. At 4000 rpm, for nB4, values of HRR are generally lower than that of NDF and therefore bsfc and effective efficiency are deteriorated. For nB6, it can be seen in Figs. 2a and 3a that the values of HRR are generally lower than that of NDF at these engine speeds; thus, effective efficiency and bsfc worsen.

Figures 2b and 3b represent the variations of in-cylinder pressure versus crank angle for different n-butanol percentages at 2000 and 4000 rpm, respectively. For 2000 rpm, the peak pressure values for nB2 and nB4 are slightly higher than that of NDF. This can be attributed to the higher heat release ratios for nB2 and nB4

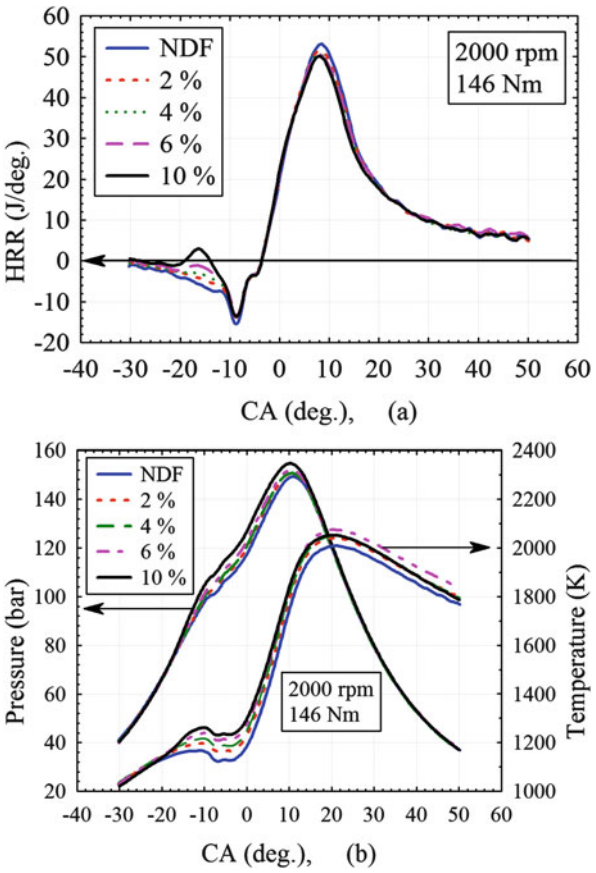

Fig. 4 (**a**, **b**) HRR, in-cylinder pressure and temperature versus CA for NDF and different nBF ratios at 2000 rpm

compared to NDF at that period, revealing some improvement of combustion for these n-butanol ratios. However, the peak pressure values for nB6 are slightly lower than that of NDF. As can be seen in Fig. 2b, for NDF the peak pressure is 152.69 bar and it occurs at 10.59 °CA, while for nB2, nB4, and nB6, the peak pressure values become 153.38, 153.16, and 151.67 bar and they occur at 11.07, 10.75, and 10.52°CA, respectively. For 4000 rpm, similar in-cylinder pressure behavior can also be observed in Fig. 3b. These results indicate that the cylinder peak pressure values exhibit only minor differences in magnitude for different n-butanol ratios. Similar results have also been reported in literature (Chen et al. 2012a, b).

Figures 2b and 3b also display the cylinder mean temperature values for different n-butanol percentages at 2000 and 4000 rpms. It can be seen from these figures that the cylinder mean temperature reduces generally with the addition of n-butanol. Since n-butanol has a higher latent heat of evaporation, a larger amount of heat is required to evaporate the blended fuel. Besides, the lower heating value of n-butanol is smaller than that of NDF. Both of these factors result in a reduction tendency of the cylinder mean temperature (Chen et al. 2012a, b).

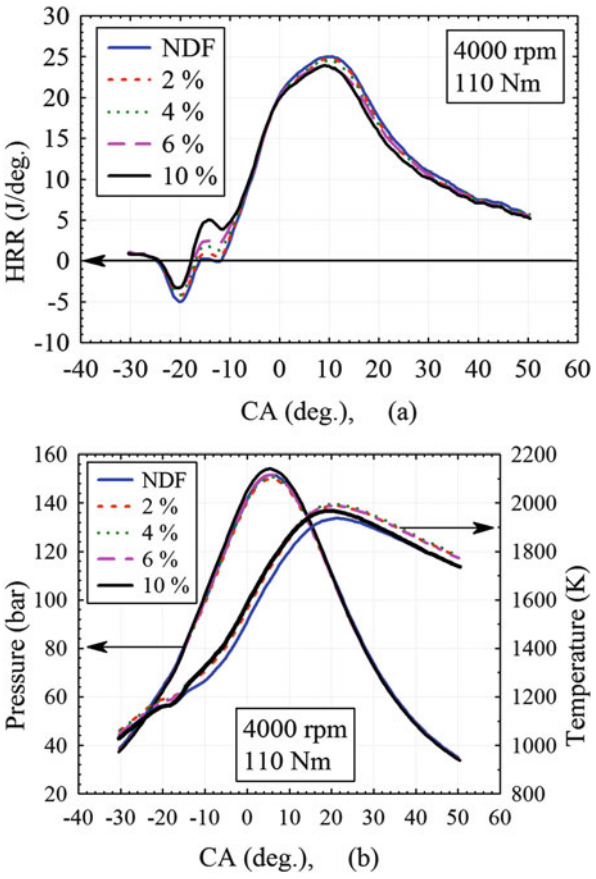

Fig. 5 (**a**, **b**) HRR, in-cylinder pressure and temperature versus CA for NDF and different nBF ratios at 4000 rpm

n-Butanol fumigation: In this study the engine performance parameter and exhaust emission results for nBF10 were not presented. However, HRR, in-cylinder pressure, and temperature variations for this percentage were given to see the flammability and combustion features of n-butanol fumigation. HRR, in-cylinder pressure, and temperature versus crank angle for different nBF ratios at 2000 and 4000 rpms were shown in Figs. 4a, b and 5a, b. As can be seen in these figures, maximum HRR values are lower than that of NDF for all of the selected n-butanol percentages. For nBF, HRR exhibits slightly different pattern compared to NDF and there is a double peak in each of the HRR diagrams. The first peak occurs earlier than the baseline maximum and the second peak occurs later. In addition, this diagram shows that the first peak becomes larger and the second peak diminishes as n-butanol ratio is increased. This feature can also be clearly observed for nBF10. Possible causes of the occurrence of two peaks in the HRR diagram can be explained as follows.

It is thought that prepared n-butanol-air mixture during intake period is ready to burn at the end of the compression stroke, and after a small amount of diesel fuel is

injected, the evaporated n-butanol/diesel fuel and air mixture burn instantaneously when this mixture exceeds lean flammability limit. This instantaneous burning of the n-butanol-air mixture ahead of the diesel fuel jet could lead to local depletion of oxygen, resulting in reducing HRR after the first peak, even though diesel fuel is still being injected. Actually, the instantaneous burning of n-butanol-air mixtures only takes minor role in the HRR, but the burning of these mixtures creates additional gas motions, and this enhances the mixing of diesel fuel, injected after this instant, with air more fastly and homogenously. Improving fuel-air mixing by this additional gas motions means that combustion process would get better and engine performance could be improved and exhaust pollution would be reduced (Goldsworthy 2013; Sahin et al. 2015; Chen et al. 2014).

Figures 4b and 5b indicate that in-cylinder pressure rises with the increase of butanol percentages at 2000 and 4000 rpms. This is a consequence of a higher heat release ratio for nBF compared to NDF at premixed combustion period. As can be seen in Fig. 4b, for NDF the peak pressure is 149.23 bar and it occurs at 11 °CA, while for nBF2, nBF4, nBF6, and nBF10, the peak pressure values are 150.71, 150.67, 151.97, and 154.67 bar and they take place at 10.69, 10.58, 10.37, and 10.13 °CA, respectively. It can be seen in Fig. 4b that the peak pressures occur at the angles of 0.61, 0.42, 0.63, and 0.87 °CA earlier than that of NDF for 2, 4, 6, and 10% n-butanol at 2000 rpm, respectively. It can be said that n-butanol ignites in premixed combustion mode and combustion starts slightly earlier than that of NDF (Chen et al. 2014). These observations are also supported by the apparent HRR variations presented in Fig. 4a. Similar behaviors are also observed at 4000 rpm as can be seen in Fig. 5a, b.

The cylinder mean temperature for NDF and different nBF ratios at 2000 and 4000 rpms are presented in Figs. 4b and 5b. It can be seen in these figures that maximum in-cylinder mean temperature increases with increasing nBF ratios. However, for nBF10 approximately 10 °CA after TDC, values of temperature start to decrease at selected engine speeds. For nBF, the premixed combustion interval tends to enlarge, so to cause higher combustion temperature.

3.2 Smoke

The effect of nBDFBs and nBF on the smoke emission is shown in Fig. 6a, b. Smoke decreases significantly for both n-butanol blending and fumigation and decrement ratios of smoke for fumigation method are higher than that of blending method. Smoke production involves a number of conflicting factors. Generally speaking, enhancing of the premixed combustion would reduce smoke and vice versa (Giakoumis et al. 2013). It can be seen clearly from HRR figures that, in the fumigation method, premixed combustion occurs before TDC and amount of burned fuel increases in the premixed combustion period with increasing n-butanol percentages. Also, additional gas motions occur by the effect of instantaneously burning of butanol-air mixture surrounding diesel fuel spray, and this

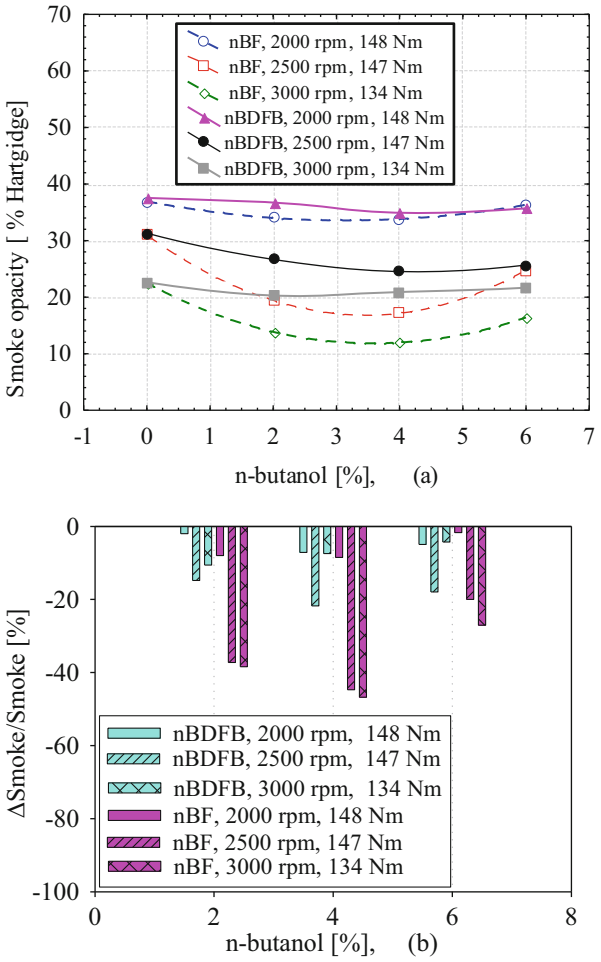

Fig. 6 (**a**, **b**) Variations of smoke and variations of the variation ratios of smoke at different engine speeds for different n-butanol ratios

could improve air utilization and combustion process. Thus, fuel-rich regions could diminish and this results in soot reduction (Yao et al. 2010).

Ignition delay generally increases for n-butanol blending because of lower cetane number of n-butanol. In this case mixing of n-butanol/diesel fuel-air before combustion could be enhanced, and this contributes to the reduction of smoke and NO_x emission simultaneously. But it can be seen in the HRR figures that premixed combustion for nBDFB is considerable smaller than that of n-butanol fumigation. For this reason decrement ratio of smoke is lower than that of fumigation. Also, the volatility of n-butanol is higher than diesel fuel and therefore n-butanol breaks up easier and evaporates more effectively compared to diesel fuel. Thus, the spray penetration length becomes shorter and this could enhance the mixing process, which reduce soot formation for nBDFBs (Yao et al. 2010).

Moreover, diesel fuel has higher tendency to soot formation due to its lower H/C ratio and its combustion process nature. For n-butanol blends and fumigation, the

hydrogen content of the mixture increases and eventually engine smoke formation would reduce and this results in reducing of soot formation (Chen et al. 2012a; Rakopoulos et al. 2014; Sahin et al. 2015). On the other hand, the use of n-butanol provides leaner running of the engine than that of NDF and thus combustion assisted by the presence of the fuel-bound oxygen of the n-butanol even in locally rich zones. This characteristic seems to result in the dominant effect for decreasing smoke (Rakopoulos et al. 2014; Giakoumis et al. 2013).

3.3 NO_x Emission

The variations of NO_x emission and the variation of the variation ratios of NO_x emission for various n-butanol blends and fumigation for two different loads at 2000 and 4000 rpms are given in Fig. 7a, d, respectively. As can be observed in these figures, for n-butanol blends, NO_x emission decreases for nB2, but it increases for nB4 and nB6 at selected engine speeds and loads. It is well known that NO_x emission mainly depends on the combustion temperature and the presence of excess

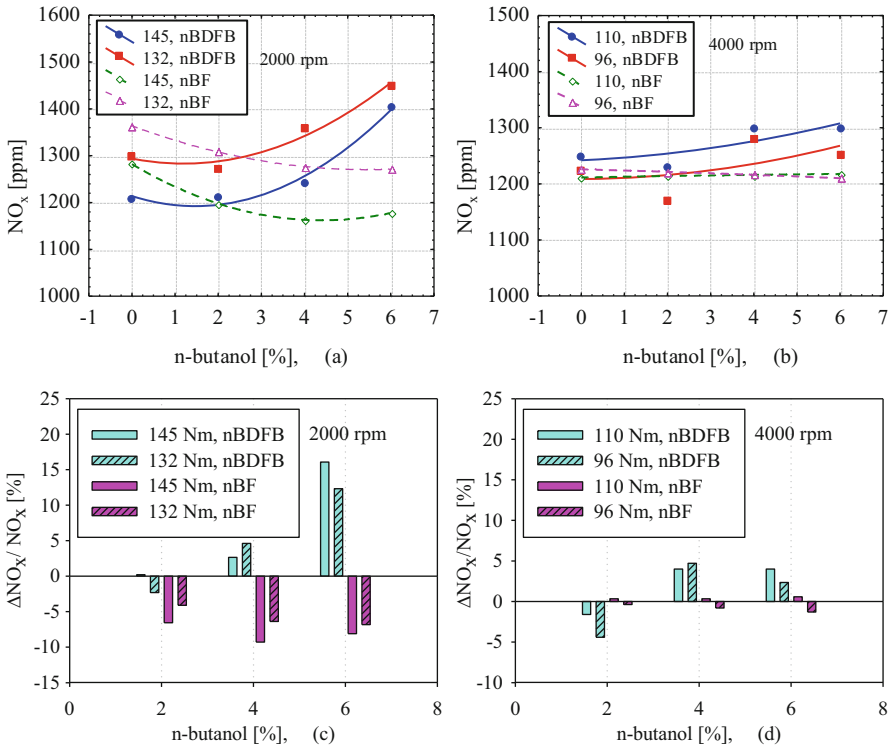

Fig. 7 (**a**, **b**) Variation of NO_x emission, (**c**, **d**) the variation ratios of NO_x emission versus different n-butanol ratios for two different loads at 2000 and 4000 rpms, respectively

oxygen (Heywood 1988). As observed in Figs. 3b and 4b, in-cylinder temperature decreases generally for selected n-butanol percentages. However, excess air coefficient increases for ethanol percentages. As a result, decreasing of the combustion temperatures becomes more dominant than that of increasing of the excess air coefficients and at the end NO_x emission decreases for nB2. However, for nB4 and nB6, increasing of excess air coefficient would become more effective than that of decreasing temperature, which results in the increase of NO_x emission ratio.

For nBF, NO_x emission decreases for selected n-butanol percentages, and decrement ratios of NO_x emission are higher than that of nBDFB at 2000 rpm. At 4000 rpm NO_x emission increases slightly for high load but it decreases at low load. As explained in the above paragraph, instantaneous burning of n-butanol-air mixture surrounding diesel fuel spray would create some additional gas motions, and main diesel fuel injected after this period could mix with air homogenously and fastly. By this way, combustion process could be improved and NO_x formation would decrease. Besides, instantaneous burning of n-butanol-air mixture could lead to depletion of oxygen around the diesel fuel spray. Thus, as the combustion of diesel fuel could occur in the leaner oxygen region, formation of NO_x emission would decrease. In the relevant literature, it has also been stated that NO_x and soot formation in homogeneous charge compression ignition engine is lower than that of conventional diesel engine (Chen et al. 2013). Also, it is well known that combustion process of fumigation method is similar to homogeneous charge compression ignition engine combustion. Thus, both NO_x and smoke emissions decrease in the fumigated engines. Similar results were reported for diesel fuel, methanol, ethanol, and dimethyl ether fumigations in the literature (Chapman and Boehman 2008; Sahin et al. 2015; Tutak 2014; Zhang et al. 2011).

3.4 bsfc and Brake Effective Efficiency

The variation and variation ratios of bsfc and effective efficiency versus n-butanol ratios for blending and fumigation methods at 2000 and 4000 rpms are presented in Figs. 8a–d and 9a–d, respectively. As can be seen in Fig. 9a, c, bsfc slightly decreases for nB2, but it generally increases for nB4 and nB6 at selected engine loads and speeds. As lower heating value of n-butanol is smaller than that of diesel fuel, naturally bsfc takes higher values as n-butanol ratio increases. That is, the engine consumes more fuel to produce the same effective power and consequently bsfc increases. However, in the present study, considerably increments in bsfc have not been observed for nBDFBs. Similar behavior can be observed for brake effective efficiency in Fig. 9b, d.

For nBF, bsfc increases for selected engine loads and speeds. As can be seen in Eq. 2b, in the fumigation method, the amount of diesel fuel has not been changed and n-butanol has been introduced to intake air in the intake channel as additional fuel. As n-butanol is added to diesel fuel, bsfc naturally decreases. Improvement effect of nBF could not result in considerable enhancement in bsfc because

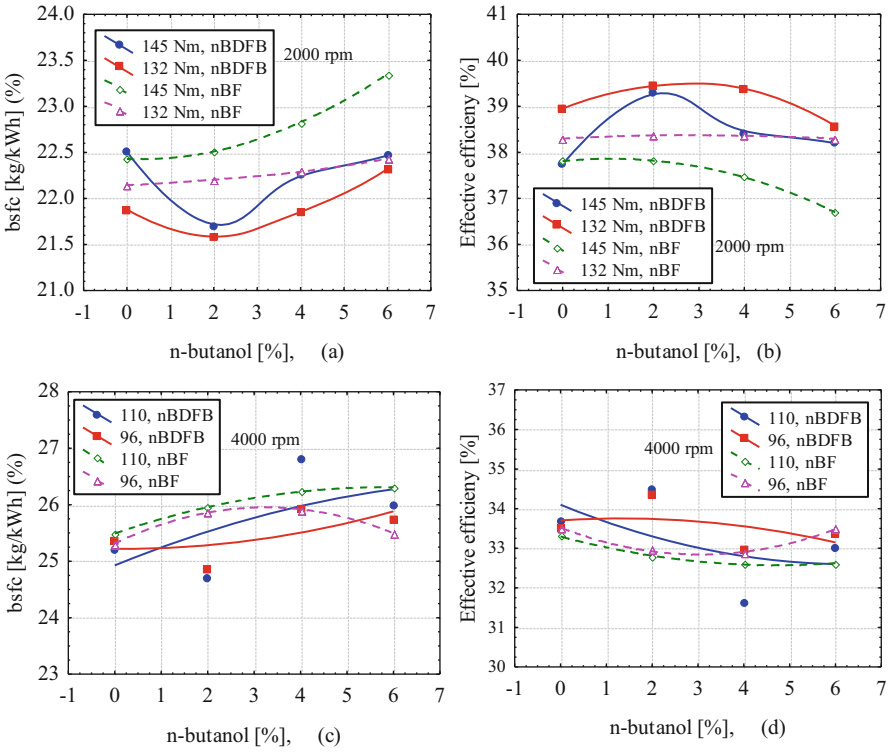

Fig. 8 (**a**–**d**) Variations of bsfc and effective efficiency versus different n-butanol ratios for two different loads at 2000 and 4000 rpms, respectively

n-butanol at small percentages is used and, therefore, bsfc slightly increases for nBF. It can be seen from HRR figures that incomplete combustion occurs for small n-butanol percentages. However, premixed combustion becomes more efficient and the amount of burned fuel is higher for nBF10 than that of lower n-butanol percentages.

3.5 Fuel Economy

Variations of variation ratios of total fuel cost for the nBDFBs and nBF compared to NDF for different loads at 2000 and 4000 rpms were presented in Fig. 10a, b, respectively. As can be seen from these figures, the total cost of fuel takes higher values than that of NDF for nBDFBs and nBF. Total fuel cost becomes higher than that of diesel fuel, because the price of n-butanol is approximately nine times of diesel fuel in Turkey. Also, combined cost of fuel for nBF is higher than that of nBDFBs because of rising bsfc for fumigation method.

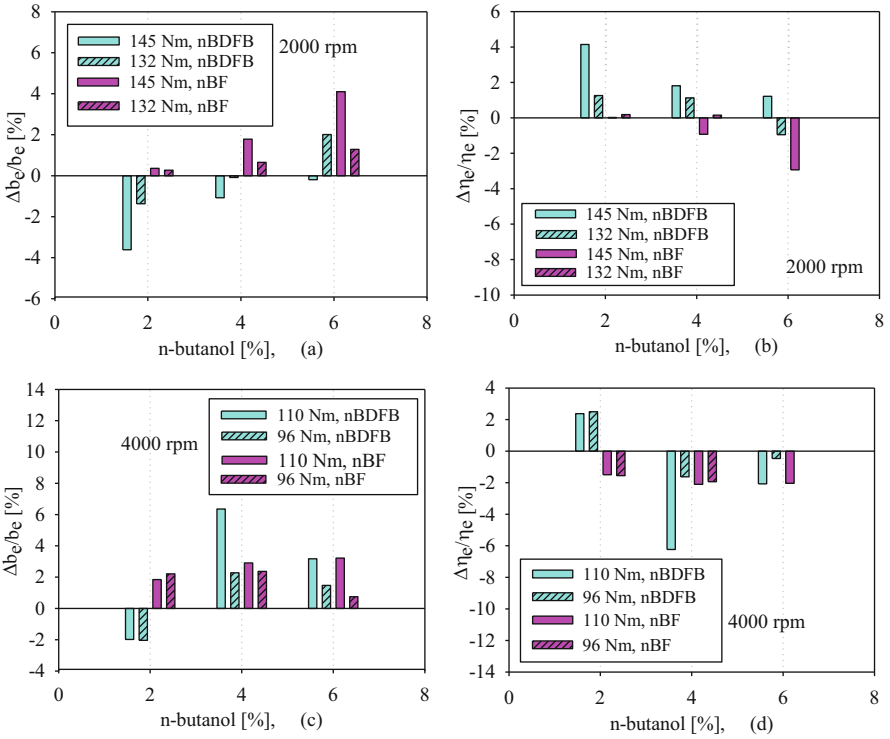

Fig. 9 (**a**–**d**) Variations of the variation ratios of bsfc and effective efficiency versus different n-butanol ratios for two different loads at 2000 and 4000 rpms, respectively

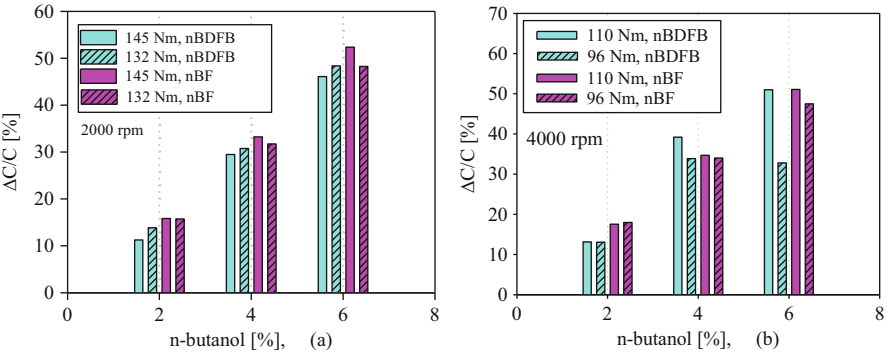

Fig. 10 (**a**, **b**) Variations of the variation ratios of cost versus different n-butanol ratios for two different loads at 2000 and 4000 rpms, respectively

4 Conclusions

From the experimental results and their discussions, the following conclusions could be drawn:

1. n-Butanol/diesel fuel blend and n-butanol fumigation methods reduce significantly smoke. Moreover, improvement effect of n-butanol fumigation on smoke is higher than that of n-butanol/diesel fuel blends.
2. NO_x emission decreases slightly for nB2, but it increases for nB4 and nB6 at selected loads and speeds. For n-butanol fumigation, NO_x emission decreases for all of the operating conditions at 2000 rpm. However, it remains almost unchanged at 4000 rpm. The NO_x reduction effect of n-butanol fumigation is better than n-butanol/diesel fuel blends.
3. For nB2 and nB4, effective efficiency improves; however, it deteriorates for nB6. However, bsfc increases; also, effective efficiency decreases slightly for n-butanol fumigation at selected loads and speeds.
4. Generally improvement effects of n-butanol/diesel fuel blends, especially nB2, on engine performances parameters are slightly better than that of n-butanol fumigation. Being the cost of n-butanol approximately nine times of diesel fuel, both two applications become more expensive.
5. For nBDFBs, heat release rate (HRR) diagrams follow similar typical characteristic of NDF, and the effect of nBDFB on the maximum value of HRR is small. However, for nBF, HRR exhibits slightly a different pattern in respect of NDF and there are double peaks in the HRR diagram. The first peak occurs earlier than that of NDF and the second peak occurs later. In addition, these diagrams show that the first peak becomes larger and the second peak diminishes as n-butanol percentage is increased.
6. As an overall conclusion, it may be affirmed that n-butanol can be used safely in the turbocharged automotive diesel engine used in the experiments by applying blending and fumigation methods. n-Butanol/diesel fuel blends reduce soot formation without any significant effect on performance characteristics and NO_x emission of used engine. However, nBF results for exhaust emissions are better than that of NBDFs. Instead of this, engine characteristic results for 2% n-butanol/diesel fuel blend are more promising than n-butanol fumigation.

References

Abu-Qudais, M., Haddad, O., Qudaisat, M.: The effect of alcohol fumigation on diesel engine performance and emissions. Energy Convers. Manag. **41**, 389–399 (2000)

Chapman, E.M., Boehman, A.L.: Pilot ignited premixed combustion of dimethyl ether in a Turbodiesel engine. Fuel Process. Technol. **89**, 1262–1272 (2008)

Chauhan, B.S., Kumar, N., Pal, S.S., Jun, Y.D.: Experimental studies on fumigation of ethanol in a small capacity diesel engine. Energy. **36**, 1030–1038 (2011)

Chen, G., Yu, W., Li, Q., Huang, Z.: Effects of n-butanol addition on the performance and emissions of a turbocharged common-rail diesel engine, SAE Tech. Papers, 2012-01-0852 (2012a)

Chen, Z., Liu, J., Han, Z., Du, B., Liu, Y., Lee, C.: Study on performance and emissions of a passenger-car diesel engine fueled with butanol diesel blends. Energy. **55,** 638–646 (2012b)
Chen, Z., Liu, J., Wu, Z., Lee, C.: Effects of port fuel injection (PFI) of n-butanol and EGR on combustion and emissions of a direct injection diesel engine. Energy Convers. Manag. **76**, 725–731 (2013)
Chen, Z., Wu, Z., Liu, J., Lee, C.: Combustion and emissions characteristics of high n-butanol/diesel ratio blend in a heavy-duty diesel engine and EGR impact. Energy Convers. Manag. **78**, 787–795 (2014)
Dogan, O.: The influence of n-butanol/diesel fuel blends utilization on a small diesel performance and emissions. Fuel. **90**, 2467–2472 (2011)
Durgun, O.: Experimental methods in engines. Lecturer notes for laboratory. Karadeniz Technical University, Engineering Faculty, Mechanical Eng. Dep., (1990)
Durgun, O., Ayvaz, Y.: The use of diesel fuel–gasoline blends in diesel engines. Proceedings of the First Trabzon International Energy and Environment Symposium, pp. 905–912. Trabzon, Turkey (1996)
Ferreira, V.P., Martins, J., Torres, E.A., Pepe, I.M., De Souza, J.M.S.R.: Performance and emissions analysis of additional ethanol injection on a diesel engine powered with a blend of diesel-biodiesel. Energy Sustain. Dev. **17**, 649–657 (2013)
Giakoumis, E.G., Rakopoulos, C.D., Dimaratos, A.M., Rakopoulos, D.C.: Exhaust emissions with ethanol or n-butanol diesel fuel blends during transient operation: a review. Renew. Sust. Energ. Rev. **17**, 170–190 (2013)
Goldsworthy, L.: Fumigation of a heavy duty common rail marine diesel engine with ethanol–water mixtures. Exp. Thermal Fluid Sci. **47**, 48–59 (2013)
Heywood, J.B.: Internal Combustion Engine Fundamentals. McGraw Hill Press, New York (1988)
Holman, J.P.: Experimental Methods for Engineers. McGraw Hill Press, New York (2001)
Kolchin, A., Demidov, V.: Design of Automotive Engines. Mir Publishers, Moscow (1984)
Lounici, M.S., Loubar, K., Tarabet, L., Balistrou, M., Niculescu, D.C., Tazerout, M.: Towards improvement of natural gas-diesel dual fuel mode: an experimental investigation on performance and exhaust emissions. Energy. **64**, 200–211 (2014)
Mohsin, R., Majid, Z.A., Shihnan, A.H., Nasri, N.S., Sharer, Z.: Effect of biodiesel blends on engine performance and exhaust emission for diesel dual fuel engine. Energy Convers. Manag. **88**, 821–828 (2014)
Park, S.H., Lee, C.S.: Applicability of dimethyl ether (DME) in a compression ignition engine as an alternative fuel. Energy Convers. Manag. **86**, 848–863 (2014)
Rakopoulos, D.C., Rakopoulos, C.D., Giakoumis, E.G., Papagiannakis, R.G., Kyritsis, D.C.: Influence of properties of various common bio-fuels on the combustion and emission characteristics of high-speed DI diesel engine: vegetable oil, bio-diesel, ethanol, n-butanol, diethyl ether. Energy. **73**, 354–366 (2014)
Sahin, Z., Durgun, O., Kurt, M.M.: Experimental investigation of improving diesel combustion and engine performance by ethanol fumigation-heat release and flammability analysis. Energy Convers. Manag. **89**, 175–187 (2015)
Siwale, L., Kristof, L., Adam, T., Bereczky, A., Mbarawa, M., Penninger, A., Kolesnikov, A.: Combustion and emission characteristics of n-butanol/diesel fuel blend in a turbo-charged compression ignition eng. Fuel. **107**, 409–418 (2013)
Tutak, W.: Bioethanol E85 as a fuel for dual fuel diesel engine. Energy Convers. Manag. **86**, 39–48 (2014)
Yao, M., Wang, H., Zheng, Z., Yue, Y.: Experimental study of n-butanol additive and multi-injection on HD diesel engine performance and emissions. Fuel. **89**, 2191–2201 (2010)
Zhang, Z.H., Tsang, K.S., Cheung, C.S., Chan, T.L., Yao, C.D.: Effect of fumigation methanol and ethanol on the gaseous and particulate emissions of a direct-injection diesel engine. Atmos. Environ. **45**, 2001–2008 (2011)

Effects of Temperature and Biodiesel Fraction on Densities of Commercially Available Diesel Fuel and Its Blends with the Highest Methyl Ester Yield Corn Oil Biodiesel Produced by Using NaOH

Atilla Bilgin and Mert Gülüm

1 Introduction

Diesel engines are being extensively utilized in a number of sectors such as road and train transport, agriculture, military, construction, mining, and stationary electricity production in the world (Esteban et al. 2012). They have appealing features including robustness, higher torque, and lower fuel consumption under certain conditions (Esteban et al. 2012). Diesel engines can use many fuels such as light and heavy diesel fuels, straight vegetable oils (SVO), kerosene, gas fuels, short-chain alcohols, and biodiesel (Esteban et al. 2012; Iwasaki et al. 1995). Biodiesel is described as a fuel comprising mono-alkyl esters of long-chain fatty acids (FA) derived from vegetable oils or animal fats (Yuan et al. 2005). It is usually produced through transesterification reaction, either under low-temperature heterogeneous conditions using alkaline, acid, enzyme, or heterogeneous solid catalysts or under high-temperature (usually $> 250\ ^{\circ}C$) homogeneous conditions without using any catalyst (Lin et al. 2014). Biodiesel is receiving increasing attention day by day (Canakci 2007) because of its many great benefits over diesel fuel as following: (1) it is renewable (Yuan et al. 2009), biodegradable (Mejia et al. 2013), and a non-toxic fuel (Ozcanli et al. 2012); (2) it has a higher cetane number than diesel fuel and contains about 10–11% oxygen by mass in the molecular structure, thus improving combustion efficiency and reducing the emission of carbon monoxide (CO), un-burnt hydrocarbons (HCs), and particulate matter (PM) in exhaust emissions (Canakci 2007); (3) it has a higher flash point temperature, making its handling, use, and transport safer than diesel fuel (Gaurav et al. 2013); (4) it

A. Bilgin (✉) • M. Gülüm
Karadeniz Technical University, Faculty of Engineering, Mechanical Engineering Department, Trabzon 61080, Turkey
e-mail: bilgin@ktu.edu.tr

© Springer International Publishing AG, part of Springer Nature 2018

F. Aloui, I. Dincer (eds.), *Exergy for A Better Environment and Improved Sustainability 2*, Green Energy and Technology,
https://doi.org/10.1007/978-3-319-62575-1_5

improves lubricity and reduces premature wearing of fuel pumps (Stalin and Prabhu 2007); (5) the use of biodiesel can help reduce the world's dependence on fossil fuels because biodiesel can be produced by using domestic renewable feedstock (Basha and Gopal 2012); and (6) it can be completely miscible with diesel fuel in any proportion because of the similar chemical structures of these two fuels. Although these properties make it an ideal fuel for diesel engines, it also has some disadvantages such as higher feedstock cost and NO_x exhaust emissions in some cases, inferior storage and oxidative stability, and lower energy content (Rahimi et al. 2014; Sivanathan and Chandran 2014; Moser 2012).

As the use of biodiesel has become more widespread, researchers have shown a strong interest in modeling the combustion process in order to understand the fundamental characteristics of biodiesel combustion (Yuan et al. 2003). They often use the physical properties of biodiesel as input data in their combustion models for the computational softwares (KIVA, Fluent, and AVL Fire). However, it may not be practical at every turn to make measurements of physical properties of biodiesel or biodiesel–diesel fuel blends for each blending ratio or temperature in any study. Regression models as a function of temperature, percentage of blend, and chemical structure have been generally used to calculate these properties without measurements. Some studies reporting these models are summarized as follows. Sivaramakrishnan and Ravikumar (2011) developed an equation depending on kinematic viscosity, density, and flash point temperature for estimating higher heating values (HHV) of methyl esters of various vegetable oils. The equation was able to predict HHV with 0.949 accuracy. Pratas et al. (2011) measured densities of various biodiesels in the temperature range of 273–363 K at atmospheric pressure. Three versions of Kay's mixing rules and two versions of the group contribution method for predicting saturated liquid (GCVOL) models were derived by using experimental data in this study. Tong et al. (2011) presented the relationship between cetane number of pure biodiesel and FAME composition (carbon number of fatty acid chain) by developing a linear regression. According to results, the linear equation showed excellent correlation with $R^2 = 0.9904$ and a maximum average absolute error of 0.49.

The present chapter deals with the investigation of the effects of biodiesel fraction in blend (X) and temperature (T) on densities of the highest methyl ester content corn oil biodiesel (B100) and its blends (B5, B15, B20, and B25) with commercially available diesel fuel (D). Some new one- and two-dimensional models were also derived for predicting the densities of biodiesel–diesel fuel blends, and these models were compared with other equations published in the literature.

Nomenclature

$a, b, c, d \ldots, g$	Regression constants
B5,B10,B15,B20	Biodiesel–diesel fuel blends
B100	Pure corn oil biodiesel
D	Pure diesel fuel
HHV	Higher heating value (kJ/kg)

(continued)

K_{ball}	Coefficient of the viscometer ball (mPa·s·cm^3/g/s)
m_{total}	Mass of the pycnometer filled with biodiesel (g)
R	Correlation coefficient
t	Falling time of the viscometer ball (s)
T	Temperature (°C)
$w_1, w_2, w_3, \ldots, w_n$	Uncertainties of independent variables
$x_1, x_2, x_3, \ldots, x_n$	Independent variables
X	Biodiesel fraction in blend (%)
Greek letters	
μ	Dynamic viscosity (cP ≡ mPa.s)
ν	Kinematic viscosity (cSt ≡ mm^2/s)
ρ	Density (kg/m^3), (g/cm^3)

2 Experimental Methods

2.1 Biodiesel Production

In this study, commercially available refined corn oil was used for biodiesel production. There was no need to perform a pretreatment to the oil because the oil was refined. Methanol (CH_3OH) of 99.8% purity as alcohol and pure-grade sodium hydroxide (NaOH) as a catalyst were used in the transesterification reaction. To produce corn oil biodiesel having the highest methyl ester yield, optimum reaction parameters were 0.90% catalyst concentration (mass of NaOH/mass of corn oil), 50 °C reaction temperature, 60 min reaction time, and 6:1 alcohol/oil molar ratio, as given by Gülüm (2014). The transesterification reaction was carried out in a 1-L flat-bottomed flask, equipped with a magnetic stirrer heater, thermometer, and spiral reflux condenser. Haake falling ball viscometer, Isolab pycnometer, top loading balance with an accuracy of 0.01 g, Haake water bath, and a stopwatch with an accuracy of 0.01 s were used to measure dynamic viscosity and density. Before starting the reaction, the catalyst was dissolved in methanol to make an alcoholic solution of the catalyst in a narrow-neck flask. In the flat-bottomed flask, the alcoholic solution was added to the 200 g of corn oil that was formerly warmed to about 80 °C in a beaker. These reactants were mixed with a stirring speed of 500 rpm using the magnetic stirrer heater. The transesterification reaction was carried out with the spiral reflux condenser for avoiding loss of alcohol. Also, reaction temperature was controlled using a thermometer to remain constant during the reaction. At the end of reaction, the resulting products mixture was transferred to a separating funnel. After a day, two phases formed in the separating funnel. The upper phase consisted of methyl esters (biodiesel), while the lower one consisted of glycerol, excess methanol, and the remaining catalyst together with soap. After separation of the two layers by gravity, the biodiesel phase was washed with warm

distilled water until the water became clear. The washed biodiesel was heated up to about 100 °C to remove methyl alcohol and water residuals.

2.2 Density Measurements

The densities of the produced biodiesel and its blends were determined by means of Eq. (1) and measurements in accordance with ISO 4787 standard:

$$\rho_{\text{blend}} = \frac{m_{\text{total}} - m_{\text{pycnometer}}}{m_{\text{water}}} \rho_{\text{water}} \tag{1}$$

where ρ and m represent density and mass, respectively. In order to minimize measurement errors, all measurements were conducted three times for each sample and the results were averaged. Also, an uncertainty analysis was carried out, depending on the sensitivities of measurement devices.

2.3 Dynamic Viscosity Measurement

The dynamic viscosities were determined in accordance with DIN 53015 standard using Eq. (2) and making measurements by means of the Haake falling ball viscometer, Haake water bath, and stopwatch:

$$\mu_{\text{blends}} = K_{\text{ball}}(\rho_{\text{ball}} - \rho_{\text{blends}})t \tag{2}$$

where μ is dynamic viscosity, K_{ball} is coefficient of the viscometer ball, and t is falling time of the ball moving between two horizontal lines marked on the viscometer tube at limit velocity. K_{ball} and ρ_{ball} are 0.057 mPa·s·cm^3/g/s and 2.2 g/cm^3, respectively.

The kinematic viscosities were determined from Eq. (3) by dividing dynamic viscosity to density at the same temperature:

$$\nu_{\text{blend}} = \frac{\mu_{\text{blend}}}{\rho_{\text{blend}}} \tag{3}$$

In Eq. (3), if $\mu_{\text{biodiesel}}$ and ρ_{biodisel} are in the unit of (cP) and (kg/L), respectively, then $\nu_{\text{biodiesel}}$ is obtained in the unit of cSt.

In this study, dynamic and kinematic viscosities and densities were measured in the Internal Combustion Engines Laboratory in the Mechanical Engineering Department at Karadeniz Technical University. The fatty acid methyl esters of the produced corn oil biodiesel were qualitatively and quantitatively analyzed by gas chromatography using a Hewlett-Packard HP-6890 Series GC system fitting

Table 1 Some fuel properties of diesel fuel, produced biodiesel and their blends, and corresponding standard values for biodiesel

Properties	Unit	D	B5	B10
Viscosity at 40 °C	cSt	2.700	3.154	3.332
Density at 15 °C	kg/m^3	832.62	835.47	838.11
Flash point	°C	63	70	76
HHV	kJ/kg	45950	45632	45359

B15	B20	B100	EN14214	ASTM-D6751
3.658	3.865	4.137	3.50–5.00	1.90–6.00
839.13	842.18	882.07	860–900	[a]
80	88	173	101≤	130≤
45051	44758	39981	[a]	[a]

[a]Not specified

Table 2 Fatty acid methyl ester composition of the produced biodiesel

Fatty acid	Mass, %
Palmitic (C16:0)	15.776
Oleic (C18:1)	47.703
Linoleic (C18:2)	33.415
α-Linolenic acid (C18:3)	1.101
Arachidic (C20:0)	0.805
Gadoleic acid (C20:1)	0.493
Behenic (C22:0)	0.347
Lignoceric (C24:0)	0.359
Average molecular mass	292.561 g/mol[a]
Typical formula	$C_{18.74}H_{35.12}O_2$[a]

[a]Calculated from fatty acid distribution

with a HP-6890 mass selective detector (1909N-133 innowax capillary column of 30 m length, 0.25 mm I.D, and 0.25 μm film thickness) in the Science Research and Application Center at Mustafa Kemal University. The other properties of the pure fuels and fuel blends such as flash point temperature (EN ISO 3679) and higher heating value (DIN 51900-2) were measured at the Prof. Dr. Saadettin GÜNER Fuel Research and Application Center at Karadeniz Technical University. These properties and EN 14214 and ASTM D 6751 standard values are given in Table 1. Also, the fatty acid compositions of the produced corn oil biodiesel and its calculated average molecular mass and typical formulae are given in Table 2.

2.4 Uncertainty Analysis

The results obtained from experimental studies are generally calculated from measured physical quantities. These quantities have some uncertainties due to uncertainties of measuring tools and measurement systems. Therefore, uncertainty

analysis should be applied for proving reliability of the calculated results. In this study, uncertainties of the measured and calculated physical quantities such as dynamic and kinematic viscosities and density values were determined by the method proposed by Holman (2001). According to this method, if the result R is a given function of the independent variables $x_1, x_2, x_3, ..., x_n$ and $w_1, w_2, w_3, \ldots, w_n$ are the uncertainties of each independent variable, then the uncertainty of the result w_R is calculated by using the equation:

$$w_R = \left[\left(\frac{\partial R}{\partial x_1} \cdot w_1 \right)^2 + \left(\frac{\partial R}{\partial x_2} \cdot w_2 \right)^2 + \ldots + \left(\frac{\partial R}{\partial x_n} \cdot w_n \right)^2 \right]^{1/2} \quad (4)$$

According to Eq. (4), the highest uncertainty was determined as 0.0364%. Therefore, it can be said that the results have fairly high reliability.

3 Results and Discussions

3.1 One-Dimensional Linear Models

3.1.1 Effects of Biodiesel Fraction on Density

The variations of densities of fuel blends (B5, B10, B15, and B20) with respect to biodiesel fractions (X) for different temperatures (T) are shown in Fig. 1. In this

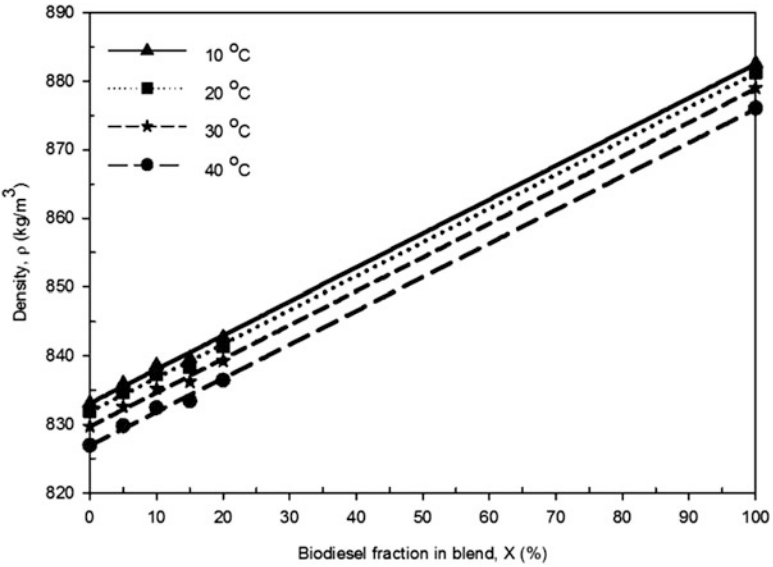

Fig. 1 Changes of density values of fuel blends with respect to biodiesel fraction for various temperatures

figure, the points correspond to measured density values at studied temperatures and biodiesel fractions, while the lines are plots of a curve-fit equation. As well-known, densities increase with increase in biodiesel fraction for a specific temperature, and these are directly proportional to biodiesel content. For these reasons, the linear model, given in Eq. (5), is fitted to the measured data:

$$\rho = \rho(X) = a + bX \tag{5}$$

where ρ is density of the blends in kg/m^3 and a and b are regression constants.

The measured and calculated density values from Eq. (5), error rates between measured and calculated values, regression constants, and correlation coefficients (R) are given in Table 3. The correlation coefficient is a quantitative measure of goodness of fit of the regression equation to the measured data. For a perfect fit, for example, R becomes 1, which means that the equation explains 100% of the

Table 3 The measured densities, calculated densities from Eq. (5), error rates between measured and calculated densities, regression constants, and correlation coefficients for different temperatures

	Measured, ρ(kg/m^3)					
	Blend, X(%)					
Temp. T(°C)	0	5	10	15	20	100
10	833.12	835.97	838.62	839.63	842.69	882.60
20	831.87	834.71	837.36	838.37	841.42	881.28
30	829.74	832.58	835.22	836.23	839.27	879.03
40	826.95	829.78	832.41	833.42	836.45	876.07

Regression constants		
a	b	R
833.1000	0.4941	0.9996
831.8000	0.4934	0.9996
829.7000	0.4922	0.9996
826.9000	0.4905	0.9996

Calculated, ρ(kg/m^3)					
Blend, X(%)					
0	5	10	15	20	100
833.1000	835.5705	838.0410	840.5115	842.9820	882.5100
831.8000	834.2670	836.7340	839.2010	841.6680	881.1400
829.7000	832.1610	834.6220	837.0830	839.5440	878.9200
826.9000	829.3525	831.8050	834.2575	836.7100	875.9500

Relative error rates (%)					
Blend, X(%)					
0	5	10	15	20	100
0.0024	0.0478	0.0690	0.1050	0.0347	0.0102
0.0084	0.0531	0.0748	0.0991	0.0295	0.0159
0.0048	0.0503	0.0716	0.1020	0.0326	0.0125
0.0060	0.0515	0.0727	0.1005	0.0311	0.0137

variability of the measured data (Chapra and Canale 1998). All correlation coefficients and the maximum relative error rate for B15 blend were obtained as 0.9996 and 0.1050%, respectively. These results and Fig. 1 show that the linear model yields the excellent agreement between measured and calculated density values, as expected.

3.1.2 Effects of Temperature on Density

Figure 2 presents the effects of temperature on densities of pure fuels and biodiesel–diesel fuel blends. As shown in the figure, the densities, as expected, decrease with increasing temperature and there are similar trends for all fuels and blends in the studied temperature range. The distributions of densities with temperature were correlated with the following linear and power models:

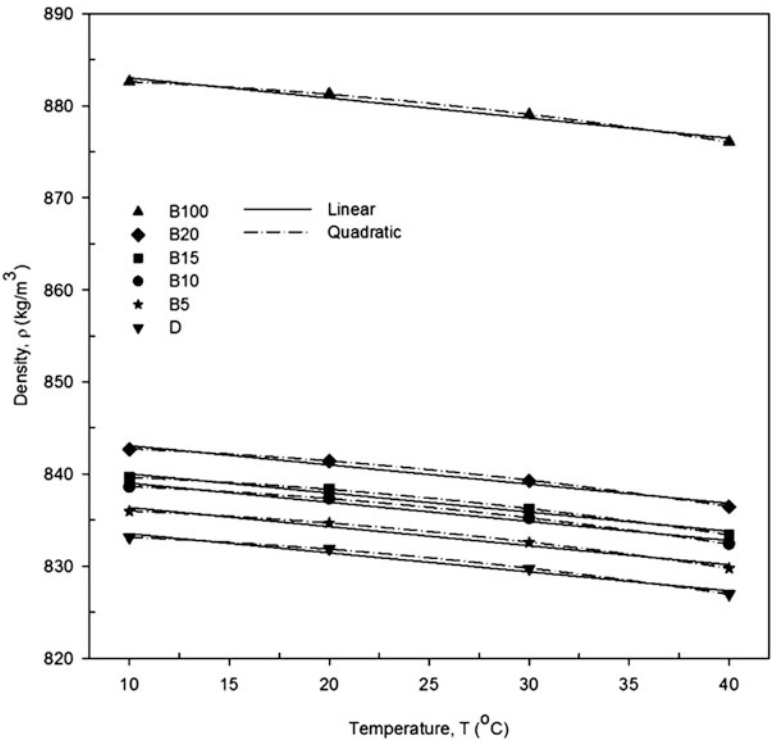

Fig. 2 Variations of density values of pure fuels and fuel blends with respect to temperature for different regression models

The linear model:

$$\rho = \rho(T) = a + bT \tag{6}$$

The power model:

$$\rho = \rho(T) = aT^b + c \tag{7}$$

where T is temperature in $^{\circ}$C and a, b, and c are regression constants.

Tables 4 and 5 list the measured and calculated (from Eqs. (6) and (7)) densities of the blends and pure fuels, error rates between them, regression constants, and correlation coefficients. For linear and power models, the maximum relative error rates were computed as 0.0539% and 0.0002%, respectively. The R values are between 0.9862 and 0.9865 for the linear model, while they all have a value of 0.9999 for the power model. According to these results, the power model as a function of T has higher accuracy in calculating densities of fuels and blends.

3.2 Two-Dimensional Surface Models

In this study, two-dimensional surface models were also improved to make quick estimates of densities for a given X and a specific T simultaneously. As mentioned previously, there was a linear relationship between density and biodiesel fraction, while linear and power models were tried to represent changes of densities with temperature, which may have non-linear characteristics. In the light of this knowledge, the experimental density values were correlated using new two-dimensional surface models represented as following:

The linear surface model:

$$\rho = \rho(T, X) = a + bT + cX \tag{8}$$

The model linear with respect to X and power with respect to T:

$$\rho = \rho(T, X) = aT^b + cX \tag{9}$$

where ρ is density in (kg/m^3) and a, b, and c are regression constants.

Tables 6 and 7 show the regression constants, measured densities, calculated densities from Eqs. (8) and (9), relative error rates between them, and correlation coefficients. The maximum relative error rates and R values from Eqs. (8) and (9) are 0.1506%, 0.1867% and 0.9993, 0.9983, respectively. These results indicate that variations of densities with X and T simultaneously are observed to be well correlated by the linear surface model.

Figures 3 and 4 depict plots of changes of constant density lines for fuel blends as functions of T and X calculated from these models. According to linear surface model by which changes of densities are well correlated, because the change of

Table 4 The measured densities, calculated densities from Eq. (6), error rates between measured and calculated densities, regression constants, and correlation coefficients for different biodiesel fractions

Blend X(%)	Measured, ρ(kg/m^3) Temp., T(°C)			
	10	20	30	40
0	833.12	831.87	829.74	826.95
5	835.97	834.71	832.58	829.78
10	838.62	837.36	835.22	832.41
15	839.63	838.37	836.23	833.42
20	842.69	841.42	839.27	836.45
100	882.60	881.28	879.03	876.07

Regression constants		
a	B	R
835.6000	−0.2064	0.9863
838.4000	−0.2070	0.9864
841.1000	−0.2077	0.9863
842.1000	−0.2077	0.9863
845.2000	−0.2087	0.9865
885.2000	−0.2184	0.9862

Calculated, ρ(kg/m^3) Temp., T(°C)			
10	20	30	40
833.5360	831.4720	829.4080	827.3440
836.3300	834.2600	832.1900	830.1200
839.0230	836.9460	834.8690	832.7920
840.0230	837.9460	835.8690	833.7920
843.1130	841.0260	838.9390	836.8520
883.0160	880.8320	878.6480	876.4640

Relative error rates (%) Temp., T(°C)			
10	20	30	40
0.0499	0.0478	0.0400	0.0476
0.0431	0.0539	0.0468	0.0410
0.0481	0.0494	0.0420	0.0459
0.0468	0.0506	0.0432	0.0446
0.0502	0.0468	0.0394	0.0481
0.0471	0.0508	0.0435	0.0450

density with respect to both temperature and biodiesel fraction is linear, the constant density lines become linear in characteristic and have constant gradients, as shown in Fig. 3. Therefore, if temperature is changed in a unit amount, in order to keep the density of the fuel blend constant, the temperature change should be multiplied by a factor corresponding to the slope of the constant density line, i.e., to change the biodiesel fraction in the blend.

Table 5 The measured densities, calculated densities from Eq. (7), error rates between measured and calculated densities, regression constants, and correlation coefficients for different biodiesel fractions

Blend X(%)	Measured, ρ(kg/m^3) Temp., T(°C) 10	20	30	40
0	833.12	831.87	829.74	826.95
5	835.97	834.71	832.58	829.78
10	838.62	837.36	835.22	832.41
15	839.63	838.37	836.23	833.42
20	842.69	841.42	839.27	836.45
100	882.60	881.28	879.03	876.07

Regression constants			
a (10^{-3})	B	c	R
−5.5610	1.9210	833.6000	0.9999
−5.6270	1.9190	836.4000	0.9999
−5.5860	1.9220	839.1000	0.9999
−5.5860	1.9220	840.1000	0.9999
−5.7140	1.9170	843.2000	0.9999
−5.7370	1.9280	883.1000	0.9999

Calculated, ρ(kg/m^3) Temp., T(°C) 10	20	30	40
833.1364	831.8444	829.7744	826.9517
835.9330	834.6342	832.5552	829.7223
838.6332	837.3312	835.2441	832.3971
839.6332	838.3312	836.2441	833.3971
842.7280	841.4176	839.3222	836.4689
882.6139	881.2504	879.0582	876.0619

Relative error rates (%) Temp., T(°C) 10	20	30	40
0.0020	0.0031	0.0041	0.0002
0.0044	0.0091	0.0030	0.0070
0.0016	0.0034	0.0029	0.0015
0.0004	0.0046	0.0017	0.0027
0.0045	0.0003	0.0062	0.0023
0.0016	0.0034	0.0032	0.0009

Table 6 The measured densities, calculated densities from Eq. (8), error rates between measured and calculated densities, regression constants, and correlation coefficient for different biodiesel fractions and temperatures

Temp. $T(^{\circ}C)$	Blend $X(\%)$	Measured $\rho(kg/m^3)$	Calculated $\rho(kg/m^3)$	Relative error rates (%)
10	0	833.12	833.5070	0.0465
	5	835.97	835.9695	0.0001
	10	838.62	838.4320	0.0224
	15	839.63	840.8945	0.1506
	20	842.69	843.3570	0.0792
	100	882.60	882.7570	0.0178
20	0	831.87	831.4140	0.0548
	5	834.71	833.8765	0.0999
	10	837.36	836.3390	0.1219
	15	838.37	838.8015	0.0515
	20	841.42	841.2640	0.0185
	100	881.28	880.6640	0.0699
30	0	829.74	829.3210	0.0505
	5	832.58	831.7835	0.0957
	10	835.22	834.2460	0.1166
	15	836.23	836.7085	0.0572
	20	839.27	839.1710	0.0118
	100	879.03	878.5710	0.0522
40	0	826.95	827.2280	0.0336
	5	829.78	829.6905	0.0108
	10	832.41	832.1530	0.0309
	15	833.42	834.6155	0.1434
	20	836.45	837.0780	0.0751
	100	876.07	876.4780	0.0466

Regression constants	Correlation coefficient
$a = 835.6000$	$R = 0.9993$
$b = -0.2093$	
$c = 0.4925$	

4 Conclusions

In this chapter, the effects of biodiesel fraction and temperature on the densities of the highest methyl ester content corn oil biodiesel and its blends with commercially available diesel fuel were investigated. One- and two-dimensional regression models were also developed to predict the densities of the pure fuels and blends at different temperatures. The following conclusions can be drawn from this study:

Table 7 The measured densities, calculated densities from Eq. (9), error rates between measured and calculated densities, regression constants, and correlation coefficient for different biodiesel fractions and temperatures

Temp. $T(^{\circ}C)$	Blend $X(\%)$	Measured $\rho(kg/m^3)$	Calculated $\rho(kg/m^3)$	Relative error rates (%)
10	0	833.12	833.8099	0.0828
	5	835.97	836.2724	0.0362
	10	838.62	838.7349	0.0137
	15	839.63	841.1974	0.1867
	20	842.69	843.6599	0.1151
	100	882.60	883.0599	0.0521
20	0	831.87	830.8555	0.1220
	5	834.71	833.3180	0.1668
	10	837.36	835.7805	0.1886
	15	838.37	838.2430	0.0152
	20	841.42	840.7055	0.0849
	100	881.28	880.1055	0.1333
30	0	829.74	829.1321	0.0733
	5	832.58	831.5946	0.1184
	10	835.22	834.0571	0.1392
	15	836.23	836.5196	0.0346
	20	839.27	838.9821	0.0343
	100	879.03	878.3821	0.0737
40	0	826.95	827.9115	0.1163
	5	829.78	830.3740	0.0716
	10	832.41	832.8365	0.0512
	15	833.42	835.2990	0.2255
	20	836.45	837.7615	0.1568
	100	876.07	877.1615	0.1246

Regression constants	Correlation coefficient
$a = 843.7000$	$R = 0.9983$
$b = -0.005121$	
$c = 0.4925$	

- In linear models, the linear and power ones were quite suitable to represent density–biodiesel fraction and density–temperature variations, respectively. Correlation coefficients (R) and maximum relative error rates were determined as 0.9996, 0.1050% and 0.9999, 0.0002% for the linear and power models, respectively.
- Two-dimensional linear surface model with the correlation coefficient of 0.9993 showed the higher degree of accuracy for representing the change in density with temperature and biodiesel fraction in the blend simultaneously. Maximum

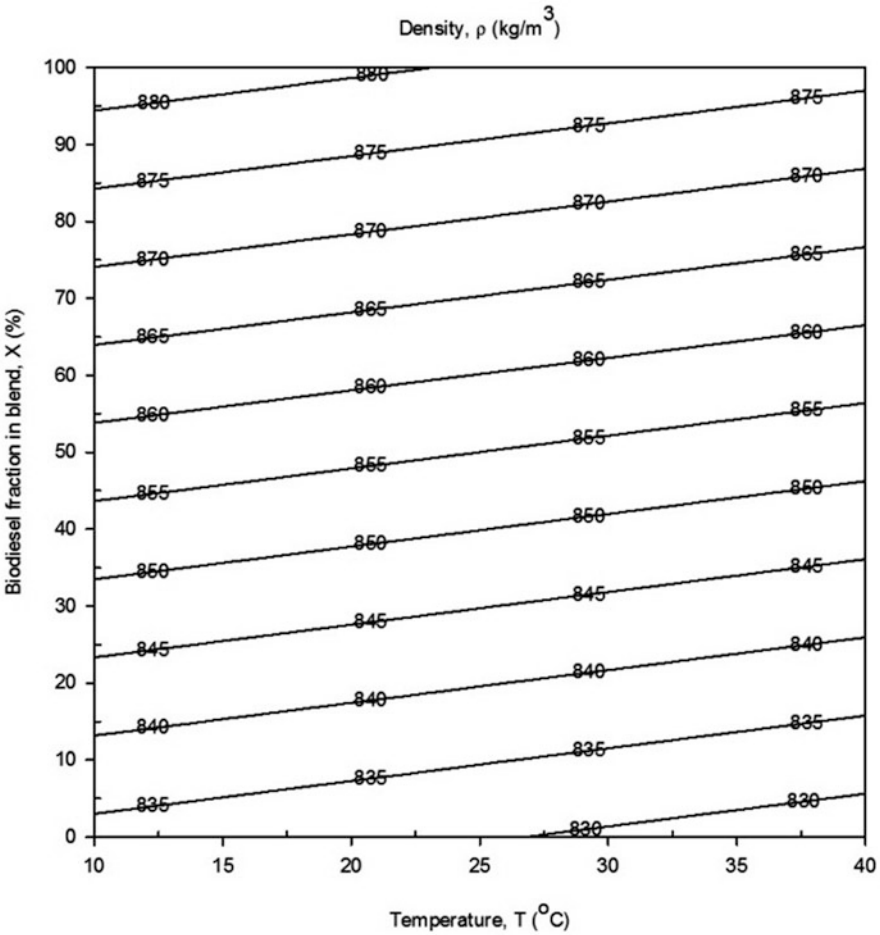

Fig. 3 Variations of constant density lines of fuel blends as functions of temperature and biodiesel fraction simultaneously calculated from Eq. (8)

relative error rate between the measured and calculated density values were computed as 0.1506% for this model.

- The two-dimensional constant density line plot obtained by the linear surface model has constant gradients, as shown in Fig. 3. This means that when temperature is changed in a unit amount, the temperature change should be multiplied by a factor corresponding to the slope of the constant density line for keeping the density of the fuel blend constant.

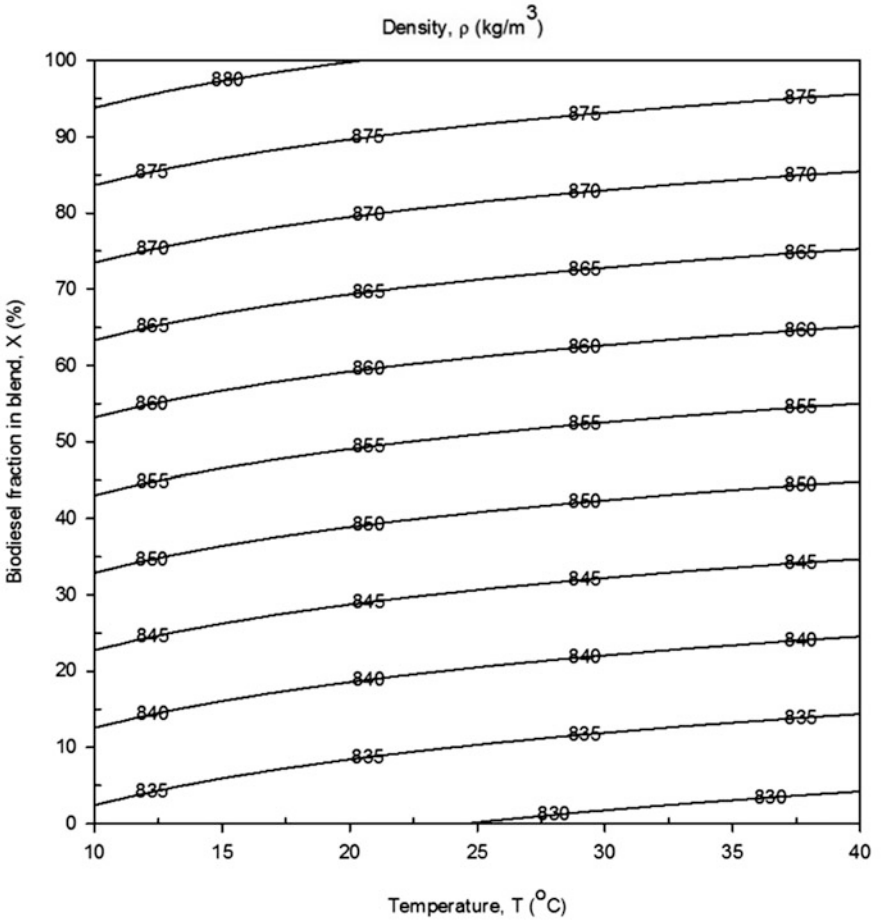

Fig. 4 Variations of constant density lines of fuel blends as functions of temperature and biodiesel fraction simultaneously calculated from Eq. (9)

Acknowledgments The authors express their gratitude to Karadeniz Technical University Scientific Research Projects Fund for financial support received (Project No: 9745).

References

Basha, S.A., Gopal, K.R.: A review of the effects of catalyst and additive on biodiesel production, performance, combustion and emission characteristics. Renew. Sust. Energ. Rev. **16**, 711–717 (2012)

Canakci, M.: Combustion characteristics of a turbocharged DI compression ignition engine fueled with petroleum diesel fuels and biodiesel. Bioresour. Technol. **98**, 1167–1175 (2007)

Chapra, S.C., Canale, P.R.: Numerical Methods for Engineers with Software and Programming Applications, 3rd edn. Mc-Graw-Hill, New York (1998)
Esteban, B., Riba, J.R., Baquero, G., Rius, A., Puig, R.: Temperature dependence of density and viscosity of vegetable oils. Biomass Bioenergy. **42**, 164–171 (2012)
Gaurav, A., Leite, M.L., Ng, F.T.T., Rempel, G.L.: Transesterification of triglyceride to fatty acid alkyl esters (biodiesel): comparison of utility requirements and capital costs between reaction separation and catalytic distillation configurations. Energy Fuel. **27**, 6847–6857 (2013)
Gülüm, M.: Experimental investigation of the effect of various production parameters on the some fuel properties of produced biodiesels from corn and hazelnut oils, Master's Thesis, Karadeniz Technical University, Turkey (2014)
Holman, J.P.: Experimental Methods for Engineers, 7th edn. McGraw-Hill, New York (2001)
Iwasaki, M., Ikeya, N., Itoh, M., Itoh, M., Yamaguchi, H.: Development and evaluation of catalysts to remove NOx from diesel engine exhaust gas, Sae Technical Paper, doi:10.4271/950748 (1995)
Lin, R., Zhu, Y., Tavlarides, L.L.: Effect of thermal decomposition on biodiesel viscosity and cold flow property. Fuel. **117**, 981–988 (2014)
Mejia, J.D., Salgado, N., Orrego, C.E.: Effect of blends of diesel and palm-castor biodiesels on viscosity, cloud point and flash point. Ind. Crop. Prod. **43**, 791–797 (2013)
Moser, B.R.: Biodiesel from alternative oilseed feedstocks: camelina and field pennycress. Biofuels. **3**, 193–209 (2012)
Ozcanli, M., Serin, H., Saribiyik, O.Y., Aydin, K., Serin, S.: Performance and emission studies of castor bean (ricinus communis) oil biodiesel and its blends with diesel fuel. Energy Sources. **34**, 1808–1814 (2012)
Pratas, M.J., Freitas, S.V.D., Oliveira, M.B., Monteiro, S.C., Lima, A.S., Coutinho, J.A.P.: Biodiesel density: experimental measurements and prediction models. Energy Fuel. **25**, 2333–2340 (2011)
Rahimi, M., Aghel, B., Alitabar, M., Sepahvand, A., Ghasempour, H.R.: Optimization of biodiesel production from soybean oil in a microreactor. Energy Convers. Manag. **79**, 599–605 (2014)
Sivanathan, S., Chandran, H.P.: Investigation on the performance and emission characteristics of biodiesel and its blends with oxygenated additives in a diesel engine, Sae Technical Paper, doi:10.4271/2014-01-1261 (2014)
Sivaramakrishnan, K., Ravikumar, P.: Determination of higher heating value of biodiesels. Int. J. Eng. Sci. Technol. **3**, 7981–7987 (2011)
Stalin, N., Prabhu, H.J.: Performance test of IC engine using karanja biodiesel blending with diesel. ARPN J. Eng. Appl. Sci. **2**, 32–34 (2007)
Tong, D., Hu, C., Jiang, K., Li, Y.: Cetane number prediction of biodiesel from the composition of the fatty acid methyl esters. J. Am. Oil Chem. Soc. **88**, 415–423 (2011)
Yuan, W., Hansen, A.C., Zhang, Q., Tan, Z.: Temperature-dependent kinematic viscosity of selected biodiesel fuels and blends with diesel fuel. J. Am. Oil Chem. Soc. **82**, 195–199 (2005)
Yuan, W., Hansen, A.C., Zhang, Q.: Predicting the temperature dependent viscosity of biodiesel fuels. Fuel. **88**, 1120–1126 (2009)
Yuan, W., Hansen, A.C., Zhang, Q.: Predicting the physical properties of biodiesel for combustion modeling. Am. Soc. Agric. Eng. **46**, 1487–1493 (2003)

Effects of Temperature and Biodiesel Fraction on Dynamic Viscosities of Commercially Available Diesel Fuels and Its Blends with the Highest Methyl Ester Yield Corn Oil Biodisel Produced by Using KOH

Gülüm Mert and Bilgin Atilla

1 Introduction

Biodiesel, defined as the mono-alkyl esters of long-chain fatty acids derived from a renewable lipid feedstock, has received considerable attention worldwide as a medium-term alternative to diesel fuel (Apostolakoua et al. 2009) because of its many advantages as follows:

1. It does not produce greenhouse effects because the balance between the amount of carbon dioxide (CO_2) emission and the amount of CO_2 absorbed by the plants producing vegetable oil is about equal (Barabás et al. 2010).
2. It has similar fuel characteristics to diesel fuel; therefore, it can be used either as blends or in pure form without major modifications of the diesel engine (Mittelbach and Enzelsberger 1999).
3. It is nontoxic, contains no aromatics and sulfur, degrades about four times compared to diesel fuel, and pollutes water and soil to a lesser extent (Serdari et al. 2000; Yusuf et al. 2011).
4. It improves lubricity, which results in longer engine component life (Ferrão et al. 2011).
5. When biodiesel and its blends are used, carbon monoxide (CO), smoke opacity, and unburnt hydrocarbon (UBHC) emissions are less than those with diesel fuel because biodiesel has oxygen in its molecular structure, leading to better combustion (Kumar et al. 2012; Swaminathan and Sarangan 2009).
6. It can be produced by using domestic renewable feedstock, thus reducing the dependence on imported petroleum.

G. Mert (✉) • B. Atilla
Karadeniz Technical University, Faculty of Engineering, Mechanical Engineering Department, Trabzon 61080, Turkey
e-mail: gulum@ktu.edu.tr

© Springer International Publishing AG, part of Springer Nature 2018

F. Aloui, I. Dincer (eds.), *Exergy for A Better Environment and Improved Sustainability 2*, Green Energy and Technology,
https://doi.org/10.1007/978-3-319-62575-1_6

7. Flash point of biodiesel (>130 °C) is higher than that of diesel fuel, which makes biodiesel safer from handling and storage point of view (Rao et al. 2010).
8. Depending on used biomass or plant and type of production method, it generally has a higher cetane number than diesel fuel, which causes a shorter ignition delay period and increases autoignition capability (Karabektas 2009).

Nevertheless, biodiesel also has some disadvantages, such as lower calorific value and volatility; higher viscosity, cloud point temperature, and (generally) nitrogen oxide (NO_x) emissions; and corrosive nature against copper and brass (Jain and Sharma 2010).

Viscosity, defined as a measure of the internal friction or resistance of a substance to flow, is one of the most important rheological property regarding fuel atomization and distribution as well as lubrication (Verduzco et al. 2011). Fuel with high viscosity has poor atomization and penetration and leads to more problems in cold weather (Al-Hamamre and Al-Salaymeh 2014). Poor atomization increases exhaust emissions and decreases engine performance. On the other hand, fuel with low viscosity may not provide sufficient lubrication for fuel injection pumps, resulting in leakage and increased wear (Al-Hamamre and Yamin 2014).

As the use of biodiesel has become more widespread, researchers have shown a strong interest in modeling the combustion process in order to understand the fundamental characteristics of biodiesel combustion (Yuan et al. 2003). They often use physical properties of biodiesel as input data in their combustion models for the most computational software (KIVA, Fluent, AVL Fire). However, it may not be practical at every turn to make measurements of physical properties of biodiesel or biodiesel–diesel fuel blends for each blending ratio or temperature in any study. Regression models as a function of temperature, percentage of blend, and chemical structure have been generally used to calculate these properties without measurements. Some studies reporting these models were summarized as follows. Krisnangkura et al. (2006) proposed an empirical model for the determination of kinematic viscosities of saturated fatty acid methyl esters (FAMEs) having various chain lengths (C12:0-C18:0) at different temperatures (20–80 °C). The suggested linearity of natural logarithm model as a function of viscosity-carbon number matched very well with the experimental values. In the study by Do Carmo et al. (2012), a new model based on one and two reference fluid corresponding states was evaluated for the prediction of the dynamic viscosities of pure biodiesels and their mixture, which takes into account the effects of temperature and compositional change. The model in this study presented the best results when compared with Ceriani's, Yuan's, and revised Yuan's models. Benjumea et al. (2008) measured some basic properties (viscosity; density; heating value; cloud point; calculated cetane index; and T10, T50, and T90 distillation temperatures) of several palm oil biodiesel–diesel fuel blends. Arrhenius-type equation and Kay's mixing rules were used in order to predict kinematic viscosity and the other properties, respectively.

In this chapter, the effects of biodiesel fraction in blend (X) and temperature (T) on dynamic viscosities of the highest methyl ester yield corn oil biodiesel (B100)

and its blends (B5, B15, B20, and B25) with commercially available diesel fuel (D) were investigated. Some new one- and two-dimensional models were also fitted to the measurements for predicting dynamic viscosities of the biodiesel–diesel fuel blends, and these models were compared to previously published models and measurements to show their validities.

Nomenclature

$a, b, c, d, \ldots, g$	Regression constants
$B5, B10, B15, B20$	Biodiesel–diesel fuel blends
$B100$	Pure biodiesel
D	Pure diesel fuel
HHV	Higher heating value (kJ/kg)
K_{ball}	Coefficient of the viscometer ball ($\text{mPa} \cdot \text{s} \cdot \text{cm}^3/g/s$)
m_{total}	Mass of the pycnometer filled with biodiesel (g)
$m_{\text{pycnometer}}$	Mass of pycnometer (g)
m_{water}	Mass of pycnometer filled with pure water (g)
R	Correlation coefficient
t	Falling time of the viscometer ball (s)
T	Temperature ($^{\circ}C$)
$w_1, w_2, w_3, \ldots, w_n$	Uncertainties of independent variables
$\tilde{w}$	Dimensionless uncertainty
$x_1, x_2, x_3, \ldots, x_n$	Independent variables
X	Biodiesel fraction in blend (%)
Greek letters	
μ_{blend}	Dynamic viscosity of blend ($cP \equiv mPa.s$)
ν_{blend}	Kinematic viscosity of blend ($cSt \equiv mm^2/\text{s}$)
ρ_{ball}	Density of viscometer ball (g/cm^3)
ρ_{blend}	Density of blend (kg/m^3)
ρ_{water}	Density of pure water (kg/m^3)

2 Experimental Methods

2.1 Biodiesel Production

In this study, commercially available refined corn oil was used in biodiesel production. Pretreatment to the oil was not required as the oil was refined. Thus, methanol (CH_3OH) of 99.8% purity as alcohol and pure-grade potassium hydroxide (KOH) as catalyst were used in the transesterification reaction. To produce corn oil biodiesel having the highest methyl ester yield, optimum reaction parameters were 1.10% catalyst concentration (mass of KOH/mass of corn oil), 60 °C reaction temperature, 60 min reaction time, and 6:1 alcohol/oil molar ratio, as given by Gülüm (2014). The transesterification reaction was carried out in a 1-L flat-

bottomed flask, equipped with a magnetic stirrer heater, thermometer, and spiral reflux condenser. Haake falling ball viscometer, Isolab pycnometer, top loading balance with an accuracy of 0.01 g, Haake water bath, and a stopwatch with an accuracy of 0.01 s were used to measure dynamic viscosity and density. Before starting the reaction, the catalyst was dissolved in methanol to make an alcoholic solution of the catalyst in a narrow-neck flask. In the flat-bottomed flask, the alcoholic solution was added to the 200 g of corn oil that was formerly warmed to about 80 °C in a beaker. These reactants were mixed with a stirring speed of 500 rpm using the magnetic stirrer heater. The transesterification reaction was carried out with the spiral reflux condenser for avoiding loss of alcohol. Also, reaction temperature was controlled using a thermometer to remain constant during the reaction. At the end of the reaction, the resulting products mixture was transferred to a separating funnel. After a day, two phases formed in the separating funnel. The upper phase consisted of methyl esters (biodiesel), while the lower one consisted of glycerol, excess methanol, and remaining catalyst together with soap. After the separation of the two layers by gravity, the biodiesel phase was washed with warm distilled water until the water became clear. The washed biodiesel was heated up to about 100 °C to remove methyl alcohol and water residuals.

2.2 Density Measurement

The densities of the produced biodiesel and its blends were determined by means of Eq. (1) and measurements in accordance with ISO 4787 standard:

$$\rho_{\text{blend}} = \frac{m_{\text{total}} - m_{\text{pycnometer}}}{m_{\text{water}}} \rho_{\text{water}} \tag{1}$$

where ρ and m represent density and mass, respectively. In order to minimize measurement errors, all the measurements were conducted three times for each sample and the results were averaged. Also, an uncertainty analysis was carried out, depending on the sensitivities of measurement devices.

2.3 Dynamic Viscosity Measurement

The dynamic viscosities were determined in accordance with DIN 53015 standard by using Eq. (2) and making measurements by means of the Haake falling ball viscometer, Haake water bath, and stopwatch:

$$\mu_{\text{blend}} = K_{\text{ball}}(\rho_{\text{ball}} - \rho_{\text{blend}})t \tag{2}$$

where μ is dynamic viscosity, K_{ball} is coefficient of the viscometer ball, and t is falling time of the ball moving between two horizontal lines marked on the viscometer tube at limit velocity. K_{ball} and ρ_{ball} are 0.057 mPa · s · cm^3/g/s and 2.2 g/cm^3, respectively.

The kinematic viscosities were determined from Eq. (3) by dividing dynamic viscosity to density at the same temperature:

$$\nu_{blend} = \frac{\mu_{blend}}{\rho_{blend}} \tag{3}$$

In Eq. (3), if μ_{blend} and ρ_{blend} are in unit of (mPa . s) and (kg/L), respectively, then ν_{blend} is obtained in the unit of mm^2/s.

In this study, dynamic viscosities and densities were measured in the Internal Combustion Engines Laboratory in the Mechanical Engineering Department at Karadeniz Technical University. The fatty acid methyl esters of the produced corn oil biodiesel were qualitatively and quantitatively analyzed by gas chromatography using a Hewlett-Packard HP-6890 Series GC system fitted with a HP-6890 mass selective detector (1909 N-133 innowax capillary column of 30 m length, 0.25 mm I.D, and 0.25 μm film thickness) in the Science Research and Application Center at Mustafa Kemal University. The other properties of the pure fuels and fuel blends, such as flash point temperature (EN ISO 3679) and higher heating value (DIN 51900-2), were also measured at the Prof. Dr. Saadettin GÜNER Fuel Research and Application Center at Karadeniz Technical University. These properties and EN 14214 and ASTM D 6751 standard values are given in Table 1. Moreover, the fatty acid compositions of the produced corn oil biodiesel and its calculated average molecular mass and typical formula are given in Table 2.

Table 1 Some fuel properties of diesel fuel, produced corn oil biodiesel and their blends, and corresponding standard values for biodiesel

Properties	Units	B100	D	B5	B10
Viscosity at 40 °C	mm^2/s	4.094	2.700	2.944	3.240
Density at 15 °C	kg/m^3	882.68	832.62	835.67	837.91
Flash point	°C	178	63	70	74
HHV	kJ/kg	39,959	45,950	40,263	40,574

B15	B20	EN14214	ASTM-D6751
3.470	3.671	3.50–5.00	1.90–6.00
839.94	842.59	860–900	[a]
83	90	101≤	130≤
40,867	41,169	[a]	[a]

[a]Not specified

Table 2 Fatty acid methyl ester composition of the produced biodiesel

Fatty acid	Mass, %
Palmitic (C16:0)	15.343
Oleic (C18:1)	47.305
Linoleic (C18:2)	34.122
α-Linolenic acid (C18:3)	1.183
Arachidic (C20:0)	0.811
Gadoleic acid (C20:1)	0.506
Behenic (C22:0)	0.362
Lignoceric (C24:0)	0.368
Average molecular mass	292.681 g/mol[1]
Typical formula	$C_{18.72}H_{35.25}O_2$[1]

[1]Calculated from fatty acid distribution

2.4 Uncertainty Analysis

The results obtained from experimental studies are generally calculated from measured physical quantities. These quantities have some uncertainties due to uncertainties of measuring tools and measurement systems. Therefore, uncertainty analysis should be applied for proving reliability of the calculated results. In this study, uncertainties of the measured and calculated physical quantities, such as dynamic and kinematic viscosities and density values, were determined by the method proposed by Holman (2001). According to this method, if the result R is a given function of the independent variables x_1, x_2, x_3, ..., x_n and are the uncertainties of each independent variable, then the uncertainty of the result w_R is calculated by using the equation:

$$w_R = \left[\left(\frac{\partial R}{\partial x_1} \cdot w_1 \right)^2 + \left(\frac{\partial R}{\partial x_2} \cdot w_2 \right)^2 + \ldots + \left(\frac{\partial R}{\partial x_n} \cdot w_n \right)^2 \right]^{1/2} \tag{4}$$

For example, by using Eqs. (1) and (4), the uncertainty of density of B10 at 15°C ($w_{\rho_{B10,15°C}}$) was calculated as:

$$\rho_{B10,15°C} = \frac{m_{total} - m_{pycnometer}}{m_{water}} \rho_{water,15°C}$$

$$x_1 \equiv m_{total} = 83.91 \text{ g}$$

$$x_2 \equiv m_{pycnometer} = 42.74 \text{ g}$$

$$m_{water} = 49.09 \text{ g}$$

$$\rho_{B10,15°C} = \frac{83.91 \text{ g} - 42.74 \text{ g}}{49.09 \text{ g}} 999.10 \text{ kg/m}^3$$

$$\rho_{\mathrm{B10,15^\circ C}} = 837.91\ \mathrm{kg/m^3}$$

$$\rho_{\mathrm{B10,15^\circ C}} = \rho_{\mathrm{B10,15^\circ C}}\left(m_{\mathrm{total}}, m_{\mathrm{pycnometer}}\right)$$

$$R \equiv \rho_{\mathrm{B10,15^\circ C}}$$

$$\frac{\partial \rho_{\mathrm{B10,15^\circ C}}}{\partial m_{\mathrm{total}}} = \frac{1}{m_{\mathrm{water}}} \cdot \rho_{\mathrm{water,15^\circ C}}$$

$$\frac{\partial \rho_{\mathrm{B10,15^\circ C}}}{\partial m_{\mathrm{pycnometer}}} = \frac{-1}{m_{\mathrm{water}}} \cdot \rho_{\mathrm{water,15^\circ C}}$$

$$w_{\rho_{\mathrm{B10,15^\circ C}}} = \left[\left(\frac{1}{m_{\mathrm{water}}} \cdot \rho_{\mathrm{water,15^\circ C}} \cdot w_{\mathrm{m_{total}}}\right)^2 + \left(-\frac{1}{m_{\mathrm{water}}} \cdot \rho_{\mathrm{water,15^\circ C}} \cdot w_{\mathrm{m_{pycnometer}}}\right)^2\right]^{1/2}$$

$$w_{\rho_{\mathrm{B10,15^\circ C}}} = \left[\left(\frac{1}{49.09\ \mathrm{g}} \cdot 999.10\mathrm{kg/m^3} \cdot 0.01\mathrm{g}\right)^2 + \left(-\frac{1}{49.09\ \mathrm{g}} \cdot 999.10\mathrm{kg/m^3} \cdot 0.01\mathrm{g}\right)^2\right]^{1/2}$$

$$w_{\rho_{\mathrm{B10,15^\circ C}}} = 0.2878\ \mathrm{kg/m^3}$$

Since the density of the B10 at 15°C was determined as 837.91 kg/m^3, dimensionless uncertainty of density becomes:

$$\tilde{w}_{\rho_{\mathrm{B10,15^\circ C}}} = \frac{0.2878\ \mathrm{kg/m^3}}{837.91\ \mathrm{kg/m^3}} \cdot 100 = 0.0343\%$$

Similarly, the highest uncertainty was determined as 0.0354%. Therefore, it can be said that the results have fairly high reliability.

3 Results and Discussions

3.1 One-Dimensional Linear Models

3.1.1 Effects of Biodiesel Fraction on Viscosity

Figure 1 shows the variations of dynamic viscosities of fuel blends (B5, B10, B15, and B20) with respect to biodiesel fractions (X) for different temperatures (T). In this figure, the points correspond to the measured viscosity values at studied temperatures and biodiesel fractions, while the lines are plots of curve fit equations. Viscosities increase with increase in biodiesel fraction for a specific temperature, as expected, and the change of them tends to be about linear with increase in biodiesel fraction as temperature is decreasing. Exponential and rational models were suggested and compared to the well-known Arrhenius model (Joshi and Pegg 2007) for characterizing these changes as:

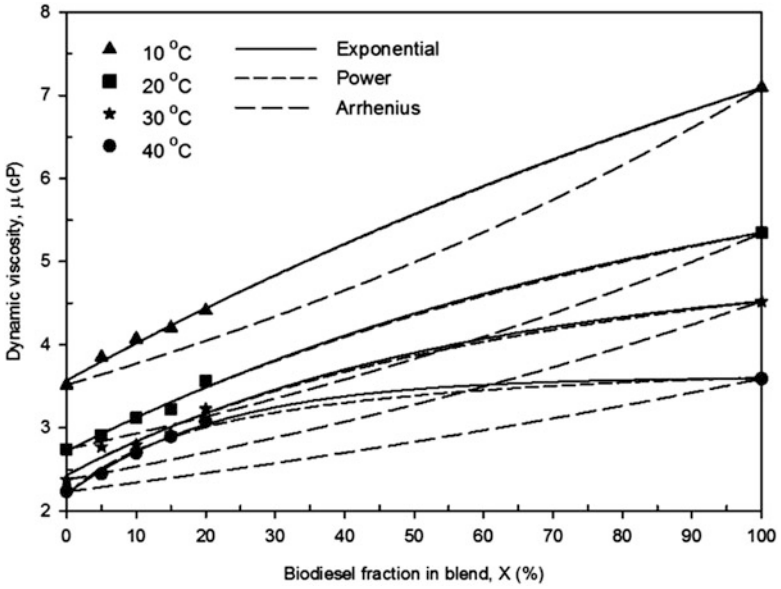

Fig. 1 Changes in viscosity values of fuel blends with respect to biodiesel fraction for different models

$$\mu = \mu(X) = \mu_0 + a \cdot e^{bX} \tag{5}$$

$$\mu = \mu(X) = (aX + 1)/(b + c) \tag{6}$$

$$\text{In}\mu = X_{\text{diesel}} \ln \mu_{\text{diesel}} + X_{\text{biodiesel}} \text{In}\mu_{\text{biodiesel}} \tag{7}$$

where μ is dynamic viscosity in cP, and μ_0, a, b, and c are regression constants.

Tables 3, 4, and 5 list the calculated (from Eqs. (5), (6), and (7)) and measured viscosities of the blends and pure fuels (D and B100), error rates between measured and calculated values, regression constants, and correlation coefficients (R). As known, the correlation coefficient is a quantitative measure of goodness of fit of the regression equation to the measured data. For a perfect fit, for example, R becomes 1 and the equation explains 100% of the variability of the measured data (Chapra and Canale 1998). The maximum relative error rates between the measured and calculated viscosity values were computed as 4.7059%, 4.5976%, and 20.0944% for Eqs. (5), (6), and (7), respectively. Also, the lowest R values are 0.9941, 0.9942, and 0.5738 for these equations, respectively. According to these results, the power model seems the best fit to the data. Moreover, as seen in Fig. 1, Arrhenius model does not fairly reflect the changes of viscosities with respect to biodiesel content for all studied temperatures, and the relation between dynamic viscosity and biodiesel fraction in blend was found to be better expressed by the rational model than the exponential model.

Table 3 Measured viscosities, calculated viscosities from Eq. (5), error rates between measured and calculated viscosities, regression constants, and correlation coefficients for different temperatures

Temp. T (°C)	Measured, μ (cP)					
	Blend, X (%)					
	0	5	10	15	20	100
10	3.514	3.850	4.068	4.204	4.409	7.094
20	2.743	2.912	3.119	3.221	3.563	5.346
30	2.376	2.771	2.791	2.923	3.229	4.520
40	2.233	2.443	2.697	2.894	3.072	3.589

Regression constants			
μ_0	a	b	R
11.9200	−8.3490	0.005481	0.9994
6.7470	−4.0300	0.010580	0.9984
4.9700	−2.5400	0.017310	0.9941
3.6110	−1.4080	0.044990	0.9982

Calculated, μ (cP)					
Blend, X (%)					
0	5	10	15	20	100
3.5710	3.7967	4.0163	4.2300	4.4378	7.0939
2.7170	2.9246	3.1216	3.3084	3.4856	5.3480
2.4300	2.6406	2.8337	3.0108	3.1733	4.5201
2.2030	2.4866	2.7131	2.8940	3.0384	3.5953

Relative error rates (%)					
Blend, X (%)					
0	5	10	15	20	100
1.6221	1.3844	1.2709	0.6185	0.6532	0.0014
0.9479	0.4327	0.0834	2.7134	2.1723	0.0374
2.2727	4.7059	1.5299	3.0038	1.7250	0.0022
1.3435	1.7847	0.5970	0.0000	1.0937	0.1755

3.1.2 Effects of Temperature on Viscosity

The effects of temperature on the viscosities of pure fuels and biodiesel–diesel fuel blends are given in Fig. 2. The viscosities of all the blends and fuels follow a similar trend: they decrease with increase in temperature, as expected. In this figure, the experimental data matched predicted values computed by exponential and power models:

$$\mu = \mu(T) = \mu_0 + a\mathrm{e}^{-bT} \tag{8}$$

$$\mu = \mu(T) = a\mathrm{T}^{\mathrm{b}} + c \tag{9}$$

where T is temperature in °C and μ_0, a, b, and c are regression constants.

Tables 6 and 7 also present the measured viscosity data, the calculated values from Eq. (8) and (9), relative error rates between them, regression constants, and correlation coefficients. The maximum relative error rates and the lowest R values

Table 4 Calculated viscosities from Eq. (6), error rates between measured and calculated viscosities, regression constants, and correlation coefficients for different temperatures

Regression constants			
a	b	c ($\times 10^{-4}$)	R
0.015990	0.2802	8.6220	0.9994
0.022310	0.3681	23.6100	0.9983
0.031040	0.4122	49.5700	0.9942
0.079000	0.4554	201.3000	0.9952

Calculated, μ (cP)					
Blend, X (%)					
0	5	10	15	20	100
3.5689	3.7958	4.0160	4.2297	4.4371	7.0930
2.7167	2.9259	3.1225	3.3076	3.4821	5.3476
2.4260	2.6436	2.8378	3.0122	3.1697	4.5203
2.1959	2.5088	2.7257	2.8851	3.0070	3.6056

Relative error rates (%)					
Blend, X (%)					
0	5	10	15	20	100
1.5623	1.4078	1.2783	0.6113	0.6373	0.0141
0.9588	0.4773	0.1122	2.6886	2.2706	0.0299
2.1044	4.5976	1.6768	3.0517	1.8365	0.0066
1.6614	2.6934	1.0641	0.3075	2.1159	0.4625

Table 5 Calculated viscosities from Eq. (7), error rates between measured and calculated viscosities, regression constants, and correlation coefficients for different temperatures

	Calculated, μ (cP)					
	Blend, X (%)					
R	0	5	10	15	20	100
0.9787	3.5140	3.6404	3.7705	3.9052	4.0447	7.0940
0.9710	2.7430	2.8359	2.9320	3.0315	3.1343	5.3460
0.8980	2.3760	2.4527	2.5330	2.6159	2.7015	4.5200
0.5738	2.2330	2.2859	2.3408	2.3971	2.4547	3.5890

Relative error rates (%)					
Blend, X (%)					
0	5	10	15	20	100
0.0000	5.4442	7.3132	7.1075	8.2626	0.0000
0.0000	2.6133	5.9955	5.8833	12.0320	0.0000
0.0000	11.4868	9.2440	10.5063	16.3363	0.0000
0.0000	6.4306	13.2073	17.1700	20.0944	0.0000

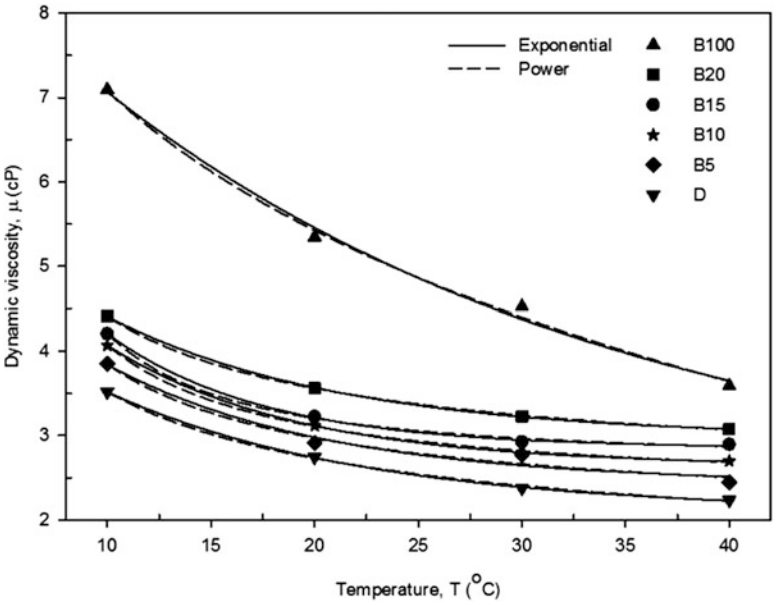

Fig. 2 Changes in viscosity values of pure fuels and fuel blends with respect to temperature for different models

were computed as 4.5868%, 0.9881 and 3.9733%, 0.9914 for Eqs. (8) and (9), respectively. When relative error rates and maximum correlation coefficients in Tables 6 and 7 are analyzed and Fig. 2 is observed, it can be said that power model matches better with the experimental data of pure fuels and fuel blends throughout the studied temperature ranges.

On the other hand, in order to test their validities, these models were also fitted to the dynamic viscosities of the coconut, colza, and soybean oil biodiesels measured by Feitosa et al. (2010), as shown in Fig. 3. Tables 8 and 9 show the dynamic viscosities measured by Feitosa et al., calculated viscosities from Eqs. (8) and (9), % errors between measured and calculated values, regression constants, and correlation coefficients. The maximum errors computed from Eqs. (8) and (9) are 2.3935% and 2.1726%, while the minimum R values are determined as 0.9996 and 0.9998, respectively. These results and Fig. 3 show that the changes of kinematic viscosity measurements given by Feitosa et al. are also better demonstrated by the power model.

3.2 Two-Dimensional Surface Models

In this study, two-dimensional polynomial and combination of exponential and linear terms surface models were also derived for changes of dynamic viscosities with respect to T and X simultaneously:

Table 6 Measured viscosities, calculated viscosities from Eq. (8), error rates between measured and calculated viscosities, regression constants, and correlation coefficients for different biodiesel fractions

	Measured, μ (cP)			
	Temp., T (°C)			
Blend X (%)	10	20	30	40
0	3.514	2.743	2.376	2.233
5	3.850	2.912	2.771	2.443
10	4.068	3.119	2.791	2.697
15	4.204	3.221	2.923	2.894
20	4.409	3.563	3.229	3.072
100	7.094	5.346	4.520	3.589

Regression constants			
μ_0	a	b	R
2.0970	3.1420	0.079580	0.9999
2.4320	3.6260	0.094660	0.9881
2.6400	4.2900	0.110000	0.9999
2.8530	5.1000	0.132700	0.9995
2.9760	3.4660	0.088350	0.9999
2.1700	7.2950	0.039870	0.9972

Calculated, μ (cP)			
Temp., T (°C)			
10	20	30	40
3.5147	2.7367	2.3856	2.2272
3.8391	2.9780	2.6439	2.5142
4.0680	3.1153	2.7982	2.6927
4.2059	3.2119	2.9482	2.8783
4.4086	3.5681	3.2208	3.0772
7.0663	5.4564	4.3758	3.6505

Relative error rates (%)			
Temp., T(°C)			
10	20	30	40
0.0199	0.2297	0.4040	0.2597
0.2831	2.2665	4.5868	2.9144
0.0000	0.1186	0.2580	0.1594
0.0452	0.2825	0.8621	0.5425
0.0091	0.1431	0.2539	0.1693
0.3905	2.0651	3.1903	1.7136

$$\mu = \mu(T, X) = a + bT + cX + dT^2 + eTX + fT^3 + gT^2 \tag{10}$$

$$\mu = \mu(T, X) = a \cdot e^{bT} + c \cdot e^{dX} + eX \tag{11}$$

where μ is dynamic viscosity in cP, and a, b, c, d, e, f, and g are regression constants.

Tables 10 and 11 list the measured viscosities, calculated viscosities from Eqs. (10) and (11), regression constants, R values, and relative error rates. The

Table 7 Calculated viscosities from Eq. (9), error rates between measured and calculated viscosities, regression constants, and correlation coefficients for different biodiesel fractions

Regression constants			
a	*b*	*c*	*R*
9.5140	−0.6310	1.2910	0.9994
15.1800	−0.9093	1.9720	0.9914
26.1800	−1.1820	2.3480	0.9995
57.7400	−1.5840	2.7010	0.9989
12.5300	−0.7946	2.3980	0.9999
−15.9000	0.1115	27.630	0.9997
Calculated, μ(cP)			
Temp., $T(^{\circ}C)$			
10	20	30	40
3.5162	2.7279	2.4035	2.2188
3.8426	2.9680	2.6609	2.5023
4.0697	3.1068	2.8179	2.6825
4.2058	3.2029	2.9651	2.8684
4.4087	3.5572	3.2379	3.0663
7.0760	5.4244	4.3975	3.6402
Relative error rates (%)			
Temp., $T(^{\circ}C)$			
10	20	30	40
0.0626	0.5505	1.1574	0.6359
0.1922	1.9231	3.9733	2.4273
0.0418	0.3912	0.9638	0.5376
0.0428	0.5619	1.4403	0.8846
0.0068	0.1628	0.2756	0.1855
0.2537	1.4665	2.7102	1.4266

maximum relative error rates and R values were computed as 5.1606%, 0.9958 and 6.5139%, 0.9952 for Eqs. (10) and (11), respectively.

Figures 4 and 5 present plots of the changes of constant dynamic viscosity curves for fuel blends as functions of T and X calculated from Eqs. (10) and (11), respectively. These plots can be used to make quick estimates of viscosities for a given blending ratio at a specific temperature.

Increasing characteristic with decreasing rate of constant viscosity curves (concave characteristic) converts to increasing behavior with increasing rate (convex characteristic) because of T^3 term of the polynomial surface model at the higher temperature and biodiesel fraction regions, as shown in Fig. 4. However, this change is not physically meaningful. Accordingly, the combination surface model including exponential and linear terms can be recommended within 0–20% blending ratio range for predicting dynamic viscosity values in spite of higher correlation coefficient and lower maximum relative error rate of the polynomial surface model.

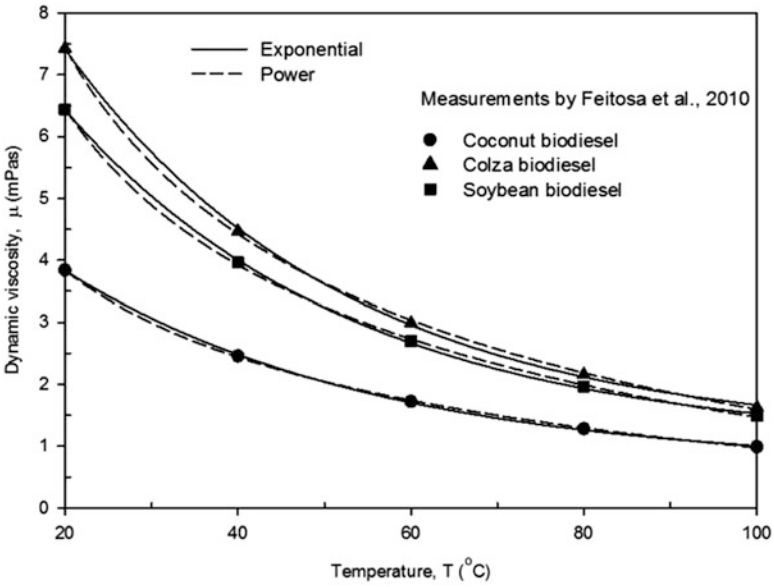

Fig. 3 Changes in viscosity values of coconut, colza, and soybean biodiesels measured by Feitosa et al. (2010) with respect to temperature for different models

There are two different characteristic regions in Fig. 5. Constant viscosity curves are sparser and closer to horizontal in the first region where temperature is higher and biodiesel fraction is lower. On the other hand, constant viscosity curves are more frequent and closer to vertical in the second region where temperature is lower and biodiesel fraction is higher. Consequently, less temperature changes at lower temperatures or more temperature changes at higher temperatures are needed for a unit change of viscosity for a given blending ratio. On the other hand, less biodiesel fraction changes at lower temperatures or more biodiesel fraction changes at higher temperatures are needed for a unit change of viscosity at a specific temperature.

4 Conclusions

In this chapter, the dynamic viscosities of corn oil biodiesel–diesel fuel blends were measured at different temperatures. Measurements were correlated by one- and two-dimensional models through regression analysis, and the compatibilities of the models have been investigated by comparing each other. The following conclusions can be drawn from the study:

Table 8 Viscosities measured by Feitosa et al. (2010), calculated viscosities from Eq. (8), error rates between measured and calculated viscosities, regression constants, and correlation coefficients for different biodiesel fractions

	Measured, μ (cP)				
	Temp., T (°C)				
Biodiesel	20	40	60	80	100
Coconut	3.8417	2.4574	1.7226	1.2816	0.9880
Colza	7.4296	4.4727	2.9959	2.1577	1.6294
Soybean	6.4440	3.9640	2.6979	1.9659	1.4959
Regression constants					R
μ_0	a		b		
0.6650	5.5310		0.02783		0.9997
1.1410	11.6600		0.03096		0.9998
1.0340	9.8130		0.02987		0.9996
Calculated, μ (cP)					
Temp., T (°C)					
20	40	60	80	100	
3.8351	2.4820	1.7064	1.2619	1.0071	
7.4185	4.5206	2.9605	2.1206	1.6684	
6.4335	4.0050	2.6688	1.9335	1.5290	
Relative error rates (%)					
Temp., T (°C)					
20	40	60	80	100	
0.1718	1.0011	0.9404	1.5371	1.9332	
0.1494	1.0709	1.1816	1.7194	2.3935	
0.1629	1.0343	1.0786	1.6481	2.2127	

Table 9 Calculated viscosities from Eq. (9), error rates between measured and calculated viscosities, regression constants, and correlation coefficients for different biodiesel fractions

Regression constants			R
a	b	c	
18.4200	−0.2997	−3.6590	0.9998
42.1400	−0.4252	−4.3530	0.9999
34.0700	−0.3819	−4.4020	0.9998
Calculated, μ (cP)			
Temp., T (°C)			
20	40	60	80	100
3.8463	2.4385	1.7408	1.2947	0.9743
7.4365	4.4271	3.0367	2.1858	1.5940
6.4500	3.9261	2.7314	1.9892	1.4671
Relative error rates (%)				
Temp., T (°C)				
20	40	60	80	100
0.1197	0.7691	1.0565	1.0222	1.3866
0.0929	1.0195	1.3619	1.3023	2.1726
0.0931	0.9561	1.2417	1.1852	1.9253

Table 10 Measured viscosities, calculated viscosities from Eq. (10), error rates between measured and calculated viscosities, regression constants, and correlation coefficient for different biodiesel fractions and temperatures

Temp. T (°C)	Blend X(%)	Measured μ (cP)	Calculated μ (cP)	Relative error rates (%)
10	0	3.514	3.5773	1.8014
	5	3.850	3.7930	1.4805
	10	4.068	4.0087	1.4577
	15	4.204	4.2244	0.4853
	20	4.409	4.4401	0.7054
20	0	2.743	2.7292	0.5031
	5	2.912	2.9202	0.2816
	10	3.119	3.1113	0.2469
	15	3.221	3.3023	2.5241
	20	3.563	3.4934	1.9534
30	0	2.376	2.4383	2.6221
	5	2.771	2.6280	5.1606
	10	2.791	2.8177	0.9566
	15	2.923	3.0074	2.8874
	20	3.229	3.1971	0.9879
40	0	2.233	2.2443	0.5060
	5	2.443	2.4559	0.5280
	10	2.697	2.6676	1.0901
	15	2.894	2.8792	0.5114
	20	3.072	3.0909	0.6152

Regression constants	Correlation coefficient
$a = 5.4430$	$R = 0.9958$
$b = -0.2528$	
$c = 5.2730 \times 10^{-2}$	
$d = 7.3900 \times 10^{-3}$	
$e = -1.1920 \times 10^{-3}$	
$f = -7.6730 \times 10^{-5}$	
$g = 2.3300 \times 10^{-5}$	

- The relation between dynamic viscosity and biodiesel fraction for the biodiesel–diesel fuel blends was found to be better expressed by the one-dimensional rational model.
- The one-dimensional power model as a function of temperature better predicted the dynamic viscosities of pure fuels and fuel blends than the one-dimensional exponential one.

Table 11 Calculated viscosities from Eq. (11), error rates between measured and calculated viscosities, regression constants, and correlation coefficient for different biodiesel fractions and temperatures

Calculated μ (cP)	Relative error rates (%)	Regression constants	Correlation coefficient
3.6025	2.5185	$a = 3.8190$ $b = -9.9890 \times 10^{-2}$ $c = 2.1960$ $d = -8.9800 \times 10^{-6}$ $e = 4.0760 \times 10^{-2}$	$R = 0.9952$
3.8062	1.1377		
4.0099	1.4282		
4.2136	0.2284		
4.4173	0.1883		
2.7140	1.0572		
2.9177	0.1957		
3.1214	0.0769		
3.3251	3.2319		
3.5288	0.9599		
2.3868	0.4545		
2.5905	6.5139		
2.7942	0.1147		
2.9979	2.5624		
3.2016	0.8486		
2.2663	1.4913		
2.4700	1.1052		
2.6737	0.8639		
2.8774	0.5736		
3.0811	0.2962		

- The two-dimensional combination surface model with higher correlation coefficient of 0.9952 matched the change of dynamic viscosities with biodiesel fraction and temperature at the same time within 0–20% blending ratio range. According to the plot of change of constant dynamic viscosity curves calculated by the surface model, less temperature changes at lower temperatures or more temperature changes at higher temperatures are requisites for a unit change of viscosity for a given blending ratio. On the other hand, less biodiesel fraction changes at lower temperatures or more biodiesel fraction changes at higher temperatures are required for a unit change of viscosity at a specific temperature.

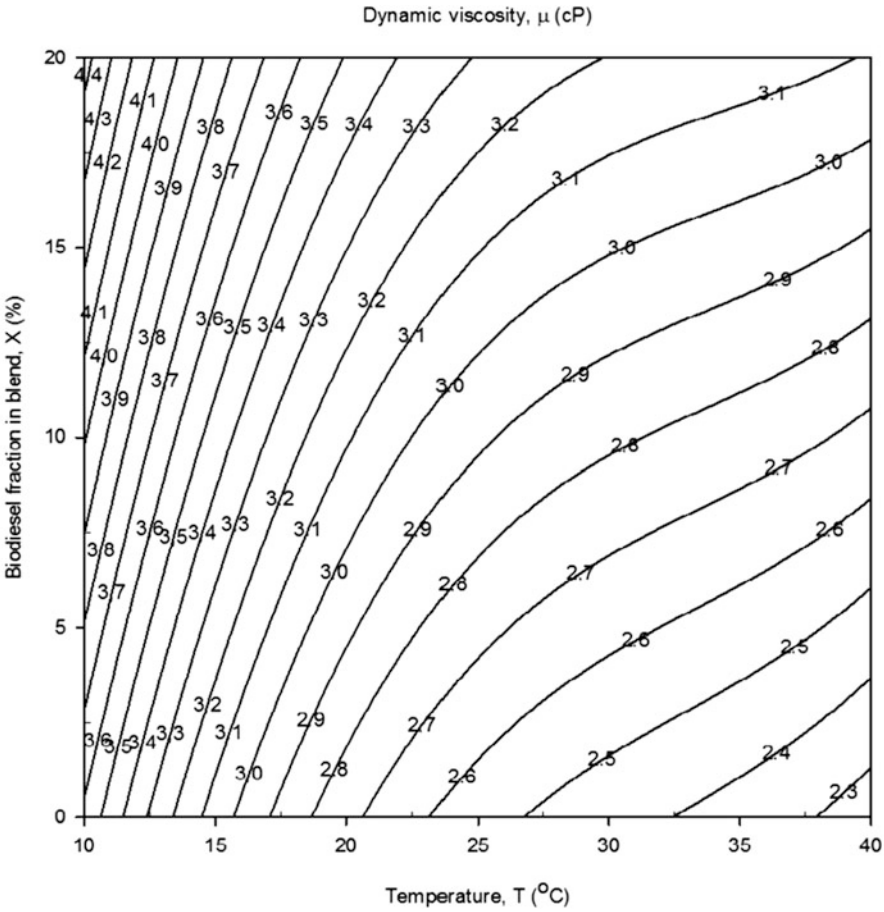

Fig. 4 Changes of constant viscosity curves of fuel blends as functions of temperature and biodiesel fraction calculated from Eq. (10)

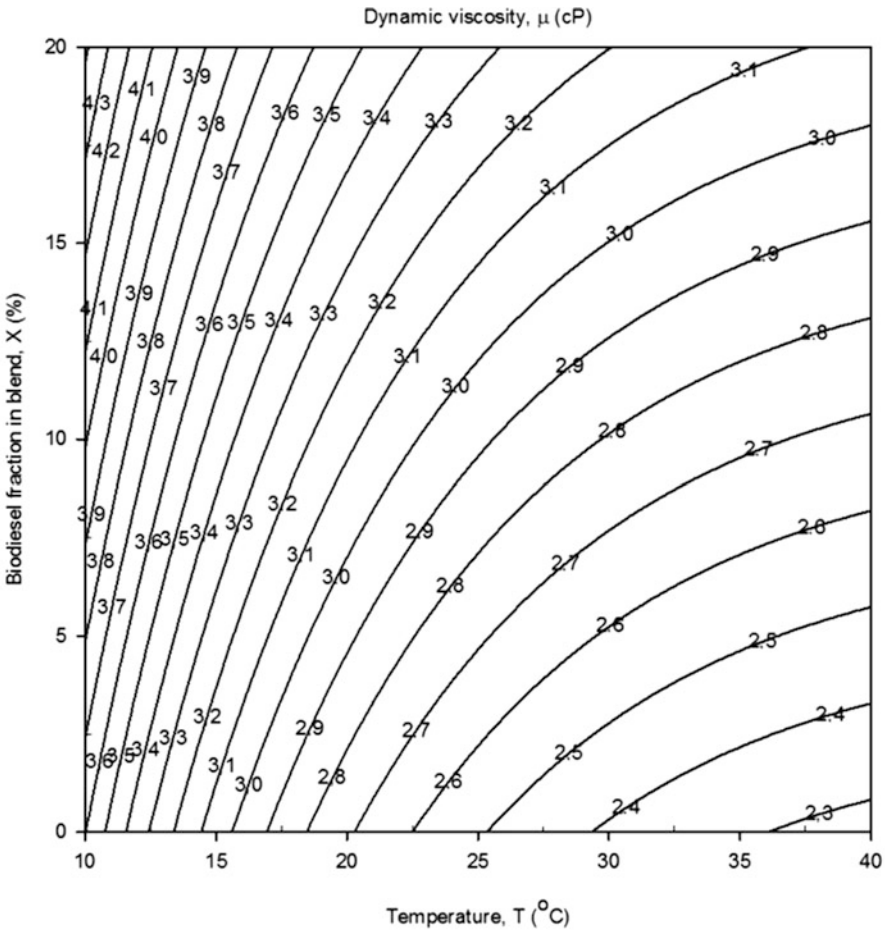

Fig. 5 Changes of constant viscosity curves of fuel blends as functions of temperature and biodiesel fraction calculated from Eq. (11)

Acknowledgments The authors express their gratitude to Karadeniz Technical University Scientific Research Projects Fund for the financial support received (Project No: 9745).

References

Al-Hamamre, Z., Al-Salaymeh, A.: Physical properties of (jojoba oil+biodiesel), (jojoba oil+diesel) and (biodiesel+diesel) blends. Fuel. **123**, 175–188 (2014)

Al-Hamamre, Z., Yamin, J.: Parametric study of the alkali catalyzed transesterification of waste frying oil for Biodiesel production. Energy Convers. Manag. **79**, 246–254 (2014)

Apostolakoua, A.A., Kookosa, I.K., Maraziotia, C., Angelopoulosb, K.C.: Techno-economic analysis of a biodiesel production process from vegetable oils. Fuel Process. Technol. **90**, 1023–1031 (2009)

Barabás, I., Todorut, A., Băldean, D.: Performance and emission characteristics of a CI engine fueled with diesel–biodiesel-bioethanol blends. Fuel. **89**, 382–3832 (2010)

Benjumea, P., Agudelo, J., Agudelo, A.: Basic properties of palm oil biodiesel-diesel blends. Fuel. **87**, 2069–2075 (2008)

Chapra, S.C., Canale, P.R.: Numerical Methods for Engineers with Software and Programming Applications, 3rd edn. Mc-Graw-Hill, New York (1998)

Do Carmo, F.R.D., Sousa Jr., P.M., Santiago-Aguiar, R.S., De Sant'Ana, H.B.: Development of a new model for biodiesel viscosity prediction based on the principle of corresponding state. Fuel. **92**, 250–257 (2012)

Feitosa, F.X., Rodrigues, M.D.L., Veloso, C.B., Cavalcante, C.L., Albuquerque, J.M.C.G., De Sant'Ana, H.B.: Viscosities and densities of binary mixtures of coconut + colza and coconut + soybean biodiesel at various temperatures. J. Chem. Eng. Data. **55**, 3909–3914 (2010)

Ferrão, M.F., Viera, M.D.S., Pazos, R.E.P., Fachini, D., Gerbase, A.E., Marder, L.: Simultaneous determination of quality parameters of biodiesel/diesel blends using HATR-FTIR spectra and PLS, iPLS or siPLS regressions. Fuel. **90**, 701–706 (2011)

Gülüm, M.: Experimental investigation of the effect of various production parameters on the some fuel properties of produced biodiesels from corn and hazelnut oils, Master's thesis, Karadeniz Technical University, Turkey (2014)

Holman, J.P.: Experimental Methods for Engineers, 7th edn. McGraw-Hill, New York (2001)

Jain, S., Sharma, M.P.: Prospects of biodiesel from Jatropha in India: a review. Renew. Sust. Energ. Rev. **14**, 763–771 (2010)

Joshi, R.M., Pegg, M.J.: Flow properties of biodiesel fuel blends at low temperatures. Fuel. **86**, 143–151 (2007)

Karabektas, M.: The effects of turbocharger on the performance and exhaust emissions of a diesel engine fuelled with biodiesel. Renew. Energy. **34**, 989–993 (2009)

Krisnangkura, K., Yimsuwan, T., Pairintra, R.: An empirical approach in predicting biodiesel viscosity at various temperatures. Fuel. **85**, 107–113 (2006)

Kumar, S., Chaube, A., Jain, S.K.: Critical review of jatropha biodiesel promotion policies in India. Energy Policy. **41**, 775–781 (2012)

Mittelbach, M., Enzelsberger, H.: Transesterification of heated rapeseed oil for extending diesel fuel. J. Am. Oil Chem. Soc. **76**, 545–550 (1999)

Rao, G.L.N., Ramadhas, A.S., Nallusamy, N., Sakthivel, P.: Relationships among the physical properties of biodiesel and engine fuel system design requirement. Int. J. Energy Environ. **1**, 919–926 (2010)

Serdari, A., Fragioudakis, K., Kalligeros, S., Stornas, S., Lois, E.: Impact of using biodiesels of different origin and additives on the performance of a stationary diesel engine. J. Eng. Gas Turbines Power. **122**, 624–631 (2000)

Swaminathan, C., Sarangan, J.: Reduction of NOx emission using EGR in biodiesel fueled engine with ether based additives, Sae Technical Paper. doi:10.4271/2009-01-1793 (2009)

Verduzco, L.F.R., Flores, B.E.G., Rodriguez, J.E.R., Jacob, A.D.R.J.: Prediction of the density and viscosity in biodiesel blends at various temperatures. Fuel. **90**, 1751–1761 (2011)

Yuan, W., Hansen, A.C., Zhang, Q.: Predicting the physical properties of biodiesel for combustion modeling. Am. Soc. Agric. Eng. **46**, 1487–1493 (2003)

Yusuf, N.N.A.N., Kamarudin, S.K., Yaakub, Z.: Overview on the current trends in biodiesel production. Energy Convers. Manag. **52**, 2741–2751 (2011)

Sankey and Grassmann Diagrams for Mineral Trade in the EU-28

Guiomar Calvo, Alicia Valero, and Antonio Valero

1 Introduction

Raw materials, particularly fossil fuels and non-fuel minerals, are crucial to maintain the European Union's economy. Despite having a rich endowment of mineral deposits, producing 1.2% and 1.4% of the world level needs of iron and aluminum respectively (British Geological Survey 2011), European countries depend on raw material secure supply. As this is a critical issue, in November 2008 the European Commission published the Raw Materials Initiative to establish the raw material strategy along with a list of actions that the member states should carry out (European Commission 2008).

While historically the importance of fossil fuels has been regarded as a priority issue, non-fuel minerals, which are essential both for electronic equipment and for the development of renewable energies, have only gained importance in the recent years. Since minerals are a non-renewable resource that is linked to geological features of the ground, it is important to analyze its use and the mineral trade between the different countries.

Material flow analysis has demonstrated to be a key tool to monitor and quantify the use of natural resources. Usually this analysis of material use, consumption and trade is carried out through aggregated indicators that take into account minerals as a whole, sometimes differentiating at most industrial minerals, construction minerals and fossil fuels (Weisz et al. 2006; Schandl and Eisenmenger 2006; Steinberg et al. 2010; Bruckner et al. 2012; Kovanda et al. 2012). Nevertheless it is important to have disaggregated studies to observe the impact and supply risk of the different

G. Calvo (✉) • A. Valero • A. Valero
Research Centre for Energy Resources and Consumption (CIRCE), Campus Río Ebro, Mariano Esquillor Gómez, 15, 50018 Zaragoza, Spain
e-mail: gcalvose@unizar.es

© Springer International Publishing AG, part of Springer Nature 2018

F. Aloui, I. Dincer (eds.), *Exergy for A Better Environment and Improved Sustainability 2*, Green Energy and Technology,
https://doi.org/10.1007/978-3-319-62575-1_7

materials (Achzet and Helbig 2013) and so provide valuable input for decision-making processes aiming at improving the sustainable use of raw materials (Tiess 2010; Tiess and Kriz 2011; Marinescu et al. 2013).

This chapter undertakes an analysis of the mineral trade in the European Union (EU-28) from 1995 to 2012. This analysis is done firstly using tonnage as a yardstick, accounting for the tons of input (production and imports) and output materials (recycling, exports and consumption). Then, the same analysis is carried out using exergy, particularly the so-called exergy replacement costs, which is explained in the next section. This allows us to compare both methodologies and bring out the significant differences regarding reliability and representativeness. The final aim is to observe the trend and evolution of the mineral trade in Europe and highlight which of the analyzed minerals can be considered critical due to external dependency.

2 Methodology

The analysis of the mineral trade of Europe is going to be firstly undertaken in tonnes. Domestic extraction, export and import data for the 1995–2012 period have been obtained from the British Geological Survey European Mineral Statistics (2014), completed with data from United States Geological Survey yearbooks of mineral statistics and national services from some European countries. As individual data for recycling rates of each of the member states of the European Union are not available, average recycling rates for several metallic minerals have been obtained from the Recycling Rates of Metals report (UNEP 2011).

In order to assess the mineral depletion more comprehensively, we are going to apply the exergoecology method initially proposed by Valero (1998) to analyze the mineral trade in Europe (EU-28) for both fossil fuels and non-fuel minerals. With this methodology we can evaluate the loss of natural resources through exergy, a property that is based on the second law of thermodynamics and that can be used to measure the quality of a system with respect to a given reference. This methodology is based on calculating the exergy that would be needed to replace a mineral deposit starting from an environment where all the minerals are dispersed in the crust into the initial conditions of composition and concentration found in the mine where it was originally extracted. To perform these calculations we need a model of average dispersed crust, *Thanatia*, a planet that represents a possible state of the Earth where all minerals have been dispersed, all fossil fuels have been consumed and which has specific atmospheric conditions (Valero et al. 2011a, b). This Thanatia model includes a list of minerals with their respective concentration in the crust which delimits the lowest ore grades of the minerals and that can serve as a boundary to our calculations. Therefore, the exergy replacement costs of a mineral can be calculated as the exergy required to restore the minerals from Thanatia into the conditions found in nature with the current available technology. As quality is being taken into account in those calculations, scarcer and difficult-to-extract minerals

(in terms of energy expended) will have a higher weight in the final accounting process as the exergy needed to recover a mineral that is dispersed increases exponentially with scarcity. Accordingly for instance, in the case of limestone, a material that can be easily extracted and that is very abundant in the crust, its exergy replacement costs are 2.6 GJ/ton. If we look at scarcer minerals, such as gold or mercury, these values go up to 583668.4 and 28298.0 GJ/ton, respectively. These numbers provide hints of which minerals would be the most complicated to replace hence also giving information about their quality. Thus, carrying out the analysis using only tonnage can result in biased information since it seems logical that 1 tonne of limestone should not have the same weight in the calculations as 1 tonne of gold in quality terms.

Since reliable and comparable data are not always easy to find, the substances that are included in this study are the following: aluminum, antimony, arsenic, barite, bismuth, boron, cadmium, chromium, cobalt, copper, feldspar, fluorspar, gold, graphite, gypsum, indium, iron ore, lead, limestone, lithium, magnesium, manganese, mercury, molybdenum, nickel, phosphate rock, potassium, selenium, silicon, silver, sodium, tantalum, tin, titanium, uranium, vanadium, wolfram, zinc and zirconium. The exergy replacement costs of these minerals have already been calculated in previous studies (Valero and Valero 2014). As for fossil fuels, their exergy replacement costs can be approximated to their high heating values as once they are consumed and burned they cannot be recovered (Valero and Valero 2012).

To better depict mineral trade, the analysis of EU-28 as a general system is conducted using Sankey and Grassmann diagrams. The main difference between both types of graphic representations is that the first usually depicts energy or material flows of a system with the width of the arrows being proportional to the flow quantity. Grassmann diagrams in turn are essentially the same but represent such flows in exergy units. These types of representations are very visual and can be used to evaluate the evolution of the mineral trade of a country or several countries and also the self-sufficiency and external dependency. Additionally, several dependency indicators based on domestic material consumption will be calculated for the year 2011 in order to evaluate the self-sufficiency and foreign dependency and have a complete picture of mineral trade in the European Union.

3 Mineral Trade in the EU-28

Over the last decades there has been a decreasing tendency in the domestic extraction, especially notable in the case of fossil fuels. In Fig. 1 we have the total mineral extraction of the EU-28 from 1995 to 2012, separated by countries. As it can be seen, the United Kingdom, Spain, Poland, Italy and Germany are historically the main producers of minerals in EU-28.

Regarding non-fuel minerals, Spain, Italy, the United Kingdom and Germany are the main extractors. Limestone accounted for an average of 85.3% of the yearly total non-fuel mineral production, followed by gypsum (8.7%) and salt (4.4%).

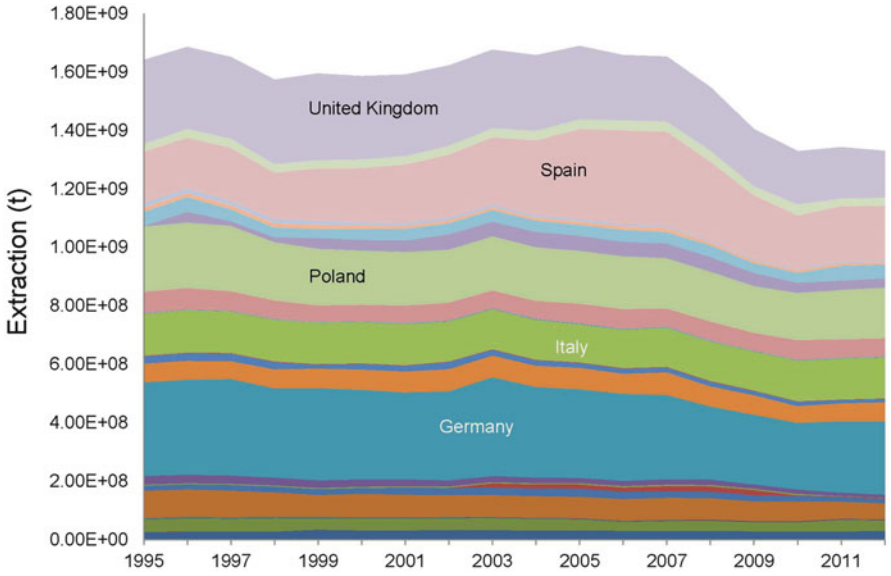

Fig. 1 Tonnes of fossil fuels and non-fuel minerals extracted in Europe from 1995 to 2012 disaggregated by countries

From 2007 onwards the non-fuel mineral domestic production has been decreasing, a change that can be attributed, among other factors, to a combination of resource management improvements and resource efficiency policies but also to the financial crisis which has been affecting the member states.

As for fossil fuels, during the period under consideration, the United Kingdom, France, Germany and Poland were the main European extractor countries. Coal remained the principal fossil fuel extracted, accounting as an average for 66.7% of the total EU-28 fossil fuel yearly production. Still, between 1995 and 2012 the total fossil fuel EU-28 domestic production decreased approximately 28%.

Figure 2 shows a general overview of the imported minerals. Although the total amount of imported materials is increasing, the fluctuations caused by the financial crisis can also be appreciated. Between 2003 and 2004 the total amount of imported fossil fuels increased 27%, but from 2007 onwards there has been a sharp decrease.

Between the years 2001 and 2011, the amount of minerals imported in Europe increased around 35% while the domestic extraction decreased almost 6% during that same period. The substances mainly imported were metallic minerals and fossil fuels, the latter mainly coming from Russia, Norway and North Africa. Even if Europe is rich in natural resources, both domestic production and import values approximately move within the same range, which highlights the importance of imports for the states belonging to the European Community.

Material trade deficit (exports minus imports) was analyzed for the 1995–2012 period. Imports exceed exports during the whole time period, generating a substantial trade deficit. The maximum amount of imported non-fuel minerals was

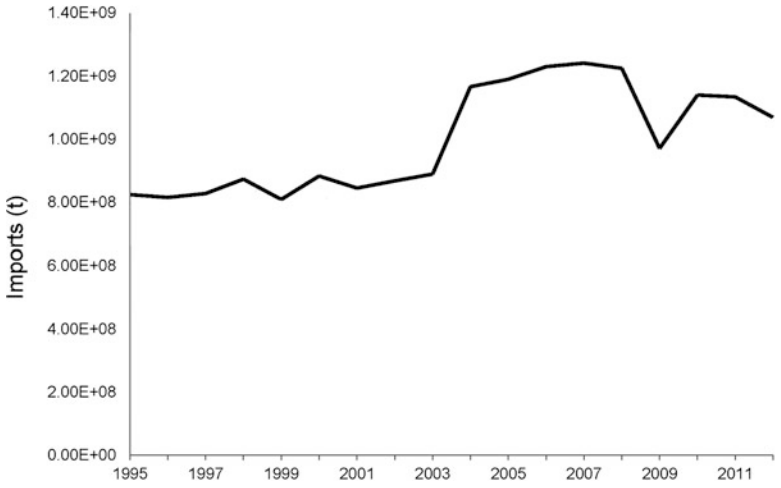

Fig. 2 Total tonnes of fossil fuels and non-fuel minerals imported in Europe from 1995 to 2012

257 million tonnes in 2007 and the maximum exports were 63.3 million tonnes in 2001. On average, exports were equivalent to 23.7% of the imports, and the maximum trade deficit, 210 million tonnes, occurred in 1998.

4 Using Year 2011 as a Case Study

A detailed analysis of the mineral trade in the EU-28 for the year 2011 was made in order to better observe the weight of the different substances. In Fig. 3 we can see the European mineral balance for 2011 expressed in tonnes for the 40 minerals and the three main fossil fuels that were selected in this study.

The general behavior that can be inferred is that European member states mainly imported oil, natural gas and iron. The domestic production consisted of coal and limestone in large quantities and oil, natural gas, iron and potash in lower quantities. Still scarcer minerals, which are usually critical and more important from an economic point of view, here remain hidden because in mass terms they have a considerably lower weight.

As stated before, import dependency for European countries is very high, and we can see that in 2011 approximately 45.8% of the input materials came from other countries. It is also noteworthy that all of the imported and produced minerals ended up being consumed within the European member states' borders, stressing that, at least regarding these substances, Europe is an extremely dependent economy.

An alternative to reducing imported materials lies in recycling, saving both energy consumption and natural resources. The low weight of recycling in Europe is striking: less than 3.2% of the total inputs (domestic production plus imports) were recycled in 2011. Although some countries have higher recycling rates, such

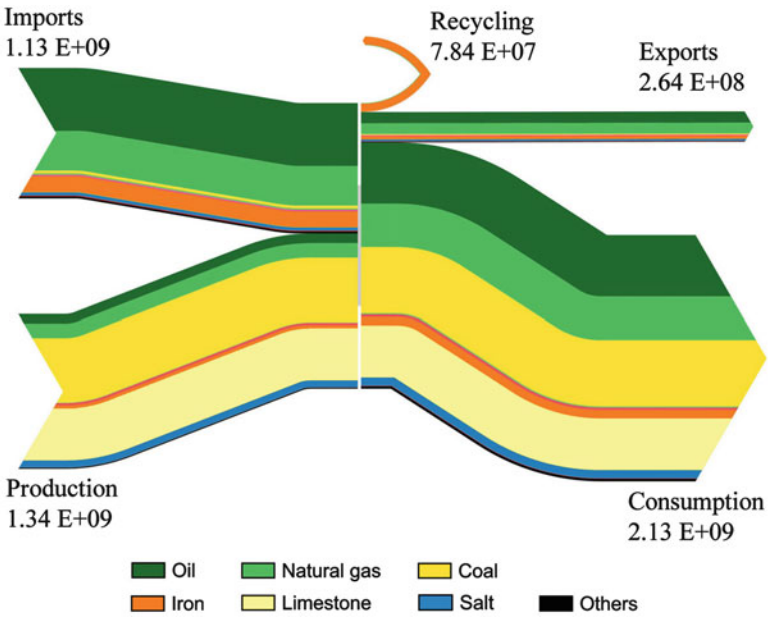

Fig. 3 Sankey diagram for the European mineral balance for 2011(data in tonnes) (Source: British Geological Survey (2014))

as Austria, Germany or Belgium, Europe is still wasting vast quantities of valuable resources and sending them to landfills. Due to low efficiencies in the processing and collection of metal-bearing products that are discarded and because primary materials are often abundant, the end-of-life recycling rates are very low. At world level, of the 60 metals analyzed by the United Nations Environment Programme (UNEP 2011), only 18 had above 50% end-of-life recycling ratios while more than 34 had lower than 1% ratios.

Exports represented 10.7% of the total output and they mainly consist of oil, natural gas and iron. On the other hand, internal consumption in the EU-28 accounted for 86.2%. These data can help emphasize that Europe is a region mainly based on domestic consumption.

In Fig. 4 fossil fuel trade data have been removed from the scenario, so we can specifically focus on non-fuel mineral trade.

If we compare the mineral trade in mass terms and in exergy replacement costs, we can clearly see that minerals have different weight. When expressed in mass terms, limestone and iron are the most traded minerals, accounting for 77.1% of the total input materials. If we express the same data in exergy replacement costs, limestone and iron only represent 10.8%, as they are abundant minerals in the crust and easier to extract. A counter example of limestone is gold, which seemed negligible in mass units but that in exergy replacement costs represents almost 12% of the total imports.

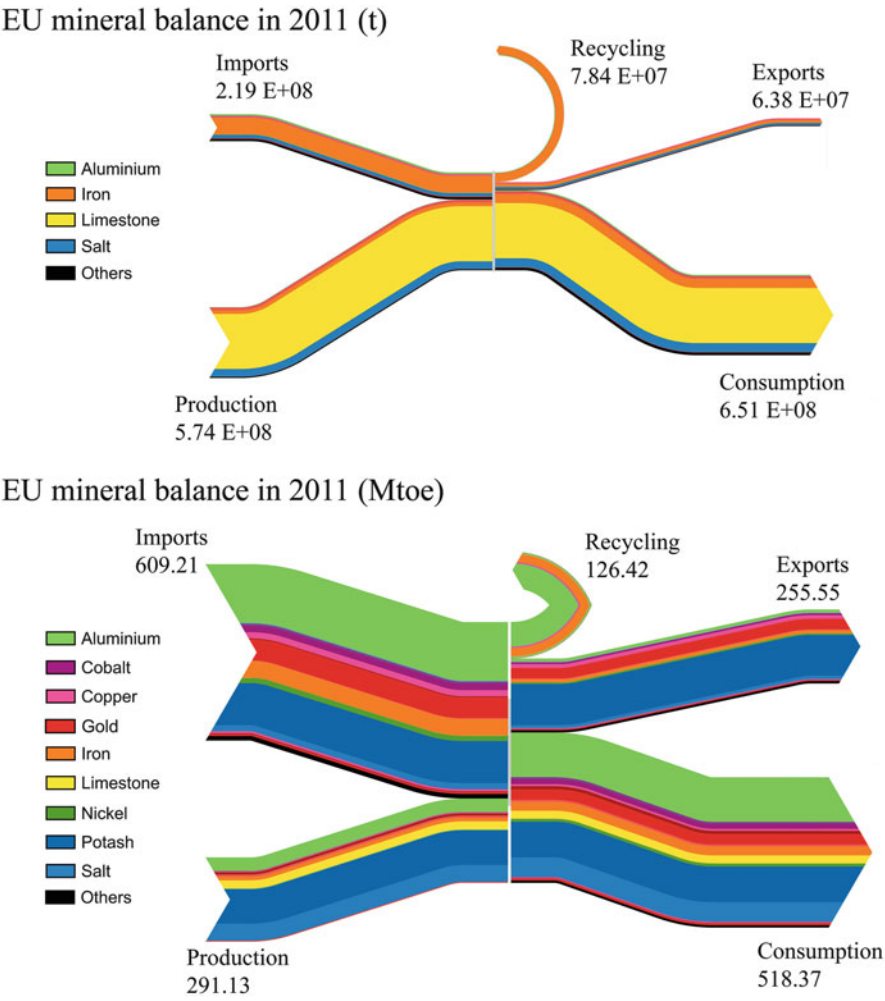

Fig. 4 Sankey and Grassmann diagrams for the European mineral balance for 2011 in tonnes (t) and in exergy replacement costs (Mtoe) for non-fuel minerals

Therefore, with data in tonnes we can display quantities, which can give us a general idea of the mineral trade, but at the same time it also gives biased information as many minerals are not extracted in sufficient quantity to be represented in the graphics. With exergy replacement costs we can evaluate the quality of the minerals, bringing out those that are scarcer or less concentrated in the crust.

In 2014 the European Commission updated the list of critical minerals for the European Union (European Commission 2014), which now includes antimony, beryllium, borates, chromium, cobalt, fluorspar, gallium, germanium, indium, magnesite, magnesium, natural graphite, niobium, PGM, phosphate rock, REE,

silicon and tungsten, of which the vast majority has been taken into account in this study. For this reason, comparing the results in mass terms and in exergy replacement costs becomes fundamental to analyze the mineral trade as scarcer minerals are better represented with the latter analysis.

When evaluating the mineral depletion caused by trade in 2011 in the EU-28, we can see for instance that the internal production of 10 of the 20 minerals considered critical by the EC in its 2014 report accounted for 0.88% of the total production expressed in tonnes and 3.19% when expressed in exergy replacement costs. The critical minerals that were imported from other countries accounted for 5.01% of the total imports expressed in tonnes and 6.74% when expressed in exergy replacement costs.

In 2011 consumption played an important role both in mass terms and in exergy terms, representing respectively 86.2% and 74.5% of the total outputs. What draws our attention is that in tonnes, the percentage corresponding to production (54.2%) is higher than the one corresponding to imports (45.8%), but in the case of exergy replacement costs we have the opposite situation (34.1% and 65.9%). The fact that consumption is always very important is not surprising; what is noteworthy is the reversed importance of production and imports depending on how the resources are being evaluated. If we only add tonnes of minerals the production is higher than imports, but if we take into account the quality of those minerals it is the imports that become more relevant since as stated before, Europe imports scarcer and more valuable minerals (from a physical point of view) than those that are domestically extracted.

5 Mineral Dependency in the EU-28 in 2011

With domestic extraction, imports, exports, consumption and recycling data we can calculate a number of ratios to evaluate several factors of dependency.

The indicator Domestic Material Consumption (DMC) is calculated as follows: DMC = extraction + imports − exports. Proceeding from this information, we can also obtain the ratio of Domestic Extraction to Domestic Material Consumption (DE/DMC), that is, the self-sufficiency ratio. If this value is 1 or more, it means the self-sufficiency ratio is high and thus the country does not need to rely on mineral trade.

We can also obtain the import-to-DMC (I/DMC) and export-to-DMC (E/DMC) ratios, used to evaluate the foreign dependency and trade intensity. These ratios will be calculated using initial data expressed both in tonnes and exergy replacement costs.

In Table 1 we can see the ratios obtained for the case of non-fuel minerals. In this first case the DE/DMC ratio is 0.79 with data expressed in tones and 0.45 with data expressed in exergy replacement costs. If we used only the first value to evaluate external dependency on non-fuel minerals, we could conclude that EU-28 is not very dependent on external supply since it is relatively close to 1. However, there is

Table 1 Ratio between domestic extraction and domestic material consumption (DE/DMC), imports/DMC and exports/DMC for EU-28 for the year 2011 for non-fuel minerals

	DE/DMC	I/DMC	E/DMC
Mass terms	0.79	0.30	0.09
Exergy terms	0.45	0.94	0.40

a 34% difference between these two DE/DMC values. Again, this is mainly due to the relevance in mass terms of the limestone extracted in the EU-28, which was 295 million tonnes or 74.5% of the total mineral extraction in 2011. As construction materials are hardly traded due to their lower price and abundance, putting them at the same level as scarcer minerals can mask the real situation. Therefore, the ratio with data expressed in tonnes does not truly reflect the situation of external dependency, which is expected to be higher if those materials were removed from the calculations. Using exergy replacement costs we have a better approximation of DE/DMC (0.45) which shows a more accurate value of the EU-28 self-sufficiency.

As for the import and export ratios, I/DMC and E/DMC, we have the opposite situation. These two ratios expressed in exergy replacement costs are higher than when data are expressed in tonnes, which indicates that EU-28 is extremely dependent on foreign trade for non-fuel mineral supply (0.94 in the case of imports and 0.40 for exports).

In Table 2 we can see the ratios obtained for the case of fossil fuels, using data from natural gas, oil and several types of coal. In this case the ratios are not so distant from each other when expressed in tonnes or in exergy replacement costs.

The dependency on imports becomes clear when observing the I/DMC ratio, 0.62 when using data in tonnes and 0.76 when using exergy replacement costs.

As it happens with non-fuel minerals, Europe is also very dependent on fossil fuel supply.

The EU-28 average ratios for DMC, DE/DMC, I/DMC and E/DMC are represented in Table 3.

In Europe there is a large variation between each of the member states regarding size, GDP, economic growth, geology, characteristics of the mining industry, etc. This is why the average ratios obtained must be taken only as a reference. The average self-sufficiency (0.54) and the elevated import dependency (0.77) make clear that Europe must rely on other regions to cover its own needs.

6 Conclusions

In this chapter we have analyzed mineral trade in Europe from 1995 to 2012, using the year 2011 as a case study to obtain several ratios to evaluate self-sufficiency and external dependency.

For the period under consideration, domestic extraction has been decreasing continuously. Especially notable is the case of fossil fuels, which decreased 28%

Table 2 Ratio between domestic extraction and domestic material consumption (DE/DMC), imports/DMC and exports/DMC for EU-28 for the year 2011 for fossil fuels

	DE/DMC	I/DMC	E/DMC
Mass terms	0.52	0.62	0.13
Exergy terms	0.41	0.76	0.17

Table 3 Average EU-28 ratios for the year 2011. Data are expressed in exergy replacement costs

	DMC	DE/DMC	I/DMC	E/DMC
EU-28 average	62.51	0.52	0.73	0.29

between 1995 and 2012. This general decrease can be attributed to emphasis on resource efficiency policies as well as to the financial crisis. With the recent initiatives promoting raw material strategies, increasing recycling rates and creating synergies between industries, these results are expected to improve in the following years.

As shown by the results, Europe mainly extracts construction and bulk materials (limestone, gypsum and salt) and depends on other regions for scarcer minerals and fossil fuel supply. Considering the elevated trade deficit, the average self-sufficiency ratio of the EU-28 (0.54) and the import dependency (0.77), it can be stated that the European Union heavily relies on imports and consumption rather than on domestic production or exports.

As demonstrated by the data presented in this chapter, a conventional Multiple Factor Analysis (MFA) analysis does not truly reflect the real situation of mineral dispersion, as all the minerals, regardless of their quality, are considered at the same level. Thus, applying the exergoecology methodology can be useful for policy makers to obtain more realistic data for the loss of mineral natural capital since it allows for more robust and reliable analysis. It also avoids subjectivity issues associated with monetary assessments and places the focus on scarcer resources. Accordingly, complementing the data in mass terms with exergy replacement costs we can have a better picture about the current situation with the help of Grassmann diagrams. Representing the data with both Sankey and Grassmann diagrams has demonstrated to be a practical way to better differentiate material flows separated by minerals and to assess external dependency.

Acknowledgments We would like to thank Teresa Brown from the British Geological Survey for her assistance for obtaining the historical data.

References

Achzet, B., Helbig, C.: How to evaluate raw material supply risks – an overview. Resour. Policy. **38**, 435–447 (2013)

British Geological Survey: European Mineral Statistics 2007–2011. A Product of the World Mineral Statistics Database. British Geological Survey, Keyworth (2011)
British Geological Survey: European Mineral Statistics 2008–2012. British Geological Survey, Keyworth (2014)
Bruckner, M., Giljum, S., Lutz, C., Svenja Wiebe, K.: Materials embodied in international trade – global material extraction and consumption between 1995 and 2005. Glob. Environ. Chang. **22**, 568–576 (2012)
European Commission: The raw materials initiative – meeting our critical needs for growth and jobs in Europe. Available online at http://eur-lex.europa.eu/LexUriServ/LexUriServ.do?uri=COM:2008:0699:FIN:EN:PDF (2008)
European Commission: Report on critical raw materials for the EU. Report of the Ad hoc working group on defining critical raw materials. Available online at http://ec.europa.eu/enterprise/policies/raw-materials/files/docs/crm-report-on-critical-raw-materials_en.pdf (2014)
Kovanda, J., van de Sand, I., Schütz, H., Bringezu, S.: Economy-wide material flow indicators: overall framework, purposes and uses and comparison of material use and resource intensity of the Czech Republic, Germany and the EU-15. Ecol. Indic. **17**, 88–98 (2012)
Marinescu, M., Alexander, K., Günter, T.: The necessity to elaborate minerals policies exemplified by Romania. Resour. Policy. **38**, 416–426 (2013)
Schandl, H., Eisenmenger, N.: Regional patterns in global resource extraction. J. Ind. Ecol. **10**, 133–147 (2006)
Steinberg, J.K., Krausmann, F., Eisenmenger, N.: Global pattern of material use: a socioeconomic and geophysical analysis. Ecol. Econ. **69**, 1148–1158 (2010)
Tiess, G.: Minerals policy in Europe: some recent developments. Resour. Policy. **35**, 190–198 (2010)
Tiess, G., Kriz, A.: Aggregates resources policies in Europe. Int. J. Environ. Prot. **1**, 63–66 (2011)
UNEP – United Nations Environment Programme: Recycling Rates of Metals: a Status Report. Nairobi: United Nations Environment Programme, 48 pp (2011).
Valero, A.: Thermoeconomics as a conceptual basis for energy-ecological analysis. In: Ulgiati, S. (ed.) Advances in Energy Studies. Energy Flows in Ecology and Economy, pp. 415–444. Musis, Roma (1998)
Valero, A., Valero, A., Gómez, J.B.: The crepuscular planet. A model for the exhausted continental crust. Energy. **36**, 694–707 (2011a)
Valero, A., Agudelo, A., Valero, A.: The crepuscular planet. A model for exhausted atmosphere and hydrosphere. Energy. **36**, 3745–3753 (2011b)
Valero, A., Valero, A.: What are the clean reserves of fossil fuels? Resour. Conserv. Recycl. **68**, 126–131 (2012)
Valero, A., Valero, A.: Thanatia: the Destiny of the Earth's Mineral Resources: a Thermodynamic Cradle-to-Cradle Assessment. World Scientific Publishing Company, Hackensack (2014)
Weisz, H., Krausmann, F., Amann, C., Eisenmenger, N., Erb, K.-H., Hubacek, K., Fischer-Kowalski, M.: The physical economy of the European Union: cross-country comparison and determinants of material consumption. Ecol. Econ. **58**, 676–698 (2006)

Development of Solid Waste Management System for Adana Metropolitan Municipality

Kadir Aydin and Çağrı Ün

1 Introduction

Several categories of waste are discussed in terms of their arisings, treatment, and disposal options. The wastes described in detail are municipal solid waste, hazardous including clinical waste, household hazardous waste, and sewage sludge. Other wastes described are agricultural waste, industrial, construction, and demolition wastes, mines and quarry wastes, power station ash, scrap tires, and end of life vehicles (Williams 2005).

Municipal solid waste is a term usually applied to a heterogeneous collection of wastes produced in urban areas, the nature of which varies from region to region. The characteristics and quantity of the solid waste generated in a region are not only a function of the living standard and lifestyle of the region's inhabitants but also of the abundance and types of the region's natural resources. Urban wastes can be subdivided into two major components; organic and inorganic. In general, the organic components of urban solid waste can be classified into three broad categories: putrescible, fermentable, and nonfermentable. Putrescible wastes tend to decompose rapidly and, unless carefully controlled, decompose with the production of objectionable odors and visual unpleasantness. Fermentable wastes tend to decompose rapidly, but without the unpleasant accompaniments of putrefaction. Nonfermentable wastes tend to resist decomposition and therefore break down very slowly. A major source of putrescible waste is food preparation and consumption.

K. Aydin (✉)
Department of Mechanical Engineering, Cukurova University, Adana, Turkey
e-mail: kdraydin@cu.edu.tr

Ç. Ün
Department of Special Waste Management, Adana Metropolitan Municipality, Adana, Turkey

© Springer International Publishing AG, part of Springer Nature 2018

F. Aloui, I. Dincer (eds.), *Exergy for A Better Environment and Improved Sustainability 2*, Green Energy and Technology,
https://doi.org/10.1007/978-3-319-62575-1_8

As such, its nature varies with lifestyle, standard of living, and seasonality of foods. Fermentable wastes are typified by crop and market debris.

Wastes generated in countries located in humid, tropical, and semitropical areas usually are characterized by a high concentration of plant debris, whereas those generated in areas subject to seasonal changes in temperature or those in which coal or wood is used for cooking and heating may contain an abundance of ash. The concentration of ash may be substantially higher during winter. Regardless of climatic differences, the wastes usually are more or less contaminated with night soil. These differences prevail even in wastes generated in large metropolitan areas of a developing country.

The primary difference between wastes generated in developing nations and those generated in industrialized countries is the higher organic content characteristic of the former. The extent of the difference is indicated by the data in Table 1, in which is presented information relative to the quantity and composition of municipal solid wastes generated in several countries (UNEP 2005).

In the municipal solid waste stream, waste is broadly classified into organic and inorganic. Waste composition is categorized as organic, paper, plastic, glass, metals, and "others." These categories can be further refined; however, these six categories are usually sufficient for general solid waste planning purposes. Table 2 describes the different types of waste and their sources.

An important component that needs to be considered is "construction and demolition waste" (C&D), such as building rubble, concrete, and masonry. In some cities this can represent as much as 40% of the total waste stream.

Figure 1 shows the MSW composition for the entire world in 2009. Organic waste comprises the majority of MSW, followed by paper, metal, other wastes, plastic, and glass. These are only approximate values, given that the data sets are from various years (Hoornweg and Bhada-Tata 2012).

Nomenclature

Subscripts	
MSW	Municipal solid waste
EU	European Union
MOEF	Ministry of Environment and Forestry
MEDWP	Medical waste plastic fuel

2 Waste Generation and Management in Turkey

Waste generation and management have been recognized as a priority for Turkey and policies are being developed to overcome existing obstacles. Furthermore, MSW management has been a pressure point for Turkey while being a candidate country for EU accession.

Table 1 Comparison of solid waste characterization worldwide (% wet wt)

Location	Putrescibles	Paper	Metals	Glass	Plastics, rubber, leather	Textiles	Ceramics, dust, stones	Wt (g)/cap/day
Bangalore, India	75.2	1.5	0.1	0.2	0.9	3.1	19.0	400
Manila, Philippines	45.5	14.5	4.9	2.7	8.6	1.3	27.5	400
Asunción, Paraguay	60.8	12.2	2.3	4.6	4.4	2.5	13.2	460
Seoul, Korea	22.3	16.2	4.1	10.6	9.6	3.8	33.4[a]	2000[a]
Vienna, Austria	23.3	33.6	3.7	10.4	7.0	3.1	18.9[b]	1180
Mexico City, Mexico	59.8[c]	11.9	1.1	3.3	3.5	0.4	20.0	680
Paris, France	16.3	40.9	3.2	9.4	8.4	4.4	17.4	1430
Australia	23.6	39.1	6.6	10.2	9.9	–	9.0	1870
Sunnyvale, California, USA	39.4[d]	40.8	3.5	4.4	9.6	1.0	1.3	2000

[a]Includes briquette ash (average)
[b]Includes "all others"
[c]Includes small amounts of wood, hay, and straw
[d]Includes garden waste

Table 2 Types of waste and their sources

Type	Sources
Organic	Food scraps, yard (leaves, grass, brush) waste, wood, process residues
Paper	Paper scraps, cardboard, newspapers, magazines, bags, boxes, wrapping paper, telephone books, shredded paper, and paper beverage cups. Strictly speaking paper is organic, but unless it is contaminated by food residue, paper is not classified as organic
Plastic	Bottles, packaging, containers, bags, lids, cups
Glass	Bottles, broken glassware, light bulbs, colored glass
Metal	Cans, foil, tins, nonhazardous aerosol cans, appliances (white goods), railings, bicycles
Other	Textiles, leather, rubber, multi-laminates, e-waste, appliances, ash, other inert materials

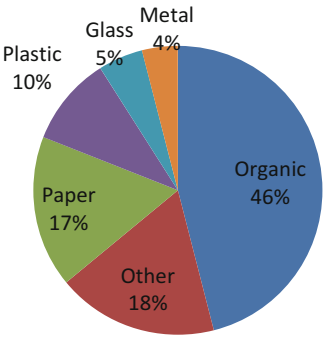

Fig. 1 Global solid waste composition (2009)

Environment Law No 2872 was rectified on 9 August 1983 and was amended in 1988 and 2001 and modified by Law No: 5491 on 26.04.2006. This Framework law aimed protection and improvement of environment in line with the sustainable protection and development principles; it puts forward the rules and principles for environmental protection, defines the responsible and authorized institutions and organizations, determines the processes for the implementation, and establishes punishments for improper acts and liabilities of the concerned within the framework of the principle "polluter pays." It also emphasized the efficient use of natural resources. Environmental Protection Institutes were established later by the year 1989 to ensure the environment law is implemented successfully. The law also paved the way for the establishment of provincial environment boards to oversee environmental protection in their respective regions.

In its 3rd section, the law prohibits disposal of all types of waste and scraps into recipient environment unless necessary precautions have been taken, determined by specific regulations. Environment-friendly technologies must be used during all kinds of activities so as to efficiently use natural resources and energy, which also means reduction of waste production at source and recycling of waste. The law also determined the status and procedure for protected areas and defines penalty mechanism for those who do not comply with the standards.

Regulation on Solid Waste Control was approved on 14 March 1991 (No 20814) and was later amended in 1991, 1992, 1994, 1998, 1999, 2000, 2002, and finally on 5 April 2005 (No 25777). The general framework of waste management system requires the reduction of waste generation as far as possible, separation of recoverable waste at source and recycling the valuable wastes and disposal of nonrecyclable wastes by means of environment-friendly methods. The purpose of this regulation is to forbid all waste management activities posing a threat to the environment. It also aimed at the protection of natural flora and fauna.

This regulation provides general information about different types of wastes like packaging waste, construction and demolition waste, waste sorting, waste transport and disposal, as well as information about landfills and incineration. However, each of these components is governed by a specific regulation for itself.

Solid waste collection and management is one of the most significant local public services. The manner in which such services are delivered is of utmost importance for public health as well as for the protection of the environment. As per the below laws and regulations, liabilities for the collection, transportation, recycling, and disposal of solid wastes are entrusted to the municipalities and metropolitan municipalities.

The By-Law on Solid Waste Control is the first important step toward successful waste management in Turkey. Although it is shown to have some shortcomings in its implementation, the MSW management system has been improved by new studies and new regulations. The main reasons for the shortcomings can be identified as:

- Waste management systems development was not a priority policy area.
- Duties and powers are distributed among many institutions and organizations, with inadequate coordination and cooperation among them.
- The fees and taxes collected in return for services were inadequate.
- The infrastructure (facilities and the existing technical capacity) was limited and the majority of facilities were in need of modernization.

According to the Metropolitan Municipality Law (10.7.2004, 5216) and the Municipality Law (3.7.2005, 5393), sole responsibility for the management of municipal waste falls on the municipalities. They are responsible for providing all services regarding collection, transportation, separation, recycling, disposal, and storage of solid wastes, or to appoint others to provide these services. Nevertheless, while fulfilling their duties in collecting and transporting the solid waste to a great extent, they do not show the required level of activity and attention in solid municipal waste management. The great majority of solid waste in the country is still not being disposed in accordance with the legislation. This situation has been improving by newly adopted management perspectives.

It has been reported that 54% of household waste is disposed in sanitary landfill sites, while the remaining 44% is dumped into dumpsites, according to the Turkish Statistical Institute. 2% was reported as either undergoing biological treatment or disposed of by other methods. The number of sanitary landfills is increasing rapidly in Turkey, as in 2003 there were 15 sanitary landfills, whereas in the 3rd quarter of

2012 this number has increased to 68. There are references in the literature to an informal recycling sector which could be responsible for up to 30% of MSW material recycling. But there is no information on the current situation concerning this informal recycling practice. Regarding the situation around packaging waste, an important part of MSW, the Turkish Ministry of Environment and Urbanization has provided the following information.

The first particular regulation on packaging waste control came into force in 2004 with the "By-Law on Control of Packaging Waste" and was revised in August 2011. The aim of the by-law is to minimize the generation of packaging waste and to also increase the rate of recycled packaging waste which cannot be avoided within the method of production. The regulation also includes principles and standards for packaging waste to be collected separately at its source, then sorted and transported within a certain system. Institutions and suppliers who are not members of authorized organizations are obliged to recover packaging waste. Recycling targets are given to authorized institutions and suppliers with this by-law. The number of economic operators registered to the system is increasing rapidly in Turkey, from 350 in 2003 to 15,192 in 2012.

The Turkish Ministry of Environment and Urbanization gives licenses to collection, separation, and recycling facilities. Whereas there were only 28 licensed facilities in 2003, this number increased to 562 in 2012. Development plans are the main tools for the coordination of public policy in Turkey and they form the basis of policy documents on solid waste. There have been a number of National Waste Management Plans covering the period 2009–2013. The main aim of the Plan is to determine national policies and the decision-making structure for the preparation of detailed waste management plans for separate waste streams. The latest plan was made with the aim of fulfilling criteria according to the EU harmonization process.

Finally, in 2008, the "By-law on General Principles of Waste Management" (05.07.2008, 2697) set the framework for waste management in Turkey from waste generation to disposal so that the procedures are followed in an environmentally sound way (Bakas and Milios 2013).

The Turkish Ministry of Environment and Urbanization has carried out various regional fieldworks in order to determine the domestic waste composition of households in Turkey in addition to solid waste surveys sent to cities that are representative of Turkey. The outcome of these studies, municipal waste composition in Turkey, is shown in Fig. 2 (Anonymous 2014).

3 Waste Management of Adana Municipalities

Adana Province is located at the Mediterranean Sea Region among the 35–38° northern latitude and 34–36° eastern longitude. The surface area is 14,030 km^2 and the altitude is approximately 23 m. The province has a 160 km coastline on the Mediterranean Sea. It comprises 15 districts, 55 municipalities, and 517 villages. The forest land in the province forms approximately 39% of the total area. Total

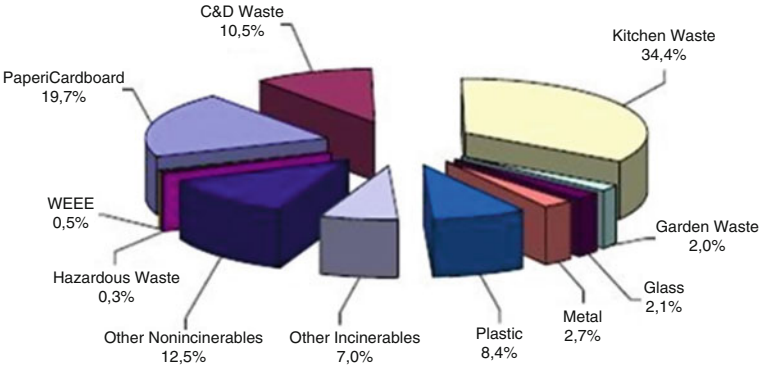

Fig. 2 Composition of domestic wastes in Turkey

meadow land in the region is equal to 3% of the total area. Various types of agricultural practices are performed in the region, total agricultural land is equal to 38% of the total area, and 19% of the total area is used for other purposes.

With the construction of Seyhan Dam and improvements in agricultural techniques, there was an explosive growth in agricultural production during the 1950s. Large-scale industries were built along D-400 state road and Karataş road. Service industry, especially banking, also developed during this period.

Adana is the marketing and distribution center for Çukurova agricultural region, where cotton, wheat, corn, soy bean, barley, grapes, and citrus fruits are produced in great quantities. Farmers of Adana produce half of the corn and soy bean in Turkey. 34% of Turkey's peanuts and 29% of Turkey's oranges are harvested in Adana. Most of the farming and agricultural-based companies of the region have their offices in Adana.

Adana has been the agricultural and economical center of attention. As one of the most fertile plains in Turkey, Çukurova produces sunflower, olive, corn, citrus (orange, mandarin, and lemon), kiwi, sugarcane, rice, soy bean, cotton, grape, peanut, almond, melon, loquat, etc. The economy of the city is generally based on agriculture and stockbreeding. Since land and climate structures are convenient, all kinds of agricultural produce are grown. Irrigated farming is done in a 49,330 ha section of total agricultural land. Olive, grain, tomatoes, pepper, tobacco, corn, sugar beet, cotton, melon, watermelon, and peach are the main produce that are grown.

According to the new Metropolitan Municipalities Law No. 6360, after the March 2014 elections, the service area of Adana Metropolitan Municipality has been expanded to cover the entire geographical area of Adana. Adana Metropolitan Municipality has to collect, transport, and dispose of solid wastes produced by its 2,149,260 people. Adana Metropolitan Municipality collects on an average 554,139.06 tons per year of solid wastes and 2,831.79 tons per year of medical wastes, excluding Yedigöze Union. The seven municipalities and their villages of Yedigöze Union also collect 94,285 tons/year of solid wastes. About 42.5% of this

waste was collected from Center of Ceyhan municipality, 40.5% from Center of Kozan municipality, 7.5% from the Center of İmamoğlu municipality, 4.5% from Center of Yumurtalık municipality, 1.9% from Center of Feke municipality, and 1.6% from Center of Saimbeyli and Aladağ municipalities (Turkstat 2013). All solid wastes collected from Adana Metropolitan Municipality, except Yedigöze Union, were transported to Adana Metropolitan Municipality Landfill Site for recycling and disposal. Solid wastes collected from Yedigöze Union are disposed of in uncontrolled dumping areas, except Ceyhan that transfers its waste to Adana Landfill site using the transfer station in Ceyhan, situated in each district. All medical wastes collected from Adana Metropolitan Municipality including Yedigöze Union are transferred to the Adana Metropolitan Medical Waste Sterilization Unit, which is located in Adana Metropolitan Municipality landfill. After sterilization, all medical waste is disposed of at the sanitary landfill of Adana as nonhazardous waste (Draft Master Plan for Yedigöze Union 2014) (Fig. 3) (Tables 3, 4, 5, and 6).

The average compositions of solid wastes in Adana Metropolitan Municipality are 60–64.5% organic wastes, 8.07% plastic materials, 2.42% papers, 0.25 metals, 1.87% glasses, and 22–25% others (tire, leather, textile wastes, ash, stone, and soil). All organic wastes are transferred to the dry plug flow anaerobic digestion with gas exploitation, followed by composting after separation process. 22,604,832 Nm^3 per year landfill gas is produced from the organic wastes and the landfill gas is converted to 2,712,580 kW of electricity per year by gas engines. 249,318 tons per year of composts is also produced from the organic wastes. 68,928,799 kg medical wastes were collected from 1449 health institutions in Turkey in 2012. 46% of medical wastes were sterilized and disposed of at a controlled landfill site, 28% of medical wastes were not sterilized and were disposed of at a controlled landfill site, 16% of medical wastes were sterilized and disposed of at municipal dumping site, 1% of medical wastes were not sterilized and were disposed of at municipal dumping site, and 8% of medical wastes were disposed of in an incinerator. 2,959,837 kg medical wastes were collected from 26 health institutions in Adana in 2012 and nearly all medical wastes in Adana were sterilized and disposed of at Adana Metropolitan Municipality dumping site.

The Yedigöze Union currently (2014) has a population of 386,848 inhabitants including seven districts: Ceyhan, Kozan, İmamoğlu, Yumurtalık, Saimbeyli, Feke, and Aladağ.

The 7 municipalities and their villages in Yedigöze Union also collect 94,285 tons/year of solid wastes. About 42.5% of this waste was collected from Center of Ceyhan municipality, 40.5% from Center of Kozan municipality, 7.5% from the Center of İmamoğlu municipality, 4.5% from Center of Yumurtalık municipality, 1.9% from Center of Feke municipality and 1.6% from Center of Saimbeyli and Aladağ municipalities. All solid wastes collected from Adana Metropolitan Municipality, except Yedigöze Union, were transported to Adana Metropolitan Municipality Landfill Site for recycling and disposal. Solid wastes collected from Yedigöze Union are disposed to uncontrolled dumping areas, except Ceyhan that

Fig. 3 Location of Yedigöze Union cities in Adana

transfers its waste to Adana Landfill site using the transfer station in Ceyhan, situated in each district.

The 7 municipalities and their villages in Yedigöze generated 156,031 tons/year of waste in 2012. About 60.4% of this waste was generated in urban locations and 39.6% was generated in rural locations. About 36.4% of this waste is generated from middle income, 12.4% from high income, 39.6% from rural locations, 7.2% from low income, 2.9% from the commercial strata, and 1.5% from the tourist strata. The population of Yedigöze is affected during the summer season; therefore, waste generation is affected as well. The average per capita waste production in Yedigöze Union was 0.98 kg/inhabitant*day in 2012 (Draft Master Plan for Yedigöze Union 2014).

Table 3 Waste composition for Yedigöze Union in 2012, (tonnes)

Material category	High income	Middle income	Low income	Commercial	Rural	Tourism	Total (ton)
Organic	11,439	32,566	6523	2046	35,396	1245	89,214
Kitchen/ Cant. Waste	11,041	30,999	5208	1510	28,189	1145	78,092
Garden/ Park Waste	398	1567	1315	536	7207	100	11,123
Wood	32	247	26	10	137	6	458
Paper/ Cardboard	1689	4564	440	776	2520	272	10,261
Paper	1037	2626	301	479	1716	178	6338
Cardboard	651	1938	139	296	804	94	3922
Glass	488	1534	148	350	816	90	3426
Plastics	1929	5254	613	569	3428	257	12,051
Textiles	297	2273	391	90	2157	60	5267
Metals	63	274	23	30	127	7	525
Hazardous Waste	158	248	101	25	555	18	1105
Composites	184	410	73	33	396	23	1119
WEEE	4	18	6	7	34	0	69
Other Composites	180	392	67	26	362	23	1050
Inert Materials	170	373	1324	94	7535	26	9521
Other Categories	2502	4798	685	193	3779	307	12,264
Fine $<$ 10 mm	462	4178	911	280	4899	89	10,820
Total	19,411	56,719	11,259	4497	61,745	2400	156,031

4 Experimental Facility

4.1 Setup

In this study, a pilot cracking reactor was designed and used for thermal cracking. The reactor consists of a heat exchanger, a PT 100 type thermocouple in order to measure the variation of temperature inside the reactor, a digital temperature indicator, a filler cap, a drain cover, and a manometer. Stainless steel number 316 L is used as the main material for the reactor manufacture. Figure 4 shows the technical drawing of the reactor.

Hospital disposals, like PP and PVC syringes, infusion sets, latex medical gloves, blood, and diffusion bags, were collected from Adana State Hospitals (Fig. 5).

Firstly, medical waste plastics were dried, triturated, and loaded into the thermal cracking reactor. The reactor was heated up to the starting temperature of reaction;

Table 4 Generation rate forecast for Yedigöze Union 2012–2045

Material category/year	2012	2015	2025	2045
Organic waste	199.1	207.1	211.0	220
Biodegradable kitchen/Cant. waste	174.3	181.8	186.7	198.4
Biodegradable garden/Park waste	24.8	25.4	24.3	21.6
Wood	1.0	1.1	1.1	1.2
Paper/cardboard	22.9	24.9	29.3	41.9
Paper	14.1	15.5	19.0	28.7
Cardboard	8.8	9.3	10.3	13.2
Glass	7.6	8.0	8.5	9.6
Plastics	26.9	29.9	38.1	62.5
Textiles	11.8	12.2	12.4	12.8
Metals	1.2	1.2	1.4	1.7
Hazardous waste	2.5	2.6	2.7	2.9
Composites	2.5	2.6	2.7	3.0
WEEE	0.2	0.2	0.2	0.3
Other composites	2.3	2.4	2.5	2.7
Inert materials	21.3	21.4	19.5	15.2
Other categories	27.4	29.9	36.0	53.3
Fine < 10 mm	24.2	23.0	17.6	10.3
Total	**348.3**	**364.1**	**380.4**	**405.6**

Table 5 Medical waste generation and management in the Yedigöze Union, 2012

District	Medical waste (tonnes)	Medical waste collection, transport and disposal
Ceyhan	146	Collected by ITC and, after sterilization, disposed of in Adana Metropolitan Municipality Sanitary Landfill
Kozan	109	
İmamoğlu	28	
Yumurtalık	7	
Saimbeyli	5	
Feke	6	
Aladağ	6	
Total	**307**	

Table 6 Existing dumpsites in Yedigöze Union

No. district ownership	No. district ownership	No. district ownership
1	Ceyhan	Transfer Station, No Dumpsite
2	Yumurtalık	Treasury
3	Kozan	Treasury
4	İmamoğlu	Treasury
5	Aladağ	Forest
6	Feke	Treasury
7	Saimbeyli	Treasury

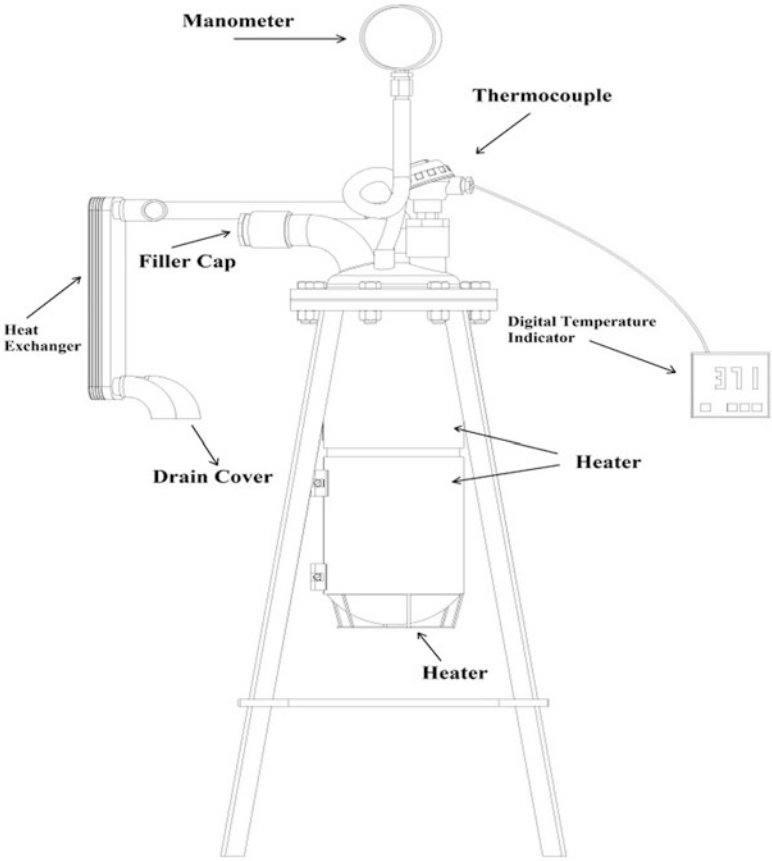

Fig. 4 Technical drawing of reactor

Fig. 5 Medical waste plastic samples

Fig. 6 Distilled medical waste plastic fuel samples

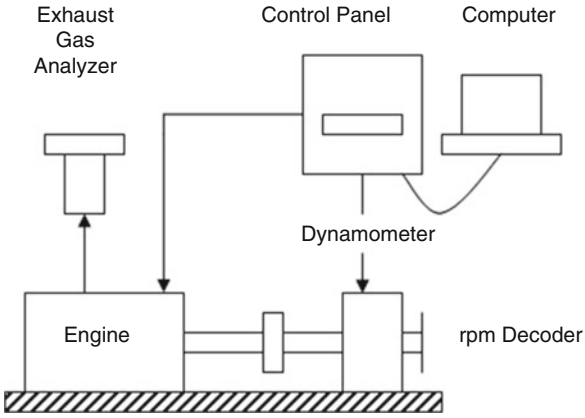

Fig. 7 Experimental setup

subsequently the reaction was started and continued between 450 °C and 475 °C. The reaction was carried out for 1.5 h. During the thermal cracking reaction, the gaseous phase formed, and then the gaseous phase was transformed to the liquid form by using plate type heat exchangers. The product was distilled into a drain cab and the final product was taken from the cab. Distilled medical waste plastic fuels are shown in Fig. 6.

In this study, three different medical waste plastic fuel (MEDWP) blends were prepared (10% Medical Waste Plastic Fuel + 90% Diesel Fuel, 20% Medical Waste Plastic Fuel + 80% Diesel Fuel, and 50% Medical Waste Plastic Fuel + 50% Diesel Fuel). The blends have been analyzed by the standards of ASTM test methods. At the engine experiments, Mitsubishi 4D34-2A type four stroke-four cylinder diesel engine, which has a 3907 cc engine volume, 89 kW maximum power at 3200 rpm and 295 Nm at 1800 rpm, was used. Torque and brake power of the engine were measured with a dynamometer. The exhaust emissions were measured by a Testo 350XL gas analyzer (Fig. 7). All experiments were repeated three times.

5 Results and Discussions

5.1 Fuel Properties

Measured fuel properties of MEDWP and its blends are shown in Table 7.

5.2 Engine Performance

Brake power and torque output values of diesel fuel + 10%, 20%, and 50% MEDWP blends are shown in Figs. 8 and 9.

Table 7 MEDWP fuel properties

Properties	Diesel fuel	MEDWP 10	MEDWP 20	MEDWP 50	MEDWP 100
Density (kg/l)	0.830	0.845	0.858	0.894	0.940
Cetane number	55.57	54.52	53.20	51.48	46.58
Pour point (°C)	−16.0	−13	−10.5	−6.0	3.0
Viscosity (cSt)	2.45	2.42	2.41	2.39	2.30
Calorific value (kcal/kg)	11,320	11,105	10,980	10,650	9850
Flash point (°C)	70.5	65.5	65.5	65.5	65.5

Only MEDWP 10 blends met the EN 590 diesel fuel standards

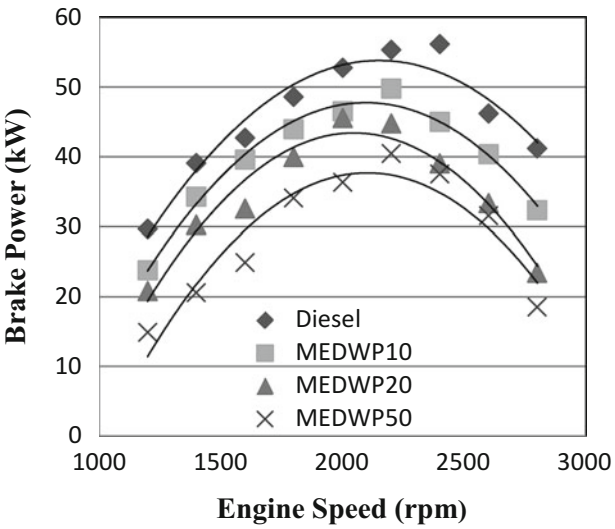

Fig. 8 Brake power outputs of diesel and MEDWP blends

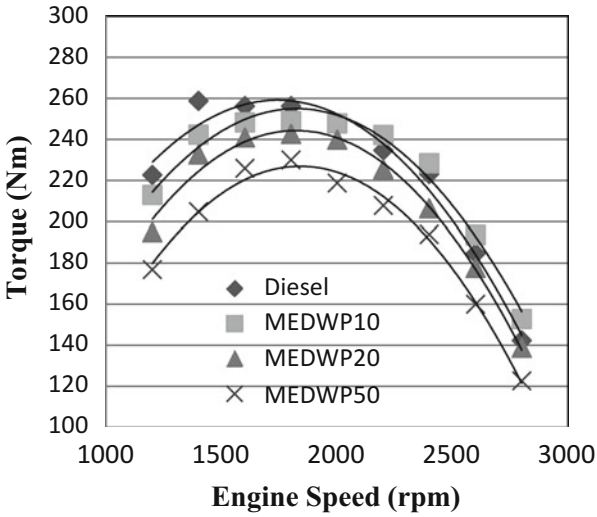

Fig. 9 Torque outputs of diesel fuel and MEDWP blends

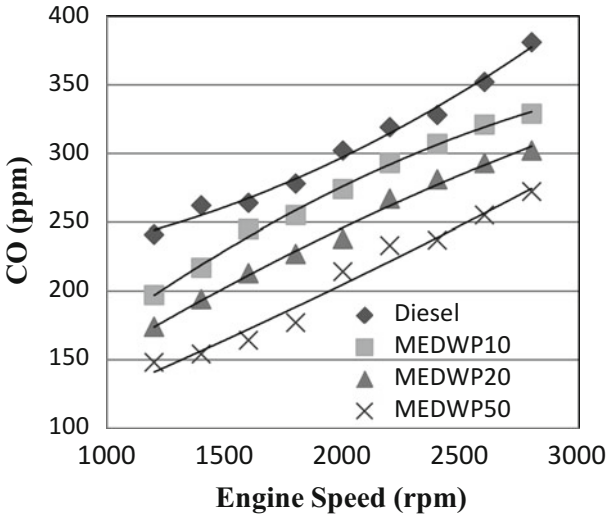

Fig. 10 CO values of diesel fuel and MEDWP blends

5.3 Exhaust Emissions

CO, CO_2, and NO_x values of diesel fuel+ 10%, 20%, and 50% MEDWP blends are shown in Figs. 10, 11, and 12.

CO values of MEDWP blends are lower than diesel fuel because of the lower viscosity of MEDWP (Fig. 10). Lower viscosity increases atomization of fuel injection during injection. CO_2 values of MEDWP blends are also lower because

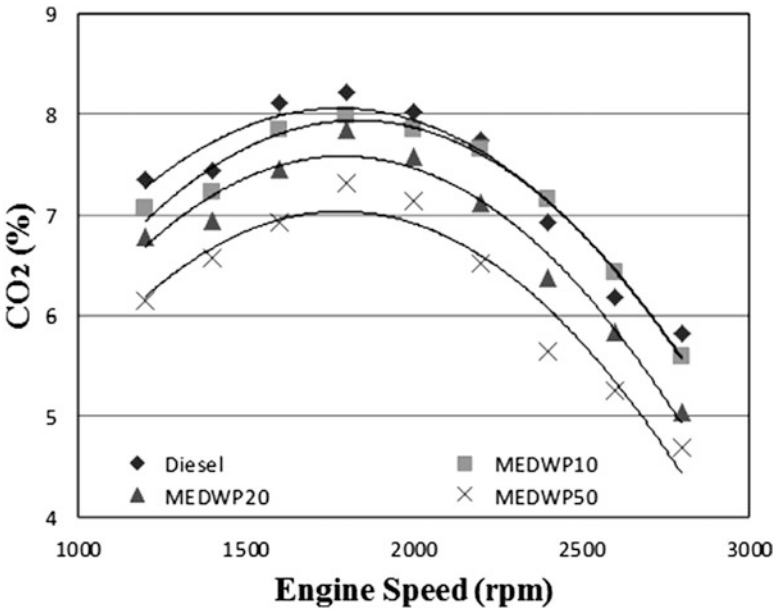

Fig. 11 CO_2 values of diesel fuel and MEDWP blends

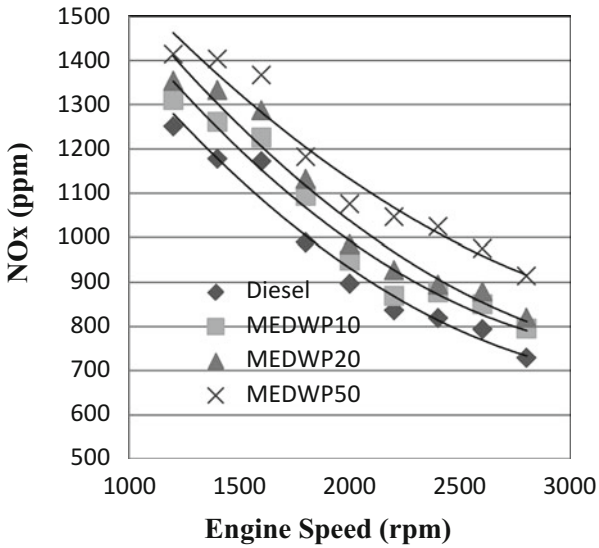

Fig. 12 NO_x values of diesel fuel and MEDWP blends

of lower ratio of Carbon atoms in MEDWP fuels than diesel fuel (Fig. 11). NO_x values of MEDWP blends are higher than diesel fuel because better atomization creates higher combustion temperature in the engine cylinder (Fig. 12). NO_x emissions are only dependent on in-cylinder combustion temperature.

6 Conclusions

The main aim of this study is to develop a new infrastructure for integrated solid waste management for Adana Metropolitan Municipality including Yedigöze Union. New transfer stations have to be located in Yedigöze Union to transfer all collected solid wastes to Adana Metropolitan Municipality Landfill Site for recycling and disposal. All plastic materials including medical wastes collected from Adana Metropolitan Municipality including Yedigöze Union have to be transferred to the thermal and catalytic cracking unit for producing plastic fuel. All medical wastes will be sterilized and converted to plastic fuel without any Medical Waste Sterilization Unit. This solution reduces the medical waste disposal without spending any energy for sterilization. Experiments showed that medical waste plastic fuel can be blended with diesel fuel by the ratio of 10% and can be used for waste collection trucks without any modification. 10% MEDWP fuel addition to diesel fuel also reduces CO and CO_2 emissions (Aydın and Ün 2014). MEDWP fuel addition to diesel fuel results in better environmental impact. Creating an all type waste plastic (municipal and medical) collection infrastructure, producing and using waste plastic fuel are one of the innovative approaches for waste management.

References

Anonymous.: http://www.eea.europa.eu/soer/countries/tr/waste-state-and-impacts-turkey (2014). Accessed 20 Dec 2014

Aydın, K., Ün, Ç.: Production, engine performance and emission studies of medical waste plastic fuel and its blends with diesel fuel. In: Proceedings of Venice 2014, Fifth international symposium on energy from biomass and waste, San Servolo, Venice, 2014

Bakas, I., Milios, L.: Municipal waste management in Turkey. European Environment Agency (2013)

Draft Master Plan for Yedigöze Union.: Technical assistance to prepare integrated solid waste management projects-lot 1. Parsons Brinckerhoff, New York (2014)

Hoornweg D., Bhada-Tata P.: What a waste: a global review of solid waste management. World Bank, Urban Development Series Knowledge Papers, No. 15., (2012)

Turkstat.: Waste statistics of health institutions at turkey. Turkish Statistical Institute Press Releases, Issue: 16117 (2013)

UNEP.: Solid waste management, vol. I, United Nations Environmental Programme, CalRecovery Inc. (2005)

Williams, P.T.: Waste treatment and disposal, 2nd edn, p. 390. John Wiley & Sons, Ltd. (2005)

Regeneration of Peel of Peas (*Pisum sativum*) After Zinc Adsorption

Sabah Menia, Amina Abbaci, and Noureddine Azzouz

1 Introduction

Heavy metal ions have become an ecotoxicological hazard because of their accumulation in living organisms. Wastewater polluted with heavy metals requires a system of treatment that can eliminate these pollutants efficiently (Rao et al. 2006).

There are many methods to remove metal ion solutions including chemical precipitation, ion exchange, adsorption, and membrane filtration. However, it is necessary to have cheap materials to treat large volumes of wastewater (Mazzi 2002).

Natural materials or waste products from industrial or agricultural processes with large adsorptive capacities can be ideal sorbents, since they are abundant in nature and require little processing (Mazzi 2002).

In our study, we have regenerated peels of peas after zinc adsorption; we have used demineralized water, hydrochloric acid, and sodium hydroxide in our process.

Nomenclature

C_o	Initial concentration ($mg.L^{-1}$)
C_e	Equilibrium concentration ($mg.L^{-1}$)
C_f	Final concentration after adsorption ($mg.L^{-1}$)
V	Volume of solution (L)
m	Mass of adsorbent (g)
q_a	Quantity of adsorbed metal on the solid phase ($mg.g^{-1}$)
q_d	Quantity of desorbed metal ($mg.g^{-1}$)

S. Menia (✉) • A. Abbaci • N. Azzouz
University of Jijel, Laboratoire des Interactions Matériaux Energie Environnement, B.P. 98, 18000 Jijel, Algeria
e-mail: sabah.menia@yahoo.fr

© Springer International Publishing AG, part of Springer Nature 2018

F. Aloui, I. Dincer (eds.), *Exergy for A Better Environment and Improved Sustainability 2*, Green Energy and Technology,
https://doi.org/10.1007/978-3-319-62575-1_9

2 Material and Method

2.1 Adsorbent Preparation

Preparation of adsorbents is as follows:

- Cut vegetables into small pieces.
- Put vegetables (10 $g.L^{-1}$) into a beaker and wash them with distilled water for 2 h at a speed of 500 revolutions per minute.
- Dry them in an oven at 80 °C for 24 h.
- Sift with a sieve of 0.05 mm.

2.2 Desorption Procedure

In order to determine the capacity of regeneration of our substrate, we have done tests of adsorption/desorption. We have used the following substances, demineralized water, HCl (0.5 M), and NaOH (0.5 M), by performing five consecutive cycles. For all tests, initial concentration of zinc is equal to 100 $mg.L^{-1}$, mass of substrate is equal to 0.4 g, temperature is of 293 K, and stirring speed is of 500 RPM.

3 Results and Discussions

The quantities of adsorbed and desorbed metals are calculated as follows:

$$q_{\mathrm{a}} = \frac{(C_{\mathrm{o}} - C_{\mathrm{e}}) \times V}{m} \tag{1}$$

$$q_{\mathrm{d}} = \frac{C_{\mathrm{f}} \times V}{m} \tag{2}$$

with

C_o: Initial concentration ($mg.L^{-1}$)
C_e: Equilibrium concentration ($mg.L^{-1}$)
C_f: Final concentration after desorption ($mg.L^{-1}$)
V: Volume of solution (L)
m: Mass of adsorbent (g)
q_a: Quantity of adsorbed metal on the solid phase ($mg.g^{-1}$)
q_d: Quantity of desorbed metal ($mg.g^{-1}$)

Results of our study indicate that hydrochloric acid is the most effective substance for desorption. The maximum amount of zinc desorbed by HCl is equal to

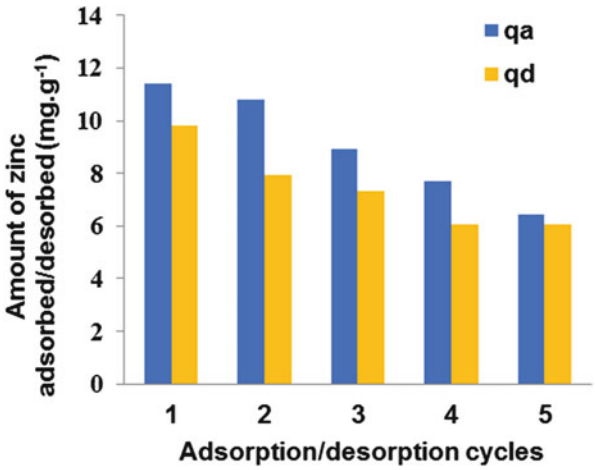

Fig. 1 Regeneration of adsorbent by hydrochloric acid

10 mg.g^{-1} (Fig. 1), whereas it is 5 mg.g^{-1} with NaOH and demineralized water (Figs. 2 and 3). We can deduce that elimination of zinc by peels of peas is done by ion exchange.

According to literature, sulfuric acid is the most effective substance for regeneration of moringa (*Moringa oleifera*) after adsorption of zinc (Kalavathy and Miranda 2010).

4 Conclusions

The objective of our study was to regenerate an adsorbent after elimination of heavy metals; we deduct:

- Hydrochloric acid is the most effective substance for regeneration of our substrate.
- The regeneration does not reach 100%.
- According to the above results, we can confirm that adsorption of zinc on peels of peas is done by ion exchange.

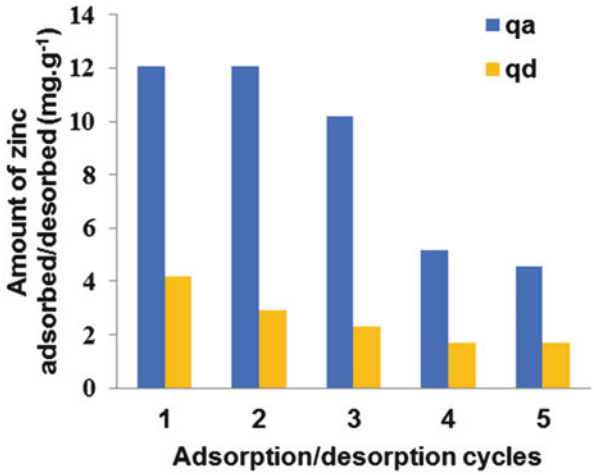

Fig. 2 Regeneration of adsorbent by sodium hydroxide

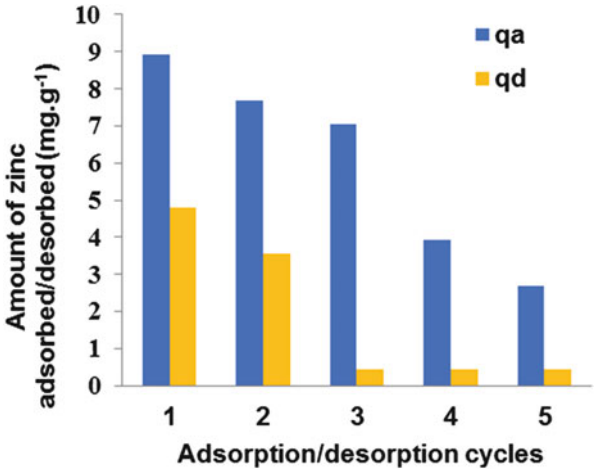

Fig. 3 Regeneration of adsorbent by demineralized water

Acknowledgments The laboratory of interactions materials-energy-environment of the University of Jijel, Algeria, supported this research.

References

Kalavathy, M.H., Miranda, L.R.: *Moringa oleifera*-a solid phase extractant for the removal of copper, nickel and zinc from aqueous solutions. Chem. Eng. J. **158**, 188–199 (2010)

Mazzi, E.: Effectiveness of some low-cost sorbents for treating mixtures of heavy metals in runoff from the first major storm even after the extended dry period. Aquat. Des. Rehabil. CHBE. **465**, 1–75 (2002)

Rao, M.M., Ramesh, A., Rao, G.P.C., Seshaiah, K.: Removal of copper and cadmium from the aqueous solutions by activated carbon derived from *Ceiba pentandra* hulls. J. Hazard. Mater. **B129**, 123–129 (2006)

Diesel Engine Performance and Emission Study Using Soybean Biodiesel Blends with Fossil Diesel

A.K. Azad, M.G. Rasul, B. Giannangelo, and S.F. Ahmed

1 Introduction

Energy demand is increasing gradually throughout the world. More consumption of energy leads to increased environmental pollution (Grossman 2015). The increasing energy demand should be met by eco-friendly, low-emission and renewable sources of energy. The total energy is consumed by different sectors like electricity generation, transport, manufacturing, industrial, commercial, residential sector, etc. The transport sector is one of the faster growing, energy and emission intensive sectors in the world (Azad et al. 2014a). This sector mainly consumes liquid fuels like diesel, gasoline, octane, etc. Biodiesel is one of the sustainable, alternative transport fuels which emit low greenhouse gases (Azad et al. 2015b). It can be produced from different sources and wide arrays of feedstock are available in the world. Biodiesels are produced from biological resources. It can be used directly or by blending in different proportions with fossil diesel. The inventions of different resources of biodiesel are ongoing. New feedstock is being discovered day-by-day to meet the increasing energy demand. One of the main sources of biodiesel production is edible oil such as soybean oil, sunflower oil, mustard oil, canola oil, coconut oil, linseed oil, etc. (Azad et al. 2012; Ameer Uddin et al. 2013; Azad and Uddin 2013). The high oil yield of these edible sources makes it more sustainable and a prospective source of biodiesel. Soybean oil has been selected as a potential source of biodiesel in this study. At present, it is one of the major feedstocks for biodiesel production (Xie and Li 2006). The widely used method for biodiesel conversion is transesterification reaction (Azad et al. 2015a). By this reaction,

A.K. Azad (✉) • M.G. Rasul • B. Giannangelo • S.F. Ahmed
Central Queensland University, School of Engineering and Technology,
Rockhampton, QLD 4702, Australia
e-mail: azad.cqu@gmail.com; a.k.azad@cqu.edu.au

© Springer International Publishing AG, part of Springer Nature 2018

F. Aloui, I. Dincer (eds.), *Exergy for A Better Environment and Improved Sustainability 2*, Green Energy and Technology,
https://doi.org/10.1007/978-3-319-62575-1_10

yielded methyl esters as biodiesel and glycerine as byproducts is produced (Du et al. 2004). After conversion of biodiesel, it can be blended with diesel and used in compression ignition (CI) engine in transport and mining. The study presents the prospect of soybean biodiesel as a sustainable transport fuel in Australia. The physiochemical fuel properties of the biodiesel were determined by ASTM and EN standards. Biodiesel blends like B5, B10, B20 and B50 were used for this experiment. The performance and emission of these blends were tested in a 4-stroke, 4-cylinder diesel test bed engine. ISO 8178–4 international standard was maintained during the experimental study.

Nomenclature

B5	5% biodiesel and 95% diesel (volume %)
B10	10% biodiesel and 90% diesel (volume %)
B20	20% biodiesel and 80% diesel (volume %)
B50	50% biodiesel and 50% diesel (volume %)
BSFC	Brake-specific fuel consumption (*kg*/*h*)
BP	Brake power (*kw*)
CO	Carbon monoxide emission (%)
CO_2	Carbon-di-oxide emission (%)
NO_x	Nitrogen oxides emission (ppm)
HC	Hydrocarbon emission (ppm)
ASTM	American Society for Testing and Materials

2 Soybean Biodiesel

Soybean is one of the widely used biodiesel feedstock in the world. This oil is edible, biodegradable and can be used as biodiesel feedstock. It is also called soy biodiesel. The production of biodiesel involves several steps, namely, seed collection, feedstock preparation, oil extraction, transesterification, blending and is finally used in transport vehicles (Milazzo et al. 2013b). The production of soybean is increasing day by day. World total production rose to 243.9 metric tons in 2010 and is predicted to be 311.1 metric tons in 2020 (Milazzo et al. 2013a; Masuda and Goldsmith 2009). Soybean biodiesel production steps are presented in Fig. 1. There are several methods available for oil extraction. Generally, the mechanical extraction method is used for crude oil extraction due to the simplicity, low cost and quick method. For large-scale production, the n-hexane method is widely used. In transesterification reaction, crude or refined vegetable oil is used to convert biodiesel by alkaline catalyst, heating and pressurizing condition as reaction agents. Glycerine is removed after conversion as the byproduct. The produced methyl ester requires washing, fractionation and drying. This methyl ester is called pure biodiesel which is denoted as B100. It is then ready to blend and use in CI engine.

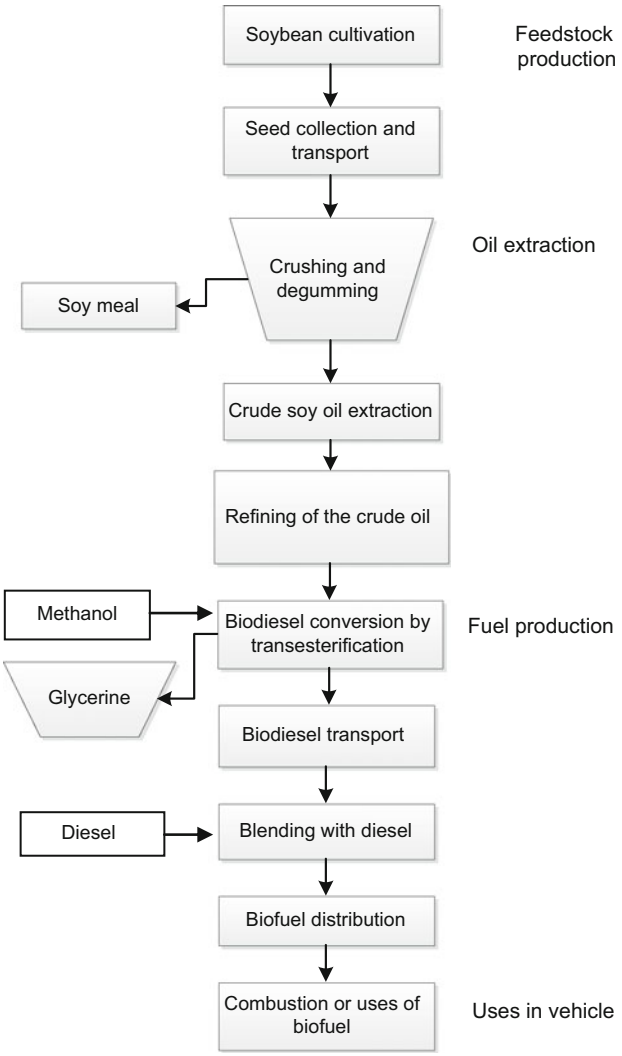

Fig. 1 Biodiesel production steps from soybean oil (Milazzo et al. 2013b)

3 Material and Methods

3.1 Materials

Soybean biodiesel was supplied by National Biodiesel Limited (NBL), Australia. NBL is one of the leading suppliers of premium quality soy biodiesel in Australia. They produce and distribute B100 and biodiesel blends, namely, B5 and B20 in the Australian biofuel market.

3.2 Production of Biodiesel

Virgin oil for CI engine as a substitute of fossil diesel is not practical due to its high viscosity, low volatility, free fatty acid content and polyunsaturated characteristics (Ma and Hanna 1999; Nigam and Singh 2011). To resolve these problems, lots of efforts have been made globally to develop and improve vegetable oil properties as a substitute of fossil fuel. Many scientist and engineers developed many technologies and methods to overcome the problems for biodiesel conversion from different feedstocks (Atabani et al. 2013). There are four methods, namely, thermal cracking, chemical cracking, dilution and transesterification available in the literatures for biodiesel conversion (Atabani et al. 2012, 2013; Balat and Balat 2010; Demirbas 2008; Fukuda et al. 2001; Demirbaş 2002; Lin et al. 2011; Srivastava and Prasad 2000; Canakci and Sanli 2008; Moser 2011; Karmakar et al. 2010; Demirbas and Demirbas 2007; Chauhan et al. 2010). Transesterification is one of the most common and economic techniques for biodiesel conversion where the chemical reaction of alcohol with vegetable oil was used due to its high conversion efficiency with minimum time (Meher et al. 2006; Leung et al. 2010). This technique has been widely used to reduce the viscosity of the vegetable oil and conversion of the triglycerides into ester. The transesterification reaction is presented in Fig. 2.

There are two available ways for transesterification reaction, namely, catalytic transesterification and non-catalytic transesterification (Atabani et al. 2012, 2013; Balat and Balat 2010; Salvi and Panwar 2012; Meher et al. 2006; Agarwal 2007; Balat and Balat 2008; Jain and Sharma 2010; Koh and Mohd. Ghazi 2011; Mahanta and Shrivastava 2004; Murugesan et al. 2009; Singh and Singh 2010; Yusuf et al. 2011; Dias et al. 2012; Berrios and Skelton 2008). In the catalytic reaction, a catalyst is used to commence the reaction. The catalyst enhances the solubility of alcohol and thus increases the reaction rate. The most frequently used process is the catalytic transesterification reaction. Catalytic transesterification method includes acid and base catalyst as well as enzyme catalyst (Royon et al. 2007). The alkaline catalysts include catalysts such as NaOH, $NaOCH_3$, $KOCH_3$, KOH, NaMeO and K_2CO_3 (Atabani et al. 2012; Narasimharao et al. 2007; Kim et al. 2004; Rashid and Anwar 2008; Liu et al. 2008; Dorado et al. 2004; Demirbas 2009a; Suehara et al. 2005). Acid catalyst includes sulfuric, hydrochloride, ferric sulfate, phosphoric and

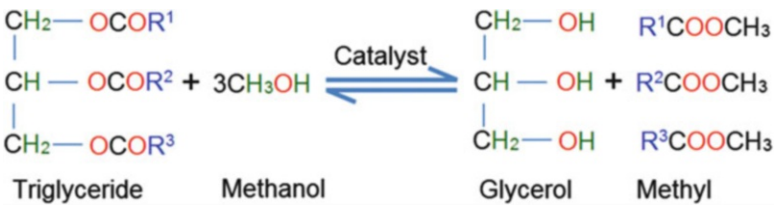

Fig. 2 General equation for transesterification reaction (Demirbas 2009b; West et al. 2008; Hincapié et al. 2011)

Table 1 Fatty acid composition of soybean oil (Milazzo et al. 2013a; Rahman et al. 2014)

Fatty acid	Formula	Molecular weight	Structure	Content (%)
Palmitic	$C_{16}H_{32}O_2$	256	16:0	10
Palmitoleic	$C_{16}H_{30}O_2$	254	16:1	1
Stearic	$C_{18}H_{36}O_2$	284	18:0	4
Oleic	$C_{18}H_{34}O_2$	282	18:1	18
Linoleic	$C_{18}H_{32}O_2$	280	18:2	55
Linolenic	$C_{18}H_{30}O_2$	278	18:3	10
Stearidonic	$C_{18}H_{28}O_2$	276	18:4	2
Saturated				0
Monounsaturated				0
Polyunsaturated				63
Total				100

organic sulfonic acid (Canakci and Van Gerpen 1999; Lotero et al. 2005). Non-catalytic transesterification includes supercritical, alcohol and BIOX co-solvent (Kusdiana and Saka 2004; Demirbaş 2002; Minami and Saka 2006; He et al. 2007).

3.3 *Fatty Acid Composition*

The fatty acid composition is very important to analyze characteristics of soybean biodiesel. This analysis can be performed by using gas chromatography. Literatures reported that there are six main fatty acid compositions in soybean oil. The fatty acid composition, molecular weight, structure and percent of contents are presented in Table 1.

3.4 *Biodiesel Properties*

The physiochemical fuel properties of the biodiesel are very important to analyze before using it in the IC engine. The engine performance and exhaust gas emission depends on the properties of fuel used in the engine. The fuel properties, namely, density, viscosity, calorific value, cetane number, flash point, poor point, etc., were determined using ASTM D6751 and EN 14214 standards and compared with standard biodiesel and petroleum diesel. The properties of the fuels are presented in Table 2. The table shows that almost every property of the fuels is within the acceptable range. The biodiesel has higher density compared with petroleum diesel but it has some good fuel properties like higher flash point, pour point and cloud point.

Table 2 The fuel properties of the soybean biodiesels (Ramadhas et al. 2005; Mofijur et al. 2013)

Properties	Unit	Diesel	Soybean biodiesel	Standard biodiesel
Density at 15 °C	kg/m^3	827.2	885	880
Viscosity	mm^2/s	3.23	4.08	1.9–6.0
Calorific value	MJ/kg	47.5	39.76	–
Cetane number	–	58	47–52	47
Flash point	°C	68.5	69	130
Pour point	°C	0	−3	– 16
Cloud point	°C	5	−4	−3 to −12
Saturated fatty acid	% mass	–	14.0	–
Monoun-SFA	% mass	–	19.0	–
Polyun-SFA	% mass	–	67.0	1.0
Degree of unsaturation	–	–	153	–
Iodine value	g12/100 g	–	151.53	120
Oxidation stability	hr	–	4.40	–
Allylic position equivalent	–	–	152	–
Bis-allylic position equivalent	–	–	75	–
Saponification value	–	–	201.59	–

3.5 *Biodiesel Blending with Diesel*

The soybean biodiesel was blended with ultra-low sulfur diesel in different proportions. The blend samples were prepared by blending 5% biodiesel and 95% diesel denoted as B5, 10% biodiesel with 90% diesel refried as B10, 20% biodiesel and 80% diesel presented as B20, and 50% biodiesel with 50% diesel denoted as B50 for soybean biodiesel.

3.6 *Test Bed Engine Setup*

The Kubota 4 stroke diesel engine was used as test engine for this study. The specification of the engine is Kubota V3300 diesel engine with a bore of 98 mm and a stroke of 110 mm. The rated power output of the engine is 50.7 kW at 2600 rpm and the rated torque is 230 Nm at 1400 rpm. The dynamometer that was used for testing is a Dyno Dynamics engine dynamometer. It works by placing a load on the engine and then measuring the amount of power the engine produces against the load. The dynamometer is coupled with test bed engine controlled by a computer. The schematic diagram of the test bed engine is presented in Fig. 3. Table 3 presents the detail specification of the test engine and its dynamometer.

The exhaust gas analyzer (EGA) that was used during testing is an Andros 6241A, 5 gas analyzer. This EGA takes instantaneous readings of the exhaust gas and can measure carbon monoxide, carbon dioxide and hydrocarbons using a non-dispersive infrared (NDIR) sensor. The EGA can also measure oxygen and

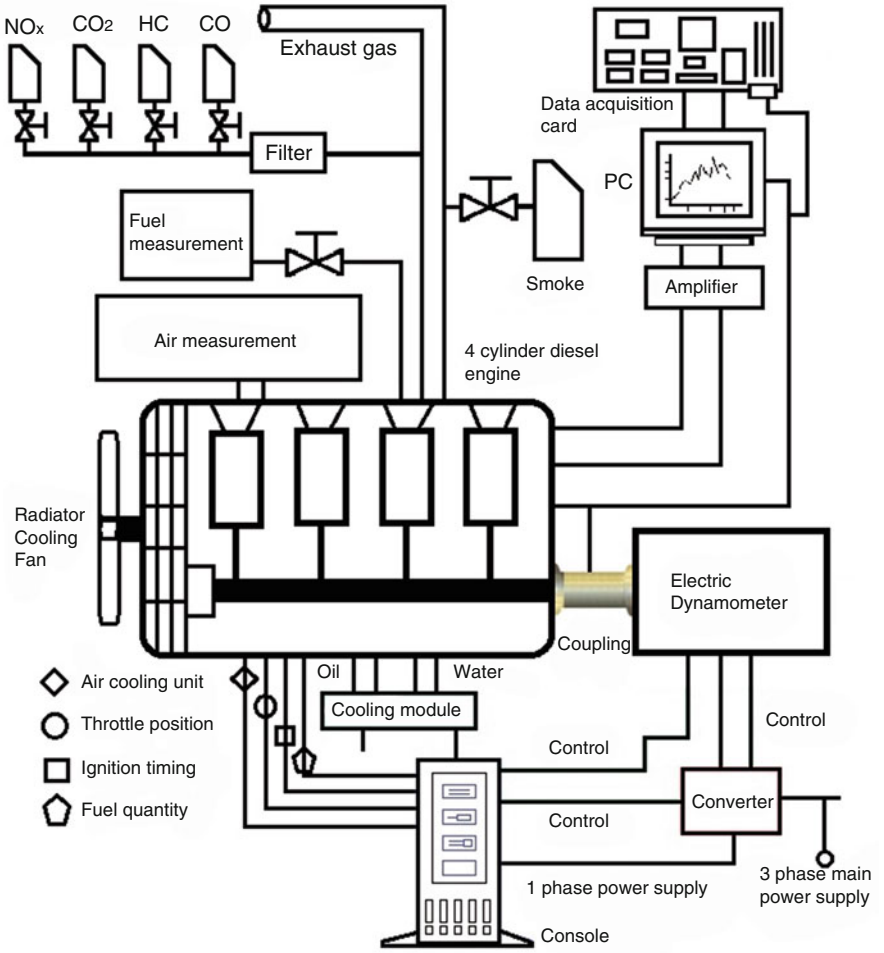

Fig. 3 Schematic diagram of the test bed engine setup

Table 3 The detail specification of the test bed engine

Items	Unit	Specifications
Type	–	Vertical, 4 stroke, liquid cooled
No. of cylinders	–	4
Bore	mm	98
Stroke	mm	110
Total displacement	L	3.318
Combustion type	–	Spherical type (E-TVCS)
Rated speed	rpm	2800
Compression ratio	–	22.6:1
Rated power	kw	53.9
Fuel injection timing	–	16° before TDC
Injection pressure	MPa	13.73

Table 4 The detail specification of the EGA

	Measurement		
Measured gas	Range	Resolution	Accuracy
HC	0–30,000 ppm (n-Hexane)	1 ppm	±4 ppm abs.
CO	0–15%	0.001%	±0.02% abs.
CO_2	0–20%	0.01%	±0.3% abs.
O_2	0–25%	0.01%	±0.1% abs.
NO_x	0–5000 ppm	1 ppm	±20 ppm abs.

Table 5 The ISO 8178–4 test procedure with speed and load

Mode	1	2	3	4	5	6	7	8
Speed (rpm)	Rated speed 2400				Intermediate speed, 1440			Idle speed, 800
Torque (Nm)	180	135	90	18	210	158	105	0
Weight factor	0.15	0.15	0.1	0.1	0.1	0.1	0.1	0.15

nitrogen oxides using an electrochemical sensor. More information like measurement range, resolution and accuracy of the EGA is presented in Table 4.

3.7 Engine Test Method

The international standard ISO 8178–4 C1 testing method was used in this experimental study. This standard is widely used to measure the exhaust emissions of non-road internal combustion engines. Table 5 shows the testing procedure for the C1 test cycle where the mode is defined as engine operating point by speed and torque, rated speed. The standard also defines that the intermediate speed shall be the declared maximum torque speed if it occurs between 60% and 75% of the rated speed. If the maximum torque speed is less than 60% of the rated speed, then the intermediate speed shall be 60% of the rated speed. Likewise, if the maximum torque speed is greater than 75% of the rated speed the intermediate speed shall then be 75% of the rated speed. The measurements were only taken in the last 3 min as it allows the system to stabilize allowing for more accurate results. At the start of each test, the engine must also be preconditioned by running the engine at its rated power for 40 min.

3.8 Neural Network for the Test

Different thermodynamic system neural network has been used to predict the performances of that particular system from some decades (Ghobadian et al. 2009). Recently, this technique is used for modeling the operation in internal

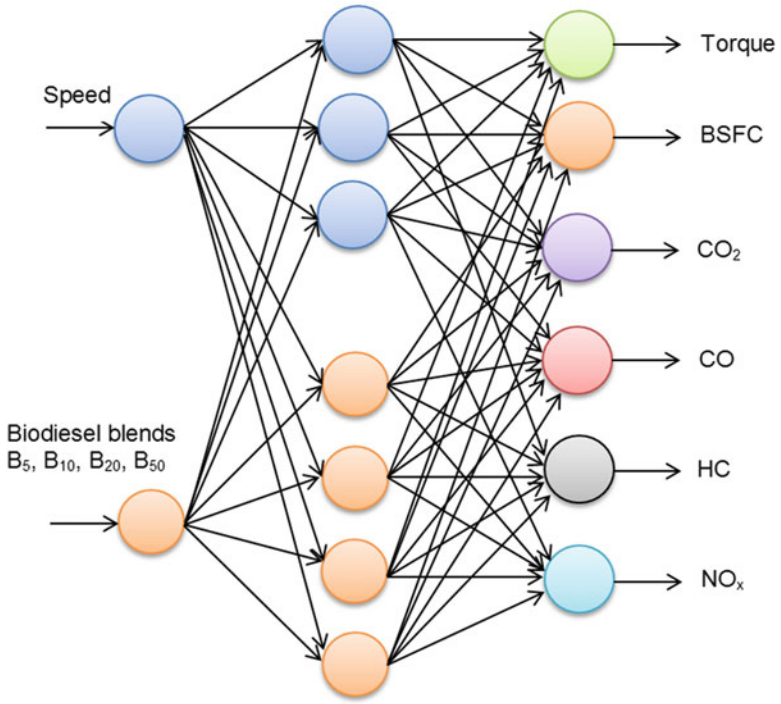

Fig. 4 Neural network for the experimental test bed engine

combustion engine. Specially, this approach is well efficient to predict the performance and emission characteristics of diesel engine, specific fuel consumption and air fuel ration in in-cylinder combustion. The neural network for this experimental work is presented is Fig. 4.

Table 5 shows the speeds and torques that were tested. The dynamometer ran a performance curve of the diesel engine and it was found that the engine was not able to reach its rated power of 50.7 kW. From the performance curve it was determined that the maximum torque of the engine occurred at 2300 rpm and as this is less than 60% of the rated speed the intermediate test speed used was instead 60% of the rated speed, 1440 rpm. The idle speed for the dynamometer is 800 rpm which was chosen as engine idle speed.

4 Results and Discussions

The key parameters for diesel engine performance are brake power, brake torque and brake-specific fuel consumption. In emission study, exhaust gases like, CO, CO_2, HC and NO_x were measured in the experiment. The diesel engine performance and emission study using soybean biodiesel and fossil diesel is briefly discussed below.

4.1 Brake Power (BP)

Figure 5 shows the variation of BP with engine speeds for diesel and biodiesel blends. The trend of the curves is similar to the diesel engine performance curves as mentioned in previous studies. The power production of the engine decreases compared with diesel fuel with the increase of biodiesel percentage. This trend is expected as biodiesel has less energy content (Table 2) than fossil diesel. The figure clearly shows the comparison between diesel and soybean biodiesel blends. Over the entire range of engine speed, biodiesel blends B5, B10, B20 and B50 produces 2.28%, 5.10%, 9.72% and 17.24% less power compared to diesel fuel, respectively. The B5 produced maximum output power (average 26.90kw) compared to other blends (average BP values are 26.13kw (B10), 24.86kw (B20) and 22.78kw (B50) under ISO 8178 test procedure). However, B5 and B10 produced very close BP over the entire range of engine speed. The result also shows that output BP decreases with the increase of biodiesel percentage in the fuel blends. The difference between the BP values is not a significant amount. For example, maximum BP drops occurred from B5 to B50 is only 0.77kw, 2.05kw and 4.12kw, respectively. It can be noted that biodiesel blends except B50 produced very close BP to diesel fuel at higher engine speed at 2400 rpm. B5 and B10 biodiesel blends can be considered as sustainable alternative fuels in terms of maximum power output in diesel engine.

4.2 Brake Torque (BT)

Figure 6 illustrates another important performance curve like total output BT variation with engine speed. The trends for each blend can be analyzed and compared with each other. The biodiesel blends appear to have the expected effect on torque as higher blends content results in a lower BT in a consistent manner. By comparing Figs. 5 and 6, it is evident that maximum torque and power reflect each other which are to be expected, as torque and power are directly proportional. For B5 and B10 biodiesel blends, total torque output is slightly lower than the diesel fuel; however, lower torque production for B50 is expected because the property of the biodiesel blends influenced the in-cylinder combustion in diesel engine. One of the main reasons is that soybean oil contains more than 55% of linoleic acid which may cause higher viscous fuel by mixing 50% with fossil diesel. The decrease of BP and BT can be attributed to the biodiesel blends due to the lower energy content (Table 1) and higher viscosity. Considerable differences of BT between B5 and B10 biodiesel have been found in this study. According to these two performance curves (Figs. 5 and 6), B5 and B10 blends have better performance than other blends.

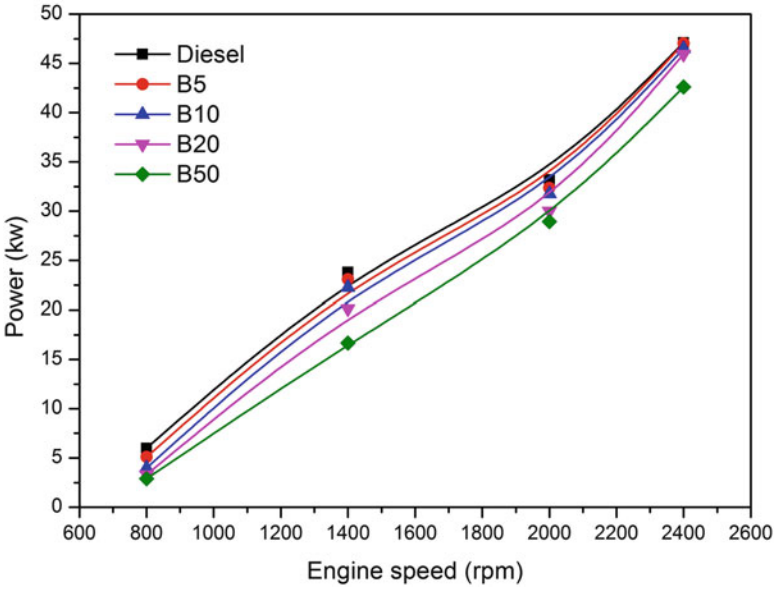

Fig. 5 Variation of total power output with engine speed for different fuel blends

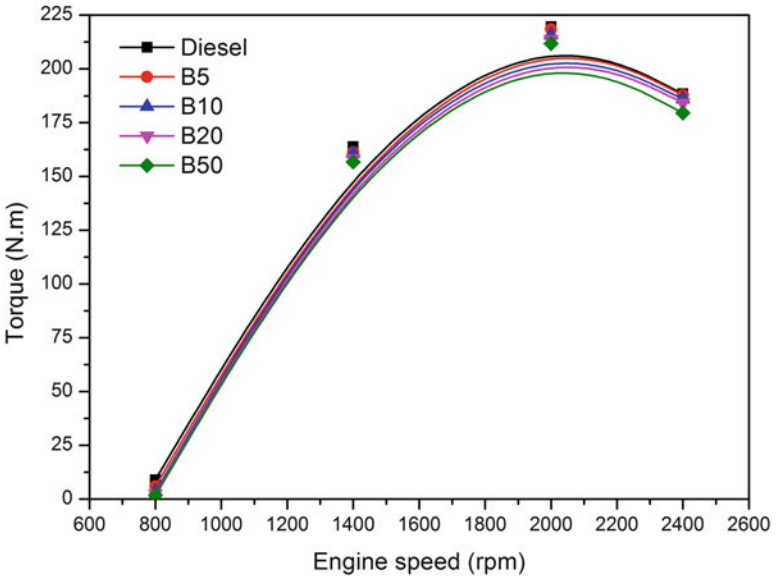

Fig. 6 Relationship between engine speed and torque for different biodiesel blends

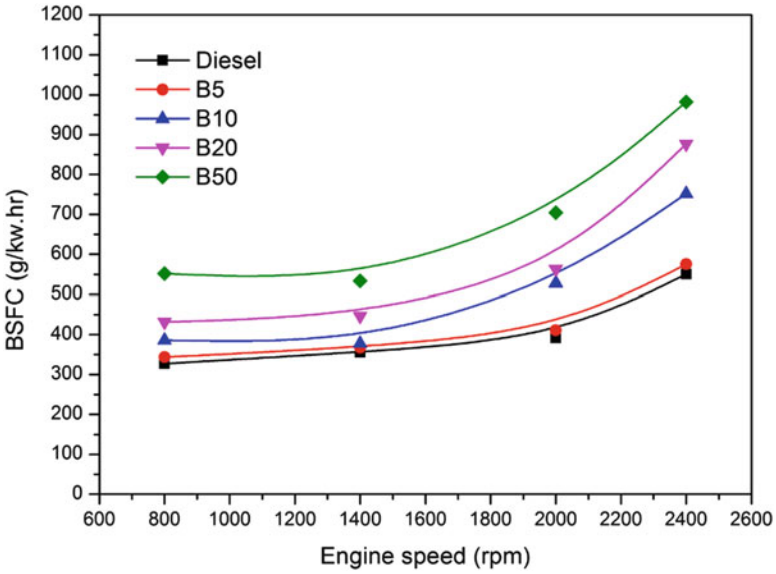

Fig. 7 Variation of BSFC with engine speed for different fuel blends

4.3 Brake-Specific Fuel Consumption (BSFC)

BSFC is one of the important factors for engine performance of the fuels. Figure 7 shows the fuel consumption of the different fuel blends over the ISO 8178 test procedure. As shown from the figure, biodiesels have higher fuel consumption than fossil diesel. The BSFC for B5 biodiesel is closer with diesel. As compared with other blends, B10 has lower BSFC in a consistent way. The trends of this curve are acceptable according to the literature as biodiesel has greater fuel consumption due to its lower energy content (Table 1). The average BSFC increases by 15.87%, 28.24% and 36.42% for B10, B20 and B50 blends compared to diesel fuel, respectively. It has been evidenced that BSFC increases with the increase of biodiesel blends (Mofijur et al. 2014). So, the experimental results are acceptable according to the literatures (Wang et al. 2013; Shahabuddin et al. 2012). More fuel consumption can be attributed to the lower energy content (Table 1) of biodiesel blends compared with fossil diesel. So, B10 soybean biodiesel blends showed better performance considering total output power, torque and BSFC compared with other blends.

4.4 Engine Emission Analysis

4.4.1 Carbon Dioxide (CO_2) Emission

Emission analysis is another part of fuel testing in CI engine. In this experiment, using exhaust gas analyzer, CO, CO2, HC and NOx emissions have been measured

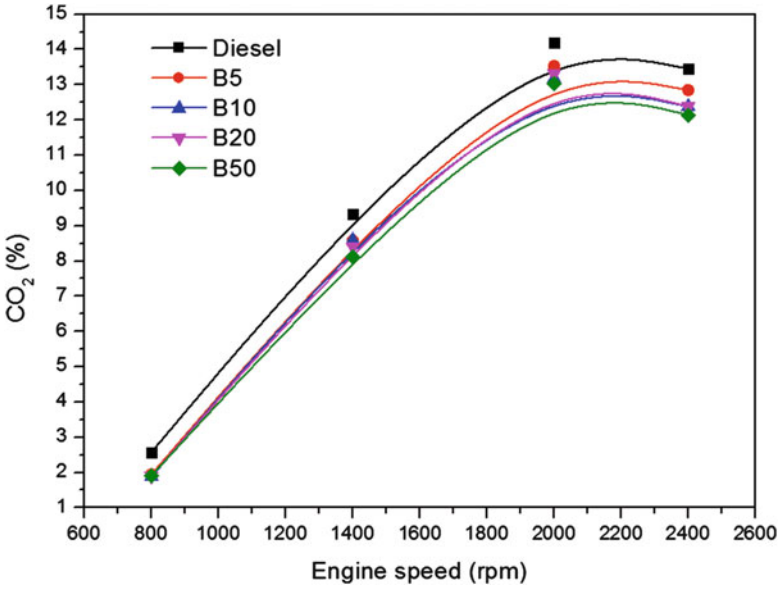

Fig. 8 Variation of CO_2 emission with engine speed for different fuel blends

as emission parameters for diesel and biodiesel blends. Figure 8 illustrates the total CO_2 emissions for diesel and biodiesel blends over the engine speed in ISO 8178 test procedure. It has been found that CO_2 emission decreases with increase of biodiesel percentage. The literature reported that biodiesel is carbon neutral fuel and the combustion of biodiesel in CI engine emits lower greenhouse gases than fossil diesel (Azad et al. 2014b; Usta et al. 2005). The trend shows the decrease in CO_2 emission compared with diesel which is expected from the experiment. The average CO_2 emission decreases by 6.73%, 8.96%, 8.99% and 11.04% for B5, B10, B20 and B50 blends compared with fossil diesel, respectively. It can be noted that the decrease of CO_2 emission for B10 and B20 blends are very close; however, for B20 other performances like BP, BT and BSFC are lower than B10 biodiesel blend. But for each blend CO_2 emission has a more distinct trend as the more biodiesel is added to the fuel the less CO_2 emission is given off. As the drop in emission does continue between B5 to B50, it may therefore be assumed that the relationship between CO_2 emissions is linear. The highest CO_2 reduction occurred using B50 blend.

4.4.2 Carbon Monoxide (CO) Emission

CO emission is another important emission parameter for diesel engine. Literature reported that CO emission occurred when excess oxygen is not present in the fuel (Rahman et al. 2014). Some other factors, namely, air/fuel ratio, injection timing, engine speed, injection pressure, fuel characteristics, etc., are also related to CO

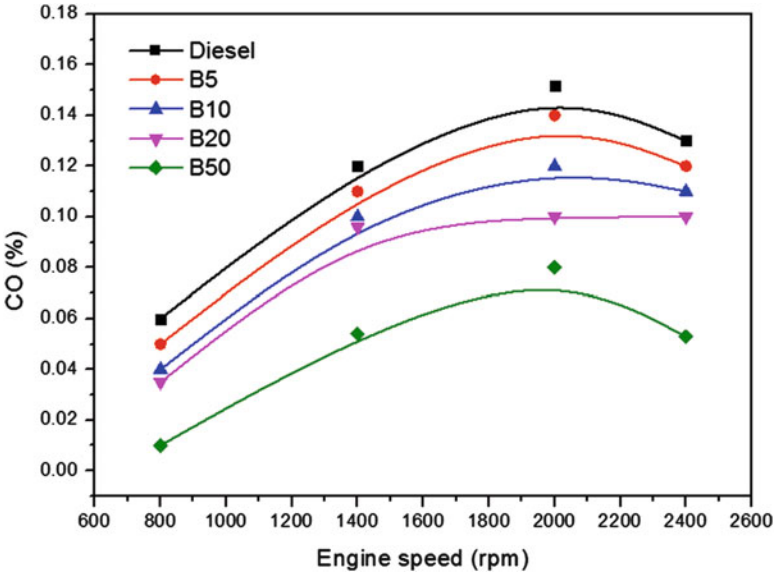

Fig. 9 Variation of CO emission with engine speed for different fuel blends

emission by combustion of fuel in CI engine (Gumus et al. 2012). Figure 9 presents the variation of CO emissions for diesel and biodiesel blends where most of the blends emit lower CO except B5 compared with diesel fuel. The CO emission reduction of about 33.12%, 28.01% and 62.83% for B10, B20 and B50 compared to diesel fuel is recorded from this study. There is no major trend of CO reduction for biodiesel blends. The experimental data shows that the amount of biodiesel in the fuel blend has positive impact on CO emission. Apart from the B5 blend, higher CO emissions were identified than that of diesel. The lower CO reading for different biodiesels could be attributed to biodiesel having higher oxygen content. A higher oxygen content results in a more complete combustion and less CO emission in the exhaust. Due to the instrumental error, every fuel has almost the same CO emission at higher speed at 2400 rpm.

4.4.3 Hydrocarbon (HC) Emission

Incomplete combustion of fuel and flame quenching results in the unburned HC emission in CI engine. Figure 10 shows the HC emission in exhaust stream for diesel and biodiesel blends under the ISO 8178 test procedure. As seen from the figure, HC emission has not been consistent with biodiesel blends. The United States Environmental Protection Agency (USEPA) determined that an increase in biodiesel percentage should decrease the amount of HC in the exhaust stream. The results obtained from the test for HC emissions roughly follow the USEPA statement. It could be mentioned here that some more error happened during the

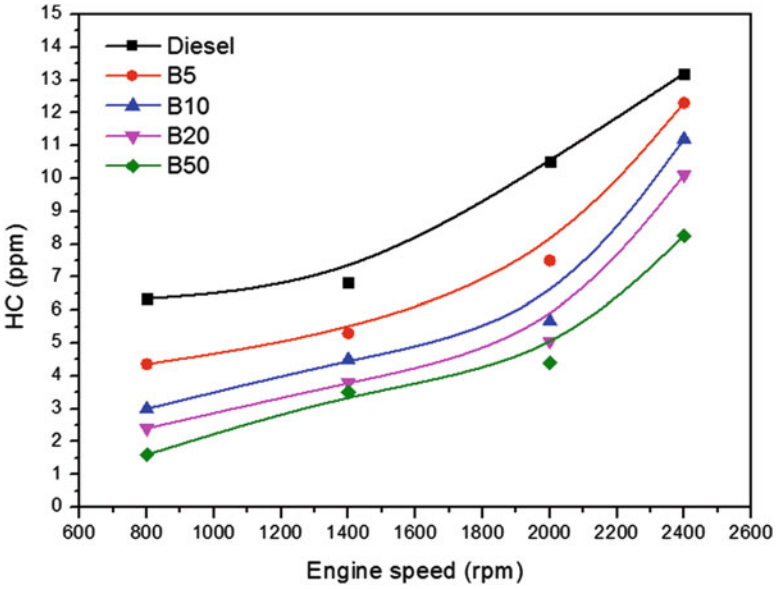

Fig. 10 Variation of HC emission with engine speed for different fuel blends

experiment at 2000 rpm for diesel fuel. A reason for these results varying so much is because hydrocarbons make up a very small amount of the exhaust stream. The maximum HC reading was 13 ppm which equates to 0.0013% of the exhaust gas. As the amount of HC being measured is really small, the error in HC in exhaust gas will not have significant effect on the results.

4.4.4 Nitrogen Oxide (NO_x) Emission

Figure 11 illustrates NO_x emission by combustion of biodiesels in CI engine, over the speed range in ISO 8178 test procedure. It has been evidenced from previous studies that NO_x emission is one of the most important problems of biodiesel combustion in CI engine (Mofijur et al. 2014). From the graph, it is clearly seen that biodiesels have positive impact on NO_x emission, that is, a greater percentage of biodiesel leads to increase NO_x emission in exhaust gas. The experimental results show that NO_x emission increases by 24.51%, 30.56%, 41.74% and 56.16% for B5, B10, B20 and B50 biodiesel blends compared with diesel, respectively. The comparison between biodiesel blends shows that B5 and B10 emit relatively lower NO_x emission than B20 and B50. The increasing trends of NO_x emission have been identified in this experiment. The USEPA report shows that an increase in biodiesel percentage leads to increase of NO_x emissions. The maximum amount of NO_x measure for the B50 blend was 2.25 ppm and this equates to 0.000225% of the total exhaust gas. As such a small amount of NO_x was measured, it is

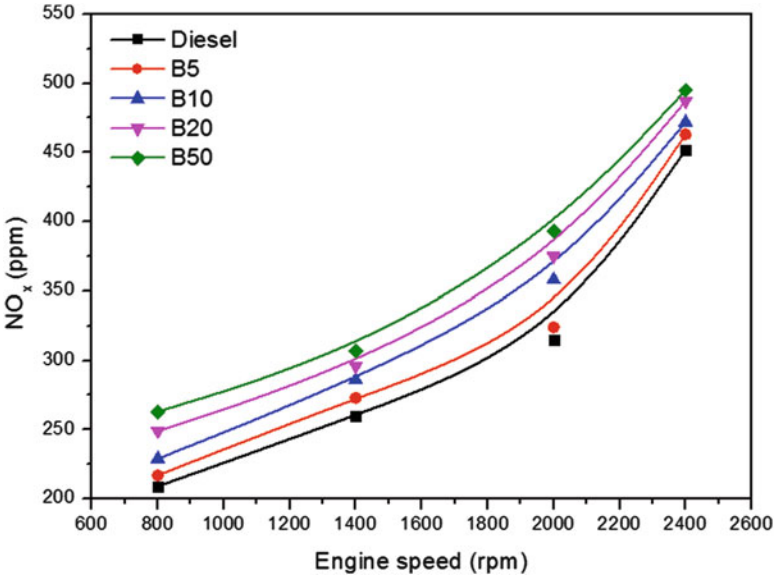

Fig. 11 Variation of NO_x emission with engine speed for different fuel blends

understandable that some of the results may be slightly off due to the accuracy of the exhaust gas analyzer. As discussed earlier, NO_x has a global warming potential of nearly 300, meaning that it is 300 times worse for the atmosphere than CO_2 emission. So, the small amounts of NOx emission have greater importance than that of the other exhaust emissions.

5 Conclusions

The study investigated the use of soybean biodiesel as a sustainable alternative fuel for diesel engine because it has excellent capability to decrease the environmental impact, it can potentially reduce the dependency on fossil fuel and it can be used in different proportion without modification of diesel engine. The following conclusions can be drawn from the experimental study. The characteristics of these biodiesels and their blends meet the requirements of ASTM D6751 and EN 14214 standards. The ISO 8178 test procedure was followed during the engine performance test and emission study and found that more biodiesel blends produce less BP, BT and higher BSFC compared to diesel fuel; however, it gives off fewer emissions than fossil diesel. The overall performance of B5 and B10 soybean biodiesel blends has been found better than other biodiesel blends. They produce an average 26.90 kw and 145.22 N.m BP and BT which is only 2.28% and 5.10% lower BP compared to diesel fuel. The BSFC for B10 blend shows relatively lower value compared to other blends but a bit higher than diesel. With the various

emission gasses such as CO, CO_2, HC and NO_x there was decreasing linear trend found for CO, CO_2 and HC emission but increasing trend for NO_x emission with the increase in biodiesel blends. Finally, it can be concluded that both B5 and B10 are the optimum soybean biodiesel blends that produce more consistent and expected results than other biodiesel blends.

References

Agarwal, A.K.: Biofuels (alcohols and biodiesel) applications as fuels for internal combustion engines. Prog. Energy Combust. Sci. **33**(3), 233–271 (2007)

Ameer Uddin, S.M., Azad, A.K., Alam, M.M., Ahamed, J.U.: Performance comparison of DI diesel engine by using esterified mustard oil and pure mustard oil blends with diesel. In: The 2nd International Conference on Mechanical Engineering and Renewable Energy, Chittagong (2013)

Atabani, A.E., Silitonga, A.S., Badruddin, I.A., Mahlia, T.M.I., Masjuki, H.H., Mekhilef, S.: A comprehensive review on biodiesel as an alternative energy resource and its characteristics. Renew. Sust. Energ. Rev. **16**(4), 2070–2093 (2012)

Atabani, A.E., Silitonga, A.S., Ong, H.C., Mahlia, T.M.I., Masjuki, H.H., Badruddin, I.A., Fayaz, H.: Non-edible vegetable oils: a critical evaluation of oil extraction, fatty acid compositions, biodiesel production, characteristics, engine performance and emissions production. Renew. Sust. Energ. Rev. **18**, 211–245 (2013)

Azad, A.K., Uddin, S.M.A.: Performance study of a diesel engine by first generation bio-fuel blends with fossil fuel: an experimental study. J. Renew.Sust. Energy **5**, 013118(1–12) (2013)

Azad, A.K., Uddin, S.M.A., Alam, M.M.: Mustard oil, an alternative fuel: an experimental investigation of bio-diesel properties with and without trans-esterification reaction. Glob. Adv. Res. J. Eng. Technol. Innov. **1**(3), 75–84 (2012)

Azad, A.K., Rasul, M.G., Khan, M.M.K., Ahasan, T., Ahmed, S.F.: Energy scenario: production, consumption and prospect of renewable energy in Australia. J. Power Energy Eng. **2**(4), 19–25 (2014a)

Azad, A.K., Rasul, M.G., Khan, M.M.K., Sharma, S.C., Islam, R.: Prospect of Moringa seed oil as a sustainable biodiesel fuel in Australia: a review. Procedia Eng. (Accepted) (2014b)

Azad, A.K., Rasul, M.G., Khan, M.M.K., Sharma, S.C., Bhuiya, M.M.K., Mofijur, M.: A review on socio-economic aspects of sustainable biofuels. Int. J.Global Warming (Accepted) (2015a)

Azad, A.K., Rasul, M.G., Khan, M.M.K., Sharma, S.C., Hazrat, M.A.: Prospect of biofuels as an alternative transport fuel in Australia. Renew. Sust. Energ. Rev. **43**, 331–351 (2015b)

Balat, M., Balat, H.: A critical review of bio-diesel as a vehicular fuel. Energy Convers. Manag. **49** (10), 2727–2741 (2008)

Balat, M., Balat, H.: Progress in biodiesel processing. Appl. Energy. **87**(6), 1815–1835 (2010)

Berrios, M., Skelton, R.L.: Comparison of purification methods for biodiesel. Chem. Eng. J. **144** (3), 459–465 (2008)

Canakci, M., Sanli, H.: Biodiesel production from various feedstocks and their effects on the fuel properties. J. Ind. Microbiol. Biotechnol. **35**(5), 431–441 (2008)

Canakci, M., Van Gerpen, J.: Biodiesel production via acid catalysis. Trans. Am. Soc. Agric. Eng. **42**(5), 1203–1210 (1999)

Chauhan, B.S., Kumar, N., Du Jun, Y., Lee, K.B.: Performance and emission study of preheated Jatropha oil on medium capacity diesel engine. Energy. **35**(6), 2484–2492 (2010)

Demirbaş, A.: Biodiesel from vegetable oils via transesterification in supercritical methanol. Energy Convers. Manag. **43**(17), 2349–2356 (2002)

Demirbas, A.: Biodiesel – A Realistic Fuel Alternative for Diesel Engine. Springer, London (2008)

Demirbas, A.: Biodiesel from waste cooking oil via base-catalytic and supercritical methanol transesterification. Energy Convers. Manag. **50**(4), 923–927 (2009a)

Demirbas, A.: Progress and recent trends in biodiesel fuels. Energy Convers. Manag. **50**(1), 14–34 (2009b)
Demirbas, A.H., Demirbas, I.: Importance of rural bioenergy for developing countries. Energy Convers. Manag. **48**(8), 2386–2398 (2007)
Dias, J.M., Alvim-Ferraz, M.C.M., Almeida, M.F., Méndez Díaz, J.D., Polo, M.S., Utrilla, J.R.: Selection of heterogeneous catalysts for biodiesel production from animal fat. Fuel. **94**(0), 418–425 (2012)
Dorado, M.P., Ballesteros, E., López, F.J., Mittelbach, M.: Optimization of alkali-catalyzed transesterification of brassica C arinata oil for biodiesel production. Energy Fuel. **18**(1), 77–83 (2004)
Du, W., Xu, Y., Liu, D., Zeng, J.: Comparative study on lipase-catalyzed transformation of soybean oil for biodiesel production with different acyl acceptors. J. Mol. Catal. B Enzym. **30**(3), 125–129 (2004)
Fukuda, H., Kondo, A., Noda, H.: Biodiesel fuel production by transesterification of oils. J. Biosci. Bioeng. **92**(5), 405–416 (2001)
Ghobadian, B., Rahimi, H., Nikbakht, A.M., Najafi, G., Yusaf, T.F.: Diesel engine performance and exhaust emission analysis using waste cooking biodiesel fuel with an artificial neural network. Renew. Energy. **34**(4), 976–982 (2009)
Grossman, P.Z.: Energy shocks, crises and the policy process: a review of theory and application. Energy Policy. **77**(0), 56–69 (2015)
Gumus, M., Sayin, C., Canakci, M.: The impact of fuel injection pressure on the exhaust emissions of a direct injection diesel engine fueled with biodiesel–diesel fuel blends. Fuel. **95**, 486–494 (2012)
He, H., Wang, T., Zhu, S.: Continuous production of biodiesel fuel from vegetable oil using supercritical methanol process. Fuel. **86**(3), 442–447 (2007)
Hincapié, G., Mondragón, F., López, D.: Conventional and in situ transesterification of castor seed oil for biodiesel production. Fuel. **90**(4), 1618–1623 (2011)
Jain, S., Sharma, M.P.: Prospects of biodiesel from Jatropha in India: a review. Renew. Sust. Energ. Rev. **14**(2), 763–771 (2010)
Karmakar, A., Karmakar, S., Mukherjee, S.: Properties of various plants and animals feedstocks for biodiesel production. Bioresour. Technol. **101**(19), 7201–7210 (2010)
Kim, H.-J., Kang, B.-S., Kim, M.-J., Park, Y.M., Kim, D.-K., Lee, J.-S., Lee, K.-Y.: Transesterification of vegetable oil to biodiesel using heterogeneous base catalyst. Catal. Today. **93**, 315–320 (2004)
Koh, M.Y., Mohd. Ghazi, T.I.: A review of biodiesel production from Jatropha curcas L. oil. Renew. Sust. Energ. Rev. **15**(5), 2240–2251 (2011)
Kusdiana, D., Saka, S.: Two-step preparation for catalyst-free biodiesel fuel production. Appl. Biochem. Biotechnol. **115**(1–3), 781–791 (2004)
Leung, D.Y.C., Wu, X., Leung, M.K.H.: A review on biodiesel production using catalyzed transesterification. Appl. Energy. **87**(4), 1083–1095 (2010)
Lin, L., Cunshan, Z., Vittayapadung, S., Xiangqian, S., Mingdong, D.: Opportunities and challenges for biodiesel fuel. Appl. Energy. **88**(4), 1020–1031 (2011)
Liu, X., He, H., Wang, Y., Zhu, S., Piao, X.: Transesterification of soybean oil to biodiesel using CaO as a solid base catalyst. Fuel. **87**(2), 216–221 (2008)
Lotero, E., Liu, Y., Lopez, D.E., Suwannakarn, K., Bruce, D.A., Goodwin, J.G.: Synthesis of biodiesel via acid catalysis. Ind. Eng. Chem. Res. **44**(14), 5353–5363 (2005)
Ma, F., Hanna, M.A.: Biodiesel production: a review. Bioresour. Technol. **70**(1), 1–15 (1999)
Mahanta, P., Shrivastava, A.: Technology Development of Bio-diesel as an Energy Alternative, pp. 1–19. Department of Mechanical Engineering Indian Institute of Technology, Guwahati (2004)
Masuda, T., Goldsmith, P.D.: World soybean production: area harvested, yield, and long-term projections. Int. Food Agribus. Manag. **12**(4), 143–162 (2009)
Meher, L.C., Vidya Sagar, D., Naik, S.N.: Technical aspects of biodiesel production by transesterification—a review. Renew. Sust. Energ. Rev. **10**(3), 248–268 (2006)

Milazzo, M.F., Spina, F., Cavallaro, S., Bart, J.C.J.: Sustainable soy biodiesel. Renew. Sust. Energ. Rev. **27**(0), 806–852 (2013a)

Milazzo, M.F., Spina, F., Primerano, P., Bart, J.C.J.: Soy biodiesel pathways: global prospects. Renew. Sust. Energ. Rev. **26**(0), 579–624 (2013b)

Minami, E., Saka, S.: Kinetics of hydrolysis and methyl esterification for biodiesel production in two-step supercritical methanol process. Fuel. **85**(17), 2479–2483 (2006)

Mofijur, M., Atabani, A.E., Masjuki, H.H., Kalam, M.A., Masum, B.M.: A study on the effects of promising edible and non-edible biodiesel feedstocks on engine performance and emissions production: a comparative evaluation. Renew. Sust. Energ. Rev. **23**(0), 391–404 (2013)

Mofijur, M., Masjuki, H.H., Kalam, M.A., Atabani, A.E., Arbab, M.I., Cheng, S.F., Gouk, S.W.: Properties and use of Moringa oleifera biodiesel and diesel fuel blends in a multi-cylinder diesel engine. Energy Convers. Manag. **82**, 169–176 (2014)

Moser, B.R.: Biodiesel production, properties, and feedstocks. In: Biofuels, pp. 285–347. Springer, New York (2011)

Murugesan, A., Umarani, C., Subramanian, R., Nedunchezhian, N.: Bio-diesel as an alternative fuel for diesel engines—a review. Renew. Sust. Energ. Rev. **13**(3), 653–662 (2009)

Narasimharao, K., Lee, A., Wilson, K.: Catalysts in production of biodiesel: a review. J. Biobaased Mater. Bioenergy. **1**(1), 19–30 (2007)

Nigam, P.S., Singh, A.: Production of liquid biofuels from renewable resources. Prog. Energy Combust. Sci. **37**(1), 52–68 (2011)

Rahman, M.M., Hassan, M.H., Kalam, M.A., Atabani, A.E., Memon, L.A., Rahman, S.M.A.: Performance and emission analysis of Jatropha curcas and Moringa oleifera methyl ester fuel blends in a multi-cylinder diesel engine. J. Clean. Prod. **65**, 304–310 (2014)

Ramadhas, A.S., Jayaraj, S., Muraleedharan, C.: Biodiesel production from high FFA rubber seed oil. Fuel. **84**(4), 335–340 (2005)

Rashid, U., Anwar, F.: Production of biodiesel through optimized alkaline-catalyzed transesterification of rapeseed oil. Fuel. **87**(3), 265–273 (2008)

Royon, D., Daz, M., Ellenrieder, G., Locatelli, S.: Enzymatic production of biodiesel from cotton seed oil using *t*-butanol as a solvent. Bioresour. Technol. **98**(3), 648–653 (2007)

Salvi, B.L., Panwar, N.L.: Biodiesel resources and production technologies – a review. Renew. Sust. Energ. Rev. **16**(6), 3680–3689 (2012)

Shahabuddin, M., Masjuki, H., Kalam, M., Mofijur, M., Hazrat, M., Liaquat, A.: Effect of additive on performance of CI engine fuelled with bio diesel. Energy Procedia. **14**, 1624–1629 (2012)

Singh, S.P., Singh, D.: Biodiesel production through the use of different sources and characterization of oils and their esters as the substitute of diesel: a review. Renew. Sust. Energ. Rev. **14** (1), 200–216 (2010)

Srivastava, A., Prasad, R.: Triglycerides-based diesel fuels. Renew. Sust. Energ. Rev. **4**(2), 111–133 (2000)

Suehara, K.-i., Kawamoto, Y., Fujii, E., Kohda, J., Nakano, Y., Yano, T.: Biological treatment of wastewater discharged from biodiesel fuel production plant with alkali-catalyzed transesterification. J. Biosci. Bioeng. **100**(4), 437–442 (2005)

Usta, N., Öztürk, E., Can, Ö., Conkur, E., Nas, S., Con, A., Can, A., Topcu, M.: Combustion of biodiesel fuel produced from hazelnut soapstock/waste sunflower oil mixture in a diesel engine. Energy Convers. Manag. **46**(5), 741–755 (2005)

Wang, X., Ge, Y., Yu, L., Feng, X.: Comparison of combustion characteristics and brake thermal efficiency of a heavy-duty diesel engine fueled with diesel and biodiesel at high altitude. Fuel. **107**, 852–858 (2013)

West, A.H., Posarac, D., Ellis, N.: Assessment of four biodiesel production processes using HYSYS.Plant. Bioresour. Technol. **99**(14), 6587–6601 (2008)

Xie, W., Li, H.: Alumina-supported potassium iodide as a heterogeneous catalyst for biodiesel production from soybean oil. J. Mol. Catal. A Chem. **255**(1), 1–9 (2006)

Yusuf, N.N.A.N., Kamarudin, S.K., Yaakub, Z.: Overview on the current trends in biodiesel production. Energy Convers. Manag. **52**(7), 2741–2751 (2011)

The Valorization of the Green Alga *Spirogyra*'s Biomass in the Region of Ouargla-Algeria into Renewable Biofuel

Souad Zighmi, Mohamed Bilal Goudjil, Salah Eddine Bencheikh, and Segni Ladjel

1 Introduction

Biofuels are an effective substrate for fossil energy's existing sources; they offer the prospect of ecological sustainability and reduce greenhouse gases' emissions (Saharan et al. 2013). Indeed, the algae are presented as a potential source of biofuel; with their various important advantages (Ramachandra 2013), they got a great deal of attention as an alternative and renewable source of biomass for bioethanol production (John et al. 2011; Wibowo et al. 2013).

Bioethanol is defined as an ethyl alcohol produced by various biological processes that convert biomass into ethanol (Deenanath et al. 2012). It is a liquid transport fuel with a high octane number; it is generally mixed with gasoline in order to contribute to the reduction of vehicles' carbon monoxide emissions (Tucho 2013).

Fermentation is the well-known process used for alcohol production from a variety of biomass sources containing sugar, starch, or cellulose. This process involves the action of yeast, which decompose and convert the sugar into ethanol (Tucho 2013).

S. Zighmi (✉)
University of Ouargla, Faculty of Sciences of the nature and life, Laboratory of Engineering Laboratory of Water and Environment in Middle Saharian, Ouargla 30000, Algeria

University of Ouargla, Faculty of Applied Sciences, Department of Process Engineering, Ouargla 30000, Algeria
e-mail: zighmi.so@univ-ouargla.dz; souad.zighmi@gmail.com

M.B. Goudjil • S.E. Bencheikh • S. Ladjel
University of Ouargla, Faculty of Applied Sciences, Laboratory of Process Engineering, Ouargla 30000, Algeria

© Springer International Publishing AG, part of Springer Nature 2018

F. Aloui, I. Dincer (eds.), *Exergy for A Better Environment and Improved Sustainability 2*, Green Energy and Technology,
https://doi.org/10.1007/978-3-319-62575-1_11

Simultaneous saccharification and fermentation (SSF) is an important strategy of the bioethanol production process where the enzyme hydrolysis and the fermentation are performed in the same container; the inhibition of the final product and of the glucose in the hydrolysis is gradually assimilated by the yeast during the fermentation process. Therefore, in SSF, the requirement of enzymes is lesser while the bioethanol yield is higher (Balat et al. 2008).

At present, recent attempts to produce ethanol are focused on the use of algal biomass as a raw material for the fermentation process, for microalgae are rich in carbohydrates and proteins that can be used as carbon sources for the fermentation and do not compete with the food chain – in addition to its none requirement for the use of large areas (Singh and Gu 2010).

The alga with the potential to be developed as a raw material for bioethanol production is *Spirogyra* (Sulfahri and Nurhidayati 2011). It has been demonstrated that *Spirogyra* species are able to accumulate high levels of polysaccharides and starch in their complex cells walls, which allows using it in bioethanol production (Nguyen and Vu 2012).

In this study, we present a research that addresses the valorization of the algal biomass in the energy field. An experimental effort has been expanded by converting *Spirogyra* biomass into ethanol through fermentation. The alga *Spirogyra* was collected from a natural lake in the region of Touggourt, a part of the city of Ouargla-Algeria. This study was conducted to determine the feasibility of using algae to produce ethanol in Algeria.

2 Materials and Methods

2.1 Sampling Site

The sampling of stem was done in the region Touggourt-Ouargla, from a natural lake (Fig. 1).This region is located in the southeast of Algeria. It corresponds to the upper part of Oued (river) Righ. It is bordered on the southeast by the Grand Erg Oriental, on the north by Megarine's palm groves, and on the west by sand dunes (Hadjoudj et al. 2011).

2.2 Sample Preparation

The strains are put into sterile glass vials and then transferred to the laboratory. The alga sample was identified by microscopic examination, as being part of the *Spirogyra* species (Fig. 2).

Fig. 1 Stem sampling site

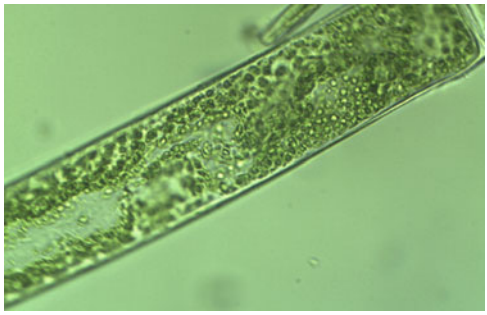

Fig. 2 Photo of *Spirogyra* species

Strains were washed with distilled water and subjected to drying away from the sun. The fine powder of *Spirogyra*'s biomass, obtained after being dried, crushed, and then filtered through a sieve of 1 mm, is used for all experiments (Fig. 3).

2.3 Extraction of Spirogyra*'s Oil*

A step of oil extraction was performed on *Spirogyra*, with hexane as the solvent used for the extraction with Soxhlet; this operation aims to reduce the fermentation time and to increase the yield of bioethanol.

2.4 Depigmentation

The extracted residue of oil subsequently undergoes a step of depigmentation. The dry material is placed for 12 h under stirring in acetone in a proportion of 150 ml of

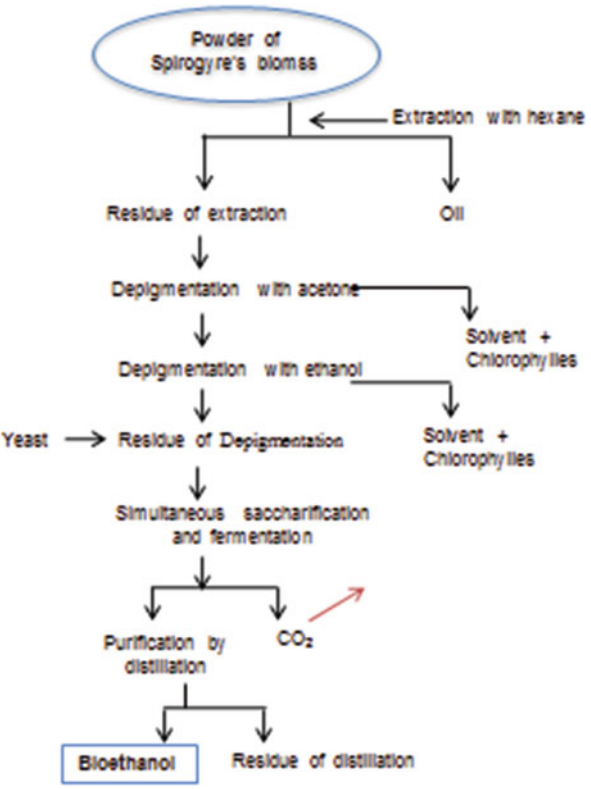

Fig. 3 Set-up for experiments

solvent for 5 g of the used material. Afterward, the mixture is filtered on sintered glass of porosity 3 and rinsed with absolute ethanol until disappearance of the green color that reflects the elimination of chlorophylls. The residue is then depigmented with 200 ml of absolute ethanol (for 5 g of material) and boiled for 1 h. This step is repeated two times, and between each depigmentation step, the mixture is filtered and washed with absolute ethanol until the color disappears. The obtained residue is dried in an oven (50 °C) for 12 h and then weighed.

2.5 Simultaneous Saccharification and Fermentation

Experimentally, for the saccharification of the developed algal biomass, we used a commercial yeast "Saf-Instant" consisting mainly of the *Saccharomyces cerevisiae* that produces enzymes, hydrolyzes the cellulose and starch present in the studied algae, and releases simple sugars that are subjected to fermentation, carried out for 24 h.

In addition, we used 3 g of yeast for 5 g of depigmentated algae's residue, heated at a temperature of 30 °C. After 24 h of experimentation, it is estimated that the fermentation is complete and that all of the glucose contained in the alga is converted into ethanol. To confirm this, we performed the Fehling's solution test.

2.6 Fehling Solution Tests

We know that the blue Fehling's solution has a property to become orange red in the presence of glucose. We put in the first test tube our solution before fermentation and, into a second tube, the solution obtained after fermentation. We add to each tube a few drops of Fehling's solution, heating them in a water bath for a few seconds with gentle agitation.

2.7 Purification

We obtained a fermented solution containing ethanol; however, the product still contains a large part of water. In order to purify the obtained ethanol, fractional distillation is carried out.

2.8 The Infrared Spectrophotometer Analysis

To confirm that the obtained product is of ethanol, an infrared spectrophotometry analysis was carried out, which allows characterizing the major functional groups in one molecule.

3 Results and Discussion

3.1 Oil Yield

The yield of the extracted oil from the *Spirogyra* algae is equal to 0.589%, which is a small quantity; therefore, the use of *Spirogyra* algae for bioethanol production is a wise choice.

Table 1 Properties of the product obtained

Properties	Obtained product
Physical state	Liquid at room temperature
Color	Transparent
Odor	Characteristic
Refractive index	1.3714
Density (g/cm^3)	0.787

3.2 Fehling's Solution Test

It was observed that the first tube containing the solution before fermentation became orange, while the second containing the fermented solution does not change color. It is deduced that the solution not fermented contains glucose, which by fermentation gives another product. Reminding that this test does not indicate if the obtained product is ethanol, this requires further experiments to confirm the result.

3.3 Purification

3.3.1 Bioethanol Yield

After completing the experiment, we obtain a clear liquid, of which the recorded yield is 16.83% of ethanol after only 24 h of fermentation. The obtained result from the analysis shows that the bioethanol yield is 28.57 times higher than the one obtained from the extracted oil, which confirms the choice of these algae for the production of bioethanol.

The characteristics of the product obtained are summarized in the following table (Table 1):

3.3.2 Checking of Bioethanol Quality

In order to see if the obtained product is consistent with the international standards, a comparison between the obtained bioethanol and gasoline is essential. Table 2 includes some parameters used for the comparison.

The comparison concerns certain properties, from the analysis results, shown in Table 2, and their comparison with gasoline can draw the following conclusions:

- The present bioethanol is renewable with a simple structure.
- Bioethanol's molecular weight is low compared to gasoline.
- Bioethanol's density is higher than that of gasoline

Table 2 Checking of bioethanol quality

Parameters	Obtained product	Gasoline
Physical state	*Liquid*	*Liquid*
Density (g/cm^3)	*0.787*	0.719
Source	*Algae (renewable)*	Crude oil
Chemical formula	C_2H_5OH	*C4 to C12*
Molecular weight	*46*	*100–105*

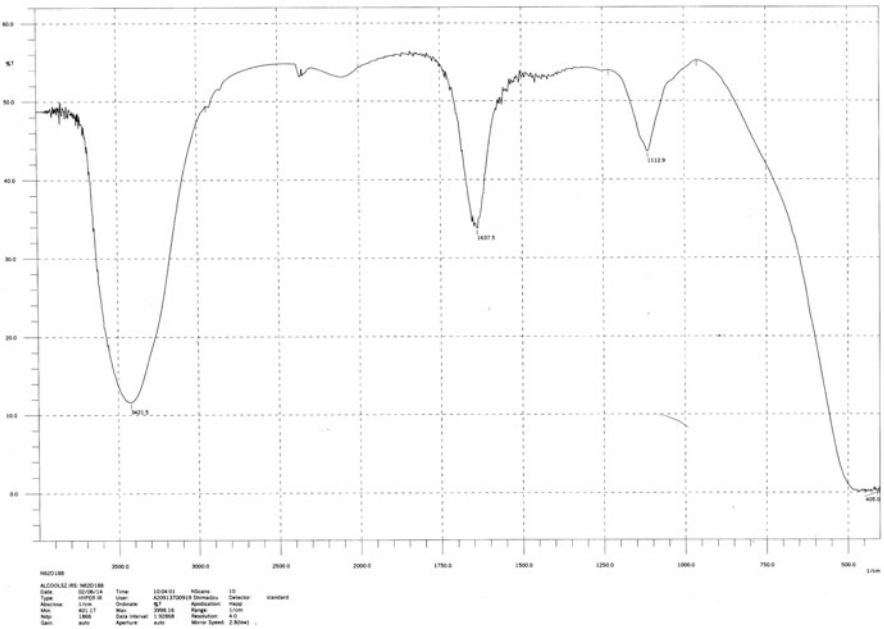

Fig. 4 IR spectrum of the obtained product

3.4 Infrared Spectrum Analysis

The analysis of the infrared spectrum of the studied samples (Fig. 4) shows that the product has a broad band around 3400 cm^{-1} which confirms the presence of an alcohol and a stretching vibration at 2900 cm^{-1} that corresponds to a group of CH. These data confirm the presence of an alcohol, which is none other than ethanol.

4 Conclusion

Bioethanol has become one of the most important biofuels on a worldwide level. In this study, the production of bioethanol is done by a fermentation process of the algae *Spirogyra* biomass, collected from a natural lake in the region of Touggourt, a part of the city of Ouargla-Algeria.

The results show that the hydrolysis and simultaneous fermentation are an important strategy for bioethanol production, which are carried out in the same place since the yield recorded is 16.83% of ethanol after only 24 h of fermentation.

Following this study, the analysis of the experimental data and of the obtained results shows that the *Spirogyra* algae is one of the green photosynthetic algae that are ideal candidates for bioethanol production. It has the potential to be an alternative solution for the production of clean and renewable energy, for it is rich in polysaccharides that can be extracted to produce fermentable sugars. In this study, we showed that algal biomass is an effective raw material for the production of bioethanol. Indeed, the experience made it clear that algae are a promising solution to the energy crisis with a very low cost and modest technological exploitation means and much more with no negative impact on the environment.

References

Balat, M., Balat, H., Oz, C.: Progress in bioethanol processing. Prog. Energy Combust. Sci. **34**(5), 551–573., ISSN 03601285 (2008)

Deenanath, E.D., Iyuke, S., Rumbold, K.: The bioethanol industry in Sub-Saharan Africa: history, challenges, and prospects. J. Biomed. Biotechnol. **2012**, 416491, 11 pages (2012)

Hadjoudj, M., Manaa, A., Derdoukh, W., Guerzou, A., Souttou, K., Sekour, M. et Doumandji, S.: LES RONGEURS DE LA REGION DE TOUGGOURT Actes du Séminaire International sur la Biodiversité Faunistique en Zones Arides et Semi-arides p. 244 (2011)

John, R.P., Anisha, G.S., Madhavan Nampoothiri, K., Pandey, A.: Micro and macroalgal biomass: a renewable source for bioethanol. Bioresour. Technol. **102**, 186–193 (2011)

Nguyen, T.H.M., Vu, V.H.: Bioethanol production from marine algae biomass: prospect and troubles. J. Viet. Env. **3**(1), 25–29 (2012)

Ramachandra, T.V., Madhab, M.D., Shilpi, S., Joshi, N.V.: Algal biofuel from urban wastewater in India: scope and challenges. Renew. Sust. Energ. Rev. **21**, 767–777 (2013)

Saharan, B.S., Sharma, D., Sahu, R., Sahin, O., Warren, A.: Towards algal biofuel production: a concept of greenbio energy development. Innov Roman Food Biotechnol. **12**, 1–21 (2013)

Singh, J., Gu, S.: Commercialization potential of microalgae for biofuels production. Renew. Sust. Energ. Rev. **14**, 2596–2610 (2010)

Sulfahri, S.N., Nurhidayati, T.: Aerobic and anaerobic processes of spirogyra extractusing different doses of Zymomonas mobilis. J. Appl. Environ. Biol. Sci. **1**(10), 420–425 (2011)

Tucho, G.T.: Feasible biomass energy conversion technologies in developing countries. Int. J. Eng. Res. Technol. (IJERT), ISSN: 2278-0181. **2**(6), 2720–2728 (2013)

Wibowo, A.H., Mubarokah, L., Suratman, A.: The fermentation of green algae (Spirogyra majuscule Kuetz) using immobilization technique of Ca-alginate for Saccharomyces cerevisiae entrapment. Indo. J. Chem. **13**(1), 7–13 (2013)

Plasma Technologies for Water Electrolyzers

V. Fateev, V. Kulygin, S. Nikitin, V. Porembskiy, S. Ostrovskiy, A. Glukhov, and A. Pushkarev

1 Introduction

Water electrolyzer development with polymer electrolyte membranes (PEM) was started in the 1950s with the first pilot electrolyzers being produced by General Electric for space projects 20 years later (Porter 1972). But commercial application of such electrolyzers is very limited up to now though it is rather intensively developed by different companies (i.e., Proton Energy Systems, Hydrogenics, Norsk Hydro Electrolysers AS, CETH2, and others) and research centers and universities (CNRS Institute of Advanced Technology for Energy Nicola Giordano (Italy), Laboratory of Electrocatalysis, CNRS UMR, Universite Paris SUD (France), NRC Kurchatov Institute (Russia), Fraunhofer Institute for Solar Energy Systems ISE Freiburg (Germany), Institute of Applied Chemistry CAS (China), and many others). Such electrolyzers considered being most safe and very efficient when high purity hydrogen production is needed, for example, for PEM fuel cells. They demonstrate high efficiency (about 4.0–4.2 kWh per m^3 of hydrogen), high specific productivity (current density up to 2–3 A/cm^2), and very high gas purity ($H_2 > 99.99\%$, $O_2 > 99.98\%$ in dry gas) (Carmo et al. 2013; Grigoriev et al. 2006). Possibility of hydrogen production at an increased pressure in a stack (up to 30 bars) without use of additional compressors makes them very attractive for renewable energy systems as it permits to solve the hydrogen storage problem rather efficiently and cheap due to use of traditional hydrogen tanks.

One of the most important limitations for their commercialization is the electrolyzer's high price which is tightly connected with large precious metal

V. Fateev (✉) • V. Kulygin • S. Nikitin • V. Porembskiy • S. Ostrovskiy
A. Glukhov • A. Pushkarev
NRC "Kurchatov Institute", Kurchatov sq., 1, Moscow 123182, Russia
e-mail: fateev_vn@nrcki.ru

© Springer International Publishing AG, part of Springer Nature 2018

F. Aloui, I. Dincer (eds.), *Exergy for A Better Environment and Improved Sustainability 2*, Green Energy and Technology,
https://doi.org/10.1007/978-3-319-62575-1_12

(mainly platinum metal) loading as these metals are used as electrocatalysts and for stack components' protection from corrosion and oxidation. Due to acidic membrane properties, corrosion is very intensive and other catalytic active metals as Ni, Co, Fe, and so on are not stable at electrolysis conditions. Different methods are used for stack component protection including CVD, PVD, magnetron sputtering, and even protective foil application to the surface of bipolar plates or current collectors (Carmo et al. 2013; Kozlov and Fateev 2009).Different methods were developed for the synthesis of the electrocatalyst (see, e.g., Carmo et al. 2013; Kozlov and Fateev 2009). The main group of such methods is a liquid phase catalyst synthesis by reduction of some catalyst precursors by different reducing agents. The second group is a "high temperature" synthesis (thermal decomposition or gas phase reduction). The first group of methods is widely used and permits to obtain nanostructured catalysts with very small particle size (up to 1–2 nm), but it is characterized by multistage procedure and requires scrupulous catalyst purification after synthesis. It also has some limitations with alloy synthesis and crystalline structure of catalyst particles. The second group often has problems of small particle synthesis due to particle agglomeration and limitations in catalyst crystalline structure. It is also worth to stress that multistage catalyst synthesis procedure results in a very high catalyst price. Due to all last decades' developments, platinum metal loading was decreased from the level of about 10 to 2–3 mg/cm^2 used now (Carmo et al. 2013). But it is still one of the main problems of PEM electrolyzers. Certainly a lifetime of PEM electrolyzer is strongly connected with the amount of used precious metals. It is well known that magnetron sputtering provides a method of protective film or thin catalyst layer (onto either the membrane or the gas diffusion layer) depositing (Arnell and Kelly 2004; Litster and McLean 2004). Earlier we established that magnetron sputtering could be rather efficient for catalyst on carbon carrier synthesis (Fedotov et al. 2013; Grigoriev et al. 2014), and in our research we investigated the possibility of ion implantation method and its combination with magnetron sputtering.

2 Experimental Facility

An ion implantation process is illustrated with Fig. 1. Ion implantation experiments were carried out on the experimental installation "Kremen 1" with implanter "Sokol-30/100" (vacuum 10^{-4} Pa, flow of ions up to 5×10^{14} ion/cm^2 per second, diameter of Pt/Pd ion source 6 mm, distance between ion source and implantable target 200 mm, time of implantation up to 24 minutes). The energy of implantable ions was 1–50 keV. An ion implantation was carried out in an impulse mode due to technical specification of the installation (25–35 impulse/s) and to provide a more uniform implanted atoms distribution and to avoid a large target heating. Amount of implanted ions was controlled by weight of a test sample and data of electron microscopy. Numerical model for estimation of the depth of implanted ion penetration and their concentration distribution was developed using "one particle

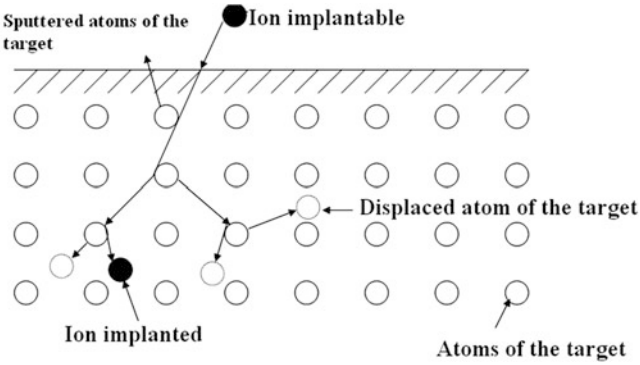

Fig. 1 Schematic illustration of an ion implantation process

implantation" approach for an isotropic and homogeneous medium. The calculations were realized with using the TRIM program. Magnetron sputtering was carried out at a modified laboratory magnetron installation (MIR 1) with a negative pulse potential bias applied to the implantable sample. Such a bias reached 200 V and permitted to combine sputtering with additional low-energy ion implantation to provide surface cleaning and fixation of the sputtered metal particles on the surface of stack components (and catalyst carrier). At the same time, such an additional implantation created sputtered atoms of protective film material and provided creation of a more uniform protective coating (or new catalytic centers). Pulse bias mode (up to 60 impulse/s) was used to avoid electric arc formation and to provide more uniform catalyst distribution on a catalyst carrier surface. The base pressure in the chamber was set to 10^{-3} Pa and the working pressure of argon was set to 4×10^{-1} Pa. Sputtering of Pt (Pd) was carried out at a current 0.1 A, distance to the target was 85 mm, and speed of metal atom deposition was about 10^{13} atoms/s*cm^2. Metal loadings deposited onto the targets were controlled by weight measurements of "sample witness". For mixing of catalyst carrier particles, a special device was used (Grigoriev et al. 2014). Electrochemical measurements were carried out in a standard three-electrode glass cell (saturated silver chloride reference electrode) in 1 M solution of H_2SO_4 using a Solartron 1285 potentiostat/galvanostat (potentiodynamic measurements in a potential range of −0.2 to +1.1 V vs. Ag/AgCl electrode with 20 mVs^{-1} sweep rate) and in laboratory electrolysis cells with a round shape catalyst layer area 7 cm^2. In PEM water electrolysis cells, catalyst layers are prepared by spraying of iridium black (anode) or platinum black on carbon (cathode) dispersion in Nafion solution on the cathode side. Porous titanium sheets (thickness 1 mm, porosity 37%) were used as current collectors. Material composition and structures were tested using transmission electron microscopy (TEM) analysis (microscope CM30 Philips) and X-ray diffraction (XRD) analysis (Bruker D8 Advance). As experimental results were rather similar for Pt and Pd, we'll concentrate on the discussion of results obtained with Pt.

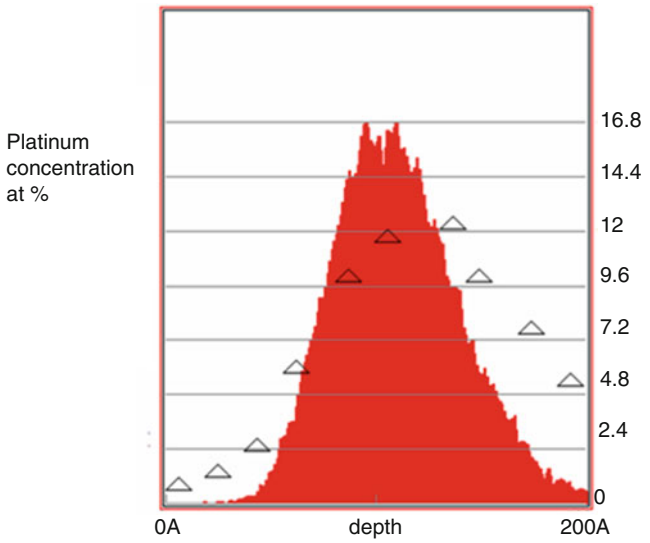

Fig. 2 Distribution of Pt ions (atoms) in Ti at $E = 20$ keV and dose 10^{15} ion/cm^2. Triangles are experimental data

3 Results and Discussions

Numerical estimations of the depth of implanted ion penetration and their concentration distribution (see Fig. 2) showed that at energies about 10–50 keV at low doses (less than 10^{15} ion/cm^2), the maximum of Pt ion distribution is relatively deep (about 30 nm at 50 keV) and surface concentration of implanted ions (atoms) is less than 1%. With increase of the value of the dose, the surface concentration is increasing mainly due to sputtering of the surface layer which at the same time results in precise metal losses. At energies about 1–2 keV, sputtering is practically absent and surface concentration could reach 40–50% (if a diffusion of implanted atoms is excluded) though the depth of implanted layer is relatively small (about 1–2 nm). Experimental data of implanted ion distribution did not differ too much from numerical estimations (see Fig. 2) though in case of Pt and Pd, ions with different charges are produced and at a constant accelerating voltage they have different energies. Most of the Pt implanted ions are in a one- and two-charge state (the last one is dominating) according to Yushkov et al. (2014), and it was taken into account for further estimations. On potentiodynamic curves, we did not observe any typical peaks of hydrogen adsorption/desorption for Ti implanted by Pt ions at energies more than 5 keV even at doses 5×10^{17}. Only at energies about 1 keV and the same or even higher doses, small and deformed peaks were observed but not regularly. At the same time, one could observe a significant increase of implanted Ti electrode activity in reactions of oxygen evolution (Fig. 3) even at relatively high energies of implanted atoms (same for hydrogen evolution).

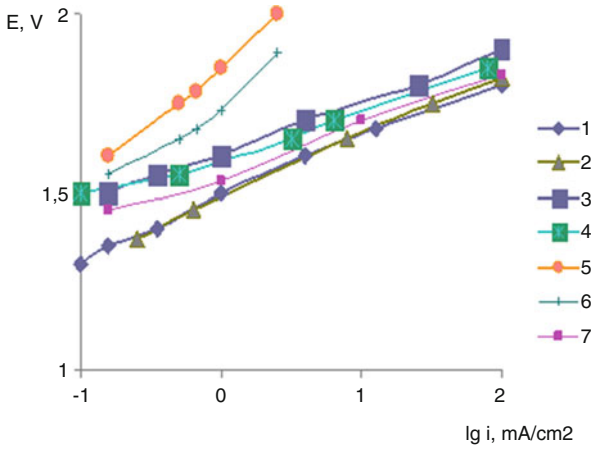

Fig. 3 Quasi stationary polarization curves (30 s at each potential) in 1 N H_2SO_4 at 20 °C for Ti foil with (1) Pt coating (23 nm) implanted with Ar^+ $E = 10$ keV, 10^{16} ion/cm^2; (2) Pt coating (42 nm) implanted with Ar^+ $E = 15$ keV, 10^{16} ion/cm^2; (3) Pt coating (23 nm) not implanted; (4) Pt foil, (5) Ti implanted with Pt $E = 10$ keV, $D = 10^{17}$ ion/cm^2; (6) Ti implanted with Pt $E = 5$ keV, 10^{17} ion/cm^2; (7) Ti implanted with Pt $E = 1$ keV, 10^{17} ion/cm^2

Table 1 Dependence of the time when electrode reached potential 2.6 V (SCE) at 80 mA/cm^2 upon Ti foil electrode treatment conditions. Pt foil thickness about 10–13 nm

Electrode treatment	Time
Not treated	<1 s
Implanted with Ar ions (2×10^{17}, 40 keV)	~1 s
Implanted with Pt ions (2×10^{17}, 40 keV)	47 min
Implanted with Pt ions (2×10^{17}, 2 keV)	61 min
Implanted with Pt ions (10^{17}, 40 keV, and then 10^{17}, 2 keV)	87 min
Sputtered Pt film	184 min
Sputtered Pt film treated with Ar^+ (5×10^{14}, 20 keV)	248 min

So during implantation of Pt, a solid solution of Pt in Ti was produced with a rather high electrochemical activity and stability in spite of a low surface Pt concentration. For accelerated tests of Ti electrode stability at anode polarization, the electrodes were polarized with current density 80 mA/cm^2, and the time during which the electrode potential was reaching 2.6 V (SCE) was taken as a reference value. Our experiments (see Table 1 and Fig. 3) showed that at large energies, surface stability for oxidation does not increase significantly though a produced oxide film has lower resistivity as it is doped by precise metal atoms. The surface layer obtained at low energies is significantly more stable against oxidation even at a relatively low amount of implanted precise metal. One can suppose that here additional effects also play rather significant role – increase of the surface roughness and creation of radiation defects and partial amorphization of the surface layer during implantation.

For example, when Ti foil was implanted by Ar ions, only one could observe significantly larger current at potentiodynamic polarization curves in comparison with not treated Ti. But these effects were not dominating at precise metal implantation, and it is possible to suppose that radiation defects are additionally decreasing the oxide film resistance. Combination of large- and low-energy implantation modes permitted to reach rather high surface stability with a rather high lifetime at Pt (Pd) concentrations less than 0.02 mg/cm^2. For bipolar plates and current collectors from porous Ti, a combined technology based on magnetron sputtering of Pt (Pd) assisted by ion (Ar, O) implantation demonstrated even more efficient results due to additional chemical and radiation surface modification but at slightly larger platinum metal loadings.

Implantation of C and N ions (10^{18} ion/cm^2, $E = 50$ keV) resulted in a significant decrease (3–4 times) of hydrogen penetration in Ti.

To obtain thick films, magnetron sputtering is significantly more attractive. But titanium plates with mechanically polished surface after Pt deposition by magnetron sputtering mainly demonstrated relatively low stability during potential cycling. We observe anode current decrease with each next cycle and sometimes even exfoliation of the Pt film. When Pt was sputtered onto porous (sintered) Ti, the stability was better but still not sufficient for long-term use. One can see (Fig. 4) that there was a strong dependence of the current on potentiodynamic curves (and obviously Pt-specific surface) upon Pt film thickness. Roughness factor (ratio or real to visible surface) was continuously increasing from 3.72 for Pt film 11 nm to 29.5 for Pt film 147 nm.

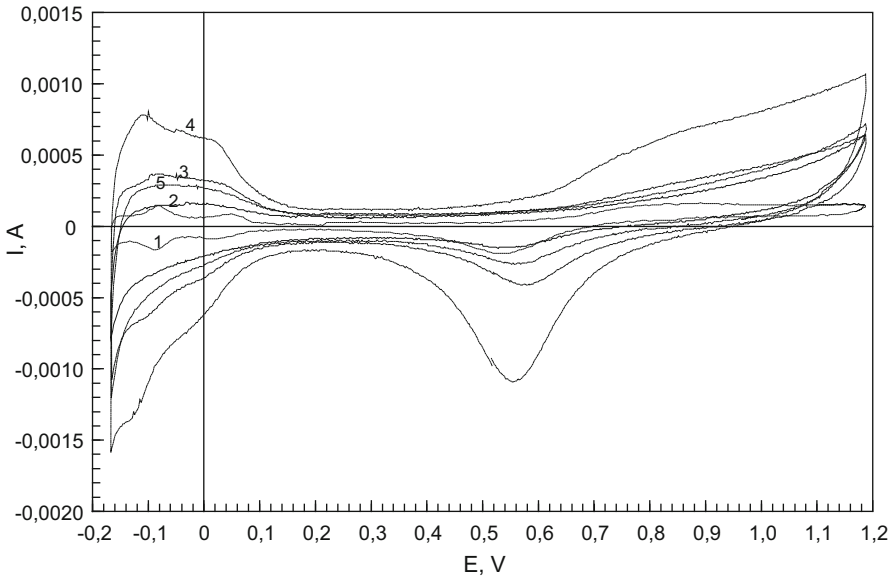

Fig. 4 Potentiodynamic polarization curves (20 mV/s in 1M H_2SO_4) for 1-Pt foil and porous Ti with sputtered Pt films with different thickness: 2–11 nm, 3–26 nm, 4–147 nm, and Ti implanted with Pt ($E = 5$ keV, 2×10^{17} ion/cm^2)

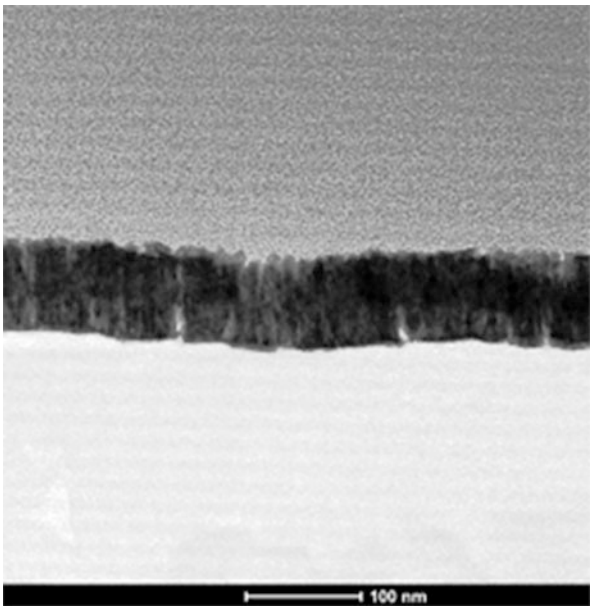

Fig. 5 SEM data on sputtered Pt film

It was possible to suppose that Pt film is rather porous and did not protect Ti surface efficiently from oxidation. Data of electron microscopy (Fig. 5) confirmed such an assumption as Pt film had a columnar structure.

A preliminary Ar ion implantation (10^{15} ions/cm^2, $E = 10$ keV) provided a significant improvement due to increase in surface roughness and purity in such electrode stability. In such a case, Pt nuclei are more uniformly distributed on the Ti surface at the initial stage, and film structure is also becoming more uniform. But the most efficient appeared to be simultaneous or consecutive ion implantation (Ar or same metal ions) together or after sputtering (see Fig. 3). When implantation was carried out by Ar ions during magnetron sputtering, energies up to 5 keV were used and such an implantation was most important at initial stage. It provided some increase of Pt atom energy due to Ar^+ flow directed to Ti surface and some sputtering of the Pt particles created on Ti surface. The accelerated by Ar^+ flux and sputtered atoms were introduced in the Ti surface layer providing some intermediate layer (Pt solid solution in Ti) and more uniform surface coverage by Pt. After magnetron sputtering for about 10 nm, film intensity of ion implantation could be reduced. Implantation after magnetron sputtering has one important disadvantage – one needs relatively high ion energies to reach Pt-Ti boarder through magnetron-sputtered Pt film (about 10 keV for Ar + ions for 10 nm film) and sputtering of Pt atoms (~5.8 atoms per ion) results in significant Pt losses. In case of Pd, sputtering is only slightly lower – 4 atoms/ion. So such a treatment could be efficient for thin (less than 10 nm) films. From data in Table 1 and Fig. 3, one can see that Pt films obtained by using such technique are significantly more efficient for Ti protection. Further improvement of oxidation resistance could be obtained by

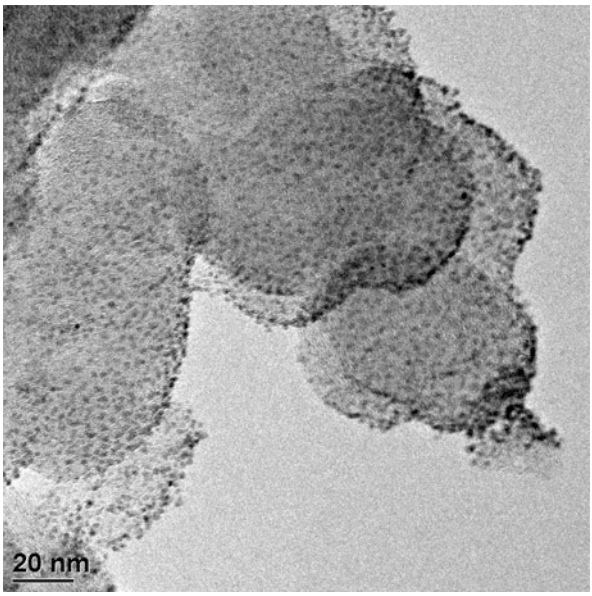

Fig. 6 SEM photo (Philips CM30) of Pt catalyst particles obtained by magnetron sputtering on Vulcan

additional chemical modification of Ti surface by implantation of O and N ions. It is necessary to mention that combination of magnetron sputtering with ion implantation could be a very efficient technology for catalyst layers and catalyst synthesis. Plasma-assisted deposition of platinum and Ir nanoparticles onto carbon carriers was carried out using the standard DC magnetron sputtering system, but with pulsed system of potential bias, application to carbon carrier was investigated. Size of Pt catalyst particles (3% weight) obtained on Vulcan and reduced graphene oxide was about 1–3 nm (Fig. 6) and specific surface about 110 m^2/g. For Ir 6–8 nm, Volt-ampere curves of PEM electrolysis cell with such catalysts were practically same as with catalysts obtained by "polyol" method (Tunold et al. 2010) but with lower (about 10–20%) precise metal loading. Certainly such catalyst synthesis technique cannot significantly decrease precise metal catalysts use but can significantly decrease catalyst price as it is practically one-stage process.

It is necessary to mention that in case of cathode materials based on titanium (bipolar plates and current collectors), implantation of carbon and nitrogen permitted to increase the stability of the construction material for about 3–4 times for hydrogen penetration. Tests of PEM electrolysis stack (5 cells) based on materials described above at operating pressure 30 bar, 80 °C, and current density 1.4 A/cm^2 for 400 h did not show any degradation of the stack parameters.

Ion implantation method was also tested for modification of alkaline electrolyzer electrode (Ni) surface. Implantation of Co, Pd, and Pt ions resulted in an increase of current density at a constant voltage of about 20–30%, but optimum parameters of implantation must be chosen for proper electrode lifetime.

4 Conclusions

Ion implantation and magnetron sputtering assisted by ion implantation were studied. It was shown that ion implantation of Pt and Pd in Ti results in solid solution production and significantly increases electrochemical stability (and even catalytic activity) for hydrogen and oxygen evolution at a rather low loading of precise metals (about less than 0.02 mg/cm^2). Combination of low- and high-energy ion implantation appeared to be most efficient for lifetime increase as it provided rather deep surface layer modification and high surface concentration of Pt (Pd). Magnetron sputtering resulted in a surface film with a columnar structure production which did not protect Ti surface efficiently from oxidation. Additional ion implantation with Ar^+ or O^+ ions of such films significantly improved electrode stability. Implantation of Ni by Co, Pt, or Pd ions increases electrode activity up to 30% in water alkaline electrolysis. Ion implantation of C and N ions provided decrease of hydrogen penetration in Ti in 3–4 times. Magnetron sputtering assisted by ion implantation gives a good possibility for efficient and relatively cheap catalysts synthesis for PEM electrolyzers. Pt particles (diameter 1–3 nm, specific surface area about 110 m^2/g) on carbon carrier were synthesized and successfully tested. Ir on carbon carrier also demonstrated high activity. The developed techniques give possibility for precise metal loading decrease in PEM electrolyzers and decrease the price of protecting coatings and catalysts themselves due to more cheap production technology – decrease of amount of synthesis stages.

This research was supported by the Russian Scientific Foundation Grant №14–29-00111.

References

Arnell, R.D., Kelly, P.J., Bradley, J.W.: Recent developments in pulsed magnetron sputtering. Surf. Coat. Technol. **188–189**, 158–163 (2004)

Carmo, M., Fritz, D.L., Mergel, J., Stolten, D.: A comprehensive review on PEM water electrolysis. Int. J. Hydrog. Energy. **38**, 4901–4934 (2013)

Fedotov, A.A., Grigoriev, S.A., Lyutikova, E.K., Millet, P., Fateev, V.N.: Characterization of carbon-supported platinum nano-particles synthesized using magnetron sputtering for application in PEM electrochemical systems. Int. J. Hydrog. Energy. **38**, 426–430 (2013)

Grigoriev, S.A., Porembskiy, V.I., Fateev, V.N.: Pure hydrogen production by PEM electrolysis for hydrogen energy. Int. J. Hydrog. Energy. **31**, 171–175 (2006)

Grigoriev, S.A., Fedotov, A.A., Martemianov, S.A., Fateev, V.N.: Synthesis of NanostructuralElectrocatalytic materials on various carbon substrates by ion plasma sputtering of platinum metals. Russ. J. Electrochem. **50**(7), 638–646 (2014)

Kozlov, S.I., Fateev, V.N.: Hydrogen Energy, p. 520. Gazprom VNIIGAZ, Mascow (2009) (in Russian)

Litster, S., McLean, G.: PEM fuel cell electrodes. J. Power Sources. **130**, 61–76 (2004)

Porter, Jr. F.J.: Development of a solid polymer electrolyte electrolysis cell module and ancillary components for a breadboard water electrolysis system, Technical Report NASA-CR-112183, (1972), U.S. NASA

Tunold, R., Marshall, A., Rasten, E., Tsypkin, M., Owe, L.-E., Sunde, S.: Materials for Electrocatalysis of oxygen evolution process in PEM water electrolysis cells. ECS Trans. **25**, 103 (2010)

Yushkov, G.Y., Vodopyanov, A.V., Nikolaev, A.G., Izotov, I.V., Savkin, K.P., Golubev, S.V., Oks, E.M.: Generation of high charge state platinum ions on vacuum arc plasma heated by gyrotron radiation. Rev. Sci. Instrum. **85**, 02B902 (2014)

Determination of Metals in Water and Sediment Samples of the Sürmene River, Turkey

Nigar Alkan, Ali Alkan, and Coşkun Erüz

1 Introduction

River water is used for many purposes such as drinking; irrigation; hydroelectric power plant; industrial and municipal facilities' discharge area for uncontrolled industrial, agricultural, and domestic wastes; and fishing (Camelo et al. 1997; Guieu et al. 1998; Mendiguchía et al. 2007). The quality of water is determined by physical, chemical, and microbiological properties (Alkan et al. 2013). Anthropogenic inputs are major source of metals and affected the quality of waters. Concentration of most metals in river is very low and produced from rock and soil. The main anthropogenic sources of heavy metal in rivers are mining, fertilizer, and pesticides in agricultural fields. Pollutants that come from domestic, industrial, and agricultural activities are first released into rivers and reach the sea and lakes through rivers. Between heavy metals and organic substances in the aquatic environment is a strong interest and this profile can change water quality. Metals, unlike other pollutants, can accumulate in sediments, uptake to toxic levels, and affect river organisms over time (Gedik and Boran 2012). Therefore, the determination of physicochemical profile, heavy metals, and organic substance for the water quality in coastal areas is important for the future estimation of the pollutant load of the rivers (Alkan et al. 2014). The aim of this study is to understand temporal and spatial changes of the land-based metal pollutions in the Sürmene stream.

N. Alkan (✉) • C. Erüz
Karadeniz Technical University, Faculty of Marine Sciences, Sürmene, Trabzon, Turkey
e-mail: nalemdag@ktu.edu.tr; anigar@gmail.com

A. Alkan
Karadeniz Technical University, Institute of Marine Sciences and Technology, Trabzon, Turkey

© Springer International Publishing AG, part of Springer Nature 2018

F. Aloui, I. Dincer (eds.), *Exergy for A Better Environment and Improved Sustainability 2*, Green Energy and Technology,
https://doi.org/10.1007/978-3-319-62575-1_13

2 Material and Methods

2.1 Study Area

Water and sediment samples were collected from three stations located between Sürmene and Köprübaşı cities on Sürmene river (Station 1: 40°54′ 32.68″N, 40° 06′ 22.66″E, Station 2: 40°52′ 06.79″N, 40° 06′ 20.60″E, Station 3: 40°50′ 04.28″N, 40° 06′ 42.14″E) in Trabzon between 2010 and 2011 during the autumn, winter, spring, and summer seasons.

Sürmene river flows into the Black Sea basin starting from the coast and up to 2700 m altitude rough land. The average flow of the river is 5.40 m^3/s, precipitation basin is 227.2 km^2, and river length is 41.3 km. The average annual rainfall varies between 1300 and 2400 mm. There are two towns and 52 neighborhood villages in the basin that generally carry on agricultural activities. There are no industrial plants in the basin except six hydroelectric power plants and a tea factory (Boran and Sivri 2001).

2.2 In Situ Measurements

Temperature (°C), pH, electrical conductivity (μs/cm), dissolved oxygen (mg/L), oxygen saturation (%), salinity (‰S), and total dissolved solid (mg/L) were measured seasonally in situ by Hach Lange HQ40D multimeter.

2.3 Water Sampling

Water samples were collected in acid-washed bottles from three stations and filtered through 0.45 μm pore-sized filters for dissolved metals analysis. After adding the acid, the samples were stored at −20 °C until analysis.

2.4 Sediment Sampling

Sediment samples were collected from 3 stations and they were preserved in acid-washed bags and placed in ice bags in the field. They were stored in deep freeze at −20°C in the laboratory until analysis.

2.5 *Laboratory Analyses*

Dissolved metal (μg/L) concentrations in water samplings were measured according to the method of EPA (1994). Sediment grain sizes were classified according to Folk (1954). Total organic carbon (TOC) was determined by using modified Walkley-Black titration method (Gaudette 1974). Carbonate levels were measured by Piper (1974) method. Metal analyses (Cr, Mn, Al, Co, Ni, Cu, Zn, As, Mo, Cd, Sb, and Pb) were performed using sediment passed through a sieve with 63 micron. All data in sediment were given mg/kg dry weight. After sediment samples digested in the closed microwave digestion system, dissolved and particulate trace metals were determined using ICP-MS (inductively coupled plasma mass spectrometry). The collision reaction interface (CRI) was used during the determination of As. Both Sc and In (50 ppb) were added to all standards, blanks, and samples and acted as internal standards.

The results obtained were classified regarding the criterias of European Commission Directive (EC 1998), National Recommended Water Quality Criteria (US EPA 2009), and World Health Organization (WHO 2004) for drinking water.

3 Results and Discussions

Seasonal water and sediment samples were collected from three stations located on Sürmene stream in Trabzon between 2010 and 2011.

Average seasonal in situ measurment results in the Sürmene river stations were given in Table 1. The pH of water is indication of its quality and dependent on carbon dioxide and carbonate-bicarbonate equilibrium. Temperature, dissolved oxygen, and total dissolved solid of three stations in the river were directly related with seasons.

As a result of grain size analysis in the sediment samples that the sand-medium grain sized fraction (32–36%) was generally dominant in the all stations. The sand-coarse grain sized fraction was varing from 12% to 33% in all stations which was noticed maximum in the Station 3. The maximum silt fraction was found as 10% in Station 2 (Fig. 1).

Organic matter is one of the most important factors in metal mobility in sediment. Minimum and maximum values were determined for pH as 8.18–8.59, for organic matter as 1.64–2.09%, for carbonate as 7.60–12.45%, and for total organic carbon as 0.08–0.13% in sediment samples of the three stations (Table 2).

As a result of dissolved metal in the Sürmene stream water, there were statistical differences ($p < 0.05$) and higher than stations 2 and 3 for Zn concentration in the station 1. There are no statistical differences for other metals ($p < 0.05$) among the stations (Fig. 2).

According to seasonal distributions, there are no statistical differences for Pb, Cd, Mo, As, Zn, Cu, and Co concentrations. Al concentration in winter period was

Table 1 Seasonal average of some physico-chemical parameters in Sürmene Stream

Parameters	Station no		
	1	2	3
Temperature (°C)	12.26 ± 4.13	14.20 ± 4.48	16.66 ± 3.72
pH	7.51 ± 0.27	7.62 ± 0.49	7.94 ± 0.43
Dissolved oxygen (mg/L)	9.98 ± 0.73	9.70 ± 0.72	9.11 ± 0.4
Oxygen saturation (%)	92.73 ± 3.96	93.75 ± 3.52	71.8 ± 34.27
Conductivity (µs/cm)	0.11 ± 0.03	0.10 ± 0.03	0.11 ± 0.02
Salinity (‰ S)	0.06 ± 0.01	0.05 ± 0.01	0.06 ± 0.02
TDS (mg/L)	0.08 ± 0.01	0.06 ± 0.02	0.08 ± 0.01

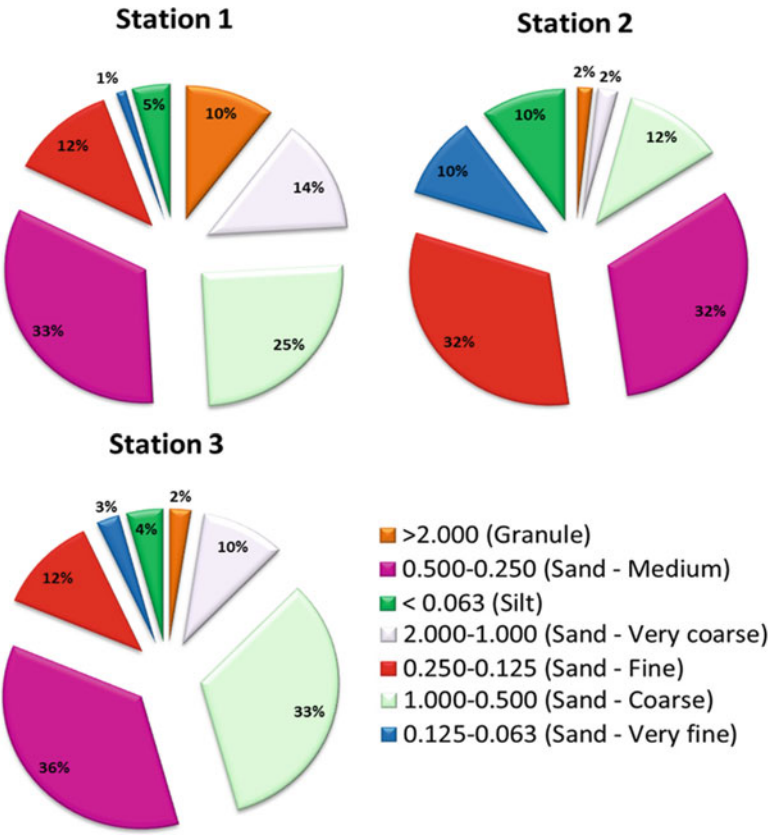

Fig. 1 Grain size distributions of sediment samples

statistically different and lower than other seasons. Similar situation persisted during the spring for Cr and Ni concentrations. Sb concentration was statistically different ($p < 0.05$) and higher in autumn than second and third stations in other seasons. There is similar distribution for Mn concentration in spring and autumn.

Table 2 Average pH, organic matter, carbonate, and total organic carbon concentrations in sediment samples

St. no	pH	Organic matter (%)	Carbonate (%)	Total organic carbon (%)
1	8.59	1.64	12.05	0.08
2	8.32	2.09	7.60	0.13
3	8.18	1.66	10.32	0.11
Average	8.36	1.80	9.99	0.11
Std. Dev.	0.21	0.25	2.25	0.02

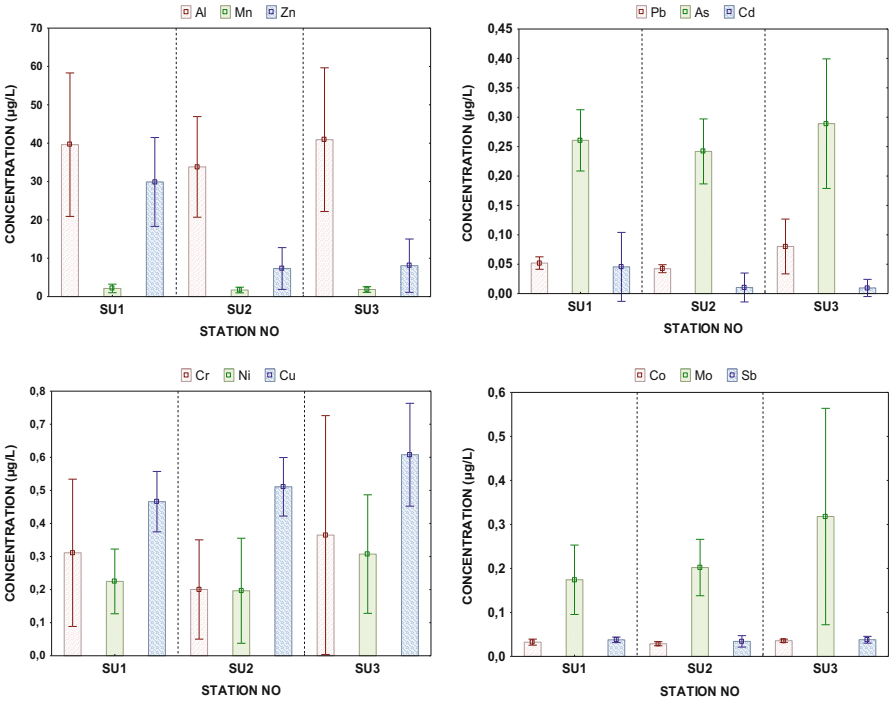

Fig. 2 Average dissolved metal concentrations of stations in the Sürmene Stream

However, there were statistical differences ($p < 0.05$) and higher level in winter and summer (Fig. 3, Table 3).

4 Conclusions

Physicochemical quality parameters are required for ecological status of river waters and sediments, but dynamic systems of river may change during the times. The surface water chemistry of river can influence the atmospheric inputs, climatic

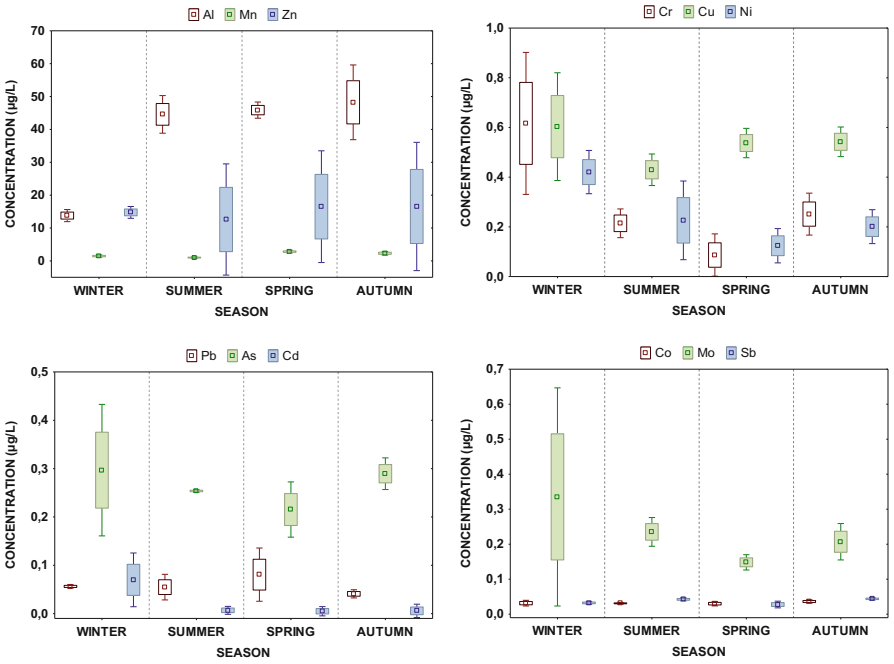

Fig. 3 Seasonal dissolved metal distrubitions

Table 3 Average metal concentrations in sediment samples of the Sürmene stations

	Stations				
Metals (mg/kg)	1	2	3	Average	SD
Al	34,237	33,183	33,083	33,501	639
Fe	31,759.8	30,525.0	30,637.7	30,974	682
Mn	1086.6	840.7	882.4	936.6	131.6
Cr	39.0	33.0	32.5	34.8	3.6
Co	13.5	12.5	13.5	13.2	0.6
Ni	18.5	15.5	19.0	17.7	1.9
Cu	39.5	37.0	32.5	36.3	3.5
Zn	68.0	72.5	62.5	67.7	5.0
As	11.0	12.0	7.5	10.2	2.4
Pb	27.0	23.0	17.5	22.5	4.8

conditions, and anthropogenic inputs. Metal concentrations in fresh water resources are important for human health and aquatic ecosystem.

All results obtained were classified regarding the criteria of European Commission Directive (1998/83/EC), National Recommended Water Quality Criteria (US EPA 2009), and World Health Organization (WHO 2004). Results obtained

from Sürmene river were found to be lower than legal limits proposed by EC L 330/05 (1998), US EPA (2009), and WHO (2004).

Hydroelectric power plant in water environment can affect living sources and impair the quality for use of river water. The usage of these natural resources must be optimum. Protection of ecological status of rivers and supporting local people sustainable development (irrigation, controlled flooding, hydroelectric power plant, waste discharges, etc.) must be balanced.

Acknowledgments This research was supported by the Scientific Research Project of Karadeniz Technical University (Project code: 890).

References

Alkan, A., Serdar, S., Fidan, D., Akbaş, U., Zengin, B., Kılıç, M.B.: Physico-chemical characteristics and nutrient levels of the eastern Black Sea rivers. Turk. J. Fish. Aquat. Sci. **13**, 847–859 (2013)

Alkan, N., Alkan, A., Akbaş, U., Fisher, A.: Metal pollution assessment in sediments of the southeastern Black Sea coast of Turkey. Soil Sediment Contam. **24**, 290–305 (2014)

Boran, M., Sivri, N.: Trabzon (Türkiye) İl Sınırları İçerisinde Bulunan Solaklı ve Sürmene Derelerinde Nütrient ve Askıda Katı Madde Yüklerinin Belirlenmesi, E.U. J Fish Aquat Sci. **18**, 343–348 (2001)

Camelo, L.G.L., Miguez, S., Marbán Rato de, L.: Heavy metals input with phosphate fertilizers used in Argentina. Total Environ. **204**, 245–250 (1997)

EPA (United States Environmental Protection Agency), Determination of Trace Elements in Waters and wastes by Inductively Coupled Plasma-Mass Spectrometry, Method 200.8, Revision 5.4, EMMC Version. (1994)

European Community Council Directive 98/83/EC (1998). Council Directive 98/83/EC of 3 November 1998 on the quality of water intended for human consumption. (1998)

Folk, R.L.: The distinction between grain size and mineral composition in sedimentary- rock nomenclature. J. Geol. **62**, 344–359 (1954)

Gaudette, H.E., Flight, W.R., Toner, L., Folger, D.W.: An inexpensive titration method for the determination of organic carbon in recent sediments. J. Sedimant Petrol. **44**, 249–253 (1974)

Gedik, K., Boran, M.: Assesment of metal accumulation and ecological risk around Rize Harbor, Turkey (southeast Black Sea) affected by copper ore loading operations by using different sediment indexes. Bull. Environ. Contam. Toxicol. **90**, 176–181 (2012)

Guieu, C., Martin, J.M., Tankere, S.P.C., Mousty, F., Trincherini, P., Bazot, M., Dai, M.H.: On trace metal geochemistry in the Danube River and western Black Sea. Estuar. Coast. Shelf Sci. **47**, 471–485 (1998)

Mendiguchía, C., Moreno, C., García-Vargas, M.: Evaluation of natural and anthropogenic influences on the Guadalquivir River (Spain) by dissolved< heavy metals and nutrients. Chemosphere. **69**, 1509–1517 (2007)

Piper, D.J.W.: Manuel of Sedimentological Techniques. Dalhousie Univ. Publ. Romankevich, E. A., 1984, Geochemistry of Organic Matter in the Ocean. Springer and Verlag, Berlin, Heidelberg, New York (1974)

U.S. Environmental Protection Agency, United States Environmental Protection Agency National Recommended Water Quality Criteria, (2009)

WHO: Chap. 12, Annex 4. In: Guidelines for Drinking-Water Quality, 3rd edn. World Health Organization, Geneva (2004)

Biodiesel Production by Transesterification of Recycled Vegetable Oils

Souad Zighmi, Mohamed Bilal Goudjil, Salah Eddine Bencheikh, and Segni Ladjel

1 Introduction

The orientation of researches toward renewable energy has become an important element of energy policy worldwide. Indeed, the development of renewable energy has become a necessity especially for the environment protection from the various problems caused by the use of fossils, especially global warming.

In a search for new energy sources, our attention is mainly focused on biomass as a reliable and renewable source that can satisfy the demand in energy. Currently, the methyl esters of vegetable oils and animal fats are considered as a real alternative to liquid fossil fuels (Cvengro and Cvengrošova 2004). However, biofuels constitute also an effective alternative to existing fossil fuels, for they offer the prospect of ecological sustainability and reduce greenhouse gas emissions (Saharan et al. 2013). Among the current biofuels, biodiesel represents an alternative to petroleum-based fuels (Balat and Balat 2008; Azcan and Yilmaz 2013). Biodiesel is produced from vegetable oils, animal fats, frying oils, and used wastes (Mustafa Balat). Biodiesels have many advantages compared with those derived from petroleum such as producing less smoke, having a higher cetane number, and releasing small amounts of carbon monoxide; they are renewable and specially nontoxic (Stavarache et al. 2005). The FAME (Fatty Acid Methyl Ester) produces fewer greenhouse gas emissions than petrodiesel; CO_2 emissions in the engine

S. Zighmi (✉)
University of Ouargla, Faculty Sciences of the Nature and Life, Ouargla 30000, Algeria

University of Ouargla, Faculty of Applied Sciences, Department of Process Engineering, Ouargla 30000, Algeria
e-mail: zighmi.so@univ-ouargla.dz

M.B. Goudjil • S.E. Bencheikh • S. Ladjel
University of Ouargla, Faculty of Applied Sciences, Ouargla 30000, Algeria

© Springer International Publishing AG, part of Springer Nature 2018

F. Aloui, I. Dincer (eds.), *Exergy for A Better Environment and Improved Sustainability 2*, Green Energy and Technology,
https://doi.org/10.1007/978-3-319-62575-1_14

output is reduced slightly (1%) with biodiesel if the equipment (tanks and vehicles) are compatible with the use of biodiesel.Biodiesel is often used after being mixed at different percentages with conventional diesel oil. It can be used in compression-ignition diesel engines with little or no modification (Kim et al. 2004). Currently, most biodiesel factories rely on the use of refined vegetable oils as their main raw materials. However, these types of oil contribute to the increase of the overall production cost of biodiesel to about 80%; while the use of frying oil for biodiesel production reduces raw materials cost to about half the price of the ordinary oil (Azcan and Yilmaz 2013). Note that the edible oils and fats used are considered as a waste contributing to the environmental pollution and thus their reinjection into sewers and the underground will cause degradation of the environment. Therefore, any attempt to use the frying oil as feed for biodiesel synthesis offers a dual benefit of preserving nature and of producing energy (Nair et al. 2012). The objective of this contribution is to highlight frying oil as a source of raw material for biodiesel synthesis.

Nomenclature

t	Time per minute
μ	Viscosity in centipoise (cp)
ρh	The oil density (g/cm^3)
ρb	: Ball density (8.03 g/cm^3)
k	Viscometer constant 3.3 for size 2
MKOH	Molar mass of KOH (56 g.mol^{-1})
VKOH	KOH solution volume used (mL)
CKOH	KOH titrated solution exact concentration (mol.L^{-1})
Moil	Mass of the test sample (g)
v'	Volume in ml of the hydrochloric acid solution (HCl) at 1 mol/l for the blank titration
V	Volume in ml of the hydrochloric acid solution (HCl) at 1 mol/l for the sample titration
N	Exact normality of the hydrochloric acid solution
m	Mass of the sample
Subscripts	
NO	Normal oil
RO	Recycled oil
BNO	Biodiesel for normal oil
BRO	Biodiesel for recycled oil

2 Materials and Methods

Today, rapeseed and soybean are the two most commonly used raw materials for biodiesel production. Rapeseed produces about 435 l to 550 l of biodiesel per hectare, while soybean produces about 160 l per hectare; also, sunflower can

produce 280 l of biodiesel per hectare (Balat and Balat 2008), (Kojima and Johnson 2005). Note that the majority of biodiesel in the USA is produced from soybean oil, estimated at more than 90% (Collins 2006). In the present work, we have chosen an edible oil widely used in Algeria, sold under the name "ELIO." Thus, two varieties of this oil are used in this study: the first is the unused ELIO oil and the second one is the same oil, used at most three times for frying.

The ELIO oil is edible vegetable oil composed of 20% sunflower and 80% soybean. The formulas of the corresponding triglycerides are as follows:

$$\text{Sunflower oil (High linoleic)} : C_{57}H_{98}O_6$$
$$\text{Soybean oil} : C_{57}H_{106}O_{10}$$
$$\text{ELIO Oil} : 20\% \text{ sunflower and } 80\% \text{ soybean}$$

The molecular weight of this oil is given by

$$M = 0.8 \times M_{\text{soybean}} + 0.2 \times M_{\text{sunflower}} \tag{1}$$
$$M = 943.6\,\text{g/mol}$$

2.1 Characterization of the Studied Oils

Some parameters characterizing these oils were determined as follows: the refractive index, the cetane number, the acid number, and the saponification number, in addition to the evaluation of density and viscosity variation at different temperatures.

2.1.1 Variation in the Density of Oils

The oils' density variation based on temperature is accomplished by means of a standard densitometer of type DMA 35_N (Density Meter, Anton Paar, Serial: 80,306,269, from 0 to 2 g/cm^3).

2.1.2 Variation in Viscosity of Oils

The viscosity of the oils based on the temperature was monitored using a falling ball viscometer (from stainless steel ball). The dynamic viscosity was determined through the following formula:

$$\mu = k(\rho_b - \rho_h)\,t \tag{2}$$

The unit of viscosity obtained is centipoise (1 cp = mPa/s), the kinematic viscosity is calculated by the following formula: $\upsilon = \mu/\rho_h$.

2.1.3 The Acid Number

In our work it is believed that the free acids are represented by only linoleic acid; the IA is given by the following formula:

$$\mathrm{IA} = \frac{M_{\mathrm{KOH}} \times V_{\mathrm{KOH}} \times C_{\mathrm{KOH}}}{m_{\mathrm{oil}}} \tag{3}$$

The IA in this work is determined by titration.

2.1.4 Saponification Number

$$S = \frac{(V' - V) \times 56.1 \times N}{m} \tag{4}$$

The saponification value is given by the following formula (4):The saponification number in this work is determined by titration.

2.2 Biodiesel Synthesis in Laboratory

Methyl esters are obtained by reaction of triglycerides transesterification by methanol using KOH as catalyst; our choice of catalyst is based on a previous study by May (2004), which showed that $Na_{(s)}$, NaOH and KOH are effective catalysts for the transesterification reaction.

For all the tests made we used a heating reflux apparatus that consists of a 1000 ml flask equipped with a condenser, the stirring system was provided by a magnetic bar. The flask was immersed into a water bath; the reaction was carried out for 2 transesterification at a temperature of 50 °C. The quantities of materials used are shown in Table 1.

The molecular weight of methanol is: M (methanol) = 32.04 g/mol; and the molecular weight of oil is: 943 g/mol.

Table 1 Quantities of reagents used

Oil	Methanol	Catalyst
250 g	85 g (report 1: 10)	2.5 g (1% weight of oil)
250 g	72 g (report 1: 8)	2.5 g (1% weight of oil)

2.2.1 Characterization of Biodiesel

Physicochemical characterization touches the following parameters: the acid number and the flash point with the evaluation of density and viscosity variation at different temperatures.

2.2.2 Characterization by IR Spectroscopy

We used as a method of analysis, infrared rays (IR) by means of Infrared Spectrophotometer type IR-408 (SHIMADZU corporation, Serial N°. A200129,031,261).

3 Results and Discussion

3.1 Characterization of Oils Used

The characteristics of the two types of oil used in this study, namely: ordinary oil (NO) and recycled oil (RO) (used for frying) are summarized in Table 2.

The fire point and the flash point were monitored using a semi-Automatic Tag open cup flash point tester (Stanhope-Stea (mindex) serial 1,027,348, ios 9001:2008), and the index of refraction was measured by ABBE Refractometer (147434).

From Table 2 we note that the acidity and saponification values for RO are higher than those of NO, caused by the presence of an important gap between the two types of oil, due, on one hand, to the fact that the edible refined oil (ELIO) was treated to reduce its acidity and to eliminate the undesirable components (AGL, Phospholipids, etc.), and, on the other hand, the frying or storage may have caused the formation of free fatty acids inside the HF, which proves that a good quality oil possesses a low acid ratio and that a low saponification value corresponds to fatty acids containing a longer chain of carbon. Concerning the other properties mentioned in the table (index of refraction, flash point, cetane number), we notice that, overall, the values recorded for both types of oil are close, with only a thin difference.

Table 2 Oils physicochemical characteristics and properties

The characteristics	(NO)	(RO)
The acid number	0.5	1.83
Saponification number	74.66	253.86
Index of refraction	1.4756	1.4762
Fire point (°C)	346	340
Cetane number	48	47
Flash point (°C)	312	305

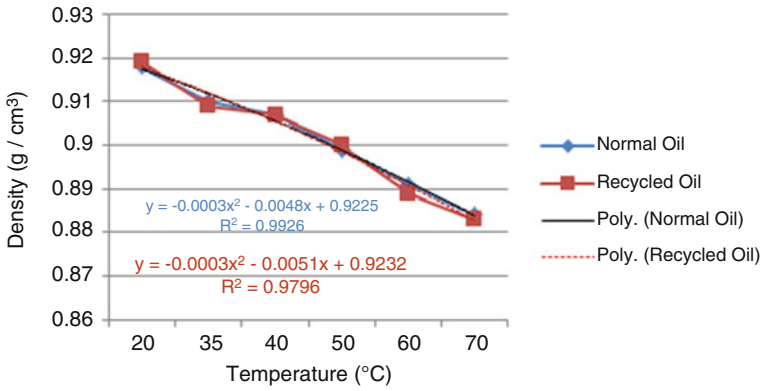

Fig. 1 NO and RO densities variation based on temperature

3.2 Oils Density Variation

Based on the recorded values in Fig. 1, it is noted very clearly that the density of the two oils decreases with increasing temperature. Moreover, this decrease is similar for both types of oil between 20 and 50 °C; however, from 50 °C we notice that the frying oil has lower densities compared with those recorded for the unused oil.

3.3 Oils Viscosity Variation

From the curves (Fig. 2) it is noted that the oils viscosity has decreased when the oil temperature increased. Moreover, it is noted that there is a more or less significant difference between the values of the two types of oil. The measured viscosity values for both oils are very high, which constitutes a handicap for their direct use as biofuels. These results are consistent with those obtained by Kerschbaum and Rinke (2004), who have demonstrated that vegetable oils can be used as fuel for diesel engines, but with a viscosity much higher than that of regular diesel, their use requires engine modifications (Kerschbaum and Rinke 2004). Indeed, the high viscosity seems to be the principal cause of many problems associated with the direct use of vegetable oils as biofuel (Ryan et al. 1984); knowing that vegetable oils are extremely viscous with viscosities 10–20 times higher than that of diesel (Çetin and Yuksel 2007).

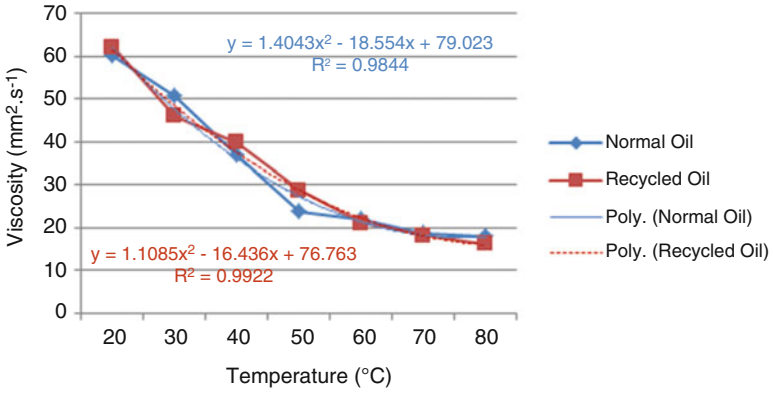

Fig. 2 NO and RO viscosity variation based on temperature

3.4 Yield of Biodiesel

The yield of the synthesized biodiesels from the two types of oil and with the two molar ratios (1/10 and 1/8) is calculated by the following formula:

$$\eta = \frac{\text{experimental mass of biodiesel}}{\text{theoritical mass of biodiesel}} \tag{5}$$

Theoretically, 1 kg of oil gives 1 kg of biodiesel by transesterification reaction while the theoretical mass of biodiesel is the mass of oil that we used in the reaction.

The obtained results are shown schematically in Fig. 3.

From Fig. 3, firstly, we notice that the yield achieved with the unused ELIO oil is higher than that achieved with the used oil for both molar ratios. Secondly, the yield of the ratio (1/8) is greater than that obtained with the ratio (1/10) in this case. In addition, the analysis of the results presented in Fig. 3 indicates that the difference in yield between the two types of oil is 07.58% and 20.4% with the ratios (1:8) and (1:10), respectively, after being exposed at the same temperature, reaction time, and for the same amount of catalyst. Following these results, it can be said that the use of frying oil with a molar ratio of 1:8, in 2 h only of reaction and under a temperature of 50 °C, improves the yield of oil conversion by transesterification. Thus, it is a wise choice, for it helps to contribute to environmental remediation, with costs more or less acceptable. The yield results also confirm that the molar ratio is an important factor and that our results are consistent with those obtained by Tomasevic and Siler-Marinkovic (2002), who have found that the molar ratio is far more effective than the catalyst of the transesterification reaction. We notice that the superior molar ratios are used to improve the solubility and to increase the contact between the triglyceride molecules and the alcohol (Noureddini et al. 1998).

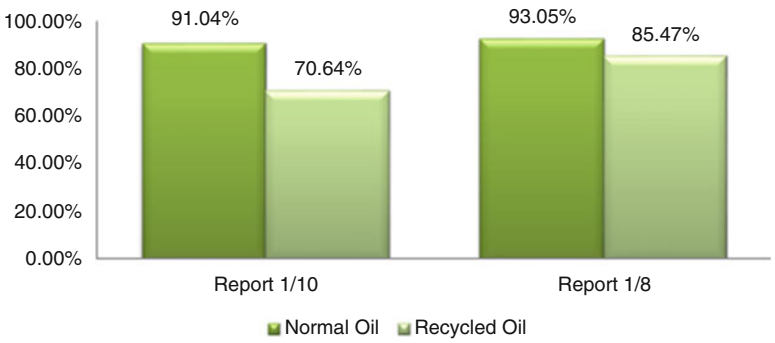

Fig. 3 The yield of biodiesel from regular oil ELIO and from frying oil with the two ratios (1/8 and 1/10)

Table 3 Biodiesel characteristics

Characteristics	BNO	BRO
The acid number	0.56	1.12
Flash point (°C)	198	249

3.5 Biodiesels Characterization

The biodiesel characteristics obtained by transesterification from the two types of oil are summarized in Table 3.

The measured values for the acid number and the flash point show that there is a significant difference between the two types of biodiesel. Indeed, the frying oil biodiesel possesses excessive values in comparison with those of the ordinary oil biodiesel.

3.6 Biodiesel Density Variation

The biodiesel density variations are presented in Fig. 4.

From the results shown in Fig. 4, we notice that the density values for both biodiesels are less than those of oils, and also the fact that they are decreasing with an increasing temperature.

3.7 Biodiesel Viscosity Variation

Viscosity is another important property of biodiesel since it affects the functioning of the injection system. The variation of viscosity based on two biodiesels temperature is presented in Fig. 5.

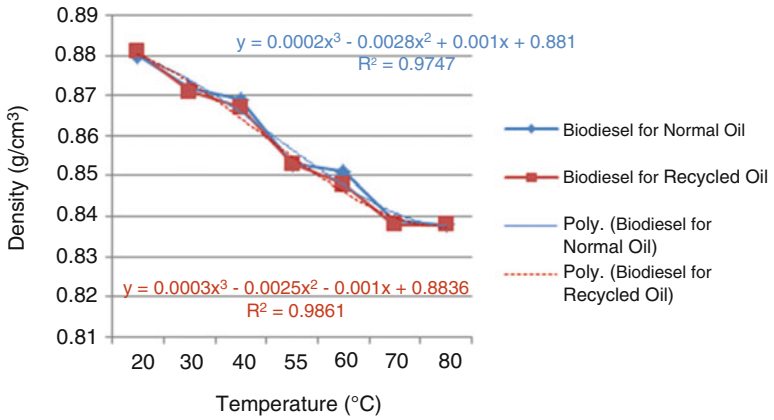

Fig. 4 BNO and BRO density variation based on temperature

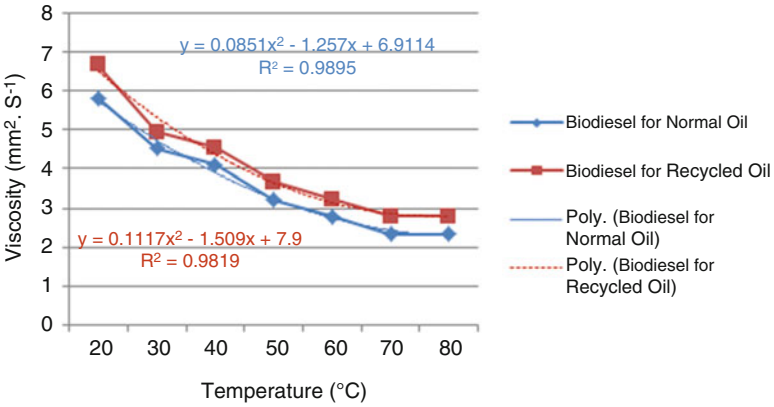

Fig. 5 BNO and BRO viscosity variation based on temperature

From Fig. 5 it is noted that the biodiesels viscosity decreases with an increasing temperature. Also the viscosity of the biodiesel synthesized from unused oil (BNO) is considerably lower than that obtained by the use of frying oils (BRO) and this while using, for all values, the same temperatures from 20 to 80 °C. The most interesting thing is that the gap between the two is thin, which allows us to say that the use of frying oil for biodiesel production is better.

Furthermore, comparing the viscosity values of the unused (NO) and the used oils (RO) with those measured for the synthesized biodiesels (BNO and BRO) at temperatures of 20 and 80 °C, shows that there is a significant decrease in viscosity depending on the temperature increase for the oils and biodiesels, and adding to that, the values of the biodiesels viscosities are significantly lower than those of oils

for both temperatures of 20 and 80 °C. The comparison of the viscosity values for biodiesel and oils was also done; the obtained results are summarized in Table 4.

The analysis results of Table 4 show that the viscosity variation gap during the transition from oil to biodiesel is significant for both oils. However, this gap is much wider for the unused oil compared to that of the frying oil, for both temperatures values. It is also observed that this gap is doubled to 3.28% for the unused oil and to 6.56% for the frying oil, when the temperature increases from 20 to 80 °C. Following these results, we can conclude that the use of frying oil for biodiesel production offers the advantage of a significant decrease in viscosity, which presents the major obstacle for the direct use of vegetable oils as diesel engines fuel Figs. 6 and 7.

Table 4 Percentage of oils and biodiesel viscosity reduction based on temperature

Oil to Biodiesel	20 °C	80 °C	Difference
NO to BNO	90.32%	87.04%	3.28%
RO to BRO	89.24%	82.68%	6.56%

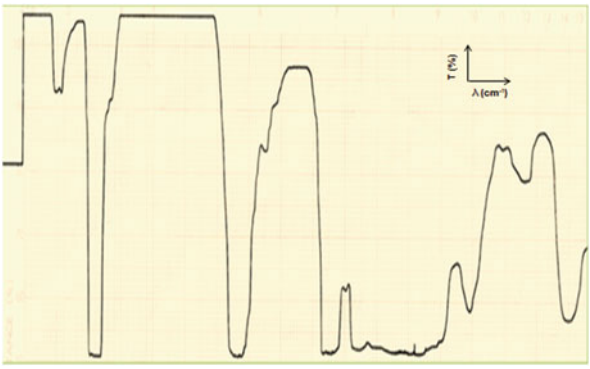

Fig. 6 IR spectrum of produced biodiesel from unused oil

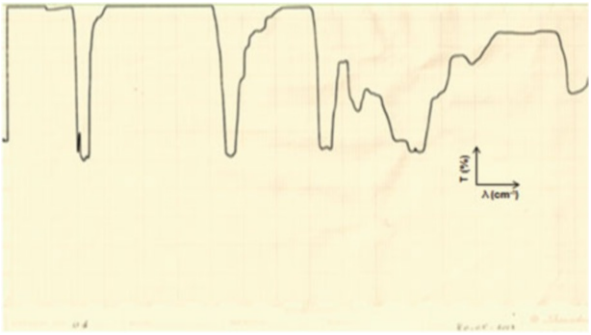

Fig. 7 IR spectrum of produced biodiesel from used frying oil

3.8 Biodiesels Characterization by IR Spectroscopy

The main functional groups of biodiesels are summarized in Table 5.

The analysis of the Table 5 and spectrum samples allows us to draw the following information:

- A stretching vibration between 2900 and 3000 cm^{-1} corresponds to an ester grouping C-H.
- A stretching vibration at 1100 cm^{-1} for (BNO) and 1155 cm^{-1} for (BRO) corresponds to a grouping of C-O.
- A stretching vibration at 1740 cm^{-1} corresponds to a grouping of C = O.

These data confirm the presence of an ester.

3.9 Checking of Biodiesels Quality

In order to see if the synthesized biodiesels are consistent with the international standards, a comparison between the two types of synthesized biodiesels and those standards is essential. Table 6 includes some parameters used for the comparison.

The comparison concerns certain properties, namely, density, viscosity, and the acid number. Firstly, our present biodiesels are characterized by densities and viscosities, which are consistent with the standards. Secondly, the ordinary oil has an acid number conforming to the standards, while the frying oil possesses a noncompliant acid number. From the analysis results, shown in Table 5, concerning the flashpoint, we can say that the synthesized biodiesels have, for the high values recorded, low flammability, as follows: 198 and 248, respectively, for the unused oil biodiesel and for the frying oil biodiesel. These results confirm that the biodiesel provides advantages in terms of safety compared to petroleum diesel, for it is much less flammable compared to petroleum diesel, which is characterized by a 77 °C according to Balat (2005).

Table 5 Biodiesel functional groups IR spectrum

Functional group		C-H	C = O	C = C	C-O
cm^{-1}	BBNO	3000	1750	1640	1100
	BBRO	2900–3000	1740	1645	1155

Table 6 Checking of biodiesels quality

Parameters	BNO	BRO	Standard	Diesel
Density at 15 °C	0.884	0.883	0.86–0.9	0.820–0.850
Kinematic viscosity at 40 °C	4.1	4.54	3.5–5	2–4.5
Acid number	0.56	1.12	0.8 max	–
Flash point	–	–	101	55 min
Cetane number	–	–	51	49–53
Fire point (°C)	198	249	–	–

4 Conclusion

Biodiesel is one of the most important renewable energy sources due to its various advantages. It is synthesized by transesterification, which is the most recommended technique. In this recent study, we applied this technique to synthesize biodiesels from two types of oil, first the ordinary oil ELIO, the second one is the frying oil. We also used methanol for the reaction and KOH as catalyst. The analysis results showed that a molar ratio of oil/alcohol of 1:8 is better in our experience, for it provides a yield of approximately 93.05% of ordinary oil and 85.07% of frying oil. The characterization of the synthesized biodiesels was initiated thereafter; we used infrared spectroscopy to identify the functional group of the formed biodiesel, which confirms that the synthesized biodiesels are methyl esters of fatty acids.

Other parameters were also checked for the oils and biodiesels, namely, acid number, saponification value, refractive index, cetane number (the latter for oil only), and also the variation of density and viscosity based on temperature. The analysis of these parameters and their comparison with the standards can draw the following conclusions:

- Biodiesels densities are low compared to those of oils.
- Biodiesels flash point and cetane number are higher than those of diesel.
- The frying oil relatively high acidity is a priori due to the changes that it has undergone due to the high temperatures and impurities during its use.

References

Azcan, N., Yilmaz, O.: Microwave assisted transesterification of waste frying oil and concentrate methyl ester content of biodiesel by molecular distillation. Fuel. **104**, 614–619 (2013)

Balat, M.: Current alternative engine fuels. Energy Sour. **27**, 569–577 (2005)

Balat, M., Balat, H.: A critical review of bio-diesel as a vehicular fuel. Energy Convers. Manag. **49**, 2727–2741 (2008)

Çetin, M., Yüksel, F.: The use of hazelnut oil as a fuel in pre-chamber diesel engine. Appl Thermal Eng. **27**, 63–67 (2007)

Collins, K.: Economic issues related to biofuels. United States Department of Agriculture (USDA) – The Office of the Chief Economist (OCE), Washington (DC). www.usda.gov/oce/index.htm (2006)

Cvengroš, J., Cvengrošova, Z.: Used frying oils and fats and their utilization in the production of methyl esters of higher fatty acids. Biomass Bioenergy. **27**, 173–181 (2004)

Kerschbaum, S., Rinke, G.: Measurement of the temperature dependent viscosity of biodiesel fuels. Fuel. **83**, 287–291 (2004)

Kim, H.J., Kang, B.S., Kim, M.J., Park, Y.M., Kim, D.K., Lee, J.S., et al.: Transesterification of vegetable oil to biodiesel using heterogeneous base catalyst. Catal. Today. **93–95**, 315–320 (2004)

Kojima, M., Johnson, T.: Potential for Biofuels for Transport in Developing Countries. Energy Sector Management Assistance Programme (ESMAP). Energy and Water Department, The World Bank Group, Washington (DC) (2005)

May, C.Y.: Transesterification of palm oil: effect of reaction parameters. J. Oil. Palm Res. **16**, 1–11 (2004)

Nair, P., Singh, B., Upadhyay, S.N., Sharma, Y.C.: Synthesis of biodies el from low FFA waste frying oil using calcium oxide derived from Mereterix mereterix as a heterogeneous catalyst. J. Clean. Prod. **29-30**, 82–e90 (2012)

Noureddini, H., Harkey, D., Medikonduru, V.: A continuous process for the conversion of vegetable oils into methyl esters of fatty acids. JAOCS. **75**, 1775–1783 (1998)

Ryan, T.W., Dodge, L.G., Callahan, T.J.: The effects of vegetable oil properties on injection and combustion in two different diesel engines. J. Am. Oil Chem. Soc. **60**, 1610–1619 (1984)

Saharan, B.S., Sharma, D., Sahu, R., Sahin, O., Warren, A.: Towards algal biofuel production: a concept of green bio energy development. Innovative Romanian Food Biotechnology. **12**, 1–21 (2013)

Stavarache, C., Vinatoru, M., Nishimura, R., Maed, Y.: Fatty acids methyl esters from vegetable oil by means of ultrasonic energy. Ultrason. Sonochem. **12**, 367–372 (2005)

Tomasevic, A.V., Siler-Marinkovic, S.S.: Methanolysis of used frying oil. Fuel Proc Tech. **80**, 1–6 (2002)

Membrane Desalination Technology in Algeria: Reverse Osmosis for Coastal Areas

Z. Tigrine, H. Aburideh, M. Abbas, S. Hout, N. Kasbadji Merzouk, D. Zioui, and M. Khateb

1 Introduction

Seawater desalination is necessary in a number of countries that witness water shortage, as an option for securing the supply of drinking water to the population, given the rapid increase in water demand in the sectors of agriculture and industry. The biggest constraints of the desalination system are its energy consumption per cubic meters product and environmental impacts due to discharges of brine in the natural environment. Despite these constraints, desalination plants grow around the world, including desalination processes to deal with the increasing water demands. Resources are limited in quality and quantity, resulting in the establishment of treatment solutions of brackish water and seawater.

Currently, on the industrial scale more than 15,000 desalination plants have been installed worldwide with a production capacity of about 56 million m^3/day with 64% seawater while the global capacity of drinking water production is about 500 million m^3/day. In the Mediterranean, the production of desalination plants is 10 million m^3/day. The total production capacity is estimated to be more than 8.5 billion gallons/day (Quteishat and Abu-Arabi 2006).

Z. Tigrine (✉)
Unité de Développement des Equipements Solaires, UDES/Centre de Développement des, Energies Renouvelables, CDER, Bou Ismail 42415, W. Tipaza, Algeria

USTHB, BP32 El Alia, Bab-Ezzouar, 16111, Algiers, Algeria
e-mail: phyzahia@yahoo.fr

H. Aburideh • M. Abbas • S. Hout • N.K. Merzouk • D. Zioui
Unité de Développement des Equipements Solaires, UDES/Centre de Développement des, Energies Renouvelables, CDER, Bou Ismail 42415, W. Tipaza, Algeria

M. Khateb
Myah Tipaza, Usine de dessalement d'eau de mer Fouka Marine, W. Tipaza, Algeria

© Springer International Publishing AG, part of Springer Nature 2018

F. Aloui, I. Dincer (eds.), *Exergy for A Better Environment and Improved Sustainability 2*, Green Energy and Technology,
https://doi.org/10.1007/978-3-319-62575-1_15

In remote regions, particularly in the Middle East and North African countries MENA, freshwater scarcity is a huge problem. The exploitation of groundwater aquifers and surface water has contributed to the decrease in quantity and quality of existing natural water resources (Mohamed et al. 2008).

Availability of electricity networks in these regions is frequently limited; technologies that are able to remove pathogens and dissolved contaminants require large amounts of energy (Eltawil et al. 2009; Schafer et al. 2007). Different economic constraints encouraged the spread of desalination technologies in the Arab countries where potable water is an essential resource as electricity (Al-Karaghouli et al. 2009). The total population is around 325 million with a very high growth rate of 2.7%; the per capita share of the total annual renewable water resources (TARWR) has dropped well below the UN threshold for water poverty (1000 m^3/year) with most of the Gulf Arab countries reaching per capita TARWR below 200 m^3/year (El-Nashar et al. 2007).

One of the most common membrane desalination methods is reverse osmosis; it has emerged as the dominating technology to produce freshwater from seawater for many industrial and domestic applications (Greenlee et al 2009). Several technologies allow the production of freshwater from seawater and brackish water. In general, desalination technologies can be classified into two different processes of separation, namely, thermal and membrane-based desalination. Among the known thermal processes, multiple effect distillation (MED), multistage flash (MSF), and vapor compression distillation (VCD) can be cited while the membrane processes include reverse osmosis (RO), electrodialysis (ED), and nanofiltration (NF).

Processes based on separations' membranes know in this context a great interest. They seem to be very powerful tools for desalination, purification, and recycling of fluids for a "zero waste" goal.

The reverse osmosis technique is the most commonly used technology for desalination where it comprises up to 45% of the total world desalination capacity. The development of desalination applications and positioning of membrane processes compared to thermal processes can boost technological and process innovations in this field. The changes aim to reduce energy consumption, investment, and operating costs.

Furthermore, the reverse osmosis facilities are mainly concentrated in the regions situated around the Mediterranean Sea where energy consumption is lower compared to the other water desalination technologies. The energy consumption of seawater reverse osmosis plants decreased in time from 20 kWh/m^3 in the 1970s to 3.5 kWh/m^3 in the 1990s due to energy recovery, pumping systems, and the development of efficient membranes destined and characterized for seawater (MacHarg and Truby 2004).

However, the costs of water desalination are very high for its intensive use of energy. As seawater has a higher osmotic pressure than brackish water, the energy requirement to desalinate brackish water was estimated below 1.5 kWh/m^3, and it remains lower than that for seawater (Kehal 1991). As the cost to desalinate brackish water is less than other existing alternatives, desalination in many arid and semiarid regions can be the best way to obtain clean and freshwater.

More recently, membrane technology has witnessed an enhancement, resulting in a significant increase in water production with high quality and cost saving.

More improvements of membrane desalination efficiency, namely, the development of new fouling resistant membranes, use of appropriate pretreatment, optimization of reverse osmosis operating factors, brine management, as well as renewable energy coupling to desalination technologies, can contribute to reducing water production cost. Due to rising environmental concerns, renewable energy technologies are most interesting for powering water desalination facilities.

For well over a decade, there have been a large number of experimental and theoretical works on characters that have been carried out in order to make changes and improve the performance of this type of desalination plant. However, in some cases, for example in small rural sites or during disasters where potable water is not available, small RO systems operating using photovoltaic (PV) systems could also be used to obtain drinking water, to help people survive.

Many attempts and experiments have been conducted to find appropriate coupling processes between the RO desalination processes and PV systems as renewable energy resources. This area has continued to attract the interest of many researchers. Several studies focused on this type of configuration by carrying out experimental small plants. With support from the Canadian government, Keefer et al. (1985) developed two small reverse osmosis systems powered by photovoltaic energy in Vancouver, British Columbia, to demonstrate the use and optimization of solar energy consumed with storage batteries (panels have a power of 480 W). To produce demineralized water 0.5–1 m^3/day, they examined the differences between the direct connections of PV reverse osmosis system, the maximum power tracking, and included storage battery. Using a positive displacement pump with variable speed, with energy recovery of the rejected brine, they claim to be able to reduce life cycle costs by 50% compared to conventional systems OI/PV. Other investigations illustrated that power consumption can be reduced to 0.89 kWh/m^3 (Maurel 1991; Kehal 1991), and an attempt was made to model this type of coupling without using batteries as given by Thomson (Fritzmann et al. 2007).

Hanafi (1994) studied the different desalination technologies associated with renewable energy, mainly solar, wind, tidal, and geothermal. He presented some control limits for the use of energy sources including wind, which are more recommended than RO/PV. A systematic approach to renewable energy-powered desalination considering all the alternatives was presented by Rodriguez et al. (1996). Of all the combinations studied, they concluded that RO powered by PV is interesting in very specific cases, such as in sunny remote sites.

A small reverse osmosis system (RO) powered by photovoltaic (PV) systems has been installed and tested at the island of Gran Canada by Herold et al. (1998). A feasibility study of this small PV system RO of 1 m^3/day was presented. The pilot plant, with an average production capacity of 3.2 m^3/day of freshwater, is coupled to a stand-alone PV system and storage batteries. The rated power consumption is 2.35 kW. They described in detail the technical characteristics of the installation (RO) as regards its operating constraints and energy consumption.

Antho Joyce et al. (2001) described a small pilot reverse osmosis unit powered by a PV system that was implemented in the Department of Renewable Energy, INETI. This small compact unit with a daily production of 100–500 L operating at low pressure (<5 bar) with a PV module 3 × 50Wp can produce drinking water from brackish water containing salt concentrations of about 5000 ppm. They presented the preliminary results of laboratory tests carried out in the summer of 2000 in Lisbon. A spiral membrane-type MP-TA50 with a filtration mode coupled with the low pressure operation (<5 bar) enables low power consumption, around 100 kJ/kg impregnation. However, these results related to daily production have been confirmed by other operating conditions by comparing the quality of impregnation and the energy consumed according to pressure. Nevertheless, they may conclude that the energy consumption of the small pilot of reverse osmosis system decreases as the feed water recovery and supply pressure increase. The results of these experiments are used to validate a mathematical model of a system based on the I-V characteristics of PV modules. This model predicts the annual production of drinking water of this unit and the cost of the water produced by this type of system.

In Algeria, Sadi and Kehal (2002) and Kehal (2003) conducted experiments on a reverse osmosis desalination plant installed in Hassi Khebi (south-eastern Algeria) with a capacity of 0.85/h driven by a photovoltaic generator. This unit was acquired as part of the collaboration between the research center CDER (Algeria) and the Commissariat à l'Energie Atomique (CEA France). They presented the evolution of power and pressure versus time; the results were encouraging during the experimentation period, giving a conversion rate of 40.7%. Subsequently, the rate dropped to 24% due to neglect and lack of skilled technicians. Unfortunately, the membranes were clogged, causing a loss of production. They also presented the perspectives and desalination opportunities along the Algerian coast with 1200 km and within the country where several aquifers are characterized by high salinity, 2–5 g/l salts dissolved.

Badreddine et al. (2004) were able to build a prototype of a reverse osmosis desalination unit with 100 L/h at the laboratory scale powered by a photovoltaic energy source (550 W–4.2 A). This innovative concept was installed at AAST in Egypt in the framework of a cooperation project with PROAUT UASZ and supported by SwissContact. The plant is intended for educational and research purposes. This preliminary operation experience shows that skilled personnel is required for operating and maintaining these kinds of desalination systems. They briefly discussed some of the issues of research that can be studied at laboratory scale, by modeling the system to optimize energy consumption, system availability, and production of water under variable weather conditions.

In Jordan S. Abdallah et al. (2005) have presented an experimental study which aims to investigate the potential for water desalination development using a solar-powered system. The results have shown that the reverse osmosis system powered by photovoltaic energy can be easily applied. They may conclude that a gain of 25 and 15% of electrical energy and the flow of desalinated water, respectively, is possible using the tracking system on east-west axis with flat fixed plate. The results are presented in curve form, namely, the electric current, voltage, electric power,

and the production rate for a fixed surface and a tracking PV system versus time. Furthermore, the production rate for a fixed surface and a tracking PV system according to electric current was introduced. They reported that more experimental work must be done to study the continuous performance of the system, and further investigation should be directed to the membrane fouling and system recovery.

Different possibilities of coupling RO with the most appropriate sources of renewable energy as hybrid systems (photovoltaic and wind) are presented by Bourouni et al. (2011) using a new model based on the genetic algorithms to minimize the total water cost. Village of Ksar Ghilène located in the south of Tunisia was chosen for this study that presents the case study of PV/RO unit installed since 2007. A comparative analysis with reference software (ROSA for the RO unit and HOMER for the PV modules) was validated.

Numerical simulations on a small-scale, stand-alone, solar-PV-powered (RO) system, with or without battery storage, were reported by Daniel et al. (2013). They note that the system scalability influences the sensitivity of simulations and the type of I-V characteristics used. The results confirm that including batteries to store excess renewable energy has a significant impact on the performance of smaller systems compared to larger ones. Various alternative systems can be used for desalination technology integrating the RO desalination process. Ibarra et al. (2014) analyzed the performance of a specific solar desalination organic Rankine cycle (ORC) system at part load operation. They tried to understand its behavior from a thermodynamic perspective and were able to predict the total water production with changing operation conditions. It is seen that the water production is stable during day and night through the thermal storage where the rate flow was around 1.2 m^3/h.

Current desalination technologies were described by Youssef et al. (2014) by comparing their performance in terms of input and output water quality, amount of energy required, and environmental impact. They suggest that adsorption desalination technology is a suitable technology for seawater desalination with its low running cost and low environmental impact as it uses waste energy resources.

To meet the demand for potable water in areas where reserves are insufficient, the recourse to desalination remains the best solution.

The Algerian government has launched several large-scale programs to eradicate the problem of drinking and irrigation water shortage. Among them are the construction of new dams, water transfer, the implementation of desalination plants, and the development of new treatment plants and wastewater treatment. The aim of this chapter is to review the water shortage problem in Algeria and to present several plants of desalination that can be implemented on the Algerian Mediterranean coastal areas using reverse osmosis technology which are very effective for solving water scarcity problem from economic and environmental viewpoints. As the Algerian population is growing, the need for drinking water is increasing; water desalination is a promising means for producing clean water from saline water abundant in sea and also in the large Saharan region. We choose a case study: Fouka seawater desalination plant by providing its monthly rate production and energy consumption for 1 year.

Water and energy are two main topics for any country's development plan. A small reverse osmosis equipment coupled with a solar energy system such as PV, wind, and CSP (Concentrating Solar Power) could be useful to produce electricity which is able to generate the energy required by membrane desalination reverse osmosis applications. It seems that according to bibliographic research, photovoltaic energy system is an alternative to provide electricity and clean water. The most promising PV energy conversion technologies are available for remote and arid areas. This technology is in development in many regions where various technologies used to desalinate saline water have different performance and characteristics. We conclude that this type of technology is destined to remote areas where the access to electricity and water is a challenge.

2 Problematic and Hydric Resource in Algeria

Algeria is an important Mediterranean country; it faces increasing water shortages due to climate change (low rainfall, desertification, etc.). It stretches from east to west on a long coastline of 1200 km in length. The continual population growth, of which 80% is concentrated in the coastal cities, and business growth in socioeconomic sectors such as agriculture, industry, and tourism have led to increased consumption of water. Desalination and wastewater reuse solutions are imperative for Algeria to overcome water shortage.

Algeria still faces drinking water supply problem; first, mechanisms must be employed to reduce wastage and water leaks, as water remains insufficient in semiarid and arid regions. One solution is the production of freshwater from brackish water and/or seawater. With its ideal location, Algeria has the largest solar resource in the Mediterranean basin. The average duration of the Algerian territory sunshine exceeds 2000 h annually, reaching nearly 3500 h of sunshine in the Sahara desert. The total received power is estimated at 169,400 TWh/year, that is to say 5000 times the annual electricity consumption of the country. Algeria has limited water resources that are unevenly distributed in time and space, and the imbalance between supply and demand of water becomes a major constraint.

Algeria has very limited water resources, largely insufficient to cover domestic, agricultural, and industrial needs. A population of 90% is concentrated in the coastal strip where all economic activities of the country are concentrated, and it requires a considerable water supply. Its climate is diverse according to its geographical diversity and interannual rainfall variability. A variability in rainfall between West (350 mm average rainfall), East (1000 mm) and high relief (2000 mm), which becomes almost absent from the Sahara (average below 100 mm) and a concentration of precipitation over time, is noticed. The evolution of rainfall during 1922–2005 is presented in Fig. 1 for three regions, namely, Algiers, Constantine, and Oran. The figures show strong decrease in rainfall, especially in the Oran region. This situation causes drought cycles. Practically,

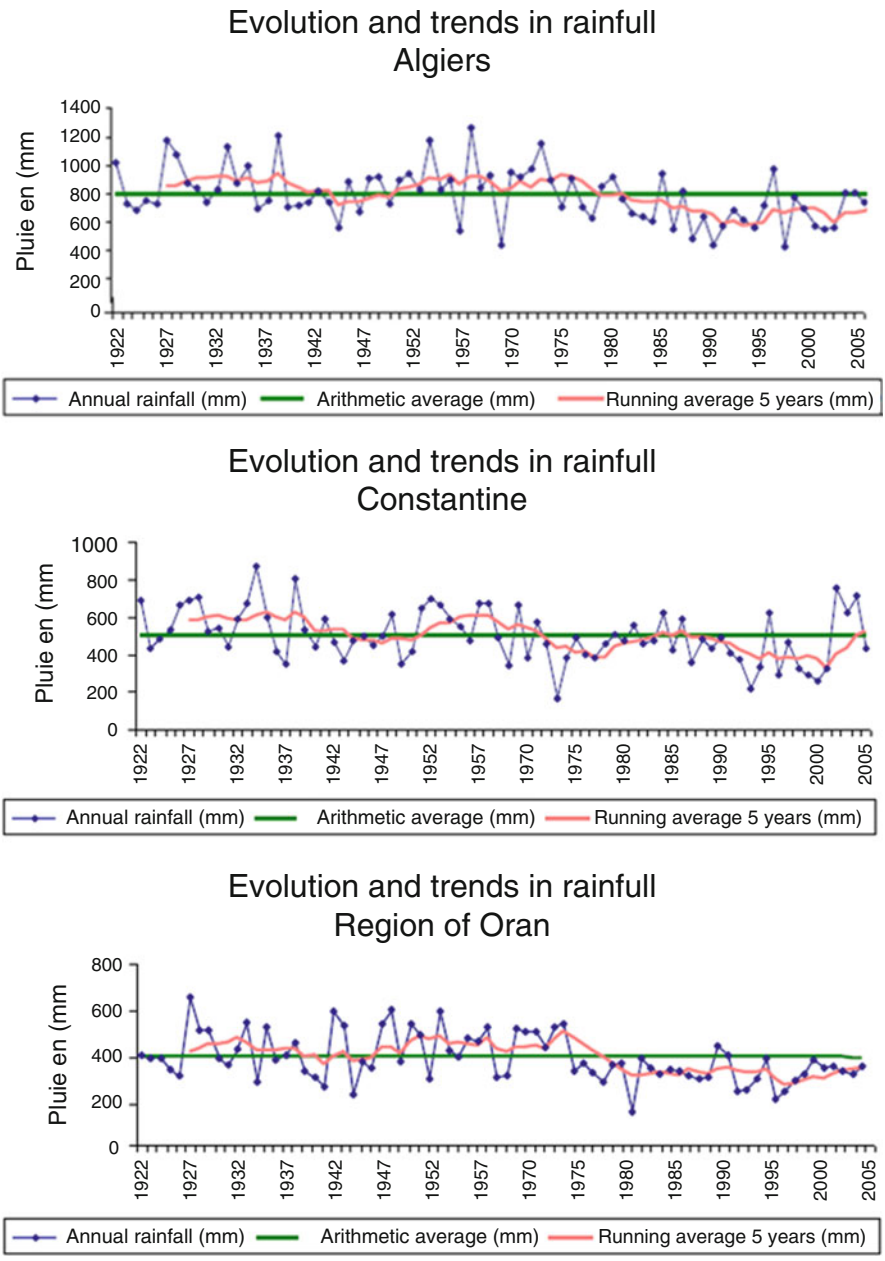

Fig. 1 Evolution of rainfall in three regions (Algiers, Constantine, and Oran) in 1922–2005 (Services de l'eau en Algerie Faire 2011)

Table 1 Total actual renewable water resources in the North African countries in 2005 according to AQUASTAT, FAO

Country	Population (1000 s)	Precip rate (mm/year)	TARWR volume (km^3/year)	TARWR per capita (m^3/year)	TARWR per capita (m^3/year)
Algeria	32,339	100	14	478	440
Tunisia	9937	300	4.6	482	460
Egypt	73,390	100	58	859	790
Morocco	31,064	300	29	971	930
Mauritania	2980	100	11	4278	3830
Libya	5659	100	1	113	106
Sudan	34,333	400	65	2074	1880

the North African countries have a low precipitation rate as shown in Table 1 that depicts water availability in the North African countries in 2005 according to FAO.

The hydrological context of Algeria is summarized within exorheic watersheds whose wadis have the outflow to the Mediterranean Sea, and the endorheic watersheds are formed of the chotts and sebkhas (saline lakes). The Sahara regions have an important subsoil rich in water and oil slicks (fossil fuel) according to Remini (2010).

Among the main technical problems encountered in the dams that affect the quantity and quality of water resources in the north of the country are the evaporation of dam lakes, the leaks in dams, the eutrophication of dam reservoirs, and the intrusion of seawater into coastal aquifers.

The country has five hydrography networks, by grouping 17 watersheds as shown in Fig. 2. Water resources are not equally distributed, in terms of either their geographical distribution, quantity, or nature (surface or groundwater). Water potential is estimated at 19.4 billion m^3/year among them; 12.5 billion m^3/year is distributed in the northern regions (superficial and underground resources) and 5.5 billion m^3/year in the Saharan regions (Problématique du secteur de l'eau 2009).

The country currently has 66 dams with a storage capacity of nearly 7 billion m^3. This number is expected to increase as 19 dams are under construction at present to allow regularize half of the total contribution of the wadis, or 5 billion m^3/year for an installed capacity of around 10 billion, and 20 new dams are planned for 2015. It is estimated that 1.6 billion is their average annual volume. Figure 3 represents the total surface water and groundwater resources and their distribution. In 1962, the annual water availability per capita was recorded about 1500 m^3.

This value was rapidly lowered over time; it recorded 720 m^3, 680 m^3, and 630 m^3 in 1990, 1995, and 1998, respectively. Today, owing to population pressure the annual water availability per capita is 500 m^3; this availability will be only 430 m^3 per capita by 2020. In terms of water potential, Algeria is below the theoretical scarcity threshold set by the World Bank (1000 m^3 per capita per year). Table 2 shows the water availability per capita in Algeria by 2020 (Problématique du secteur de l'eau 2009).

According to the Ministry of Water Resources, Algeria has 50 dams in operation, 11 are under construction, and 50 other dams are being studied; they should be

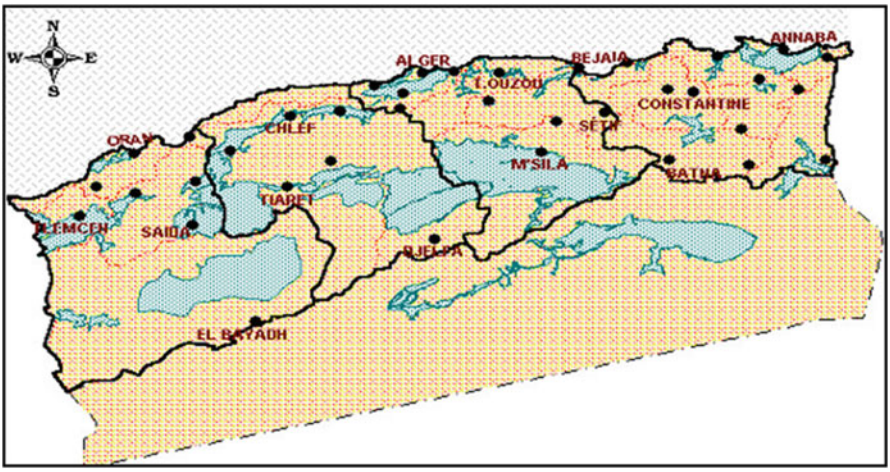

Fig. 2 Map of five geographic planning areas (Problématique du secteur de l'eau 2009)

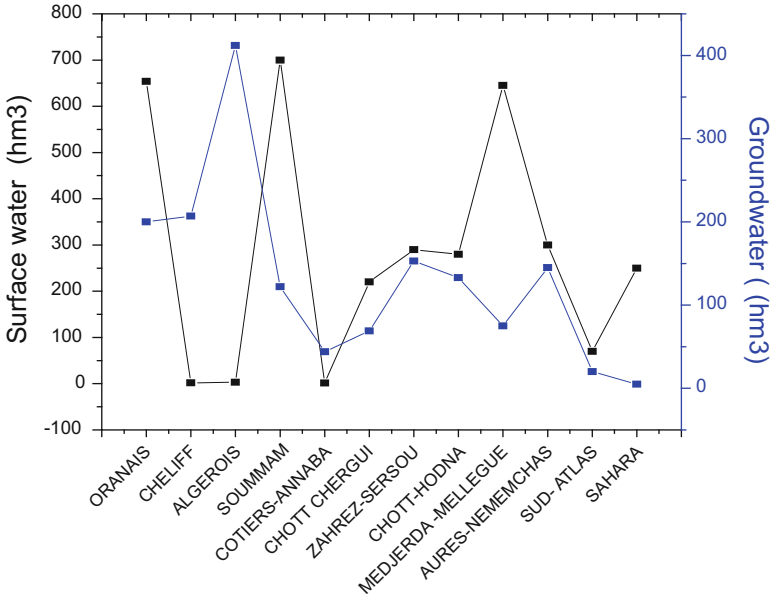

Fig. 3 Potential distribution per basin

completed before 2020 in order to catch up a delay found because of water losses estimated at 50%. Despite the construction of new dams and the use of desalination, Algeria will record a water deficit of 1 billion m^3 by 2025. The lack of resources is compounded by the poor spatial and temporal distribution of these resources, the soil erosion and siltation of dams, and the losses due to the obsolescence of

Table 2 Water availability per capita in Algeria by 2020 (Problématique du secteur de l'eau 2009)

Basin hydrographic	Resources (hm)	Population (106 capita)	Availability (m^3/capita)
Oranie chott Chergui	1400	6.3	220
Chélifer	2072	7.0	300
Algérois Soumma-Hadna	5125	15.8	320
Const-mejd Mellegue	5048	10.0	500
Sud	5436	4.9	1120
Total	64,518	44.0	430

distribution networks and insufficient management. In particular, the desalination of seawater and brackish water is one of the promising techniques for some regions of the country. It responds primarily to drinking water supply and irrigation of agricultural land. For this purpose, desalination is encouraged by the state whose government has installed several desalination plants in Algeria. Several major centers, such as Arzew which provides 90,000 m^3 or center of Beni Saf, have solved the problem of water scarcity in some cities.

3 Seawater Desalination Technology in Algeria

Water and energy are two main topics for any country's development plan. Algeria is the second largest country in Africa and the Arab world after Sudan in terms of surface area, and the largest around the Mediterranean whose southern areas include a significant part of the Sahara (80%). To meet the demand for freshwater in areas where reserves are insufficient, several countries have called on water desalination. The Algerian government has launched several national large-scale programs to eradicate the problem of drinking and irrigation water shortage. Among them are the construction of new dams, water transfer, the implementation of desalination plants, and the development of new treatment plants and wastewater treatment.

Desalination is a process that removes salts from water so that it may be used in municipal and industrial applications. With advanced techniques, desalination processes are becoming cost competitive with other methods of producing freshwater. Two main categories of technologies used for desalination can be classified as thermal and membrane. These technologies need energy to operate and produce clean water. Desalination processes using different techniques are determined by category as shown in Fig. 4.

Due to a severe continuous drought, the Algerian government has adopted a huge desalination program to overcome the water deficit. Thirteen seawater

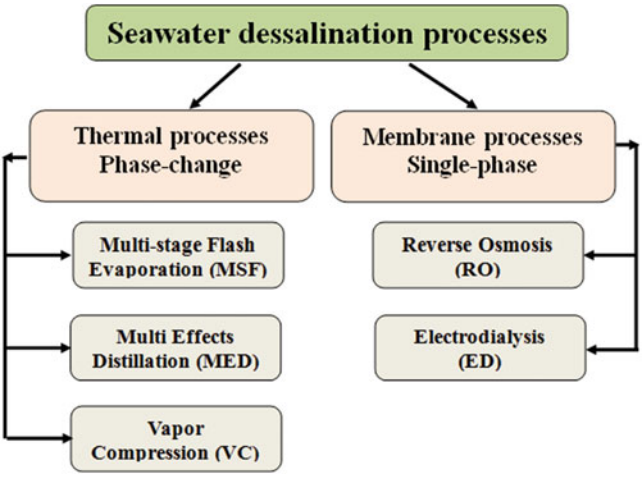

Fig. 4 The main desalination technologies and processes

desalination projects are operational with a total capacity of 2260 million cubic meters, that is, 2.26 billion liters per day. A determined program launched by the government in the last decade aims to deal with the lack of conventional drinking water resources and meet the domestic needs of more than 20 million Algerians. Moreover, 75 dams in construction will bring the overall volume of 6 billion m^3; they will be operational by 2025. Seawater desalination capacity in Algeria increased from 152,500 m^3/day in 2006 to 1. 2 Mm^3/day in 2011. At the end of 2012, the production capacity was 1.3 Mm^3/day, and the total capacity in 2014 reached 2.1 Mm^3/day. In Algeria, reverse osmosis technology is the most used for desalination that represents more than 95% as reported by Fig. 5. The general location and distribution of water desalination plants in Algeria is provided in Fig. 6.

Desalination of seawater in Algeria is an ambitious program; it is implemented through the installation of large seawater desalination plants as El-Magtaâ méga plant near Oran, which is operational since the first semester 2014. It is one of the largest in the world; it uses reverse osmosis process with a capacity of 500,000 m^3/day for the long-term coverage of needs for drinking water of 5 million people. The station of Hamma, called to ensure drinking water supply to Algiers, was inaugurated in February 2008, with a production capacity of 200,000 m^3/day. Figure 6 shows the different desalination plants implemented in Algeria with their capacity in cubic meters per day. We observe that the west region has benefited from a strong desalination capacity in comparison to the center region. The progress of these plants is presented in Fig. 7. This program concerned several regions, namely, Sahara, east, and west cities (Table 3 and Fig. 8).

Now, let us present the evolution of the installed capacity of water desalination in Algeria between 2006 and 2014 as given in Fig. 4 (MacHarg and Truby 2004). It can be seen that the total production capacity of drinking water increases along

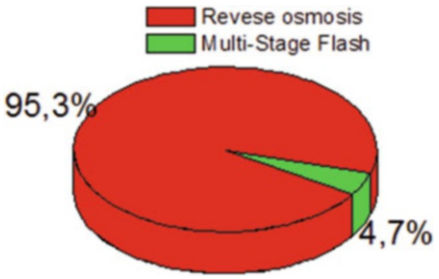

Fig. 5 Energy recovery in reverse osmosis sea water desalination (Ibarra et al. 2014)

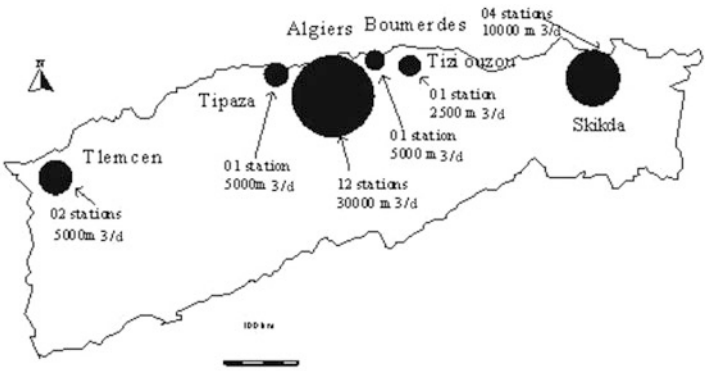

Fig. 6 Distribution of water desalination plants in Algeria (Remini 2010)

time. The following table provides estimates of the capacity that was installed between 2005 and 2010 and which will be installed during 2020–2030. Near-future water needs are estimated according to regions. We note that 16 projects of large units bring the desalted water volume to 942 m^3H for the horizon 2025. The achievement of these 13 seawater desalination plants with a total capacity of about 2260,000 m^3/day made up for the actual need for water despite different technical problems encountered at the station due to electricity cuts (Table 4 and Fig. 9).

In addition to these great stations, the desalination program reveals the presence of some monobloc stations of small capacity (between 2500 and 7000 m^3/day), some of which have been relocated to provide water to the most affected areas (see table 4).

The various stations that exist in Algeria are managed by production companies piloted by the Algerian Energy Company (AEC) which is created by Sonatrach and Sonelgaz groups. The production of freshwater from desalinated water is sold to the Algerienne Des Eaux (ADE) that is a public body of industrial and commercial character. This public body is under the authority of the minister responsible for water resources that was created in April 2001 year by executive Decree No. 01-101. We emphasize that desalinated water prices remained constant for consumers despite the development of desalination plants (Table 5).

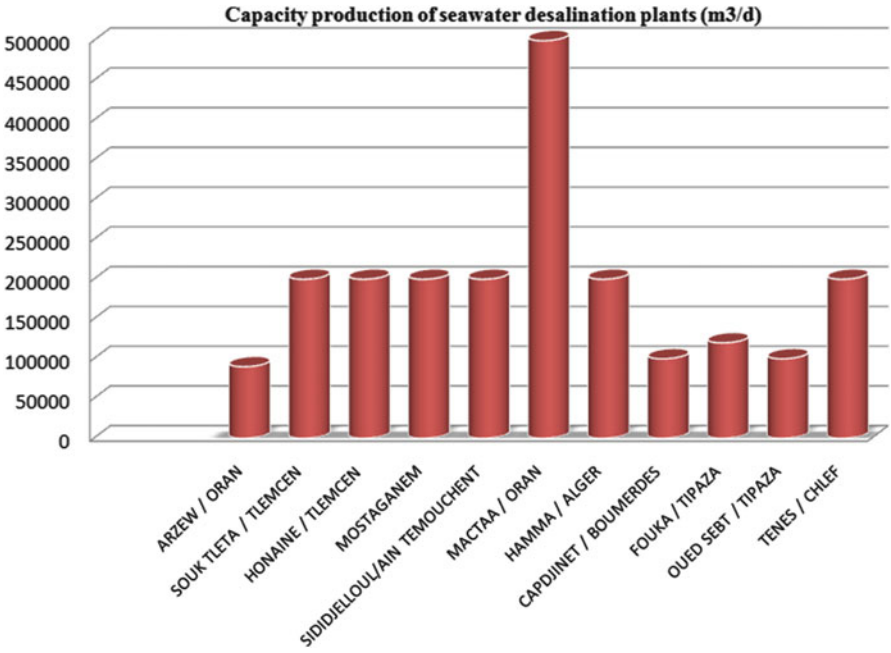

Fig. 7 Capacity of the seawater desalination plants in Algeria

The cost of desalinated water is estimated according to three important elements, namely, financial expenses, energy cost, driving operation and maintenance costs. Over the past decade, the cost of desalination declined by half as the raw materials cost has increased and will continue to increase in the near future. Investment costs are estimated at 900–1000 €/m^3/h for reverse osmosis. The cost of desalinating brackish water is significantly low (0.2–0.3 €/m^3) in comparison to seawater which varies in the range of 0.4–0.6 €/m^3. The desalinated water for large units costs about two times more than conventional water (Ibarra et al. 2014).

4 Case Study: Seawater Desalination Plant of Fouka

The realization of the seawater desalination plant of Fouka is a part of the national program of realization of 13 plants. It is the third station established in the wilaya of Tipaza along with the Bou Ismail station which delivers 5000 m^3/day and Oued Sebt station Gouraya which also delivers 100,000 m^3/day. The seawater desalination plant of Fouka is intended to cover the drinking water needs of the eastern part of the province of Tipaza and part of the western region of Algiers. It is functional since 2011, located in the town of Fouka, Douaouda wilaya of Tipaza and implemented on a surface of 10 ha. This station uses the membrane separation reverse osmosis technique to desalinate seawater; its daily desalination capacity is 120,000 m^3/day.

Table 3 Progress and localization of seawater desalination stations in Algeria (http://www.mre.dz/baoff/fichiers/PROGRAMME_DESSALEMENT.pdf)

Desalination stations of seawater				
Region	Project location	DIM (km) $\ldots < \Phi$ mm $\leq \ldots$	Progress	Investors (SDEM)
West	Ouest Arzew/Oran	37 km $\Phi = 1250$	Operating (August 2005)	Black-Veach (South Africa)
	Souk Tleta/ Tlemcen	157 km $250 < \Phi \leq 1400$	Operating (May 2011)	Hyflux-Malakoff (Singapore)
	Honaine/Tlemcen	160 km $500 < \Phi \leq 1200$	Operating (July 2012	Geida (Spain)
	Mostaganem	117 km $200 < \Phi \leq 1400$	Operating (September 2011)	Inima-Aqualia (Spain)
	Sidi Djelloul/Ain Temouchent	160 km $250 < \Phi \leq 1400$	Operating (December 2009)	Geida (Spain e)
	Mactaa/Oran	21 km $700 < \Phi \leq 1800$	Works in progress	Hyflux-Malakoff (Singapore)
Center	Hamma/Alger	12 km $700 < \Phi \leq 900$	Operating (February 2008)	Ge.Ionix (USA)
	Cap Djinet/ Boumerdes	30 km $900 < \Phi \leq 1000$	Operating (August 2012)	Inima-Aqualia (Spain)
	Fouka/Tipaza	15 km $350 < \Phi \leq 900$	Operating (July 2011)	Snc Lavalin-Predisa (Canada- Spain)
	Oued Sebt/Tipaza	127 km $200 \leq \Phi \leq 1000$	SDEM not launched	Biwater (Angleterre)
	Tenes/Chlef	254 km $200 < \Phi \leq 1400$	Travaux en cours	Befesa Agua (Spain)
East	Echatt/Tarf	20 km $\Phi = 800$	SDEM not launched	–
	Skikda	54 km $400 < \Phi \leq 1000$	Operating (March 2009)	Geida (Spain)
Total	1164 km			

Water produced by the desalination plant will be acquired by Sonatrach, the Algerian waters (ADE) for 25 years. It is equipped with two pumping stations and seven tanks with a capacity of 14,000 m^3 for a total volume of 60,000 m^3 affected for each wilaya. This hydraulic project will cover the needs of 17 municipalities with a total population estimated at 476,372 inhabitants distributed between the two wilayas. The communes supplied with drinking water by this station are Douaouda, Fouka, Bou Ismail, Ain Tagourait, Hattatba, and Chaiba and also the adjoining communes of the province of Tipaza, namely, Zéralda, Mahelma, and Ain Benian Staoueli. This station was carried out by the company "Myah Tipasa" which represents a consortium consisting of AEC (Algerian Electrical Energy) and the Canadian "SNC Lavalin."

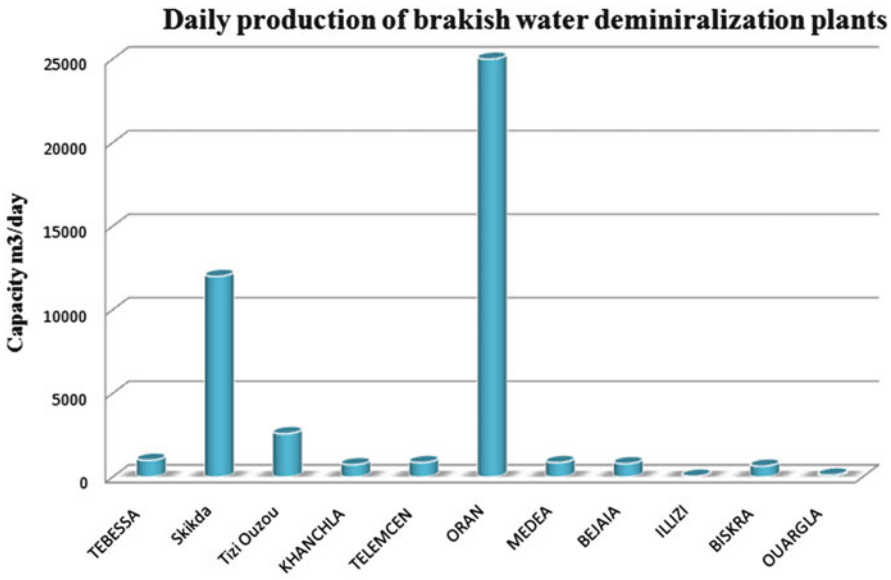

Fig. 8 Capacity of the brackish water demineralization plants in Algeria

Table 4 Seawater desalination program (Services de l'eau en Algerie Faire 2011)

Desalination plants' proposed capacity, m^3/day			
Region	Number of plants	2005–2010	2020–2030
Nord Ouest	6	1,090,000	1,090,000
Nord Center	6	650,000	740,000
Nord Est	4	150,000	380,000
Total program	16	1,890,000	2,210,000
Total desalination program in million m^3/year		690	807

4.1 Basic Diagram of RO

By definition, reverse osmosis is a membrane separation process in which pure water passes from the high pressure seawater side of a semipermeable membrane to the low pressure side of the membrane. It is the most important part of the seawater desalination system. Following the pretreatment (flocculation, chemical treatment, and filtering) and supercharging using the high pressure pump, the seawater enters the membrane and is separated into freshwater that is the permeated water and concentrated brine under the high pressure effect. After further treatment, the clean water is pumped to the terminal users from the storage tanks. The clean water goes to the storage tanks, and after further treatment, water becomes potable. The brine is evacuated into the sea, then further treatment is provided using an energy recovery device (Fig. 10).

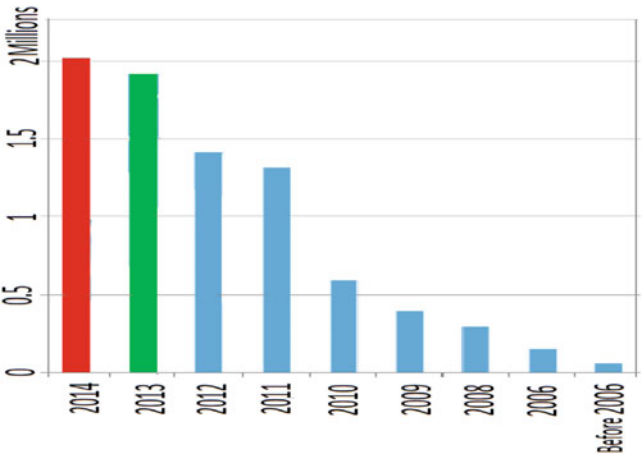

Fig. 9 Evolution of the installed capacity of water desalination in Algeria between 2006 and 2014 (Recuperation D'energie 2014)

Table 5 Monobloc stations of small capacity (Algérienne des eaux. http://www.ade.dz/index.php/projets/dessalement)

Province (Wilaya)	Town	Capacity m^3/day	Population to be served
Alger	Zéralda	5000	33,330
Alger	Staoueli	2500	16,660
Alger	Ain Benian	5000	33,330
Tlemcen	Ghazaouet	5000	33,330
Tipasa	Bou Ismail	5000	33,330
Skikda	L.BenMhidi	7000	47,000
Tizi Ouzou	Tigzirt	2500	16,660
Oran	Bou Sfer	5000	33,330
Oran	Ain Turk	2×2500	33,330
Ain Temouchent	Bou Zdjer	5000	33,330
Ain Temouchent	Bou Zdjer	5000	33,330
Boumerdes	Corso	5000	33,330

4.2 Desalination Production

Now let us present some characteristics and data of Fouka seawater plant that has a capacity of 120,000 m^3/day. It is a private BOO (Build, Own, Operate) contract. The seawater of Fouka is characterized by an electrical conductivity of 56.6 ms/cm and a pH = 8.01 at a temperature $T = 23.3$ °C.

This plant is directly related to the water distribution network of the town. The aim of the Fouka plant is durable supply of freshwater with high quality to several

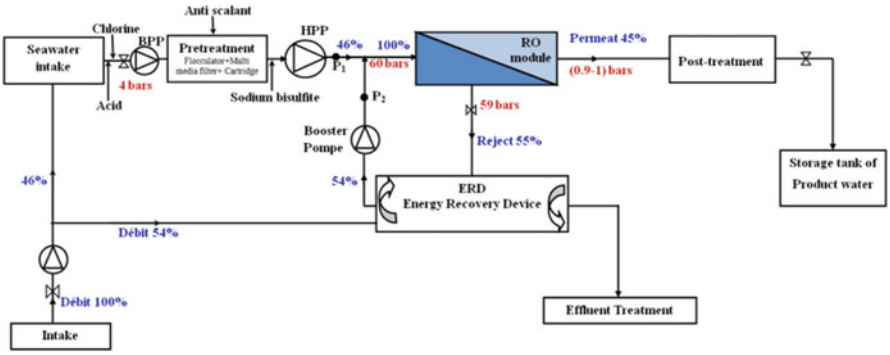

Fig. 10 General diagram of the seawater desalination plant

populations. The table shows the variation of total dissolved solids (TDS) with temperature of the raw water (seawater of Fouka) during 1 year (Table 6).

Figure 11 shows monthly production of freshwater for 2013 and 2014. The monthly production increases when the temperature of water to be desalinated is increased. Indeed, temperature has a significant impact on the production rate. It is seen that the production achieved the optimal range between July and October for the 2 years (2013–2014) when the recorded temperature of the raw water varied in the range 23–24 °C. We note that the minimum production is obtained in December in the case of 2014. As Fouka is a Mediterranean area, the total dissolved solids (TDS) in this region is relatively greater within the range 38–39.5 g/l as illustrated above in Table 6. The variation values of some characteristics such as TDS are very important. From these parameters the quality of freshwater production and the desalination cost can be determined. However, the increase of TDS allows operating the pump for reaching the pressure of 65–70 bar in which this pump HPP (Italian compagny for pumps' manufacturing) consumes more energy. Regarding parameters that can contribute to defining the recovery ratio, seawater has to be analyzed regularly. The evaluation of monthly production of freshwater with energy for 2014 is shown in Fig. 12.

Figure 13 shows the obtained data in which the membrane production of Fouka plant increases and where conversion rate reaches up to a maximum of 46%. The data relates to a plant that is supplied with an average of 38,000 TDS water. We note that, when the conversion rate increases the energy consumption rate increases strongly. It is seen that in the range where the conversion rate of membrane varies between 44.6 and 45.5% the energy consumption does not exceed the value 4 kWh/m^3, while if the conversion rate exceeds this value a rise of 5% of the energy can be achieved (from 44.6 to 46%); it corresponds to an increase of energy of about 0.215 kWh/m^3. As a result, the reverse osmosis desalination technology requires high rates of energy and generates brackish water discharges.

In fact, the existence of energy recovery systems decreases power consumption, and these are efficient for the production of potable water. Actually, renewable energy can provide a sustainable and alternative solution for reverse osmosis

Table 6 Monthly characteristics of the raw water during 2014

Month 2014	TDS (mg/l) of raw water	T (°C) of raw water
January	38.50	16.00
February	38.90	15.60
March	39.10	15.60
April	39.40	16.40
May	39.50	17.90
June	38.85	21.39
July	38.88	23.99
August	38.68	24.04
September	38.61	24.93
October	38.95	23.20
November	38.38	19.51
December	38.37	17.17

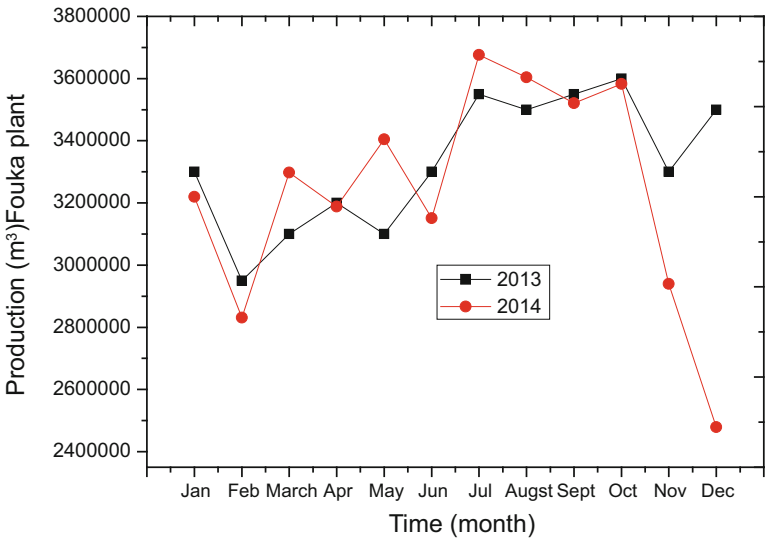

Fig. 11 Monthly production of freshwater for 2013 and 2014

systems that are driven by solar energy. Water desalination technologies operating with renewable energy for the production of drinking water are considered to be a sustainable solution to address the deficit of water in rural areas that have no access to safe drinking water and electrical energy. This principle is currently developed industrially for water purification and seawater desalination (Fig. 14).

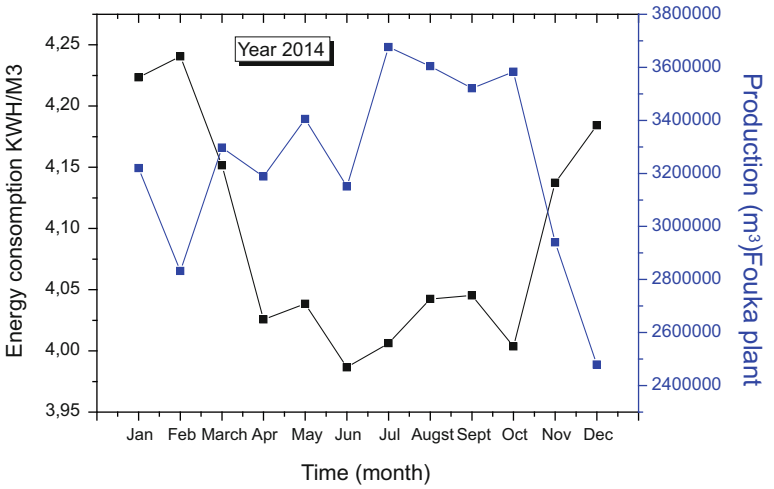

Fig. 12 Variation of monthly production of freshwater with energy consumption versus time for 2014

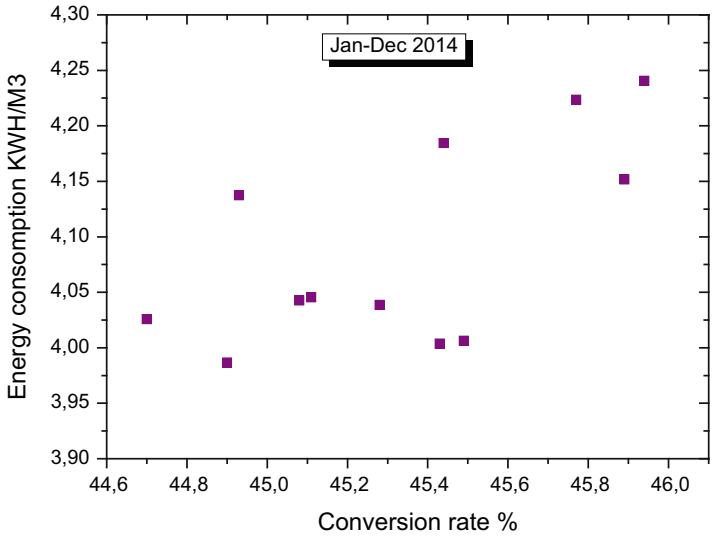

Fig. 13 Plant energy consumption as a function of conversion rate for 2014

5 Conclusions

Seawater desalination technology is used in many regions of North Africa due to population growth, drought, and water scarcity. Different technologies are developed, and they demand high power consumption. Reverse osmosis is the most

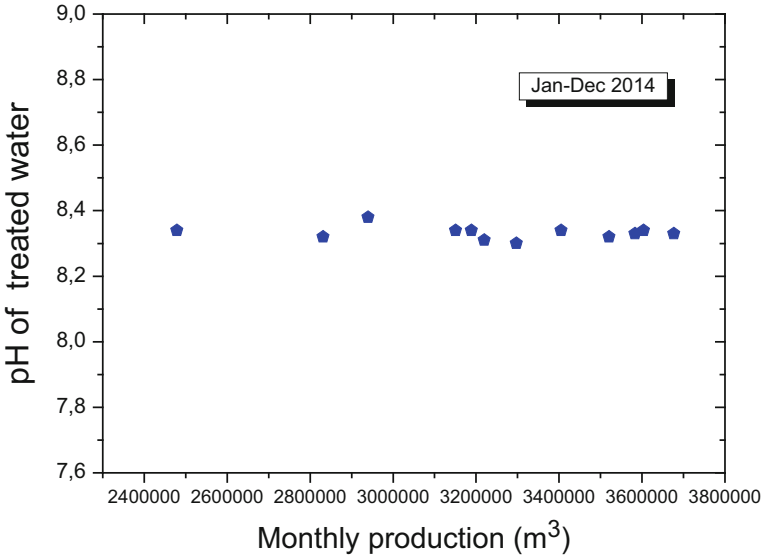

Fig. 14 Variation of treated water pH versus monthly production of freshwater for 2014

suitable process for extracting salt from seawater to meet the increasing water demand.

In this present work, we assessed the currently available seawater desalination plants which are implanted in Algeria. We reviewed the water shortage problem in our country by presenting the main problematic and hydric resources in Algeria. Several plants of desalination located on Algerian Mediterranean coastal areas using reverse osmosis technology and their capacity in cubic meters per day are presented. Case study of seawater desalination plant of Fouka is discussed. Mainly, we show the monthly production of potable water for 2013 and 2014 and their variation of energy consumption with time. Seawater desalination requires much energy and as water demand increases, desalinated water cost increases.

References

Abdallah, S., Abu-Hilal, M., Mohsen, M.S.: Performance of a photovoltaic powered reverse osmosis system under local climatic conditions. Desalination. **183**, 95–104 (2005)

Algérienne des eaux. http://www.ade.dz/index.php/projets/dessalement

Al-Karaghouli, A., Renne, D., Kazmerski, L.L.: Solar and wind opportunities for water desalination in the Arab regions. Renew. Sustain. Energy Rev. **13**(9), 2397–2407 (2009)

Badreddin, E., Gambier, A., Aboul-Fotouh, F.: Laboratory set-up for education and research on automation of reverse osmosis plants employing a sustainable energy source. Desalination. **166**, 307–314 (2004)

Bourouni, K., Ben M'Barek, T., Al Taee, A.: Design and optimization of desalination reverse osmosis plants driven by renewable energies using genetic algorithms. Renew. Energy. **36**, 936e950 (2011)

Clarke, D.P., Al-Abdeli, Y.M., Kothapalli, G.: The effects of including intricacies in the modelling of a small-scale solar-PV reverse osmosis desalination system. Desalination. **311**, 127–136 (2013)

El-Nashar, A.M., Al Gobaisi, D., Makkawi, B.: Solar energy for desalination in the Arab world. Proceedings of Ises Solar World Congress 2007: Solar Energy and Human Settlement, Vols I–V, p. 213–221 (2007)

Eltawil, M.A., Zhengming, Z., Yuan, L.Q.: A review of renewable energy technologies integrated with desalination systems. Renew. Sustain. Energy Rev. **13**(9), 2245–2262 (2009)

Fritzmann, C., Löwenberg, J., Wintgens, T., Melin, T.: State-of-the-art of reverse osmosis desalination. Desalination. **216**, 1–76 (2007)

Greenlee, L.F., Lawler, D.F., Freeman, B.D., Marrot, B., Moulin, P.: Reverse osmosis desalination: water sources, technology, and today's challenges. Water Res. **43**, 2317–2348 (2009)

Hanafi, A.: Desalination using renewable energy sources. Desalination. **97**, 339–352 (1994)

Herold, D., Horstmann, V., Neskakis, A., Plettner-Marliani, J., Piernavieia, G., Calero, R.: Small scale photovoltaic desalination for rural water supply demonstration plant in Gran Canaria. Renew. Energy. **14**(1–4), 293–298 (1998)

Ibarra, M., Rovira, A., Alarcón-Padilla, D.C., Zaragoza, G., Blanco, J.: Performance of a 5 kWe solar-only organic Rankine unit coupled to a reverse osmosis plant. Energy Procedia. **49**, 2251–2260 (2014)

Joyce, A., Loureiro, D.: Carlos Rodrigues & Susana Castrob :small reverse osmosis units using PV systems for water purification in rural places. Desalination. **137**, 39–44 (2001)

Keefer, B.G., Hembree, R.D., Scharach, F.C.: Desalination. **54**, 89–103 (1985)

Kehal, A.: Reverse osmosis unit of 0.85 m3/h capacity driven by photovoltaic generator in South Algeria. Proceedings of the New Technologies for the Use of Renewable Energies Sources in Water Desalination Conference, Session II, Athens, p. 8e16 (1991)

Kehal, S.: Retrospectives and perspectives of desalination in Algeria. Desalination. **152**(1–3), 113–124 (2003)

MacHarg, J., Truby, R.: West coast researchers seek to demonstrate SWRO affordability. Desalin. Water Reuse Q. **14**(3), 1–18 (2004)

Maurel, A.: Desalination by reverse osmosis using renewable energies (SolarWind). In: Proceedings of the New Technologies for the Use of Renewable Energies Sources in Water Desalination Conference, Session II, Athens, p. 17e26 (1991)

Mohamed, E.S., et al.: A direct coupled photovoltaic seawater reverse osmosis desalination system toward battery based systems - a technical and economical experimental comparative study. Desalination. **221**(1–3), 17–22 (2008)

Problématique du secteur de l'eau et impacts liés au climat en Algérie. 07 Mars 2009. Algerie, Rapport, national,eau,adaptation.pdf

Quteishat, K., Abu-Arabi, M.: Promotion of solar desalination in the MENA region. Middle East Desalination Centre, Muscat. http://www.menarec.com/ docs/Abu-Arabi.pdf. Accessed 28 March 2006

Recuperation D'energie Dans Le Dessalement D'eau Mer Par Osmose Inverse. Journée Mondiale de l'Eau 19 Mars 2014. http://www.cuniv-ntemouchent.dz/files/eau42014.pdf

Remini, B.: La Problematique De L'eau En Algerie Du Nord: Larhyss Journal, ISSN 1112–3680, n° 08, Juin, pp. 27–46 2010

Rodriguez-Girones, M., Rodriguez, M., Pérez, J., Veza, J.: Proceedings of the Medical Conference on Ren. Energy Sources for Water Production, Santorini, June, p. 173–179 1996

Saadi, A., Kehal, S.: Retrospectives and potential use of saline water desalination in Algeria. Desalination. **152**, 51–56 (2002)

Schafer, A.I., Broeckmann, A., Richards, B.S.: Renewable energy powered membrane technology. 1. Development and characterization of a photovoltaic hybrid membrane system. Environ. Sci. Technol. **41**(3), 998–1003 (2007)

Services de l'eau en Algerie Faire du droit à l'eau une réalité pour tous communication à la consultation des acteurs étatiques sur les bonnes pratiques dans les domaines de l'eau et de l'assainissement Genève janvier 2011 : State Actors /AlgeriaCOMHCDHGeneva.pdf.

Youssefa, P.G., Al-Dadaha, R.K., Mahmouda, S.M.: Comparative analysis of desalination technologies. Energy Procedia. **61**, 2604–2607 (2014.) The 6th International Conference on Applied Energy – ICAE2014.

A Study on Energy and Environmental Management Techniques Used in Petroleum Process Industries

A.K. Azad, M.G. Rasul, Rubayat Islam, and S.F. Ahmed

1 Introduction

The energy and environment is one of the major concerns in the present world nowadays (DOE). The environment is a combination of matters and energies around us. The coordination among the resources of an organization is called management. So, environmental management is a broad area of research which is important for the global environment. Environmental pollution can be defined as the unfavourable alteration of our surroundings by human actions, through direct or indirect effects of changes in energy patterns, radiation levels, chemical and physical constitution of organisms, etc. (Hossain 2009; Azad and Alam 2011). These changes may affect directly or indirectly the environment (MEF 2007; Cholakov 2010). The first environmental activities in Bangladesh were taken soon after the Stockholm conference on human environment. As a follow-up action to the Stockholm conference, the Bangladesh Government funded, under the aegis of the department of public health engineering and with a staff level of 27 and after promulgating the water pollution control ordinance in 1973, a project primarily aimed at water pollution control. In the subsequent years, various events took place (Hossain 2009). In 1977, the Environment Pollution Control Board (EPCB) with 16 members ruled by a member of the planning commission and environment pollution control cell was formed and renamed as Department of Environment in

A.K. Azad (✉) • M.G. Rasul • S.F. Ahmed
Central Queensland University, School of Engineering and Technology, Rockhampton, QLD 4702, Australia
e-mail: azad.cqu@gmail.com; a.k.azad@cqu.edu.au

R. Islam
Department of Mechanical Engineering, Bangladesh University of Engineering and Technology, Dhaka 1000, Bangladesh

© Springer International Publishing AG, part of Springer Nature 2018

F. Aloui, I. Dincer (eds.), *Exergy for A Better Environment and Improved Sustainability 2*, Green Energy and Technology,
https://doi.org/10.1007/978-3-319-62575-1_16

1985. The department discharges its responsibilities through a head office and six divisional offices located in Dhaka, Chittagong, Khulna, Rajshahi (Bogra) and Sylhet in Bangladesh (DoE 2007, Hossain 2009, DoE 2008). The following policy, acts and rules facilitate the activities of DoE (Department of Environment) in Bangladesh: Environment Policy, 1992; Environment Conservation Act, 1995, and subsequent amendments; Environment Conservation Rules, 1997, with amendments; Environment Court Act, 2000, and subsequent amendments; Ozone Depleting Substances Control Rules, 2004; and Noise Control Rules in 2006 (Hossain 2009).

The environment can be polluted in many ways. One of the major sources of environment pollution is industrial waste water which can be defined as any physical, biological or chemical change in water quality that adversely affects living organisms or makes water unsuitable for desired uses. The polluted water has some signs like bad taste, offensive odour, oil and grease floating on water surface, etc. (Abdel-Gawad and Abdel-Shafy 2002; El-Gohary et al. 1987; Ramalho 1977). The waste water sources can be categorized into, namely, point source and non-point source. The factories, power plant, sewage treatment plants, underground coal mines, gas processing plants and oil well are classified as point sources. Non-point sources include runoff from farm fields, feedlots, lawns and gardens, construction sites, logging areas, roads, streets, parking lots, etc. (Correia et al. 1994). Waste water treatment is very important to save the environment. This pollution can be managed by applying some treatment techniques such as effluent treatment plant (ETP). ETP is the most commonly and widely used technique for industrial waste water treatment. The treatment techniques mainly depend on the quality of untreated waste water.

This study summarizes the energy and environmental management practices in natural gas process industries in Bangladesh. Management and treatment system of the hazardous pollutant like waste water which is more intensive for environmental pollution is developed in this study. The rational use of energy and its management system are also reported, and further recommendation is made for energy-efficient process industries in Bangladesh.

2 Environmental Management

2.1 Pollution Abatement Technique

Waste water treatment system can be categorized as preliminary treatment, primary or physical treatment, secondary or biological treatment and tertiary or advanced treatment (Fakhru'l-Razi et al. 2009; Brindle and Stephenson 1996; Knoblock et al. 1994; Kirk et al. 2002; Cummings 1991; Van Loosdrecht et al. 1998; Glaze et al. 1987; Kuba et al. 1997). The primary treatment involves screening; grit removal and settling give about 30–35% reduction in biological oxygen demand (Fakhru'l-Razi et al. 2009; Brindle and Stephenson 1996; Parinos et al. 2007;

Carballa et al. 2005). It can be performed by (a) sedimentation tank, (b) septic tank, (c) Imhoff tank and (d) dissolved air floatation (DAF). Secondary treatment generally consists of biological aeration steps in which the dissolved organic matter is converted into an able settled form and removed as sludge by settling in a secondary settling tank. This sludge having been previously aerated is referred to as activated sludge, a part of it is recycled back to the aeration tank and the remaining part is withdrawn from the system as excess sludge (Brindle and Stephenson 1996; Kornaros and Lyberatos 2006; Lin et al. 2001). The excess sludge and primary settled sludge are mixed, thickened and sent to a sludge digester for further stabilization followed by de-watering. Sometimes primary and secondary treatment can be accomplished together. Treatment in lagoons and ponds is the best example of this type of treatment (Svenson et al. 1992; Gurbuz et al. 2009; Legrini et al. 1993; Henze 2002; Scott and Ollis 1995; Fuhs and Chen 1975). The tertiary treatment is also called as advanced treatment. If more treatment is needed to achieve the standard of the effluent water, then advanced treatment is required. The actual steps needed for this treatment depend on the purpose for which the effluent is to be used for. Tertiary treatment consists of air stripping, the step which removes ammonia, nitrogen or other gases (Kornaros and Lyberatos 2006; Knoblock et al. 1994; Owen et al. 1995; Oliveros et al. 1997), nitrification process (Focrrr and Chang 1975), denitrification process (Focrrr and Chang 1975), chlorination process (Takht Ravanchi et al. 2009), dechlorination process (Focrrr and Chang 1975), chemical precipitation (Dean et al. 1972), reverse osmosis (Wang et al. 2005) and ion exchange process (Namasivayam and Ranganathan 1995). A typical flow diagram for waste water treatment plant is shown in Fig. 1. This abatement technique can be used in petroleum process industries for their waste water treatment.

2.2 *Oil and Water Separation Technique Used in Petroleum Industries*

Bangladesh is blessed with natural gas and black coal. Raw natural gas contains about 0.5–2.0% water (Mondal et al. 2013b). This raw gas is processed in gas processing plant. In this plant, one of the main challenges is to remove water and higher hydrocarbons from the raw gas. The water which comes out with the raw gas is called produced or underground waste water (Barbosa et al. 2007; Lettinga 1995). At the initial stage, a two- or three-phase knockout separator can separate the produced water from the gas but has some oil component mixed with it (Mondal et al. 2013a). API separator is one of the most important devices to remove oil from the waste water (Dobson and Burgess 2007). It is mainly a couple chambered vessel containing trash trap (including rods), oil retention baffles, flow distributers (vertical rods), oil layer, slotted pipe skimmer, adjustable overflow wire and sludge sump, chain and flight scraper. The waste water samples were tested for the

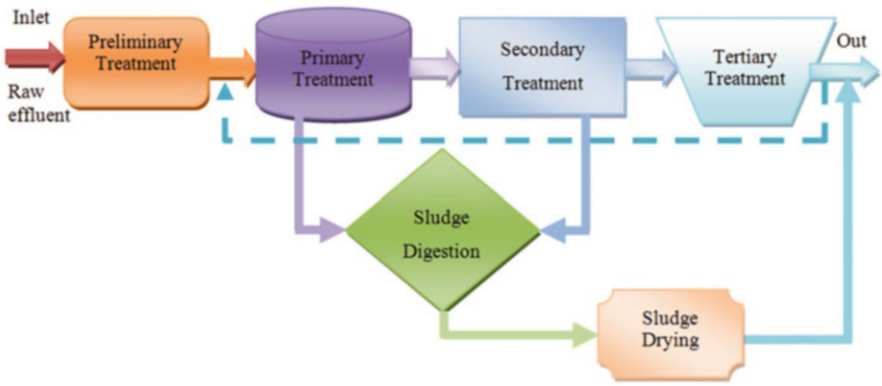

Fig. 1 Typical flow diagram for waste water treatment plant

following 14 parameters: dissolved oxygen, biochemical oxygen demand (at 20 °C), chemical oxygen demand, chloride, ammonia, ammonium, nitrate, chromium, cadmium, lead, total suspended solid, total dissolved solid, phosphate and sulphate (Fuhs and Chen 1975; Kornaros and Lyberatos 2006; Lund and Lund 1971). Table 1 shows some standard parameters for industrial effluent and their discharge limit in three discharge points.

2.3 Study on Industrial Effluents

Produced water or waste water is the largest waste stream generated in oil and gas industries. It is a mixture of different organic and inorganic compounds, minerals and hydrocarbons. Due to the increasing volume of waste water all over the world in the current decade, the outcome and effect of discharging produced water on the environment has lately become a significant issue of environmental concern. The study was made on waste water management and treatment for three natural gas processing industries in Bangladesh. Due to confidentiality, the names of the industries have been removed and indicated as Industry A, B and C, respectively. For the study, the effluent compositions were tested which are presented in Table 2. From the Table, it seems that the waste water contains a significant amount of oil and grease in petroleum industries. Figure 2 shows the designated process flow diagram for effluent treatment in petrochemical industries. Produced water is conventionally treated through different physical, chemical and biological methods. However, current technologies cannot remove small suspended oil particles and dissolved elements. Besides, many chemical treatments require high initial running cost. In onshore facilities, biological pretreatment of oily waste water can be a cost-effective and environment-friendly method. Table 3 shows the quality of effluent after treatment.

Table 1 Standard parameters for industrial effluent

Parameters	Unit	Discharge to		
		Inland surface water	Secondary treatment plant	Irrigable land
BOD at 20 °C	mg/L	50	250	100
COD	mg/L	200	400	400
Dissolved oxygen, DO	mg/L	4.5–8	4.5–8	4.5–8
Electric conductivity	μohm/cm	1200	1200	1200
Total dissolved solid	mg/L	2100	2100	2100
Oil and grease	mg/L	10	20	10
pH	mg/L	6–9	6–9	6–9
Suspended solid	mg/L	150	500	200

Table 2 Waste water composition in studied industries

Items	Unit	Name of the industry		
		A	B	C
pH	–	6.5–8.0	8.5–10.0	8.73–11.5
BOD	mg/L	37	26	19
COD	mg/L	400	424	378
Electric conductivity	μohm/cm	–	3.74	2.98
Oil and grease	mg/L	20	263	428
Suspended solid (SS)	mg/L	180	215	231
NH_3 (as N)	mg/L	150	–	130
Total Kjeldahl nitrogen	mg/L	200	–	–
Nitrate (NO_3-N)	mg/L	50	38	46
Phosphate (PO_4-P)	mg/L	30	45	63
Cyanide, CN	mg/L	–	0.1	0.3
Colour	Pt-Co unit	298	303	305
Turbidity	NTU	5.6	6.3	8.6

3 Energy Management

Rationalization of an industrial operation is quite complex for an existing industrial system. However, in order to save energy, the following time frame measures can be implemented depending on the size of the investment and their cost-effectiveness as short-term measure, medium-term measure and long-term measure. In the case study, processing plants used short-term and medium-term measures to efficiently run process using existing process facilities. These three terms are briefly discussed below.

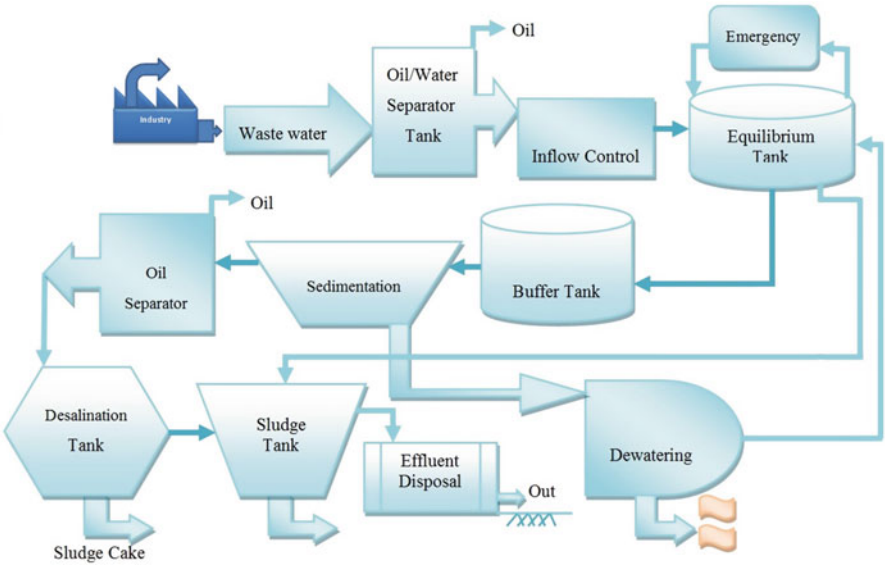

Fig. 2 Designated process flow diagram for effluent treatment plant in petroleum industries

Table 3 Effluent quality after treatment

Items	Unit	Name of the industry		
		A	B	C
pH	–	6.5–8.0	7.5	9.2
DO	mg/L	–	5.2	2.5
BOD	mg/L	30	14	11
COD	mg/L	192	101	137
Electric conductivity	µohm/cm	–	1.32	1.75
Oil and grease	mg/L	8.9	9.3	10.2
Suspended solid	mg/L	97.3	82.1	98.7
NH_3 (as N)	mg/L	48.2	–	52
Colour	Pt-Co	–	219	136
Turbidity	NTU	3.4	1.8	0.79

3.1 Short-Term Measures

In the short-term measure, schedule maintenance for energy conservation is needed. Under this term, no new investment is required except for increased maintenance task. It only leads to increase labour cost for maintenance. The main objective is to improve the energy efficiency of the equipment by enforcing better schedule for the maintenance programme. Using exhaust gas analyser for improving combustion efficiency in the furnace and power generator can save more than 5% fuel consumption. The associated work is the better adjustment of the inlet air quality to improve combustion efficiency. Regular cleaning and reduction of pressure drop

can improve the heat transfer efficiency of the heat exchangers. Proper cooling system can help to increase the lifetime of the equipment and enable it for proper functioning (Azad et al. 2015b).

3.2 Medium-Term Measures

Small investment is required in medium-term measures on the energy consumption network. It's neither change principal of operation nor general engineering aspect. The objective is to reduce the consumption of high-quality energy and use low-quality energy; some changes are done on the existing network with additional investment. For example, installation of heat recovery unit is done to reheat or preheat the feedstock. It will reduce heat loss and save fuel consumption of the main heating source. Inefficient equipment can be replaced by more efficient one with the small investment. Repair of leakages and proper insulation or re-insulation could save energy as well as money. Waste reduction and waste recovery for reuse can increase productivity and save energy.

3.3 Long-Term Measures

Long-term measures require large investments on the interconnections of the processes. This can be a combination of various measures. Petroleum process industry requires both heat and power for continuing the process run. By-products reprocessing unit installation with the large investment will increase multi-products and will make healthy gross profit as well. Installation of power line to supply excess power to grid or other associated organization will save excess produced power for process run. Very large investments on the principle of the process are also included in this term. Though the finished product is not changed, process itself is modified or redesigned. Older technologies can be replaced by new and advanced technologies which are the major contributing factor for lower specific energy consumption, especially in the case of energy-intensive sector. The case study plants are not using long-term measure for energy management due to very big investment and sophisticated process equipment required. This term of measure is not suitable for the present condition. Energy-efficient and upgrading process principals will get property for any new installation in the future.

3.4 Rational Use of Energy

The process industries are the more energy- and pollution-intensive sector throughout the world. To understand the energy scenario of petrochemical process

Table 4 Types of energy used in case studied petroleum process industries

Process	Type of fuel
Raw materials pumping and storing	Electricity
Feedstock preheating	Heat energy
Heating/furnace running	Natural gas
Gas generator used for power generation for process run	Natural gas
Product pumping	Electricity
Product cooling	Electricity
Product testing in laboratory	Natural gas and electricity
Others (AC for equipment, fan, lighting, etc.)	Electricity
Office, administration and security light	Electricity

industries, energy auditing is needed. The main energy consumption is in the form of heat and power (electricity). The types of energy used by the industry are presented in Table 4. For petroleum process industries, about 80–85% energy is consumed by furnace for heating and 15–19% energy consumed by power generator for process run. The rest of the 1% energy is used in laboratory for property testing of the finished products. So, energy conservation measures should be implemented for more energy-intensive processes such as heating furnace and power generation (Azad et al. 2015a).

The rational use of energy considering energy utilization through the most suitable and economically viable methods can save energy and environment concurrently. The better energy management proved to be a better form of energy conservation, saving as much as 10–30% without capital investments (Rasul 1994; Mondal et al. 2014). Worrell et al. (Worrell et al. 1994) investigated the energy consumption by industrial processes and suggested that by applying best practice technology, potential improvement in energy efficiency on an average $15 \pm 4\%$ for oil petrochemical industries, $21 \pm 2\%$ for ammonia, $25 \pm 5\%$ for paper, $13 \pm 1\%$ for cement and $27 \pm 3\%$ for steel can be achieved (Worrell et al. 1994). Rasul et al. reviewed the rational use of energy in process industries like textile, steel and alumina refining, respectively (Rasul 1994; Rasul et al. 2004; Rasheed et al. 2003). So, energy conservation is important for long-term economic well-being and security. Utlu and Hepbasli (Utlu and Hepbasli 2007) reviewed the energy efficiency in Turkish industrial sector and reported 90% efficiency increase in energy use in petroleum refining due to its energy recovery system. The chemical and petrochemical industries account for 30% of industrial energy use globally (Gielen and Taylor 2007). A generalized energy distribution of the petroleum process industries is presented in Fig. 3, and the energy flow diagram of petrochemical industries is presented in Fig. 4.

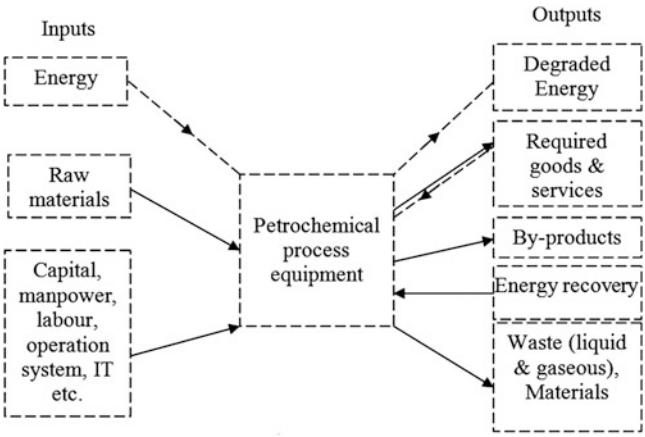

Fig. 3 Energy distribution of petroleum industries

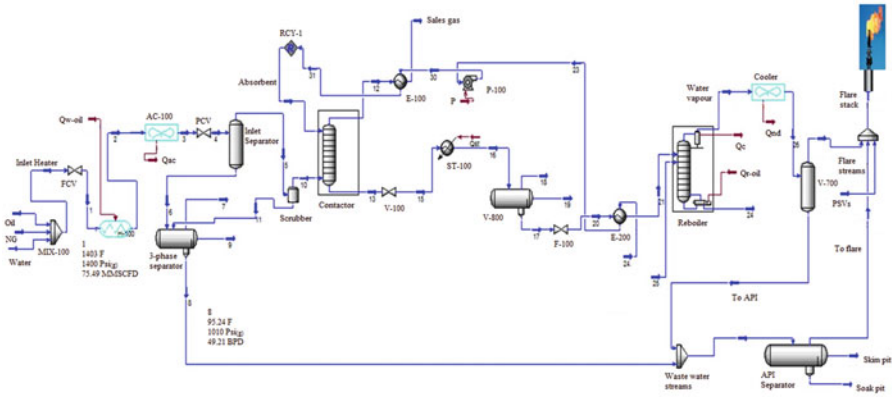

Fig. 4 Energy flow diagram for the petroleum industries with liquid and gaseous effluent handling unit

4 Conclusions and Recommendations

The study reviewed the energy and environmental management for petroleum process industries in Bangladesh. Pollution abatement techniques, main pollutants and the problems associated with waste water treatment are identified in this study. Oil-water separator used in petroleum process industries and the standard of industrial effluents are also outlined. It has been found that high salinity and oil and grease contents of the influent characteristics have direct influence on the turbidity of the effluent of petroleum waste water. The effluent characteristics before and after treatment and the process flow diagram have been analysed. The rational use of energy with energy flow diagram has been developed and briefly

discussed. The time frame energy management process is also presented in this study for petroleum industries in order to save energy. The study found from the literature that it is possible to save about 15% of energy uses in petroleum process industries by implementing the proper energy management system. The study recommended the proper selection of treatment technique which can be used to remove the oil, grease and salinity from the waste water by secondary treatment. It is also important to eliminate the heavy metals dissolved as divalent metal oxide as Fe, Mn, Zn, Ni or Cr in produced water. By considering the above-mentioned parameters, an effluent treatment plant can be designed to maintain environmental quality standards (EQS) in waste water treatment for environment-friendly effluent.

References

Abdel-Gawad, S., Abdel-Shafy, M.: Pollution control of industrial wastewater from soap and oil industries: A case study. Water Sci. Technol. **46**(4–5), 77–82 (2002)

Azad, A.K., Alam, M.M.: Analysis of total power consumption and carbon dioxide emissions in Asia and Oceania. In: 1st International Conference on Mechanical Engineering Research, Kuantan, pp. 259–266 (2011)

Azad, A.K., Rasul, M.G., Bhuiya, M.M.K., Mondal, S.K., Sattar, M.K.: Energy and waste management for petroleum refining effluents: A case study. Int. J. Automot. Mech. Eng. **11**, 2170–2187 (2015a)

Azad, A.K., Rasul, M.G., Khan, M.M.K., Mondal, S.K., Islam, R.: Modelling and simulation of heat and mass flow by Aspen HYSYS for petroleum refining process in field application. Thermofluids modeling for energy efficiency applications. Oxford, Elsevier, 227–257 (2015b)

Barbosa, V.L., Tandlich, R., Burgess, J.E.: Bioremediation of trace organic compounds found in precious metals refineries' wastewaters: A review of potential options. Chemosphere. **68**(7), 1195–1203 (2007)

Brindle, K., Stephenson, T.: The application of membrane biological reactors for the treatment of wastewaters. Biotechnol. Bioeng. **49**(6), 601–610 (1996)

Carballa, M., Omil, F., Lema, J.M.: Removal of cosmetic ingredients and pharmaceuticals in sewage primary treatment. Water Res. **39**(19), 4790–4796 (2005)

Cholakov, G.S.: Control of pollution in petroleum industry. Pollut. Control Technol. **3**, 1–10 (2010)

Correia, V.M., Stephenson, T., Judd, S.J.: Characterisation of textile wastewaters-A review. Environ. Technol. **15**(10), 917–929 (1994)

Cummings Jr, P.W.: Waste Water Treatment Process. Google Patents, Australia (1991)

Dean, J.G., Bosqui, F.L., Lanouette, K.H.: Removing heavy metals from waste water. Environ. Sci. Technol. **6**(6), 518–522 (1972)

Dobson, R.S., Burgess, J.E.: Biological treatment of precious metal refinery wastewater: A review. Miner. Eng. **20**(6), 519–532 (2007)

DoE 'Guide lines for submissions of information/ data for Effluent Treatment Plant (ETP): Bangladesh Environmental Institutional Strengthening Project, Department of Environment, Bangladesh. [Cited on 23 December 2013]; Available at: http://www.doe-bd.org/ETP_Guideline.pdf. (2007)

DOE. Department of Environment, Guide for Assessment of Effluent Treatment Plant: Ministry of Environment and Forest, Bangladesh. [Cited on 24 December 2013]; Available at: http://www.doe-bd.org/ETP_Assessment_Guide.pdf. [Online] (2008)

El-Gohary, F.A., Abo-Elela, S.I., Ali, H.I.: Management of wastewater from soap and food industries: A case study. Sci. Total Environ. **66**, 203–212 (1987)

Fakhru'l-Razi, A., Pendashteh, A., Abdullah, L.C., Biak, D.R.A., Madaeni, S.S., Abidin, Z.Z.: Review of technologies for oil and gas produced water treatment. J. Hazard. Mater. **170**(2), 530–551 (2009)

Focrrr, D., Chang, A.: Nitrification and denitrification processes related to waste water treatment. Adv. Appl. Microbiol. **19**, 153 (1975)

Fuhs, G., Chen, M.: Microbiological basis of phosphate removal in the activated sludge process for the treatment of wastewater. Microb. Ecol. **2**(2), 119–138 (1975)

Gielen, D., Taylor, M.: Modelling industrial energy use: The IEAs energy technology perspectives. Energy Econ. **29**(4), 889–912 (2007)

Glaze, W.H., Kang, J.-W., Chapin, D.H.: The chemistry of water treatment processes involving ozone, hydrogen peroxide and ultraviolet radiation. Ozone Sci. Eng. **9**(4), 335–352 (1987)

Gurbuz, F., Ciftci, H., Akcil, A.: Biodegradation of cyanide containing effluents by Scenedesmus obliquus. J. Hazard. Mater. **162**(1), 74–79 (2009)

Henze, M.: Wastewater Treatment: Biological and Chemical Processes. Springer, Germany, 11–41 (2002)

Hossain, I.: Department of Environment and its role in protecting the environment of Bangladesh, Available at: http://www.academia.edu/3832861/Department_of_Environment_and_its_role_in_protecting_the_environment_of_Bangladesh (2009). Accessed on 23 Dec'2013. [Online]

Kirk, L.A., Tyler, C.R., Lye, C.M., Sumpter, J.P.: Changes in estrogenic and androgenic activities at different stages of treatment in wastewater treatment works. Environ. Toxicol. Chem. **21**(5), 972–979 (2002)

Knoblock, M., Sutton, P., Mishra, P., Gupta, K., Janson, A.: Membrane biological reactor system for treatment of oily wastewaters. Water Environ. Res. **66**(2), 133–139 (1994)

Kornaros, M., Lyberatos, G.: Biological treatment of wastewaters from a dye manufacturing company using a trickling filter. J. Hazard. Mater. **136**(1), 95–102 (2006)

Kuba, T., Van Loosdrecht, M., Heijnen, J.: Biological dephosphatation by activated sludge under denitrifying conditions pH influence and occurrence of denitrifying dephosphatation in a full-scale waste water treatment plant. Water Sci. Technol. **36**(12), 75–82 (1997)

Legrini, O., Oliveros, E., Braun, A.: Photochemical processes for water treatment. Chem. Rev. **93** (2), 671–698 (1993)

Lettinga, G.: Anaerobic digestion and wastewater treatment systems. Antonie Van Leeuwenhoek. **67**(1), 3–28 (1995)

Lin, C.-K., Tsai, T.-Y., Liu, J.-C., Chen, M.-C.: Enhanced biodegradation of petrochemical wastewater using ozonation and BAC advanced treatment system. Water Res. **35**(3), 699–704 (2001)

Lund, H.F., Lund, H.F.: Industrial Pollution Control Handbook. McGraw-Hill, New York (1971)

MEF: Bio-safety guide lines of Bangladesh, Ministry of Environment and Forest, Government of the People's Republic of Bangladesh, Available at: http://www.doe-bd.org/BiosafetyGuidelineBD.pdf (2007). Accessed on 24 Dec'2013. [Online]

Mondal, S.K., Uddin, M.R., Azad, A.K.: Aspen-Hysys simulation of a condensate fractionation plant. In: International Conference on Mechanical, Industrial and Materials Engineering, Bangladesh, pp. 912–917. (2013a)

Mondal, S.K., Uddin, M.R., Azad, A.K.: Simulation and optimization of natural gas processing plant. In: International Conference on Mechanical, Industrial and Materials Engineering, Bangladesh, pp. 485–490. (2013b)

Mondal, S.K., Uddin, M.R., Paul, P., Deb, A., Azad, A.K.: Minimization of the process loss in condensate fractionation plant. Procedia. Eng. **90**, 524–529 (2014)

Namasivayam, C., Ranganathan, K.: Removal of Cd (II) from wastewater by adsorption on "waste" Fe (III) Cr (III) hydroxide. Water Res. **29**(7), 1737–1744 (1995)

Oliveros, E., Legrini, O., Hohl, M., Müller, T., Braun, A.M.: Industrial waste water treatment: Large scale development of a light-enhanced Fenton reaction. Chem. Eng. Process. Process Intensif. **36**(5), 397–405 (1997)

Owen, G., Bandi, M., Howell, J., Churchouse, S.: Economic assessment of membrane processes for water and waste water treatment. J. Membr. Sci. **102**, 77–91 (1995)

Parinos, C.S., Stalikas, C.D., Giannopoulos, T.S., Pilidis, G.A.: Chemical and physicochemical profile of wastewaters produced from the different stages of Spanish-style green olives processing. J. Hazard. Mater. **145**(1–2), 339–343 (2007)

Ramalho, R.: Introduction to Wastewater Treatment Processes. Academic Press, New York (1977)

Rasheed, T., Rasul, M.G., Khan, M.M.K.: Energy Savings Potential in an Alumina Refinery Central Region Engineering Conference (CREC2003), Rockhampton, 2–5 September 2003

Rasul, M.G.: A review on rational use of energy and its conservation measures in process industry: a case of textile industry. International Mechanical Engineering Congress and Exhibition: Resource Engineering, Institution of Engineers, Australia, 109 (1994)

Rasul, M.G., Tanty, B.S., Khan, M.M.K.: Energy savings opportunities in iron and steel industry. In: 2nd BSME-ASME International Conference on Thermal Engineering 2–4 January'2004, Dahka, pp. 1116–1122. (2004)

Scott, J.P., Ollis, D.F.: Integration of chemical and biological oxidation processes for water treatment: Review and recommendations. Environ. Prog. **14**(2), 88–103 (1995)

Svenson, A., Linlin, Z., Kaj, L.: Primary chemical and physical characterization of acute toxic components in wastewaters. Ecotoxicol. Environ. Saf. **24**(2), 234–242 (1992)

Takht Ravanchi, M., Kaghazchi, T., Kargari, A.: Application of membrane separation processes in petrochemical industry: A review. Desalination. **235**(1), 199–244 (2009)

Utlu, Z., Hepbasli, A.: A review and assessment of the energy utilization efficiency in the Turkish industrial sector using energy and exergy analysis method. Renew. Sust. Energ. Rev. **11**(7), 1438–1459 (2007)

Van Loosdrecht, M., Brandse, F., De Vries, A.: Upgrading of waste water treatment processes for integrated nutrient removal—The BCFS® process. Water Sci. Technol. **37**(9), 209–217 (1998)

Wang, C., Hu, X., Chen, M.-L., Wu, Y.-H.: Total concentrations and fractions of Cd, Cr, Pb, Cu, Ni and Zn in sewage sludge from municipal and industrial wastewater treatment plants. J. Hazard. Mater. **119**(1), 245–249 (2005)

Worrell, E., Cuelenaere, R.F.A., Blok, K., Turkenburg, W.C.: Energy consumption by industrial processes in the European Union. Energy. **19**(11), 1113–1129 (1994)

Generating Temperature Maps of a Solar Receiver for a Domestic Parabolic Concentrator for Cooking Purposes Under Algerian Environment

Fatiha Yettou, Boubekeur Azoui, Ali Malek, Narayan Lal Panwar, and Amor Gama

1 Introduction

When considering thermal applications of solar energy, solar cooking is the best option and the solar cooker is the most promising appliance. The use of these cookers provides many advantages, such as fuel economy, greenhouse gases emission reduction, firewood utilization saving, lower cost, and high durability (Hager and Morawicki 2013). However, in many parts of the world, especially in developing countries, wood and fossil fuel-based cooking still predominate with the highest share in the global energy consumption of the residential sector. This situation poses some serious ecological problems such as deforestation (Toonen 2009); economical and health problems are also among the consequences of firewood use.

Algeria lies in the sunny belt of the world (Fig. 1). The insulation time over the quasi-totality of the national territory exceeds 2000 h annually and can reach 3900 h in the high plains and Sahara. The daily solar energy obtained on a horizontal

F. Yettou (✉) • A. Gama
Unité de Recherche Appliquée en Energies Renouvelables, URAER, Centre de Développement des Energies Renouvelables, CDER, 47133 Ghardaïa, Algeria
e-mail: yettou.t@gmail.com

B. Azoui
Laboratoire de Recherche LEB, Département d'Electrotechnique, Université Hadj Lakhdar, Boukhlouf Med ElHadi, Batna, Algéria

A. Malek
Centre de Développement des Energies Renouvelables, CDER, 16340 Algiers, Algeria

N.L. Panwar
Department of Renewable Energy Engineering, Maharana Pratap University of Agriculture and Technology, Udaipur, Rajasthan 313001, India

© Springer International Publishing AG, part of Springer Nature 2018

F. Aloui, I. Dincer (eds.), *Exergy for A Better Environment and Improved Sustainability 2*, Green Energy and Technology,
https://doi.org/10.1007/978-3-319-62575-1_17

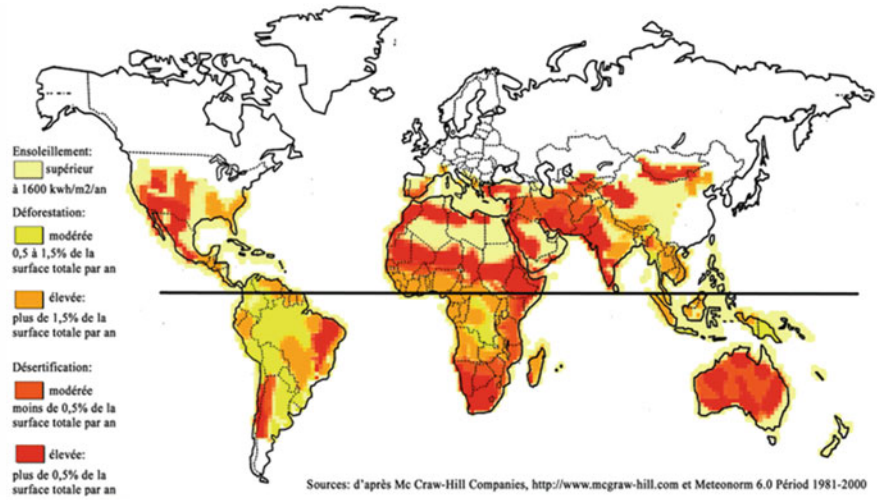

Fig. 1 Priority areas of the world for the development of solar cooking

surface is 5 kWh/m^2 over the major part of the national territory, or about 1700 kWh/m^2/year for the North and 2263 kWh/m^2/year for the South of the country (Boudghene Stambouli 2011). These are very favorable climatic conditions for all solar energy applications, especially for residential cooking, considering that the global Algerian demand for cooking energy is expected to increase greatly with the increasing population over the coming years and that actual demand is currently met through the use of natural gas in cities and through forest wood in rural and isolated areas.

The amount of power produced by solar cookers depends on the amount of sunlight to which it is exposed. As the sun's position changes throughout the day, the solar cookers must be adjusted several times during cooking. For this purpose, booster mirrors are usually added to box-type solar cookers (BSCs), and single- or two-axis tracking systems are used by parabolic solar cookers (PSCs). For both types of cookers, the tracking is difficult, especially when the cooker is loaded (case of BSCs) and when the manual device is used to rotate the assembly (case of PSCs). The performance of solar cookers can be optimized when the cookers are oriented in such a way that the incident sun lights fall onto solar cookers with an incident angle equal to zero and therefore the total losses in the absorber/focal point are the least, so as to reduce the high accuracy requirement for tracking and to overcome the need of standing in the sun, which are the main drawbacks of most solar cookers (Yettou et al. 2014).

In our recent work (Yettou et al. 2014), the absorber temperature maps of a box-type solar cooker with inclined aperture area were established. In this work, the authors attempted to evaluate the thermal efficiency of a paraboloid concentrator solar cooker in Algerian climatic conditions using a new approach based on optical simulation of concentrated solar radiation. The estimated temperature maps of the

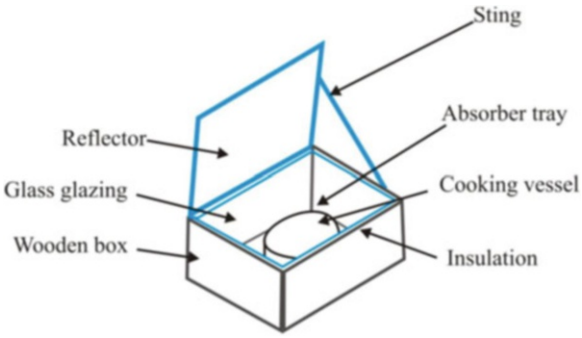

Fig. 2 Components of a box solar cooker

concentrator receiver were generated by this study for all Algerian cities and for several cases. In order to validate the results of simulation experimentally, the parabolic solar cooker was designed and realized by the authors at Applied Research Unit on Renewable Energies of Ghardaïa (Algeria) for domestic cooking applications.

2 Solar Cookers: Definition and Types

Solar cookers absorb solar energy and convert it into heat, which is utilized to cook food. Solar cookers also enable some significant processes, such as pasteurization and sterilization (Cuce and Cuce 2013). Several types of solar cookers have been developed and are still being modified by researchers and scientists worldwide. The available solar cookers can be classified according to different manners, the main categories are: box type, concentrating type, and indirect type. The most recent classification was proposed by Yettou et al. in their review (Yettou et al. 2014).

2.1 Box Solar Cookers

A solar box cooker (SBC) consists of an insulated box with a transparent glass cover and a plate absorber painted black in order to absorb a maximum amount of sunlight (Cuce and Cuce 2013; Saxena et al. 2011). The box is usually equipped with a mirror booster to reflect solar radiation into the box. A description of solar box cooker is shown in Fig. 2. A maximum of four cooking vessels can be placed inside the box cooker (Khan 2008; Kothari et al. 2008). Using the box type, a temperature around 100 °C is achieved; this temperature is suitable for cooking by boiling (Lahkar and Samdarshi 2010). Box-type solar cookers are slow to heat up but work satisfactorily under conditions in which there is diffuse radiation, convection heat loss caused by wind, intermittent cloud cover, and low ambient temperature (Funk and Larson 1998; Panwar et al. 2012).

Many scientists and manufacturers over the world are interested in box solar cookers (Mirdha and Dhariwal 2008; Anderson et al. 2009; Nahar et al. 1994; Mullick et al. 1997; Srinivasan Rao 2007). In recent years, researchers highly focused on developing novel designs of solar cookers. In 2012, Mahavar et al. (2012) presented the design development and thermal and cooking performance studies of a novel Single Family Solar Cooker (SFSC) in early 2013, and they fabricated a Solar Rice Cooker (SRC) (Mahavar et al. 2013). Kumar et al. (2008) fabricated and tested a multipurpose domestic solar cooker-cum-dryer based on truncated pyramid geometry, at the Sardar Patel Renewable Energy Research Institute of India. They also designed and constructed a truncated pyramid geometry-based multipurpose solar device, which could be used for domestic cooking as well as for water heating (Kumar et al. 2010). In early 2013, Farooqui presented an innovative work (Farooqui 2013), which consists of a novel mechanism for one-dimensional tracking of box-type solar cookers.

2.2 Concentrating Solar Cookers

Concentrating-type cookers utilize multifaceted mirrors, Fresnel lenses, or parabolic concentrators to attain higher temperatures (up to 200 °C) (Lahkar and Samdarshi 2010). The most popular is the parabolic solar cooker (Fig. 3), which consists of a parabolic reflector supported by a stand with a cooking pot placed at the focal point of the cooker. Concentrating-type cookers are suitable for frying and food cooking but need frequent adjustment to track the sun's position. Therefore, these cookers are usually equipped with sun-following devices. The most recent work done in this field is the sun tracking system with absorber displacement of (Gama et al. 2013).

Concentrating-type cookers have attracted more attention, and several concepts are being brought into reality around the world (Arenas 2007; Sharaf 2002; Sonune and Philip 2003). Recently, more advanced concentrating-type designs have been developed, such as the parabolic solar cooker constructed by Al-Soud et al. (2010), the spherical-type solar cooker with automatic two-axis sun tracking system realized by Abu-Malouh et al. (2011), and the solar cooking stove, which uses a Fresnel lens for concentration of sunlight, designed and tested in 2011 by (Valmiki et al. 2011). A solar coffee maker was also realized and operated by Sosa-Montemayor et al. (2009), a solar fryer was designed and developed by Gallagher (2011), a solar cooker and a water heater were designed and built in 2010 by Badran et al. (2010), and mostly recently, a new portable solar cooker with PCM-based heat storage was created by Lecuona et al. (2013).

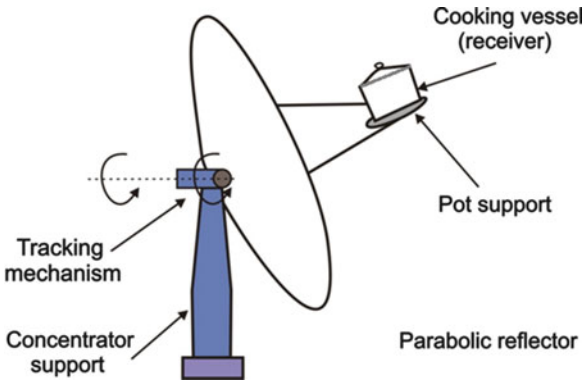

Fig. 3 Components of a parabolic solar cooker

2.3 Indirect Solar Cookers

The indirect-type solar cookers use a heat-transfer fluid to carry thermal energy from the point of collection to the cooking vessel(s) (Lahkar and Samdarshi 2010). This mode of energy collection is useful for indoor cooking applications. One of such types is the cooker realized by Esen (2004), which uses a vacuum-tube collector with heat pipes containing different refrigerants, and the cooker employing flat-plate collectors with the possibility of indoor cooking experimented by Hussein et al. (2008).

3 Theoretical Study

3.1 Solar Radiation Model

The position of the sun with respect to a horizontal surface is given by the two coordinates: solar altitude γ_s and solar azimuth χ, and is calculated as follows (Yettou et al. 2009; Hofierka and Súri 2002):

$$\mathrm{Sin}(\gamma_s) = \mathrm{Cos}(\phi) \cdot \mathrm{Cos}(\delta) \cdot \mathrm{Cos}(\omega) + \mathrm{Sin}(\phi) \cdot \mathrm{Sin}(\delta) \tag{1}$$

$$\mathrm{Cos}(\chi) = \frac{[\mathrm{Cos}(\delta) \cdot \mathrm{Cos}(\omega) \cdot \mathrm{Sin}(\phi) - \mathrm{Sin}(\delta) \cdot \mathrm{Cos}(\phi)]}{\mathrm{Cos}(\gamma_s)} \tag{2}$$

where δ is the sun declination, ω is the hour angle, and φ is the geographical latitude of the location.

The clear-sky normal beam irradiance IN [W/m^2] has been calculated using the module r.sun of the GRASS GIS platform (Sùri and Hofierka 2004; GRASS Development Team 2009). It computes the solar radiation using the model of the European Solar Radiation Atlas (Rigollier et al. 2000):

$$I_N = G_0 \cdot \exp\{-0.8662\, T_{LK}\, m_A\, \delta_R(m_A)\} \quad (3)$$

in which G_0 is the extraterrestrial solar radiation, δ_R is the spectrally integrated optical thickness of the clean dry atmosphere, and m_A is the relative optical air mass. The term $-0.8662\, T_{LK}$ is the air mass 2 Linke atmospheric turbidity factor corrected by Kasten (1996). The web-based solar radiation resource SoDa (SoDa Service e Knowledge in Solar Radiation, www.soda-is.com/) can be used to calculate monthly values of T_{L2} for any location in the world by entering geographical coordinates and elevation data (Gama et al. 2010).

For an assessment of normal beam irradiances for overcast conditions, a sunshine fraction factor σ_o is used. A sunshine fraction data for Algerian cities is available in Capderou's books (1987).

3.2 *Description of the Parabolic Solar Cooker*

The realized parabolic solar cooker (SPC) consists of a parabolic reflector supported by a stand with a cooking pot placed at the focal point of the cooker.

The shape of the cooker is paraboloidal type (Fig. 4) having 0.9 m aperture diameter. This solar cooker has a steel structure and uses small mirror facets as the reflector. The reflective area of the solar cooker is 0.72 m^2. The focal length of the cooker is 0.5 m while the focal area of the cooker is 0.10 m^2. The concentration ratio of this cooker is calculated about 24. The reflectivity of the mirror facets is 0.80. The aluminum cooking pot (20 cm in diameter and 10 cm in height) filled with water and equipped with a black cover was placed at the focus area of the cooker. Parabolic reflector was assigned a reflectivity of 100%, and its receiver is considered as a perfect absorber. The solar tracking in this cooker is done manually.

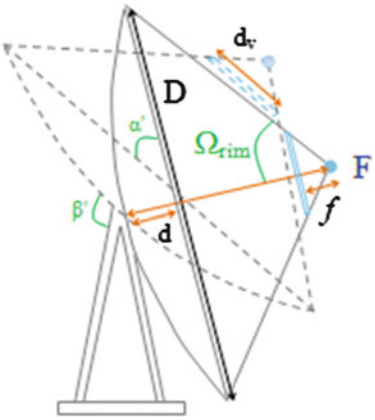

Fig. 4 Schematic of a parabolic solar cooker with tracking system

3.3 Mathematical Equations

According to Duffie and Beckman (1991), the optimal PSC positions can be defined by two angles: λ (surface slope) and χ (the surface azimuth angle). For two-axes tracking, the cooker positions are determined as follows:

$$\lambda = \theta_z \tag{4}$$

$$\chi = \theta_a \tag{5}$$

where θ_z is the zenith angle of the sun and θ_a is the solar azimuth angle.

It is a great challenge to maintain the position of the SPC focused image on the focal point at all times; it results in a lower concentration factor and thus needs more frequent adjustments of the concentrator. Therefore, it is necessary to move the cooking pot by a distance f from the focal point (Fig. 4) to increase the focused area and reduce rays path corrections and then to improve the concentration factor.

The mathematical formulas for calculating the distance f are presented below:

$$\tan\psi = \frac{d_v/2}{f} = \frac{D/2}{F-d} \tag{6}$$

The parametric equation of the parabola is as follows:

$$d = \frac{1}{4F} \cdot \frac{D^2}{2} \tag{7}$$

By inserting Eq. (7) into Eq. (6) and solving the equation, the new focal point distance from the parabolic vertex is known by calculating the value of f as follows:

$$f = \frac{(F-d) \cdot d_v}{D} \tag{8}$$

3.4 Adjustment Tracking Time

It is important to choose the correct tilt angles (γ,χ) of the parabolic cooker, a minor error will result in a reduced number of incident rays on the receiver. Figure 5 is a simplified graphic representation showing the incident rays with a reduced number of rays to improve readability. The figure demonstrates a simulation of the ray path of the parabolic solar cooker for all incident rays and reduced number of incident rays due to a non-normal incidence.

To deduce the optimum adjustment time, the receiver losses were evaluated for parabolic solar cookers every 5 min. As a starting time, we chose to simulate the

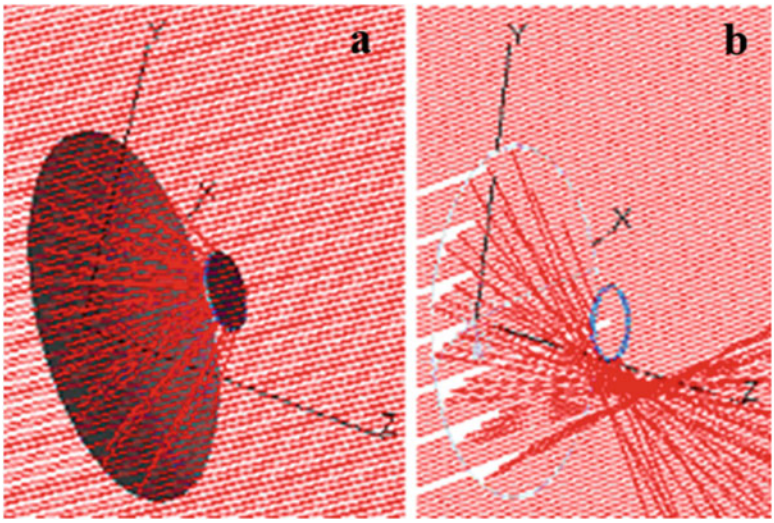

Fig. 5 Simulation showing the ray path for parabolic solar cooker: (**a**) when the collector is oriented directly to sun; (**b**) when the collector is tilted at an incorrect angle

solar cooker for 1 day at winter solstice from 12:00 (angle of solar incidence equal to 0) to 12:45 and reported the results every 5 min. The solar flux distribution graphs are plotted in terms of solar concentrated irradiance (in W/m^2).

The parabolic reflector focuses the incident radiation to a point, and the profile of the concentrated spot for the PSC at noon on 23 December is shown in Fig. 6. Figure7 reveals the simulated flux distribution results of focused image on the focal point on 23 December at 12:30.

The concentrated irradiance depends on the losses in the receiver of the solar cooker. The losses in the receiver change with the sun's position. Therefore, the concentrated irradiance changes with the sun's position. Facing south, the receiver achieved highest concentrations at noon. However, it offered poor efficiency after 30 min of operation without adjusting as seen in Fig. 7. Therefore, parabolic solar cookers need adjustments so as to always face the sun, and the titled angles must be corrected from the initial values.

In our recent paper (Yettou et al. 2013), we explained a new method based on optical losses to determine the time adjustment for PSC. According to the results, a time adjustment of 8 min is required for the parabolic solar cooker.

4 Methodology

In order to draw different cooker maps, several steps are necessary (Fig. 8):

- Modeling normal beam solar irradiances for clear and cloudy skies based on sun position parameters, data for Linke turbidity and sunshine fraction factors using Matlab language (Matlab/Simulink Tutorial (2010)).

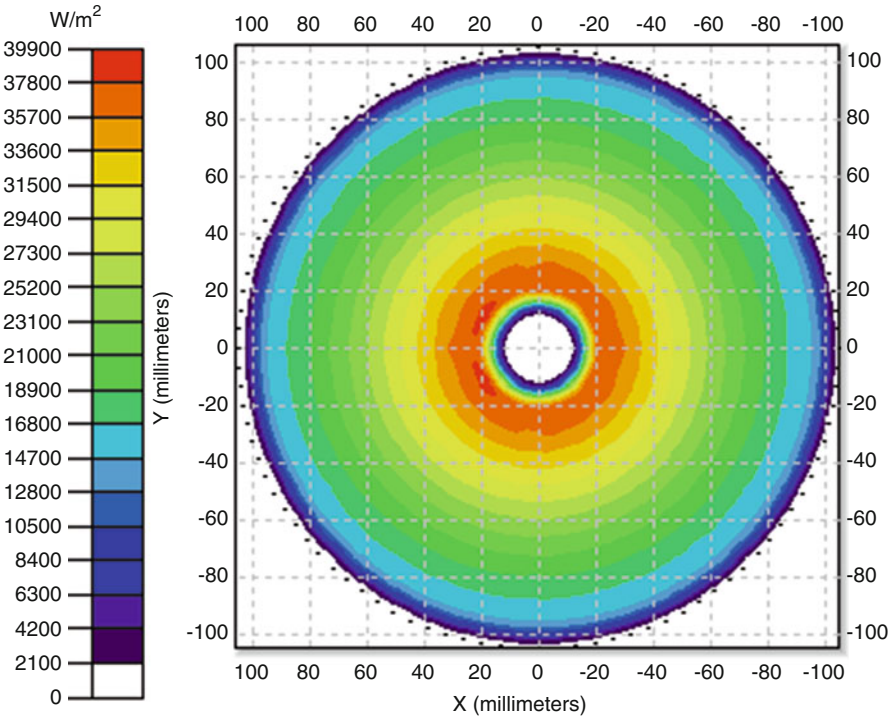

Fig. 6 The profile of the concentrated spot for the parabolic solar cooker on 23 December at 12:00

- By importing the conception design of parabolic solar cooker from Solid Works software (SolidWorks Corporation), a simulation of concentrated solar irradiance on a concentrator receiver was done for 48 cities in Algeria by inserting modeling results as inputs into TracePro software (Lambda Research Corporation USA (2010)).
- Solar cookers are a direct application of the laws of heat transfer by radiation (Stephan-Boltzmann law), which states that the flux density emitted or received by a body is proportional to the fourth power of its temperature. Thus, the next step is the conversion of the obtained optical results for concentrated irradiance to thermal values using Stephan-Boltzmann law as follows (Chong et al. 2011):

$$C_{\max} R_1 R_2 I_S = \sigma_s T^4 \tag{9}$$

where $\mathbf{C_{max}}$ is the concentration ratio, it is equal to the concentrated radiation/incident radiation, $\mathbf{R_1R_2} = \mathbf{R}$ is the reflectivity of the glasses, **I** is the incident solar radiation in W/m^2, $\boldsymbol{\sigma_s}$ is the Stefan-Boltzmann constant (5.67×10^{-8} W/m^2 K^4), $\boldsymbol{T^4}$ is the temperature in °K.

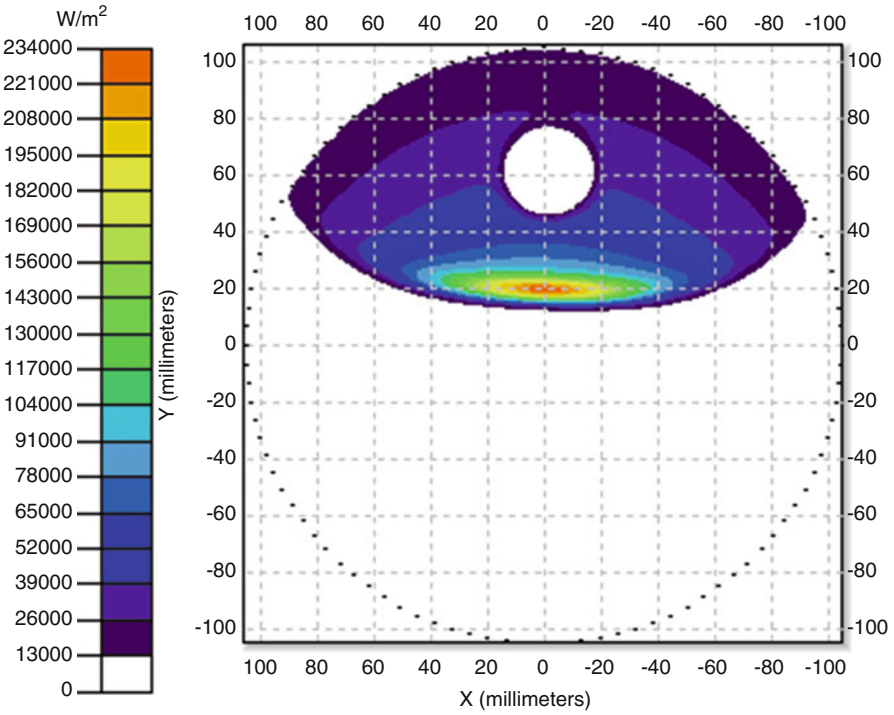

Fig. 7 The simulated flux distribution results of the parabolic concentrator on the target on 23 December at 12:30

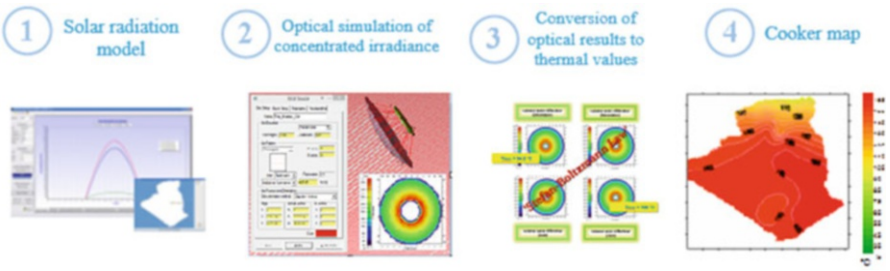

Fig. 8 Steps to obtain parabolic solar cooker maps based on optical approach

- The above steps are applied to 62 points (including the 48 cities) for several geographical locations of Algeria to create a compatible matrix format for Surfer Golden Software (Surfer User's guide). The Golden Software Surfer Inc. software is a universal tool path contours, surfaces, and 3D cartographic representations. It also allows to interpolate between two adjacent points with high accuracy. Reading the matrix file XYZ by the Surfer software offers the possibility to project the obtained results on illustrative and analyzable maps. So, maps of solar irradiance, concentrated solar radiation, and temperatures are obtained.

5 Optical Simulation, Experimental Work, and Validation

For each city (Lat, Long, Alt) in Algeria, an optical simulation of concentrated solar irradiance on a concentrator receiver was done. Figures 9a–d represent the results of simulation, by TracePro software, of concentrated irradiance on the absorber area for clear and cloudy days in December and June months, respectively.

By applying the Stefan-Boltzmann formula for thermal conversion of optical values, the following results were obtained for pot water temperatures in December month at Ghardaïa city: 92.6 °C for clear sky and 84.3 °C for cloudy sky. By comparing the theoretical results with experimental data measured at Ghardaïa

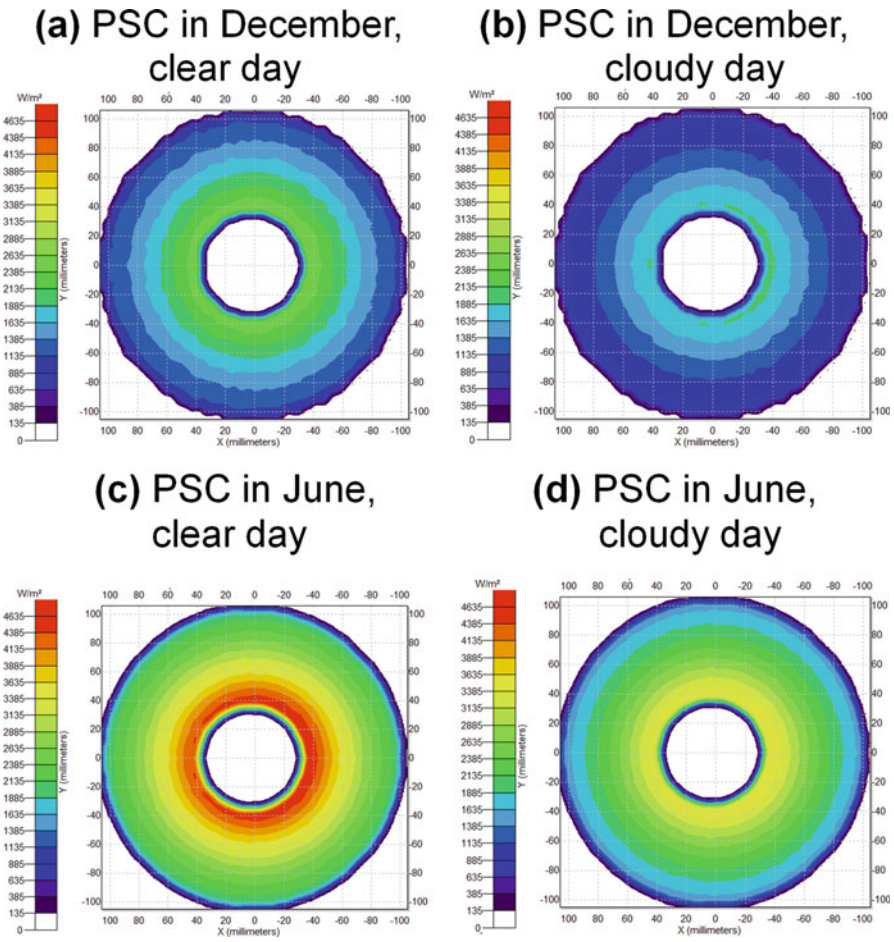

Fig. 9 Results of the simulation for the concentrated irradiance on the focal area of the PSC in Ghardaïa sites. (**a**) PSC in December, clear day, (**b**) PSC in December, cloudy day (**c**) PSC in June, clear day (**d**) PSC in June, cloudy day

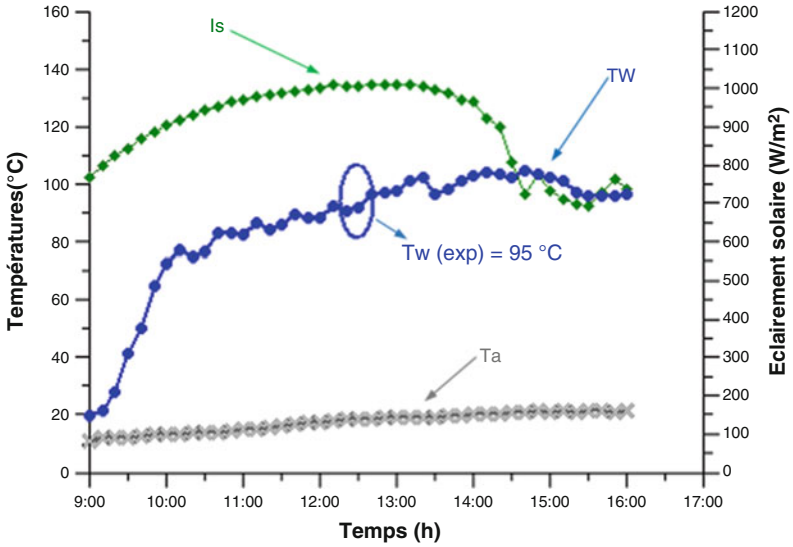

Fig. 10 Practical results of the temperature profile for the PSC's focal area with solar radiation, measured on the Ghardaïa site for one of the tests carried out in December

(Fig. 10), it was found that the values are in good agreement with an acceptable average error of ±3 °C. Under direct sun exposition, the cooker water temperatures achieved 95 °C for clear sky and 82 °C for overcast sky conditions, just afternoon, the ambient temperatures were 19 °C and 17 °C, respectively.

6 Mapping Results

To generate various maps (direct normal radiation, concentrated radiation, temperature receivers), we applied the approach detailed above, namely mathematical modeling, optical simulation, and data conversion, for the entire Algerian territory. For this, and in order to cover most of the country's area, we chose 62 points including 48 cities with different geographic coordinates (Lat, Lon, Alt) original of Google Earth Service.

6.1 Solar Radiation and Concentrated Radiation Maps

Figures 11 and 12 show the map of mean values of Linke turbidity factor used for calculating direct normal irradiance on the parabolic receiver, for clear sky in winter and summer seasons, respectively. Mapping in Figs. 13 and 14 represents

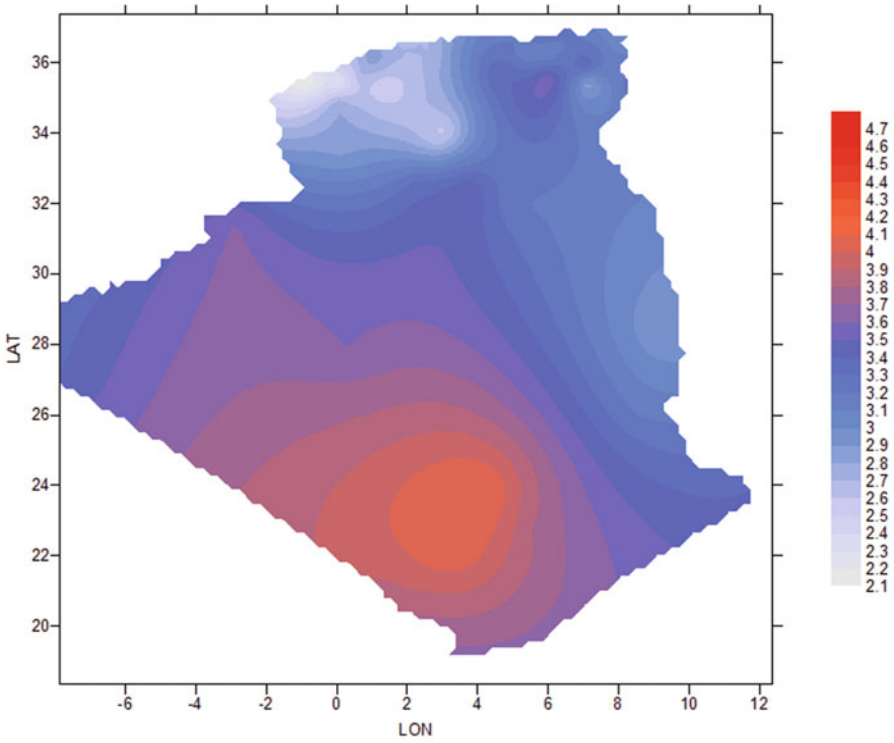

Fig. 11 Mapping of Linke turbidity factor mean values for December month in Algeria

the instantaneous incident irradiances for December and June months obtained from our Matlab program. We also present, in Figs. 15 and 16, the maps of sunshine fraction for all Algerian cities used for calculating the solar irradiance incident on the cooker receiver in cloudy skies.

Figures 17, 18, 19, and 20 represent the mapping of the obtained results for concentrated irradiances on the receiver for clear skies in winter and summer months and for cloudy skies in winter and summer months, respectively.

We can easily notice, from these cards, the important quantity of concentrated solar radiation incident on the cooker receiver in summer season compared to winter. This remark is also valuable for cloudy days, especially in the south of the country. The amount of average concentrated irradiance at the receiver of the cooker is estimated as 2676 W/m^2 for a typical day of June month at noon (Fig. 20) and as 1393 W/m^2 for a typical day of December month (Fig. 19). These quantities are significantly increased for clear skies with 4104 W/m^2 average value in summer (Fig. 18) and 2240 W/m^2 in winter (Fig. 17), and this is mainly due to the significant amount of direct normal solar radiation received throughout the Algerian territory during the year. The average value of direct normal irradiance in June month at noon is estimated at 877 W/m^2 (Fig. 14), and an average value in the month of December is estimated as 867 W/m^2 (Fig. 13).

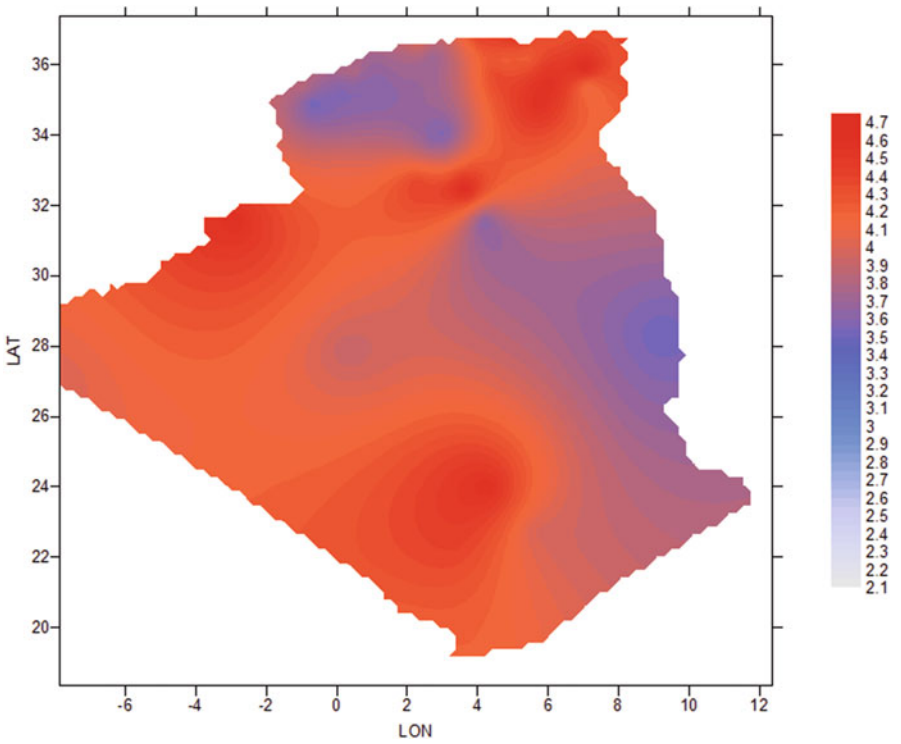

Fig. 12 Mapping of Linke turbidity factor mean values for June month in Algeria

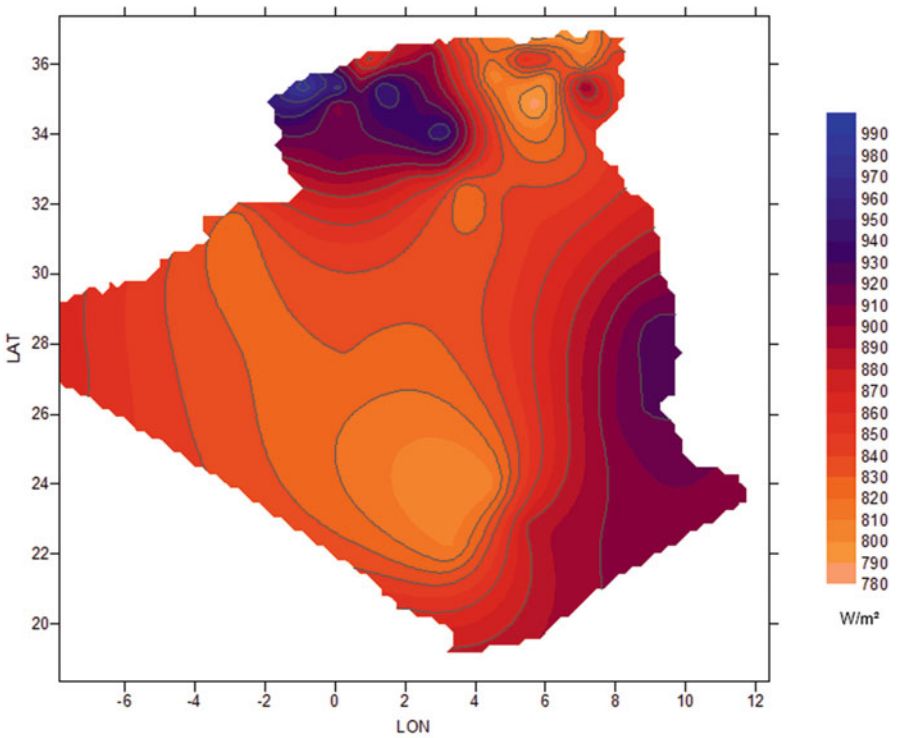

Fig. 13 Mapping of normal beam solar irradiances for December month in Algeria

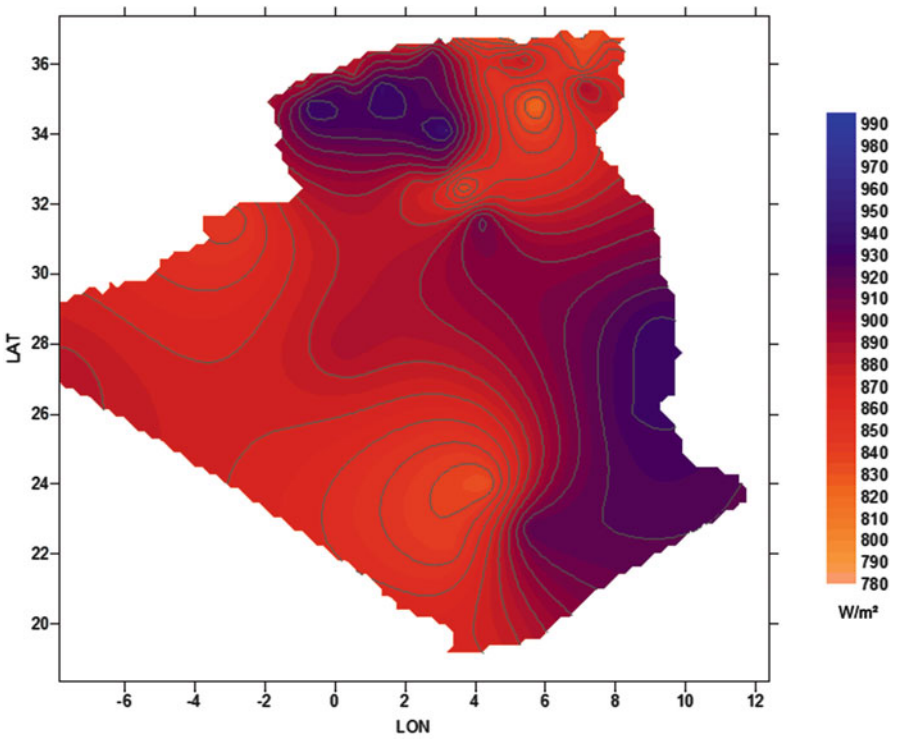

Fig. 14 Mapping of normal beam solar irradiances for June month in Algeria

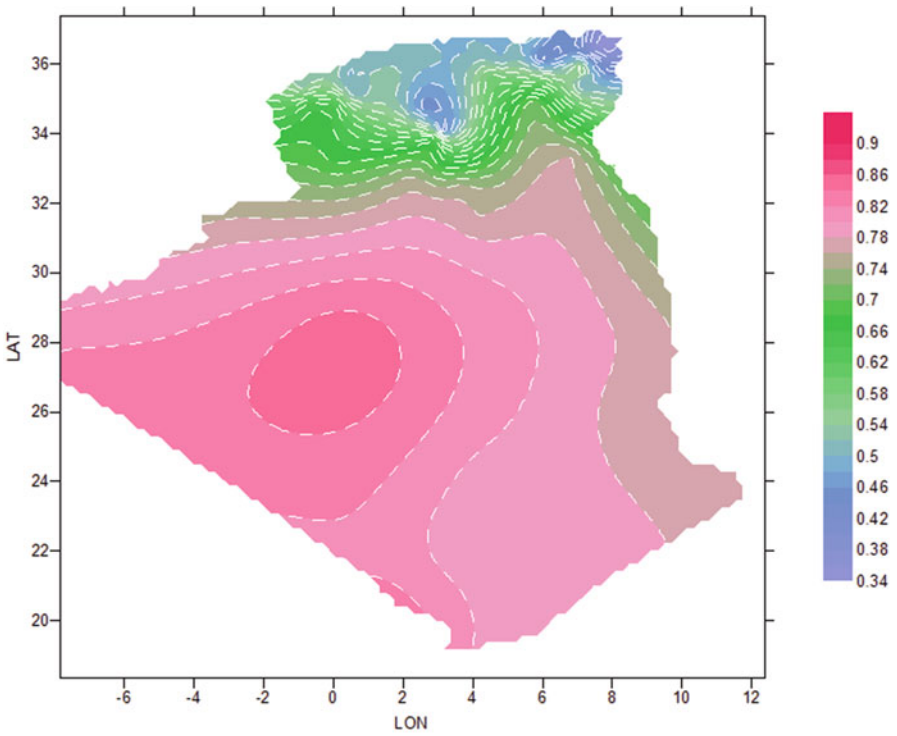

Fig. 15 Mapping of sunshine fraction mean values for December month in Algeria

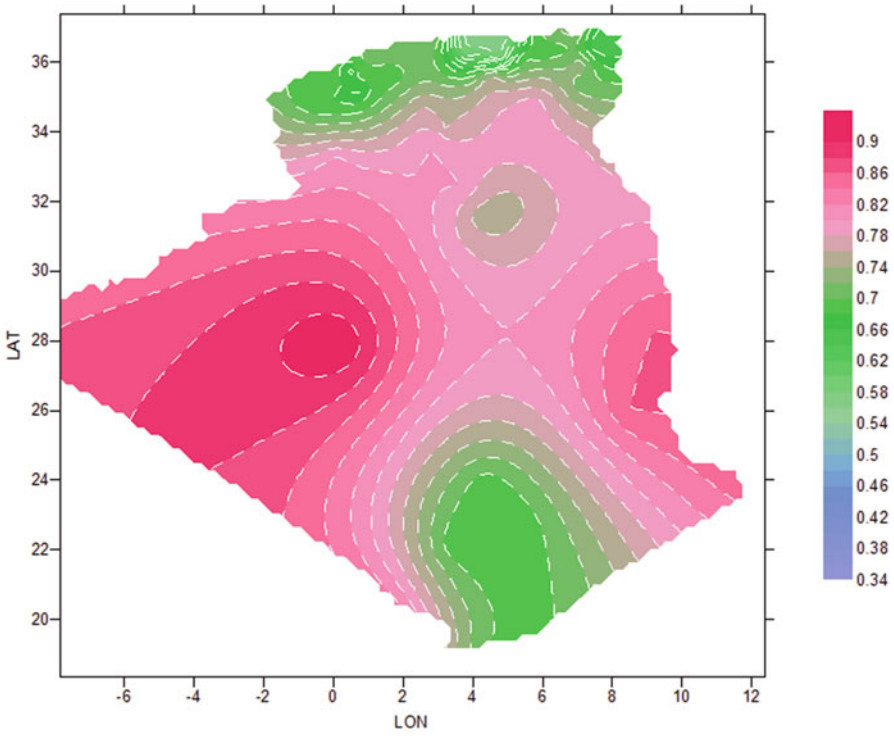

Fig. 16 Mapping of sunshine fraction mean values for June month in Algeria

6.2 Cooker Receiver Temperature Maps

Figures 21 and 22 show the mapping of temperatures attained by the cooker receiver obtained for winter and summer months under clear sky in Algeria, respectively. The receiver temperatures for winter and summer months under overcast conditions are also presented in Figs. 23 and 24.

According to the iso-temperature map distributions, it is clear that the solar cooker can be used in all Algerian territories in clear sky summer season (Fig. 22) with temperatures exceeding 110 °C. For the winter season, the use duration of the cooker is reduced from the southern to the northern cities (Fig. 21) depending on the amount of solar radiations. The recorded temperatures are between 62.7 and 68.4 °C for sites with latitude greater than 36 °N and between 70.2 and 86.2 °C for sites with latitude $34° < \varphi < 36$ °N, the estimated temperatures are above 93 °C for South of the country.

The use of the solar cooker under overcast conditions became inefficient in North and height plains regions (Fig. 23) due to low temperatures (below 80 °C). However, the cooker is exploitable in most of the areas of the country during summer season almost under cloudy sky; temperatures are estimated between 81.3 and 90.7 °C in the north and between 94.6 and 167.7 °C in the south (Fig. 24).

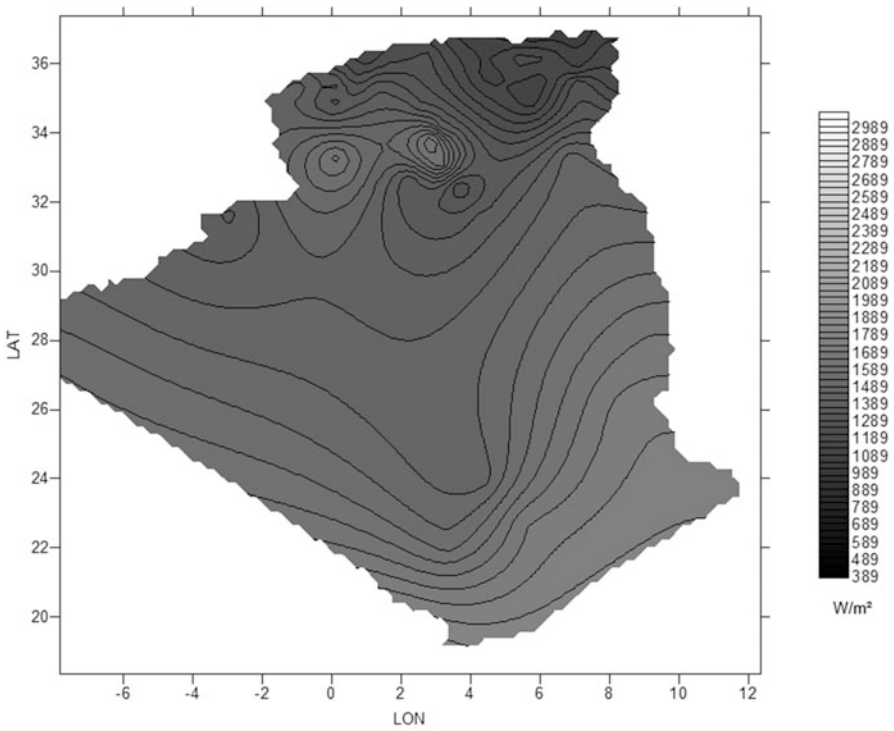

Fig. 17 Obtained map for concentrated solar irradiance on PSC's receiver for typical winter season clear days

7 Conclusion

A new approach was employed to generate temperature maps of a solar receiver for a domestic parabolic concentrator used for cooking purposes. A model was developed to calculate solar irradiance for 48 cities in Algeria; an optical simulation of concentrated solar radiation was applied to each location. The simulation results are converted to temperature values based on Stefan-Boltzmann law. The hourly temperature maps produced can predict the cooker efficiency under Algerian climatic conditions for clear and cloudy skies. Nevertheless, solar cooking remains a reality that allows healthy cooking of food with energy savings and respect for the environment.

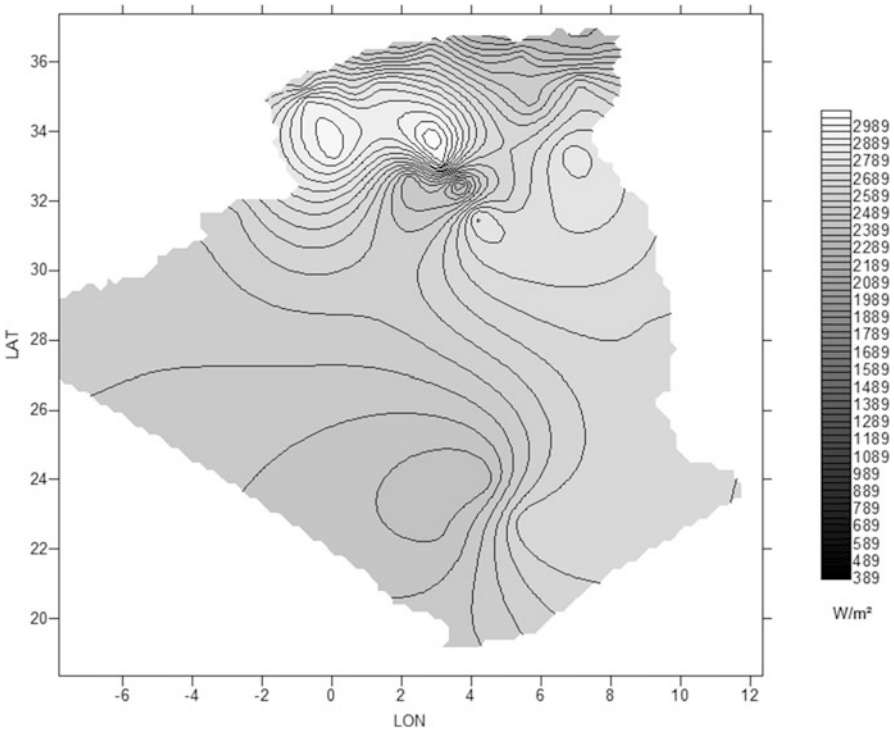

Fig. 18 Obtained map for concentrated solar irradiance on PSC's receiver for typical summer season clear days

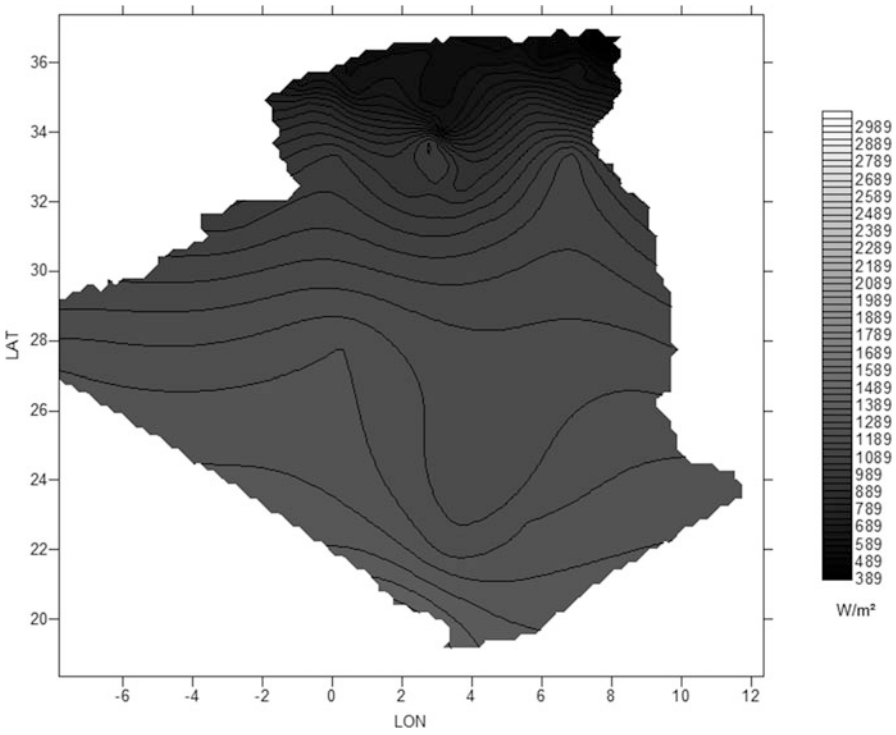

Fig. 19 Obtained map for concentrated solar irradiance on PSC's receiver for typical winter season cloud days

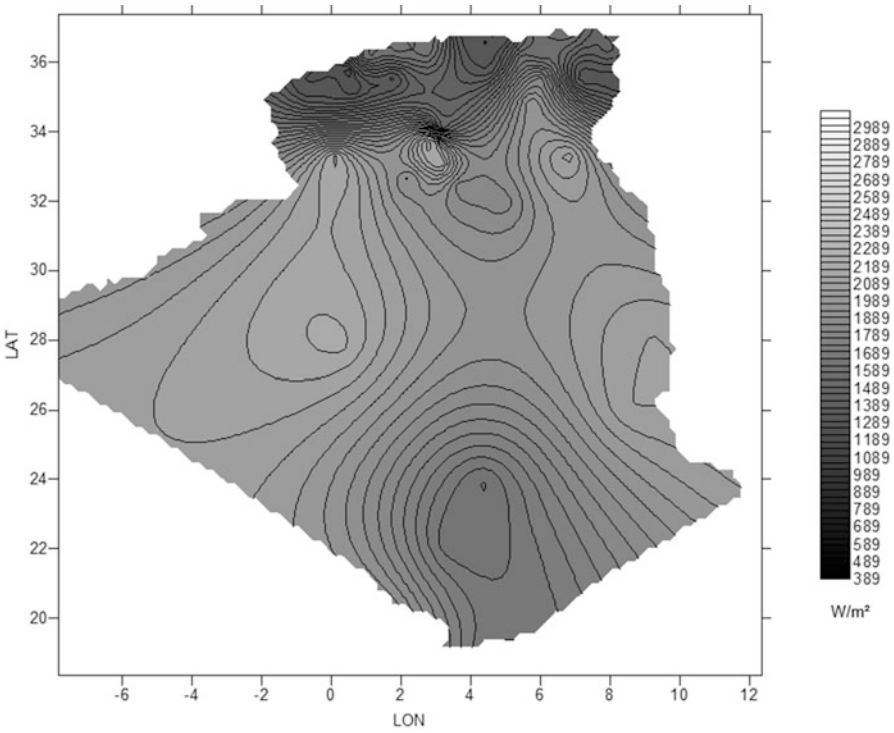

Fig. 20 Obtained map for concentrated solar irradiance on PSC's receiver for typical summer season cloud days

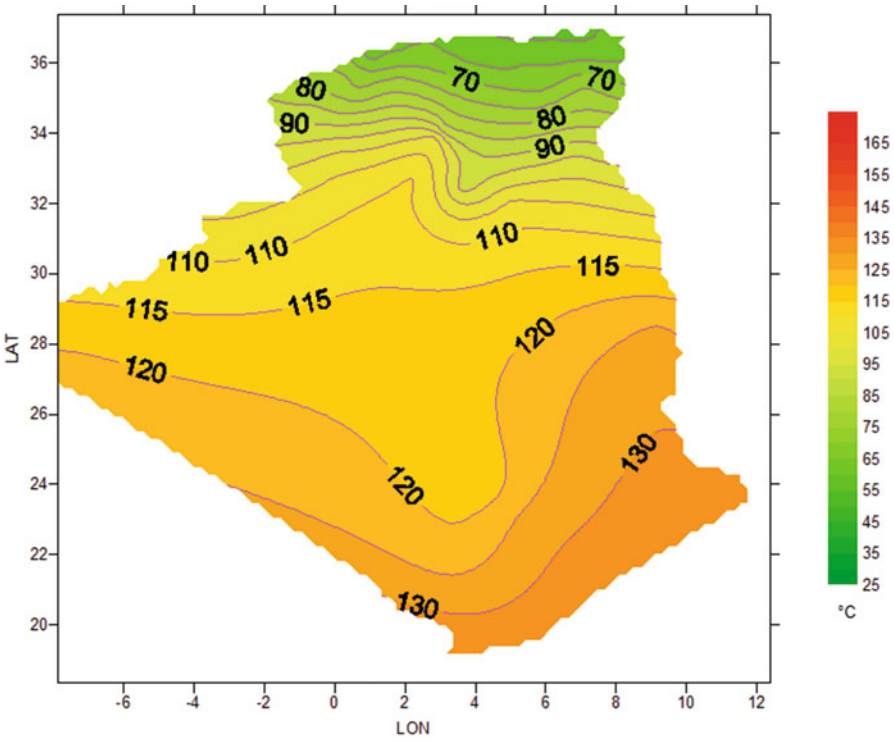

Fig. 21 Receiver temperature maps of parabolic solar cooker for Algerian clear sky as obtained by the proposed approach for typical winter season

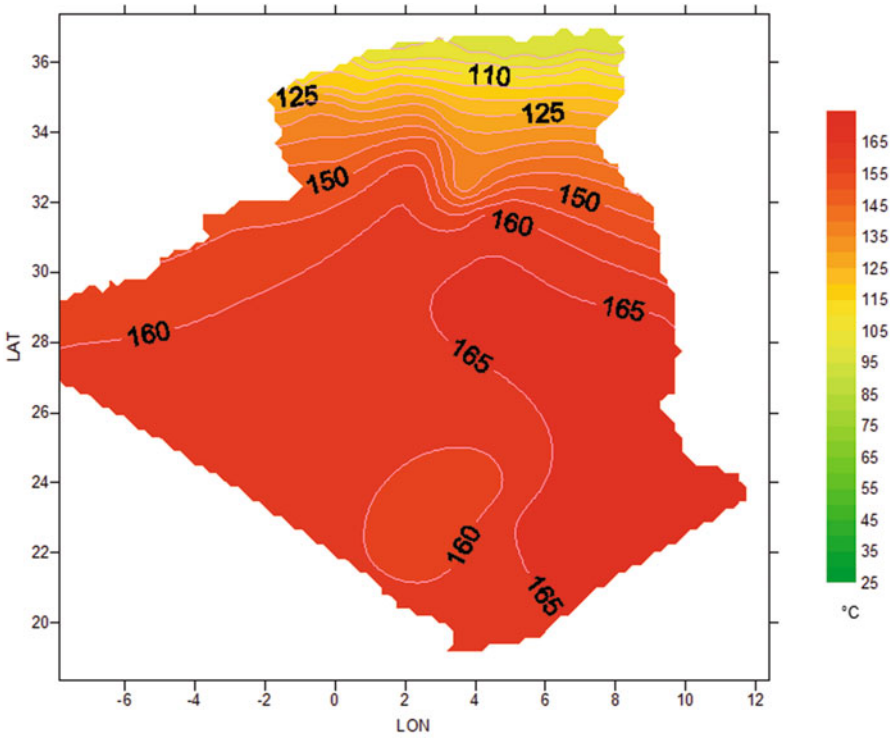

Fig. 22 Receiver temperature maps of parabolic solar cooker for Algerian clear sky for typical summer season

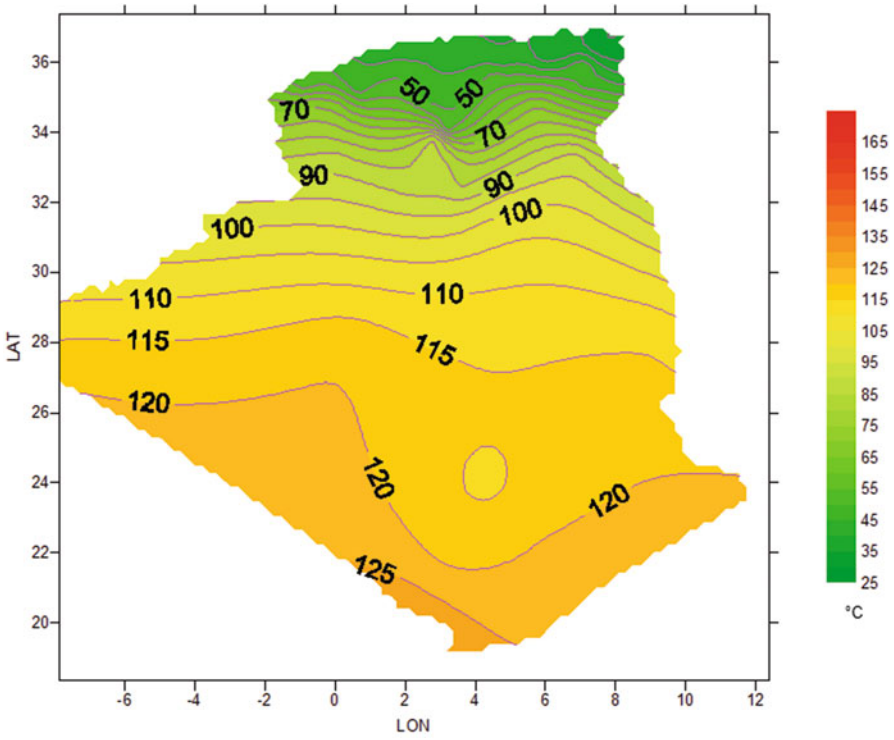

Fig. 23 Receiver temperature maps of parabolic solar cooker for Algerian cloudy sky as obtained by the proposed approach for typical winter season

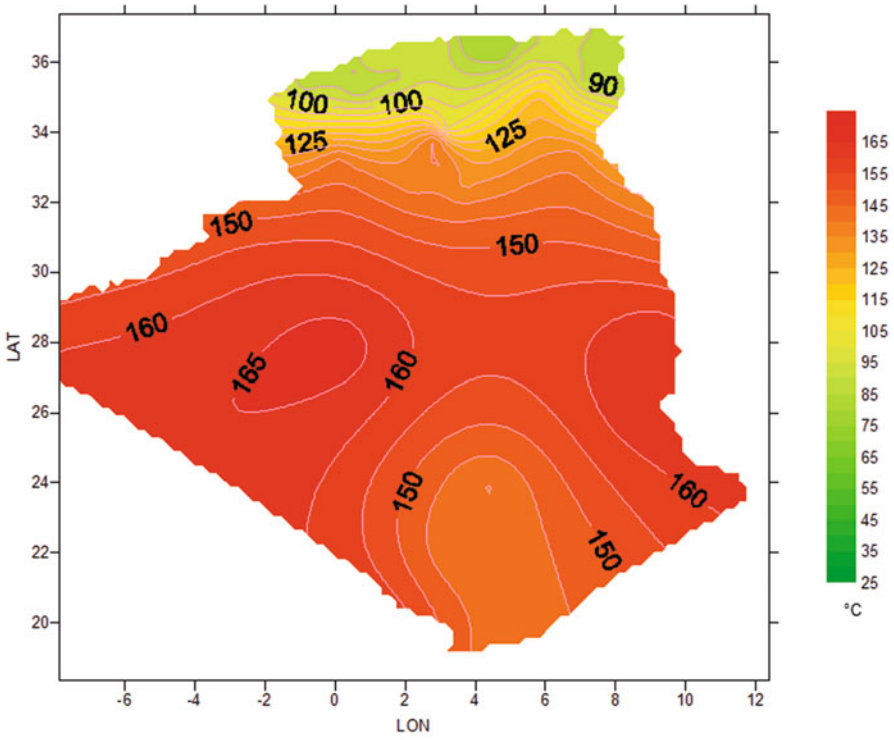

Fig. 24 Receiver temperature maps of parabolic solar cooker for Algerian cloud sky for typical summer season

References

'Matlab/Simulink Tutorial', School of Electrical, Electronic and Computer Engineering, Version 7.10, 1st edn, 2010. 'Matlab/Simulink Tutorial', School of Electrical, Electronic and Computer Engineering, Version 7.10, 1st edn (2010). [Rapport]

Abu-Malouh, R., Abdallah, S., Muslih, I.M.: Design, construction and operation of spherical solar cooker with automatic sun tracking system. [Revue]. Energy Convers. Manag. **52**, 615–620 (2011)

Al-Soud, M.S., Abdallah, E., Akayleh, A., Abdallah, S., Hrayshat, E.S.: A parabolic solar cooker with automatic two axes sun tracking system. [Revue]. Appl. Energy. **87**, 463–470 (2010)

Anderson, T., Duke, M., Carson, J.: Performance of coloured solar collectors. [Conférence] Proceedings of the First International Conference on Applied Energy (ICAE09), University of Hong Kong (CD), Hong Kong, 5–7 Jan 2009

Arenas, J.M.: Design, development and testing of a portable parabolic solar kitchen. [Revue]. Renew. Energy. **32**, 257–266 (2007)

Badran, A.A., Yousef, I.A., Joudeh, N.K., Al Hamad, R., Halawa, H., Hassouneh, H.K.: Portable solar cooker and water heater. [Revue]. Energy Convers. Manag. **51**, 1605–1609 (2010)

Boudghene Stambouli, A.: [Revue]. - Promotion of renewable energies in Algeria: strategies and perspectives. : [s.n.] Renew Sust Energy Rev. **15**, 1169–1181 (2011)

Capderou, M.: Atlas solaire de l'Algérie, Aspect géométrique, Synthèse géographique. [Ouvrage]. - [s.l.], vol. 1, T3. Office des Publications Universitaires, EPAU, Algérie, 405 p (1987)

Chong, K.K., Lim, C.Y., Hiew, W.: Cost-effective solar furnace system using fixed geometry Non-Imaging Focusing Heliostat and secondary parabolic concentrator. [Revue]. Renew. Energy. **36**, 1595–1602 (2011)

Cuce, E., Cuce, P.M.: A comprehensive review on solar cookers. [Revue]. Appl. Energy. **87**, 1399–1421 (2013)

Duffie, J., Beckman, W.: Solar Engineering of Thermal Processes. [Ouvrage]. - [s.l.], 2nd edn. John Wiley & Sons, New York (1991)

Esen, M.: Thermal performance of a solar cooker integrated vacuum-tube collector with heat pipes containing different refrigerants. [Revue]. Sol. Energy. **76**, 751–757 (2004)

Farooqui, S.Z.: A gravity based tracking system for box type solar cookers. [Revue]. Sol. Energy. **92**, 62–68 (2013)

Funk, P.A., Larson, D.L.: Parametric model of solar cooker performance. [Revue]. Sol. Energy. **62** (1), 63–68 (1998)

Gallagher, A.: A solar fryer. [Revue]. Sol. Energy. **85**, 496–505 (2011)

Gama, A., Larbes, C., Malek, A., Yettou, F., Adouane, B.: Design and realization of a novel sun tracking system with absorber displacement for parabolic trough collectors [Revue]. J Renew Sustain Energy. **5**, 033108 (2013)

Gama, A., Yettou, F., Malek, A., Larbes, C., Azoui, B.: Determination of atmospheric turbidity using solar radiation measurements for two Algerian sites. [Conférence] 2nd International Conference on Nuclear and Renewable Energy Resources (NURER10), Ankara, 04–07 Juillet 2010

GRASS Development Team Geographic Resources Analysis Support System (GRASS GIS) Software [Rapport]. - [s.l.] : Open Source Geospa. Found., USA., 2009

Hager, T.J., Morawicki, R.: [Revue]. - Energy consumption during cooking in the residential sector of developed nations: a review. : [s.n.] Renew. Sust. Energ. Rev. **40**, 54–63 (2013)

Hussein, H.M.S., El-Ghetany, H.H., Nada, S.A.: Experimental investigation of novel indirect solar cooker with indoor PCM thermal storage and cooking unit. [Revue]. Energy Convers. Manag. **49**, 2237–2246 (2008)

Hofierka, J., Súri, M.: The solar radiation model for open source GIS: implementation and applications. [Conférence] Proceedings of the Open source GIS – GRASS users conference, Trento, 11–13 Sept 2002

Kasten, F.: The Linke turbidity factor based on improved values of the integral Rayleigh optical thickness. [Revue]. Sol. Energy. **56**, 239–244 (1996)
Khan, B.H.: Non-conventional energy resources. [Ouvrage]. Tata McGraw Hill Publications, New Delhi (2008)
Kothari, D.P., Singal, K.C., Ranjan, R.: Renewable Energy Resources and Emerging Technologies. [Ouvrage]. Prentice-Hall, New Delhi, India, (2008)
Kumar, N., Agravat, S., Chavda, T., Mistry, H.N.: Design and development of efficient multipurpose domestic solar cookers/dryers. [Revue]. Renew. Energy. **33**, 2207–2211 (2008)
Kumar, N., Chavda, T., Mistry, H.N.: A truncated pyramid non-tracking type multipurpose domestic solar cooker/hot water system. [Revue]. Appl. Energy. **87**, 471–477 (2010)
Lahkar, P.J., Samdarshi, S.K.: A review of the thermal performance parameters of box type solar cookers and identification of their correlations. [Revue]. Renew. Sust. Energ. Rev. **14**, 1615–1621 (2010)
Lambda Research Corporation USA. TracePro software for opto-mechanical modeling user manual release 6 revision 03 et 2.7–2.13. 2010. p. [En ligne]
Lecuona, A., Nogueira, J.I., Ventas, R., Rodríguez-Hidalgo, M.C., Legrand, M.: Solar cooker of the portable parabolic type incorporating heat storage based on PCM [Revue]. Appl. Energy. **111**, 1136–1146 (2013)
Mahavar, S., Rajawat, P., Marwal, V.K., Punia, R.C., Dashora, P.: Modeling and onfield testing of a solar rice cooker. [Revue]. Energy. **49**, 404–412 (2013)
Mahavar, S., Sengar, N., Rajawat, P., Verma, M., Dashora, P.: Design development and performance studies of a novel single family solar cooker. [Revue]. Renew. Energy. **47**, 67–76 (2012)
Mirdha, U.S., Dhariwal, S.R.: Design optimization of solar cooker. [Revue]. Renew. Energy. **33**, 530–544 (2008)
Mullick, S.C., Kandpal, T.C., Kumar, S.: Top heat-loss factor of double-glazed box type solar cooker from indoor experiments. [Revue]. Energy. **22**, 559–565 (1997)
Nahar, N.M., Marshall, R.H., Brinkworth, B.J.: Studies on a hot box solar cooker with transparent insulation materials. [Revue]. Energy Convers. Manag. **35**, 787–791 (1994)
Panwar, N.L., Kaushik, S.C., Kothari, S.: State of the art of solar cooking: an overview. [Revue]. Renew. Sust. Energ. Rev. **16**, 3776–3785 (2012)
Rigollier, C., Bauer, O., Wald, L.: On the clear sky model of the esraeuropean solar radiation atlas with respect to the Heliosat method. [Revue]. Sol. Energy. **68**(1), 33–48 (2000)
Saxena, A., Varun, Pandey, S.P., Srivastav, G.: A thermodynamic review on solar box type cookers. [Revue]. Renew Sust Energy Rev. **15**, 3301–3318 (2011)
Sharaf, E.: A new design for an economical, highly efficient, conical solar cooker. [Revue]. Renew. Energy. **27**, 599–619 (2002)
SoDa Service e Knowledge in Solar Radiation. [En ligne]. www.soda-is.com/
SolidWorks SolidWorks Corporation, 300 Baker Avenue, Concord, MA 01742. Available from: http://www.solidworks.com/. SolidWorks, SolidWorks Corporation, 300 Baker Avenue, Concord, MA 01742. Available from: http://www.solidworks.com/. [En ligne]
Sonune, A.V., Philip, S.K.: Development of a domestic concentrating cooker. [Revue]. Renew. Energy. **28**, 1225–1234 (2003)
Sosa-Montemayor, F., Jaramillo, O.A., Del Rio, J.A.: Thermodynamic analysis of a solar coffee maker. [Revue]. Energy Convers. Manag. **50**, 2407–2412 (2009)
Srinivasan Rao, K.V.N.: Innovative solar cooking vessel design [Conférence]. Fifth international energy conversion engineering conference and exhibit, St. Louis, 25–27 June 2007
Surfer User's guide 3ème edition, Golden Software Inc., 1999. [En ligne]
Sùri, M., Hofierka, J.: A new GIS-based solar radiation model and its application to photovoltaic assessments. [Revue]. Trans. GIS. **8**(2), 175–190 (2004)
Toonen, H.M.: [Revue]. - Adapting to an innovation: solar cooking in the urban households of Ouagadougou (Burkina Faso).: [s.n.] Phys. Chem. Earth. **34**, 65–71 (2009)
Valmiki, M.M., Li, P., Heyer, J., Morgan, M., Albinali, A., Alhamidi, K.: A novel application of a Fresnel lens fora solar stove and solar heating. [Revue]. Renew. Energy. **36**, 1614–1620 (2011)

www.soda-is.com/ [En ligne]
www.soda-is.com/ SoDa Service e Knowledge in Solar Radiation. [En ligne]. www.soda-is.com/
Yettou, F., Azoui, B., Malek, A.: Determination of adjustment tracking time in two types of solar cookers by ray-tracing method [Revue]. Power Eng. Energy Electrical Drives' (POWERENG), 2013. 822–827 (2013). doi:10.1109/PowerEng.2013.6635716
Yettou, F., Azoui, B., Malek, A., Gama, A., Panwar, N.L.: Estimation et cartographie des températures d'un cuiseur solaire boite avec et sans réflecteur en Algérie. [Conférence] // 3ème Séminaire International sur les Energies Nouvelles et Renouvelables (SIENR14), Ghardaïa, 13–14 Octobre 2014a
Yettou, F., Azoui, B., Malek, A., Gama, A., Panwar, N.L.: Solar cooker realizations in actual use: an overview. [Revue]. Renew. Sust. Energ. Rev. **37**, 288–306 (2014b)
Yettou, F., Malek, A., Haddadi, M., Gama, A.: Etude comparative de deux modèles de calcul du rayonnement solaire par ciel clair en Algérie. [Revue]. Revue des Energies Renouvelables CDER. **12**(2), 331–346 (2009)

Experimental Investigations on the Effects of Low Compression Ratio in a Direct Injection Diesel Engine

M. Viveganantth, K. Ashwin Kanna, and A. Ramesh

1 Introduction

Diesel engines are based on the concept of compression ignition. They rely mainly on the high temperature achieved during the compression stroke for autoignition of the injected diesel. So, higher the compression ratio, better is the cold starting ability. However, high compression ratios lead to many disadvantages like bulky and heavy engine components, high friction, low rated engine speed, and high NO_x and soot emission levels. On account of these conflicting requirements, optimization of the compression ratio is one of the major challenges often faced by designers, Gardner and Henein (1988). In order to achieve maximum benefit at all engine operating conditions, variable compression ratio operation in diesel engines has been explored. However, the complexity of this method makes it impractical for production engines.

At present, considerable research is being carried out in order to achieve very low NO_x and soot emissions. In diesel engines, reducing the compression ratio is one of the promising ways to meet these stringent demands. While reducing the compression ratio, the in-cylinder gas temperature decreases, which in turn reduces the thermal nitric oxide (NO) formation. It also increases the ignition delay, hence leading to better fuel-air mixing and thus more fuel burns in the premixed phase of combustion which leads to low smoke. Beatrice et al. (2008) and MacMillan et al. (2012) showed that soot/NO_x trade-off was improved in low compression ratio diesel engines. On the other hand, due to incomplete combustion, a significant increase in CO, HC emission, and fuel consumption was also observed. The injection timing can be advanced in a low compression ratio engine, because of

M. Viveganantth (✉) • K.A. Kanna • A. Ramesh
Mechanical Engineering, Indian Institute of Technology Madras, Chennai 600036, India
e-mail: viveganantth@gmail.com

© Springer International Publishing AG, part of Springer Nature 2018

F. Aloui, I. Dincer (eds.), *Exergy for A Better Environment and Improved Sustainability 2*, Green Energy and Technology,
https://doi.org/10.1007/978-3-319-62575-1_18

its low peak cylinder pressure when compared to the conventional engines. Hence, the drop in thermal efficiency in a low compression ratio engine can be addressed. Cursente et al. (2008) reported a 12% increase in brake power at 4000 rpm by changing the compression ratio from 18:1 to 14:1, because of advanced fuel injection timing in which the combustion center occurred close to TDC.

Another major issue in operating a low compression ratio diesel engine at high loads is combustion noise. At high loads the drop in cylinder air temperature during fuel evaporation was observed to be considerable, and it increased the ignition delay period which led to high combustion rates. Suh (2011) showed that for the same peak pressure, the heat release rate could be reduced by about 47% with two pilot injections, when compared to the single injection at a compression ratio of 15.3:1.

Though researchers are trying to lower compression ratios to about 14:1, poor cold starting ability and warm-up stability are issues that are to be solved. Diesel engine cold start problems include long cranking time, combustion instabilities, and high emissions. Figure 1 shows the various parameters that can affect the starting of a diesel engine. One of the main challenges in cold starting is to understand the various thermodynamic processes during engine cranking. Liu et al. (2003) used a thermodynamic simulation model to study the key parameters that affect the cranking time and combustion instability during idling. They found that accumulated fuel in the combustion chamber during misfiring cycles has a major impact on engine cold starting. Further, cranking speed should be at an optimum level for effective cold starting, because lower speed causes high heat transfer and blowby losses, whereas time available for evaporation is reduced in case of higher cranking speeds.

Henein et al. (1992) and Han et al. (2001) investigated combustion instabilities during cold starting and found that misfiring is not random but is repeatable. The engine may often skip one or two cycles during starting because the vaporized fuel quantity is not sufficient, due to the slow evaporation rate and the net energy produced from combustion in one cycle not being capable of overcoming the frictional/inertial losses.

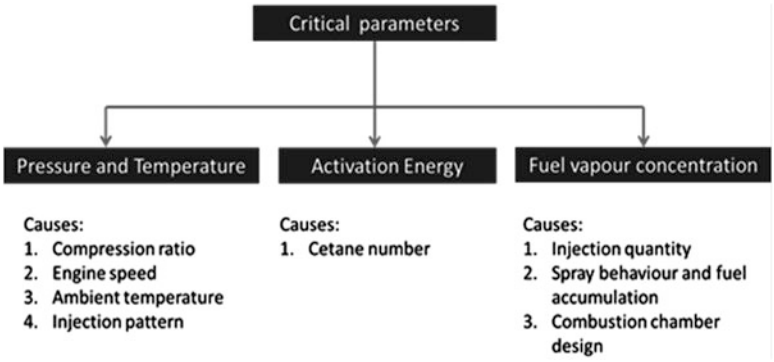

Fig. 1 List of critical parameters affecting the engine starting

Zahdeh (1990) found that the peak compression temperature was decreased by 254 °C, when the ambient temperature was reduced from +20 to −20 °C. So, cold starting becomes much more challenging in a low compression ratio diesel engine at very low ambient conditions. Pacaud et al. (2008), improved the cold starting ability of a low compression ratio diesel engine with the aid of a glow plug and by the use of multiple pulse fuel injection techniques. They found that the pilot injection of diesel promoted the cold flame combustion reaction which in turn reduces the ignition delay. However, the pre-glowing duration (time required for the glow plug tip to reach 800 °C) will increase drastically at low ambient temperatures and, hence, leads to long cranking time. In order to improve warm-up stability, additional methods to trap hot exhaust gases were needed. Peng et al. (2008) found that recirculating fuel-rich exhaust gases back into the cylinder through the intake manifold reduced ignition delay and improved combustion stability. Added advantage of recirculating exhaust gases is the reduction of HC emission (white smoke) during engine warm-up.

In order to implement suitable cold starting strategies, a proper understanding of the transient behavior of an engine during starting is essential. Thus, this work is aimed at understanding the advantages in performance and emissions and also the challenges in cold starting a low compression ratio diesel engine.

Nomenclature

CR	Compression ratio (−)
NO	Nitric oxide (ppm)
HC	Hydrocarbon (ppm)
CO	Carbon monoxide (% volume)
BMEP	Brake mean effective pressure (bar)
IMEP	Indicated mean effective pressure (bar)
TDC	Top dead center (TDC)
degCA	Degree crank angle (degree)
P	Cylinder pressure (bar)
V	Displacement volume (m^3)
n	Polytropic constant (−)
Q	Heat release rate (J/degCA)
SOI	Start of injection

2 Experimental Facility

The schematic arrangement of the experimental setup is shown in Fig. 2. A 0.55 L single cylinder diesel engine was used for this experimental study. Detailed specifications of the engine are provided in Table 1. The geometric compression ratio was modified from 16.5:1 (as in the production engine) to 15:1 and 14:1 progressively by increasing the volume of the piston bowl and also maintaining its shape similar to the original as shown in Fig. 3. Hereafter, these compression ratios will be referred to as CR16.5, CR15, and CR14, respectively. The engine was coupled to an

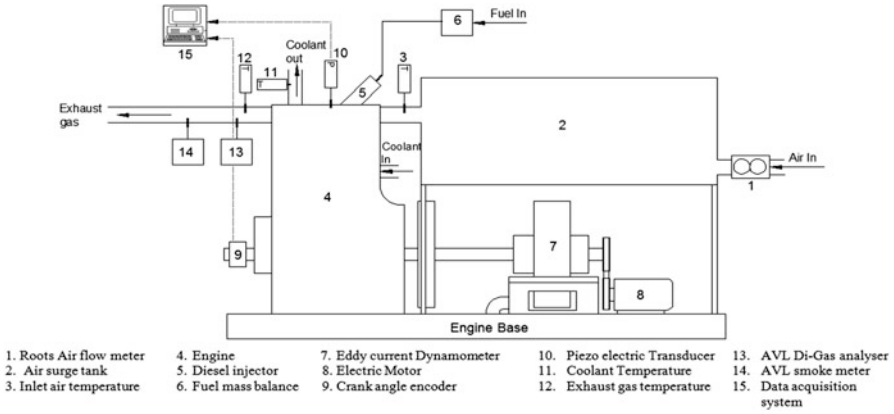

Fig. 2 Schematic layout for the single cylinder diesel engine experimental setup

Table 1 Engine specifications

Engine type	Single cylinder, water cooled, diesel engine
Bore × stroke	80 × 110 mm
Displacement volume	553 CC
Compression ratio	16.5, 15 and 14
Connecting rod length	231 mm
Max. torque and power	23.5 Nm at 1500 rpm 3.7 kW at 1500 rpm
Fuel injection system	Mechanical (NOP = 220 bar)

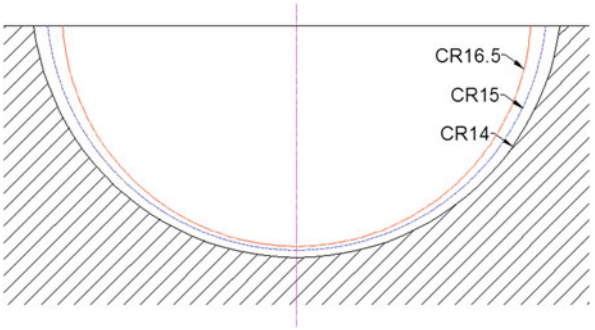

Fig. 3 Piston bowl profile for three compression ratio configuration

eddy current dynamometer for loading and to maintain its speed. The airflow rate to the engine was measured using a positive displacement-type airflow meter (make, Dresser, model, Roots Series B3). Fuel consumed by the engine was measured directly on the mass basis. Exhaust gas emissions (HC, CO, and NO) were measured using a NDIR-based (AVL Di-gas 444) portable analyzer, while an AVL 415S smoke meter was used for smoke measurements. K-type thermocouples were

used to measure the intake air and exhaust gas temperatures. A resistance temperature detector was used to measure the outlet temperature of the coolant.

In-cylinder pressure was measured using a flush-mounted piezoelectric pressure transducer (make, Kistler, model, 6043A60) along with a charge amplifier. An optical encoder was used to determine the position of the crankshaft. A high-speed data acquisition system (NI data acquisition card 6070E) with in-house developed software was used to record the in-cylinder pressure on the crank angle basis. An average of 100 consecutive cycles of cylinder pressure data was used for the calculation of heat release rate. The heat release rate was determined through a first law analysis of the cylinder pressure data as given below:

$$\frac{dQ_n}{d\theta} = \frac{n}{n-1} P \frac{dV}{d\theta} + \frac{1}{n-1} V \frac{dP}{d\theta} \tag{1}$$

Engine was maintained in the required ambient temperature through cold air and coolant conditioning systems. Engine cooling was achieved by circulating chilled water in to the engine coolant jacket. Cold air was supplied through a refrigeration system mounted on the engine intake. Intake air temperature was controlled by adjusting the refrigerant temperature in the evaporator coil of the air conditioner. The engine was also equipped with a starter motor and a 12 V cranker (rectifier which converts 220 V AC to 12 V DC) for starting. To maintain constant cranking condition and to ensure repeatability during starting, the cranker was used instead of a battery. Another in-house developed data acquisition software was used for acquiring the instantaneous cylinder pressure and engine speed data of first 100 cycles at 1° intervals during engine starting. Starting was considered to be successful if the engine fired and accelerated to the idle speed. As mentioned earlier, engine cranking time will vary for different compression ratios and different ambient temperatures, so it was necessary to control the starter motor in order to disengage it once the engine operation became stable. A control system was developed using a microcontroller for this application. This system measures the engine speed and disengages the starter motor when it crosses the set threshold; at this condition it was considered that the engine attains stability and has started accelerating steadily toward the idling speed. The start ability experiments were performed in the following order: First, the data acquisition was started; then it triggers the starter motor control system to crank the engine; this control system disengages the starter motor if the engine crosses the threshold speed of 700 rpm.

3 Results and Discussions

Experiments were initilally conducted at different compression ratios under different constant injection timings, while the load (brake mean effective pressure – BMEP) was varied. Parameters like brake thermal efficiency, cylinder pressure, heat release rate, and emissions were obtained under steady operating conditions. These are reported and discussed to evaluate the influence of compression ratio.

Subsequently experiments were conducted to evaluate the startability under different ambient temperatures that were simulated as explained earlier.

3.1 NO and Smoke Emissions

Figure 4 indicates the variation of NO emissions under different BMEPs at three compression ratios with a static injection timing of 23°bTDC. The nitric oxide (NO) emission decreased with a reduction in the compression ratio. This was mainly due to the low peak in-cylinder temperatures reached after combustion which were influenced by the lower charge temperatures at the end of compression stroke with reduced compression ratios. At BMEPs lower than 3 bar, reduction in NO levels was significant with respect to reduction in compression ratios. However, at higher BMEPs, NO levels were higher in case of CR14 than CR15 due to the higher rate of combustion. This is explained in detail later with heat release rate data. Figure 5 shows that smoke levels get reduced with a reduction in the

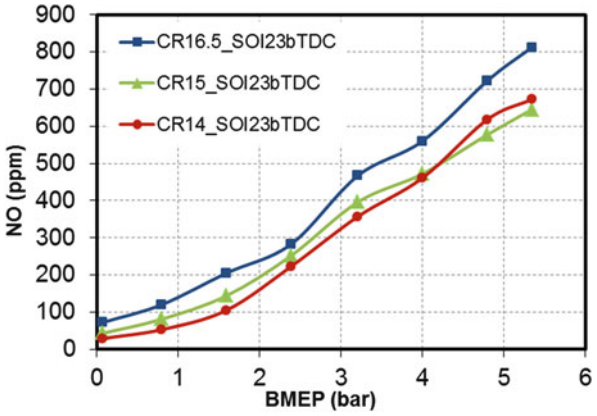

Fig. 4 Variation of nitric oxide emissions with load

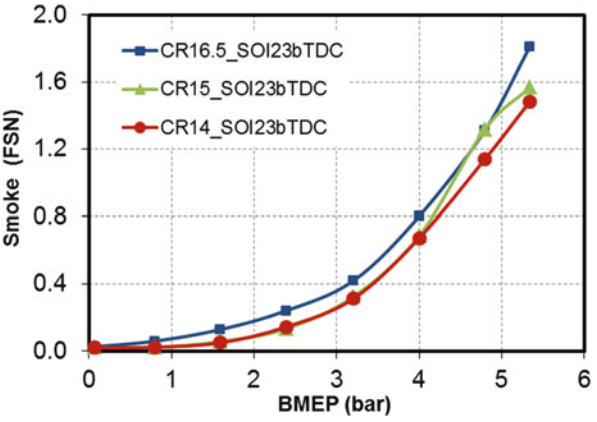

Fig. 5 Variation of smoke emissions with load

compression ratio. This is due to increase in the premixed phase of diesel combustion, i.e., with a reduction in the compression ratio, the ignition delay is longer and majority of injected diesel is burnt in the premixed combustion phase. The higher ignition delay in the case of low compression ratios thus leads to improved fuel-air mixing. However, the lower charge temperatures at low compression ratios will also affect fuel vaporization and mixing under these conditions.

3.2 Combustion Characteristics

Brake thermal efficiencies at the three compression ratios were almost similar as shown in Fig. 6. At higher BMEPs (85% and 100% load), a marginal drop in efficiency of about 1% was observed with CR14. Figure 7 shows the variation in peak cylinder pressure with load for various compression ratios. It was observed that for same BMEP the peak cylinder pressure in low compression ratio engines is

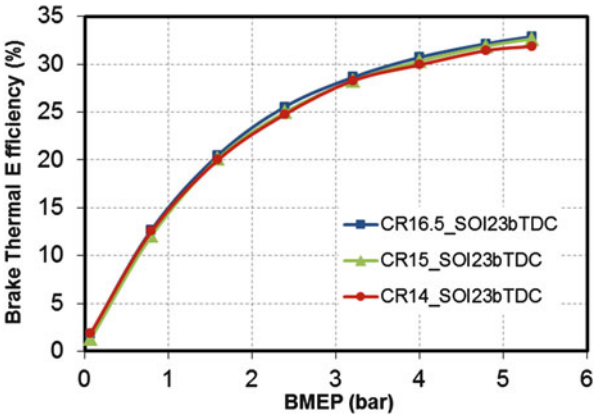

Fig. 6 Variation of brake thermal efficiency with load

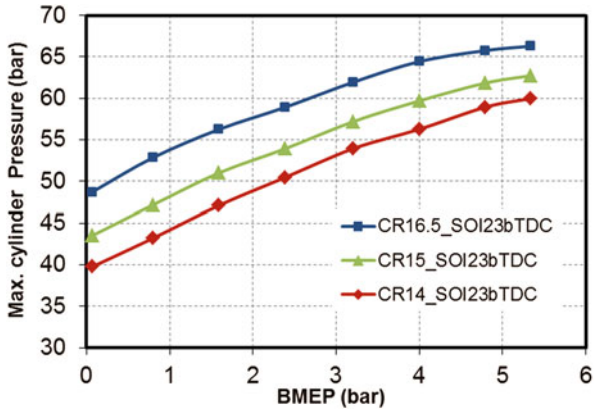

Fig. 7 Variation of peak cylinder pressure with load

reduced. This reduced in-cylinder pressure leaves scope for improving the brake thermal efficiency by advancing the fuel injection timing and also by reducing engine friction through reduction in the size and weight of other engine components.

The variation of heat release rate at fixed BMEPs of 5.3 bar and 2.4 bar under a constant static injection timing of 23°bTDC is depicted in Figs. 8 and 9. It is observed that combustion gets retarded as the compression ratio is reduced. This is because of the low cylinder pressure and temperature during the compression stroke. At high BMEPs (>4 bar), the combustion rate is high in CR15 and CR14 because of the high ignition delay caused due to the drop in cylinder temperature during fuel evaporation. This leads to high local temperatures inside the cylinder during combustion which in turn results in high NO emissions and high combustion noise. At low BMEPs (refer to Fig. 9), the start of combustion gets retarded

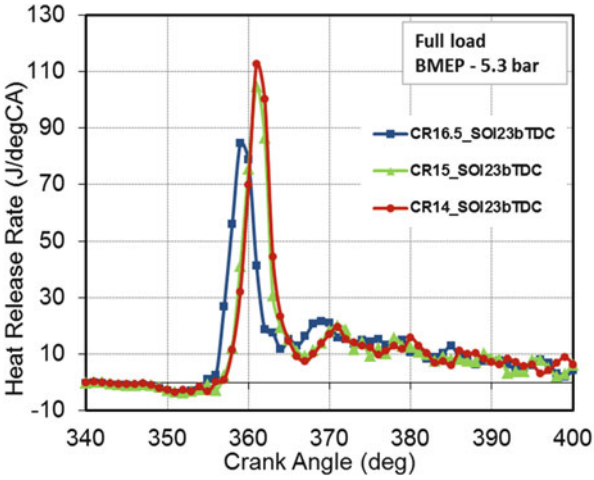

Fig. 8 Effect of reducing compression ratio on heat release rate (HRR) at 5.3 bar BMEP

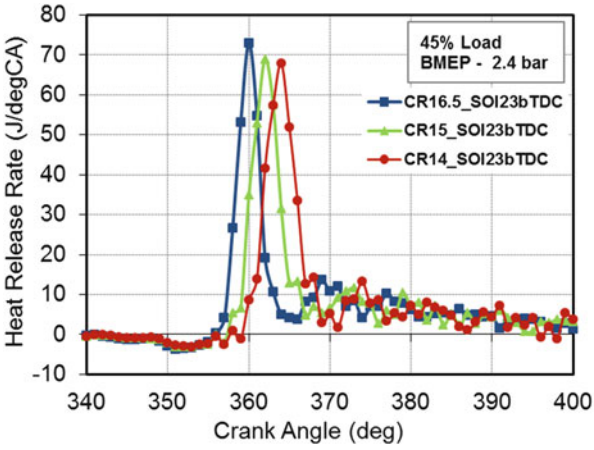

Fig. 9 Effect of reducing compression ratio on heat release rate at 2.4 bar BMEP

(ignition delay is increased) in CR14 and CR15 because of low in-cylinder pressure and temperature. However, the peak heat release rate is lower at lower compression ratios because of the low temperatures in the cylinder that affect mixture preparation during the ignition delay period. This leads to low NO and smoke but affects effective expansion of the combusted gases.

3.3 Cold Starting

The effect of lowering the ambient temperature on engine startability was evaluated in subsequent experiments. Startability of the engine at two compression ratios, namely, CR14 and CR16.5, was evaluated at 10 °C, 15 °C, 20 °C, and 28 °C. Figures 10 and 11 show the instantaneous engine speed and cylinder pressure plots for the first 30 cycles during engine cranking and starting. At the highest intake temperature of 28 °C, there was no difference in startability between the two compression ratios as seen in Fig. 10. Combustion occurred right from the first cycle which is inferred from the cylinder pressure plot. The engine started accelerating right from the first cycle and reached the governor-controlled idle speed after 25 cycles. The initial peak pressures were higher with CR16.5 as compared to CR14. Cylinder pressure plot shown in Fig. 10 is at the starting condition.During starting, the fuel injection pump of this engine injects more fuel than at full load. Hence, this leads to high cylinder pressures (Pmax) during starting.

At the intake temperature of 10 °C (Fig. 11), the engine with compression ratio of 16.5 (CR16.5) fired in all cycles from the beginning, and this shows that the engine startability did not deteriorate while reducing the ambient temperature from 28 to 10 °C. However, in the case of CR14, the engine misfired in the first 6 cycles, and the first firing occurred only at the seventh cycle because of the fuel accumulated during the previous cycles.

Combustion instabilities were there till the first 20 cycles. The engine fired in every other cycle or every third cycle till it attained stability. After the twentieth cycle, the engine was stable and accelerated steadily because of the reduced heat transfer and blowby losses at high engine speeds and slightly warm engine walls. For CR14 at ambient temperature of 10 °C, the engine took 36 cycles to reach the governor-controlled idle speed of 1500 rpm.

In order to determine whether the misfiring cycles that occurred in between the firing cycles are due to irregularities in injection or actual lack of combustion, heat release rates were obtained for the fired and misfired cycles and also for a cycle where the fuel injection was completely absent. This is seen in Fig. 12. We see that in the fired cycle, the heat release rate (HRR) shows a sharp positive peak. It also shows a negative portion after fuel injection as indicated in Fig. 12. This is due to vaporization of the fuel accumulated before ignition. This negative portion is not seen in the cycle where fuel injection is not present. In the misfiring cycle, we see that the negative HRR portion is present, but the positive HRR portion is absent indicating that fuel was injected but combustion was not initiated in the misfired

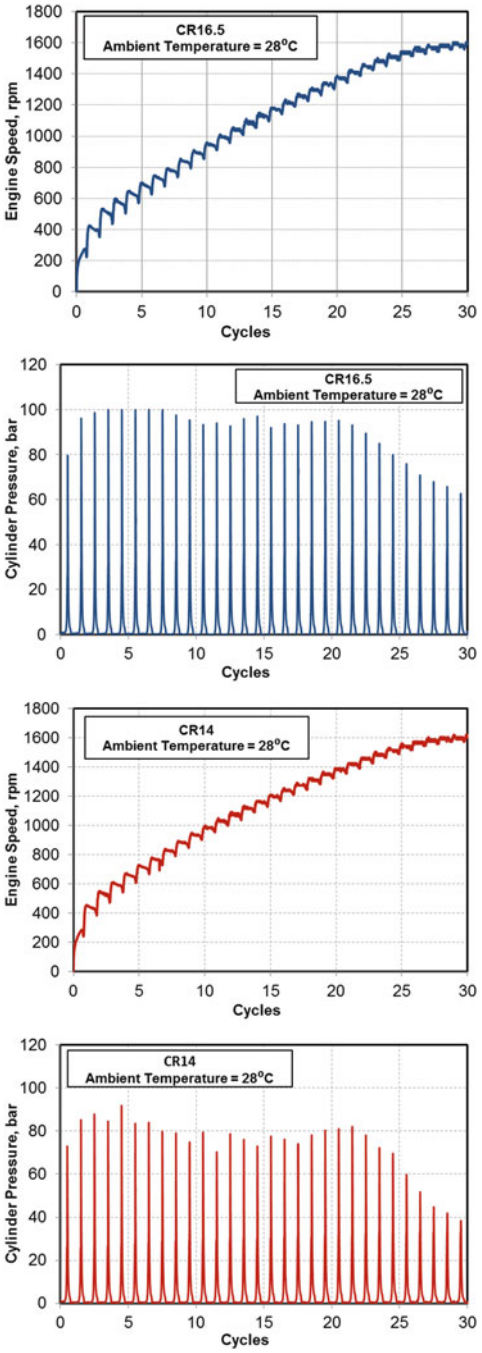

Fig. 10 Engine startability trials at 28 °C ambient temperature

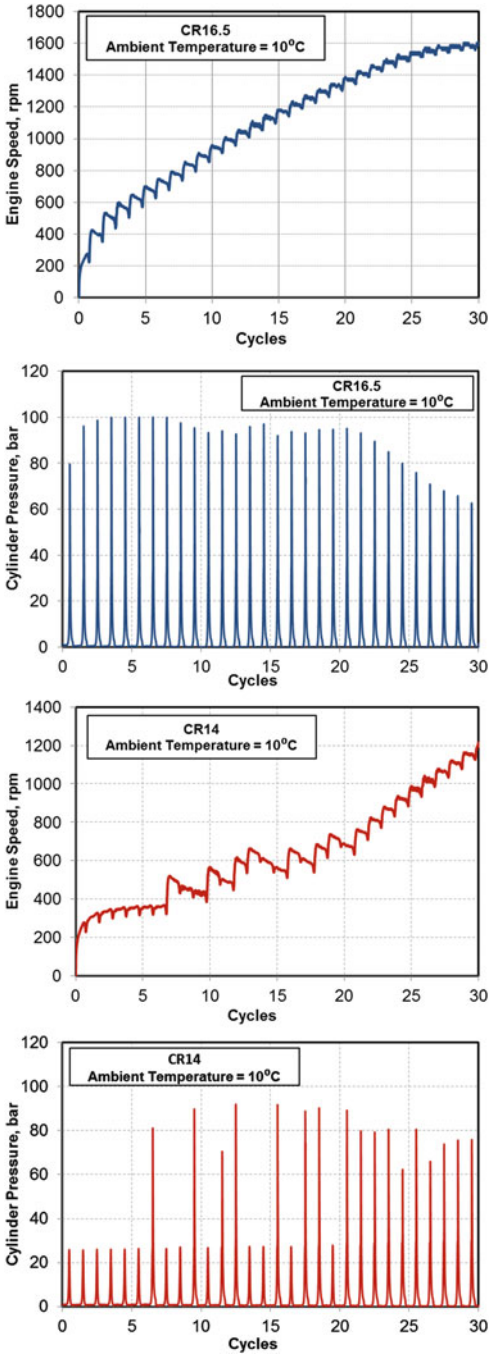

Fig. 11 Engine startability trials at 10 °C ambient temperature

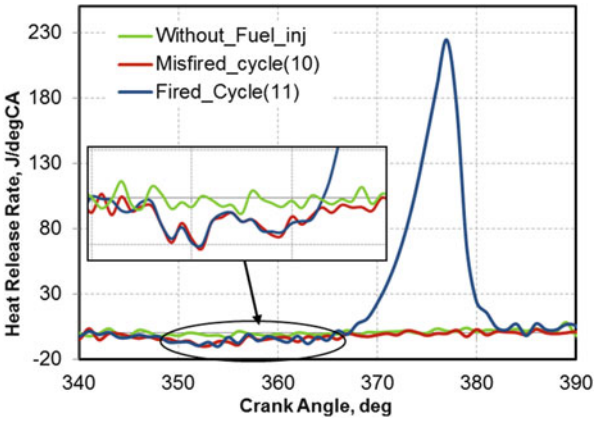

Fig. 12 Rate of heat release plot during cranking with CR14 at 10 °C

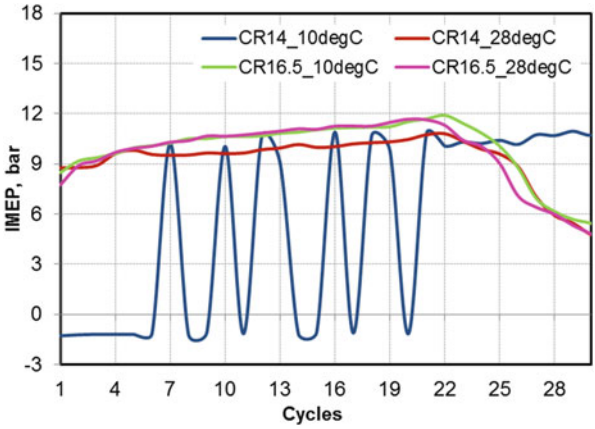

Fig. 13 Indicated mean effective pressure (IMEP) plot during cranking at different ambient temperatures

cycle. Hence, some of the cycles even after a firing cycle misfire under cold start conditions in the case of CR 14. This could be because during cold start the concentration of fuel vapor is insufficient for ignition. Hence, repeated injection of fuel in consecutive cycles that misfire raises the vapor concentration and aids ignition in a following cycle. It is seen that the sequence of firing and misfiring cycles is not entirely random. Such observations have also been reported in literature [Henein (1992)]. It may also be noted that the heat release shows only premixed combustion. This also indicates that only the fuel that is vaporized participates in combustion during the initial cycles of cold starting.

The severe IMEP fluctuations seen at starting in CR14 at 10 °C are indicated in Fig. 13.

Figure 14 shows how the starting delay (number of cycles to reach idling speed) of the engine increases with reduced ambient temperatures. It is evident that even below ambient temperatures of 15 °C, reduction in the compression ratio significantly affects startability. This will also have a significant influence on emissions during starting.

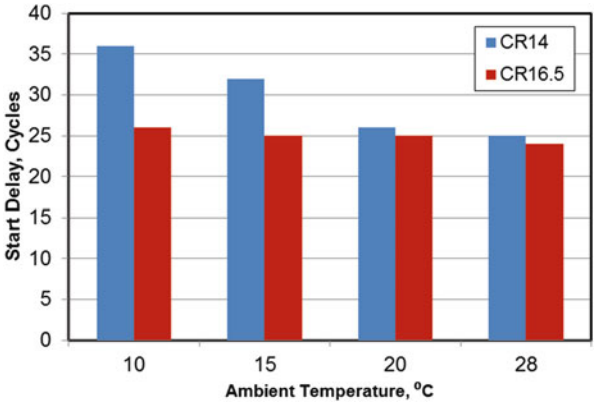

Fig. 14 Start delay for CR16.5 and CR14 at different ambient temperatures

4 Conclusions

Based on the experimental investigations on a direct injection diesel engine with three different compression ratios (CR14, CR15, and CR16.5), the following conclusions were made.

(a) Reducing the compression ratio in the diesel engine reduces the nitric oxide (NO) emissions at all load conditions by reducing the peak in-cylinder temperature. Particularly significant reductions are seen at lower loads (BMEP < 3 bar) where the combustion rate is minimum. At a BMEP of 1.6 bar, the reduction in NO with CR14 and CR15 was 49% and 30%, respectively, as compared to CR16.5. Smoke at all load conditions is also reduced at low compression ratios due to longer ignition delay. At a BMEP of 1.6 bar, the reduction in smoke with CR14 and CR15 was 62% and 55%, respectively, as compared to CR16.5.
(b) Brake thermal efficiency was not significantly affected with reduction in compression ratio.
(c) Starting delay of the engine with CR14 was increased at reduced ambient temperatures, because of misfiring (combustion failure) during the intial cycles when the engine is cold.
(d) During cold starting only the fuel that is vaporized participates in combustion and the remaining gets accumulated in the bowl. Repeated injection of fuel in consecutive misfiring cycles raises the fuel vapor concentration and aids combustion in the following cycle.

References

Beatrice, C., Avolio, G., Del Giacomo, N., Guido, C.: Compression Ratio Influence on the Performance of an Advanced Single-Cylinder Diesel Engine Operating in Conventional and Low Temperature Combustion Mode, SAE Technical Paper 2008-01-1678 (2008)

Cursente, V., Pacaud, P., Gatellier, B.: Reduction of the Compression Ratio on a HSDI Diesel Engine: Combustion Design Evolution for Compliance the Future Emission Standards, SAE Technical Paper 2008-01-0839 (2008)

Gardner, T., Henein, N.: Compression Ratio Optimization in a Direct-Injection Diesel Engine: A Mathematical Model, SAE Technical Paper 880427 (1988)

Henein, N.A., Zahdeh, A.R., and Yassine, M.K., Bryzik, W.: Diesel Engine Cold Starting: Combustion Instability, SAE Technical Paper 920005 (1992)

Liu, H., Henein, N.A., Bryzik W.: Simulation of Diesel Engines Cold Start, SAE International, 2003-01-0080 (2003)

MacMillan, D.J., Law, T., Shayler, P.J., Pegg, I.: The Influence of Compression Ratio on Indicated Emissions and Fuel Economy Responses to Input Variables for a D.I Diesel Engine CombustionSystem, SAE Technical Paper 2012-01-0697 (2012)

Pacaud, P., Perrin H., Laget O.: Cold Start on Diesel Engine: Is Low Compression Ratio Compatible with Cold Start Requirements? SAE Technical Paper 2008-01-1310 (2008)

Peng, H., Cui, Y., Shi, L., Deng, K.: Improve Combustion during Cold-Start of DI Diesel Engine by EGR under normal ambient temperature, SAE 2008-01-1084 (2008)

Suh, H.K.: Investigations of multiple injection strategies for the improvement of combustion and exhaust emissions characteristics in a low compressionratio (CR) engine. Appl. Energy. **88**, 5013–5019 (2011)

Zahdeh, A., Henein, N., Bryzik, W.: Diesel Cold Starting: Actual Cycle Analysis Under Border-Line Conditions, SAE Technical Paper 900441 (1990)

Zhiping Han, Naeim Henein, Bogdan Nitu and Walter Bryzik.: Diesel engine cold start combustion instability and control strategy. SAE 2001-01-1237 (2001)

Control of Cement Slurry Formulation for an Oil Well in a Critical Geological Layer

Soumia Bechar and Djamal Zerrouki

1 Introduction

Cementing is an essential operation during construction of an oil or gas well (Choolaei et al. 2012). The quality of cement in a casing plays a vital role during drilling and has a serious impact on secondary cementing, stimulation operation, and protection of casing against corrosion (Backe et al. 1997; Ershadi et al. 2011). The oil and gas industry has worked for a long time to respond to the challenge of ensuring the protection of the environment. However, the exploitation of oil and gas reserves has not always been without secondary ecological effects. However, in all cases, environmental impacts can be avoided, minimized, or mitigated (Ershadi et al. 2011). During construction of an oil or gas well, oil well cementing is the process of placing cement slurry in the annulus space between the well casing and the geological formations surrounding the well bore, from the injection horizon to the surface. This procedure is used for providing zonal isolation of different subterranean formations in order to prevent the exchange of gas or fluids among different geological formations, as well as for protecting oil-producing zones from corrosion and collapse. Oil well cementing is less tolerant of errors than conventional cementing works, and long-term performance of the oil well cement slurries is of great concern (Le Saout et al. 2006). In this way, cementing of oil wells requires new materials that provide long-term stability in critical conditions.

S. Bechar (✉) • D. Zerrouki
Ouargla University, Applied Science, Process Engineering, Dynamic Interactions and Reactivity of Systems Laboratory, Ouargla 30000, Algeria
e-mail: soumiabechar1@gmail.com

© Springer International Publishing AG, part of Springer Nature 2018

F. Aloui, I. Dincer (eds.), *Exergy for A Better Environment and Improved Sustainability 2*, Green Energy and Technology,
https://doi.org/10.1007/978-3-319-62575-1_19

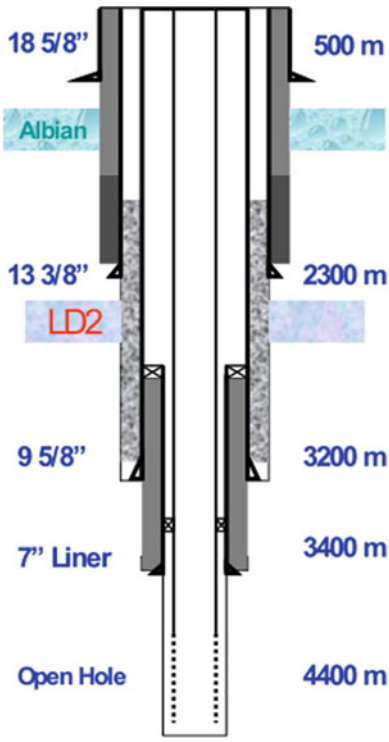

Fig. 1 A typical well profile in the Hassi Messaoud field

The protective characteristics of oil well cements can be controlled by the addition of a specific additive (Bensted 1996). The main challenge in the Hassi Hessaoud field is zonal isolation for the Lias Dolomitic (LD2), called Horizon B. This high pressure zone is located at a depth that varies from 2400 to 2700 m with a thickness of about 30–60 m (Figs. 1, 2, and 3). The zone is characterized by a high pore pressure gradient up to 2.25SG (Bouras et al. 2007). The difficulty is in keeping a hydrostatic column to check pore pressure, but this hydrostatic pressure must be below the pressure of the fracturing formation. Poor quality and bed placing of the cement slurry in the annulus space lead to the need for remedial cementing and will increase the time and cost of the cement job (Nelson 1990). The cost for workover operations on wells in production can easily reach US$40,000 /day; for example, for the MD-174 well, 24 days were spent on repairing casing corrosion, as casing corroded at 2614 m in front of the LD2 formation (Bouras et al. 2007). As provided in the severe downhole severities, the control of formulation properties is crucial for obtaining a good cement bond to protect the casing from corrosive fluids.

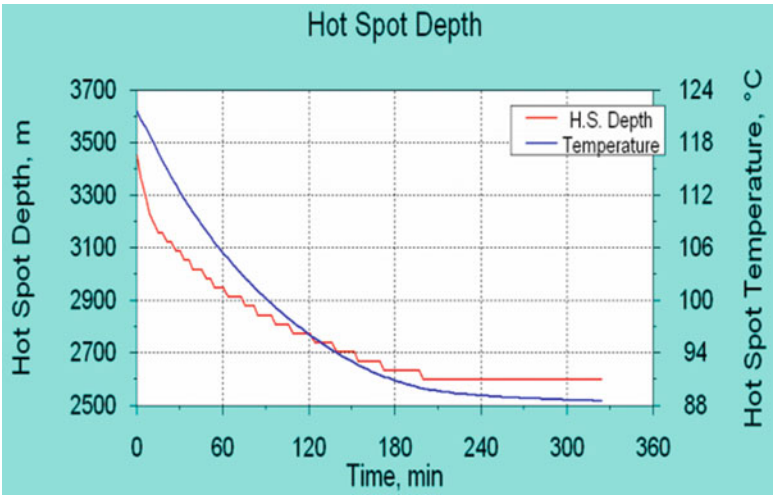

Fig. 2 Bottom hole static temperature (BHST) simulation

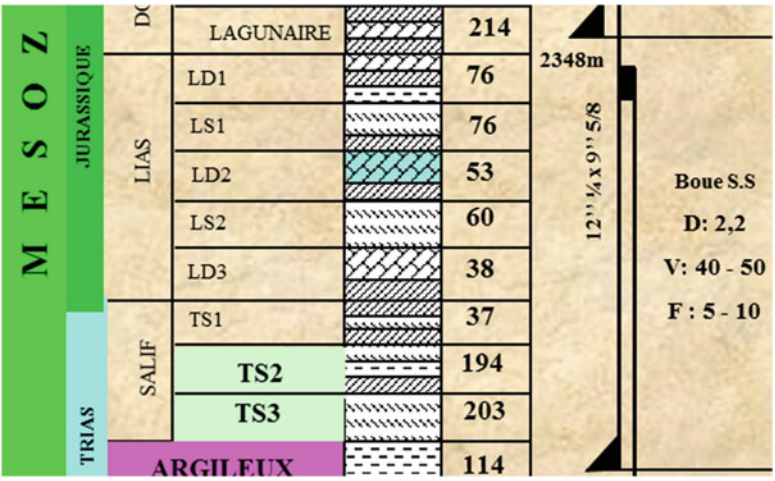

Fig. 3 Lithology example of a typical case (Hassi Messaoud field)

2 Background Information

The collection of temperature data takes account of the recording at the bottom. The bottom hole static temperature (BHST) of this well has been estimated to be 120 °C, and the bottom hole circulating (BHCT) temperature is predicted to be 88 °C. The temperature gradient is 2.73 °C/100 m.

Table 1 Analysis of the water taken from the geological layer Horizon B (LD2)

Ions	Chloride calcic waters
HCO_3^- (g/L)	1.37
Cl^- (g/L)	2520
So_4^{--} (g/L)	0
Ca^{++} (g/L)	1160
Mg^{++} (g/L)	10
Ba^{++} (g/L)	0
Na^+	63.3
K^+ (g/L)	9.24
PH	6
Density à 25 °C	1.28
Depth (m)	2400–2800

The water in the geological formation that causes the dilution of cement slurry during its introduction was sampled and analyzed and the results are shown in Table 1.

3 Experiments

3.1 Reagents

Portland cement is used a lot in oil well cementing operations, and is a very important link in the process of oil well construction (Garnier et al. 2007; Neuville 2008; Shenglai et al. 2014). The cement powder used in this study is class "G" HSR cement according to the American Petroleum Institute (API) standards (API 2002). It was obtained from Dyckerhoff and the phase composition of class G cement is presented in Table 2. The cement powder was blended in dry with silica fume (35 % by weight of cement). The particle size (100-mesh) and crystalline nature of the silica (98 % of SiO_2 or greater), as well as the addition of the mineral pozzolanic admixture can affect the properties of cement slurry both in a fresh and in a hardened state (Lohtia and Joshi 1996; Plassais 2003). It extends the mechanical integrity of the cement over the life of the well and prevents cement strength retrogression, which would otherwise lead to severe well integrity problems in abnormal conditions. We used hematite powder to provide stable rheology values due to the kit's better suspending properties; it increases cement slurry density to maximize well control under high well pressures (Johnston et al. 1992). Sodium chloride (NaCl) 37.2 % by weight of water (bwow) was dissolved to obtain a salt-saturated water for mixing in order to minimize the deference potential of the interstitial solution and the exterior environment to avoid the dissolution of the salt form forming a slurry and thus to avoid a resulting hydrostatic imbalance. Other

Table 2 Composition of class G cement

C3S (wt. %)	53.7
C2S (wt. %)	26.46
C3A (wt. %)	2.8
C4AF (wt. %)	12
SO_3	2.0
MgO	0.7
Free lime	0.4

classic additives such as antifoam agents, dispersants, retarders, anti-gel agents, and fluid loss control are also used in the admixture of cement slurry.

3.2 Material

The cement slurries were prepared in the laboratory according to the API guidelines with the following standard mixing procedures described in API RP 10B-2: First, NaCl was dissolved in water for 15 min, after that an anti-gel agent was added to the water mix with an antifoam agent, dispersant, fluid loss control, retarder, and hematite powder. Thereafter it was transferred into the cup of the warring blender. Then, the cement was added within 15 s to the aqueous solution and mixed using two speeds, 4000 and 1200 RPM (API 2002).

At first the cement slurry was poured into a slurry container for the preconditioning process. After achieving the desired conditions, the slurry was stirred for about 20 min, and then it was immediately poured into a viscometer cup. Throughout this time the slurry was stirred in order to prevent it from remaining static. The first reading was taken 10 s after continuous rotation at the lowest rotating speed. After that, the remaining readings were taken in ascending order, following continuous rotation of 10 s at each speed. After reading each speed, in order to continue the reading process, the speed was immediately shifted to the next considered speed. The rheological measurements were reported (R3, R6, R100, R200, and R300), and at the end gel at 10 s and gel at 10 min were also measured. These tests were carried out according to API specification 10A standard (API 2002) using the Fann 35 device.

3.2.1 Thickening Time

The apparatus for measuring the thickening time consists of a pressurized consistometer, which has a rotating cylindrical slurry container, equipped with a stationary paddle assembly. At first the slurry was loaded into a slurry container and was placed in a pressure vessel. The temperature and pressure of the cement slurry were increased according to the appropriate specification schedule. The thickening

Table 3 Fann 35 data

RMP	
300	92
200	75
100	50
6	22
3	20

time was recorded as the passed time between the first application of temperature and pressure to the pressurized consistometer and the time at which a consistency of 100 Bc was reached (the Bearden unit of consistency (Bc) is the measure of the consistency of a cement slurry). Finally, the maximum consistency between 15 and 30 min of the stirring period was reported (API 2002).

3.2.2 Compressive Strength

By measuring the variation of the speed of an acoustic signal, the ultrasonic cement analyzer provides a continuous method for determining the compressive strength as a function of time (API 2002). See Table 3.

4 Results and Discussion

4.1 Rheological Parameters

The density of the slurry was calculated at 2.24 SG and checked after mixing using the Halliburton densimeter. We were obliged to readjust the concentration of dispersant and anti-gel agent to acquire normative values.

- Viscosity and yield value:
  Vp = (R300) − (R100t) *1.5 (Centipoise)
  Pv = 67.5 Cp
  Yv = lecture 300 t/min−Vp (en lbf/100ft^2)
  Yv = 27.5 lbf/100ft^2
- Gel strength
  10 s: 10 s: 20 (lbf/100 ft^2)
  10 min: 10 min: 50 (lbf/100ft^2)

4.2 Fluid Loss and Free Water

FL: 66 cc/30 min @ 1000 psi
FW: 0% cc

4.3 Thickening Time

The pumpability of the cement slurry is the crucial parameter for concretization of the cementing operation. A multitude of tests have been carried out in order to obtain a suitable thickening time (pumpabilty time), which was at 05 h but it is strongly recommended to have enough thickening time for a safety margin (Fig. 4).

4.4 Compressive Strength

- Ultrasonic cement analyser: The transit time from the slurry is inversely proportional to the compressive strength. This formulation has developed good mechanical resistance (1500 PSI) (Fig. 5).

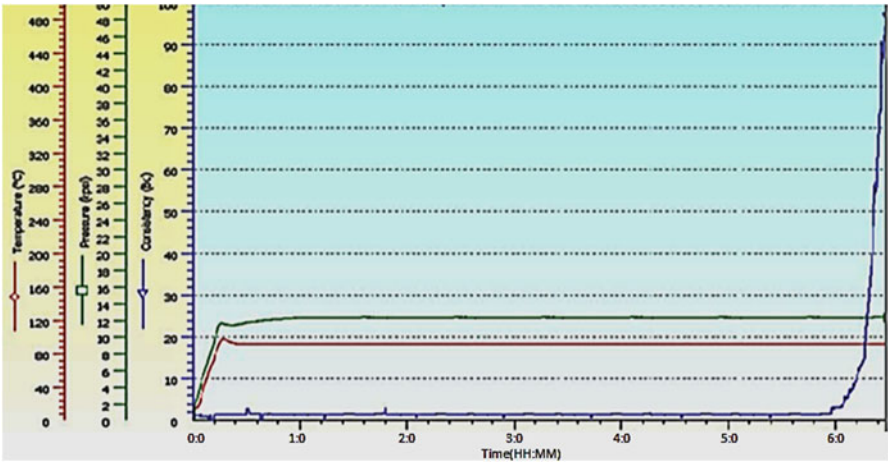

Fig. 4 Variation in consistency according to time

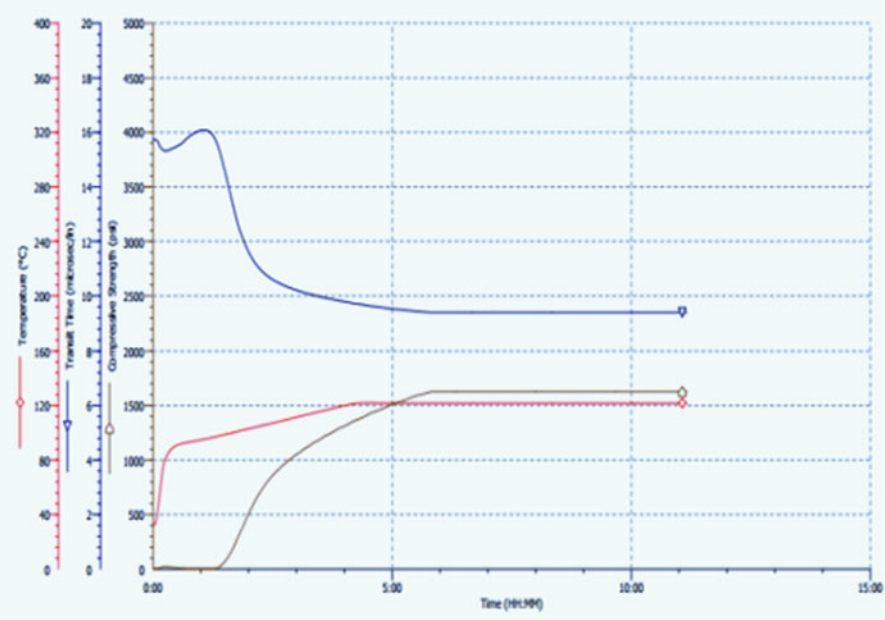

Fig. 5 Compressive strength and transition time (recorded by UCA)

- By Crushing Cube after curing for 36 h in a curing chamber at BSHT (Fig. 6)

Compressive Strength = force/Area
5447/4(inch) = 1361 (Psi)

The hardened cement has developed an adequate compressive strength.

5 Conclusion

The correct introduction of the cement slurry between the drilled hole and the casing in place is important to provide good control of rheological properties. The important in this is the correct use of additives and the precise prediction of pumpability time, which are crucial factors for the success of the cementation job and sustainability of the hardened sheath, as well as the longevity of the well and reliability of production. This paper presents an initiative study for understanding the behavior of weighting cement slurry under several constraints in downhole conditions. Many perspectives are shown in this study to begin to work on improving the sustainability and strength of the cement-hardened face in the complexity of the geology in the Hassi Messaoud field.

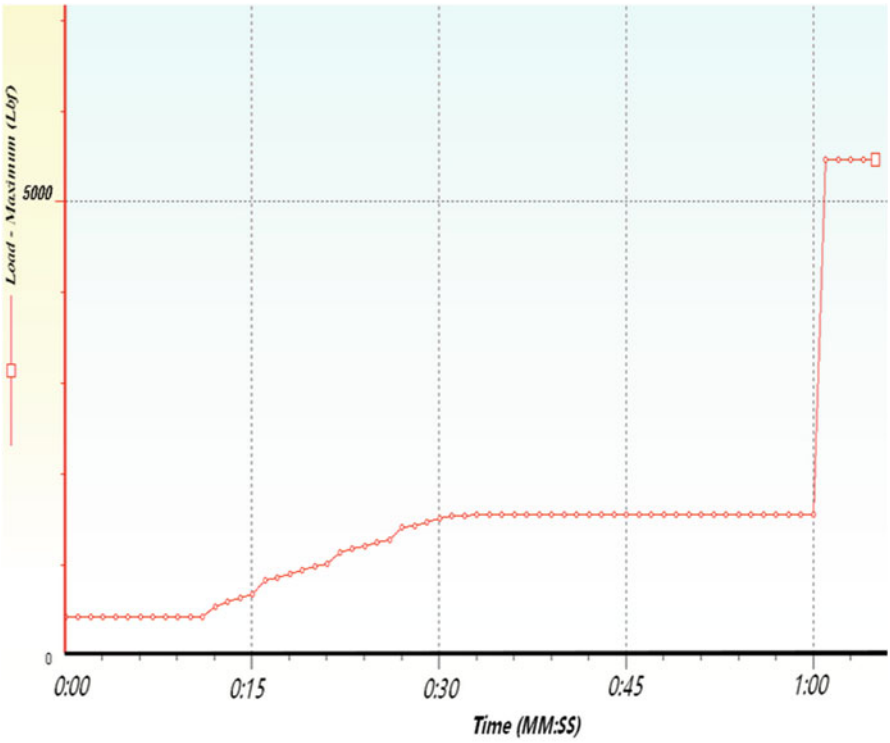

Fig. 6 Chart showing the destructive test of compressive strength

Acknowledgments This research was supported by the Laboratory Dynamic Interactions and Reactivity of Systems, Ouargla University and Bjsp Laboratory Hassi Messaoud.

References

American Petroleum Institute: Recommended Practice for Testing Well Cements, 23rd edn, http://www.api.org/, (2002)

Backe, K.R., Lile, O.B., Lyomove, S.K., Elvebakk, H., Skalle, P.: Characterising curing cement slurries by permeability, tensile strength, and shrinkage. Soc. Pet. Eng. SPE38267, p. 159 (1997)

Bensted, J.: Concrete Admixtures Handbook. Properties, Science, and Technology, 2nd edn. pp. 1077–1111. Noyes publications (1996). Available online 23 Oct 2008

Bouras, H. Sonatrach, Toukam, E., Martin, F.V., Bedel, J.-P.: Successful application of novel cementing technology in Hassi-Messaoud, Algeria SPE/IADC 108249 (2007)

Choolaei, M., Rashidi, A.M., Ardjmand, M., Yadegari, A., Soltanian, H.: The effect of nanosilica on the physical properties of oil well cement. Mater. Sci. Eng. A. **538**, 288–294 (2012)

Ershadi, V., Ebadi, T., Rabani, A.R., Ershadi, L., Soltanian, H.: The effect of nanosilica on cement matrix permeability in oil well to decrease the pollution of receptive environment. Int. J. Environ. Sci. Develop. **2**, 128–132 (2011)

Garnier, A., Frauoulet, B., Saint-Marc, J.: Characterization of cement systems to ensure cement sheath integrity. In: Offshore Technology Conference, Houston (2007)

Guo, S., Bu, Y., Liu, H., Guo, X.: The abnormal phenomenon of class G oil well cement endangering the cementing security in the presence of retarder. Constr. Build. Mater. **54**, 118–122 (2014)

Johnston, N.C., Senese, M.: New approach to high density cement slurries for cementing high-pressure/high-temperature wells. Paper SPE 16011 presented at the European Petroleum Conference, Cannes, 16–18 November 1992

Le Saout, G., Lecolier, E., Rivereau, A., Zanni, H.: Chemical structure of cement aged at normal and elevated temperatures and pressures. Part II. Low permeability class G oil well cement. Cem. Concr. Res. **36**, 428–433 (2006)

Neuville, N.: Etude et modelisation de l'alteration physico-chimique de materiaux de cimentation des puits pétroliers, 25–26 (2008)

Nelson, E.B.: Well Cementing, Chap. 11. In: Rae, P. (ed.) Cement Job Design, pp. 301–335. Schlumberger Educational Services, Houston (1990)

Plassais, A.: Nanoporosité, texture et propriétés mécaniques de pâtes de ciments. (2003)

Paul Lohtia, R., Joshi, R.C.: Concrete Admixtures Handbook. Properties, Science, and Technology, 2nd edn, pp. 657–739. Noyes publications (1996). Available online 23 October 2008

Recovery of Farm Waste After Methanization by Evaporation on Inclined Plate

Hiba Zouaghi, Souad Harmand, and Sadok Ben Jabrallah

1 Introduction

Wastes present problem to the entire population because of the nuisance it causes. In rural communities, it is rather animal waste, which causes a big problem (pollution of soil, rivers, water table, etc.). However, these releases have a product rich in nutrients and fertilizers (Granier and Texier 1993). On this basis, several farmers choose recovery of such wastes by anaerobic digestion. The development of biogas plants not only reduces agricultural emissions by converting biomass but also produces thermal energy. This thermal energy can have other uses.

After anaerobic digestion, it leads to the production of two types of energy. One is related to the production of electricity and the other is reused in methanation process. However, the disadvantage is that the digestate, after anaerobic digestion, causes problems on many levels. It has high water content (up to 97%), particularly pig manure. That is why storage or reuse is required. This product is the material remaining residue at the end of the process. It has excellent agronomic value and can be used as a fertilizer (Latimier et al., 1996; Levasseur 1998).

The field of waste recovery appeared since a long time, especially in regard to farm waste, because of organic matter and fertilizers. Drying presents an important process for the management of farm waste, as it reduces the mass and volume of the

H. Zouaghi (✉)
National Engineering School of Monastir, Avenue Ibn El Jazzar, Monastir 5019, Tunisia
e-mail: hibazouaghi@yahoo.fr

S. Harmand
University of Lille Nord, UVHC, LAMIH UMR CNRS 8201, Mont Houy, Valenciennes Cedex 09, 59300, France

S.B. Jabrallah
Sciences Faculty of Bizerte, Zarzouna, Bizerte 7021, Tunisia

© Springer International Publishing AG, part of Springer Nature 2018

F. Aloui, I. Dincer (eds.), *Exergy for A Better Environment and Improved Sustainability 2*, Green Energy and Technology,
https://doi.org/10.1007/978-3-319-62575-1_20

product and therefore cost of storage, workforce, and transportation. It is a method based on evaporation. This process, which is a change of vapor–liquid phase, can be achieved by exposure to air. But, it can be intensified by the use of solar energy. This is one of the most practical methods of preserving the quality of agricultural products and of recycling waste and effluents. Studies on drying after anaerobic digestate are rare. However, other waste streams drying exist.

Drying process can reduce the weight and volume of the product and therefore cost of storage, handling, and transportation. Solar drying plant of sewage sludge treatment was built as a tunnel-type greenhouse with a ceiling height of 2.5 m in Turkey (Salihoglu et al., 2006). It has been completely covered by two walls, with a thickness of 10 mm of transparent polycarbonate with light transmitting sheet of 80%. Solar dryer was constructed with the principle of increasing the difference between vapor pressure of sludge compared to interior and relative vapor pressure to obtain an effective drying. Lei et al., (2009) developed a greenhouse solar dryer in China for drying sludge from wastewater treatment. The greenhouse is made of glass. Its inner lower surface is painted black in order to increase the absorption of solar radiation. A high stack of 180 cm was placed on top of the greenhouse. Samples of fresh sludge were obtained from wastewater treatment plant located in Shanghai. Before drying, the humidity is 5.16 kg/kg dry and dried at 0.78 kg/kg dry. It was rolled to 25 mm in thickness in a plate made from 0.1 mm steel mesh and a surface area of 0.22 m $\times$ 0.36 m. The drying process lasts 125 h in summer and about 550 h in winter with a nonregular decrease in moisture content (Bennamoun, 2011).

Tannery effluent, ejected into the environment, pollutes terrestrial and aquatic organisms in and around tanneries and evaporates over long periods. Drying may be accomplished by allowing the effluent to flow on an inclined plane solar sensor. While the liquid flows over the collector, it is heated by solar energy that helps increase the evaporation rate. In tannery, water effluent evaporation and recovery of salt is a method that uses solar energy available in abundance (Mani et al., 1993, 1994; Srithar et al., 2003a, 2003b, 2006), driers having sensor solar plates, and a spray system to increase evaporation flow. In the case of plate sensor, effluent flows over the manifold. Therefore, the effluent temperature at the exposure area with air increases, which increases the rate of evaporation.

This work is about drying of pig digestate after undergoing anaerobic digestion and phase separation by centrifugation. The treated effluent has a solid content of 2.3%. In this context, an inclined stainless steel plate, 2 m long, 1 m wide, and inclined by 30°, has been put in place. The device is without a glass cover, and tests were carried out in a laboratory using a 6000-W solar simulator. This device is designed to be placed on barn roofs.

This study is divided into two parts. In the first part, evaporation tests were conducted by varying the inlet temperature of the effluent. The second part focuses on the comparison between the experimental and calculated results by solving equations of heat and mass balances on plate and film.

Nomenclature

Cp	Heat capacity (J/kg.°C)
e	Thickness (mm)
h	Convection coefficient (W/m^2.°C)
I	Radiated flux (W/m^2)
L	Plate length (m)
Lv	Latent heat of vaporization (J/kg)
m	Flow (m^3/s)
Pr	Prandtl number
S	Area (m^2)
T	Temperature (°C)
X	Horizontal axis (m)
Y	Vertical axis (m)
Greek letters	
α	Absorptivity μ: viscosity (*Pa.s*)
ε	Emissivity υ kinematic viscosity (m^2/s)
ζ	Transmissivity σ: Boltzmann constant
λ	Thermal conductivity (W/m.°C)
Superscripts	
*	par unit width
Subscripts	
ev	Evaporated in: initial
ext,out	Outside int: inside
f	Fluid
p	Plate
pair	Between plate and air
pf	Between plate and film

2 Effluent Characteristics

A thermo-physical characterization of the effluent is performed to determine thermal conductivity "λ," heat capacity "Cp," and dynamic viscosity "μ"; the effluent is the liquid phase of pig manure that has already undergone methanation and phase separation by centrifugation.

Analyses were performed on three samples (E_0, E_1, and E_2) having different concentrations. The sample E_0 is the liquid effluent having a concentration of C_0 and a dry matter content of 2.3%. The sample E_1 was prepared by evaporation of E_0 so as to lose one third of its initial volume. As for E_2, evaporated volume is about two thirds of E_0. The characteristics of each sample are shown in Table 1.

The thermal conductivity measurements use a device called FP2C. This is a thermal conductivity meter which is based on hot wire method for measuring the overall thermal conductivity of a material from the evolution of temperature

Table 1 Characteristics of samples to analyze

Sample name	E_0	E_1	E_2
Concentration	C_0	$C_1 = 1.5C_0$	$C_2 = 3C_0$
Density (g/l)	960	900	850

Table 2 Thermal conductivity of samples

Sample	E_0	E_1	E_2	*Water*
$T = 30\ °C$	0.593	0.560	0.598	0598
$T = 60\ °C$	0.700	0.805	0.713	0.651

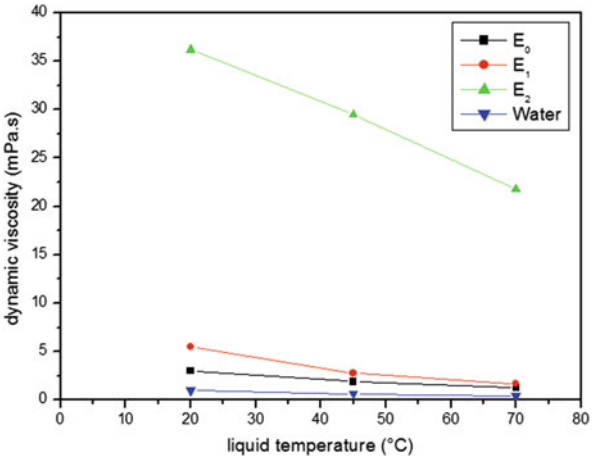

Fig. 1 Graph of dynamic viscosity as function of temperature for shear rate of 100 s^{-1}

measured by a thermocouple placed near a resistive wire. The values of thermal conductivity λ are expressed in W/m.K. We were able to determine thermal conductivities of samples for 30 and 60 ° C (Table 2).

Knowing that the measurement accuracy is 5%, and by referring to Table 2, we see that thermal conductivity does not depend on the concentration of the samples but depends on its temperature. When temperature is about 30 °C, it is 0.584 W/m. K almost equal to that of the water of 0.598 W/m.K. At 60 ° C, $\lambda = 0.739$ W/m.K, whereas $\lambda_{water} = 0.651$ W/m.K (Brau 2006).

Measurements of dynamic viscosity use a rheometer DHR III having TA Instrument mark. The measurements are performed at atmospheric pressure for three temperatures (20 °C, 45 °C, and 70 °C). Each test was performed twice on different samples to assess the reproducibility.

Before starting measurements, each sample is deposited on the bottom plate and spread with a top plate. Excess product is removed with a spatula. The gap is then adjusted and the temperature of the sample conditioned to be measured with an accuracy of 0.5 °C.

The flowing curve of different samples is obtained using a measuring method based on a constant shear rate. The values of shear stress and viscosity are noted as soon as the flow is established. Results are given with an accuracy of 10%, considering geometric imperfections and rheometer accuracy (Fig. 1).

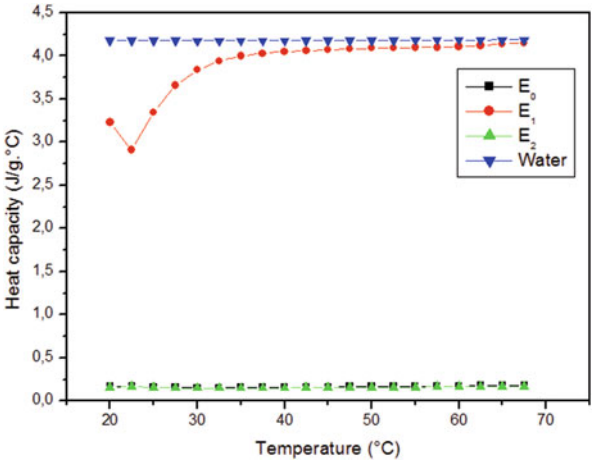

Fig. 2 Heat capacity function of temperature for each sample

The influence of temperature on viscosity of each sample is shown. If temperature increases, viscosity decreases for different shear rates. However, this influence is less depending on sample, well-marked for E_0 and E_1 (especially between 20 °C and 45 °C), and less important for E_2. Viscosity of sample E_0 is the closest to that of water (Brau 2006).

As for the measures of the heat capacity, they are made with the DSC Mettler Toledo DSC1. This device uses the differential scanning calorimetry (DSC), which measures the change in enthalpy in sample using a standard sapphire.

This method uses the following experimental conditions:

- Temperature stabilizing at 20 °C for 5 min, heating from 20 to 70 °C (20 °C/min)
- Stabilization at 70 °C for 5 min
- Continuous wipe neutral gas (nitrogen) to 50 ml/min

The analysis results show that for samples E_0 and E_2, heat capacity is constant over the temperature range of 20–67.5 °C. It is an average of 0.166 J/g.°C for E_0 and 0.16 Jg.°C for E_2. For E_1, the heat capacity varies depending on the temperature. It is from 3.23 J/g.°C to T = 20 °C. It comes down to 2.91 J/g.°C to 22.5 °C and gradually increases. A slight increase is observed for temperatures between 30 and 67.5 °C, and it is on average 4.08 J/g.°C. Results are shown in Fig. 2.

3 Experimental Facility

This process consists of flowing the aqueous liquid effluent on an inclined plate subject to solar flux. The purpose is to produce solid fertilizer from aqueous liquid waste, such as anaerobic digestate. The system should be inexpensive to purchase and should consume as little energy as possible as it is for farmers who make liquid methane.

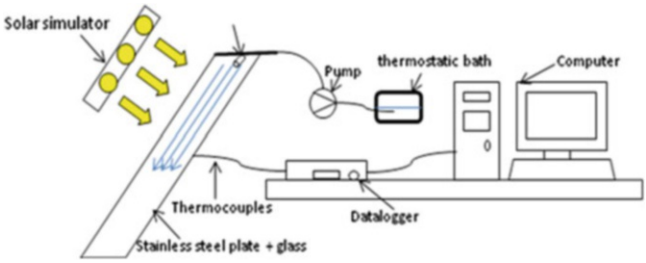

Fig. 3 Experimental installation

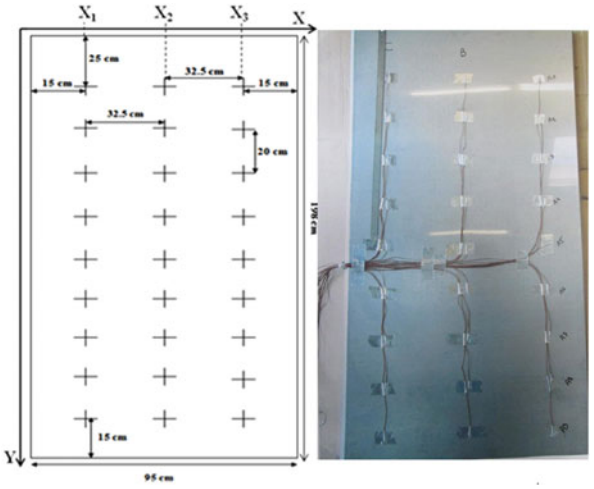

Fig. 4 Layout of thermocouples on the plate

This device is an evaporator composed of a stainless steel plate with a tilt angle of 30°. This plate is 2 m long and 1 m wide. The liquid is injected from the top of the plate with an injection nozzle. Fluid flows along the plate and is recovered in a gutter (Fig. 3).

The steel plate is not covered with glass wool. It is heated using a 6000-W solar simulator. The solar simulator is placed parallel to the evaporator at a distance of 2 m such that the flow will be focused on the upper part of the plate and there will be a flux density similar to that of the sun.

Thermocouples are fixed to the stainless steel plate, as shown in Fig. 4. The thermocouples are positioned into three rows of nine lines. The first line of thermocouples is approximately 20 cm from the top and 15 cm from the edge. Thermocouples are spaced at a distance of 20 cm. K-type thermocouples were used and had a margin of error of ± 2.5 ° C.

Once steady state was achieved, the liquid was injected from the top of the plate using a pump that feeds the dispense manifold. The input flow measurement was performed by weighing the liquid before and after injection for a predetermined time before the start of the solar simulator.

The evaporated flow was measured when the simulator was powered and after stabilization of the temperature. The measurement was achieved by weighing the liquid at the output of the plate over a given time.

4 Numerical Scheme

Before circulating the liquid film, the plate was exposed to radiation simulator and its back was isolated (no heat loss). Based on the sum of the incoming flux that equals the amount of outgoing flux, the heat balance on the plate can then be written:

$$\alpha_p I_0 - \varepsilon_p \sigma \left(T_p^4 - T_{\text{air}}^4 \right) - h_{\text{ext,pa}} \left(T_p - T_{\text{air}} \right) = 0 \tag{1}$$

The natural convection coefficient in steady state is a function of temperature of the plate and that of air (Chen et al. 1986; Huetz et al., 1981):

$$h_{\text{ext,pa}} = 0.225 \left(T_p - T_{\text{air}} \right)^{1/5} \tag{2}$$

Heat balance becomes

$$\alpha_p I_0 - \varepsilon_p \sigma \left(T_p^4 - T_{\text{air}}^4 \right) - 0.225 \left(T_p - T_{\text{air}} \right)^{6/5} = 0 \tag{3}$$

Once the plate temperature is stabilized, the liquid is circulated (Fig. 5).
Heat balance on film can be written:

$$\alpha_p \tau_f I_0 + \varepsilon_p \alpha_p \sigma T_f^4 - \varepsilon_p \sigma T_p^4 - h_{\text{int},pf} \left(T_p - T_f \right) = 0 \tag{4}$$

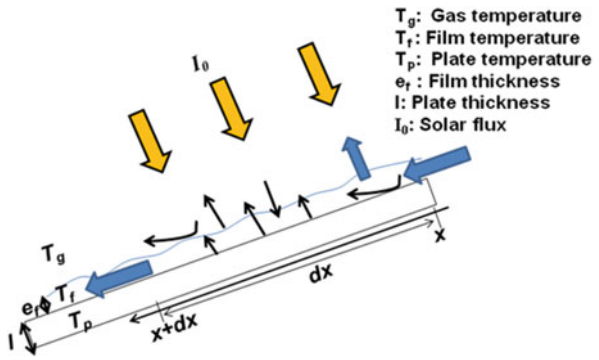

Fig. 5 Balance on liquid film

The forced convection coefficient is a function of the thickness of the water film. In steady state, for an inclined plate of 30°, the forced convection coefficient between the effluent and the plate takes the following form:

$$h_{\text{int},pf} = \left(0.332.\frac{\lambda}{L}\text{Pr}^{1/3}\sqrt{\frac{\dot{m}_{\text{in}}}{\upsilon}}\right)\frac{1}{\sqrt{e_f}} \tag{5}$$

As regards the liquid film, the mass balance is (Bouchekima et al. 2001)

$$\begin{aligned}\dot{m}\,(x)Cp\frac{T_f(x)}{dx} + \alpha_f I_0 + \alpha_f\tau_f\rho_p I_0 + h_{\text{int},pf}\left(T_p(x) - T_f(x)\right) + \alpha_p\varepsilon_p\sigma T_p^4 \\ = \left(\dot{m}\,(x) - \dot{m}\,(x+dx)\right)Lv + h_{\text{int,fair}}\left(T_f - T_{air}\right) + \varepsilon_f\sigma T_f^4 \\ + \dot{m}\,(x+dx)Cp\frac{T_f(x+dx)}{dx}\end{aligned} \tag{6}$$

where $S_p = dx\,.\,L$ and

$$\dot{m}_{ev} = \dot{m}_{\text{in}} - \dot{m}_{\text{out}} \tag{7}$$

The film thickness along the plate is variable and depends on the evaporated flow. Assuming the volume is constant, the film thickness is defined by:

$$e_f(x) = e_f(0).\frac{\dot{m}\,(x)}{m_{\text{in}}} \tag{8}$$

The equations are solved using the programming language MATLAB. Solving equations is performed one by one, as the number of equations is less than the number of unknowns. Once the temperature along the plate is determined from eq. (3), it is known and entered as data in (4). Knowing $T_p(0)$ and $T_f(0)$, we can determine the convection coefficient. Thus, eq. (6) is solved at initial status. Using the equation (7) the film thickness can be derived to estimate x, and the same approach can be followed to solve (4) and (6).

5 Results and Discussions

The cartography of the flux on plate is shown in Fig. 6. We chose the same points as thermocouples (three columns of nine lines). The solar flux is measured by a pyranometer with accuracy ±4–10 μV/W/m^2.

The maximum flux is at $Y = 0.45$ m according to the different positions X_1, X_2, and X_3. It is 805 W/m^2 at $Y = 0.45$ m for position X_2. The minimum flux is 111 W/m^2 for $Y = 1.85$ m for position X_1. The mean flux along the plate is approximately 424 W/m^2.

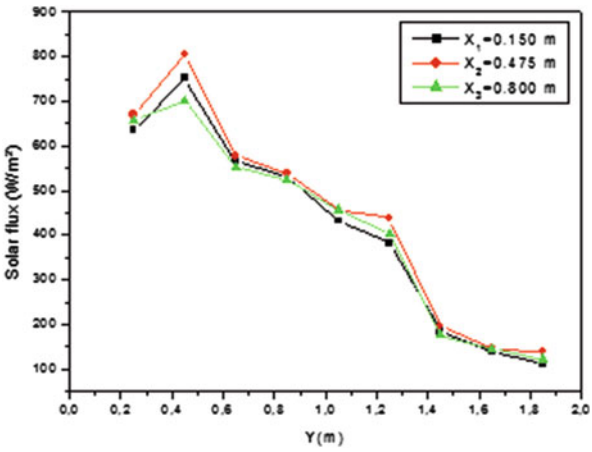

Fig. 6 Cartography of the fluxes on the plate

The shape of this curve can be explained by the position of simulator in which the plate is exposed. Therefore, the flux is not distributed evenly; only the upper part of the plate is exposed to radiation. Simulator radiates this partly explains the fall of the stream up to 116 W/m^2.

By solving eq. (1), we were able to compare the temperature of plate in different experimental and calculated positions. Results are shown in Fig. 7.

Results indicate that following columns X_1, X_2 and X_3, curves representing temperature of plate after have the same shape. It is maximum at $Y = 0.45$ m and decreases along plate. This can be explained by the solar flux which is focused on the top plate when it reaches 805 W/m^2.

From eq. (1), the temperature of plate depends on radiation flux and temperature of the air. The flux is not uniformly distributed on the plate, whose upper portion only is exposed to radiation. This explains the drop in temperature of the plate from $Y = 1.45$ m. This curve has the same shape as the distribution curve of flux along the plate. Then, the temperature of the plate is strongly dependent of radiated flux.

The slight variation of the calculated and measured plate temperature may depend on several factors such as laboratory temperature and temperature of the air between the plate and the simulator.

The liquid flows over the plate. By varying the inlet temperature of the effluent, the temperature of the effluent on the plate varies as shown in Fig. 8, according to eq. (4).

The temperature of the effluent is important on top of the plate, at $Y = 0.45$ m; it starts to decrease until stable at the bottom of the plate. When the liquid inlet temperature is 40 °C, the fluid reaches a maximum temperature of 69 °C at $Y = 0.45$ m and for $X_2 = 0.475$ m. Then its temperature decreases to 38 °C at $Y = 1.85$ m and for X_2.

In each case, the film temperature is maximal for X_2. This can be explained by the distribution of flux, which is maximum at the top of the plate. Moreover, from

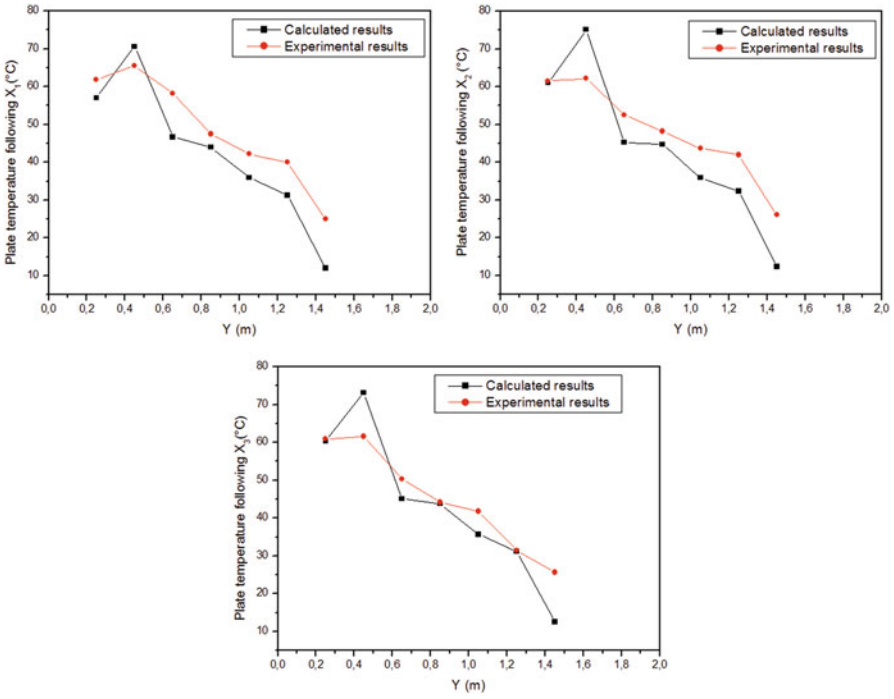

Fig. 7 Evolution of plate temperature

eq. (4), the variation in T_p causes the variation of T_f. This implies that fluid temperature curve along the plate has the same shape as that of the plate. The fall of fluid temperature is due to the low temperature of the plate as it is not exposed to the rays of the simulator.

On the top, the temperature of the plate is higher than that of the fluid. The fluid is heated by the plate. Its temperature increases and becomes close to that of the plate. In the bottom of the plate, the effluent cools because its temperature is higher than the plate temperature.

We compared the inlet and outlet liquid temperatures, results are shown in Fig. 9:

When the liquid is preheated at 20 and 30 °C, its outlet temperature is higher than that of the input. It is respectively 24 and 34 °C experimentally and 23 and 31 °C calculated. Hot liquid having a temperature around 35 °C is cooled on the bottom of the plate. The difference between the plate and fluid temperatures is low. However if the liquid is preheated at 40 and 50 °C, the difference of the temperature between the plate and the fluid is large, which explains the temperature drop of the latter in the outlet. As for the maximum difference between the measured and the calculated results, it is 10%.

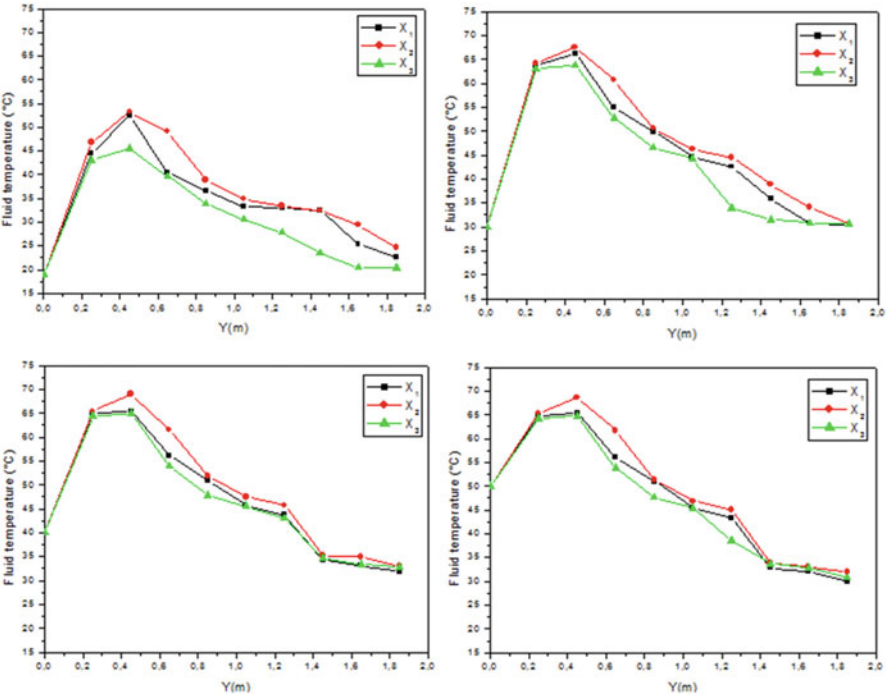

Fig. 8 Film temperature along the plate

Fig. 9 Outlet temperatures of fluid

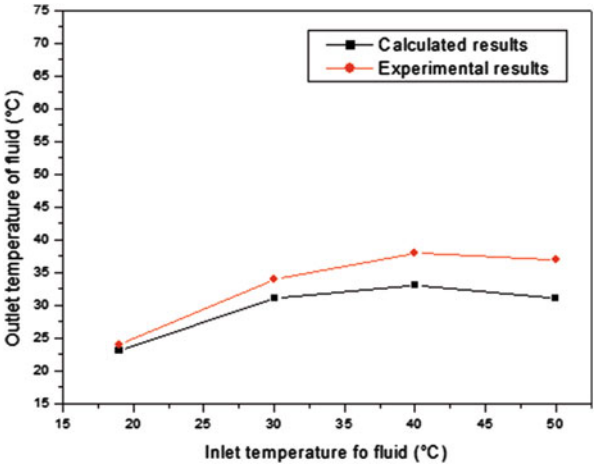

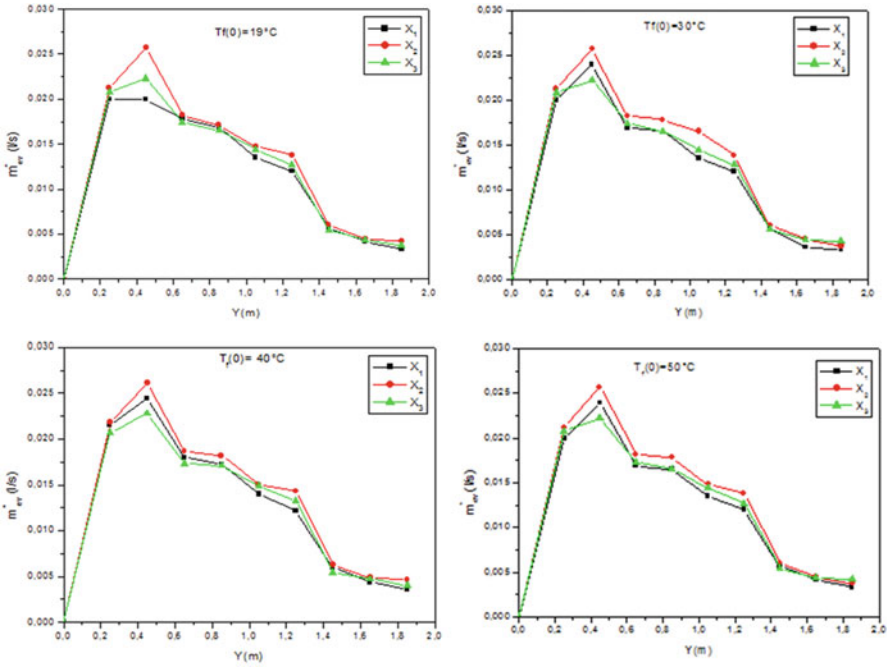

Fig. 10 Variation of local evaporated flow along the plate

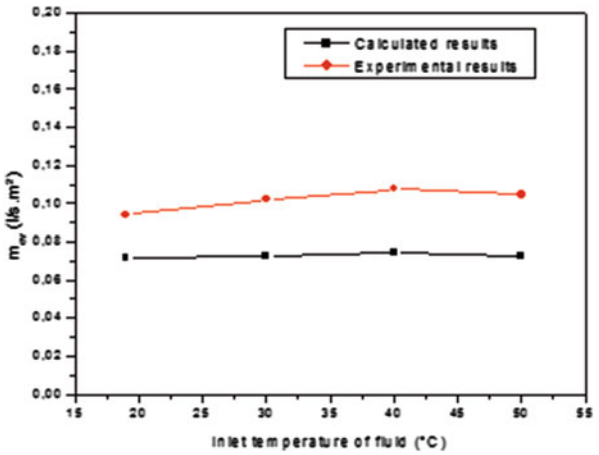

Fig. 11 Comparison between calculated and experimental evaporated flow

Evaporated local flow is maximum when the liquid temperature is high. It gradually decreases. It is low in the bottom of the plate because the fluid temperature is low (Fig. 10).

Experimentally, we measured the total throughput evaporated. Theoretically, it is determined by integrating the local flow evaporated. We obtained results presented in Fig. 11.

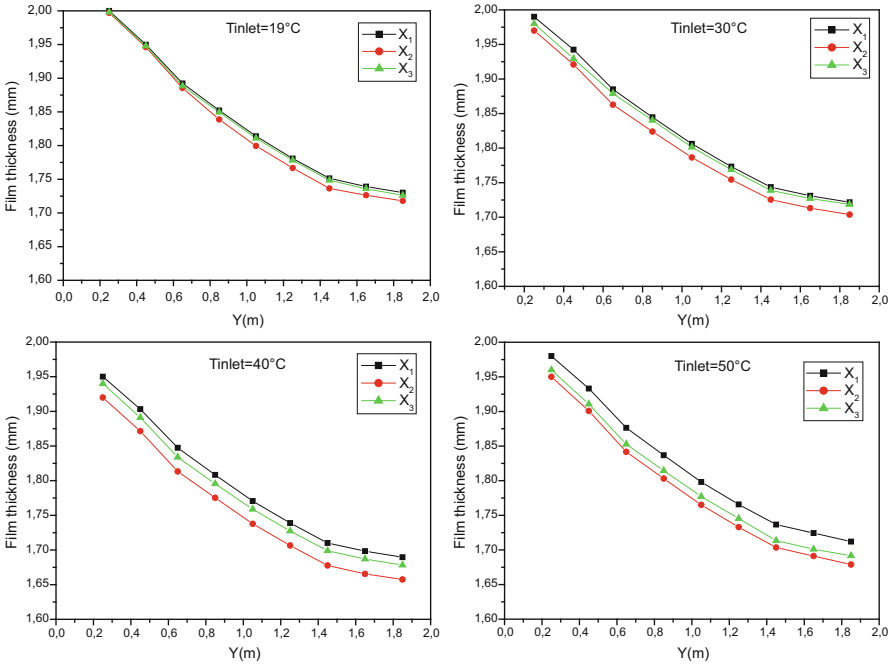

Fig. 12 Variation of film thickness along the plate

When the liquid is preheated at temperatures between 19 and 40 °C, the total flow evaporated increases if the inlet temperature is increased. At an inlet temperature of 50 °C, the liquid becomes warmer than the plate, producing heat, thus explaining the decrease in total evaporated flow at this temperature. The maximum difference between the measured and calculated results is 10%.

The film thickness is variable; it decreases along the plate until it stabilizes when the evaporated flow becomes weak. The curves in Fig. 12 present the result in solving eq. (7).

Film thickness is the lowest for X_2 for each case where the evaporated flow is maximum. The more the evaporated flow increases, the lower the film thickness, and vice versa. The significant decrease in film thickness is due to the high evaporated flow. In the bottom of the plate, the evaporated flow is low, and the film thickness is almost constant.

The volume concentration of the effluent increases following Y. Flowing liquid evaporates and loses its water content. It becomes more concentrated. Note that the initial volume concentration of the liquid is 0.0229%. At its release, its maximum concentration reached 0.0274% (Fig. 13).

At the bottom of the plate, the liquid concentration stabilizes due to low evaporated flow. The volume concentration is maximum following X_2, the maximum evaporated flow along this axis. The concentration of liquid at output is maximum (reaching 0.0274) when the liquid is preheated to 40 °C.

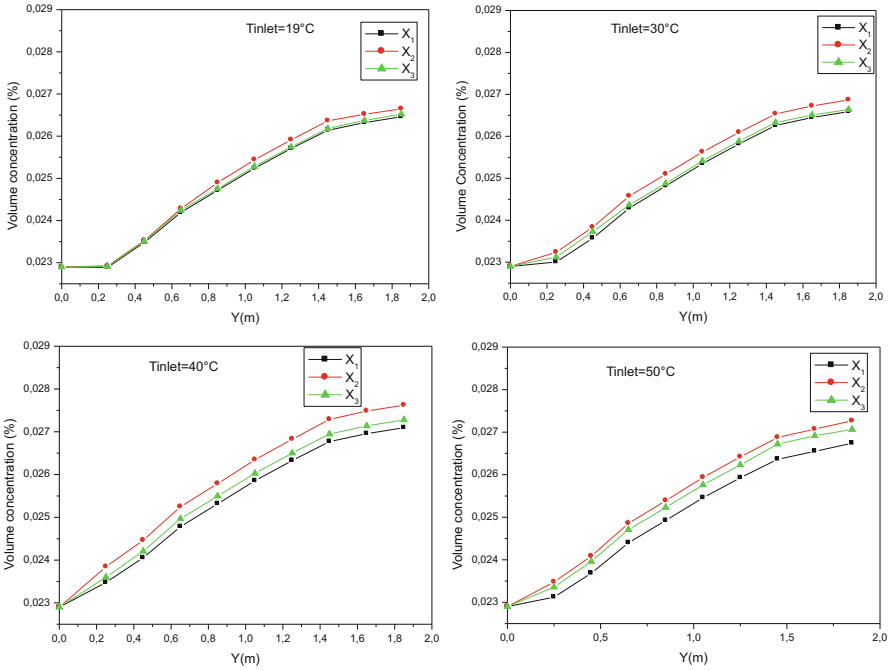

Fig. 13 Variation of effluent concentration along the plate

6 Conclusion

In a study on the evaporation of pig digestate after centrifugation, the effluent having 2.3% of dry matter flows as film on a stainless steel plate inclined by 30°. A thermophysical characterization of three samples of different concentrations shows that heat capacity and viscosity depends on the concentration of the liquid. On the contrary, thermal conductivity does not depend on liquid concentration but on its temperature.

A comparison between the experimental and calculated results by determining heat and mass balance on plate and film was completed. The difference between the measured and experimental results did not exceed 7%. We found that since heating flow is not constant over the plate, the temperature of the plate depends on flux distribution. If it is maximum, then the plate temperature is maximum, and vice versa. Once the film circulates, its temperature is affected by the temperature of the plate. Therefore, evaporated flow is proportional to film temperature.

Evaporated flow is maximum on the central part of the plate, where flux is maximum. The final concentration of product reached 0.0274%. The liquid lost nearly 20% of its volume when it was introduced at 40 °C. Therefore, when we preheat liquid between 19 and 40 °C, evaporated flow improves. So, liquid temperature becomes higher than that of the plate. In addition, the liquid transfers its heat to the plate that blocks evaporation phenomenon.

Acknowledgments This research is part of a PhD study in National Engineering School of Monastir, Tunisia. It is supported by the Laboratory TEMPO of the University of Valenciennes and Hainaut Cambresis.

References

Bennamoun, L.: Solar drying of wastewater sludge: A review. Faculté des Sciences Exactes, Sciences Naturelles et de la Vie, Université Larbi BenM'hidi, Oum El Bouaghi, Algeria Article history (2011).

Bouchekima, B., Gros, B., Ouahes, R., Diboun, M.: Brakish water desalination with heat recovery. Desalination. **138**, 147–155 (2001)

Brau, J.: Support de cours de convection pour 3 GCU. Insa de Lyon, département de Génie Civil et Urbanisme (2006).

Chen, T.S., Tien, J.P., Armaly, B.F.: Natural convection on horizontal, inclined and vertical plates with variable surface temperature or heat flux. Int. J. Heat Mass Transf. **29**(10), 1465–1478 (1986)

Granier, R., Texier, C.: Production du lisier de porc à l'engrais: quantité et qualité. Techni-porc. 23–31 (1993)

Huetz-Aubert, J., Sacadura, F.: Mesure des émissivités et des réflectivités monochromatiques directionnelles des matériaux opaques. Revue Phys. Appl. **17**(p), 251–260 (1981)

Latimier, P., Gallard, F., Corlouër, A.: Actualisation des volumes et des quantités d'azote, de phosphore et de potasse rejetés dans le lisier par un élevage naisseur-engraisseur. Journées Rech. Porcine en France. **28**, 241–248 (1996)

Levasseur, P.: Composition et volume de lisier produit par le porc : Données bibliographiques. TECHNI. **21**(4), 16–19 (1998)

Lei Z, Dezhen C, Jinlong X. Sewage sludge solar drying practise and characteristics study. In: Proceedings of power engineering conference, IEEE (2009).

Mani, A., Srinivasa Murthy, S.: Solar Evaporation Ponds for Tannery Effluent Treatment. A Technical Report, TALCO Ltd., Chennai (1993)

Mani, A., Srinivasa Murthy, S.: Analysis of an open type flat plate collector for tannery effluent treatment. Energ. Conver. Manage. **35**(12), 1061–1071 (1994)

Salihoglu, N.K., Pinarli, V., Salihoglu, G.: Solar drying in sludge management in Turkey. Renew. Energy. **32**, 1661–1675 (2006)

Srithar, K., Mani, A.: Comparison between simulated and experimental performance of an open solar flat plate collector for treating tannery effluent. Int. Commun. Heat Mass Transfer. **30**(4), 505–514 (2003a)

Srithar, K., Mani, A.: Analysis of a single cover FRP flat plate collector for treating tannery effluent. Appl. Therm. Eng. **24**(5–6), 873–883 (2003b)

Srithar, K., Mani, A.: Studies on solar flat plate collector evaporation systems for tannery effluent (soak liquor). J. Zheijang Univ. Sci. A. **7**(11), 1870–1877 (2006)

Optimal Operation of MEA-Based Post-combustion Carbon Capture Process for Natural Gas Combined Cycle Power Plants

Xiaobo Luo and Meihong Wang

1 Introduction

Using carbon capture and sequence (CCS) technology to control CO_2 emissions from fossil fuel (e.g. coal and natural gas), fired power plants play an important role to achieve the target of limiting average global temperature increase to 2 °C in 2050 (IEA 2012). MEA-based post-combustion absorption is considered as the most matured technology for carbon capture from fossil fuel-fired power plants (Wang et al. 2011). However, when power plants are integrated with capture plants, the two big barriers observed for CCS deployment are: (1) its massive capital cost and (2) high thermal energy penalty (Luo et al. 2015).

Currently, 20% of global electricity production capacity is supplied from gas-fired power generation (British Petroleum 2014). This number is expected to become larger in the next several decades because of the advent of cheap natural gas and carbon emission mitigation policy. However, the cost of electricity will increase from £66 to £144.1 per MWh for NGCC power plant integrated with PCC plant (DECC 2013). Except for an enormous capital investment, the parasitic energy penalty is also significant for NGCC power plant integrated with PCC process. Therefore, research efforts are required for potential improvements to reduce both the capital cost and the energy penalty to gain a better economic profile of commercial deployment of carbon capture.

One of the most important engineering tools for addressing these cost issues is optimization (Edgar et al. 2001). Optimization of a large scale of configuration plant, such as NGCC power plant integrated with PCC process in this study, can involve several levels such as process configurations, features of equipment designs

X. Luo • M. Wang (✉)
School of Engineering, University of Hull, Cottingham Road, Hull HU6 7RX, UK
e-mail: Meihong.Wang@hull.ac.uk

© Springer International Publishing AG, part of Springer Nature 2018

F. Aloui, I. Dincer (eds.), *Exergy for A Better Environment and Improved Sustainability 2*, Green Energy and Technology,
https://doi.org/10.1007/978-3-319-62575-1_21

and control variables of plant operations. Most early studies are carried out for the parametric studies for coal-fired power plants. Key variables such as lean solvent loading, solvent/gas ratio (L/G ratio), MEA concentration in solvent and stripper operating pressure have been investigated. The results shows they have big impacts on the energy consumptions (Abu-Zahra et al. 2007b; Canepa and Wang 2015) and are highly sensitive to the economic performance of the whole plant (Abu-Zahra et al. 2007a). However, their optimal values exhibit a large range in different studies. For example, the optimal value of lean loading is in a big range of 0.18–0.32 mol CO_2/mol MEA with corresponding special duty at a range of 4.5–3.8 GJ/ton CO_2 (Abu-Zahra et al. 2007b; Mac Dowell and Shah 2013). For the design parameters, the diameter and packing height of the absorber and the stripper have large impacts on the capital cost. The optimal values of these design parameters are coupled with other process variables. Their interactions are highly nonlinear based on chemical principles. Then it is hard to make fast cost estimation by simply formatting cost calculation equations.

Another approach to minimize the total cost is optimal operation towards the changes of marketing, such as volatile electricity demand and pricing, fuel price as well as carbon price. Mores et al. (2012) found that the total annual cost of carbon capture plant varies linearly for carbon capture level within a range of 70–80% but it rises exponentially when carbon capture level increases from 80–95%. Cohen et al. (2012) investigated the economic benefits of a 500-MW coal-fired power plant with CO_2 capture for a carbon pricing from 0-200USD/ton CO_2 and concluded CO_2 capture investment is unjustifiable at low CO_2 prices. In the study by Mac Dowell and Shah (2013), optimal CO_2 capture level is 95% for £30/ton CO_2 and £90/MWh scenario and is around 70% for £8/ton CO_2 and £55/MWh scenario for a 660-MW_e coal-fired power plant integrated with a capture plant. The study concludes carbon price should be more than 40£/ton CO_2 to justify the total cost of carbon capture for an objective of capture level greater than 90% without considering the costs of CO_2 compression, transport and storage.

Compared with coal-fired power plant, the CO_2 concentration in flue gas is much lower for a gas-fired power plant which causes some major different features in terms of the economic performance, such as bigger equipment size and lower L/G ratio. Thus the optimization results of carbon capture for a coal-fired power plant may not be transferred to NGCC power plant directly. This paper aims to explore the optimal operation of MEA-based post-combustion carbon capture plant for gas-fired NGCC power plant. The novelties of this study are claimed as follows: (1) whole chain economic estimate was conducted for NGCC power plant integrated with carbon capture, transport and storage; (2) the optimizations were carried out for the carbon capture level under different carbon price, natural gas (NG) price and CO_2 T&S price; (3) this study pointed out the coactions of carbon price, NG price and CO_2 T&S cost will affect the decision-making about optimal carbon capture level for operating PPC process for a NGCC power plant.

2 Process Model Development

For this large-scale plant optimization, process model is the core part of this nonlinear programming. Process model contains the bulk of parameters, variables and constraints in an optimization problem (Edgar et al. 2001). Accurate process model offer better predictions of process variables in terms of both technical and economic performance. In this study, the process model includes NGCC power plant, PCC process and CO_2 compression train. In this section, the sub-models were developed using Aspen Plus®, based on our previous studies (Luo et al. 2015; Canepa et al. 2013).

2.1 NGCC Power Plant Model

A 453-WM_e NGCC reference model with a GE 9351FB gas turbine and a triple-level pressures reheat HRSG was developed using Aspen Plus®. Peng-Robinson (Peng and Robinson 1976) with Boston Mathias modifications (Neau et al. 2009a, b) (PR-BM), equation of state (EOS) is used for the gas cycle and STEAMNBS (Aspen-Tech 2012), and EOS is used for the steam cycle for the calculation of thermodynamic properties.

At the ambient conditions (ambient temperature is assumed to be 9 °C and ambient pressure is assumed to be 1.01 bar in this study), fresh air is compressed to mix with natural gas to enter the combustion chamber (see in Fig. 1). The hot gas leaves the combustion chamber and enters the gas turbine to expand to generate a part of electricity. Exhaust gas from gas turbine, through HRSG, provides the heating to the steam cycle to generate three kinds of steams at different pressures of 170 bar, 40 bar and 5 bar, which go to the high pressure steam turbine (HP-ST), the intermediate pressure steam turbine (IP-ST) and the low pressure steam turbine (LP-ST), respectively, to generate another part of electricity.

The model parameters are presented in Table 1, referring to IEAGHG report (IEAGHG 2012). The simulation results using this model were compared with the simulation results using another software package, GT Pro® (IEAGHG 2012), in order to make a brief validation. The comparison results of Aspen Plus® and GT Pro® appear to be in good agreement (Luo et al. 2015).

2.2 PCC and Compression Model

For the reactive absorption process using MEA solvent to absorb CO_2, Aspen Plus® rate-based approach was proven to be capable to provide an acceptable accuracy for the performance prediction of PCC process (Zhang et al. 2009). The model of PCC process used in this study is developed with Aspen Plus® based on the previous

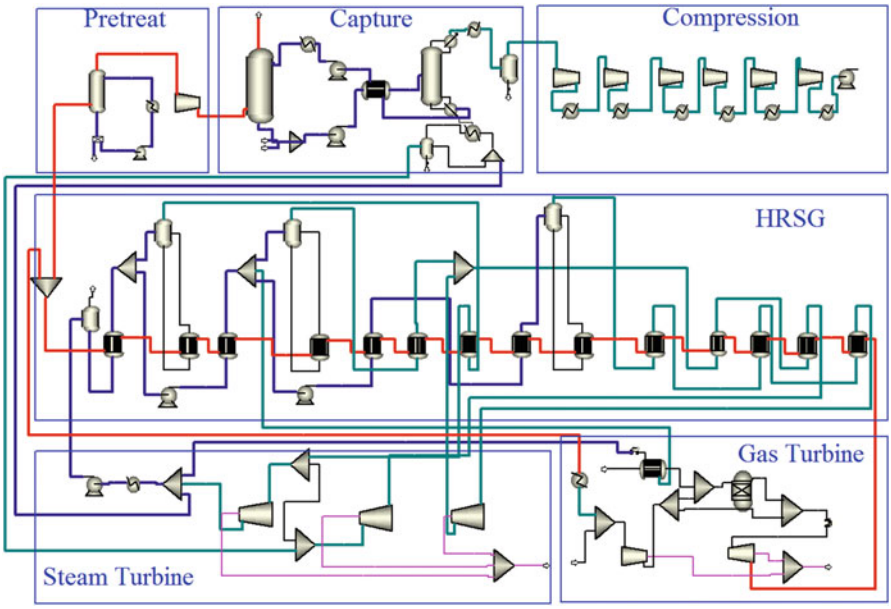

Fig. 1 The flowsheet of NGCC power plant integrated with PCC process and compression with EGR

researches (Canepa et al. 2013; Luo et al. 2015). Electrolyte NRTL (Chen and Song 2004) property method is used to describe the thermodynamic and physical properties. The simulation results from this model were compared with the experimental data and also Zhang's study for a validation purpose. The validation shows a good agreement of several key design parameters and operational variables, such as lean solvent loading, rich solvent loading, capture level and the temperature profiles of both the absorber and the stripper (Canepa et al. 2013; Canepa and Wang 2015). Table 2 shows the model parameters of the PCC process after scaling up to match the NGCC power plant.

A compression train is needed to pressurize the captured CO_2 to reach a high entry pressure, as high as 110–150 bar for pipeline transport and geologic sequestration. By our previous study (Luo et al. 2014), an optimal option was selected to get a minimum annual cost including annualized capital cost, operating and maintenance cost and energy cost. The optimal configuration compromises six stages integrally geared compressor following a pump with intercoolers at an exit temperature of 20 °C, which was also adopted in this study Table 3.

Table 1 Model parameters of NGCC power plant

Parameters	Value
Natural gas composition (vol %)	
CH_4	89
C_2H_6	7
C3-C5	1.11
CO_2	2
N_2	0.89
Gas turbine	
Type	GE 9371FB
Pressure ratio	18.2
Steam turbine	
Steam inlet of HP turbine (bar/°C)	172.6/601.7
Steam inlet of IP turbine (bar/°C)	41.5/601
Steam inlet of LP turbine (bar/°C)	5.8/293.1
HP/IP/LP turbine efficiencies (%)	92/94/90
Minimum temperature approach of HRSG	
Steam and gas (°C)	25
Gas and boiling water (°C)	10
Water liquid and gas (°C)	10
Approach of Economizer (°C)	5
Condenser pressure and temperature (bar/°C)	0.039/29.0

Table 2 Model parameters of PCC process with EGR

Parameter	Value
CO_2 concentration in flue gas (mol%)	7.32
CO_2 capture level (%)	90
CO_2 captured (kg/s)	40.92
Columns flooding (%)	65
Lean loading (mol CO_2/mol MEA)	0.32
L/G (mol/mol)	2.71
Reboiler duty (MW)	176.227
Reboiler duty (GJ/tonne CO_2)	4.31
Lean solvent MEA concentration (wt%)	30
Lean solvent temperature (°C)	30
Absorber column numbers	1
Absorber column diameter (m)	16.2
Absorber column pressure (bar)	1.0
Absorber column packing	Mellapack 250Y
Absorber column packing height (m)	20
Stripper column numbers	1
Stripper column diameter (m)	8.6
Stripper column pressure (bar)	2.1
Stripper column packing	Mellapack 250Y
Stripper column packing height (m)	20

Table 3 Parameters of compression train

Parameter	Unit	Value
Suction pressure	bar	1.8
Suction temp.	°C	20
Pumping suction pressure	bar	80.0
Pumping suction temp.	°C	20
Exit pressure	bar	136.0
Stage	–	6
Isentropic efficiency	%	75
Intercooler exit temperature	°C	20
Last stage exit temp.	°C	20

2.3 NGCC Integrated with PCC and Compression

When the NGCC power plant is integrated with PCC process and compression, there are several basic interfaces (see Fig. 1), including: (1) Flue gas is lined from HRSG to the capture process after gas processing. (2) Low pressure steam is extracted for solvent regeneration. (3) Steam condensate returns to the steam cycle of NGCC power plant. (4) NGCC power plant provides electrical power supply for PCC process and CO_2 compression. Compared with NGCC stand-alone, carbon capture case has a total 9.58% net power efficiency decrease according to the previous study. The power plant output is reduced by three main factors: (1) steam extraction causing a reduction in steam flow rate through the LP-ST and therefore in its power output; (2) the power consumption of CO_2 compression; and (3) auxiliary power consumption, including the blower and solvent circulation powers. Out of the three factors, the power reduction due to steam extraction is the main one.

Another process modification for NGCC power plant when integrated with PCC process is to recirculate a fraction of flue gas (the ratio is 0.38) leaving from the HRSG back to the compressor inlet where it is mixed with fresh air (see Fig. 1). The CO_2 content in the flue gas from NGCC power plant is as low as 3–4 mol%, whilst it is 11–13 mol% for a coal-fired power plant, which causes bigger equipment size requirement and lower absorption efficiency of the absorber in PCC capture plant (Jonshagen et al. 2011). Exhaust gas recirculation (EGR) is an effective solution for smaller capital cost and better thermal performance for a NGCC power plant integrated with a PCC process (Luo et al. 2015; Canepa and Wang 2015).

3 Cost Model Formulation

3.1 Cost Breakdown

For operating an industrial process plant, the total cost includes capital expenditure (CAPEX) and operational expenditure (OPEX). OPEX can be split into fixed OPEX (operating and maintenance (O&M) cost) and variable OPEX (mainly the energy and utilities cost) (IEA-GHG 2002). CAPEX includes equipment material and installation, labour cost, engineering and management EPC cost and other costs happened during the project contracture and commissioning. Fixed OPEX includes overhead cost, operating and maintenance (O&M) cost and other fixed costs regardless of the plant running at partial or full loading or shutdown. Variable OPEX mainly includes fuel cost, energy and utilities costs and solvent make-up cost. For a NGCC power plant integrated with PCC process, it is noticed that the variable cost should also include the emission penalty cost of CO_2 discharged into the atmosphere and T&S cost of the CO_2 captured.

3.2 Objective Function

For techno-economic evaluation or cost optimization of a power plant integrated with carbon capture process, different economic indexes have been used in different studies, including (1) total annual operating profits, (2) total annualized cost, (3) levelized cost of electricity (LCOE), and (4) cost of CO_2 avoided. In this study, LCOE was formulated to be the objective function of the optimization. LCOE was calculated by dividing total annual cost by annual net power output. The total annual cost is the sum of annualized CAPEX, fixed OPEX and variable OPEX.

$$\text{LCOE} = \frac{\text{Total annual cost}}{\text{Net power output}}$$

$$\text{Total annual cost} = \text{Annualized CAPEX} + \text{Fixed OPEX} + \text{Variable OPEX}$$

The annualized CAPEX is the total CAPEX multiplied by capital return factor (McCollum and Ogden 2006). It would be noticed that this study focuses on the optimal operation of NGCC power plant with PCC process. Its annualized CPAEX and fixed OPEX are supposed to be fixed negating the tax and labour cost changes. Only the variable OPEX was considered to change in response to different market situations. In this study, the variable OPEX includes fuel cost, cooling utilities cost, solvent make-up cost, carbon emission cost and CO_2 T&S cost.

4 Techno-Economic Evaluation of Base Case

In this section, the technical performance was evaluated according to the process simulation results. Then the cost of whole chain for capturing carbon from NGCC power plant was evaluated for the base case by combining simulation results and the literature data, in order to give a basis for later optimal operation study.

4.1 Technical Performance

The base case was set up based on the PCC process described in Sect. 2.2 with 90% carbon capture level and with EGR for NGCC power plant. The key technical performance parameters of the base case were compared with the reference case of NGCC stand-alone and are summarized in Table 4.

4.2 LCOE of the Base Case

For the economic evaluation, CAPEX and fixed OPEX referred to the benchmark report (IEAGHG 2012). The variable OPEX was summarized from each sub-cost calculated based on the simulation results from the process model. To harmonize results for comparison with other studies, the following assumptions are made: (1) all costs are corrected to €2015 using the harmonized consumer price index (HICP) in Europe zone; (2) the captured CO_2 mixture has no economic value; (3) cooling water is sourced from a nearby body of water at the cost of pumping and operation of a cooling tower. Other important cost inputs are provided in Table 5, with the costs given in Euro.

Table 4 Process performance of the base case

Description	Reference	Base case
Gas turbine power output (MW_e)	295.03	294.64
Steam turbine power output (MW_e)	170.71	117.69
Power island auxiliary power consumption (MW_e)	11.69	9.7
CO_2 compression power consumption (MW_e)	–	14.8
Mechanical power consumption in capture process (MW_e)	–	2.035
Stripper reboiler duty (MW_{th})	–	176.2
Steam extracted for reboiler (kg/s)	–	71.06
CO_2 captured (kg/s)	–	40.92
CO_2 emission (kg/MWh)	348.3	40.98
Specific duty (MJ_{th}/kg CO_2)	–	4.31
Net plant power output (MW_e)	453.872	385.795
Net plant efficiency (%, LHV)	58.74	49.93

Table 5 Key economic evaluation cost inputs

Description	Unit	Value	Reference
Refrigerant price	€/t	0.17	Aspen Tech (2012a)
Carbon price	€/kg	7.0	FML (2015)
NG price	€/GJ	6.58	Ycharts (2015)
MEA solvent price	€/ton	1452	Alibaba.com (2015)
CO_2 T&S cost	€/ton	39.54	DECC (2013)
Project economic life	year	25	IEAGHG (2012)

Table 6 Model parameters of PCC process with EGR

Description	Unit	Reference	Base case
Annualized CAPEX of NGCC[a]	M€/year	44.226	41.257
Annualized CAPEX of PCC[a]	M€/year	–	39.158
Fixed OPEX of NGCC[a]	M€/year	8.344	7.784
Fixed OPEX of PCC[a]	M€/year	–	9.078
Variable OPEX			
Fuel	M€/year	160.424	160.424
Carbon emission	M€/year	9.695	0.970
T&S	M€/year	–	51.025
Solvent make-up	M€/year	–	2.999
Refrigerant	M€/year	–	0.673
Total annual cost	M€/year	231.034	330.230
LCOE	€/MWh	58.10	97.70

[a]The cost refers to a benchmark report from IEAGHG (2012)

Table 6 shows the comparison results of reference case of NGCC stand-alone and the base case of carbon capturing. In the base case, the annualized CAPEX of PCC process is close to the annualized CAPEX of NGCC power plant, and the variable OPEX accounts for 65% of the total annual cost. For the variable OPEX of NGCC stand-alone, the fuel cost is the biggest part and carbon emission cost is the second largest part. However, when NGCC is integrated with PCC process, the fixed OPEX increases obviously because of new expense items such as CO_2 T&S cost and MEA solvent make-up cost. According to this result, the scenarios of different fuel price and CO_2 T&S price will be analysed to see their impacts on the optimal study on carbon capture level in response to carbon price.

5 Optimal Operation

The economic evaluation of the base case in Sect. 4.2 shows the high capital cost as well as great variable operating cost occurs for capturing carbon from NGCC power plant. For the optimal operation of an assumed existing NGCC power integrated

with PCC process, two major questions are concerned: (1) What is the optimal carbon capture degree under different market conditions? (2) What are the optimal values of key operational variables for an optimal capture level?

To answer these questions, in this section, the studies were carried out for the optimal carbon capture level in response to carbon price first. And then the impacts of fuel price and CO_2 T&S price were analysed. Lean loading was chosen to be the key operational feature variable for optimization.

5.1 LCOE Under Carbon Price

In order to achieve the target of global climate control, CO_2 allowance price was set to drive the actions of reducing CO_2 emission. Current carbon price in EU is around €7/ton CO_2 (FML 2015), but future carbon price is highly uncertain with different paths predicted by DOE of US (see in Fig. 2). The economic performances with a representative of LCOE were examined under different carbon price conditions of €7, €50, €100 and €150 per tonne of CO_2 in this study.

The results are summarized in Fig. 3. Under low carbon price of €7/ton CO_2, LCOE gets the minimum value of €83.4/MWh with 60% CL at an optimal lean loading of 0.26 mol CO_2/mol MEA. Figure 3 (a) also shows LCOE increases obviously with higher CL no matter what the lean loading would be. That trend may indicate that under low carbon price, the carbon emission penalty cost cannot justify the higher operating cost of PCC process. The optimal operation in terms of minimum LCOE is discharging the flue gas to the atmosphere by bypassing PCC process. With higher carbon price of €50/ton CO_2, the differences of LCOE of different CL become smaller. For the scenario of carbon price of €100/ton CO_2, the

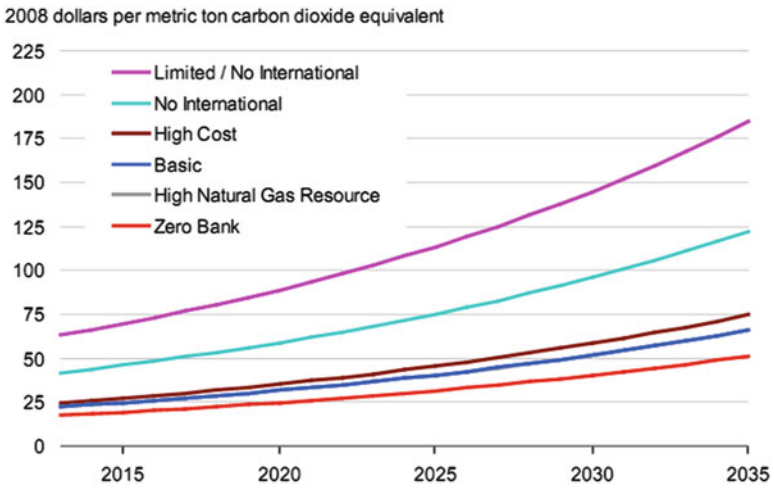

Fig. 2 Carbon price paths (USDOE 2010)

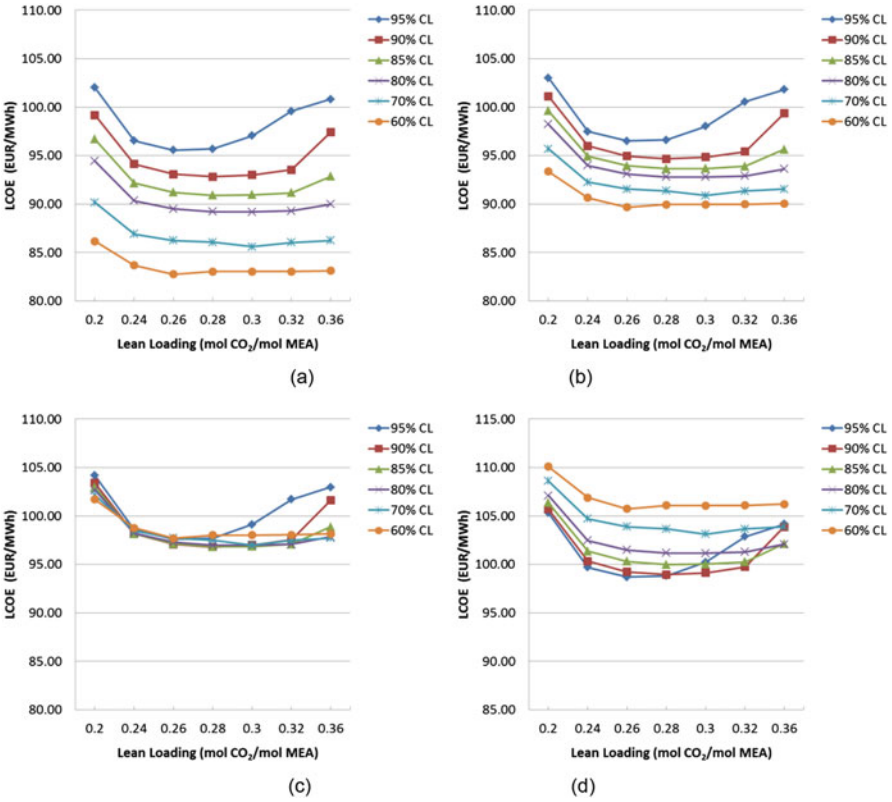

Fig. 3 LCOE in response to different carbon prices: (**a**) carbon price is €7/ton CO_2, (**b**) carbon price is €50/ton CO_2, (**c**) carbon price is €100/ton CO_2, (**d**) carbon price is €150/ton CO_2

values of LCOE distribute in a very narrow range which means the carbon emission penalty cost can just justify the extra variable OPEX cost for carbon capture. With high carbon price of €150/ton CO_2, the optimal value of LCOE of 90% CL and 95% is very close at a lean loading of 0.26–0.28 mol CO_2/mol MEA.

This optimization study indicates that the minimum value of carbon price may be around €100/ton CO_2 to justify the investment of CCS deployment for NGCC power plant. And the carbon price needs to rise up to around €150/ton CO_2 to drive the optimal operation strategy to meet 90% and 95% carbon capture target.

5.2 *The Effect of NG Price*

In Sect. 4, the economic evaluation results show fuel cost is the largest part of the variable OPEX and is a huge expense even compared with the annualized CAPEX. It is realized that the uncertain NG price would have a big impact on deciding the

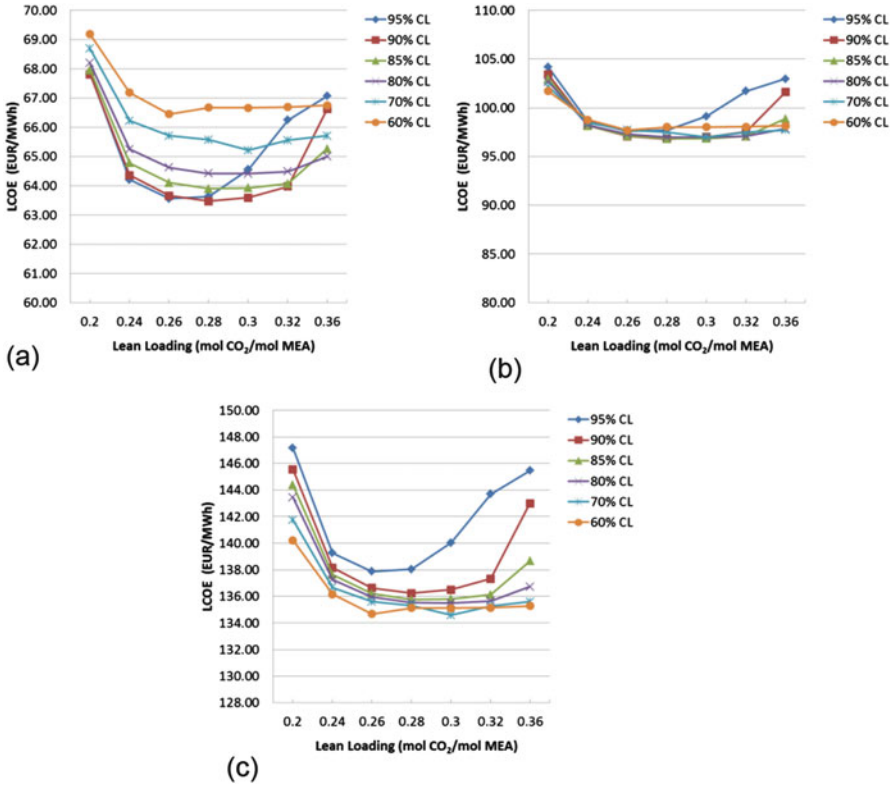

Fig. 4 LCOE in response to different fuel price with carbon price of €100/ton CO_2: (**a**) NG price is €2/GJ, (**b**) NG price is €6.58/GJ, (**c**) NG price is €12/GJ

optimal operation strategy. Figure 4 shows the results of the optimal capture level under different fuel prices assuming a scenario with carbon price at €100/ton CO_2. At the low NG price scenario (see in Fig. 4a), the higher capture level shows a low LCOE because the CO_2 emission penalty can more easily justify the fuel cost. However, the situation reverses when NG price rises up to €12/GJ. Then a carbon price higher than €100/ton CO_2 is needed to draw the balance back for carbon capture.

5.3 The Effect of CO_2 T&S Price

The CO_2 transport and storage cost is a significant part of variable OPEX of running a PCC process for the power plant. DECC of UK (2013) issued a report, in which the transport and storage cost accounts for a big part of the increment of LCOE. Under FID 2013, FID 2020 and FID 2028 CCS technology scenarios, the CO_2 T&S cost is £40.7, £15.7 and £3.7 per MWh of electricity. The change of the CO_2 T&S

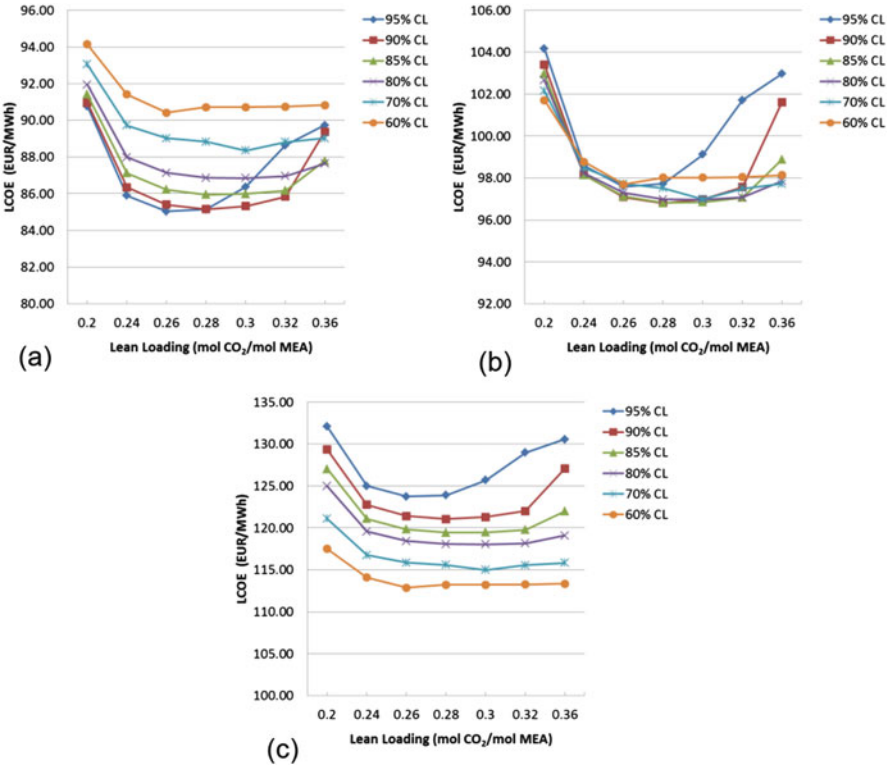

Fig. 5 LCOE in response to different CO_2 T&S price with carbon price of €100/ton CO_2: (**a**) CO_2 T&S price is €9.32/ton CO_2, (**b**) CO_2 T&S price is €39.54/ton CO_2, (**c**) CO_2 T&S price is €102.5/ton CO_2

price may affect the optimal operation decision largely. In this section, the optimizations were carried out on three different CO_2 T&S equivalent prices of €102.5, €39.54 and €9.32 per tonne of CO_2 assuming a scenario with carbon price at €100/ton CO_2. The results are displayed in Fig. 5. With low CO_2 T&S price of €9.32/ton CO_2, the optimal capture level is 90–95% compared with 80–90% at the intermediate price of €39.54/ton CO_2. At the high CO_2 T&S price of €102.5/ton CO_2, the high cost of carbon capture would not be justified (see in Fig. 5a) and a carbon price higher than €100/ton CO_2 is needed to provide driving force for carbon capture. Otherwise, bypassing PCC process is the optimal choice.

6 Conclusions

In this paper, the optimal operation of NGCC power plant integrated with PCC process was investigated under different market conditions such as carbon price, fuel price and CO_2 T&S cost. To be a part of the optimization program, a rate-based

steady-state process model including NGCC, PCC and compression train was developed using Aspen Plus®. The objective function to be minimized in the optimization is formulated for LCOE with dividing total annual cost, a sum of annualized CAPAX, fixed OPEX and variable OPEX, by annual net power output. The economic evaluation was carried out for the reference case and the base case for whole chain of NGCC integrated with PCC, CO_2 T&S. The base case was set up based on a PCC process with 90% carbon capture level and with EGR for NGCC power plant. The optimal operations were carried out for the carbon capture level under different carbon price, fuel price and CO_2 T&S price by minimizing LCOE. Some conclusions from this study were summarized for the optimal operation of a 453-WM_e NGCC power plant integrated with PCC process, as follows:

- Fuel cost, carbon emission cost and CO_2 T&S cost are major parts of the variable OPEX cost.
- Carbon price needs to be more than €100/ton CO_2 to justify the cost of carbon capture.
- Carbon price needs to be around €150/ton CO_2 to drive optimal carbon capture level to 90–95%.
- Higher carbon price is required to get same optimal carbon capture level when NG price rises up.
- Higher carbon price is required to get same optimal carbon capture level when CO_2 T&S cost rises up.
- The optimal range of lean loading is 0.26–0.3 mol CO_2/mol MEA.

Acknowledgements The authors would like to acknowledge the financial support from EU FP7 Marie Curie International Research Staff Exchange Scheme (Ref: PIRSES-GA-2013-612230) and 2013 China–Europe small- and medium-sized enterprises energy saving and carbon reduction research project (No.SQ2013ZOA100002).

References

Abu-Zahra, M.R.M., Niederer, J.P.M., Feron, P.H.M., Versteeg, G.F.: CO_2 capture from power plants: part II. A parametric study of the economical performance based on mono-ethanolamine. Int. J. Greenhouse Gas Control. **1**(2), 135–142 (2007a)

Abu-Zahra, M.R.M., Schneiders, L.H.J., Niederer, J.P.M., Feron, P.H.M., Versteeg, G.F.: CO_2 capture from power plants part I. A parametric study of the technical performance based on monoethanolamine. Int. J. Greenhouse Gas Control. **1**(1), 37–46 (2007b)

Alibaba.com: Monoethanolamine price. Available at: http://www.alibaba.com/products/F0/monoethanolamine_price/----------GGS.html (2015). Accessed 05 Feb 2015

Aspen Tech: Aspen Physical Property System: Physical Property Methods. Aspen Technology, Inc., Burlington (2012)

Aspen-Tech: Aspen Icarus Reference Guide: Icarus Evaluation Engine (IEE) V8.0. Aspen Technology, Inc., Burlington (2012)

British Petroleum: BP statistical review of world energy. Available at: http://www.bp.com/content/dam/bp/pdf/Energy-economics/statistical-review-2014/BP-statistical-review-of-world-energy-2014-full-report.pdf (2014). Accessed on 16 Sept 2014

Canepa, R., Wang, M.: Techno-economic analysis of a CO_2 capture plant integrated with a commercial scale combined cycle gas turbine (CCGT) power plant. Appl. Therm. Eng. **74**, 10–19 (2015)

Canepa, R., Wang, M., Biliyok, C., Satta, A.: Thermodynamic analysis of combined cycle gas turbine power plant with post-combustion CO_2 capture and exhaust gas recirculation. Proc. Inst. Mech. Eng. E J. Process. Mech. Eng. **227**(2), 89–105 (2013)

Chen, C.C., Song, Y.: Generalized electrolyte-NRTL model for mixed-solvent electrolyte systems. AICHE J. **50**(8), 1928–1941 (2004)

Cohen, S.M., Rochelle, G.T., Webber, M.E.: Optimizing post-combustion CO_2 capture in response to volatile electricity prices. Int. J. Greenhouse Gas Control. **8**, 180–195 (2012)

DECC of UK: CCS cost reduction task force: final report'. Available at: https://www.gov.uk/government/publications/ccs-cost-reduction-task-force-final-report (2013). Accessed on 16 Sept 2014

Edgar, T.F., Himmelblau, D.M., Lasdon, L.S.: Optimization of chemical processes. McGraw-Hill, New York (2001)

FML: Carbon emissions futures – Dec 15 (CFI2Z5). Available at: http://www.investing.com/commodities/carbon-emissions (2015). Accessed on 5 Feb 2015

IEA: Energy technology perspectives 2012. International Energy Agency, Paris (2012)

IEAGHG: Pipeline transmission of CO_2 and energy. Transmission study report. International Energy Agency (2002)

IEAGHG: CO_2 capture at gas fired power plants. International Energy Agency (2012)

Jonshagen, K., SipÃķcz, N., Genrup, M.: A novel approach of retrofitting a combined cycle with post combustion CO_2 capture. J. Eng. Gas Turbines Power. **133**(1), 011703 (2011)

Luo, X., Wang, M., Oko, E., Okezue, C.: Simulation-based techno-economic evaluation for optimal design of CO_2 transport pipeline network. Appl. Energy. **132**(0), 610–620 (2014)

Luo, X., Wang, M., Chen, J.: Heat integration of natural gas combined cycle power plant integrated with post-combustion CO_2 capture and compression. Fuel. **151**, 110–117 (2015)

Mac Dowell, N., Shah, N.: Identification of the cost-optimal degree of CO_2 capture: an optimisation study using dynamic process models. Int. J. Greenhouse Gas Control. **13**(0), 44–58 (2013)

McCollum, D.L., Ogden, J.M.: Techno-Economic Models for Carbon Dioxide Compression, Transport, and Storage & Correlations for Estimating Carbon Dioxide Density and Viscosity. University of California (2006)

Mores, P., Rodríguez, N., Scenna, N., Mussati, S.: CO_2 capture in power plants: minimization of the investment and operating cost of the post-combustion process using MEA aqueous solution. Int. J. Greenhouse Gas Control. **10**(0), 148–163 (2012)

Neau, E., Hernández-Garduza, O., Escandell, J., Nicolas, C., Raspo, I.: The soave, Twu and Boston–Mathias alpha functions in cubic equations of state: part I. Theoretical analysis of their variations according to temperature. Fluid Phase Equilib. **276**(2), 87–93 (2009a)

Neau, E., Raspo, I., Escandell, J., Nicolas, C., Hernández-Garduza, O.: The soave, Twu and Boston–Mathias alpha functions in cubic equations of state. Part II. Modeling of thermodynamic properties of pure compounds. Fluid Phase Equilib. **276**(2), 156–164 (2009b)

Peng, D.Y., Robinson, D.B.: A new two-constant equation of state. Ind. Eng. Chem. Fundam. **15**(1), 59–64 (1976)

USDOE: Energy Market and Economic Impacts of the American Power act of 2010, Washington, DC (2010)

Wang, M., Lawal, A., Stephenson, P., Sidders, J., Ramshaw, C.: Post-combustion CO_2 capture with chemical absorption: a state-of-the-art review. Chem. Eng. Res. Des. **89**(9), 1609–1624 (2011)

Ycharts: European Union natural gas import price. Available at: http://ycharts.com/indicators/europe_natural_gas_price (2015). Accessed on 10 Feb 2015

Zhang, Y., Chen, H., Chen, C.-C., Plaza, J.M., Dugas, R., Rochelle, G.T.: Rate-based process modeling study of CO_2 capture with aqueous Monoethanolamine solution. Ind. Eng. Chem. Res. **48**(20), 9233–9246 (2009)

Experimental and Numerical Investigations of "Fabrication of TiO_2 Compact Layer by the Spray Pyrolysis Deposition System for Dye-Sensitized Solar Cells"

Pernebayeva Damira, Upadhyaya Hari, and Prabhakara Bobbili

1 Introduction

Environmental concerns and the escalating demand for power generation are key drivers for the research and development of environmentally friendly and cost-effective technologies and products. As fossil fuels diminish and the world becomes increasingly reliant on the generation of electric power, the use of renewable energy is being sought as an alternative way for power supply. Among other renewable energy technologies, photovoltaic (PV) devices could be recognized as the most promising technology due to the abundance and inexhaustibility of solar radiation (1361 W/m^2 by Kopp et al. 2005).

Generally, solar cell technologies can be divided into the first, second, and third generations. The first generation, such as crystalline silicon PV panels, is a more mature technology, whereas the second includes the emerging thin-film technologies that have just entered the market, and the third covers future technologies (Hagfeldt et al. 2012). Although silicon wafer PV technology that relies on expensive bulk multi-crystalline or single-crystal semiconductors has been considered as a dominant in the solar industry, new generation solar cells such as dye-sensitized or "Gratzel" cell can be considered as a competitor device. The dye-sensitized solar cell (DSC) is an emerging device that is based on molecular and nanometer-scale components and could have many commercial applications owed to a large

P. Damira (✉)
Nazarbayev University, School of Engineering, Mechanical Engineering Department, 53 Kabanbay Batyr Ave, Astana, Republic of Kazakhstan, 010000
e-mail: damira.pernebayeva@nu.edu.kz

U. Hari • P. Bobbili
Heriot-Watt University, Engineering and Physical Science, Mechanical Engineering Department, Edinburgh EH14 4AS, UK

© Springer International Publishing AG, part of Springer Nature 2018

F. Aloui, I. Dincer (eds.), *Exergy for A Better Environment and Improved Sustainability 2*, Green Energy and Technology,
https://doi.org/10.1007/978-3-319-62575-1_22

flexibility in shape, light weight, color, and transparency (Hagfeldt et al. 2012). Moreover, DSCs could eclipse traditional PV cells due to their simple fabrication process at relatively low cost (40% lower compared with silicon PV) and at reduced material consumption (Hashmi 2011).

Basically, DSC is a photoelectrochemical solar cell device that converts sunlight into electricity with efficiency above 12% for small cells and about 9% for mini modules (Hagfeldt et al. 2012). Initially, O'regan and Gratzel innovated nanocrystalline dye-sensitized solar cells (Oregan and Gratzel 1991). Common DSCs contain the following structure: a mesoporous TiO_2 working electrode, a Ru-complex sensitizer, electrolyte containing I^-/I_3^- redox couple, and transparent conductive oxides (TCO) counter electrode coated with a thin layer of platinum (Hagfeldt et al. 2012). A mesoporous and nanostructured TiO_2 film is one of the key components of the DSCs. It provides a large surface area for photon absorption and electron transport to the substrate (Hagfeldt et al. 2012). Generally, the mesoporous TiO_2 electrode is composed of the following structures: TiO_2 compact layer (with a thickness of ~50 nm), a light-absorbing layer with a thickness of ~10-μm (with ~20 nm particle size), a light-scattering layer with a thickness of ~3 μm porous layer (with ~400 nanometer-sized TiO_2 particles), and an overcoating of TiO_2 throughout the whole structure, formed by aqueous $TiCl_4$ with a further annealing treatment (Hagfeldt et al. 2012).

Basically, the working principle of the DSC is the following: the energy of an incident photon is absorbed by a dye molecule and the electrons with sufficient energy are excited from the valence band to the conduction band of each dye. Then the electron is injected from the photoexcited dye to the lower energy conduction band of the semiconductor. Following this, the electrons diffuse through TiO_2 semiconductor toward the transparent conductive oxides substrate, and simultaneously the oxidized dye molecules are regenerated by oxidizing I^- to I_3^- ions (Li 2012). The electrons of the I_3^- ions are replaced by the ones arriving from the external circuit toward the counter electrode. This cycle repeats its process and electricity is produced.

As it has been previously said, the electrons diffuse through the semiconductor and therefore its properties are worth mentioning. Titanium dioxide, an n-type wide-bandgap semiconductor, is an efficient photocatalyst and has been considered as one of the most proposed semiconductor materials for DSCs. It takes the leading position among other materials due to its abundance and unique photoelectric and photocatalytic properties such as high refractive index, high dielectric constant, wide energy bandgap, and transparency. TiO_2 photocatalytic activity was first explored by Fujishima and Honda (1972).

Despite all the advantages of DSCs, its commercialization is a major challenge due to technical constraints such as low light absorption and instability. The factor causing cell instability is referred to the liquid electrolyte which limits the shape of the device and introduces risks of evaporation and leakage of the solvent (De Freitas et al. 2008). Another issue relates to the charge recombination processes that occur due to the physical contact between the electrolyte and the FTO substrate surface. Backside electron transfers can occur if the electrons of the semiconductor

recombine with the oxidized electrolyte species before diffusing to the TCO. If this undesired process takes place, it will lead to reduced cell efficiency.

However, this process can be overcome by introducing a compact layer (CL) or blocking layer (BL) between the interfaces of FTO and porous TiO_2 that can effectively prevent the electron recombination due to its high density structure (Yu et al. 2009). Furthermore, the thickness, doping density, and band alignment of titanium dioxide blocking layer on FTO are critical parameters (Cameron et al. 2003). Due to the compact layer properties, many research papers have been focused on compact layer development and fabrication methods, and a variety of techniques have been already established. Seo et al. investigated the fabrication of TiO_2 blocking layer using Ti sputter deposition and acid-treatment methods (Seo et al. 2011). As a result, researchers obtained improvements in DSC performance as the efficiency increased by 1.3% compared to DSC without a compact layer. However, Yu et al. have introduced a better result with a dip-coating technique (Yu et al. 2009). Blocking layer was formed from TiO_2 organic sol and the outcomes showed that the efficiency, short-circuit current, and open-circuit potential of DSCs with the compact layer were improved by 33.3%, 20.3%, and 10.2%, respectively. Another work by Patrocínio et al. applied the blocking layer TiO_2/PSS (sodium sulfonated polystyrene) using layer-by-layer method (Patrocionio et al. 2012). This research presented an increase in the cell efficiency from 5.7% to 7.3%. A different method of the formation of blocking layer was proposed by Li et al. (2012). BL was fabricated by slow intermolecular electrostatic action between the 4-tert-butylpyridine and the 1,2-dimethyl-3-propylimidazolium ions. Researchers highlighted the influence of the posttreatment effect as aging in the dark on DSC performance. It was reported that improvements were achieved due to delayed interaction between electrons and I_3^- ions in the electrolyte.

However, among the methods described above, there is another technique called the spray pyrolysis deposition which is a simple and versatile method of making thin films. This method is considered as the most promising due to its simple work principle and low operational cost. Moreover, due to its viability, it has been already applied to the deposition of uniform thin films for photovoltaic solar cells, sensors, powder, and glass production. One of the benefits of spray pyrolysis deposition system is the deposition on large surface areas. In addition, thin film fabrication process is carried out in the open atmosphere and does not require expensive vacuum equipment. It also enables the use of a variety of chemicals in liquid form instead of powders and minimizes the impact on the working environment and reduces the risks associated with handling toxic solvents (Weber et al., 2012). Thus, SPD technique could be easily scalable to industrial level based on these advantages.

The simple apparatus of spray pyrolysis deposition system typically consists of an atomizer, precursor solution, substrate heater, and temperature controller (Fig. 1). Basically, SPD technique operates three process stages: the atomization of precursor solution, spraying the liquid source onto the heated substrate surface, and the decomposition of the precursor (Perednis et al. 2003).

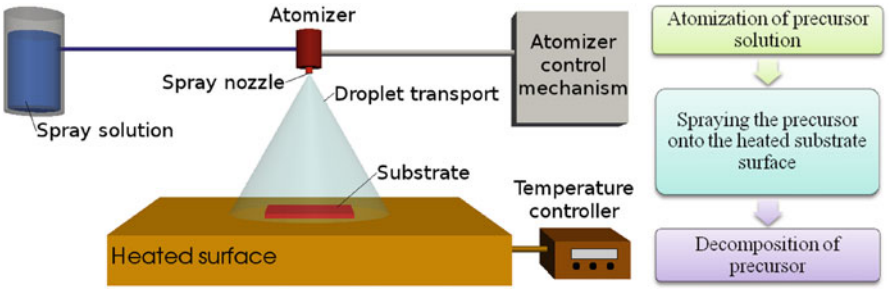

Fig. 1 Schematic representation of the typical SPD setup

Table 1 Properties of TiO_2

Properties	Anatase phase	Rutile phase
Energy bandgap (eV)	3.26	3.05
Density (g/cm3)	3.90	4.27
Dielectric constant	55	170
Refractive index	2.49–2.55	2.61–2.90

Therefore, SPD is of great practical interest in processing dense and porous films for dye-sensitized solar cells by optimizing deposition variables such as the substrate temperature, the composition of precursor solution, the nozzle-to-substrate distance, the deposition time, the flow rate, the amount of the spread precursor solution, the droplet size, and the cooling rate after deposition. Since a high homogeneous structure is needed to produce good-quality thin films, the optimization and control of the system parameters are essential factors.

Many research papers have focused on the development of thin films processing with an employed SPD technique. Table 1 shows the recent research papers that focused on the SPD system development and optimized the spraying process. Initially, the system was pioneered by Viguie and Spitz (1975) and the importance of substrate temperature was highlighted. Later Perednis and Gauckler (2003) as well as Duta et al. (2006) carried out further research, reviewed SPD parameters, and developed the Viguié and Spritz model. It was observed that qualitative and quantitative precursor compounds, substrate temperature, carrier gas, and droplet size affect the film quality. Another work by Nakaruk and Sorrel investigated the spray pyrolysis mechanism and they have found that the droplet size depends on atomization method and film thickness that can be controlled by air induction (Nakaruk and Sorrell 2010). Atomization process refers to the production of droplets and their scattering into the gas. Ultrafine particles can be produced and determined by the concentration and velocity of the droplet generated by atomizers (Miki-Yoshida et al. 2006). Frequently, three different atomization methods have been used in spray pyrolysis including electrostatic, ultrasonic, and pressurized methods.

Electrostatic spray deposition (ESD) method produces precursor spraying by an electrohydrodynamic (EHD) force (Zaouk et al. 2000). Basically, a spray is created by DC voltage applied between the nozzle and the substrate by an electrostatic force. Regarding ultrasonic spray deposition (USD), ultrasonic atomization relies on an electromechanical device that vibrates at a very high frequency.

Pressurized spray deposition (PSD) employs a high-speed air to generate an aerosol. Air under high pressure generates spray toward the substrate; the quality of spray and droplet size distribution are influenced by pressure variation (Perednis 2003). Moreover, the aerosol transport to the substrate is also affected by the chemistry of the precursor solution, the type of the solvent, and the nozzle-to-substrate distance (Weber et al., 2012).

Eventually, several papers have focused on the system parameters that influence film properties. Among the large number of processing parameters, substrate temperature and precursor solution are determined as the most influencing factors on film quality.

Precursor solution can considerably change the film structure, the morphology, and the surface roughness. The most used precursor materials are titanium, nitrate, chloride, acetate, etc. Furthermore, different quantity of additives, salt concentrations, and solvents can be added to the precursor solution to modify the film morphology (Jiang et al. 2011). The additives within the solvents enable to develop a film surface structure, adhesion on a substrate surface, improved evaporation rate (Duta, 2006). $TiCl_3$, HCl, ethyl alcohol, and $TiCl_4$ vapors, titanium(IV)-oxyacetylacetonate (TiO(acac)), and Ti powder and H_2O concentration were investigated as a precursor solution for TiO_2 thin film (Jiang et al. 2011). In the paper of Perednis et al., it was concluded that due to the variation in the precursor solution with the addition of acetic acid, TiO_2 film morphology has changed from cracked to crack-free (Perednis 2003). This was a great achievement in the use of this chemical composition.

The substrate temperature is another critical parameter. The research article by Patil investigated the influence of substrate temperature on film porosity and crystallinity (Jiang et al. 2011). An increase in substrate temperature led to subsequent film porosity. Obtained tests in thin film fabrication showed that the anatase phase at 325 °C has less optical transmittance than at 450 °C. In another experiment by Yanagi et al. (1998), the surface morphology differed from inconstant particles at 200 °C to uniform with 400 °C. It was indicated that a homogeneous particle formation was achieved at higher temperature. Similarly, Masayuki et al. (2003) attained the anatase type TiO_2 film by enhancing the substrate temperature from 450 to 500 °C.

Research conducted by Perednis et al. (2003) highlighted that the morphology and the porosity of films highly depend on the substrate temperature. For that reason, the film structures were modified from a cracked form into microporous due to the temperature increase from 420 to 490 °C and above. Although there are other factors such as deposition time, type of precursor solvents, and salts that can affect the film, the conducted research proves the significant role of substrate temperature.

Nomenclature

T	Substrate temperature (°C),
Q	Flow rate ()
Ø	Nozzle diameter
D	Nozzle-to-substrate distance
T	Spraying time
σ	Surface roughness
R	Resistance
P	Pressure
T%	Transmittance
Subscripts	
XRD	X-ray diffraction
TEM	Transmission electron microscopy
EDS	Energy dispersive spectroscopy
AFM	Atomic force microscopy
SEM	Scanning electron microscopy

Current research aims to enhance the DSCs' performance via introducing the deposited TiO_2 compact layer (CL) between FTO and TiO_2 mesoporous film interface. Research focuses on the fabrication of a high quality TiO_2 CL by SPD technique. This work consists of two main objectives: the first is to design and develop the experimental aerosol-assisted SPD setup and optimize the process parameters; and the second is to fabricate the TiO_2 compact layer and assemble the dye-sensitized solar cell based on it. The final part is to investigate the optical and structural properties of the compact layer and photovoltaic performance of DSCs by instruments such as HITACHI (S-2700) scanning electron microscopy (SEM), the BRUKER (D500) X-ray diffractometer (XRD), JENWAY 7310 UV-Vis spectrophotometer, and Newport 29,950–1000 solar simulator.

Eventually, several papers have focused on the system parameters that influence film properties. Among the large number of processing parameters, substrate temperature and precursor solution are determined as the most influencing factors on film quality.

Precursor solution can considerably change the film structure, morphology, and the surface roughness. The most used precursor materials are titanium, nitrate, chloride, acetate, etc. Furthermore, different quantity of additives, salt concentrations and solvents can be added to the precursor solution to modify the film morphology (Jiang et al. 2011). The additives within the solvents enable to develop a film surface structure, adhesion on a substrate surface, improved evaporation rate (Duta, 2006).$TiCl_3$, HCl, ethyl alcohol and $TiCl_4$ vapors, titanium(IV)-oxyacetylacetonate (TiO(acac)), and Ti powder and H_2O concentration were investigated as a precursor solution for TiO_2 thin film (Jiang et al. 2011). In the paper of Perednis et al., it was concluded that the variation in the precursor solution with an addition of acetic acid, TiO_2 film morphology has changed from cracked to cracked-free (Perednis 2003). This was a great achievement in the use of this chemical composition.

The substrate temperature is another critical parameter. The research article by Patil investigated the influence of substrate temperature on film porosity and crystallinity (Jiang et al. 2011). An increase in substrate temperature leaded to a subsequent film porosity. Obtained tests in thin film fabrication showed that the anatase phase at 325 °C has less optical transmittance than at 450 °C. In another experiment by Yanagi et al. *(*1998*)*, the surface morphology differed from inconstant particles at 200 °C to uniform with 400 °C. It was indicated that a homogeneous particle formation was achieved at higher temperature. Similarly, Masayuki et al. (2003) attained the anatase type TiO_2 film by enhancing the substrate temperature from 450 to 500 °C.

Research conducted by Perednis et al. (2003) highlighted that the morphology and the porosity of films highly depend on the substrate temperature. For that reason, the film structures were modified from a cracked form into micro porous due to the temperature increase from 420 to 490 °C and above. Although there are other factors such as deposition time, type of precursor solvents and salts that can effect on film, the conducted research proves the significant role of substrate temperature.

Current research aims to enhance the DSCs performance via introducing the deposited TiO_2 compact layer (CL) between FTO and TiO_2 mesoporous film interface. Research focuses on the fabrication of a high quality TiO_2 CL by SPD technique. This work consists of two main objectives: the first is to design and develop the experimental aerosol assisted SPD set up and optimize the process parameters; and the second is to fabricate the TiO_2 compact layer and assemble the dye-sensitized solar cell based on it. The final part is to investigate the optical and structural properties of the compact layer and photovoltaic performance of DSCs by instruments such as HITACHI (S-2700) scanning electron microscopy (SEM), the BRUKER (D500) X-ray diffractometer (XRD), JENWAY 7310 UV-Vis spectrophotometer spectrophotometer, and Newport 29,950–1000 solar simulator.

2 Experimental Facility

2.1 Experimental Aerosol-Assisted SPD Setup

The apparatus used for spray pyrolysis was designed and assembled for laboratory spraying tests. Generally, the system consisted of a spray bottle with a nozzle diameter of 2 mm, a hot plate, and carrier gas provided by the silicon tube. Pressurized air was used as an atomizer. The system was constructed in the laboratory fume board. The image of SPD system is presented in Fig. 2. Through designed set of experiments, the range of initial spray conditions, such as deposition temperature, the concentration of precursor solution, the nozzle-to-substrate distance, the flow rate of carrier gas, and the spraying time over which the film could be reproducibly deposited, were defined. Based on the literature review, it was found that the substrate temperature has a major impact on the film quality.

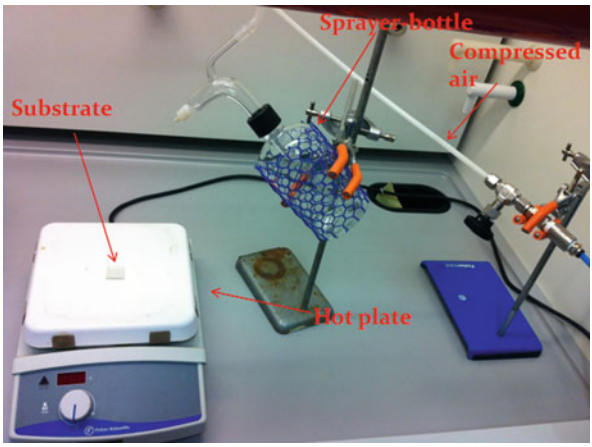

Fig. 2 Image of experimental aerosol-assisted SPD setup

Therefore, this parameter was chosen to be investigated while others were kept constant. The temperature range was set between 300 and 500°C, since the quality of the films gradually decreased with lower temperature and at temperature above 500°C the substrate glass tended to crack.

2.2 *Fabrication of TiO_2 Compact Layer by the SPD Setup*

The TiO_2 suspension was prepared by mixing 0.5 ml of Ti(IV) isopropoxide and 100 ml of ethanol solution. The precursor solution was atomized by compressed air (0.1–0.2 bar) through the nozzle and toward the preheated substrate glass on the hot plate. Fluorine-doped tin oxide (FTO) glass substrates with a size of 20 × 20 × 2 mm were used. Before spraying, the FTO glass was cleaned in a soap solution using an ultrasonic bath for 15 min, and then rinsed with DI water and isopropyl alcohol (IPA) followed by drying with nitrogen stream. The temperature range of the hot plate was set between 300 and 500 °C with an increasing rate of 100 °C. After spraying, the samples were sintered at 500 °C for 30 min and then cooled to room temperature. The distance between the nozzle and the substrate was about 20–30 cm. The following table presents the range of chosen working parameters for spraying process (Table 2).

2.3 *The Working Electrode Fabrication by Screen-Printing Technique*

The screen-printing process includes several procedures: coating, storing, and heating. The working electrode was formed from five layers: three layers of a transparent and a double layer of scattering paste resulting in the thickness of

Table 2 Working parameters of SPD system

Temperature	300–500 °C with 100 °C step
Air pressure	0.1 bar
Nozzle-to-substrate distance	20–30 cm
Spraying time	5–10 s
Nozzle diameter	2 mm
Substrate glass	FTO (20 × 20 × 2 mm^3)
Precursor	0.5 wt% of the (IV)-isopropoxide

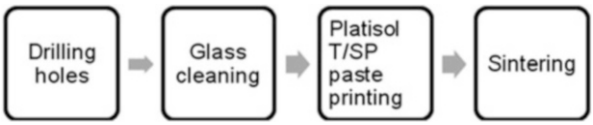

Fig. 3 Flow chart of the counter-electrode preparation

15 μm. For the transparent and scattering layer, the TiO_2 (DSL 18 NR-T) and TiO2 paste (DSL 18NR-AO) were used, respectively. Transparent paste was applied on the top of the TiO_2 compact layer by screen printing and kept in a clean box for 45 s with acetone so that the paste can relax to minimize the surface irregularity and then dried for 3 min at 120 °C. This procedure was repeated for each layer. Finally, electrodes coated with the TiO_2 paste were subjected to gradual heating at 325 °C for 5 min, at 375 °C for 5 min, at 450 °C for 15 min, and at 500 °C for 15 min.

2.4 Dye and Electrolyte Preparation

The TiO_2 photoelectrode was dipped into N-719 dye solution in a mixture of absolute ethanol and stored at room temperature for 16–20 h. As regards the electrolyte, the same preparation suggested by Seigo et al. was used. This method utilizes 0.6 M BMII, 0.03 M I2, 0.10 M guanidinium thiocyanate, and 0.5 M 4-tert-butylpyridine in a mixture of acetonitrile and valeronitrile (volume ratio, 85:15) (Yu et al. 2009).

2.5 Counter-Electrode Preparation

Counter electrode was prepared by the following procedure. A hole was drilled in the FTO glass by sand blasting for 50 seconds, which was then washed with DI water and cleaned with acetone in a sonicated bath for 15 min. Thereafter, the Platisol T/SP catalyst (purchased from Solaronix) was printed on the FTO glass by coating which was then heated at 400 °C for 15 min (Fig. 3).

2.6 Dye-Sensitized Solar Cell Assembling

Dye-sensitized solar cells were formed based on differences on the compact layer. The first group of cells was assembled on the bare FTO substrate. The second group was fabricated on TiO_2 compact layer deposited by the SDP system at different temperatures, and the third group was based on a standard $TiCl_4$ treated. DSCs were assembled into a sandwich-type cell composed of the Pt-counter electrode, the electrolyte, and the dye-sensitized electrode. A drop of the electrolyte was injected by the syringe into the hole in the back of the counter electrode and introduced into the cell via the vacuum machine. The cell was placed in a small chamber to remove inside air. Finally, the hole was sealed using a hot-smelt ionomer film (Surlyn). The fabrication process of the cell is illustrated in Figs. 4 and 5.

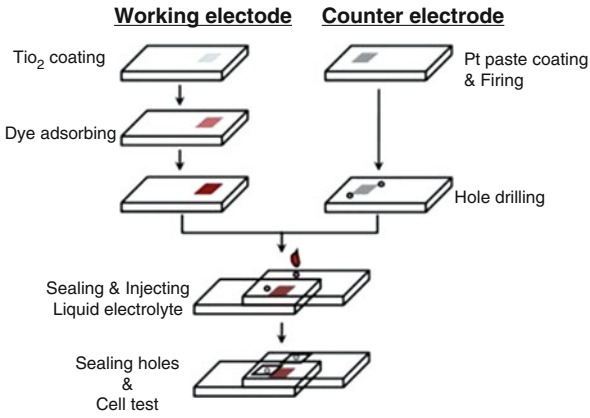

Fig. 4 Schematic representation of the DSC fabrication procedure

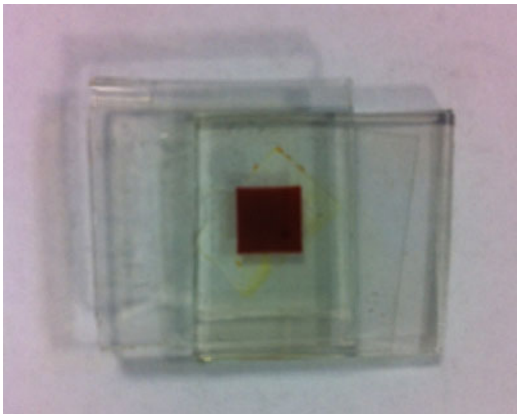

Fig. 5 Dye-sensitized solar cell assembled

2.7 Characterization Instruments

The surface morphology of the transparent TiO_2 compact film was studied by using HITACHI (S-2700) scanning electron microscopy (SEM). The crystal structure of the film structure was studied by the BRUKER (D500) X-ray diffractometer (XRD). The optical transmittance was measured by the JENWAY 7310 spectrophotometer in the wavelength range of 320–900 nm, and the J–V characteristics of the DSCs were measured using a Newport 29,950–1000 solar simulator.

3 Results and Discussions

3.1 Transmittance of the TiO_2 Compact Layer

The transmittance spectra of the bare FTO, the $TiCl_4$-treated compact layer, and the TiO_2 blocking layer fabricated by the SPD at 300°C, 400 °C, and 500°C are shown in Fig. 6. It can be clearly observed that the transmissivity of FTO treated with TiO_2 and $TiCl_4$ decreased by 10%. The bare FTO glass presented about ~85% of transmittance spectra in the visible range, whereas with a TiO_2 compact layer it

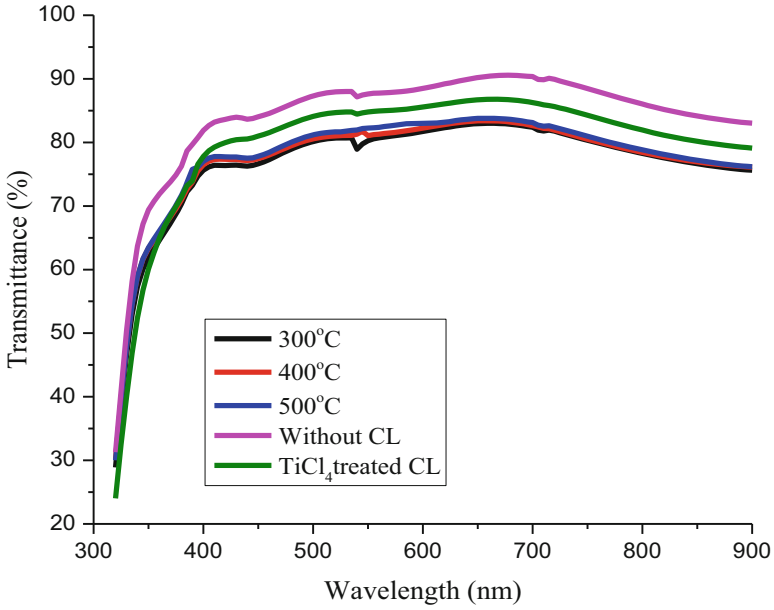

Fig. 6 Transmittance spectra of the compact layers of TiO_2 deposited at a temperature of 300 °C, 400°C, and 500°C and $TiCl_4$ treated. The data of a bare FTO glass substrate are presented as a reference

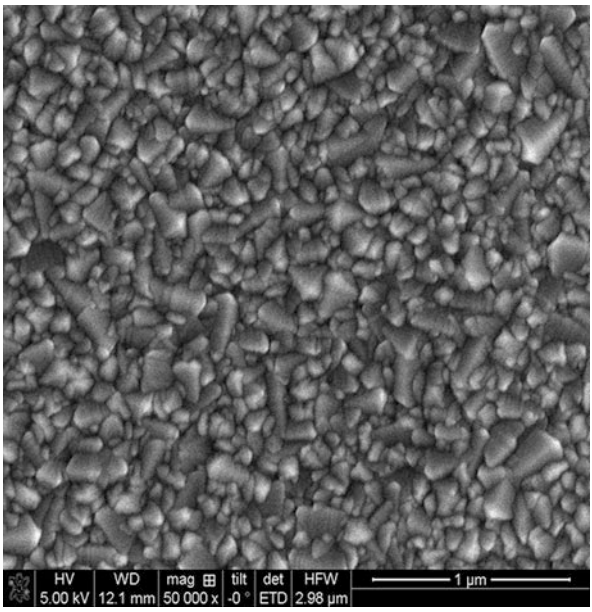

Fig. 7 SEM images of the surface morphology of the TiO_2 compact layer deposited at 300 °C

was less. At 500°C, the compact film showed a slightly better transmittance (~70%) than those deposited at 300 and 400°C (>70%). However, the transmittance of the FTO treated with $TiCl_4$ (~82%) was not influenced significantly. Similar results of the transmittance of TiO_2 films were obtained in the literature.

3.2 Structure and Surface Morphology of the TiO_2 Compact Film

The SEM study of the TiO_2 compact films at 300°C, 400°C, and 500°C is illustrated in Fig. 7. From the images, the uniformity and the roughness of the surface morphology of TiO_2 compact layer can be observed as well as the crack-free films that were obtained. This achieved surface morphology is beneficial for the overall cell performance.

The X-ray diffraction spectra of the deposited TiO_2 films are shown in Fig. 8. SnO_2 and TiO_2 peaks are visible. In very thin layer deposited at 300°C, 400°C and 500°C, three peaks are found for TiO_2 anatase form. Anatase phase, with an energy bandgap of 3.2 eV, is preferred than the rutile phase, which has an energy bandgap of 3.0 eV, due to its morphology. The small and spherical grains of anatase phase allow for higher dye absorption and enhanced electron transport according to Zaouk et al. (2000) (Figs. 9 and 10).

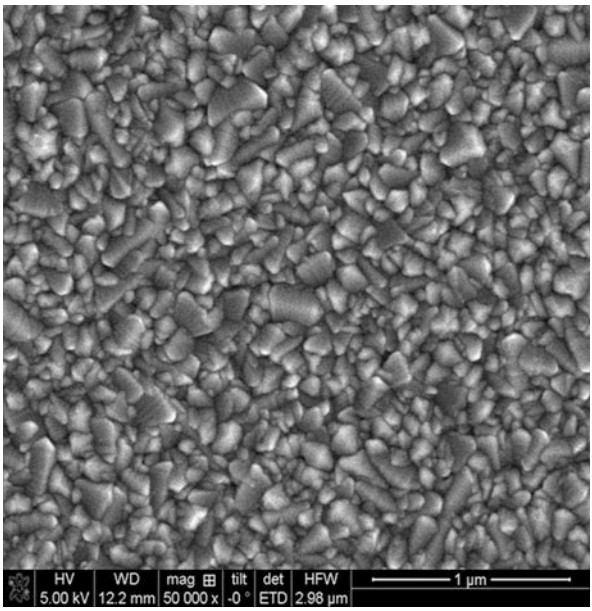

Fig. 8 SEM images of the surface morphology of the TiO_2 compact layer deposited at 400 °C

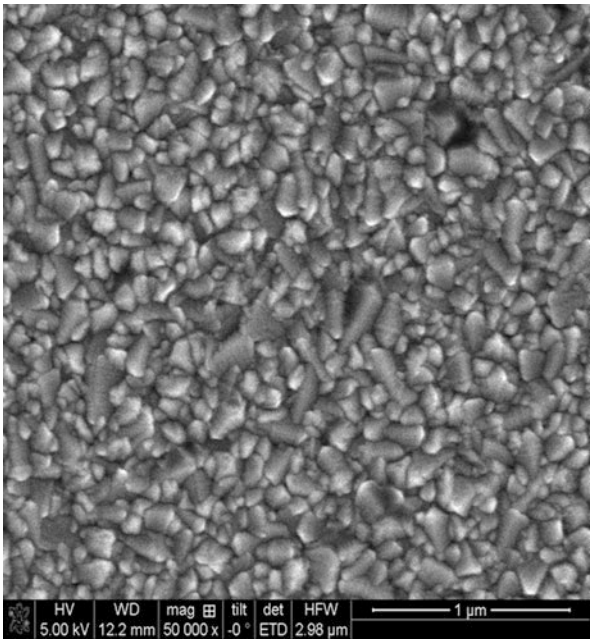

Fig. 9 SEM images of the surface morphology of the TiO_2 compact layer deposited at 500 °C

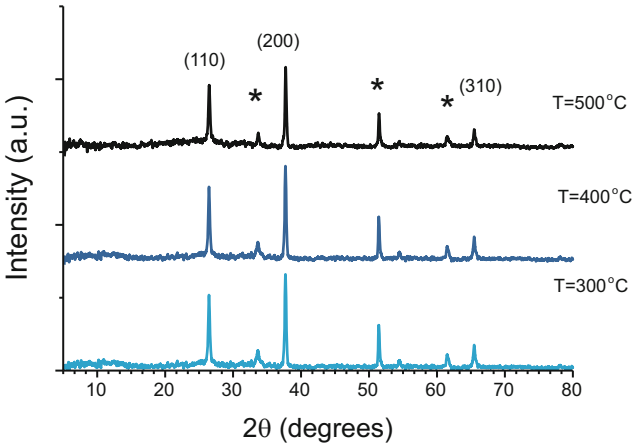

Fig. 10 XRD patterns for the TiO2 compact films deposited at different substrate temperatures indicate peaks of the anatase phase based on JCPDS no 88–1175 for TiO2, (*) refers to the (SnO2: F) substrate based on JCPDS card: 00–035-0907 for FTO

3.3 Electrical Conductivity Measurement of DSCs

A Newport 29950-1000 solar simulator was used to measure current–voltage values to determine the power conversion efficiencies of solar cells. Measurements were carried out in the dark and under illumination. The cells were covered with a black mask with a hole (2 mm in diameter) around the active area (1 cm^2) of the cells. The energy conversion efficiency, η, was calculated by the J–V characteristic curve and following equations:

$$\eta = \frac{J_{SC} \cdot V_{OC} \cdot ff}{P_{in}} \cdot 100\%$$

$$ff = P_{max} \cdot J_{sc} \cdot V_{oc}$$

where J_{SC} is the short-circuit density, V_{OC} is the open circuit voltage, ff is the fill factor, P_{in} is the illumination intensity, and P_{max} is the maximum power output of the solar cell (Hagfeldt et al. 2012).

DSC based on the TiO_2 blocking layer showed better energy conversion efficiency, higher current density, and fill factor than the cell without the blocking layer. At 300°C, the compact layer has improved the DSC's overall energy efficiency from 3.8% to 6.4%, the current density increased from 11.31 to 12.8 mA/cm^2, and the fill factor enhanced from 0.51 to 0.76. However, the efficiency of the cells declined for the layers that were prepared at 400 and 500°C. The best cell performance was achieved by traditional $TiCl_4$ treatment that gave efficiency of 7.4%, the short-circuit current density of 13.08 mA/cm^2, the open circuit voltage of 0.68 V, and fill factor of 0.82. The open circuit voltage remained low for all cells which might be due to the lower shunt resistance and an internal electron leakage from the FTO (Fig. 11 and Table 3).

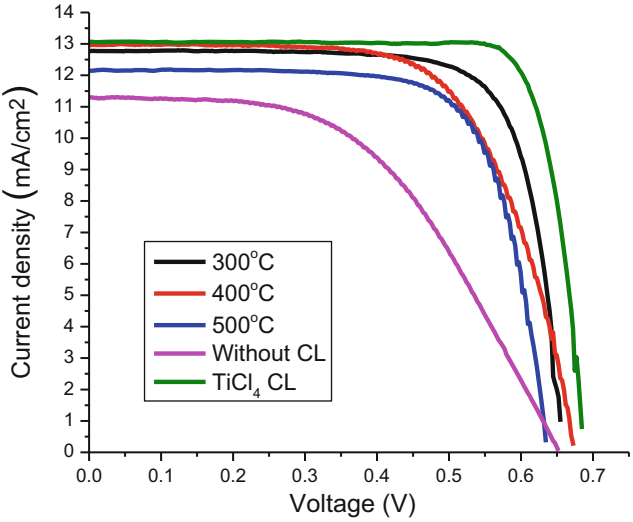

Fig. 11 J–V curve of DSCs with CL deposited at different substrate temperatures by the SPD system, CL treated with $TiCl_4$, and DSC without CL

Table 3 Photovoltaic parameters of DSCs without CL, with TiO_2 CL deposited at different temperatures and $TiCl_4$ treated

Sample	Voltage, V_{oc} (V)	Current density, J_{sc} (mA/cm^2)	Fill factor, *ff*	Efficiency ŋ, (%)
Without CL	0.65	11.31	0.51	3.76
300 °C	0.65	12.80	0.76	6.40
400 °C	0.67	13.00	0.66	5.77
500 °C	0.63	12.19	0.73	5.61
$TiCL_4$-treated CL	0.68	13.08	0.82	7.35

4 Conclusions

The TiO_2 compact film as a means of blocking layer has been introduced between the FTO and nanoporous TiO_2 film in DSC. The spray pyrolysis deposition technique was employed to fabricate the compact films. The process parameters of the SPD system were optimized through the number of tests to obtain high-quality films. The results based on the DSC performance revealed that a good quality of TiO_2 compact layer can be obtained at 300°C substrate temperature. By X-ray diffraction, the anatase phase of the TiO_2 layer that was deposited at 300°C, 400°C, and 500°C was found. In addition, the transmittance spectra of the compact layers were around 70% which is 10% lower than that of the bare FTO transmittance. Overall, owing to the introduction of the compact layer, the direct contact between

FTO and electrolyte interfaces was avoided and therefore the electron recombination was prevented. As a result, J_{sc} value increased from 11.31 to 12.8 mA/cm^2, and the overall cell efficiency was improved almost two times from 3.8% to 6.4%. Thus, these results indicate the significant role of the compact oxide blocking layer in DSC. Although the cell based on the compact layer treated with $TiCl_4$ remains at higher performance (the efficiency is 7.35%, current density is 13.08 mA/cm^2, the open circuit voltage is 0.68 V, and fill factor is 0.82), the compact layer prepared by the SPD technique has a great potential. Moreover, the SPD system can be applied for the fabrication of photoelectrodes and dyes and sequentially reduces the cost of DSCs.

Acknowledgments This research was supported by Professor Hari Upadhyaya, Dr. Prabhakara Bobbili, and Dr. Senthilarasu Sundaram, the Laboratory of Energy of Heriot-Watt University.

References

Cameron, P.J., et al.: Characterization of titanium dioxide blocking layers in dye-sensitized nanocrystalline solar cells. J. Phys. Chem. B. **107**(51), 14394–14400 (2003)

De Freitas, J.N., et al.: Solar module using dye-sensitized solar cells with a polymer electrolyte. Sol. Energy Mater. Sol. Cells. **92**(9), 1110–1114 (2008)

Duta, A.: TiO2 thin layers with controlled morphology for ETA (extremely thin absorber) solar cells. Thin Solid Films. **511-512**, 195–198 (2006)

Hagfeldt, A., et al.: Dye-sensitized photoelectrochemical cells. Ractical Handbook of Photovoltaics (ISBN: 978-0-12-385934-1), p.479–542, Elsevier Inc. (2012)

Honda, K.: Electrochemical photolysis of water at a semiconductor electrode. Nature (London). **238**, 37–38 (1972)

Li, B., et al.: Photovoltaic performance enhancement of dye-sensitized solar cells by formation of blocking layers via molecular electrostatic effect. Electrochim. Acta. **59**, 207–212 (2012)

Masayuki, O., Koji, N., Shoji, K.: Porous TiO2 thin films synthesized by a spray pyrolysis deposition (SPD) technique and their application to dye-sensitized solar cells. Sol. Energy Mater. Sol. Cells. **70**, 425–435

Masayuki, O., et al.: Fabrication of dye-sensitized solar cells by spray pyrolysis deposition (SPD) technique. J. Photochem. Photobiol. A Chem. **164**, 167–172 (2003)

Miki-Yoshida, M., et al.: Growth and structure of TiO2 thin films deposited inside borosilicate tubes by spray pyrolysis. Surf. Coat. Technol. **200**, 4111–4116 (2006)

Nakaruk, A., Sorrell, C.C.: Conceptual model for spray pyrolysis mechanism: Fabrication and annealing of titania thin films. J. Coat. Technol. Res. **7**(5), 665–676 (2010)

Oregan, B., Gratzel, M.: A low-cost, high-efficiency solar cells based on dye-sensitized colloidal TiO2 films. Nature. **353**(6346), 737–740 (1991)

Patrocionio, A.O.T., Paterno, L.G., Iha, N.Y.M.: Layer-by-layer TiO2 films as efficient blocking layers in dye-sensitized solar cells. J. Photochem. Photobiol. A Chem. **205**, 23–27 (2012)

Perednis, D.: Thin film deposition by spray pyrolysis and the application in solid oxide fuel cells. PhD Thesis, Zurich, Switzerland (2003)

Seo, H., et al.: Method for fabricating the compact layer in dye-sensitized solar cells by titanium sputter deposition and acid-treatments. Sol. Energy Mater. Sol. Cells. **95**(1), 340–343 (2011)

Viguie, J.C., Spitz, J.: Chemical vapor deposition at low temperatures. J. Electrochem. Soc. **122**, 585 (1975)

Weber, A.Z., et al.: Redox flow batteries: A review. J. Appl. Electrochem. **10**, 1137 (2012)

Yanagi, H., et al.: Characterization of dye-doped TiO2 films prepared by spray-pyrolysis. Charakterisierung von farbstoffdotierten TiO2-Dunnschichten hergestellt durch Spruhpyrolyse, p. 426. (1998(Complete))

Yu, H., et al.: An efficient and low-cost TiO2 compact layer for performance improvement of dye-sensitized solar cells. Electrochim. Acta. **54**(4), 1319–1324 (2009)

Zaouk, D., et al.: Fabrication of tin oxide (SnO2) thin film by electrostatic spray pyrolysis. Microelectron. Eng. **51**, 627–631 (2000)

Experimental Investigation on *Citrullus colocynthis* Oil as Alternative Fuel

Aida Cherifa AHMIA, Fetta DANANE, Rhiad ALLOUNE, and Rahma BESSAH

1 Introduction

The increase in energy demand and pollution problems caused by industrialization has urged researchers and economists to find new sources of energy. One of the feasible energy sources is the use of plant oils, which is readily available and environmentally acceptable (Meher et al. 2006).

The concept using vegetable oil as a fuel dates back to 1895 when Dr. Rudolf Diesel developed the first diesel engine to run on vegetable oil.

Biodiesel is an alternative diesel fuel that consists of alkyl monoesters of fatty acids from vegetable oils or animal fats. Its acceptance as a substitute for fossil-derived diesel has grown the world over.

Pure vegetable oils have been used in the past in diesel engine. However, there have been many problems linked with the direct use of vegetable oils in diesel engine, such as high viscosities and lower volatilities (Kansedo et al. 2008).

Transesterification is one of the accepted processes for the production of biodiesel from oils and fats with alcohols in the presence of homogeneous catalysts (Zhang et al. 2003) or heterogeneous catalysts (Taufiq-Yap et al. 2011; Siddiquee et al. 2011). The homogeneous catalysts have been proven to be more practical in application (Liu et al. 2008). The alkaline catalyst is capable of producing higher yield and purity of biodiesel with a reaction time of between 30 and 60 min

A.C. AHMIA (✉)
Centre de Développement des Energies Renouvelables, CDER, 16340 Algiers, Algeria

Université des Sciences et de la Technologie Houari Boumediene, USTHB, 16111 Algiers, Algeria
e-mail: ahmia.a.c@gmail.com

F. DANANE • R. ALLOUNE • R. BESSAH
Centre de Développement des Energies Renouvelables, CDER, 16340 Algiers, Algeria

© Springer International Publishing AG, part of Springer Nature 2018

F. Aloui, I. Dincer (eds.), *Exergy for A Better Environment and Improved Sustainability 2*, Green Energy and Technology,
https://doi.org/10.1007/978-3-319-62575-1_23

(Liu 1994) and limits the free fatty acids (FFA) content not more than 1.0% (Leung and Guo 2006).

Owing to their availability, various oils have been in use in different countries as feedstocks for biodiesel production. Rapeseed and sunflower oils in Europe, soybean oil in the U.S., palm oil in Malaysia and Indonesia, and coconut oil in the Philippines are being used for biodiesel production. Also, the *Jatropha* tree (*Jatropha curcas*), karanja (*Pongamia pinnata*) and mahua (*Mangifera indica*) are used as major biodiesel fuel sources in India (Demirbas 2009).

However, the food-fuel debate over conventional vegetable oils has rekindled research interest in exploring non-edible and lesser-known oil crops. Among oleaginous and non-edible plants is *Citrullus colocynthis*, commonly known as the colocynth, bitter apple, bitter cucumber or egusi. It is a creeper, short period crop grown naturally wild in arid zones. It is a viny plant with butter pulp native to the Mediterranean Basin, tropical Africa and Asia. *C. colocynthis* is among the 300 species of melon found in Africa and it is cultivated for its seeds, which are rich in oil (53%) and protein (28%) (Ntui et al. 2009).

The main objective of the present study is to investigate the use of *C. colocynthis* as a potential feedstock for biodiesel production by its seed oil transesterification, to measure the physicochemical properties of the methyl ester produced (refractive index, density) and to compare them with the standards limits. The great potential of *C. colocynthis* oil (CCO) in biodiesel production will be highlighted.

Nomenclature

v	Kinematic viscosity (mm^2/s)
Yd	Yield of reaction (%)
nR	Refractive index
gp	Grams of pycnometer (g)
St	Surface tension (mNm^{-1})
Cp	Cloud point (°C)
Greek letters	
ρ	Density (gcm^{-3})
Subscripts	
CCO	*C. colocynthis* oil
CCOME	*C. colocynthis* oil methyl ester
dw	Distilled water

2 Materials and Methods

2.1 CCO Extraction

Crude *C. colocynthis* seed oil was purchased from Bou Saada (239 km South Algiers). Crushed seeds were introduced to a soxhlet extraction system fitted with a 500 mL three-necked round bottom flask and a condenser. The extraction was

employed, according to the AOAC official method of 963.15 (Association of Official Analytical Chemist 1976).

Prior to transesterification, oil quality properties of *C. colocynthis* were determined. The density was evaluated with a pycnometer and using empirical formula reported in the literature. The refractive index was determined using a SCT-105.001.26 refractometer. The kinematic viscosity was determined using a Cannon-Fenske viscometer.

2.2 Transesterification Process and CCOME Analysis

The reversible transesterification reactions are the most common method of converting triglycerides from oils into biodiesel, as shown in Fig. 1, and the most promising solution of the high viscosity oil problem.

The transesterification reaction can be non-catalyzed or catalyzed by an acid, a base or an enzyme. Depending on the solubility of the chemical catalyst in the reaction mixture, transesterification reaction can be homogeneously or heterogeneously catalyzed. These reactions can be accomplished as one-step (base or acid) or two-step (acid/base) processes, depending on the content of free fatty acids.

The reaction was carried out at 60 °C for 1 h with 1 wt% of NaOH and methanol-to-oil molar ratio of 6:1 (Rashid et al. 2008). In order to maintain the catalytic activity, a mixture of NaOOH and methanol was freshly prepared to avoid methanol losses and prevent moisture build-up. This was mixed until the complete dissolution of the catalyst. The solution was added into the reactor and stirred at 600 rpm. The reaction time started as soon as the catalyst/methanol solution was added to the reactor. On completion of the reaction, the resulting product was cooled to room temperature without any agitation and transferred to a separatory funnel for glycerol and methyl ester separation. It was left overnight to allow separation by gravity. After the two phases have separated, the upper phase was collected and the excess alcohol was removed.

The resulting *C. colocynthis* oil methyl ester (CCOME) obtained was purified by successive washing with distilled water (50 ml, 30% of the mass of the mixture) to remove residual catalyst, glycerol, methanol and soap. A small quantity (0.5 ml) of sulfuric acid was used in the second washing to neutralize the remaining soaps and catalyst. Drying was carried out by heating and stirring the CCOME at 100° (Boiling temperature of water).

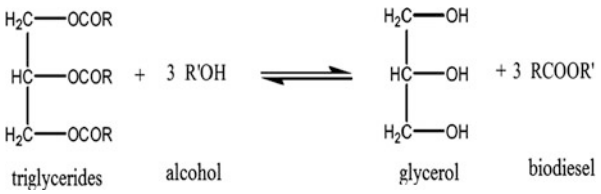

Fig. 1 Transesterification reaction of triglycerides with alcohol

The CCOME yield (Yd) was calculated using empirical formula reported in the literature (Rashid et al. 2010). The density was evaluated with a pycnometer and using empirical formula reported in the literature.

The choice of the viscometer depends on the nature of the liquid. Like ours is transparent, we chose a type Cannon-Fenske viscometer size 150, Type 464.

The apparatus used for the calculation of the surface tension is a tensiometer TD 2000 Prolabo provided with a very thin platinum blade and perfectly wettable.

3 Results and Discussion

3.1 CCO Characterization

The empirical formula (1) was reported from the literature to determine the density of CCO:

$$\rho = \frac{\text{gp filled with CCO - gp empty}}{\text{gp filled with dw - gp empty}} \tag{1}$$

The density was determined to be ρ =0.9046 g/cm^3. This result is well within the range reported for conventional vegetable oils.

The kinematic viscosity at 40 °C is v = 31.52 mm^2/s. The result is also well within the range reported for conventional vegetable oils in the literature (Srivastava and Prasad 2000).

The SCT-105.001.26 refractometer gave that the refractive index of CCO is nR = 1.473. The result fits into the limits given by the literature.

3.2 CCOME Characterization

3.2.1 Reaction Yield

Biodiesel (CCOME) yield estimation was done after the separation and purification of the transesterified product. The 82% yield ($Yd = 82\%$) of CCOME synthesized was calculated according to Eq. (2) (Rashid et al. 2010):

$$Yd(\%) = \frac{\text{grams of CCOME produced} \times 100}{\text{grams of CCO used}} \tag{2}$$

3.2.2 Density

Density is an important parameter for diesel fuel injection systems. It is the weight of a unit volume of fluid. A higher density for biodiesel results in the delivery of a

slightly greater mass of fuel since fuel injection equipment operates on a volume metering system.

The density of CCOME calculated using the empirical formula (1) was found to be ρ =0.8731 g/cm^3.

3.2.3 Kinematic Viscosity

Kinematic viscosity is a very important fuel property and it represents the flow characteristics of fuel. One of the reasons why biodiesel is used as an alternative fuel instead of pure vegetable oils or animal fats is as a result of its reduced viscosity which enhances fuel flow characteristics.

The kinematic viscosity of CCOME obtained from Crude *C. colocynthis* seed oil used in our work, measured at 40 °C was $v = 3.98$ mm^2/s. The result conforms with the kinematic viscosity of CCOME obtained from Crude *C. colocynthis* seed oil found in North and tropical Africa measured at 40 °C which was about 3.83 mm^2/s (Giwa et al. 2010) and 4.486 mm^2/s (Elsheikh and Akhtar 2014).

3.2.4 Surface Tension

The surface tension is an important property of the fuel, it influences the spray characteristics of the fuel droplets, as well as the combustion efficiency (De-gang et al. 2005). It is defined as a force per unit length resulting from the surface free energy, energy that is manifested in the work required to raise a unit surface area of a liquid, isothermally and reversibly.

The tensiometer displays the value St = 34.3 mN/m at 25 °C.

3.2.5 Cloud Point

The injection system of an engine cannot function properly if the biofuel is perfectly smooth. Low temperatures lead to the formation of solid crystals invisible to the naked eye in the fluid, so that the presence of these crystals in biofuels can edit blocking the motor power by partially or totally the filters. This situation affects engine performance, especially when starting vehicles (Owen and Coly 1990).

The cloud point of oil is the temperature at which it begins to solidify when cooled under standard conditions. The more the temperature decreases, the more the crystals form. When the crystals become visible to the naked eye (diameter ≥ 5 . mu.m) we see the emergence of a cloudy suspension and the cloud point is defined at this temperature (Coley 1989).

The temperature representing the cloud point at 25 ° C according to standard ASTM D 2500 is Cp = 0.9 ° C.

Table 1 Properties of CCOME, biodiesel and diesel fuel

Properties	Unit	CCOME	Biodiesel standard values	Diesel standard values
Density	gcm^{-3}	0.8731	0.86–0.9	0.82–0.85 Serdari and Lois (1999)
Kinematic viscosity	mm^2s^{-1}	3.98	1.9–6.0	2.0–4.5
Surface tension	mNm^{-1}	34.3	–	–
Cloud point	°C	0.9	–	−16 (Chavan et al., 2014)

3.3 Properties Comparison

For comparison purpose, the properties of CCOME, biodiesel and diesel fuels are listed in Table 1.

The density found in this work fits into the limits specified by the EN 14214 (0.860–0.900 g/cm^3 at 15 °C) standard.

The kinematic viscosity also conformed to both biodiesel standards EN 14214 (3.5–5 mm^2/s at 40 °C) and ASTM D 6751-02 (1.9–6.0 mm^2/s at 40 °C). The cloud point of CCOME conforms with the value of cloud point of biodiesel from soybean oil (1 °C).

4 Conclusions

An increasing demand of fossil fuels has being a critical problem for us. The natural resources of fossil fuel are dwindling day by day. Biodiesel that may called natural fuel may be a good source or substitute for fossil fuel in the future. In this paper, CCO was transesterified using methanol in the presence of sodium hydroxide to produce CCOME as biodiesel. The yield is satisfactory and the determined biodiesel fuel properties of CCOME conformed to EN 14214 and ASTM D 6751-02 standards. The potential of *C. colocynthis* oil as biodiesel feedstocks was clearly presented in this study.

Acknowledgements The authors gratefully acknowledge “University of Valenciennes” for the organization of this important conference and “Centre de Developpement des Energies Renouvelables” to support this investigation. Our sincerest and deep gratitude goes to Doctor A.M. Aziza and Doctor R. Bessah for their valuable advice.

References

Association of Official Analytical Chemist, Official Methods of Analysis of AOAC International, Method 963.15, Association of Official Analytical Chemist, Washington, DC, USA (1976)

Chavan, S.B., Kumbhar, R.R., Sharma, Y.C.: Transesterification of Citrullus colocynthis (Thumba) oil: Optimization for biodiesel production. Adv. Appl. Sci. Res. **5**(3), 10–20 (2014)
Coley, T.R.: Flow and storage properties in critical reports on applied chemistry. Gasoline and Diesel Fuel Additives. **25**, 105–123 (1989)
De-gang, L., Huang, Z., Lu, X.: Physico-chemical properties of ethanol–diesel blend fuel and its effect on performance and emissions of diesel engines. Renew. Energy. **30**, 967–976 (2005)
Demirbas, A.: Progress and recent trends in biodiesel fuels. Renew. Sustain. Energy. **50**, 14–34 (2009)
Elsheikh, Y., Akhtar, F.: Biodiesel from Citrullus colocynthis oil: Sulfonic-ionic liquid-catalyzed. Sci. World J.., Article ID 540765. **2014**, (2014)
Giwa, S., Chuah, A.L., Adam, N.M.: Investigating "Egusi" seed oil as potential biodiesel feedstock. Energies. **3**, 607–618 (2010)
Kansedo, J., Lee, K.T., Bhatia, S.: Feasibility of palm oil as the feedstock for biodiesel production via heterogeneous transesterification. Chem. Eng. Technol. **31**(7), 993–999 (2008)
Leung, D.Y.C., Guo, Y.: Transesterification of neat and used frying oil. Fuel Process. Technol. **87** (10), 883–890 (2006)
Liu, K.S.: Preparation of fatty acid methyl esters for gaschromatographic analysis of lipids in biological materials. J. Am. Oil Chem. Soc. **71**(11), 1179–1187 (1994)
Liu, X., He, H., Wang, Y., Zhu, S., Piao, X.: Transesterification of soybean oil to biodiesel using CaO as a solid base catalyst. Fuel. **87**(2), 216–221 (2008)
Meher, L.C., Dharmagadda, V.S.S., Naik, S.N.: Optimization of alkali-catalyzed transesterification of Pongamia pinnata oil for production of biodiesel. Bioresour. Technol. **97**(12), 1392–1397 (2006)
Ntui, V.O., Thirukkumaran, G., Iioka, S.: Efficient plant regeneration via organogenesis in "egusi" melon (Colocynthis citrullus L.) Scientia Hort. **119**, 397–402 (2009)
Owen, K., Coly, T.: Automotive Fuel Handbook, pp. 353–403. Society of Automotive Engineers, Warrendale (1990)
Rashid, U., Anwar, F., Jamil, A., Bhatti, H.N.: Jatropha curcas seed oil as a viable source for biodiesel. Pak. J. Bot. **42**(1), 575–582 (2010)
Rashid, U., Answar, F., Moser, B.R.: Moringa oleifera oil: A possible source of biodiese. Bioresour Technol. J. **99**, 8175–8179 (2008)
Serdari, A., Lois, E.: Impact of esters of mono and dicarboxylic acid on diesel fuel quality. Ind. Eng. Chem. Res. **38**, 3543–3548 (1999)
Siddiquee, M.N., Kazemian, H., Rohani, S.: Biodiesel production from the lipid of wastewater sludge using an acidic heterogeneous catalyst. Chem. Eng. Technol. **34**(12), 1983–1988 (2011)
Srivastava, A., Prasad, R.: Triglycerides-based diesel fuels. Renew. Sustain. Energy Rev. **4**, 111–133 (2000)
Taufiq-Yap, Y.H., Lee, H.V., Yunus, R., Juan, J.C.: Transesterification of non-edible Jatropha curcas oil to biodiesel usin binary Ca-Mg mixed oxide catalyst: Effect of stoichiometric composition. Chem. Eng. J. **178**, 342–347 (2011)
Zhang, Y., Dub´e, M.A., McLean, D.D., Kates, M.: Biodiesel production fromwaste cooking oil: 2. Economic assessment and sensitivity analysis. Bioresour. Technol. **90**(3), 229–240 (2003)

A Novel Approach to Local-Level Design of Bioenergy Supply Chains Integrated with District Heating Systems

Yılmaz Balaman Şebnem and Selim Hasan

1 Introduction

Decision models for biomass to energy supply chain network design of increasing scope and sophistication with an emphasis on environmental issues have been devised recently. Among them, Ayoub et al. (2009) develop a methodology and use a multiobjective MILP model to design and evaluate biomass utilization networks in local areas. Ekşioğlu et al. (2009) develop a mathematical model that integrates long-term biomass to biorefinery supply chain design and midterm logistics decisions. Giarola et al. (2013) present a multiperiod, multiechelon MILP framework to optimize the environmental and financial performances of corn grain and stover-based bioethanol supply chains simultaneously. Marufuzzaman et al. (2014), Kanzian et al. (2013), Osmani and Zhang (2014), and Akgül et al. (2012) are among the other studies that propose bioenergy supply chain design models.

However, it is necessary to develop models that incorporate inherent uncertainties. In addition, these models should incorporate multiple objectives considering economic, technical, environmental, and social aspects to provide more effective solutions to real-life problems. This study aims to develop a comprehensive DSS for design and management of local biomass to energy supply chain networks integrated with district heating systems considering inherent uncertainties. The proposed DSS integrates MODM and fuzzy modeling approaches to consider multiple objectives simultaneously and deal with the uncertainties in biomass to energy supply chains effectively. To treat uncertainties in aspiration

Y.B. Şebnem (✉) • S. Hasan
Dokuz Eylül University, Faculty of Engineering, Department of Industrial Engineering, Tınaztepe Campus, İzmir 35397, Turkey
e-mail: s.yilmaz@deu.edu.tr

© Springer International Publishing AG, part of Springer Nature 2018

F. Aloui, I. Dincer (eds.), *Exergy for A Better Environment and Improved Sustainability 2*, Green Energy and Technology,
https://doi.org/10.1007/978-3-319-62575-1_24

levels for the goals and obtain the preferred compromise solution, fuzzy goal programming (FGP) approach is employed.

The decisions that can be made by the proposed DSS include strategic and tactical decisions about locations of the energy production facilities and biomass storages, logistics, and transportation, and the optimal heat distribution system. The aim is to minimize the costs of district heating system and local transportation while maximizing the service level, which is the level of meeting heat demand of the residential area.

Once the decisions for all localities in the regional supply chain corresponding to procurement and allocation of the resources, configuration of the supply chain network with related connections and capacities and inventory, production and logistics management are made, the local-level supply chain design model provide deals with the comprehensive planning of local supply chain network along with a district heating system. In this study, we use the findings of Yılmaz Balaman and Selim (2014) which present a regional design model and its application.

Biomass to energy conversion plants with CHP generators offer the possibility of installing district heating systems that are used for distributing heat generated in a centralized location for residential and commercial heating requirements such as space heating and water heating. The heat is often obtained from a cogeneration plant burning fossil fuels. After generation, the heat is distributed from the energy station to the heat consumers through a district heating network that consists of a network of insulated pipes. Cost of heat distribution system depends on the length of the network and thermal energy flow in unit time where investment and operational costs of the main transfer station depend on the installed capacity of the system.

2 Formulation of the Proposed Model

Notations and related descriptions for model indices, input parameters, and decision variables are presented in Nomenclature.

Nomenclature

Indices	
I	Bioenergy plant sites
l j	Plant capacity levels for heat production Heat demand nodes
K	Waste storage sites
M	Energy crop storage sites
P	Crop storage capacity levels
E	The sites including arable out of use area for energy crop cultivation
F	The sites including cultivated agricultural area
T	Time periods
P	Crop storage capacity levels
E	The sites including arable out of use area for energy crop cultivation

(continued)

Parameters	
Dem_{jt}	Heat demand of demand node j at time period t (kWh)
PHC_c	Heat production capacity of the plant with capacity level c (kW)
PC_c	Biomass capacity of the plant with capacity level c (ton)
N_c	Number of plants in the selected county with capacity level c
C_p	Energy crop capacity of the energy crop storage with capacity level p (ton)
$H1_W$	Biomass to heat conversion rate of waste biomass W (kWh/ton)
$H2_E$	Biomass to heat conversion rate of energy crop E (kWh/ton)
$R1$	The remaining of the produced heat in plant after internal consumption and heat losses (%)
$R2$	The remaining of the stored heat in heat storage after heat losses (%)
EA_{et}	Arable empty area in site e at time period t (da)
TEA_t	Total arable empty area in the selected locality at time period t (da)
CA_{ft}	Cultivated area in site f at time period t (da)
F	Fertilizer requirement in the cultivated agricultural area (ton/da)
CHN_{ij}	Length dependent cost of heat distribution network per kWh of distributed energy between plant at site i and heat demand node j (€/kWh-km)
CHI	Investment cost of DHS (€/kW)
CHO	Operational cost per kWh of distributed energy of DHS (€/kWh)
CHS	Cost per kW of installed capacity of thermal storage (€/kW_{th})
TC_{kitW}	Unit transportation cost of waste biomass W from storage k to the bioenergy plant at site i at time period t (€/ton)
TC_{mitE}	Unit transportation cost of energy crop E from storage site k to the bioenergy plant at site i at time period t (€/ton)
TC_{emtE}	Unit transportation cost of energy crop E from arable out of use area e to the energy crop storage at site m at time period t (€/ton)
TCF_{ift}	Unit transportation cost of organic fertilizer from the bioenergy plant at site i to cultivated area f at time period t (€/ton)
$MAXSC$	Capacity limit for thermal storage (kW)
DEC_t	Amount of energy crop stored in the energy crop storages at the selected locality at time period t (ton)
$EAPt$	Proportion of energy crop cultivation area to total arable empty area in the selected locality at time period t (%)
$TWPIm_t$ / $TWPIn_{tW}$	Total imported / local waste biomass W amount distributed to the selected locality's plants at time period t (ton)
Dem_{jt}	Heat demand of demand node j at time period t (kWh)
PHC_c	Heat production capacity of the plant with capacity level c (kW)
PC_c	Biomass capacity of the plant with capacity level c (ton)
N_c	Number of plants in the selected county with capacity level c
C_p	Energy crop capacity of the energy crop storage with capacity level p (ton)
$H1_W$	Biomass to heat conversion rate of waste biomass W (kWh/ton)
$H2_E$	Biomass to heat conversion rate of energy crop E (kWh/ton)
$R1$	The remaining of the produced heat in plant after internal consumption and heat losses (%)
$R2$	The remaining of the stored heat in heat storage after heat losses (%)
EA_{et}	Arable empty area in site e at time period t (da)

(continued)

TEA_t	Total arable empty area in the selected locality at time period t (da)
CA_{ft}	Cultivated area in site f at time period t (da)
F	Fertilizer requirement in the cultivated agricultural area (ton/da)
CHN_{ij}	Length dependent cost of heat distribution network per kWh of distributed energy between plant at site i and heat demand node j (€/kWh-km)
CHI	Investment cost of DHS (€/kW)
CHO	Operational cost per kWh of distributed energy of DHS (€/kWh)
CHS	Cost per kW of installed capacity of thermal storage (€/kW_{th})
TC_{kitW}	Unit transportation cost of waste biomass W from storage k to the bioenergy plant at site i at time period t (€/ton)
TC_{mitE}	Unit transportation cost of energy crop E from storage site k to the bioenergy plant at site i at time period t (€/ton)
TC_{emtE}	Unit transportation cost of energy crop E from arable out of use area e to the energy crop storage at site m at time period t (€/ton)
TCF_{ift}	Unit transportation cost of organic fertilizer from the bioenergy plant at site i to cultivated area f at time period t (€/ton)
$MAXSC$	Capacity limit for thermal storage (kW)
DEC_t	Amount of energy crop stored in the energy crop storages at the selected locality at time period t (ton)
$EAPt$	Proportion of energy crop cultivation area to total arable empty area in the selected locality at time period t (%)
$TWPIm_t$ / $TWPIn_{tW}$	Total imported / local waste biomass W amount distributed to the selected locality's plants at time period t (ton)
$TEPIm_{tE}$ / $TECPIn_{tE}$	Total imported / local energy crop E amount distributed to the selected locality's plants at time period t (ton)
$TWSIm_{tW}$ / $TWSIn_{tW}$	Total imported / local waste biomass W amount distributed to the selected locality's waste storages at time period t (ton)
$TESIm_{tE}$ / $TESIn_{tE}$	Total imported / local energy crop E amount distributed to the selected locality's energy crop storages at time period t (ton)
$TWPEx_{tW}$ / $TEPEx_{tE}$	Total exported waste biomass W / energy crop E amount that goes to other localities' plants from the selected locality's waste storages / energy crop storages at time period t (ton)
$TESEx_{tE}$	Total exported energy crop E amount that goes to other localities' energy crop storages from the selected locality's energy crop fields at time period t (ton)
$TFIn_t$	Total local fertilizer amount that goes to the selected locality's cultivated areas from the selected locality's plants at time period t (ton)
Decision Variables	
$WPIm_{itW}$ / $WPIn_{itW}$	Imported / local waste biomass W amount distributed to plant in site i at time period t (ton)
$EPIm_{itE}$ /$EPIn_{itE}$	Imported / local energy crop E amount distributed to plant in site i at time period t (ton)
$WSIm_{ktW}$ / $WSIn_{ktW}$	Imported / local waste biomass W amount distributed to waste storage in site k at time period t (ton)
$ESIm_{mtE}$ / $ESIn_{mtE}$	Imported / local energy crop E amount distributed to energy crop storage in site m at time period t (ton)

(continued)

$ESPIn_{mitE}$ / $WSPIn_{kitW}$	Local energy crop E / waste biomass W amount distributed to plant in site i from energy crop storage in site m / waste storage in site k at time period t (ton)
$EAIn_{emtE}$	Local energy crop amount distributed to energy crop storage in site m from energy crop field in site e at time period t (ton)
$EPEx_{mtE}$ / $WPEx_{ktW}$	Exported energy crop E / waste biomass W amount that goes to other localities' plants from the selected locality's energy crop storage in site m / waste biomass storage in site k at time period t (ton)
$ESEx_{etE}$	Exported energy crop E amount that goes to other localities' energy crop storages from the selected locality's energy crop field in site e at time period t (ton)
FIn_{it}	Local fertilizer amount produced at plant in site i at time period t (ton)
$FPIn_{ift}$	Local fertilizer amount distributed from selected locality's plant in site i to the selected locality's cultivated area in site f at time period t (ton)
DSE_{mt}	Amount of energy crop stored in the energy crop storage in site m at time period t (ton)
OH_{it}	Heat production amount of plant in site i at time period t (kWh)
Q_{ijt}	Heat distribution amount from plant in site i to demand node j at time period t (kWh)
SH_{it}	Stored heat amount of plant in site i at time period t (kWh)
SC_i	Thermal storage capacity of plant in site i (kW)
A_{et}	Size of area for energy crop cultivation in arable empty area in site e at time period t (da)
W_{it}	Amount of water used in plant at site i (ton)
Y_{ic}	Binary variable that indicates whether or not a plant with capacity level c is constructed in site i
D_k	Binary variable that indicates whether or not a waste storage is constructed in site k
S_{mp}	Binary variable that indicates whether or not an energy crop storage with capacity level p is constructed in site m
$WPIm_{itW}$ / $WPIn_{itW}$	Imported / local waste biomass W amount distributed to plant in site i at time period t (ton)

2.1 The Objective Function

The proposed model includes the following economic and service-level related objectives:

- Minimization of district heating system cost and local transportation cost
- Minimization of the unmet heat demand which leads to maximization of total service level

First objective: Minimization of district heating system and local transportation costs.

1. *Total cost of district heating system*

Total cost of district heating system consists of the following cost components:

- Investment cost of district heating system,
- Operational cost of district heating system,
- Cost of heat distribution network,
- Cost of thermal storage.

Eq. 1 represents the total cost of the district heating system.

$$\begin{aligned}\text{Total district heating system cost} = & \left(\text{CHI}^* \sum_i \sum_j \sum_t Q_{ijt}\right) \\ & + \left(\text{CHO}^* \sum_i \sum_j \sum_t Q_{ijt}\right) \\ & + \left(\sum_i \sum_j \sum_t \text{CHN}_{ij} * Q_{ijt}\right) \\ & + \left(\text{CHS}^* \sum_i \text{SC}_i\right)\end{aligned} \tag{1}$$

2. *Local transportation costs*

Local transportation costs include the following cost components:

- Cost of waste biomass transportation from waste storages to plants,
- Cost of energy crop transportation from crop storages to plants,
- Cost of energy crop transportation from energy crop fields to crop storages,
- Cost of fertilizer transportation from plants to cultivated areas in the selected locality.

The following equation calculates the local transportation costs:

$$\begin{aligned}\text{Local Transportation Cost} = & \left(\sum_k \sum_i \sum_t \sum_W \text{TC}_{kitW} * \text{WSPIn}_{kitW}\right) \\ & + \left(\sum_m \sum_i \sum_t \sum_E \text{TC}_{mitE}{}^* \text{ECSTPIn}_{mitE}\right) \\ & + \left(\sum_e \sum_m \sum_t \sum_E \text{TC}_{emtE}{}^* \text{ECAIn}_{emtE}\right) \\ & + \left(\sum_i \sum_f \sum_t \text{TCF}_{ift}{}^* \text{FERPIn}_{ift}\right)\end{aligned} \tag{2}$$

Second objective: Minimization of the unmet heat demand. This objective function ensures maximization of the total service level. The second objective function is represented by Eq. (3):

$$\text{Unmet Heat Demand} = \sum_{j} \sum_{t} \left(\text{Dem}_{jt} - \sum_{i} Q_{ijt} \right) \tag{3}$$

2.2 The Constraints

Constraints of the local-level supply chain design model and their definitions are presented in this section.

Heat flow conservation and heat storage capacity constraints: Heat flow conservation constraints are represented by Eqs. (4) and (5):

$$(\text{OH}_{it} * R1) + \left(\text{SH}_{i(t-1)} * R2\right) = \sum_{j} Q_{ijt} + \text{SH}_{it} \quad \forall i, \ \forall t \tag{4}$$

$$\sum_{i} Q_{ijt} \leq \text{Dem}_{jt} \quad \forall j, \ \forall t \tag{5}$$

Eq. (6) presents the constraint that ensures the amount of heat stored in a conversion plant at each time period must not exceed the thermal storage capacity in that plant. Eq. (7) limits the thermal storage capacity in each plant to the capacity limit:

$$\text{SH}_{it} \leq \text{SC}_{i} \quad \forall i, \ \forall t \tag{6}$$

$$\text{SC}_{i} \leq \text{MAXSC} * \sum_{c} Y_{ic} \quad \forall i \tag{7}$$

Plant number and heat production capacity constraints: Eq. (8) ensures that the heat production amount of each conversion plant must not exceed the heat production capacity of that plant. Eqs. (9) and (10) limit the plant number in the selected locality to the value determined in the regional level and ensure that only one plant must be constructed in a plant location:

$$\text{OH}_{it} \leq \sum_{c} \text{PHC}_{c} * Y_{ic} \quad \forall i, \ \forall t \tag{8}$$

$$\sum_{i} Y_{ic} = N_{c} \quad \forall c \tag{9}$$

$$\sum_{c} Y_{ic} \leq 1 \quad \forall i \tag{10}$$

Biomass and fertilizer flow conservation constraints: Biomass and fertilizer that are stored, processed, and produced in the selected locality are subdivided into three categories, namely imported, local, and exported biomass. Equations that represent the biomass and fertilizer flow conservation constraints are given in the following along with the related explanations.

1. Eqs. (11, 12, 13, and 14) present the constraints that calculate the amounts of "imported biomass" that is distributed:
   - To the selected locality's conversion plants from other localities' biomass storages,
   - To the selected locality's biomass storages from other localities' biomass source sites.

$$\mathrm{TWPIm}_{tW} = \sum_{i} \mathrm{WPIm}_{itW} \quad \forall t, \ \forall W \tag{11}$$

$$\mathrm{TEPIm}_{tE} = \sum_{i} \mathrm{EPIm}_{itE} \quad \forall t, \forall E \tag{12}$$

$$\mathrm{TWSIm}_{tW} = \sum_{k} \mathrm{WSIm}_{ktW} \quad \forall t, \ \forall W \tag{13}$$

$$\mathrm{TESIm}_{tE} = \sum_{m} \mathrm{ESIm}_{mtE} \quad \forall t, \ \forall E \tag{14}$$

2. Eqs. (15, 16, 17, 18, 19, 20, and 21) present the constraints that calculate the amounts of "local biomass" that is distributed:
   - To the selected locality's conversion plants from that locality's biomass storages,
   - To the selected locality's biomass storages from that locality's biomass source sites.

$$\mathrm{TWPIn}_{tW} = \sum_{i} \mathrm{WPIn}_{itW} \quad \forall t, \ \forall W \tag{15}$$

$$\mathrm{WPIn}_{itW} = \sum_{k} \mathrm{WSPIn}_{kitW} \quad \forall i, \ \forall t, \ \forall W \tag{16}$$

$$\mathrm{TEPIn}_{tE} = \sum_{i} \mathrm{EPIn}_{itE} \quad \forall t, \ \forall E \tag{17}$$

$$\mathrm{EPIn}_{itE} = \sum_{m} \mathrm{ESPIn}_{mitE} \quad \forall i, \ \forall t, \ \forall E \tag{18}$$

$$\mathrm{TWSIn}_{tW} = \sum_{k} \mathrm{WSIn}_{ktW} \quad \forall t, \ \forall W \tag{19}$$

$$\mathrm{TESIn}_{tE} = \sum_{m} \mathrm{ESIn}_{mtE} \quad \forall t, \ \forall E \tag{20}$$

$$\mathrm{ESIn}_{mtE} = \sum_{e} \mathrm{EAIn}_{emtE} \quad \forall m, \ \forall t, \ \forall E \tag{21}$$

3. Eqs. ((22, 23, and 24) present the constraints that calculate the amounts of "exported biomass" that is distributed
   - To the other localities' conversion plants from the selected locality's biomass storages,
   - To the other localities' biomass storages from the selected locality's biomass source sites.

$$\mathrm{TWPEx}_{tW} = \sum_{k} \mathrm{WPEx}_{ktW} \quad \forall t, \ \forall W \tag{22}$$

$$\mathrm{TEPEx}_{tE} = \sum_{m} \mathrm{EPEx}_{mtE} \quad \forall t, \ \forall E \tag{23}$$

$$\mathrm{TESEx}_{tE} = \sum_{e} \mathrm{ESEx}_{etE} \quad \forall t, \ \forall E \tag{24}$$

4. Eqs. (25) and (26) present the constraints that calculate the amount of "local fertilizer" that is distributed to the selected locality's cultivated areas from the selected locality's conversion plants:

$$\mathrm{TFIn}_{t} = \sum_{i} \mathrm{FIn}_{it} \quad \forall t \tag{25}$$

$$\mathrm{FIn}_{it} = \sum_{f} \mathrm{FPIn}_{ift} \quad \forall i, \ \forall t \tag{26}$$

Eqs. (27) and (28) ensure that no more biomass is transported from a storage than what is actually available in that storage at the time of shipment:

$$\left(\sum_{i} \sum_{E} \mathrm{ESPIn}_{mitE} + \mathrm{EPEx}_{mtE} \right) + \mathrm{DSE}_{mt} = \left(\sum_{E} \mathrm{ESIn}_{mtE} + \mathrm{ESIm}_{mtE} \right) + \mathrm{DSE}_{m(t-1)} \quad \forall m, \ \forall t \tag{27}$$

$$\sum_{i} \mathrm{WSPIn}_{kitW} + \ \mathrm{WPEx}_{ktW} = \mathrm{WSIm}_{ktW} + \mathrm{WSIn}_{ktW} \quad \forall k, \ \forall t, \ \forall W \tag{28}$$

Eq. (29) limits the fertilizer distribution amount to fertilizer requirement of the areas:

$$\sum_{i} \mathrm{FPIn}_{ift} \leq \mathrm{CA}_{ft} {}^{*} V \quad \forall f, \ \forall t \tag{29}$$

Production and capacity constraints: Eq. (30) calculates the heat production amount in each plant for each time period:

$$\begin{aligned} &\left(\sum_{W} \mathrm{WPIm}_{itW} {}^{*} H1_{W}\right) + \left(\sum_{W} \mathrm{WPIn}_{itW} {}^{*} H1_{W}\right) \\ &+ \left(\sum_{E} \mathrm{EPIm}_{itE} {}^{*} H2_{E}\right) + \left(\sum_{E} \mathrm{EPIn}_{itE} {}^{*} H2_{E}\right) = \mathrm{OH}_{it} \forall i, \ \forall t \end{aligned} \tag{30}$$

Eq. (31) ensures that the total solid content of the biomass slurry in each plant must be between MinTS and MaxTS. This constraint also determines the amount of water required to satisfy the total solid content limits:

$$\mathrm{MinTS} \leq \frac{\left(\sum_{W} \mathrm{TS}_{W} {}^{*} (\mathrm{WPIm}_{itW} + \mathrm{WPIn}_{itW})\right) + \left(\sum_{E} \mathrm{TS}_{E} {}^{*} (\mathrm{EPIm}_{itE} + \mathrm{EPIn}_{itE})\right)}{\left(\sum_{W} \mathrm{WPIm}_{itW} + \mathrm{WPIn}_{itW}\right) + \left(\sum_{E} \mathrm{EPIm}_{itE} + \mathrm{EPIn}_{itE}\right) + \mathrm{W}_{it}} \leq \mathrm{MaxTS} \forall i, \quad \forall t \tag{31}$$

Eq. (32) limits the biomass handling of the plants to the maximum biomass handling capacity of the plant:

$$\begin{aligned} &\left(\sum_{W} \mathrm{WPIm}_{itW} + \mathrm{WPIn}_{itW}\right) + \left(\sum_{E} \mathrm{EPIm}_{itE} + \mathrm{ECPIn}_{itE}\right) \\ &\leq \sum_{c} \mathrm{PC}_{c} {}^{*} \mathrm{Y}_{ic} \quad \forall i, \ \forall t \end{aligned} \tag{32}$$

Storage number and capacity constraints: Eqs. (33) and (34) limit the waste storage number in the selected locality to the value determined by the regional-level model and ensure that only one energy crop storage is constructed in a crop storage location. Eqs. (35, 36, and 37) calculate the capacities of energy crop and waste storages and also limit the total biomass capacity of the storages:

$$\sum_{p} \mathrm{S}_{mp} \leq 1 \quad \forall m \tag{33}$$

$$\sum_{k} \mathrm{D}_k = \mathrm{XW} \tag{34}$$

$$\mathrm{DEC_t} = \sum_{m} \mathrm{DSE}_{mt} \quad \forall t \tag{35}$$

$$\left(\sum_{E} \mathrm{ESIn}_{mtE} + \mathrm{ESIm}_{mtE}\right) + \mathrm{DSE}_{mt} \leq \sum_{p} \mathrm{C}_p{}^{*}\mathrm{S}_{mp} \quad \forall m, \ \forall t \tag{36}$$

$$\left(\sum_{W} \mathrm{WSIn}_{ktW} + \mathrm{WSIm}_{ktW}\right) \leq \mathrm{MAXDC}^{*} D_k \quad \forall k, \ \forall t \tag{37}$$

Energy crop field constraints: This constraint set calculates the size of area to be used for energy crop cultivation in each arable empty area location e at time period t and limits this value to the total size of arable empty area in that location:

$$\sum_{e} \mathrm{A}_{et} \leq \mathrm{EAP}_t{}^{*}\mathrm{TEA}_t \quad \forall t \tag{38}$$

$$\sum_{m} \sum_{E} \mathrm{EAIn}_{emtE} + \mathrm{ESEx}_{etE} = \mathrm{A}_{et}{}^{*}\mathrm{VE}_t \quad \forall e, \ \forall t \tag{39}$$

$$\mathrm{A}_{et} \leq \mathrm{EA}_{et} \quad \forall e, \ \forall t \tag{40}$$

3 Case Study

As stated before, we use the application results of Yılmaz Balaman and Selim (2014) regional-level model.

The regional-level model was applied to all 20 counties of İzmir. Among these counties, we selected Kiraz as the local application area which means the model in the local design phase is applied to Kiraz, and the optimal configuration of the supply chain network with district heating system is obtained.

The number of candidate sites for anaerobic digestion plants, waste storage, and energy crop storage locations are 15, 10, and 10, respectively. There exist five locations including arable empty area for energy crop cultivation and five locations for cultivated agricultural area. Total sizes of agricultural and surplus arable areas in Kiraz are 26,000 da and 185,565 da, respectively. The length of the time period used in our computational experiments is 1 month, and the planning horizon is 1 year. The thermal energy produced by plants is assumed to be consumed in residential area in the centre of Kiraz, which is divided into ten heat demand nodes. The thermal energy is distributed from the energy station to the heat customers via insulated pipes. We obtain the data on average heat requirement of a household per m^2, which depend on the climatic conditions of the region and the season, by a literature survey on district heating system installations and by utilizing expert

opinion. For more detailed information about heat demand in different countries, Dong et al. (2012), Marinova et al. (2008), and Uhlemair et al. (2014) can be referred. Figure 1 presents the results of our computational experiments obtained by "modified fuzzy and" operator using six different γ values corresponding to six solution alternatives. At this stage, a sensitivity analysis is conducted to explore the impact of "coefficient of compensation" on the results.

In real-life decision problems, relative importance of the objectives assigned by the decision-makers may change according to decision-maker or over time. To provide a broader decision spectrum to decision-makers, the solutions are obtained by using three different relative weight combinations for the objectives (WCost and WUnmet Heat Demand). Any solution alternative can be selected as the best one concerning the priorities of the decision-maker on different supply chain performance indicators. In this regard, trade-offs among the alternative solutions need to be considered. If meeting heat demand of the demand nodes is more important than the cost objective for the decision-maker, then the weight structure of WCost = 0.25 and WUnmet Heat Demand = 0.75 can be considered.

In this case, one of the alternatives of third, fourth, fifth, and sixth ($\gamma = 0.6$, $\gamma = 0.4$, $\gamma = 0.2$, $\gamma = 0$) can be chosen where the unmet heat demand is 114,547 kWh/year. Among these alternatives, the sixth one ($\gamma = 0$) also satisfies the cost objective (€ 306,099). Among the solution alternatives for this weight structure, the second solution alternative $\gamma = 0.8$ offers the minimum cost but offers a high value for unmet heat demand (7,515,843kWh/year). If the decision-maker prefers the weight structure of WCost = 0.25 and WUnmet Heat Demand = 0.75, comparison of the results with $\gamma = 0$ and $\gamma = 0.8$ reveals that a 98.47% decrease in unmet heat demand can be attained with an 18% increase in cost.

If the objectives are equally important for the decision-maker, then the weight structure of WCost = 0.5 and WUnmet Heat Demand = 0.5 can be preferred. In this case, the second alternative with $\gamma = 0.8$ outperforms the other alternatives in terms of the cost value (€ 259,526), but it offers a high value for unmet heat demand (7,515,883 kWh/year). The fourth, fifth, and sixth alternatives ($\gamma = 0.4$, $\gamma = 0.2$, $\gamma = 0$) offer the minimum unmet heat demand (114,547 kWh/year) with the costs of € 306,442, € 305,929, and € 306,099, respectively. Among these alternatives, the sixth one ($\gamma = 0$) also satisfies the cost objective (€ 306,099). If the decision-maker prefers the weight structure of WCost = 0.5 and WUnmet Heat Demand = 0.5, comparison of the results with $\gamma = 0$ and $\gamma = 0.8$ reveals that a 98.47% decrease in unmet heat demand can be attained with an 18% increase in cost.

If minimization of the cost is more important than minimization of unmet heat demand, the decision-maker may chose the weight structure of WCost = 0.75 and WUnmet Heat Demand = 0.25. Hence, the fourth alternative ($\gamma = 0.4$) with the smallest value for WCost can be treated as the best solution. In this case, the cost, which is sum of district heating system and local transportation costs, is € 259,526. In addition, the unmet heat demand is 7,515,849 kWh/year in this alternative. The sixth alternative ($\gamma = 0$) offers the minimum unmet heat demand (114,547 kWh/year), whereas the cost is € 305,922. If the decision-maker prefers the weight structure of WCost = 0.75 and WUnmet Heat Demand = 0.25, comparison of the

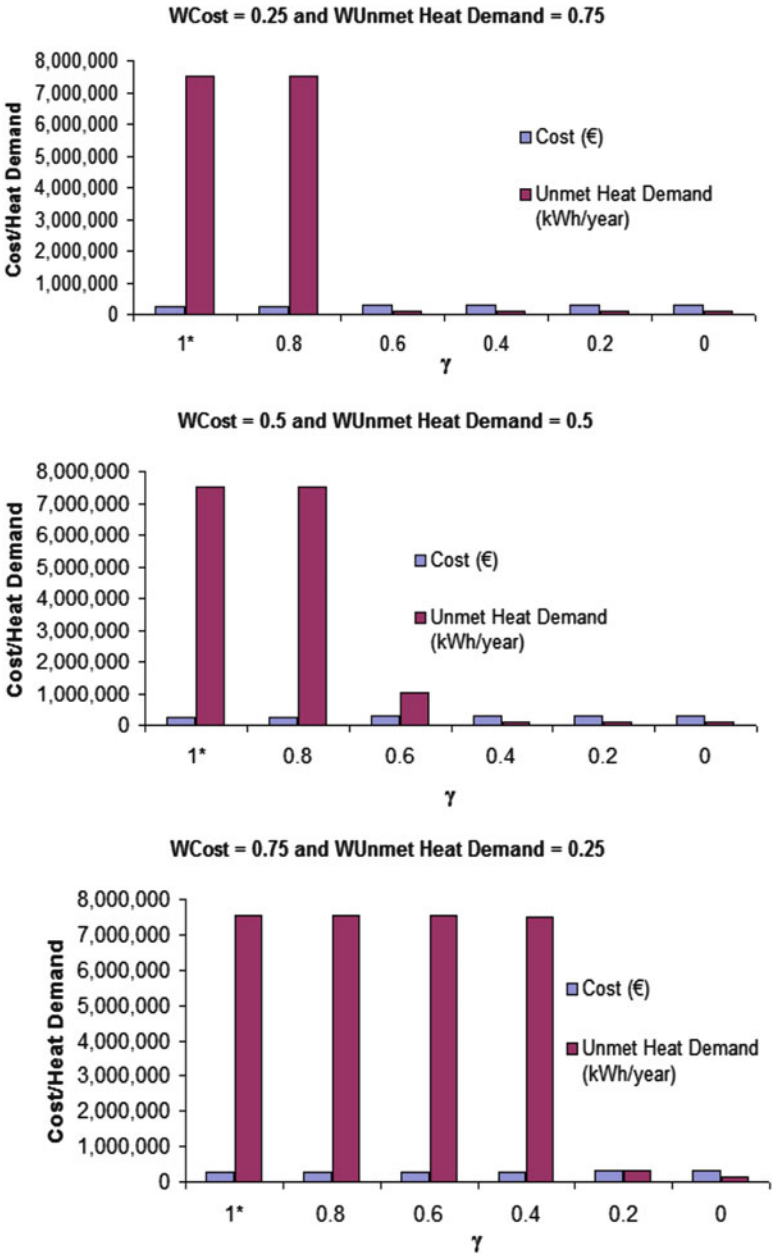

Fig. 1 The results of computational experiments

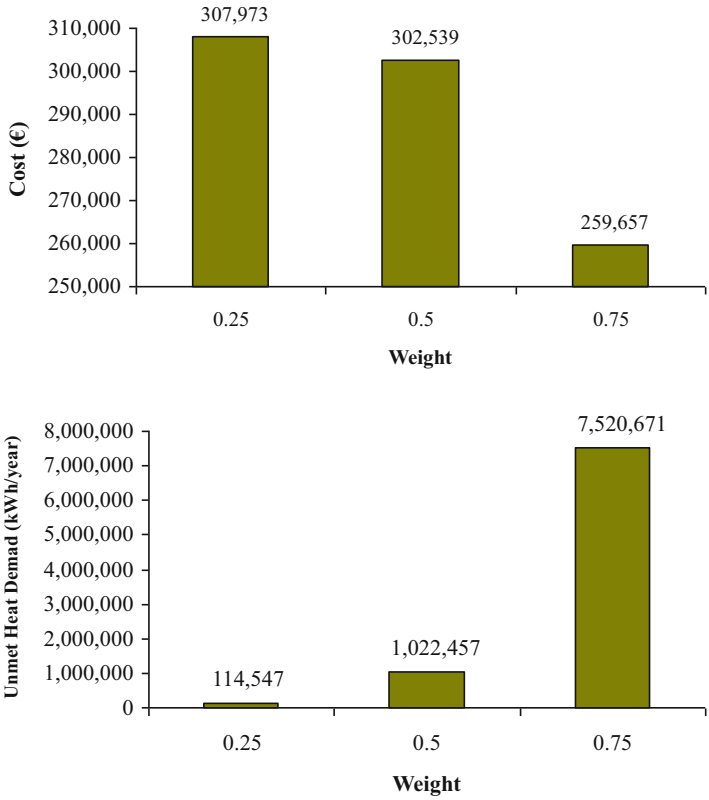

Fig. 2 Changes in the cost and unmet demand values corresponding to $\gamma = 0.6$ with three different weight structures

results with $\gamma = 0$ and $\gamma = 0.4$ reveals that a 98.47% decrease in unmet heat demand can be attained with a 17.8% increase in cost.

Let us suppose that the decision-makers accept the results of the model with $\gamma = 0.6$. The changes in the cost and unmet demand values corresponding to $\gamma = 0.6$ with three different weight structures can be observed in Fig. 2.

4 Summary and Conclusions

This study deals with effective design and management of comprehensive local biomass to energy supply chain networks integrated with district heating systems by considering inherent uncertainties. In this regard, a DSS is developed to make strategic and tactical decisions for design and management of sustainable and efficient biomass to energy supply chains, under the condition of limited and seasonally variable resources and fluctuations in the system parameters caused by

unstable economic, environmental, and social policy actions and natural conditions. The proposed DSS employs FGP as the solution approach.

Once the numbers and capacities of the plants and storages are obtained and logistics decisions are made in the regional-level bioenergy supply chain design, the proposed local-level model is utilized to obtain comprehensive design of the local biomass to energy supply chain network along with district heating system for the selected locality. Besides the decisions related to the spatial and logistical structures of the local supply chain network, allocation of heat demand nodes to plants in terms of heat transmission and heat production/storage decisions is made for each plant in the selected locality through the proposed model. The aim of the proposed local-level design model is to minimize local transportation costs for local bioenergy supply chains, which constitute the regional supply chain, and maximize the service level which is the level of meeting heat demand of the residential area in the handled local part of the regional supply chain.

References

Akgül, O., Shah, N., Papageorgiou, L.G.: Economic optimisation of a UK advanced biofuel supply chain. Biomass Bioenergy. **41**, 57–72 (2012)

Ayoub, N., Seki, H., Naka, Y.: Superstructure-based design and operation for biomass utilization network. Comput. Chem. Eng. **3**, 1770–1780 (2009)

Dong, M., He, F., Wei, H.: Energy supply network design optimization for distributed energy systems. Comput. Ind. Eng. **63**(3), 546–552 (2012)

Ekşioğlu, S.D., Acharya, A., Leightley, L.E., Arora, S.: Analyzing the design and management of biomass-to-biorefinery supply chain. Comput. Ind. Eng. **57**, 1342–1352 (2009)

Giarola, S., Bezzo, F., Shah, N.: A risk management approach to the economic and environmental strategic design of ethanol supply chains. Biomass Bioenergy. **58**, 31–51 (2013)

Kanzian, C., Kühmaier, M., Zazgornik, J., Stampfer, K.: Design of forest energy supply networks using multi-objective optimization. Biomass Bioenergy. **58**, 294–302 (2013)

Marinova, M., Beaudry, C., Taoussi, A., Trépanier, M., Paris, J.: Economic assessment of rural district heating by bio-steam supplied by a paper mill in Canada. Bull. Sci. Technol. Soc. **28**, 159–173 (2008)

Marufuzzaman, M., Eksioglu, S.D., Huang, Y.: Two-stage stochastic programming supply chain model for biodiesel production via waste water treatment. Comput. Oper. Res. **49**, 1–17 (2014)

Osmani, A., Zhang, J.: Economic and environmental optimization of a large scale sustainable dual feedstock lignocellulosic-based bioethanol supply chain in a stochastic environment. Appl. Energy. **114**, 572–587 (2014)

Uhlemair, H., Karschin, I., Geldermann, J.: Optimizing the production and distribution system of bioenergy villages. Int. J. Prod. Econ. **147**, 62–72 (2014)

Yılmaz Balaman, S., Selim, H.: A fuzzy multiobjective linear programming model for design and management of anaerobic digestion based bioenergy supply chains. Energy. **74**, 928–940 (2014)

Kinetic Study of Plastic Wastes with and Without Catalysts

Emna Berrich Betouche and Mohand Tazerout

1 Introduction

Energy valorization from thermoplastic wastes to produce "considerable quantities" of a "good-quality" fuel is still an actual aim. In 2009, France produced 1.65 million tons of plastic wastes which take one to four centuries to be decomposed in nature. France recycled 18% and processed about 37% by energy valorization. The remaining 45% is landfilled. "Recovery" in the field of plastic production in France is only 20% against 44% for glass or 60% for paper and cardboard. One ton of energetic valorized plastic could yet "save" 830 l of oil. Compliance with environmental standards and minimizing energy costs of fuel production processes require the development of an optimal energy process for plastic wastes recycling to produce fuels. This process should be reliable and least expensive (in raw material, energy consumption, and production time, etc.).

Pyrolysis process is based on the thermal degradation of an organic compound to obtain (gas, liquid, solid). It is performed in the absence of oxygen or oxygen-deficient atmosphere to prevent oxidation and combustion. It enables us to obtain a

E.B. Betouche (✉)
Department Energetic systems and Environment, Laboratory CNRS, GEPEA,UMR6144 Engineering school École des Mines de Nantes, 4 rue Alfred KASTLER, BP20722, 44307 Nantes, France

Department of Physique, LUNAM Université, Université de Nantes, Faculté des Sciences et des Techniques, 2, rue de la Houssinière BP, 92208-44322 Nantes, France
e-mail: emna.berrich@univ-nantes.fr

M. Tazerout
Department Energetic systems and Environment, Laboratory CNRS, GEPEA,UMR6144 Engineering school École des Mines de Nantes, 4 rue Alfred KASTLER, BP20722, 44307 Nantes, France

© Springer International Publishing AG, part of Springer Nature 2018

F. Aloui, I. Dincer (eds.), *Exergy for A Better Environment and Improved Sustainability 2*, Green Energy and Technology,
https://doi.org/10.1007/978-3-319-62575-1_25

carbonaceous solid, liquid (fuel), and gas. It begins at a relatively low level of temperature and can be continued up to approximately 800 °C depending on the primary material and the operating conditions. Different transformations occur simultaneously depending on different parameters.

The most widely used catalysts for catalytic conversion of plastic polymers to chemical products and fuels are zeolite ZSM-5 (Miskolczi et al. 2004), ZSM-2 (Covarrubiasa et al. 2010), $BaCO_3$ (Jan et al. 2010), bimetallic catalyst Al-Zn composite (Tang et al. 2003), commercial FCC (Lin et al. 2010; Miskolczi et al. 2006), SO_3 (Almustapha and Andresen 2011), and ZnO, MgO, CaC_2, SiO_2, Al_2O, and mixture of SiO_2 and Al_2O_3 (Shah et al. 2010). However, most of these catalysts need either high cost of production or an operating mode which may not be industrially feasible due to high degradation temperature and/or high residence time with low conversion rate.

"Free" catalysts are obtained from shells because they generally contain $CaCO_3$ as a main Ca-based component. The high temperature range above 700 °C is required to transform $CaCO_3$ to CaO catalyst. The temperature of 800 °C was thus selected as a suitable condition to produce CaO catalyst from shells according to preparation time and energy consumption (Viriya-empikul et al. 2010).

Nomenclature

A	: Pre-exponential factor (s^{-1})
T	: Temperature (°C)
m	: Weight (kg)
x	: Conversion rate
Subscripts	
Ea	: Activation energy (kJ/mol)
TGA	: Thermogravimetric analysis

2 Experimental Facility and Thermogravimetric Analysis

Thermogravimetry is a technique for measuring the mass variation of a sample when it is subjected to a temperature program in a controlled atmosphere. This variation can be a loss of mass (vapor transmission) or weight gain (fixing gas oxidation), the measures used to monitor the decomposition of the substance and evaluate their thermal stability.

This analysis provided critical thresholds during the thermal decomposition of the plastic and the typical range for thermal mass loss. Furthermore, the thermogravimetric analysis (TGA) provides information according to the following reaction conditions: the inert gas flow rate, heating rate, and the final reaction temperature set initially.

Fig. 1 Experimental installation

Table 1 Operating conditions

Period	Initial T(°C)	Final T (°C)	Residence time (s)	Heat rate (°C/mn)
1	25	25	300	
2	25	550	6300	5
3	550	550	5400	

The essential elements to be defined for the study of plastic are optimal temperature plastic decomposition, the initial temperature of decomposition, pic-temperature corresponding to the maximum degradation temperature, the conversion rate, the variation of the proportions, or nature of catalysts.

The equipment used for the analysis (Fig. 1) is the SETSYS Evolution. This is composed of an integrated structure: the controller, the furnace, gas and piloting systems, the security features, a measuring head, and thermogravimetry (TG). The structure can accommodate various measurement heads and a multitasking SETSOFT software controlling one or more appliances.

Catalysts used are the commercial zeolite (as a reference catalyst): zeolite ZSM-5 (10%), ZSM-5 (20%), oysters' shell (10%), oysters' shell (20%), eggs' shell (10%), eggs' shell (20%), and blends of oysters' shell (10%) with eggs' shell (10%). Experiments were conducted under N_2 atmosphere at heating rate of 5 °C/min from room temperature to 500–550 °C (Table 1) and then a heating for 30 min or 90 min at constant temperature 500 °C, 525 °C, or 550 °C. A first-order decomposition reaction was assumed (Khaghanikavkani and Farid 2011; Zhou et al. 2009).

3 Kinetic Analysis

The kinetic study of the decomposition of the plastic was determined using data from the thermogravimetric analysis. The parameters of the kinetic analysis are the activation energy and pre-exponential factors. These parameters were determined by the fact that the thermal decomposition of the polymers usually takes this form:

A(solid) → B(volatil) + C(solid)

The polymer degradation rate is generally proportional to the concentration of reactants; there was thus eq. (1) (Almustapha and Andresen 2011):

$$r = -\frac{dx}{dt} = kf(x) \tag{1}$$

where x is the conversion rate:

$$x = \frac{m_i - m_0}{m_i - m_f} \tag{2}$$

and m_0, m_i, and m_f are, respectively, the actual, initial, and final weights:

$$f(\alpha) = (1-\alpha)^n \tag{3}$$

Using Arrhenius law:

$$k = Ae^{-\frac{E_a}{RT}} \rightarrow \frac{dx}{dT} = kf(x) = Ae^{-\frac{E_a}{RT}}(1-x)^n \tag{4}$$

For a fixed heat rate β:

$$\beta = \frac{dT}{dt} \rightarrow \frac{dx}{dt} = \frac{A}{\beta}Ae^{-\frac{E_a}{RT}}(1-x)^n \tag{5}$$

The integration of the equations gives:

$$\frac{1-(1-x)^{1-n}}{1-n} = \frac{A}{\beta}\int_0^T Ae^{-\frac{E_a}{RT}}dT \tag{6}$$

However, as $\int_0^T Ae^{-\frac{E_a}{RT}}dT$ is not an exact primitive, $e^{-\frac{E_a}{RT}}$can be assumed to an asymptotic series and integrated:

$$\frac{1-(1-x)^{1-n}}{T^2(1-n)} = \frac{ART^2}{\beta E}\left[1-\frac{2RT}{E}\right]e^{-\frac{E_a}{RT}} \tag{7}$$

Thus:

$$\ln\left[\frac{1-(1-x)^{1-n}}{T^2(1-n)}\right] = \ln\left[\frac{ART^2}{\beta E}\left[1-\frac{2RT}{E}\right]\right] - \frac{E_a}{RT} \tag{8}$$

As $RT/E \approx 1$ and $1 - \frac{2RT}{E} \approx 1$, we can write:

$$\ln\left[\frac{1-(1-x)^{1-n}}{T^2(1-n)}\right] = \ln\left[\frac{AR}{\beta E}\right] - \frac{E_a}{RT}\,(n \neq 1) \tag{9}$$

$$\ln\left[\frac{-\ln(1-x)}{T^2}\right] = \ln\left[\frac{AR}{\beta E}\right] - \frac{E_a}{RT}\,(n = 1) \tag{10}$$

The energy activation and the pre-exponential factor can thus be determined.

4 Results and Discussions

4.1 Effect of Zeolite Catalyst on Kinetic Parameters of PE Degradation

The activation energy corresponds to the minimum necessary energy needed so that the reaction takes place, while the pre-exponential factor corresponds to the collision frequency between molecules. The calculated overall activation energy and the pre-exponential factor of HDPE are 241.6 kJ/mol and 3 10^6 (1/s) for the operation conditions of 20 ml/min of N_2, heat rate of 5 °C/mn from 25 to 525 °C, and then heating at constant temperature of 525 °C for 30 min. Comparing our results to Khaghanikavkani and Farid (2011), for 15.5 mg of HDPE, under isothermal conditions at three temperatures (477 °C, 466 °C, and 455 °C), in the presence of 0.7 l/min of N_2, they found an activation energy and a pre-exponential factor of 113.17 kJ/mol and 4.85 10^5 (s^{-1}). Almustapha and Andresen (2011) conducted TG analysis to study the catalytic degradation of HDPE. They found that HDPE degradation begins at about 420 °C with only 3% at 460 °C for a heating rate of 10 °C/min and a nitrogen flow rate of 20 ml/min. The sample is weighed between 20 and 30 mg. The activation energy and the frequency factor are, respectively, equal to 342.95 kJ/ mol and 5.22 10^{19} s^{-1}. Their low conversion rate and their relatively high-frequency factor are maybe caused by the plastic particle size which was between 125 and 150 micron. Co-pyrolysis behaviors of HDPE and LDPE were investigated by Zhou et al. (2009) using TGA. They found that, for a nitrogen flow rate of 30 ml/min and a heating rate of 20 °C/min from room temperature to 750 °C, the degradation temperature range is 439–523 °C for HDPE and

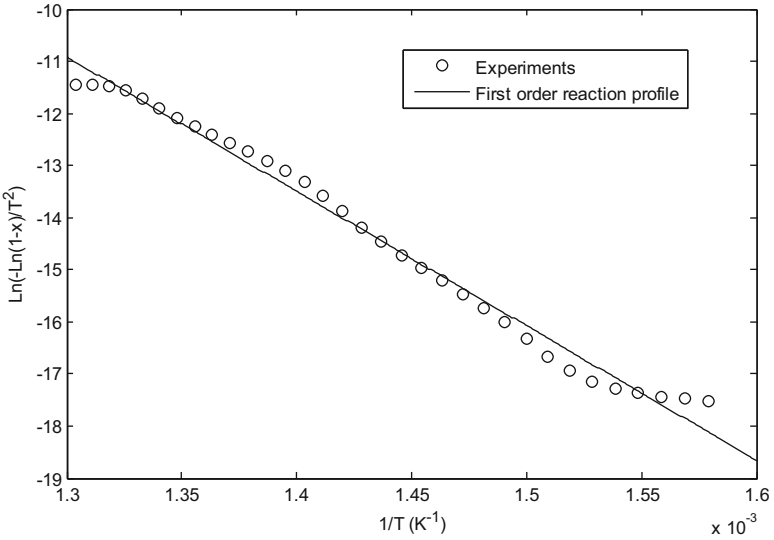

Fig. 2 Plots of $\mathrm{Ln}(-\mathrm{Ln}(1-x)/T^2)$ vs. $1/T$ of PE 90% + ZSM-5 10%

426–526 °C for LDPE with a conversion rate, respectively, of 97% and 99%. The activation energy and the pre-exponential factor are equal to 457.2 kJ /mol and 3.5 10^{30} s^{-1} for HDPE and 300.4 kJ /mol and 2.2 10^{20} s^{-1} for LDPE. The sample is weighed 5 mg. The particle size was lesser than 500 µm. Thus, the distribution particle size has an important effect on the activation energy and the pre-exponential factor even for approximately the same operating conditions.

Figure 2 presents the evolution of $\mathrm{Ln}(-\mathrm{Ln}(1-x)/T^2)$ vs. 1/T of PE 90% + ZSM-5 10%). It can be seen that the pyrolysis process can be described by one first-order reaction. The activation energy and the pre-exponential factor for HDPE with zeolite as catalyst (PE 90% + ZSM-5 10%) are 216.6 kJ/mol and 3 10^6 (1/sec), while they are equal to 84.7 kJ/mol and 3.47 10^4 (1/s) for PE 80% + ZSM-5 20% if we consider that the global pyrolysis process can be described by one first-order reaction (Fig. 3). However, the evolution of $\mathrm{Ln}(-\mathrm{Ln}(1\text{-}x)/T^2)$ vs. 1/T is a quadratic one. Thus, we opted for Zhou et al. (2009) who described the pyrolysis processes of LVC-LDPE and LVC-HDPE blends as a series of consecutive first-order reactions. So we tried one and then two independent first-order reactions to describe the plastic pyrolysis catalyzed by ZSM-5. The (PE 80% + ZSM-5 20%) pyrolysis can be described by two consecutive first-order reactions (Fig. 4). The activation energy decreases while using catalysts. Twenty percent of zeolite as catalyst can reduce the activation energy more than the half. The pre-exponential factor characterizes the "disorder" generated by the thermal decomposition, i.e., it is proportional to the frequency of collisions between molecules. This factor can be reduced if the catalyst proportion is considerable.

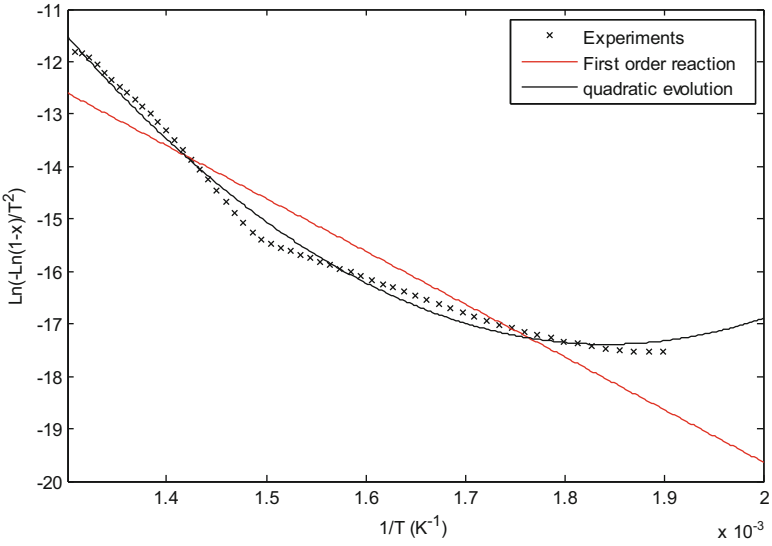

Fig. 3 Plots of $\mathrm{Ln}(-\mathrm{Ln}(1-x)/T^2)$ vs. $1/T$ of PE 80% + ZSM-5 20%

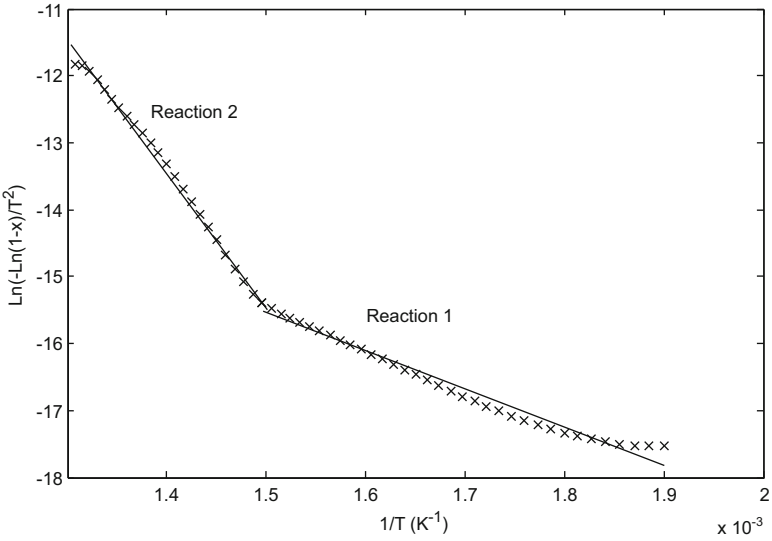

Fig. 4 Plots of $\mathrm{Ln}(-\mathrm{Ln}(1-x)/T^2)$ vs. $1/T$ of PE 80% + ZSM-5 20%: consecutive first-order reactions

This interception point between the two first-order reaction profiles corresponds to a temperature $T = 395.3°\mathrm{C} \pm 5°\mathrm{C}$ which is the maximum pyrolysis temperature. For the first reaction which takes place from $T = 253$ °C to Tpic, the $Ea_1 = 47.40$ kJ/mol and $A_1 = 19.95\ 10^4$ (1/s), while for the second reaction

which takes place form T peak to the temperature at the end of the thermal degradation = 494 °C, Ea_2 = 166.37 kJ/mol and A_2 = 140 10^4 (1/s).

4.2 *Effect of Oysters' Shell on Kinetic Parameters of PE Degradation*

Oyster shell is mainly composed of calcium carbonate $CaCO_3$ and a conchyoline matrix. It was tested as a catalyst on the pyrolysis process of PE. The thermal degradation range of (PE 90% + oysters' shell 10%) is 394–512 °C and of (PE 80% + oysters' shell 20%) is 378–503 °C. The maximum degradation temperature is, respectively, 484 °C for PE 90% + oysters' shell 10% and 480 °C for PE 80% + oysters' shell 20%.

The activation energy and the pre-exponential factor are 202.4 kJ/mol and 2.26 106 (1/s) for PE 90% + oysters' shell 10% for 20 ml/min of N_2, at a heat rate of 5 °C/mn from 25 to 550 °C and then heating at constant temperature, if the pyrolysis process is described as a first-order reaction (Fig. 5). However, it can be described by two successive first-order reactions.

The intersection point between the two profiles corresponds to T = 436 °C which is lesser than the T_{peak}. For the first reaction which takes place from T = 394 °C to 436, the Ea_1 = 58.5 kJ/mol and A_1 = 24.18 10^4 (1/s), while the second reaction takes place from 436 to 512 °C with Ea_2 = 355.85 kJ/mol and A_2 = 9.28 10^6 (1/s) (Fig. 6).

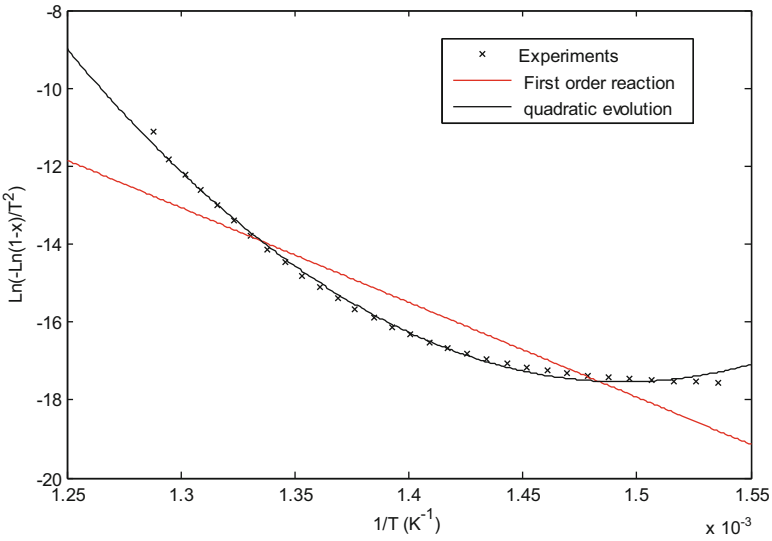

Fig. 5 Plots of Ln(−Ln(1−x)/T^2) vs. 1/T of PE 90% + oysters' shell 10%

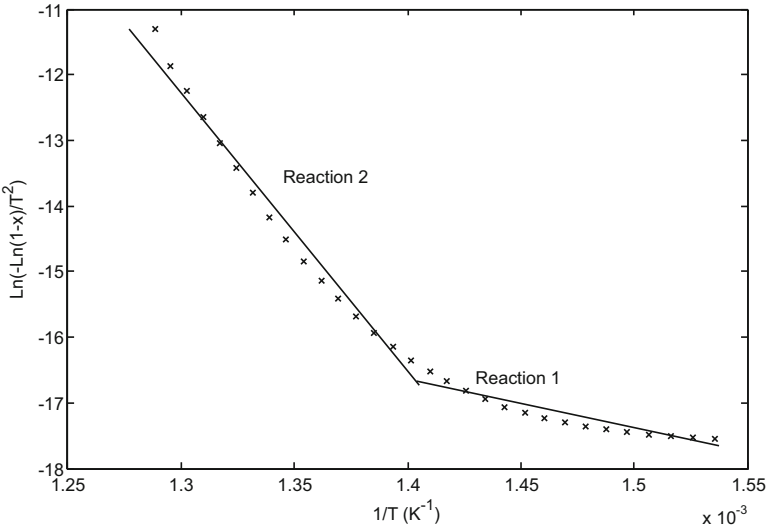

Fig. 6 Plots of $\mathrm{Ln}(-\mathrm{Ln}(1-x)/T^2)$ vs. $1/T$ of PE 90% + oysters' shell 10%: consecutive first-order reactions

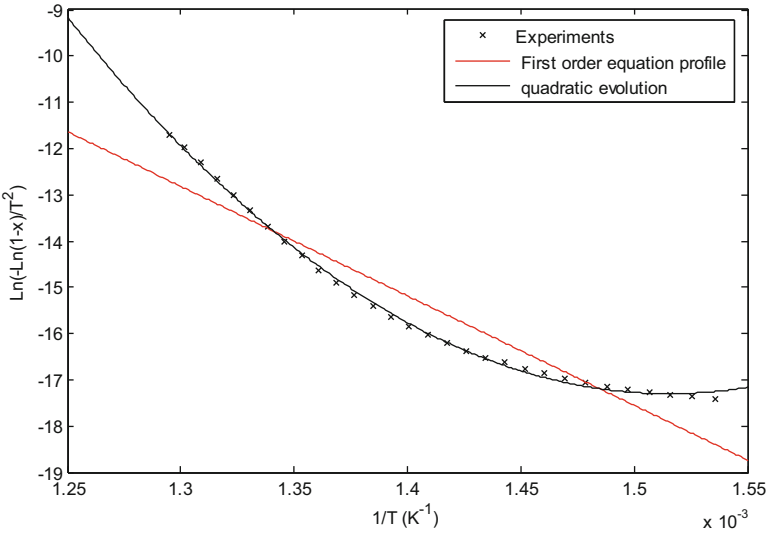

Fig. 7 Plots of $\mathrm{Ln}(-\mathrm{Ln}(1-x)/T^2)$ vs. $1/T$ of PE 80% + oysters' shell 20%

The intersection point between the two profiles of the two successive first-order reactions describing the pyrolysis process of (PE 80% + oysters' shell 20%) (Figs. 7 and 8) corresponds to $T = 436$ °C which is the same intersection

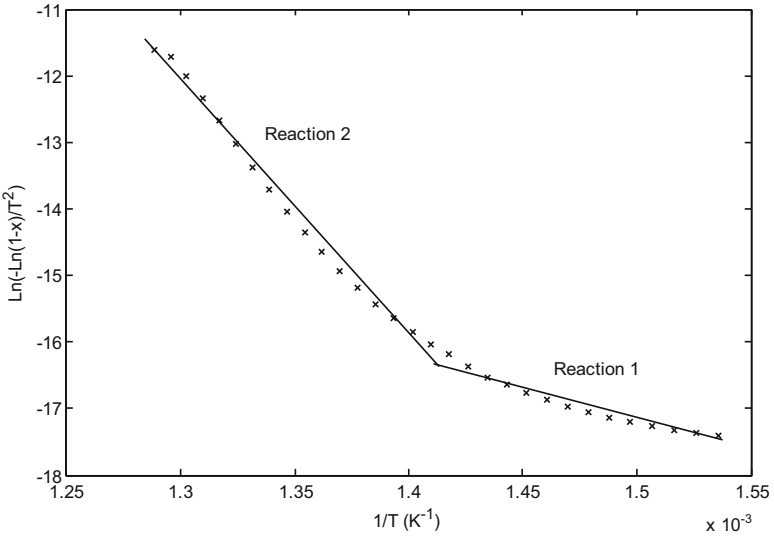

Fig. 8 Plots of $\mathrm{Ln}(-\mathrm{Ln}(1-x)/T^2)$ vs. $1/T$ of PE 80% + oysters' shell 20%: consecutive first-order reactions

temperature point of the blend (PE 90% + oysters' shell 10%). This temperature is lesser than the maximum temperature degradation of (PE 80% + oysters' shell 20%) which is equal to 480 °C.

4.3 Effect of Eggs' Shell on Pyrolysis Process

The evolution of weight losses (TG) and its derivative (dTG) vs. the temperature for HDPE (pellet) with eggs' shell is, respectively, shown in Figs. 9 and 10 (PE 90% + eggs' shell 10%) and in Figs. 11 and 12 (PE 80% + eggs' shell 20%). The results proved that the thermal degradation temperature range (PE 90% + eggs' shell 10%) is 387–512 °C. For the blend (PE 80% + eggs' shell 20%), TG profile illustrates that the pyrolysis reaction starts at 248 °C for a heat rate of 5 °C/min and that the reaction is almost complete at 530 °C. The maximum degradation temperature corresponds to the peak of the dTG profile function of the temperature, i.e., the red point on the curves of Figs. 10 and 12. It is equal to 481 °C for PE 90% + eggs' shell 10% and 479 °C for PE 80% + eggs' shell 20%. The eggs' shell decreases the maximum temperature needed to have a good conversion rate. The conversion rates are more than 99%.

The plots of $\mathrm{Ln}(-\mathrm{Ln}(1-x)/T^2)$ vs. $1/T$ of PE 90% + eggs' shell 10% and PE 80% + eggs' shell 20% are shown in Figs. 13 and 14. They prove that the pyrolysis process does correspond neither to one first-order reaction equation nor to a

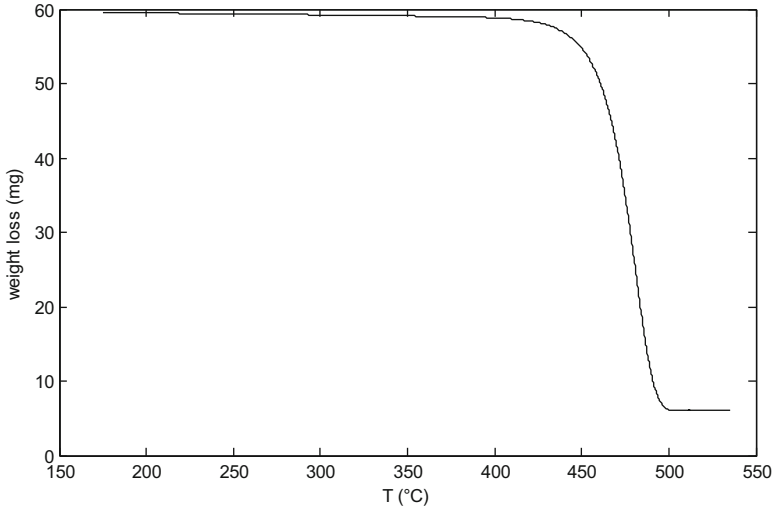

Fig. 9 Plots of weight losses (TG) and its derivative dTG function of temperature for PE 90% + eggs' shell 10%

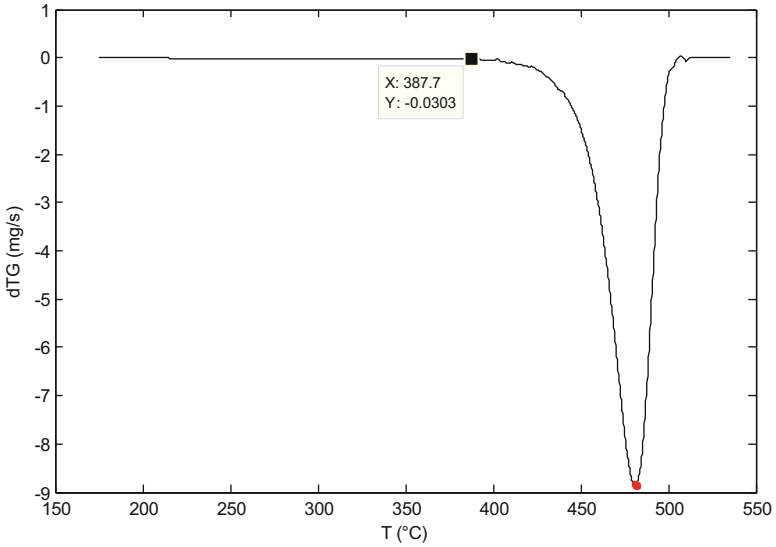

Fig. 10 Weight losses and derivative dTG function of temperature for PE 90% + eggs' shell 10%

quadratic evolution. The pyrolysis process can be described by a three consecutive first-order reactions for PE 90% + eggs' shell 10% (Fig. 15) and four consecutive first-order reactions for PE 80% + eggs' shell 20% (Fig. 16).

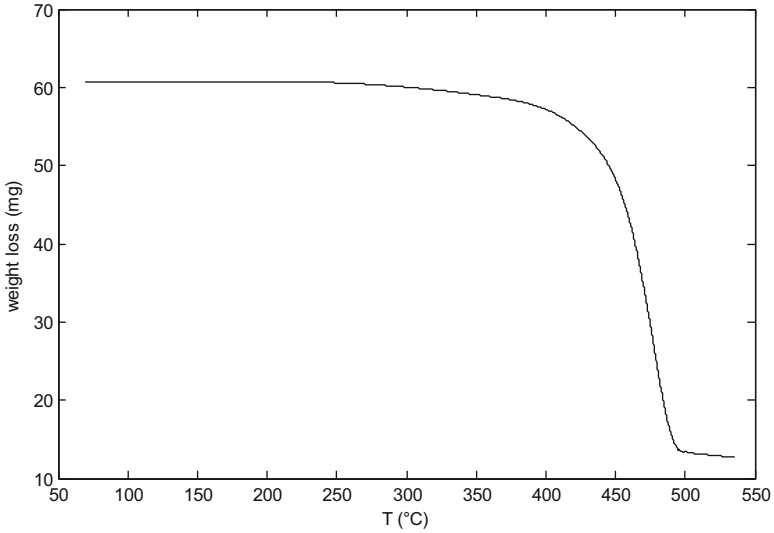

Fig. 11 Plots of weight losses (TG) and its derivative dTG function of temperature for PE 80% + eggs' shell 20%

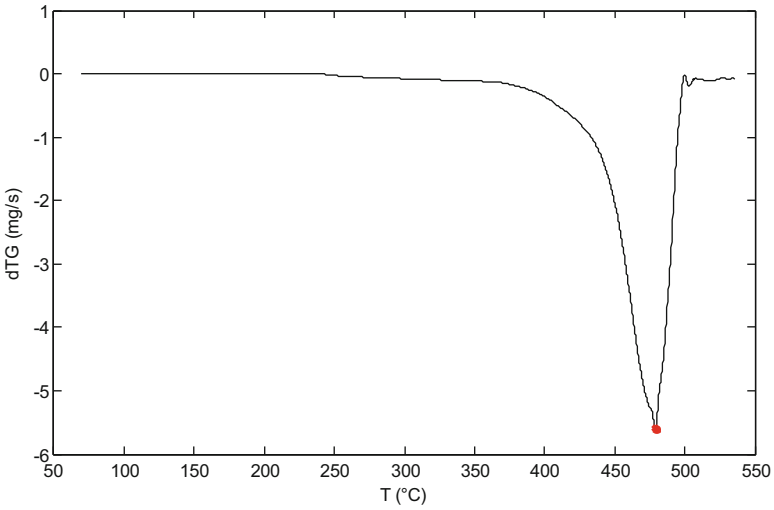

Fig. 12 Weight losses and derivative dTG function of temperature for PE 80% + eggs' shell 20%

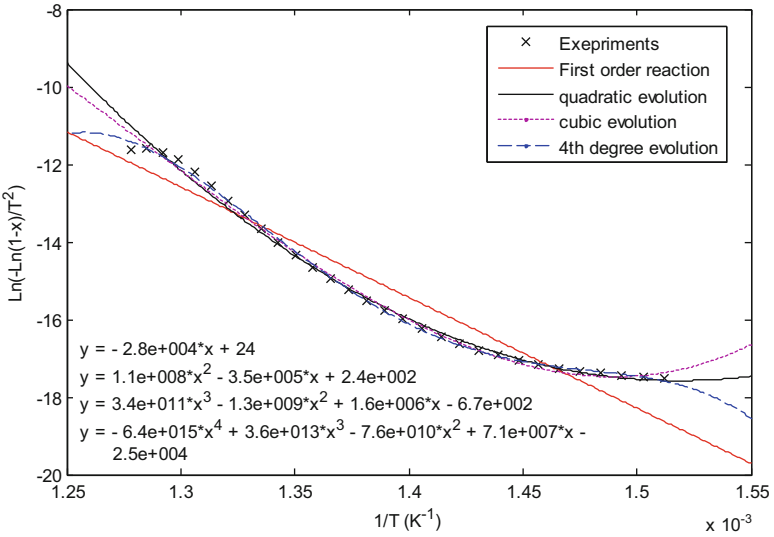

Fig. 13 Plots of $\mathrm{Ln}(-\mathrm{Ln}(1-x)/T^2)$ vs. $1/T$ of PE 90% + eggs' shell 10%

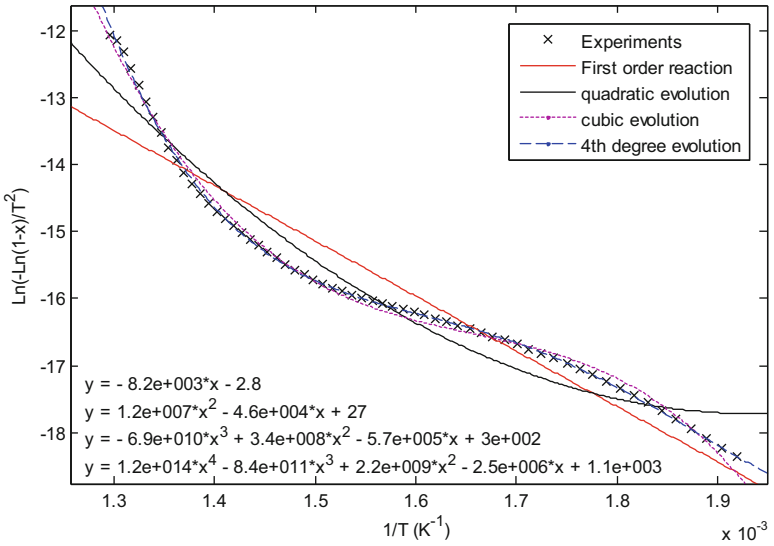

Fig. 14 Plots of $\mathrm{Ln}(-\mathrm{Ln}(1-x)/T^2)$ vs. $1/T$ of PE 80% + eggs' shell 20%

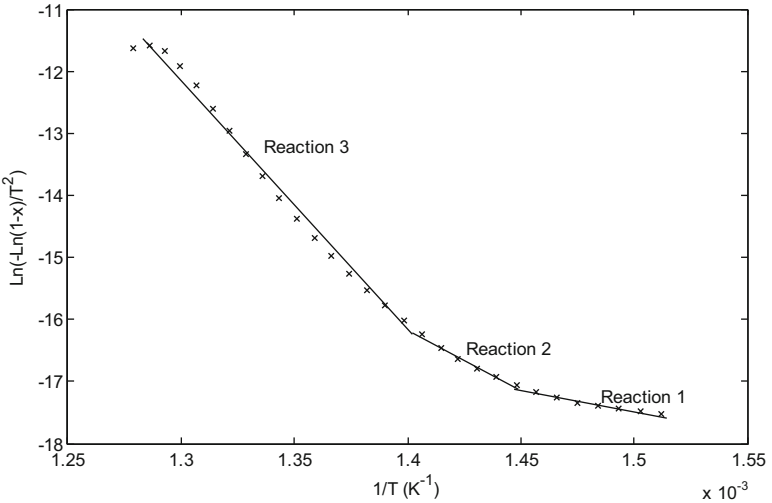

Fig. 15 Plots of $\mathrm{Ln}(-\mathrm{Ln}(1-x)/T^2)$ vs. $1/T$ of PE 90% + eggs' shell 10%: consecutive first-order reactions

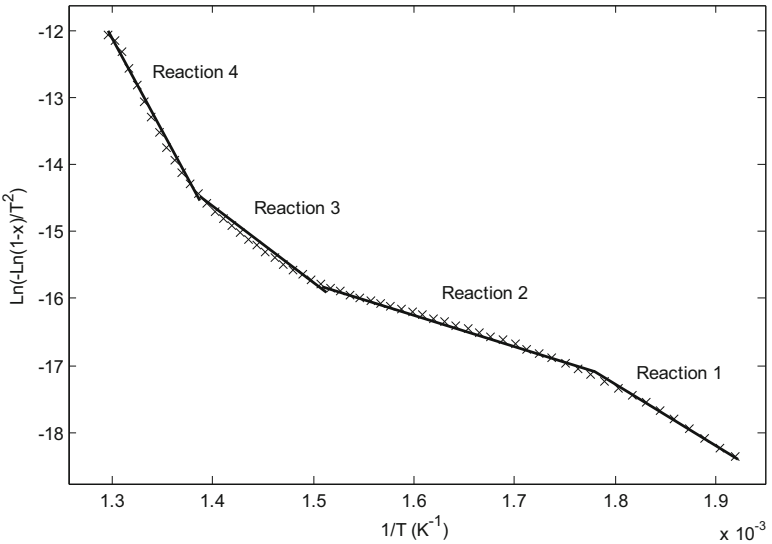

Fig. 16 Plots of $\mathrm{Ln}(-\mathrm{Ln}(1-x)/T^2)$ vs. $1/T$ of PE 80% + eggs' shell 20%: consecutive first-order reactions

5 Conclusions

The kinetic parameters strongly depend on operating conditions, especially on the catalyst nature and quantities. According to these two parameters and under the same operating parameters (temperature range of heat, heat rate, nitrogen rate), the pyrolysis process can be described by one first-order reaction or consecutive two, three, or four first-order reactions. The activation energy and the pre-exponential factor were determined for every case. The activation energy generally decreases while using catalysts. For example, 20% of zeolite as catalyst can reduce the activation energy more than the half. The pre-exponential factor characterizes the "disorder" generated by the thermal decomposition due to the frequency of collisions between molecules. This factor can be reduced if the catalyst proportion is considerable.

References

Almustapha M.N., Andresen J.M., Catalytic conversion of high density polyethylene (HPE) polymer as a mean of recovering valuable energy content from the plastic wastes, IPCBEE, 21 (2011).

Covarrubiasa, C., Graciab, F., Palza, H.: Catalytic degradation of polyethylene using nanosized ZSM-2 zeolite. Appl. Catal. A Gen. **384**, 186–191 (2010)

Jan, M.R., Shah, J., Gulab, H.: Catalytic degradation of waste high-density polyethylene into fuel products using BaCO3 as a catalyst. Fuel Process. Technol. **91**, 1428–1437 (2010)

Khaghanikavkani, E., Farid, M.M.: Thermal pyrolysis of polyethylene: Kinetic study. Energy Science and Technology. **2**(1), 1–10 (2011)

Lin, Y.H., Yang, M.H., Wei, T.T., Hsu, C.T., Wu, K.J., Lee, S.L.: Acid-catalyzed conversion of chlorinated plastic waste into valuable hydrocarbons over post-use commercial FCC catalysts. J. Anal. Appl. Pyrolysis. **87**, 154–162 (2010)

Miskolczi, N., Bartha, L., Deák, G., Jóver, B., Kalló, D.: Thermal and thermo-catalytic degradation of high-density polyethylene waste. J. Anal. Appl. Pyrolysis. **72**, 7 (2004)

Miskolczi, N., Bartha, L., Deak, G.: Thermal degradation of polyethylene and polystyrene from the packaging industry over different catalysts into fuel-like feed stocks. Polym. Degrad. Stab. **91**, 517–526 (2006)

Shah, J., Jan, M.R., Mabood, F., Jabeen, F.: Catalytic pyrolysis of LDPE leads to valuable resource recovery and reduction of waste problems. Energy Convers. Manag. **51**, 2791–2801 (2010)

Tang, C., Wang, Y.Z., Zhou, Q., Zheng, L.: Catalytic effect of Al-Zn composite catalyst on the degradation of PVC containing polymer mixtures into pyrolysis oil. Polym. Degrad. Stab. **2003** (81), 89–94 (2003)

Viriya-empikul, N., Krasae, P., Puttasawat, B., Yoosuk, B., Chollacoop, N., Faungnawakij, K.: Waste shells of mollusk and egg as biodiesel production catalysts. Bioresour. Technol. **101**, 3765–3767 (2010)

Zhou, L., Luo, T., Huang, Q.: Co-pyrolysis characteristics and kinetics of coal and plastic blends. Energy Convers. Manag. **50**, 705–710 (2009)

Effect of Ballast Water on Marine Ecosystem

Hacer Saglam and Ertug Duzgunes

1 Introduction

Modern shipping cannot operate without ballast water, which provides balance and stability to unladen ships. Shipping has a share about 90% of world trade in volume and a mere 10 billion tons of ballast water globally transferred annually from one place to another. However, it may also cause serious ecological, economic, and health threats (IMO 2010).

Introduction of invasive aquatic species to the new environment by ballast water, attaching to hulls and via other vectors has been identified as one of the four greatest threats to the world's oceans. The other three are land-based sources of marine pollution, overexploitation of marine living resources, and physical alteration/destruction of marine habitat (Raj 2014).

In major oil spills, the ecological impacts are the most likely to occur very fast, be catastrophic and acute, and highly visible. However, impacts will decrease over time as the oil degrades and cleanup and rehabilitation activities are undertaken. In aquatic bio-invasion, the initial impacts may be nonexistent to minor and invisible. However, as the population increases, the impacts will increase over time, in an insidious, chronic, and irreversible manner (Fig. 1) (Raaymakers 2002).

Shipping is one of the sources of transfer of non-native aquatic organisms. Ballast water acts as a vector for such organisms while at the same time being absolutely essential to the safe and efficient operation of ships at present (IMO 2013).

H. Saglam (✉) • E. Duzgunes
Karadeniz Technical University Faculty of Marine Science, Camburnu, Trabzon 61530, Turkiye
e-mail: hacersaglam@yahoo.com

© Springer International Publishing AG, part of Springer Nature 2018

F. Aloui, I. Dincer (eds.), *Exergy for A Better Environment and Improved Sustainability 2*, Green Energy and Technology,
https://doi.org/10.1007/978-3-319-62575-1_26

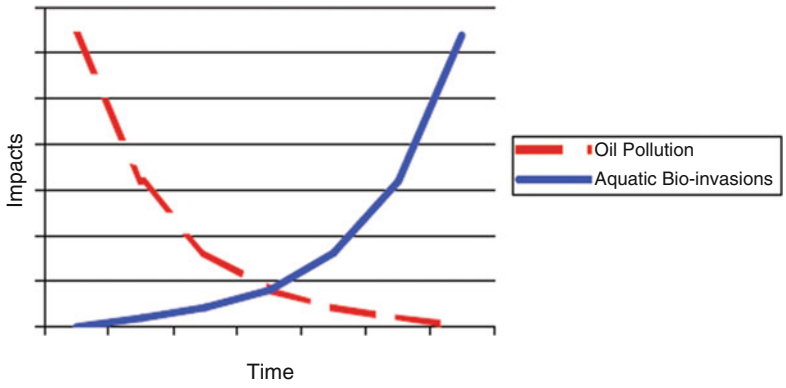

Fig. 1 Impacts over time, major oil spill versus aquatic bio-invasions (Raaymakers 2002)

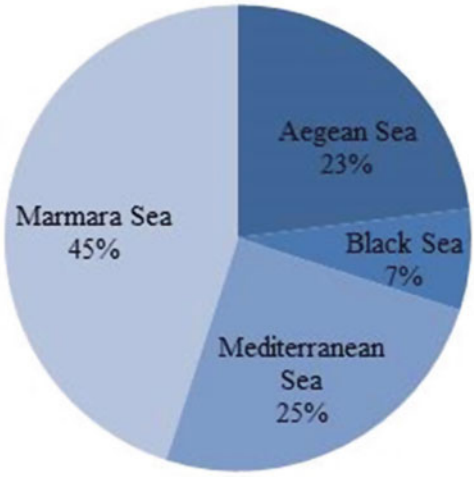

Fig. 2 Ballast water discharged in Turkey coasts (Korcak 2010)

Turkey has a competitive advantage in maritime transport since it is surrounded by the Mediterranean, the Aegean, and the Black Sea, together with the straits of the Dardanelles and the Bosporus. The length of coasts of Turkey is 8333 kilometers and has 295 port facilities. According to the recent reports, Turkey has one of the most vulnerable coasts due to intensive maritime traffic in surrounding seas. Currently, 23 million tons of ballast water was discharged to Turkish coastal waters. Most of the ballast is discharged to four hot spots in Izmit, Iskenderun, Izmir, and Istanbul bays (Fig. 2) (Korcak 2011). Ballast water discharged to Turkish seas comes from the Mediterranean (54%), Black Sea (27%), Northeastern Atlantic (6%), Northwestern Atlantic (3%), Indian Pacific (3%), and other countries (Red Sea, Persian Gulf, etc.) (Tıktık 2010).

This review will focus on impacts, treatments, and management of the ballast water with its regulations through the IMO to protect ecosystem.

Nomenclature

IMO	International Maritime Organization
BWM	Ballast water management
BWE	Ballast water exchange
D1	Ballast water exchange standard
D2	Ballast water treatment standards
μm	Micrometer (1 μm = 10^{-3} mm)
Cfu	Colony forming unit
Nm	Nautical mile

2 Ballast Water and Invasive Species

Ballast is any material used to weight and/or balance an object. Ballast water is the water carried by ships to ensure stability, trim, and structural integrity. Ships have carried solid ballast, in the form of rocks, sand, or metal, for thousands of years. Since modern times, mainly water has been used as ballast. It is much easier to load on and off and is therefore more efficient and economical than solid ballasts. When a ship is empty of cargo, it fills ballast water. When it loads cargo, the ballast water is discharged (Fig. 3).

Ballast water capacities depend on ship type. Large tankers and bulk carriers carry the highest ballast water volumes (Table 1) (Hewitt et al. 2009).

Ballast water usually contains a variety of biological organisms including animals, plants, and pathogens. If the organisms survive in the new environment, they can cause major ecological and economic damage to the ecosystem (MIT Sea Grant 2002). The rate of ship types arriving to national ports is given in Fig. 4.

According to the surveys, there are 66 different invasive species carried by ships to Turkish coasts, of which 19 of them can be categorized as harmful organisms (Fig. 5). In particular, three major alien and invasive species – namely, *Mnemiopsis leidyi* from the North Atlantic, *Rapana venosa* from the Japan Sea, and *Beroe ovata* from the North Atlantic – were transferred to the Black Sea, where they collapsed the entire fish stock and caused significant economic losses in the region.

3 Ecological and Economic Impacts of Ballast Waters

The success of introduced species can depend on several factors including lack of natural predators, abundance of food sources, better tolerance of pollution, disease and other stressors, and out-competing a less aggressive species that currently occupies a biological niche that suits the introduced species (Deacutis and Richard 2002).

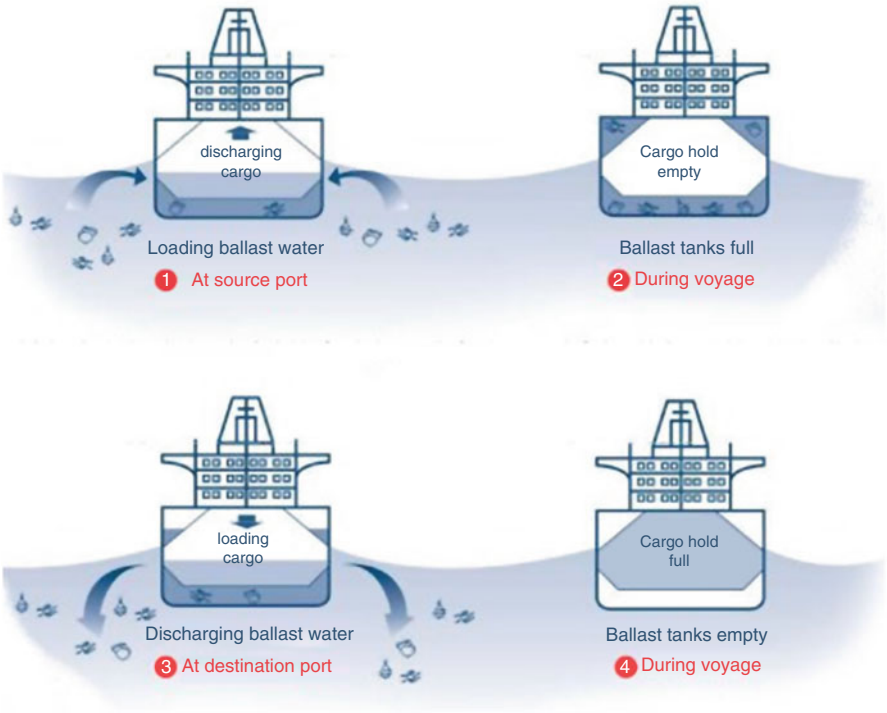

Fig. 3 Loading and discharging ballast water exchange between ports (IMO GloBallast)

Table 1 Ballast water capacities for different types of ships (IMO GloBallast)

Vessel type	DWT	Normal (tons)	% of DWT	Heavy (tons)	% of DWT
Bulk carrier	250,000	75,000	30	113,000	45
Bulk carrier	150,000	45,000	30	67,000	45
Bulk carrier	70,000	25,000	36	40,000	57
Bulk carrier	35,000	10,000	30	17,000	49
Tanker	100,000	40,000	40	45,000	45
Tanker	40,000	12,000	30	15,000	38
Container	40,000	12,000	30	15,000	38
Container	15,000	5000	30	–	–
G. Cargo	17,000	6000	35	–	–
G. Cargo	8000	3000	38	–	–
Passenger/RORO	3000	1000	33	–	–

A successful invader in its new environment can cause a range of ecological impacts. These include competing with native species for space and food; preying upon native species; altering habitat, environmental conditions (e.g., increased water clarity due to mass filter feeding), food web, and the overall ecosystem; and displacing native species by reducing native biodiversity and even causing local extinctions (Raj 2014).

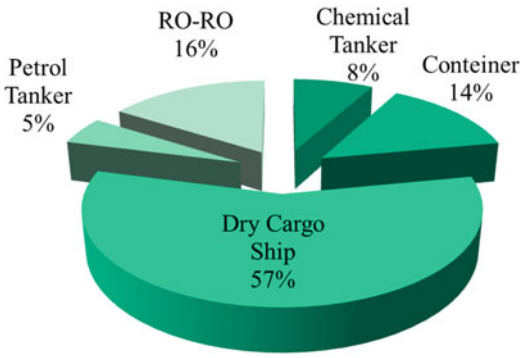

Fig. 4 The rate of ship types arriving to national ports (Tıktık 2010)

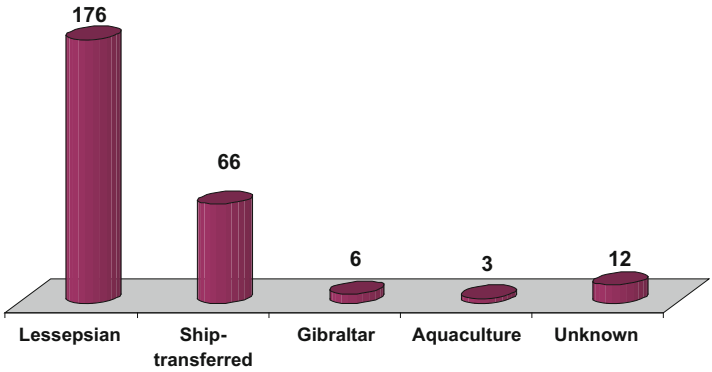

Fig. 5 The number of invasive species in the Turkish coast according to introduction pathways (Tıktık 2010)

In the past, when the Black Sea was in a healthy ecological state, all the niches were occupied, and the chances for newcomers to develop in the Black Sea sustainable populations were at minimum. When the ecological conditions were drastically damaged as a consequence of pollution, eutrophication process, the empty niches were ready to absorb new populations. Now the Black Sea environmental resistance is very fragile (Gomoiu 2001).

Food web structure may change completely after the introduction of a single species. An example of food web destabilization due to the introduction of alien species is the invasion of the Black Sea by the Asian carnivorous whelk *Rapana venosa*. This gastropod, a voracious consumer of bivalves, has been responsible of a drastic reduction in the local oyster and mussel stocks, limiting also their larval recruitment. The scarcity of bivalve larvae in the water column led to a decline of the plankton-eating fish populations (Drapkin 1963).

Another one is the comb jelly *Mnemiopsis leidyi*, which had been affecting the Black Sea food web. This ctenophore eats large quantities of zooplankton and is the most important reason for the sharp decline of anchovy and other pelagic fish stocks in the Black Sea (Kideys 1994).

The major economic impact is the reduction in fisheries production (including collapse of the fishery) due to competition and predation and impacts on aquaculture (including closure of fish farms), especially from introduced harmful algal blooms which was not the case for Turkey.

The economic impacts of invasive alien species can be very high. By 1989, the biomass of *Mnemiopsis leidyi* was estimated as 1 billion tons consumed vast quantities of fish eggs and larvae, as well as the zooplankton that commercially important fish feed on. In 1992, the annual losses caused due to decline of commercial catches were estimated to be at least 240 million US$ (IMO 2010).

4 Ballast Water Legislation and Regulations

In 2004, IMO adopted "The International Convention for the Control and Management of Ships' Ballast Water and Sediments" (BWMC) with the aim of protecting the marine environment from the transfer of the harmful aquatic organisms in ballast water carried by ships.

The convention will enter into force 12 months after it has been ratified by 30 states representing 35% of the world's merchant shipping tonnage. The convention will apply to all ships and offshore structures that carry ballast water and are engaged in international voyages. Turkey joined other 43 states which had ratified the BWM Convention. BWM Convention applies to all ships greater than 400 gross tons. The convention will come into force at different times depending on ballast tank capacity and date of vessel construction (IMO 2014). The BWM Convention was ratified by a sufficient number of states on 8 September 2016, bringing the total gross tonnage to over 35% from the signatory states. This means the convention will enter into force 12 months later, on 8 September 2017 (GloBallast Monograph 25, 2017). The BWM Convention is a key international measure for environmental protection that aims to stop the spread of potentially invasive aquatic species through ships' ballast water.

4.1 Ballast Water Management (BWM) Convention

The convention stipulates two standards for discharged ballast water. The D1 standard covers ballast water exchange, while the D2 standard covers ballast water treatment systems and specifies levels of viable organisms left in water after treatment.

The criteria for selecting a treatment method can be summarized as follows:

- Safety of the crew and passengers
- Ease of operating treatment equipment
- Amount of interference with normal ship operations and travel times

- Structural integrity of the ship
- Size and effectiveness of treatment equipment
- Amount of potential damage to the environment
- Ease for port authorities to monitor for compliance with regulations (IMO 2013)

The convention requires either D1 or D2 standards after entry into force.

4.2 Ballast Water Exchange (BWE) (Regulation D1)

Ballast water exchange is the oldest method and usually recommends minimizing the risk of introducing non-native species in the open ocean. This method is effective because organisms from coastal waters do not survive in the open ocean. But some of the disadvantages are difficulty to completely remove sediments and residual water from the bottom of ballast tanks, organisms being stuck to the sides of the tank and structural supports within the tank which will not be readily removed, and during stormy or rough seas unsafe exchange of ballast water for a ship.

Mid-ocean ballast exchange that occurs at least 200 nm from the shore and in water at least 200 m in depth currently provides the best available option to reduce the risk of alien species introduction and transfer; however, it is subject to serious ship safety limits. In cases where the distance requirement cannot be met, it is permissible to perform BWE at a distance of 50 nm from the shore. The convention specifies at least 95% volumetric exchange of ballast water. The two most common approaches to ballast water exchange are sequential exchange and flow-through exchange (IMO 2013; ABS 2014).

Sequential exchange: A process by which a ballast tank is first emptied and then refilled with replacement ballast water.

Flow-through exchange: A process by which replacement ballast water is pumped into a ballast tank, allowing water to flow through overflow or other arrangements. At least three times the tank volume is to be pumped through the tank (ABS 2014).

4.3 Ballast Water Treatment (Regulation D2)

D2 standard specifies that treated and discharged ballast water must be in line with the criteria shown in Table 2.

In general, ballast water treatment technologies are divided into two groups: separation technologies or disinfection technologies. Separation technologies remove organisms from ballast water upon intake or prior to discharge. Disinfection technologies kill or render organisms incapable of reproducing (ABS 2014).

Table 2 IMO D2 standards for discharged ballast water (ABS 2014)

Organism category	Regulation
Organisms >50 μm	<10 cells/m^3
50 μm > organisms ≥ 10 μm	<10 cells/ml
Toxicogenic *Vibrio cholera*	<1 cfu/100 ml
Escherichia coli	<250 cfu/100 ml
Intestinal enterococci	<100 cfu/100 ml

4.3.1 Separation Technologies

The most predominant type of separation technology in BWM system is filtration systems. Filtration is the passage of a fluid through a porous medium to remove suspended matter, such as sediment, organisms, and silt. BWM system filters are reported to remove organisms from 10 to 200 μm in diameter. Various other types of separation technologies are being used. A hydrocyclone uses centrifugal force to separate items of different densities for removal of organisms.

4.3.2 Disinfection Technologies

Several disinfection technologies are used in BWM system, including chlorination, ozone, deoxygenation, ultraviolet (UV), and heat treatments. The ability for technologies to be effective disinfectants is impacted by the salinity and turbidity of the seawater.

- Chlorination is a traditional technique for waste water disinfection and can be accomplished through conversion of naturally occurring chlorine in seawater or direct injection of chlorine containing compounds.
- Ozone treatment is an effective disinfectant. In seawater, ozone treatment initiates chemical reactions similar to chlorination that result in the formation of the highly effective biocide/germicide of hypobromous acid.
- UV treatment is used to break down cell membranes killing organisms outright or destroying its ability to reproduce. The effectiveness depends on the turbidity of the ballast water (i.e., the concentration of sediments) as this could limit the transmission of the UV treatment (ABS 2014).
- Heat treatment involves heating the ballast water to reach a temperature that will kill the organisms between 35 and 45 °C.

All treatment options are under research for improving because no one method has yet been proven to remove all organisms from ballast water. Scientists improve existing treatment methods (Alkan and Satır, 2005). There are currently 23 treatment systems homologated by the IMO to meet IMO-D2 standards.

5 Conclusions

Shipping is one source of unwanted aquatic organisms. The introduction of invasive aquatic species into new environments by ballast water, attached to ship's hulls and via other vectors, has been identified.

Ballast water discharge typically contains a variety of biological materials, including plants, animals, viruses, and bacteria. These materials often include non-native, nuisance, exotic species that can cause extensive ecological and economic damage to marine ecosystems. Various studies have shown that thousands of different species are carried in ballast tanks, which significantly threaten the biodiversity in the seas around the globe.

The International Maritime Organization (IMO) aims to assist developing countries to reduce the transfer of harmful organisms in ships. In order to the overcome ballast water problem, the International Convention for the Control and Management of Ship's Ballast Water and Sediments was adopted in 2004 to prevent, minimize, and eliminate the risk of introduction of harmful aquatic organisms through ships.

References

American Bureau of Shipping (ABS).: Ballast Water Treatment Advisory. ABS, Houston (2014)

Alkan, G. B., Satır, T.: Ballast Water Problem in the Black Sea and Turkish Straits, October 8–12, 2005, 13th International Symposium on Environmental Pollution Pollution and its impact Life in the Mediterranean Region, MESAEP, Thessaloniki, Greece (2005)

Deacutis, C.F., Richard,C.R.: Ballast water and introduce species: Management options for Narragansett Bay and Rhode Island. A report prepared to fulfill the requirements of Chapter 46–17.3 of the Rhode Island general laws related to ballast water. Narragansett Bay Estuary Program, R.I. Department of environmental management (2002)

Drapkin, E.: Effect of *Rapana bezoar* Linné (Mollusca, Muricidae) on the Black Sea fauna. Doklady Akademii Nauk SRR. **151**, 700–703 (1963)

GloBallast Monograph 25: The GloBallast Story: Reflections from a Global Family GEF-UNDP-IMO GloBallast Partnerships (2017)

Gomoiu, M.T.: Impacts of naval transport development on marine ecosystems and invasive species. J. Environ. Prot. Ecol. **2**, 475–481 (2001)

Hewitt, C.L., Gollasch, S., Minchin, D.: The vessel as a vector-Biofouling, ballast water and sediments. In: Rilov, G., Crooks, J.A. (eds.) Biological Invasions in Marine Ecosystems, pp. 117–132. Springer, Berlin/Heidelberg (2009)

IMO GloBallast: http://globallast.imo.org/

IMO.: Economic assesments for ballast water management: A guideline. GloBallast Monography Series No. 19 (2010)

IMO.: Identifying and managing risks from organisms carried in ships'ballast water. Globallast Monography Series No. 21 (2013)

IMO.: Ballast water treatment advisory 2014 (Retrieved 4 Dec 2008) (2014)

Kideys, A.E.: Recent dramatic changes in the Black Sea ecosystem: The reason for the sharp decrease in Turkish anchovy fisheries. J. Mar. Syst. **5**, 171–181 (1994)

Korcak, M.: Türkiye için Balast Suyu Değerlendirme Raporu. Denizcilik Müsteşarlığı (2010)

Korcak, M.: Ballast water management in Turkey-an overview. In: Telli, O.A., Karakoç, F., Haag, F. (eds.) Ballast Water Management Systems 26–28 October 2011. İstanbul, Turkey (2011)

MIT Sea Grant.: Marine bioinvasions fact sheet: Ballast water (2002)

Raaymakers, S.: The ballast water problem: Global ecological, economic and human health impacts. RECSO / IMO Joint Seminar on Tanker Ballast Water Management & Technologies Dubai, UAE, 16–18 Dec 2002

Raj, C.Y.: Ballast water its impact on ecology and human health. Int. J. Appl. Eng. Res. **15**, 2881–2892 (2014)

Tıktık, O.: Ballast Water Management in Turkey. International Black Sea Day. 31 Oct 2010. Trabzon Turkey (2010)

Regeneration of Waste Frying Oil for Biodiesel Production

Fetta Danane, Aida Cherifa Ahmia, Rhiad Alloune, and Rahma Bessah

1 Introduction

The increasing energy demand, together with the depletion of fossil fuels and environmental issues, is posing great challenges for researchers and the scientific community worldwide today. The present energy scenario has stimulated very active research interest in the production of renewable biofuels. Biodiesel is considered as a viable alternative to petroleum-derived diesel in the near future due to its interesting characteristics. Chemically, biodiesel is composed of monoalkyl esters of long chain fatty acids derived from renewable lipid feedstocks such as vegetable oils or animal fats (Leung et al. 2010). Biodiesel offers several advantages, including renewability, biodegradability, negligible toxicity, environmentally friendly emission profile, higher combustion efficiency, higher cetane number, higher flash point, and contains 10–11% oxygen by weight and better lubrication (Nair et al. 2012). The energy content and the physicochemical properties of biodiesel are almost similar to conventional diesel fuel; therefore, it can be used on its own or mixed with conventional diesel in the existing conventional compression-ignition engines without any major modifications (Leung et al. 2010). However, the high cost of biodiesel production is the major obstacle to its commercialization. It has been reported that approximately 70–95% of the total biodiesel production cost is related to the cost of the raw materials (Azócar et al. 2010).

F. Danane (✉) • A.C. Ahmia
Centre de Développement des Energies Renouvelables, CDER, 16340 Algiers, Algeria

Université des Sciences et de la Technologie Houari Boumediene, USTHB,
16111 Algiers, Algeria
e-mail: f.danane@cder.dz

R. Alloune • R. Bessah
Centre de Développement des Energies Renouvelables, CDER, 16340 Algiers, Algeria

© Springer International Publishing AG, part of Springer Nature 2018

F. Aloui, I. Dincer (eds.), *Exergy for A Better Environment and Improved Sustainability 2*, Green Energy and Technology,
https://doi.org/10.1007/978-3-319-62575-1_27

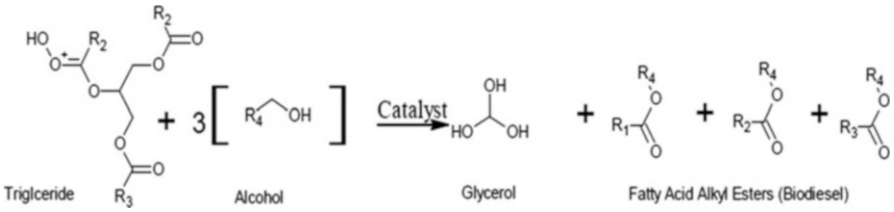

Fig. 1 Transesterification reaction of triglycerides

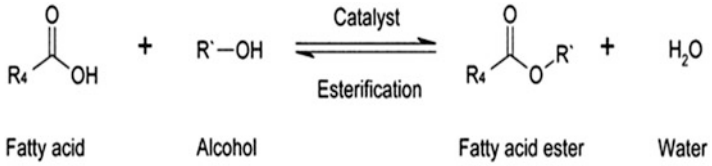

Fig. 2 Esterification reaction

In this context, waste cooking oil (WCO) is considered a promising feedstock where the biodiesel production cost could be effectively reduced by 60–70% when using this low cost raw material (Math et al. 2010).

Moreover, the production of biodiesel from WCO will not only avoid competition for the same oil resources for food and fuel but will also solve the problems associated with WCO disposal.

Usually, biodiesel is produced by the transesterification reaction (Fig. 1).

Frequently, the actual amount of methanol or ethanol used for transesterification is higher than the stoichiometric amount in order to achieve acceptable conversions. For instance, a methanol or ethanol to oil molar ratio of 6:1 is a good choice for achieving 95% conversion at 60 °C with one (1) gr of NaOH as catalyst. Obtaining such good results, however, requires certain precautions. First, triglyceride should be nearly pure. Studies show that the presence of water or Free Fatty Acids (FFA) acts as poison for the catalyst. Second, the price of pure triglyceride does not allow biodiesel to compete with diesel fuel in cost (Klass 1998) and (Kemp 2006). These disadvantages are the main reasons why researchers have recently focused on other feedstock for biodiesel production. Acid oils, which have high FFA content, are well known as a potential alternative raw material. The presence of FFA requires the addition of a pretreatment step before transesterification, in which FFAs react with methanol or ethanol in the presence of acidic catalyst reacts, as shown in Fig. 2.

In this context, the main objective of our study is to eliminate the fatty acids before starting transesterification and testing the effectiveness of ethanol and methanol to ensure a better yield in the production of biodiesel from used frying oil.

2 Basic Chemical Aspects of Cooking

Cooking is a dehydration process; it means that water and soluble compounds are transferred from fried food to oil. At the same time, fried products absorb a part of the surrounding oil. Edible oils are constantly exposed to chemical reaction during cooking due to their composition and external influences. The reactions are led by oxygen, light, and heat. Three main reactions take place: oxidation, polymerization, and hydrolysis (Berrios et al. 2010).

(a) *Oxidation* produces oil aging due to contact with atmospheric oxygen. Oxidation is accelerated because of temperature and light. Triglycerides, which are present in oil, are oxidizable organic compounds. In fact, when the number of double bonds rises, oxidation takes place easily. As well as degraded products, oxidation produces hydroperoxides, aldehydes, and ketones.
(b) *Polymerization* is a chemical reaction where unsaturated fatty acids due to the influence of heat, heavy metals (Cu, Fe), or light, and by means of the breakage of the double bond, react to form dimers (molecule composed of two identical subunits or monomers linked together) and polymers of triglycerides. As a consequence of polymerization, the oil's molecular weight rises and the oil becomes more viscous.
(c) *Hydrolysis* is led by water acquisition in the fried product and is supported by certain products deep-fried in batter. Free fatty acids (FFAs) are generated because triglycerides are broken down. Moreover, when the water evaporates through the oil, monoglycerides, diglycerides, and FFAs are created.

Thus, the new products formed during frying are polymers, dimers, oxidized triglycerides (hydroperoxides, aldehydes and ketones), as well as diglycerides and fatty acids (Ruiz et al. 2008). Therefore, used frying oils are heterogeneous as compared to crude or refined oils. All these groups possess higher polarity than the initial triglycerides and can be easily quantified by means of adsorption chromatography (Ruiz et al. 2008) and (IUPAC 1992) to find out the total degradation of frying oils.

Oil, containing a large quantity of free fatty acids, cannot be directly used for biodiesel fuel production applying the commonly used alkaline transesterification procedure; free fatty acids have to be esterified before the transesterification of triglycerides can take place (Berrios et al. 2010). Canakci and Van Gerpen (Canakci and Van Gerpen 2001) recommend this pretreatment since, if the FFA level exceeds 5%, saponification will hinder the separation of the ester from glycerin and reduce the yield and formation rate of FAME due to alkaline catalyst consumption. This is the case of a few used frying oils. Then, an esterification step is necessary before transesterification.

3 Experimental Setup

3.1 Pretreatment of Waste Cooking Oil

After collecting the waste frying oil (used sunflower oil), it was filtered to remove any inorganic residues and suspended matters and heated at 110 °C in order to get rid of water.

The acid value was determined by means of the titration with KOH solution in accordance with the EN 14104 Standard (EN 14104 2003). The result shows that the FFA level exceeds 5 wt. %. Therefore, an esterification reaction to eliminate the FFAs is required. The esterification reaction is catalyzed by acid, a sulfuric acid (H_2SO_4), which is the most commonly used because of its low cost and ready availability. The dosage of sulfuric acid taken is 0.5 wt.% and agitated at 600 rpm during 1 h.

3.2 Transesterification of Waste Cooking Oil

Transesterification of vegetable oils with alcohol is the best method for biodiesel production and reducing viscosity.

Many different alcohols can be used in this reaction, such as, ethanol, methanol, propanol, and butanol. The alkali catalysts often used are NaOH, KOH, and $CH_3{-}ON_a$.

After pretreatment, the transesterification process was carried out. The different steps are illustrated in the diagram below (Fig. 3) (Awad et al. 2013).

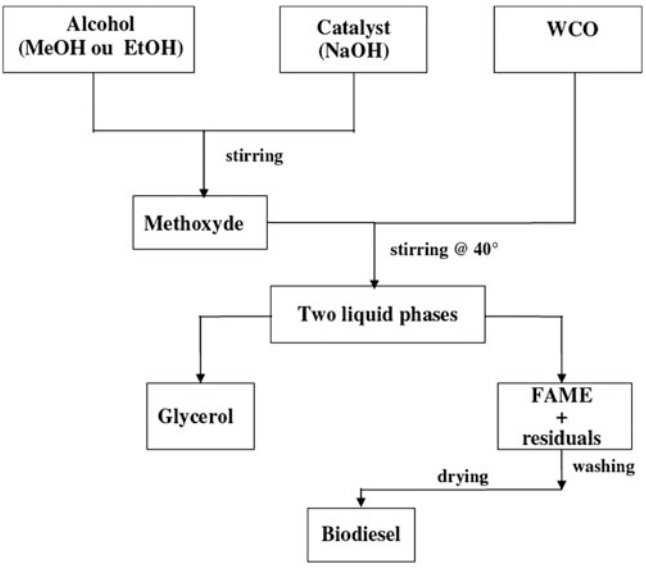

Fig. 3 Transesterification process

4 Results and Discussions

The main factors affecting the transesterification reaction are reaction temperature, reaction time, alcohol type, quantity, and catalyst concentration.

In this work, for the transesterification reaction, we used NaOH (2%) mixed with alcohol; 1:6 molar ratio methanol or ethanol to oil was taken. Then, the mixture was stirred by means of a magnetic stirrer under constant temperature (60 °C) and at 600 rpm until no traces of solid NaOH are observed, which means that the reaction is accomplished. The time varies between 30 and 120 min.

At the end of the reaction, the products were poured through a separating funnel in order to separate the glycerol phase from biodiesel. As both phases contain alcohol and catalyst, after the separation step, the biodiesel was washed several times with water until the aqueous phase became clear and neutral. Finally, the biodiesel is filtered and weighed. The yield of biodiesel was calculated.

In this work, we have chosen to test the effectiveness of methanol and ethanol in the transesterification process. For this, we calculated the yields (Yd) of the transesterification of used sunflower oil according to reaction time. The results are grouped in Fig. 4.

Results show that methanol gives a higher yield compared to ethanol, and this whatever the reaction time. These results are consistent with the work of Ramadhas et al. (2005), indicating that the production of biodiesel using ethanol is more complicated than that using methanol. This is explained by the fact that the use of ethanol leads to the formation of a stable emulsion. Indeed, during the transesterification reaction, there is always emulsion formation.

In the case of methanol, emulsions are easily decomposed to form an upper layer rich in methyl esters and a lower layer rich in glycerol. For ethanol, emulsions are more stable and complicate the separation of the two layers because of the physical structure of ethanol, which has a larger nonpolar group than that of methanol.

In literature, we also found that the most commonly used alcohols are ethanol and methanol, especially the latter, given its low cost and its physical benefits (chains shorter and more polar alcohol) (Kansedo et al. 2009). However, ethanol has the advantage of coming from a renewable source through fermentation of sugar derived from sugarcane or beet. Biodiesel thus obtained is 100% renewable.

5 Conclusions

In this work, biodiesel was obtained from used sunflower oils with a high percentage of free fatty acids (>0.5%). It was necessary to carry it out in two steps: esterification and transesterification, testing two types of alcohol—methanol and ethanol.

It is concluded that the FFA content has a negative effect on the whole process. The FFAs form soap with the catalyst, which reduce considerably its efficiency for

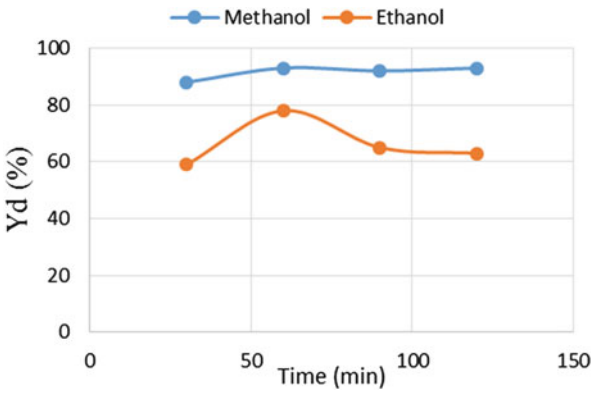

Fig. 4 Effect of alcohol type on the yield of the used sunflower oil transesterification

transesterification. Thus, higher amounts of catalyst are required. The formation of soap during alkali-catalyzed reaction creates proper conditions for the emulsion's appearance so that the esters are captured into a stable emulsion with glycerol and excess alcohol, and at the end of the process the phase's separation will not be possible.

Based on this work, it is recommended to use methanol in alkali-catalyzed transesterification of waste oils with relatively high FFA contents. To avoid their negative effects, FFAs in the base oil are both converted to soap and removed from the process, or they may be esterified (yielding more biodiesel) using an acidic catalyst.

References

Awad, S., Paraschiv, M., Varuvel, E.G., Tazerout, M.: Optimization of biodiesel production from animal fat residue in wastewater using response surface methodology. Bioresour. Technol. **129**, 315–320 (2013)

Azócar, L., Ciudad, G., Heipieper, H., Navia, R.: Biotechnological processes for biodiesel production using alternative oils. Appl. Microbiol. Biotechnol. **88**, 621–636 (2010)

Berrios, M., Martín, M.A., Chica, A.F., Martín, A.: Study of esterification and transesterification in biodiesel production from used frying oils in a closed system. Chem. Eng. J. **160**, 473–479 (2010)

Canakci, M., Van Gerpen, J.: Biodiesel production from oils and with high free fatty acids. Trans. ASAE. **44**, 1429–1436 (2001)

EN 14104.: Fat and oil derivates. Fatty Acid Methyl Esters (FAME). Determination of acid value (2003)

IUPAC: Standard Methods for the Analysis of Oils, Fats and Derivates. Standard Method 2507–International Union of Pure and Applied Chemistry, 1st supplement to 7th edn. Pergamon Press, Oxford (1992)

Kansedo, J., Lee, K.T., Bhatia, S.: Cerbera odollam (sea mango) oil as a promising non-edible feedstock for biodiesel production. Fuel. **88**, 1148–1150 (2009)

Kemp, W.H.: Biodiesel basics and beyond: a comprehensive guide to production and use for the home and farm. Aztext Press, Ontario (2006)

Klass, L.D.: Biomass for renewable energy, fuels and chemicals. Academic Press, New York (1998)

Leung, D.Y.C., Wu, X., Leung, M.K.H.: A review on biodiesel production using catalyzed transesterification. Appl. Energy. **87**, 1083e–11095 (2010)

Meher, L.C., Vidya, S.D., Naik, S.N.: Technical aspects of biodiesel production by transesterification—a review. Renew. Sust. Energ. Rev. **10**, 248–268 (2006)

Math, M.C., Kumar, S.P., Chetty, S.V.: Technologies for biodiesel production from used cooking oil – a review. Energy Sustain. Dev. **14**, 339–345 (2010)

Nair, P., Singh, B., Upadhyay, S.N., Sharma, Y.C.: Synthesis of biodiesel from low FFA waste frying oil using calcium oxide derived from Mereterix mereterix as a heterogeneous catalyst. J. Clean. Prod. **29–30**, 82–90 (2012)

Ramadhas, A.S., Jayaraj, S., Muraleedharan, C.: Biodiesel production from high FFA rubber seed oil‖. Fuel. **84**, 335–340 (2005)

Ruiz- Méndez, M.V., Marmesat, S., Liotta, A., Dobarganes, M.C.: Analysis of used frying fats for the production of biodiesel. Grasas Aceites. **59**, 45–50 (2008)

Talebian-Kiakalaieh, A., Aishah Saidina Amin, N., Mazaheri, H.: A review on novel processes of biodiesel production from waste cooking oil. Appl. Energy. **104**, 683–710 (2013)

The Effect of Air with Supplementary Oxygen on Power and Fuel Consumption of Spark-Ignition Engine

Mojtab Tahani, Mohammadhossein Ahmadi, and Keayvan Keramati

1 Introduction

With the fast growth of society and industry, the requirement of fossil fuels is rising higher and higher; thus, there is great concern about the dearth of energy due to finite reserves or for additional political reasons (such as the petroleum crisis). Furthermore, environmental protection problems have been emphasized upon all over the world in recent years; therefore, it is critical to reduce fuel consumption to meet environmental needs. Besides, the torque of a spark-ignition engine varies with air/fuel ratio (AFR). This means the engine torque will change with change in fuel consumption.

Motor vehicle energy demand through motion depends mostly on rolling, aerodynamic drag, acceleration, and gravitational losses. Depending on the engine efficiency of a vehicle and the energy required by vehicle accessories, a definite amount of the fuel energy is spent to overcome forces resisting the motor vehicle's motion through a driving cycle (Tolouei and Titheridge 2009). Delayed injection produces a lower temperature and pressure during most of the combustion. Advancing the injection leads to an input of fuel at the time that the temperature and pressure in the combustion chamber are lower, which retards the start of the

M. Tahani
University of Tehran, Faculty of New Sciences and Technologies,
North Kargar St., Tehran 1439955941, Iran

M. Ahmadi (✉)
Razi University, Department of Mechanical Engineering of Agricultural Machinery,
Kermanshah, Iran
e-mail: mmhahmadi@gmail.com

K. Keramati
Iran University of Science and Technology, Department of Automotive
Engineering, Tehran, Iran

© Springer International Publishing AG, part of Springer Nature 2018

F. Aloui, I. Dincer (eds.), *Exergy for A Better Environment and Improved Sustainability 2*, Green Energy and Technology,
https://doi.org/10.1007/978-3-319-62575-1_28

combustion and growths the amount of fuel that enters throughout the ignition delay (Duran et al. 2012). Oxygen percentage in the air is an important variable having the potential to noticeably affect the fuel consumption.

Numerous researchers have been aggressively investigating the special effects of oxygenates on diesel engine combustion, and reviews of several relevant papers have been published by Litzinger (Litzinger et al. 2000) and Natarajan (Natarajan et al. 2001). Boehman and coworkers have considered oxygenation of diesel engine by alternative fuels, additives, and oxygen enrichment of intake air (Boehman et al. 2005; Litzinger et al. 2000; Song et al. 2002, 2004, 2006). Most of the literature on oxygen-enriched combustion reports significant decrease in smoke emissions, upper peak cylinder pressure, improved power output, and considerably reduced ignition delay by increasing oxygen in the intake air (Desai et al. 1993; Ghojel and Hilliard 1983; Karim 1968). However, the effect of oxygen percentage in the air on fuel consumption remains unclear in their study.

Reduction in fuel consumption would be very important to energy saving and environment protection. Numerous scientists have conveyed that high energy efficiency and low emission could be achieved if air with supplementary oxygen was used so it induced complete combustion (Arrègle et al. 2003; Song et al. 2003). There have been several reports regarding the result of oxygen-enriched air on the emission gas and efficiency of a blast furnace (Kondo 1992; Petela et al. 2002). There have been little studies on the presentation of gas membranes to the spark-ignition engine in order to figure out the special effects of air with supplementary oxygen on the emission gases (Saito et al. 1991; Rigby and Watson 1994; Byun et al. 2006).

The features of oxygen-enriched combustion would moreover be of advantage to decrease the necessities of compression, which would cause to lower manufacturing costs, improved fuel conversion efficiency, and increased durability (Perez and Boehman 2010). Therefore, oxygenating the air causes wide flammability and improvement in power output.

So, in this study, the effects of air with supplementary oxygen on fuel consumption and torque of a spark-ignition engine in new way were investigated. Here, we can find out the research innovations and suggestions in the field of the effect of air with supplementary oxygen on power and fuel consumption of spark-ignition engine:

- As usual, for increasing the amount of oxygen in combustion reaction to perform complete combustion, premixed reactant of oxygen like hydrogen-oxygen-air, methane-air, etc., are used as supplementary oxygen feeding. But in this study, the supplementary oxygen is fed into the engine directly and without any mediated mixture.
- The survey results of the study among the performed researches have shown that the best Method to increasing power of spark-ignition engine is increasing of oxygen percentage by oxygenating inlet air.
- In this study a new method to oxygenating inlet air directly has been found by using a gas mixing chamber.

- The structure of testing instruments used in this study could be an invention to tune cars by decrement and increment of fuel consumption and power of the spark-ignition engine, respectively, in the future.
- The results of this study could be a way for other studies in the field of CFD to simulate the in-cylinder combustion and the reaction products, in future.
- From an economic perspective, adding pure oxygen instead of premixed reactant to air has very little cost to increase oxygen content of air in the engine.

From an industrial perspective, availability and safety of pure oxygen instead of premixed reactant are the benefits of using pure oxygen to increase oxygen content of air in the engine.

Nomenclature

T_w	: Torque obtained from wheel (N.m)
T_e	: Torque of the engine (N.m)
n_e	: Rotational speed of the engine (rpm)
n_w	: Rotational speed of the wheels (rpm)
hp	: Horsepower (hp)
AFR_{stoich}	: Stoichiometric air–fuel ratio
b	: Hydrogen/carbon ratio
MW_{O_2}	: Molecular weight of oxygen (kg/kmole)
MW_{N_2}	: Molecular weight of nitrogen (kg/kmole)
X_{O_2}	: Oxygen molar fraction

2 Experimental Facility

2.1 Setup

The components of the system to produce air with different percentage of oxygen include an air compressor, an oxygen tank, and a gas mixing chamber.

An electric motor air compressor was used to supply air. Specifics: 8.7 cfm air displacement, 50 L air receiver, 2.5 hp, 230 V, 8 bar maximum in work pressure, equipped with thermal overload protection, controlled by a completely automatic pressure switch.

An up to 8495 L of oxygen Steel "T" medical oxygen cylinder with a CGA540 valve and STANDM60T01-A adjustable cylinder stand was employed to supply pure oxygen.

An oxygen pressure regulator (specifics: 20,700 KPa Maximum inlet pressure, Includes a Swagelok™ 1/4 in and NPT to 1/8 in) was installed to regulate and adjust desired pressure of oxygen flow. Oxygen was carried to the gas-mixing chamber at an ultimate pressure of 40 KPa as measured on output gauge indicator of pressure regulator. Then the flow rate of oxygen gas was regulated to chosen rate by passing

it over rotameter (specifics: Tube-cube model, Azmoon Motamem Instruments Tehran Iran, 0–500 cc/min was used to measure O_2 flow rate). The rotameter was calibrated by using water displacement method and verified by a digital flow meter (Jour Research Company, Sweden). Directed whole flow rate of gas mixture was calculated on the basis of the some of the flow rates necessary for each mixture, flow rate of every gas (air and pure oxygen) being proportional to its concentration in the mixture.

A gas-mixing chamber was used to mix the compressor air and pure oxygen to produce air with different percentage of oxygen (specifics: 6750 cc capacity, developed by Rameshbabu et al. (1991) but with different configuration and optimization by Momen (2002)). The unit consisted of 26 pieces of (5 and 3 mm thickness) Perspex plates and two threaded rods (5 mm diameter) for holding the entire mixer assembly together (Fig. 1c).

A 100 × 120 cm bates cargo pack was used as an air bag to store air with different percentage of oxygen (Fig. 1d).

After preparing the air with different percentage of oxygen, the valve of the air bag was attached to the air manifold before the air filter of the engine.

Tests were performed in a spark-ignition engine Pride (Saba) M13NI (specifics: 1323 cm3, 4 cylinder arranged in-line, four-stroke, direct-injection, water-cooled, 9.7:1 compression ratio) (Fig. 1f). The maximum torque was 103.3 N.m at 2800 rpm and the maximum engine power was 62.5 hp at 5500 rpm. There were three engines for tests. The engines were not new but were reconditioned to usual specifications.

Fuel consumption tests were performed with fuel flow meter DFM 50CK. Fuel flow meter DFM has 3D ring type measuring cavity. DFM produces the impulse, while the volume of fuel (which is equivalent to the volume of measuring cavity)

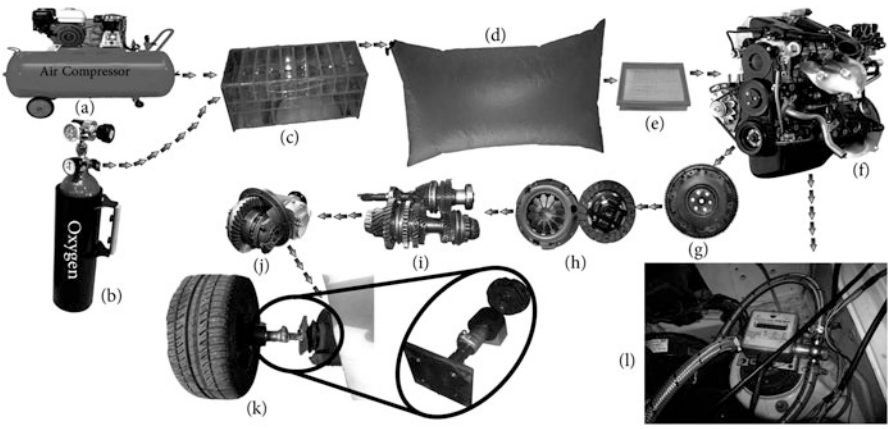

Fig. 1 A schematic diagram of the experimental setup: (**a**) air compressor, (**b**) oxygen tank, (**c**) gas mixing chamber, (**d**) voluminous air bag (bates cargo pack), (**e**) air filter, (**f**) spark-ignition engine, (**g**) flywheel, (**h**) clutch, (**i**) gearbox, (**j**) differential, (**k**) Datum Electronics Series 420 PTO (Power Take Off) and tire, (**l**) fuel flow meter DFM 50CK

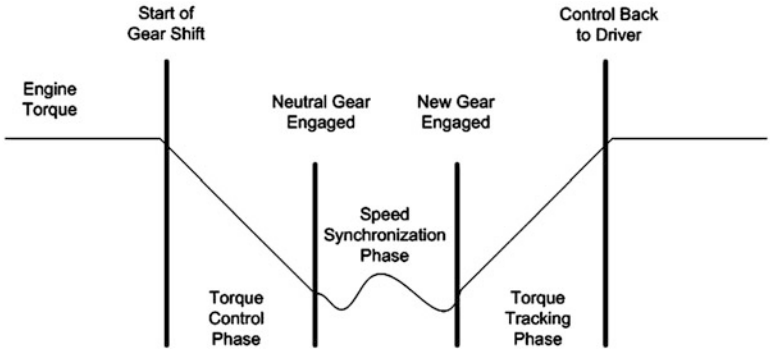

Fig. 2 Gear shifting stages for an automatic manual transmission (Pettersson and Nielsen 2000)

passes over it. For 1 L of spent fuel, DFM produces the number of impulses which is indicated on the meter harness. DFM allows solving the following jobs: fuel consumption rationing, fuel monitoring, sensing and avoiding theft of fuel, optimization of fuel consumption and real-time monitoring, and tests of engine fuel consumption. The inaccuracy of the fuel flow meter DFM 50CK was ±1% (Fig. 1l).

A gear shift involves three stages: (1) torque regulator phase, (2) speed rate synchronization stage, and (3) torque tracking stage (Fig. 2) (Pettersson and Nielsen 2000).

2.2 Measurements

Through the torque control stage, the engine is controlled till zero brake torque is reached. Once reached, neutral gear is engaged decoupling the engine from the transmission. Through the decoupled phase, the engine speed is synchronized to the transmission speed by the correct conversion ratio of the new gear. Once synchronization is achieved, the new gear is engaged and the engine torque is regulated to track the required torque till finally giving complete control to the driver. The most influential stage in a gear shift is the torque control stage. During this stage, it is important to precisely estimate brake torque. For instance, if a big torque mismatch happens when the neutral gear is engaged, the driveline will resonate, which translates to engine and transmission wear, driver discomfort, and noise (Pettersson and Nielsen 2000). In this study, the torque obtained after control was given to driver phase was measured.

Torque measurement tests were carried out with Datum Electronics Series 420 PTO (Power Take Off). Datum Electronics Series 420 PTO shaft torque and power monitoring system will display and log transmitted power, shaft speed and the torque accurately while testing new systems driven from entirely standard PTO Shafts. The Series 420 PTO System has a noncontact transmissions system that runs a digital output rightly proportional to torque. Provided as a wide-ranging

transducer with bearings to support the stator component, this strong design provides performance data through real measurement on the revolving drive shaft. The PTO structure has a female coupling on one end and a male fitting on the other. The male and female ends were coupled to the female and male end of the Power transducer linkage designed by author, respectively. The PTO system turns like an extension device, with the male end copying the male end of the application. The speed and torque signals are transferred from the shaft to a static cover assemblage. Datum Electronics Series 420 PTO operating speed and torque ratings are up to 3000 rpm and up to 2500 N.m, respectively (Fig. 1k).

By torque transducer (Datum Electronics Series 420 PTO) we measured the torque of the wheels, but we needed the torque of the engine, then we needed the rotational speed of the wheels (rpm). By stopping one wheel all of the speed goes to the other wheel.

The rotational speed of the wheel measurement was carried out with Lutron Photo/Contact Tachometer – DT-2230. The accuracy, resolution, and amplitude of this device were $\pm(0.1\ \% + 1\text{digit})$@ reading, 0.1 RPM (<1000 RPM), 1 RPM ($\geq$1000 RPM) and Photo Tachometer (5–99,999 RPM), Contact Tachometer (0.5–19,999 RPM), respectively.

The fuel used in this study was Euro 5 type.

After setting up the experimental instrument, the engine was started and the air contained in the air bag was sucked in by the engine automatically and without any loading on it.

Each running phase was held for 10 min till engine performance was stabilized and continued while every parameter was measured and logged in three engine speeds through the last 3 min of every running step. A first test was performed with natural atmospheric air content at the beginning, in order to compare engine performance. Engine tests were performed on the same three engines the same day, so that they have almost the same environmental conditions within 3 repetitions of each test.

Fuel consumption and torque from three engines in seven different oxygen percentages of air were measured. The different percentages of oxygen contained in the air were 20.8%, 21.6%, 22.6%, 23.6%, 24.8%, and 27%. The experiments were performed at three different engine speeds ranging from 1000 rpm to 3000 rpm, at 1000 rpm increments.

3 Numerical Scheme

Assuming that all parts of the driving line are spur gears and regardless of the route of transmission with torque losses, we could have written

$$\frac{T_w}{T_e} = \frac{n_e}{n_w} \tag{1}$$

where T_w = the torque obtained from wheel (N.m), T_e= the torque of the engine (N.m), n_e= the rotational speed of the engine (rpm), and n_w = the rotational speed of the wheels (rpm).

The power of the engine is calculated by

$$\text{hp} = \frac{0.737561}{5252} \times T_e \times n_e \tag{2}$$

where hp = horsepower, T_e = torque of the engine (N.m), and n_e = the rotational speed of the engine (rpm).

4 Results and Discussions

4.1 Effect of Percentage of Oxygen in the Air and Engine Speed on Brake Engine Torque

Determination of brake engine torque isn't an unimportant task. Parameters such as the pressure and temperature of the intake manifold, pressure and temperature of the exhaust manifold, engine speed, fuel quantity, and engine geometry all have a considerable effect on engine brake torque. There are also additional complicating factors that affect the determination of brake torque such as accessory parasitic loads. Accessory parasitic loads are modules such as cooling fans, alternators, A/C compressors, oil pumps, air compressors, power steering pumps, and water pumps (Franco et al. 2008).

Figure 3 displays the increasing trend for the engine brake torque when engine speed was increased from 1000 to 3000 rpm with different percentage of oxygen content in the air.

When the oxygen percentage in the intake rises from 20.8% to 27%, engine brake torque is increased from 65.48 N.m to 78.36 N.m in 1000 rpm engine speed, 76.56 N.m to 85.96 N.m in 2000 rpm engine speed, and 80.51 N.m to 102.16 N.m in 3000 rpm engine speed. According to the results, it was found that engine brake torque increased with the increase in oxygen percentage at the intake.

Oxygen addition to the air increases gasoline's heating value, and increase in power and torque were obtained. This is described with some causes. Beneficial effect of oxygenating the air is a potential reason for more complete combustion, thus increasing the torque. Furthermore, a bigger fuel for the similar volume is injected to the cylinder because of greater concentration of oxygen. This results in an increase in power and torque.

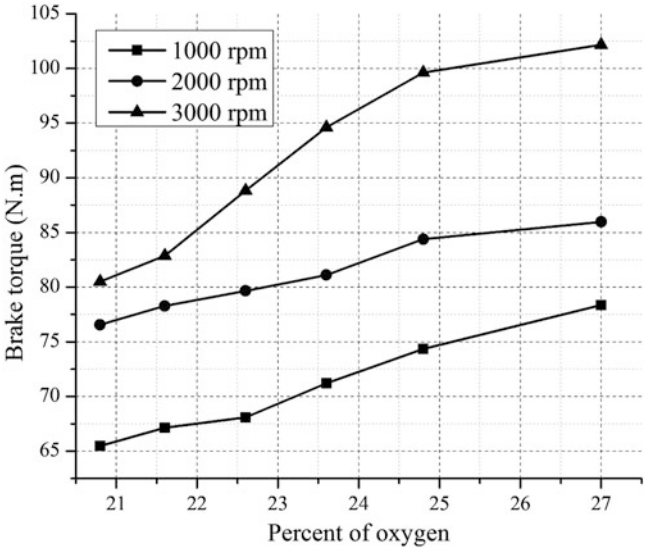

Fig. 3 Effect of percentage of oxygen in the air and engine speed on brake engine torque

While the engine rotational speed increased from 1000 to 3000 rpm, the intake of air quantity also increased. At higher engine speed, the combustion and exhaust temperature increased, which can promote higher efficiency. Additionally, the air–fuel mixing procedure improved because the turbulence intensity increased at the upper engine rotational speeds, thus providing more complete combustion. This was primarily because of an increase in both the volumetric efficiency and flow rate of the reactant mixture at upper engine speeds.

4.2 Effect of Percentage of Oxygen in the Air and Engine Speed on Brake Engine Power

One of the theories in this Investigation was to prove the capability of oxygen-enriched gasoline combustion to increase the power output in a spark-ignition engine because of the potential to burn extra fuel at a certain stoichiometry (oxygen-to-fuel ratio). Related to this theory Assanis and coworkers found that an increase in oxygen volume fraction at the intake air from 21% to 35% leads to increase in brake power by up to 90%.

Figure 4 displays the increasing trend in engine power when engine speed is increased from 1000 to 3000 rpm at different percentages of oxygen content in the air.

When the oxygen percentage at the intake rises from 20.8% to 27%, the engine torque increases from 9.19 hp to 11.00 hp in 1000 rpm engine speed, 21.50 hp to 24.14 hp in 2000 rpm engine speed, and 33.91 hp to 43.04 hp in 3000 rpm engine speed.

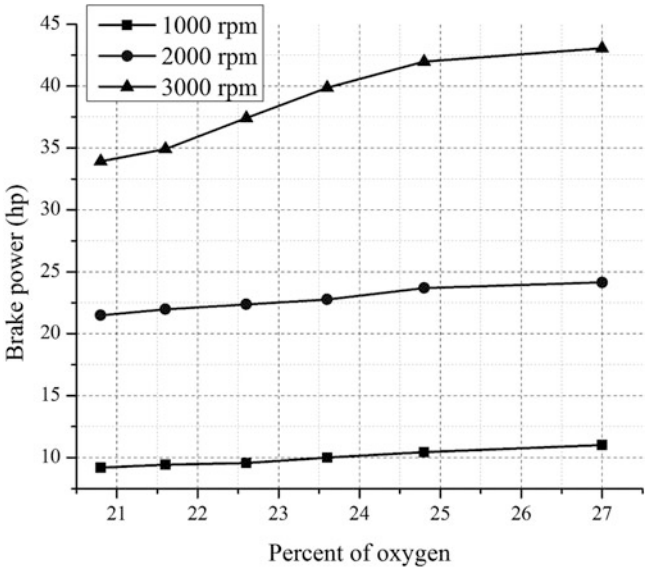

Fig. 4 Effect of percentage of oxygen in the air and engine speed on brake power of the engine

According to the results, it was found that the engine power increased by the increase in oxygen percentage at the intake. The air with supplementary oxygen causes the complete combustion of a spark-ignition engine. This means that almost all of the fuel carbons reacted with oxygen and produced more power. Consequently, it can be seen from the graph that the engine brake power were increased by increasing the oxygen percentage inside the intake. Therefore, Addition of oxygen increases the thermal efficiency resulting in engine power enhancement. Assanis et al. (2001) obtained similar results.

This oxygen enrichment stratagem, mentioned as rich oxygen-to-fuel ratio (Poola and Sekar 2003), has been the most used in the oxygen enrichment investigations reported in the literature. According to the literature, brake power output is not affected a great deal by oxygen enrichment unless the fuel amount injected is also increased, keeping a constant oxygen-to-fuel ratio (Assanis et al. 2001; Poola and Sekar 2003), or by using greater fuel flow rates (Rakopoulos et al. 2004).

4.3 Effect of Percent of Oxygen in the Air and Engine Speed on Fuel Consumption of the Engine

Also, the results indicated that the higher the engine speed, the higher the engine brake power. This was primarily because of an increase in both the flow velocity and volumetric efficiency of the reactant mixture at greater engine speeds.

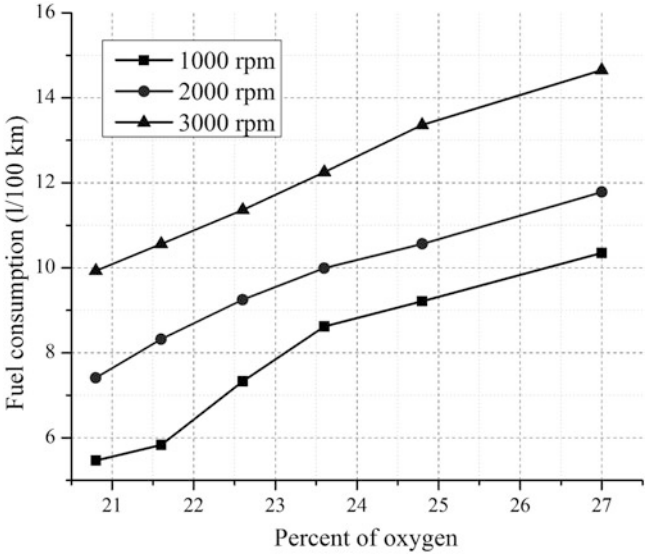

Fig. 5 Effect of percentage of oxygen in the air and engine speed on fuel consumption of the engine

To determine fuel consumption at stable working situations (constant speeds, constant torques), consumption of a certain quantity of fuel in 100 km was measured. It is well known that the amount of heating value of fuel affects the fuel consumption of a spark-ignition engine.

Figure 5 displays the increasing trend for engine fuel consumption when the engine speed is increased from 1000 to 3000 rpm at different percentages of oxygen content in the air.

Fuel consumption is affected through oxygen enrichment because of the variation in the equivalence ratio as oxygen concentration at the intake air manifold changes. The relationship below is described as the stoichiometric air–fuel ratio (Heywood 1988), where it is simply seen that, for a constant hydrogen to carbon molar ratio (H/C), the stoichiometric air–fuel ratio ($\mathrm{AFR}_{\mathrm{stoich}}$) decreases while the oxygen concentration in air increases. This means that lesser air is required for complete combustion of gasoline fuel. When air mass flow is constant, as in these experiments, the extra oxygen could be used to burn extra fuel to improve fuel consumption:

$$\mathrm{AFR}_{\mathrm{stoich}} = \frac{\left(1+\frac{b}{4}\right) \times \left[\mathrm{MW}_{\mathrm{O}_2} + \left(\frac{1-X_{\mathrm{O}_2}}{X_{\mathrm{O}_2}} \mathrm{MW}_{\mathrm{N}_2}\right)\right]}{(12.011+b)} \tag{3}$$

where $b = H/C$ molar ratio, $\mathrm{MW}_{\mathrm{O}_2}$ and $\mathrm{MW}_{\mathrm{N}_2}$ are molecular weight of oxygen and nitrogen, respectively, and X_{O_2} is the oxygen molar fraction (or volume fraction) in the combustion air.

When the oxygen percentage at the intake rises from 20.8% to 27%, fuel consumption of the engine is increased from 5.46 $^{l}/_{100\ km}$ to 10.35 $^{l}/_{100\ km}$ in 1000 rpm engine speed, 7.41 $^{l}/_{100\ km}$ to 11.78 $^{l}/_{100\ km}$ in 2000 rpm engine speed, and 9.93 $^{l}/_{100\ km}$ to 14.65 $^{l}/_{100\ km}$ in 3000 rpm engine speed.

According to the results, we found that the presence of greater oxygen concentration resulted in a slight increase in the fuel consumption rate.

In the graph, it is shown that the fuel consumption rate increased approximately in proportion with engine rotational speed under constant engine torque conditions. This is attributed to the fact that when engine speed increased, the friction horsepower increased according to the drop in the mechanical efficiency to maintain a constant torque output (Lin and Wang 2004), leading to an increase in the fuel consumption rate.

5 Conclusions

The use of oxygen enrichment on a spark-ignition engine was studied, and some variables in engine performance, such as brake torque output, brake power output, and fuel consumption, were examined. The main conclusions can be summarized as follows:

1. The brake torque output and the brake power output increased with the increase in oxygen concentration at the air inlet manifold, representing that air with supplementary oxygen induced the complete combustion of engine. Also, when the engine speed was increased from 1000 to 3000 rpm, the brake torque output and the brake power output were increased. At higher engine speed, the combustion and exhaust temperature increased, which can promote higher efficiency.
2. The fuel consumption increased with the increase in oxygen concentration at the air inlet. When air mass flow is constant, the extra oxygen could be used to burn extra fuel to improve fuel consumption, leading to decrease air–fuel ratio. When engine speed increases, the friction horsepower rises according to the drop in the mechanical efficiency to maintain a constant torque output, leading to an increase in the fuel consumption amount.

References

Arrègle, J., López, J.J., García, J.M., Fenollosa, C.: Development of a zero-dimensional diesel combustion model. Part 1: analysis of the quasi-steady diffusion combustion phase. Appl. Therm. Eng. **23**(11), 1301–1317 (2003)

Assanis, D.N., Poola, R.B., Sekar, R., Catal, G.R.: Study of using oxygen-enriched combustion air for locomotive diesel engines. J. Eng. Gas Turbines Power. **123**, 157–166 (2001)

Boehman, A.L., Song, J., Alam, M.: Impact of biodiesel blending on diesel soot and the regeneration of particulate filters. Energy Fuel. **19**, 1857–1864 (2005)

Byun, H., Hong, B., Lee, B.: The effect of oxygen enriched air obtained by gas separation membranes from the emission gas of diesel engines. Desalination. **193**, 73–81 (2006)

Desai, R.R., Gaynor, E., Watson, H.C.: Giving standard diesel fuels premium performance using oxygen-enriched air in diesel engines, SAE Technical Paper 932806 (1993)

Duran, V., Uriondo, Z., Moreno-Gutiérrez, J.: The impact of marine engine operation and maintenance on emissions. Transp. Res. Part D. **17**, 54–60 (2012)

Franco, J., Franchek, M.A., Grigoriadis, K.: Real-time brake torque estimation for internal combustion engines. Mech. Syst. Signal Process. **22**, 338–361 (2008)

Ghojel, J., Hilliard, J.C.: Effect of oxygen enrichment on the performance and emissions of I. D. I. diesel engines, SAE Technical Paper 830245 (1983)

Heywood, J.B.: Internal combustion engine fundamentals. McGraw-Hill, Singapore (1988)

Karim, G.: Examination of combustion processes in compression–ignition engine by changing the partial pressure of oxygen in the intake charge, SAE Technical Paper 680767 (1968)

Kondo, T. (ed.): New development in gas separation technology. Toray Research Center Inc. Chūō, Tokio, Präfektur Tokio, Japan (1992)

Lin, C.Y., Wang, K.H.: Diesel engine performance and emission characteristics using three-phase emulsions as fuel. Fuel. **83**(4/5), 537–545 (2004)

Litzinger, T., Stoner, M., Hess, H., Boehman, A.L.: Effects of oxygenated blending compounds on emissions from a turbocharged direct injection diesel engine. Int. J. Eng. Res. **1**, 57–70 (2000)

Momen R.F.: Development of a laboratoy- scale device for disinfestation of stored product insects using controlled atmospheres. Paper number 026124, ASAE Annual Meeting. (doi:10.13031/2013.10944) (2002)

Natarajan, M., Frame, E.A., Naegeli, D.W., Asmus, T.W., Clark, W., Garbak, J., Gonzalez, M.A., Liney, E., Piel, W.J., Wallace, III J.P.: Oxygenates for advanced petroleum-based diesel fuels: Part 1. Screening and selection methodology for the oxygenates, SAE Technical Paper 2001–01-3631 (2001)

Perez, P.L., Boehman, A.L.: Performance of a single-cylinder diesel engine using oxygen-enriched intake air at simulated high-altitude conditions. Aerosp. Sci. Technol. **14**, 83–94 (2010)

Petela, R., Hutny, W., Price, J.T.: Energy and exergy consumption and CO_2 emissions in an iron making process. Adv. Environ. Res. **6**(2), 157–170 (2002)

Pettersson, M., Nielsen, L.: Gear shifting by engine control. IEEE Trans. Control Syst. Technol. **8** (3), 495–507 (2000)

Poola, R.B., Sekar, R.: Reduction of NO and particulate emissions by using oxygen-enriched combustion air in a locomotive diesel engine. J. Eng. Gas Turbines Power. **125**, 524 (2003)

Rakopoulos, C.D., Hountalas, D.T., Zannis, T.C., Levendis, Y.A.: Operational and environmental evaluation of diesel engines burning oxygen-enriched intake air or oxygen-enriched fuels: a review. SAE Trans. **113**, 1723–1743 (2004)

Song, J., Alam, M., Boehman, A.L., Kim, U.: Examination of the oxidation behavior of biodiesel soot. Combust. Flame. **146**, 589–604 (2006)

Song, J., Cheenkachorn, K., Wang, J., Perez, J., Boehman, A.L., Young, P.J., Waller, F.J.: Effect of oxygenated fuel on combustion and emissions in a light-duty turbo diesel engine. Energy Fuel. **16**, 294–301 (2002)

Song, J., Zello, V., Boehman, A.L., Waller, F.J.: Comparison of the impact of intake oxygen enrichment and fuel oxygenation on diesel combustion and emissions. Energy Fuel. **18**, 1282–1290 (2004)

Song, K.H., Nag, P., Litzinger, T.A., Haworth, D.C.: Effects of oxygenated additives on aromatic species in fuel-rich, premixed ethane combustion: a modeling study. Combust. Flame. **135**(3), 341–349 (2003)

Tolouei, R., Titheridge, H.: Vehicle mass as a determinant of fuel consumption and secondary safety performance. Transp. Res. Part D. **14**, 385–399 (2009)

Saito, M., Sato, M., Murata, H., Sadakata, M.: Combustion rates of pulverized coal particles in hightemperature/high-oxygen concentration atmosphere. Combust. Flame. **87**(1), 1–12 (1991)
Rigby, G.R., Watson, H.C.: Application of membrane gas separation to oxygen enrichment of diesel engines. J. Membr. Sci. **87**, 159–169 (1994)
Rameshbabu, M., Jayas, D.S., White, N.D.G.: Mortality of Cryptolestes ferrugineus(Stephens) adults and eggs in elevated carbon dioxide and depleted oxygen atmospheres. J. Stored Prod. Res. **27**, 163–170 (1991)

A Comparative Study on Some Methods to Use Tyre Pyrolysis Oil as an Alternative Fuel in a DI Diesel Engine

Sivalingam Murugan, Hariharan Sundaramoorthi, Govindan Nagarajan, and Bohumil Horak

1 Introduction

Increase in automobile vehicles is a growing concern, and in the coming years, the disposal of waste tyres will become complex. Issues associated with waste tyres have exercised the minds of both government policymakers and sections of the tyre industry around the world for many years. Yet there remains a strong perception that waste tyres are not being managed as well as they might. It is a fact that waste tyre management techniques adopted in India are very less when compared to the other developed countries. A majority of waste tyres are disposed through landfill, or there are reportedly significant numbers that are dumped illegally or disposed off in other inappropriate ways as reported by Christian Roy et al. (1999). The current disposal methods of waste automobile tyres are (i) landfill, (ii) crumbing, (iii) remould, (iv) incineration, (v) tyre-derived fuel and (vi) energy recovery through pyrolysis and gasification as reported by Cunliffe and Williams (1998). Effective waste minimisation benefits industry, community and environment. At present, about 50% of the waste automobile tyres are used for landfill. Some tyres are also used for engineering purposes in landfill sites. If disposed off in large volumes, tyres in landfill sites can lead to fires and instability by rising to the surface. This

S. Murugan (✉) • B. Horak
Department of Mechanical Engineering, National Institute of Technology, Rourkela, India

Department of Biomedical and Cybernatics, VSB Technical University, Ostrava, Czech Republic
e-mail: s.murugan@nitrkl.ac.in; muruganresearch@yahoo.com

H. Sundaramoorthi
Development Engineer, AVL MTC AB, Haninge, Sweden

G. Nagarajan
Department of Mechanical Engineering, Anna University, Chennai, India

© Springer International Publishing AG, part of Springer Nature 2018

F. Aloui, I. Dincer (eds.), *Exergy for A Better Environment and Improved Sustainability 2*, Green Energy and Technology,
https://doi.org/10.1007/978-3-319-62575-1_29

affects long-term settlement and may cause problems for future use and land reclamation.

The current disposal method of waste tyres by landfilling causes a loss of valuable resource. Other methods merely delay the inevitable need for disposal. Pyrolysis is a better method of disposing waste automobile tyres as reported by Isabel de Marco Rodriguez (2001). Another method of disposal is crumbing. This method involves cutting of tyres at several stages until rubber attains crumb form. These are several possible outlets for tyre crumb. But the current use is only around 25% of the total waste. Remould of waste tyres requires a lot of work on the part of the manufacturers, as many designs of tyres are not suitable for remould. About 20% of total waste automobile tyres are remouldable, and in turn this will increase by 5% more in the future. An alternative method for disposal of waste automobile tyres is incineration. By incineration of waste automobile tyres, electricity can be generated. However, high investment cost and high pollution are the two major problems associated with incineration of waste automobile tyres. Tyre has a high energy value and can be utilised for generation of heat and electrical power. The substance obtained from tyre for such purposes is called tyre-derived fuel (TDF). Instead of coal, TDF is burnt in cement kilns for heating purpose. However, because of chemicals in the tyres, the manufacturing ability of cement kiln decreases. There is also a potential problem of atmospheric pollution. Pyrolysis is a better method of disposing waste automobile tyres as reported by Yu Min Chang (1996).

Pyrolysis is the thermal cracking of organic substance in a theoretically oxygen-free environment (Zabaniotou and Stavropoulos 2003). Several researchers have studied on pyrolysis of biomass, waste automobile tyres, plastics and other organic materials. Pyrolysis of waste automobile tyres yields three principal products, namely, tyre pyrolysis oil (TPO), pyrogas and carbon black. Pyrolysis oil obtained from the organic substances can be used as alternative fuels for internal and external combustion engines (Bertoli et al. 2000; Farid Nasir and Kawser Jamil 1999). For instance, Yrjo Solantausta et al. (1993) studied the flash wood pyrolysis oil as an alternative fuel for diesel power plants. In this study, engine tests were carried out on a single-cylinder, diesel engine in three steps: (i) only with wood pyrolysis oil, (ii) ignition improver-enhanced pyrolysis oil and ethanol (iii) and poor-quality reference fuel. Engine test was also conducted on a multi-cylinder high-speed diesel engine with pilot injection. It was reported that NO_x emissions were higher by about 28%, and smoke was lesser by about 23% for wood pyrolysis oil compared to diesel. It was also reported that both NO_x and smoke have reduced by about 80% when ignition improver was added to pyrolysis oil. The ignition delay was found to be 6 °CA for diesel fuel, and with poor-ignition-quality reference fuel, it was 8 °CA. It was observed that the ignition improver was not as effective with pyrolysis oil as with ethanol. The minimum concentration of additive used was 3% and the ignition delay was 15 °CA and the engine operation was unstable. Only a small difference was noticed in ignition delay (i.e. 1 °CA), when improver concentration was increased from 5% to 9% in pyrolysis oil, and ignition delay was still longer than that of poor- quality reference fuel. Combustion started late with ethanol, pyrolysis oil containing 3% additive and poor-quality reference fuel (10% heat released at

5–16 °ATDC). Pyrolysis oil with 5% and 9% improver and conventional diesel were considerably faster (10% heat release at 3 °ATDC). Combustion duration for 50% heat release was almost the same for pyrolysis oil (5% and 9% additive) and diesel. The time taken for 90% heat release was the shortest with pyrolysis oil, approximately 15 °CA for pyrolysis oil when compared to that of 25 °CA for diesel operation. The time taken between 10% and 90% heat release was roughly 22 °CA for diesel and 13–17 °CA for pyrolysis oil. Frigo et al. (1996) investigated cylinder high-speed diesel engine with pilot injection. It was reported that NO_x was higher by about 28%, and smoke was lesser by about 23% for wood pyrolysis oil compared to diesel. It was also reported that both NO_x and smoke have reduced by about 80% when ignition improver was added to pyrolysis oil. The ignition delay for diesel fuel was 6 °CA, and with poor-ignition-quality reference fuel, it was about 8 °CA. It was observed that the ignition improver was not as effective with pyrolysis oil as with ethanol.

In the present investigation samples of waste truck tyres were subjected to vacuum pyrolysis process to obtain the TPO. Then the physico-chemical properties of the derived TPO were determined and compared with those of diesel fuel (DF) properties. Then, attempts were to explore the possible methods to use TPO as an alternative fuel in a compression ignition (CI) engine by adopting few fuel and engine modifications. The combustion, performance and emission parameters of the engine run on crude TPO and modified fuels were tested in a single-cylinder, four-stroke, air-cooled, direct injection (DI) engine. The experimental results were compared with those of diesel fuel operation in the same engine and presented in this paper.

2 Materials and Methods

2.1 Tyre Pyrolysis Oil (TPO)

In the present investigation, waste tyres originated from trucks were collected from disposal areas and shredded into smaller pieces. The shredded tyre chips were washed and then dried for removal of moisture. The elemental composition of tyre sample (tread rubber) is given in Table 1.

The detailed description of the vacuum pyrolysis carried out in this study is described in (Murugan et al. 2008a, b). Nitrogen was used to purge the oxygen from the reactor. The process was carried out between 450 and 650 °C in the reactor for 4 h and 30 min. The fuel properties are important in predicting the engine behaviour (Watanabe et al. 1998). The heat energy required to convert the waste tyres into the products was around 7.8 MJ/kg. The properties of TPO obtained in the pyrolysis process are compared and given in Table 2.

Table 1 Elemental composition of waste tyres (Murugan 2008)

Elemental composition (wt %)	Proximate analysis (Dry air wt %)
Carbon: 88.87	Volatile matter: 67.06
Hydrogen: 7.09	Fixed carbon: 28.13
Oxygen: 2.17	Moisture content: Nil
Nitrogen: 0.24	Ash content: 4.81
Sulphur: 1.63	
Total: 100.00	100.00

Table 2 Comparison of properties of TPO and DTPO with petroleum fuels (Murugan et al. 2008a, b)

Property		Diesel	Gasoline	TPO	DTPO
Density @ 15 °C, kg/m^3		830	740	923.9	771
Kinematic Viscosity, cSt @ 40 °C		2.58	–	3.77	1.7
Net Calorific Value, MJ / kg		43.8	45	38	39
Flash Point, °C		50	−42.78	43	36
Fire Point, °C		56	−48.89	50	48
Sulphur Content, %		0.29	_	0.72	0.26
Ash content, %		0.01	_	0.31	–
Carbon residue, %		0.35	0.7		0.02
Aromatic content, %		26		60	
Distillation temperature, °C	Boiling Point	198.5		70	
	10%	240.5		114.5	
	50%	278.5		296.1	
	90%	330.5		386.4	
	EP	344		388.7	

2.2 *Experimental Setup*

The schematic layout of the experimental setup is shown in Fig. 1. The specifications of the engine are given in Table 3. An electrical dynamometer was used to provide the engine load. An air-box was fitted to the engine for airflow measurements. The fuel flow rate was measured on volumetric basis using a burette and a stopwatch. Chromel-alumel thermocouple in conjunction with a digital temperature indicator was used to measure the exhaust gas temperature. A pressure transducer in conjunction with Kistler makes charge amplifier, and a cathode ray oscilloscope (CRO) was used to measure the cylinder pressure. The pressure pickup was mounted on the cylinder head and before mounting it was calibrated with a dead weight tester. A TDC optical sensor with a signal conditioner was used to detect the engine crank angle.

A gas analyser was used to measure NOx/HC/CO emissions in the exhaust. The accuracy of the instrument is ±1 ppm. Smoke was measured by a Bosch smoke metre. The specifications of the exhaust gas analyser and smoke metre are given in

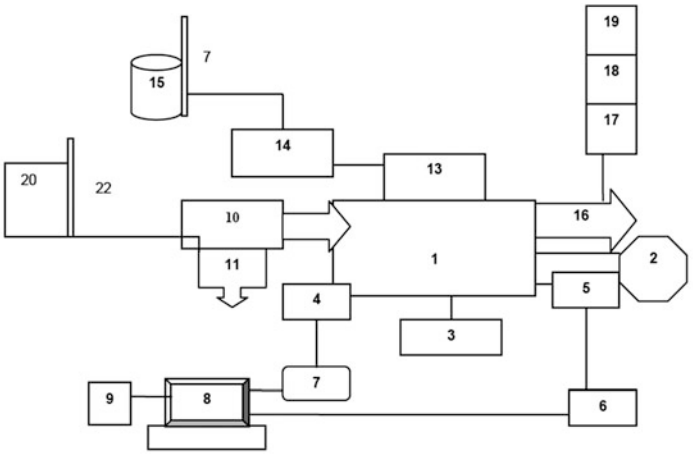

1. Engine
2. Dynamometer
3. Control Panel
4. Pressure Pickup
5. TDC optical sensor
6. Signal conditioner
7. Charge Amplifier
8. C.R.O
9. Printer
10. Inlet Manifold
11. Surge tank
12. Air flow meter
13. Fuel Injector
14. Fuel Injection pump
15. Fuel Tank
16. Exhaust Manifold
17. CO/HC Analyser
18. NO_x Analyser
19. Bosch Smokemeter
20. DEE Tank
21. Burette for DF/TPO
22. Burette for DEE

Fig. 1 Experimental setup

Table 3 Engine details

Name of the engine	Kirloskar
General details	Four stroke, CI, air cooled, single cylinder
Bore (mm)	87.5
Stroke (mm)	110
Compression ratio	17.5:1
Rated output at 1500 rpm (kW)	4.4
Fuel injection pressure (bar)	210
Injection timing (°CA)	23 BTDC

Appendix 3. Initially experiments were carried out using base diesel fuel (DF). All the experiments were conducted at the rated engine speed of 1500 rpm. A series of performance and exhaust emission tests were carried out on the engine using TPO-/DTPO-based fuels and DF. All the tests were conducted by starting the engine with DF only. After the engine was warmed up, it was then switched to TPO-DF run for sometime with DF to flush out the TPO-DF from the fuel line and the injection system.

2.3 TPO-Diesel Fuel (DF) Blends

Initially, 10–70% of TPO on volume basis was blended with DF and was under observation for 15 days to check for the miscibility. It was observed that no separation took place in the blend of TPO and DF. TPO blended with DF is indicated as TPO xx, like TPO 10 denotes 10% TPO blended with 90% DF.

2.4 Engine Modification: Higher Injection Pressure

Increasing the injection pressure improves the atomisation of fuel (Mbarawa et al. 1999; Yoshiyuki Kidoguchi et al. 2000). Normal injection pressure of engine in which the tests were conducted was 210 bar. In this study, various nozzle opening pressures, viz., 220 bar, 230 bar and 250 bar, with the same fuel injection pump and injectors were used.

2.5 Distilled Tyre Pyrolysis Oil-DF Blends

As the crude TPO contained moisture, foreign particles and impurities, the performance and other factors would be affected. The desulphurisation and distillation of TPO improved a few physico-chemical properties. Hence, DTPO was blended with DF from 10% to 40% (in steps of 10%) and used as a partial fuel in the same engine. The injection pressure was kept at original injection pressure of 210 bar. The performance, emission and combustion characteristics of the single-cylinder, four-stroke, air-cooled, DI diesel engine were studied.

2.6 TPO-DEE Dual Fuel Mode

Initially the engine was able to run up to 70% of TPO blended with 30% DF. After distillation of TPO, the DTPO was blended with DF up to 90 percent (90% of DTPO and 10% of DF) and used as a fuel in the engine. But the engine was not able to run with 100% TPO or DTPO as fuel. The probable reason was due to lower cetane number of the fuel that resulted in a longer ignition delay, thereby delaying the start of combustion. Fuels with very high cetane numbers can reduce the ignition delay to a greater extent (Nagarajan and Prabhu Kumar 2004). Low cetane fuels can be solely used in a diesel engine on dual fuel mode (Eugene Ecklund et al. 1984). There are a number of such fuels such as dimethyl ether, diethyl ether and diglyme [Anand and Mahalakshmi (2006) and Nicos Ladommatos et al. (1996)]. Out of these fuels, diethyl ether was found to be the most potential fuel. Diethyl ether

Table 4 Properties of DEE (Hariharan et al. 2013)

Property	DEE
Viscosity at 20 °C, centipoise	0.23
Specific gravity	0.714
Density, kg/m^3	713
Heating value, MX kg	33.89
Cetane number	>125
Autoigniton temperature, °C	160
Boiling point, °C	34.4

(DEE) has a cetane number greater than 125 as reported by Subramanian and Ramesh (2002). Dimethyl ether is more volatile than diethyl ether and is prone to create vapour lock problems in the fuel lines. Diglyme is also a high cetane fuel that can be used as an ignition enhancer but it is costly. Normally IC engines can be operated with two fuels such as gaseous or high volatile fuel and another liquid fuel. Such an engine is called a dual fuel engine. The two fuels can be admitted in varying proportions. In this investigation, TPO was injected into the cylinder as main fuel, and DEE was inducted into the cylinder along with air. The properties of DEE are given in Table 4.

A plastic container storing DEE was connected to a burette through a stopcock. From the burette, the DEE was allowed to flow through an inlet valve (I.V) needle of 2 mm diameter directly into the intake pipe located at 5 cm before the inlet manifold. The DEE was admitted into the intake pipe in the form of droplets. As DEE is highly volatile, it readily mixes with the air drawn and enters into the cylinder. The engine started easily with TPO. The time taken for DEE and TPO was recorded to determine the flow rates, respectively. Experiments were conducted at various flow rates of DEE.

DEE aspirated into the intake air was gradually varied to achieve the constant speed of 1500 rpm at various loads. At each load, three flow rates of DEE, viz., 65 g/h, 130 g/h and 170 g/h, were maintained in such a way that the onset of unstable operation or misfiring and knocking was observed from the pressure crank angle trace. The quantities of DEE required for starting the engine and for idling was 16.5% by mass. The energy share of DEE at different loads on mass basis is given in Table 5.

During the engine operation on dual fuel mode, there was no knocking noticed at low loads. This was ensured through the pressure crank angle diagram recorded in an oscilloscope.

3 Results and Discussions

Based on the fuel economy and emission results, the following were considered in each mode of test conducted:

Table 5 Energy share of DEE at different loads on mass basis (in percentage)

	DEE inducted at different flow rates (g/h)		
Load (%)	65	130	170
No load	1.6	16.5	21.1
25	7.2	15.2	20.4
50	6.5	12.8	16.9
75	5.3	9.9	13.1
90	4.7	8.7	11.7
100	4.0	7.4	10.8

(i) TPO30 (30% TPO in crude form + 70% DF on volume basis) subjected to fuel injection pressure of 220 bar was chosen as optimum in the case of TPO-DF blend operation.
(ii) DTPO40 (40% distilled tyre pyrolysis oil + 60% DF on volume basis) was chosen as optimum when the engine was run on DTPO-DF fuel blends.
(iii) When TPO was injected as a pilot fuel and DEE was inducted at three different flow rates on the dual fuel mode, TPO + 130 g/h was chosen as an optimum condition.

3.1 Pressure Crank Angle Diagram

Figure 2 shows the pressure crank angle diagram for TPO operation for different techniques and DF. The peak cylinder pressure in a CI engine is influenced by the ignition delay and mixture formation (Heywood 1998). It can be observed from the figure that the cylinder peak pressure for DF is 71 bar. Fuels with a high cetane number and better mixture formation result in higher cylinder pressure (Nicos Ladommatos et al. 1996). In the case of TPO 30 at 220 bar, DTPO 40 and TPO-DEE at 130 g/h, the cylinder peak pressures at full load are 73 bar and 68 bar and 74 bar, respectively. Longer ignition delay of TPO 30 at 220 bar may be the reason for increase in cylinder peak pressure. In the case of DTPO 40, the peak pressure is lesser by about 3 bar than DF.

Higher latent heat of evaporation may be the reason for the decrease in the peak pressure. For TPO-DEE at 130 g/h, the peak pressure increases by 3 bar compared to DF as a result of longer ignition delay. Longer ignition delay may be attributed to the interaction of DEE with the aromatics in the TPO, delaying the onset of combustion.

3.2 Ignition Delay

Ignition delay is the time difference in crank angle between the start of injection and start of combustion. Figure 3 shows the variation of ignition delay with brake power while using TPO and DF.

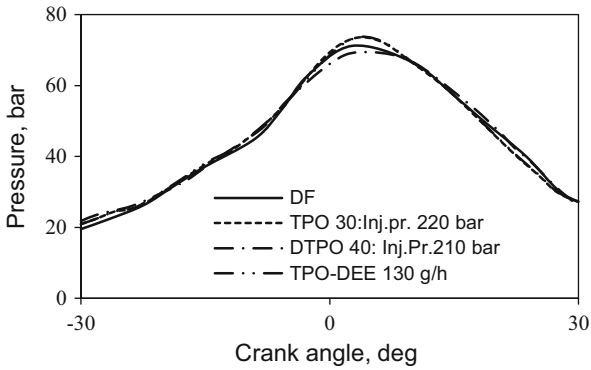

Fig. 2 Variation of cylinder pressure with crank angle

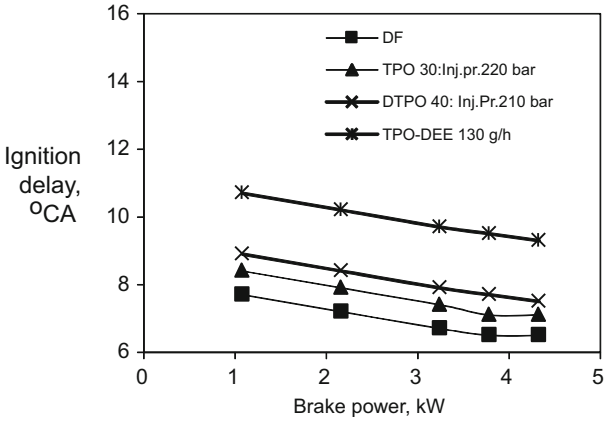

Fig. 3 Ignition delay with brake power

It may be seen from the figure that the ignition delay for DF varies from 7.7 °CA at low load to 6.5 °CA at full load. For TPO 30 with fuel injection pressure of 220 bar, it varies from 8.4 °CA at low load to 7.1 °CA. In the case of DTPO 40, it varies from 8.9 °CA at low load to 7.5 °CA at full load. For TPO-DEE operation, it varies from 10.7 °CA at low load to 9.3 °CA at full load. Longer ignition delay is noticed in TPO-DEE operation since TPO is a low-quality fuel. And also, the quality of TPO is inferior compared to that of DTPO 40 and TPO 30 with fuel injection pressure of 220 bar.

3.3 Cylinder Peak Pressure

It can be noticed that the cylinder peak pressure is higher for TPO 30 and TPO-DEE and lower for DTPO 40 operation compared to DF. The cylinder peak pressure for

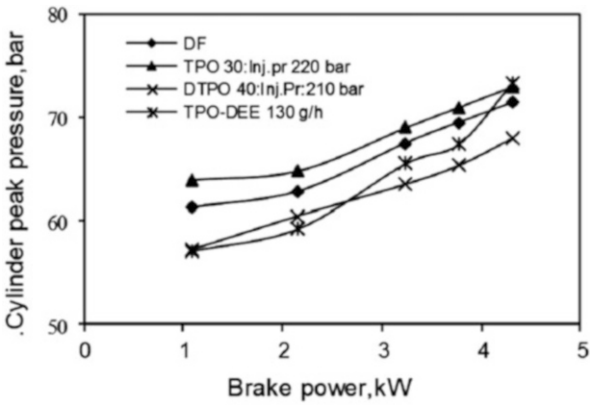

Fig. 4 Maximum cylinder pressure with brake power

DF increases from 58 bar at low load to 71 bar at full load, and for the fuel injection pressure of 220 bar for TPO 30 operation, it varies from 59 bar at low load to 73 bar at full load. For DTPO 40, the peak pressure varies from 57 bar at low load to 68 bar, and in the case of TPO-DEE operation, it ranges from 57 bar at low load to 73 bar at full load. Higher viscosity and lower volatility of the TPO 30 blend may be the reason for higher peak pressure. The variation of cylinder peak pressure with brake power is shown in Fig. 4.

The increase in the peak pressure in the case of TPO-DEE operation may be due to longer ignition delay, and the increase in heat release rate occurs before TDC by the early combustion of DEE (Nagarajan et al. 2002). Higher latent heat of evaporation of DTPO 40 may be the reason for lower cylinder peak pressure.

3.4 Rate of Heat Release

The heat release rate in a CI engine depends on the ignition delay and initial stages of combustion (Huang et al. 2004; Jamil Ghojel and Damon Honnery 2005). The heat release pattern of each technique of TPO operation and DF at full load is shown in Fig. 5.

DF shows lesser heat release rate at the initial stage and longer combustion duration at full load. For DF the maximum heat release rate is 57.4 J/°CA which occurs at 6.7 ° before TDC. The maximum rate of heat release for TPO 30 with fuel injection pressure of 220 bar is 60 J/°CA which occurs at 6.5 ° before TDC. In the case of DTPO 40 operation, the maximum heat release rate is 56.3 J/°CA which occurs at 5.9 °CA before TDC. For TPO-DEE operation it is 59.5 J/°CA occurring at 6.4 °CA. This may be due to the higher vaporising tendency of DEE even though the ignition delay is longer when compared to that of DF. Longer ignition delay is the reason for higher peak pressures and heat release for TPO 30 and DTPO40. The heat of evaporation of DEE is comparatively higher than that of DF. In the case of

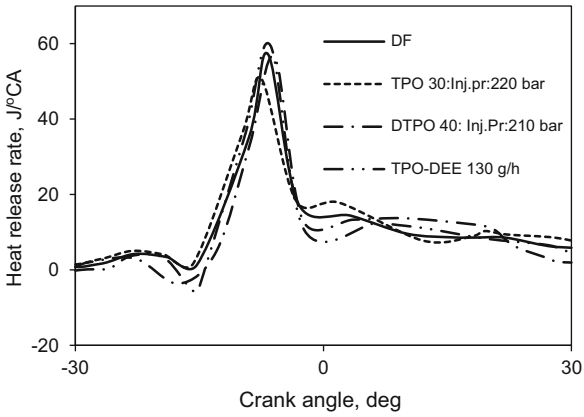

Fig. 5 Heat release rate with crank angle at full load

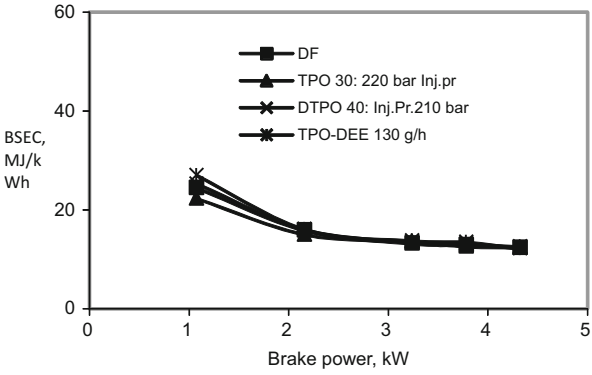

Fig. 6 BSEC with brake power

TPO-DEE operation, the diffusion combustion is longer though the cetane number of DEE is higher. This may be due to lower volatility of TPO compared to that of DF.

3.5 Brake Specific Energy Consumption (BSEC)

Figure 6 shows the comparison of BSEC with brake power for different TPO blended fuels and DF.

It can be noticed from the figure that the BSEC for DF varies from 24.4 MJ/kWh at low load to 12.2 MJ/kW h at full load. At the fuel injection pressure of 220 bar for TPO 30 operation, the BSEC varies from 22.2 MJ/kW h at low load to 12.3 MJ/kW h at full load. Low viscous and higher calorific value fuels consume less fuel (Prabhakar Reddy 1999; Pradeep and Sharma 2005). The BSEC for TPO at 220 bar is marginally lesser compared to that of DF, due to better spray formation. In the case of DTPO 40, the BSEC varies from 25.2 MJ/kW h at low load to 12.4 MJ/

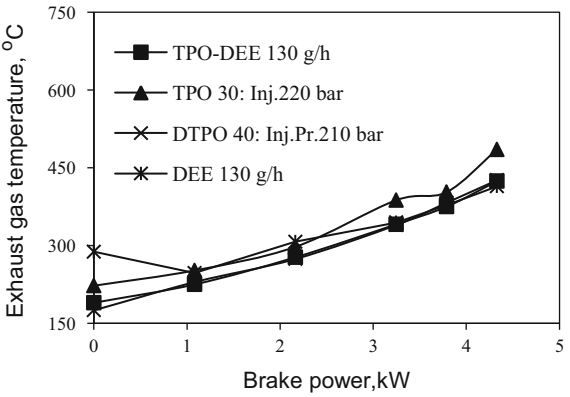

Fig. 7 Exhaust gas temperature with brake power

kW h at full load. The BSEC for DTPO 40 is the same as that of DF operation. It varies from 28.03 MJ/kW h at low load to 12.7 MJ/kW h at full load for TPO-DEE operation. It is observed that the energy required for TPO-DEE operation, to develop the same power output, is higher than DF, and hence, more amount of fuel is consumed. This is due to the lower heating value of TPO and DEE than DF.

3.6 Exhaust Gas Temperature

The comparison of exhaust gas temperature with brake power is shown in Fig. 7. Exhaust gas temperature is used to predict the useful work in an internal combustion (IC) engine (Ganesan 2003). The exhaust gas temperature for DF varies from 190 °C at no load to 424 °C at full load. At the fuel injection pressure of 220 bar for TPO 30 operation, the exhaust gas temperature varies from 223 °C at no load to 485 °C at full load. In the case of DTPO 40, the exhaust gas temperature varies from 171 °C at no load to 426 °C at full load. Longer ignition delay is the reason for higher exhaust gas temperatures in the TPO-DF and DTPO-DF operation. It varies from 238 °C at low load to 414 °C at full load for TPO-DEE operation.

Higher latent heat evaporation of DEE is the reason for the lower exhaust gas temperature for TPO-DEE operation.

3.7 Oxides of Nitrogen (NO_x) Emission

Figure 8 depicts the variation of NO_x emissions with brake power for TPO 30 with fuel injection pressure of 220 bar, DTPO 40, TPO-DEE and DF. The NOx emission in a compression ignition (CI) engine depends on the oxygen availability and the cylinder temperature (Yakup Icingur and Duran Altiparmak 2003). NO_x for DF varies from 16.9 g/kW h at low load to 14.9 g/kW h at full load, whereas it varies

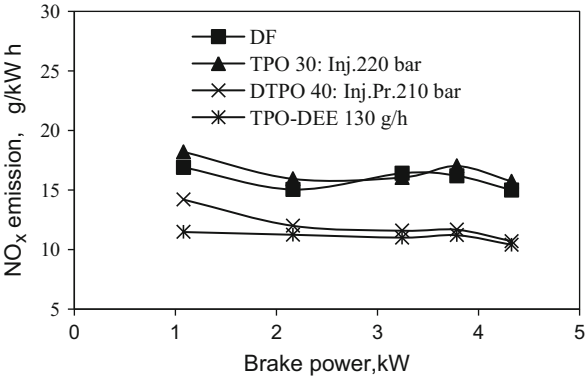

Fig. 8 NO_x emissions with brake power

from 18.2 g/kW h at low load to 15.7 g/kW h at full load for TPO 30 at 220 bar. In the case of DTPO 40, NO_x varies from 14.2 g/kW h at low load to 10.7 g/kW h at full load and from 10.4 g/kW h at low load to 14.2 g/kW h at full load with the induction of DEE at 130 g/h. In comparison, TPO 30 shows the highest NO_x values compared to DF and the other best of techniques. Increasing fuel injection pressure to certain pressure increases the mixture formation (Reddy et al. 2000).

This may be attributed to lower volatility, higher viscosity of TPO 30. DTPO-DF operation and TPO-DEE operation produce lower NO_x levels compared to that of DF and TPO-DF operation. Higher latent heat of a fuel reduces the intensity of the premixed phase combustion due to lower cylinder temperature (Lu Xing-Cai et al. 2004). The reason for lesser NO_x may be due to the higher latent heat of evaporation of DTPO. In the case of TPO-DEE operation, lower combustion temperature caused by DEE is the reason for lower NO_x formation.

3.8 Smoke Emission

Aromatic content and fuel properties play important role in smoke emission of a CI engine (Kent et al. 1994, 1995). The variation of smoke emission with brake power for the tested fuels is shown in Fig. 9. The smoke density for DF varies between 0 BSU at no load and 1.45 BSU at full load. Smoke reduces marginally for TPO 30 operation with fuel injection pressure of 220 bar at full load, and the value lies between 0.1 BSU at no load and 1 BSU at full load. Diesel has a high cetane number and less aromatic content than the TPO and DTPO; hence, the smoke is lower than TPO-based operation except when it is subjected to higher injection pressure.

For DTPO 40, it varies from 0.2 BSU at no load to 1.65 BSU at full load, while for TPO-DEE operation, it varies from 1.8 BSU at low load to 3.2 BSU at full load. In comparison, TPO 30 with fuel injection pressure is found to emit lesser smoke value compared to that of DF. But DTPO-DF operation and TPO-DEE operation give higher smoke compared to that of TPO 30 and DF. Higher injection pressure of

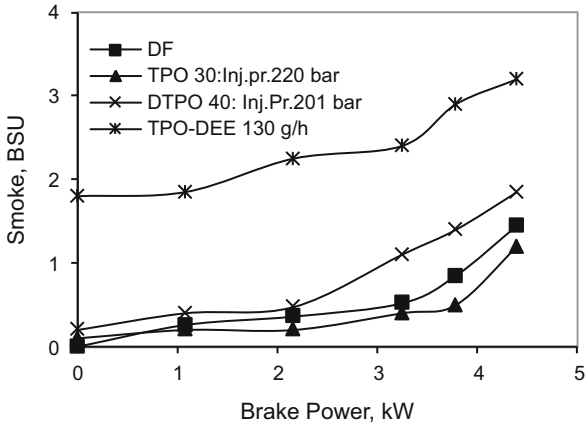

Fig. 9 Smoke with brake power

TPO 30 would improve the atomisation of fuel results in a slightly lower smoke emission. But in the case of DTPO-DF operation, lower cylinder temperature is caused due to higher latent heat of evaporation, in addition to PAH present in the DTPO which may be the reasons for higher smoke. Smoke emission at full load in each of the techniques is given in Table 5.10.

4 Conclusion

Based on the investigations carried out on a single-cylinder, four-stroke, air-cooled, DI diesel engine fuelled with diesel and tyre pyrolysis oil (TPO) using different techniques, the following conclusions are drawn:

- Increasing injection pressure of fuel nozzle reduced the ignition delay with improvement in the brake thermal efficiency. But the exhaust gas temperature increased. The NO_x emission increased, while the smoke emission reduced. The rate of pressure rise was higher than that of diesel at full load. Brake thermal efficiency for DF at full load is 29.5%, whereas it is 28.9% for the engine fuelled with TPO 30.NOx for TPO 30 is 4.5% higher compared to DF at full load. Smoke decreases by about 1 BSU when the nozzle opening is increased to 220 bar from 210 bar.
- Although the ignition delay was marginally higher for DTPO40 than that of TPO30 at 220 bar, the NOx emission was reduced, but with marginal increase in the smoke emission at full load. NOx reduces by about 29% in DTPO 40 operation compared to DF operation. Smoke density is 14% higher in DTPO 40 compared to DF.
- By running the engine TPO-DEE on the dual fuel mode, the ignition delay was higher than the other operations, at full load. However, the results prove that utilisation of TPO as a sole fuel in a diesel engine is possible. Thermal efficiency

reduced by about 2.5% with TPO-DEE operation at full load compared to DF. NOx is 5% lesser for TPO-DEE operation than DF at full load. Thirty-eight percentage increase in smoke emission is observed for TPO-DEE compared to DF at full load.

- Overall, the DTPO 40 blend shows a better performance with reduced emissions compared to that of TPO 30, TPO-DEE and DF operations.

Acknowledgements This paper has been elaborated in the framework of the project new creative teams in priorities of scientific research, reg. no. CZ.1.07/2.3.00/30.0055, supported by Operational Programme Education for Competitiveness and cofinanced by the European Social Fund and the state budget of the Czech Republic.

References

Anand, R., Mahalakshmi, N.V.: Simultaneous reduction of NO_x and smoke from a direct injection diesel engine with exhaust gas recirculation and diethyl ether. In: Proceedings of IMechE. **22** (1), Part D: Journal of Automobile Engineering, 109–116 (2006)

Bertoli, C., D'Alessio, J., Del Giacomo, N., Lazzaro, M., Massoli, P. Moccia, V.: Running light duty DI diesel engines with wood pyrolysis oil. SAE paper no. 2000–01-2975, 3090–3096 (2000)

Chang, Y.-M.: On pyrolysis of waste Tyre: degradation rate and product yields. J. Resour. Conserv. Recycl. **17**, 125–139 (1996)

Cunliffe, A.M., Williams, P.T.: Composition of oils derived from the batch pyrolysis of tyres. J. Anal. Appl. Pyrolysis. **44**, 131–152 (1998)

Eugene Ecklund, Richard L Bechtold, Thomas J.Timbario and Peter W. McCallum, State of the art report on the use of alcohols in diesel engines. SAE paper no.840118, 684–700 (1984)

Frigo, S., Gentil, R., Tognotti, L., Zanforlin, S.: Feasibility of using flash wood pyrolysis oil in diesel engines. SAE paper no. 962529, 165–173 (1996)

Ganesan, V.: Internal combustion engines, 2nd edn. Tata McGraw Hill Publications, New Delhi (2003)

Ghojel, J., Honnery, D.: Heat release model for the combustion of diesel oil emulsions in DI diesel engines. J. Appl. Therm. Eng. **25**, 2072–2085, Elsevier Publications (2005-A)

Hariharan, S., Murugan, S., Nagarajan, G.: Effect of diethyl ether on Tyre pyrolysis oil fueled diesel engine. Fuel. **104**, 109–115 (2013)

Heywood, J.B.: Internal combustion engines fundamentals. McGraw Hill, New York (1998)

Huang, Z.H., Lu, H.B., Jiang, D.M., Zeng, K., Liu, B., Zhang, J.Q., Wang, X.B: Combustion characteristics and heat release analysis of a compression ignition engine operating on a diesel/methanol blend. In: Proceedings of the Institution of Mechanical Engineers: Pro Quest Science Journal, pp. 1011–1024 (2004)

Icingur, Y., Altiparmak, D.: Effect of fuel cetane number and injection pressure on a DI diesel engine performance and emissions. Energy Convers. Manag. **44**, 389–397 (2003)

Kent, B,Terry, L,Ullman, L,Robert, L.M.: Effects of cetane number , cetane improver, aromatics and oxygenates on 1994 heavy duty-diesel engine emissions. SAE paper no.941020 (1994)

Kent, B, Terry, L, Ullman, L, Robert, L.M.: Effects of cetane number, cetane improver, aromatics and oxygenates on 1994 heavy duty-diesel engine emission with exhaust catalyst. SAE paper no.95020 (1995)

Kidoguchi, Y., Yang, C., Kato, R., Miwa, K.: Effects of fuel cetane number and aromatics on combustion process and emissions of a direct-injection diesel engine. JSAE Rev. **21**, 469–475 (2000)

Ladommatos, N., Parsi, M., Knowles, A.: The effect of fuel cetane improver on diesel pollutant emissions. Journal of Fuel. **75**(1), 8–14 (1996)

Mbarawa, M., Millton, B.E., Casey, R.T., Miao, H.: Fuel injection characteristics of diesel stimulated natural gas combustion. Int. J. Energy Res. **23**(5), 1359–1371 (1999)

Murugan, S., Ramaswamy, M.C., Nagarajan, G.: The use of tyre pyrolysis oil in diesel engines. Waste Manag. **28**(12), 2743–2749 (2008a)

Murugan, S., Ramaswamy, M.C., Nagarajan, G.: Performance, emission and combustion studies of a DI diesel engine using distilled Tyre pyrolysis oil-diesel blends. Fuel Process. Technol. **89** (2), 152–159 (2008b)

Nagaraja, A.M., Prabhu Kumar, G.M.: Characterization and Optimization of rice bran oil methyl ester for CI engine at different injection pressures. SAE paper no.2004–28-0048, pp. 320–325 (2004)

Nagarajan, G., Renganarayanan, R., Rao, A.N.: Emission and performance characteristics of neat ethanol fueled DI diesel engine. International Journal of Ambient energy. **23**(3), 149–158 (2002)

Nasir, F., Jamil, Md.K.: Pyrolysis rubber oil as an alternative renewable fuel in diesel engines. In: Proceedings of 5th Asia Pacific International Symposium on Combustion and Energy, pp. 38–43, China (1999)

Prabhakar Reddy, C; Studies on droplet size measurement and engine performance using non edible oils as alternate fuels. In: Proceedings of the IC Engines and Combustion Conference, pp. 197–204 (1999)

Pradeep, V., Sharma, R.P.: Evaluation of performance, emission and combustion parameters of a CI engine fueled with biodiesel from rubber seed oil and its blends. SAE paper no. 2005-26-353, 339–352 (2005)

Reddy, K.V., Babu, K.R., Ganesan, V.: Effect of Injection pressure on diesel engine performance with vegetable oil: diesel blends, In: Proceedings of I.C Engines and Combustion Conference, Narora Publishers, New Delhi (2000)

Rodriguez, I.d.M., Laresgoiti, M.F., Cabrero, M.A., Torres, A., Chomon, M.J., Caballero, B.: Pyrolysis of scrap tyres. Fuel Processing Technology. **72**(1), 9–22 (2001)

Roy, C.: Blaise Labrecque and Bruno de Caumia recycling of scrap tyres to oil and carbon black by vacuum pyrolysis, Journal of Resources. Conservation and Recycling. **4**, 203–213 (1990)

Roy, C., Chaala, A., Darmstadt, H.: The vacuum pyrolysis of used tyres end-uses for oil and carbon black products. J. Anal. Appl. Pyrolysis. **51**, 201–221 (1999)

Subramaniam, K.A., Ramesh, A.: Use of diethyl ether along with water–diesel emulsion in a DI diesel engine. SAE paper no. 2002-01-2720, 1361–1367 (2002)

Watanabe, H., Tahara, T., Tamanouchi, M., Iida, J.: Study on the effects on exhaust emissions in direct injection diesel engines: effect of fuel injection system, distillation properties and cetane number. JSAE. Rev. **19**(1), 21–26 (1998)

Xing-Cai, L., Jian-guang, Y., Wu-gao, Z., Zhen, H.: Effect of cetane number improver on heat release rate and emissions of high speed diesel engine fueled with ethanol-diesel blend fuel. Journal of Fuel. **83**, 2013–2020 (2004)

Zabaniotou, A.A., Stavropoulos, G.: Pyrolysis of used automobile tyres and residual char utilization. J. Anal. Appl. Pyrolysis. **70**, 711–722 (2003)

Investigation of Effects of Natural Gas Composition on One-Dimensional Comprehensive Engine Model Calibration

Seyed Vahid Ghavami, Ali Salavati-Zadeh, Ahmad Javaheri, Bahram Bahri, Vahid Esfahanian, and Masoud Masih Tehrani

1 Introduction

Natural gas as a potential clean alternative fuel is playing a growing role in stationary and transportation industries. Large reservoirs have made this fuel to be even more promising. On the other hand, employment of natural gas comes with an inevitable shortcoming of considerable deviation in composition of gases extracted from different resources, which causes change in these gases' combustion features.

Concerns over the energy crisis and rising environmental issues have made combustion system designers to face challenges in the design of modern systems. The development of numerous prototypes is not feasible or even possible anymore. Therefore, computer simulation can be an efficient tool. In spite of this, three-dimensional high-resolution modelling strategies are very time-consuming and won't be suitable tools for providing the rapid responses obliged by market demands or regulatory agenda. Reduced-order modelling strategies would be a

S.V. Ghavami • A. Salavati-Zadeh (✉) • A. Javaheri
Vehicle, fuel and Environment Research Institute, University of Tehran, North Kargar Ave, Tehran, Iran
e-mail: alisalavati@ut.ac.ir

B. Bahri
Automotive Engineering Department, Shahreza Branch, Islamic Azad University, Shahreza, Iran

V. Esfahanian
School of Mechanical Engineering, Engineering College, University of Tehran, Tehran, Iran

M. Masih Tehrani
School of Automotive Engineering, Iran University of Science and Technology, Tehran, Iran

© Springer International Publishing AG, part of Springer Nature 2018

F. Aloui, I. Dincer (eds.), *Exergy for A Better Environment and Improved Sustainability 2*, Green Energy and Technology,
https://doi.org/10.1007/978-3-319-62575-1_30

favourable option in analysis and optimization of combustion systems, i.e. internal combustion engines. An example of these simulation strategies is comprehensive one-dimensional engine cycle modelling, which since its development in the late 1970s has undergone many developments and plays a pivotal role in the design and optimization processes of internal combustion engines. The main assumption in this modelling strategy is that the engine pipes and runners' length to diameter ratios are large enough, so that the flow could be considered to be one dimensional. It is also assumed that the flow rate is high enough to neglect the influences of viscosity (Benson 1982; Ramos 1989). It is therefore convenient to employ inviscid one-dimensional Euler system of equations known as gas dynamic system of equations (White 2003) to simulate the flow field inside the engine pipes. Other elements such as cylinder, air cleaner, plenums, junctions, injectors, catalytic converters, throttle, etc. are simulated using the thermodynamic zero-dimensional models. Meanwhile, another methodology for in-cylinder flow field simulation with more accuracy follows the general lines of multi-zone modelling technique, which considers the cylinder to be divided to different thermodynamic zero-dimensional zones, i.e. burned and unburned. The results of flow simulation in different elements are implemented as boundary conditions to gas dynamic system of equations. On the other hand, this approach suffers a great drawback. It has a very low accuracy where the three-dimensional effects take part in flow features, homentropic assumption does not apply or the flow bending radius is very small. Similar to all other reduced-order simulation procedures, this technique also involves employment of empirical correction factors which should be calibrated against experimental observations. Examples of these factors can be flow or discharge coefficients at the connection keypoints of elements and runners, in which the gas dynamic system of equations is solved. Besides these coefficients, several factors are required and should be calibrated for adjustment of results obtained from simulation of flow inside other elements. Examples of these coefficients would be factors considered in combustion thermodynamic function, i.e. Wiebe function (Ghojel 2010), or in-cylinder wall heat transfer coefficients and temperatures.

In this framework, the position of calibration process is of crucial necessity when employing reduced-order modelling techniques. A one-dimensional model may end in several results, one of which correctly predicts the engine intake and exhaust masses and reconstructs the in-cylinder pressure and heat release profile with high accuracy (Winterbone and Pearson 2000; Caton 2016). When the engine cycle 1D comprehensive model is fully calibrated, it could be employed for predicting of engine performance in several conditions (Benson 1982; Ramos 1989; Winterbone and Pearson 2000; Caton 2016), whereas in case of charge in many other performance conditions, such as valve lift timing and profile, it is mandatory to recalibrate the model with experimental observations and/or high-fidelity multidimensional simulation results.

It should be noted that by change in the fuel of an engine, the calibration of the thermodynamic cycle won't be reliable anymore. This fact follows the high dependency of burn rate function, Wiebe function as an example, on fuel bond types and

energies, transport factors, etc. (Ghojel 2010). In addition, the change in the density of fuel and air mixture may influence the flow coefficients at the boundaries and may therefore harm the model correctness (Medina et al. 2014).

The natural gas consists of several small normal or branched aliphatic C_1 to C_5 hydrocarbons along with inert species, mainly nitrogen (N_2) and carbon dioxide (CO_2) molecules. On the other hand, its composition differs among various wells. Additionally, it may also change based on the petrochemical process. In most of the simulation tools, pure methane is considered as the main surrogate candidate for natural gas, whose composition may differ and alter significantly from one area to another, and this matter has caused concerns about the correctness of reduced models of CNG-fuelled combustion systems.

Considering the above-mentioned facts, and bearing in mind that natural gas shares about 70% of the Iran total energy consumption basket, along with the fact that approximately 3 million vehicles consume compressed natural gas (CNG) in Iran, the most in the world, this research aims to investigate the effects of deviations in composition of natural gas within Iran's range on the calibration of engine one-dimensional cycle model. To accomplish this, a gas-fuelled spark ignition engine is simulated using AVL BOOST v2013 software. The model results are calibrated for three different engine loads at three different compression ratios versus experimental observations for engine working with pure methane as fuel. The goal functions during the calibration process are air and fuel mass flow rates and in-cylinder open cycle pressure profile. After finalizing the model calibration, the models are used for predicting the performance of the same engine without change in the model-calibrated parameters when working with natural gases distributed in Mashhad and Tehran. The simulation results are compared with experimental observations on the same engine working with Mashhad and Tehran natural gases, which the latter is proved to have the maximum deviation from pure methane in composition. The findings indicate that the results of the model remain valid for air flow rate, fuel consumption and in-cylinder open cycle pressure profile, in spite of change in the composition of the fuel. This proves that the range of deviation in composition of natural gases distributed in Iran does not affect the calibration correctness of the engine comprehensive thermodynamic cycle model.

2 Studied Engine

The test engine employed in this study is a spark ignition single-cylinder natural gas-fuelled engine. The engine is developed by AVL GmbH and is currently installed in Vehicle, Fuel and Environment Research Institute, University of Tehran. The engine compression ratio can be varied between 6 and 16, by altering the shims between the cylinder head and engine block. General specifications of the engine are shown in Table 1. In addition, the test bed is also illustrated in Fig. 1. More information on the engine and test bed specifications is brought by Javaheri et al. (2014).

Table 1 Main engine information (Javaheri et al. 2014)

Engine type	4 Stroke
Cylinder	1
Valve	4
Bore	86 mm
Course	86 mm
Connecting rod	143 mm
Compression ratio	6–16
Injection	Intake port injection

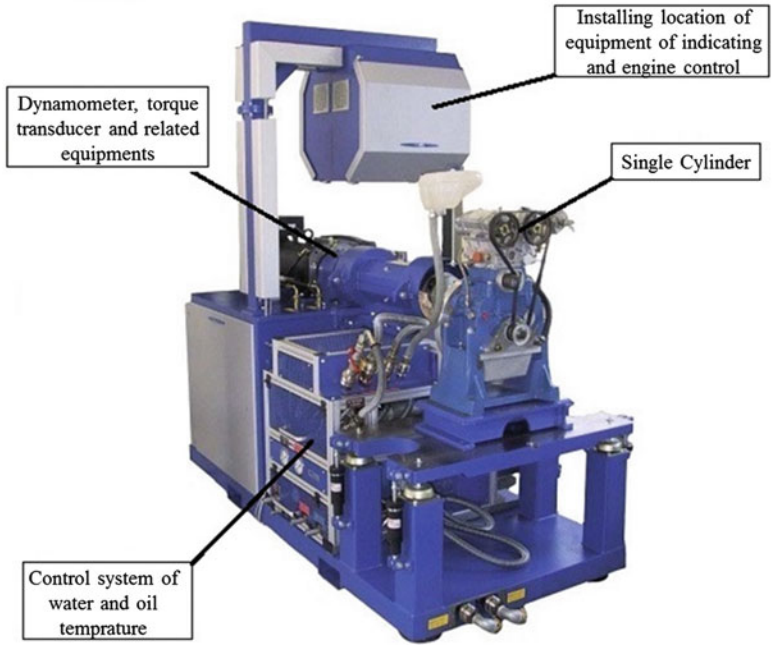

Fig. 1 Illustration of the test bed (Javaheri et al. 2014)

The experiments are carried out at three different compression ratios of 12, 14 and 16. Three different engine loads are also considered. For part-load conditions, the break mean effective pressure is set to be equal to 2 and 4 bar. The full load conditions are also investigated.

3 Simulation and Calibration Approach

In this research, it is aimed to create a baseline model with high accuracy based on experimental observations for a single-cylinder spark ignition natural gas-fuelled test engine at three different compression ratios, i.e. 12, 14 and 16. In all of the tests,

Table 2 Studied fuel compositions (mass fraction based)

	Fuel 1	Fuel 2	Fuel 3
Methane	100	94.778	77.696
Ethane	0	1.221	6.621
Propane	0	0.694	6.498
Carbone dioxide	0	2.052	2.689
Nitrogen	0	1.255	6.496

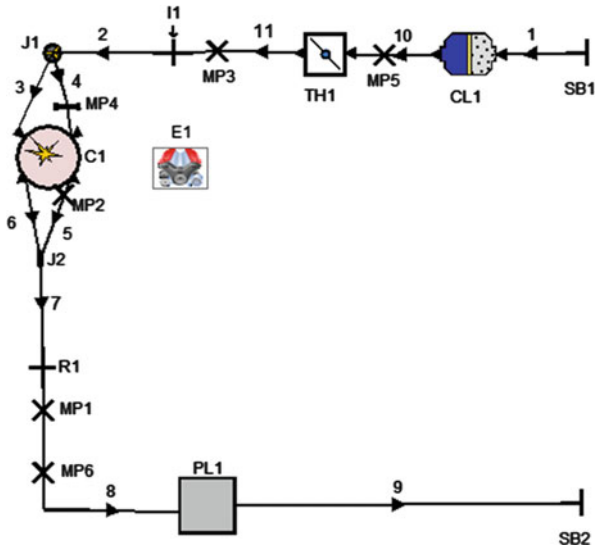

Fig. 2 One-dimensional comprehensive model developed in AVL BOOST v2013

the engine speed is held constant at 2000 rpm. All of the tests are repeated for three different throttle angles:

1. Wide open throttle (WOT) state, i.e. full load conditions
2. Partially open throttle state, so that the brake mean effective pressure equals to 4 bar
3. Partially open throttle state, so that the brake mean effective pressure equals to 2 bar

As described earlier, the tests are repeated for three different natural gas compositions. These compositions are shown in Table 2.

Fuel 1 is pure methane, fuel 2 is the natural gas distributed in Mashhad and fuel 3 represents the natural gas typically used in Tehran.

The engine one-dimensional comprehensive model is developed using AVL BOOST v2013 software, schematic of which is shown in Fig. 2. The general strategy of the modelling and calibration methodology will be described here briefly.

An internal combustion engine could be considered as a system of pipes connecting different elements. The important point which should be considered

here is that each pipe's length to diameter ratio is large enough, so that the flow could be considered one dimensional (Benson 1982; Winterbone and Pearson 2000). On the other hand, with the relatively high flow speed, it would be convenient to employ the inviscid assumption. Hence, the one-dimensional Euler system of inviscid equations could be used for simulating the fluid flow characteristics inside the pipes. After creating the overall model topology, geometrical parameters, such as pipe lengths, elements, volumes, bore, stroke, connecting rod length, compression ratio, etc., are set. The simulation process could be started after setting up the operating parameters and required factors for numerical simulation process. The calibration will be started after the model setup is complete.

The air flow rate at each node of the pipe is calculated under the light of solving system of one-dimensional gas dynamics equations using fourth-order MacCormack (Tannehill et al. 1997) scheme. All the boundary conditions related to different elements are implemented using the non-homentropic approach (Benson 1982).

The fuel flow rate is found by setting the equivalence ratio in the injector element based on the results of gas dynamic system of equations. It is worth mentioning that the same applies for experimental results. During the test procedure, only the air flow rate is observed directly as raw data from the test cell and the fuel flow rate is calculated using the injector control instruments based on the input air-fuel ratio and is then reported to the user.

Combustion thermodynamic simulation is carried out using Wiebe two-zone algorithm, following the general lines of multi-zone modelling strategy (Heywood 1988; Medina et al. 2014). To simulate the heat transfer phenomenon, the AVL 2000 model is used (Schwarz 2012).

The calibration process is started for motoring conditions and the main focus is on the in-cylinder pressure profile. To finalize the calibration process at this step, various model parameters and coefficients are set based on trial and error strategy. These parameters include 24 flow coefficients, 7 heat transfer coefficients and temperatures for cylinder components, i.e. piston, cylinder head, liner at both conditions of piston at bottom dead centre and top dead centre. In addition, due to non-homentropic treatment of boundary conditions, and the necessity for correct positioning of interaction point of the characteristic curve with energy ellipse, the temperatures and heat transfer coefficients at the intake and exhaust ports are also set. After finalizing the calibration process for motoring condition, fuel injection and combustion-related parameters are added to begin the second step of calibration process. Therefore, four factors are added to calibrate the two-zone Wiebe function. It should be considered that, after adding fuel injection and combustion to the model developed initially for motoring conditions, all the parameters including flow coefficients, heat transfer coefficients and temperatures should be readjusted.

As it was mentioned earlier, one of the main goal functions during the calibration process is the minimum error between the experimentally achieved in-cylinder pressure profile and the numerical simulation results. To this end, the trial and error procedure was designed so that minimum error exists during combustion, expansion, exhaust and intake periods of the cycle. In addition, during the

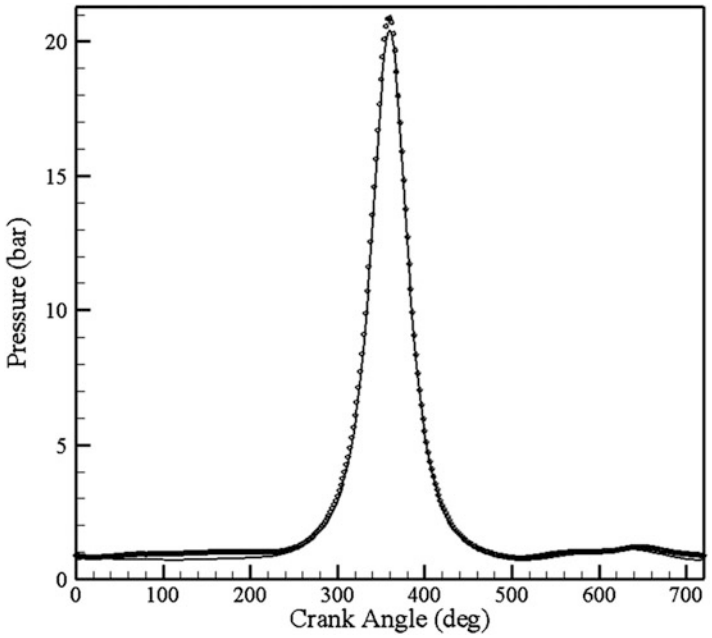

Fig. 3 In-cylinder pressure profile for motoring condition at CR = 12

compression stroke, the numerically and experimentally obtained pressure profile should be completely identical, so that one can assure the agreement between the in-cylinder-trapped mass obtained from experiment and numerical simulation. The calibrated results for motoring condition are shown in Figs. 3, 4 and 5 for the compression ratios 12, 14 and 16, respectively.

From Fig. 3, it is evident that the root mean square of errors between experimental and numerical in-cylinder profile during the compression stroke does not exceed 0.8%. On the other hand, the overall root mean square of experiment and simulation results on in-cylinder pressure profile remains less than 1.5%. For compression ratio of 14, as depicted in Fig. 4, the situation is the same. The root mean square of errors during the compression stroke remains less than 0.65%, while the overall error does not exceed 1.2%. For compression ratio of 16, as illustrated in Fig. 5, the root mean square of errors during the compression stroke remains less than 0.9%, while the overall error does not exceed 1.5%.

The air and fuel mass flow rates obtained from experimental data and numerical simulation results for engine working with stoichiometric mixture of air and pure methane (fuel 1) at constant engine speed of 2000 rpm in three different compression ratios of 12, 14 and 16 are shown in Tables 3, 4 and 5 for engine working at part-load condition of brake mean effective pressure (BMEP) of 2 and 4 bar and full load conditions, respectively. From the tables, it is obvious that the errors always stay below 1%, which proves acceptable consistency of the numerical simulation results and experimental findings.

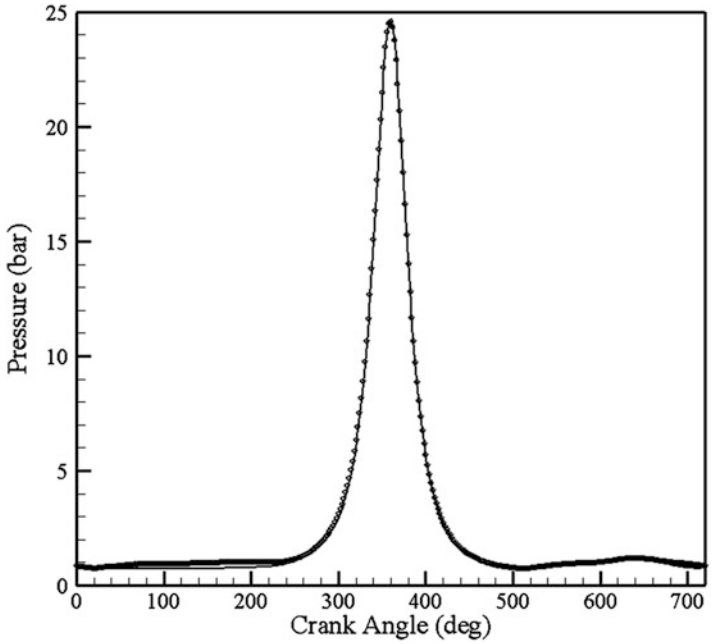

Fig. 4 In-cylinder pressure profile for motoring condition at CR = 14

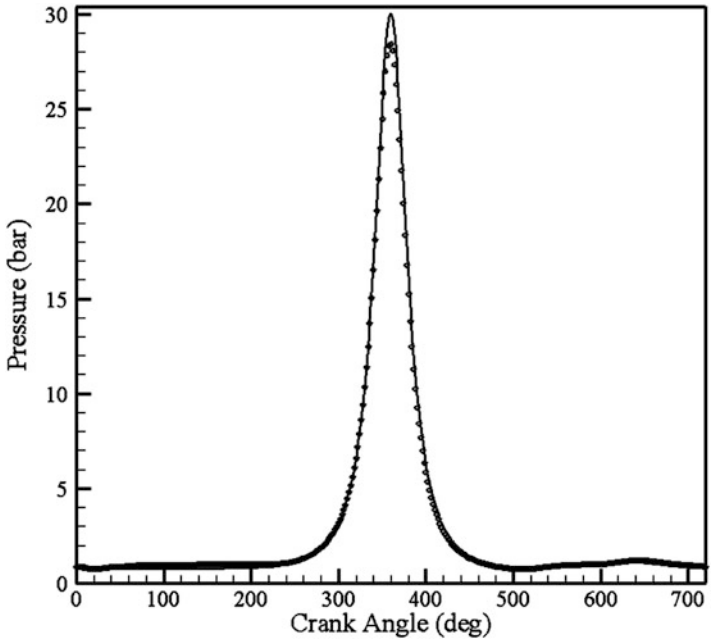

Fig. 5 In-cylinder pressure profile for motoring condition at CR = 16

Table 3 Experimental and simulation results of air and fuel mass flow rates for fuel 1 in BMEP = 2 bar

CR		Exp. (gr/s)	Sim. (gr/s)	Error (%)
12	Air	2.860	2.866	0.209
	Fuel	0.166	0.167	0.602
14	Air	2.764	2.779	0.542
	Fuel	0.161	0.162	0.621
16	Air	2.907	2.889	0.619
	Fuel	0.169	0.168	0.591

Table 4 Experimental and simulation results of air and fuel mass flow rates for fuel 1 in BMEP = 4 bar

CR		Exp. (gr/s)	Sim. (gr/s)	Error (%)
12	Air	4.004	4.034	0.749
	Fuel	0.233	0.235	0.858
14	Air	3.956	3.971	0.379
	Fuel	0.230	0.231	0.434
16	Air	4.051	4.018	0.814
	Fuel	0.236	0.234	0.847

Table 5 Experimental and simulation results of air and fuel mass flow rates for fuel 1 in full load

CR		Exp. (gr/s)	Sim. (gr/s)	Error (%)
12	Air	5.434	5.407	0.501
	Fuel	0.316	0.315	0.316
14	Air	5.196	5.252	1.082
	Fuel	0.302	0.305	0.993
16	Air	5.106	5.093	0.244
	Fuel	0.297	0.296	0.336

The in-cylinder pressure profile for three different engine loads and compression ratios of 12, 14 and 16 are depicted in Figs. 6, 7 and 8, respectively. In addition, the root mean squares of the errors between numerical and experimental results are shown in Table 6. These results indicate that in spite of negligible discrepancy of simulation results from experimental findings, the model calibration for engine working on pure methane (fuel 1) is promising.

During the calibration, the following results are also obtained for tuning the temperatures of different combustion chamber parts at different engine loads and compression ratios.

As the compression ratio rises, the gas temperature at the exhaust will decrease, due to higher work obtained during combustion period (Ferguson and Kirkpatrick 2000; Heywood 1988). Experimental data on exhaust gas temperatures at 5 cm after cylinder for pure methane is shown in Table 7. Therefore, the following results are obtained during the calibration of cylinder part temperatures:

1. All the temperatures are lowered about 2.5 °C when the compression ratio is reduced from 16 to 14 and from 14 to 12.

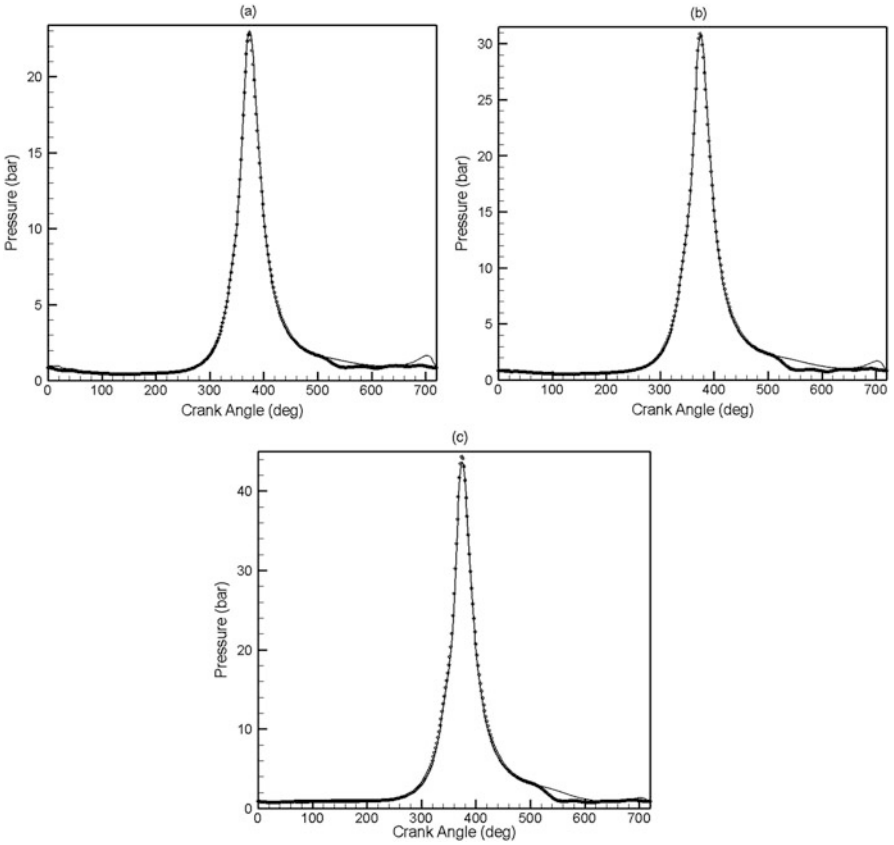

Fig. 6 In-cylinder pressure profile for fuel 1 at compression ratio of 12 for (**a**) BMEP = 2 bar, (**b**) BMEP = 4 bar and (**c**) full load conditions. Solid lines denote simulation and symbols denote experimental results

2. The engine part temperatures don't change when the engine load is lowered from full load to brake mean effective pressure of 4 bar.
3. With decrease in load at part-load condition from 4 to 2 bar, the engine part temperatures are reduced about 4 °C at all the compression ratios.

4 Results and Discussion

In the next step, the model parameters are held fixed, and the fuel composition is changed. Figure 9 illustrates the in-cylinder pressure profile obtained from simulation and experiment at three different engine compression ratios of 12, 14 and 16, respectively. The natural gas is gathered from Mashhad (fuel 2) and the same composition is considered for the simulation. As it is evident from the figures, the

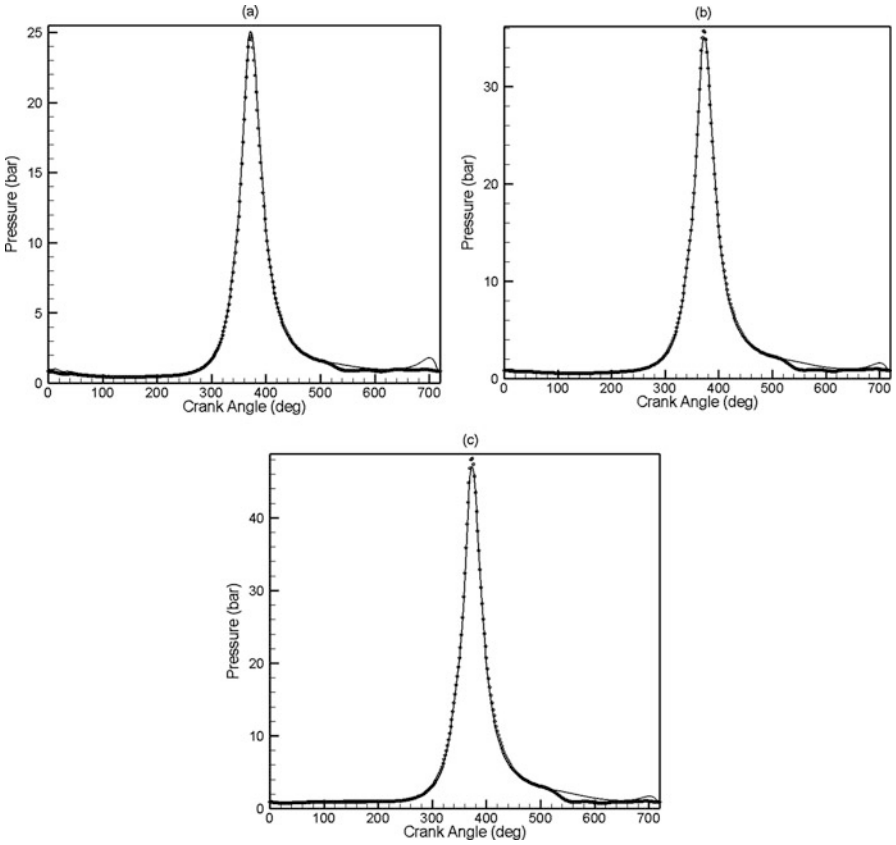

Fig. 7 In-cylinder pressure profile for fuel 1 at compression ratio of 14 for (**a**) BMEP = 2 bar, (**b**) BMEP = 4 bar and (**c**) full load conditions. Solid lines denote simulation and symbols denote experimental results

root mean squares of the errors don't exceed 1.1%, proving proper agreement of the simulation results and experimental data.

Once again, it is important to note that all of the experiments and simulations are carried out at a constant engine speed of 2000 rpm and stoichiometric mixture conditions at the injector. Meanwhile, the mass flow rates of air and fuel are shown in Table 8. The numerical and experimental results in the table are at the full load condition (throttle at wide open state).

It is evident from the table that the errors between numerical and experimental results for natural gas distributed in Mashhad (fuel 2) always stay below 4.5%. This small and negligible discrepancy indicates good agreement of the gas dynamic system of equation results with experimental data. These numerical results are calibrated using flow coefficients at the boundaries of each pipe, i.e. engine elements. Therefore, one can conclude that in addition to the thermodynamic combustion model (Fig. 9), the Euler equation calibration remains also valid.

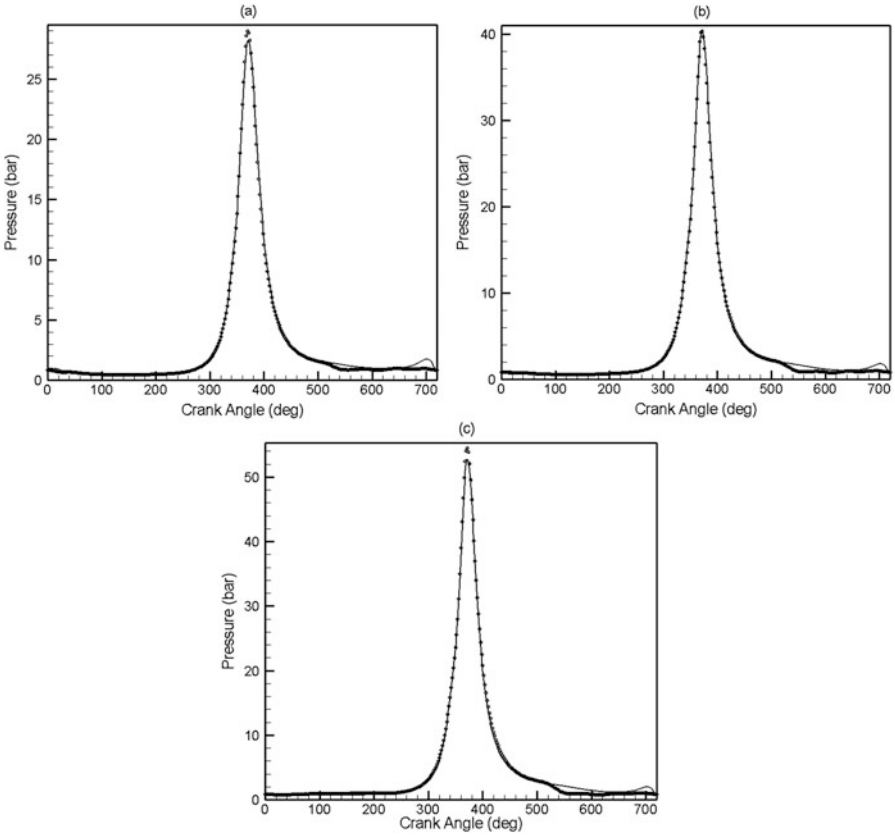

Fig. 8 In-cylinder pressure profile for fuel 1 at compression ratio of 16 for (**a**) BMEP = 2 bar, (**b**) BMEP = 4 bar and (**c**) full load conditions. Solid lines denote simulation and symbols denote experimental results

Table 6 Exhaust gas temperatures at different engine loads and compression ratios

	CR = 16	CR = 14	CR = 12
Full load	458	467	481
BMEP = 4 bar	457	467	479
BMEP = 2 bar	442	453	460

Table 7 Root mean squares of errors for numerical and experimental pressure profiles for fuel 1

	CR = 16 (%)	CR = 14 (%)	CR = 12 (%)
Full load	0.93	0.69	0.73
BMEP = 4 bar	0.64	0.77	0.82
BMEP = 2 bar	0.88	0.79	0.77

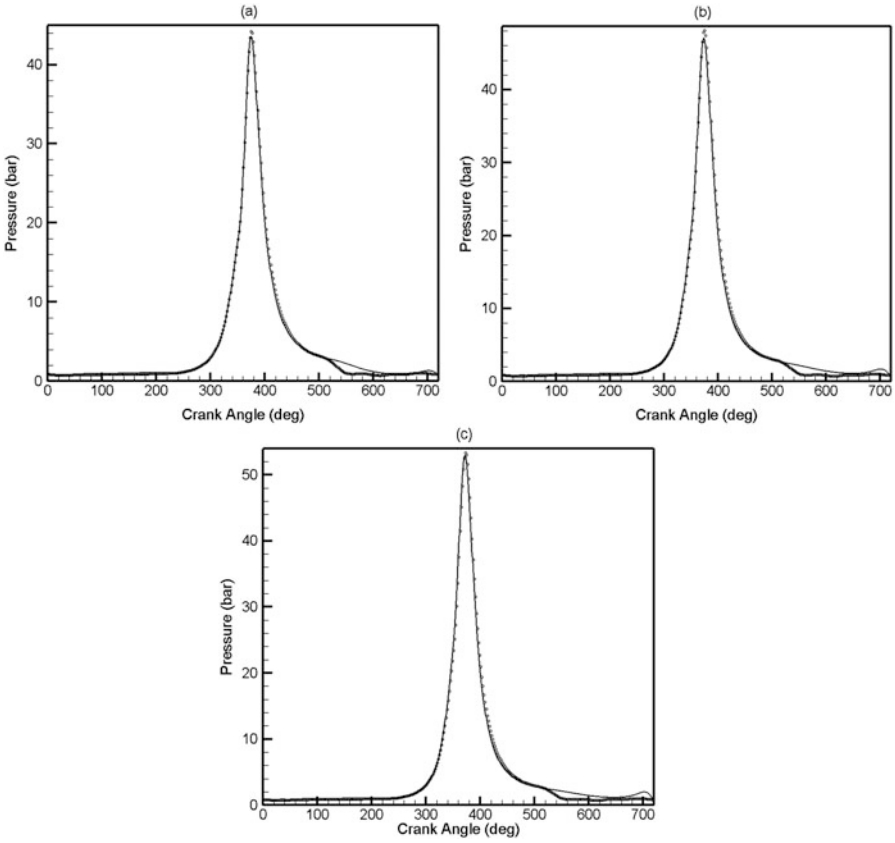

Fig. 9 In-cylinder pressure profile for fuel 2 at (**a**) CR = 12 bar, (**b**) CR = 14 bar and (**c**) CR = 16. Solid lines denote simulation and symbols denote experimental results

Table 8 Experimental and simulation results of air and fuel mass flow rates for fuel 2 in full load

CR		Exp. (gr/s)	Sim. (gr/s)	Error (%)
12	Air	5.527	5.534	0.132
	Fuel	0.331	0.332	0.591
14	Air	5.573	5.374	3.563
	Fuel	0.333	0.324	2.664
16	Air	5.480	5.234	4.485
	Fuel	0.328	0.317	3.228

The simulation and experiment procedures are then repeated for the natural gas distributed in Tehran. It was mentioned earlier that Tehran natural gas has the maximum deviation from pure methane in composition. Hence, if the model remains calibrated for this composition of natural gas, it will be valid for all types of natural gas found in Iran.

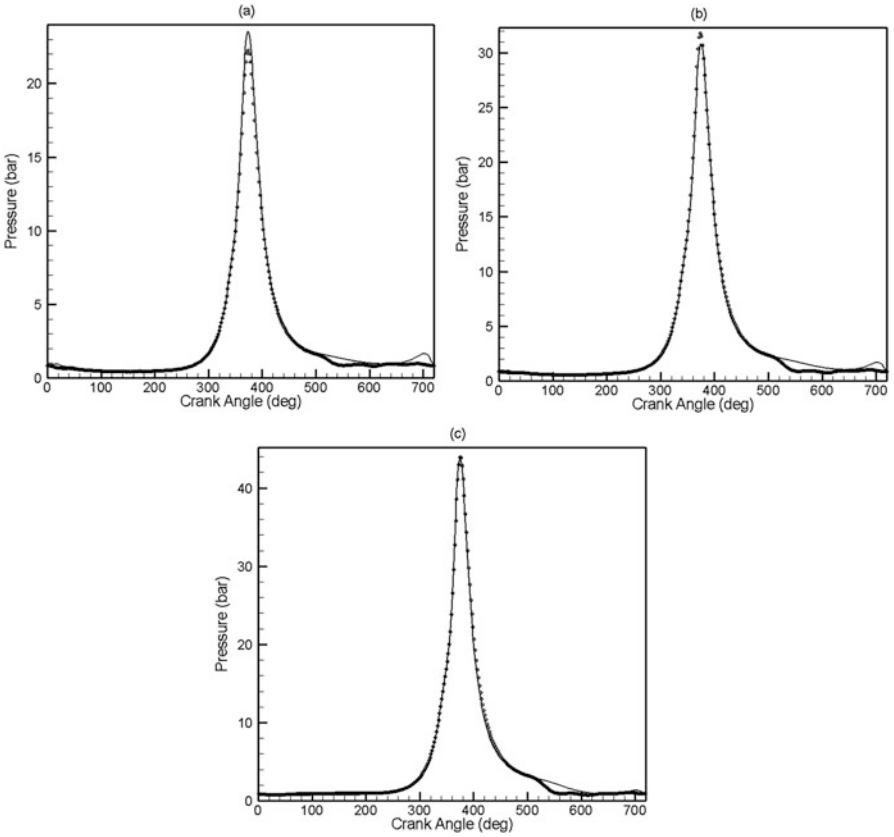

Fig. 10 In-cylinder pressure profile for fuel 3 at compression ratio of 12 for (**a**) BMEP = 2 bar, (**b**) BMEP = 4 bar and (**c**) full load conditions. Solid lines denote simulation and symbols denote experimental results

As for fuels 1 and 2, the verification of the model's calibrated results is investigated at two different steps.

First, it is investigated that the cylinder-related part temperatures and heat transfer coefficients are still correct or not. In addition, the calibration of the combustion zero-dimensional thermodynamic model, i.e. Wiebe function, is also controlled. To accomplish this step, the in-cylinder pressure profiles obtained from simulation and experiment should be compared. This is done in Figs. 10, 11 and 12. As can be seen in the figures, for all the case studies, the pressure curves are still in good agreement. The root mean squares of experimental and simulation data discrepancies are shown in Table 9. The root mean square of errors does not exceed 1.9%, which could be regarded as a very good agreement.

For the second step, the performance of the gas dynamic system of equations with calibrated flow coefficients is qualified. To this end, the experimental and simulation results for the mass flow rates of air and fuel are shown in

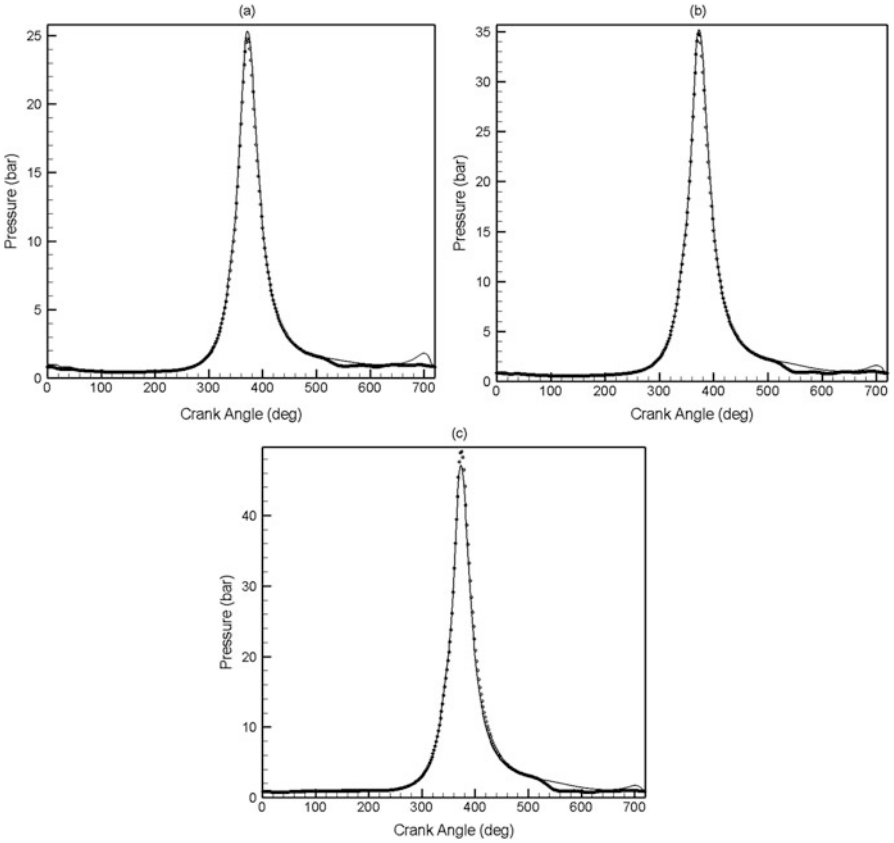

Fig. 11 In-cylinder pressure profile for fuel 3 at compression ratio of 14 for (**a**) BMEP = 2 bar, (**b**) BMEP = 4 bar and (**c**) full load conditions. Solid lines denote simulation and symbols denote experimental results

Tables 10, 11 and 12. The data in the table indicate that errors are larger than those for Mashhad gas, which was also predictable due to larger deviation of Tehran gas composition. Nevertheless, these errors do not exceed 4.5%, proving that the results are still in good agreement and the model results are still reliable.

5 Concluding Remarks

Natural gas burns through a clean combustion process and has large resources throughout the world. These key features let natural gas be considered as a promising alternative fuel. In spite of all these, it faces severe drawback of deviation in composition between different reservoirs, which affects its combustion characteristics.

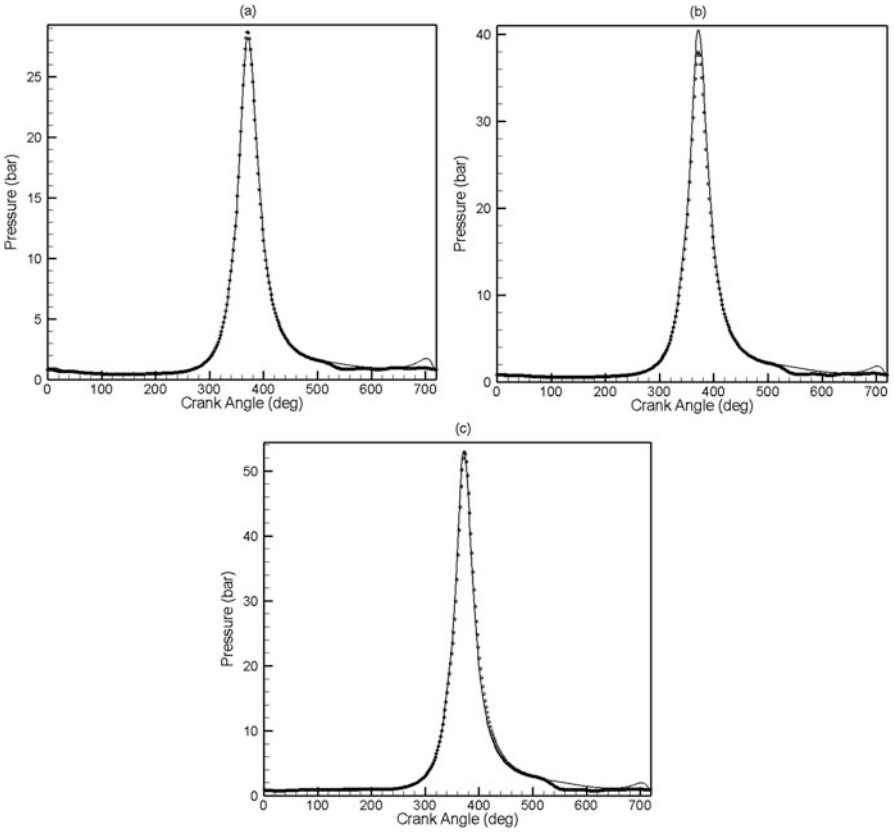

Fig. 12 In-cylinder pressure profile for fuel 3 at compression ratio of 16 for (**a**) BMEP = 2 bar, (**b**) BMEP = 4 bar and (**c**) full load conditions. Solid lines denote simulation and symbols denote experimental results

Table 9 Root mean squares of errors for numerical and experimental pressure profiles for fuel 3

	CR = 16 (%)	CR = 14 (%)	CR = 12 (%)
Full load	0.87	1.82	0.93
BMEP = 4 bar	1.84	0.89	1.80
BMEP = 2 bar	1.31	1.10	1.89

Table 10 Experimental and simulation results of air and fuel mass flow rates for fuel 3 in BMEP = 2 bar

CR		Exp. (gr/s)	Sim. (gr/s)	Error (%)
12	Air	2.728	2.827	3.641
	Fuel	0.197	0.203	2.861
14	Air	2.775	2.840	2.332
	Fuel	0.180	0.184	2.377
16	Air	2.842	2.930	3.071
	Fuel	0.184	0.190	3.008

Table 11 Experimental and simulation results of air and fuel mass flow rates for fuel 1 in BMEP = 4 bar

CR		Exp. (gr/s)	Sim. (gr/s)	Error (%)
12	Air	3.970	3.955	0.377
	Fuel	0.258	0.257	0.256
14	Air	3.800	3.967	4.392
	Fuel	0.247	0.257	4.269
16	Air	3.872	4.047	4.505
	Fuel	0.252	0.263	4.420

Table 12 Experimental and simulation results of air and fuel mass flow rates for fuel 3 in full load

CR		Exp. (gr/s)	Sim. (gr/s)	Error (%)
12	Air	5.379	5.518	2.583
	Fuel	0.350	0.359	2.662
14	Air	5.294	5.316	0.414
	Fuel	0.344	0.346	0.486
16	Air	5.150	5.187	0.727
	Fuel	0.335	0.337	0.687

One-dimensional comprehensive engine models have key importance during the engine design or optimization processes. This modelling technique consists of solving one-dimensional Euler system of inviscid flow equations inside the engine pipes and embedding them with zero-dimensional thermodynamic models for other engine elements such as cylinders. This methodology engages employment of several empirical factors which have to be calibrated and may differ as the working fluid composition changes. These parameters can be divided into three main categories:

1. Flow coefficients: The one-dimensional system of gas dynamic equations considers the flow to be homentropic (Benson 1982; Winterbone and Pearson 2000), i.e. having constant entropy over the flow domain. Therefore, the mass flow rates of working fluid into and out from the elements should be adjusted with flow coefficients, which are computed as the ratio of actual to isentropic flow rates.
2. Zero-dimensional combustion thermodynamic function is Wiebe function in this work. For Wiebe function, there are four calibration parameters.
3. Cylinder parts, i.e. liner, cylinder head, piston, valve and port temperatures and heat transfer coefficients which influence the in-cylinder thermal losses during the cycle.

Hereby, it is worth mentioning again that the present work's aim is not to investigate the effects of natural gas composition on the performance of the gas engine, but it aims to answer the question that does the change in composition of natural gas affect the calibration of the engine comprehensive gas dynamics model?

To answer this question, a one-dimensional comprehensive gas dynamics model is developed and calibrated for a single-cylinder spark ignition gas engine working with pure methane as fuel for three different engine compression ratios and three different engine loads. All the tests are carried out at constant engine speed of

2000 rpm at stoichiometric condition. The engine used in this research is designed and manufactured by AVL List Gmbh. Details on the test cell and engine are provided by Javaheri et al. (2014). In addition, the AVL BOOST v2013 software is employed for the simulations. The following results are achieved during the calibration process:

1. As the compression ratio rises, the engine part temperatures are reduced. This was predictable, because with increase in compression ratio, the temperature of cylinder exhaust gas will reduce (Heywood 1988; Ferguson and Kirkpatrick 2001; Pulkrabek 1997). In this work, as the compression ratio is increased from 12 to 14 and from 14 to 16, the temperature of piston, cylinder head, liner, ports and valves is considered to be 2.5 °C lower. This consideration yielded to the numerical predictions with most agreement with experimental findings.
2. In relatively high engine loads, the engine part temperature can be considered equal to those at engine full loads. In the present work, as the engine brake mean effective pressure is reduced from 6.2 at full load condition to 4, the engine part temperature remains constant in the model. Nevertheless, with further reduction of engine load to 2, the engine part temperatures should be reduced by 4 °C to achieve the best possible agreement.

To study the effects of changes in gas composition, the range of natural gas compositions in Iran is brought under consideration. Therefore, the natural gas distributed in Tehran which has the maximum deviation from pure methane is chosen. Another natural gas is also chosen from Mashhad, the second great city in Iran. Nine tests (three engine loads at three different compression ratios of 12, 14 and 16) are repeated for the engine working with each of the fuels. It is worth mentioning that in these tests, the engine speed is held constant at 2000 rpm, and the mixture is stoichiometric. The calibrated model is employed to simulate the engine cycle, without any change in parameters. The following results are obtained:

1. Despite the fact that the discrepancies between numerical predictions and experimental observations for in-cylinder pressure profile and mass flow rates of air and fuel increase as the deviation in the composition rises (the discrepancies of the simulation results from experimental data are higher for Tehran gas compared to Mashhad); the simulation results and experimental data remain in good agreement for fuels 2 and 3. Therefore, one can conclude that when studying an engine working the natural gases distributed in Iran, it would be sufficient to calibrate the engine comprehensive one-dimensional model with pure methane or each of the gas compositions that exist in Iran. The model predictions will be accurate enough for other gases.
2. The model validity with change in composition of the natural gases in the range that exist in Iran is regardless of engine compression ratio and load.
3. Considering the above-mentioned facts, it seems that the influence of natural gas composition inside Iran, on the gas-fuelled internal combustion engine working parameters, such as engine temperature, is very negligible.

Acknowledgements This research was supported by the Vehicle, Fuel and Environment Research Institute (VFERI), University of Tehran. The authors gratefully acknowledge this support.

References

Benson, R.S.: The Thermodynamics and Gas Dynamics of Internal Combustion Engines. Oxford University Press, London (1982)

Caton, J.A.: An Introduction to Thermodynamic Cycle Simulations for Internal Combustion Engines. John Wiley and Sons, West Sussex (2016)

Ferguson C.R., Kirkpatrick A.T., Internal Combustion Engines, Applied Thermosciences. 2nd edn, Wiley (2000)

Ferguson, C.R., Kirkpatrick, A.T.: Internal Combustion Engines. Applied Thermosciences, New York, John Wiley and Sons (2001)

Ghojel, J.I.: Review of the development and applications of the Wiebe function: a tribute to the contribution of Ivan Wiebe to engine research. International Journal of Engine Research. **11**, 297–312 (2010)

Heywood, J.B.: Internal Combustion Engine Fundamentals. McGrawHill, New York (1988)

Javaheri, A., Esfahanian, V., Salavati-Zadeh, A., Darzi, M.: Energetic and exergetic analyses of a variable compression ratio spark ignition gas engine. Energy Convers. Manag. **88**, 739–748 (2014)

Medina, A., Curto-Risso, P.L., Hernandez, A.C., Guzman-Vargas, L., Angulo-Brown, F., Sen, A. K.: Quasi-Dimensional Simulation of Spark Ignition Engines from Thermodynamic Optimization to Cyclic Variability. Springer, London (2014)

Pulkrabek, W.W.: Engineering Fundamentals of the Internal Combustion Engine. Prentice Hall, Upper Saddle River (1997)

Ramos, J.I.: Internal Combustion Engine Modelling. Taylor and Francis, London (1989)

Schwarz, C.: Calculation of real working process. In: Merker, G.P., Schwarz, C., Teichmann, R. (eds.) Combustion Engines Development: Mixture Formation, Combustion Emissions and Simulation. Springer, Berlin (2012)

Tannehill, J.C., Anderson, D.A., Pletcher, R.H.: Computational Fluid Mechanics and Heat Transfer. Taylor and Francis, Washington DC (1997)

White, F.M.: Fluid Mechanics. McGrawHill, Boston (2003)

Winterbone D.E., Pearson R.J., Theory of engine manifold design: wave action methods for IC engines. Professional Engineering Pub (2000)

Experimental Results of Split-Flow Modification for Post-combustion CO_2 Capture Process

Marcin Stec, Adam Tatarczuk, Lucyna Więcław-Solny, Aleksander Krótki, Tomasz Spietz, Andrzej Wilk, and Dariusz Śpiewak

1 Introduction

Carbon capture from flue gases is gaining interest in the European Union due to current council obligations (Więcław-Solny et al. 2012) concerning reduction of greenhouse gas emissions. To fulfil council liabilities, it is necessary to develop technically feasible CO_2 separation processes allowing the reduction of greenhouse gases from fossil fuel power plants. Amine-based flue gas scrubbing is the most promising technology which may be used in CO_2 separation processes. The main advantage of this process is simplicity of incorporation into existing power plants (Skorek-Osikowska et al. 2012). However, amine-based CO_2 separation processes add serious energy penalty, reducing the efficiency of the power plant (Chen and Rochelle 2011). Therefore, current research concentrates on examination of energy-saving design approaches (Spietz et al. 2014) and on solvent developments (Wilk et al. 2013).

This paper deals with the results of tests of the split-flow modification of amine scrubbing flow sheet. Splitting the flow of the solvent is advantageous and can reduce energy consumption of the process (Thompson and King 1987) and increases CO_2 recovery (Polasek et al. 1983). Description and modelling of the split-flow process have been well established. The numerous papers deal with energy considerations, capital costs (Karimi et al. 2011), evaluation of different split-flow configurations (Ahn et al. 2013) or thermodynamic aspects of the flow splitting (Leites et al. 2003). In contrast, studies describing experimental

M. Stec (✉) • A. Tatarczuk • L. Więcław-Solny • A. Krótki • T. Spietz • A. Wilk • D. Śpiewak
Institute for Chemical Processing of Coal, Zamkowa 1, 41-803 Zabrze, Poland
e-mail: mstec@ichpw.pl

© Springer International Publishing AG, part of Springer Nature 2018

F. Aloui, I. Dincer (eds.), *Exergy for A Better Environment and Improved Sustainability 2*, Green Energy and Technology,
https://doi.org/10.1007/978-3-319-62575-1_31

Fig. 1 Overview of the PDU for amine-based post-combustion carbon capture at Clean Coal Technologies Centre in Zabrze, Poland

implementation of the split-flow process are scarce (Cousins et al. 2012) or out of date (Polasek et al. 1983). This conjuncture encouraged the authors to present the results of tests carried out at process development unit (PDU) for amine-based post-combustion carbon capture located at Clean Coal Technologies Centre in Zabrze, Poland.

Process development unit having capacity up to 100 m^3_n/h was designed to test the amine scrubbing carbon capture process from flue gases or mixtures of technical gases. PDU (Fig. 1) incorporates novel process flow sheet introducing both concepts: split-flow process and rich split; therefore, the results are a valuable material for model validation. Flexible configuration of the PDU allows straightforward changes in process flow sheet; therefore, tests of conventional as well as novel flow sheets are possible. This feature of the PDU makes comparisons between configurations effortless.

This paper deals with the detailed description of four tests: two tests for standard process flow sheet and two tests carried out with split-flow arrangement. Process conditions were carefully selected to make the comparison between standard and split-flow flow sheets possible. Vast number of process parameters are included, making this paper a valuable source of data for model validation.

The tests presented in this paper were carried out using 30 wt% MEA (monoethanolamine) aqueous solution considered baseline solvent for pilot plant studies of post-combustion carbon dioxide capture by reactive absorption (Mangalapally et al. 2009).

2 Experimental

2.1 Chemicals

Concentrated ethanolamine (MEA, CAS: 141-43-5, technical grade) was obtained from Brenntag NV. Aqueous solution of ethanolamine was prepared on site using mains water.

The following additives were used in minor quantities: Silpian W-3 purchased from Silikony Polskie sp. z o.o. as antifoaming agent, potassium metavanadate (KVO_3, CAS: 13769-43-2) as corrosion inhibitor and hydrazine hydrate solution (H_4N_2 H_2O, CAS: 7803-57-8) as antioxidant.

2.2 Process Development Unit Description

The overview of the process development unit for amine-based post-combustion carbon capture is shown in Fig. 1.

In Fig. 2 process flow sheet of the PDU is introduced. The PDU allows CO_2 separation from gas streams. Either flue gas fed by blower or mixture of technical gases can be treated. The CO_2-rich gas (volumetric flow up to 100 m^3_n/h) is fed into the pretreatment scrubber where the temperature of the gas is set, and gas is saturated with water. Pretreatment scrubber suits therefore as direct contact cooler using water as cooling medium. To avoid excessive amine degradation while testing the process on flue gases, the activated coal SO_x adsorber is located downstream of the scrubber. The CO_2-rich gas enters the absorber at the bottom. The absorber is built of three sections. Middle section, where gas contacts counter currently with semi-lean amine, top section where lean amine is fed and water wash

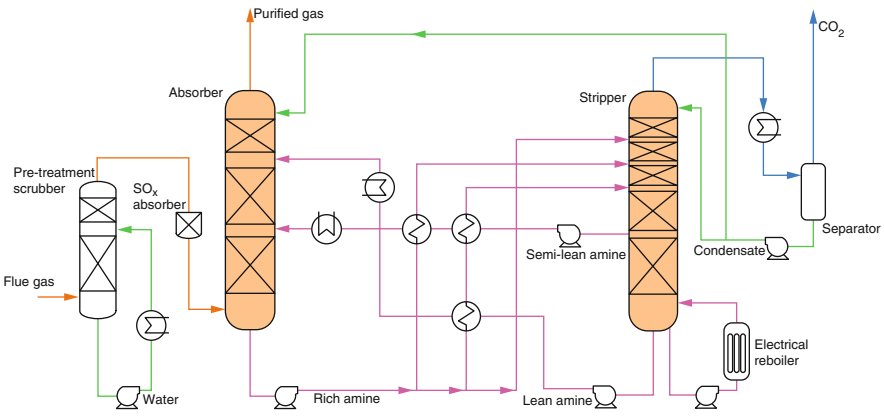

Fig. 2 Flow sheet of the process development unit

Table 1 Column size, packing heights and packing materials at the process development unit for amine-based post-combustion carbon capture

Column	Diameter (mm)	Packing height (mm)	Packing material
Absorber	273	1400	Cylindrical ring 5 mm
			VFF GmbH
		1200	Berl saddles 10 mm
			VFF GmbH
		2000	Novalox saddles 13
			VFF GmbH
Stripper	273	320	Sulzer CY
		320	Sulzer CY
		480	Sulzer CY
		1600	Interpack #2
			VFF GmbH
		1000	Interpack #1
			VFF GmbH

section above the lean solvent inlet. The water wash section, where make-up water is added, acts as cooler and prohibits the increase of amine concentration in the solvent. Packing parameters and dimensions of the absorber are given in Table 1.

Carbon dioxide from CO_2-rich gas is absorbed into the liquid phase. The rich solvent is pumped into the stripper through rich lean and rich semi-lean heat exchangers. The rich solvent is heated to higher temperatures through hot solvents leaving the stripper. Such split-flow configuration is based on the invention proposed by Shoeld (1934). In Fig. 2 additional line of rich solvent, bypassing heat exchangers, can be noticed. Using this line, small portion of rich solvent remains unheated and enters the top of the stripper. This modification known as 'rich split' was suggested by Eisenberg and Johnson (1979). Concluding, the rich amine can be fed to the stripper by means of three feed points: as unheated or heated either with semi-lean or lean solvent.

The solvent in the bottom of the stripper is heated using electrical heating element. Energy delivered to the rich solvent is spent on its regeneration. A portion of the solvent is drawn from the intermediate section (semi-lean solvent) of the stripper and fed to the absorber at some mid-column feed point. Because of the side draw, remaining amine flow to the reboiler is lower, resulting lower lean amine loading. Lean amine is pumped back to the absorber and enters the top of the column, as for conventional process flow sheet. Further details regarding construction, packing and dimensions of the stripper are given in Table 1.

Product CO_2 saturated with water vapours is collected from the top of the stripper. Remaining part of water is removed in condenser installed downstream of the column and almost pure CO_2 is obtained.

Effects of foregoing modifications will be described in detail in consecutive sections.

The PDU uses 30 wt% MEA (monoethanolamine) aqueous solution as solvent.

For additional details concerning the PDU as well as other facilities located at Clean Coal Technologies Centre in Zabrze, Poland, see (Lajnert and Latkowska 2013).

2.3 Gas and Liquid Analysis

Gas and liquid analysis are the most important and sophisticated measurements and therefore will be described in detail.

Gas analysis is conducted online by using a ULTRAMAT 23 gas analyser. The measuring principle of the instrument is based on the molecule-specific absorption of bands of infrared radiation. Prior to feeding the gas to analyser, it is dedusted and cooled to separate water vapours. The CO_2 concentration from the instrument is given directly as volumetric percent.

A liquid samples of rich, semi-lean and lean amine are collected during the steady state, before the trial is stopped. The liquid samples are further analysed to determine the amine concentration and CO_2 loading.

The concentration of the solvent is checked by titration, and CO_2 loading is estimated based on the density of the solvent using correlations given by Hartono et al. (2014).

3 Results and Discussions

3.1 Split-Flow Process Analysis

A literature review on description of the split-flow process is outlined below.

The concept of the flow splitting was first suggested by Shoeld (1934) in patent aiming to remove H_2S from fuel gases using sodium phenolate. Shoeld suggested splitting the streams of both lean and rich amine and claims that such modification reduces steam usage by 50% comparing to conventional single flow process.

Shoeld's idea has been improved by several authors (Condorelli et al. 2001; Freguia et al. 2004; Towler et al. 1997). Despite the differences in various split-flow modifications, there is one common feature present in every split-flow configuration. Because of semi-lean amine drawn off the middle of the stripper, the amount of the solvent remaining in the stripper for further regeneration is lower; therefore, it can be regenerated to a higher extent than for conventional process. Resulting lean amine is very clean and can be fed to the top of the absorber to 'polish' the gas (Polasek et al. 1983). Semi-lean amine recycled to an intermediate stage of the absorber is used to absorb the bulk of CO_2. Additionally semi-lean amine, which is cooled before being fed to the column, suits as interstage absorber cooling. More

optimal temperature profile obtained makes better absorption of CO_2 possible (Leites et al. 2003).

In split-flow designs lean amine is fed to the stripper at various heights (Fig. 2). Forcing the lean solvent at different column heights changes temperature and concentration in the stripper, bringing together the operating and the equilibrium line (Thompson and King 1987). According to the second law of thermodynamics, in order to reduce heat consumption of the process, it is necessary to reduce driving force (Leites et al. 2003). Therefore, split-flow designs are advantageous in terms of the reduction of the heat consumption.

Comprehensive analysis of the heat reduction potential of the split-flow designs, based on exergy losses, was presented by Amrollahi et al. (2011).

Flow sheet of the PDU shown in Fig. 2 contains also rich-split modification suggested by Eisenberg and Johnson (1979). One of the streams of the lean amine is routed directly to the amine stripper bypassing heat exchangers. This stream is heated by condensing steam in the column which would normally be lost from the stripper. Reducing the losses of the steam and heating of a portion of amine reduce the overall energy requirements of the process.

Simulations of CO_2 removal in split-flow processes confirm beneficial character of split-flow modifications. The reduction of the reboiler heat duty by 5–18% than for conventional process was claimed by Hyung Kun Bae (2011). In (Cousins et al. 2011) authors presented simulations of rich-split and split-flow modifications where the reduction of the reboiler heat duty over standard process reached 10.3% and 11.6%, respectively.

3.2 Experimental Data

In this section, the measurement results of the test cases are presented. Cases 1 and 2 should be analysed together as presenting the comparison of standard and flow sheet process, for reboiler heating element power set to 33.0 kW. Similarly, cases 3 and 4 are the same comparison for the reboiler heating element power set to 29.7 kW.

The gas for the separation process using PDU was prepared as mixture of carbon dioxide (concentration: 12.30 vol %) and nitrogen (concentration: 87.7 vol %). Such CO_2 concentration is typical for flue gases from coal-fired power plant. Detailed specification of the gas at the absorber inlet is shown in Table 2.

Prior to feeding the gas into the absorber, it is saturated with water in pretreatment scrubber using water wash. Generally, the pretreatment scrubber is intended to dedust and cool flue gases; however, presented experiments were conducted using technical gases; therefore, such operations were not required.

The gas is treated in the absorber, contacting amine solvent counter currently. The solvent absorbs CO_2, treated gas (CO_2-lean gas) is vented to the atmosphere, and CO_2-rich solvent is pumped to the stripper. The operation conditions of the experiments, including solvent flows, temperatures, solvent loadings, etc., are presented in Table 4.

Table 2 Gas conditions and composition at the absorber inlet

Process variable	Case			
	1	2	3	4
Conditions				
Volumetric flow (m^3/h)	94.4	94.4	92.9	92.9
Mass flow (kg/h)	126.3	126.3	124.2	124.2
Pressure (kPa)	34.8	38.6	38.3	38.1
Temperature (°C)	17.3	15.4	15.2	15.2
Composition (vol % – dry)				
Nitrogen	87.7			
Carbon dioxide	12.3			

Table 3 Gas conditions and composition at the absorber inlet

Process variable	Case			
	1	2	3	4
CO_2-lean gas leaving absorber				
Pressure (kPa)	29.99	29.99	29.98	30.00
Temperature (°C)	37.9	41.1	36.2	38.8
CO_2 concentration (vol% – dry)	1.19	1.00	1.11	0.95
CO_2 leaving stripper				
Pressure (kPa)	45.02	45.01	44.99	44.98
Temperature (°C)	97.9	99.2	95.3	94.9

The conditions and composition of CO_2-lean gas collected from the absorber, together with conditions of CO_2 leaving the stripper, are summarised in Table 3.

In every case, carbon dioxide leaving the stripper is cooled to 25 °C, and water is removed, in condenser installed downstream of the stripper. Water collected in the separator is afterwards pumped back to the absorber to avoid excess water losses from the solvent.

Contrary, water vapours leaving the absorber with CO_2-lean gas are not returned to the process; therefore,

water balance is disturbed. Fortunately partial pressure of water vapours at the outlet of the absorber is not high, thanks to moderate temperatures of CO_2-lean gas stream.

However, to maintain the concentration of the solvent constant, the levels in the bottoms of absorber and stripper are carefully controlled, and water is added in case of level deviations.

The reboiler heat duties shown in Table 4 are gross values, therefore include heat losses to the ambient. The losses depend on many parameters, and its estimation is not straightforward; however, for comparable pilot plant, authors claim than an average value of 10% of the reboiler heat duty could be an acceptable simplification for the heat losses (Stec et al. 2015).

Table 4 Operation conditions of the experiments

Process variable	Case			
	1	2	3	4
CO_2 recovery (%)	91.1	92.5	91.8	93.0
Reboiler heat duty (MJ/kg_{CO2})	5.25	5.05	4.74	4.46
Absorber pressure (kPa)	29.99	29.99	29.98	30.00
Stripper pressure (kPa)	45.02	45.01	44.99	44.98
L/G (kg/kg)	5.20	5.22	5.31	5.32
Overall rich amine mass flow (kg/h)	694.9	685.3	694.3	693.3
Rich amine mass flow – top stripper inlet (kg/h)	60.5	60.5	60.6	60.6
Rich amine mass flow – middle stripper inlet (kg/h)	19.5	267.0	16.7	274.8
Rich amine mass flow – bottom stripper inlet (kg/h)	614.9	357.7	617.0	357.9
Lean amine mass flow (kg/h)	656.7	323.8	659.7	324.4
Semi-lean amine mass flow (kg/h)	–	335.5	–	336.3
Rich amine mass loading (mol_{CO2}/mol_{MEA})	0.411	0.420	0.427	0.423
Lean amine mass loading (mol_{CO2}/mol_{MEA})	0.273	0.234	0.296	0.240
Semi-lean amine loading (mol_{CO2}/mol_{MEA})	–	0.329	–	0.336
Rich amine temperature – at absorber outlet (°C)	54.6	52.5	53.0	51.9
Rich amine temperature – top stripper inlet (°C)	54.6	52.5	53.0	51.9
Rich amine temperature – middle stripper inlet (°C)	–	97.0	–	95.9
Rich amine temperature – bottom stripper inlet (°C)	102.0	105.5	101.0	103.3
Lean amine temperature (°C)	110.5	111.5	109.8	110.7
Semi-lean amine temperature (°C)	–	107.6	–	106.4
Reboiler heating element power (kW)	33.0	33.0	29.7	29.7

The temperature at the absorber inlet is always 40 °C for the solvent

3.3 Absorber Operating Lines

Figures 3 and 4 show a comparison between absorber operating lines for standard and split-flow process flow sheets and equilibrium curves. The equilibrium curves are plotted based on experimental data taken from (Jou et al. 1995). Temperature in the absorber varies along the columns' height from 40 to 60 °C for a typical test, and the equilibrium data for this temperature range are presented in Figs. 3 and 4.

The experimental data for the CO_2 partial pressure is available at three points of the absorber: at the inlet, in the middle section and at the outlet; however, straight lines were used to connect experimental data, but these lines serve only to join the data points.

Despite the semi-lean amine loading is higher than the lean amine loading for standard case, the slope of the operating lines for both process flow sheets remains similar for lower section of the absorber. This fact is clearly visible in Fig. 4, where the operating lines almost overlap for higher partial pressures of CO_2 (lower section of the absorber), which in terms of driving force means the same CO_2 absorption capabilities.

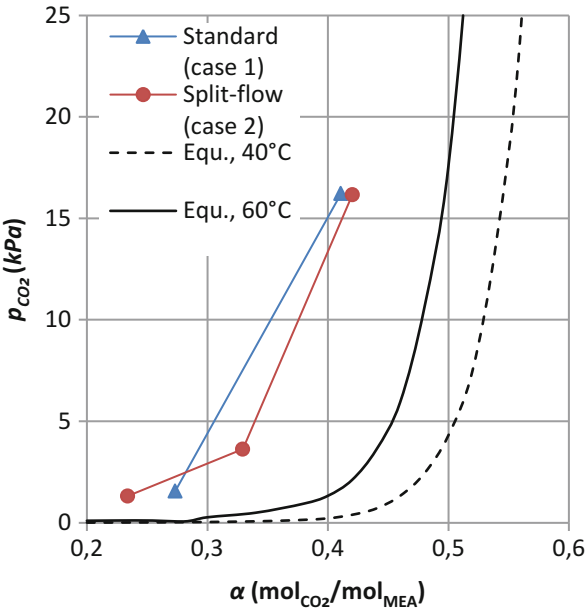

Fig. 3 Comparison of absorber operating lines for cases 1 and 2 to equilibrium curve

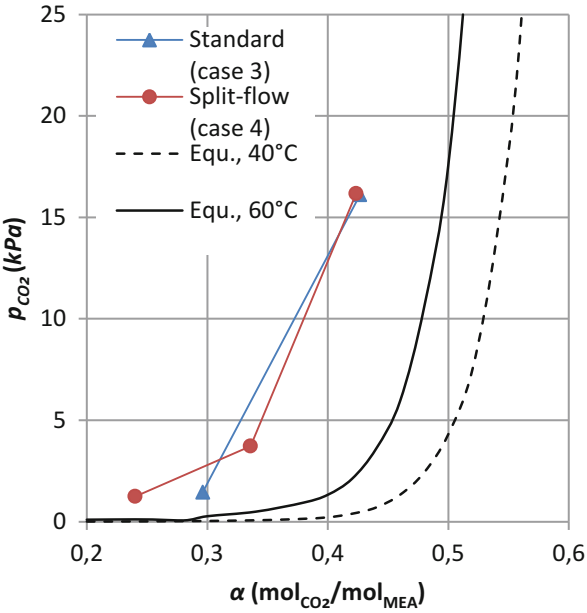

Fig. 4 Comparison of absorber operating lines for cases 3 and 4 to equilibrium curve

Contrary, the driving force for top section of the absorber in split-flow process is much higher than for standard process flow sheet. This is expected because the lean solvent loading for split-flow process is lower than for standard process flow sheet.

Summarising, the CO_2 recovery in lower part of the absorber remains similar for both process flow sheets, as the driving force is also at a similar level. However, split-flow process becomes beneficial in top part of the absorber where the gas is contacting the solvent having very low loading. Thanks to increased driving force in upper part of the column, overall CO_2 recovery is higher for split-flow process by 1.4% when comparing case 1 and case 2, and by 1.2% for cases 3 and 4. It should be noted here that comparisons between standard and split-flow process were carried out for constant power delivered to the process.

As shown above the split-flow process increases CO_2 recovery comparing to standard process. The advantage of split-flow designs would reveal more significantly for systems where the lean solvent loading is very low. The split-flow designs are particularly preferred when high-quality CO_2 lean gas is required (Polasek et al. 1983).

3.4 Absorber Temperature Profiles

Figures 5 and 6 show absorber temperature profiles for standard and split-flow processes. The presence of the pronounced temperature increase is common for every case. This temperature bulge (Kvamsdal and Rochelle 2008) can be explained

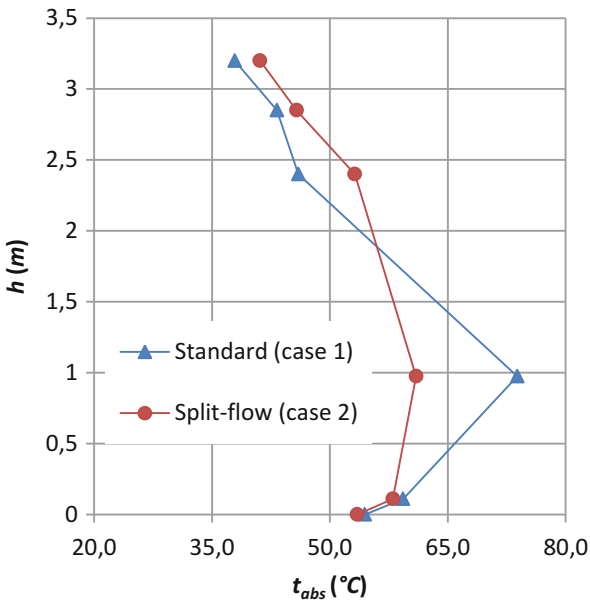

Fig. 5 Absorber temperature profiles for cases 1 (standard) and 2 (split-flow process)

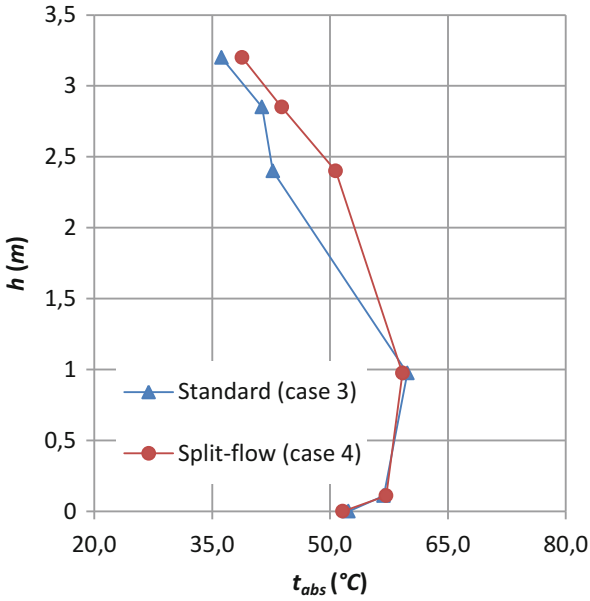

Fig. 6 Absorber temperature profiles for cases 3 (standard) and 4 (split-flow process)

by the fact that during absorption, the heat is released and flows towards the top of the column causing the temperature increase.

It can be noticed that the temperature bulge for split-flow process is less prominent (Fig. 5). This is intercooling effect caused by the injection of cool semi-lean solvent. The semi-lean solvent is fed into the absorber at 40 °C and cools interior of the absorber. Additionally the heat released in lower part of the absorber with split-flow designs is slightly lower comparing to standard process due to lower loading of the semi-lean amine. Both reasons together cause temperature decrease below semi-lean solvent inlet for split-flow process.

The opposite effect occurs in top section of the absorber where the temperature increase can be noticed for split-flow process (Figs. 5 and 6). The lean solvent fed into the top inlet of the absorber has the same temperature either for standard or split-flow process; therefore, the intercooling effect is equal for both configurations. However, the loading of the solvent is lower for split-flow designs; therefore, the amount of CO_2 absorbed in upper part of the column increases. Higher CO_2 absorption causes higher heat release and the increase of the temperature.

Feeding the solvent, having different loadings, at various heights of the absorber causes that the temperature profile of the column for split-flow process is uniform and slightly lower on average than for standard process flow sheet. Lower average temperature of the absorber is in favour of higher driving forces for the absorption process and also increases the absorption capacity of the solvent (Amrollahi et al. 2012).

4 Conclusions

The effects of splitting the flow of the solvent being injected into the absorber have been described in detail. It must be mentioned that split-flow modifications in absorber are intended to increase CO_2 absorption driving force and according to the second law of thermodynamics cause the increase in energy demand of the process. However, introduction of colder rich solvent to the top of the stripper, hotter rich streams below, taking the semi-lean amine from the stripper, changes its temperature profile. Changed temperature profile causes the operating line of the stripper parallel more closely the equilibrium curve thereby the condition necessary to reduce the energy consumption in the stripper is fulfilled.

Analysing energy demand of the split-flow process modification, we are facing contradictory effects: the increase of energy demand in the absorber and decrease in the stripper. However, the total energy consumption of the process is reduced comparing to the standard flow sheet, making this modification profitable.

The reduction in the reboiler heat duty for split-flow process during trials presented in this paper ranges from 4 to 6%. Apart from the reboiler heat duty reduction, the increase in CO_2 recovery is also observed with split-flow designs.

Split-flow process improvement proved its value during experimental tests because with minor increase in process complexity, noticeable increase in process efficiency was perceived.

It can be expected that split-flow modification coupled with new solvent would drastically decrease the energy demand and increase the CO_2 recovery of the amine-based post-combustion CO_2 capture process.

Acknowledgements The results presented in this paper were obtained during research cofinanced by the National Centre of Research and Development in the framework of Contract SP/E/1/67484/10 – Strategic Research Programme – Advanced technologies for energy generation: Development of a technology for highly efficient zero-emission coal-fired power units integrated with CO_2 capture.

References

Ahn, H., Luberti, M., Liu, Z., Brandani, S.: Process configuration studies of the amine capture process for coal-fired power plants. Int. J. Greenh. Gas Control. **16**, 29–40 (2013)

Amrollahi, Z., Ertesvåg, I.S., Bolland, O.: Optimized process configurations of post-combustion CO2 capture for natural-gas-fired power plant—exergy analysis. Int. J. Greenh. Gas Control. **5**, 1393–1405 (2011)

Amrollahi, Z., Ystad, P.A.M., Ertesvåg, I.S., Bolland, O.: Optimized process configurations of post-combustion CO2 capture for natural-gas-fired power plant – power plant efficiency analysis. Int. J. Greenh. Gas Control. **8**, 1–11 (2012)

Chen, X., Rochelle, G.T.: Aqueous piperazine derivatives for CO2 capture: accurate screening by a wetted wall column. Chem. Eng. Res. Des. **89**, 1963–1710 (2011)

Condorelli, P., C. Mariz, J. Scherffius, and R. Won.: Split flow process and apparatus. Google Patents. http://www.google.com/patents/EP1152815A1?cl=en (2001)

Cousins, A., Wardhaugh, L.T., Feron, P.H.M.: Preliminary analysis of process flow sheet modifications for energy efficient CO2 capture from flue gases using chemical absorption. Chem. Eng. Res. Des. **89**, 1237–1251 (2011)

Cousins, A., Cottrell, A., Lawson, A., Huang, S., Feron, P.H.M.: Model verification and evaluation of the rich-split process modification at an Australian-based post combustion CO2 capture pilot plant. Greenh. Gases Sci. Technol. **2**, 329–345 (2012)

Eisenberg, B., and Johnson, R.R.: Amine regeneration process. Google Patents. http://www.google.com/patents/US4152217 (1979)

Freguia, S., Gilmartin, J., Reddy, S., and Scherffius, J.: Improved split flow process and apparatus (Google patents). (2004) https://www.google.com/patents/WO2004005818B1?cl=en

Hartono, A., Orji Mba, E., Svendsen, H.F.: Physical properties of partially CO2 loaded aqueous Monoethanolamine (MEA). J. Chem. Eng. Data. **59**, 1808–1816 (2014)

Hyung Kun Bae, S.Y.K.: Simulation of CO2 removal in a split-flow gas sweetening process. Korean J. Chem. Eng. **28**, 643–648 (2011)

Jou, F.-Y., Mather, A.E., Otto, F.D.: The solubility of CO2 in a 30 mass percent monoethanolamine solution. Can. J. Chem. Eng. **73**, 140–147 (1995)

Karimi, M., Hillestad, M., Svendsen, H.F.: Capital costs and energy considerations of different alternative stripper configurations for post combustion CO2 capture. Chem. Eng. Res. Des. **89**, 1229–1236 (2011)

Kvamsdal, H.M., Rochelle, G.T.: Effects of the temperature bulge in CO2 absorption from flue gas by aqueous Monoethanolamine. Ind. Eng. Chem. Res. **47**, 867–875 (2008)

Lajnert, R., Latkowska, B.: Clean Coal Technologies Center in Zabrze – possibilities of technological research. Przem. Chem. **92**, 215–221 (2013)

Leites, I.L., Sama, D.A., Lior, N.: The theory and practice of energy saving in the chemical industry: some methods for reducing thermodynamic irreversibility in chemical technology processes. Energy. **28**, 55–97 (2003) doi: 10.1016/S0360-5442(02)00107-X

Mangalapally, H.P., Notz, R., Hoch, S., Asprion, N., Sieder, G., Garcia, H., Hasse, H.: Pilot plant experimental studies of post combustion CO2 capture by reactive absorption with MEA and new solvents. Energy Procedia. **1**, 963–970 (2009)

Polasek, J.C., Bullin, J.A., Donnelly, S.T.: How to reduce costs in amine sweetening units. Chem. Eng. Prog. **79**, 63–67 (1983)

Shoeld, M.: Purification and Separation of Gaseous Mixtures. (1934)

Skorek-Osikowska, A., Kotowicz, J., Janusz-Szymańska, K.: Comparison of the energy intensity of the selected CO2-capture methods applied in the ultra-supercritical coal power plants. Energy Fuel. **26**, 6509–6517 (2012)

Spietz, T., Więcław-Solny, L., Tatarczuk, A., Krótki, A., Stec, M.: Technological modifications in pilot research on CO2 capture process. Chem. Sci. Tech. Mark. **68**, 884–892 (2014)

Stec, M., Tatarczuk, A., Więcław-Solny, L., Krótki, A., Ściążko, M., Tokarski, S.: Pilot plant results for advanced CO2 capture process using amine scrubbing at the Jaworzno II power Plant in Poland. Fuel. **151**, 50–56 (2015)

Thompson, R.E., King, C.J.: Energy conservation in regenerated chemical absorption processes. Chem. Eng. Process. Process Intensif. **21**, 115–129 (1987)

Towler, G., Shethna, H., Cole, B., Hajdik, B.: Improved absorber-stripper Technology for gas Sweetening to ultra-low H2S concentrations. In: Proceedings of the Annual Convention-Gas Processors Association, pp. 93–100. Gas Processors Association, San Antonio (1997)

Więcław-Solny, L., Tatarczuk, A., Krótki, A., Wilk, A., Śpiewak, D.: Dotrzymać kroku polityce energetyczno-klimatycznej UE – postęp badań procesów usuwania CO2 z gazów spalinowych. Polityka Energ. **15**, 111 (2012)

Wilk, A., Więcław-Solny, L., Tatarczuk, A., Krótki, A., Śpiewak, D.: Effect of composition of absorption solution on carbon dioxide removal efficiency. Przem. Chem. **92**, 120–125 (2013)

Hydrogen Production from Methanol Electrolysis

Sabah Menia, Fatiha Lassouane, Hamou Tebibel, and Abdallah Khellaf

1 Introduction

Various methods are available for hydrogen production and each of these methods has its own advantages and disadvantages. Currently, steam reforming of natural gas is considered as the most cost-effective route for large-scale hydrogen production. Due to various issues related to the storage and transport of hydrogen, there is an immediate requirement of small-scale methods for on-site hydrogen production and for applications such as for fuel cells. Though compact steam reformers using natural gas and methanol are under development, there are many issues associated with them, such as carbon monoxide removal, long start-up time, and poor transient response (Sasikumar et al. 2008).

Electrolysis is the best option for producing hydrogen very quickly and conveniently. Electrolysis of water can generate very high pure hydrogen and is considered as the most promising technology for small-scale production of hydrogen. The disadvantage of this process is that the energy requirement is very high. Theoretically, the energy consumption is 39.4 kWh/kg or 3.54 kWh/Nm^3 of hydrogen, while for a commercial water electrolyser, it is about 50–55 kWh/kg or 4.5–5 kWh/Nm^3 of hydrogen. Though various methods have been reported for reducing energy consumption of water electrolysis, theoretical requirement itself is very high. This method will become more attractive if low-cost electricity or electricity from renewable sources is available (Sasikumar et al. 2008).

Electrolysis of aqueous methanol is another promising method for on-site hydrogen production, and it has been reported that hydrogen can be generated by

S. Menia (✉) • F. Lassouane • H. Tebibel • A. Khellaf
Centre de Développement des Energies Renouvelables, CDER, B.P. 62, Route de l'Observatoire, 16340 Bouzareah, Algiers, Algeria
e-mail: s.menia@cder.dz

© Springer International Publishing AG, part of Springer Nature 2018

F. Aloui, I. Dincer (eds.), *Exergy for A Better Environment and Improved Sustainability 2*, Green Energy and Technology,
https://doi.org/10.1007/978-3-319-62575-1_32

electrolysis of methanol–water mixture, at a very low operating voltage, compared to water electrolysis. Though carbon dioxide, a greenhouse gas, is produced during this process, the net carbon dioxide emission will be negligible, since methanol can be produced from biomass, a renewable source. When aqueous methanol is electrolyzed, hydrogen and carbon dioxide are produced, at ambient temperature and pressure (Sasikumar et al. 2008).

The reaction at the anode and cathode and overall reaction are represented as follows:

$$\text{Anode} : CH_3OH + 6\,OH^- \rightarrow 5\,H_2O + CO_2 + 6\,e^- \quad (1)$$

$$\text{Cathode} : 2\,H_2O + 2\,e^- \rightarrow 2OH^- + 3H_2 \quad (2)$$

$$\text{Overall reaction} : CH_3OH + H_2O \rightarrow 3\,H_2 + CO_2 \quad (3)$$

The theoretical voltage required for the above methanol–water solution electrolysis is 0.02 V only, which is very much lower compared to 1.23 V required for water electrolysis. Hence, the corresponding theoretical energy consumption for aqueous methanol electrolysis is very low (Sasikumar et al. 2008).

In this paper, the basic concept of methanol–water solution electrolysis with an alkaline membrane is introduced.

2 Methanol Electrolysis

Liquid alcohols could serve as a bridge between gasoline and gaseous H_2. They possess high energy densities and can be easily stored and distributed through the existing gasoline infrastructure. It has also been argued that alcohols are the next liquid fuels to use after the depletion of petroleum resources. Methanol can be economically mass-produced from nonrenewable resources, such as natural gas and coal, or from renewable resources such as biomass. Alcohols can be used to produce electricity in direct fuel cells or mechanical energy in internal combustion engines. However, an alcohol electrochemical reformer or electrolyser can be used to produce clean H_2, which can be used in other systems, resulting in an improvement in the overall system performance. Electrochemical reforming or electrolysis is a process in which an organic or alcohol fuel is electro-oxidized to form H_2. Electrical power is required to split the chemically bonded species (Cloutier and Wilkinson 2010).

The aqueous solution of CH_3OH fed to the anode is electro-oxidized via a dehydrogenation process to produce carbon dioxide (CO_2), hydrogen ions (H^+), and electrons (e^-) (Cloutier and Wilkinson 2010).

Most H_2 is currently produced by the well-established catalytic steam reforming (SR) process for hydrocarbon-based fuels, which requires higher temperatures in the range of 250–1100 °C. It can be carried out externally, integrated with a fuel cell, or directly inside a fuel cell such as a molten-carbonate fuel cell (MCFC, 600–700 °C) or a solid oxide fuel cell (SOFC, 600–1000 °C). On-board gasoline reforming was originally believed to be the best way of generating H_2 for transportation, but it was determined that it did not offer clear advantages over other available technologies, such as gasoline ICE and battery hybrids. The practical issues of durability, size and weight, resistance to vibration, cold start, transient response, and H_2 purity concerns complicate the application of SR for H_2 generation in transportation. An important approach to achieve the ultimate performance targets, including start-up time and start-up energy, could be to efficiently carry out on-board reforming at temperatures lower than that of a conventional SR. It was reported that methanol catalytic reforming can be carried out in the aqueous phase at lower temperatures (80–200 °C). It seems that no studies have verified if low-temperature methanol reforming could meet the on-board fuel processing targets and if its adoption could serve as a bridge toward the implementation of a H_2 economy. Under certain operating conditions, the alcohol electrochemical reformer or electrolyser may result in reduced energy consumption over comparable existing technologies. First, the single-step electrochemical reforming process could be conducted in the liquid phase at a lower operating temperature and has the potential to have a higher overall system efficiency compared to conventional high-temperature multi-reactor SR systems. Secondly, H_2 production from methanol electrolysis should result in lower power consumption than H_2 production from water electrolysis, the large-scale commercialization of which is restrained by its significant electricity requirements. In fact, the standard potential for the oxidation of CH_3OH in the liquid phase is only −0.016 V versus the standard H_2 electrode (SHE) compared to -1.23 V versus standard H_2 electrode for the oxidation of water. It has been estimated that H_2 production from the electrolysis of CH_3OH costs about 50% less compared to that of water, even when the cost of CH_3OH is taken into account. The main disadvantages of alcohol electrolysis are issues also faced by direct alcohol fuel cells: the slow kinetics of the anode alcohol electrooxidation and the loss of fuel resulting from the alcohol and water crossover from the anode to the cathode. Although CO_2, a greenhouse gas, is produced whether CH_3OH is thermally or electrochemically reformed, it is more localized and concentrated in an electrochemical reforming process. This has an advantage for effective capture for sequestration and reduces the cost for CO_2 disposal in many applications. The cost of CO_2 capture and disposal for various coal-fired generation technologies ranges from 1.1 to 4.9 cent/ kWhe and 0.6 to 6.7 cent/kWhe, respectively (Cloutier and Wilkinson 2010).

Reichman and William demonstrated the electrochemical production of H_2 gas from CH_3OH in aqueous NaOH or KOH media at temperatures between 23 and 60 °C. The inclusion of a base permits the generation of H_2 without CO_2 emission. As H_2 would be the only gas produced, it would not require separation from other gaseous by-products, and single-chamber configurations might be possible.

However, in a dual-chamber configuration, the bicarbonate ions and/or carbonate ions generated as soluble by-products might degrade the performance of the electrolyser. Teruo et al. efficiently produced H_2 by the electrochemical decomposition of an aqueous solution of liquid fuel via electrolysis in a two-chamber electrolytic cell using a diaphragm and metals dispersed on carbon as the anode and cathode catalysts. Woods et al. developed an electrochemical reformer and fuel cell system, which uses a solid-state or liquid state acidic or basic electrolyte and relies on electricity and/or thermal energy to supply the necessary reaction energy to reform organic fuels into H_2 and CO_2, while the H_2 generated produces electricity in a fuel cell (Cloutier and Wilkinson 2010).

To date, all literature published studies pertaining to the performance of alcohol electrolysers have been carried out in a recycle operation mode or flowing mode. In these studies, the anode is fed with unacidified CH_3OH aqueous solution, which is fed using a pump, while the cathode compartment containing H_2 is purged with argon. In the recycle operation studies, e.g., carbon paper, typical anode catalysts used are Pt/C or Pt–Ru/C, and although Pt/C is typically the most studied cathode catalyst, cathode catalysts such as Pt–WC/C have also been investigated (Cloutier and Wilkinson 2010) (Fig. 1).

3 Comparison with Ethanol Electrolysis

Electrolysis of aqueous alcohols has been proposed as a promising method for on-site hydrogen production with lower power demands, since part of the energy required for the electrolysis is provided by the organic molecule. For instance, it has been reported that hydrogen can be produced by the electrolysis of methanol–water mixtures, at a very low operating voltage compared with water electrolysis. This process of water–alcohol mixture electrolysis has also been named as electrochemical reforming or electro-reforming and is based on the use of electrical power to split the chemically bonded species by the electrooxidation of the alcohol fuel. Although CO_2 is produced, this process is considered as an environment-friendly one, if a bio-alcohol is used as the fuel. Then, the produced CO_2 can be recaptured by living plants to regenerate the required biomass. In addition, a clear advantage of this method compared to the catalytic steam reforming of alcohols is the production of pure hydrogen in the cathode compartment of the cell, which is automatically separated from the other reaction products (Caravaca et al. 2012).

Hence, the electrochemical reforming of methanol and glycerol has been studied in the literature showing very promising results for pure H_2 production. However, to the best of our knowledge, there are no previous works related to the electrochemical reforming of ethanol. This latter is expected to be the most widely used biofuel around the globe since it can be produced from abundant supplies of starch/cellulose biomass. In addition, ethanol is harmless to humans and can be easily transported and stored (Caravaca et al. 2012) (Fig. 2).

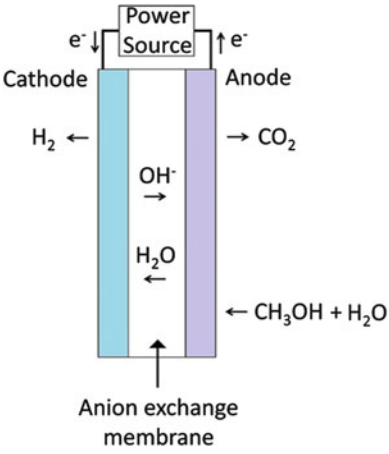

Fig. 1 Schematic of methanol–water solution electrolysis with an alkaline membrane (Tuomi et al. 2013)

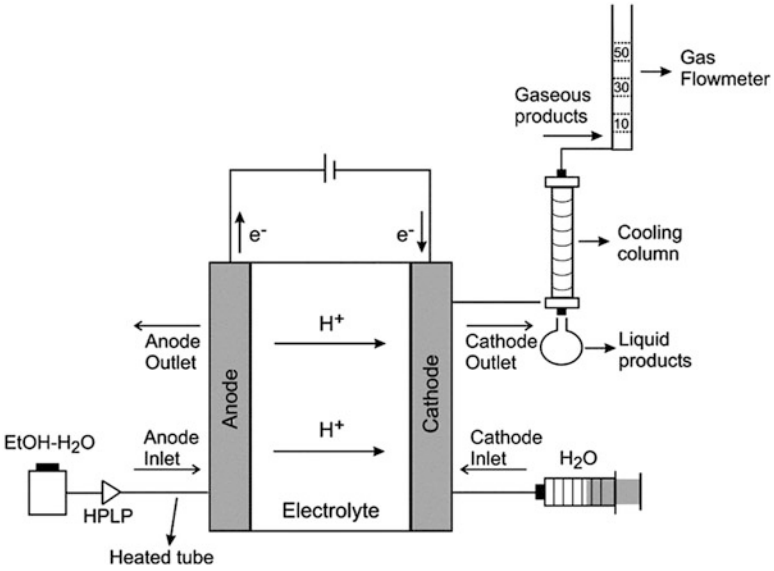

Fig. 2 Representation of the setup used for the ethanol electro-reforming process (Caravaca et al. 2012)

4 Conclusions

The concept of methanol–water solution electrolysis in a fuel cell equipped with an alkaline membrane for hydrogen production is introduced, offering the possibility for lower power consumption in hydrogen production when compared to traditional water electrolysis.

The alkaline membrane electrolyser is an attractive alternative to the conventional electrolysers with proton exchange membranes enabling the utilization of low-cost membrane materials offering savings with material expenses.

This novel method opens a new area for investigation in hydrogen production and enables alternative material choices to produce commercially viable methanol electrolysers although further development is required.

Acknowledgments Development center of renewable energy in Algeria supported this research.

References

Caravaca, A., Sapountzi, F.M., De Lucas-Consuegra, A., Molina-Mora, C., Dorado, F., Valverde, J.L.: Electrochemical reforming of ethanol water solutions for pure H_2 production in a PEM electrolysis cell. Int. J. Hydrog. Energy. **37**, 9504–9513 (2012)

Cloutier, C.R., Wilkinson, D.P.: Electrolytic production of hydrogen from aqueous acidic methanol solutions. Int. J. Hydrog. Energy. **35**, 3967–3984 (2010)

Pham, A.-T., Baba, T., Sugiyama T., Shudo T.: Efficient hydrogen production from aqueous methanol in a PEM electrolyzer with porous metal flow field: Influence of PTFE treatment of the anode gas diffusion layer. Int. J. Hydrog. Energy. **38**(1), 73–81 (2013)

Sasikumar, G., Muthumeenal, A., Pethaiah, S.S., Nachiappan, N., Balaji, R.: Aqueous methanol electrolysis using proton-conducting membrane for hydrogen production. Int. J. Hydrog. Energy. **33**, 5905–5910 (2008)

Tuomi, S., Santasalo-Aarnio, A., Petri, K.P., Kallio, T.: Hydrogen production by methanol water solution electrolysis with an alkaline membrane cell. J. Power Sources. **229**, 32–35 (2013)

Experimental Investigation of Polypropylene Pyrolysis for Fuel Production

Emna Berrich Betouche, Asma Dhahak, Abdel Aziz Touati, and Fethi Aloui

1 Introduction

Waste plastics have a long biodegradability lifetime of between 100 and 1000 years (Dussud and Ghiglione 2014). The treatment of such waste is carried out by several methods (Panda 2011). The thermo-chemical processes seek waste valorization through their high calorific value. Indeed, this power is equivalent to that of coal or oil, and is 3.5 times higher than that of paper or cardboard (Carrega and Verney 2012).

The pyrolysis of waste plastics is very interesting. It is based on an endothermic reaction that takes place in a low-oxygen atmosphere (less than 2% of O_2). The waste is decomposed under three phases: a solid residue (pyrolysis coke or coal), liquid (mixture of condensable heavy and light condensable), and gas (CO, H_2,

E.B. Betouche (✉)
LUNAM University, Nantes University, UFR Sciences et Technology, 2 Chemin de la Houssinière, 44300 Nantes, France

CNRS, GEPEA, UMR6144, IMT Atlantique École des Mines de Nantes, 4 Rue Alfred Kastler, 44300 Nantes, France
e-mail: Emna.berrich@univ-nantes.fr

A. Dhahak
Ecole Nationale d'Ingénieurs de Gabes, Chemical Engineering-Processes Department, Avenue Omar Ibn El Khattab, Zrig Eddakhlania, GABES 6072, Tunisia

A.A. Touati
LAMIH CNRS UMR 8201, Department of Mechanics, University of Valenciennes (UVHC), Campus Mont Houy, F-59313 Valenciennes Cedex 9, France

F. Aloui
LAMIH CNRS UMR 8201, Department of Mechanics, University of Valenciennes (UVHC), High Engineering School (ENSIAME), Campus Mont Houy, F-59313 Valenciennes Cedex 9, France

© Springer International Publishing AG, part of Springer Nature 2018

F. Aloui, I. Dincer (eds.), *Exergy for A Better Environment and Improved Sustainability 2*, Green Energy and Technology,
https://doi.org/10.1007/978-3-319-62575-1_33

Fig. 1 The commercial symbol of polypropylene (PP)

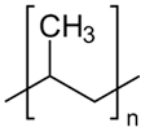

Fig. 2 Chemical structure of polypropylene (PP)

CO_2, CH_4, C_2H_4, and C_2H_6) (Léger and Lafortune 2001). This process is efficient. Its advantages are (Patni et al. 2013):

- The ability to develop all the products obtained: pyrolysis oil that can be used as fuel for engines, gas can be used for heating or electricity generation, and coke can later be converted into products such coal assets or material used in the building industry.
- Reducing waste volume (<50–90%)
- The use of low oxygen provides the reduced emission of pollutants such as dioxins.
- The ease of storage and transportation fuel.

Polypropylene (PP) was discovered in 1955 by Prof. Natta. It is generally used in automobiles, packaging, bags, bottle caps, and clingfilm. The commercial symbol of polypropylene (PP) is shown is Fig.1. Its chemical structure is shown in Fig. 2. It is formed from naphtha, which is produced between the kerosene and gasoline production steps. It then undergoes steam cracking to produce the monomers (ethylene and propylene). The reaction mechanism (series of transformations) involved in producing PP is produced by a low-pressure propene polymerization reaction (Mc et al. 2010). It has an asymmetrical chemical structure (Karger-Kocsis 1994).

2 Experimental Facility

2.1 Setup

The experiments were conducted in a semi-batch reactor in an inert atmosphere. The experimental installation is shown in Fig. 3. It comprises a batch reactor, a gas analyser, a pressure sensor, two temperature sensors, a heater, a condenser, a nitrogen tank, a flowmeter, a thermometer, a liquid bottle, and acquisition software.

Initially, the sample is collected, cut, weighed, and then loaded into the reactor. The latter has to be tightly closed, purged with a stream of nitrogen to remove oxygen from the reactor, covered by insulation to limit heat loss, and then heated through a heater. The sample weights were 100 g. The nitrogen flow is fixed to

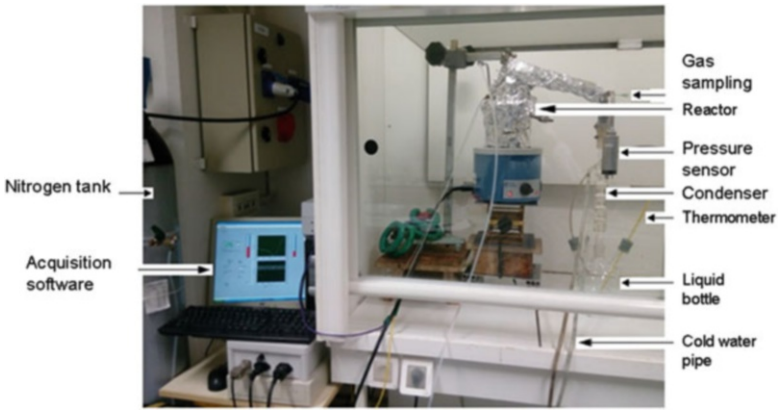

Fig. 3 Experimental installation

20 ml/min. A heating rate equal to 10 °C/min was maintained until a well-fixed temperature depending on the functional parameters and the thermo-gravimetric analysis resulted. Then the heating was decreased to 2 °C/min. During experiments, there are two types of products: non-condensable gases and condensable gases that became liquid using the condenser.

3 Results and Discussion

The heat flow rate was initially fixed to 10 °C/min up to a temperature of 325 °C. It was then reduced to 2 °C/min. Based on the thermo-gravimetric analysis, before a temperature of 325 °C, no reaction was detected, thus the heat rate can be increased in order to reduce residence time on the reactor. The set-point temperature was fixed to 550 °C because after this temperature, no important reaction was generated under the heat rate given. Thus, heating after reaching this temperature should be considered as heat losses, which reduce the process's efficiency. The water flow was fixed to 6.84 ± 0.18 L/min. Development of the quantity and quality of liquid of the pyrolysis product during one of the experiments carried out is shown in Fig. 4.

Condensation begins after 43 min of heating, and is very slow. The first gas condensation temperature is equal to 385.8 °C. At the beginning of the condensation, the liquid has a yellowish color, and then it becomes reddish.

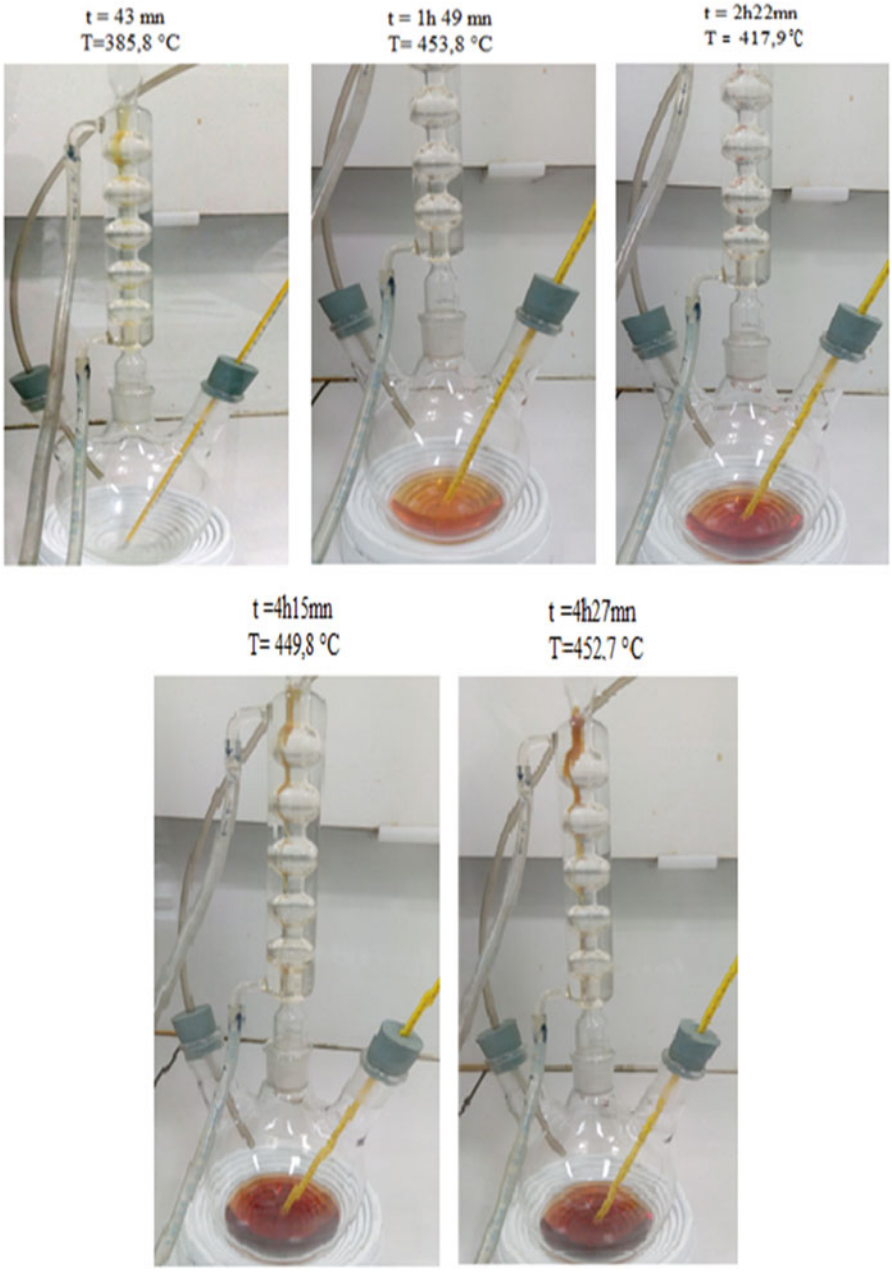

Fig. 4 Development of the quantity and quality of the PP pyrolysis liquid

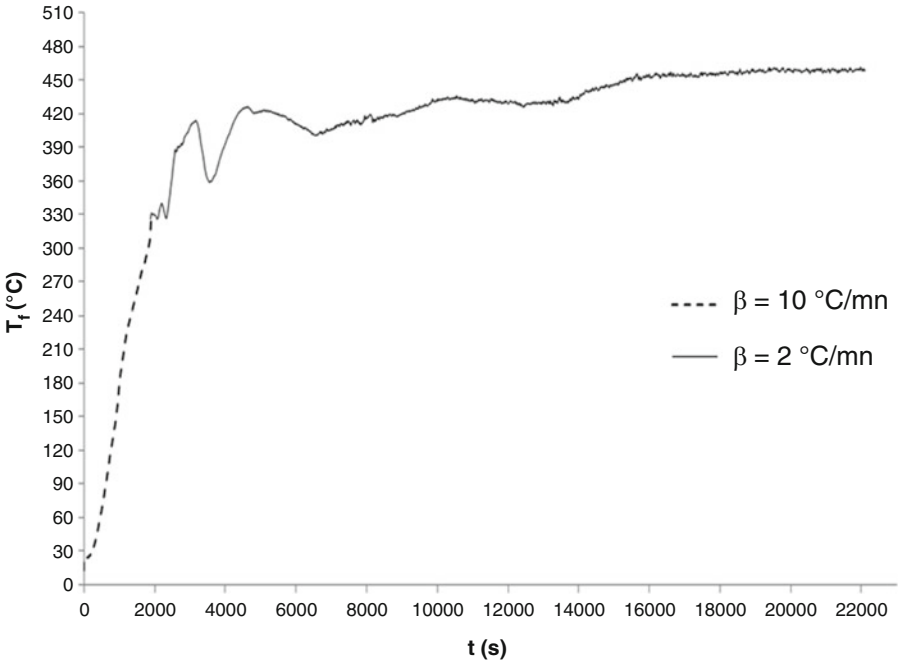

Fig. 5 Time-evolution of the temperature at the bottom of the reactor

3.1 Temporal Development of the Reactor Temperature

The time-evolution of the temperature at the bottom of the reactor is illustrated in Fig. 5.

The reactor residence time was 6 h 8 min, and the final temperature was 458.2 °C. The condensation temperature was more or less stabilized and the condensation became very slow.

Figure 6 shows the temporal development of the temperature differences between the bottom T_f and the middle height T_m of the reactor ΔT:

$$\Delta T = T_f - T_m \tag{1}$$

The solid and liquid products obtained are shown in Fig. 7. ΔT decreases when T_f reaches 330.9 °C after 32 min (1920 s) of heating. Degradation begins at this temperature. There are three peaks in the temperature profile (Fig. 6). The first peak appears at 2342 s, and corresponds to a production of propane. More details are given below and in Fig. 8 which illustrates the time-evolution of volumetric percentage of PP pyrolysis gases.

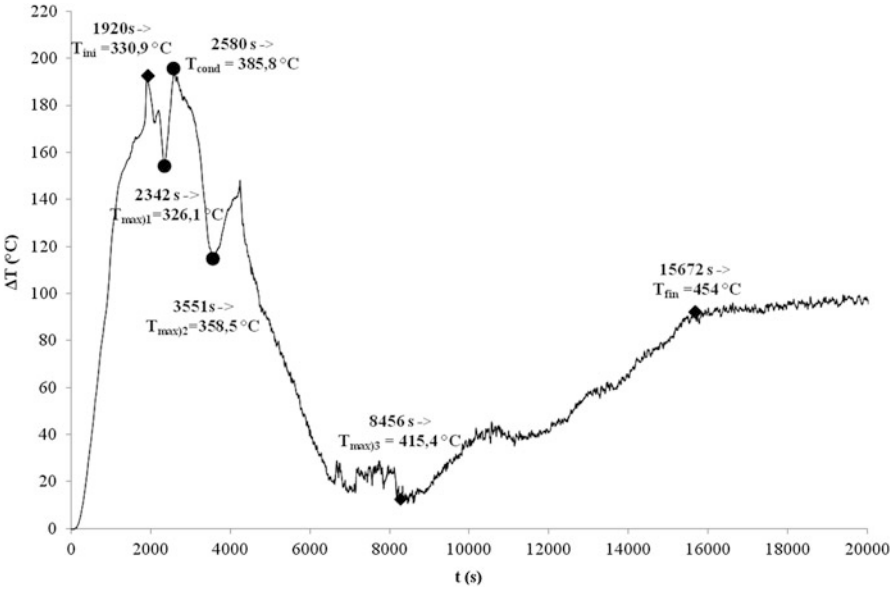

Fig. 6 Time-evolution of PP pyrolysis temperature difference between the bottom and the middle of the reactor

Fig. 7 PP pyrolysis products

The second peak appears at 3551 s. Figure 8 shows that between 3448 and 3751 s, the volatile gas volumetric percentage decreases. Therefore, it corresponds to the condensation phase of gases having a carbon number greater than 6.

The broad peak between 4250 and 15672 s is due to the release of non-condensable gases (at approximately 6498 s) and condensable gases (at approximately 8456 s). Condensation was rapid in the following situations:

- After 2 h 22 min (8520 s), at a temperature equal to 417.9 °C.
- After 2 h 39 min (9540 s), at a temperature equal to 420 °C.
- After 3 h 05 min (11,100 s), at a temperature equal to 432.5 °C.

The degradation is almost complete at 454 °C, after 4 h 21 min of PP pyrolysis.

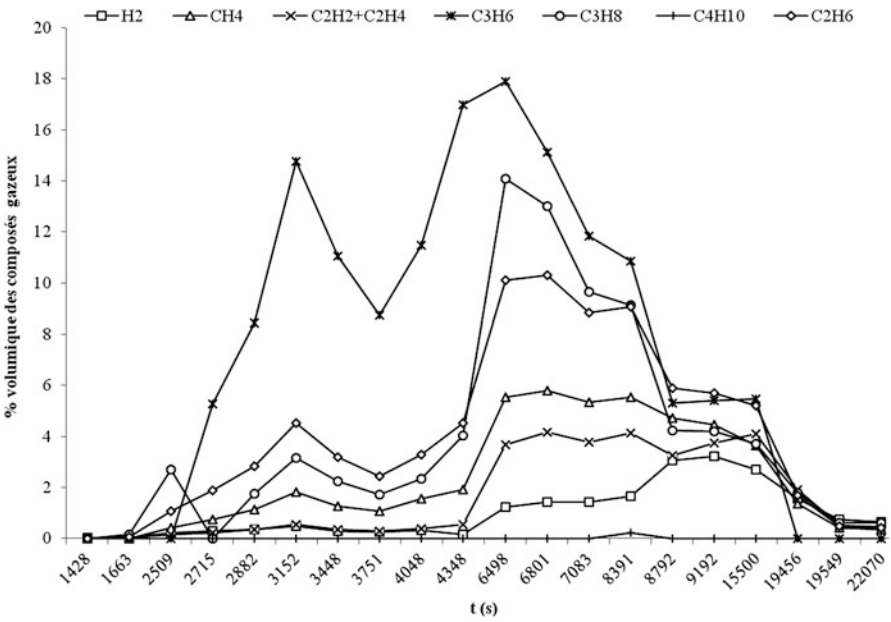

Fig. 8 Time-evolution of volumetric percentage of PP pyrolysis gases

3.2 PP Pyrolysis Product Analysis

Under the fixed operational parameters, the pyrolysis of 100 g of PP enables 63.13 g of liquid to be obtained (a volume of 84 ml) and 0.36 g of solid. Thus, the liquid, solid, and gas products mass yields are, respectively, 63.13%, 0.36%, and 36.51%. The performance of the gas obtained is very important so that good condensation is achieved for cooling the gas released.

3.2.1 Gas Analysis

The time-evolution of the volumetric percentages of gases obtained by PP pyrolysis is presented on Fig. 8.

In the alkene family, propene has a higher percentage of approximately 17.91% at 401.3 ° C. This has been confirmed in the literature (Wong and Broadbelt 2001). For alkanes, ethane and propane are predominantly formed.

3.2.2 Liquid Analysis

The liquid chromatograph of PP pyrolysis is represented in Fig. 9. The compounds identified in this liquid are listed in Table 1. The liquid is made up essentially with

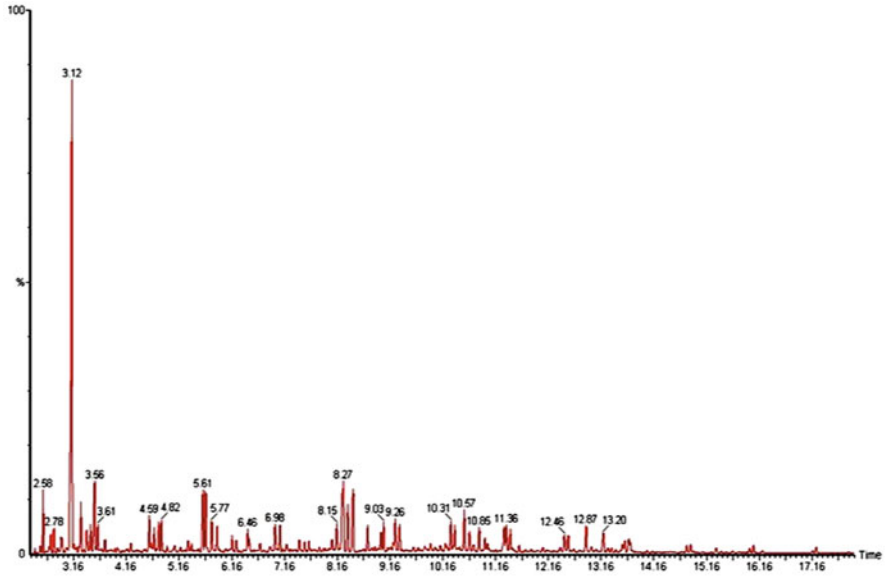

Fig. 9 Liquid chromatogram of PP pyrolysis

Table 1 List of the major components in the PP pyrolysis liquid

Retention time min	Component	Molar mass (g/mol)	Chemical formula
2.586	2,3-dimethyl-Hexane	114	C_8H_{18}
2.782	Octane	114	C_8H_{18}
3.121	2,4-dimethyl-1-heptene	126	C_9H_{18}
3.563	(S)-3-ethyl-4-methylpentanol	130	$C_8H_{18}O$
3.602	Oxalate d'isobutyle et de nonyle	272	$C_{15}H_{28}O_4$
4.589	1-decene	140	$C_{10}H_{20}$
4.827	2,6-dimethyl-Nonane	156	$C_{11}H_{24}$
5.615	isotridecanol	200	$C_{13}H_{28}O$
5. 768	(Z)-3-tetradecene	196	$C_{14}H_{28}$
6.459	(2,4,6-trimethylcyclohexyl) methanol	156	$C_{10}H_{20}O$
6.979	1-dodecene	168	$C_{12}H_{24}$
8.158	1-tridecene	182	$C_{13}H_{26}$
8.272	2-isopropyl-5-methyl-1-heptanol	172	$C_{11}H_{24}O$
9.031	Acetate de 11,13-dimethyl-12-tetradecen-1-yle	282	$C_{18}H_{34}O_2$
9.262	(E)- 9-octadecene	252	$C_{18}H_{36}$
10.306	(E)-5-eicosene	280	$C_{20}H_{40}$
10.566	1-tricosene	322	$C_{23}H_{46}$
10.855	2-hexyl- 1-decanol	242	$C_{16}H_{34}O$
12.461	(E)-9-eicosene	280	$C_{20}H_{40}$
11.364	cyclohexadecane	224	$C_{16}H_{32}$
13.206	1-hentetracontanol	592,592	$C_{41}H_{84}O$

Table 2 Comparison of PP liquid to other fuels

Properties	Gasoline	Kerosene	Diesel	PP pyrolysis liquid obtained
Density (kg/m^3)	743–751 (20–30 °C)	760–767 (20–30 °C)	870–1000	751.644
Flash point (°C)	−46	38	38–58	31
HHV (MJ/kg)	47	46	45	46.151 ± 1.33
Viscosity (cP) at 40 °C	0.41	1.7	3.35	0.67
Composition on carbon	C_7–C_{11}	C_{12}–C_{15}	C_{16}–C_{18}	C_8–C_{41} (C_8–C_{11}: 38.09% C_{12}–C_{15}: 14.28% >C_{15}: 47.63%)

42.86% alkenes and 19.04% alkanes whose carbon number is greater than 8. Among the constituents, there are also oxygenates (38.1%), which are mainly composed of alcohols. This is may be due to the oxidation of polypropylene in the presence of the limited oxygen quantity inside the reactor. The polypropylene contains tertiary carbons, which promote oxidation compared to other types of heat treatments. In the presence of oxygen, tertiary radicals form the peroxide chemical formula-C-O-O-H even at 150 °C. The peroxides are decomposed later in more stable oxygenated groups such as hydroxyl and carbonyl groups (Panda and Singh 2013).

The liquid characteristics are presented in Table 2. The liquid obtained has almost the density of gasoline, while its higher heating value (HHV) and its flash point are closer to those of kerosene.

The PP liquid dynamic viscosity obtained is higher than that of gasoline and lower than that of kerosene.

The liquid is a mixture of 47.63% of heavy hydrocarbons (>C15) and 52.37% of light hydrocarbons (C8–C15). Thus PP pyrolysis promotes the production of unsaturated light hydrocarbons.

4 Conclusions

The pyrolysis of polypropylene is realised to produce fuel. Under the operational parameters, the obtained liquid mass yield is 63.13%. It is made up of 47.63% heavy hydrocarbons and 52.37% light hydrocarbons. It has approximately the same gasoline density but a higher heating value (HHV). Its flash point is closer to that of kerosene.

Acknowledgements This work was supported by LUNAM University, Nantes University, UFR Sciences et Technology, the "Processes engineering, Environment and Agri-food" laboratory (GEPEA), Energetic Systems and Environment (DSEE) Department, IMT Atlantique, Mines

Engineering school of Nantes in FRANCE and the Engineering School of Gabes, Chemical Engineering-Processes of Gabes, Tunisia. This support is gratefully acknowledged.

References

Carrega, M., Verney, V.: Matières plastiques, 3ème édition, Paris, DUNOD, coll "Technique et Ingénierie", 680 (2012)

Dussud, C., Ghiglione, J. F.: La dégradation des plastiques en mer, SFE report, december. http://www.sfecologie.org/regards/2014/12/26/r63-plastiques-en-mer-dussud-et-ghiglione/#comment-259688 (2014)

Karger-Kocsis, J.: Polypropylene Structure, Blends and Composites, Structure and Morphology, p. 169. Chapman & Hall/Springer, London (1994)

Léger, S., Lafortune, F.: Pyrolyse et gazefication des pneus hors d'usage. http://www.recyc-quebec.gouv.qc.ca/upload/publications/pneus/pyrolyse.pdf (2001)

Mc Guigan, J., Moyer, R., Harris, F.: Managerial Economics: Applications, Strategy and Tactics, 12ème édition, USA, Cengage Learning, 403 (2010)

Panda, A. K.: Studies on process optimization for production of liquid fuels from waste plastics, Doctorat en génie chimique: Département de génie chimique Institut national de technologie (2011)

Panda, A. K., Singh, R. K.: Experimental Optimization of Process for the Thermo-catalytic Degradation of Waste Polypropylene to Liquid Fuel, Advances in Energy Engineering (AEE), 1 (2013)

Patni, N., Shah, P., Agarwal, S., Singhal, P.: Alternate Strategies for Conversion of Waste Plastic to Fuels, ISRN Renewable Energy, ID 902053. http://www.hindawi.com/journals/isrn/2013/902053/ [page consultée le 13.04.2015] (2013)

Wong, H.-W., Broadbelt, L.J.: Tertiary resource recovery from waste polymers via pyrolysis: neat and binary mixture reactions of polypropylene and polystyrene. Ind. Eng. Chem. Res. **40**, 22 (2001)

Experimental Analysis of Hydrogen-Fueled Homogeneous Charge Compression Ignition (HCCI) Engine

M. Mohamed Ibrahim and A. Ramesh

Nomenclature

HCCI	Homogeneous charge compression ignition
HHCCI	Hydrogen homogeneous charge compression ignition
HDHCCI	Hydrogen diesel homogeneous charge compression ignition
HER	Hydrogen energy ratio
BMEP	Brake mean effective pressure
CI	Compression ignition
SI	Spark ignition
EGR	Exhaust gas recirculation
CO_2	Carbon dioxide
CO	Carbon monoxide
HC	Hydrocarbon
NO_X	Oxides of nitrogen
NO	Nitric oxide
PM	Particulate matter
TDC	Top dead center
IMEP	Indicated mean effective pressure
°C	Degree Celsius
°CA	Degree crank angle
RTD	Resistance temperature detector
CRI	Common rail injection
ICT	Intake charge temperature
rpm	Revolution per minute

(continued)

M.M. Ibrahim (✉) • A. Ramesh
Department of Mechanical Engineering, Indian Institute of Technology Madras, Tamilnadu, Chennai 600 036, India
e-mail: ibrahimengine@gmail.com

© Springer International Publishing AG, part of Springer Nature 2018

F. Aloui, I. Dincer (eds.), *Exergy for A Better Environment and Improved Sustainability 2*, Green Energy and Technology,
https://doi.org/10.1007/978-3-319-62575-1_34

ppm	Parts per million
J/°CA	Joule per degree crank angle
°BTDC	Degree crank angle before top dead center
ϕ	Equivalence ratio
BTE	Brake thermal efficiency
ITE	Indicated thermal efficiency
IT	Injection timing of diesel
COV	Coefficient of variation
LTR	Low-temperature reaction
HTR	High-temperature reaction
SOC	Start of combustion
SOI	Start of injection
FSN	Filter smoke number

1 Introduction

Research in internal combustion engines is currently focused on decreasing the level of emissions without sacrificing fuel economy. A relatively new alternative combustion strategy known as homogeneous charge compression ignition (HCCI) can lead to ultralow oxides of nitrogen (NO_X) and particulate matter (PM) emissions. It also has the potential to operate at high thermal efficiency. In this combustion mode, a lean and nearly homogeneous mixture of air and fuel is ignited by compression. Combustion of this mixture occurs at multiple ignition locations in the combustion chamber almost simultaneously (Yao et al. 2009; Zhao 2007; Jittu et al. 2007). HCCI combustion was studied initially by Onishi et al. (1979) in a two-stroke engine. One of the earliest experiments on a four-stroke HCCI engine fueled with a mixture of isooctane and n-heptane in the HCCI combustion by Najt and Foster (1983) reported that in these engines, combustion is controlled by chemical kinetics. Thring (1989) studied the four-stroke diesel HCCI mode with control by changing the intake temperature and exhaust gas recirculation (EGR) over a range of equivalence ratios and was the first to name this kind of combustion mode as homogeneous charge compression ignition. The HCCI combustion can be experimented in both modified spark ignition (SI) and compression ignition (CI) engines with different types of fuels like gasoline, diesel, alcohols, natural gas, liquefied petroleum gas (LPG), biogas, and hydrogen (Yao et al. 2009; Zhao 2007). However, most of the research work focuses mainly on diesel and natural gas.

Investigations on diesel-fueled HCCI operation with intake manifold injection indicated the requirement of high intake temperature for effective mixture formation (Ryan and Callahan 1996). The problems faced were very high HC emissions, advanced combustion phasing, and low thermal efficiency. However, the levels of NO_X and PM emissions were significantly reduced. In-cylinder injection of diesel

was also found to be advantageous as compared to manifold injection of diesel as it could eliminate intake heating and minimize the level of lubricating oil dilution (Nathan et al. 2007; Walter and Gatellier 2002; Ibrahim and Ramesh 2013). In order to overcome the problems such as poor vaporization of diesel, lubricating oil dilution, and high HC emissions, multi-pulse injection method (up to eight injections per cycle) with a common rail system at high injection pressure was employed. On modifying the injection strategy, HC emission was reduced when the injection timing was moved toward top dead center (TDC) to minimize wall impingement of diesel. A reduction of CO emissions was obtained by increasing the boost pressure or by late-injection strategy. EGR (about 61%) could extend the operating range of IMEPs to 9 bar (Zheng and Kumar 2009). Gaseous fuels are suitable for HCCI operation as this readily form a homogeneous mixture. Neat natural gas-fueled HCCI operation needs relatively too high intake temperatures as methane has a high self-ignition temperature (Kobayashi et al. 2011; Yap et al. 2004). Most researchers have experimented with the natural gas in the HCCI mode with inlet heating, use of fuel additives like dimethyl ether (DME) or hydrogen, and addition of pilot diesel to aid the ignition (Kobayashi et al. 2011; Yap et al. 2004; Srinivasan et al. 2007; Din et al. 2010; Zhao 2007). Hydrogen has also been used to improve natural gas HCCI operation with residual gas trapping, and it was shown that it reduces the intake temperatures required for autoignition (Yap et al. 2004).

Biogas has also been used in the HCCI mode. It requires relatively too high intake charge temperature of about 200 °C to sustain the HCCI combustion because of its high autoignition temperature (Bedoya et al. 2012). A significant reduction in the intake temperature needed for sustaining combustion was observed when diesel was injected into the manifold of a biogas-fueled HCCI engine. The intake charge also had to be heated, and a temperature of 135 °C was found to be optimal. The presence of CO_2 in biogas was found to lower the high heat release rates that are normally encountered in diesel HCCI operation (Nathan et al. 2010).

Limited work has been reported on the use of hydrogen in the HCCI mode. Neat hydrogen HCCI combustion needs relatively high intake temperatures in the range of 80–100 °C. Though the load range is limited, the thermal efficiency is high. Emissions are very low as compared to the diesel-fueled CI mode (Caton and Pruitt 2009; Gomes et al. 2008). The maximum IMEP that can be reached is about 3.5 bar which is restricted by knocking mode (Stenlaas et al. 2004). Addition of CO_2 extended the load range of operation in the hydrogen HCCI mode to an IMEP to 4.5 bar (Ibrahim and Ramesh 2014). Studies have been conducted with diesel being injected into the manifold along with hydrogen in order to extend the load range. However, the intake had to be heated to about 75 °C to vaporize the diesel (Guo et al. 2011). In-cylinder injection of diesel along with manifold induction of hydrogen eliminated the need to heat the intake charge. Hydrogen retards the combustion of diesel and results in improvements in performance and emissions in the HCCI mode (Ibrahim and Ramesh 2013).

In this work a single-cylinder diesel engine was modified to run in the HCCI mode with hydrogen as the fuel. Influences of intake charge temperature and equivalence ratio were studied. Further, the same engine was equipped with a

common rail diesel injection system, and experiments were done with manifold injection of hydrogen and in-cylinder injection of diesel. The injection timing of diesel, exhaust gas recirculation ratio, and hydrogen-to-diesel-energy ratio were optimized. The results of combustion and emissions in the above two modes of operation are presented. Further, the different modes have been compared at the best operating conditions with the neat diesel CI mode to bring out the relative performance and emission benefits of using hydrogen in the HCCI mode.

2 Engine Setup and Experiments

The engine whose specifications are given in Table 1 was coupled to an eddy current dynamometer with closed loop control. The schematic diagram of engine setup and the accessories used to operate the engine in the hydrogen-fueled HCCI mode are depicted in Fig. 1. An air preheater with a controller was installed in the intake manifold to set the required intake charge temperature. Hydrogen was inducted into the engine through the intake manifold after this heater. A thermal mass flow meter was used to measure the mass flow rate of hydrogen. The air flow rate was measured using a positive displacement volumetric flow meter.

A high-pressure common rail diesel system with completely flexible fuel injection controls was adopted on the single-cylinder diesel engine for the hydrogen diesel HCCI mode. The flow rate of diesel fuel was measured directly on the mass basis. The intake charge temperature was measured using the K-type thermocouple. The exhaust system was also provided with an arrangement to extract exhaust gases for recirculation, i.e., EGR. The level of NO emission was measured using chemiluminescence analyzer. AVL DiGas analyzer was used for the measurement of CO and HC emissions. Smoke emission was measured using an AVL smoke meter.

A piezo electric cylinder pressure transducer was flush mounted on the cylinder head for the measurement of cylinder pressure on the basis of crank position. An optical encoder (Make: Kistler, Switzerland) was mounted on the crank shaft to provide crank angle information to the data acquisition system. The pressure signals

Table 1 Specifications of the engine

Engine type	Single-cylinder, four-stroke, naturally aspirated, water-cooled, direct injection, diesel engine
Bore	80 mm
Stroke	110 mm
Connecting rod length	231 mm
Compression ratio	16:01
Rated power	3.7 kW @1500 rpm
Injection system	Modified- to high-pressure common rail system

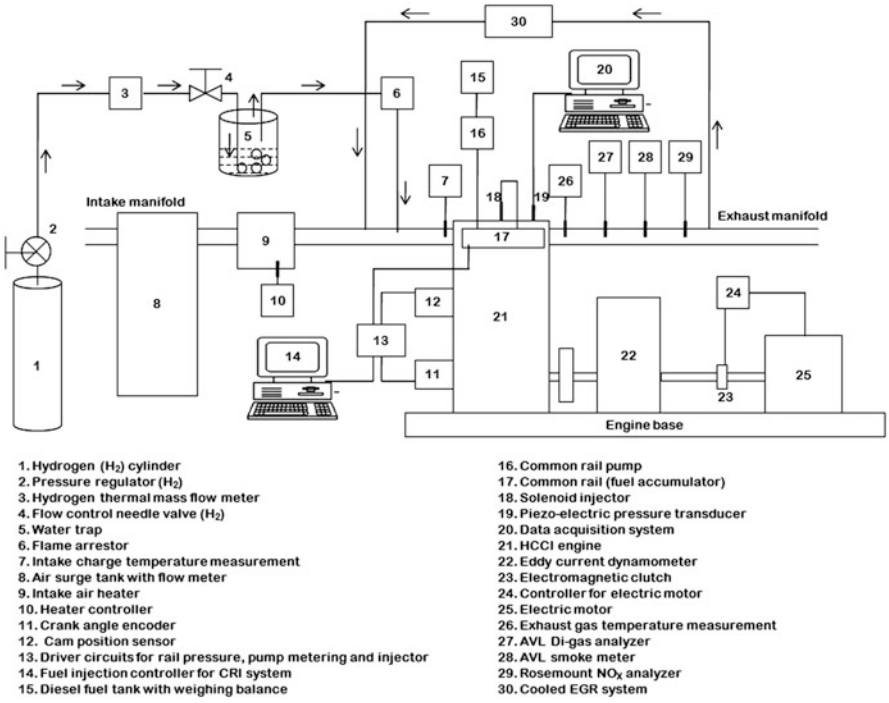

Fig. 1 The schematic diagram of engine setup and the accessories used to operate the engine in the hydrogen-fueled HCCI mode

were then recorded by an in-house developed high-speed data acquisition system (National Instruments, 6070E data acquisition card). The heat release rate was determined using an average of cylinder pressure data for 100 consecutive cycles. In this case, the cyclic dispersion was adequately low. This was checked. The coefficient of variation (COV) of IMEP was 3–4%, and hence, this method was used. The coolant temperature was measured using a resistance temperature detector (RTD). To check the leakage of hydrogen, a leak detector was used.

In order to perform experiments in the HHCCI mode, the engine was motored initially without introduction of hydrogen. Intake charge temperature was raised up to a level where combustion could be sustained with little amounts of hydrogen being admitted. This temperature was around 130 °C. Thereafter the intake charge temperature was set at the required value, while the quantity of hydrogen was varied at the same instant to achieve stable HCCI combustion. Subsequently the intake charge temperature was maintained at different values, and the hydrogen flow rate was also varied to perform experiments at different equivalence ratios. The range of equivalence ratios was limited by knock on the higher hydrogen flow rates and misfire on the lower hydrogen flow rates. These experiments were repeated at various constant intake charge temperatures ranging from 80 to 130 °C. In all cases, the coolant outlet temperature was maintained at 50 °C by adjusting its

flow rate. During the HDHCCI mode of operation, the engine was initially motored and started in the CI mode. Once the coolant temperature reached a fixed value of 50 °C, a mode switch over from CI to HCCI was feasible by advancing the injection timing of diesel using the common rail injection (CRI) system. The intake charge temperature was maintained at 30 °C for all operating range of BMEPs. Using the electronic controller of the CRI system, the injection timing of diesel was always set at the best value for thermal efficiency. Additionally the influence of different levels of EGR was studied. The intake charge temperature was maintained by the heater described earlier. All these experiments were conducted at a constant speed of 1500 rpm.

3 Results and Discussion

Experiments were performed on the single cylinder stationary diesel engine in three different modes of operation, namely, hydrogen-fueled HCCI (HHCCI), hydrogen diesel HCCI (HDHCCI), and neat diesel compression ignition (CI). Results of combustion, emissions, and performance in these different modes and also a comparison to quantify the potential benefits of switching between the modes are presented.

3.1 Combustion Characteristics of the Hydrogen-Fueled HCCI (HHCCI) Engine

It is seen from Fig. 2 that the start of combustion was significantly retarded when the intake charge temperature (ICT) was decreased from 90 to 80 °C at a constant hydrogen flow rate of 0.18 kg/h. The highest brake thermal efficiency was obtained at the lowest possible ICT of 80 °C with hydrogen. Therefore, retarded combustion phasing led to better thermal efficiency, and further reduction in the ICT resulted in misfire. Thermal efficiency values in the HHCCI mode were higher than in the conventional CI mode of operation because of shorter combustion duration. In HHCCI mode, ignition starts due to the temperature reached during compression. Ignition is the point where the heat release rate curve becomes positive. The range of intake charge temperatures (80–130 °C) was adequate to sustain hydrogen-fueled HCCI combustion at a compression ratio of 16:1.

A drastic reduction of NO emission as indicated in Fig. 2 was observed as compared to the CI mode. The concentration of smoke, HC, and CO emissions as expected were negligible.

Increase in the equivalence ratio (ϕ) also raised the combustion rate and also advanced it as shown in Fig. 3. Though the combustion gets advanced to crank angles much before TDC, we see that the brake thermal efficiency has also

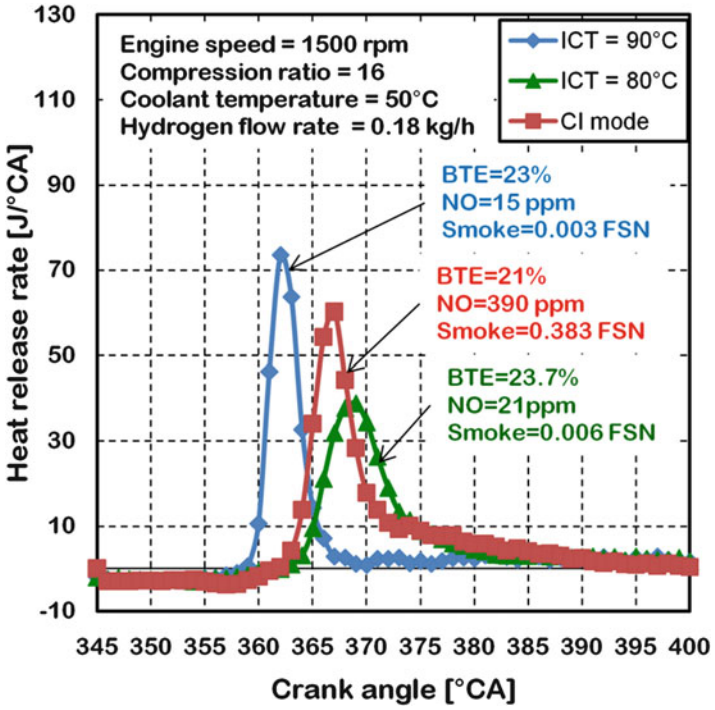

Fig. 2 Effect of intake charge temperature on HHCCI operation and its comparison with CI mode

increased. This is because higher equivalence ratios lead to higher torque (BMEP output) and thus the mechanical efficiency increases.

However, we see that the indicated thermal efficiency (ITE) actually decreases with increase in equivalence ratio because of advanced combustion. With increase in equivalence ratio, the level of NO emission increases slightly only. On the whole, extremely low NO emission was seen, and high intake charge temperatures were needed to sustain neat hydrogen-fueled HCCI combustion.

3.2 Effect of Hydrogen Energy Ratio in the HDHCCI Mode

In order to eliminate intake charge heating, in-cylinder injection of diesel was employed long with hydrogen. Initially these experiments were conducted at a BMEP of 2 bar where the engine could be operated in the HDHCCI mode and also in the diesel-fueled HCCI (DHCCI) modes and also with EGR. The variables whose effect was studied are hydrogen energy ratio, injection timing, and EGR level. The effect of varying the hydrogen energy ratio (HER) which is defined as the energy derived from hydrogen to the total energy derived from diesel and hydrogen while maintaining the injection timing (at 93°BTDC) without EGR was initially studied.

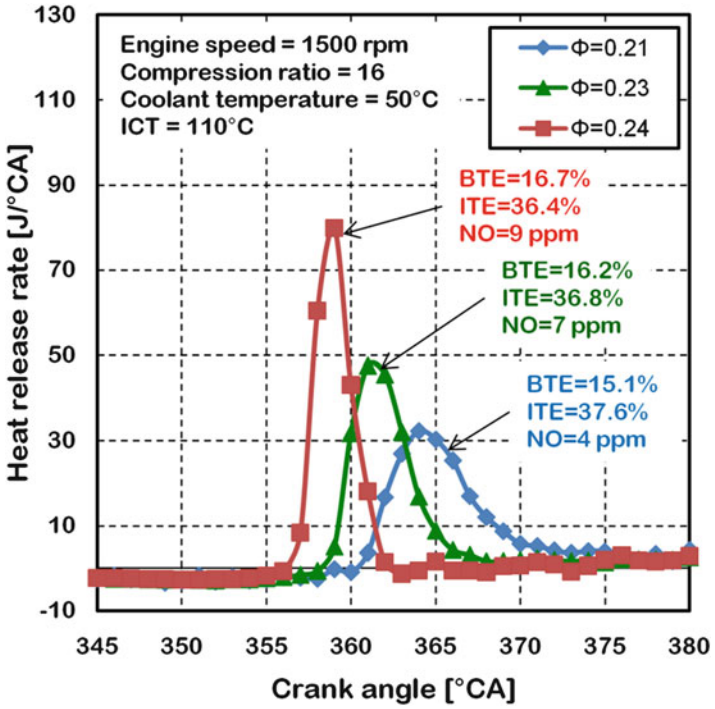

Fig. 3 Effect of equivalence ration on HHCCI mode at a constant intake charge temperature of 110 °C

Figure 4 shows that the addition of hydrogen increased the thermal efficiency. This is because in the diesel-fueled HCCI operation (HER = 0), combustion occurs too early due to the low self-ignition temperature of diesel. Hydrogen delays the combustion to crank angles where energy conversion to work is effective. The combustion process gets retarded with hydrogen because of dilution and chemical effects as reported in literature (Guo et al. 2011). However, after a particular amount of hydrogen (33.8% energy ratio), the engine began to misfire because of too retarded combustion on account of the small amount of diesel that was used.

The level of NO emissions depicted in Fig. 4 decreases with introduction of hydrogen due to lowered combustion rates and retarded combustion which lead to lower temperatures.

In the HDHCCI mode, smoke emission is mainly due to the injected diesel. Hence, increase in the fraction of hydrogen lowers smoke concentrations as seen. HC and CO are also only contributed by the injected diesel, and hence, similar trends are seen for these pollutants as well (Fig. 4). In the case of 0% energy ratio, the combustion is too advanced, and this is the reason for the low thermal efficiency. Even with the highest hydrogen flow rate, most of the combustion gets completed before TDC. Though still retarded, combustion could have yielded better thermal efficiencies, and it was not possible due to misfire.

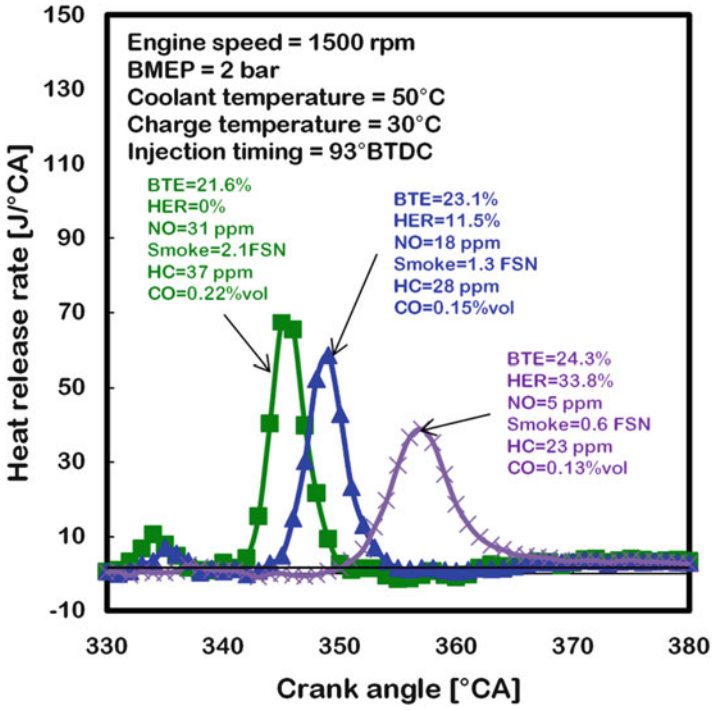

Fig. 4 Influence of adding hydrogen on diesel HCCI mode at a constant BMEP of 2 bar

3.3 Effect of Injection Timing of Diesel with HDHCCI Mode of Operation

Experiments were done with fixed hydrogen and diesel flow rates (fixed energy ratio of hydrogen) and no EGR. The highest thermal efficiency was obtained at an injection timing of 80°BTDC. The heat release rate versus crank angle curves depicted in Fig. 5 show that as the injection timing was advanced, the combustion was retarded. This is because earlier injection timings of diesel give it increased residence time to form a more homogeneous mixture which leads to retarded combustion. Such an occurrence has been indicated by other researchers also in diesel-fueled HCCI engines. The best injection timing is a compromise between combustion rate and combustion phasing (combustion occurring close to TDC). Operation in the HDHCCI mode was restricted by severe knocking below an injection advance of 60°BTDC, and the engine started to misfire above an injection timing of 120°BTDC at this condition. Advancing the injection timing significantly lowers the NO levels (Fig. 5) due to reduced temperatures as a result of retarded and slower combustion. Smoke emissions are due to the injected diesel. It may be noted that in these results, the amounts of diesel and hydrogen are fixed. Smoke formed in the combustion chamber can be oxidized if there is sufficient oxygen and

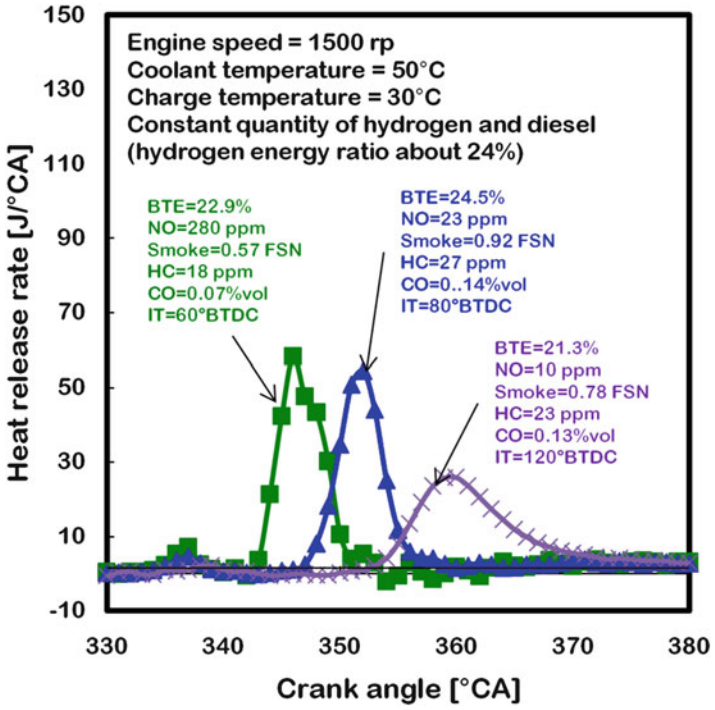

Fig. 5 Effect of injection timing of diesel on HDHCCI mode of operation

the temperature is also high. In all these cases, the overall equivalence ratios are very low.

The impingement of diesel on the bowl of the combustion chamber is high when the injection timing is retarded (piston is near top dead center). It is to be noted that the injector in this case is with a single hole along the axis of the cylinder. Advanced injection timings led to more homogeneous mixtures and thus could result in lower smoke levels. A combination of these factors influences the variation of smoke indicated in Fig. 5. Smoke peaked at a particular injection timing. The concentration of HC and CO emissions increased as the injection timing of diesel was advanced, and this is because of lower in-cylinder gas temperatures which affect oxidation of these components.

3.4 Effect of EGR Ratio in the HDHCCI Mode

The following results are at a constant hydrogen energy ratio and injection timing and indicate the influence of EGR level. Adding EGR increases the thermal efficiency as seen in Fig. 6 due to proper combustion. Introduction of EGR lowers the level of NO emissions because of lower combustion rates as seen in Fig. 6. The

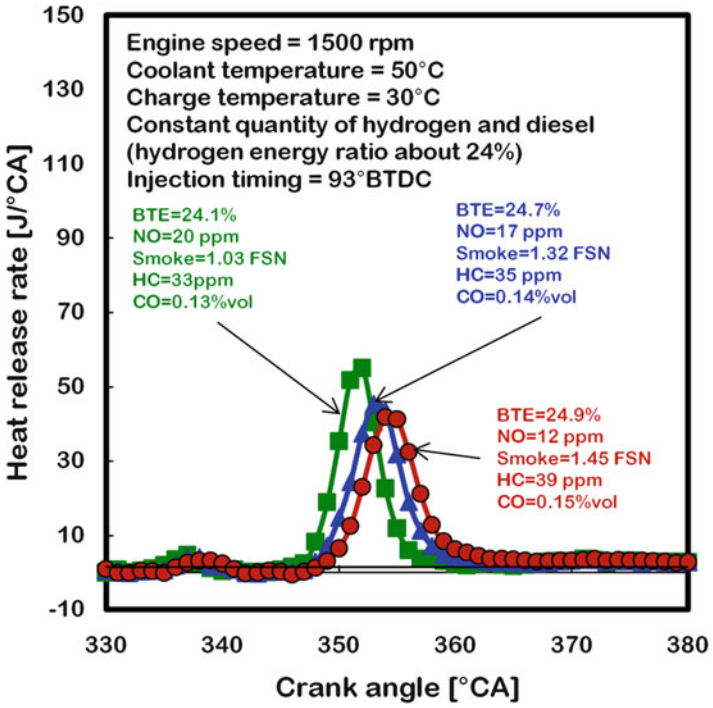

Fig. 6 Effect of EGR on HDHCCI mode

concentration of smoke, HC, and CO emissions are increased with EGR as depicted due to lower oxygen availability. On the whole, it is seen that EGR, injection timing, and hydrogen energy ratio affect performance and emissions significantly. Further studies were done at fixed BMEPs under variable hydrogen energy ratio, while the injection timing of diesel was always adjusted for best thermal efficiency.

3.5 Comparison of HHCCI, HDHCCI, and CI Modes of Operation

In this section the different modes of operation are compared at the respective best operating conditions at every BMEP. It may be noted that in the HHCCI mode, only BMEPs in the range 0.5 to 2.2 bar were possible and that too with intake charge heating, whereas in the HDHCCI mode, best results were obtained only without intake charge heating. In some cases in the HDHCCI mode, EGR was needed to properly phase the combustion process. Hence, the results in the HDHCCI mode are with the optimum levels of EGR and injection timings. BMEPs in the range 2 to 4 bar were only possible in the HDHCCI mode of operation.

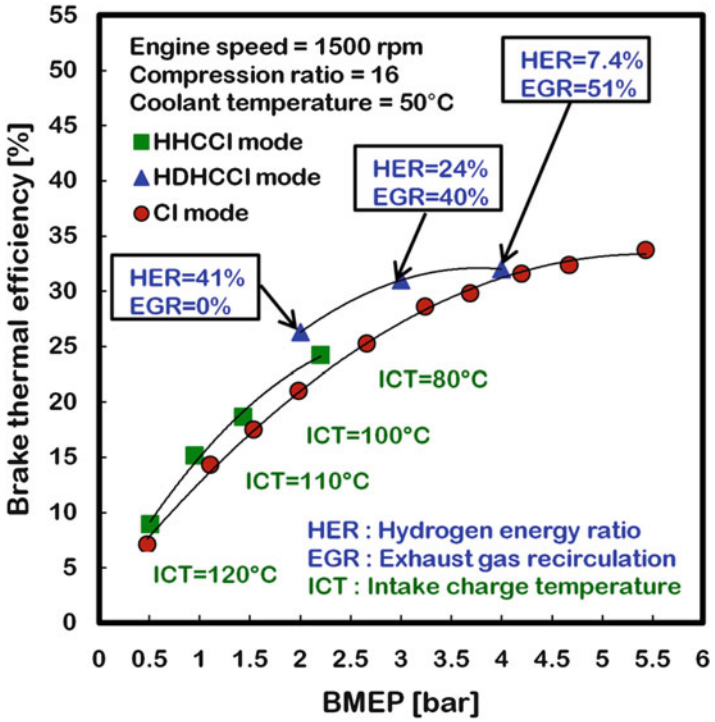

Fig. 7 Comparison of brake thermal efficiency with BMEP among HHCCI, HDHCCI, and CI modes

HHCCI mode was only possible in the low BMEP range (0.5–2.2 bar) as seen in Fig. 7. However, at these conditions, the brake thermal efficiency was better than the CI mode due to better combustion phasing and faster combustion. However, high intake charge temperatures (ICT) were needed. At a BMEP of 2.2 bar, i.e., as the equivalence ratio went up, HHCCI operation is not possible due to too rapid combustion that results in knock. Thereafter, only HDHCCI was possible. In this mode, no heating of the intake charge was needed. As the BMEP went up, it was required to lower the hydrogen energy ratio. In fact at the highest possible BMEP of 4 bar, the HER was only 7.4%, and the operation resembled the neat diesel HCCI mode. High EGR levels were needed to control the combustion rate, and this led to the use of low amounts of hydrogen in order to avoid misfire. In the entire range, the operation in both the HCCI modes was higher in terms of thermal efficiency than the CI mode. Thus, the use of hydrogen in the HCCI mode along with diesel or in the single fuel mode is advantageous. However, the range of operation is still restricted.

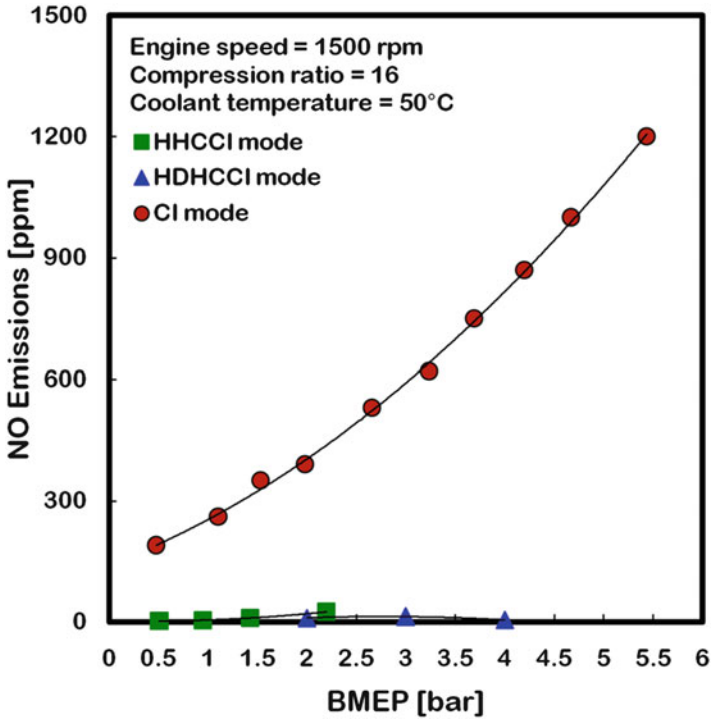

Fig. 8 Comparison of NO emissions with BMEP among HHCCI, HDHCCI, and CI modes

An additional consideration is the impingement of diesel on the cylinder walls when the hydrogen energy ratio is low which leads to dilution of the lubricating oil, HC, CO, and smoke emissions. This will mean that operation in the HDHCCI mode has to be limited to high HERs, i.e., low BMEPs. The NO emissions in the HHCCI and HDHCCI modes (Fig. 8) were extremely lower than in the CI mode as expected to low combustion temperatures.

Smoke emission in the HDHCCI mode was higher than in the CI mode as seen in Fig. 9. This is because of fuel impingement on the bowl of the combustion chamber.

We see that from Figs. 10 and 11, the HC and CO emissions are also influenced by this effect in the case of the HDHCCI mode. Of particular importance is the rise in CO, HC, and smoke with BMEP in the HDHCCI mode. This is due to the increase in the amount of diesel that was injected because the hydrogen energy ratio had to be reduced with increase in BMEP.

The start of injection and start of combustion (low-temperature combustion and main combustion) have been indicated in Table 2 for the HDHCCI mode.

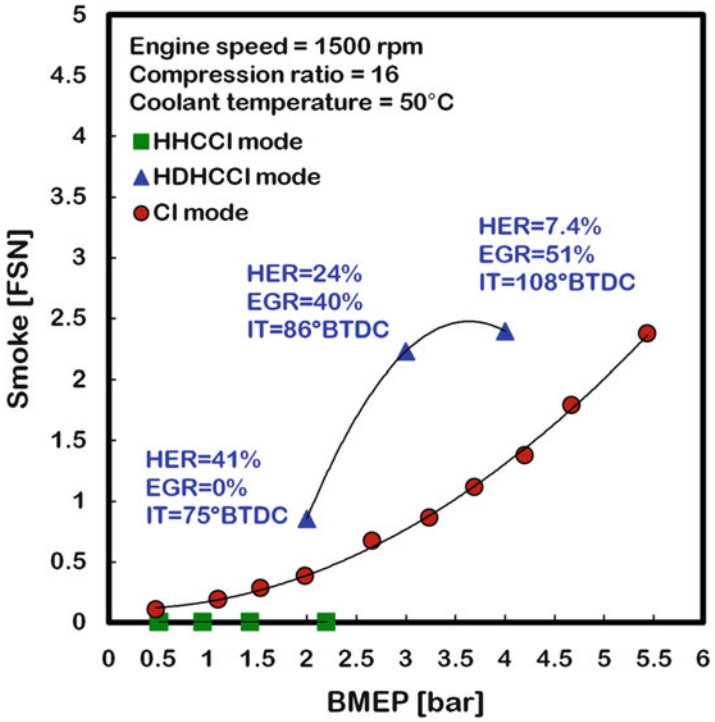

Fig. 9 Comparison of smoke emissions with BMEP among HHCCI, HDHCCI, and CI modes

4 Conclusions

Based on the experiments conducted in the neat hydrogen HCCI (HHCCI) mode and the hydrogen diesel HCCI (HDHCCI) mode, the following conclusions are drawn:

- The load range in the HHCCI mode is restricted by knocking at about 2 bar, and intake charge heating is essential. However, the thermal efficiency is higher, and the NO emission is significantly lower than normal diesel operation.
- Hydrogen can be used to phase the combustion in diesel-fueled HCCI engines. However, even in the HDHCCI mode, only BMEPs of about 4 bar can be reached when EGR is also employed. HDHCCI operation is also better than conventional diesel operation in terms of efficiency and NO emissions. No heating of the intake charge is needed, and the upper limit of operation is restricted by knock.

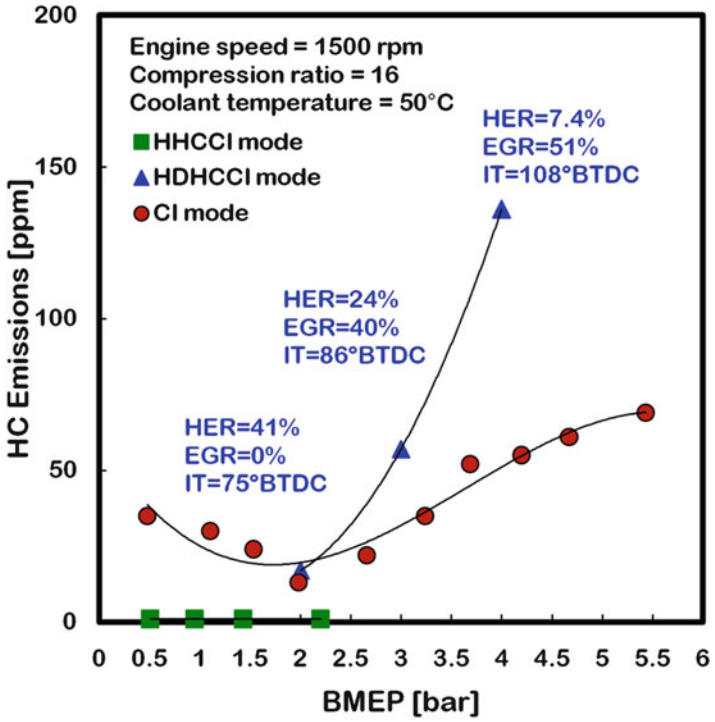

Fig. 10 Comparison of HC emissions with BMEP among HHCCI, HDHCCI, and CI modes

- HDHCCI results in higher levels of smoke and HC emissions particularly at the higher end of BMEPs as EGR levels are high and hydrogen amount is low at these conditions. The high amount of diesel and advanced injection timing result in impingement of the diesel on the bowl of the combustion chamber in this mode.

On the whole, by shifting from the HHCCI mode at low BMEPs to the HDHCCI mode at medium BMEPs and to the CI mode at high BMEPs, operation with high thermal efficiency and low NO emission is possible. However, control of intake charge temperature in the HHCCI mode and elevated smoke and HC levels in the HDHCCI mode are issues to be further tackled.

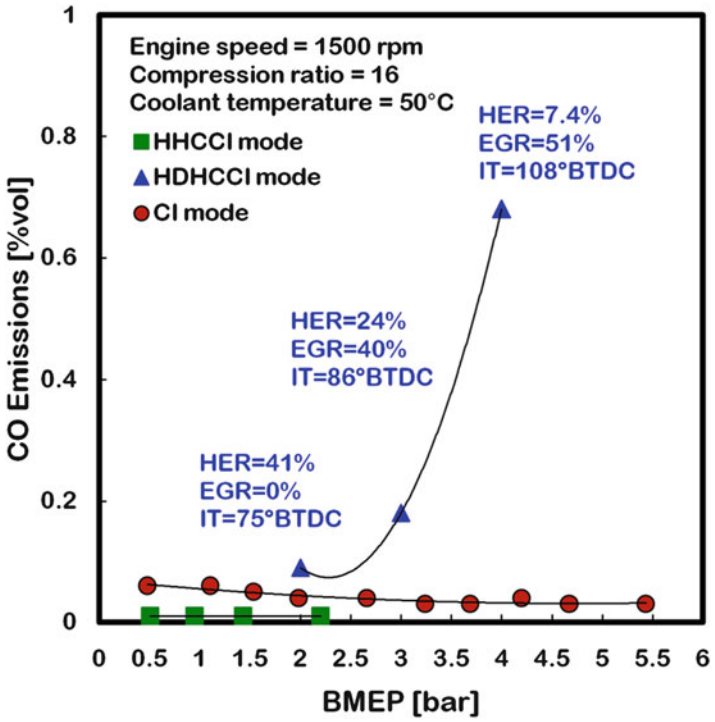

Fig. 11 Comparison of CO emissions with BMEP among HHCCI, HDHCCI, and CI modes

Table 2 The SOI and SOC (LTR and HTR) for the HDHCCI mode at best operating condition

BMEP [bar]	2	3	4
Start of injection of diesel [°BTDC]	75	86	108
Start of combustion (LTR) [°CA]	334	333	340
Start of combustion (HTR) [°CA]	348	348	350

References

Bedoya, I.D., Saxena, S., Cadavid, F.J., Dibble, R.W., Wissink, M.: Experimental evaluation of strategies to increase the operating range of a biogas-fueled HCCI engine for power generation. Appl. Energy. **97**, 618–629 (2012)

Caton, P.A.., Pruitt, J.T.: Homogeneous charge compression ignition of hydrogen in a single-cylinder diesel engine. Int. J. Engine Res. **10**, 45–63 (2009)

Din H.A.E., Elkelawy M., Sheng Z.Y.: HCCI engines combustion of CNG fuel with DME and H2 additives. SAE paper no. 2010-01-1473 (2010)

Gomes, A.J.M., Milkalsen, R., Roskilly, A.P.: An investigation of hydrogen-fuelled HCCI engine performance and operation. Int. J. Hydrog. Energy. **33**, 5823–5828 (2008)

Guo, H., Hosseini, V., Neill, W.S., Chippior, W.L., Dumitrescu, C.E.: An experimental study on the effect of hydrogen enrichment on diesel fueled HCCI combustion. Int. J. Hydrog. Energy. **36**, 13820–13830 (2011)

Ibrahim, M.M., Ramesh, A.: Experimental investigations on a hydrogen diesel homogeneous charge compression ignition engine with exhaust gas recirculation. Int. J. Hydrog. Energy. **38**, 10116–10125 (2013)

Ibrahim, M.M., Ramesh, A.: Investigations on the effects of intake temperature and charge dilution in a hydrogen fueled HCCI engine. Int. J. Hydrog. Energy. **39**, 14097–14108 (2014)

Jittu S., Thipse S.S., Marathe N.V., Babu M.K.G.: Homogeneous charge compression ignition (HCCI): a new concept for zero and particulate matter (PM) from diesel engine combustion. SAE paper no. 2007-26-020 (2007)

Kobayashi, K., Sako, T., Sakaguchi, Y., Morimoto, S., Kanematsu, S., Suzuki, K., Nakazono, T., Ohtsubo, H.: Development of HCCI natural gas engines. J. Nat. Gas Sci. Eng. **3**, 651–656 (2011)

Najt P.M., Foster D.E.: Compression ignited homogeneous charge combustion. SAE paper no. 830264 (1983)

Nathan, S.S., Mallikrajuna, J.M., Ramesh, A.: The effect of mixture preparation in a diesel HCCI engine using early in-cylinder injection during the suction stroke. Int. J. Automot. Technol. **8**, 543–553 (2007)

Nathan, S.S., Mallikarjuna, J.M., Ramesh, A.: An experimental study of the biogas–diesel HCCI mode of engine operation. Energy Convers. Manag. **51**, 1347–1353 (2010)

Onishi S., Jo S.H., Shoda K., Jo P.D., Kato S.: Active Thermo – Atmosphere Combustion (ATAC) – a new combustion process for internal combustion engines. SAE paper no. 790840 (1979)

Ryan T.W., Callahan T.J.: Homogeneous charge compression ignition of diesel fuel. SAE paper no. 961160 (1996)

Stenlaas O., Christensen M., Egnell R., Johanson B.: Hydrogen as homogeneous charge compression ignition engine fuel, SAE paper no. 2004-01-1976 (2004)

Srinivasan, K.K., Krishnan, S.R., Qi, Y., Midkiff, K.C., Yang, H.: Analysis of diesel pilot-ignited natural gas low-temperature combustion with hot exhaust gas recirculation. Combust. Sci. Technol. **179**, 1737–1776 (2007)

Thring, R.H.: Homogeneous Charge Compression Ignition (HCCI) engines. SAE paper no. 892068 (1989)

Walter B., Gatellier B.: Development of the high power NADI concept using dual mode diesel combustion to achieve zero NOX and particulate emissions. SAE paper no. 2002-01-1744 (2002)

Yap D., Megaritis A., Peucheret S., Wyszynski M.L., Xu H.: Effects of hydrogen addition on natural gas HCCI combustion. SAE paper no. 2004-01-1972 (2004)

Yao, M., Zheng, Z., Liu, H.: Progress and recent trends in homogeneous charge compression ignition (HCCI) engines. Prog. Energy Combust. Sci. **35**, 398–437 (2009)

Zhao, H.: HCCI and CAI engines for the automotive industry. Woodhead Publishing Limited/CRC Press, Cambridge (2007)

Zheng, M., Kumar, R.: Implementation of multiple-pulse injection strategies to enhance the homogeneity for simultaneous low-NO_X and soot diesel combustion. Int. J. Therm. Sci. **48**, 1829–1841 (2009)

Part II
Sustainable Buildings

Investigations of Thermal Comfort of Building Integrated Phase Change Materials

Mustapha Faraji

1 Introduction

The overheating/subcooling is the major problem of the most modern constructions because of the use of lightweight materials with low thermal inertia. As a possible solution to this problem, we propose the use of phase change materials (PCM) that allow changing the thermal behavior of the building by improving the thermal inertia. The wallboards are cheap and widely used in a variety of applications, making them very suitable for PCM encapsulation. On the other hand, the principles of latent heat storage can be applied to any appropriate building materials. The latent heat of fusion increases the thermal mass of the building. Ahmed et al. (2006) presented a study of different types of walls containing PCM. The partitions consist of a locally marketed panel. Three types of panels are tested: (1) polycarbonates with granulated paraffin, (2) polycarbonate filled with polyethylene glycol (PEG 600 PCM), and (3) polyvinyl chlorite (PVC) filled with PEG 600. The experimental setup makes possible to measure the thermal response of these different types of walls. The experimental results obtained are compared with those of the numerical simulations based on the apparent capacity method. The results showed that type (3) is the best appropriate panel. Lightweight structures are frequently used in modern buildings; they are characterized by low thermal inertia. The possible solution is the incorporation of PCMs in the envelope of these structures. In this sense, Potvin and Gosselin (2009) studied the thermal performance of a cell made of lightweight materials with PCM. The walls of the cell are subjected to local climatic conditions. The obtained results are compared with those of a reference

M. Faraji (✉)
Hassan II University, Faculty of Sciences Ain Chock, Physics Department, LPMMAT Laboratory, Casablanca, Morocco
e-mail: farajimustapha@yahoo.fr

© Springer International Publishing AG, part of Springer Nature 2018

F. Aloui, I. Dincer (eds.), *Exergy for A Better Environment and Improved Sustainability 2*, Green Energy and Technology,
https://doi.org/10.1007/978-3-319-62575-1_35

one without PCM. The study revealed that the apparent capacity of the PCM cell was found to be higher than that of the reference cell. The solar energy transmitted inside the PCM cell via a glass window is stored in the walls. The thickness of the walls with PCM is reduced in comparison with that of the cell without PCM. Several measurements of the temperatures and the heat flow are taken for the different walls. Experimental results and numerical simulation are confronted, and they showed good agreement. Stetiu and Feustel (1998) used a thermal building simulation program based on the finite difference approach to numerically evaluate the latent heat storage performance of PCM wallboard in a building environment. The capability of PCMs to reduce peak loads is well documented. Kissock et al. (1998) measured peak temperature reductions of up to 10 °C in side-by-side testing of unconditioned experimental houses with and without paraffinic PCM wallboard. Kosny et al. (2006) reported that PCM-enhanced cellulose insulation can reduce wall-generated peak-hour cooling loads by about 40%.

2 Physical Model

Figure 1 shows the physical model proposed as a heating system. It is a composite wall with three layers. Their thicknesses are respectively e_1, e_m, and e_2. The internal layers e_1 and the external layers e_2 are made of concrete, and the layer e_m consists of a capsulated PCM, which is stratified in the direction of the width of the wall. The PCM is located in the position x_m. The wall is located in Casablanca, Morocco (33°36′N, 07°36′W). Temperature of the first external node is denoted $T_{2,\ out}$ and that of the first internal node is denoted $T_{1,\ in}$. The radiative heat flux density γQ_{ext} is absorbed by the outer surface of the wall. The radiative heat flux exchanged between the wall and the sky is $Q_{w,\ rad}$. The sky is considered as a black body. The absorptivity and the emissivity of the wall are respectively γ and ε. During the day, solar energy is stored in the concrete and the PCM as a sensible and latent heat.

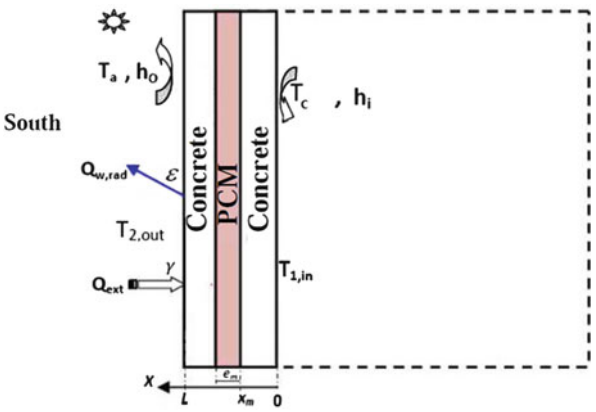

Fig. 1 Concrete/phase change material wall

The melted PCM accumulates a significant amount of heat during the period of charge. During the night, room temperature decreases to relatively low levels; the PCM solidifies and discharges from heat stored during the day. This heat is used for the night heating purposes.

Indoor air of local is heated by an active system regulated in the temperature of comfort: $T_c = 22$ °C. All the borders of the local are thermally isolated with the exception of the concrete/PCM left façade. This wall is facing south and is subject to boundary conditions generally encountered in buildings. The objective of this study is to reduce uptime of active heating system (air conditioner, radiator, convector, etc.).

To simplify the mathematical formulation of the problem, the following assumptions were made (ASHRAE n.d.):

- The interface resistances between the different layers of the wall are neglected.
- The PCM is considered homogeneous and isotropic.
- Heat transfer conduction in the composite wall is monodimensional; the end effects are neglected; and vertical surfaces of the wall are isotherms.
- Thermophysical properties of concrete and PCM are supposed constants; the PCM liquefied at T_m.
- The internal convective heat coefficient h_i is assumed to be 10 W/m^2 K, and the external convective heat coefficient h_o is assumed to be 21 W/m^2 K.
- The chosen encapsulated PCM are rectangular panels with respectively a thickness and a length of 0.5 cm and 1 m. These panels are vertically arranged between the lining up of bricks as it is used in buildings. Natural convection in melted PCM is neglected (encapsulated PCM).

The energy transport in PCM/wall may be written using the enthalpy formulation (Voller and Peng 1994) as follows:

$$\frac{\partial H}{\partial t} = \nabla(k \nabla T) \tag{1}$$

where

$$H(T) = h(T) + \rho \lambda f \Delta H_f \tag{2}$$

and

$$h(T) = h(T_m) + \int_{T_m}^{T} \rho c_p \mathrm{d}T \tag{3}$$

$\lambda = 1$ in the PCM and $\lambda = 0$ in the concrete.

Using sensible enthalpy h, Eq. (2) is rewritten as

$$\frac{\partial h}{\partial t} = \alpha \frac{\partial^2 h}{\partial x^2} \rho \lambda \Delta H_{\mathrm{f}} \frac{\partial f}{\partial t} \tag{4}$$

The liquid fraction f in the PCM layer is estimated as

$$f = \begin{cases} 1 & \text{if} \quad T > T_{\mathrm{m}} \\ 0 & \text{if} \quad T_{\mathrm{m}} < T \\ 0 < f < 1 & \text{if} \quad T = T_{\mathrm{m}} \end{cases} \tag{5}$$

The following relations provide the thermal properties at interfaces:

$$k_{\mathrm{i}} = \frac{k_+ k_- (\delta_- + \delta_+)}{k_+ \delta_- + k_- \delta_+}, k_{\mathrm{m}} = f k_1 + (1 - f) k_{\mathrm{s}} \tag{6}$$
$$\rho c_{\mathrm{p}} = f \left(\rho c_{\mathrm{p}}\right)_l + (1 - f) \left(\rho c_{\mathrm{p}}\right)_s$$

where δ_+ is the distance between the interface and the first node material '+', and δ_- is the distance between the interface and the first node on the inside of the material '−'. The boundary conditions are as follows:

- The continuity of flow and temperatures in interfaces PCM / concrete:

$$k_+ \left.\frac{\partial T}{\partial x}\right|_{x_+} = k_- \left.\frac{\partial T}{\partial x}\right|_{x_-} \quad , T_+ = T_- \tag{7}$$

- At $x = 0$,

$$-k \left.\frac{\partial T}{\partial x}\right|_{x=0} = h_{\mathrm{i}} (T_{\mathrm{c}} = T) \tag{8}$$

- At $x = L$,

$$-k \left.\frac{\partial T}{\partial x}\right|_{x=L} = h_{\mathrm{o}} (T_{\mathrm{a}} - T) + Q_{\mathrm{w,rad}} + \gamma Q_{\mathrm{ext}} \tag{9}$$

with

$$Q_{\mathrm{w,rad}} = \sigma \varepsilon F \left(T_{\mathrm{sky}}^4 - T^4\right) = h_{\mathrm{sky}}^{\mathrm{r}} (T_{\mathrm{a}} - T) \tag{10}$$

The sky is considered as a black body. The sky temperature T_{sky} is given by (Swinbank 1963)

$$T_{\mathrm{sky}} = 0.0552 \times (T_{\mathrm{a}} + 273.15)^{1.5} - 273.15 \tag{11}$$

The coefficient of radiative transfer $h_{\mathrm{sky}}^{\mathrm{r}}$ is given as follows:

$$h_{\text{sky}}^{\text{r}} = \frac{\sigma\varepsilon\left(T_{\text{sky}}^4 - T^4\right)}{T^{\text{a}} - T} \tag{12}$$

The heat flux at interfaces $x = x_{\text{m}}$ and $x = x_{\text{m}} + e_{\text{m}}$ between the PCM and the concrete is evaluated by

$$q_i'' \approx \frac{k_+ k_-}{k_+\delta_- + k_-\delta_+}(T_+ - T_-) \tag{13}$$

3 Results and Discussion

Thermal properties of the concrete wall and the RT 22 PCM (Rubitherm Technologies GmbH 2013) are summarized in Table 1. Figure 2 shows the timewise variations of the ambient temperature and total solar radiations received by wall faces during the typical days of the cold period of the year (winter – January, Casablanca – Morocco, 33°36′ N, 07°36′ W).

Figure 2 shows that minimum temperatures are obtained during the night. On average, minima and maxima temperatures range between 3 °C and 15 °C, respectively, and the ambient temperature swings between these extremes. Radiations remain zero during the night and increase in the following day. Solar radiations, Q, received by a wall are zero during the first 7 h every day and increase with sunrise, and the ambient temperature increases. Solar radiation reaches a maximum value (720 W/m^2) between solar noon and 15 h 00 and falls to 0 W/m^2 at 18 h 00 (sunset and cancellation of solar radiations). Radiations remain zero during the night. The climate of Casablanca is characterized by significant temperature fluctuations with lower nocturnal values of temperature.

Table 1 Thermal properties of the RT 22 PCM

Parameter	Value
Melting area	20–23 °C
Congealing area	23–20 °C
Combined heat storage capacity (latent and sensible heat in a temperature range of 14–29 °C)	200 kJ/kg
Specific heat capacity	2 kJ/kg K
Density	0.73 kg/l
Heat conductivity Concrete wall thermal conductivity	0.2 W/m K 1.04 W/m K

Rubitherm Technologies GmbH (2013)

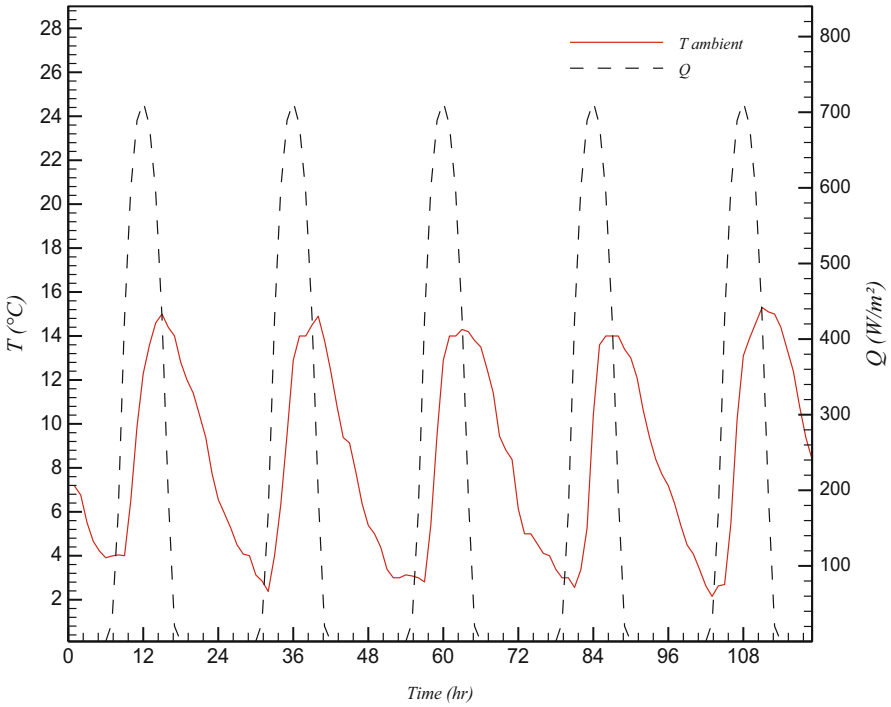

Fig. 2 Timewise variations of the ambient temperature, T_a, and the global solar radiations, Q, received by walls (January – Casablanca, Morocco 33°36′N, 07°36′W)

Figure 3 compares the thermal behavior of the ordinary and the PCM walls. Data analysis shows that even though both walls undergo the same climatic conditions, during night, the internal temperature (at a height of 1.5 m) decreases depending on the heat dissipation capacity of each constructive system. The thermal reduction is slower in the PCM wall case since it has stored more heat (latent) during the day. On average, inside temperature varies from 16 to 22 °C for PCM wall and from 14 to 26 °C for an ordinary wall without PCM. Remember that ambient temperature varies between 3 and 15 °C (Fig. 2), but the building walls receive also a radiative heat flux due to the solar radiations absorbed by the concrete (mortar solar absorption, $\alpha = 0.8$) combined with convective heat flux, and leads to the increase of the PCM temperature to its melting point. When the PCM undergoes phase change, the slope of T curve weakens because the melting and solidification of PCM occur at a nearly constant temperature; as a consequence, sensible heat dissipation weakens and the decrease of the PCM wall's nocturnal temperature is shifted. During the day, the rise of solar radiations accumulates sensible heat in concrete and stores latent heat in the PCM layer. The results showed, for the wall with PCM envelope, a significant reduction of indoor temperature due to absorption of solar gains in the composite walls in conjunction with melting of the PCM. In fact, composite PCM–

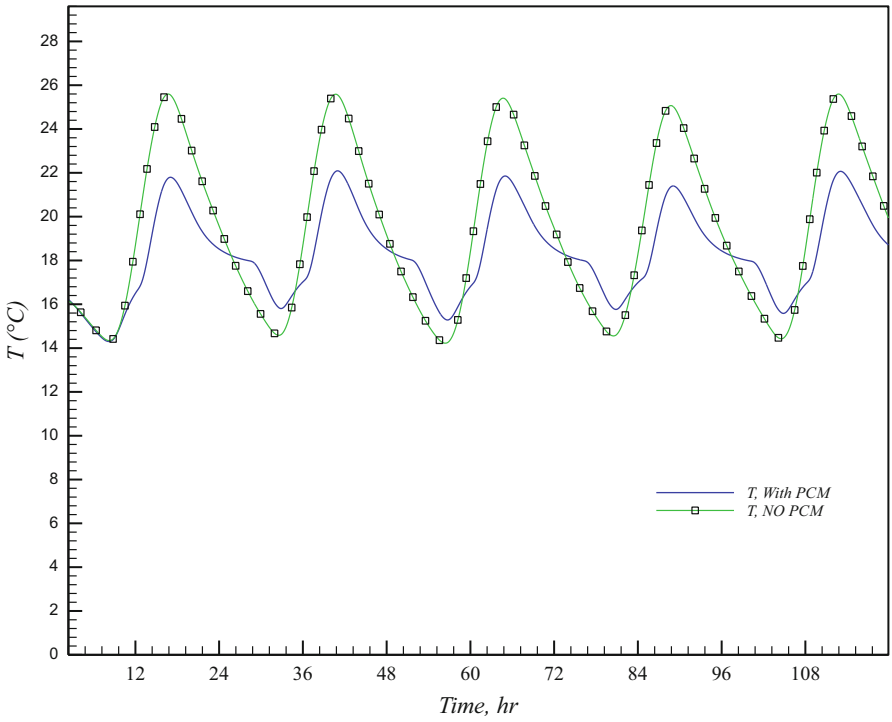

Fig. 3 Variations of the wall's inner temperature

concrete walls can be considered as important heat storage devices. During the day, an important amount of the solar heat is stored in the PCM wall structure with less temperature fluctuations until the full melting of PCM. The stored heat during a day is naturally released for heating needs in the following cold night.

Figure 4 represents the total heat flux, q, measured at walls for the two test cases. Negative values correspond to the indoor thermal gain and positive values quantify the thermal loss. For the case without PCM, heat flux penetrates and leaves the wall easily and, therefore, important temperature fluctuations take place. The heating of the wall is due to the rise of the sensible heat storage during the day. The ordinary wall loses heat from 21 00 h to 12 00 h, and inner air temperature falls after a certain delay due to the thermal inertia and to the relatively weak value of thermal conductivity of concrete. Note that the temperature minima in case of the wall with PCM, as shown by Fig. 3, is clearly greater than that achieved without PCM, because the nocturnal heat lost to the ambient by the walls is shifted by the release of the important diurnal latent heat stored in PCM. Day/night cycles allow for charging/discharging of the PCM panels. Figure 4 shows also that the wall with PCM is more insulated and that PCM is melted and solidified periodically. The fluctuation amplitude of the inner temperature (wall with PCM case) decreases because the accumulated heat during the melting processes added to the sensible

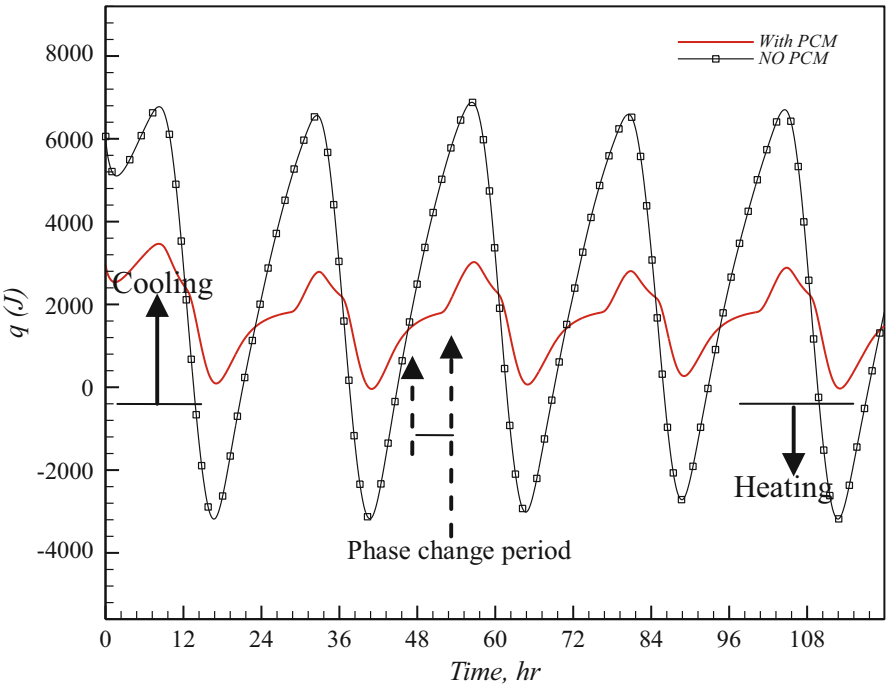

Fig. 4 Heat fluxes

heat stored in the wall/PCM structure brake the fast decrease of the temperature during the night. Notice that, for walls without PCM case, the heat flux increases to a high value at night, and that explains the lower temperatures achieved with more pronounced fluctuations.

The performance of the wall with PCM (RT 22) as a heating system for the building has been evaluated in terms of thermal load leveling, TLL, using the following equation:

$$\mathrm{TLL} = \frac{T_{\max} - T_{\min}}{T_{\max} + T_{\min}} \tag{14}$$

Thermal load leveling, TLL, puts a figure on the fluctuations of temperature inside the room. The less the fluctuations the better is the environment for the occupants. In winter, without heating arrangement for thermal comfort requirements, thermal load leveling should have *lower value* by incorporating heating method due to the increase of $((T_{\mathrm{i,in}})_{\max} + (T_{\mathrm{i,in}})_{\min})$ and the decrease of $((T_{\mathrm{i,in}})_{\max} - (T_{\mathrm{i,in}})_{\min})$.

The results for daily variation of thermal load leveling, TLL, for the walls with and without PCM are summarized in Table 2. It can be seen that the value of TLL is maximum for the wall without PCM, and it is reduced to about 28% for the wall with PCM. The lower values of thermal load leveling indicate that, due to the PCM

Table 2 Thermal load leveling

Day	TLL (with PCM)	TLL (no PCM)
1	0.20	0.28
2	0.16	0.27
3	0.17	0.28
4	0.15	0.26
5	0.17	0.27

layer, less fluctuations of indoor temperature are obtained and, thereby, there occurs an improvement of thermal comfort environment in the building.

4 Conclusion

Investigation of the thermal performance of composite concrete/PCM wall was performed. The results showed a significant reduction of indoor temperature fluctuations due to absorption and release of solar gains in the composite wall in conjunction with the melting of the PCM. The results showed that thermal load leveling of the wall containing PCM was reduced compared to the case without PCM with more constant conditions, It emerged that the wall with PCM/concrete wall is able to provide good performance. The thermal conditions of the indoor environment achieved with the presence of PCM panels were considerably improved compared to the wall without PCM.

Nomenclature

c_p	Specific heat (kJ/kg K)
f	Liquid fraction
e_m	PCM layer thickness (m)
h	Enthalpy (J)
h_i	Inner wall convective heat transfer coefficient (W/m^2 K)
h_o	Outside wall convective heat transfer coefficient (W/m^2 K)
h^r_{sky}	Irradiative heat transfer coefficient (W/m^2 K)
k	Thermal conductivity (W/m K)
L	Total wall thickness (m)
Q_{ext}	Solar radiation (W/m^2)
$Q_{w,rad}$	Heat lost to the ambient by radiations (J)
x	Cartesian coordinate (m)
t	Time (s)
T	Temperature (°C)
Indices	
i	Interface
m	Melting, PCM
c	Comfort
In	Inner wall face

(continued)

Out	Outer wall face
+,−	Right, left nodes
f	Fusion
Greeks	
ρ	Density (kg/m^3)
γ	Absorptivity
α	Thermal diffusivity (m/s^2)
σ	Stefan-Boltzmann constant
ε	Concrete emissivity
ΔH_f	Latent heat of PCM (kJ/kg)

References

Ahmad, M., Bontemps, A., Sallée, H., Quenard, D.: Experimental investigation and computer simulation of thermal behaviour of wallboards containing a phase change material. Energ. Buildings. **38**(4), 357–366 (2006)

ASHRAE: Handbook – fundamental(SI). http://www.techstreet.com/ashrae /products/ 1858361?ashrae_auth_token=

Kelly Kissock, J., Michael Hannig, J., Thomas I.: Testing and simulation of phase change wallboard for thermal storage in buildings. In: Morehouse, J.M., Hogan, R.E. (eds.) Proceedings of 1998 International Solar Energy Conference, Albuquerque, June 14–17. American Society of Mechanical Engineers, New York (1998)

Kosny, J., Yarbrough, D., Wilkes, K., Leuthold, D., Syad, A.: "PCM-Enhanced Cellulose Insulation –Thermal Mass in Lightweight Natural Fibers" 2006 ECOSTOCK Conference, IEA, DOE, Richard Stockton College of New Jersey, June 2006 (2006)

Potvin, F.M., Gosselin, L.: Thermal shielding of multilayer walls with phase change materials under different transient boundary conditions. Int. J. Therm. Sci. **48**, 1707–1717 (2009)

Rubitherm Technologies GmbH: Internet: www.rubitherm.com, Data sheet, Date: 23.07.2013

Stetiu, C., Feustel, H.E.: Phase change wallboard and mechanical night ventilation in commercial buildings. Lawrence Berkeley National Laboratory Berkeley(1998)

Swinbank, W.C.: Long-wave radiation from clearskies. Q. J. R. Meteorol. Soc. **381**(89), 339–348 (1963)

Voller, V.R., Peng, S.: An enthalpy formulation based on an arbitrarily mesh for solution of the stefan problem. Comput. Mech. **14**, 492–502 (1994)

Determining Optimum Insulation Thickness of a Building Wall Using an Environmental Impact Approach

Özel Gülcan, Açıkkalp Emin, Karakoc T. Hikmet, Hepbasli Arif, and Aydın Ahmet

1 Introduction

In the world, environmental problems have become widespread along with population growth, energy consumption, and industrialization (Dinçer 1999). At the present time, the most important indicator of environmental problems is global warming. Gases (carbon dioxide, methane, nitrous oxide, and fluorinated gases) that trap heat in the atmosphere are called greenhouse gases (United States EPA 2014) Carbon dioxide which is the output of the energy conversion process has the largest effect on global warming by a rate of 81% (Karakoc et al. 2011). The effects of global warming have reached sensible levels, and environmental impact analysis has gained greater importance in the energy policies of the countries.

In Turkey, buildings are responsible for 30% of the total green gas emissions (Karakoc et al. 2011). To decrease CO_2 emissions and fuel consumption, energy losses from the building must be minimized. Thermal insulation is an important, applicable, and rational solution to achieve this aim by altering the properties of

Ö. Gülcan (✉) • A. Emin
Bilecik S.E. University, Engineering Faculty, Department of Mechanical and Manufacturing Engineering, Bilecik, Turkey
e-mail: gulcan.ozel@bilecik.edu.tr

K.T. Hikmet
Anadolu University, Faculty of Aeronautics and Astronautics, Department of Airframe and Powerplant Maintenance, Eskisehir, Turkey

H. Arif
Yasar University, Faculty of Engineering, Department of Energy Systems Engineering, Izmir, Turkey

A. Ahmet
Sakarya University, Faculty of Engineering, Department of Mechanical Engineering, Sakarya, Turkey

© Springer International Publishing AG, part of Springer Nature 2018

F. Aloui, I. Dincer (eds.), *Exergy for A Better Environment and Improved Sustainability 2*, Green Energy and Technology,
https://doi.org/10.1007/978-3-319-62575-1_36

building envelopes. In addition to this, thermal insulation provides cost savings and thermal comfort (Ekici and Aksoy 2011).

Many studies have been performed on the optimum insulation thickness in the literature (Hasan 1999; Bolattürk 2006; Sisman et al. 2007; Yıldız et al. 2008; Yu et al. 2009; Kaynakli 2008). These studies determine optimum thickness using energy, exergy, economic, and emissions methods (Balli et al. 2008). Ucar and Balo (2010) and Ucar et al. (2011) determined optimum insulation thickness by using exergy-based analysis methods for the different climatic regions and fuels. A parametric study that investigated all the parameters affecting the optimum thermal insulation thickness for building walls was carried out by Kaynakli (2011). He used an economic model based on the life cycle cost analysis to determine the optimum insulation thicknesses. Bolattürk (2008) investigated the optimum insulation thickness for the external walls of buildings with respect to cooling and heating degree-hours in the warmest zone of Turkey. He calculated that the optimum insulation thickness varies between 3.2 and 3.8 cm depending on the cooling degree-hours and 1.6 and 2.7 cm for the heating loads. Effect of the fuel type, wall configuration, and combustion parameters on optimum insulation thickness was determined by Arslan et al. (2010). He calculated optimum insulation thicknesses between 0.291 and 0.1352 m depending on the fuel types, wall types, and combustion parameters. Environmental impact obtained from the LCA is combined with exergy analysis, and it is called as exergoenvironmental analysis. This new method is used for calculating environmental impact of the energy conversion systems (Meyer et al. 2009; Tsatsaronis 2008). Environmental impacts of several materials are associated with points and listed in the ECO indicator 95 and ECO indicator 99 (Goedkoop and Spriensma 2000; Goedkoop 1995).

In this study, to determine the optimum insulation thickness, a novel method based on the environmental impact analysis is performed to an external building wall. In our analysis, the rockwool and polystyrene are used as the insulation materials. LCC analysis is commonly used in studies mentioned above for evaluating the optimum insulation thickness. LCC analysis is applied for the investigated wall, and the results of LLC and environmental analyses are compared.

b	Environmental impact point (mPts/kg)
B	Total environmental impact of the system (mPts/m^2-year)
E	Annual energy (J/ m^2-year)
h	Convection heat transfer coefficient (W/m^2.K)
Hu	Heating value (J/kg)
HDD	Annual heating degree day (°C.day)
k	Thermal conductivity (W/m.K)
L	Thickness of the wall component (m)
m	Annual fuel mass (kg/m^2-year)
q	The annual heating loss (J/m^2-year)
R	Thermal resistance (m^2.K/W)
S	Annual net saving of environmental impact (mPts/ m^2-year)

(continued)

SE	Annual net saving of energy loss (J/ m^2-year)
T	Temperature (°C or K)
U	Heat transfer coefficient (W/ m^2.K)
V	Volume (m^3)
x	Insulation thickness (m)
Greek letters	
η	Efficiency of the heating system (%)
φ	Chemical exergy factor of the fuel
ρ	Density (kg/m^3)
Subscripts	
br	Brick
CO_2	Carbon dioxide
c	Cost
en	Environmental
F	Fuel
i	Inside air
ip	Inside plaster
ener	Inside air
ins	Insulation
Loss	Loss
o	Outside air
op	Outside plaster
nins	No-insulation
T	Total

2 Modeling and Analysis

2.1 Environmental Impact Analysis

A composite wall investigated in this study is presented schematically in Fig. 1. The building wall consists of parallel layers of inside plaster, brick, insulation material, and outside plaster. Rockwool and polystyrene are chosen as the insulation materials in the calculations. Some properties of the building wall components are given in Table 1. Temperatures of the outside and inside air are assumed at constant T_o and T_i. Natural gas is used as fuel for the heating system operated in 90% efficiency. Calculations are made annually for unit area of an external building wall.

The annual heating loss (J/m^2-year) from the unit area of the wall is determined from Eq. (1) by the way of heating degree-day (Başoğul and Keçebaş 2011):

$$q = 86400\,\mathrm{HDD}U \tag{1}$$

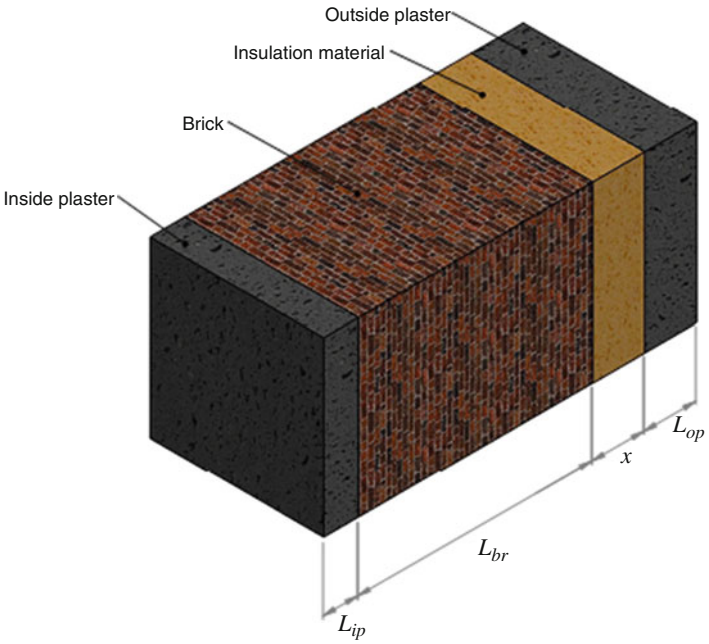

Fig. 1 Investigated building wall system

Table 1 Some properties of the building wall materials

Layer	Thickness (m)	Conductivity (W/mK)
Inside plaster	0.02	0.87
Brick	0.19	0.45
İnsulation material		
Rockwool	0–0.4	0.04
Polystyrene	0–0.4	0.032
Outside plaster	0.03	0.87

Bolattürk (2006) and Izocam (2014)

where HDD is the heating degree-days (°C.day) and U is the heat transfer coefficient (W/m^{2}K). Heat transfer coefficients (W/m^{2}K) for no-insulation and the insulated wall conditions can be calculated using Eqs. (2) and (3), respectively:

$$U_{\text{nins}} = \frac{1}{R_{\text{i}} + R_{\text{ip}} + R_{\text{br}} + R_{\text{op}} + R_{\text{o}}} = \frac{1}{R_{\text{T,nins}}} \tag{2}$$

$$U_{\text{ins}} = \frac{1}{R_{\text{i}} + R_{\text{ip}} + R_{\text{br}} + R_{\text{ins}} + R_{\text{op}} + R_{\text{o}}} = \frac{1}{R_{\text{T,ins}}} \tag{3}$$

$R_{T,nins}$ is the total thermal resistance of the wall without the insulation material, which is

$$R_{T,nins} = \frac{1}{h_i} + \frac{L_{ip}}{k_{ip}} + \frac{L_{br}}{k_{br}} + \frac{L_{op}}{k_{op}} + \frac{1}{h_o} \tag{4}$$

where h_i and h_o are the convection heat transfer coefficients on the inside and outside of the wall. L and k are the thickness and the thermal conductivity of the wall components, respectively. Subscripts ip, br, and op denote the inside plaster, brick, and outside plaster, respectively.

Also, $R_{T,ins}$ is the total thermal resistance of the insulated wall, and it is defined as follows:

$$R_{T,nins} = R_{T,ins} + \frac{x}{k_{ins}} \tag{5}$$

where x and k_{ins} are the thickness and the thermal conductivity of the insulation material, respectively. Annual energy (J/m^2-year) need from the unit area of the wall is calculated by using efficiency of the heating system (η) and the annual heating loss (q):

$$E = \frac{86400\,\mathrm{HDD}U}{\eta} \tag{6}$$

Annual fuel consumption (kg/m^2-year), depending on the annual energy need, is determined using Eq. (7):.

$$m_F = \frac{86400\,\mathrm{HDD}U}{\mathrm{Hu}\eta} \tag{7}$$

where Hu is the lower heating value of the fuel (J/kg). More than 90% of natural gas is composed of methane (CH_4); so, methane can be used in the combustion equation, and the combustion process is assumed as complete to facilitate calculations.

Combustion equation can be written as follows:

$$CH_4 + 2(O_2 + 3.76N_2) \rightarrow CO_2 + 2H_2O + 7.52N_2$$

From this equation, CO_2 emission (kg/m^2-year) can be given as in Eq. (8):

$$m_{CO_2} = 2.75\left(\frac{86400\,\mathrm{HDD}U}{\mathrm{Hu}\eta}\right) \tag{8}$$

Total environmental impact function of the system (Özel et al. 2014), B_T (mPts/m^2-year), is calculated from Eq. (9):

$$B_T = b_F m_F + b_{CO_2} m_{CO_2} + b_{ins} \rho_{ins} x_{ins} \tag{9}$$

Here, b_F is the environmental impact of the fuel (mPts/kg), b_{CO_2} is the environmental impact of CO_2 (mPts/kg), and b_{ins} is the environmental impact of the insulation material (mPts/kg). Also, ρ_{ins} (kg/m^3) is the density of the insulation material. The optimum insulation thickness is obtained by getting the derivative of B_T with respect to x and set equal to zero as follows:

$$x_{en} = -k_{ins} R_{T,nins} + 487.44 \sqrt{\frac{(b_{CO_2} + 0.36 b_F) \mathrm{HDD} k_{ins}}{b_{ins} \mathrm{Hu} \eta \rho_{ins}}} \tag{10}$$

B_T will receive the minimum value at the optimum insulation thickness. The net saving of the environmental impact (mPts/m^2-year) is

$$\begin{aligned} S = {} & (b_F m_F + b_{CO_2} m_{CO_2})_{nins} \\ & - (b_F m_F + b_{CO_2} m_{CO_2} + b_{ins} \rho_{ins} x_{ins})_{ins} \end{aligned} \tag{11}$$

The net saving of energy loss from the pipe surface (J.K/m) is

$$\mathrm{SE} = E_{nins} - E_{ins} \tag{12}$$

2.2 Life Cycle Cost Analysis

Life cycle cost analysis is an economic evaluation method that determines the total cost of system components over a period of time. For a building wall, LCC analysis is used to determine the optimum insulation thickness to take into account the change in interest and inflation (Ucar 2010).

The annual fuel cost per unit area is

$$c_F = c_f m_F \tag{13}$$

where c_f is the cost of fuel. The fuel cost over a lifetime is calculated using the present worth factor (PWF) in the life cycle cost. The PWF depends on the inflation rate, g, and interest rate, i, and is adjusted for inflation as (Ekici et al. 2012)

$$i^* = \begin{cases} \dfrac{i-g}{1+g} & ; \quad i > g \\ \dfrac{g-i}{1+i} & ; \quad i < g \end{cases} \tag{14}$$

and then PWF is defined as follows (Arslan and Kose 2006):

$$\mathrm{PWF} = \begin{cases} \dfrac{1-(1+i^*)^{-N}}{i^*} & ; \quad i \neq g \\ (1+i)^{-1} & ; \quad i = g \end{cases} \tag{15}$$

where i^* is the interest rate adjusted for the inflation rate and N is the lifetime of the insulation material.

Finally, the annual fuel cost can be shown as

$$C_{\mathrm{F}} = c_{\mathrm{f}} \mathrm{PWF} m_{\mathrm{F}} \tag{16}$$

The annual cost of the insulation material per unit volume can be calculated as

$$C_{\mathrm{ins}} = c_{\mathrm{i}} V_{\mathrm{ins}} \tag{17}$$

where c_i is the cost of insulation material per m^3 and V_{ins} is the volume of the insulation material.

The annual total cost of the building wall is

$$C_{\mathrm{T}} = c_{\mathrm{f}} \mathrm{PWF} m_{\mathrm{F}} + c_{\mathrm{i}} V_{\mathrm{ins}} \tag{18}$$

The annual cost saving per unit area of the wall is

$$\mathrm{SC} = C_{\mathrm{T,nins}} - C_{\mathrm{T,ins}} \tag{19}$$

The optimum insulation thickness is obtained by getting the derivative of SC with respect to x and set equal to zero. SC will receive maximum value at the optimum insulation thickness. Data used in the calculations can be seen in Table 2.

$$x_{\mathrm{C}} = 293.94 \sqrt{\frac{C_{\mathrm{F}} \mathrm{HDD} k_{\mathrm{ins}} \mathrm{PWF}}{C_{\mathrm{ins}} \mathrm{Hu} \eta}} - k_{\mathrm{ins}} R_{\mathrm{T,ins}} \tag{20}$$

3 Results and Discussion

In the present study, the environmental analysis and life cycle cost analysis are applied to an external building wall to determine the optimum insulation thickness. Rockwool and polystyrene are chosen as the insulation materials for building walls in the city of Bilecik, Turkey.

It is seen from Fig. 2 that the total environmental impact of the system decreases with the insulation thickness until a certain point called as optimum point. Environmental impact of the system gets the minimum value at this point named optimum insulation thickness. The optimum insulation thicknesses for the rockwool and polystyrene are calculated as 0.232 and 0.219 m, respectively by using Eq. (10). At optimum points, environmental impacts of the system are

Table 2 Parameters used in calculations

Parameter	Unit	Value
Environmental impact point	mPts/kg	
Rockwool (Goedkoop and Spriensma 2000)		4.2
Polystyrene (Goedkoop and Spriensma 2000)		8.3
Fuel (Goedkoop 1995)		114
CO_2 (Goedkoop 1995)		5.45
Mean temperature for heating period (Turkish Meteorological Office 2014)	°C	9
Heating degree-days (Dombaycı 2009)	°C-days	2966
Boiler efficiency		0.9
Density of insulation material	kg/m^3	
Rockwool (Izocam 2014)		105
Polystyrene (Kaya and Aydin 2006)		45
Lower heating value of the fuel (Arin and Akdemir 2002)	kJ/kgK	50×10^3
Fuel cost (Aksa Natural Gas 2014)	$/kg	0.53
Inflation rate (Central Bank of the Republıc of Turkey 2014)		8.39
Interest rate (Central Bank of the Republıc of Turkey 2014)		9.65
Lifetime (N)	year	10
Glass wool cost (Kaynakli 2008)	$/$m^3$	75
Rockwool cost (Izocam 2014)	$/$m^3$	132

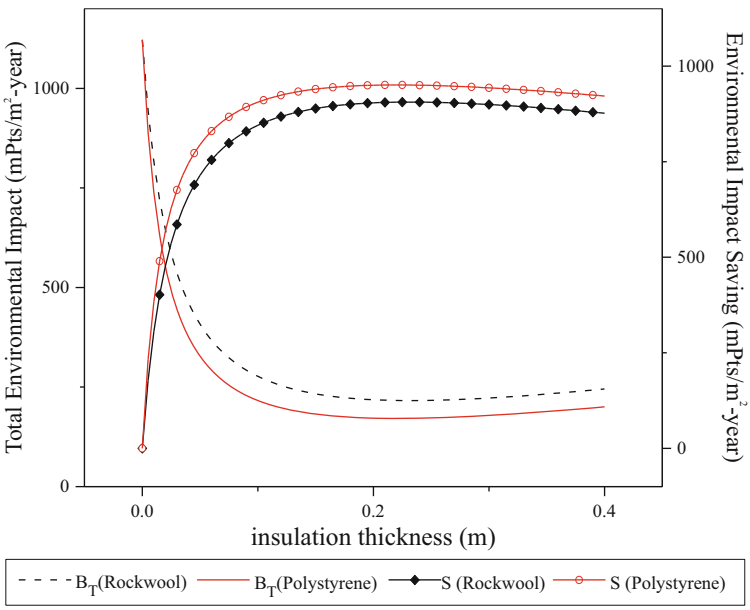

Fig. 2 Changes of the total environmental impact and the net environmental impact saving according to the insulation thickness

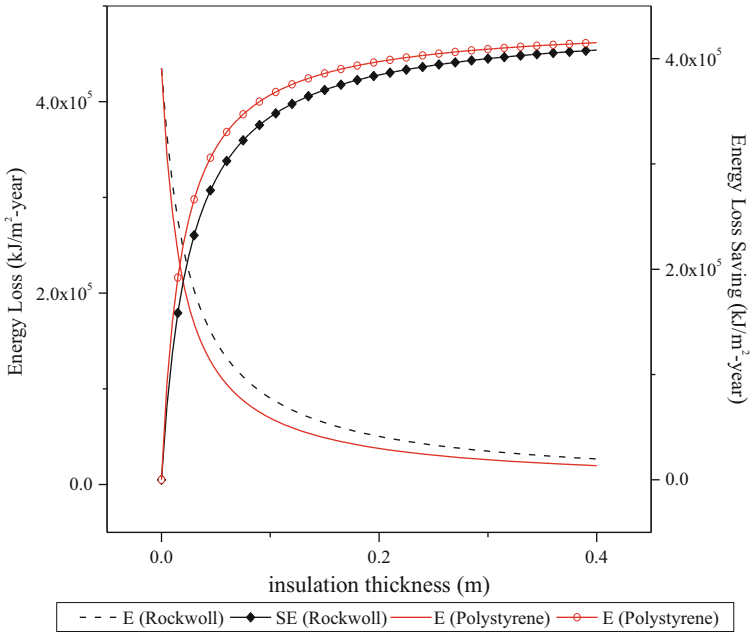

Fig. 3 Effect of the insulation thickness on energy loss and energy loss saving

determined as 216.12 and 171.304 mPts/m^2-year. The net environmental impact saving of the system tends to increase logarithmically up to the optimum insulation thickness while the total environmental impact decreases.

As it appears in Fig. 3, application of the insulation material decreases the energy loss from the building wall. Until the environmental optimum insulation thickness, energy loss decreases significantly, and after the optimum point, its decrease continues negligibly. According to these results, when rockwool and polystyrene are used at the optimum thickness, energy loss from the building wall decreases by 89% and 92%.

Variations of the fuel consumption and the CO_2 emission versus the insulation thickness are presented in Fig. 4. As insulation thickness increases, the fuel consumption and CO_2 emission decrease. Similar to the energy loss, fuel consumption and CO_2 emission decrease logarithmically. Up to the environmental optimum point, a rapid decrease in fuel consumption and CO_2 emission is observed. The results show that for rockwool, decreasing of the no insulation condition up to 0.4 m insulation thickness is 94% for fuel consumption and CO_2 emission. Eighty-nine percent of these are obtained up to the optimum insulation thickness. For polystyrene, decrease in fuel consumption and CO_2 emission is 95% between no insulation condition and 0.4 m insulation thickness. Ninety-two percent of these are obtained up to the optimum insulation thickness.

As a part of the LCC analysis, insulation and fuel costs are evaluated, and results are presented in Fig. 5. Investigating the graphics, it can be seen that initially fuel

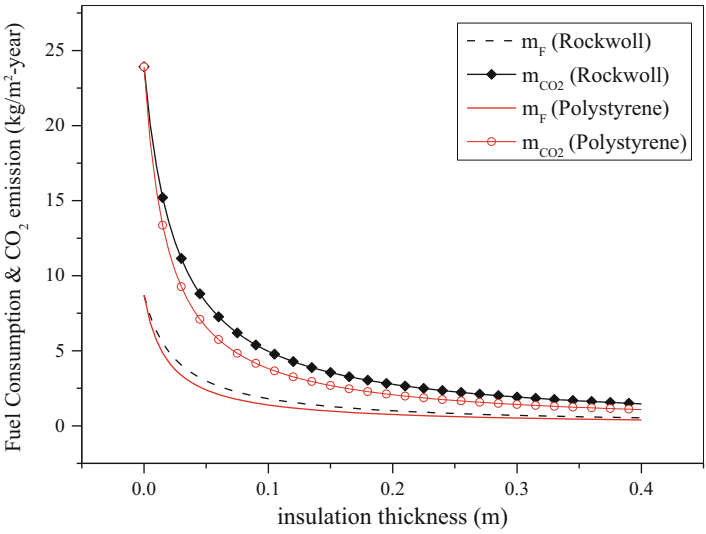

Fig. 4 Fuel consumption and CO_2 emission versus insulation thickness

cost decreases in larger steps up to a certain point, and then decreasing steps get smaller. Insulation cost increases linearly because it only depends on the insulation thickness. Total cost of the system decreases logarithmically up to the minimum point, called the economical optimum point, after which it starts to increase (Fig. 6). For rockwool and polystyrene, economical optimum points are calculated as 0.065 and 0.085 m, respectively. The net cost saving of the system tends to increase logarithmically up to the optimum insulation thickness while the total cost decreases.

4 Conclusions

In this study, optimum insulation thickness of a building wall is determined by using two different analysis methods. First, the environmental impact analysis based on the life cycle assessment is performed for the wall system. And then results are compared with the LCC analysis which is most commonly used for determining the optimum insulation thickness of a building wall. Some concluding remarks can be summarized as follows:

- For rockwool, environmental and economical optimum insulation thicknesses are calculated as 0.232 and 0.065 m, respectively.
- For polystyrene, environmental and economical optimum insulation thicknesses are calculated as 0.219 and 0.085 m, respectively.

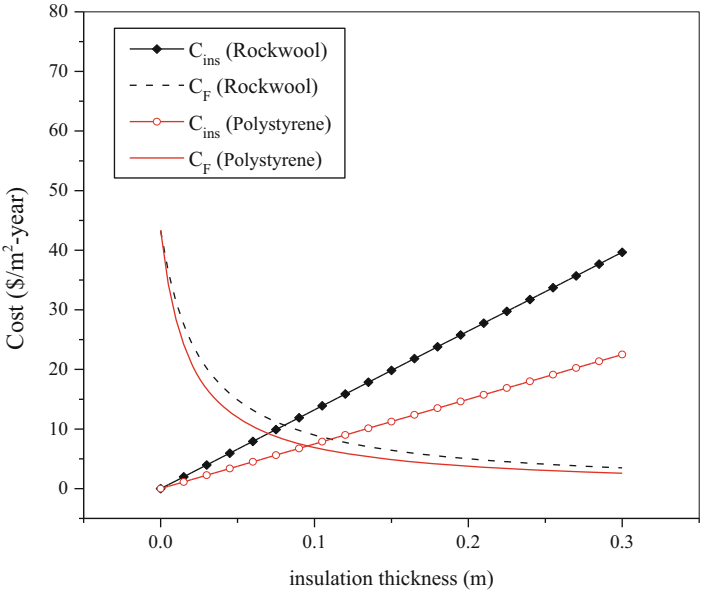

Fig. 5 Variations of insulation and fuel cost with insulation thickness

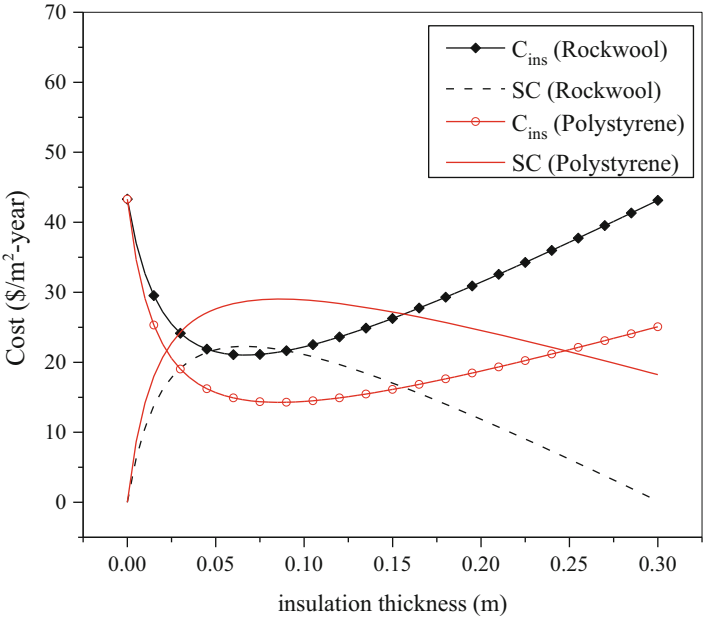

Fig. 6 Variations of total cost and cost saving with insulation thickness

- For different insulation materials and wall components, optimum insulation thicknesses based on the environmental impact and LCC analysis can be calculated by using Eqs. (10, 20)
- In comparing the two methods, the optimum insulation thickness with the life cycle cost analysis is lower than that with the environmental impact analysis.

References

Aksa Natural Gas.: http://www.beygaz.com/Turkish/FiyatTarifesi.aspx (2014)
Arin, S., Akdemir, S.: Seralarda doğal gazın ısıtma amaçlı kullanılabilirliği (Applicability of the natural gas in greenhouses for heating purposes). Sci. Res. J. Series B. **3**(1), 89–99. (in Turkish), www.trakya.edu.tr./enstituler/fenbilimleri/dergi/arsiv/2002-1/12sel.pdf (2002)
Arslan, O., Kose, R.: Thermoeconomic optimization of insulation thickness considering condensed vapor in buildings. Energy Build. **38**, 1400–1408 (2006)
Arslan, O., Ozgur, M.A., Yıldızay, H.D., Kose, R.: Fuel effects on optimum insulation thickness: an exergitic approach. Energy Sources Part A. **32**, 128–147 (2010)
Balli, O., Aras, H., Hepbasli, A.: Exergoeconomic analysis of a combined heat and power (CHP) system. Int. J. Energy Res. **32**, 273–289 (2008)
Başoğul, Y., Keçebaş, A.: Economic and environmental impacts of insulation in district heating pipelines. Energy. **36**(10), 6156–6164 (2011)
Bolattürk, A.: Determination of optimum insulation thickness for building walls with respect to various fuels and climate zones in Turkey. Appl. Therm. Eng. **26**, 1301–1309 (2006)
Bolattürk, A.: Optimum insulation thicknesses for building walls with respect to cooling and heating degree-hours in the warmest zone of Turkey. Build. Environ. **43**, 1055–1064 (2008)
Central Bank of the Republıc of Turkey.: http://www.tcmb.gov.tr/yeni/bgm/yfaagrmev/agrmev_TRL.html (2014)
Dincer, I.: Environmental impacts of energy. Energy Policy. **27**(14), 845–854 (1999)
Dombaycı, O.A.: Degree-days maps of Turkey for various base temperatures. Energy. **34**, 1807–1812 (2009)
Ekici, B.B., Aksoy, T.U.: Prediction of building energy needs in early stage of design by using ANFIS. Expert Syst. Appl. **38**(5), 5352–5358 (2011)
Ekici, B.B., Gulten, A.A., Aksoy, T.U.: A study on the optimum insulation thicknesses of various types of external walls with respect to different materials, fuels and climate zones in Turkey. Appl. Energy. **92**, 211–217 (2012)
Goedkoop, M.: The Eco-Indicator 95. Final Report, Pré Consultants, Amersfoort (1995)
Goedkoop, M., Spriensma, R.: The Eco-indicator 99: a damage oriented method for life cycle impact assessment. Methodology Report, Amersfoort (2000)
Hasan, A.: Optimizing insulation thickness for buildings using life cycle cost. Appl. Energy. **63**, 115–124 (1999)
Izocam Insulation material: http://www.izocam.com.tr/tr-tr/urunler/yalitim-malzemeleri.aspx. Access date: March (2014)
Karakoc, T.H., Turan, O., Binyildiz, E., Yildirim, E.: Thermal Insulalation, 1st edn. Rota, Istanbul (2011)
Kaya, M., Aydın, H.: Production methods and Properties of polyurethane foam (Isi yalitim malzemesi poliüretan köpüğün üretim yöntemleri ve özellikleri), Soma Meslek Yüksekokulu Teknik Bilimler Dergisi, No:6 (2006)
Kaynakli, O.: A study on residential heating energy requirement and optimum insulation thickness. Renew. Energy. **33**(6), 1164–1172 (2008)
Kaynakli, O.: Parametric investigation of optimum thermal insulation thickness for external walls. Energies. **4**, 913–927 (2011)

Meyer, L., Tsatsaronis, G., Buchgeister, J., Schebek, L.: Exergoenvironmental analysis for evaluation of the environmental impact of energy conversion systems. Energy. **34**, 75–89 (2009)

Özel G., Açıkkalp E., Karakoc T.H., Hepbasli A.: Novel method for determining optimum insulation thickness of a piping system, 1th International Conference on Energy (ICOE 2014), 12–13 Aug 2014, Colombo

Sisman, N., Kahya, E., Aras, N., Aras, H.: Determination of optimum insulation thicknesses of the external wallsand roof (ceiling) for Turkey's different degree-day regions. Energy Policy. **35**, 5151–5155 (2007)

Tsatsaronis, G.: Recent developments in exergy analysis and exergoeconomic. Int. J. Exergy. **5**, 489–499 (2008)

Turkish Meteorological Office.: http://www.meteoroloji.gov.tr/. Access date: March (2014)

Ucar, A.: Thermoeconomic analysis method for optimization of insulation thickness for the four different climatic regions of Turkey. Energy. **35**, 1854–1864 (2010)

Ucar, A., Balo, F.: Determination of the energy savings and the optimum insulation thickness in the four different insulated exterior walls. Renew. Energy. **35**, 88–94 (2010)

Ucar, A., Inalli, M., Balo, F.: Application of three different methods for determination of optimum insulation thickness in external walls. Environ. Prog. Sustain. Energy. **30**, 709–719 (2011)

United States Environmental Protection Agency.: http://www.epa.gov/climatechange/ghgemissions/gases.html, June (2014)

Yıldız, A., Gürlek, G., Erkek, M., Özbalta, N.: Economical and environmental analyses of thermal insulation thickness in buildings. J. Therm. Sci. Technol. **28**, 25–34 (2008)

Yu, J., Yang, C., Tian, L., Liao, D.A.: Study on optimum insulation thicknesses of external walls in hot summer and cold winter zone of China. Appl. Energy. **86**, 2520–2529 (2009)

Energetic and Exergetic Design Evaluations of a Building Block Based on a Hybrid Solar Envelope Method

Mert Yelda and Saygın Nicel

1 Introduction

Nowadays, buildings are usually designed with an abstract and single perspective. This study shows that the context in which it will be located and the climate in which it is built also need to be considered.

At all levels of land-use planning decisions, the use of energy has to be taken into account and urban planners have to develop solutions for efficient use of energy. Land-use patterns directly affect energy consumption and influence energy systems. This is seen, for example, from the small scale of "a house" to the large scale of "a country." No matter what the scale of land investigated, it is crucial to understand the significance of efficient energy planning in the contribution to global energy conservation.

When looking from an energy-efficiency point of view, the different properties of the spatial structure are important. The fundamentals exercised when planning and decision making for local energy-efficiency planning are as effective for decisions on a regional scale (Owens 1990). Beside properties like orientation and microclimate on the smaller scale, wider spatial properties are also important on a larger scale. On a small scale, direct forward changes bring considerable improvements, for instance, adjusting the orientation of the building for the sake of energy saving and not adding extra cost to the construction. For comprehensive

M. Yelda (✉)
Yüzüncü Yil University, Faculty of Engineering and Architecture, Department of City and Regional Planning, Kampüs, Van 65080, Turkey
e-mail: mertyelda@gmail.com

S. Nicel
İzmir Institute of Technology, Faculty of Architecture, Department of City and Regional Planning, Gülbahçe, İzmir 35100, Turkey

© Springer International Publishing AG, part of Springer Nature 2018

F. Aloui, I. Dincer (eds.), *Exergy for A Better Environment and Improved Sustainability 2*, Green Energy and Technology,
https://doi.org/10.1007/978-3-319-62575-1_37

energy effectiveness on a larger scale, climatic and microclimatic properties of the urban area have to be considered with great care because of the loads arising from the heating and cooling needs.

It was concluded by Ovalı (2009) in her study that 50 % of energy consumed in buildings can be conserved when a climate-friendly building and built-environment design is applied. The situation in Turkey, where there is only one Building Act, underestimates the effects of different climate regions in the country. According to Act 3030, a building is designed and placed 5 m from the frontage and 3 m from flank front. These standards were taken from German standards during the planning of Ankara. However, this plan was for a building in Germany with 2–3 stories, while in Turkey other standards have been implemented so that the distance between the buildings increases 0.5 m for every storey in the building (Tokuç 2005). Planning, design, and implementation regulations do not take local and regional differences into account. As a result the urban environment is not in harmony with the local properties (Aydemir et al. 2004). Similarly, on a building scale, implementation for the regulation of energy performance in a building only focuses on decreasing the energy demand instead of applying the tools for increasing energy efficiency (Çakmanus 2010), although it deals with issues like the importance of orientation, passive solar gain, and microclimatic effects.

Morello and Ratti (2009) applied a solar envelope method to extensive urban areas and have made this method simple to apply to urban planning. Digital elevation models are used with a computerized method for dealing with this massive model.

Knowles (2003a, b) analyzed the solar enveloped method in detail. Its importance is pointed out in the context of sustainable development and improved esthetic possibilities for architecture and urban design.

When energy-efficient planning and design are taken into consideration, a relationship between land use and building design comes to the mind (Mangan and Oral 2013; Ovalı 2009; Owens 1990) . Energy-efficient planning principles systematically investigate the city on four scales, namely the building (small scale), the neighborhood (building block), the settlement (city), and the region (large scale). Figure 1 shows the basics of this framework and the relationship between energy and spatial properties. The relationship between the dominant properties in energy consumption and scales of investigation is identified and given considering intrinsic energy need and efficient use of energy in the framework. Land-use decisions should be made taking into consideration how to reduce the effects on climate change, ensuring efficient and effective use of energy, and providing sustainable urban policies (Ayan 1985). Moreover, the aim of energy-efficient planning is to help people carry out their daily activities in the most efficient way from an energy point of view, and to minimize energy usage (Owens 1990).

This study aimed to state the amount of energy conservation in a building block when hybrid solar envelope design strategies are applied. In other words, how energy and exergy can be saved when hybrid solar envelope design strategies are applied and what differences that they will bring, compared to the existing design of the building block.

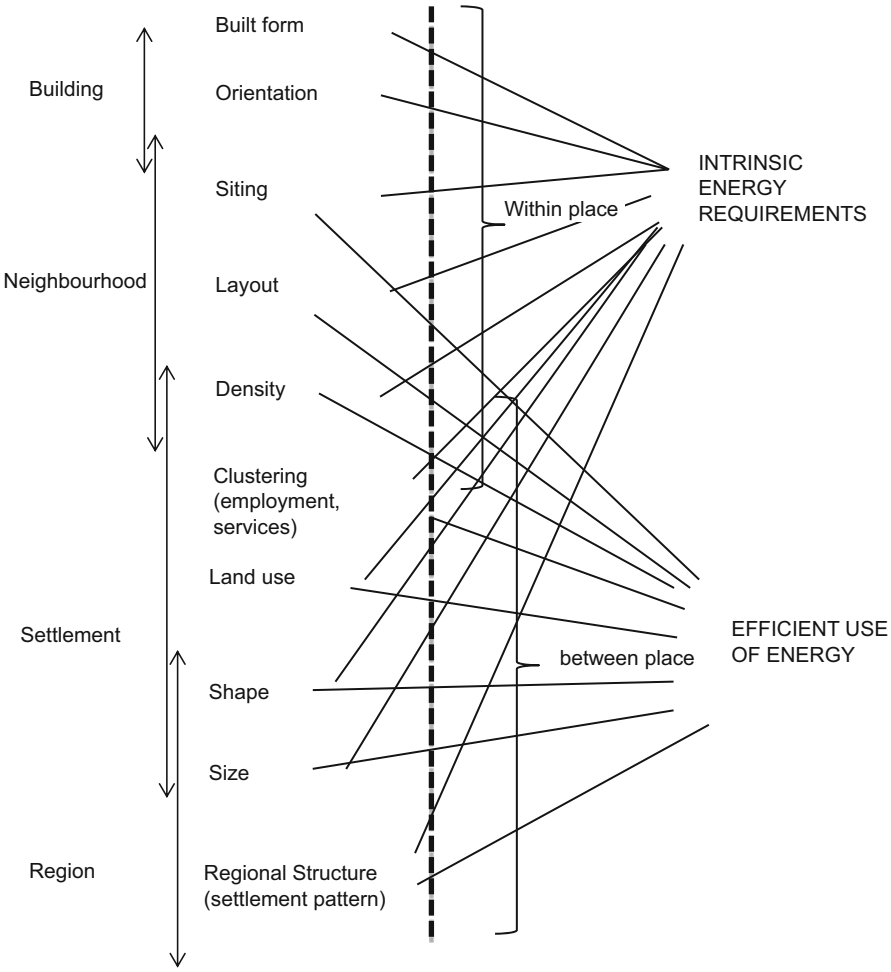

Fig. 1 Framework for analysis of energy/spatial structure relationship (Source: Owens 1990, p. 60)

2 Hybrid Solar Envelope Method

The solar envelop method depends on the arrangement of the height of the building(s) in accordance with the sun's path in the effective hours of radiation. The effective sun is the time between 10:00 am and 02:00 pm in which the sun has a greater heating capacity than the other hours of the day. The design is developed according to the angle of sunlight during this period (Canan 2008; Knowles 2003a, b).

The method aims at a scale impact and the height is not limited, only adjusted, depending on the solar angle and the topography. High-rises can also be considered

with this method (Canan 2008; Knowles, 2003a, b). Generally, a terraced structure is the result of this method being applied to building heights or to a building's singular design.

Various parameters such as physical environmental parameters, which include temperature, wind, sun path, climate, orientation, building form, distance between buildings, building organization, building envelope, and materials and landscaping are taken into account in designing energy-efficient alternatives.

The angle 12° from south towards east is chosen as the main orientation for a case area (Tokuç 2005) depending on the latitude. Based on the findings in the literature, for a hot-humid climate region optimum building form is taken as 1:1.7 in this study (Olgyay 1973). In the design, the width of the building is chosen as 30 m and the length as 18 m. Moreover, the long side of the building faces southward to increase the solar gain.

The spacing allowed between the buildings is of particular importance when the shadow effect is taken into account. The building's shadow must not block another building's solar input. The calculation used with this in mind is based on the sun's radiation angle to the earth. In this calculation, the angular value for 21 December is used, as the solar radiation's angle is at its lowest in the year on this date. An angular value of 29° is used in calculations at 12:00 pm, which is selected as the maximum radiation occurs at noon. Based on the calculations, the x/y ratio must be 0.55 and the maximum shadow length should be 1.96 times the height of the building. In this study the ratio of the spacing between the buildings is thus determined to be a rounded "2" in order to prevent a shadow effect.

In addition to the energy-efficient design parameters, a criterion for the solar envelop method is integrated in a single method. This hybrid method includes the requirements of orientation, spacing, landscaping, and building form as well as the building height properties as proposed in the solar envelop method.

Figure 2 shows a calculated solar enveloped for an area. Using these calculated angles of the solar path the building's height is adjusted for achieving maximum use of passive solar energy.

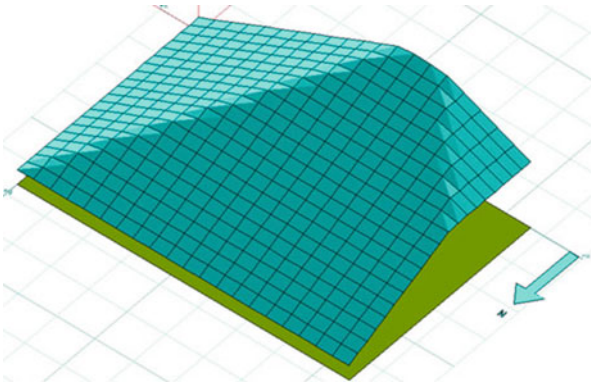

Fig. 2 Solar envelope method (Source: Knowles and Koenig 2002, p. 3)

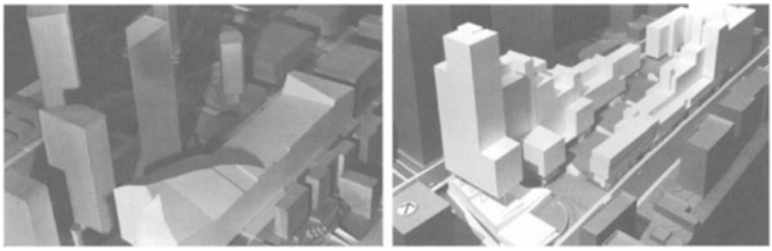

Fig. 3 Solar envelope method in high-rise buildings (Source: Knowles 2003a, p. 13)

The solar envelop method depends on understanding the changing position of the sun throughout the day and year. If this dynamic behavior is a factor in the design of the urban area environmental friendliness, sustainability and reduced energy consumption in cities can be achieved (Canan 2008; Knowles 2003a, b; Topaloğlu 2003). Figure 3 shows an example of an application of a solar enveloped-based design to an urban area. The terraced structure depending on the peak of the solar envelope and the angles of facades can be clearly seen in this design alternative.

3 Exergy Analysis of a Residential Area

The calculations for the exergy load of residential building blocks are complicated. This process starts with the data-handling, which is composed of some major design parameters of buildings and building blocks, as listed below (Mert 2014):

- Building scale: location of the building, orientation of the building, building form, area/volume ratio of the building, openings to building ratio, size of the building, design of the building, insulation of the building, resident information, heating and cooling system properties.
- Building block scale: building block form, size of building block, perimeter-to-area ratio, landscaping and planting of building block, microclimatic properties (wind, average temperature, etc.), shadowing due to the configuration of buildings, topography of the building block.

After completion of processing and analyzing data, exergy calculations take place:

- Calculation of the Shadow Effect Factor (SEF).
- Calculation of the exergy load of each building for heating and cooling.
- Calculation of the exergy loads for the building blocks.

This procedure calculates $\dot{E}\,x_{demand}$, which shows us the exergy need of the building. For the calculation of exergy demand, the fundamental procedure proposed by LowEx (Hepbaşlı 2012) is used:

$$\dot{E}\,x_{demand} = \dot{E}\,x_{loss} - \dot{E}\,x_{gain} \tag{1}$$

The transmission losses through the doors, walls, windows, and roofs cause exergy loss $\dot{E}\,x_{loss}$;

$$\dot{E}\,x_{loss} = \dot{E}\,x_{loss,transmission} + \dot{E}\,x_{loss,ventillation} \tag{2}$$

$$\dot{E}\,x_{loss,transmisson} = \sum U_i.A_i.(T_i - T_o) \tag{3}$$

The transmission losses are calculated by taking the heat transfer coefficient of walls, doors, roofs, and ceilings (U_i) as well as the areas (A_i) and the indoor (T_i) and exterior (T_o) air temperature differences into consideration.

$$\dot{E}\,x_{loss,ventillation} = C_p\rho.V.n_d.(1 - n_v).(T_i - T_o) \tag{4}$$

where ρ and C_p are the density [kg/m^3] and specific heat [kJ/kgK] of air, respectively. n_d and n_v are the air exchange rate [m^3/h] and the efficiency constants, respectively. V represents the volume [m^3].

Solar gains through the openings in the buildings are the source of exergy gain $\left(\dot{E}\,x_{gain}\right)$ that is a function of SEF. Other gains, such as lighting (2 W/m^2), that arise from the auxiliary equipment in the settlements are also taken into account. In order to calculate the gain, the determinations of the facades of the buildings are necessary, since the effect of the orientation of the buildings on the energy and exergy performance of the building depends on it. Each separate building is taken into account in this perspective. Facades that face from southwest to southeast and from northwest to northeast are also calculated and taken into consideration correspondingly.

$$\dot{E}\,x_{gain} = \dot{E}\,x_{gain,solar} + \dot{E}\,x_{gain,internal} \tag{5}$$

$$\dot{E}\,x_{gain,solar} = I_s.\left(\frac{100 - SEF}{100}\right).(1 - F_f).A_w\,g \tag{6}$$

Here, solar radiation is shown by I_s [W/m^2], F_f is the window frame fraction that is taken as 0.3, A_w is the window area [m^2], and g is the total transmittance.

$$SEF = \left(\frac{t_{shadow}}{t_{daytime}}100\right) \tag{7}$$

The SEF is an indication of a building's blockage by the shadow of other objects and buildings. This is the result of the overlapping shadow on the buildings standing behind another one. The 3D models are used for computing the SEF for both

summer and winter periods. In SEF, calculation models of the existing situation and the proposed plan are developed separately. These models allow us to simulate the time-dependent effect of the sunlight with regard to the attitude of the case are. SEF is evaluated by determining the ratio of the time under shadow (t_{shadow}, [min]) of the building to the daytime ($t_{daytime}$, [min]) with direct sunlight access in an approximate manner by using the 3D model of the area.

$$\dot{E}\,x_{gain\ ,in} = n_o.\varphi_{i,o} + A_N.\varphi_{i,e} \tag{8}$$

where n_o is the number of occupants, A_N is the floor area of the building [m^2], $\Phi_{I,o}$ and $\Phi_{I,e}$ are specific internal gains of occupants [W/occupant] and specific internal gains of equipment [W/m^2], respectively.

$\dot{E}\,x_{input}$ is calculated by taking $\dot{E}\,x_{demand}$ into consideration in addition to the efficiency of the heat production and heat distribution systems, which are used as 0.95 and 0.93, respectively.

The exergy flexibility factor shows the possibility of replacing a thermal system with another system, especially renewable, to meet the exergy demand (Hepbaşlı 2012).

$$EFF = \frac{\dot{E}\,x_{demand}}{\dot{E}\,x_{input}} \tag{9}$$

$$\dot{E}\,x_{input} = \frac{\dot{E}\,x_{demand}}{\eta_{heat\_sys}} + \dot{E}\,x_{loss} + \dot{E}\,x_{axu} \tag{10}$$

The heat gains of the buildings are also effective with regard to the values of the cooling exergy load of the building. The average temperature value is taken as 26.8 °C (MGM 2013) for the summer season.

$$\dot{E}\,x_{cooling} = Ex_{axu} + \dot{E}\,x_{gain,solar} + \dot{E}\,x_{gain,transmisson} \tag{11}$$

4 Case Study: Mavişehir Mass Housing Area

The case area is located in Izmir, which is in the western part of Turkey (Fig. 4). Izmir has a hot-humid climate; the summers are hot and dry while the winters are mild and rainy. According to the climactic and geographic characteristics, both the solar potential and the wind potential of Izmir are noticeably high. July and August are the hottest months in the city, with temperatures of 27.3 °C and 27.6 °C, respectively; the coldest months are January and February, with temperatures of 8.6 °C and 9.6 °C, respectively (MGM 2013).

Fig. 4 Location of Mavişehir in Izmir Bay (Source: Google 2013)

Moreover, the prevailing winds in Izmir come from the southeast and the west (MGM 2013; Serin 2011). The prevailing wind direction of the Izmir–Ciğli station was selected for the study because the station is located very close to the case area (Fig. 5).

The sun path diagram of Izmir is given in Fig. 6. The green curve on the upper side of the diagram represents the path of the sun from east to west during the daytime and indicates the angles on 21 June. The blue curve represents the path of the sun on 21 December. As seen in Fig. 6, the angle of sunlight reaching Izmir varies between the maximum angles of 72°–29° at 12 pm during the year.

The existing situation of the selected case area is a mass housing area and consists of high-rise (from 12-storey to 23-storey) buildings (Fig. 7). In addition to the housing units, the area also includes social and leisure facilities such as sports areas, green areas, parking areas, playgrounds, and education and commercial areas. Having a central gas heating system, double-glazed windows, sun blinds, decorative coated doors, and double bathrooms, each type of accommodation in Mavişehir is a luxury residential high-rise apartment or villa (Fig. 8) (Aydoğan 2005; Koç 2001; Özçelik 1998).

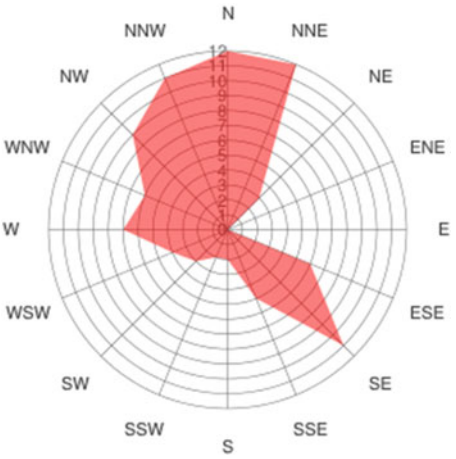

Fig. 5 The prevailing wind direction in Izmir–Ciğli Station (Source: Windfinder 2013)

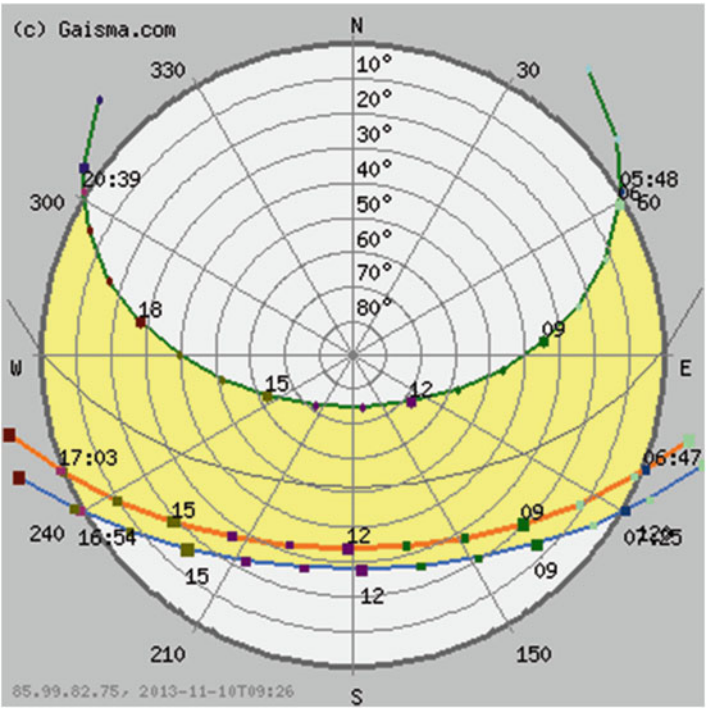

Fig. 6 Sun path diagram of Izmir (Source: Gaisma 2013)

Fig. 7 View of the case area (Source: Google 2013)

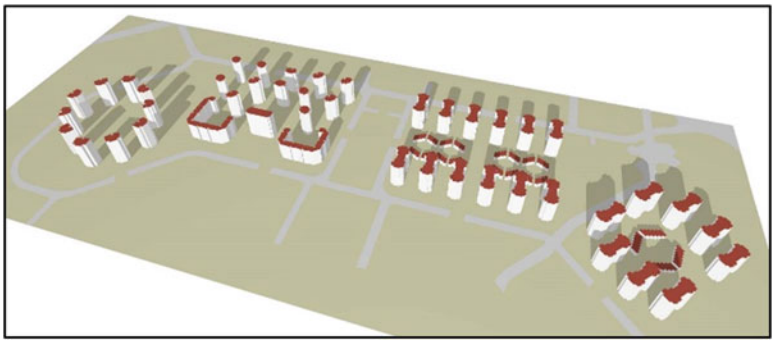

Fig. 8 Site model of the existing building block

5 Redesign of a Building Block: Hybrid Solar Envelope Method

The structure of a building block is designed as a terraced structure in accordance with the solar envelope values developed for Izmir (Fig. 6) and the structure of this model. The number of storeys changes within the range of 2 to 12 (Fig. 9) and the area of each housing unit is about 110 m^2. This selection is based on the peak point of the solar envelope and the prevailing angles of the solar envelope for east, west,

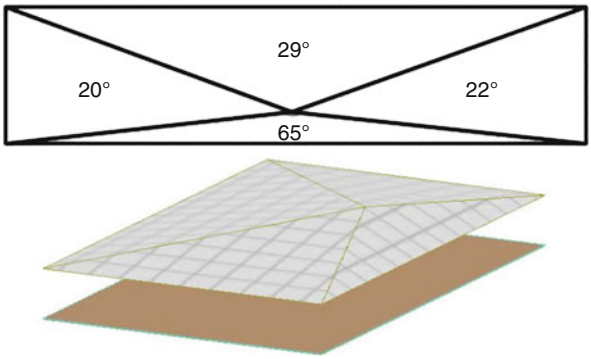

Fig. 9 Developed solar envelope of the case area

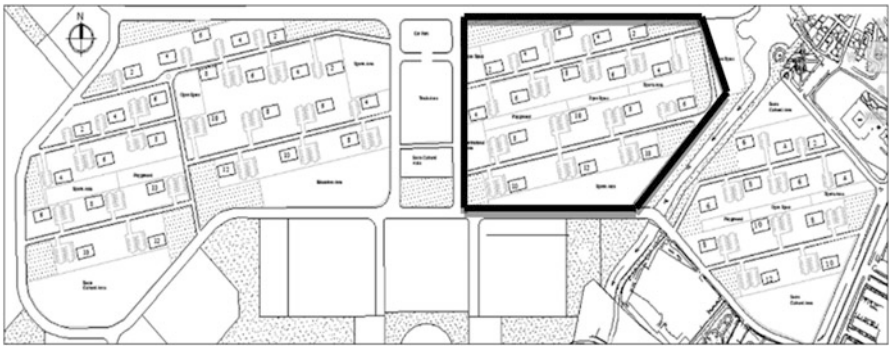

Fig. 10 Site plan of solar envelope-based alternative

north, and south. Green areas, playgrounds, sports area, parking area, and social, cultural, and educational areas are also considered, and areas are demarcated for these needs. The number of storeys of the buildings and height of the buildings change according to the solar envelope calculation. As a result, the distances between the buildings are also affected and changing.

Figures 10, 11, 12, and 13 show the developed site plan in detail for building blocks with regard to the hybrid solar enveloped-based energy-efficient design method. The effect of the solar envelop can be seen in Fig. 12. In Table 1 the number of buildings and housing units in the proposed solar enveloped-based design is shown.

6 Results and Discussion

In this study, exergy analysis is used to investigate a building block located in İzmir Mavişehir. Exergy concepts in relation to the environment ease the quantification of economic and ecological problems by underlining the potential of a successful

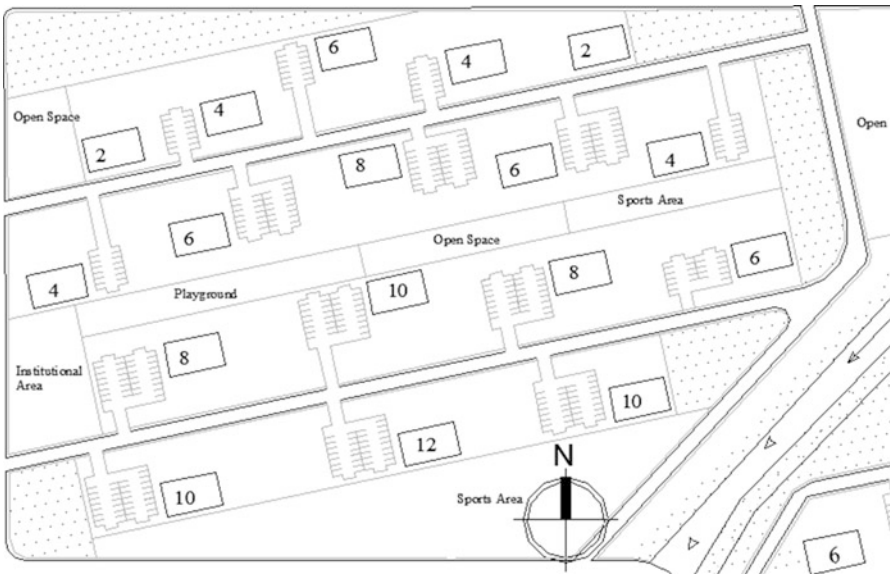

Fig. 11 Site plan of solar envelope-based alternative in detail

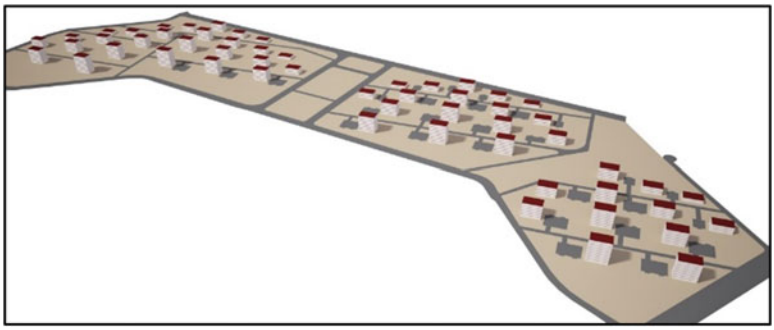

Fig. 12 Site model of solar envelope-based alternative

exergy analysis (Mert 2006). The important effects of the relationship between exergy and the environment are seen in the reduction of waste energy emissions, a decrease in resources of energy-related sectors, and more efficient use of energy (Dinçer 2002).

Some assumptions made in the analysis are listed below:

- The reference state for exergy analysis is selected as 298 K temperature and 1 atm pressure in atmospheric concentrations.
- Indoor air temperature is 21 °C.
- Outdoor temperature is 10.9 °C, the average winter temperature of Izmir (between the years of 1960–2012) (MGM 2013).

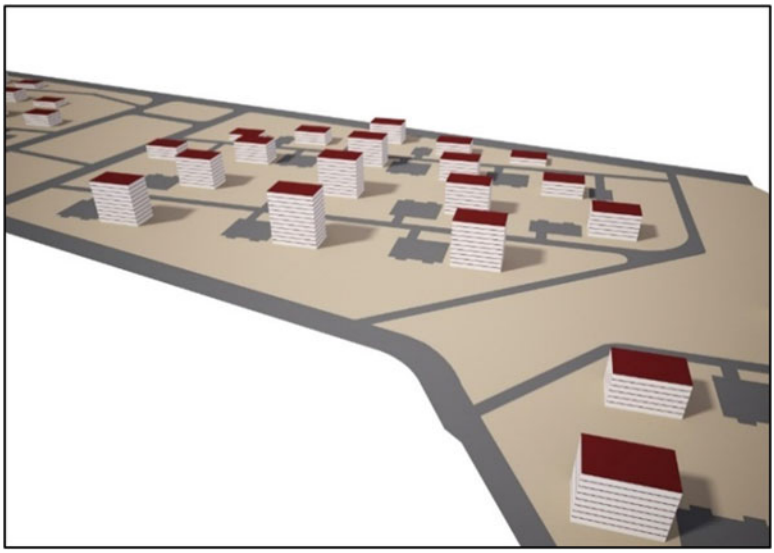

Fig. 13 Site model of solar envelope-based alternative

Table 1 Details for the solar envelop-based design

Storey	No. of buildings	No. of housing units
12	4	192
10	9	360
8	11	352
6	13	312
4	12	192
2	7	56
Total	**56**	**1464**

- Outdoor temperature is 28.6 °C, the average summer temperature of Izmir (MGM 2013).
- The heat transfer coefficients of the walls and doors are gathered from real values depending on the plan details of the buildings, which are obtained from the Karşıyaka Municipality, and on the reported data of the construction company (Karşıyaka Municipality 2012).
- An average value of four residents is assumed during the calculations.
- 70°/50° heating system (inlet/outlet temperature of the radiators) is used in calculations in accordance with the reality and the condensing boiler systems.

In Table 2 results for exergy analysis of a residential area for solar envelope-based design is given. It must be mentioned that the summer exergy load and winter exergy load is in accordance with the expectation that cooling load is higher than the heating load and the exergy efficiency is in the range of 7–11, depending on the

Table 2 Results for the solar envelop-based design

Storey	Exergy load summer [W]	Exergy load winter [W]	Exergy by fuel [W]	Exergy efficiency [%]	Exergy flexibility factor [%]
12	16,753	8,330	6,200	10.1	39
10	14,048	7,078	5,183	10.5	38
8	9,848	5,425	3,438	10.9	36
6	8,638	4,575	3,148	11.0	33
4	5,932	3,323	2,131	11.2	29
2	3,227	2,071	1,113	7.4	19

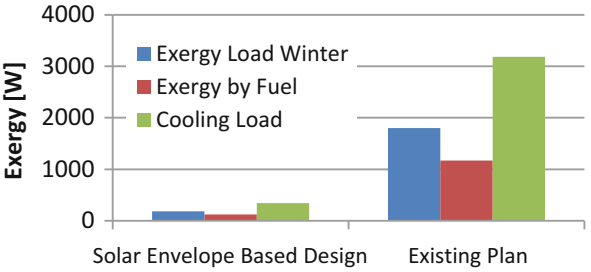

Fig. 14 Exergy load and exergy according to fuel values of proposed alternative and existing plans

local climate properties. The higher the building height the larger the exergy loads, whereas lower exergy loads are also seen in the investigation.

The exergy efficiency values are in the range of 10.8–11.2 % and the exergy by fuel value changes from 2,845.7 to 5,424.9 kW. These results are in accordance with the literature, as Hepbaşlı (2012) pointed out that the efficiency of buildings with a LowEx design reaches 7–8 %. When the existing plan and the proposed plan alternative are compared it is seen that the exergy load value for the existing plan is ten times higher than the new design. It can be seen that the hybrid solar envelope design can lead to high ratios of energy conservation. In Fig. 14, the exergy per separate housing unit is shown. It is seen that a solar enveloped-type housing has better energy conservation with lower than 184 W, while in the existing plan this value lies in the range of 1,800 W. The proposed design's exergy load values are lower than the others mainly because of the general high performance of the heating system in a great number of housing units. This investigation is carried out per housing unit since the housing unit numbers are different in the proposed design alternative and to the existing situation. So in order to achieve a logical discussion, comparison per housing unit is applied.

From a cooling load point of view in the summer period, it is seen that the saving is much higher since the exergy load value decreases from 3,181 to 346. This is a result of proper airing and particularly use of excellent construction materials (Table 3). When the values from the literature (Hepbaşlı 2012) of cooling loads are investigated it is seen that cooling loads for hot-humid zones are higher than heating loads and it is seen that the results of this study are in accordance with the literature.

Table 3 The savings by energy-efficient design per housing unit

	Solar envelope based design	Existing plan
Exergy load winter [W]	184.80	1798.0
Exergy by fuel [W]	125.37	1173.0
Exergy load summer [W]	346.89	3181

Table 4 The annual saving using an energy-efficient design

Conservation type	Conservation amount (per year)
Exergy winter [W]	2,188.67
Exergy summer [W]	1,583.68
Money [TL]	1,072.48
CO_2 emission [kg]	1,787.46

Table 5 Design values of existing and proposed plan alternatives

	Existing building block	Solar envelop-based building block
Number of buildings	155	56
Housing unit (number)	5320	1464
Floor area of housing unit (m^2)	56 m^2–150 m^2	117 m^2
Total housing area (m^2)	54,135	30,240

The amount of money and greenhouse emissions saved is shown in Table 4 per housing unit in the building block. It is seen that every housing unit saves 1,072.48 TL (nearly US$500) in a year according to the effect of the energy-efficient design. This value is very important for most of the families in Turkey. Of more importance than the monetary savings, nearly 1.79 tons of greenhouse gas emissions per housing unit have not been emitted into the atmosphere, which is a magnificent contribution to the environment for the sake of a sustainable and green future. These values are calculated using the energy price of US$0.08 /kW for cost and using reaction stoichiometry calculations with natural gas as the fuel in the case area.

The exergy calculations are concluded with determinations of exergy efficiency and exergy loads in addition to the annual conservation of exergy, money, and greenhouse gases.

In Table 5, general features of the existing building block and the proposed design alternative are summarized. The design alternative has less housing units than the existing building block. As seen in Table 3, the housing unit number is decreased in the alternative proposed design. This result mostly arises from the fact that the spacing between the buildings is increased in the energy-efficient design, which brings a low density to the built area.

From an energy-efficiency point of view it is seen from this study that when the planning and design are carried out taking into consideration the energy-efficient design parameters, the efficiencies increase considerably. That brings us to a position to propose considering these parameters in every planning and design study as well as implementing these in building and planning acts.

7 Conclusions

The building block is redesigned in order to increase energy. The results of the exergy analysis of the proposed design alternative show that the exergy efficiency values have increased to 11 % from 1.5 % in the existing design. Since the efficiency value is the representation of the performance of using the energy in an effective manner, it is free of the magnitude (size of the area) and can be evaluated for understanding the energetic behavior of the existing and proposed design alternative. The exergy efficiency was increased considerably, and a large amount of energy and money can be conserved through the application of the proposed design. The results also show that the annual exergy load of a single housing unit was decreased from 1,800 to 184.8 W for winter and from 3,180 to 346 W in summer.

It is seen that when energy-efficient design parameters are taken into account, such as proper distance allocation among the buildings for sunlight purposes, a lower density building block is needed. In the existing plan the parking area is also larger than the proposed building block because of the high number of housing units. Moreover, the high housing unit number creates a decrease in the green open spaces, sports areas, and playground areas. It was also found out that the alternative design proposed larger green areas, open spaces, and social areas with respect to the existing situation in the area. That also mostly arose from the spacing between the buildings.

As a result of this study, it was found that by applying a solar envelope design to the selected building block, 1,613 and 2,834 W of energy could be conserved during the winter and the summer periods, respectively, for a housing unit. With this energy conservation, 1,072 TL (nearly US$500) per housing unit was saved annually. Of more importance, 1,787 kg of emission gases (CO_2, etc.) per housing is not released into the atmosphere. This results in the formation of a more sustainable neighborhood. When the total area is taken into account, the exergy efficiency reaches up to 11 %. The Exergy by Fuel Value is 125.37 kW, with a Summer Exergy Load of 346.89 kW and a Winter Exergy Load of 184.80 kW. These are the main indications of the importance of the exergetic analysis in a building block.

In this study, it is revealed that according to energy efficiency, efficiencies increase considerably when a hybrid solar envelope design is considered during the planning and design periods. Furthermore, the results show that the concept of energy efficiency should be taken seriously from every urban planning and design stage to implementation.

References

Ayan, M.: Konut Alanları Tasarım İlkeleri. Batıkent Konut Üretim Yapı Kooperatifleri Birliği, Ankara (1985)

Aydemir, Ş., Erkonak, A., Şen, S., Beyazlı, D.Ö., Öksüz, N., Ahmet, M., Sancak, C., Özyaba, M., Türk, Y.A.: Kentsel Alanların Planlanması ve Tasarımı. Akademi Kitabevi, Trabzon (2004)

Aydoğan, A.: Residential satisfaction in high-rise buildings. Master diss., İzmir Institute of Technology (2005)

Çakmanus, İ.: Binalarda Enerji Verimliliğinin Değerlendirilmesi. Yeşil Bina. **4**, 1–3 (2010)

Canan, F.: Enerji etkin tasarımda parametrelerin denetlenmesi için bir model denemesi. Unpublished PhD Thesis, Selçuk University (2008)

Dinçer, İ.: The role of exergy in energy policy making. Energy Policy. **30**, 137–149 (2002)

Gaisma. Sun path diagram. http://www.gaisma.com (2013). Accessed on 3 Nov 2013

Google Earth.: http://www.google.com/earth/ (2013). Accessed on 3 Feb 2013

Hepbaşlı, A.: Low Exergy (LowEx) heating and cooling systems for sustainable buildings and societies. Renew. Sust. Energ. Rev. **16**, 73–104 (2012)

Karşıyaka Municipality: Approved plan of Mavişehir mass housing. Accessed on June, 2012, Department of Planning Archive (2012)

Knowles, R.: The solar envelope in time-saver standards for urban design. The McGraw-Hill Companies, New York (2003a)

Knowles, R.L.: The solar envelope: its meaning for energy and buildings. Energ. Build. **35**(1), 15–25 (2003b)

Knowles, R., Koenig, P.: A dynamic approach to solar-access zoning. School of Architecture, University of Southern California, Los Angeles (2002)

Koç, H.: Cumhuriyet Döneminde İzmir'de Sosyal Konut ve Toplu Konut Uygulamaları. Dokuz Eylül University Faculty of Architecture Publications, Izmir (2001)

Mangan, S.D., Oral, G.K.: Türkiye'nin Farklı İklim Bölgelerinde Bir Konut Binasının Enerji Etkin İyileştirilmesi. In 11.Ulusal Tesisat Mühendisliği Kongresi, Izmir, 921–931 (2013)

Mert, S.O.: Exergoeconomic analyisis of pem fuel cell systems for transportation application. Unpublished Master diss., Ege University (2006)

Mert, Y. Application of exergy analysis method to energy efficient building block design. Unpublished PhD Thesis, İYTE (İzmir Institute of Technology) (2014)

MGM (Turkish State Meteorology Service).: İklim Sınıflandırması.. http://www.mgm.gov.tr/iklim/iklim-siniflandirmalari.aspx?m=IZMIR (2013). Accessed on 3 Sept 2013

Morello, E., Ratti, C.: Sunscapes: 'solar envelopes' and the analysis of urban DEMs. Comput. Environ. Urb. Syst. **33**(1), 26–34 (2009)

Olgyay, V.: Design with climate-bioclimatic approach to architectural regionalism. Princeton University Press, New Jersey (1973)

Ovalı, P.K.: Türkiye İklim Bölgeleri Bağlamında Ekolojik Tasarım Ölçütleri Sistematiğinin Oluşturulması- "Kayaköy Yerleşkesinde Örneklenmesi. PhD diss., Trakya University (2009)

Owens, S.: Land use planning for energy efficiency. In: Cullingworth, B. (ed.) Energy, land and public policy, energy policy studies, vol. 5, pp. 53–98. Transaction Publishers, New Jersey (1990)

Özçelik, A.A.: İzmir'deki Toplu Konutların Türkiye Emlak Bankası Uygulamaları Örneğinde İrdelenmesi. Master diss., Dokuz Eylül University (1998)

Serin, E.: Ekolojik Konut Tasarımı Kriterlerinin Araştırılması ve İzmir İli İçin Bir Tasarım Modeli Önerisi. Master diss., Dokuz Eylül University (2011)

Tokuç, A:. İzmir'de Enerji Etkin Konut Yapıları İçin Tasarım Kriterleri. Master diss., Dokuz Eylül University (2005).

Topaloğlu, B. Solar envelope and form generation in architecture. Unpublished Master diss., Middle East Technical University (2003)

Windfinder.: Wind & weather statistics for Izmir-Ciğli. www.windfinder.com (2013). Accessed on 3 Nov 2013

Natural Ventilation Around and Through Building: A Numerical Study

A. Kaddour and S.M.A. Bekkouche

1 Introduction

In the planning process of a building, the heating and cooling concepts are developed, and both have the ventilation concept as an integrated part. Mechanical, natural, and even hybrid ways of ventilation are nowadays in use. Natural ventilation of buildings, relying on pressure or on difference in temperature, is the most common form of ventilation. The air is exchanged through doors and open or tilted windows. For layout purposes, it is important to estimate the magnitude of the air change rates correctly. Ventilation through tilted windows is sparsely represented in the literature to date Teppner (2014).

The 1970s housing crisis had inspired the interest in bioclimatic architecture, as the most nowadays built houses are intact and combustible energy reserves are exhausted. The case study of this research is the agglomeration of Ghardaia situated in M'zab valley in the northern part of Algeria Bekkouche (2011).

Ghardaia region is situated at the south of the capital (600 km) between 32° and 33°20° northern latitude and 2°30° longitude east at an average altitude of 500 m. The climate is hot and dry in summer, with large temperature swings, intense solar irradiation, and strong winds. The winter is cold and moderately wet, characterized by very low precipitations (160 mm/year), very high temperatures in summer, and low temperatures in winter (frosty from December to mid-February). The temperatures vary between a maximum of around 50 °C and a minimum of 20 °C, thus

A. Kaddour (✉) • S.M.A. Bekkouche
Unité de Recherche Appliquée en Energies Renouvelables URAER, Centre de Développement des Energies Renouvelables (CDER), 47133 Ghardaia, Algeria
e-mail: kaddour.majid@gmail.com

© Springer International Publishing AG, part of Springer Nature 2018

F. Aloui, I. Dincer (eds.), *Exergy for A Better Environment and Improved Sustainability 2*, Green Energy and Technology,
https://doi.org/10.1007/978-3-319-62575-1_38

Fig. 1 Descriptive plan of studied housing

giving a large diurnal temperature swing. Winter temperatures vary between a maximum of 24 °C and a minimum of 0 °C. Its normal temperature in January is 10.4 °C; it is 36.3 °C in July. And the average annual range is about 12.2 ° amplitudes of monthly average temperatures. They are more moderate in winter than in summer (average 11° in winter cons 13.5° in summer). The monthly maximum amplitudes are larger in summer than in winter, which fluctuates around 20 °C. Solar irradiation is intense throughout the year with a maximum of 700 Wm-2 in winter and 1000 Wm-2 in summer, measured on the horizontal surface Mingozzi (2009).

In Ghardaia region, stone is the most used material for construction because of its widespread availability. In carrying out the current work, our inspiration stems from Ghardaia traditional housing architecture. It is adapted to contemporary life convenience, where local materials such as stone, plaster, and mortar cement are used. Figure 1 represents a schematic view of typical housing of 88 m^2 areas, and walls' height is equal to 2.8 m.

Temperatures of windows and doors, made of ordinary wood, depend on several factors including local climate, orientation, frame (frame + insert), relative area (window, flooring), and solar and nocturnal occultation performances. When external temperatures are moderate, these surfaces would yield a higher gain.

Nomenclature

g	Gravitational constant ($m.s^{-1}$)
A	Area (m^2)
A_i	Area of the zone surface I, (m^2)
A_L	
C_p	Specific heat of the air (J/(kg.K)
C_w	Coefficient for wind-induced infiltration ($(L/s)^2/(cm^4\ (m/s)^2)$)
C_z	Air capacitance (J/K)

(continued)

F_{schedule}	Value from a user-defined schedule [0,.. .,1]
h_{i}	Heat transfer coefficient (W/(m^2. K))
$\times$	Mass airflow due to infiltration (kg/s)
$\dot{m}_{\text{i}}$	Mass airflow due to interzone air mixing (kg/s)
$\dot{m}_{\text{sys}}$	Mass airflow of the systems (kg/s)
$\dot{Q}_{\text{i}}$	Convective internal loads (J/s)
$\dot{Q}_{\text{sys}}$	Heat power of the air systems (W)
s_{wind}	Local wind speed (m/s)
t	Time (s)
T_{z}	Indoor air temperature (K)
T_z^t	Indoor air temperature at the time b step t
$T_z^{t-\delta t}$	Indoor air temperature at the previous time step t (K)
T_{si}	Temperature in the surface I (K)
T_∞	Outdoor air temperature (K)
T_{sup}	Temperature of the supply of air (K)
$\sum_{i=1}^{\text{N}_{\text{sl}}} \dot{Q}_i$	Sum of the convective internal loads (J/s)
$\sum_{i=1}^{N_{\text{surfaces}}} h_i A_i \ (T_{\text{si}} - T_{\text{z}})$	Convective heat transfer from the zone surfaces (J/s)
$\sum_{i=1}^{N\ \text{zones}} \dot{m}_i C_p \ (T_{\text{zi}} - T_{\text{z}})$	Heat transfer due to interzone air mixing (J/s)
$\dot{m}_{\text{inf}} C_{\text{p}}(T_\infty - T_{\text{z}})$	Heat transfer due to infiltration of outsider air (J/s)
$\dot{Q}_{\text{sys}}$	Air system output (J/s)
$C_z \frac{\text{d}T_z}{\text{dt}}$	Power stored in the zone air (J/s)

2 Energetic Balance

If we seek to optimize comfort by minimizing bought consumed energy, thus it is vital to understand the importance and behavior of heat flow. Otherwise, it would be difficult and costly to measure all heat fluxes passing through the building and practically impossible in case of a building under construction. Therefore, the energy balance determination is of paramount importance Fanger (1982).

Building energy balance is based upon the fact that practically all energy fluxes penetrating a given building end up transformed to heat. Given that on average basis the building's inside temperature remains constant, thus all energy fluxes would exit.

Energy balance penetrating and exiting a building is compatible for a given period of time. It is evident that this balance must be equilibrated by energy conservation.

Table 1 Housing energy balance

Gradual losses	Gains
Heat transmission through envelope	Solar radiation penetrating through windows and other passive collectors
Heat transmission through floor	Inhabitants' metabolic heat
Heat losses in stale air	Solar collectors
Heat loss in sewage (hot water) and structure-accumulated heat	Heat returned by the structure
Technical installation gradual loss	Fuel electrical energy supply
Total losses	Total gains

Energy balance includes all gains and losses and the consumption (see Table 1) period is equal and is relatively high (a year as a typical example, even a month if no high storage capacity exists).

The housing receives energy of different forms:

- Fuels: diesel, gas, and woods
- Electricity

Solar radiation and external thermal radiation

3 Instantaneous Thermal Balance

Heat transfers may be carried out in several processes: conduction in stationary material, convection in case poof fluid, radiation in transparent medium, and vaporization-condensation of water vapor.

It is evident that a relatively precise resolution, of all dynamical equations that model heat transfer, coupled with limit conditions (between different materials and meteorological data) and subject to a given initial condition, in real housing comprising hundreds of construction elements and occupied by a resident with varying living conditions, is only achieved using powerful computers equipped with a dedicated software.

If by means of dynamical method, one knew all fluxes and temperatures present in housing at each time instant, one can integrate these values over a given time period (month, season, and year as example) and determine consumed thermal energy by housing and comfort conditions over that period.

Thermal instantaneous balance may be written in the following manner: required power to heating Pc is equal to the sum of losses (transmission and ventilation) minus solar gains and internal gains plus accumulated heat inside housing.

Air thermal balance of a given zone of housing is given by Perez (2012):

$$C_z \frac{dT_z}{dt} = \sum_{i=1}^{\text{Nsl}} \dot{Q}_i + \sum_{i=1}^{\text{Nsurfaces}} h_i A_i (T_{si} - T_z) + \sum_{i=1}^{\text{Nzones}} \dot{m}_i C_p (T_{zi} - T_z) + \dot{m}_{\text{inf}} C_p (T_\infty - T_z) + \dot{Q}_{\text{sys}} \quad (1)$$

This balance depends on internal convection loads, heat transfer by convection with different zone surfaces, heat transfer due to air infiltration, and any existing aeration systems.

In order to solve Eq. 1, an algorithm is designed to obtain internal temperature of the studied zone. The solution is given by:

$$T_z^t = \left(T_z^{t-\delta t} - \frac{\sum_{i=1}^{N_{\text{sl}}} \dot{Q}_i + \sum_{i=1}^{N_{\text{surfaces}}} h_i A_i T_{si} + \sum_{i=1}^{N_{\text{zones}}} \dot{m}_i C_p T_{zi} + \dot{m}_{\text{inf}} C_p T_\infty + \dot{m}_{\text{sys}} C_p T_{\text{sup}}}{\sum_{i=1}^{N_{\text{surfaces}}} h_i A_i + \sum_{i=1}^{N_{\text{zones}}} \dot{m}_i C_p + \dot{m}_{\text{inf}} C_p + \dot{m}_{\text{sys}} C_p} \right) \times \exp\left(- \frac{\sum_{i=1}^{N_{\text{surfaces}}} h_i A_i + \sum_{i=1}^{N_{\text{zones}}} \dot{m}_i C_p + \dot{m}_{\text{inf}} C_p + \dot{m}_{\text{sys}} C_p}{C_z} \delta t \right) + \frac{\sum_{i=1}^{N_{\text{sl}}} \dot{Q}_i + \sum_{i=1}^{N_{\text{surfaces}}} h_i A_i T_{si} + \sum_{i=1}^{N_{\text{zones}}} \dot{m}_i C_p T_{zi} + \dot{m}_{\text{inf}} C_p T_\infty + \dot{m}_{\text{sys}} C_p T_{\text{sup}}}{\sum_{i=1}^{N_{\text{surfaces}}} h_i A_i + \sum_{i=1}^{N_{\text{zones}}} \dot{m}_i C_p + \dot{m}_{\text{inf}} C_p + \dot{m}_{\text{sys}} C_p} \quad (2)$$

4 Gradual Losses Through Ventilation

Housing ventilation may engender energy consumption for the following:

1. To heat, cool, and condition external air in order to bring its temperature and its moisture to comfortable values Fanger (1988)
2. To move the cold air and the stale air.

Energy consumption to conditioning air is done in such way that housing is whether equipped or not with a dedicated ventilation system or air conditioning facility. This consumption is basically given by

$$Q_V = m\ \Delta H(1 - \eta_r) = \rho\ \dot{V}\ t\ \Delta H(1 - \eta_r) \quad (3)$$

Q_V is energy consumption over a considered time period [J].
m is air mass passing through housing [kg].
ΔH is enthalpy difference between internal and external air, including the amount of energy required for varying temperature and humidity [J/kg] (not to be confused with between H, enthalpy in J/kg, and coefficient of gradual losses in W/K).
ρ is air volumic mass [kg/m^3].
$\dot{V}$ is air rate [m^3/h].
t is considered the time period.

$\eta_r$is heat recovered from fouled air efficiency.

In housing without an air conditioning system, in winter, moisture contribution is largely ensured by human activities and moistener is often unnecessary. Besides that, ventilation is often natural.

In this case, the demand of energy is restricted to that required for heating:

$$Q_V = m\, C_p \Delta T(1 - \eta_r) = \rho\, \dot{V}\ t\, C_p \Delta T(1 - \eta_r) \tag{4}$$

where ΔT is the difference in temperature between inside and outside and C_p is air-specific heat (1000 J/kg·K).

For coefficient of gradual loss caused by ventilation, H_V is thus

$$H_V = \dot{m}\ C_p(1 - \eta_r) = \rho\, \dot{V}\ t\, C_p(1 - \eta_r) \tag{5}$$

At ambient temperature, ρC_p is equal to 1200 J/(m^3 K) or 0.33 Wh/(m^3 K).

5 Heat Recovery

In case of building equipped with heat return system between fresh and extracted air, gradual losses caused by mechanical ventilation are reduced by a factor $(1 - \eta_r)$, where η_r is global efficiency of the heat return system.

For system with heat recovery capacity from fouled air toward water heating system or local heater using heat pump, the rate of air renewal is calculated without reduction. The lowering of energy need due to heat recovery is thus taken into account when calculating the considered energy consumption system.

It is important to note here that η_r is the global efficiency of recovered heat which is always less than the exchanger recovery capacity efficacy, determined in the production site. According to measurement done by the author, the global real efficiency is at best near 85% of the theoretic efficacy and be equal to nil in most extreme critical cases (see Fig. 2). Only heat of fouled air that passes through the exchanger is recovered. Indeed, heat within the air is lost through exfiltration along the envelope of the housing or in air circulating through opening located between extraction canal and pulse canal, is not recovered. In addition to that, the recirculation increases pulsed air rate without improving air quality. All carried out calculation is done to obtain a relationship between exchanger recovery efficacy, $\varepsilon_{\mathrm{HR}}$, and global heat recovery and is given by:

$$\eta_r \cong \frac{(1 - \gamma_{\mathrm{exf}})(1 - R_{\mathrm{e}})}{1 - R_{\mathrm{e}}\, \gamma_{\mathrm{exf}}}\ \varepsilon_{\mathrm{HR}} \tag{6}$$

γ_{exf} is the exfiltration ratio, including fresh air rate and the amount of fresh air that penetrates the housing and escapes through envelope openings.

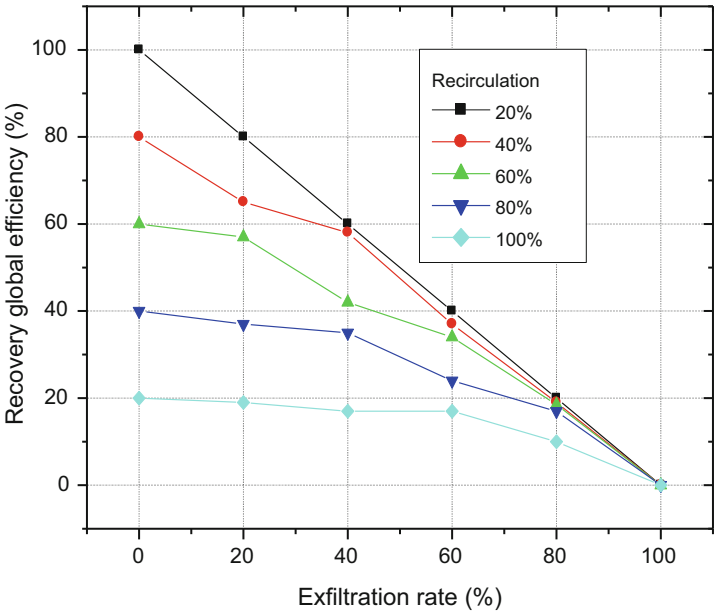

Fig. 2 Recovery global efficiency in function of internal recirculating and exfiltration rate, respectively

R_e is the recirculation rate including extracted air rate that recirculate.

6 Internal Gains

These heat gains "free of charge" emanate from metabolic heat of inhabitants and heat radiated by appliances, lighting, etc. that are not specifically devoted to heating but resulting from other energy consumption processes inside the heated volume.

Thermal power evacuated by inhabitants present during a time period h may be calculated using Eq. (5):

$$\phi_h = N\frac{\mathrm{Ph}}{24} = A\frac{\mathrm{Ph}}{24D} \tag{7}$$

N Number on inhabitants present in heated zone
P Evacuated power by inhabitant
h Presence time in hour per day
A Heated flooring crude surface occupied by inhabitants
D Available surface to inhabitants

Table 2 Thermal power evacuated by inhabitants, according to SIA (2001)

Housing type	Occupation (m^2/pers)	Presence (h/j)	Power (W)
Collective housing	40	12	70
Individual housing	60	12	70
Office	20	6	80
School	10	4	70
Restaurant	5	3	100

Table 3 Thermal power dissipated by appliances, associated with heated crude floor surface, according to SIA (2001)

Housing type	Annual consumption (MJ/m^2)	Correction factor
Collective housing	100	0.7
Individual housing	80	0.7
Office	80	0.9
School	40	0.9
Restaurant	120	0.7

The presence rate depends on inhabitant type that can be classified into two categories: housing or establishment such as school. The evacuated power depends on activities and inhabitants' size. We can however admit that there is an average activity and classify inhabitants into two categories: adults and infants. SIA 380/1 proposes figures given in Table 2.

The power supplied by appliances is generally calculated from electrical power P_{el} consumed by appliances:

$$\phi_a = P_{el} f_e \tag{8}$$

where f_e is a correction factor taking into account the fact that electrical apparatus are not present in heated space together (e.g., public lighting, freezer in the basement, etc.).

[SIA, 2001 #328] proposed figures given in Table 3 for average consumed electrical power for heated floor surface P_{el}/SPC and for factor f_e.

Thus, the internal energy is given in period t by

$$Q_i = t\ (\phi_h + \phi_a) \tag{9}$$

At the first approximation, internal gain rates for a given family are in the order of 1300 MJ for a month period, having an average power of 500 W. Another method consists in counting an average power of 5 W/m^2 of flooring in the housings.

7 Heating Needs

The gradual loss, Q_l, and heat supplies, Q_g, are calculated for each step of period calculation. The need of heating of locals for each period is summarized as follows:

$$Q_h = Q_l - \eta Q_g \tag{10}$$

where:

Q_l Heat gradual losses
Q_g Heat gains
η Utilization rate

8 Results and Discussions

The rate of utilization takes into account the fact that we have from time to time whether to reject or not to collect a part from internal gains and/or solar in order to avoid overheating. According to Fig. 3, the utilization rate depends on the ratio of gain to losses γ, of housing thermal inertia expressed by a time constant τ, and amplitude of admitted temperature variation in case of internal temperature.

We see in Fig. 4 the regulation system of the heater has also influence on utilization of gains, but in practice, we prefer to take into account this fact separately. Housing thermal balance is calculated as possible independently of heating system, and imperfect control effects are then included in global efficiency of the heating system.

The heating system is supposed to be perfectly regulated; parameters presenting a major influence on utilization rate are the following:

The ratio of gradual loss, γ, is defined as

$$\gamma = \frac{Q_g}{Q_l} \tag{11}$$

The variation of utilization rate with its variables is well described by empirical relationship:

$$\eta = \frac{1 - \gamma^a}{1 - \gamma^{a+1}} \quad \text{si } \gamma \neq 1 \tag{12}$$

$$\eta = \frac{a}{a+1} \quad \text{si } \gamma = 1$$

where a is numerical parameter depending on time constant τ.

Figure 3 gives utilization rate for period of calculation on a monthly basis for several time constants.

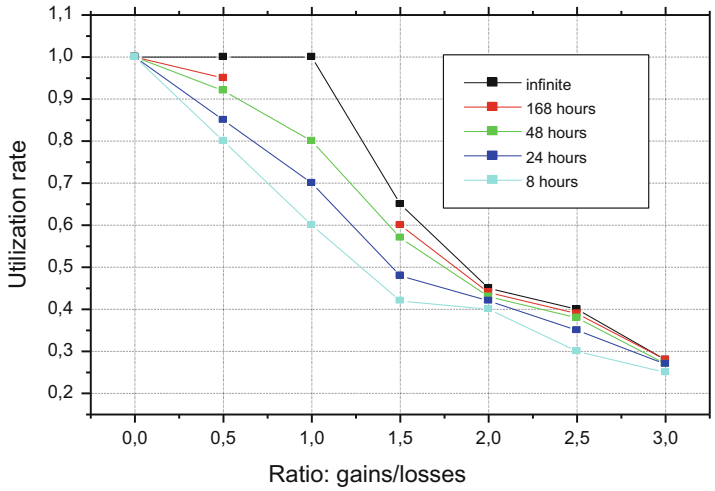

Fig. 3 Utilization rate in function of gains/gradual loss ratio for constant times 8 h, 1 day, 2 days, 1 week, and infinite, valid for calculating period of 1 month

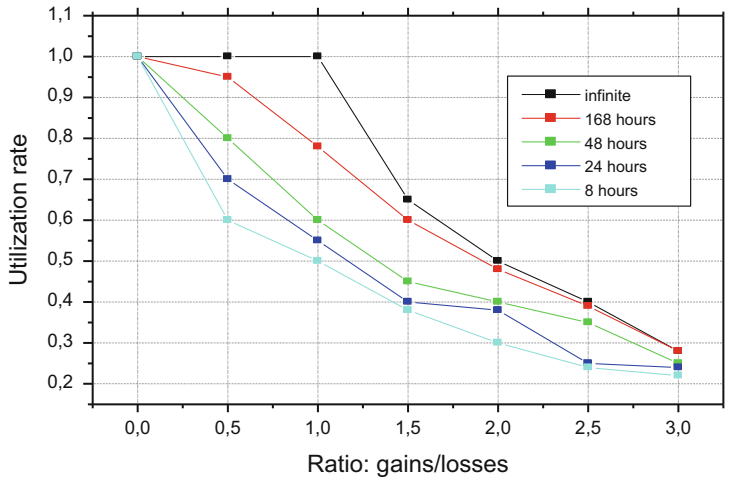

Fig. 4 Utilization rate in function of gains/gradual loss ratio for housing lightly permanently heated and housing heated during day only

According to Fig. 5, an important difference between external and internal air temperature is spotted.

Furthermore, semi-open windows contribute to reduce internal air temperature; we can notice that the opening effect represents the important factor of internal temperature variation.

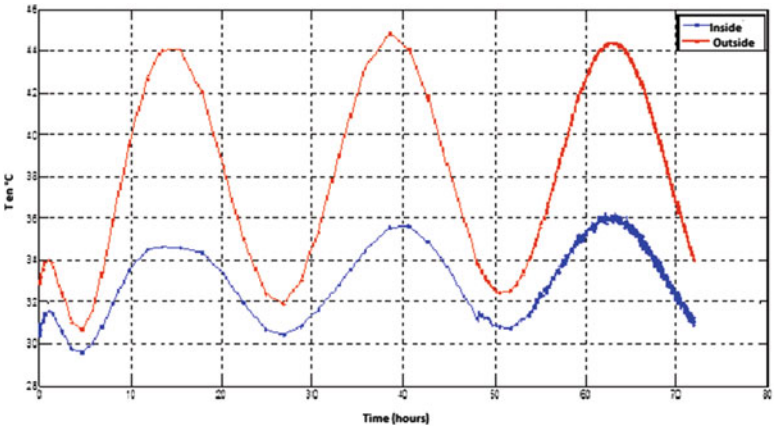

Fig. 5 Comparison between internal and external temperature variation (21–23 July 2013)

The building forms a single entity including the structure, installations, and occupants. An action on one of its components may have secondary effects on other components. In this section, we examine some of these interactions.

Strong moisture favors the growth of moisture agents and other microorganisms that can demolish building structure and its occupant. In order to limit the risk, it is most recommended to avoid the following:

Leaks in envelop (mainly ceiling) and in water pipes or sewer
Any condensation over internal surfaces of housing's outer walls during the most coldest periods
That relative local moisture exceeds 80% on surfaces susceptible to favor the growth of moisture (plasters, woods, wall paper, paintings, etc.)
Water vapor can be condensed in sufficient quantity inside walls.

It is generally also admitted that the risk of growth of moisture on walls increases strongly when local humidity relatively exceeds 80%. This humidity depends on several factors:

Wall surfaces' temperature
Ventilation rate
Vapor production in air

The simple developed model given below allows estimating this risk. Temperature of internal surface of the element is given by

$$T_{s,i} = T_e + f_{Rsi}(T_i - T_e) \tag{13}$$

where T represents temperatures, index i designs inner and e outer, and f_{Rsi} is peripheral temperature coefficient that can be computed in all places at all times by solving heat equation.

Partial pressure of water vapor of external air depends also of its external temperature. The following mixture ratio is deduced:

$$x_e = \frac{M_w}{M_a}\frac{P_e}{P_a - P_e} = 0.62198\frac{P_e}{P_a - P_e}\ [\text{kg/kg}] \tag{14}$$

where:

M is molar mass (index e for water, a for air)
P_a is atmospheric pressure (101,300 Pa in normal conditions at sea level)

Minimum air rate $\dot{V}_{min}$ is allowed to avoid moisture growth risk and is given by

$$\dot{V}_{min} = \frac{S_{e,i}}{\rho_a(x_i - x_e)} \quad [\text{m}^3/\text{h}] \tag{15}$$

where:

$S_{e,i}$ is rate production of water vapor inside [kg/h]
ρ_a is volumic mass of internal air [kg/m^2]

By solving this equation, we obtain mixture ratio of internal air for a given air rate and rate of production and a given humidity rate production:

$$x_i = \frac{S_{e,i}}{\rho_a \dot{V}} + x_e \quad [\text{kg/kg}] \tag{16}$$

Hence, pressure vapor inside is

$$p_i = \frac{M_a P_a x_i}{M_a x_i + M_e} = \frac{P_a x_i}{x_i + 0.62198} \quad [\text{Pa}] \tag{17}$$

This model allowed to plot the Fig. 6. We show minimum air rate necessary to evacuate water vapor produced by a person and avoid the risk of moisture. Air rate can be reduced because of cold when external air is particularly dry but may significantly be increased at midseason.

Note that temperature factor (see Fig. 7) in insulated walls according to modern norms ($U < 0.3$ W/m^2 K) is at least 0.85. It is with thermal bridges that this factor may be reduced and achieves its critical value.

At the time of appearance of moisture in the housing, it often happens that the landlord blamed the occupant of producing too much humidity or insufficient ventilation. However, occupant claims that the insulation is absent.

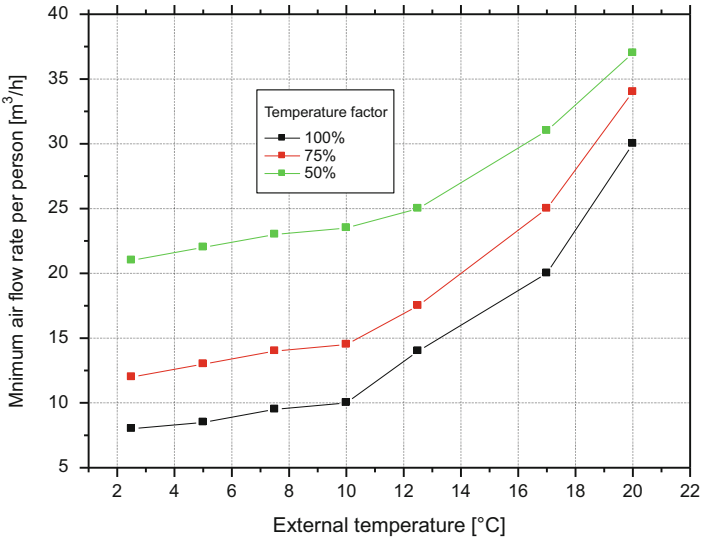

Fig. 6 Minimum air flow rate per person, at 20 °C internal temperature

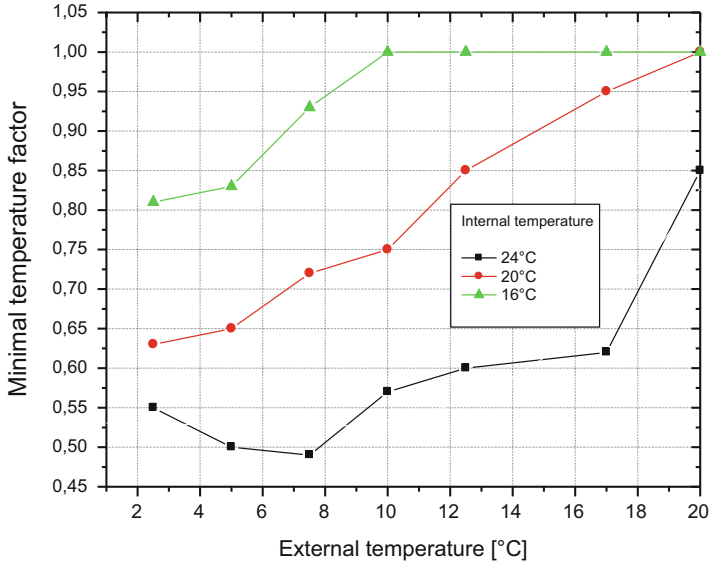

Fig. 7 Minimal temperature factor f_{Rsi} minimal at 15 m^3/h per person

9 Conclusions

This leads to the circulation of large quantities of air in the ventilated space, without producing any real dilution effect, which in turn leads to great heat losses. The right solution is the natural ventilation, which makes it possible to minimize heat losses because the air mixing occurs during the ventilation stop period.

To demonstrate the influence of the internal and external temperatures, this study also conducted housing energy simulations associated with air change rates deduced by the energy simulation program and calculations based on Matlab software.

The natural ventilation of building that successively open and close at regular time intervals can limit the excessive circulation of air masses, which in turn limits heat losses.

The ratio of gain to losses, γ, of housing thermal inertia has a big effect on the utilization rate. The natural ventilation concepts are evaluated.

References

Bekkouche, S.M.A., Benouaz, T., Yaiche, M.R., Cherier, M.K., Hamdani, M., Chellali, F.: Introduction to control of solar gain and internal temperatures by thermal insulation, proper orientation and eaves. Energ. Buildings. **43**(9), 2414–2421 (2011)

Fanger, P.O.: Thermal Comfort. R. E Krieger, Florida (1982)

Fanger, P.O., Melikov, A.K., Hansawa, H., Ring, J.: Air turbulence and the sensation of draught. Energ. Buildings. **12**, 21–39 (1988)

Mingozzi, A., Bottiglioni, S., Medola, M.: Passive cooling of a bioclimatic building in the continental climate of the padan plain: analyzing the role of thermal mass with dynamic simulations. Int J Sustainable Energy. **28**, 141–156 (2009)

Perez, I.V., Østergaarfb, P.A., Remmenb, A.: Model of natural ventilation by using a coupled thermal-airflow simulation program. Energ. Buildings. **49**, 388–393 (2012)

Teppner, R., Langensteiner, B., Meile, W., Brenn, G., Kerschbaumer, S.: Air change rates driven by the flow around and through a building storey with fully open or tilted windows: An experimental and numerical study. Energ. Buildings. **80**, 570–583 (2014)

Mathematical Filtering Analysis of Infrared Images in Integrated-Circuit Techniques

Imre Benkö

1 Introduction

This paper covers only the data obtained through the computer processing of infrared (IR) thermograms which had to be evaluated because the IR images were gained from various measurements and because of the nature of the objectives (Benkő 1992, 1997). The methods of filtering can be grouped as follows: smoothing filters, sharpening filters, band filters and gradient filters. It is important to emphasize that, after the filters are applied, the colours and temperatures indicated in the resultant image have no relation to the actual temperatures but to the physical essence of the filtering method selected. The illustrations for IR image analysis are taken from the electronics industry (see Fig. 1a, b) (Benkö 1998).

2 Generalities

The principal objective of image enhancement techniques is to process an image so that results are more suitable for a specific application than the original image. In the IR thermogrammetry the goal of the image processing is to obtain a new IR image showing some thermal faults or singularities in the temperature field. It is to be noted that the image enhancement techniques are very much problem oriented.

I. Benkö (✉)
Budapest University of Technology and Economics, Budapest, Hungary

Faculty of Mechanical Engineering, Institute of Thermal Engineering,
Cirmos u.1, H-1112 Budapest, Hungary
e-mail: ibenko@freestart.hu

© Springer International Publishing AG, part of Springer Nature 2018

F. Aloui, I. Dincer (eds.), *Exergy for A Better Environment and Improved Sustainability 2*, Green Energy and Technology,
https://doi.org/10.1007/978-3-319-62575-1_39

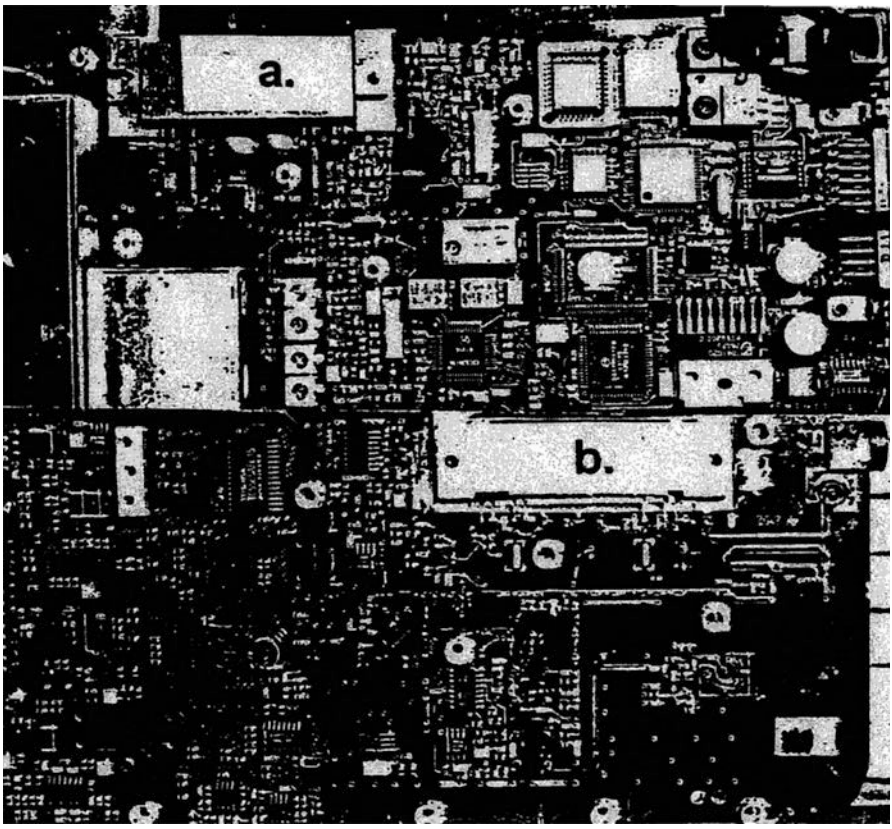

Fig. 1 (**a**) The component side and (**b**) the chip side of an integrated circuit

Generally, image enhancement methods are based on either spatial or frequency domain techniques. The spatial domain refers to the image plane itself, and approaches in this category are based on direct manipulation of pixels in an image. Frequency domain processing techniques are based on modifying the Fourier transform of an image (see Sect. 6).

3 Spatial Domain Methods of Image Filtering

The term spatial domain refers to the aggregate of pixels composing an image, and spatial domain methods are procedures that operate directly on these pixels (Gonzales and Woods 1977). Image processing functions in the spatial domain may be expressed as

$$g(x, y) = T[f(x, y)] \tag{1}$$

where $f(x,y)$ is the input image, $g(x,y)$ is the processed image and T is an operator on f, defined over some neighbourhood of (x,y).

One of the principal approaches in eq. (1) is based on the use of so-called masks (also referred to as templates, windows or filters). Basically, a mask is a small two-dimensional array, in which the values of the coefficients determine the nature of the process, such as sharpening. Enhancement techniques based on this type of approach often are referred to as mask processing or filtering.

4 Smoothing Filters

Smoothing filters are used for blurring and for noise reduction. Blurring is used in preprocessing steps, such as removal of small details from an image prior to (large) object extraction, and bridging of very small gaps in line or curves. Noise reduction can be accomplished by blurring with a linear filter and also by non-linear filtering.

4.1 Neighbouring Filter

In this filtering function the value of the pixel is calculated by averaging the values of the neighbouring pixels. Either four or eight neighbouring pixels can be included. For four pixels the equation $g(x,y)$ is defined as follows:

$$g(x, y) = \frac{1}{4}\sum\nolimits_{(n,m)} f(n, m) \tag{2}$$

In the above equation, $g(x,y)$ is the modified pixel and $f(n,m)$ is the neighbouring pixels.

4.2 Sharpening Filters

The principal objective of sharpening is to highlight fine details in an image or to enhance detail that has been blurred, either in error or as a natural effect of a particular method of image acquisition. Uses of image sharpening vary and include applications ranging from electronic printing and medical imaging to industrial inspection and detection of some thermal faults in a printed circuit in electronic technology.

4.3 Derivative Filters

Averaging of pixels over a region tends to blur detail in an image. As averaging is analogous to integration, differentiation can be expected to have opposite effect and thus to sharpen an image. The most common method of differentiation in image processing applications is the gradient.

4.4 Gradient Filter

The gradient filter assesses a pixel with regard to the numerical difference to its neighbourhood pixels. Either of the two gradient equations can be selected:

(a) Common (or normal) gradient equation
(b) The so-called Roberts gradient equation

They differ in how the neighbouring pixels are viewed.

The normal gradient. The gradient (difference) equation is defined as follows:

$$g(x,y) = [f(x,y) - f(x+1,y)] + [f(x,y) - f(x,y+1)] \tag{3}$$

The result $g(x,y)$ replaces $f(x,y)$.

The Roberts gradient. The gradient equation is defined as follows:

$$g(x,y) = [f(x,y) - f(x+1,y+1)] + [f(x+1,y) - f(x,y+1)] \tag{4}$$

The result $g(x,y)$ replaces $f(x,y)$.

In both gradient filter functions, the calculated value of the pixel can be modified by further parameter options.

5 Matrix Filter

Within the function, three filter sub-functions are available:

(a) Low pass
(b) High pass
(c) User

The matrix filter works according to the following mathematical operation. The pixel value of a 3x3 matrix is replaced by the relation

$$g(m_1,m_2) = \sum\nolimits_{n1}\sum\nolimits_{n2} \boldsymbol{F}(n_1,n_2) \times \boldsymbol{H}(m_1 - n_1 - 1, m_2 - n_2 + 1) \tag{5}$$

where $\boldsymbol{F}$ and $\boldsymbol{H}$ represent the image matrix and the convolution matrix, respectively.

5.1 Sobel Filter

The Sobel filter is a special matrix filter which is particularly suitable for recognizing contours. The results are similar to those achieved with the gradient filter.

In the Sobel filter, the gradient equation is as follows:

$$g = \mathbf{w_1 x} + \mathbf{w_1}^{\mathbf{t}}\mathbf{x} \tag{6}$$

where $\mathbf{w_1}$ is the 3×3 weight matrix that the user has to define, and $\mathbf{w_1}^{\mathbf{t}}$ is the weight matrix transposed from $\mathbf{w_1}$ and $\mathbf{x}$ is the 3×3 image section matrix. For pixel modification, the centre pixel of the image section matrix $\mathbf{x}$ is replaced. This is always taken from the original image.

6 Analysis of Thermal Singularities of an Integrated Circuit

The applicability (advantages and limitation) of IR images and their scientific value are determined in the technical practice by the following main features:

(a) The type of the technical phenomenon investigated
(b) Consideration of rules of IR optics during the IR image taking
(c) Proper selection of ambient parameters

Under optimum conditions, the IR image will contain important information on the thermal character of the temperature field of the examined object or phenomenon. As a consequence, the evaluation of IR images, the thermal physical characteristics and the interpretation will contribute to the scientific value of IR images.

In the actual practice of IR image analysis, the following general methods may be chosen, while their relative advantages and disadvantages must be decided in the light of the test being done. The first is the traditional phenomenological analysis, e.g. determination of the temperature at specified points (e.g. the centre point of the cross hairs) (see Fig. 3a), a comparison between temperature distribution along the horizontal, vertical or optional lines (see Fig. 3a) and relief representation of the temperature field (see Fig. 3c). Two new methods serve for mathematical evaluation of temperature fields:

(a) Histographic analysis, i.e. the application of the distribution curve of temperature histogram for process monitoring (see Fig. 3b) (Benkö et al 1998)
(b) Mathematical filtering of IR images to reveal the sites of highest temperature or of the largest temperature alteration (see Fig. 2)

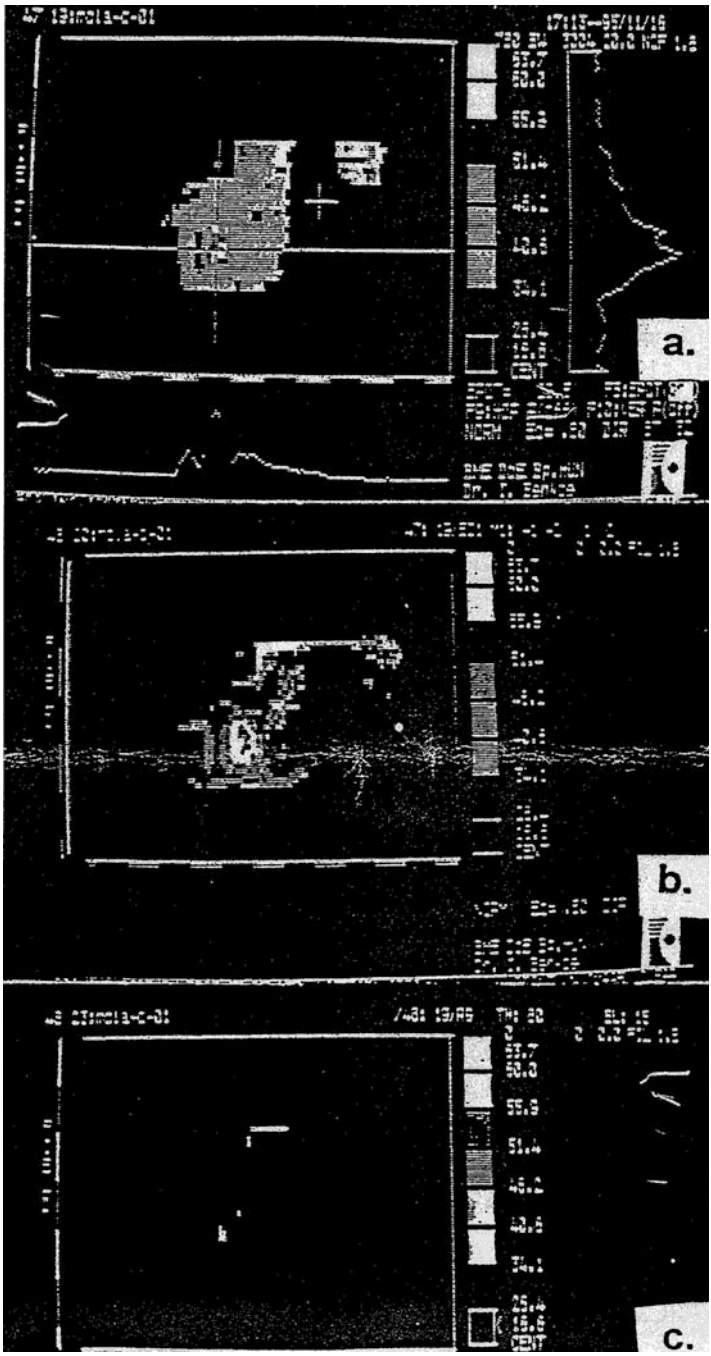

Fig. 2 Series of IR images concerning the filtering of (**a**) original IR image, (**b**) first step (the Sobel filter) of filtering and (**c**) second step (*the Roberts gradient*) of filtering

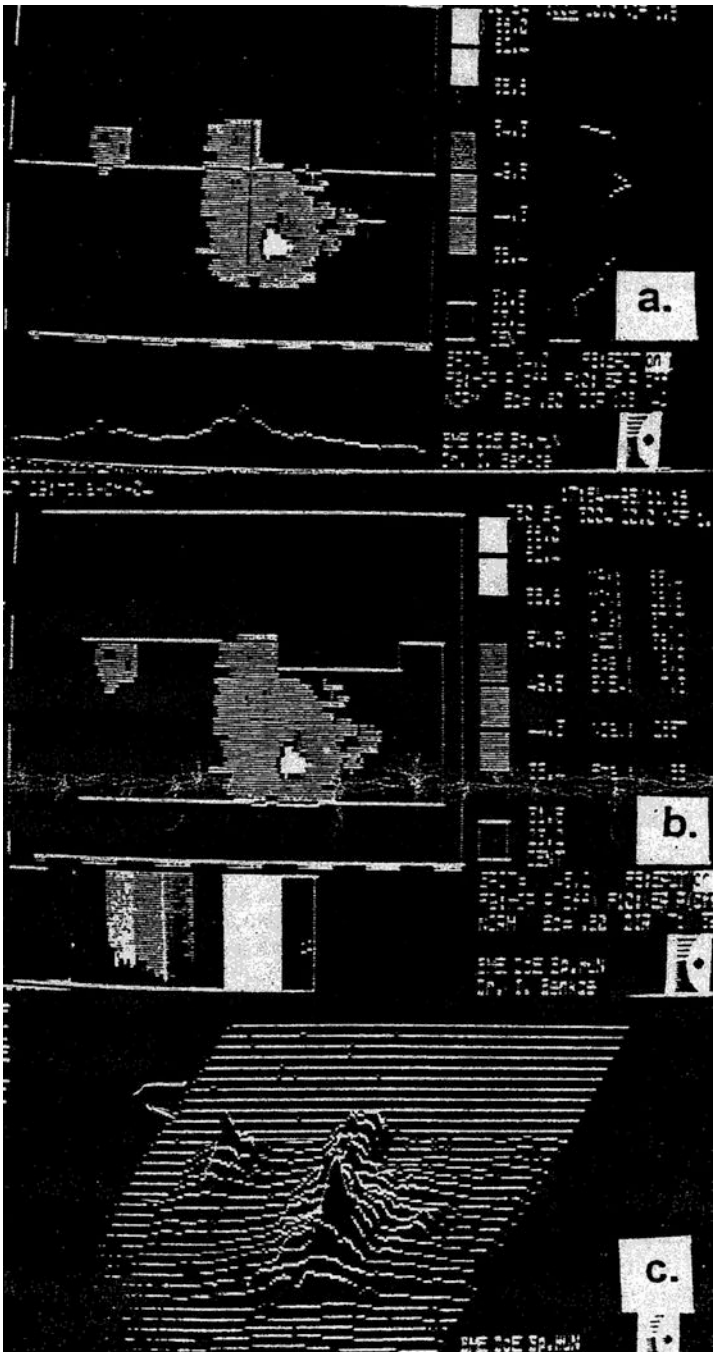

Fig. 3 Common evaluation of IR images on the chip side (**a**) line thermogram, (**b**) histogram and (**c**) reli

(c) In the section, several techniques are from the field of integrated-circuit techniques (Fig. 1). An example for the filtering of the component side is shown in Fig. 2b (Sobel) and the applied Roberts gradient in Fig. 2c, where the thermal singularities can be seen. Therefore the recommendable process of mathematical filtering applying to the original IR images in similar technical cases is as follows. The first step is the Sobel filter which is a sharpening step, equalizing the smaller temperature differences so that the contours of the high-temperature field can be achieved (Fig. 2b). The second step is subsequent filtering of Fig. 2b by the Roberts gradient. The Roberts gradient filtering ensures that all the pixels have a gradient value larger than a threshold and the other filtering provides a background level value. Therefore Fig. 2 has a threshold of 80 and a background of 15 and shows the 'hot field' of the component side of the integrated circuit.

A common evaluation for analysis of the chip side (Fig. 1b) is presented in Fig. 3. For comparison of 'classical' and filtering evaluation of IR images, Fig. 3 presents some possibilities for chip side of the integrated circuit (Fig. 1b). Figure 3a shows the temperature distribution along lines created horizontally and vertically, similar to Fig. 2a. Figure 3b is the histographically processed result of Fig. 3a, representing the more significant characteristics of the histogram in the specified area in Fig. 3b: the highest (maximum 65.4 °C), the lowest (minimum 28.6 °C) and the middle (average 37.7 °C) temperature, etc. Figure 3c is a three-dimensional relief display of Figs. 3a and 4.

When the spots with the highest temperatures on both the chip and the component sides are known, the faulty or improperly sized elements can be replaced. Thus unexpected later failures due to the high local thermal load can be prevented.

7 Conclusions

IR image filtering is a practical, quick and normalizable evaluation method with the aim of analysing the temperature field initially. The topic presented in this paper is representative of techniques that are commonly used in practice for digital IR image enhancement. However, this area of image processing is basically problem oriented, and a dynamic field in the literature, too. For this reason, the methods included in this paper have to select both the topic and the goal of thermal analysis.

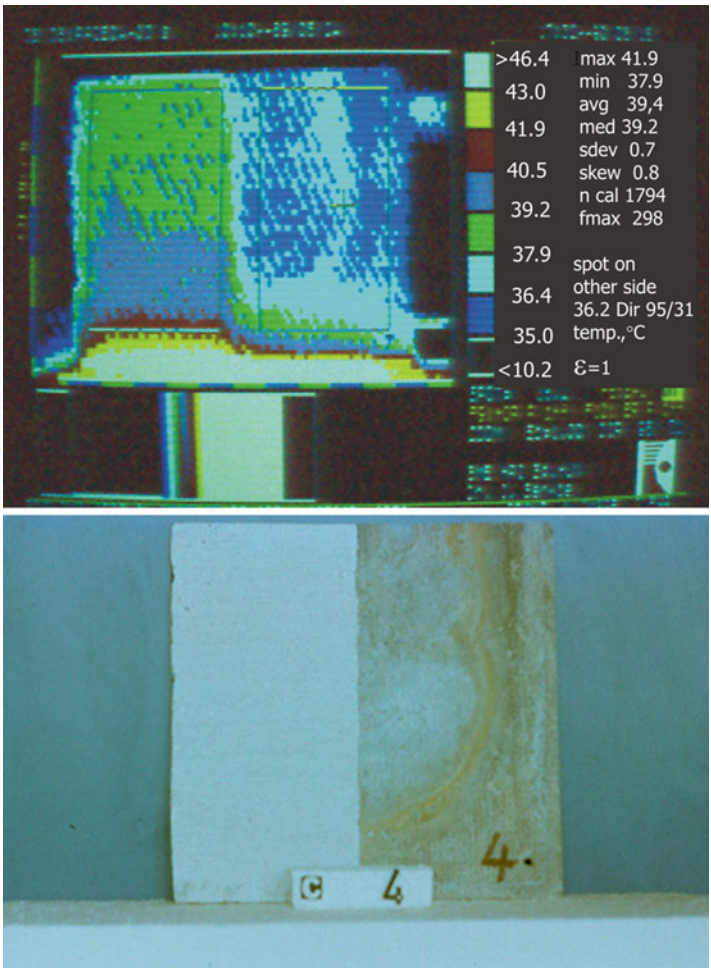

Fig. 4 Infrared thermogram (above) of a sample (Pace-04) and picture of coated slate roof

References

Benkő, I.: Applications of infrared thermogrammetry in thermal engineering. In: Proceeding of the Conference on Quantitative Infrared Thermography (QIRT 92). Eurotherm Séries 27, pp. 343–349. Edition Européennes Thermique et Industrie, Paris (1992)

Benkö, I.: Infra-red picture analysis in thermal engineering. In: Benkő, I. (ed.) Proceedings of the Tenth International Conference on Thermal Engineering and Thermogrammetry, pp. 46–52. MATE TE and TGM, Budapest (1997)

Benkö, I.: Applications of infrared filtering in electronic technology. In: Wiecek, B. (ed.) Book of Abstracts of Quantitative Infrared Thermography (QIRT 98), pp. 86–87. PKOptoSEP, Lodz (1998)

Benkö, I., Köteles, G.J., Németh, G.: New infrared histographic investigation of the effect of beta-irradiation in medical field. In: Balageas, D., Busse, G., Carlomagno, C.M., Wiecek, B. (eds.) Proceedings of the Conference on Medical Infrared Thermography (MIRT 98), pp. 40–45. PKOptoSEP, Lodz (1998)

Gonzales, R.G., Woods, R.E.: Digital image processing. Addison-Wesley, Wokingham (1977)

Performance Analysis of Ceramic Composite Thermal Protection System Tiles

Arjunan Pradeep, Suryan Abhilash, and Kurian Sunish

1 Introduction

When a space craft enters a planetary atmosphere from space, the surface exposes to high heat fluxes generated by dissipation of kinetic energy due to aerobraking and friction with atmospheric gases, which depends on many parameters including entry velocity, entry angle, ballistic coefficient, vehicle bluntness, enthalpy characteristics, and density and temperature of atmospheric gases. The design of a successful thermal protection system (TPS) is a significant engineering challenge as its failure will ultimately breakup the entire craft including its payload, structure, and crew. Reusable TPSs are primarily developed for extended flight durations with much better insulating capacity than ablators and to maximize reradiation of the incident aerothermodynamic heat to atmospheric environment (Shukla et al. 2006).

Reentry vehicles with sharp leading edges imply lower aerodynamic drag, improved performance, safety, and maneuverability but results higher surface temperature than blunt vehicles. As the leading edge radius decreases, the surface temperature increases (Savino et al. 2010). Therefore, in order to achieve maximum performance, materials are needed, which are both capable of withstanding the reentry environment at temperatures greater than 2000 K and have a high thermal conductivity that will direct more energy away from the tip of the leading edge allowing for even further improvements in vehicle performance. It leads to the demand of development of high-temperature materials which can find applications in hypersonic flight vehicles with sharp leading edges. From the family of ceramic materials known as ultrahigh-temperature ceramics (UHTCs), refractory metal

A. Pradeep (✉) • S. Abhilash • K. Sunish
University of Kerala, Department of Mechanical Engineering, College of Engineering Trivandrum, Thiruvananthapuram 695016, India
e-mail: pradeeparch@gmail.com

© Springer International Publishing AG, part of Springer Nature 2018

F. Aloui, I. Dincer (eds.), *Exergy for A Better Environment and Improved Sustainability 2*, Green Energy and Technology,
https://doi.org/10.1007/978-3-319-62575-1_40

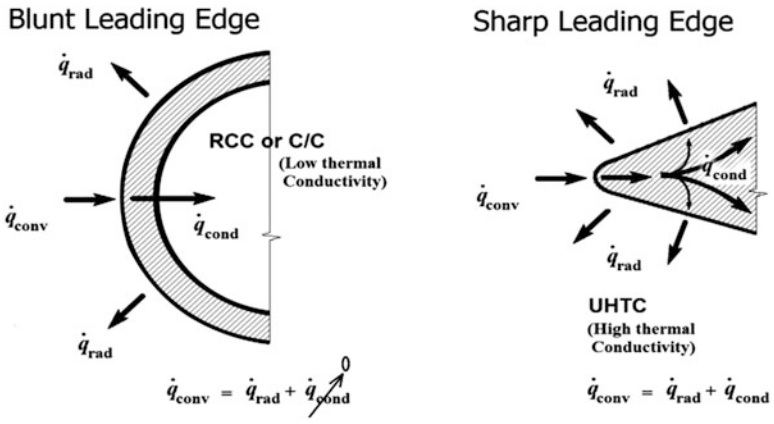

Fig. 1 Effect of conductivity for a blunt and sharp leading edge of a reentry vehicle

diborides with some additives such as SiC (e.g.: HfB_2-SiC) and/or refractory metal carbides (HfC), can be identified as most promising candidates as an effective thermal protection system for nose cap and other sharp leading edges. These materials are characterized by improved mechanical and thermal properties, excellent chemical stability like good oxidation resistance, and high melting point (>3000 K) (Savino et al. 2008).

Figure.1 shows how the surface temperature for the sharp UHTC leading edge is determined by an energy balance of incident heat flux, reradiated energy, and energy pulled away from the leading edge tip and reradiated out the sides of the component in which the incident heat flux is lower (Kontinos et al. 2001).

When a steady state is achieved, global radiative equilibrium is established, in the sense that the overall convective heat flux is perfectly balanced by the overall surface radiative flux, and, if the material thermal conductivity is high, a relatively low equilibrium temperature is achieved. Thus, the need for highly conducting yet refractory materials is essential in the design of sharp vehicles (Gasch et al. 2005).

Nomenclature

1-D,2-D,3-D	One, two, three dimensional
TPS	Thermal protection system
UHTC	Ultrahigh temperature ceramics
SiC	Silicon carbide
HfB_2	Hafnium diboride
ZrB_2	Zirconium diboride
HfC	Hafnium carbide
ZrC	Zirconium carbide
HfN	Hafnium nitride
$MoSi_2$	Molybdenum disilicide
Si_3N_4	Silicon nitride

(continued)

q	Heat flux
RCC	Reinforced carbon/carbon
MFI	Multifoil insulation
RSI	Reusable surface insulation
H	Specific total enthalpy
PWT	Plasma wind tunnel
SHS	Sharp hot structures
FEM	Finite element method
k	Conductivity
T	Temperature
C_p	Specific heat at constant pressure
C_v	Specific Heat at constant volume
Kn	Knudsen number
E	Extinction coefficient
Greek letters	
τ	Time in seconds
μ	Dynamic viscosity
γ	Ratio of specific heats
α	Accommodation coefficient
σ	Stefan-Boltzmann constant
ρ	Density
Subscripts	
rad	Radiative
cond	Conductive
conv	Convective
s	Solid
g	Gas

1.1 Problem Definition

The main objective of this work is to investigate the temperature distribution by conduction, convection, and radiation through ceramic composite porous tile. Currently, studies on thermal response of nonablating pure ceramic tiles are available as a TPS material applying on surface other than leading edges of wings and nose cone of a space vehicle, and in this study, performance analysis of TPS Tile made of silica-based ceramic composite is considered instead of a single-component silica tile.

2 Review of Literature

Comparison of measured and predicted temperature profiles of selected multicomponent TPS to an aerodynamic arc-jet environment was studied at surface heating rates high enough to include radiation heat transfer by Stewart and Leiser (1985).

Stauffer et al. (1992) developed a model for evaluating the steady-state heat transfer through multifoil insulation (MFI). The model enables the calculation of an effective thermal conductivity as a function of temperature and pressure. The heat transfer through MFI, a composite insulation system consisting of thin metallic foils held apart by tiny ceramic particles, consists of three components: foil to foil radiation heat transfer, gas conduction via interstitial gas molecules, and solid conduction through ceramic spacer particles. The radiation heat transfer and gaseous conduction models are validated by comparison with test data reported in the literature. Empirical correlations are developed to describe the nondimensional contact conductance, and these show that contact conductance is a function of configuration and operating conditions. The model can provide important information to designer of thermal protection system (TPS) of advanced hypersonic vehicles.

Chiu (1992) developed a simulation model and illustrates the thermal response of reusable surface insulation (RSI) tiles and blankets during aeropass. For some cases, experimental measurements were available from arc-jet testing, and comparison between calculated and measured temperature is also carried out. Thermal analyses of both tiles and blankets have been conducted in this study. Comparison between the in-depth temperatures of an advanced tile calculated using transient thermal conductivities and those measured under stagnation heating during arc-jet test show good agreement, which indicates the accuracy of the transient thermal conductivities. The analysis in this paper was carried out to predict the temperature performance of a spectrally reflective coating on a tile, to access the temperature errors in a tile due to thermo couple lead wires installations, to determine the extent of thermal distortion in a blanket due to adjacent tiles, and to correlate the temperature measurements of a thermocouple probe in a blanket.

The need of research and development of UHTC materials for low thrust rocket propulsion and hypersonic spacecraft applications are emphasized by Upadhya et al. (1997). They observes that by developing an ultrahigh-temperature material with temperature capabilities in the range of 2200–3000 °C, the fuel-film and regenerative cooling can be significantly reduced and/or eliminated resulting in cleaner burning of rocket engine. Thus, fuel utilization can be vastly improved, more payloads can be sent to space, higher specific impulse can be achieved, and finally, the cost of the rocket engine could be reduced. Mechanical, thermal, and oxidation behavior of refractory metals and alloys, refractory carbides, refractory borides, and carbon–carbon composites are summarized in the paper.

Opeka et al. (1999) reported mechanical, thermal, and oxidation properties of HfB2, HfC, HfN, ZrB_2, ZrC, and SiC ceramics. It was found that HfB_2 had a much

lower ductile-to-brittle transition temperature than HfN or HfC. The effect of lowering the carbon stoichiometry was also to decrease the transition temperature. The thermal conductivity of HfB_2 was much greater than the carbides or nitride. The coefficient of thermal expansion of all materials tested was approximately the same up to 1500 °C, with HfN exhibiting a higher expansion than the others up to 2500 °C. The HfB_2 ceramics had the highest modulus of the materials tested, whereas HfC had the lowest. The oxidation behavior of the ceramics was characterized as a function of phase composition. The SiC-containing ZrB_2 ceramics had high oxidation resistance up to 1500 °C compared with pure ZrB_2 and ZrC ceramics. The ZrB_2/SiC ratio of about 2 (25 vol% SiC) is necessary for the best oxidation protection. The presence of ZrC in ZrB_2 ceramics negatively affects their oxidation resistance. A hypothesis describing oxidation behavior of the ZrB_2/ZrC/SiC ceramics is proposed.

Daryabeigi (2002) investigated the use and optimization of high-temperature insulation for metallic thermal protection systems. The multilayer insulation considered consists of ceramic foils with high-reflectance gold coatings. Here, the author's main aim was to model the combined radiation/conduction heat transfer through multilayer insulations with a numerical model validated by experimental lists and to use the numerical model to design optimum multilayer configurations. The effective thermal conductivity of a multilayer insulation was measured over an extended temperature of 373–1273 K and a pressure range of 1.33×10^{-5} – 101.32 kPa. A numerical model was developed for modeling combined radiation/conduction heat transfer in high-temperature multilayer insulations. The numerical model was validated by comparison with steady-state effective thermal conductivity measurements and by transient thermal tests simulating reentry aerodynamic heating conditions. A design of experimental approach was used to determine the optimum design for multilayer insulations subjected to reentry aerodynamic heating condition.

The need for materials development, ground testing, and sophisticated modeling techniques for the development of new TPS material for future space missions are emphasized by Laub and Venkatapathy (2003). As a base information, they describe about two classes namely ablative and reusable TPS materials and a brief history of ablative TPS so far. They also describes the lessons learned and TPS challenges for future missions based on the Jupiter, Venus, Titan, Mars, Neptune, and other sample return missions. The authors pointed out that TPS innovations are required because above missions were done with materials developed over many decades ago. The authors emphasize on the establishment of a cross-cutting TPS Technology program with elements focused on sustaining current technologies and elements focused on enabling future higher speed return missions.

Matthew et al. (2005) summarizes experimental results on HfB_2- and ZrB_2-based compositions. They focused on identifying additives like SiC to improve mechanical and thermal properties and to improve oxidation resistance. These are characterized by high melting points, chemical inertness, and good oxidation resistance in

extreme environments at temperatures greater than 2000 °C as experienced during reentry. They are providing variation of thermal properties with rise in temperature.

Shukla et al. (2006) studied thermal response of the nonablating ceramic tiles by finite element method. A continuum model for the porous materials is used for the determination of thermal conductivity. The temperature distribution for the one-dimensional model is compared with the available arc-jet result. The 1-D and 2-D temperature contours and the heat flux distributions for the silica tiles are also presented. The expression for the pressure distribution in a silica tile is derived. They used pure silica material and developed a methodology to analyze the performance of ablative thermal protection system and proved that, by using temperature limits provided from the materials used for the structure of the spacecraft, a TPS can be designed to prevent the structure from overheating. The models used were validated with experimental arc-jet data. The assumptions used in the computations were an adiabatic back wall, low surface catalysis, and no convective cooling during soak out.

Upon reviewing this literature, it was realized that performance analysis of TPS tile made of silica-based ceramic composite can also be considered by a similar methodology done by them. The application of these tile materials can be found in nose cap and wing tips of the reentry vehicle or locations where the vehicle structure interacts with the heat flux to cause the temperature to rise to its peak values.

Scatteia et al. (2006) reported results of an experimental investigation into the efficiency of sintered ZrB_2-SiC compounds and of plasma-sprayed ZrB_2-SiC coating for heat radiation and for the recombination of atomic oxygen. Experiments on emissivity measurements of ZrB_2-SiC ceramic composite at 200 Pa and 0.001 Pa pressure conditions are performed. The results under vacuum conditions are lower than the ones obtained at high pressure. High emissivity values and low recombination coefficients were found in agreement with previous experimental studies performed on similar ceramic compounds but at lower temperatures using a different measurement technique. According to the surface analysis, the oxide scale is a silica or borosilicate glassy layer. This represents a rather promising result, because the radiative efficiency of silica-based glassy compounds is reportedly higher than that of pristine UHTCs.

Loehman et al. (2006) reported results of thermal diffusivity, thermal conductivity, and specific heat measurements of ZrB_2 and HfB_2. Thermal diffusivities were measured to 2000 °C for ZrB_2 and HfB_2 ceramics with SiC contents from 2 to 20%. Thermal conductivities were calculated from thermal diffusivities and measured heat capacities. Thermal diffusivities were modeled using different two-phase composite models. They prove that these materials exhibit excellent high-temperature properties and are attractive for further development for thermal protection systems.

Zhang et al. (2008) conducted ablation tests of the flat-face models for ZrB_2–20vol%SiC ultrahigh-temperature ceramic (UHTC) which was prepared by hot pressing. The tests conducted under ground simulated atmospheric reentry conditions using arc-jet testing with heat fluxes of 1.7 and 5.4 MW/m^2 under subsonic

conditions, respectively. For temperatures in the order of 1600–1700 °C, the material was able to endure the heating conditions; however, for temperatures in the order of 2300 °C, evident oxidation and ablation occurred, and the material was unable to offer a valuable resistance to the applied aerothermal load. Results indicate that ZrB_2–SiC ultrahigh-temperature ceramics are the potential candidates for leading edges. Results indicated that ZrB_2–SiC can maintain the high-oxidation resistance coupled with configurational stability at temperatures lower than that point which results in significant softening and degradation of the oxide scale, and that point will be the temperature limit for UHTC.

Savino et al. (2008) investigated the behavior of pressure less sintered two different ultrahigh-temperature ceramics, HfB_2 + 5% $MoSi_2$ and HfC +5%$MoSi_2$, which were exposed to an average specific total enthalpy of the flow around the body of the order of 5–10 MJ/kg and at atmospheric pressure typical of atmospheric reentry environment, with an arc-jet facility at temperatures exceeding 2000 °C. The surface temperature and emissivity of the materials were evaluated during the test. The microstructure modifications were analyzed after exposure. The HfB_2 + 5%$MoSi_2$ model surface reached a peak value of 1950 °C for specific total enthalpy *(H)* approaching 8 MJ/kg. The cross section after exposure showed the formation of a compact silica oxide (about 15 μm) which sealed the underlying HfO_2 scale. The HfC + 5% $MoSi_2$ model surface reached peak values of 2100 and 2400 °C. Cross-sectional analysis showed a layered structure, constituted of an outer layer of porous HfO_2 and an inner layer mainly constituted of HfO_2 and silica.

Borrellia et al. (2009) tested a nose cap demonstrator in the plasma wind tunnel (PWT) facility to focus on the assessment of the applicability of UHTCs to the fabrication of high performance and sharp hot structures (SHS) for reusable launch vehicles. In this paper, the FEM-based thermo-structural analyses are presented. Comparisons with experimental data measured in the PWT have been introduced to validate the FEM model and to help in interpreting the experimental test itself. Synergies between numerical and experimental activities have been finalized to the improvement of knowledge on the physical phenomenon under investigation. The effects on the thermal response due to the assumption of the catalytic condition of the wall, due to the uncertainties related to heat flux and pressure measurements on the probe (which influence the heat flux computation), and due to uncertainties in the determination of some UHTC thermal properties, have been investigated. Discrepancies between the numerical results and experimental ones in terms of wall temperature distribution on the massive UHTC nose tip were found, and possible sources of error have been analyzed. The experimental temperatures curves fall very close to the numerical envelope (taking in account several sources of error) for all the test duration and the noncatalytic wall model was found more reliable in reproducing thermal behavior of the nose cap.

Savino et al. (2010) deal with arc-jet experiments on different UHTC models which have been carried out in two different facilities, to analyze the aerothermal environment and to characterize the material behavior in high enthalpy hypersonic nonequilibrium flow. Typical geometries of interest for nose tip or wing leading edges of hypersonic vehicles, as rounded wedge, hemisphere, and cone are

considered. The ZrB_2-based UHTC material sample tested for several minutes to temperatures up to 2050 K showing a good oxidation resistance in extreme conditions. The flow conditions and the sharpness of the models are similar in both facilities, but the larger model (rounded wedge) is characterized by a heat flux distributions (peaking at the leading edge and strongly decreases downstream) resulting in a lower average surface heat flux and therefore (also due to the relatively high thermal conductivity) in a smaller equilibrium temperature in comparison with the smaller specimens. Numerical-experimental correlations show a good agreement with proper modeling of the surface catalytic behavior. As expected, the higher temperature achieved in the small-sized specimens, submitted to hypersonic arc-jet conditions than in the rounded wedge tests and the lower pressure in comparison with the subsonic arc-jet tests increase the oxidation phenomena. The change in surface composition can justify the lower value (0.6–0.65) of the surface emissivity estimated in their work in comparison with the subsonic experiments (0.9) where poor oxidation phenomena were observed.

Levinskas et al. (2011) report the experimental investigations of the new composite material based on light silicate frame impregnated by polymer composite tested in high-temperature air jet and generated by means of plasma torch (temperature – (1320–2420) °C, velocity – (40–50) m/s). Data of composite material ablation rate and temperature of protective sample set surface during experiment are presented. Recent advances in polymer-layered silicate nanocomposites, especially with the improved thermal stability, flame retardancy, and enhanced barrier properties promote the investigation of these materials as potential ablatives. Introduction of the layered nanosilicates (montmorillonite, tobermorite) into polymer matrix results in the increase of thermal stability of polymer nanocomposites and ablation resistance, which are not observed in each component. Experimental investigations of the ablation resistance of the set with protective shell were provided in two different plasma flows–air plasma jet (for first set of samples in which ablation resistance is found remarkably high in air gas flow environment) and combustion gases plasma jet with reduced oxygen content (for second set of samples in which existence of the reinforcement coating remarkably decreased the ablation rate initially). The light silicate shell has demonstrated good resistance to the impact of high-temperature gas flow initiated by plasma jet. The additional impregnation of light silicate shell with epoxy nanocomposite reinforcement coating increased the temperature on the shell surface due to exothermic reactions but decreased the ablation rate accordingly. The experiments in reduced oxygen flow have shown good thermal stability of the protective shell. The structure imparts high thermal shock resistance and dimensional stability.

Justin and Jankowiak (2011) present ZrB_2-SiC and some other composites developed for leading edges or air intakes of future hypersonic civilian aircrafts flying up to Mach 6. Addition of 20 vol% of SiC is found optimal for good oxidation resistance. They observe that these composites possess high hardness, high flexural stress, good machinability, high emissivity, good thermal conductivity, and thermal shock resistance.

Mallik et al. (2012) investigated thermal properties of ZrB_2–SiC, HfB_2–SiC, ZrB_2–SiC–Si_3N_4, and ZrB_2–ZrC–SiC–Si_3N_4 composites within temperature range between 25 and 1300 °C. Thermal conductivity increases with addition of SiC, while it decreases on ZrC addition. Variations of thermal conductivity, specific heat, and thermal diffusivity with temperature are plotted. Gregory et al. (2012) reviewed results on thermal conductivity of HfB_2 and ZrB_2. Pure HfB_2, pure ZrB_2, and composites of HfB_2 and ZrB_2 with various vol% of SiC are reviewed in detail.

Can and Yue (2013) are developing a numerical model combining radiation and conduction for porous materials based on the finite volume method. The model can be used to investigate high-temperature thermal insulations that are widely used in metallic thermal protection systems on reusable launch vehicles and high-temperature fuel cells. The effective thermal conductivities which are measured experimentally can hardly be used separately to analyze the heat transfer behaviors of conduction and radiation for high-temperature insulation. By fitting the effective thermal conductivities with experimental data, the equivalent radiation transmittance, absorptivity and reflectivity, as well as a linear function to describe the relationship between temperature and conductivity can be estimated by an inverse problems method.

Yang et al. (2013) compared and investigated the effect of high-temperature oxidation on mechanical properties and anti-ablation property of ZrB_2/SiC as a protective coating that was obtained on the surface of C/SiC composites. The following are the observations done by the authors: C/SiC composites are good thermal shielding for aerospace applications, provided that they are protected from oxidation by suitable coatings. UHTC, and in particular ZrB_2, is among the best oxidation resistant materials as known. Mechanical tests were conducted before and after oxidation test. Anti-ablation property was tested under oxy-acetylene torch. Compared with the uncoated composites, the linear and mass ablation rates of the coated composites decreased by 62.1% and 46.1%, respectively, after ablation for 30s. The formation of zirconia and silicon dioxide from the oxidation of ZrB_2/SiC improved the ablation resistance of the composites because of the evaporation at elevated temperature, which absorbed heat from the flame and reduced the erosive attack to carbon fibers and SiC matrix. They tried to prove that ZrB_2/SiC coating for C/SiC composites could fully fulfill the advantages of refractory compounds.

3 Heat Transfer Through Porous Ceramic/Ceramic Composite Tile

3.1 Heat Transfer by Gas Conduction in Pores

Conduction is one of the main modes of heat transfer in tiles. The heat is transmitted along the solid skeleton of the tile and through the gas filling the space in the insulation. With increasing porosity of the insulator, the second way becomes

dominant. Accordingly, the thermal conductivity of high-quality insulators comes close to that of the contained gas, which is usually considered as air/inert gas. According to the fundamental equation of the theory of heat conduction, the steady-state (stationary) thermal fluxes across an isothermal surface in a body are

$$q = k\nabla T \tag{1}$$

In general form, the transient equation of heat conduction is

$$\rho\, C_{\mathrm{p}} \frac{\partial T}{\partial \tau} = k\, \nabla^2 T \tag{2}$$

The kinetic theory of gas usually consider two extreme cases of heat transfer by gas conduction: $L << \delta$ and $L >> \delta$ where L is the mean free path of the gas molecules and δ is the distance between the heat exchanging surfaces (/characteristic length). The atmospheric pressure under reentry condition at high altitude is taken as 0.01 atm. The value of L at this pressure and altitude is very high as compared with δ (In this case, δ is. pore diameter, which is in the range of micrometers). So, $\mathrm{Kn} >> 1$. According to the kinetic theory of gas, when Knudsen number, $\mathrm{Kn} << 1$, the conductivity is independent of the gas pressure. If the pressure is sufficiently low and $\mathrm{Kn} >> 1$, the gas molecules bounce from wall to wall without colliding with each other. The amount of heat transferred is then proportional to the number of molecules participating in the transfer and thus to the gas pressure. When the distance between the walls is larger, the path of the molecule becomes longer, but their number per unit surface also increases. As a result, the rate of heat transfer is independent of the separation of the walls. For a monatomic gas, the thermal conductivity of gas can be expressed as

$$k_{\mathrm{g}} = \frac{k_0}{(1 + 2a_{\mathrm{c}} \times \mathrm{Kn})} \tag{3}$$

where k_0 = thermal conductivity of the gas at atmosphere pressure and can be obtained by $k_0 = e\ \mu\ \mathrm{C_V}$ where $e = (9\gamma - 5)/4$

$$a_{\mathrm{c}} = \left(\frac{2\mathrm{e}}{1+\gamma}\right)\left(\frac{2-\alpha}{\alpha}\right)$$

α = accommodation coefficient that allows for incomplete energy exchange between the gas molecules and surface and is defined by

$$\alpha = \frac{T_2' - T_1}{T_2 - T_1}$$

where T_1 is the temperature corresponding to the energy of the molecule colliding with the wall, the temperature of which is T_2, and T'_2 is the temperature corresponding to the energy of the reflected molecules.

3.2 Transient Heat Transfer by Radiation

The mode of heat transfer across TPS materials is by solid conduction, gaseous conduction through gases trapped in the pores, free and forced convection, as well as radiation in pores. The convection is generally neglected and will not be considered here. However, it should be noted that especially when considering the case of an applied rigid fibrous refractory insulation for a space vehicle during reentry, forced convection may affect the overall heat transfer. The mechanism of conduction by residual gas and solid conduction, if not similar physically, is similar mathematically in the sense that the heat flux is proportional to the thermal conductivity and local heat gradient. Radiation, on the other hand, is a complex process and has to be treated separately. The local inhomogenities in the material affect the transmission of radiant energy. For example, radiation leaving a surface, on passing through the material may (i) pass through voids in the fibrous material, (ii) be absorbed by the residual gas and subsequently reemitted, (iii) be absorbed by the particle and subsequently reemitted, (iv) be scattered by particles, and (v) be scattered by fibers. The TPS material will be considered as homogeneous and continuous. These assumptions may be justified if the gas voids and the particles of the insulation are essentially in the equilibrium with the surrounding gas, and if the particle spacing is sufficiently small, so that the temperature difference between the adjacent solid particles is small compared with the total temperature. For a radiative flux,

$$q_{\text{rad}} = -\frac{16}{3E}\sigma\, n^2\, T_{\text{rad}}^3 \frac{\partial T}{\partial x} = -k_{\text{rad}} \frac{\partial T}{\partial x} \tag{4}$$

where E is extinction coefficient, n is refractive index (taken as 1), and σ is Stefan-Boltzmann constant.

$$T_{\text{rad}}^3 = \frac{\left(T^2 + T_a^2\right)(T + T_a)}{4}$$

where T is temperature of the body, and T_{a} is temperature of the atmosphere.

The energy flux vector by combined radiation and conduction at any position in the medium can be expressed as

$$q = q_{\text{rad}} + q_{\text{g}} = -\left(k_{\text{rad}} + k_{\text{g}}\right)\frac{\partial T}{\partial x} \tag{5}$$

This can be used as heat conduction equation, to obtain an energy balance on a differential volume element within an absorbing–emitting medium. The medium behaves like a conductor with thermal conductivity dependent on temperature.

3.3 Effective Thermal Conductivity

Effective thermal conductivity of the bulk material is as follows:

$$k = \eta A_1(\theta)k_s + (1-\theta)k_g + \beta A_2(\theta)k_{\text{rad}} \tag{6}$$

where $\eta = 1.93\theta$ (η is called bonding efficiency factor), θ = volume faction, $\beta = -8.571(1.0-\theta)+0.84$ for porosity >0.84, and $\beta = 1.2$ for porosity <0.84 (β is called density scale factor on the change in emittance of composite insulation). The two adjustment parameters η and β which relate to solid conduction and radiation heat transfer are found to be independent of composition and fiber structure and to depend only on the solid volume fraction and porosity.

One-dimensional transient energy equation without internal heat source can be now expressed as

$$\rho\, C_{\text{p}}\frac{\partial T}{\partial \tau} = k\,\frac{\partial^2 T}{\partial x^2} \tag{7}$$

4 Modeling Details

The tile gets heat flux due to air friction. It emits a part of this heat as reradiated energy. Remaining part is conducting through porous material. Effective conductivity value, k is applied in governing equation. The thermal analysis is done across the cross section of tile, and temperature profile is observed on selected nodes in the line through the center of tile. Upper and bottom surfaces of the tile are considered as insulated to examine the maximum heat penetration across the tile. A one-dimensional thermal analysis is sufficient for design purpose to determine the transient temperature response near the center of the tiles for stagnation heating. Aerothermal heat flux of 400,000 W/m^2 is applied at the surface of the tile ($x = a$). Heat is reradiated from the surface (at $x = a$) to deep space as well as conducted through TPS component. The emittance and specific heat are functions of temperature and pressure. The normal density, thermal conductivity, heat capacity, and emittance of various RSI are listed by Chiu and Pitts (1991) and applied for analysis of pure ceramic TPS tile in phase I. A numerical model built by COMSOL

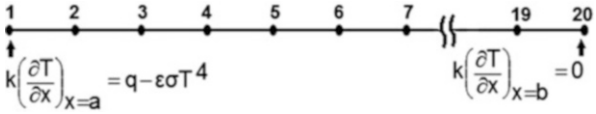

Fig. 2 1-Dimensional Analysis rod element of blunt/sharp leading edge of a reentry vehicle

Multiphysics is used in the present study. Added physics is heat transfer in porous media with time-dependent study. Materials listed in COMSOL material library and material properties collected from the literature reviews are applied for analysis of composite ceramic tile in phase II. The details of geometry, governing equation, and boundary condition are described below.

4.1 Geometry and Meshing

The geometry of the present computational model is based on Shukla et al. (2006). The silica tile is considered as one-dimensional rod element having length of its cross section and is divided into 20 nodes of equal size. Figure 2 shows the geometry marked with first seven nodes from which variation of temperature with respect to time is observed during analysis.

The mesh sequence type is selected as physics-controlled mesh having extremely fine element size.

4.2 Governing Equation

The main objective of this work is to investigate the temperature distribution through ceramic composite porous tile. As phase I, the analysis with numerical model built by COMSOL Multiphysics is validated by predicting the thermal response of the reusable surface insulations made of porous pure ceramic material and compared with the results of Shukla et al. (2006). In the phase II, tile with material selected from UHTCs are analyzed. For both cases, the governing equation can be written as

$$\rho c_{\mathrm{p}} \frac{\partial T}{\partial t} = \nabla(k \nabla T) \tag{8}$$

4.3 Initial and Boundary Conditions

To obtain the temperature distribution in the medium, Eq. (8) will be solved subjected to initial and boundary conditions. The boundary conditions would often be specified temperatures of the enclosure surfaces. However, near a boundary, the diffusion approximation is not valid; consequently, the solution is incorrect near the wall and cannot be matched directly to the boundary conditions. To overcome this difficulty, the boundary conditions at the edge of the absorbing–emitting medium are modified, so the resulting solution to the diffusion equation with this effective boundary condition will be correct in the region away from the boundaries where the diffusion approximation is valid. In the pure radiation case, a temperature slip was introduced to overcome difficulty of matching diffusion solution in the medium to the wall temperature. For combined conduction–radiation, a similar concept was introduced by Howell and Seigel (1981). With the diffusion approximation, results for combined radiation and conduction can be obtained for both energy transfer and temperature profile.

Governing Eq. (8) is subjected to following initial and boundary conditions:

$$T(x,0) = T_0 \tag{9}$$

$$k\left(\frac{\partial T}{\partial x}\right)_{x=\mathrm{a}} = q - \varepsilon\sigma T^4 \tag{10}$$

$$k\left(\frac{\partial T}{\partial x}\right)_{x=\mathrm{b}} = 0 \tag{11}$$

5 Identification of Ceramic Composites

The temperature at the tip of the leading edge is inversely proportional to the square root of the leading edge nose radius, and the reduced curvature radius results in higher surface temperature than that of the actual blunt vehicles that could not be withstood by the conventional thermal protection system materials (Savino et al. 2010). As per the data collected from review of literature, the family of ceramic matrix composites named as UHTCs are identified as promising candidates of for such structure materials, because they posses high melting point, dimensional stability, high hardness, good chemical inertness, and oxidation resistance at elevated temperatures. However, the good thermal conductivity and high melting point values of UHTCs bound its application in sharp nose cones and leading edges of space vehicles than in other structures of vehicle. Other TPS materials having low thermal conductivity like pure ceramic are having comparatively low melting point and very high value of heat flux developing due to aerobraking of vehicle with sharp nose cone can melt them. As an RSI system, such materials are not preferable for sharp nose cone and leading edges.

The incident convective heat flux is balanced by reradiated energy and energy conducted away from the leading edge tip to other surface of tile near to another layer of low thermal conductivity TPS material/substructure of the vehicle. When a steady state is achieved, global radiative equilibrium is established, and because the material thermal conductivity is high, a relatively low equilibrium temperature is achieved. Thus, the need for highly conducting refractory materials can be met with UHTCs in the design of sharp vehicles (Gasch et al. 2005).

Paul et al. (2012) report that Carbides and borides of transition metal elements such as Hf and Zr are widely studied due to their desirable combinations of mechanical and physical properties, including high melting points (>3000 °C), high thermal and electrical conductivities, and chemical inertness against molten metals. Even though carbides have higher melting points than borides, the latter have much higher thermal conductivities and thus good thermal shock resistance making HfB_2 and ZrB_2 more attractive for ultrahigh-temperature applications.

The following observations contribute to the selection of HfB_2-20vol%SiC and ZrB_2-20vol%SiC as the tile materials. Reviews by Upadhya et al. (1997) explore that addition of SiC can improve oxidation resistance of both HfB_2 and ZrB_2. They pointed out the experimental results in the temperature range of 1300–1500 °C with SiC addition to ZrB_2. Inner layer of Zirconium Oxide and outermost rich glassy layer of Silicon oxide is forming. The formation of this glass provides oxidation resistance at high temperature due to good wettability and good surface coverage. As reported by Scatteia et al. (2006), these layers of oxides which partially cover the pores are characterized by higher emissivity, and that causes an increase in emissivity as the temperature rises. This behavior will yield to increase in reradiated flux and hence attains steady state at much lower equilibrium temperature.

Addition of 20 vol% SiC to either ZrB2 or HfB2 matrix composites is an optimum composition which leads to significant increase in their thermal conductivities as well as effective densification during its production by sintering (Loehman et al. 2006).

Hereafter, HfB_2-20vol%SiC and ZrB_2-20vol%SiC are given sample names HB20S and ZB20S.

6 Results and Discussions

6.1 Heat Transfer Analysis on Pure Ceramic Tile

The primary objective of this phase-I analysis is to predict the temperature distribution through TPS tile of pure ceramic porous material and to compare with the results of Shukla et al. (2006) as part of the validation of analysis with numerical model built by COMSOL Multiphysics. The material properties used are listed in Table 1.

Table 1 Properties of pure silica TPS tile

Property	Value
Material	Silica
Density, ρ (kg/m^3)	352
Volume Fraction, θ	0.8
Pore Diameter, δ (μm)	0.8
Extinction Coefficient, E (m-1)	14900

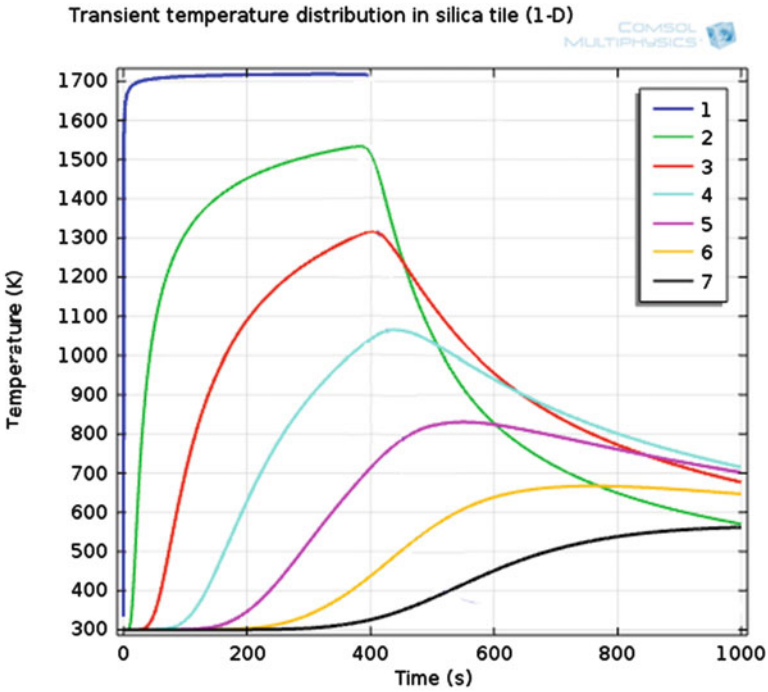

Fig. 3 1-D transient temperature distribution in silica tile

The pressure considered here is 0.01 atm. The heat flux value of 400,000 W/m^2 is taken as a time-dependent value, which means after 400 s the heat flux is assumed as zero.

The thermal conductivity plays a major role in determining accuracy of calculated temperature response. The silica tile is considered as one-dimensional rod element and is divided into 20 nodes. Figure 3 shows the in-depth temperature response of first 7 nodes of the TPS tile. The rod will absorb a part of the heat flux which is conducted through it, and the remainder is reflected as reradiated heat energy to the outer space. The rod attains a maximum temperature of 1720 K in the outer surface. The values of the thermal conductivity, specific heat at constant pressure, and emissivity were used from listed tables/graphs showing variation of

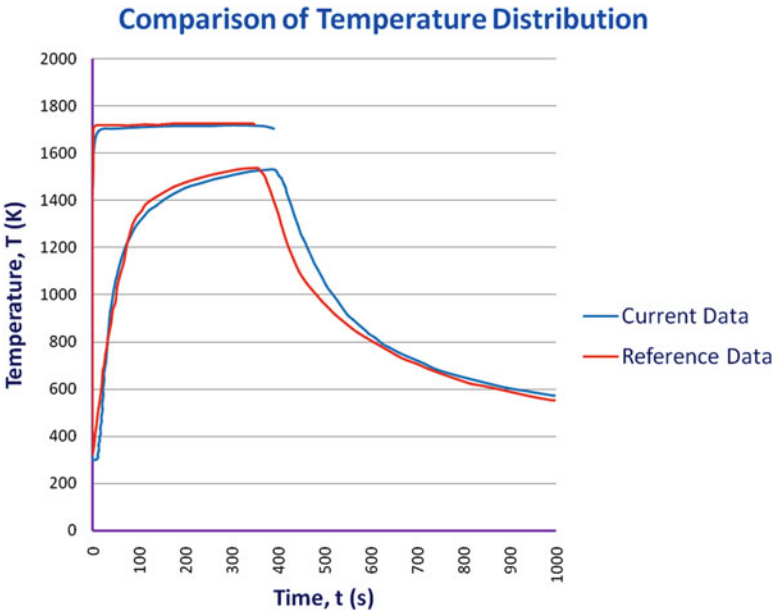

Fig. 4 Comparison of temperature distribution

respective property with temperature as given by Chiu (1992), and Touloukian and Buyco (1970).

These inputs were used in COMSOL Multiphysics model builder. This analysis helps to find how a tile responds to a high heat load, from one end to another end.

Due to the low value of effective thermal conductivity, each node shows a finite amount of decrease in temperature as proceeding from outer surface to inner surface. The nodes beyond 7th node is showing temperature readings converging to a constant safe value, which is an important observation for designers to fix the thickness required for the ceramic tile as a TPS.

Figure 4 compares the present temperature profile of nodes 1 and 2 with the temperature profiles of same nodes reported by Shukla et al. (2006).

The present software gives same values for maximum temperature attained by these nodes, but current data show the extreme temperature values up to 400 s, and thereafter, the heat flux is withdrawn suddenly. As per reference data, a gradual withdrawal of heat flux initiated just before reaching 400 s. Otherwise, the two graphs hardly show any difference in the temperature distribution. Based on these satisfactory observations, the phase II of the analysis is done with ceramic composite tiles.

6.2 Heat Transfer Analysis on Ceramic Composite Tile

The primary objective of this phase-II analysis is to predict the temperature distribution through TPS tile of composite ceramic porous material and to identify its ability as TPS. It is reported by Parthasarathy et al. (2012) that UHTC-based leading-edge samples proved to withstand the simulated hypersonic conditions up to Mach 7. At this speed, heat flux in the range of 2 MW/m^2 can be evolved. So, by following the same procedure of phase-I analysis, this heat flux value is applied, and after 400 sec, the heat flux is assumed as zero. However, during reentry conditions, the heat flux will be vanished before 400 s due to the increased flight velocity and lesser time to descent to an altitude of "cooler" conditions. The pressure applied is 0.01 atm. Volume fraction of 0.8 is applied for selected HB20S and ZB20S.

The material used for HB20S is chosen from COMSOL Multiphysics material library, and HfB_2-20SiC [solid, 99% dense] is selected. Input parameters such as thermal conductivity, emissivity, specific heat, and density are obtained from material library. The density observed from COMSOL material library is ranging from 9338 to 8962 kg/m^3 with respect to temperature ranging from 300 to 2500 K. Figure 5 shows 1-D transient temperature distribution of all node points in HB20S tile. The rod attains a maximum temperature of 2408 K in the outer surface. All

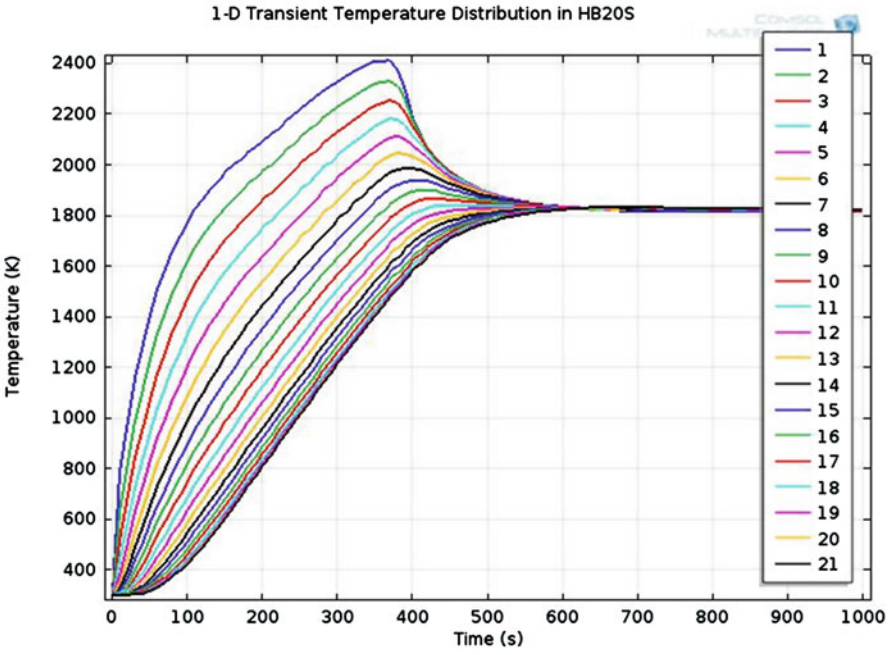

Fig. 5 1-D Transient Temperature distribution in HB20S tile

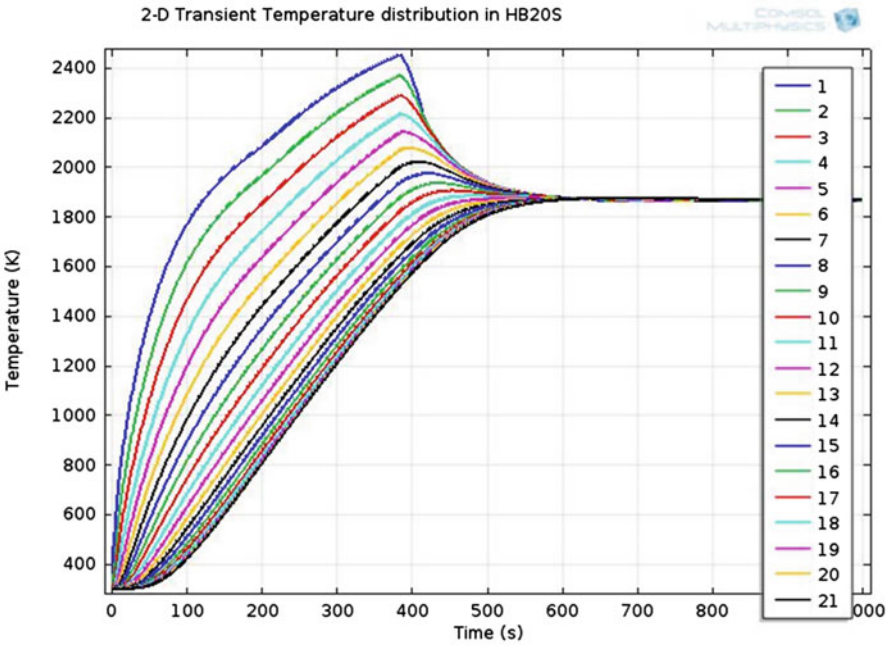

Fig. 6 2-D Transient Temperature distribution in HB20S tile

node points reaches a final temperature of 1816 K. Due to high conductivity, the equilibrium temperature is reached at a faster rate.

Figure 6 shows 2-D transient temperature distribution of all node points in HB20S tile. A maximum temperature of 2452 K is observed, which reaches to 1862 K after withdrawing heat flux. All input parameters are kept same as that applied in 1-D analysis. The temperature distribution shows 2–3% increase in temperature than 1-D analysis, and in a broad sense, both temperature distribution curves can be considered as same.

The material used for ZB20S is chosen from COMSOL Multiphysics material library, and ZrB_2-20SiC (solid, 99% dense) is selected. Input parameters such as thermal conductivity, emissivity, specific heat at constant pressure, and density are obtained from COMSOL Multiphysics material library. Figure 7 shows 1-D transient temperature distribution of all node points in ZB20S tile.

The rod attains a maximum temperature of 2446 K in the outer surface. All node points reach a final temperature of 1886 K. The temperature distribution shows 2% increase in maximum value of temperature in outer surface than maximum value of temperature obtained in 1-D analysis of HB20S sample whereas an increase of 4% is observed for steady-state equilibrium temperature of both cases.

The density observed from COMSOL material library is 5560 kg/m^3 at 300 K, which is applied.

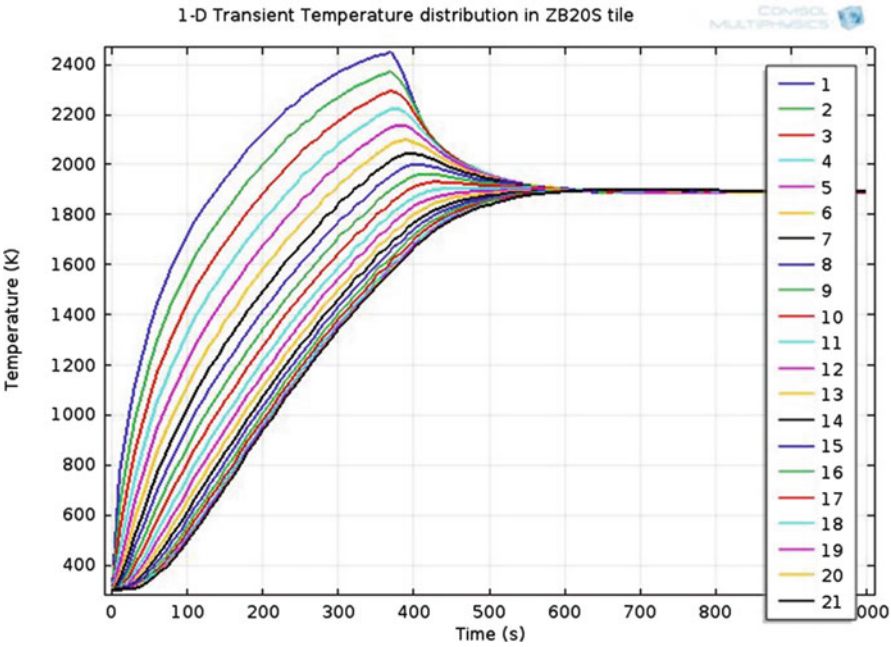

Fig. 7 1-D Transient Temperature distribution in ZB20S tile

Figure 8 shows 2-D transient temperature distribution of all node points in ZB20S tile. A maximum temperature of 2501 K is observed, which reaches to 1936 K after withdrawing heat flux. The temperature distribution of ZB20S sample shows 2–3% increase in temperature than 1-D analysis of the same.

When comparing the temperature distributions of both HB20S and ZB20S samples during 2-D analysis, the rise in maximum temperature of outside surface is 2%, and the rise in steady-state equilibrium temperature is 4%.

Figure 9 shows 3-D transient temperature distribution of all node points in ZB20S tile. A maximum temperature of 2495 K is observed, which reaches to 1944 K after withdrawing heat flux. The temperature distribution shows 2–3% increase in temperature than 1-D analysis of ZB20S sample, whereas the percentage difference with temperature of 2-D analysis is negligible.

7 Conclusions

7.1 Summary

The transient temperature distribution of HB20S and ZB20S samples are almost same. The density of HB20S sample is 68% greater than that of ZB20S. In other

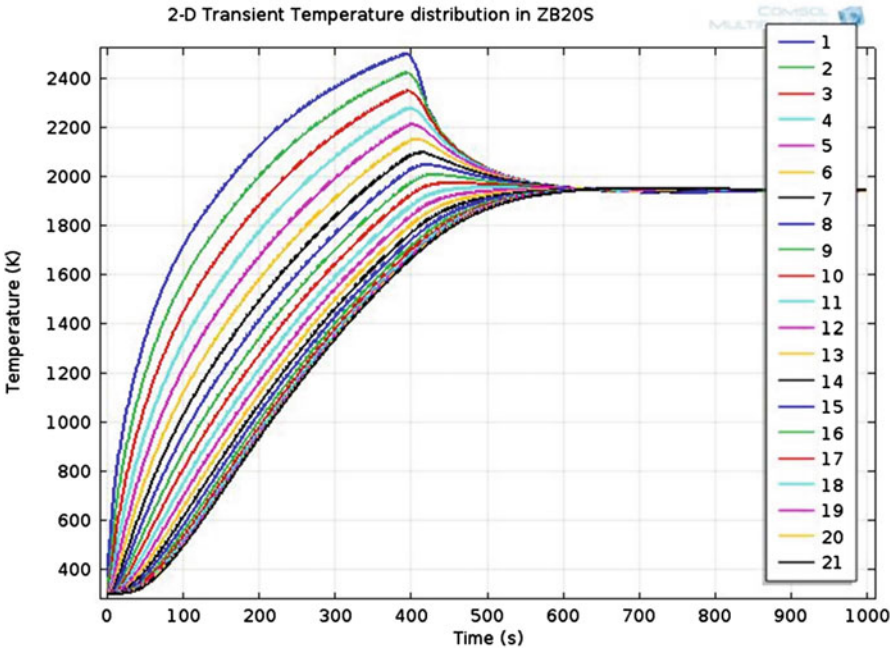

Fig. 8 2-D Transient Temperature distribution in ZB20S tile

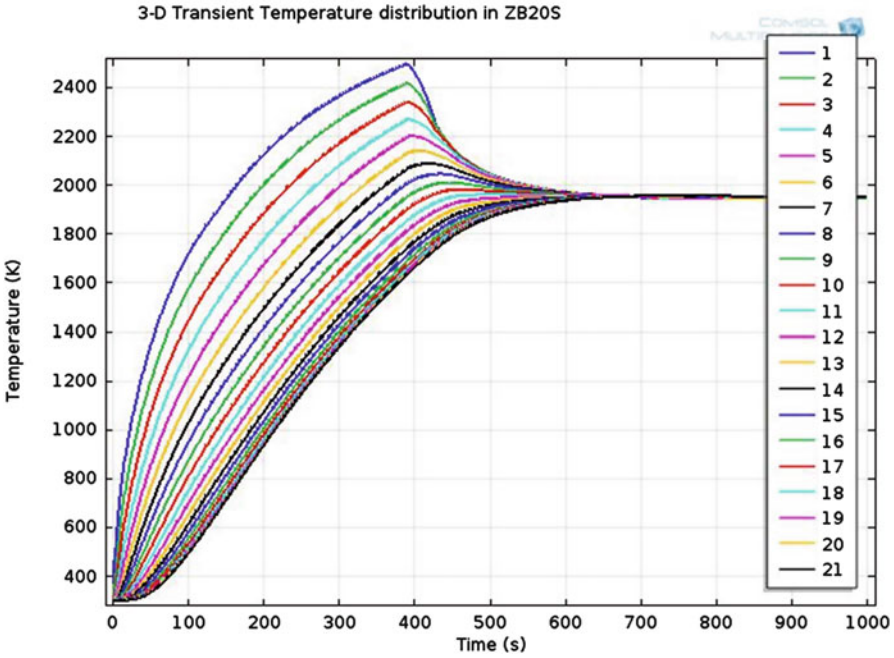

Fig. 9 3-D Transient Temperature distribution in ZB20S tile

words, weight of ZB20S TPS tile having same dimensions of HB20S TPS tile is 40% less than weight of HB20S tile. This is an important contribution to gain in weight of the vehicle, if TPS of ZB20S samples are selected. The melting points of both samples are above 3000 K with a difference less than 4%. The evaluation of these properties and along with other fantastic observations in terms of chemical and mechanical properties available from the literature survey, even under limited research facilities, shows that ceramics based on ZrB_2, especially ZrB_2-20vol%SiC, offer promise for use as structural materials in extreme environments.

The HB20S and ZB20S sample materials can find potential applications in microelectronics, molten metal containments, nuclear reactors, high-temperature electrodes, wear-resistant surfaces, heat shield structures under extreme environments, etc. For aerospace vehicles, the leading edges under elevated temperatures can find its proper candidate from this sample. In rocket propulsion system and reentry vehicles, extreme heat flux is experienced in sharp structures like leading edges, nose cones, and nozzles. The proposed type of materials can improve the ability of these types of vehicle structures in terms of mechanical, thermal, and chemical perspectives. Sharp leading edges would imply lower aerodynamic drag, improved flight performances and crew safety, due to the larger cross range and maneuverability along with more gentle reentry trajectories.

7.2 Scope for Future Work

In this paper, heat penetration across the cross section of a pure ceramic and two samples of ceramic composites are evaluated. If the incident heat flux value is again increased beyond Mach 7, phase changes will occur due to melting, which require another detailed study. Different combinations of UHTCs with low-conductivity TPS materials like pure ceramic tiles can be examined. It can be in the form of a UHTC-coated or UHTC–ceramic multilayer TPS tile keeping an eye on the benefit of weight reduction when the secondary material is having low density. 2-D or 3-D thermal analysis of a UHTC nose cone model with maximum heat flux at nose cone tip, which is gradually decreasing in the downstream surface of cone, can be done.

References

Borrellia, R., Riccioa, A., Tescionea, D., Gardib, R., Marinob, G.: Thermo-structural behavior of an UHTC made nose cap of a re-entry vehicle. Acta Astronaut. **65**, 442–456 (2009)

Can, H., Yue, Z.: Calculation of high-temperature insulation parameters and heat transfer behaviors of multilayer insulation by inverse problems method. Chin. J. Aeronaut. **27**(4), 791–796 (2013)

Chiu, S.A. Thermal Analyses of Reusable Surface Insulations, AIAA Paper 92–0852, Reno, (1992)

Chiu, S.A. Pitts, W.C., Reusable Surface Insulations for Reentry Spacecraft, AIAA Paper 91–0695, (1991)

Daryabeigi, K.: Thermal analysis and design optimization of multilayer insulation for re-entry aerodynamic heating. J. Spacecr. Rocket. **39**(4), 509–514 (2002)

Gasch, M.J., Ellerby, D.T., Johnson, S.M.: Ultra High Temperature Ceramic Composites, Handbook of Ceramic Composites, pp. 197–224. Kluwer Academic Publishers, Boston (2005)

Gregory, J., Harrington, K., Hilmas, G.E.: Thermal conductivity of ZrB2 and HfB2. In: Ultra-High Temperature Ceramics Materials for Extreme Environment Applications, pp. 197–235. Wiley, US (2012)

Howell, J.R., Siegel, R.: Thermal Radiation Heat Transfer. McGraw-Hill, Tokyo (1981)

Justin, J.F., Jankowiak, A.: Ultra high temperature ceramics: densification, properties and thermal stability. Aerospace Lab. **3**, AL03–AL08 (2011)

Kontinos, D. A., Gee, K. , Prabhu, D. K..Temperature Constraints at the Sharp Leading Edge of a Crew Transfer Vehicle, AIAA 2001–2886 (2001)

Laub, B., Venkatapathy, E..Thermal Protection System Technology and Facility Needs for demanding Future Planetary Missions, International Workshop on Planetary Probe Atmospheric Entry and Descent Trajectory Analysis and Science, Lisbon, Portugal, 6–9 October, (2003)

Levinskas, R., Kezelis, R., Brinkiene, K., Grigaitiene, V., Valincius, V., Lukosiute, I., Kavaliauskas, Z., Baltusnikas, A.: High temperature ablation of composite material under plasma jet impact. Mater. Sci. **17**(4), 423–427 (2011)

Ronald, Loehman., Erica, Corral., Hans Peter Dumm, Paul Kotula, Raj Tandon. Ultra high temperature ceramics for hypersonic vehicle applications, Sandia report, SAND2006–2925, Sandia National Laboratories, U.S. Department of Energy, (2006)

Mallik, M., Kailath, A.J., Ray, K.K., Mitra, R.: Electrical and thermophysical properties of ZrB2 and HfB2 based composites. J. Eur. Ceram. Soc. **32**, 2545–2555 (2012)

Opeka, M.M., Talmy, I.G., Wuchina, E.J., Zaykoski, J.A., Causey, S.J.: Mechanical, thermal, and oxidation properties of refractory hafnium and zirconium compounds. J. Eur. Ceram. Soc. **19**, 2405–2414 (1999)

Triplicane A. Parthasarathy., Michael K. Cinibulk & Mark Opeka. Modeling and evaluating the environmental degradation of UHTCs under hypersonic flow, Ultra-High temperature ceramics materials for cxtreme environment applications, pp.267–290. Wiley, US, (2012)

Paul, A., Binner, J., Vaidhyanathan, B.: UHTC composites for hypersonic applications. In: Ultra-High Temperature Ceramics Materials for Extreme Environment Applications, pp. 144–166. Wiley, US (2012)

Savino, R., Fumoa, M.D.S., Silvestroni, L., Sciti, D.: Arc-jet testing on HfB2 and HfC-based ultra-high temperature ceramic materials. J. Eur. Ceram. Soc. **28**, 1899–1907 (2008)

Savino, R., Fumo, M.D.S., Paterna, D., Di Maso, A., Monteverde, F.: Arc-jet testing of ultra-high-temperature-ceramics. Aerosp. Sci. Technol. **14**, 178–187 (2010)

Scatteia, L., Cosentino, G., Cantoni, S., Balat-Pichelin, M., Beche, E., Sans, J.L.. An investigation upon the catalytic and radiative behaviors of ZrB2-SiC ultra high temperature ceramic composites, Proceedings 5th European Workshop on Thermal Protection Systems and Hot Structures, Noordwijk, The Netherlands, 17–19 May (2006)

Shukla, K.N., Pradeep, A., Suneesh, S.S.: Thermal performance analysis of silica tiles. J. Eng. Phys. Thermophys. **79**(6), 1157–1163 (2006)

Stauffer, T. R., Jog, M., & Ayyaswamy, P. The effective thermal conductivity of multi foil insulation as a function of temperature and pressure. AIAA paper (1992)

Stewart, D.A. , Leiser, D.B., Thermal response of integral multi- component composite thermal protection systems, AIAA 20th Thermo physics Conference, Williamsburg, VA., June 19–21, pp. 420–427, (1985)

Touloukian, Y.S., Buyco, E.H.: Specific Heat Nonmetallic Solids Thermophysical Property of Matter, vol. 5. IFI / PLENUM, Washington (1970)

Upadhya, K., Yang, J.M., Hoffman, W.: Materials for ultrahigh temperature structural applications. Am. Ceram. Soc. Bull. **76**(12), 51–56 (1997)

Yang, X., Wei, L., Wang, S., Bi-feng, Z., Zhao-hui, C.: ZrB2/SiC as a protective coating for C/SiC composites: effect of high temperature oxidation on mechanical properties and anti-ablation property. Compos. Part B. **45**, 1391–1396 (2013)

Zhang, X., Hu, P., Han, J., Meng, S.: Ablation behavior of ZrB2–SiC ultra high temperature ceramics under simulated atmospheric re-entry conditions. Compos. Sci. Technol. **68**, 1718–1726 (2008)

Developing High-Resolution Remote Sensing Technology into an Advanced Knowledge Management System to Assess Small-Scale Hydropower Potential in Kazakhstan

Kabiyeva Marzhan, Kaskina Dina, and Bradshaw Roland

1 Introduction

For the last several decades, remote sensing technology and image processing have made a significant influence on the field of environmental protection and water management. This project aims to advance the application of remote sensing in the context of managing water resource by integrating high-resolution remote sensing technology into a knowledge management system for the management of water resources and the infrastructure to control them. Remote sensing technology is used to complement the development of a knowledge management system by advancing the remote sensing capability and image processing to near real time. This capability can be used to monitor and assess a river basin to develop flood extent and predictions but also to assess hydrological capacities for hydropower generation.

The application of high-resolution remote sensing technology and advanced image processing using advanced algorithms and statistical pattern recognition will considerably advance the ability to assess water resources. Remote sensing technology is used to complement the development of a knowledge management system by advancing the remote sensing capability and image processing to near real time.

In this research, we address how the integration of remote monitoring technology into a knowledge management framework provides water resource management organizations with a model for continuous improvement in making credible and defensible decisions for managing water resources and their associated infrastructure.

K. Marzhan • K. Dina • B. Roland (✉)
Nazarbayev University, School of Engineering, Civil Engineering Department, 53 Kabanbay Batyr Av, Astana 010000, Republic of Kazakhstan
e-mail: roland.bradshaw@nu.edu.kz

© Springer International Publishing AG, part of Springer Nature 2018

F. Aloui, I. Dincer (eds.), *Exergy for A Better Environment and Improved Sustainability 2*, Green Energy and Technology,
https://doi.org/10.1007/978-3-319-62575-1_41

The project corresponds to the Supreme Science and Technology Commission Protocol (№ 20–55/372) to advance the science in the field of energy research, deep processing of raw materials and products, information and communication technology, life sciences, and the continued development of intellectual potential of the country by aligning water resource technology and management issues to these priority areas.

2 Background

Based on its historic legacy from economic policies in the Soviet Union, Kazakhstan faces a real environmental threat from intensively polluted water bodies arising from its mining, metallurgical, and chemical industries as well as untreated wastewater discharges to the environment from urban and rural settlements (Nazarbayev 2013).

Over the last two decades, economic development policies marginalized many of the existing problems in the water sector of which one of the main areas of concern is the natural imbalance between available water resources and a growing water demand for consumption. This water scarcity in many of Kazakhstan's catchments has a negative impact on river water qualities. With the amount of river water in steadily decline, increases in the level of accumulated contaminants in the flood plains of rivers become increasingly evident. Thus, it is negatively affecting the quality of agricultural products and the health of the human population (Zàuìrbek 2013).

Another major issue in Kazakhstan is that only half of the water set aside for irrigation reaches the fields due to unrecoverable losses of water occurring within the irrigation networks and fields. In the period 1990–2012, this has led to an alarming reduction in irrigated land from 2.5 million hectares to 2.1 million hectares, of which no more than 1.4 million hectares is used today. This is estimated to cost the country 700 billion tenge to compensate for the shortfalls in agricultural production (Nazarbayev 2013).

Another concern is the increase in water salinity. Continuous monitoring studies have shown that currently more than 50% of irrigated lands have increased levels of salinity, while—at the same time—large amounts of land drainage pollute natural water resources. As a result, the productivity of agricultural land decreases, and their products do not meet environmental requirements (Zàuìrbek 2013).

The acute water resource deficit for the Ishim, Nura-Sarysu, and Tobol-Torgai river basins in Kazakhstan is considered an obstacle to the development of the mining industry in these locations, which constitutes a significant opportunity cost for the country. Besides coal, copper, and iron ore, the region also possesses large reserves of manganese and lead-zinc, ore, tungsten, molybdenum, bauxite, and asbestos raw materials for the development of the chemical industry and others. With 90% of the drainage for the Ishim, Nura-Sarysu, and Tobol-Torgai rivers occurring during 1–2 months in the spring and the potential to continue developing

the raw material sector, a water resource strategy is required to retain and possibly divert water resources from neighboring river basins as a solution to the local deficit (UNDP 2004). Beyond its vast amount of oil, gas, and coal, the Republic of Kazakhstan has a hydraulic potential of about 170 billion kWh per year, with the technological potential being 62 billion kWh per year. Despite this enormous potential, only 27 billion kWh is being generated with hydroelectric power systems. The economic potential of small hydropower generating units alone is estimated at 7.5–11.0 terawatt-hours per year, of which only 5% is produced (UNDP 2004).

These requirements demand a thorough restructuring of the existing system of natural water resource allocation and use as suggested by Zàuìrbek (2013) which is largely in line with the literature on Integrated Water Resource Management (IWRM) (Al Radif 1999; Biswas 2004; Jewitt 2002; Jonch-Clausen and Fugl 2001; Mitchell 2005; Thomas, Durham 2003; van der Brugge and Rotmans 2007). The major list of suggestions includes (1) developing and implementing international principles of water allocation and management in trans-boundary river basins, (2) developing and implementing mechanisms for the rational and efficient use of water resources, (3) developing and implementing the water-saving technologies that will transform industries into nonconsuming or low water-consuming industries, (4) developing and implementing the water pollution control technologies that will transform industries into nonpolluting or low-pollution industries, (5) developing and implementing action plans to improve water quality in the water bodies, (6) developing water rates that promote water-saving and water pollution control objectives, and (7) establishing a network monitoring service for accounting and allocation of water resources.

With respect to the latter, the current draft state program on water management of the Republic of Kazakhstan for 2014 to 2040 anticipates a significant investment in hydrological observation stations which—upon completion—will monitor and control 75% of the irrigation and drainage systems using modern gauging stations, water metering instruments, and automated process control system and will bring the number of state gauging stations to 500 in total by 2020. The coverage of hydrological observation network primarily concentrates on medium to large systems as well as small systems with significant impact on the economy (Nazarbayev 2013). In addition to field observation station, remote sensing technology is increasingly used to monitor and assess water resources.

3 Literature Review

3.1 Remote Sensing Technology

Increasingly, water resource management studies are conducted about the use of remote sensing techniques to understand the extent of water surfaces and their volumetric characteristics. This study will investigate how remote sensing

technology can be applied and integrated in the management of water resources and the infrastructure that control them.

Real-time remote monitoring (RTRM) systems combine a wide range of data modalities and technologies to enable high-speed visualization and analytics. In the water quality assessments, the monitoring platform usually consists of data processing device, automatic water sampler, hydrological profiler, rainfall sensor, enclosures for experimental equipment, humidity and temperature sensors, sunlight intensity sensor, lighting protector, wind speed sensor, and energy source such as solar. CAAE RTRM is an example of such a platform that can be made use in automatic data processing and alert response system making extensive use of remote monitoring techniques. There exist several RTRM programs; they are:

1. Baltic Sea Portal (http://www2.fimr.fi/en/itamerikanta.html)
2. Carolinas Coastal Ocean Observing and Prediction System (Caro-COOPS) (http://carocoops.org/carocoops_website/index.php)
3. Chesapeake Bay Program (http://www.chesapeakebay.net/overview.htm)
4. Chesapeake Bay "Eyes on the Bay" (http://mddnr.chesapeakebay.net/eyesonthebay/index.cfm)
5. MYSound monitoring-real-time observations, University of Connecticut (http://www.mysound.uconn.edu/)
6. Upper Susquehanna/Lackawanna River (http://wilkes.edu/~gisriver/)
7. US EPA Environmental Monitoring and Assessment Program (EMAP) (http://www.epa.gov/emap/)
8. Horn Point Choptank River Index Site—CISNet program, University of Maryland—(http://www.hpl.umces.edu/)
9. Hydrometeorological Automated Data System (HADS)—(http://www.nws.noaa.gov/oh/hads/)
10. Louisiana Universities Marine Consortium (LUMCON) current weather—(http://weather.lumcon.edu)
11. National Data Buoy Center (NDBC)—(http://www.ndbc.noaa.gov/)
12. National Estuarine Research Reserve System (NERRS)—(http://nerrs.noaa.gov/)
13. Rutgers University Coastal Ocean Observation Laboratory (RU-COOL) program—(http://marine.rutgers.edu/cool/)
14. San Francisco Bay, USGS RTRM SFPORTS—(http://sfports.wr.usgs.gov/)
15. South Carolina Algal Ecology Laboratory (SCAEL), South Carolina Department of Natural Resources/University of South Carolina—(http://links.baruch.sc.edu/scael/)
16. Woods Hole Oceanographic Institution (WHOI)—(http://www.whgrp.com/semb.htm)

RTRM platforms help to host the sensors and would enable the water engineers to monitor the quality and environmental conditions on a regular basis. The incorporation of imaging technologies into RTRM systems would enable better visualization and monitoring using modern satellite imaging. The high-resolution spatial data can be coupled with GPS and field computing devices. Though this is an

attractive scheme for real-time monitoring, they often suffer from feature misclassification such as resulting from shadows. In the last decade, this field has further extended to exploit the possibility to utilize very-high-resolution (VHR) multimodal/multi-temporal image fusion for different remote sensing applications. The state of the art suffers from the effects of layover, shadow, and foreshortening. These are largely open problems that affect the full utilization of VHR images for important problems of feature extraction and classification. We are interested in using VHR images to understand and study the water resources.

Detecting water bodies using remote sensing data has been described by a number of researchers who use digital imaging processing techniques to map the surface extent of water bodies. With increasing technological advances in remote sensing technology, this emphasis has shifted toward developing technologies that are capable of studying underwater depth of lake or ocean floors, and it is anticipated that remote sensing has potential to make significant contributions to river research by providing extensive, quantitative data that could yield insights on the changing nature of river dynamics at catchment scale level (Marcus and Fonstad 2008). Remote sensing of water depth in shallow marine settings has a long history (Lyzenga 1978; Philpot 1989; Maritorena et al. 1994), and the literature suggests increasing applications of remote sensing in the study of riverbed characteristics (Marcus and Fonstad 2008) using passive optical remote sensing involving the measurement of visible and near-infrared reflected solar energy that has interacted with the atmosphere, the water column, and the streambed. The relevant processes were summarized by Legleiter et al. (2009), based on previous studies by Philpot (1989), and Maritorena et al. (1994).

There are different methods for retrieving water depth from remote sensing data. Lyzenga (1979) proposed a method to retrieve water depth by removing water column effects to obtain bottom reflectance parameters from remote sensing imagery. This approach to river depth measurement is based on the transmission equation of electromagnetic radiation in water, and by measuring the optical parameters within the water body, water depth can be computed by neglecting the attenuation effect of a water body to obtain the relationship between water-leaving radiant energy and water depth (Lyzenga 1979). Alternatively, a linear relationship between water depth and a linear combination of the logarithmic radiant intensity can be assumed (Lyzenga 1978, 1981). Other methods include bottom albedo-based single-band models and multiband ratio models (Wang et al. 2007) which assume an ideal situation with vertical homogeneity for water body's photochemistry, high and invariable bottom albedo, and shallow water (Polcyn and Sattinger 1969; Polcyn and Lyzenga 1973). Under the assumption of no variability of bottom albedo in relation to bottom composition, Brown (1971) was able to increase the accuracy of water depth mapping by taking the ratio between two bands to minimize the bottom effects. Holding water quality and atmospheric conditions constant, Philpot (1989) discussed the effects of incrementing the number of influencing factors for water depth mapping, including bottom composition and water types.

Efforts to minimize the use of in situ data for light attenuation coefficients in water columns have been demonstrated by Stumpf et al. (2003) who were able to reduce five standard coefficients for bathymetry mapping down to two by developing a reflectance ratio model based on the variable radiant absorptivity among spectral bands requiring only a few water depth points from nautical charts for the calibration of the model. The estimation of the attenuation coefficients using only water levels present on multi-temporal images in reference to simultaneous sea level observations, thus obtaining absolute water depth directly from remote sensing images, was explored.

Increasingly, the ability of multispectral satellites to detect light in the blue (450–510 nm), green (510–580 nm), and red bands (630–690 nm) is leveraged to achieve good water depth estimates up to 15 meters in depth. It is anticipated that newer airborne, high-resolution, multispectral platforms with the ability to detect light between 400 and 450 may show that accurate bathymetric measurements can be achieved up to 20 meters and deeper.

The other main techniques for calculating bathymetry based on multispectral satellite imagery use a photogrammetric approach. In this method, stereoscopic images of an area are used to develop a digital elevation model (DEM) of a riverbed.

The application of a photogrammetric approach using radiometric data may be a promising, new application to develop accurate bathymetric models of shallow environments without ground truth. However, the technique has not been widely studied due to current limitations in the capabilities of remote sensing equipment and current sensors as well as image classification and analysis.

Identifying vegetations, waterways, and man-made structures from remote sensing images involves large amount of data processing and makes remote sensing data uniquely suitable for statistical pattern recognition methods. With respect to the latter, classifying objects and patterns is one of the major tasks for unsupervised classification of remote sensing imagery which are emerging to interpret the cluster centers of an image and to reveal a suitable number of classes to overcome the disadvantage of unsupervised classification (Burman 1999; Chen and Ho 2008; Pasolli et al. 2009; Schwarz and Datcu 1997; Stathakis and Vasilakos 2006; Yang and Yang 2004).

In line with current research in this field (Feng and Tian 2013; Hou et al. 2014; Li et al. 2008; Merabtene et al. 2002; Wang et al. 2009), the application of high-resolution remote sensing technology and advanced image processing using advanced algorithms and statistical pattern recognition will considerably advance the ability to monitor and assess water resources.

3.2 Knowledge Management

The exhaustive, unsustainable, and inefficient use of water resources along with the real environmental threat from intensively polluted water bodies arising from

mining, metallurgical, and chemical industries as well as untreated wastewater discharges to the environment from urban and rural settlements requires a new model for water resource allocation, consumption, use, and disposal.

Water resources and infrastructure management models are increasingly developed that promote sustainable use of water resources and infrastructures (Cardoso et al. 2012; Marlow et al. 2010; Marlow et al. 2011; Michele and Daniela 2011; Zhu et al. 2010; Zhu et al. 2011; Burns 2002), but integral to a water resource program are comprehensive knowledge management systems to support decision-making processes for water resource allocation, consumption, use, and disposal as well as infrastructure management.

Over the past few years, there has been a growing interest in treating knowledge as a significant organizational resource or asset (Alavi and Leidner 2001). Alongside, researchers have begun promoting a class of information systems, referred to as knowledge management systems (KMS), and a vast body of literature has emerged to address this interest (Alavi and Leidner 2001; Argote et al. 2003; Becerra-Fernandez and Sabherwal 2001; Earl 2001; Gold et al. 2001; Hedlund 1994; Liao 2003; McDermott 1999; Nickerson and Zenger 2004; Schultze and Leidner 2002; Spender 1996; Studer et al. 1998; Tanriverdi 2005; Tsoukas and Vladimirou 2001; Zack 1999). According to Alavi and Leidner (2001); the objective of KMS is to support creation, transfer, and application of knowledge in organizations. Asset-centric data management or dynamic asset registries depend upon the identification of significant systems, assets, or equipment via a unique identifier or spatial location in each of the supporting information systems thereby providing prospective user a comprehensive view of all relevant information. Such an aggregate upper tier system forms the initial building block for a new dynamic register that binds crucial data and information into one clear and cohesive asset-centric knowledge database for any management decision-making purposes. With the onset of the ITIS revolution and ever-increasing capability to produce, analyze, and store data, a research interest is emerging that demands a new generation of data integration forming a system that brings together disparate information irrespective of source system, location, or format type for the purpose of knowledge or intelligence building (Bradshaw et al. 2011d). Yet, knowledge and knowledge management are complex and multifaceted concepts that are developed in context.

Specific to water resource management, infrastructure management, and asset management, we find an increasing body of literature on strategies to support organizations and governments to manage resources using information and knowledge management systems. Early models and uses of decision support tools for collaborative planning in integrated water resource management have been described by Ubbels and Verhallen (2001), Boddy et al. (2007), Chen et al. (2010), Dalcanale et al. (2011), de Rezende et al. (2008), Grigg (2006), Karki et al. (2011), Jianxin et al. (2015), McNamara et al. (2009), Mikulecky et al. (2003), Quinn et al. (2010), Siontorou and Efthymiadou (2008), Toman (2007), Dewi et al. (2008), and Zhang et al. (2015).

Considering the multidimensional character of (water resource) management practices, different frameworks have been developed to encapsulate the main

aspects and requirements for knowledge-based asset management into a cohesive idea (Dalcanale et al. 2011; Champion and Leon Patterson 2012; Illaszewicz et al. 2013). The challenge is in designing a framework that is comprehensive enough to capture the key issues, but that continues to be manageable (UNDP 2009:32). As a result, one goal of the framework is to present the collective information as simply as possible in order to avoid dissuading its adoption by smaller organizations while still retaining applicability for advanced users. Alongside those goals is the need to retain flexibility for a wide range of potential situations. For this project, a conceptual water resource knowledge management framework has been developed to enquire and collect relevant information needs for water resource management and decision-making. The framework corresponds with the requirements for IWRM (Al Radif 1999; Biswas 2004; Jewitt 2002; Jonch-Clausen and Fugl 2001; Mitchell 2005; Thomas and Durham 2003; van der Brugge and Rotmans 2007; Sandhawalia and Dalcher 2008).

Recently frameworks have appeared that are designed to measure and develop organizational capability with respect to asset management in organizations (Illaszewicz et al. 2013). In the context of this review, the term "capability" is considered to represent the degree to which an organization can identify needs, plan, and implement decisions to achieve desired outcomes based on the knowledge stakeholders have. Capability development, therefore, represents "transformations that empower individuals, leaders, organizations and societies" (UNDP 2009:6). The outcomes are largely unique to the organization but are typically oriented around delivering the expected levels of service from infrastructure assets for the system users. To enable capacity development, a framework must exist to provide the frame of reference. A capability assessment model should allow an organization to locate itself on the framework, understand the opportunities that may be available to it (e.g., either for increasing or decreasing organizational capabilities), and make informed decisions and corresponding changes (e.g., competency training, capability development) as need be. To achieve process improvements, a system must be available to measure the current and target capabilities for which a variety of systems are available, such as benchmarking, total quality management, the Deming Cycle, or Capability Maturity Models.

A structured capability building framework spanning the breadth of knowledge management may offer a powerful tool for clarifying these relationships while returning the emphasis to development or improvement of organizational management capacity.

The knowledge management system has the aim to support the user to develop credible and defensible water resource management plans in line with IWRM objectives and in particular:

(a) Describe water resources and identify actual and emerging problems of water pollution and water use inefficiencies as well as infrastructure needs.
(b) Formulate plans and set priorities for water quality, water use management and infrastructure needs.

(c) Develop and implement water quality management programs, water allocation strategies and river basin asset management plans.

Such applications with the integration of geo-information systems have significant potential as a platform for managing environmental, water resource, and infrastructure data (Chen et al. 2010), and the mapping and geo-spatial analysis of information will see further advancements by integrating models and real-time monitoring thus providing comprehensive knowledge management systems used by regulators and public agencies responsible for water resource management and environmental engineering and management decision-making.

So far, the academic literature does not identify any significant maturity building knowledge management framework in the context of delivering water resource objectives and associated infrastructure. This type of knowledge management framework is considered novel and original in its conception. Developing a solution for integrating high-resolution remote sensing information into a comprehensive knowledge management system is considered original and novel.

4 Methodology

Considering the breadth of this research project and the need for ensuring compliance with the principles of scientific ethics and ethical management procedures, maintaining high standards of intellectual honesty, and avoiding the fabrication of scientific data, a clear perspective on the applied research strategy and methodology is required. A range of research strategies were considered and used in the design of this project, in particular relating to the design and information needs of a knowledge management system. Ethnography is concerned with specific people or cultural groups to describe a way of life or, in this project's context, "the way we do things here". As part of the sample group, the researcher interacts with the group. This poses a serious disadvantage since the researcher influences the information obtained in the studies. However, this may serve as an advantage from an action research perspective.

Action research has been promoted by practitioners as a moral responsibility to work socially meaningful in changing a situation for the better by the researchers' involvement. It is "research becoming praxis – practical, reflective, pragmatic action – directed towards solving the problems in the world" and has a deliberate interaction with the subject areas of study.

This project is considered to identifying an area of study and allows findings to emerge from systematically collected data. It is data driven with developed methods of collection and analysis that can stand up to rigor, reliability, and validity. It is approached by broad and exploratory search before focusing on emerging findings. This type of grounded theory allows the researcher to cover more territory while remaining relevant within the real world. It is a constant

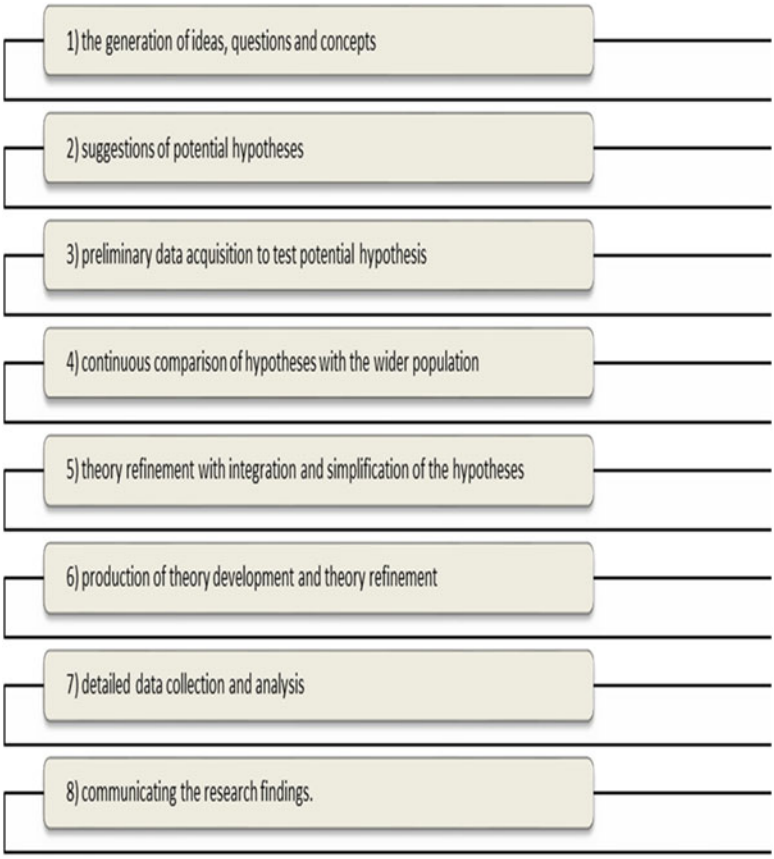

Fig. 1 Grounded theory research (According to Lee 1999)

comparative approach building on a continual review of new data against previously collected data that help to refine the development of a theory or hypothesis.

The project execution in this project follows Lee (1999) who identifies eight steps for grounded theory research (Fig.1). In this context, data acquisition strategies have to be considered for this project, and it was decided that the research scope of this project was best studied with qualitative research methods such as participant observation, interviews, surveys, document reviews, and keeping personal learning logs.

Qualitative data collection uses language, description, and expression (Trochim 2000) and emphasizes the human element in a "real" perspective. Using observational methods enables the collection of qualitative data by observing what groups or individuals do. Recording their actions and describing their activities in "real-world research" offer good advantages. Interviews provide a source of data from interacting in a conversation. The spectrum of interviews ranges from unstructured

via semi-structured to structured interviews. Whereas the former can provide very rich and detailed data with expressive and enlightening information, it lacks standardization in its results which is a definitive advantage in structured interviews. Yet, structured interviews lack in the inability to react to emergent topics raised by the interviewee. Surveys and questionnaires are an extension to interviews (Trochim 2000) and can be designed for quantitative analysis and even for self-administration. They offer a time-effective means of data acquisition, but questions arise over the quality of data obtained, e.g., unanswered questions and misinterpretation.

5 Results and Discussions

5.1 Remote Sensing Methodology Development

The scope of the work package included the following:

1. Creating and updating the inventory of water resources
2. Creating and updating the inventory of water bodies
3. River basin mapping and waterline identification
4. Detecting intermittent streams (streamflow and hollows)
5. Mapping of lakes and reservoirs and their major components (edge, coastal slope, coast, coastal shallows)
6. Determining the type of lake water cycle in nature (waste, closed drainage, flow, temporary waste, etc.)
7. Separation Lake mineralization at relatively fresh and salty
8. Identifying the elements of the structure of floodplains of major rivers (bends, meanders, furca, oxbow lakes, etc.)
9. Detecting and typing of large fluvial forms and their elements (ridge, rolls, reaches, backwaters, etc.)
10. Identifying the structure of young floodplain formations (islands, shoals, braids, blind area, bichevniki, etc.)
11. Identifying area of river flooding during flooding and flood forecasting
12. Delimiting the flooded areas during floods and a preliminary assessment of the impact of floods
13. Detecting unauthorized building in floodplains

In the initial pilot study, a methodology and algorithms were developed that were tested on imagery obtained for the Borovoy lake system (located in North Kazakhstan). The study sought to identify the structure of lake system including the bathymetric model of the lakes. The study will be complemented by field data from existing monitoring control station to determine the correlation between imagery and field data.

These image processing algorithms utilize very-high-resolution images and will synthesize any monitoring data for their presentation in tables, plots, or other graphical displays for standard computer as well as mobile phones and tablets. We would develop customized methods for segmentation, extraction of features, and learning methods to estimate the water volume and capacity within a predefined geographical region across the Ishim River basin. The identification of the water volume from the high-resolution images to be integrated to the knowledge management and data analysis framework involves the study of:

1. Imagery acquisition parameters: Identify appropriate acquisition windows and address the challenges of working with large geographic extents of high-resolution satellite data.
2. Field data sampling from multiple sensors: The reference data and recalibration of the point and polygon filed data to use with high-resolution images.
3. Spectral confusion: Solve the possible issues of spectral confusion associated with cover-type classifications.
4. Shadows: The issues of shadows on image classification and ways these errors can be accounted for or avoided.
5. Accuracy assessments: Develop techniques to model and assess the accuracy of the output maps outlining the water resources and its availability and accuracy of estimation in real-time setup. This work package will procure high-resolution remote sensing data to develop advanced algorithms to assess and monitor water resources for river basin water resource management. Data shall be provided by KGS from its own remote sensing satellites KazEOsat-1 and KazEOsat-2 or KGS partner's satellites. KGS performs distribution activities of the satellites within Astrium Geoinformation constellation and additionally RapidEye constellation. KazEOsat-1 and KazEOsat-2 operation is expected to start from the middle of 2014. The project will use remote sensing data procured from a high-resolution (1 m panchromatic and 4 m multispectral) remote sensing satellite with the following specifications: PAN, 600 nm; blue, 455–520 nm; green, 525–595 nm; red, 630–695 nm; and NIR, 775–850 nm. Middle-resolution satellite has a 6.5 m multispectral resolution with the following bandwidths: blue, 430–500 nm; green, 520–590 nm; red, 630–685 nm; red edge, 790–730 nm; and NIR, 760–850 nm.

The scope of this work package includes the development and application of algorithms to assess and monitor the hydrology of lakes, rivers, and reservoirs.

Four main groups of work with application of KazEOsat-1 and KazEOsat-2 datasets will be applied:

(A) Surface water coverage area (SWCA) extraction from the multispectral bands KazEOsat-1 and KazEOsat-2
(B) Digital elevation model (DEM) preparation from the stereo datasets KazEOsat-1 and KazEOsat-2
(C) Digital terrain model (DTM) preparation from DEM with bathymetry, water depth, and subtraction

(D) Water volume fluctuation computation and modeling with DTM applications

(A) SWCA extraction from the multispectral bands KazEOsat-1 and KazEOsat-2

From the various surveyed methods for extracting SWCA, normalized spectral indices, manual translation, and parametric classification of images are the most widely used. In comparison with other methods, the use of spectral indices has many advantages: this method relies primarily on the transformation of numerical values, which allows a decrease in background effects and reduced data dimensionality, providing a level of standardization for comparative purposes and enhancing the required signal for specific land cover and land use areas. Thus, normalized indices increase the separation ability of information extracted from remote sensing data. Because of spectral differences among diverse land cover and land use areas, surface areas can be calculated from different combinations of remotely sensed image bands depending on the type of surface analyzed, e.g., water, vegetation, or urban areas. KazEOsat-1 and KazEOsat-2 datasets are identical to RapidEye and SPOT satellites but have high pixel resolution. We developed (Sagin et al. 2015) a methodology to track contemporary water coverage changes using remote sensing. We prepared a GIS automated routine based on the modified normalized difference water index (mNDWI) to extract the surface water coverage area (SWCA) from optical satellite datasets using the surface water extraction coverage area tool (SWECAT). It was applied to measure SWCA during drought and flood peaks in the Saskatchewan River delta, Canada, from Landsat, SPOT, and RapidEye images. Landsat results were compared favorably with Canadian National Hydro Network (CNHN) GeoBase data, with deviations between SWCA classifications, and the base CNHN GeoBase shapefile of ~2%. Difference levels between the extracted SWCA layer from Landsat and the higher-resolution commercial satellites (SPOT and RapidEye) are also less than 2%. SWCA was tightly linked to discharge and level measurements from in-channel gauges ($r2 > 0.70$). We targeted to test and to adapt the SWECAT for KazEOsat-1 and KazEOsat-2 datasets. The current research adapted the approach of normalized spectral difference indices for the identification of water areas. Here, the normalized difference water index (NDWI) in the form of the modified NDWI (mNDWI) was used for the delineation of open surface water areas within the studied region:

$$\mathrm{mNDWI} = \frac{B_{\mathrm{green}} - B_{\mathrm{SWIR(NIR)}}}{B_{\mathrm{green}} + B_{\mathrm{SWIR(NIR)}}} \quad (1)$$

where B_{green} and $B_{\mathrm{SWIR(NIR)}}$ are sensor spectral and B_{green}, B_{SWIR} short-wave infrared, and $B_{(\mathrm{NIR})}$ near-infrared band values, respectively, for Landsat MMS, SPOT2 HRV, and RapidEye JSS56 that used the BNIR and for Landsat TM, SPOT4 HRVIR, and SPOT5 HRG that used the B_{SWIR} sensors. The mNDWI index varies from -1 to 1, depending on the proportions of subpixel water or non-water components (e.g., soil and/or vegetation). An application of a threshold can control the analysis output. Zero was set as the mNDWI threshold for open

surface water areas. In addition to the water index threshold, the $B_{SWIR(NIR)}$ thresholds were used for a better open surface water area identification and delineation. The $B_{SWIR(NIR)}$ thresholds were estimated for the satellite datasets using a visual assessment of the preliminary identification results and histograms of the image analysis. The different mNDWI thresholds and limits of the $B_{SWIR(NIR)}$ thresholds used for open surface water areas identification and delineation are: (a) Landsat MSS (NIR), 30; (b) Landsat TM (SWIR), 35; (c) Landsat ETM + (SWIR), 35; (d) SPOT2 HRV (NIR), 40; (e) SPOT4 HRVIR (SWIR), 40; (f) SPOT5 HRG (SWIR), 60; and (g) RapidEye JSS56 (NIR), 2500. RapidEye's threshold is higher because it has a higher radiometric resolution (16 bit data), compared to Landsat and SPOT (8 bit data). The general spatial resolution rule states that for the successful identification of the object of interest, there is a need for at least four spatial observations—pixels—in the case of remote sensing raster data. For example, the identification of a water object with a 60 m diameter would require four pixels with at least 30 m by 30 m spatial resolution. Therefore, the identified open surface areas were filtered: the objects less or equal to the area of three pixels were removed to avoid misinterpretation. After filtering, the identified open surface areas that intersect the study region were extracted as a final result.

KazEOsat-1 and KazEOsat-2 datasets have higher spectral resolution. In our search works, we will need to test for KazEOsat-1 and KazEOsat-2 datasets and find out the optimal threshold values to extract the SWCA.

(B) DEM preparation from the stereo datasets KazEOsat-1 and KazEOsat-2

DEM is one of the most important input data for any kind of hydrological, water management studies and modeling. Most of the hydrologists desire to apply the DEM from Light Detection and Ranging (LIDAR). However LIDAR is very expensive and still will be complicated to cover the big Kazakhstan territory. The other main techniques for DEM preparation is to use multispectral satellite imagery with a photogrammetric approach. In this method, stereoscopic images of an area are used to develop a DEM. Stereo SPOT, Landsat, ASTER, and RapidEye are used widely to extract a DEM. The high-resolution stereo KazEOsat-1 and KazEOsat-2 datasets are our target to extract the high-resolution DEM. The KazEOsat stereo-extracted DEM will be calibrated and verified with new German TanDEM-X (TerraSAR-X add-on for digital elevation measurement) spaceborne radar remote sensing datasets, which will be available from October 2014. Satellites were launched successfully from Kazakhstan Baikonur Cosmodrome recently and DEM data under processing by the German Space Agency, Microwave and Radar Institute. The DEMs with a spatial resolution of 12 m will be generated for the global TanDEM-X DEM as the primary mission goal. Moreover, local DEMs of higher accuracy level (spatial resolution of 6 m and relative vertical accuracy of 0.8 m) and applications based on along-track interferometry (ATI) will be available. We have submitted a science grant proposal to TanDEM-X Science Service System (https://tandemx-science.dlr.de/) to test the new high-resolution DEM. This

is one of the main research targets of the high-resolution DEM preparation for Kazakhstan's territory.

Mainly, in this project, identification of structure of lakes will be based on imagery data, and digital elevation model (DEM) of bathymetry will be created from high-resolution imagery using PCI Geomatica software. Particularly, image correlation is used to extract matching pixels in two overlapping images and then uses the sensor geometry from a computed match model to calculate x, y, and z positions.

Collecting stereoscopic imagery of the shallow ocean floor is in how light interacts with the air/water interface. At high angles of incidence, light is completely reflected off the water surface thus preventing any subaquatic profiles from being observed. In this application, a sensor is required to collect enough high-resolution stereoscopic imagery within the narrow angle to penetrate the surface of a water body. Thus, measured depth points from satellites and bathymetric data will be used to extract sensor reflectance values from each image, and then the points are divided for testing and calibrating.

(C) Digital terrain model (DTM) preparation from DEM with bathymetry, water depth, and subtraction

DTM is a bare-earth model that contains elevations of natural terrain features such as barren ridge tops and river valleys. Elevations of vegetation and cultural features, such as buildings and roads, and water parts are digitally removed. We targeted to collect the river and lakes' bathymetry, water depth, and subtract from the DEM the bathymetry data. This methodology has been used widely, including Canada, by the water resource companies and agencies. Saginatyev's research group applied the methodology for Saskatchewan and Slave River basins in Canada.

(D) Water volume fluctuation computation and modeling with DTM applications

The SWCA group of data will be prepared in the research work (A) from the multispectral bands KazEOsat-1 and KazEOsat-2 in combination with DTM data. Furthermore, using the GIS platform and the field data provided by Ministry of Environment and Water Resources in Kazakhstan, modeling of water volume fluctuation will be created by comparing water volume data in the 1980s with recent years. Further, a change in water volume comparison will be computed and shown statistically.

(C) Will be used for water volume fluctuation, computation and modeling

5.2 Methodology for Development of Water Resource Knowledge

Moreover, by now, the methodology for developing water resource knowledge has been developed. It includes implementation of the following steps:

1. Find old historical maps covering the lake research area that were 50–100 years ago.
2. Georeference all these maps in GIS and extract surface water coverage of all lakes.
3. Download all Landsat data covering the research area from 1972 till the present day from http://glovis.usgs.gov/.
4. Make all atmospheric corrections of all Landsat data, preprocess, and extract surface water coverage of all lakes.
5. Compute surface water coverage changes by using your processed data, similar to the paper in (4).
6. Prepare high-resolution digital terrain model (DTM) from stereo KazEOSat dataset, by using similar tools such as OrthoEngine and stereo DEM extraction tool from PCI Geomatica, ENVI, or ERDAS.
7. Compute water volume by compiling the surface water coverage from processed data and DTM by using GIS tools.
8. Compute water volume changes by using your processed data, and show statistics in GIS, Excel, or MATLAB.
9. Track algae pollution by using the multispectral satellite bands from Landsat or KazEOSat-1.
10. Compare the extracted water pollution data from satellites and the field hydrochemical analysis, and show statistics.
11. Apply ArcSWAT for modeling to predict the future changes, including water quantity and water quality.

By means of this scheme, it's planned to focus first of all on lakes located in Borovoy area and then on water bodies of East Kazakhstan.

Historical maps 50–100 years ago will allow conducting comparative analysis with the recent years (1); these maps will be georeferenced to existing GIS data so that it would be possible to digitize the information from them. The historical maps and satellite images, in turn, will provide us a change through time (2).Regarding monitoring change of surface water coverage, it is quite important for the management of water, biological components (Sagin et.al. 2014), and hydraulic alterations. This extraction of surface water coverage area will be possible using GIS platform and PCI Geomatica from Landsat images (3, 4, 5). Performing the water management tasks is not possible without simulation of the natural terrain elevation (6); particularly it will enable us to compute water volumes using bathymetry data (7, 8).

Further it is planning to monitor water pollution, specifically caused by algae pollution. Based on high-resolution satellite data, it is possible to track algae

pollution in terms of color of a water body; the color occurs usually because of the presence of some organic pollutants in a water body, so that it affects water quality and living organisms (9).Furthermore, once we extract water pollution data, field hydrochemical analysis will be compared statistically (10).Based on all research, prediction of future changes will be conducted using ArcSWAT platform.

5.3 Knowledge Management System

The objective of this work package was to identify information requirements for managing water resource and developing a functional description of a software platform that contains all relevant information required for water resource decision-making and management.

Alongside the requirements for IWRM, a conceptual water resource knowledge management framework has been developed to inquire and collect relevant information needs for water resource management and decision-making. The framework is an extension to the one designed by Dalcanale, Fontane, and Csapo (2011).The conceptual water resource knowledge management framework is currently in development as part of the Nazarbayev University seed grant program and was developed to include nine distinct but interrelated components (Table 1).

The testing and further refinement of knowledge management platform were conducted by inviting water resource management experts, professionals, and professional organizations and institutions to participate in workshops, interviews, and surveys. These were carried out to develop a comprehensive understanding of management decision-making and management processes as well as information and data needs, in particular relating to:

Water Resource Strategy and Policy

- Formulate strategies, policies, and plans and setting priorities for water quality, water use management, and infrastructure needs.
- Develop water quality management program, water allocation strategies, and river basin asset management plans.

Table 1 Water resource knowledge management framework

Water resource strategy and policy
Stakeholder management
Ownership, responsibility, authority, and resources
Inventory of the water resource and its infrastructure
Condition and performance of a water resource and its infrastructure
Valuations and financial review
Monitoring, control, and knowledge management
Internal process development and review
Risk assessment, management, and emergency response

Stakeholder Management

- Develop and maintain a stakeholder network with relevant government organizations involved in water resource management.

Ownership, Responsibility, Authority, and Resources

- Develop an understanding of the governance structure for a water resource river basin including ownership, responsibility, authority for decision-making, and decision-making resources.

Inventory of the Water Resources and Its Monitoring and Control Infrastructure

- Inventory key attributes of water resources and their monitoring and control infrastructure

Condition and Performance of a Water Resource and Its Infrastructure

- Assess and monitor the condition of water resource and their infrastructure assets including physical structures, monitoring and control stations, and equipment.
- Identify actual and emerging problems of water pollution, quantitative water use restrictions, and infrastructure needs.
- Obtain, analyze, and prepare monitoring data from existing flow monitoring stations.
- Specify and develop and/or assess a rainfall-surface water runoff model for the water resource.
- Valuations and financial review.
- Evaluate water resource infrastructure assets.
- Evaluate water resource as an economic resource for domestic, industrial, and commercial use.
- Evaluate the economic, commercial, and financial implications for inter-basin water conveyance systems.

Internal Process Development and Review

- Document the governing processes for water abstraction and pollution control for a water resource river basin based on the review of ownership, responsibility, authority for decision-making, and decision-making resources.

Risk Assessment, Management, and Emergency Response

- Document risk assessments and risk management systems as well as processes and procedures for responses to emergencies (floods, draughts, structural failures, etc.).

It is anticipated to further engage with experts, professionals, and professional institutions with relevant experience in water resource management and the management of water resource assets and infrastructure to further refine the framework.

5.4 Technical Knowledge Management Architecture

The knowledge management platform requires integration of many different technologies and methods including network technology, sensor technology, database technology, telecommunication technology, and information management method. In our proposal, the system consists of four parts: wireless sensor network, local server, monitoring service platform, and application server which are connected and operated coordinately. They form an integral part of real-time data collecting, management of information, comprehensive analysis and support planning, and real-time control. The algorithms developed in WP3 will be embedded into the software script to integrate (near) real-time monitoring and control into a software platform used to manage water resources and their controlling infrastructure.

The software and hardware design principle of (near) real-time monitoring and management system in water resources will be developed as shown in Fig. 2.

The main structure of the system in Fig. 1 can be divided into two parts: central management system and communication system.

The central management system includes a monitoring service platform and application server. The monitoring service platform provides real-time data collection of various parameters related to water resource management, such as temperature, moisture content (air humidity), water flow rate, water volume, water quality,

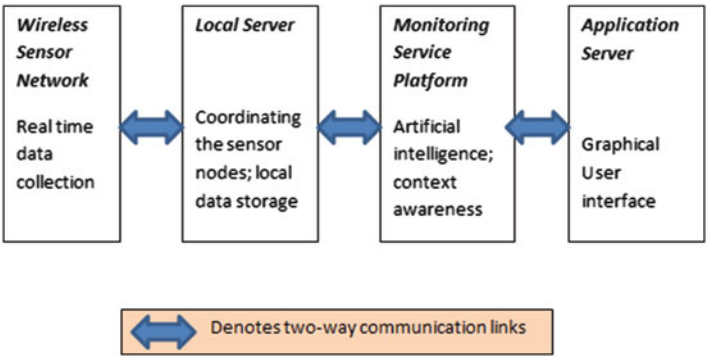

Fig. 2 Architecture of the real-time monitoring system for water resources

and rainfall. The system will analyze the validity of the data before saving it to a central database. It can output the information in a variety of charts or simulation graphs to show a trend including short-term forecasting or prediction. That involves mathematical modeling using artificial intelligence and context awareness, based on data that have been collected. Apart from that, the system can have built-in decision-making, for example, activate certain control or send alert messages, when there is a sudden change in temperature. The interface to users will be done through the application server in the form of graphical user interface (GUI).

The communication system includes both wired and wireless communications. Various sensors will be communicating wirelessly with a control terminal (local server that serves as a coordinating focal point) that is located within the coverage area using various standards, for example, ZigBee, based on IEEE 802.15.4. The control terminal will be connected to the central management system (see item A above) using high-speed cable communication link.

6 Conclusions

In this project, it is aimed to make two distinct contributions to knowledge:

1. High-resolution remote sensing: The development of a real-time online monitoring and assessment capability based on genetic algorithms and statistical pattern recognition has potential to find significant, customized application to advance the management of water resources and environmental systems by enabling real-time and remote monitoring of physical and hydraulic attributes of water resources. The integration of advanced algorithms to assess and monitor water resources for river basin water resource management into a prototype for a water resource monitoring capability that is complementary on the ground field observation stations is novel.
2. Knowledge management: The management of water resources and its infrastructure requires evidence-based decisions that are based on capabilities to monitor, evaluate, and optimize water resource management activities. Tools and processes at strategic, policy, and tactical level form an integrated monitoring and control framework to proactively and consistently identify and assess water resources. This places the identification, assessment, and control of water resources at the center of water resource management and therefore the availability and quality of information at the center of decision-making.

The application developed in this project will form a prototype for water resource and infrastructure knowledge management system. With the mapping and geo-spatial analysis of information as a basis, it is anticipated that the integration of real-time monitoring provides a comprehensive knowledge management systems to support water resource management and environmental engineering decision-making processes in regulatory and public agency organizations.

In the continuation of this project, we will develop a methodology for hydro-potential assessment using remote sensing data. The objective is to develop a water resource development strategy with specific emphasis on developing hydroelectric power generation capacity in Kazakhstan. Therefore, the project includes:

- Studying practice of water resource management and information sources as they relate to the East Kazakhstan river basin
- Obtaining remote sensing data and algorithm development to assess hydropower generation potential
- Developing an understanding of hydroelectric power generation potential on rivers in East Kazakhstan
- Developing a methodology for prioritizing more detailed investigations into the feasibility of small power stations based on parameters specified in the RFP and this pre-proposal
- Identifying three sites for a detailed feasibility analysis
- Conducting three detailed feasibility analyses

The project will result in a comprehensive technical and economic feasibility study for investing in hydropower generation by quantifying flow volumes, identify potential sites for water storage, and assess geographic elevation gradients that are suitable to produce electricity with small hydropower stations. The study includes the technical specifications and risk assessment for design and construction of three hydroelectric power generating plants and is presented with comprehensive cost estimates and revenue projections. Given the local potentialities of each particular location (flow duration curve and available head), a reservoir or a run-of-river unit will be recommended up to basic engineering level, according to local and world-wide providers. Additionally, an assessment of the economic and technical viability of each unit will be performed based on CapEx, OpEx, and general financial parameters (discount rate, inflation, energy escalation, etc.). The study will include a sensitivity and risk analysis to determine the best and worst conditions as well as to guide public policies to stimulate private or public investments in the sector with a fair profit or to value strategic decision-making.

Acknowledgments This research was supported by NURIS of Nazarbayev University. These supports are gratefully acknowledged.

References

Al Radif, A.: Integrated water resources management (IWRM): an approach to face the challenges of the next century and to avert future crises. Desalination. **124**(1–3), 145–153 (1999)

Alavi, M., Leidner, D.: Review: knowledge management and knowledge management systems: conceptual foundations and research issues. MIS Q. **25**(1), 107–136 (2001)

Argote, L., McEvily, B., Reagans, R.: Managing knowledge in organizations: an integrative framework and review of emerging themes. Manag. Sci. **49**(4), 571–582 (2003)

Becerra-Fernandez, I., Sabherwal, R.: Organizational knowledge management: a contingency perspective. J. Manag. Inf. Syst. **18**(1), 23–55 (2001)

Biswas, A.: Integrated water resources management: a reassessment - a water forum contribution. Water Int. **29**(2), 248–256 (2004)

Boddy, S., Rezgui, Y., Wetherill, M., Cooper, G.: Knowledge informed decision making in the building lifecycle: an application to the design of a water drainage system. Autom. Constr. **16** (5), 596–606 (2007)

Bradshaw R., Watt D., Anderson M.: Building First Nations Data Integration into Asset Management. In: 16th Annual OFNTSC Conference and Tradeshow, Thunder Bay on August 23–25 (2011)

Brown, W., Polcyn, F., Stewart, S.: A method for calculating water depth, attenuation coefficients, and bottom reflectance characteristics in proceedings. Seventh International Symposium on Remote Sensing of the Environment, Ann Arbor, MI, USA, pp. 663–680 (1971)

Burman, J.: Hybrid pattern recognition method using evolutionary computing techniques applied to the exploitation of hyperspectral imagery and medical spectral data. Image. Signal Process. Remote Sens. V. **3871**, 348–357 (1999)

Burns, P.: Implementing Strategic Asset Management. APWA International Public Works Congress, Kansas City (2002)

Cardoso, M., Silva, M., Coelho, S., Almeida, M., Covas, D.: Urban water infrastructure asset management - a structured approach in four water utilities. Water Sci. Technol. **66**(12), 2702–2711 (2012)

Chen, C., Ho, P.: Statistical pattern recognition in remote sensing. Pattern Recogn. **41**(9), 2731–2741 (2008)

Chen, D., Shams, S., Carmona-Moreno, C., Leone, A.: Assessment of open source GIS software for water resources management in developing countries. J. Hydro Environ. Res. **4**(3), 253–264 (2010)

Dalcanale, F., Fontane, D., Csapo, J.: A general framework for a collaborative water quality knowledge and information network. Environ. Manag. **47**(3), 443–455 (2011)

De Rezende, J., Da Silva, R., De Souza, J., Rotunno Filho O.: Sharing the knowledge generated during a water resources project. 12th International Conference on Computer Supported Cooperative Work in Design, Xi'an, China (2008)

Earl, M.: Knowledge management strategies: toward a taxonomy. J. Manag. Inf. Syst. **18**(1), 215–233 (2001)

Feng, K., Tian, J.: Water resources optimal allocation based on multi-objective differential evolution algorithm. Adv. Mechatronics Control Eng.., Pts 1–3. **278–280**, 1271–1274 (2013)

Gold, A., Malhotra, A., Segars, A.: Knowledge management: an organizational capabilities perspective. J. Manag. Inf. Syst. **18**(1), 185–214 (2001)

Grigg, N.S.: Workforce development and knowledge management in water utilities. J. Am. Water Works Ass. **98**(9), 91 (2006)

Hedlund, G.: A model of knowledge management and the N-form corporation. Strateg. Manag. J. **15**, 73–90 (1994)

Hou, J., Mi, W., Sun, J.: Optimal spatial allocation of water resources based on Pareto ant colony algorithm. Int. J. Geogr. Inf. Sci. **28**(2), 213–233 (2014)

Illaszewicz, G., Bradshaw, R., Smith, S.: Asset management capacity development using a structured framework, OWWA/OMWA Joint Annual Conference & Tradeshow, Ottawa, 5–8 May 2013

Jewitt, G.: Can integrated water resources management sustain the provision of ecosystem goods and services? Phys. Chem. Earth. **27**(11–22), 887–895 (2002)

Jianxin, L.; Rui, Z.; Yun, Z.: General Frame of Hai Basin KM System and Information Sharing. Physical and Numerical Simulation of Geotechnical Engineering; Brighton East, Iss. 20, 30–39 (2015)

Jonch-Clausen, T., Fugl, J.: Firming up the conceptual basis of integrated water resources management. Int. J. Water Resour. Dev. **17**(4), 501–510 (2001)

Karki, M.B., Shrestha, A.B., Winiger, M.: Enhancing knowledge management and adaptation capacity for integrated management of water resources in the Indus River basin. Mt. Res. Dev. **31**(3), 242–251 (2011)
Lee, T.: Using Qualitative Methods in Organizational Research. Sage Publications, Thousand Oaks (1999)
Legleiter, C.J., Roberts, D.A., Lawrence, R.L.: Spectrally based remote sensing of river bathymetry. Earth Surf. Process.Landf. **34**, 1039–1059 (2009)
Li, C., Yang, Z., Huang, G., Cai, Y.: Genetic projection pursuit interpolation model for social renewability assessment of water resources (2008)
Liao, S.H.: Knowledge management technologies and applications - literature review from 1995 to 2002. Expert Syst. Appl. **25**(2), 155–164 (2003)
Lyzenga, D.R.: Passive remote sensing techniques for mapping water depth and bottom features. Appl. Opt. **17**(3), 379–383 (1978)
Lyzenga, D.R.: Shallow-water reflectance modeling with applications to remote sensing of ocean floor. Proceeding of 13th international Symposium on remote sensing of environment, Ann Arbor, MI, USA, pp. 583–602 (1979)
Lyzenga, D.R.: Remote sensing of bottom reflectance and water attenuation parameters in shallow water using aircraft and Landsat data. Int. J. Remote Sens. **2**(1), 71–82 (1981)
Marcus, W., Fonstad, M.: Optical remote mapping of rivers at sub-meter resolutions and watershed extents. Earth Surf. Process. Landf. **33**, 4–24 (2008). doi:10.1002/esp.1637
Maritorena, S., Morel, A., Gentili, B.: Diffuse-reflectance of oceanic shallow waters – influence of water depth and bottom albedo. Limnol. Oceanogr. **39**, 1689–1703 (1994)
Marlow, D., Beale, D., Burn, S.: A pathway to a more sustainable water sector: sustainability-based asset management. Water Sci. Technol. **61**(5), 1245–1255 (2010)
Marlow, D., Pearson, L., MacDonald, D., Whitten, S., Burn, S.: A framework for considering externalities in urban water asset management. Water Sci. Technol. **64**(11), 2199–2206 (2011)
McDermott, R.: Why information technology inspired but cannot deliver knowledge management. Calif. Manag. Rev. **41**(4), 103 (1999)
McNamara, L., Cornish, P., Jacobs, B.: Improving the relevance and impact of water quality modelling for decision-making. 8th World IMACS /MODSIM Congress, Cairns, Australia 13–17 (2009)
Merabtene, T., Kawamura, A., Jinno, K., Olsson, J.: Risk assessment for optimal drought management of an integrated water resources system using a genetic algorithm. Hydrol. Process. **16** (11), 2189–2208 (2002)
Michele, D.S., Daniela, L.: Decision-support tools for municipal infrastructure maintenance management. In: World Conference on Information Technology (Wcit-2010), vol. 3. 2011
Mikulecky, P., Ponce, D., Toman, M.: A knowledge-based solution for river water resources management. Water Resour. Manag. II. **8**, 451–458 (2003)
Mitchell, B.: Integrated water resource management, institutional arrangements, and land-use planning. Environ. Plan. A. **37**(8), 1335–1352 (2005)
Nazarbayev, N.: Draft Decree of the President of the Republic of Kazakhstan on the State Program on Water Management of the Republic of Kazakhstan for 2014–2040 Years. Government of Kazakhstan, Astana (2013)
Nickerson, J.A., Zenger, T.R.: A knowledge-based theory of the firm-the problem-solving perspective. Organ. Sci. **15**(6), 617–632 (2004)
Pasolli, E., Melgani, F., Donelli, M.: Automatic analysis of GPR images: a pattern-recognition approach. IEEE Trans. Geosci. Remote Sens. **47**(7), 2206–2217 (2009)
Philpot, W.D.: Bathymetric mapping with passive multispectral imagery. Appl. Opt. **28**(8), 1569–1579 (1989)

Polcyn, F.C., Lyzenga, D.R.: Calculation of water depth from ERTS-MSS data. Proceedings Symposium on Significant Results Obtained from ERTS-1, Ann Arbor, MI, USA, pp. 1433–1436 (1973)
Polcyn, F.C., Sattinger, I.J.: Water depth determination using remote sensing techniques. Proceedings of the 6th International Symposium on Remote Sensing of Environment, Vol. II, Ann Arbor, MI, USA, pp. 1017–1028 (1969)
Quinn, P.F., Hewett, C.J.M., Muste, M., Popescu, I.: Towards new types of water-centric collaboration. Proc. Inst. Civ. Eng. Water Manage. **163**(1), 39–51 (2010)
Sagin, J., Sizo, A., Wheater, H., Jardine, T.D., Lindenschmidt, K.-E.: A water coverage extraction approach to track inundation in the Saskatchewan River Delta, Canada. Int. J. Remote Sens. **36**, 764–781 (2014)
Sagin J., Sizo A., Wheater H., Jardine T.-D., Lindenschmidt K.-E.: A water coverage extraction approach to track inundation in the Saskatchewan River Delta, Canada. Int. Journal of Remote Sensing. **36**(3), pp. 764–781 (2015)
Sandhawalia, B., Dalcher, D.: Knowledge management capability framework. Knowl. Manag. Action. **270**, 165–180 (2008)
Schultze, U., Leidner, D.E.: Studying knowledge management in information systems research: discourses and theoretical assumptions. MIS Q. **26**(3), 213–242 (2002)
Schwarz, G., Datcu, M.: Wavelets – a universal tool for the processing of remote sensing image data? Image Process. Signal Process. Synth. Aperture Radar Remote. Sens. **3217**, 427–434 (1997)
Siontorou, C.G., Efthymiadou, A.P.: Knowledge management for lake restoration strategy in protected areas. (2008)
Spender, J.C.: Making knowledge the basis of a dynamic theory of the firm. Strateg. Manag. J. **17**, 45–62 (1996)
Stathakis, D., Vasilakos, A.: Comparison of computational intelligence based classification techniques for remotely sensed optical image classification. IEEE Trans. Geosci. Remote Sens. **44** (8), 2305–2318 (2006)
Studer, R., Benjamins, V.R., Fensel, D.: Knowledge engineering: principles and methods. Data Knowl. Eng. **25**(1–2), 161–197 (1998)
Stumpf, R.P., Holderied, K., Sinclair, M.: Determination of water depth with high-resolution satellite imagery over variable bottom types. Limnol. Oceanogr. **48**, 547–556 (2003)
Tanriverdi, H.: Information technology relatedness, knowledge management capability, and performance of multibusiness firms. MIS Q. **29**(2), 311–334 (2005)
Thomas, J.S., Durham, B.: Integrated water resource management: looking at the whole picture. Desalination. **156**(1–3), 21–28 (2003)
Toman, M.: Utilization of knowledge management and information technologies theory in water resources management. Water Resour. Manag. IV. **103**, 667–676 (2007)
Trochim, W.: The Research Methods Knowledge Base, 2nd edn. Atomic Dog Publishing, Cincinnati (2000)
Tsoukas, H., Vladimirou, E.: What is organizational knowledge? J. Manag. Stud. **38**(7), 973–993 (2001)
Ubbels, A., Verhallen, A.J.M.: Collaborative planning in integrated water resources management: the use of decision support tools. Integrated Water Resour. Manag. **272**, 37–43 (2001)
United Nations Development Programme (UNDP) Kazakhstan: Water Resources of Kazakhstan in the new millennium, Report # UNDPKAZ 07, Almaty (2004)
United Nations Development Programme, 2009, Capacity Development: A UNDP Primer. Available online: http://www.undp.org/content/dam/aplaws/publication/en/publications/capacity-development/capacity-development-a-undp-primer/CDG_PrimerReport_final_web.pdf
Van der Brugge, R., Rotmans, J.: Towards transition management of European water resources. Water Resour. Manag. **21**(1), 249–267 (2007)

Wang, X., Sun, Y., Song, L., Mei, C.: An eco-environmental water demand based model for optimising water resources using hybrid genetic simulated annealing algorithms. Part I. Model development. J. Environ. Manag. **90**(8), 2628–2635 (2009)

Dewi A., Luckin R., Sheriff R.E., Lynne Dunckley L.: Development of a knowledge management system integrated with localcommunication channels and knowledge management initiatives for Kenyan rural farming communities. Proceedings of the Fifth IEEE International Conference on Wireless, Mobile and Ubiquitous Technologies in Education, WMUTE 2008, 23–26 March 2008, Beijing, China (2008)

Yang, M.D., Yang, Y.F.: Genetic algorithm for unsupervised classification of remote sensing imagery. Image Process. Algorithms Syst. III. **5298**, 395–402 (2004)

Zack, M.H.: Developing a knowledge strategy. Calif. Manag. Rev. **41**(3), 125–+ (1999)

Zàuìrbek, A.K.: National programme for water resources management in the Republic of Kazakhstan, Almaty: KazNatAGRU (2013)

Zhang, J., Shi, Z., Fu, X.: Development and application of knowledge management (KM) system information platform of GEF Haihe river project. Physical and Numerical Simulation of Geotechnical Engineering; Brighton East Iss. 20, pp. 54–58 (2015)

Zhu, H., Liu, T., Huang, Q.: Performance evaluation of water asset management in china based on entropy theory. (2010)

Zhu, H., Wang, Z., Liu, T.: Performance evaluation of water asset management in China. Front. Green Build. Mater. Civ. Eng.. Pts 1–8. **71–78**, 2116–2121 (2011)

Investigation of Thermal Characteristic of Eutectic Fatty Acid/Damar Gum as a Composite Phase Change Material (CPCM)

Hadi Fauzi, Hendrik S.C. Metselaar, T.M.I Mahlia, Mahyar Silakhori, and Hwai Chyuan Ong

1 Introduction

Thermal energy storage (TES) plays an important role in generating solar energy to be used in a wide range of applications such as heating and cooling, solar power, and industrial waste heat recovery (Al-Abidi et al. 2012; Cabeza et al. 2011; Kuravi et al. 2013; Nomura et al. 2010). Latent heat thermal energy storage (LHTES) materials known as phase change materials (PCMs) offer more advantage over sensible heat thermal energy storage (SHTES) materials, particularly the small temperature difference between melting and solidifying point, small volume, and low weight per unit of storage capacity. PCMs absorb heat as storage energy during the heating process and release it during cooling (Pielichowska and Pielichowski 2014). Phase change materials (PCM) used in thermal energy storage (TES) application have been classified into two categories: inorganic and organic phase change materials (PCMs). Although the inorganic PCMs have a great heat storage capacity and a wide range of phase transition temperature, they have a number of

H. Fauzi (✉)
Department of Mechanical Engineering, University of Malaya, Kuala Lumpur 50603, Malaysia

Department of Chemical Engineering, Syiah Kuala University, Banda Aceh 23111, Indonesia
e-mail: hadidoank@gmail.com

H.S.C. Metselaar (✉) • M. Silakhori • H.C. Ong
Department of Mechanical Engineering, University of Malaya, Kuala Lumpur 50603, Malaysia
e-mail: h.metselaar@um.edu.my

T.M.I. Mahlia
Department of Mechanical Engineering, Universiti Tenaga Nasional, Kajang 43000, Selangor, Malaysia

© Springer International Publishing AG, part of Springer Nature 2018

F. Aloui, I. Dincer (eds.), *Exergy for A Better Environment and Improved Sustainability 2*, Green Energy and Technology,
https://doi.org/10.1007/978-3-319-62575-1_42

disadvantages such as subcooling, corrosion, phase separation, phase segregation, and lack of thermal stability, compared with organic PCMs which only have a problem with low heat transfer rate due to low thermal conductivity (Fauzi et al. 2014; Zalba et al. 2003; Zhou et al. 2014). Therefore, enhancement of thermal conductivity of organic phase change materials (PCMs) has become one of the main issues in a wide application of thermal energy storage (TES).

A few different methods have been proposed to enhance the thermal conductivity of PCMs. Encapsulation was one of the methods proposed to improve the thermal conductivity of PCMs. On the other hand, this method has handled the leakage problem properly and brings a high cost in production (Zhou et al. 2014). In addition, thermal conductivity of PCM can be improved by adding high conductive porous material using simple mixing method, solution casting method, or impregnation method (Alkan and Sari 2008; Kim and Drza 2009; Nomura et al. 2009; Zhang and Fang 2006).

In this work, we prepared the composite phase change material (CPCM) by adding *Shorea javanica* obtained from purified damar gum as a porous material to improve the thermal conductivity of myristic acid/palmitic acid/sodium laurat (MA/PA/SM) eutectic mixture, combining simple mixing and impregnation methods.

Nomenclature

ΔH_{f}	Latent heat of fusion ($J.g^{-1}$)
$\Delta H_{\mathrm{f,m}}$	Latent heat of fusion at melting ($J.g^{-1}$)
$\Delta H_{\mathrm{f,s}}$	Latent heat of fusion on solidifying ($J.g^{-1}$)
T_{m}	Melting temperature ($^{\circ}C$)
T_{s}	Solidification temperature ($^{\circ}C$)

2 Material and Methods

2.1 Materials

The myristic acid/palmitic acid with the addition of 5 wt.% sodium myristate, known as MA/PA/SM eutectic mixture, proposed by Fauzi et al. (2013) was used as a base phase-change material (PCM). Natural damar gum or *Shorea javanica* collected from conventional plantation in Indonesia has been proposed for use as porous material. An additional purification process is required to obtain impurities-free *Shorea javanica* (SJ).

Purification method by organic solvent has been used to purify *Shorea javanica* (SJ) (Setianingsih 1992). Toluene MW. 92.14 (Fisher Scientific) and SJ in composition ratio of 1:8 wt.% were stirred at 2000 rpm for 20 min under ambient temperature to obtain a completely dissolved SJ solution. Furthermore, 1 wt.% of

activated charcoal (AC) supplied from Acros Organic was added for decolorizing the SJ solution, and stirred for 15 min at 45 °C. Sedimentation and filtration processes were performed to separate the impurities from the solution. Then, the pure solution of *Shorea javanica* (SJ) was placed in the evaporator to remove the solvent, and finally, the button product of SJ was dried in the oven at 80 °C for 8 h to obtain pure *Shorea javanica* powder. Furthermore, the powder of *Shorea javanica* (SJ) was ground in a rotary ball mill and further put into a sieve shaker separator to obtain particles of *Shorea javanica* (SJ) of the same size (100 μm).

2.2 Preparation and Analysis Methods

A combination of simple mixing (Kim and Drza 2009) and impregnation (Nomura et al. 2009) methods known as mixing–impregnation method has been used to prepare a novel eutectic composite phase change material (CPCM) of MA/PA/SM/SJ. The MA/PA/SM and SJ in various composition ratios of 1, 2, 3, 4, and 5 wt.% were placed together in a jacketed flask reactor at different times under vacuum pressure, and the heat absorbed from the heat transfer fluid (HTF) at 70 °C. Furthermore, stirrer mixing was applied for homogenous distribution of SJ in MA/PA/SM eutectic mixture. These preparation processes were performed for 2 h and closed by drying under ambient temperature.

The prepared eutectic composite of MA/PA/SM/SJ in different composition ratios of SJ have been separately evaluated for the thermal properties, thermal conductivity and thermal stability, using the thermal differential scanning calorimetric (DSC) thermal analysis (Metler Toledo, DSC1 Star^e system), the thermal conductivity analyzer (Hot Disc, TPS 2500 S), and Simultaneous Thermal Analyzer (STA 6000, Perkin Elmer). The Fourier transform infrared spectroscopy (FT-IR, Bruker Tensor 27) was used to identify the chemical reaction that occurred between the MA/PA/SM eutectic mixture and *Shorea javanica*. The analysis was performed using ATR sample compartment with MIR spectra in the wave number range of 4000–400 cm^{-1}.

Moreover, the thermal performance of the MA/PA/SM/SJ eutectic composite was evaluated using customized thermal performance test setup as shown in Fig. 1. The setup consisted of two fluid circulation baths for hot and cold fluids to circulate the heat transfer fluid (HTF) to the chamber. Two cylindrical glass tubes were attached inside the chamber and contacted with HTF. Furthermore, 6 g of the two samples – MA/PA/SM eutectic mixture and MA/PA/SM/SJ eutectic composite – were placed in the glass tubes. The alteration of the temperature of these samples against endothermic and exothermic time was detected by a thermocouple (J-type, Omega) on DAQ system. The temperature of hot and cold HTF was set above and below the melting temperatures of the samples, which were 65 °C and 30 °C, respectively.

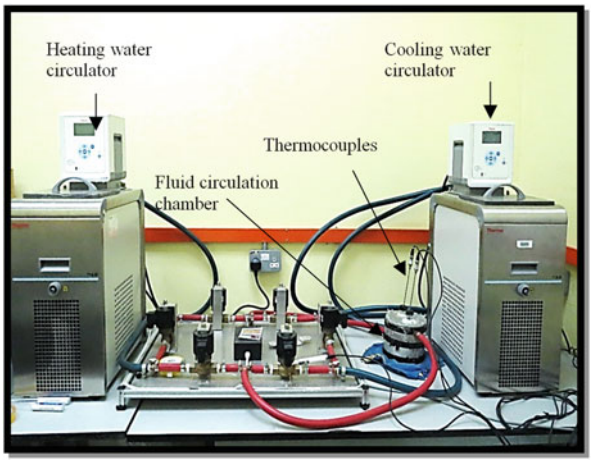

Fig. 1 Thermal performance test setup

3 Results and Discussion

3.1 Thermal Characteristic of MA/PA/SM/SJ

Fauzi et al. (2013) previously have done work on the improvement the thermal properties of myristic acid/palmitic acid (MA/PA) eutectic mixture by adding 5 wt. % sodium myristate (SM) to reduce the phase transition temperature (considering to tropical weather applications) and increase the latent heat of fusion of eutectic PCM. The studies reported that the addition of sodium myristate (SM) was able to reduce the melting temperature (T_m) and improve the latent heat of fusion (ΔH_f) of MA/PA eutectic mixture, as 11.5% and 15.3%, respectively. But it does not show a significant improvement on thermal conductivity. Therefore, this current study has been designed to achieve a good improvement on thermal conductivity of prepared PCM without much effect on reducing the thermal properties.

The DSC curve in Fig. 2 presents the thermal properties of CPCM in different compositions of SJ. The melting temperature (T_m) and solidification temperature (T_s) of MA/PA/SM/SJ were interpreted as onset points, whereas the latent heat of fusion during melting ($\Delta H_{f,m}$) and solidification phase (ΔH_{fs}) were obtained from interpolating of the chart's peak area. The results, as shown in Table 1, indicated that the phase transition temperature of MA/PA/SM/SJ eutectic composite rises up against increasing percentage composition of SJ, and at the same time, its latent heat of fusion tends to decrease with increasing SJ composition.

The thermal conductivity of MA/PA/SM/SJ eutectic composite in different compositions of SJ which is tabulated in Table 2 shows that the thermal conductivity increased simultaneously with increasing percentage composition of SJ. From these result obtained, the highest thermal conductivity value was belong to eutectic composite mixture of MA/PA/SM with 5 wt. % SJ as 0.492 Wm^{-1} K^{-1}. However, the thermal properties of MA/PA/SM + 5 wt.% SJ eutectic composite show an

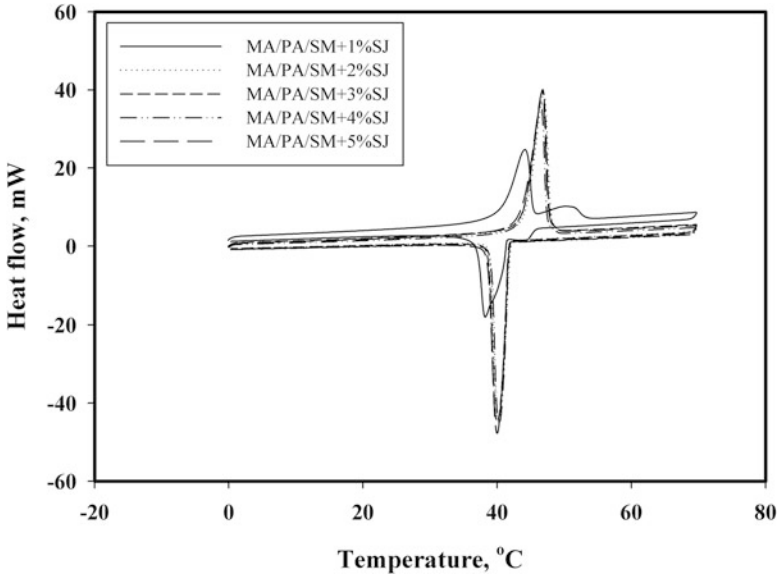

Fig. 2 DSC thermal properties curve of MA/PA/SM/SJ composite mixture

Table 1 Thermal properties of MA/PA/SM eutectic mixture with *Shorea javanica*

Composite phase change materials (CPCMs)	T_m (°C)	$\Delta H_{f,m}$ (J/g)	T_s (°C)	$\Delta H_{f,s}$ (J/g)
MA/PA/SM + 1% SJ	40.54	179.92	41.46	183.55
MA/PA/SM + 2% SJ	43.20	176.39	41.95	179.95
MA/PA/SM + 3% SJ	43.96	177.45	41.73	180.85
MA/PA/SM + 4% SJ	43.89	169.35	41.75	172.29
MA/PA/SM + 5% SJ	43.75	167.38	41.67	175.63

Table 2 Thermal conductivity of composite phase change materials (CPCMs)

Composite phase change materials (CPCMs)	Thermal conductivity, $Wm^{-1} K^{-1}$
MA/PA/SM + 1% SJ	0.463
MA/PA/SM + 2% SJ	0.475
MA/PA/SM + 3% SJ	0.488
MA/PA/SM + 4% SJ	0.489
MA/PA/SM + 5% SJ	0.492

unexpected value on latent heat of fusion that shows a significant drop to 167.38 Jg^{-1} compared with the latent heat of fusion of initial MA/PA/SM eutectic mixture as 179.92 Jg^{-1}. However, an improvement of thermal conductivity without significant drop of latent heat of fusion is shown by MA/PA/SM + 3 wt.% SJ eutectic composite. The thermal conductivity of MA/PA/SM/SJ showed a very significant improvement of 101.65% by adding 3 wt.% SJ compared with the thermal

conductivity value of MA/PA/SM eutectic mixture (Fauzi et al. 2013). Meanwhile, the latent heat of fusion only presents a small decrease of 0.93% from 179.12 to 177.45 Jg^{-1}.

Different kinds of porous materials have been used in a number of studies to improve the thermal conductivity of PCMs. Karaipekli et al. (2007) proposed a different mass fraction of expanded graphite (EG) and carbon fiber (CF) to enhance thermal conductivity of stearic acid (SA). The result of this study reported that thermal conductivity of SA increased with increasing mass fraction of EG and CF and indicated an insignificant decrease on its latent heat of fusion at the same time. Sari and Karaipekli (2007) studied the effect of addition of expanded graphite (EG) into paraffin in improving the thermal conductivity of paraffin. The results indicated that the thermal conductivity of paraffin/EG composite mixture increased with increasing mass fraction of EG. The decrease of latent heat of fusion also occurred by increasing the composition of EG in paraffin in this study. In the extended work, these authors evaluated the thermal characteristic and thermal conductivity improvement of capric acid–myristic acid/expanded perlite and some fatty acid compounds with expanded graphite. They also proved that these porous materials were able to improve the thermal conductivity of PCMs and also reduce its latent heat of fusion insignificantly (Karaipekli and Sari 2008; Sari et al. 2008).

Moreover, the improvement of thermal conductivity of MA/PA/SM + 3 wt.% SJ composite mixture was proved by the improvement of its heat transfer rate as seen in Fig. 3, which shows the heat storage/release duration time needed for the prepared MA/PA/SM and MA/PA/SM + 3 wt.% SJ to change the phase from solid to liquid and vice versa. These curves show that the MA/PA/SM + 3 wt.% SJ eutectic composite needs the shortest time to reach the melting and solidification points compared with the MA/PA/SM eutectic mixture. The heat storage/release curve of the prepared MA/PA/SM and MA/PA/SM + 3 wt.% SJ also indicates that the heat transfer rate during heat release process increases faster than theheat storage process. It is because of the fact thatthe heat transfer process during the heat storage was controlled by natural convection, and during the heat release, the heat transfer was controlled by thermal conduction. The increase of thermal conductivity of CPCM had a significant enhancement effect on the heat transfer during heat release than heat storage processes (Zhang and Fang 2006).

3.2 Compatibility of SJ with MA/PA/SM

The FT-IR spectra in Fig. 4 show the absorbance peak for each functional group of chemical structures of MA/PA/SM, MA/PA/SM + 3 wt.% SJ, and SJ. The spectra show the same peak area in every range of wave number between MA/PA/SM eutectic mixture and MA/PA/SM + 3 wt.% SJ eutectic composite. It means that the improvement of the thermal conductivity of CPCM by the addition of 3 wt. % of *Shorea javanica* (SJ) as a porous material does not occur in the chemical reaction in

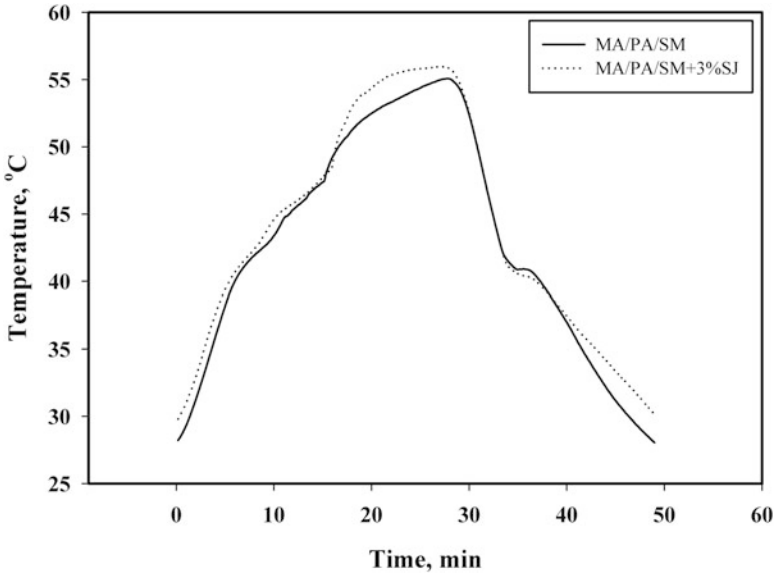

Fig. 3 Heat storage and release curves of MA/PA/SM and MA/AP/SM/SJ

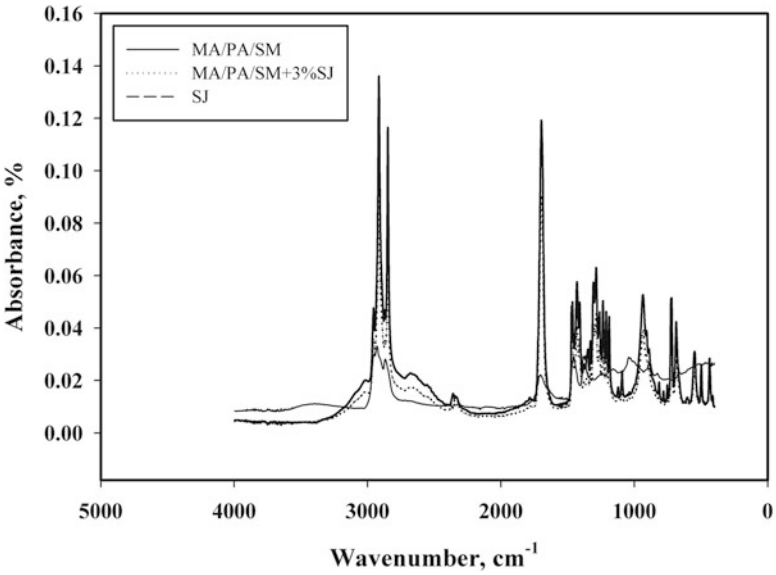

Fig. 4 FT-IR curve of MA/PA/SM, SJ, and MA/PA/SM + 3 wt.% SJ

the mixture. Thus, it can be noted that the change of thermal properties of MA/PA/SM/SJ eutectic CPCM was not caused by chemical reaction but due to the physical properties of *Shorea javanica* (SJ), namely high melting temperature and low latent

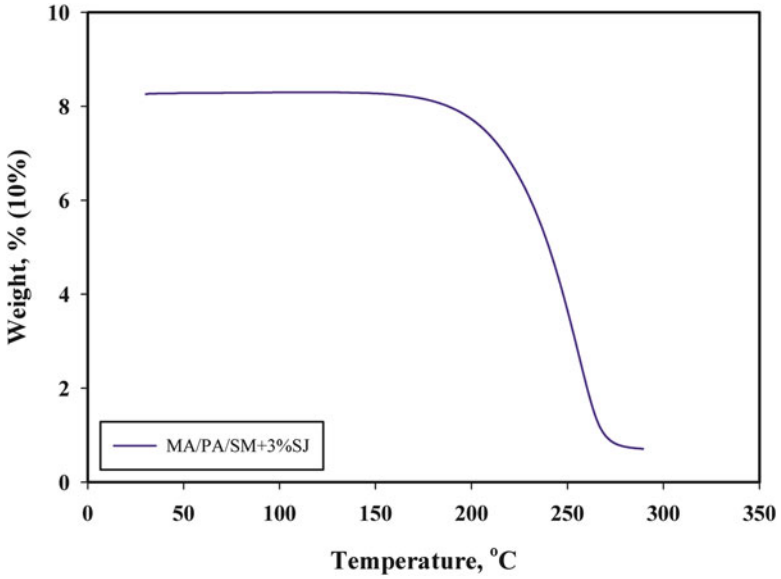

Fig. 5 TGA curve of MA/PA/SM + 3 wt.% SJ

heat of fusion, and thereby contributing to the increase in melting temperature and drop in latent heat of fusion of MA/PA/SM/SJ eutectic CPCM.

3.3 Thermal Stability of MA/PA/SM/SJ

A thermal stability curve of MA/PA/SM + 3 wt.% SJ eutectic composite demonstrated in Fig. 5 shows that the prepared MA/PA/SM + 3 wt.% SJ eutectic composite does not show any mass degradation within the work temperature 30–160 °C. The weight degradation of MA/PA/SM + 3 wt.% SJ begins to appear once the work temperature is 168.7 °C and reaches an optimum weight degradation at the work temperature of 289.39 °C. Thus, these results indicate that the MA/PA/SM + 3 wt.% SJ eutectic composite presented good stability to apply as a CPCM in thermal energy storage application (TES) with the operation temperature under 168 °C.

Thermal stability of composite phase change materials (CPCMs) have also been studied by other researchers. Kim and Drza (2009) measured thermal stability of paraffin/xGnP composite PCM at temperature range of 30–600 °C. The mass of CPCMs started decomposition at 200 °C and reached total decomposition at 280 °C. In the other work, Jeong et al. (2013) analyzed thermal decomposition of n-octadecane/diatomite CPCMs at a temperature range of 30–400 °C. In this study, we have showed that the weight decomposition of n-hexadecane/diatomite composite was 50% lower than that of pure n-hexadecane PCM at operation

temperature 200 °C. According to these studies, it can be noted that CPCMs have a higher thermal stability compared with pure PCMs.

4 Conclusions

In this current study, the preparation and thermal characteristics of a novel eutectic composite phase change material (CPCM) which involves the myristic acid/palmitic acid/sodium lautare (MA/PA/SM) and *Shorea javanica* (SJ) have been evaluated. The thermal conductivity of this CPCM was simultaneously increased with increasing the composition of SJ as 1, 2, 3, 4, and 5 wt. %, respectively. But CPCM with composition 3 wt. % SJ shows a good improvement on thermal conductivity without significant impact in the decreasing latent heat of fusion of CPCM. The eutectic composite of MA/PA/SM + 3 wt.% SJ also indicates a good thermal performance, no chemical reaction between each component in the mixture, and has a good thermal stability without any weight degradation within the work temperature of 30–168 °C. Therefore, it can be concluded that *Shorea javanica* (SJ) is acceptable to be used as a novel porous material to improve the thermal conductivity of composite phase change materials (CPCM).

Acknowledgments The authors acknowledge the Minister of Higher Education and Faculty of Engineering, University of Malaya, through High Impact Research grant (UM.R/HIR/MOHE/ENG/21-D000021-16001).

References

Al-Abidi, A. A., Bin Mat, S., Sopian, K., Sulaiman, M. Y., Lim, C. H., Th, A.: Review of thermal energy storage for air conditioning systems. Renew. Sust. Energ. Rev. **16**(8), 5802–5819 (2012) http://dx.doi.org/10.1016/j.rser.2012.05.030

Alkan, C., Sari, A.: Fatty acid/poly(methyl methacrylate) (PMMA) blends as form-stable phase change materials for latent heat thermal energy storage. Sol. Energy. **82**(2), 118–124 (2008) http://dx.doi.org/10.1016/j.solener.2007.07.001

Cabeza, L. F., Castell, A., Barreneche, C., de Gracia, A., Fernández, A. I.: Materials used as PCM in thermal energy storage in buildings: a review. Renew. Sust. Energ. Rev. **15**(3), 1675–1695 (2011) http://dx.doi.org/10.1016/j.rser.2010.11.018

Fauzi, H., Metselaar, H. S. C., Mahlia, T. M. I., Silakhori, M., Nur, H.: Phase change material: optimizing the thermal properties and thermal conductivity of myristic acid/palmitic acid eutectic mixture with acid-based surfactants. Appl. Therm. Eng. **60**(1–2), 261–265 (2013) http://dx.doi.org/10.1016/j.applthermaleng.2013.06.050

Fauzi, H., Metselaar, H. S. C., Mahlia, T. M. I., Silakhori, M.: Thermo-physical stability of fatty acid eutectic mixtures subjected to accelerated aging for thermal energy storage (TES) application. Appl. Therm. Eng. **66**(1–2), 328–334 (2014) http://dx.doi.org/10.1016/j.applthermaleng.2014.02.014

Jeong, S.-G., Jeon, J., Lee, J.-H., Kim, S.: Capric–myristic acid/expanded perlite composite as form-stable phase change material for latent heat thermal energy storage. Renew. Energy. **33** (12), 2599–2605 (2008) http://dx.doi.org/10.1016/j.renene.2008.02.024

Karaipekli, A., Sari, A.: Capric–myristic acid/expanded perlite composite as form-stable phase change material for latent heat thermal energy storage. Renew. Energy. **33**(12), 2599–2605 (2008) http://dx.doi.org/10.1016/j.renene.2008.02.024

Karaipekli, A., Sarı, A., Kaygusuz, K.: Thermal conductivity improvement of stearic acid using expanded graphite and carbon fiber for energy storage applications. Renew. Energy. **32**(13), 2201–2210 (2007) http://dx.doi.org/10.1016/j.renene.2006.11.011

Kim, S., Drza, L.T.: High latent heat storage and high thermal conductive phase change materials using exfoliated graphite nanoplatelets. Sol. Energy Mater. Sol. Cells. **93**(1), 136–142 (2009). doi:10.1016/j.solmat.2008.09.010

Kuravi, S., Trahan, J., Goswami, D. Y., Rahman, M. M., Stefanakos, E. K.: Thermal energy storage technologies and systems for concentrating solar power plants. Prog. Energy Combust. Sci. **39**(4), 285–319 (2013) http://dx.doi.org/10.1016/j.pecs.2013.02.001

Nomura, T., Okinaka, N., Akiyama, T. Impregnation of porous material with phase change material for thermal energy storage. Mater. Chem. Phys. **115**(2–3), 846–850 (2009) http://dx.doi.org/10.1016/j.matchemphys.2009.02.045

Nomura, T., Okinaka, N., Akiyama, T.: Waste heat transportation system, using phase change material (PCM) from steelworks to chemical plant. Resour. Conserv. Recycl. **54**(11), 1000–1006 (2010) http://dx.doi.org/10.1016/j.resconrec.2010.02.007

Pielichowska, K., Pielichowski, K.: Phase change materials for thermal energy storage. Prog. Mater. Sci. **65**(0), 67–123 (2014). doi:10.1016/j.pmatsci.2014.03.005

Sari, A., Karaipekli, A.: Thermal conductivity and latent heat thermal energy storage characteristics of paraffin/expanded graphite composite as phase change material. Appl. Therm. Eng. **27** (8–9), 1271–1277 (2007) http://dx.doi.org/10.1016/j.applthermaleng.2006.11.004

Sari, A., Karapekl, A., Kaygusuz, K.: Fatty acid/expanded graphite composites as phase change material for latent heat thermal energy storage. Energy Sources, Part A: Recovery, Utilization, and Environmental Effects. **30**(5), 464–474 (2008). doi:10.1080/15567030601003700

Setianingsih, N. (1992). Pemurinian Damar Shorea javanica dengan Menggunakan pelarut Organik dan Bahan Pemucat.

Zalba, B., Marín, J.M., Cabeza, L.F., Mehling, H.: Review on thermal energy storage with phase change: materials, heat transfer analysis and applications. Appl. Therm. Eng. **23**(3), 251–283 (2003). doi:10.1016/s1359-4311(02)00192-8

Zhang, Z., Fang, X.: Study on paraffin/expanded graphite composite phase change thermal energy storage material. Energy Convers. Manag. **47**(3), 303–310 (2006) http://dx.doi.org/10.1016/j.enconman.2005.03.004

Zhou, M., Bi, H., Lin, T.Q., Lu, X.J., Wan, D.Y., Huang, F.Q., Lin, J.H.: Heat transport enhancement of thermal energy storage material using graphene/ceramic composites. Carbon. **75**(0), 314–321 (2014). doi:10.1016/j.carbon.2014.04.009

Improving of the Angström-Prescott Model Using Harmonic Analysis

Yavuz Selim Güçlü, İsmail Dabanlı, Eyüp Şişman, and Zekai Şen

1 Introduction

The fossil fuels source is expected to run out in the next 50 years. This is convenient in a way because the atmosphere will not be loaded with greenhouse gases, but instead new renewable energy sources with low carbon emissions should enter the scene. In the meantime, there are numerous climate change-based researches focusing on clean and renewable energy fields (Şen 2009). The sun as the mother of almost all energy sources provides opportunities for solar energy research at different parts of the world theoretically and through technological investigations and applications. Solar irradiation calculations and predictions are among the major fields of research.

The first study in this field was presented by Angström (1924), who suggested the linear equation between solar irradiation and sunshine duration. Later, his equation was refined by Prescott (1940) in terms of extraterrestrial solar radiation. The same formulation was developed by Page et al. (1964) through changing open day solar irradiation term with lateral solar irradiation that comes outside of atmosphere. Later on, linear relation between sunshine duration and solar irradiation was studied by many researchers (Swartman and Ogunlade 1967; Sabbagh

Y.S. Güçlü
Istanbul Technical University, Faculty of Civil Engineering, Department of Hydraulics, Maslak, Istanbul 34469, Turkey

İ. Dabanlı, Assist. Prof. Dr. (✉) • Z. Şen
Istanbul Medipol University, Faculty of Engineering and Natural Sciences, Department of Civil Engineering, Beykoz, Istanbul 34810, Turkey
e-mail: idabanli@medipol.edu.tr

E. Şişman
Yildiz Technical University, Faculty of Civil Engineering, Department of Hydraulics, Davutpaşa, Istanbul 34220, Turkey

© Springer International Publishing AG, part of Springer Nature 2018

F. Aloui, I. Dincer (eds.), *Exergy for A Better Environment and Improved Sustainability 2*, Green Energy and Technology,
https://doi.org/10.1007/978-3-319-62575-1_43

et al. 1977; Rietveld 1978; Gopinathan 1988; Soler 1991; Wahab 1993; Şen 2001; Almorox et al. 2013).

Şahin and Şen (1998) contributed dynamic terms to linear relation for solar irradiations. On the other hand, a second degree relation was given by Ögelman et al. (1984), and they claimed that their method better describes the relationship between sunshine duration and solar irradiation. Similar research was examined by Akınoğlu and Ecevit (1990). Furthermore, Samuel (1991) developed a third degree relationship for the same purpose. Şen (2007) also provided non-linear relationship in the form of power function between sunshine duration and solar irradiation. Fuzzy logic approaches and neural network modelling techniques were also suggested for solar energy calculations by Şen (1998) and Benghanem et al. (2009). Neither the linear nor the non-linear modelling techniques include dependency for each term to the previous data. Along this line of research, Güçlü et al. (2014a, b) gave place to such a dependency between sunshine duration and solar irradiation in their model by using current and previous data. However, all accomplished models do not include periodicity of sunshine data.

The periodicity of meteorological data is generated from the earth's rotation around its axes and movement around the sun. These rotation and movements are formed daily, monthly, seasonally and annually in the form of solar irradiation periodicities. Some researchers used sine and cosine or harmonic analysis techniques in order not to predict sunshine duration versus solar irradiation (Balling 1983; Amato et al. 1986; Baldasano and Berna 1988; Şahin et al. 2001).

The aim of this study is to combine harmonic analysis and the Angström-Prescott model to obtain better solar irradiation predictions with their comparisons with the classical Angström-Prescott model.

2 Methodology

The harmonic and the Angström-Prescott models are used for the prediction of solar irradiation on the basis of sunshine duration data.

2.1 Angström-Prescott Model

The original Angström-Prescott (1940) equation relates to the global irradiation amount, H, to sunshine duration, S, after their division to respective astronomical (extraterrestrial) counterparts, H_0 and S_0, and also to dimensionless coefficients, a and b, and it is expressed simply as:

$$\left(\frac{H}{H_0}\right) = a + b\left(\frac{S}{S_0}\right) \tag{1}$$

2.2 Improved Model

The periodicity on sunshine duration and solar irradiation occurs from hour to annual periods naturally (Şen 2002). Periodicity can be recognized visually when the data set variation scatter diagrams are generated. The initial step of model is to get arithmetic average for each day on the basis of daily time interval for sunshine duration and solar irradiation. Hence, there are 1st, 2nd, 3rd, …, 365th daily averages for the harmonic analysis.

Harmonic analysis mathematical expression can be formulized in two different ways according to Eqs. 2 and 3 as follows:

$$Y_i = a \sin\left(2\pi\frac{i}{T} + \varphi_{\sin}\right) + \bar{Y} \tag{2}$$

$$Y_i = a \cos\left(2\pi\frac{i}{T} + \varphi_{\cos}\right) + \bar{Y} \tag{3}$$

where a is a coefficient and i refers to the count from 1 to 365, whereas T is the whole duration as 365 days, sin and cos are phase angles, $\bar{Y}$ is the average of the data and Y_i is the ith day measurement. By using trigonometric substituents, Eq. 2 can be converted to Eq. 4 as:

$$Y_i = a\cos(\varphi)\sin\left(2\pi\frac{i}{T}\right) + a\sin(\varphi)\cos\left(2\pi\frac{i}{T}\right) + \bar{Y} \tag{4}$$

In this equation, A and B constant coefficients are named succinctly as in the following equation:

$$Y_i = A\sin\left(2\pi\frac{i}{T}\right) + B\cos\left(2\pi\frac{i}{T}\right) + \bar{Y} \tag{5}$$

After calculating the numerical values of A, B, then $\bar{Y}$ and Y_i can be solved easily. The numerical solution needs first to integrate Eq. 4 from 0 to T as in the following expression:

$$\int_0^T Y_i di = A\int_0^T \sin\left(2\pi\frac{i}{T}\right)di + B\int_0^T \cos\left(2\pi\frac{i}{T}\right)di + \bar{Y}\int_0^T di \tag{6}$$

The mathematical integration results for the first and second terms in Eq. 6 go to 0 (see Eqs. 7 and 8):

$$\int_0^T \sin\left(2\pi\frac{i}{T}\right)\mathrm{di} = -\cos\left(2\pi\frac{i}{T}\right)\Big|_0^T = 0 \tag{7}$$

$$\int_0^T \cos\left(2\pi\frac{i}{T}\right)\mathrm{di} = \sin\left(2\pi\frac{i}{T}\right)\Big|_0^T = 0 \tag{8}$$

When this mathematical substition is applied in Eq. 6, then the following new formula is generated:

$$\int_0^T Y_i\mathrm{di} = \bar{Y}\int_0^T \mathrm{di} = \bar{Y}i|_0^T = \bar{Y}T \tag{9}$$

The first term in this equation expresses in serial by considering $Y_0 = 0$, then $\bar{Y}$ can be calculated as constant through the following formula:

$$\bar{Y} = \frac{1}{T}\sum_{i=1}^{T} Y_i = \text{constant} \tag{10}$$

Numerical solution of A and B coefficients can be calculated from Eqs. 11, 12 and 13. Firstly, Eq. 5 is multiplied by and then calculation is achieved through the integration as:

$$\int_0^T Y_i \sin\left(2\pi\frac{i}{T}\right)di = A\int_0^T \sin^2\left(2\pi\frac{i}{T}\right)di + B\int_0^T \cos\left(2\pi\frac{i}{T}\right)\sin\left(2\pi\frac{i}{T}\right)di + \bar{Y}\int_0^T \sin\left(2\pi\frac{i}{T}\right)di \tag{11}$$

$$\int_0^T \cos\left(2\pi\frac{i}{T}\right)\sin\left(2\pi\frac{i}{T}\right)di = -\frac{1}{2}\cos^2\left(2\pi\frac{i}{T}\right)\Big|_0^T = -\frac{1}{2}+\frac{1}{2} = 0 \tag{12}$$

$$\int_0^T \sin^2\left(2\pi\frac{i}{T}\right)di = \frac{1}{8\pi}\left(4\pi 4 - T\sin\left(4\pi\frac{i}{T}\right)\right|_0^T = \frac{T}{2} \tag{13}$$

If the results of the above equations are combined into Eq. 14 and then if the first term is expanded into a series, then Eq. 15 can be generated as a constant:

$$\int_0^T Y_i \sin\left(2\pi\frac{i}{T}\right)di = A\frac{T}{2} \tag{14}$$

$$A = \frac{2}{T}\sum_{i=1}^{T} Y_i \sin\left(2\pi\frac{i}{T}\right) = \text{constant} \tag{15}$$

The same calculation steps for determining B coefficient follows A coefficient determination procedure, and after serial expression, the following expression can be produced:

$$B = \frac{2}{T}\sum_{i=1}^{T} Y_i \cos\left(2\pi\frac{i}{T}\right) = \text{constant} \tag{16}$$

Daily average of sunshine duration and solar irradiation data are suitable for harmonic analysis. The new sequence is generated according to harmonic analyses by subtracting the daily averages, (Y_{i_mean}), from the available data for S and H. These sequences are divided by S_0 and H_0, respectively, to obtain the dimensionless sequences. These new sequences are necessary for the Angström-Prescott model production in a better way. The prediction of daily irradiation values is then calculated by use of improved model. For this purpose, H_p is predicted as solar irradiation with H_h, as harmonic model result and H_A as Angström-Prescott model results. Mathematical expression for solar irradiation prediction results as:

$$H_\text{p} = H_\text{h} + H_\text{A} \tag{17}$$

3 Application

Data obtained from the Turkish State Meteorological Service, for Diyarbakır City of Turkey, are used for the application. This location lies at latitude 40° 13.5′ E and longitude 37° 54.5′ N. The data set includes sunshine duration and solar irradiation daily measurements from 2000 to 2008. Data set is split into two groups as for testing and validation, where test data consist of 2000–2005 years and remaining data are for validation.

3.1 The Angström-Prescott Model

The classical Angström-Prescott model scatter diagram provides results as seen in Fig. 1, where a and b coefficients are calculated as 0.2893 and 0.4871, respectively.

After this stage, the predictions are achieved through the Angström-Prescott model. The estimated solar radiation values are compared with current values to determine the amount of errors.

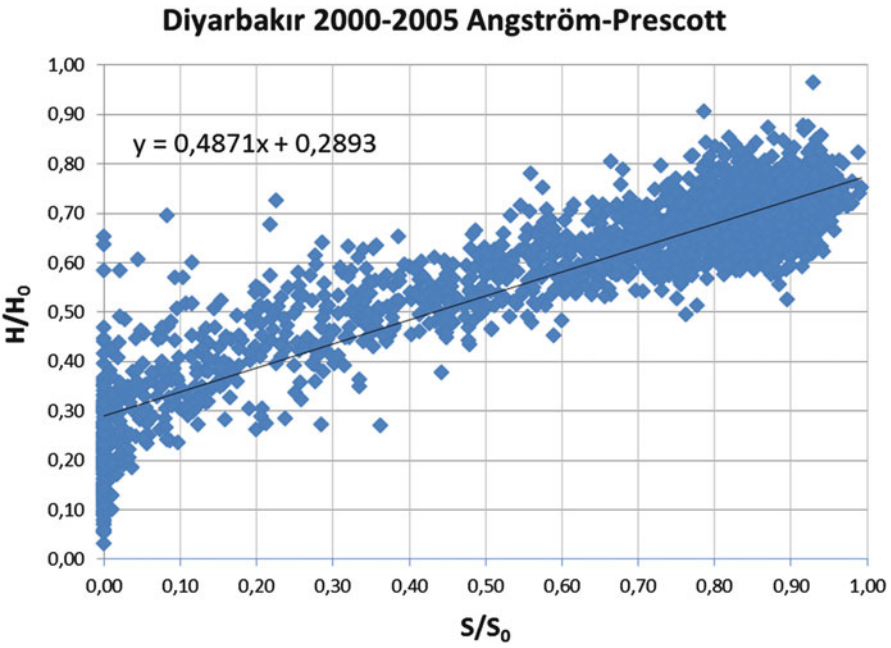

Fig. 1 Scatter diagram for the classical Angström-Prescott model

3.2 *Improved Model*

Measured time series between 2000 to 2005 for sunshine duration and solar irradiation are illustrated in Fig. 2. As seen in this figure, periodicity of solar irradiation and sunshine duration is very obvious. Harmonic analyses results are plotted for sunshine duration and solar irradiation in Figs. 3 and 4.

On the other hand, A, B and $\bar{Y}$ coefficients in Eq. 5 are calculated after harmonic analyses end up, and the results are tabulated in Table 1.

The new Angström-Prescott equation for improved model is generated by using the difference of the harmonic analysis values (Y_i) from daily averages, (Y_{i_mean}) and normalized by S_0 and H_0. The model results are illustrated in Fig. 5. Angström-Prescott equation coefficients a and b are calculated as 0.0101 and 0.5294, respectively, for this model.

The errors of predictions are calculated according to the following well-known expression as the mean absolute error (MAE), which can be written for N data values:

$$\text{MAE} = \frac{1}{N} \sum \sqrt{(\text{Measured Data} - \text{Predicted Data})^2} \tag{18}$$

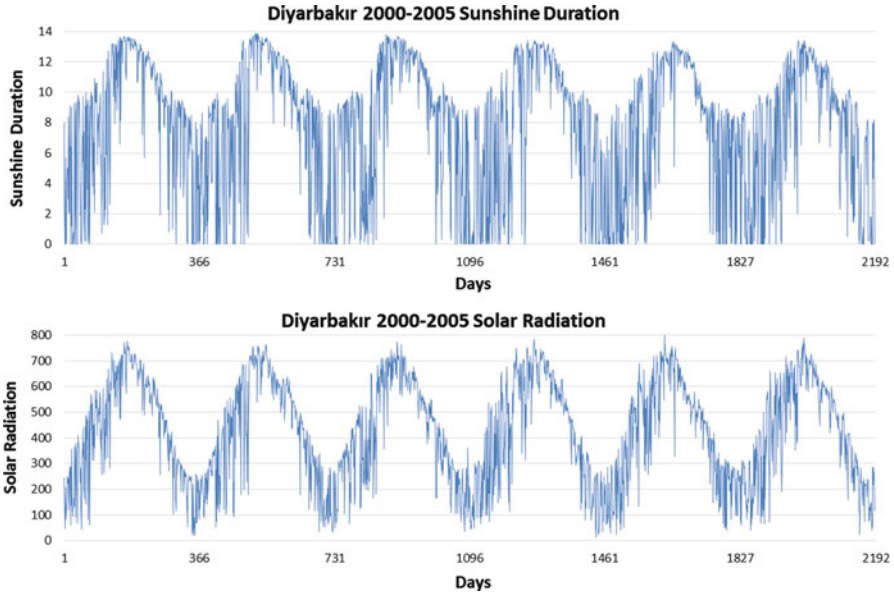

Fig. 2 Time series for measured sunshine duration and solar irradiation

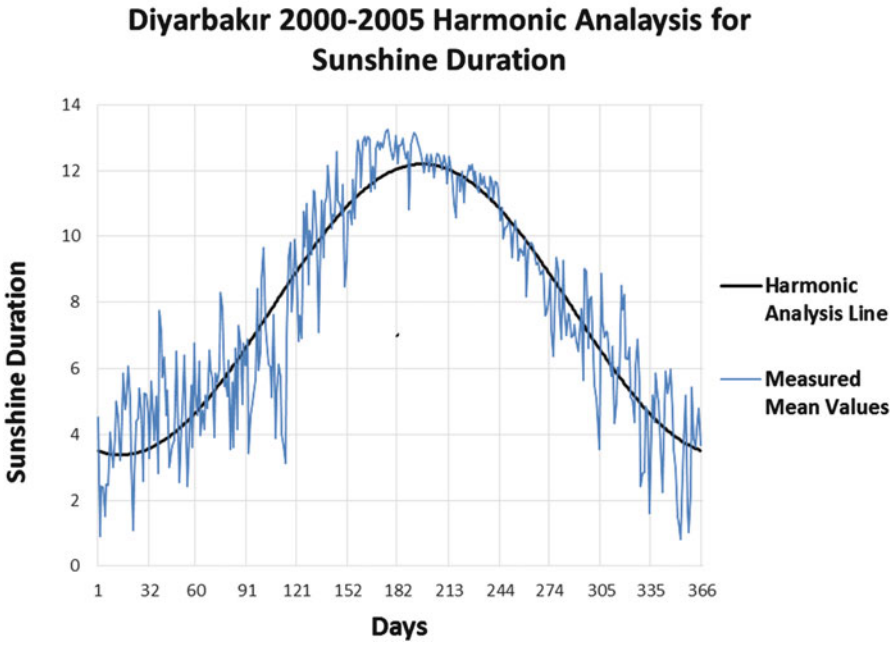

Fig. 3 Sunshine duration harmonic analysis diagram for improved model

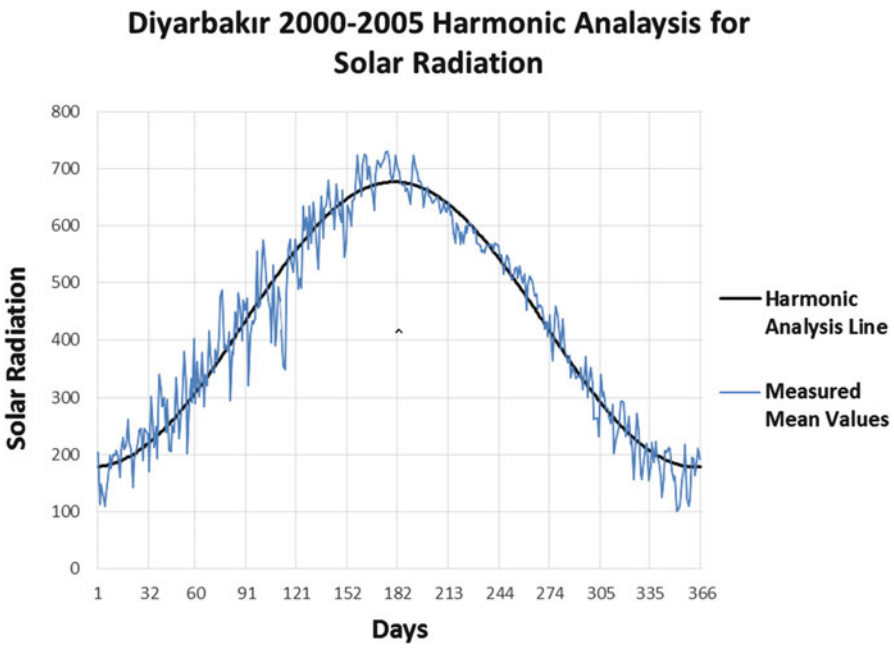

Fig. 4 Solar irradiation harmonic analysis diagram for improved model

Table 1 *A*, *B* and $\bar{Y}$ coefficients

	Sunshine duration	Solar irradiation
$\bar{Y}$	*7,790,594*	*427,5009*
A	*−1,080406*	*10,5402*
B	*−4,276,403*	*−248,7756*

The improved model's error summation is equal to 40,817.5 cal/cm^2 for solar irradiation. Besides this, the Angström-Prescott model's sum of errors equals to 43,996.2 cal/cm^2. These numerical values prove that improved model predictions are more successful than Angström-Prescott model at approximately 7.2%.

4 Conclusion

Recently clean energy resources are under intensive research all over the world due to atmospheric pollution caused by fossil fuels through global warming and greenhouse effects, which trigger climate change and variation. Consequently, clean energy sources, such as the wind, solar, solar-hydrogen and geothermal energies, are becoming increasingly under focus for technological and scientific developments. In this paper a new approach is suggested for the estimation of solar energy

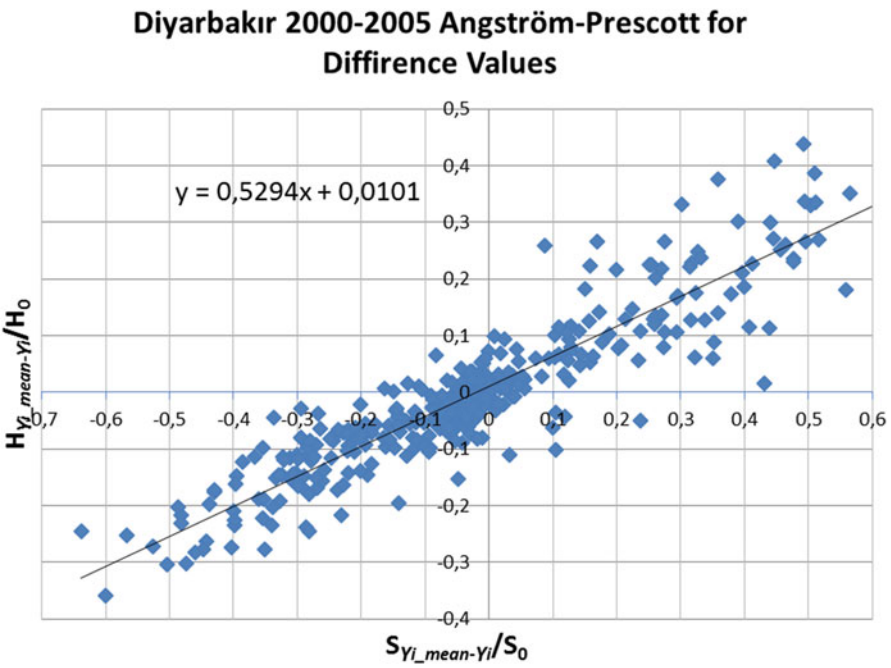

Fig. 5 Scatter diagram for the classical Angström-Prescott model for different values

by considering the combined classical Angström-Prescott equation and the harmonic analyses model. In the literature, a variety of models are suggested for solar irradiation estimation, but none of them include harmonic analyses. The suggested method is a simple and new approach for solar energy calculations. The improved model outperforms the classical linear model at approximately 7%.

Acknowledgments This paper consists same methodology but different application of Güçlü et al. (2015).

References

Akınoğlu, B.G., Ecevit, A.: Construction of a quadratic model using modified Angström coefficients to estimate global solar radiation. Sol. Energy. **45**, 85–92 (1990)

Almorox, J., Bocco, M., Willington, E.: Estimation of daily global solar radiation from measured temperatures at Cañada de Luque, Córdoba, Argentina. Renew. Energy. **60**, 382–387 (2013)

Amato, U., Andretta, A., Banoli, B., Coluzzi, B., Cuomo, V., Fontana, F., Serio, C.: Markov processes and Fourier analysis as a tool describe and simulate daily solar irradiance. Sol. Energy. **37**(3), 179–194 (1986)

Angström, A.: Solar terrestrial radiation. Q. J. R. Meteorol. Soc. **50**, 121–126 (1924)

Baldasano, J.M., Clar, J., Berna, A.: Fourier analysis of daily solar radiation data in Spain. Sol. Energy. **41**(4), 327–334 (1988)
Balling, R., Cerveny, R.S.: Spatial and temporal variations in long-term normal percent possible solar radiation levels in the United States. J. Clim. Appl. Meteorol. **22**, 1726–1732 (1983)
Benghanem, M., Mellit, A., Alamri, S.N.: ANN-based modelling and estimation of daily global solar radiation data: a case study. Energy Convers. Manag. **50**, 1644–1655 (2009)
Gopinathan, K.K.: A general formula for computing the coefficients of the correlation connecting global solar radiation to sunshine duration. Sol. Energy. **41**, 499–502 (1988)
Güçlü, Y.S., Dabanlı, İ., Şişman, E.: Short- and long-term solar radiation estimation method. In: Dincer, I., Midilli, A., Kucuk, H. (eds.) Progress in exergy, energy, and the environment. Springer, Cham (2014a). doi:10.1007/978-3-319-04681-5_48
Güçlü, Y.S., Yeleğen, M.Ö., Dabanlı, İ., Şişman, E.: Solar irradiation estimations and comparisons by ANFIS, angström-prescott and dependency models, solar energy. Sol. Energy. **109**, 118. http://dx.doi.org/10.1016/j.solener.2014.08.027 (2014b)
Güçlü, Y.S., Dabanlı, İ., Şişman, E., Şen, Z.: HARmonic–LINear (HarLin) model for solar irradiation estimation, Renew Energy, **81**, 209–218, (2015). http://dx.doi.org/10.1016/j.renene.2015.03.035
Ögelman, H., Ecevit, A., Taşemiroğlu, E.: Method for estimating solar radiation from bright sunshine data. Sol. Energy. **33**, 619–625 (1984)
Page, J.K.: The estimation of monthly ea values of daily total short wave radiation on vertical and inclined surfaces from sunshine records for latitudes 40°N–40°S. In: Proceedings of the UN conference on new sources of energy, paper no. 598, 4, pp. 378–390 (1964)
Prescott, J.A.: Evaporation from a water surface in relation to solar radiation. Trans. R. Soc. S. Aust. **64**, 114–118 (1940)
Rietveld, M.R.: A new method for estimating the regression coefficients in the formula relating solar radiation to sunshine. Agric. Meteorol. **19**, 243–252 (1978)
Sabbagh, J.A., Sayigh, A.A.M., El-Salam, E.M.A.: Estimation of the total solar radiation from meteorological data. Sol. Energy. **19**, 307–311. 13 (1977)
Samuel, T.D.M.A.: Estimation of global radiation for Sri Lanka. Sol. Energy. **45**(5), 333 (1991)
Soler, A.: Monthly specific Rietveld's correlations. Sol. Wind Technol. **2/3**, 305–306 (1991)
Swartman, R.K., Ogunlade, O.: Solar radiation estimates from common parameters. Sol. Energy. **11**, 170–172 (1967)
Şahin, A.D., Kadioğlu, M., Şen, Z.: Monthly clearness index values of Turkey by harmonic analysis approach. Energy Convers. Manag. **42**, 933–940 (2001)
Şahin, A.D., Şen, Z.: Statistical analysis of the Angström formula coefficients and application for Turkey. Sol. Energy. **62**, 29–38 (1998)
Şen, Z.: Fuzzy algorithm for estimation of solar irradiation from sunshine duration. Sol. Energy. **63**, 39–49 (1998)
Şen, Z.: Angström equation parameter estimation by unrestricted method. Sol. Energy. **71**, 95–107 (2001)
Şen, Z.: "İstatistik Veri İşleme Yöntemleri" (In Turkish), p. 243. Turkish Water Foundation (2002)
Şen, Z.: Simple nonlinear solar irradiation estimation model. Renew. Energy. **32**, 342–350 (2007)
Şen, Z.: "Temiz Enerji Kaynakları ve Modelleme İlkeleri" (In Turkish), p. 236. Turkish Water Foundation (2009)
Wahab, A.M.: New approach to estimate Angström coefficients. Sol. Energy. **51**, 241–245 (1993)

EEG Analysis Using a Wavelet Packet Transforms Mean Energy and Mean Teager Energy with an Artificial Neuro-Fuzzy System

K.S. Biju, M.G. Jibukumar, and C. Rajasekharan

1 Introduction

The human body can achieve many functions. It is one of the most perfect creations imaginable. The human body is controlled by the brain, and the efficiency of the human body in achieving assigned functions is directly related to the capability of the human brain .The brain is considered a system, which is made up of the central nervous system, which is the master controller, and the peripheral nervous system, which interconnects the brain to everything (Fauci et al. 2011). Different parts of brain have different functionality. These functions are indicated as electrical activity in the brain, which is generated from brain neurons. This electrical potential is effectively recorded using an electroencephalography (EEG).

The EEG contains different frequency bands that show the different types of brain activity. The main challenge is to develop a suitable method to detect unknown patterns that are an indication of abnormal brain function (Gotman 1999). The time-frequency analysis of EEG data has been much improved by feature extraction (Tzallas et al. 2009). However, time and frequency information

K.S. Biju (✉)
Electronics and Communication Engineering Department, Government Engineering College, Bartonhill, Thiruvananthapuram 695035, India

Electronics Engineering Division, School of Engineering, Cochin University of Science & Technology, Kochi 682022, India
e-mail: bijukarunnya@gmail.com

M.G. Jibukumar
Electronics Engineering Division, School of Engineering, Cochin University of Science & Technology, Kochi 682022, India

C. Rajasekharan
Medical College Hospital, Thiruvananthapuram 695011, India

© Springer International Publishing AG, part of Springer Nature 2018

F. Aloui, I. Dincer (eds.), *Exergy for A Better Environment and Improved Sustainability 2*, Green Energy and Technology,
https://doi.org/10.1007/978-3-319-62575-1_44

are both trade-offs for each other, depending on the duration of the window. The wavelet transform decomposes the signal for a fixed basis of functions to avoid constraints associated with non-stationary signals consisting of both time and frequency information (Khan and Gotman 2003). The EEG power spectrum is used as a computer diagnostic tool for epilepsy, an abnormal state of the brain (Kerr et al. 2012). It reduces the diagnosis time compared with conventional long-term video monitoring. EEG raw data are classified into different frequency bands of brain waves using a wavelet packet transform (Sinno and Kifah 2008; Zandi et al. 2010), which are then compared with different statistical parameters. The Teager energy measurement of electocorticography is used for functional mapping of the brain during a controlled 50-Hz cortical stimulation (Gwinn et al. 2008). It has been observed that the post-signal power occurs in the beta and gamma frequency bands.

The artificial neural network is a popular computational model for multi-input multi-output systems using back-propagation tuning (Narendra and Parthasarathy 1990). The artificial neural network is the leading performance predictor of the proton member fuel cell (Bhagavatula et al. 2012). Here four leading parameters are input, with four hidden layers, and the back-propagation method is adopted for interpreting the data. Neural networks are used for feature selection methods for EEG signals (Garrett et al. 2003).The ANFIS (adaptive neuro-fuzzy inference system) hybrid learning procedure is used for human experience with if-then rules and prescribed input-output data (Jang 1993). ANFIS is also used in the energy research field. ANFIS is effectively used for modelling proton member fuel cell-based nanocomposites and recast nafion membranes (Amirinejad et al. 2013). It compares the different neural network models. It is also used for evaluation of human emotions (Malkawi and Murad 2013). Each measured human variable has a separate input-output membership function, and a set of fuzzy rules for the different emotions can be studied. Using a combination of different classification methods improves the rate of prediction. The hybrid wavelet and neural network methods show improved forecasting of the energy usage (Voronin and Partanen 2014).

In this study the EEG is decomposed into four levels of wavelet packet transform. The selected packets contain the frequency rhythms of the EEG, i.e., delta, theta, alpha, beta, and gamma. Figure 44.1 shows the signal flow diagram of the system. They are then compared using different statistical analyses of each packet. The classification into normal and abnormal EEG is performed using ANFIS, as described above.

2 Methodology

2.1 Data Collection

The EEG data were obtained from the Department of Epileptology, University of Bonn, Bonn, Germany (Andrzejak et al. 2001). There are five sets of normal and abnormal EEG data with 500 single-channel EEG segments. The data set A and

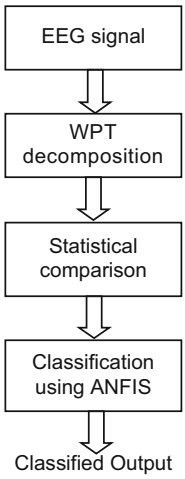

Fig. 44.1 Signal flow of the proposed system

data set B are the healthy EEG sets in open-eye and closed-eye conditions. The data set C and data set D are the unhealthy EEG sets, with an interictal condition. The data set E is an abnormal (seizure) EEG. The data are sampled at 173.61 Hz with each segment being 23.3 s in duration and having 4,096 data points (Subramaniyam and Hyttinen 2013). In this study set B and set E are only used for analysis. The raw EEG signal is fed through a low-pass filter of 0.5 Hz and also through a 64-Hz high-pass filter to eliminate high-frequency noise before it is loaded to the system.

2.2 Wavelet Packet Transform

The wavelet packet transform (WPT) is an extension of the wavelet transform. It is a collection of the linear combination multiple bases. In WPT decomposition the finite energy signal is down-sampled by a factor of two and split into a detail approximation signal. The approximation contains low-frequency information and the detail contains high-frequency information (Wu et al. 2008). Figure 44.2 shows the one-leg sub-spaces of the four-level wavelet packet decomposition. The original signal is decomposed into different sub-bands, known as packets. At each level in the decomposition, numbers of packets are 2^l, where l is the number of the level.

During the four-level wavelet packet decomposition, the selected packets are assigned to an EEG frequency rhythm, the sub-band A(4,1) as a delta band, A(4,2) as a theta band, A(4,3) as an alpha band, summation of A(4,4) and A(2,2) as the beta band, and A(1,2) as the gamma band, which are equivalent to frequency bands of the EEG. The wavelet packet energy spectrum provides time-frequency information of a time series EEG signal (Dianguo et al. 2010).

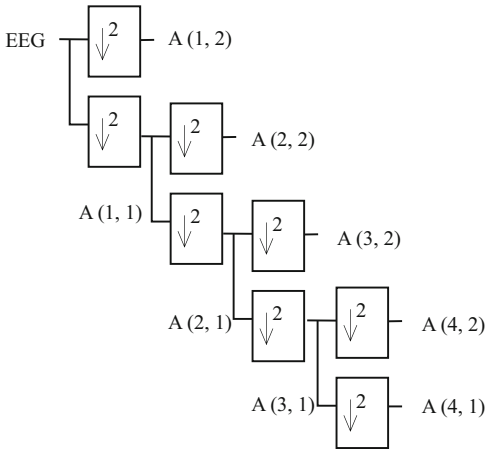

Fig. 44.2 Wavelet packet decomposition

3 Feature Vector Formation

The method involved in this study was first to load the EEG signal of the system. Taking the wavelet packet decomposition of each channel, the assigned packets for the frequency rhythms of the EEG signal, the coefficients of energy, entropy, mean energy, and mean Teager energy are calculated and the coefficients are used for training data using ANFIS (Sinno and Kifah 2008). Average errors of the epoch for a healthy EEG and an abnormal EEG are determined.

To form the feature vectors, statistical parameters like energy, entropy mean energy, and mean Teager energy are calculated by

(i) Energy(E)

The energy of a signal shows the quantum of activity. The energy of a finite signal is defined as follows (Artameeyanant et al. 2012):

$$\text{Energy}(l) = \sum_{i=1}^{n} x(i)^2 \tag{44.1}$$

where $x(i)$ is the instant quantized value of the brain wave, n is the total number of samples, and l represents the decomposed level. The energy of the abnormal EEG and normal EEG are compared, with the abnormal EEG containing maximum energy.

(ii) Entropy

Entropy is the measure of the unpredictability of a signal (Krstacic et al. 2002), which is represented as:

$$\text{Entropy}(1) = \sum_{j=1}^{N} D_{i,j}^2 \log(D_{i,j}^2) i = 1, 2, \ldots..l \tag{44.2}$$

(iii) Mean energy

The mean energy is the amount of energy over a specific period of time. When mean energy is increased in a signal associated with an abnormality of the brain, the duration of the period is given as:

$$\text{Mean Energy}(1) = \frac{1}{N} \sum_{i=l-N+1}^{l} x(i)^2 \tag{44.3}$$

where N is the length of segment in the decomposed wavelet packet transform.

(iv) Mean Teager energy (MTE)

The mean Teager energy is highly efficient for spike detection, which is characterized by localized high frequencies and an increase in instantaneous energy (Gopan et al. 2013). It can be defined as:

$$MTE(1) = \log\left[\frac{1}{N} \sum_{i=l-N+3}^{l} x(i-1)^2 - x(i)x(i-2)\right] \tag{44.4}$$

where N is the length of the corresponding wavelet decomposed segment. The feature normalization is accomplished by logarithmic scaling. Mean Teager energy gives the maximum value for abnormal EEG.

4 Results and Discussion

The EEG data used in this study contained five sets of 100 single channels of 23.3 s duration sampled at 173.6 Hz. A total of 4,096 samples were present in each segment of the dataset. The frequency band of the EEG is fixed as 0.5 Hz–64 Hz. Frequencies greater than 64 Hz are considered to be noise and can be eliminated. The signal is first decomposed into four levels of WPT. The selected decomposed packets are the sub-bands of EEG rhythm. The sub-band frequencies of 0.5–4 Hz, 4–8 Hz, 8–12 Hz, 12–32 Hz, and >32 Hz are available in A(4,1), A(4,2), A(4,3), combination of A(4,4) and A(2,2), and A(1,2) packets, respectively. Table 44.1 shows the different values of the statistical parameters.

The feature vectors of each proposed sub-band in abnormal and normal signals are calculated with the energy, entropy mean energy, and mean Teager energy parameters. The mean energy and mean Teager energy are the low values in the normal and abnormal signals. The normal EEG in all parameters has less magnitude

Table 44.1 Tabulation of statistical parameters

		Delta	Theta	Alpha	Beta	Gamma
En (10^7)	N	2	0.3	2	2	0.2
	A	62	55	53	45	23
MEn	N	9.1	5.0	9.2	5.6	5.5
	A	10.2	8.4	7.5	7.2	5.1
MTE	N	2.5	3.5	4	6	5
	A	10.1	9.5	9.5	7.1	7.4
E (10^8)	N	4.5	4.5	4.5	3	0.3
	A	93	11	150	150	100

En energy, *MTE* mean Teager energy, *MEn* mean energy, *E* entropy, *A* abnormal, *N* normal

Table 44.2 Average error for 1,000-epoch fuzzy inference system (FIS) training

Frequency band	Delta	Theta	Alpha	Beta	Gamma
En (10^5)	5.24	1.24	6.02	3.26	7.37
MEn (10^7)	0.039	0.232	0.267	0.299	0.157
MTE	0.032	0.231	0.245	0.186	0.034
E (10^6)	10.396	2.261	11.964	0.616	14.385

En energy, *MTE* mean Teager energy, *MEn* mean energy, *E* entropy, *A* abnormal, *N* normal

in abnormal EEG signals. In an abnormal EEG the delta band has the highest mean energy of all the sub-bands. Next highest mean energy is in theta sub-band. This indicates that the abnormal state (epilepsy) of the brain requires a high level of energy to demodulate to normal and pathological neuronal activities (Cloix and Hévor 2009; Wu et al. 2015).The feature vector is input into the ANFIS. Using ANFIS the given input/output data are constructed on a fuzzy inference system (FIS), the membership function parameters of which are tuned using a back-propagation algorithm. This allows fuzzy systems to learn from the input/output data and model an expert system. Table 44.2 shows the average error of FIS training for 1,000 epochs.

The mean energy and the mean Teager energy provide the maximum efficiency with minimum error compared to other features. Figure 44.3 shows the training error of mean Teager energy on the delta band in the ANFIS editor.

It was observed that in the ANFIS editor mean Teager energy has a minimum training error of 0.0325 in the delta sub-band of the EEG.

The training error in all sub-bands of the EEG was much lower for mean Teager energy compared to other parameters. This suggests that mean Teager energy is more suitable for further classification of EEG signals.

By observing the wavelet packet spectrum of normal and abnormal EEG signals, the abnormal EEG spectrum is denser than the spectrum of the normal EEG signals.

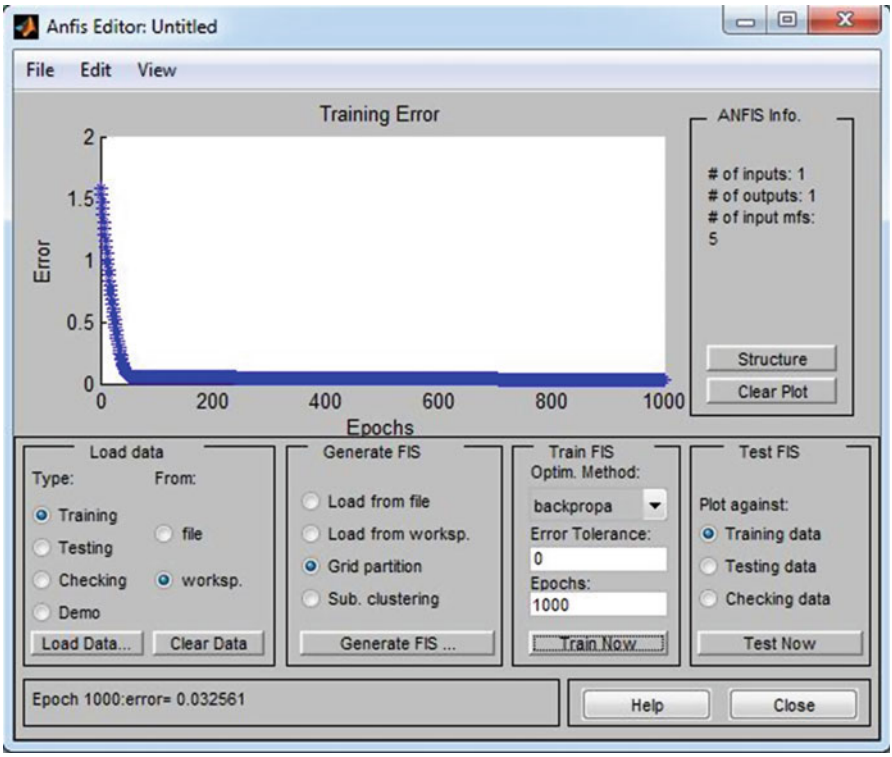

Fig. 44.3 Training error of mean Teager energy on delta band

It indicates that during the abnormal state (epilepsy) of the brain more energy is delivered to the lower frequency regions (Fig. 44.4).

5 Conclusion

In this proposed method, the EEG signal is analyzed using wavelet packet transform for feature extraction and a hybrid neuro-fuzzy system for classification. Here the signal is filtered by a band-pass filter to suppress the noise. Then the wavelet packet transform decomposes into four levels to obtain the frequency rhythm of delta, theta, alpha, beta, and gamma bands. Features of the sub-band coefficients are analysed by different statistical parameters like entropy, energy, mean Teager energy, and mean energy. If the brain produces high energy in the alpha band it reflects a normal brain state. If the brain produces high energy in the delta and theta bands, it seems to reflect an abnormal brain state (epilepsy). Finally, a constructed feature vector, the mean Teager energy, is used as an input to the artificial neuro fuzzy system to classify abnormal and normal EEG signals. Out of four parameters

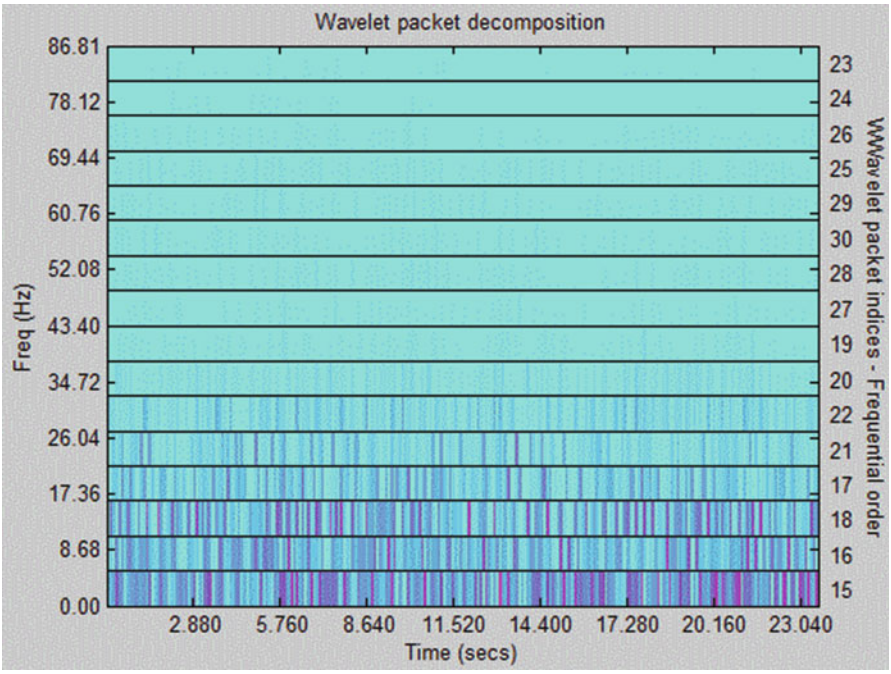

Fig. 44.4 Wavelet packet spectrum of an abnormal signal

it was shown that the mean energy and mean Teager energy coefficient of features have a minimum training error of 1,000 epochs. The mean Teager energy coefficient vector has a lower error than mean energy. Therefore mean Teager energy is used for constructing the feature vector for classification of normal and abnormal EEG signals.

References

Amirinejad, M., Tavajohi-Hasankiadeh, N., Madaeni, S.S., Navarra, M.A., Rafiee, E., Scrosati, B.: Adaptive neuro-fuzzy inference system and artificial neural network modeling of proton exchange membrane fuel cells based on nanocomposite and recast Nafion membranes. Int. J. Energy Res. **37**, 347–357 (2013)

Andrzejak, R.G., Lehnertz, K., Mormann, F., Rieke, C., David, P., Elger, C.E.: Indications of nonlinear deterministic and finite-dimensional structures in time series of brain electrical activity: dependence on recording region and brain state. Phys. Rev. E Stat. Nonlinear Soft Matter Phys. **64**, 061907 (2001)

Artameeyanant, P., Chiracharit, W., Chamnongthai, K.: Spike and epileptic seizure detection using wavelet packet transform based on approximate entropy and energy with artificial neural network. 5th Biomedical Engineering International Conference (BMEiCON), Ubon Ratchathani, 1–5(2012)

Bhagavatula, Y.S., Bhagavatula, M.T., Dhathathreyan, K.S.: Application of artificial neural network in performance prediction of PEM fuel cell. Int. J. Energy Res. **36**, 1215–1225 (2012)

Cloix, J.F., Hévor, T.: Epilepsy regulation of brain energy metabolism and neurotransmission. Curr. Med. Chem. **16**, 841–853 (2009)

Dianguo, C., Liu, L., Peng, W.: Application of wavelet packet energy spectrum to extract the feature of the pulse signal. 4th International Conference on Bioinformatics and Biomedical Engineering (iCBBE). Chengdu, 1–4 (2010)

Fauci A.S., Kasper D.L., Longo D.L., et al., Harrison's Principal of Internal Medicine, Mc Graw Hill Medical publishing division, 18th Edition, USA Vol. 2. (2011)

Garrett, D., Peterson, D.A., Anderson, C.W., Thaut, M.H.: Comparison of linear, nonlinear, and feature selection methods for EEG signal classification. IEEE Trans. Neural Syst. Rehabil. Eng. **11**(2), 141–144 (2003)

Gopan, K.G., Harsha, A., Joseph, L.A., Kollialil, E.S.: Adaptive neuro-fuzzy classifier for 'Petit Mal' epilepsy detection using Mean Teager Energy. International Conference on Advances in Computing, Communications and Informatics (ICACCI). Mysore, 752–757 (2013)

Gotman, J.: Automatic detection of seizures and spikes. J. Clin. Neurophysiol. **16**(2), 130–140 (1999)

Gwinn, R.P., Spencer, D.D., Spencer, S.S., Duckrow, R.B., Vives, K., Wu, K., Tkeshelashvili, D., Zaveri, H.P.: Local spatial effect of 50 Hz cortical stimulation in humans. Epilepsia. **49**, 1602–1610 (2008)

Jang, J.-S.R.: ANFIS: adaptive-network-based fuzzy inference system. IEEE Trans. Syst. Man Cybern. **23**(3), 665–685 (1993)

Kerr, W.T., Anderson, A., Lau, E.P., Cho, A.Y., Xia, H., Bramen, J., Douglas, P.K., Braun, E.S., Stern, J.M., Cohen, M.S.: Automated diagnosis of epilepsy using EEG power spectrum. Epilepsia. **53**, e189–e192 (2012)

Khan, Y.U., Gotman, J.: Wavelet based automatic seizure detection in intracerebral electroencephalogram. Clin. Neurophysiol. **114**, 898–908 (2003)

Krstacic, G., Krstacic, A., Martinis, M., Vargovic, E., Knezevic, A., Smalcelj, A., Jembrek-Gostovic, M., Gamberger, D., Smuc, T.: Non-linear analysis of heart rate variability in patients with coronary heart disease. Comput. Cardiol. **29**, 673–675 (2002.) 22–25

Malkawi, M., Murad, O.: Artificial neuro fuzzy logic system for detecting human emotions. Hum. Centric Comput. Inf. Sci. **3**, 3 (2013)

Narendra, K.S., Parthasarathy, K.: Identification and control of dynamical systems using neural networks. IEEE Trans. Neural Netw. **1**(1), 4–27 (1990)

Sinno, N., Kifah, T.: Analysis of epileptic events using wavelet packets. Int. Arab. J. Inf. Technol. 5(4), 165–169 (2008)

Subramaniyam, N.P., Hyttinen, J.: Analysis of nonlinear dynamics of healthy and epileptic EEG signals using recurrence based complex network approach. 6th International IEEE/EMBS Conference on Neural Engineering (NER). San Diego, 605–608 (2013)

Tzallas, A.T., Tsipouras, M.G., Fotiadis, D.I.: Epileptic seizure detection in EEGs using time–frequency analysis. IEEE Trans. Inf. Technol. Biomed. **13**(5), 703,710 (2009)

Voronin, S., Partanen, J.: Forecasting electricity price and demand using a hybrid approach based on wavelet transform, ARIMA and neural networks. Int. J. Energy Res. **38**, 626–637 (2014)

Wu, T., Yan, G., Yang, B., Sun, H.: EEG feature extraction based on wavelet packet decomposition for brain computer interface. Measurement. **41**(6), 618–625 (2008)

Wu, Y., Liu, D., Song, Z.: Neuronal networks and energy bursts in epilepsy.,Review Article. Neuroscience. **287**(26), 175–186 (2015)

Zandi, A.S., Javidan, M., Dumont, G.A., Tafreshi, R.: Automated real-time epileptic seizure detection in scalp EEG recordings using an algorithm based on wavelet packet transform. IEEE Trans. Biomed. Eng. **57**(7), 1639–1651 (2010)

Optical Simulation of Different Cavity Receivers Shape Used in Solar Tower Power Plant

Toufik Arrif, Adel Benchabane, Amor Gama, Hakim Merarda, and Abdelfateh Belaid

1 Introduction

In a CRS, the solar receiver is the heat exchanger where the solar radiation is absorbed and transformed into thermal energy useful in power conversion systems. There are different classification criteria for solar receivers, depending on the geometrical configuration and the absorber materials used to transfer the energy to the working fluid. In this survey, receivers are classified into three groups widely employed in central receiver system, volumetric receivers, cavity receivers and particle receivers (Omar et al. 2013). This paper is interested in cavity receivers group.

In a cavity receiver, the radiation reflected from the heliostats passes through an aperture into a boxlike structure before impinging on the heat transfer surface.

James and Terry (1985) have investigated the thermal performance of five cavity receivers of different geometries comprising spherical, hetero-conical, conical,

T. Arrif (✉)
Unité de Recherche Appliquée en Energies Renouvelables, URAER, Centre de Développement des EnergiesRenouvelables, CDER, 47133 Ghardaïa, Algeria

University Mohamed KhiderBiskra, Mechanical Engineering Department, Laboratory of Mechanical Engineering, PO Box145, RP07000 Biskra, Algeria
e-mail: arriftou@yahoo.fr

A. Benchabane
University Mohamed KhiderBiskra, Mechanical Engineering Department, Laboratory of Mechanical Engineering, PO Box145, RP07000 Biskra, Algeria

A. Gama • H. Merarda • A. Belaid
Unité de Recherche Appliquée en Energies Renouvelables, URAER, Centre de Développement des EnergiesRenouvelables, CDER, 47133 Ghardaïa, Algeria

© Springer International Publishing AG, part of Springer Nature 2018

F. Aloui, I. Dincer (eds.), *Exergy for A Better Environment and Improved Sustainability 2*, Green Energy and Technology,
https://doi.org/10.1007/978-3-319-62575-1_45

cylindrical, and elliptical. They have found that the rim angle and cavity geometry have a strong effect on the energy absorption efficiency.

Fang et al. (2011) have described a methodology for evaluating thermal performance of saturated steam solar cavity receiver under windy environment. To this end, the Monte Carlo method, the correlations of the flow boiling heat transfer, and the calculation of air flow field were coupled to assess absorbed solar energy.

They have concluded that the air velocity attained the maximum value when the wind came from the side of the receiver and the thermal loss of receiver also reached the highest value due to the side-on wind.

Yang et al. (2012) have used computational fluid dynamics to look into the distributions of temperature, heat flux, and the heat transfer characteristics of a molten salt tube receiver of a central receiver system. They have concluded that temperature distribution of the tube wall and HTF (Heat Transfer Fluid) is irregular and the heat flux of the exposed surface rise with the rise of molten salt velocity.

Paitoonsurikarn and Lovegrove (2006) have numerically examined three different cavity geometries. They have then established a correlation of the Nusselt number for natural convection.

Fang et al. (2011) have proposed an iterative method, based on Monte Carlo ray tracing (MCRT) technique, to determine surface temperature and to investigate the performance of cavity receiver under windy conditions.

Wu et al. (2011) have conducted a 3-D numerical study to examine the effect of geometric design of heat pipe receiver on natural convection characteristics. They have then proposed a new accurate correlation of Nusselt number that can estimate natural convection heat losses.

Garcia et al. (2008) have compared six simulation environments for solar tower power investigation: UHC, DELSOL, HFLCAL, MIRVAL, FIAT LUX, and SOLTRACE. They have then classified them into two groups. The first one comprises optimization codes HFLCAL, UHC-RCELL, and DELSOL. The second group includes performance analysis codes such as FIAT LUX, MIRVAL, UHC-NS, and SOLTRACE.

Lina et al. (2014) have investigated experimentally as well as numerically the optical and thermal performance of a linear Fresnel lens solar collector using different shapes of cavity receiver. The optical performance was analyzed by using TracePro software which uses Monte Carlo ray tracing (MCRT) method. They have found that triangular cavity receiver is suitable for solar thermal utilization in the medium temperature range (100–150 °C) without using the conventional glass-metal tube absorber.

In this paper, a new study of solar power tower systems using TracePro software to obtain a concentrated ray distribution as uniform as possible on the inner walls of the cavity receiver of different shape was carried out. It will allow us to define a reference incident flux distribution that will be used to predict thermal performance of the cavity receiver.TracePro software uses Monte Carlo ray tracing which is a technique that computes the outcome of random processes.

In Monte Carlo ray tracing method, scattering and diffraction are treated as random processes. That is, instead of propagating a distribution of light, discrete

samples of the distribution (rays) are propagated. The samples are randomly chosen, using the scattering distribution as a probability density which in turn facilitates the use of the well-developed techniques of ray tracing to model scattering (Lambda Research Corporation 2009).

Nomenclature

δ	Solar declination (radians)
φ	Latitude (radians)
n_d	Day number
$\omega_{sunrise}$	Hour angle of sunrise
ω_{sunset}	Hour angle of sunset
h	Solar altitude (radians)
$\vec{S}$	
a	Solar azimuth (radians)
H_T	Tower height (m)
(X_M, Y_M, Z_M)	Heliostat Cartesian coordinate system (m)
r	Ring radius (m)
H	Heliostat
R	Receiver
Dap	Aperture diameter (m)
Lcav	Cavity length (m)
A_w	Cavity inner wall area (m^2)
Greek letters	
ψ	Heliostat relative angle referenced to the base of the tower (radians)
β	Angle of beam rays (radians)
θ	Angle of incidence (radians)
γ	Heliostat azimuth angle (radians)
α	Heliostat inclination angle (radians)
λ	Cavity inclination angle (degree)

2 Numerical Procedure

2.1 Selecting a Reference Case

The first step in the optical study is to define a reference case to complete the following survey. In our case, a mini solar power plant was chosen to study in turn 12 heliostats on a 15 × 14 m area (each one 1 m^2) (Figs. 1 and 2), for the winter solstice (December 21) at 12 GMT. Based on the work of Siala and Elayeb (2001), Belhomme et al. (2009), and Lundy (2003) and using the DELPHI environment, we

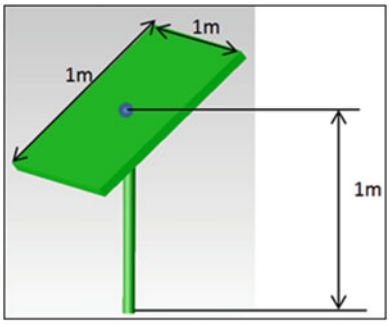

Fig. 1 The shape and dimensions of the heliostat

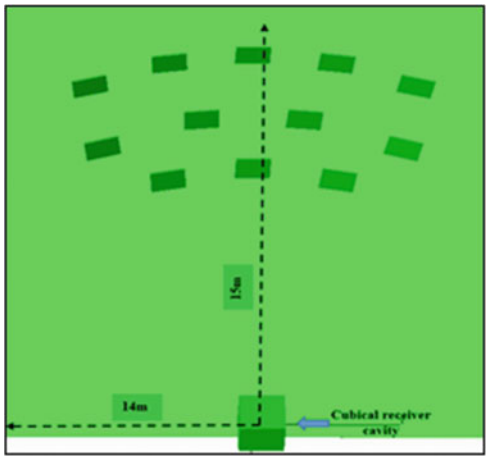

Fig. 2 Radial stagger arrangement of 12 heliostats in TracePro environment (December 21 at 12 pm)

have calculated the field layout by considering shading and blockage effects. The cavity receiver is placed at 6.5 m at the top of the tower.

Direct solar radiation incident on a horizontal plane in Ghardaia (clear day) for the selected dates (21 December) is 525 W/m^2. It was obtained using a known radiation model R_SUN which is developed in MATLAB.

Parameters relating to the heliostat field, position of the cavity receiver, sun position, angle of incidence, the reflected beam position, and orientation of the heliostat are calculated (MATLAB) to find the angles to be followed by the heliostat to reflect the incident ray of the sun toward a fixed target at the top of the tower.

2.2 Solar Position

The solar declination δ and hour angle of sunrise and sunset ω as a function of day number n_d and latitude φ (all angles in radians) are calculated as (Duffie and Beckman 2006), (Capderou 1986):

$$\delta = \frac{23.45\pi}{180} \sin\left(2\pi \frac{284 + n_d}{365}\right) \tag{1}$$

$$\omega_{sunrise} = \cos^{-1}(\tan\varphi \tan\delta) - \pi = -\omega_{sunset} \tag{2}$$

The sun's position relative to an observer on the ground is described by two angles, the solar altitude h and azimuth a:

$$\sin a = \frac{\cos\delta \sin\omega}{\cos h} \tag{3}$$

$$\sin h = \sin\varphi \sin\delta + \cos\varphi \cos\delta \cos\omega \tag{4}$$

2.3 Heliostat-Tour Relations

We consider the heliostat field, which is defined in an orthonormal reference, whose center is at the base of the tower, and the three directions are, respectively, the north, west, and the zenith. Figure 3 shows the heliostat tower together in a

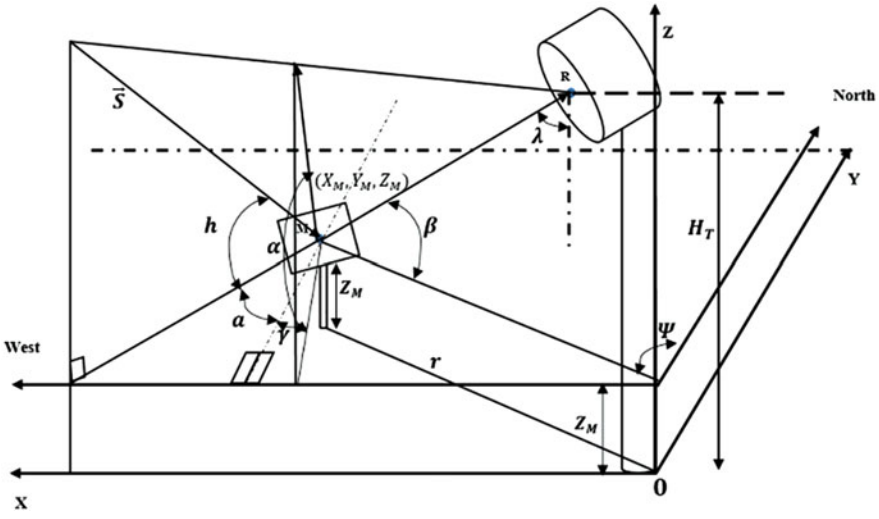

Fig. 3 Description of angles of a heliostat-tour system in Cartesian coordinates

Cartesian coordinate system associated to the tower base$(0, 0, H_T)$ with $H_T = 6.5$ m, the coordinates of heliostat (X_M, Y_M, Z_M) are defined in this orthonormal reference by:

$$\begin{cases} X_M = -r \sin \psi \\ Y_M = r \cos \psi \\ Z_M = \ Z_M \end{cases} \tag{5}$$

and

$$r = \sqrt{X_M^2 + Y_M^2} \tag{6}$$

From the coordinates of the heliostat H and cavity R, we define a positioning relative angle ψ referenced to the base of the tower in a horizontal plane (by convention, the heliostats to the west of the tower have a positive angle ψ) and a target angle of β in a vertical plane (D Claude 1983), and according to previous relations, we obtain the following relations for ψ and β:

$$\begin{aligned} \psi &= \tan^{-1}\left(\frac{X_M}{Y_M}\right) \\ \beta &= \tan^{-1}\left(\frac{H_T - Z_M}{r}\right) \end{aligned} \tag{7}$$

The angle of incidence θ of the rays on the reflective surface is calculated with the following equation (Chong and Tan 2012):

$$\theta = \frac{1}{2}\cos^{-1}(\sin h \sin \beta + \cos h \cos \beta(\sin a \sin \psi + \cos a \cos \psi)) \tag{8}$$

2.4 Normal Heliostat Orientation

Each heliostat is individually adjusted according to two angles, heliostat azimuth angle γ and heliostat inclination angle α (the normal/horizontal). To reflect the rays to the center of the cavity aperture R, the position of the heliostat is then given by the following relations (Chong and Tan 2012):

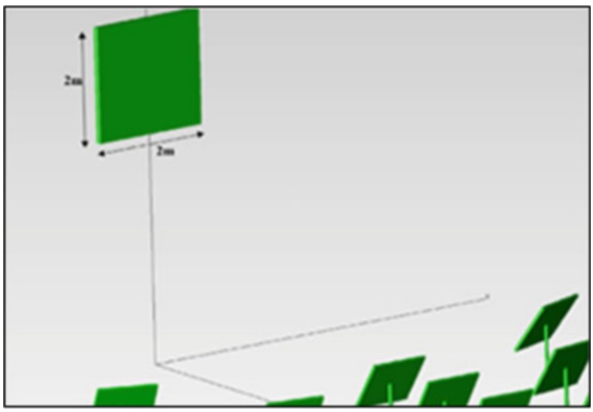

Fig. 4 Size of the rectangular flat plate

$$\alpha = \sin^{-1}\left(\frac{\sin h + \sin\beta}{2\cos\theta}\right) \tag{9}$$

$$\gamma = \sin^{-1}\left(\frac{\sin a\cos h + \cos\beta\ \sin\psi}{2\cos\theta\cos\alpha}\right) \tag{10}$$

2.5 Size of the Cavity aperture

The cavity receiver must be inclined in such a way that the normal vector to the cavity aperture is directed toward the center of the heliostat field and such that the incident flux will be intercepted in the middle area of the vertical wall opposing the cavity aperture (Benjamin n.d.), the angle was calculated as $\lambda = 32.02^{\circ}$,

In order to find the size of the cavity receiver aperture, the heliostat field reflects the rays on a 2×2 m rectangular plate target as shown in Fig. 4, and the results are shown in Fig. 5.

It is observed that the angle of inclination of a rectangular plate made the difference in the maximum value of the concentrated ray flux and in the size of the sunspot; thus, the size of the cavity receiver aperture will be $D_{ap} = 1.2$ m.

3 Types of Cavities Investigated

The current work deals with cavity receiver which has been reported in the literature (Pavlovic and Penot 1991, Fang et al. 2013, Robert n.d., Benjamin n.d.) for central receiver power plant. These are cylindrical, cubical, and trapezoidal prism shape; the 3-D cavity models were developed using *GAMBIT 2.4.6* and imported in TracePro and are shown in Fig. 6. The optical properties of heliostat

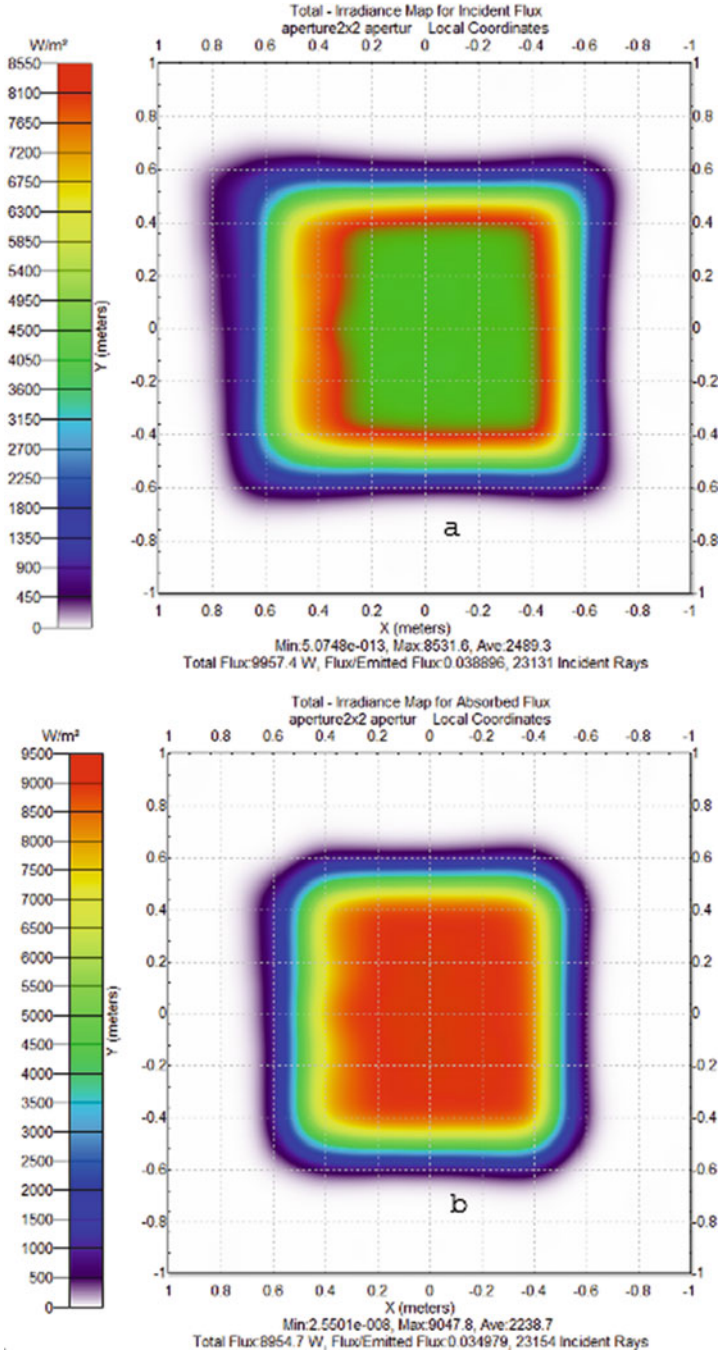

Fig. 5 Incident concentrated rays on the rectangular flat plate (2 × 2 m): (**a**) $\lambda = 0^0$ (**b**) $\lambda = 32.02^0$

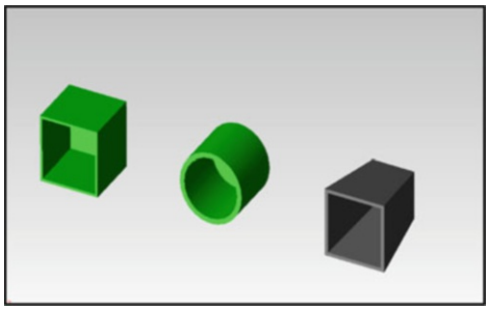

Fig. 6 Types of cavities investigated

Table 1 Optical parameters of heliostat and cavity

Device	Reflectance	Absorptance
Rectangular flat plate	0.1	0.9
Heliostat mirror	0.95	0.05
Cavity wall	0.1	0.9

mirrors, cavity wall, and rectangular flat plate used in this simulation are listed in Table 1. While comparing these different shapes, their aperture diameter is taken to be same $D_{ap} = 1.2$ m.

The effect of shape on the concentrated ray distribution is studied with the aperture diameter fixed ($D_{ap} = 1.2$ m); the length of cavity is varied to get constant inner wall area A_w equal to 7.2 m^2 for all shapes. This is due to the fact that for a given central receiver power plant, the size of the cavity is fixed and represents (an almost) 3–4 m placed on an 80–120 m high tower. In the present study, a mini solar central receiver power plant of 20 (12) heliostats (1 m^2 each) is considered, the size of the cavity can be rather small compared to a real central receiver power plant.

While comparing these different cavities, cubical cavity is taken as the base cavity with diameter of aperture $D_{ap} = 1.2$ m, and the length of the cavity $L_{cav} = 1.2$ m and cavity inner wall area $A_w = 7.2$ m^2.

4 Results and Discussions

4.1 Flux Distribution

In the present simulation, for Ghardaia region in Algeria, the solar radiation value of 525 W/m^2 was chosen as input source, which represents the maximum average radiation received over a typical day December 21 in Ghardaia (south Algeria). The simulated ray tracing results for 562,500 sunrays with heat flux of 525 W/m^2 are shown in Fig. 7. As seen, most of the rays traced by the simulation could be concentrated on the cavity receiver.

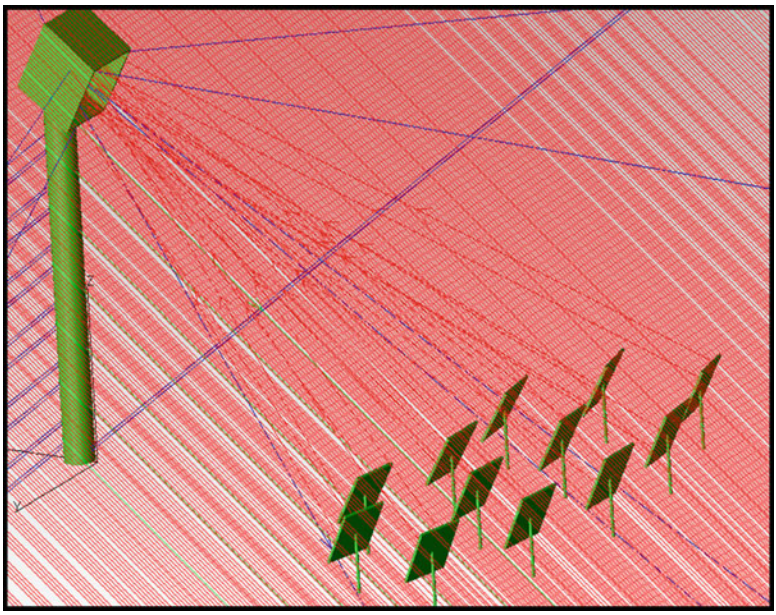

Fig. 7 Radial stagger arrangement of heliostats in TracePro with incident rays in *red* and reflected rays in *blue*

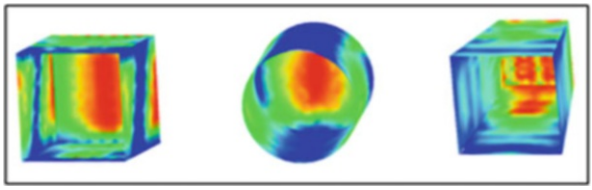

Fig. 8 Distribution of incident solar flux in internal wall of the three cavity receivers

Optical simulation was performed employing TracePro ray tracing software using MCRT method. The incident solar flux distribution on absorbing surface of three different types of cavity receiver involved was obtained and is shown in Figs. 8 and 9.

Based on incident solar flux distribution maps shown in Figs. 8 and 9 and flux reported in Table 2, it is seen that the cavity receiver in trapezoidal prism shape experiences more uniform distribution on absorbing surface, what means minimum peak flux density with minimum lost flux.

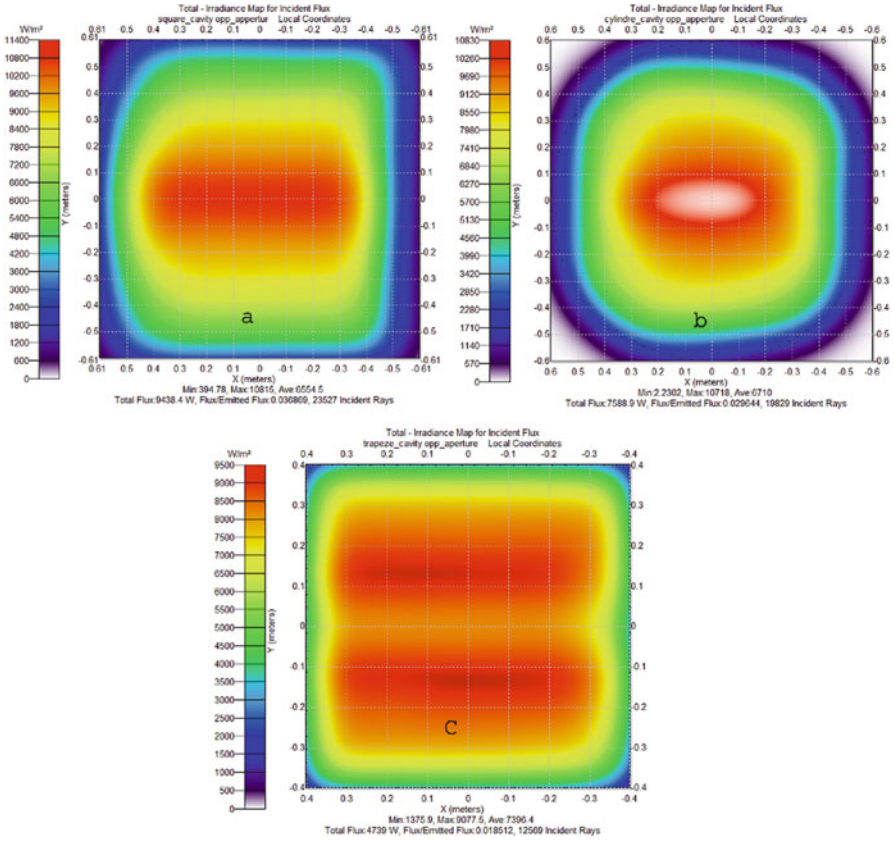

Fig. 9 Distribution of incident solar flux in the internal opposite aperture wall: (**a**) cubical (**b**) cylindrical (**c**) trapezoidal prism

5 Conclusions

This paper presents a numerical investigation on flux distribution on a solar cavity receiver using three different shapes: cubical, cylindrical, and trapezoidal prism. The heat flux distribution for three types of cavity receivers used in solar tower power plant was carried out by employing MCRT method. Ray tracing results show that the cavity with trapezoidal prism shape receives the best uniform flux distribution.

Optical efficiency is not shown in this paper and will be shown in our future work with thermal efficiency to better analyze the performance of cavity receiver; for this reason, numerical as well as experimental methods must be employed.

Table 2 Flux report of different cavities

Cavities	Incident flux (Watt)	Absorbed flux (Watt)	Lost flux (Watt)
Cylindrical			
Opp_aperture	7699.11	6929.20	41.98
Surf_int	3464.64	3118.18	62.64
Sum	11,163.75	10,047.38	104.62
Cubical			
Opp_aperture	9908.37	8917.53	71.23
Surf_int_H	231.59	208.43	18.06
Surf_int_B	271.96	244.76	23.22
Surf_int_D	751.41	676.27	20.01
Surf_int_G	1133.56	1020.21	21.45
Sum	12,296.89	11,067.20	153.98
Trapezoidal prism			
Opp_aperture	5182.66	4664.39	3.14
Surf_H	502.49	452.24	14.20
Surf_B	1310.46	1179.41	14.70
Surf_D	1502.66	1352.40	13.80
Surf_G	1505.63	1355.06	15.66
Sum	10,003.90	9003.51	61.50

References

Belhomme, B., Pitz-Paal, R., Schwarzboezl, P., Ulmer, S.: A new fast ray tracing tool for high-precision simulation of heliostat fields [Journal]. J. Sol. Energy Eng. Trans. ASME. **131**, 3 (2009)

Benjamin, G.: Modélisation et dimensionnement d'un récepteur solaire à air pressurisé pour le projet PEGASE [Journal]. Thèse univ- Perpignan [s.n.]

Capderou.: Atlas solaire de l'Algérie [Journal]. OPU Tome 2 (1986)

Chong, K.K., Tan, M.H.: Comparison study of two different sun-tracking methods in optical efficiency of heliostat field [Journal]. Hindawi Publ. Corp. Int. J. Photoenergy. **2012**, 10 (2012)

D Claude.: Performance et limites de chaudière à gaz de centrales solaires [Journal]. Thèse N° 474. Vol. Thèse N° 474 (1983)

Duffie, J.A., Beckman, W.A.: Solar Engineering of Thermal Processes [Journal]. Wiley (2006)

Fang, J.B., Tu, N., Wei, J.J.: Numerical investigation of start-up performance of a solar cavity receiver [Journal]. Renew. Energy. **53**, 35–42 (2013)

Fang, J.B., Wei, J.J., Dong, X.W., Wang, Y.S.: Thermal performance simulation of a solar cavity receiver under windy conditions [Journal]. Sol. Energy. **85**, 126–138 (2011)

Garcia, P., Ferriere, A., Bezian, J.J.: Codes for solar flux calculation dedicated to central receiver system applications: a comparative review [Journal]. Sol. Energy. **82**, 189–197 (2008)

James, A., Terry, G.: Thermal performance of solar concentrator cavity receiver systems [Journal]. Sol. Energy. **34**, 135–142 (1985)

Lambda Research Corporation User's Manual [Journal]. Lambda Research Corporation, Littleton [s.n.], Release 5.0 : Vol. Release 5.0 (2009)

Lina, M., Sumathy, K., Dai, Y.J., Zhao, X.K.: Performance investigation on a linear Fresnel lens solar collector using cavity receiver [Journal]. Sol. Energy. **107**, 50–62 (2014)

Lundy: Sargent & Assessment of Parabolic Trough and Power Tower Solar Technology Cost and Performance Forecasts [Journal]. National Renewable Energy Laboratory NREL. (NREL/SR-550-34440) : Vols. (NREL/SR-550-34440) (2003)

Omar, B., Abdallah, K., Kamal, M.: A review of studies on central receiver solar thermal power plants [Journal]. Renew. Sust. Energ. Rev. **23**, 12–39 (2013)

Paitoonsurikarn, S., Lovegrove, K.: A new correlation for predicting the free convection loss from solar dish concentrating receivers [Journal]. Proceedings of 44th ANZSES Conference. Australia : [s.n.], (2006)

Pavlovic, M., Penot, F.: Experiments in the mixed convection regime in an isothermal open cubic cavity [Journal]. Exp. Thermal Fluid Sci. **4**, 648–655 (1991)

Robert, Y.Ma.: Wind Effects on Convective Heat Loss from a Cavity Receiver for a Parabolic Concentrating Solar Collector [Journal]. Sandia National Laboratories Technical Library, Vols. SAND92–7293

Siala, F.M.F., Elayeb, M.E.: Mathematical formulation of a graphical method for a no-blocking heliostat field layout [Journal]. Renew. Energy. **23**, 77–92 (2001)

Wu, S.Y., Xiao, L., Li, Y.R.: Effect of aperture position and size on natural convection heat loss of a solar heat-pipe receiver [Journal]. Appl. Therm. Eng. **31**, 2787–2796 (2011)

Yang, X., Yang, X., Ding, J., Shao, Y., Fan, H.: Numerical simulation study on the heat transfer characteristics of the tube receiver of the solar thermal power tower [Journal]. Appl. Energy. **90**, 142–147 (2012)

Improved Wind Speed Prediction Results by Artificial Neural Network Method

Asilhan Sevinc Sirdas, Akatas Nilcan, and Izgi Ercan

1 Introduction

Recently, increase in industrialization and urbanization has brought about a rise in energy demand. Orientation to renewable energy sources is inevitable because resources used in energy production have been running out, and they cause irreversible damages to the environment. Wind is one of these renewable energy resources. The most positive impact of wind energy is to not cause the release of greenhouse gases that are formed as a result of the combustion of fossil fuels. Besides, the widespread use of wind energy will also reduce pollutant emissions as a result of reduction in fossil fuel consumption (Fig. 1 and Table 1).

Turkey is under the influence of the northern wind caused by the general circulation of the atmosphere. It is also surrounded by seas on three sides and has high valleys, especially in the eastern regions. All these lead to high wind energy potential for Turkey. Turkey's gross wind potential is thought to be 400 billion kWh per year, while technical potential is thought to be 120 billion kWh per year (Gençoğlu 2002). According to the Global Wind Report published by Global Wind Energy Council, the total installed capacity of Turkey was 2312 MW at the end of 2012; then 646 MW were added in 2013, and it increased to 2959 MW at the end of 2013 (Url-1 2014).

A.S. Sirdas (✉) • A. Nilcan
Istanbul Technical University, Faculty of Aeronautics and Astronautics, Department of Meteorological Engineering, Maslak, 34469 Istanbul, Turkey
e-mail: sirdas@itu.edu.tr; ssirdas@gmail.com

I. Ercan
Yildiz Technical University, Faculty of Electrical Engineering, Davutpasa Campus, Istanbul, Turkey

© Springer International Publishing AG, part of Springer Nature 2018

F. Aloui, I. Dincer (eds.), *Exergy for A Better Environment and Improved Sustainability 2*, Green Energy and Technology,
https://doi.org/10.1007/978-3-319-62575-1_46

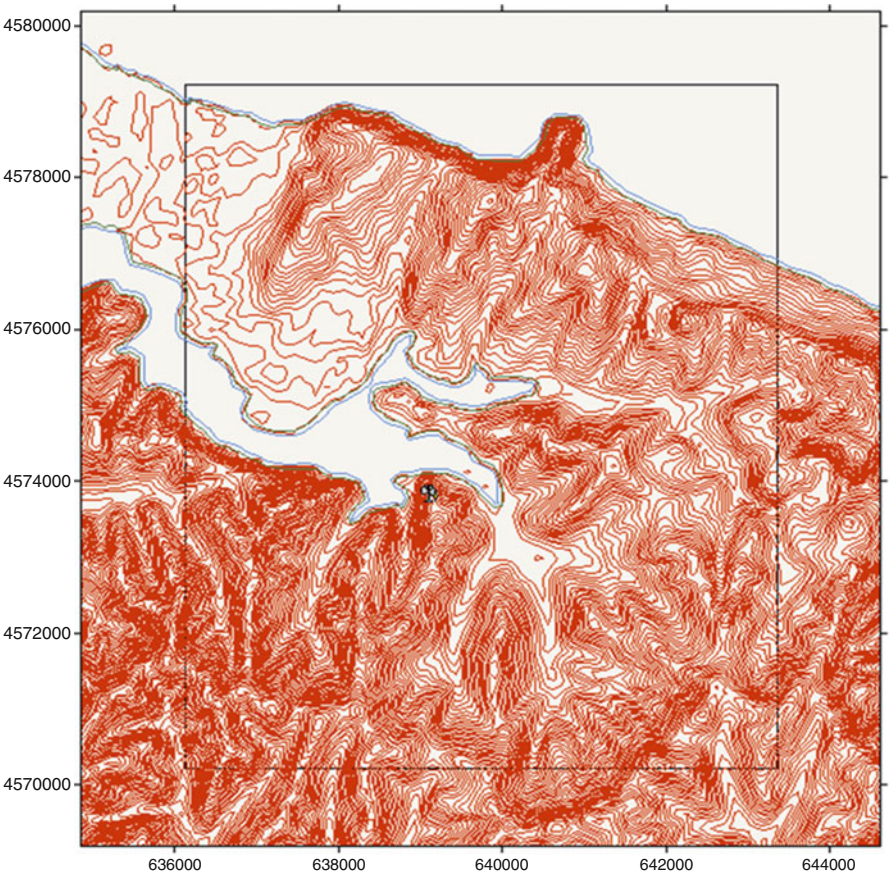

Fig. 1 Digital map of study area by WaSPV3

Turkey has continued to make new breakthroughs related to wind energy. In this respect, this work aimed to form a preliminary study for a wind turbine planned to take place in Terkos, Istanbul, as the first national turbine of Turkey. For this reason, short-term analysis and predictions of wind for Terkos region were handled in this study.

Nomenclature

V_1	The observed wind speed (m.s^{-1})
V_2	The calculated wind speed (m.s^{-1})
Z_2	The height level 2 (m)
Z_1	The height level 1 (m)
Greek letters	
α	An empirically derived coefficient that varies depending upon the stability of the atmosphere

(continued)

Superscripts	
α	0.169
Subscripts	
i	Time step
n	Number of time steps

Table 1 Roughness lengths specified in WAsP1

Physical z_0 [m]	Terrain surface characteristics	Roughness class z_0	Specified in WAsP [m]
1.5		4 (1.5 m)	1.5
>1	Tall forest		>1
1.00	City		1.00
0.80	Forest		0.80
0.50	Suburbs		0.50
0.40		3 (0.40 m)	0.40
0.30	Shelter belts		0.30
0.20	Many trees and/or bushes		0.20
0.10	Farmland with closed appearance	2 (0.10 m)	0.10
0.05	Farmland with open appearance		0.05
0.03	Farmland with very few buildings/ trees	1 (0.03 m)	0.03
0.02	Airport areas with buildings and trees		0.02
0.01	Airport runway areas		0.01
0.008	Mown grass		0.008
0.005	Bare soil (smooth)		0.005
0.001	Snow surfaces (smooth)		0.003
0.0003	Sand surfaces (smooth)		0.003
0.0002	(Used for water surfaces in the Atlas)	0 (0.0002 m)	0.0
0.0001	Water areas (lakes, fjords, open sea)		0.0

2 Data and Methodology

The study area, Terkos, is in the northwest of Istanbul, Turkey, with 41° 18′ N latitude and 28° 39′ E longitude (Fig. 2). A measurement mast with measuring instruments at 20, 40, 65, 80, and 81 m is located in the area, which is at 51 m from sea level. Temperature, pressure, wind speed, and wind direction data can be obtained on these levels at 10 min intervals. The measurement mast is shown in Fig. 3. In this study, wind speed data from August 1, 2012, to August 1, 2013, were

Fig. 2 Study area

measured at all levels. Wind direction data were obtained from 20 and 65 m of the mast for the same time period.

Due to the absence of data measured at 10 m, it was obtained from the other levels by using power law (Eq. 1):

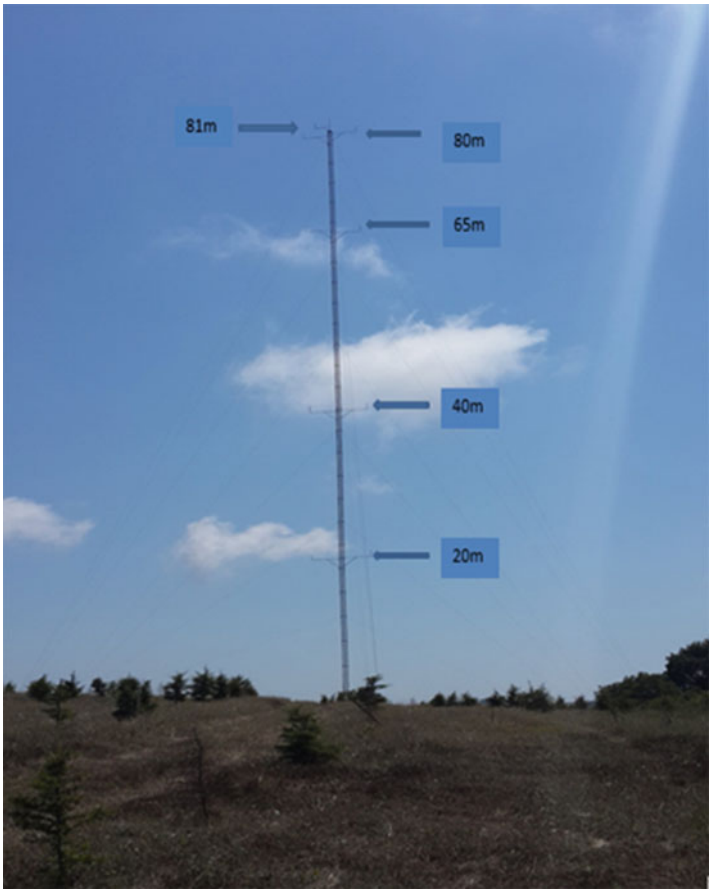

Fig. 3 Measurement mast

$$V_2 = V_1 \left(\frac{Z_2}{Z_1} \right)^{\alpha} \tag{1}$$

where V_2 (m/s) is the calculated wind speed at height z_2 (m), V_1 (m/s) is the observed wind speed at z_1 (m), and α is the power law exponent, which is affected by the roughness of the location. For the study area, α was found as 0.169.

The daily and monthly averages of wind speeds were shown by time series graphs. Daily mean wind speed time series derived from 10 min interval observation data showed that wind speeds were higher in October, November, and February (Fig. 4). Especially in the earliest days of February, wind speeds reached maximum values.

Monthly mean wind speed graphs show that wind speed values decrease in summer season of the region (May–June–July) and increase in autumn season (August–September–October) (Fig. 4). Determining the wind directions is crucial

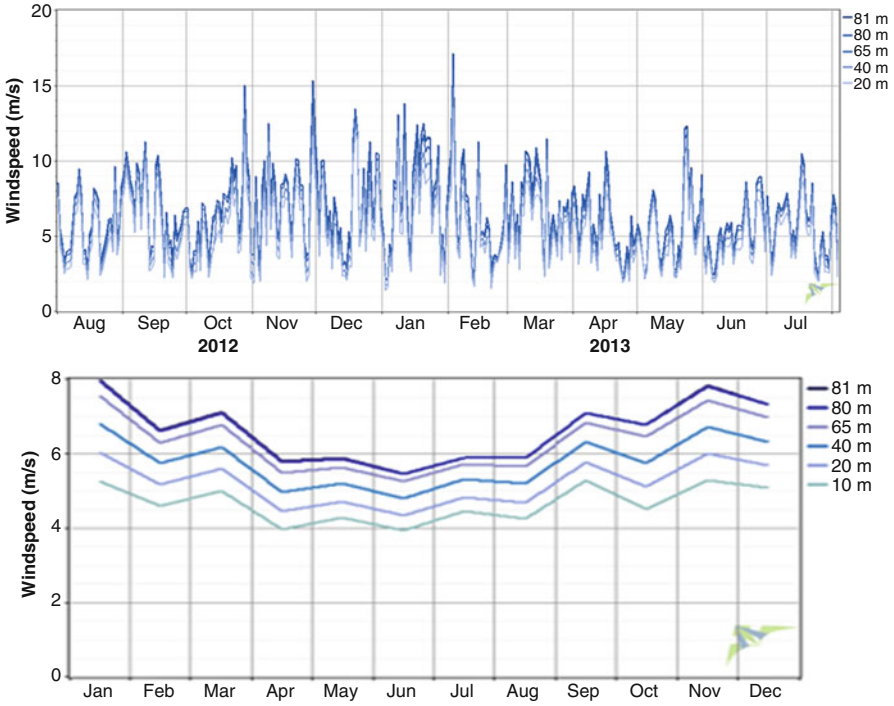

Fig. 4 Time series of daily mean wind speed

for wind energy studies. Wind roses derived from wind direction data from 20 to 65 m of measurement mast are demonstrated in Fig. 5. Accordingly, the most windward directions are northwest and southeast.

2.1 Short-Term Wind Prediction with WRF/ARW

The Weather Research and Forecasting (WRF) model has two dynamical core variants named nonhydrostatic mesoscale (NMM) and advance research (ARW). NMM is used for making operational forecasts, while ARW is used for both meteorological research and numerical weather prediction. In this study, WRF/ARW version 3.2.1 was used.

2.1.1 Initial and Boundary Conditions

The initial and boundary conditions supplied to the WRF/ARW model were provided by the National Centers for Environmental Prediction (NCEP) Final

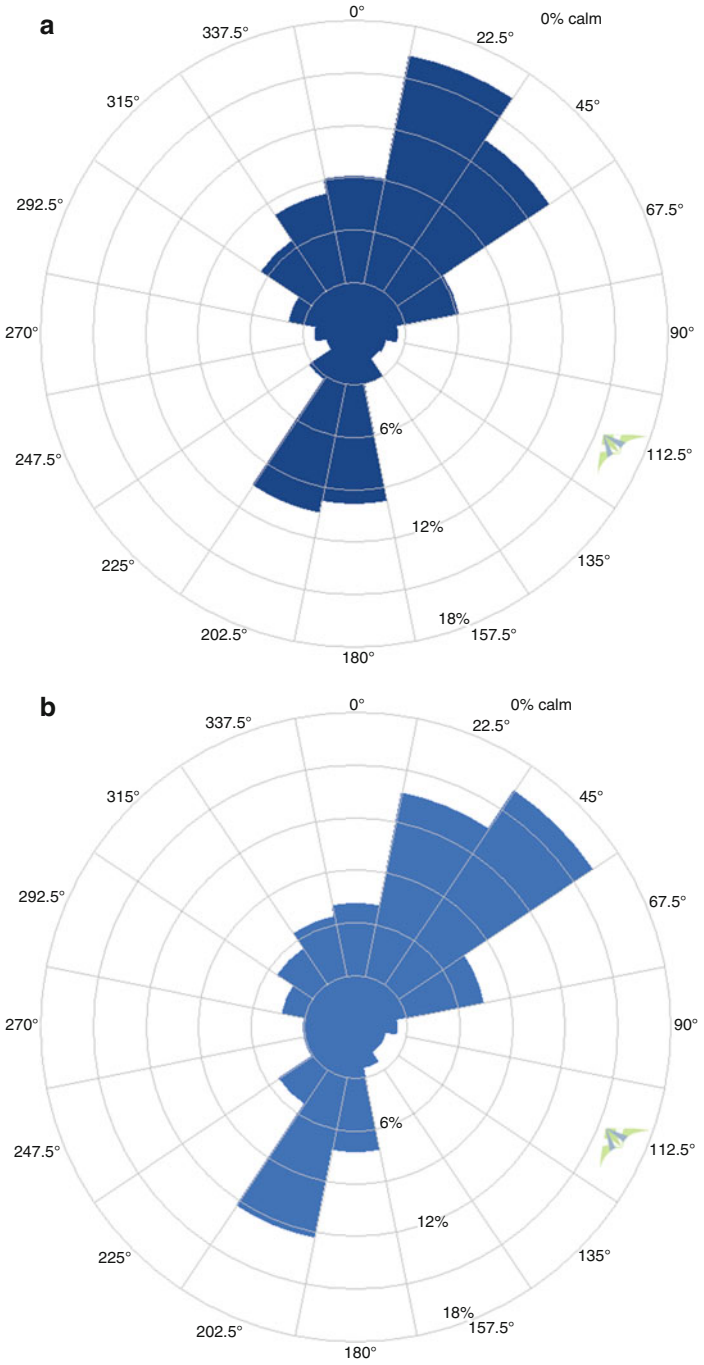

Fig. 5 Wind rose for (**a**) 65 m (**b**) 20 m

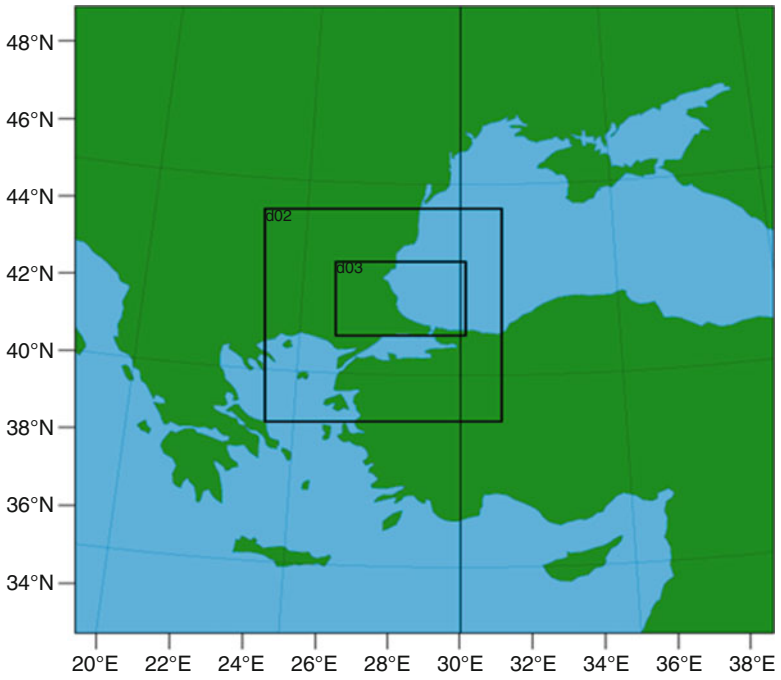

Fig. 6 WRF/ARW domain configuration

Operational Model Global Tropospheric Analyses, with 1° of spatial and 6 h of temporal resolution.

2.1.2 Design of the Simulations

The model was built over three nested domains shown in Fig. 6. The coarser domain (d01) with 30 km spatial resolution covers eastern Europe and Turkey between 33–49° N latitudes and 19–39° E longitudes. The middle domain (d02) with 10 km spatial resolution covers Marmara Region located in the northwest of Turkey. The inner domain (d03) with 3 km spatial resolution covers Thrace region and Terkos. All domains are cantered to the same point where measurement mast locates with latitude 41° 18′ N and longitude 28° 39′ E. The vertical structure of the model contains 28 layers.

There are several physical options for the WRF model predictions. These physical options consist of the combination of microphysics, cumulus parameterizations, surface physics, planetary boundary layer (PBL) physics, and atmospheric radiation physics. In this study, six different WRF/ARW simulations obtained with different physical options are listed in Table 2. It was aimed to test mainly the PBL parameterizations. In the simulations, Asymmetrical Convective Model version 2 (ACM2), Medium Range Forecast Model (MRF), Mellor–Yamada–Janjic

Table 2 WRF/ARW physics options

Parameterization	PBL	Land surface model	Surface layer physics
1	ACM2	Pleim-Xiu	Pleim-Xiu
2	MRF	Noah LSM	Monin-Obukhov
3	MYJ	Noah LSM	Eta similarity
4	MYNN2	Noah LSM	MYNN
5	YSU	Noah LSM	Monin-Obukhov
6	QNSE	Noah LSM	QNSE

Table 3 WRF/ARW PBL schemes

Scheme	WRF dynamic core	Prognostic variables	Diagnostic variables	Cloud mixing ratio
ACM2	ARW	–	–	QC, QI
MRF	ARW NMM	–	–	QC, QI
MYJ	ARW NMM	TKE_PBL	EL_PBL, exch_h	QC, QI
MYNN2	ARW	QKE	Tsq, Qsq, Cov, exch_h, exch_m	QC
YSU	ARW NMM	–	exch_h	QC, QI
QNSE	ARW NMM	TKE_PBL	EL_PBL, exch_h, exch_m	QC, QI

Url-2 (2014)

(MYJ), Mellor–Yamada Nakanishi and Niino Level 2 (MYNN2), Yonsei University (YSU), and Quasi-Normal Scale Elimination (QNSE) PBL options were used (Table 2). The differences between the PBL parameterizations are indicated in Table 3. They can differ from each other by the prognostic variables TKE_PBL (turbulent kinetic energy from PBL) and QKE (turbulent heat flux) and diagnostic variables EL_PBL (length scale from PBL), exch_h (scalar exchange coefficient), exch_m (exchange coefficient), Tsq (liquid water potential temperature variance), Qsq (liquid water variance), and Cov (liquid water-liquid water potential temperature covariance) (Url-3 2014).

According to the National Center for Atmospheric Research (NCAR) Technical Note, microphysics schemes have a wide range of options from basic physics for idealized studies to complicated mixed-phase physics for process studies and numerical weather prediction (Skamarock et al. 2008). In this study, Thompson option including both ice-phase and mixed-phase processes were chosen for all simulations as the microphysics scheme.

Another parameterization option is cumulus physics scheme. The cumulus physics schemes are responsible for the subgrid-scale effects of convective and/or shallow clouds (Skamarock et al. 2008). The Kain–Fritsch scheme including updraft and downdraft changes was used for this study. This scheme makes the calculations by using a basic cloud model bearing updrafts and downdrafts with dragging effects (Skamarock et al. 2008).

Using these parameterizations, 3-day and 10-day predictions were performed by WRF/ARW. Simulation period covered 1–4 February and 1–4 March for 3-day

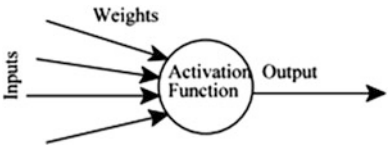

Fig. 7 An artificial neuron (Gershenson 2001)

runs. In the 10-day predictions, 1–11 February and 1–11 March periods were chosen. The results were derived as 1 h outputs.

Because the WRF/ARW gave results only for the grid points, the data on the grids were moved to Terkos where the measurement mast locates by two downscaling methods: weighted average method and nearest neighbor method.

2.2 Artificial Neural Networks (ANN)

The artificial neural network (ANN) method was used to try and reduce the errors of WRF/ARW results that were derived from different parameterizations. The ANN method is the study of cellular networks with storage of the experimental knowledge feature (Aleksander 1989). The development of ANN is known to be inspired by the neurons in the brain. The functioning of the artificial neuron is shown in Fig. 7.

An ANN model is trained using the available data and then tested with the rest of the data. The purpose of the training is to calculate the weights and minimize the errors (Aşkın et al. 2011). In this study, 70% of the WRF/ARW prediction results were used as training data and the remaining 30% data were tested.

In the ANN model, the Levenberg–Marquardt algorithm was performed. It is a least squares calculation method mainly based on the maximum neighborhood and consists of the best features of Gauss–Newton and gradient descent algorithms (Aşkın et al. 2011).

3 Applications

WRF/ARW was run with six different initial conditions, and the results were obtained. First, February 1–4 and March 1–4 results were derived. Then they were downscaled to the point where the observation data exist. Model results were achieved for the selected nesting area separately.

Hourly wind speed data (measured) were compared to the hourly model results (predicted) at 10 m. Results are shown in Figs. 8 and 9.

From a coarser domain to the inner domain, the model results were closer to the observations (Fig. 7). A bigger domain and lower resolution made predictions that

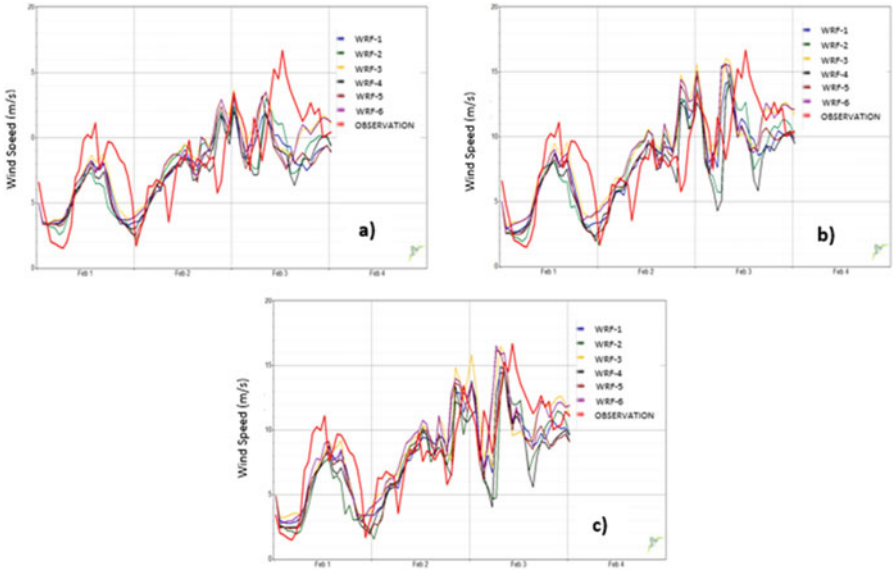

Fig. 8 1–4 February model results (downscaled by nearest neighbor method) and observations for (**a**) coarser domain (d01), (**b**) middle domain (d02), (**c**) inner domain (d03)

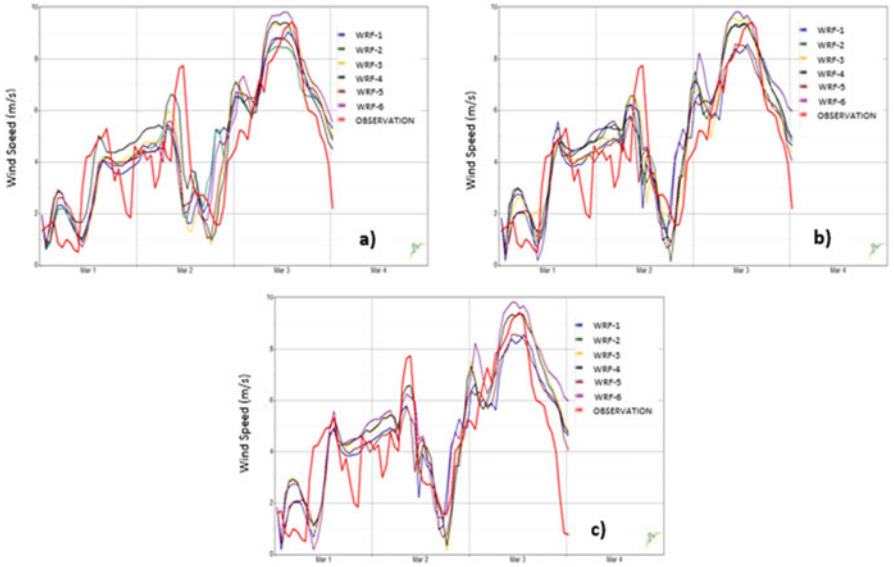

Fig. 9 March 1–4 model results (downscaled by nearest neighbor method) and observations for (**a**) coarser domain (d01), (**b**) middle domain (d02), (**c**) inner domain (d03)

were far from the observed data. The model results were seen to be close to each other, and WRF-3 results were closer to the observations.

4 Results and Discussions

4.1 WRF/ARW Predictions

Model performances were established by the root mean square error (RMSE) (Eq. 2) compared to the measured data in Terkos:

$$\mathrm{RMSE} = \sqrt{\frac{1}{n}\sum_{i=1}^{n}(F_i - O_i)} \tag{2}$$

where n is number of data, F_i is forecast values, and O_i is observed values at time i.

The RMSE calculations are given in Tables 4 and 5.

The model results belonging to March 1–4 were more successful than February 1–4 results. Where the wind speeds are high, especially in March 3, observations and predictions overlapped well (Fig. 9). Although observations had more fluctuations than the predictions, general oscillation could be followed by the simulations.

4.2 ANN Predictions

The different model predictions were used in a two-layer ANN model to get more correlated results with the observations. The first 70% of hourly March 1–11 results were inserted in the ANN as the training data. Then the remaining data were used as the test data. The predictions were attained hourly for the first 6 h. Table 6 shows the correlations and RMSE between predictions derived by using WRF/ARW simulations and observations. "1" refers to training and "2" refers to test data.

In order to make a comparison, six different WRF/ARW simulation results and ANN results using these simulations are indicated in Table 7.

Correlations between the observations and the forecasts used as the training data began to decrease at the third hour. Generated test data were more correlated to the observations when compared to the training data. Temporal variation of the correlation is noticeable in Table 5. For all WRF/ARW simulations, correlations of the first hour were very low, whereas the ANN correlations were considerably higher. The general view was that ANN increased the correlations substantially.

Table 4 RMSE results for 1–4 February

1–4 February RMSE (m/s)	WRF-1	WRF-2	WRF-3	WRF-4	WRF-5	WRF-6
D01						
Nearest neighbor	1.32	1.36	1.20	1.47	1.44	1.29
Weighted ave.	1.38	1.38	1.21	1.51	1.50	1.31
D02						
Nearest neighbor	1.16	1.17	1.09	1.20	1.17	1.12
Weighted ave.	1.35	1.38	1.20	1.44	1.39	1.27
D03						
Nearest neighbor	1.19	1.44	1.31	1.38	1.38	1.30
Weighted ave.	1.21	1.45	1.29	1.37	1.36	1.30

Table 5 RMSE results for 1–4 March

1–4 March RMSE (m/s)	WRF-1	WRF-2	WRF-3	WRF-4	WRF-5	WRF-6
D01						
Nearest neighbor	0.89	0.91	0.91	0.89	0.87	0.95
Weighted ave.	0.87	0.90	0.89	0.91	0.85	0.92
D02						
Nearest neighbor	0.70	0.71	0.80	0.86	0.70	0.87
Weighted ave.	0.78	0.89	0.84	0.86	0.70	0.83
D03						
Nearest neighbor	0.79	0.88	0.88	0.85	0.76	1.01
Weighted ave.	0.78	0.96	0.85	0.85	0.74	0.96

Table 6 ANN results

	1 h	2 h	3 h	4 h	5 h	6 h
Correlation 1	0.77	0.66	0.61	0.50	0.40	0.25
Correlation 2	0.58	0.61	0.60	0.65	0.57	0.57
RMSE 1	1.54	1.80	1.90	2.06	2.18	2.28
RMSE 2	2.23	2.17	2.34	2.29	2.46	3.05

5 Conclusions

WRF/ARW simulation results showed that inner domain results are closer to the observations than the other domains due to higher spatial resolution. In addition, the nearest neighbor downscaling method generally worked better than the weighted average method. When the wind speeds are higher than 12–13 m/s, model results were much more underestimated while comparing the rest. Because WRF/ARW is a mesoscale model, it was unable to predict the short-time variation of the winds in microscales and follow the general oscillation on time.

February results had less accuracy because of relatively high wind speed values when compared to March results. Predictions were accurate for the wind speeds less

Table 7 ANN results

	1 h	2 h	3 h	4 h	5 h	6 h
WRF-1						
Correlation	0.001	0.28	0.28	0.31	0.35	0.25
WRF-2						
Correlation	0.07	0.03	0.013	0.0008	0.22	0.44
WRF-3						
Correlation	0.013	0.17	0.19	0.25	0.21	0.17
WRF-4						
Correlation	0.016	0.18	0.24	0.28	0.25	0.23
WRF-5						
Correlation	0.046	0.011	0.001	0.034	0.039	0.06
WRF-6						
Correlation	0.02	0.27	0.29	0.35	0.34	0.22
YSA (training)						
Correlation	0.77	0.66	0.61	0.50	0.40	0.25
YSA (test)						
Correlation	0.58	0.61	0.60	0.65	0.57	0.57

than 10 m/s, especially in March results. On the contrary, the predictions were underestimated for the peak values in February.

Different parameterizations showed slightly different results. While WRF-3 and WRF-6 parameterizations had fewer errors in February predictions, WRF-1 and WRF-5 parameterizations were more successful than the others in March results.

Consequently, it was observed that different initial conditions, such as physics options or resolution, gave different results. If different scheme results are combined in ANN, much more accurate results can be obtained.

Acknowledgments This research was supported by The Scientific and Technological Research Council of Turkey (TUBITAK) 1007-KAMAG; MİLRES (National Wind Power System). We would like to acknowledge the support of TUBITAK who encouraged our research.

References

Aleksander, I.: Neural Computing Architectures: The Design of Brain-Like Machines. North Oxford Academic Publ, London (1989)

Aşkın, D., İskender, İ., Mamızadeh, A.: Farklı Yapay Sinir Ağları Yöntemlerini Kullanarak Kuru Tip Transformatör Sargısının Termal Analizi. Gazi Üniversitesi Mühendislik Mimarlık Fakültesi Dergisi Cilt. **26**(4), 9005–9913 (2011)

Gençoğlu, M.T.: Yenilenebilir Enerji Kaynaklarının Türkiye Açısından Önemi. Fırat Üniversitesi Fen ve Mühendislik Bilimleri Dergisi. **14**(2), 57–64 (2002)

Gershenson, C.: Artificial Neural Networks for Beginners, 9 pages. University of Sussex, Cognitive and computing sciences (2001)

Skamarock, W.C., Klemp, J.B., Dudhia, J., Gill, D.O., Barker, M., Duda, K.G., Huang, X.Y., Wang, W., Powers, J.G.: A description of the advanced research WRF version 3. NCAR/TN–

475+STR. National Center For Atmospheric Research Boulder Co Mesoscale and Microscale Meteorology Div (2008)
Url-1.: http://www.gwec.net/wp-content/uploads/2014/04/GWEC-Global-Wind-Report_9-April-2014.pdf . Retrieved time: 01.10.2014
Url-2.: http://www2.mmm.ucar.edu/wrf/users/docs/user_guide_V3/ARWUsersGuideV3.pdf. Retrieved time: 22.09.2014
Url-3.: http://www2.mmm.ucar.edu/wrf/users/wrfv3.5/Registry.EM_COMMON. Retrieved time: 22.09.2014

Technical and Economical Prefeasibility Study of a Solar Water Heating (SWH) System in an Apartment Building in Cape Town

Olugbeminiyi Idowu, Toluwalope Ige, Nicole Lacouve, Amin A. Mustafa, and Luis Rojas-Solorzano

1 Introduction

The centrally generated electrical power in South Africa consists of 92.6% coal-fuelled power—the aging coal-fuelled South African plants have the lowest operating efficiency in the world (de Groot and Sebitosi 2013). Moreover, water heating represents up to 48% of total electricity consumption in South African homes (Geldenhuys 1998). Although the country has a fairly high annual average solar irradiation levels of 5.4 kWh/m^2/day measured on a horizontal plane that could make solar energy recovery a favorable alternative (Boxwell 2015), only about 1% of households utilize solar water heaters (DME 2003). Rising electricity rates, capital investments in electricity production, and distribution, as well as needs to reduce CO_2 emissions, have all led the government to start promoting alternative, renewable energy solutions to meet growing energy demands (Donev et al. 2012).

Promoting solar water heating (SWH) has been at the forefront of this initiative, with significant grants being offered by Eskom, South Africa's public electricity utility. Between the years 2008 and 2011 alone, Eskom has incentivized 156,000 installations with its Solar Water Heating Rebate Programme and has partnered with the Department of Energy to reduce the demand on the public grid by 2300 GWh through the use of SWH (ESKOM 2012). The legislative capital of the country, Cape Town, has launched its own initiative in the form of the Residential

O. Idowu • T. Ige (✉) • N. Lacouve • A.A. Mustafa
Institut Mines-Télécom Atlantique, Department of Energy and Environment Systems, Nantes 44300, France
e-mail: olugbeminiyi@gmail.com; fetoige@yahoo.com; nicole.legenski@gmail.com; amin.moniem@gmail.com

L. Rojas-Solorzano
Nazarbayev University, Department of Mechanical Engineering, Astana 010000, Kazakhstan
e-mail: luis.rojas@nu.edu.kz

© Springer International Publishing AG, part of Springer Nature 2018

F. Aloui, I. Dincer (eds.), *Exergy for A Better Environment and Improved Sustainability 2*, Green Energy and Technology,
https://doi.org/10.1007/978-3-319-62575-1_47

Solar Water Heater Programme, which has encouraged residents through financial services and technical support to "invest to save" in SWH (City of Cape Town 2011). With temperatures in Cape Town ranging from 2 °C to 37 °C, an annual average of 17 °C (The Weather Channel LLC 2014), and an average of 2993 h of sunshine per year (Climatemps 2014), SWH is an attractive clean energy alternative to electric water heaters. According to a recent survey conducted by the City of Cape Town, nearly 70% of residents want a solar water heater (with energy cost savings cited as the primary reason), and half of the respondents replied that it is likely they would install one within the next 3 years (City of Cape Town and Du Toit 2013).

Given that energy cost savings are an important motivating factor for consumers who plan to install a solar water heating system (SWHS), economic feasibility studies of these types of systems could be useful decision-making tools. However, accurately predicting the long-term profitability of such investments is difficult due to the project's dependence on multiple external factors and thus requires the use of a robust scientific model and careful precision of climatic and economic parameters to achieve an accurate result. Therefore, the purpose of this study is to perform a prefeasibility study of a possible SWHS in the Cape Town area and to evaluate the sensitivity of various parameters to the long-term ability of the project to produce energy cost savings. In this study, the technical and economic prefeasibility of installing a collective domestic SWH system in an apartment building is evaluated using the RETScreen Clean Energy Project Analysis Software, an advanced model equipped to analyze feasibility and energy performance of clean energy projects. A prefeasibility study of this nature is not currently available for South Africa in the literature, although there are similar types of feasibility studies for other locations throughout the world including Taiwan (Lin et al. 2015), Morocco (Allouhi et al. 2015), Jordan (Kablam 2004), Oman (Gastli and Charabi 2011), and Serbia (Stevanovic and Pucar 2012).

In this project, the RETScreen software was used to perform energy and economic feasibility analyses on a glazed flat-plate SWHS with an electrical coil for auxiliary heating. The SWHS is designed for a new flat roof apartment building with nine domicile units, located approximately 20 km southeast of the city center and near the Cape Town International Airport. Hardware coefficients of performance are obtained for SWH units that are available for purchase in the Cape Town region, and pricing for these units and installations are provided by actual suppliers servicing the region.

The results of interest from this study include energy produced by the SWHS, energy costs avoided by using the SWHS, greenhouse gas (GHG) emissions avoided by using the SWHS, net present value (NPV), and internal rate of return (IRR) of the investment, as well as sensitivity of these results to parameters of the project such as changing electricity costs, loan interest rates, or government subsidy amount.

Nomenclature

SWH	Solar water heating
SWHS	Solar water heating system
NPV	Net present value
IRR	Rate of return
GHG	Greenhouse gas
f	Solar fraction
F_R ($\tau\alpha$)	Collector heat removal factor
$F_R U_L$	Collector heat loss coefficient [W/(m^2 K)]
H_T	Monthly average daily radiation incident on the collector plane
T_a	Monthly average ambient temperature
T_w	Hot water temperature
T_m	Monthly average water supply temperature
C_a	Actual storage capacity
C_s	Standard storage capacity

2 Literature Review

The presence of similar feasibility studies for SWHS in the literature can be noted as early as 2002, when Kablam (2004) performed a technoeconomic analysis for a SWHS in Jordan. In this study, a model was developed to determine the economic feasibility of a SWHS with an electric coil as an auxiliary fuel as compared to the base case of a conventional gas-powered water heater. It was determined that the SWHS remained economically preferable if the auxiliary electric coil was used for less than 120 days out of the year.

A study that is very similar in goal and scope to the current project was done by Gastli and Charabi (2011), who performed a full RETScreen analysis on a SWHS in Oman. In this study, the SWHS was compared to the base case of a conventional electric-powered water heater. The project for a four-person household was assumed to be financed 50% by government subsidies and 50% by the household. The pre-tax IRR for assets was calculated to be 12.2%, and the equity payback period was found to be 8.5 years. In addition, the net annual GHG emission was reduced by 3.6 tCO_2 equivalents.

There is also another study based on RETScreen aimed at determining the financial feasibility of a SWHS in Serbia (Stevanovic and Pucar 2012). This study performed a RETScreen analysis in six Serbian cities for a SHWS for a household of four people. For a government subsidy of 50% of initial costs, equity payback period ranged from 4.7 to 6 years depending on the location. In addition, this study also made a financial analysis to determine the most appropriate level of government subsidies for the project.

3 SWHS Prefeasibility Study in Cape Town

3.1 SWHS Design

The purpose of this project is to determine the feasibility of a typical SHWS in the Cape Town area. Since South Africa's public utility ESKOM has implemented grants of 40% of initial costs, it is in the public interest to demonstrate that these types of projects can be profitable and to determine financial indicators, such as equity payback period, IRR, and NPV. These results are here calculated using the support tool RETScreen, which comprises several types of analyses: energy model, GHG emission, reduction, cost, financial, and risk analyses.

In order to accomplish these objectives, it is necessary to design a SWHS with components that can be obtained in the region. For this project, a SWHS is conceived for the collective water heating of an apartment building. The area chosen for the placement of this system is near the Cape Town International Airport, as shown in Fig. 1. This location was chosen due to the abundance of meteorological solar irradiance data available for this area. Table 1, shows meteorological data for this area used by the model.

The apartment building is chosen to be a new flat-roofed structure with adequate space to accommodate the SWHS collectors and storage tanks. The SHWS comprises 20 glazed flat-plate solar panels, each with a gross area of 2.14 m^2, a 150-L storage tank, and a thermosyphon passive heat exchanger from the Jiangsu Sunrain Solar Energy Company. A thermosyphon heat exchanger uses the natural

Fig. 1 Geographic location of SWH project (Google Earth 2015)

Table 1 Meteorological data for Cape Town project area provided by RETScreen

Month	Air temperature	Relative humidity	Daily solar radiation – horizontal	Heatingdegree-days
	°C	%	KWh/m^2/d	°C-d
January	20.4	68.0	7.72	0
February	20.4	69.9	7.05	0
March	19.2	72.6	5.86	0
April	16.9	76.6	4.17	33
May	14.4	79.6	2.97	112
June	12.5	79.9	2.45	165
July	11.9	78.9	2.62	189
August	12.4	78.6	3.40	174
September	13.7	76.6	4.75	129
October	15.6	71.6	6.09	74
November	17.9	68.9	7.48	3
December	19.5	68.4	7.85	0
Annual	16.2	74.2	5.19	879

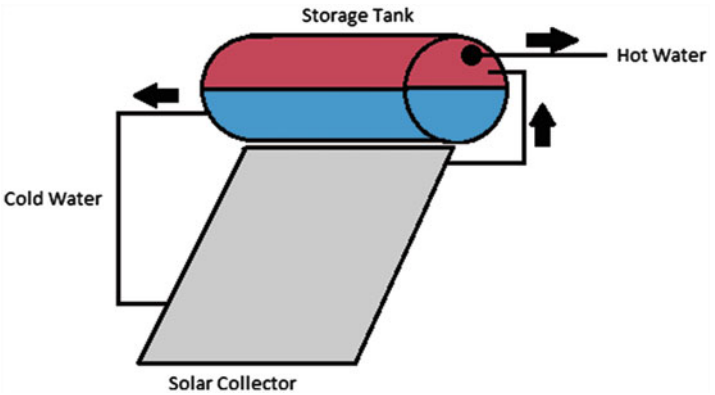

Fig. 2 Thermosyphon passive heat exchange, glazed flat-plate SWH

circulation of warm and cool water to direct flow through the solar collector and to the hot water output of the unit. Figure 2 shows the general principle of such a unit. The apartment building has nine domicile units, with four occupants each. It is assumed that each household member consumes an estimated 60 L of hot water per day (Donev et al. 2012).

An important parameter in the feasibility of a SWHS project is the electricity rate. South Africa has historically had low electricity tariffs due to abundance of coal reserves, consistent government subsidies, and centralized control of both coal supply and electricity production (de Groot and Sebitosi 2013). The electricity tariffs for domestic households of the City of Cape Town are indicated in Table 3.

3.2 Energy Model

The RETScreen energy model calculates the solar fraction f in order to determine the amount of energy produced by the SWHS. The solar fraction refers to the amount of heating demand that is met by the SWHS. The solar fraction is calculated in the following manner (Stevanovic and Pucar 2012):

$$f = 1.029Y - 0.065X - 0.245Y^2 + 0.0018X^2 + 0.0215Y^3 \tag{1}$$

where X and Y are determined as follows:

$$X = \frac{A_C F_R U_L (T_{ref} - T_a)}{L}^* \left(\frac{C_a}{C_s}\right)^{-0.25*} \frac{(11.6 + 1.18T_w + 3.86T_m - 2.32T_a)}{(T_{ref} - T_a)}$$
$$Y = \frac{A_C F_R (\tau\alpha) H_T N}{L} \tag{2}$$

where T_{ref} is 100 ° C, L is the total monthly heating load, C_a is actual storage capacity, C_s is standard storage capacity, N is the number of days in the month, A_c is the collector area in m^2, F_R $(\tau\alpha)$ is the collector heat removal factor, $F_R U_L$ is the collector heat loss coefficient in Wm^{-2} K^{-1}, H_T is the monthly average daily radiation incident on the collector plane, T_a is the monthly average ambient temperature, T_w is the hot water temperature, and T_m is the monthly average water supply temperature.

Table 2 gives the necessary input parameters used for this SWHS.

Table 2 Parameters used in energy model of SWHS

Parameter	Value	Unit
Number of units	9	
Occupancy rate	100	%
Daily hot water use	2160	L/d
Temperature of heated water	60	°C
Operating days per week	7	
Slope of collectors	30	Degrees
Aperture area per solar collector	1.86	m^2
Gross area per solar collector	2.14	m^2
Fr (tau alpha) coefficient	0.67	
FrUL coefficient	4.62	$W/m^2/°C$
Number of collectors	20	
Storage capacity/solar collector area	70	L/m^2
Electricity rate	0.11	€/kWh

Table 3 Residential electricity pricing in 2014/2015

Units received (kWh/month)		Tariff (cents/kWh)	
		Rand	Euros
Lifeline (<450)			
First 50 kWh		Free	
Block 1	0–350	96.12	7.1
Block 2	350–450	233.30	17.3
Domestic (> 450)			
Block 1	0–600	153.63	11.4
Block 2	600+	186.81	13.8

City of Cape Town (2014a, b)

3.3 Electricity Pricing

In studying this feasibility for SWHS, electric heaters are considered as the base case with the cost of electricity being the fuel in comparison with the cost of solar radiation that is free. Electricity tariff in Cape Town is set by the City of Cape Town Electricity Services, with different prices being set depending on the expected consumption of the residence (City of Cape Town 2014a, b). Table 3 shows the residential electricity pricing in place; however, the tariff used in modeling this case is that for a monthly consumption of 0–600 kWh as set in July 2014. This is after taking into account the consumption needs of the apartment model, especially regarding hot water consumption of 240 L/day. When using a rate of 5.1 kWh/100 L to increase water temperature from 16 to 60 °C (Thomson 2013), energy use for water heating could be up to 367 kWh/month. According to a survey by the (City of Cape Town and Du Toit 2013), electric water heater accounts for 30–50% of the domestic electricity bill of a household in Cape Town. Furthermore, this same survey presents that each household spends on average R764.66 (537 kWh) on electricity monthly.

According to the electricity services board of the city, the tariff is expected to increase by 9.92% in 2015 and 9.26% in 2016 (Rencontre 2013). However, although future tariff changes are expected to occur in a manner that cannot be readily modeled for the lifetime of the project, an escalation rate of 10.0% is factored in by assuming that the annual increase in electricity price during the lifetime of the project will remain at about the same rate for the 2015 and 2016 projections. Additionally, a trend analysis of the rate of price increase from 2006 to 2014 was made to define a cap of 15.34% while evaluating the sensitivity of the project to electricity price escalation.

3.4 System Cost

The selection of the system and its cost plays a fundamental role in the feasibility of the project. In defining the cost of the selected system, estimates were obtained

Table 4 Cost estimates for the selected SWHS

Item	Cost	
	Rand	Euros
Feasibility study	8605	559
SWHS (×20)	249,517	18,464
Engineering and Installation	146,356	10,830
Training and Commissioning	770	50
Unskilled Labor	847	55
Total	406,096	29,958

1 rand = 0:074 euros; Costs are inclusive of 14% VAT

from a Chinese supplier, two Eskom-approved suppliers in Cape Town, and an agent with the SWH division of Sustainable Energy Society of Southern Africa (SESSA). However, the estimate presented by one of the suppliers in Cape Town was used since they provided a breakdown of the individual components in the overall cost, as detailed in Table 4. Furthermore, the difference in the cost estimates from these four sources was small, and a contingency of 10% was factored into calculations. Apart from the system cost, it was also important to factor in the installation and maintenance costs as well as the costs of auxiliary systems such as pipes and pumps.

3.5 Financing

As with most clean energy projects, the initial costs are often a barrier. According to a market research conducted by the City of Cape Town in 2013, 67.9% of respondents are desirous of SWHs; however, the SWH unit installation and upfront costs are given as the main hindrances to installing one. Duly noting that 67.2% of interviewed persons consider upfront cost as a major drawback (City of Cape Town and Du Toit 2013), in coping with this, Eskom offers a SWH rebate program to cover the initial costs. This rebate is about 40% of the cost of the solar collector unit and ranges from €243 to €663 (R3280 to R8964) for each unit installed that meets certain specified conditions. The calculation of the exact amount depends on the type of system installed (ESKOM 2012). The system considered for this study meets the criteria for benefiting from the rebate and is estimated as €7640 (€382 per unit).

However, considering that 54.2% of persons will be motivated to obtain a system only if there are no upfront costs and that 62.5% would like to pay less than €148 (R2000) for the initial cost of the system (City of Cape Town and Du Toit 2013), financial calculations of the viability of the project are made with the assumption that the remainder of costs not covered by the rebate is taken as a bank loan to be paid over a 5-year term. The complete financial parameters for the project are specified in Table 5.

Table 5 Financial parameters for the feasibility study simulation

Financial parameter	Value	Unit
Inflation rate[a]	5.3	%
Fuel escalation rate[b]	10.0	%
Debt ratio	60.0	%
Discount rate	9.0	%
Debt term	5	Years
Debt interest rate[c]	11.0	%
System lifetime	25	Years
Government rebate for 20 units[d]	7640	€

[a]Triami Media BV (2014)
[b]Rencontre (2013)
[c]Trading Economics (2014)
[d]City of Cape Town (2011)

4 Results and Discussions

Following the simulation of these design parameters as described in the preceding sections using RETScreen, the results obtained are as follows.

4.1 Energy Savings

The designed SWHS provided 17 MWh of heating per year, which is equivalent to a solar fraction of 42%. The use of the system resulted in an electricity consumption of 23.3 MWh, compared to the base case consumption of 40.3 MWh. This represents an electricity savings of 17 MWh per annum, which is equivalent to €1934.

4.2 Emissions Reduction

The amount of emissions (normalized to tons of CO_2) estimated from the use of the SWHS is 24 tCO_2 equivalents, while with the use of electricity for water heating, it was 41.5 tCO_2 equivalents. This results in a saving of 17.5 tCO_2 equivalents, which is equivalent to 3.2 cars taken off the road in a year.

4.3 Financial Analysis

The results obtained from the simulation of the financial parameters for an investment in the SWHS taking into consideration the present situation in South Africa and the projections described above in the Financial discussion section (and Table 5

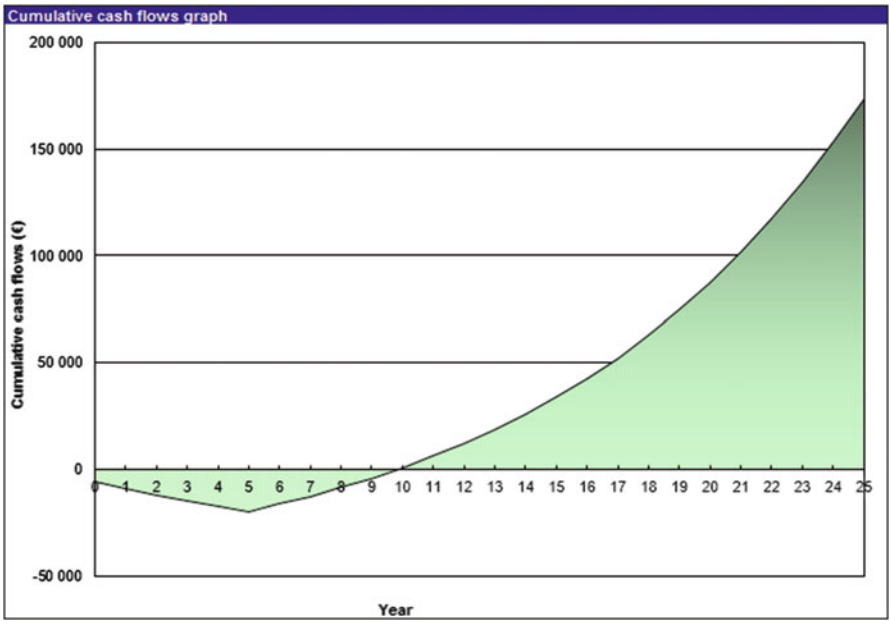

Fig. 3 RETScreen cumulative cash flow graph

above) show that the net present value (NPV) on the investment is €27,028 with an internal rate of return (IRR) of 17.3% and an equity payback time of 9.9 years. The benefit–cost ratio of the investment is 3.05. Figure 3 below shows the progression of the cumulative cash flow from the investment over time.

With all the parameters employed for this simulation, it can be seen that the parameter with the highest influence on the profitability of this investment is the cost of the electricity, as seen from the relative impact graph shown in Fig. 4, based on a Monte Carlo analysis of 500 combinations of possible scenarios with an uncertainty of 10%.

From the relative impact shown in Fig. 4, it can be seen that the cost of fuel (which is the local cost of electricity) has a high impact on the viability of this project. This parameter was analyzed by seeing how the variation of the escalation rate of electricity will affect the NPV, the payback time, and the IRR. Table 6 shows how these values vary with the different escalation rates of electricity.

Another important parameter is the availability of rebate. Presently, the rebate is 40% of the cost of the equipment, which amounts to €7386. Figure 5 shows the effect a reduction or removal of this rebate will have on the after-tax IRR of the investment. The removal of the rebate will give an after-tax IRR of 13.7%, a payback period of 11.2 years, an NPV of €19,642, and a benefit–cost ratio of 2.49.

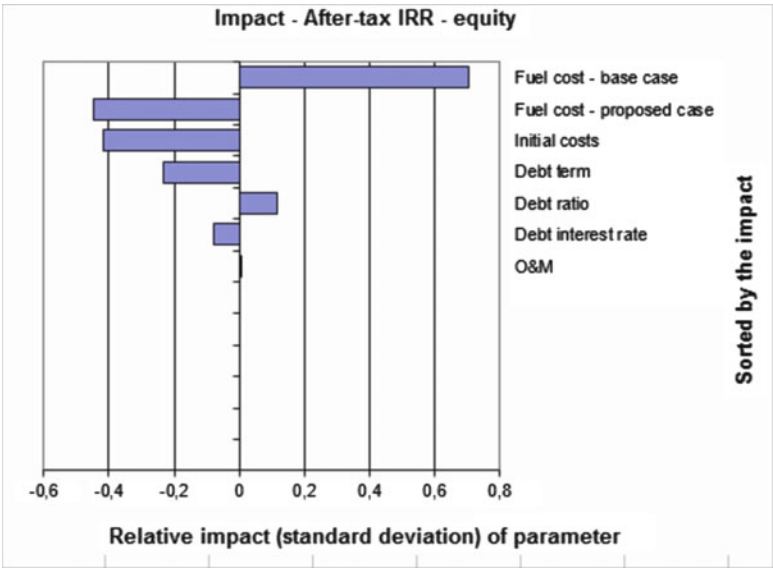

Fig. 4 RETScreen tornado diagram of sensitivity analysis on after-tax IRR

Table 6 Effects of changes in fuel escalation rates on financial returns

Fuel escalation rate	After-tax IRR asset (%)	Benefit–cost ratio	Equity payback (years)	NPV (€)
5.0	10.5	1.25	12.3	3,294
7.5	13.9	1.99	10.9	13,046
10.0	17.3	3.05	9.9	27,028
12.5	20.7	4.59	9.1	47,292
15.0	24.2	6.85	8.4	76,909

5 Conclusions

With 42% of energy savings and a matching percentage in emissions reduction, it is very reasonable to say that the justification behind the technical benefits of SWH have been validated in the case of an apartment building similar to the one defined in this work in the City of Cape Town, South Africa.

The designed SWHS yielded a yearly 17 MWh in energy savings, 17.5 tCO_2 equivalents emissions reduction, along with a net present value (NPV) on the investment of €27,028, with an internal rate of return (IRR) of 17.3%, and an equity payback period of 9.9 years.

Nevertheless, the current ESKOM rebate scheme plays a pivotal role in the attractiveness of investments in such SWH systems. The 40% rebate scheme

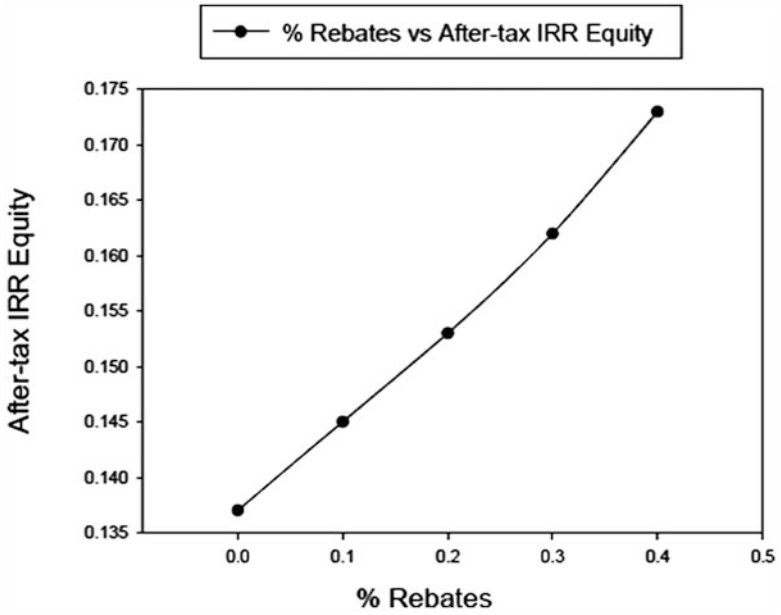

Fig. 5 After-tax IRR vs. rebates sensitivity analysis

(on initial investment) is responsible for a 1.3-year reduction of the payback period and a 5% reduction in the after-tax IRR.

Although the rebate scheme was significant as 67% of the residents of Cape Town indicated concerns regarding the initial investment, the outcomes of the study highlight a greater financial sensitivity to the fuel escalation rate. Generally, the application and adoption of SWHS in Cape Town has yielded positive overall outcomes.

Acknowledgments The team wishes to acknowledge and thank the Sustainable Energy Society of Southern Africa (SESSA), Prof. Bernard Bourges, and Prof. Luiz Crespo for their contributions toward the successful finalization of this study. Additionally, the team would also like to extend its sincere appreciation to the EU's Education, Audiovisual and Culture Executive Agency (EACEA), specifically the Erasmus Mundus program for making the project possible.

References

Allouhi, A., Jamil, A., Kousksou, T., El Rhafiki, T., Mourad, Y., Zeraouli, Y.: Solar domestic heating water systems in Morocco: an energy analysis. Energy Conv. Manag. **92**, 105–113 (2015)

Boxwell, M.: Solar irradiance. Retrieved January 20, 2015 from Solar Electricity Handbook.: http://solarelectricityhandbook.com/solar-irradiance.html (2015)

City of Cape Town.: Residential Electricity Tariffs Explanation (2014a)

City of Cape Town.: Smart Living Handbook: Making Sustainable Living a Reality in Cape Town homes. Cape Town (2011)
City of Cape Town.: Solar Water Heaters: Why get a Solar Water Heater? Retrieved November 2014 10, 2014 from Saving Electricity: http://savingelectricity.org.za/pages/water_heaters.php (2014b)
City of Cape Town, Du Toit, J.: Final Report: Market Research – Prospective Solar Water Heater / Heat Pump Market in the Cape Town Metropole. Sheryl Ozinsky Consulting, Cape Town (2013)
Climatemps.: Cape Town Climate and Temperature. Retrieved November 10, 2014 from Climatemps: http://www.cape-town.climatemps.com/ (2014)
de Groot, R.V.G.,.v.d., Sebitosi, A.: Comparing solar PV (photovoltaic) with coal-fired electricity production in the centralized network of South Africa. Energy. **55**, 823–837 (2013)
DME: White Paper for the Promotion of Renewable Energies and Clean Development. Department of Minerals and Energy, Pretoria (2003)
Donev, G., van Stark, W., Blok, K., Dintchev, O.: Solar water heating potential in South Africa in dynamic energy market conditions. Renew. Sust. Energy Rev. **16**, 3002–3013 (2012)
ESKOM.: COP17 fact sheet: Solar Water Heating Rebate Programme. Retrieved November 10, 2014 from http://www.eskom.co.za/AboutElectricity/FactsFigures/Documents/The_Solar_Water_Heating_SWH_Programme.pdf (2012)
Gastli, A., Charabi, Y.: Solar water heating initiative in Oman energy saving and carbon credits. Renew. Sust. Energy Rev. **15**, 1851–1856 (2011)
Geldenhuys, A.: ESKOM Domestic Load Research (1998)
Google Earth.: Retrieved 2015 from Google Earth: earth.google.com (2015)
Kablam, M.: Techno-economic analysis of the Jordanian solar water heating system. Energy. **29**, 1069–1079 (2004)
Lin, W., Chang, K., Chung., K.M.: Payback period for residential solar water heaters in Taiwan. Renew. Sust. Energy Rev. **41**, 901–906 (2015)
Rencontre, L.: Presentation to NERSA. City of Cape Town Electricity Services. City of Cape Town, Cape Town (2013)
Stevanovic, S., Pucar, M.: Financial measure Serbia should offer for solar water heating systems. Energy Build. **54**, 519–526 (2012)
The Weather Channel LLC.: Weather History for Cape Town, South Africa. Retrieved November 10, 2014 from Weather Underground.: http://www.wunderground.com/history/airport/FACT (2014)
Thomson, R.: Measuring residential electricity savings in South Africa after solar or heat pump installations – a simple, reliable method. Retrieved January 10, 2015 from Environment News South Africa.: http://www.environment.co.za/environmental-issues-news/measuring-residential-electricity-savings-in-south-africa-after-solar-or-heat-pump-installations-a-simple-reliable-method.html (2013)
Trading Economics.: South Africa Prime Overdraft Rate. Retrieved 2014 йил November from Trading Economics.: http://www.tradingeconomics.com/south-africa/bank-lending-rate (2014)
Triami Media BV.: Historic Inflation South Africa – CPI Inflation. From Worldwide Inflation Data: http://inflation.eu/ (2014)

Use of Straw Bundles in Buildings for a Lower Environmental Footprint of Insulated Systems

Jean-Luc Menet

1 Introduction

Population on earth is supposed to reach around ten billion people in 2050 (O'Neill et al. 2010). Consequently, building market is an industrial sector in permanent development all around the world because of two major necessities:

- More people mean more houses and buildings.
- Environmental impacts must be reduced.

This second point should lead companies to use high-performance materials, to reduce energy consumptions on the whole life of the buildings, and to limit raw materials quantities that are employed to ensure the required technical performances.

Among the objectives aimed by environmental politics and regulations all over the world, the *passive buildings* seem to be an appropriate solution permitting a decrease or at least a stabilization of climate change indicators in order to limit the greenhouse effect. To reach this goal, buildings must be correctly insulated; it is the reason why, regardless of the country, thermal regulations are developed and require high insulating performances of houses and buildings.

The regulation relative to the building's envelope performance greatly varies from one country to the other. Besides, the building systems must be adapted to each specific decision or to the design context. For example, in France, a recent thermal regulation imposes for every new construction a given insulating performance depending on the region as shown in the RT 2012 regulation (2012).

J.-L. Menet (✉)
ENSIAME, Université de Valenciennes et du Hainaut-Cambrésis,
Le Mont Houy –, 59313 Valenciennes Cedex, France
e-mail: jean-luc.menet@univ-valenciennes.fr

© Springer International Publishing AG, part of Springer Nature 2018

F. Aloui, I. Dincer (eds.), *Exergy for A Better Environment and Improved Sustainability 2*, Green Energy and Technology,
https://doi.org/10.1007/978-3-319-62575-1_48

But another problem appears: if a correct insulating system should save energy for heating and air conditioning, the real question is to evaluate its contribution to the total energy consumption, i.e., on the whole life of the buildings. Indeed, the more the buildings are isolated, the less the energy consumption will be; then the choice of the materials becomes preponderant. Consequently, in building projects a "life cycle thinking" should be systematically conducted.

More precisely, considering the energy consumption, if a conventional insulating material, such as glass wool or rock wool, is used, it is interesting to analyze if the total energy consumption "contained" in the product, namely, the *grey energy*, is not greater than the one which could be saved by using this material in the building during all its life. The *grey energy* is the energy used during the different steps of the life of the product: the extraction of the raw materials, the fabrication, the distribution, and the transportation of the different elements used for the product, and the end of life (e.g., incineration). Consequently, a study dealing with energy consumption of buildings must consider the different steps of the life cycle.

Regarding the energy consumption, this question has been studied by different authors, and fortunately the use of insulating material generally seems to be beneficial for the environment (Schmidt et al. 2004). Some of these results are available on www.inies.fr.

Now, let us presume that the indicator which should be considered is not the energy consumption but the *Non-Renewable Energy Consumption* (NREC), because it creates greenhouse effect.

Moreover, considering insulating materials, this question must be answered not only considering the energy consumption or the greenhouse gases emissions but also using different other environmental indicators. This is mainly due to the fact that the reduction of one environmental impact could lead to an increase of another; this phenomenon is called the *pollution displacement*.

But an insulating material is rarely used alone; it is generally associated to other products constituting the final element. Then, to study the environmental impact of insulating systems, it is necessary to evaluate the contribution of the different elements, i.e., the whole wall.

In other words, to evaluate the environmental effect of an insulating system, the recommended methodology must be:

- A multistep study, which is conducted on the whole life cycle of the system
- A multicriteria analysis considering few environmental impacts
- A multielement consideration

Such a methodology does exist; it is called the Life Cycle Assessment (LCA), which is described in the international standards ISO 14040 (2006) and ISO 14044 (2006).

Conventional insulating materials have been studied separately using the LCA methodology (Schmidt et al. 2004; inies.fr n.d.), i.e., independent of the existence of the wall. This can be useful for the choice of environmentally friendly materials for a given wall. This approach can be at the same time pertinent and sufficient if

only the insulating materials have to be chosen, which is generally the case when building conventional walls. But if another insulating material, such straw bundles is used, all the wall must probably be adapted and a specific study is necessary, which must includes all the elements constituting the wall.

On the other side, different authors have studied the environmental impacts of wall assemblies (Frenette et al. 2010) to evaluate few environmental impacts, for example, the global climate change indicator. But in such studies, to the authors' knowledge, natural materials, such as straw bundles, are generally not considered. Besides, comparative studies are very rare, while a pertinent choice should be made using comparisons.

Now, our question is to know if natural materials, such as the straw bundles, are better for the environment than the conventional ones, e.g., rock wool or glass wool with common breeze blocks. The LCA methodology permits this comparison and the analysis of keys parameters. This paper, following other studies on this theme (Menet and Gruescu 2013; Menet 2014), tries to answer this question; it deals with an LCA study on different insulating exterior walls in order to evaluate the environmental interest of the use of natural insulating materials, such as straw bundles, for buildings..

2 Use of Straw Bundles in Buildings

2.1 Building with Straw

Building using natural materials is not a new concept. On the contrary, it has been used for centuries all over the world and is always used here or there nowadays.

Compressed straw coming from wheat cultivation is a high-performance thermal and phonic material. It is said to regulate the humidity in the different rooms of buildings. It has a remarkable fire behavior.

Many papers have been published dealing with straw buildings (see, e.g., Minke and Mahlke 2005; King 2006; Ashour et al. 2011a, b; Chaussinand et al. 2015). It is attested that straw bundles can be used either for insulating systems or for the structural elements.

The first use of straw bundles for "modern" houses has been identified in Nebraska, United States (Marks 2005). This house was built in 1896 and still stands. This information will be useful for estimating the life duration of such a construction.

2.2 Physical Properties of Straw Bundles

Straw is the stalk of grasses, such as the wheat. It is generally conditioned as bales or bundles.

Table 1 Dimensions of the considered straw bundles

Length (cm)	100
Width (cm)	35
Height (cm)	50

Table 2 Main properties of compressed straw

Thermal conductivity (W/mK)	$0.06 < \lambda < 0.075$[a]
Thermal resistance (m^2.K/W)	$5 < R < 7$
Fire behavior (class)	M1[b]
Humidity potential storage (% of mass)	30
Acoustic absorption (dBA)	$48 < a < 57.3$
Water vapor diffusion	$1 < \mu < 2$

[a]In the following the mean value of λ has been chosen, i.e., $\lambda = 0.0675$ W/mK
[b]France

As it will be explained in the following, straw is so plentiful in the considered country (France) that it can be considered as a waste.

Straw buildings use straw bundles, which have the following dimensions (Table 1).

Let us write that these quantities can be exchanged according to the building choices. For example, either the width or the height of the bundle can constitute the wall thickness.

The previous data conduct to a mass of about 17.5 kg for each bundle. Two bundles are necessary to build a square meter of wall of 35 cm thickness.

The physical properties of straw bundles are well known. They are listed in Table 2. Let us notice that the fire behavior is M1, i.e., the material is incombustible (stones are classified as M0, absolutely incombustible; mineral wools are classified as M1).

A particular attention is needed; particularly, the presence of pests or rodents, and also the moisture resistance must be considered. These problems that have been integrated in the building procedures are widely studied (Goodhew et al. 2004).

2.3 Procedures, Regulation, and Building Modes

Professional procedures and regulations have been developed in 2012 in France (Floissac 2012). In France, these procedures, namely, CP2012, indicate four requirements to be met:

- Respect for the regulation (required technical specifications)
- Qualified material relative to the considered use
- Respect for the design and implementation rules
- Staff trained to the building mode

Such requirements exist in different countries. France has been chosen because the present study is supposed to be applied to a wall built in France.

There are many ways to use straw for building. Bales or straw can be used. In this paper, the chosen technique was proposed by the GREB (*Groupe de Recherches Ecologiques de la Batture* – http://www.greb.ca) born in Canada, where the climate leaves no place to mediocre quality houses. The wall system is composed of the following elements (see Fig. 2): the wood (brackets and beams) used for the load-bearing structure, the straw bundles, the nails or screws, and the mortar.

The needed quantities of these elements have been established by Menet 2014 and have been partially adapted for this study (see below): 30 straw bundles; 4 beams, 5 m long and 16 beams, 3 m long; 40 brackets, 35 cm long; about $1m^3$ mortar; 240 nails or screws; and 273 m string for the straw bundles. Only the exterior side of the wall assembly is considered, because the interior side generally depends on the consumer.

3 The Life Cycle Assessment Methodology

The Life Cycle Assessment (LCA) methodology leads to the quantification of the environmental footprint for goods, services, and processes, called *products* in the following. One of the attended objectives is to identify some main points allowing to do design choices permitting the diminution of the environmental impacts concerning the different life cycle steps. This approach is also called *life cycle analysis*, *ecobalance*, or *cradle-to-grave analysis*.

A Life Cycle Assessment is the investigation and valuation of the potential environmental impacts of a given product. It is a variant of an input-output analysis, but it focuses on physical rather than monetary flows. LCA is both a multicriteria and a multistep study, and it has the particularity of being "goal dependent"; this means that the goal and scope definition of the study are not only important, but they can be "redefined" during the entire study if necessary. In the same way, every phase of an LCA (see Fig. 1) is linked with at least two others.

A framework for LCA has been standardized in the ISO 14040-44 series by the International Organization for Standardization (ISO). As shown in Fig. 1, it consists of the following phases:

- *Goal and scope definition*. This phase defines the goal and the intended use of the LCA; it scopes to clarify the system boundaries, the function and the considered flows, the required data quality, and the technology and assessment parameters.
- *Life Cycle Inventory (LCI)*. This "activity" consists of collecting data on inputs (resources, such as the energy or the raw materials consumptions, and intermediate products) and outputs (emissions, wastes) for all the processes in the considered product system.
- *Life Cycle Impact Assessment (LCIA)*. It is the phase of the LCA where inventory data on inputs and outputs are translated into indicators about the product

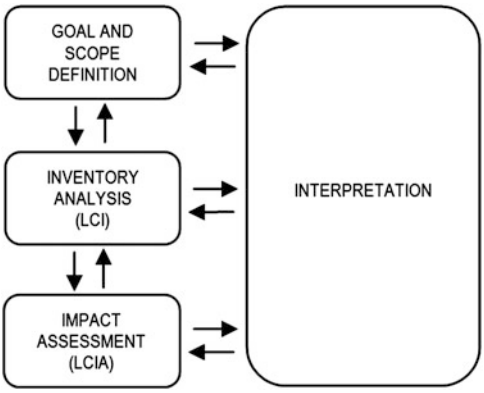

Fig. 1 Scheme of the LCA methodology

system's potential impacts on the environment, on human health, and on the availability of natural resources.

- *Interpretation*. This is the crucial phase where the results of the LCI and the LCIA are interpreted according to the goal of the study and where sensitivity and uncertainty analysis can also be performed to qualify the results and the conclusions. This phase permits the analysis of the results relative to the abovementioned first phase.

Some of these phases are divided into several steps, particularly the first phase of the methodology (goal and scope definition) which must be made very precisely.

In particular, the LCA methodology needs to precisely define a functional unit, which permits to compare one system with another.

These characteristics of the studied wall are described in Sect. 4.1.

In this paper, the study takes into account the following five classical steps of the life of a product:

- Manufacturing
- Distribution
- Installation
- Use
- End of life

4 Results and Discussion According to the LCA Methodology

In the following, the LCA methodology is applied to evaluate the potential environmental impacts of a wall made of straw bundles.

4.1 Goal and Scope Definition

In the following, the customers are defined, the main objective is described, the function and the functional unit are clarified, the keys parameters are highlighted, and the system boundaries are fixed.

The study is intended for every person (private person or builder) expecting to insulate a building or a house using straw bundles.

Insulations made from straw bundles are supposed to be ecological. The main objective of this study is to quantify the environmental impacts of these building modes on a given wall and to compare them to the ones obtained on a conventional wall made of breeze blocks and glass wool. The studied "straw wall" is made of wood structure and has a 15 m^2 area (3 m high and 5 m long).

According to the LCA methodology, the function of the products must be correctly and precisely defined. Concerning insulation, it is supposed to reach at least a thermal resistance of 5 m^2.K/W, which corresponds to the thermal resistance of a straw bundle. The use of additive wood panels will increase this thermal resistance, so that it is higher than the recommended value of 4 m^2.K/W for an insulated wall according to the RT2012 regulation.

The chosen functional unit is to build an exterior wall assembly of 15 m^2 which has the following characteristics:

- The technical building objectives are reached.
- The thermal resistance of the final assembly is at least 5 m^2.K/W (which corresponds to the thermal resistance of a straw bundle).
- The lifetime of the assembly is 100 years.

This last consideration is validated by the real lifetime of the first straw houses, and this corresponds to the mean rate of renewal of the house park which is around 1% in France.

Concerning the end of life phase, the conventional wall is landfill (dumped waste). The straw wall is treated as follows:

- The concrete is landfill (dumped waste).
- The wooden panels, the wooden structure, and the wooden brackets are incinerated with an energetic valorization.
- The straw bundles are recycled (applied in the neighborhood).

The key parameters are the straw thicknesses leading to the wished thermal resistance, as well as the life expectancy of the various materials. The thicknesses are easily determined from the thermal conductivity of both types of insulating materials. Straw reaches 100 years without any problem if correctly implemented. Concerning the structure, it will be necessary to choose a wood which can resist 100 years.

Concerning the boundaries of the study, let us remind that only the exterior side of the wall assembly is designed because a comparative study is projected.

The final casing of the exterior is not taken into account, just as the inside casing (e.g., plaster plates and painting). The LCA of the different machines used to cultivate the cereals (for straw) are not considered in this study, because the straw is in fact considered as a waste of the cultivation. Tools (saws, hammers, screwdrivers, etc.) and natural resources (e.g., water) used for the building have not been taken into account. The different elements constituting the "straw wall" are presented in Sect. 4.2.

The different steps and elements of the considered products must be determined precisely. This phase of the LCA methodology must be made very carefully. Some hypothesis can be made, for example, by neglecting some of the life cycle steps or some of the evaluated impacts.

4.2 Life Cycle Inventory (LCI)

The LCI must precisely take into account the different elements constituting the life cycle of the wall, for example, the location of the manufacturing or distribution (*life cycle tree*). These elements are not provided in this paper; let us notice that the straw bundles are made near the wall installation and that every manufacturing or distribution has been located in the neighborhood. The main information concerning the conventional wall and the "straw wall" is respectively reported in Tables 3 and 4.

The previous tables are linked with the considered walls represented in Figs. 2 (conventional wall) and 3 ("straw wall").

The data corresponding to the LCI are associated to the following five steps of the LCA methodology:

Table 3 Main information for the material constituting the conventional wall (reference)

Materials	Quantity	Mass (kg)	Life duration	Number of use	kms
Breeze blocks	99	1500	100 y	1	75
Mortar	x	1300	100 y	1	21
Glass wool	4	52	50 y	2	550

Table 4 Main information for the material constituting the "straw wall"

Materials	Quantity	Mass (kg)	Life duration	Number of use	kms
Wooden panels	7	160	100 y	1	65
Straw bundles	30	525	100 y	1	3
Concrete	X	700	100 y	1	21
Wooden structure	X	135	100 y	1	160
Wooden brackets	40	7	100 y	1	6

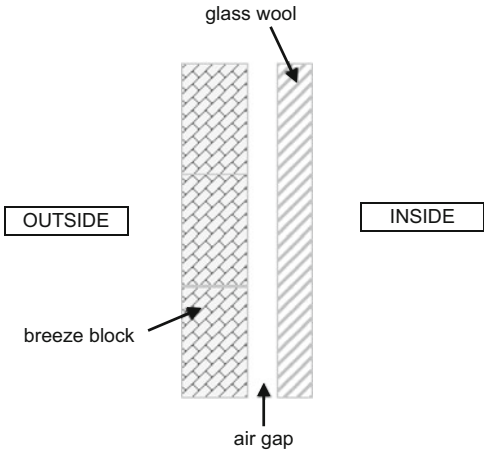

Fig. 2 Scheme of the conventional wall (side view)

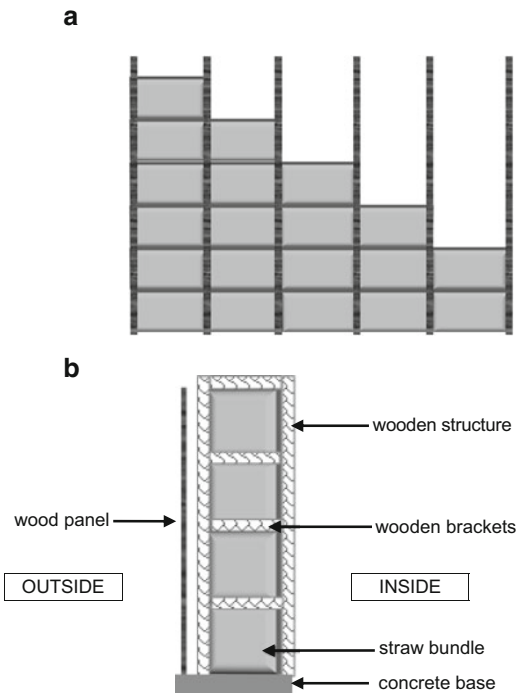

Fig. 3 (**a**) Scheme of the "straw wall" (front view). (**b**) Scheme of the "straw wall" (side view)

- *Step 1*
  The *manufacturing* takes into account the pollutions created by the use of raw materials to build the product.
- *Step 2*
  The *distribution* phase takes into account the impacts generated during the transportation of the product toward the destination where it will be used.

- *Step 3*
  The *installation phase* deals with the implementation of the wall.
- *Step 4*
  In the present case, the *consumer use* phase is not really considered because the maintenance (e.g., the wall painting or cleaning) is not included in the study.
- *Step 5*

The *end of life* phase (post-consumer use) depends on the wall (conventional or *natural*); it has been presented in Sect. 4.1.

4.3 Life Cycle Impact Assessment (LCIA)

The environmental impacts are calculated using endpoint and midpoint indicators associated with the well-known CML 2001 evaluation method (http://www.leidenuniv.nl/interfac/cml/ssp/projects/lca2/index.html).

The used data are coming from the famous Ecoinvent dataset (http://www.ecoinvent.ch/), from the INIES database (www.inies.fr), and also from the *European Life Cycle Database* (ELCD) in adequacy with the ILCD handbook (2012).

To evaluate the environmental impacts, the EIME TM v5.5.0.11 software (http://www.codde.fr/logiciel-acv.com) is used with a set of indicators coming from PEP ecopassport® (http://www.pep-ecopassport.org).

The chosen impact indicators are referenced in Table 5 and are described below (let us remind that the indicators deal with potential impacts):

- The *Air Acidification* (*AA*) indicator presents the air acidification by gases released to the atmosphere. It is expressed in grams of H^+, as if all gases were H^+, using equivalency in their acidification. The AA indicator is expressed in kilograms of H^+ equivalent (kg H^+ eq.).

Table 5 Used indicators (midpoint indicators for PEP)

Code	Name	Unit
AA	Air acidification	kg H^+ eq.
AT	Air toxicity	m^3
ED	Energy depletion	MJ
GWP	Global warning potential (100Y)	kg CO_2 eq.
HWP	Hazardous waste potential	kg
ODP	Stratospheric ozone depletion potential	CFC-11 eq.
POCP	Photochemical ozone creation potential	C_2H_4 eq.
RMD	Natural resources indicator	Y-1
WD	Water depletion	dm^3
WE	Water eutrophication	PO_4^{3-} eq.
WT	Water toxicity	dm^3

- The *Air Toxicity* (*AT*) indicator represents the air toxicity in a human environment, taking into account the usually accepted concentrations tolerated for several gases and the quantity released. The given indication corresponds to the air volume necessary to dilute "contaminated air." The limit values are expressed in g/l; consequently, the AT indicator is expressed in volume m^3.
- The *Energy Depletion* (*ED*) *indicator* accounts for energy consumption (or use), either derived from the combustion of fuels or from other sources (fossil, renewable, or nuclear for electricity production). This indicator also considers the *grey energy* in materials. The ED indicator is expressed in J or MJ.
- The *Global Warning Potential* (*GWP*) indicator represents the contribution to global warming due to specific gas emissions in the atmosphere during the product life cycle. It is expressed in grams of carbon dioxide equivalent (CO_2 eq.). The indicator implemented in the EIME TM software is the index called *IPCC-Greenhouse effect (100 years).* This indicator considers the potential direct effects on the Greenhouse Effect of the emission of 64 greenhouse gases over 100 years.
- The *Hazardous Waste Potential* (*HWP*) indicator calculates the quantity of hazardous waste produced for a given product. It is added to the flows of the LCA inventory and is expressed in kg.
- The *Stratospheric Ozone Depletion* (*OD*) indicator represents the contribution to the depletion of the stratospheric ozone layer by the emission of specific gases and is expressed in grams of CFC-11 equivalent (CFC-11 eq.).
- The *Photochemical Ozone Creation Potential* (*POCP*) indicator calculates the potential creation of ozone in troposphere (e.g., leading to "smog") by the release of specific gases which will become oxidants in the low atmosphere because of the solar radiation. It is expressed in grams of ethylene equivalent (C_2H_4 eq.).
- The *Natural Resources indicator* (*RMD*) calculates the depletion of natural resources, taking into account the size of the resource reserve in ground and the consumption rate of today's economy. It is expressed in fraction of reserve disappearing per year (Y-1).
- The *Water Depletion* (*WD*) indicator represents the water consumption during the whole life cycle of the considered product, i.e., the sum of consumptions from any kind of water source or quality. It is expressed in dm^3.

  NB.: The water used for cooling or used in a closed loop process is not taken into account in the calculation.
- The *Water Eutrophication* (*WE*) indicator represents the water enrichment in nutritive elements of lakes and marine waters by the release of specific substances in the effluents leading to eutrophication. The nitrification potential is evaluated. The WE indicator is expressed in grams or kilograms of PO_4^{3-} equivalent (PO_4^{3-} eq.).
- The *Water Toxicity* (*WT*) indicator represents the water toxicity. This indicator takes into consideration the usually accepted concentrations tolerated for several substances and the quantity released. The given indication corresponds to the water volume necessary to dilute the "contaminated water." The limit values are expressed in g/l; consequently, the WT indicator is expressed in dm^3.

In the following, the environmental impacts of the two studied walls are presented using the abovementioned indicators.

The results dealing with the environmental impacts are presented in Table 6 and Fig. 4 concerning the conventional wall schemed in Fig. 2 and in Table 7 and Fig. 5 for the "straw wall."

In fact, each indicator has a different unit, so that the impacts must be normalized, according to the specifications of the normalized ISO procedures 14040 (2006) and 14044 (2006). Consequently, Figs. 4 and 5 represent nondimensional values of each indicator for the different steps of life.

4.4 Interpretation

This fourth step of the LCA methodology does not really consist of a results analysis; it permits to assess the results obtained from the LCIA phase, relatively to the aim of the study described in part IV.1.

Let us specify that there is no environmental impact for the installation step and for the use of each studied product. This fact is directly linked to the aim of the study: the installation phase has not been taken into consideration and the use phase does not impact the system:

- In a whole system including the inside finished surface of the wall (e.g., gypsum boards, painting, etc.), the environmental impacts could be important. In the present study, a comparative calculation is conducted, so that the revetment is supposed to be the same whatever the wall; consequently it has not been taken into account in the calculation.
- The use step does not create any impact for a similar reason (the painting, for example, is considered out of the boundaries of the system).

Concerning the three other steps, the first results depend on the studied wall:

- For the conventional wall (see Table 5 and Fig. 4), the main contribution of the environmental impacts is essentially found either in the manufacturing step or at the end of life, whatever the considered indicator. This means that for the conventional wall, it is not necessary to focus on the distribution step: the manufacturing step, due to the fabrication of concrete for the breeze blocks, for example, generates high environmental impacts. On the same way, the end of life generates high impacts because of the complexity or impossibility to recycle most of the materials used in the conventional wall.
- For the "straw wall" (see Table 6 and Fig. 5) the previous results are globally similar considering the repartition of the main step generating the higher environmental impacts, but we can notice that the manufacturing step globally generates lower impacts compared with the "straw wall." It can be deduced that the natural material used (the straw) is effectively better for the environmental than the conventional wall for most of the indicators.

Table 6 Environmental footprint of the conventional wall

	AA for PEP		AT for PEP		ED for PEP	
	kg H+ eq	%	m^3	%	MJ	%
1. Manufacturing	1.04e-1	74.43	1.33e+8	66.96	7.91e+3	74.35
2. Distribution	3.99e-3	2.86	5.90e+6	2.98	3.79e+2	3.56
3. Installation	0.00e+0	0.00	0.00e+0	0.00	0.00e+0	0.00
4. Use	0.00e+0	0.00	0.00e+0	0.00	0.00e+0	0.00
5. End of life	3.17e-2	22.71	5.95e+7	30.06	2.35e+3	22.08
Σ Sum	1.39e-1	100.00	1.98e+8	100.00	1.06e+4	100.00

	GWP for PEP		HWP for PEP		ODP for PEP	
	kg CO_2 eq.	%	kg	%	kg CFC-11	%
1. Manufacturing	8.08e+2	28.04	4.94e-2	74.75	4.09e-5	62.80
2. Distribution	2.96e+1	1.03	9.75e-3	14.73	1.85e-5	28.44
3. Installation	0.00e+0	0.00	0.00e+0	0.00	0.00e+0	0.00
4. Use	0.00e+0	0.00	0.00e+0	0.00	0.00e+0	0.00
5. End of life	2.04e+3	70.93	6.96e-3	10.52	5.71e-6	8.76
Σ Sum	2.88e+3	100.00	6.62e-2	100.00	6.51e-5	100.00

	POCP for PEP		RMD for PEP		WD for PEP	
	kg C_2H_4 eq	%	Y-1	%	dm^3	%
1. Manufacturing	1.05e-1	19.41	1.37e-14	73.41	1.32e+3	64.72
2. Distribution	2.37e-2	4.37	5.21e-16	2.80	3.18e+1	1.56
3. Installation	0.00e+0	0.00	0.00e+0	0.00	0.00e+0	0.00
4. Use	0.00e+0	0.00	0.00e+0	0.00	0.00e+0	0.00
5. End of life	4.14e-1	76.22	4.43e-15	23.79	6.85e+2	33.72
Σ Sum	5.43e-1	100.00	1.86e-14	100.00	2.03e+3	100.00

	WE for PEP		WT for PEP	
	kg PO_4^{3-} eq	%	m^3	%
1. Manufacturing	1.30e-2	1.48	2.23e+2	17.45
2. Distribution	4.42e-4	0.05	5.11e+0	0.40
3. Installation	0.00e+0	0.00	0.00e+0	0.00
4. Use	0.00e+0	0.00	0.00e+0	0.00
5. End of life	8.65e-1	98.46	1.05e+3	82.16
Σ Sum	8.78e-1	100.00	1.28e+3	100.00

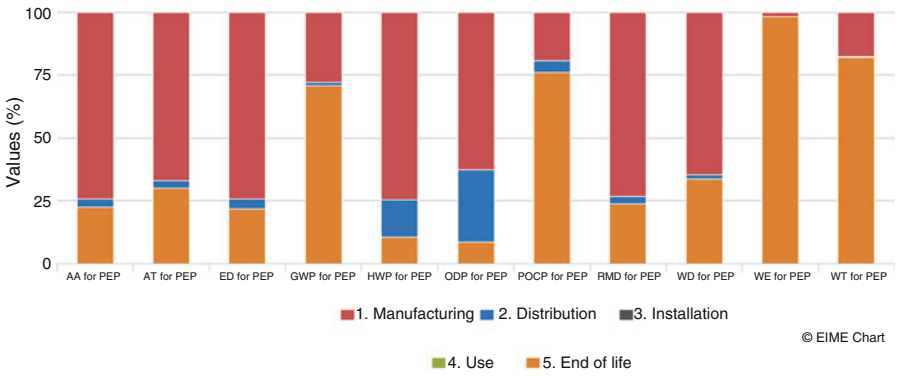

Fig. 4 Normalized impacts for the conventional wall

For the two studied walls, the end of life step is very important for the following environmental impacts: the Global Warning Potential (WWP), the Photochemical Ozone Creation Potential (POCP), the Water Eutrophication (WE), and the Water Toxicity (WT). These two last elements concerning water should have probably been more important if the water used for the installation step had been considered.

Considering the global contribution, the main impacts depend on the wall:

- For the conventional wall (see Table 5), the Air Toxicity is about 2E8 m^3, the Energy Depletion reaches 10,000 MJ, and the Global Warning Potential is just under 3000 kg CO_2 eq., which globally represents the greenhouse gases rejected by a "modern" car on around 30,000 km.
- For the "straw wall" (see Table 6), the Air Toxicity remains important and of the same order, essentially because of the manufacturing step. This is mainly due to the wood chemical treatment which should be improved if we want to reduce the environmental footprint. The Energy Depletion is about 6000 MJ and the Global Warning Potential reaches 1400 kg CO_2 eq., which globally represents the greenhouse gases rejected by a "modern" car on a distance of around 14,000 km (a mean year of use in France).

Now we aim to compare the environmental impacts of the two considered walls.

The results for the manufacturing step, the distribution, and the end of life are respectively represented in Tables 8, 9, and 10.

Concerning the manufacturing step, the environmental footprint of the "straw wall" is always inferior to the one of the conventional wall, except for Air Toxicity indicator (chemical treatment of the wood). The results concerning the distribution step are clear: the environmental impacts of the straw wall are lower; this can be explained by the fact that for the "straw wall," local production has been preferred. The end of life step leads to lower environmental impacts for the "straw wall" regardless of the indicator.

If the global environmental footprint is considered (see Table 11 and Fig. 6), it can be concluded that in comparison with the conventional wall, the "straw wall":

Table 7 Environmental footprint of the "straw wall"

	AA for PEP		AT for PEP		ED for PEP	
	kg H+ eq	%	m^3	%	MJ	%
1. Manufacturing	1.10e-2	35.21	1.46e+8	79.45	4.11e+3	71.36
2. Distribution	1.04e-3	3.34	1.54e+6	0.84	8.50e+1	1.48
3. Installation	0.00e+0	0.00	0.00e+0	0.00	0.00e+0	0.00
4. Use	0.00e+0	0.00	0.00e+0	0.00	0.00e+0	0.00
5. End of life	1.91e-2	61.45	3.62e+7	19.71	1.56e+3	27.17
Σ Sum	3.12e-2	100.00	1.84e+8	100.00	5.76e+3	100.00

	GWP for PEP		HWP for PEP		ODP for PEP	
	kg CO_2 eq.	%	kg	%	kg CFC-11	%
1. Manufacturing	1.85e+2	13.01	4.07e-2	87.39	6.29e-6	52.99
2. Distribution	6.31e+0	0.44	9.43e-4	2.02	1.79e-6	15.09
3. Installation	0.00e+0	0.00	0.00e+0	0.00	0.00e+0	0.00
4. Use	0.00e+0	0.00	0.00e+0	0.00	0.00e+0	0.00
5. End of life	1.23e+3	86.55	4.94e-3	10.59	3.79e-6	31.91
Σ Sum	1.42e+3	100.00	4.66e-2	100.00	1.19e-5	100.00

	POCP for PEP		RMD for PEP		WD for PEP	
	kg C_2H_4 eq	%	Y-1	%	dm^3	%
1. Manufacturing	2.65e-2	9.39	3.14e-15	50.79	3.69e+2	47.15
2. Distribution	3.31e-3	1.17	1.20e-16	1.95	3.42e+0	0.44
3. Installation	0.00e+0	0.00	0.00e+0	0.00	0.00e+0	0.00
4. Use	0.00e+0	0.00	0.00e+0	0.00	0.00e+0	0.00
5. End of life	2.53e-1	89.44	2.92e-15	47.26	4.11e+2	52.41
Σ Sum	2.83e-1	100.00	6.18e-15	100.00	7.83e+2	100.00

	WE for PEP		WT for PEP	
	kg PO_4^{3-} eq	%	m^3	%
1. Manufacturing	4.07e-4	0.09	2.13e+1	3.51
2. Distribution	4.90e-5	0.01	1.96e+0	0.32
3. Installation	0.00e+0	0.00	0.00e+0	0.00
4. Use	0.00e+0	0.00	0.00e+0	0.00
5. End of life	4.70e-1	99.90	5.83e+2	96.16
Σ Sum	4.71e-1	100.00	6.06e+2	100.00

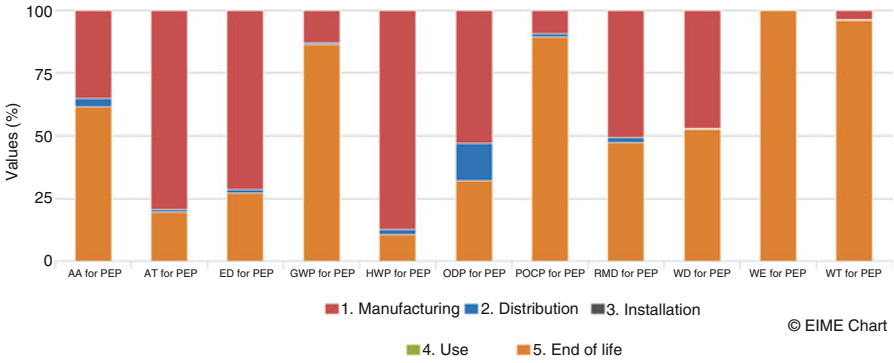

Fig. 5 Normalized impacts for the "straw wall"

Table 8 Comparison of the environmental footprint for the manufacturing step

Indicator	Conv. wall	Straw wall	"Straw/conv" (%)
AA	1.04E − 01	1.10E − 02	11
AT	1.33E + 08	1.46E + 08	110
AD	7.91E + 03	4.11E + 03	52
GWP	8.08E + 02	1.85E + 02	23
HWP	4.94E − 02	4.07E − 02	82
ODP	4.09E − 05	6.29E − 06	15
POCP	1.05E − 01	2.65E − 02	25
RMD	1.37E − 14	3.14E − 15	23
WD	1.32E + 03	3.69E + 02	28
WE	1.30E − 02	4.07E − 04	3
WT	2.23E + 02	2.13E + 01	10

Table 9 Comparison of the environmental footprint for the distribution step

Indicator	Conv. wall	Straw wall	"Straw/conv" (%)
AA	3.99E − 03	1.04E − 03	26
AT	5.90E + 06	1.54E + 06	26
AD	3.79E + 02	8.50E + 01	22
GWP	2.96E + 01	6.31E + 00	21
HWP	9.75E − 03	9.43E − 04	10
ODP	1.85E − 05	1.79E − 06	10
POCP	2.37E − 02	3.31E − 03	14
RMD	5.21E − 16	1.20E − 16	23
WD	3.18E + 01	3.42E + 00	11
WE	4.42E − 04	4.90E − 05	11
WT	5.11E + 00	1.96E + 00	38

Table 10 Comparison of the environmental footprint for the end of life step

Indicator	Conv. wall	Straw wall	"Straw/conv" (%)
AA	3.17E − 02	1.91E − 02	60
AT	5.95E + 07	3.62E + 07	61
AD	2.35E + 03	1.56E + 03	66
GWP	2.04E + 03	1.23E + 03	60
HWP	6.96E − 03	4.94E − 03	71
ODP	5.71E − 06	3.79E − 06	66
POCP	4.14E − 01	2.53E − 01	61
RMD	4.14E − 01	2.92E − 15	0
WD	6.85E + 02	4.11E + 02	60
WE	8.65E − 01	4.70E − 01	54
WT	1.05E + 03	5.83E + 02	56

Table 11 Comparison of the global environmental footprint of the two studied walls

Indicator	Conv. wall	Straw wall	"Straw/conv" (%)
AA	1.39E − 01	3.12E − 02	22
AT	1.98E + 08	1.84E + 08	93
AD	1.06E + 04	5.76E + 03	54
GWP	2.88E + 03	1.42E + 03	49
HWP	6.62E − 02	4.66E − 02	70
ODP	6.51E − 05	1.19E − 05	18
POCP	5.43E − 01	2.83E − 01	52
RMD	1.86E − 14	6.18E − 15	33
WD	2.03E + 03	7.83E + 02	39
WE	8.78E − 01	4.71E − 01	54
WT	1.28E + 03	6.06E + 02	47

- Generates around five times less kg H^+ eq.
- Depletes twice less energy
- Generates twice less CO_2 eq.
- Produces one and a half time less dangerous wastes
- Destroys five times less ozone in the troposphere
- Generates twice times less photochemical pollution
- Depletes three times less natural resources and water
- Contributes twice less to the water eutrophication and the water toxicity
- Generates toxic pollutants in the air with the same magnitude

In other words, the environmental footprint of the "straw wall" is at least twice lower regardless of the indicator, except concerning the air toxicity essentially because of the chemical treatment of the wood.

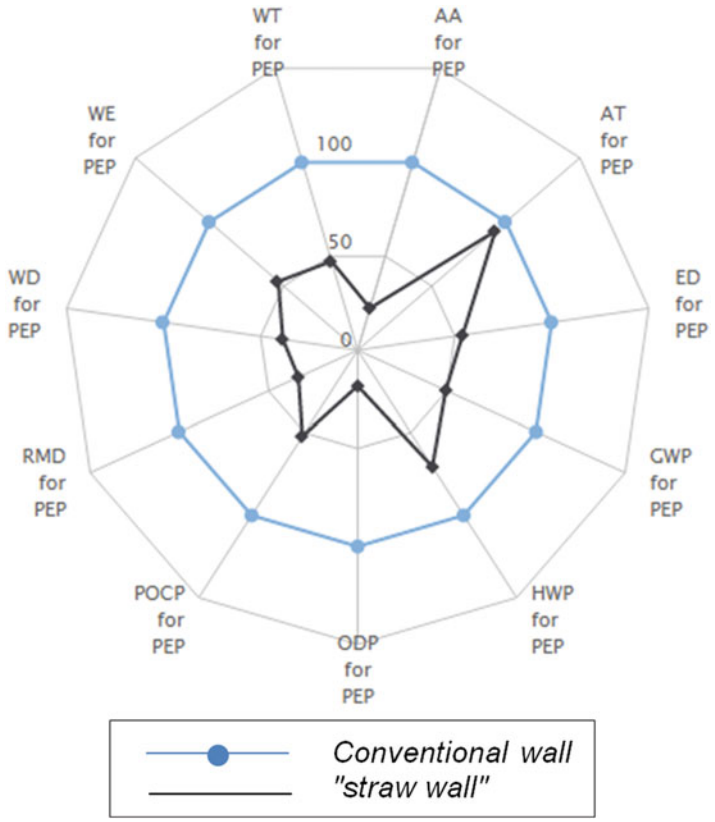

Fig. 6 Comparative environmental footprint of the two studied walls

5 Conclusion

This study deals with the use of the Life Cycle Assessment (LCA) methodology and tools to quantify the environmental impacts of two wall assemblies: a conventional wall and a "straw wall" using wood and straw bundles. The considered wall assemblies were first described from a physical and functional point of view. The LCA methodology has next been presented and applied to the previous introduced insulating systems assemblies. The goal of this study was to compare two walls for a 100-year life duration, a thermal resistance reaching 5 m^2.K/W, and a 15 m^2 area.

The obtained results show that the wall using straw bundles has a lower environmental footprint than the studied conventional wall, regardless of the indicator. Of course, this study used some restrictive hypothesis which must be verified and tested in future works. Besides, the study has been simplified to allow a first comparison, and it must be continued, notably to quantify the influence of the

different elements or steps in the life cycle of a wall assembly. However, the present results give encouraging elements for future studies concerning the use of local and/or natural material for housing as it has been shown that straw bundles associated to wood structure and panel is an interesting alternative not only for local economy but also for waste treatment (straw bundles are considered as wastes) and environmental footprint.

These three elements are linked to the three pillars of sustainable development: *planet, people,* and *profit*. A "straw house" is made of natural and renewable materials (*planet*), is said to be pleasant and comfortable for the inhabitants (*people*), and permits the development of a local and non-"relocated" economy (*profit*).

Acknowledgments The author wants to acknowledge the different students who have collaborated on this project, particularly Thomas Alglaeve and Amandine Degallaix who have especially participated in the LCIA study of this work.

References

Ashour, T., Georg, H.,Wu, W.: Performance of straw bale wall: A case of study. Energy Build. **43**(8), 1960–1967, (2011a)

Ashour, T., Georg, H., Wu, W.: An experimental investigation on equilibrium moisture content of earth plaster with natural reinforcement fibres for straw bale buildings. Article Appl. Thermal Eng. **31**(2), 293–303 (2011b)

Chaussinand, A., Scartezzini, J.L., Nik, V.: Straw bale: a waste from agriculture, a new construction material for sustainable buildings. Energy Procedia. **78**, 297–302 (2015)

Floissac, L.: .Règles professionnelles de la construction en paille, Le Moniteur (2012)

Frenette, C.D., Bulle, C., Beauregard, R., Salenikovich, A., Derome, D.: Using life cycle assessment to derive an environmental index for light-frame wood wall assemblies. Build. Environ. **45**(10), 2111–2122 (2010)

INIES: Fiches de Déclaration Environnementale et Sanitaire (FDE&S) www.inies.fr

Goodhew, S., Griffiths, R., Woolley, T.: An investigation of the moisture content in the walls of a straw-bale building. Build. Environ. **39**(12), 1443–1451 (2004)

ISO 14040: Environmental Management – Life Cycle Assessment, Principles and framework (2006).

ISO 14044: Environmental Management – Life Cycle Assessment, Requirements and guidelines (2006)

King B.: Design of straw bale buildings: the state of the art. Green Books, San Rafael, CA (2006)

Marks, L.R.: Straw bale as a viable cost effective and sustainable building material for use in Southeast Ohio. Master's thesis, Ohio University (2005)

Menet, J.-L., Gruescu, I.-C.: Environmental footprint of building elements using Life Cycle Analysis methodology, 21ème Congrès Français de Mécanique, 2013 August 26th-30th, Bordeaux (2013)

Menet, J.-L.: Environmental footprint of walls using natural insulating materials coming from agricultural wastes. J. Catal. Mater. Environ. **11**, 55–62 (2014)

Minke, G., Mahlke, F.: Building with straw: design and technology of a sustainable architecture. Birkhauser (2005)

O'Neill, B.C., Dalton, M., Fuchs, R., Jiang, L., Pachauri, S., Zigova, K.: Global demographic trends and future carbon emissions. Proc. Natl. Acad. Sci. USA, **107**(41), 17521–17526 (2010)

RT2012: Exigences réglementaires pour la construction des bâtiments neufs, chap. 1: la réglementation thermique 2012. http://www.developpement-durable.gouv.fr/Chapitre-I-La-reglementation.html (2012)

Schmidt, A.C., Jensen, A.A., Clausen, A.U., Kamstrup, O., Postlethwaite, D.: A comparative life cycle assessment of building insulation products made of stone wool, paper wool and flax. Int. J. Life Cycle Assess. **9**(1), 53–66 (2004)

Wolf, M.A., Pant, R., Chomkhamsri, K.: The International Reference Life Cycle Data System (ILCD) Handbook JRC reference reports. Publications Office of the European Union, Luxembourg (2012)

Part III
Energy Strategies and Policies

Experimental Performance Analysis of an Integrated Air Conditioning Split Heat Pump System for Application in a Mediterranean Climate

Nižetić Sandro, Kizilkan Önder, and Čoko Duje

1 Introduction

A hybrid energy system presents energy solutions where the advantage of each individual energy technology can be used and different forms of energy demands can be ensured for occupants. For example, in majority of residential facilities, there is a demand for simultaneous space heating/cooling and hot water preparation. Furthermore, hybrid energy systems can be assembled from developed market energy technologies such as heat pump technology, photovoltaic technology, solar thermal systems, and fuel cell systems. Hence, the objective is to find an appropriate hybrid energy solution that is acceptable from a techno-economic aspect and also from an aspect of environmental suitability through the implementation of renewable energy technologies. There are different studies that focus on hybrid energy system research, for example, Fong et al. (2010), Herrando et al. (2014), Hongbing et al. (2011), Huang et al. (2010), Klein et al. (2014), Ozgener (2010), Rezaie et al. (2011), Tyagi et al. (2012), Xingxing et al. (2013, 2014), Yamada et al. (2012), and Zafar and Dincer (2014).

N. Sandro (✉)
University of Split, Faculty of Electrical and Mechanical Engineering and Naval Architecture, LTEF-Laboratory for Thermodynamics and Energy Efficiency, R. Boskovica 32, Split, HR 21000, Croatia
e-mail: snizetic@fesb.hr

K. Önder
Süleyman Demirel University, Faculty of Technology, Department of Energy Systems Engineering, Isparta 32260, Turkey

Č. Duje
University of Split, Faculty of Electrical and Mechanical Engineering and Naval Architecture, Department of Electronics, R. Boskovica 32, Split, HR 21000, Croatia

© Springer International Publishing AG, part of Springer Nature 2018

F. Aloui, I. Dincer (eds.), *Exergy for A Better Environment and Improved Sustainability 2*, Green Energy and Technology,
https://doi.org/10.1007/978-3-319-62575-1_49

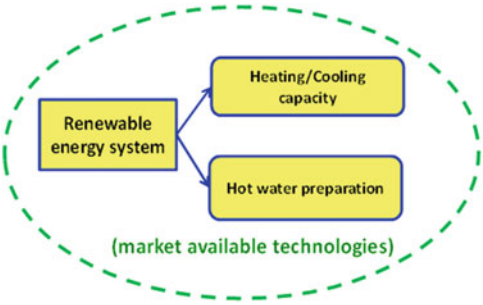

Fig. 1 General requirements for renewable hybrid energy concept

The proposed hybrid energy system by Nizetic et al. (2014) was tested at a geographical location in Croatia, in the city of Split situated on the Adriatic coast, which is a typical coast-side city with a Mediterranean climate. The advantage of a Mediterranean climate lies in the fact that heat pump systems can be used throughout the year in an efficient way, and in general, the potential for implementation of renewable energy sources (Nizetic et al. 2008) (Nizetic 2011) in a Mediterranean region is great. On the other side, the majority of building facilities in Croatia use standard heat pump systems (split-type air conditioning units) and standard boilers for preparation of hot water (with directly installed electric heaters) to cover space heating/cooling demands and hot water demands, respectively. The energy market offers a variety of available solutions but not in the form of hybrid energy systems, so consumers are more oriented on the usage of individual technologies instead of using the more efficient hybrid energy systems. Hence, our idea was to use existing market-available technologies that are installed in majority of building facilities, basically modify them, and establish a unique, more efficient energy solution.

Regarding the previously proposed hybrid energy solution, it should provide space cooling/heating capacity and simultaneously ensure hot water preparation. Additionally, the sole requirement is that the system should be a renewable one and assembled from market-available energy technologies (the base concept is shown in Fig. 1).

The objective of this chapter is to present further analysis results of the hybrid energy system proposed by Nizetic et al. (2014), where a specific design and performance parameters for cooling mode were elaborated. Additionally, in this study, performance parameters for heating mode are presented, and a comparison between summer and winter hybrid energy system operation is discussed.

2 A Specific Experimental Setup

In ensuring the previously defined goals, the hybrid energy system that was proposed by Nizetic et al. (2014) and the basic concept of the proposed hybrid energy system are shown in Fig. 2. According to Fig. 2, the hybrid energy system

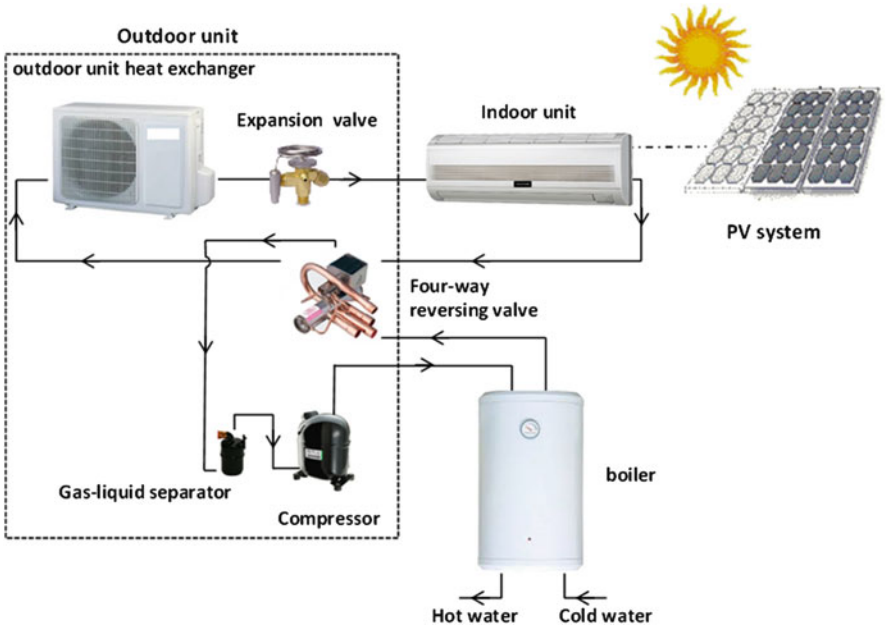

Fig. 2 Simplified scheme of the proposed hybrid energy system (Nizetic et al. 2014)

was assembled from a standard split heat pump air conditioning unit with a heating/cooling capacity of 3.7 kW/3.5 kW, and the refrigerant used was R410A. Furthermore, the air conditioning unit was connected to a standard boiler for hot water preparation in the same way that a spiral copper heat exchanger is installed into the boiler (water tank with a capacity of 80 L). Additionally, the whole system was supplied with electricity from a small PV plant (off-grid system, 1.8 kW installed electric power, four batteries, each of 330 Ah, and monocrystalline PV technology—195 W of nominal power in each panel). It is noticeable that the previously specified individual components that form the proposed hybrid energy system can be found in majority of building facilities (touristic, residential, etc.). The proposed hybrid energy system (Fig. 2) is able to produce space cooling/heating capacity and hot water and is driven by a small photovoltaic (PV) plant; it basically represents a renewable energy system that fits the requirements defined in the previous section of the manuscript.

Regarding the specificity of the Mediterranean coast, the proposed energy system is especially useful for implementation in touristic facilities (small or medium ones) as it represents an energy-efficient solution that is renewable and can cover the required energy demands (it could also be suitable for remote locations with electricity supply issues).

3 Measurement Rig

An indoor unit and water tank were installed on a test stand as shown in Fig. 3a. PV panels were mounted on the south terrace of the Faculty building (Fig. 4.), and the rest of the electronics were installed inside the laboratory of Thermodynamics at the Faculty of FESB in Split.

A simplified measurement rig is shown in Fig. 5. So, in essence, it is a conventional split heat pump system scheme but additionally expanded with an accumulation boiler (water tank). Electricity consumption was measured with an energy logger (current, voltage, and engaged electric power). A pyrometer was mounted on the PV system to measure insolation, to detect the average electrical efficiency of the PV system, and, finally, to estimate battery capacity (autonomy for specific working regimes). The PV panels were inclined at 25°, which is in accordance with the specific geographical location. As mentioned earlier, a heat exchanger (condenser 1, Fig. 5) was added to utilize waste heat and ensure heating capacity for hot water preparation. The installed heat exchanger in the boiler always acts as a condenser both in heating and cooling mode. Besides the previous modification, the electronics of a standard air conditioning unit was also modified to ensure easy handling for consumers. Namely, the device has a heating and cooling mode (where the water is also heated simultaneously in the boiler) and a water heating mode (without heating/cooling capacity).

The surrounding air temperatures, ambient air temperature inside the cooled/heated space, and the air temperature at the outlet of the indoor unit were measured with temperature sensors. Air mass flow was calculated according to the measured air velocity and temperature at the outlet of the indoor unit. The temperature of the water inside the boiler was also measured, so more than 15 parameters were measured to evaluate performance parameters for summer and winter conditions. Simulation of water consumption was also performed to investigate the impact of water consumption on the performance parameters, and a more realistic situation was analyzed, where simultaneous heating/cooling capacity was provided together with hot water preparation. In the next section, performance analysis results are presented for summer and winter operation together with a discussion of the gained experimental results.

4 Performance Analysis: An Analytical Approach

According to the measured parameters, a performance analysis was conducted for a typical winter and summer day in the geographical location of Split (Croatia), which typically represents a Mediterranean climate. An energy balance equation can be written for the proposed hybrid energy system for heating and cooling mode, respectively, to determine the COP value:

(a)

(b)

Fig. 3 (**a**) Indoor unit and water tank (boiler) on a test stand. (**b**) Adaptation of a standard air conditioning unit

Fig. 4 PV system components

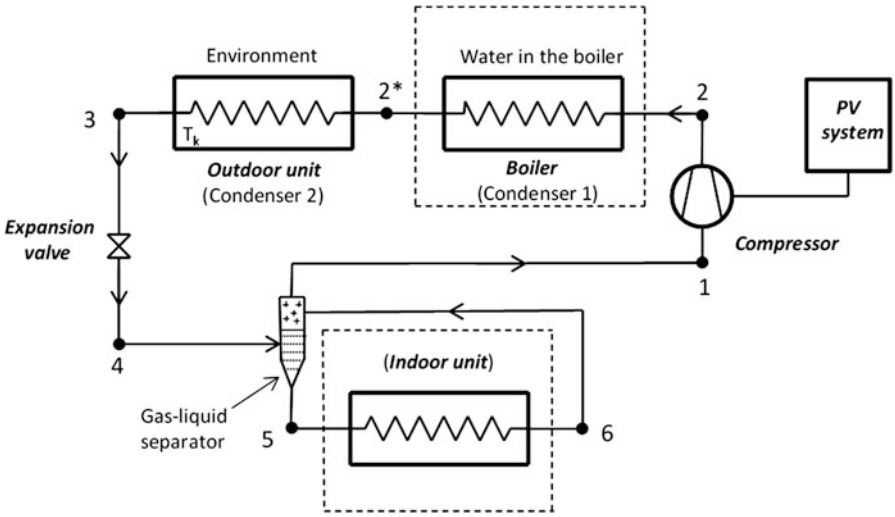

Fig. 5 Simplified measurement test rig (Nizetic et al. 2014)

$$\mathrm{COP_H} = \frac{\dot{Q}_{\mathrm{Con}}}{P_{\mathrm{Comp}}} = \frac{\dot{Q}_{\mathrm{Con1}} + \dot{Q}_{\mathrm{Con2}}}{\dot{E}_{\mathrm{El}}/\tau} \tag{1}$$

$$\mathrm{COP_C} = \frac{\dot{Q}_{\mathrm{Ev}} + \dot{Q}_{\mathrm{Con1}}}{\dot{E}_{\mathrm{el}}/\tau} \tag{2}$$

The heat rejected from the refrigerant to the water (condenser 1, Fig. 5) can be calculated from the measured water temperatures and the overall quantity of water

wasted in a certain period of time, respectively (water was wasted a few times during the experimental testing):

$$\dot{Q}_{\text{Con1}} = \sum \dot{m}_{\text{w}} c_{\text{pw}} (T_{\text{w}_2} - T_{\text{w}_1}) \tag{3}$$

The rejected and taken heat from the space, depending on the working mode, can be calculated from the measured air flow average (via air velocity) and air temperature at the outlet of the indoor unit, respectively:

$$\dot{Q}_{\text{Con2}} = \dot{m}_{\text{a}} c_{\text{pa}} \left(\bar{T}_{\text{h}} - \bar{T}_{\text{sh}}\right) \tag{4}$$

Finally, the performance coefficient for the hybrid energy system can be defined for heating and cooling modes as follows:

$$\text{COP}_{\text{H}} = \frac{\sum m_{\text{w}} c_{\text{pw}} (T_{\text{w}_2} - T_{\text{w}_1}) + \dot{m}_{\text{a}} c_{\text{pa}} \left(\bar{T}_{\text{h}} - \bar{T}_{\text{sh}}\right) \tau}{\dot{E}_{\text{el}} / \tau} \tag{5}$$

$$\text{COP}_{\text{c}} = \frac{\sum m_{\text{w}} c_{\text{pw}} (T_{\text{w}_2} - T_{\text{w}_1}) + \dot{m}_{\text{a}} c_{\text{pa}} \left(\bar{T}_{\text{sc}} - \bar{T}_{\text{c}}\right) \tau}{\dot{E}_{\text{El}} / \tau} \tag{6}$$

The above elaborated calculation framework was used to determine the hybrid energy system performance parameters based on measured parameters under realistic conditions.

4.1 Summer Period

The hybrid energy system was tested during the summer period in a daily working regime and night working regime. The daily mean air temperatures ranged from 28 °C to 34 °C and from 27 °C to 30 °C during night regime. In both analyzed cases, the set cooled space temperature was 24 °C. During the experimental measurements, solar irradiation ranged between 600 and 800 W/m^2, and the mean achieved PV electrical efficiency was around 15%. The total measurement time ranged from 3 to 4 h. Refrigerant pressure in a steady regime was around 10.0 bars on the evaporator side and around 24.0 bars on the condenser side. Furthermore, the quantity of simulated water consumption ranged between 80 and 90 L for showering and hand washing purposes. General circumstances and achieved performance parameters are summarized in Table 1.

According to the recorded electricity consumption during steady-state night operation, we calculated that the PV system autonomy is around 12 h. We also examined the influence of water consumption on the outlet temperature of the air conditioning unit and discovered that the effect was minor. Namely, the variation in air temperature at the outlet of the indoor unit was around 1 °C; therefore, the

Table 1 Performance parameters and general working circumstances for the summer period

Performance parameters (daytime and nighttime operation)	
Surrounding air temperature	27–34 °C
Indoor air temperature	24 °C
Total measurement time	3–4 h
Water consumption	80–90 l
Mean refrigerant pressure (condenser)	24 bars
Mean refrigerant pressure (evaporator)	10 bars
Mean water temperature	46–51 °C
Mean hourly electricity consumption	0.55–0.66 kWh
Mean COP number	5.3–5.4

system performance is not affected at all. Regarding hot water preparation, the hybrid energy system was able to heat the water in the boiler from 30 °C to 45 °C in approximately 20–25 min, depending on the working circumstances. However, if the water is not released from the boiler during system operation, it was possible to heat the water in the boiler up to 60 °C. The COP value during daytime operation ranged on average from 4.6 to 6.1 and nighttime operation ranged from 4.0 to 6.7. In both the previous working circumstances, the mean COP number achieved was around 5.4, which proves the good efficiency of the proposed hybrid energy system as we are dealing with a small energy system. Engaged compressor power ranged from 500 to 700 W in steady-state operation, and hourly electricity consumption was around 0.66 kWh in daytime operation and around 20% less in nighttime operation. Finally, it can be concluded that the achieved performance parameters of the proposed hybrid energy system in cooling mode are excellent as a relatively high COP value was achieved, the system was able to heat water to an appropriate temperature, and autonomy was provided during nighttime operation.

4.2 Winter Period

Regarding winter period, the hybrid energy system was tested only in daytime operation. The surrounding air temperature ranged from 8 to 13 °C, and solar irradiation ranged from 300 to 500 W/m^2. In all cases, the heating space temperature was 24 °C. Water consumption was also simulated, and it ranged from 30 to 80 L. The average measurement time varied from 2 to 4 h. The mean performance results for steady-state operation are presented in Table 2 for a heating regime.

The system was able to heat water from 20 °C to 50 °C for approximately half an hour, and the average air temperature at the indoor outlet unit ranged from 41 °C to 44 °C. However, when water was wasted, we noticed a significant decrease in air temperature at the outlet of the indoor unit. To be specific, immediately after water was released, the temperature at the indoor outlet unit decreased from 6 to 8 °C, which caused insufficient temperature level at the indoor outlet unit. An example of water waste effect is shown in Fig. 6. In this case, approximately 20 min was needed

Table 2 Performance parameters and general working circumstances for winter period

Winter performance parameters (daytime operation)	
Surrounding air temperature	8–13 °C
Indoor air temperature	24 °C
Total measurement time	2–4 h
Water consumption	30–80 L
Mean refrigerant pressure (condenser)	28 bars
Mean refrigerant pressure (evaporator)	8.5 bars
Mean water temperature	44 °C
Mean hourly electricity consumption	1.14 kWh
Mean COP number	5.3

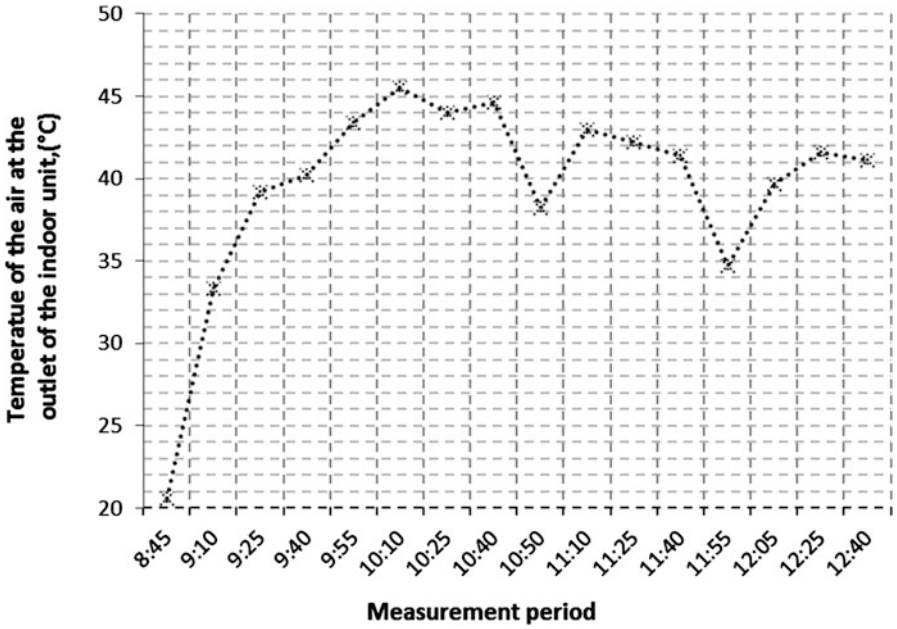

Fig. 6 Effect of water consumption on air temperature at the outlet of the indoor unit

to achieve proper air temperature at the indoor outlet unit (around 40 °C). However, the system was able to recover the temperature at the indoor outlet unit in reasonable time.

An example of COP value variation (heating mode) as the function of surrounding air temperature is shown in Fig. 7. According to the provided measurements, it is noticeable that if the average temperature of the surrounding air is above 10 °C, the mean COP value will be above 5.5, but if the temperature of the surrounding air is below 10 °C, the mean COP value will be around 20% lower. However, the proposed hybrid energy system is assumed to operate in mild climates where the mean surrounding air temperatures in winter period are around 10 °C.

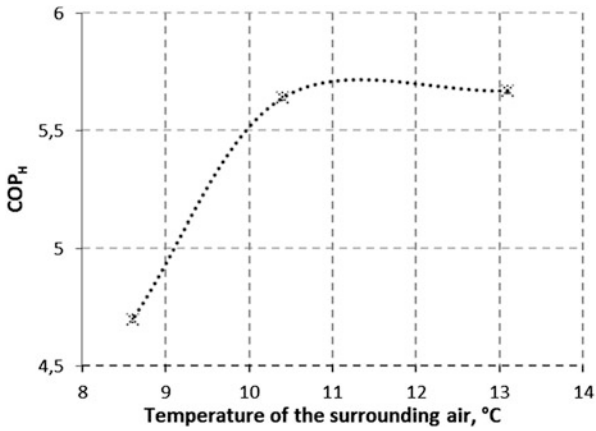

Fig. 7 COP value as the function of surrounding air temperature

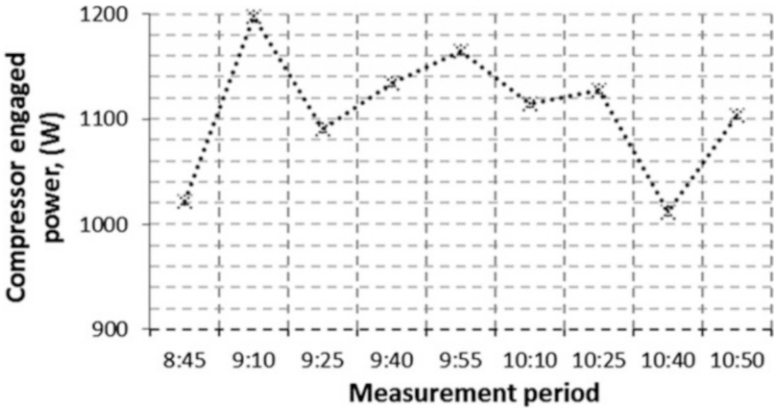

Fig. 8 Variation of compressor power in steady-state operation

Engaged compressor power in heating mode was around 1.0 kW in steady-state operation, and mean current was around 5 A. An example of engaged compressor power variation is shown in Fig. 8. The mean hourly electricity consumption was around 1.14 kWh, and in comparison with summer operation, it is a doubled amount.

Regarding the preparation of hot water in the summer period, the hybrid energy system was able to heat the water in the boiler to 56 °C, and the average temperature of hot water was 44 °C. Water consumption was also simulated, and one boiler capacity (80 L) was wasted in 4 h. The effect of water consumption on water temperature is shown in Fig. 8. According to Fig. 9, the sudden drops in water temperature correspond with the simulated water consumption. After water consumption, the water temperature in the boiler reduced, ranging from 30 to 35 °C, and the system needed around 20 min to ensure proper water temperature at around 45 °C.

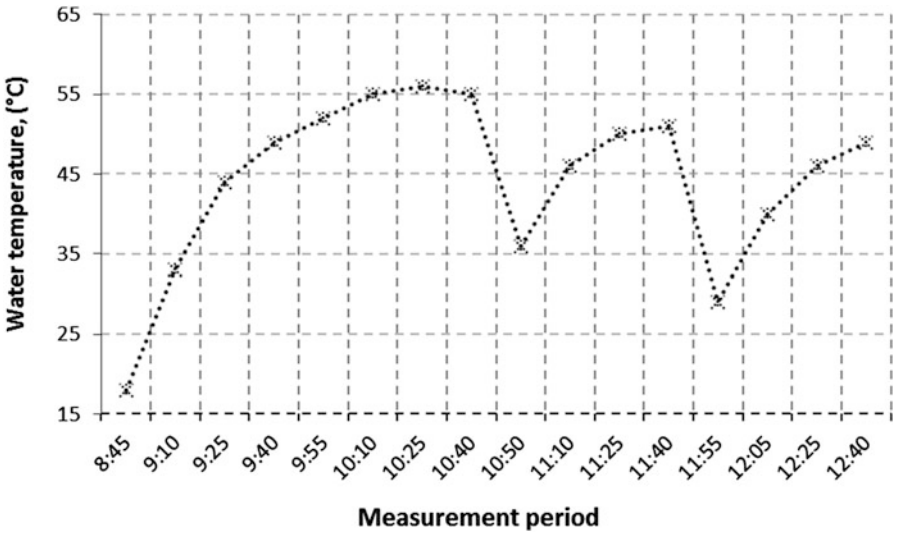

Fig. 9 Effect of water consumption on mean temperature in water tank

Performance parameters of the hybrid energy system are also satisfactory in the heating mode, although there is an issue regarding the impact of water release on air temperature at the outlet of the indoor unit. Electricity consumption is also doubled in comparison with cooling mode, and PV system autonomy is significantly reduced. Therefore, the system has got lower overall performance in heating mode in comparison to cooling mode but is still a good and applicable energy solution for building applications.

5 Conclusions

In this chapter, the specific experimental setup and design of the hybrid energy system was elaborated in detail. The proposed energy system is suitable for operation in mild climates, such as a Mediterranean climate, where a heat pump can work efficiently throughout the year. The main characteristic of the proposed system is that it has been assembled from existing market-available energy technologies to ensure fast implementation into the market through simple adjustments of existing energy systems that are already used in building applications. Moreover, the system is totally renewable, which is an important advantage in these times when climate issues are our main concern. According to experimental measurements, the system has shown promising performance parameters. The mean COP value was both 5.4 in summer and winter periods, but the mean hourly electricity consumption was around 0.5 kWh in the summer period and around 1.1 kWh in the

winter period. The PV system autonomy was up to 12 h in the summer period and 6 h in the winter period. Furthermore, the system was able to heat up water to a mean temperature of 45 °C, and the maximal achieved water temperature was 56 °C. Hence, it can be concluded that the achieved water temperature level is suitable for domestic or other needs. If we compare the summer and winter performance parameters of the hybrid energy system, it can be concluded that summer performance parameters are better. In other words, in cooling mode, electricity consumption will be halved, the COP number will be higher, water temperature in the boiler will also be higher, and PV system autonomy will be doubled; therefore, these advantages are important in the potential application of the proposed energy system. Finally, it can be concluded that the proposed hybrid energy system is efficient for summer and winter operations and has potential applications in touristic building facilities and residential facilities in mild climates as well.

References

Fong, K.F., Lee, C.K., Chow, T.T., Lin, Z., Cha, L.S.: Solar hybrid air-conditioning system for high temperature cooling in subtropical city. Renew. Energy. **35**(11), 2439–2451 (2010)

Herrando, M., Markides, C.N., Hellgardt, K.: A UK-based assessment of hybrid PV and solar-thermal systems for domestic heating and power: system performance. Appl. Energy. **122**, 288–309 (2014)

Hongbing, C., Riffat, S.B., Fu, Y.: Experimental study on a hybrid photovoltaic/heat pumps system. Appl. Therm. Eng. **31**, 4132–4138 (2011)

Huang, B.J., Wu, J.H., Hsu, H.Y., Wang, J.H.: Development of hybrid solar-assisted cooling/heating system. Energy Convers. Manag. **51**(8), 1643–1650 (2010)

Klein, K., Huchtemann, K., Müller, D.: Numerical study on hybrid heat pump systems in existing buildings. Energ. Buildings. **69**, 193–201 (2014)

Nizetic, S., Coko, D., Marasovic, I.: Experimental study on a hybrid energy system with small-and medium-scale applications for mild climates. Energy. **75**, 379–389 (2014)

Nizetic, S., Ninic, N., Klarin, B.: Analysis and feasibility of implementing solar chimney power plants in the Mediterranean region. Energy. **33**(11), 1680–1690 (2008)

Nizetic, S.: Technical utilisation of convective vortices for carbon-free electricity production: a review. Energy. **36**, 1236–1242 (2011)

Ozgener, O.: Use of solar assisted geothermal heat pump and small wind turbine systems for heating agricultural and residential buildings. Energy. **35**(1), 262–268 (2010)

Rezaie, B., Esmailzadeh, E., Dincer, I.: Renewable energy options for buildings: case studies. Energ. Buildings. **43**(1), 56–65 (2011)

Tyagi, V.V., Kaushik, S.C., Tyagi, S.K.: Advancement in solar photovoltaic/thermal (PV/T) hybrid collector technology. Renew. Sust. Energ. Rev. **16**(3), 1383–1398 (2012)

Xingxing, Z., Xudong, Z., Jingchun, S., Xiaotong, Y.J.: Dynamic performance of a novel solar photovoltaic/loop- heat-pipe heat pump system. Appl. Energy. **114**, 335–352 (2014)

Xingxing, Z., Xudong, X.Z., Xiaotong, Y.J.: Characterization of a solar photovoltaic/loop-heat-pipe heat pump water heating system. Appl. Energy. **102**, 1229–1245 (2013)

Yamada, T., Kawai, M., Zhang, P.: Development of hybrid heat pump system utilizing solar energy. Trans. Jpn. Soc. Mech. Eng. Part B. **78**, 430–434 (2012)

Zafar, S., Dincer, I.: Thermodynamic analysis of a combined PV/T-fuel cell system for power, heat, fresh water and hydrogen production. Int. J. Hydrogen Energy. **39**(19), 9962–9972 (2014)

Technical and Economic Prefeasibility Study of Mini-Hydro Power Plants in Venezuela Case Study: El Valle River

Victor Trejo, Gabriela Diaz, and Luis Rojas-Solorzano

1 Introduction

Venezuela's income derives almost exclusively from oil exports, and it is one of the few countries favored with both large amounts of fossil fuels and important renewable resources. According to statistics from the International Energy Agency (2013), 68.5% of the country's internal electricity consumption is produced by hydroelectric power plants, and the rest is covered by thermoelectric generation (Ministerio del Poder Popular para la Energía Eléctrica 2013). However, over 87% of the hydroelectric production comes from a single source, the Simón Bolívar Hydroelectric Central, which ranks as the fourth largest in the world, and no investments in small hydroelectric power are scheduled. Investments in thermoelectric power generation are instead currently being carried out. At this moment, Venezuela is also the country with the largest CO_2 generation per capita in Latin America (IEA 2013). This situation, along with typical highly competitive international fuel prices that otherwise would increase internal revenues received from oil exports, extremely needed to fund education and social programs, makes Venezuela the perfect example in the study of renewable energies. Recent changes in oil prices introduced uncertainty in the described scenario.

The RETScreen® V.4 software (RETScreen® International 2004) is a widespread clean energy project analysis tool that facilitates the execution of prefeasibility and feasibility analyses. Several different types of projects have

V. Trejo (✉) • G. Diaz
Simón Bolívar University, Department of Energy Conversion and Transport, Sartenejas, Caracas 1080, Venezuela
e-mail: victormanueltn@gmail.com

L. Rojas-Solorzano
Nazarbayev University, Faculty, Department, Institute, Astana 010000, Kazakhstan

© Springer International Publishing AG, part of Springer Nature 2018

F. Aloui, I. Dincer (eds.), *Exergy for A Better Environment and Improved Sustainability 2*, Green Energy and Technology,
https://doi.org/10.1007/978-3-319-62575-1_50

been studied with this tool, a few examples of which are the comparison between landfill gas and waste incineration for power generation in Ghana (Anaglate et al. 2012), the evaluation of prospects of wind farm development in Algeria (Himri et al. 2009) and an environmental, technical, and financial feasibility study of solar power plants in Iran (Hajiseyed Mirzahosseini and Taheri 2012) and the assessment of the prediction capacity of wind-electric generation models (Romero and Rojas-Solórzano 2014) to just name a few.

In this work, the technical and economic feasibility of the installation of a mini-hydroelectric power plant on El Valle River in Venezuela is assessed, which is supported by RETScreen® software. This chapter is organized as follows: In the first two sections, technical and economic feasibility studies and their results are described in detail. Special attention is paid to modeling Venezuela's energy and economic scenario to assess the viability of the project under these circumstances. Sensitivity and risk analysis complement the prefeasibility study and are presented in Sect. 3. In Sect. 4, the CO_2 emission analysis is described. Finally, conclusions are drawn.

2 Technical Analysis

2.1 Installation Site and Type of Power Plant

The El Valle River in the Los Salias Municipality of the Miranda State, Venezuela, was chosen for this study. The river, along with the streams Cují and El Indio, feed the La Mariposa reservoir. The water from the reservoir flows by gravity into the La Mariposa water purification facility, which, according to Hidrocapital (2013), the company in charge of its operation, has a maximum capacity of 4.3 m^3/s and provides drinking water to 80% of Los Altos' Mirandinos community and 15% of Caracas, Venezuela's capital city. In order to minimize investment costs and the effect on the environment, the installation of a run-of-the-river hydroelectric power plant was chosen.

2.2 Evaluation of Hydric Resource

The estimate of usable flow was based on hydrological data provided by Venezuela's National Institute of Meteorology and Hydrology (INAMEH). The data comprised monthly average, minimum, and maximum flows in the El Valle River during the period 1978–1991 measured at El Valle in la Mariposa hydrological station. With this information, the flow-duration curve in Fig. 1 was prepared. In accordance with the type of power plant (run-of-the-river) and turbine selection, a flow of 1.25 m^3/s exceeding 97.7% was set as design flow for the power plant.

For estimating the available hydraulic head, the computational tool Google Earth was employed. This tool is capable of providing the elevation profile along

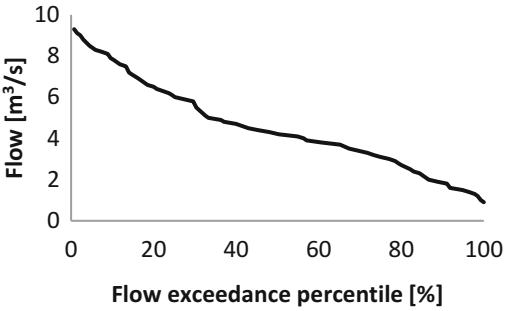

Fig. 1 Flow-duration curve of El Valle River

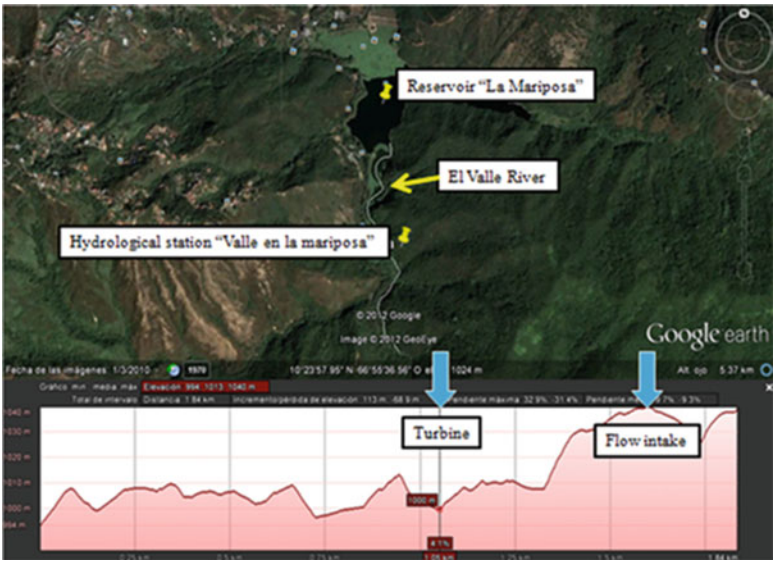

Fig. 2 Elevation curve along the El Valle River (Google Earth 2012)

a trajectory drawn by the user on a satellite view of the terrain. A trajectory along the El Valle River was traced in order to estimate the hydraulic head. The resulting elevation profile is shown in Fig. 2 with two arrows indicating possible positions for the flow intake and the turbine. The section limited by these two positions has a horizontal length of 0.55 km and a hydraulic head of 40 m.

2.3 Turbine Selection

Based on the available flow and head, a Francis turbine emerged as the most appropriate unit (Minicentrales hidroeléctricas - Manual de energías renovables 2006). A 405-kW turbine along with its accessories (generator, governor, excitation

Table 1 Key characteristics of selected turbine

Turbine features	
Max head	42 m
Design head	40 m
Runner diameter	0.5 m
Design flow	1.25m^3/s
Unit output	405 kW
Turbine efficiency	89%
Generator efficiency	92.5%
Frequency	60 Hz

system, main inlet valve, spare parts, and special tools) was chosen from the catalogue of a manufacturer, and its characteristics are summarized in Table 1.

The annual production of energy was estimated taking into consideration the operating conditions of the turbine, its type and flow-duration curve, a typical power curve, and the generator–turbine efficiencies. The obtained projected annual energy is 3121 MWh, which shows that the El Valle River is adequate for the installation of a mini-hydroelectric power plant.

3 Economic Analysis

The economic prefeasibility analysis was carried out in the RETScreen® V.4 software. Electricity prices in Venezuela are very low since they are subsidized by the government, which means that investing in electricity generation is not profitable for any private entity unless some sort or arrangement is agreed upon with the authorities. Therefore, the study was carried out from the perspective that the only possible investor is the Venezuelan Government, for whom the investment may be beneficial in the sense that it opens up the opportunity for substituting thermoelectric generation and exporting the fuels that would have been otherwise consumed. The modeling of the project is described in detail in this section.

3.1 Value of the Produced kWh

Electricity prices in Venezuela (Ministerios de la Producción y del Comercio y de la Energía y Minas 2013) has been subsidized under regulation since 2002 as indicated by the official gazette from April 3 (2002) and do not reflect inflation rates (Banco Central de Venezuela 2012). For this reason, using the commercialization price of electricity as the value of the produced kWh underestimates greatly the economic impact of any generation project in the country. Since Venezuela is an oil producer and exporter, each kWh produced via renewable energies translates into a

kWh that is not produced in thermoelectric power plants and can thus be exported at considerably higher international rates.

The investment in renewable sources of energy competes directly with the ongoing expansion of Venezuela's thermoelectric installed capacity. More specifically, hydroelectric power currently competes with power generation with gasoil (diesel); according to Venezuela's Centro Nacional de Despacho (2010), generation with fueloil and natural gas decreased by 0.57% and 6.77%, respectively, in 2010 with respect to 2009, while generation with gasoil increased by 25.4%. Therefore, the value of the saved kWh was set to $242/MWh according to gasoil prices reported by the IEA (2012) for the date of the modeling and after considering the efficiency of a typical diesel power plant according to the US Energy Information Administration (2013).

3.2 Financial Parameters

A project life of 50 years was considered since hydroelectric power plants can operate for over 50 years without major overhauls. A yearly average escalation rate for gasoil was calculated with available data corresponding to the period 2007–2014 and an average US inflation rate was calculated with data corresponding to the period 1980–2010 (Index Mundi 2014). The obtained value of the former is 1.1% and for the latter 2.6%. For the discount rate, a value of 10% was chosen, which corresponds to a typical return value of Venezuelan US$ bonds.

3.3 Costs

The costs of the selected turbine and related equipment are detailed in Table 2 and add up to a total of US$104,000, which represents the highest portion of the initial costs.

The costs of the feasibility study, development, and engineering were estimated as 10% of the equipment and civil work costs, and equal to 8.4% of the initial costs. As reported by the Instituto para la Diversificación y Ahorro de Energía (2006), civil works for a hydroelectric power plant typically represent 40% of the initial

Table 2 Costs of turbine and related equipment

Equipment	Cost [US $]
Turbine	38,000
Generator	25,000
Governor	17,000
Excitation system	12,000
Main inlet valve	6000
Spare parts and special tools	6000

Table 3 Salaries of staff during construction and start-up

Quantity	Position	$/month	Total
1	Supervisor	2400	2400
2	Engineers	1860	3720
3	Technicians	1290	3870
3	Manual workers	1000	3000
1	Operator	1290	1290
	Complete staff (3 months)	$40,260	

Table 4 Economic indicators of the project's profitability

Indicator	Value
Internal rate of return	280.30%
Payback period	0.4 years
Net present value	US$7992008
Equivalent annual savings	US$804050
Benefit-cost ratio	30.77

costs. This is a conservative value for a run-of-the-river installation, and it is meant to account for any contingencies. Transportation fees for the equipment were calculated as $10,000, near 10% of the equipment costs.

Three months was estimated as the time necessary for the construction and start-up of the power plant. It was estimated that during this period, two engineers, three technicians, and three manual workers would be required. Additionally, the turbine provider demands a supervisor, and the future operator of the power plant would require training during this period. The costs associated to the described personnel are detailed in Table 3. The salary of the supervisor is fixed by the provider, while the rest of the salaries were calculated based on Venezuela's labor market (Gonzalez 2012).

3.4 Results of the Prefeasibility Study

The economic indicators resulting from the prefeasibility analysis carried out are summarized in Table 4.

As the resulting economic indicators show, the herein described project would be highly profitable, the investment of which would be recovered rather quickly (1.1 years) and that would produce benefits during its complete lifetime. The study shows a very high internal rate of return (280.30%), which is quite superior to the discount rate (10%). Figure 3 shows the growth of the net present value in the cumulative cash flow during the project's lifetime. The benefit–cost ratio indicates that for each dollar invested, $30.77 will be gained including all expenditures, which equates to $804,050 as annual savings.

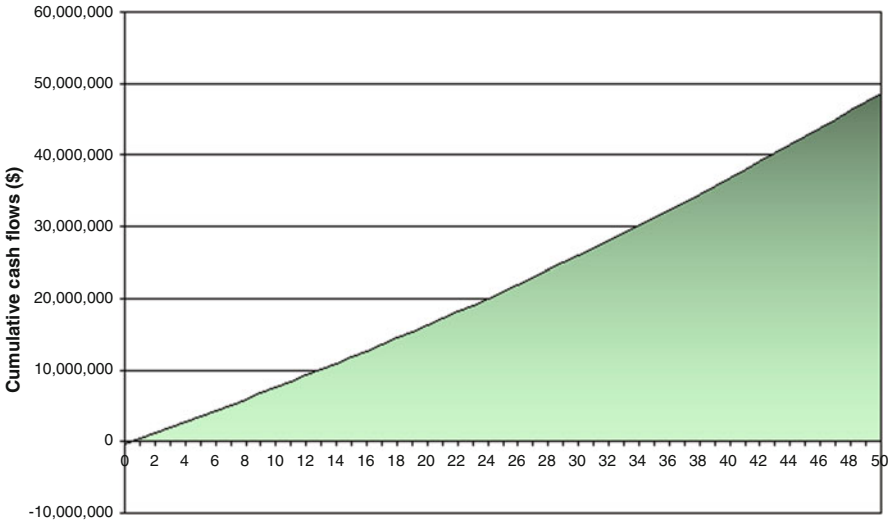

Fig. 3 Cumulative cash flow

Table 5 Results of sensitivity analysis

	Relative impact (−)		
Parameter	Internal rate of return	Payback period	Net present value
Gasoil price	0.8	−0.8	1
Initial costs	−0.55	0.6	>−0.1
Operation and maintenance costs	>−0.1	<0.1	>−0.1

3.5 Risk Analysis

The economic gains of the project are achieved through gasoil savings and sales. Fuel prices are difficult to predict since they depend heavily on international politics. For these reasons, it is especially important to assess the possible impact of a decrease in the price of gasoil on the profitability of the project. Sensitivity and risk analyses were carried out.

In the sensitivity analysis, the effects of possible variations of initial costs, maintenance costs, and the price of gasoil (modeled as the electricity export rate) on the internal rate of return, the net present value, and the payback period were considered. Results are summarized in Table 5 and show that the most influential factor is the price of gasoil followed by the initial costs. The price of gasoil has a strong influence on all three economic indicators, while the initial costs impact the internal rate of return and the payback period mostly. The operation and maintenance costs do not show an important relative impact.

Table 6 Risk analysis for the internal rate of return

Price of gasoil variation [%]	Initial costs variation [%]				
	−50	−25	0	25	50
−50	274%	183%	138%	110%	92%
−25	417%	278%	209%	167%	140%
0	559%	373%	280%	224%	187%
25	702%	468%	352%	282%	235%
50	845%	564%	423%	339%	282%

Table 7 Risk analysis for payback period

Price of gasoil variation [%]	Initial costs variation [%]				
	−50	−25	0	25	50
−50	0.4	0.5	0.7	0.9	1.1
−25	0.2	0.4	0.5	0.6	0.7
0	0.2	0.3	0.4	0.4	0.5
25	0.1	0.2	0.3	0.4	0.4
50	0.1	0.2	0.2	0.3	0.4

Following the results of the sensitivity analysis, the influence of the price of gasoil and the initial costs on the profitability of the project were quantified with the risk analysis. A wide sensitivity range of 50% was considered for both factors, that is, scenarios that combined variations of each factor ranging from 50% to 150% of the original values were considered. The results of the risk analysis are shown in Tables 5 and 6 for the internal rate of return and payback period, respectively.

An increase of 50% in the initial costs and a decrease of 50% in the price of gasoil result in the worst-case scenario: an internal rate of return of 92% and a payback period of 1.1 years. These are less attractive but still very profitable indicators, which shows that, even though the project is very sensitive to variations in initial costs and the price of gasoil, it can still be profitable when facing very unfavorable scenarios such as recent changes in oil price, as long as the gap between gasoil production costs and its sale price remains wide enough (Table 7).

4 Emission Analysis

Due to the high demand that the Venezuelan electrical network has been experiencing since the energy crisis of 2009, new thermoelectric plants have been installed along the Venezuelan territory in the recent years.

With the installation of the mini-hydropower plant in the El Valle River, it is possible to contribute to the relief of the already existing network.

Since the electric grid is overloaded, the proposed mini-hydropower plant would displace the thermoelectric power plants that are to be installed likewise

contributing to reduce the fuel consumption required for the operation of these new thermoelectric plants, and thus the greenhouse gases emissions. To determine the amount of emissions that would be reduced with the proposed project, an analysis of emissions was performed.

The resulting savings in greenhouse gases emission resulting from this study is 3079 t of equivalent CO_2 per year. Some equivalent measures to better visualize this benefit may be considered: 3079 t CO_2 are equivalent to removing 564 automobiles from circulation, to avoid consuming 7160 barrels of gasoline, or 1,322,961 l of gasoline per year.

5 Conclusions

A technical and economic prefeasibility study of the installation of a mini-hydroelectric power plant on the El Valle River in Venezuela was carried out. The technical prefeasibility study showed that the El Valle River reunites the necessary characteristics for the installation of a run-of-the-river hydroelectric power plant.

The economic prefeasibility study was carried out from the perspective that, taking Venezuela's very particular energy and economic characteristics into consideration, the national government is the only possible investor. The results of the study show very attractive economic indicators, such as a 280.3% internal rate of return, a 0.4 years payback period, and a 30.77 benefit–cost ratio.

Sensitivity and risk analyses demonstrated that, even when facing highly unfavorable variations in gasoil prices and initial costs, the project can still be profitable. The emission analysis' results indicate possible annual reductions of greenhouse gases emissions equivalent to 3079 t CO_2.

The profitability of the project, as well as its environmental advantages, is enhanced by the fuel savings and possible export. Both economic and environmental attractiveness of the installation of the mini-hydroelectric power plant are strongly reinforced by Venezuela's current energy and economic characteristics. In this sense, the positive results of the study are an indication that clean energy could find very fertile scenarios in countries such as Venezuela, where the advantages of their application may not be evident.

References

Anaglate, S.A., Rahmaputro, S., Ruiz, C., Rojas-Solórzano, L.R.: Comparison between landfill gas and waste incineration for power generation in Accra, Ghana. Int. J. Environ. Sci. Eng. Res. **3**, 1–7 (2012)

Banco Central de Venezuela: Banco Central de Venezuela – Indicadores. [Online]. Available at: http://www.Bcv.Org.Ve/c2/indicadores.Asp (2012). Accessed 10 Nov 2012

Centro Nacional de Despacho: Scribd. [Online]. Available at: http://es.Scribd.Com/doc/58926153/Comentarios-Centro-Nacional-de-Despacho-Informe-2010 (2010). Accessed 5 Nov 2013

Google Earth. El Valle River satellite view 10°23′57.95N 66°55′36.56O, elevation 1024M. [Online]. Available: http://www.Google.Com/earth/index.Html (2012). Accessed Nov 2013

González, D.: Revista económica de Venezuela. [Online]. Available at: http://revistaeconomicadevenezuela.Blogspot.Com/2011/04/salario-nominal-en-venezuela-1999-2011.Html (2012). Accessed 10 Nov 2012

Hajiseyed Mirzahosseini, A., Taheri, T.: Environmental, technical and financial feasibility study of solar power plants by RETScreen, according to the targeting of energy subsidies in Iran. Renewable Sutainable Energy Rev. **16**(5), 2806–2811 (2012)

Hidrocapital. Hidrocapital. [Online]. Available at: http://www.Hidrocapital.Com.Ve/internet/index.Php?Option=com_content&view=article&id=162:plantas-de-tratamiento-ii&catid=7:nuestras-plantas-de-tratamiento&Itemid=45 (2013). Accessed 13 Nov 2013

Himri, Y., Boundghene Stambouli, A., Draoui, B.: Prospects of wind farm development in Algeria. Int. J. Sci. Technol. Desalting Water Purif. **239**(1–3), 130–138 (2009)

Index Mundi: United States Inflation rate (consumer prices) - Economy [Online]. Available at: http://www.indexmundi.com/united_states/inflation_rate_(consumer_prices).html (2014). Accessed 10 January 2014

Instituto para la Diversificación y Ahorro de Energía: Minicentrales hidroeléctricas – manual de energías renovables. In: Madrid: s.N., p. 53 (2006)

International Energy Agency: International energy Agency. [Online]. Available at: http://www.Eia.Gov/petroleum/gasdiesel/ (2012). Accessed 2 July 2012

International Energy Agency: [Online]. Available at: http://www.Iea.Org/statistics/statisticssearch/report/?&country=VENEZUELA&year=2011&product=ElectricityandHeat (2013). Accessed 5 Nov 2013

Ministerio del Poder Popular para la Energía Eléctrica: Ministerio del Poder popular para la Energía Eléctrica. [Online]. Available at: http://mppee.Gob.Ve/inicio/guriinfo (2013). Accessed 5 Nov 2013

Ministerios de la Producción y del Comercio y de la Energía y Minas. Universidad del Zulia. [Online]. Available at: http://www.Arq.Luz.Edu.Ve/personales/rcuberos/cursos/postgrado/servicios/documentos/normas/gacetatarifaselectricas.Pdf (2002). Accessed 5 Nov 2013

RETScreen® International: Clean energy project analysis: RETScreen® Engineering & Cases Textbook. Canada: s.n. 9 (2004)

Romero, M.N., Rojas-Solórzano, L.R.: Assessment of the prediction capacity of a wind-electric generation model. Int. J. Renewable Energy Biofuels. **2014**, 1–16 (2014)

U.S. Energy Information Administration: EIA. [En línea]. Available at: http://www.eia.gov/tools/faqs/faq.cfm?id=107&t=3 (2013). Accessed 12 Nov 2013

A Study of the Effects of the External Environment and Driving Modes on Electric Automotive Air-Conditioning Load

Yew Khoy Chuah and Yu-Tsuen Chen

1 Introduction

According to the International Energy Agency (IEA) (2013) the oil consumption of OECD countries in the first quarter of 2013 amounts to 46 million barrels per day, a reduction of 200 thousand barrels with respect to the same period in 2012. However, there was an increase of 1.3 million barrels per day for non-OECD countries, up to about 44 million barrels per day.

The above figures clearly state the problem of our ever-increasing need for oil. Material needs in all aspects of comfortable modern life that are a consequence of economic growth will further aggravate our ever-growing need for energy. Inevitably the global warming problem resulting from the increasing atmospheric concentration of CO_2 is becoming worse each year.

Of all sectors of our lives, the internal combustion engine automobile is one of the largest sources of CO_2 emission. Hence electric-powered or hybrid-powered vehicles are seen to be a solution to reducing the need for oil. Conventional automobile air conditioning is powered by coupling to the engine. The air-conditioning system for hybrid- or electric-powered vehicles has to be electric powered. In addition, intelligent control adapted to driving modes is needed to reduce the power consumption and prolong the driving range. Therefore optimization of energy efficiency by control strategies is imperative. However, energy saving that does not affect driving thermal comfort has to be achieved.

Nakane et al. (2010) found that when all driving modes are considered, an air-conditioning system may reduce the driving range by one-half. Factors

Y.K. Chuah (✉) • Y.-T. Chen
Department of Energy and Refrigerating Air-Conditioning Engineering, National Taipei University of Technology, 1, Sec. 3, Zhongxiao E. Road, Taipei 10608, Taiwan
e-mail: yhtsai@ntut.edu.tw

© Springer International Publishing AG, part of Springer Nature 2018

F. Aloui, I. Dincer (eds.), *Exergy for A Better Environment and Improved Sustainability 2*, Green Energy and Technology,
https://doi.org/10.1007/978-3-319-62575-1_51

considered in their research included the external environment, driving mode such as idling or moving, solar radiation angles, etc., that would greatly affect the cooling load. They also suggested that intelligent energy saving control would elevate energy management and greatly prolong the driving time without comprising thermal comfort.

Makino et al. (2003) suggested that a commercial compact scroll compressor can be used in electric vehicles. In comparison, it is smaller in size and has higher energy efficiency. Hosoz and Direk (2006) evaluated the use of a four-way valve so to provide heating in winter. They found that the heat exchanger has to be redesigned to achieve effective heating.

Brown (2009) compared the use of a new low GWP HFO refrigerant to the current R134a applied to automobiles. Although HFO refrigerant has thermal properties close to those of R134a, he suggested that more information is needed for further evaluation. Lee and Jung (2012) compared R1234yf to R134a under the same operating experimental conditions and found that R1234yf had a lower cooling capacity.

Alkan and Hosoz (2010) found that when the condenser fan of an automobile's air conditioner has variable speed control, variable speed compressor will perform better than that of a constant speed compressor.

2 Cooling Load Computation

Air-conditioning load is fundamental to the design and selection of equipment. A cooling computation model is proposed in this paper. In the proposed model, vehicle cooling load calculation is based on inputs of ambient air temperature, wind speed, solar radiation, driving mode, and passenger metabolism heat, among other things. The calculation also considers the vehicle's shell structure and materials, radiation angle at the glass, low-e glass application, occupancy, and outdoor air. Heat conduction, convection, and radiation are all considered in the model. Radiation transmitted through the large glass area with respect to the different incidence angles was considered in the model. The model allows for part of the glass having low emissivity coating as for most vehicles sold in Taiwan. For heat conduction through the body of the vehicle, an effective temperature was used instead of outdoor air temperature to account for solar radiation effects. A prediction of the external car body temperature was also made.

The total cooling load of an automobile can be calculated using Eq. (1), which is also shown schematically in Fig. 1.

$$Q_{\text{total}} = Q_{\text{solar}} + Q_{\text{cond}} + Q_{\text{fresh}} + Q_{\text{inside}} \tag{1}$$

Q_{total}: heat removed from inside an automobile (W)
Q_{solar}: Solar radiation through glass (W)
Q_{cond}: Heat conduction into automobile(W)

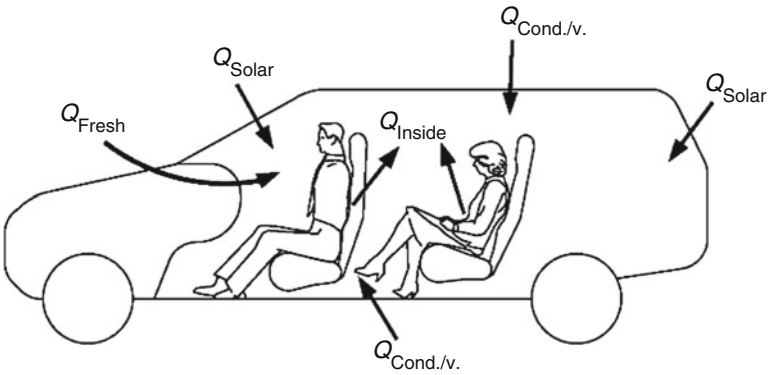

Fig. 1 Cooling load considered in the analysis

Q_{fresh}: Treating outdoor air to inside conditions (W)
Q_{inside}: Internal heat due to passengers and others (W)

2.1 *External Convective Transfer Coefficient* $\mathbf{h}_o$

Heat convection between the external automobile surface and ambient air was considered in the analysis. In this study natural convection due to temperature difference was also considered. Heat transfer coefficients were calculated by referring to chapter 4 of the ASHRAE Handbook-Fundamentals (2009a).

2.2 *Transmitted Solar Radiation* $\mathbf{Q}_{Solar}$

Automobiles with a large glass area transmitting solar radiation have a major source of air-conditioner load. The direct solar heat is affected by the transmittance, reflectivity, and absorptivity of the glass material or coating on it. Moreover, the glass thickness and solar incidence angle are also important factors to consider, as stated in chapter 14 of the ASHRAE Handbook-Fundamentals (2009b). The transmitted solar radiation can be calculated as shown in Eq. (2).

$$Q_{\text{Solar}} = \sum [T_{\text{b}} \text{E}_{\text{t,b}} + T_{\text{d}} (\text{E}_{\text{t,d}} + \text{E}_{\text{t,r}})] A_{\text{g}} \tag{2}$$

T_b: Solar direct transmittance, fraction
T_d: Solar diffuse transmittance, fraction
$E_{t,b}$: Solar direct intensity (W.m^{-2})
$E_{t,d}$:Solar diffuse intensity (W.m^{-2})

$E_{t,r}$: Surface reflectance (W.m^{-2})
A_g: Glass area (m^2)

There are some cases where the glass area has a coating to isolate some solar radiation. Normally the isolation effect can be as high as 65%. Therefore for a glass area with isolation coating Q_{solar} has to be revised, as in Eq. (3).

$$Q'_{solar} = Q_{solar}\,(1 - \text{isolation}) \tag{3}$$

2.3 *Heat Conduction* $Q_{Cond./v.}$

When the shell structure of an automobile is exposed to outside conditions, the external surface temperature is substantially higher than that of the internal surface. The external surface temperature is affected by solar radiation, outside air temperature, and driving speed. The glass area can be assumed to have a low thermal mass. However, for an opaque shell, heat conductivity has to be considered in the calculation. Moreover, the inside and outside convective heat resistance also has to be considered.

To simplify the computation the internal convective resistance is taken to be a constant value. The conduction calculation begins with the external surface temperature, therefore only internal convective resistance is considered. The calculation of heat conduction and the overall heat transfer coefficient U are calculated by Eqs. (4) and (5). In Eq. (5) ra is the resistance of the air gap in the automobile shell structure and t_{set} is the air-conditioning temperature set.

$$Q_{cond} = \sum UA(t_{es} - t_{set}) \tag{4}$$

$$\mathrm{U} = \frac{1}{\sum d_j/k_j} + \mathrm{ra} + 1/h_i \tag{5}$$

2.3.1 External Surface Temperature T_{es}

As shown in Fig. 2, the solar heat absorbed would partly be transmitted into the inside, but also partly reradiated or convected to the outside air. As can be seen in Eq. (6), heat conduction is balanced by three heat transfer mechanisms.

$$q''_{conduction} = q''_{solar} + q''_{convection} + q''_{radiation} \tag{6}$$

$q''_{conduction}$: Heat conduction flux (W.m^{-2})
q''_{solar}: Absorbed solar flux (W.m^{-2})
$q''_{convection}$: Heat convection flux (W.m^{-2})
$q''_{radiation}$: Radiation flux (W.m^{-2})

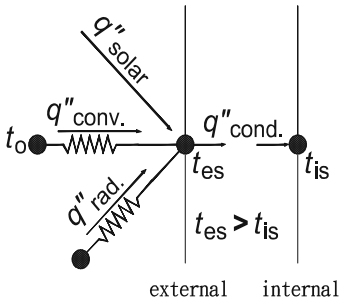

Fig. 2 Heat balance calculation Scheme

A. Absorbed solar flux q''_{solar}.

(a) *Opaque part calculated using* Eq. (7):

$$q''_{\text{solar}} = \varepsilon(E_{\text{t,b}} + E_{\text{t,d}} + E_{\text{t,r}}) \tag{7}$$

(b) *Clear part:*

For part with no isolation coating using Eq. (8):

$$q''_{\text{solar}} = \varepsilon^{\text{f}}_{1,\text{b}} E_{\text{t,b}} + \varepsilon^{\text{f}}_{1,\text{d}}(E_{\text{t,d}} + E_{\text{t,r}}) \tag{8}$$

Without isolation coating using Eq. (9):

$$q''_{\text{solar}} = \left[\varepsilon^{\text{f}}_{1,\text{b}} E_{\text{t,b}} + \varepsilon^{\text{f}}_{1,\text{d}}(E_{\text{t,d}} + E_{\text{t,r}})\right]\left(1 - \varepsilon^{\text{f}}_{2}\right) + E_{\text{t}}\varepsilon^{\text{f}}_{2} \tag{9}$$

ε: Radiation absorptivity
$\varepsilon^{\text{f}}_{1,\text{b}}$: Direct radiation absorptivity
$\varepsilon^{\text{f}}_{1,\text{d}}$: Diffuse radiation absorptivity
$\varepsilon^{\text{f}}_{2}$: Isolation coating effect, 0.65 for absorption type, 0.35 for reflective type

B. External convection $q''_{\text{convection}}$ using Eq. (10):

$$q''_{\text{convection}} = h_o(t_{\text{o}} - t_{\text{es}}) \tag{10}$$

h_{o}: External convection coefficient ($\text{W.m}^{-2}.\text{K}^{-1}$)
t_{o}: External temperature (K)

C. The solar radiative heat gain $q''_{\text{radiation}}$can be calculated using Eqs. (11, 12, 13, 14, 15, and 16):

$$q''_{\text{radiation}} = h_{\text{r,g}}\left(t_{\text{g}} - t_{\text{es}}\right) + h_{\text{r,sky}}\left(t_{\text{sky}} - t_{\text{es}}\right) \tag{11}$$

$$h_{\text{r,g}} = \varepsilon\sigma\left[\frac{F_{\text{s-g}}\left({t_{\text{g}}}^4 - {t_{\text{es}}}^4\right)}{t_{\text{g}} - t_{\text{es}}}\right] \tag{12}$$

$$h_{\text{r,sky}} = \varepsilon\sigma\left[\frac{F_{\text{s-sky}}\left({t_{\text{sky}}}^4 - {t_{\text{es}}}^4\right)}{t_{\text{sky}} - t_{\text{es}}}\right] \tag{13}$$

$$F_{\text{s-g}} = \frac{1 - \cos\alpha}{2} \tag{14}$$

$$F_{\text{s-sky}} = \frac{1 + \cos\alpha}{2} \tag{15}$$

$$t_{\text{sky}} = t_o - 6\cos\frac{\alpha}{2} \tag{16}$$

$H_{\text{r,g}}$: Surface to ground radiation transfer coefficient ($\text{Wm}^{-2}\,\text{K}^{-1}$)
$H_{\text{r,sky}}$: Surface to sky radiation transfer coefficient ($\text{Wm}^{-2}\,\text{K}^{-1}$)
t_{g}: Ground surface temperature (K)
t_{sky}: Effective sky temperature (K)
ε: Surface long wave emissivity
σ: Stefan-Boltzmann constant, 5.67×10^{-8} $\text{W.m}^{-2}.\text{K}^{-4}$
$F_{\text{s - g}}$: Surface to ground view angle factor
$F_{\text{s - sky}}$: Surface to sky view angle factor
α: Surface inclination angle relative to the normal

t_{es} can be calculated by substituting Eqs. (7), (10) and (11) into (6) to obtain Eq. (17).

$$t_{\text{es}} = \frac{Ut_{\text{set}} + aG_{\text{t}} + h_{\text{o}}t_{\text{o}} + h_{\text{r,g}}t_{\text{g}} + h_{\text{r,sky}}t_{\text{sky}}}{U + h_{\text{o}} + h_{\text{r,g}} + h_{\text{r,sky}}} \tag{17}$$

Iteration is required in the computation as $h_{\text{r,g}}$, $h_{\text{r,sky}}$ and h_{o} (for natural convection) are determined based on the external surface temperature.

2.4 Outdoor Air-Cooling Load, Q_{Fresh}

Outdoor air ventilation is required to maintain the air quality inside an automobile. The outdoor air has to be treated to meet thermal comfort conditions. The cooling load due to fresh air ventilation can be calculated using Eq. (18).

$$Q_{\text{fresh}} = Q\rho_{\text{air}} n_p (h_{\text{out}} - h_{\text{in}}) \tag{18}$$

Q: Minimum air volume per person as given in ASHRAE standard 62.1 (2004) and can be set at 0.15 $m^3 min^{-1} person^{-1}$.
ρ_{air}: Air density, taken as 1.2 kg/m^2
N_p: Number of passengers
h: Air enthalpy ($kJ.kg^{-1}$)

2.5 *Heat Gain Due to Passengers, Equipment, and Lighting,* Q_{inside}

$$Q_{\text{Inside}} = Q_{\text{human}} + Q_{\text{equ.}} + Q_{\text{light}} \tag{19}$$

Components of Eq. (19) are described below:

Q_{human}: 115 W × number of person
Q_{equ}: Include fan motor, GPS, stereo, electric equipment, estimated at 638 W
Q_{light}: Taken to zero at day time

3 Computation Software Development

Based on the cooling load computation model described above, an Excel-VBA based air-conditioning load calculation tool was developed. The cooling load calculation needs only conditions of ambient environment and the driving mode parameters such as speed and GPS information. With the highest temperature of the day known or predicted, the possible maximum load can be calculated. The design of automotive air conditioning and the control strategy can be performed with the calculation tool to save time and reduce costs. Prediction of the surface temperature of the shell structure can be calculated using the Excel-VBA based tool.

3.1 *Experimental Measurements of Automobile Surface Temperature*

A comparison of the prediction model with actual measurement of the outside shell temperature of a car was conducted. Figure 3 shows a sedan placed outside exposed to the sun. The comparison was made under the actual weather conditions such as temperature, humidity, and wind speed, car heading direction, sky clearness, and ground surface temperature.

Fig. 3 An automobile under test

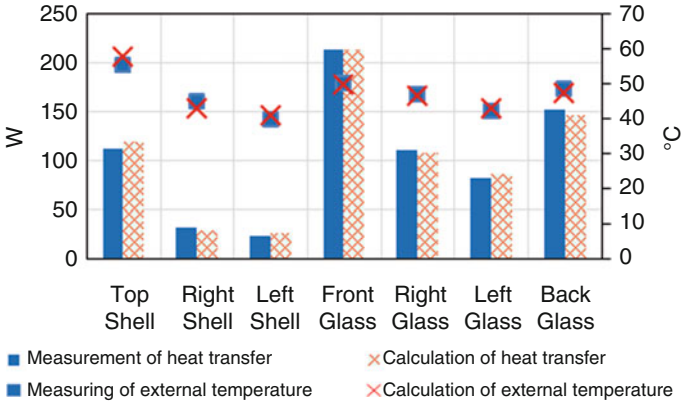

Fig. 4 Comparison of prediction and measurement of surface temperature and heat transfer

The measurements were carried out on a sunny day in 2013 at noon. Other measured data are described below:

1. Ground surface temperature was 60 °C.
2. Ambient air temperature was 32 °C.
3. Ambient air relative humidity was 49%.
4. Ambient air velocity was 1.3 m/s.

In the measurement, the automobile was headed towards south.

3.2 Verification of External Surface Temperature

The comparison between the prediction and the measurement of surface temperature and heat transfer are shown in Fig. 4. Comparison is made between the different glass and opaque areas. It can be seen that the errors for the opaque and glass areas are, respectively, ±2.2 °C and ±1 °C. The largest errors for temperature

and heat transfer are, respectively, 4.5% and ±12%. The average errors for surface temperature and heat transfer are, respectively, 0.34% and 1.07%. As a whole the inner and outside car body temperatures were predicted to an accuracy of ±1 °C.

4 Energy-Saving Potential Analysis

Energy saving has to first satisfy the thermal comfort of the passengers. However, energy saving is critical to the driving range. Air conditioning of electric vehicles is powered by the refrigerant compressor and the fans. This study focuses on the compressor power and the effects of driving modes and the ambient environment. Therefore the analysis presented in this paper reflects an energy saving potential that is closely related to the actual driving modes of electric vehicles.

4.1 Compressor Performance Curves

Figure 5 presents the performance curves of an electric vehicle refrigerant compressor as presented by Hsiao (2011). The compressor curves were used in the analysis of the compressor according to the needs of the air-conditioning capacity. It can be seen that the refrigerating capacity changes with the compressor speed, and compressor power changes with compressor speed. Note also the coefficient of performance (COP) for compressor peak at lower speed. COP peaks at about 4.6 at around 1300 rpm; however, at 3500 rpm COP reduces to about 1.5. Therefore it can

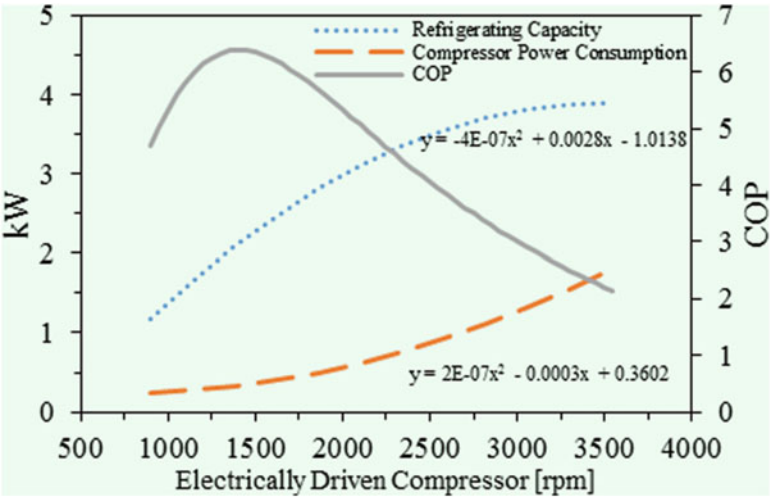

Fig. 5 The performance curves of a compressor

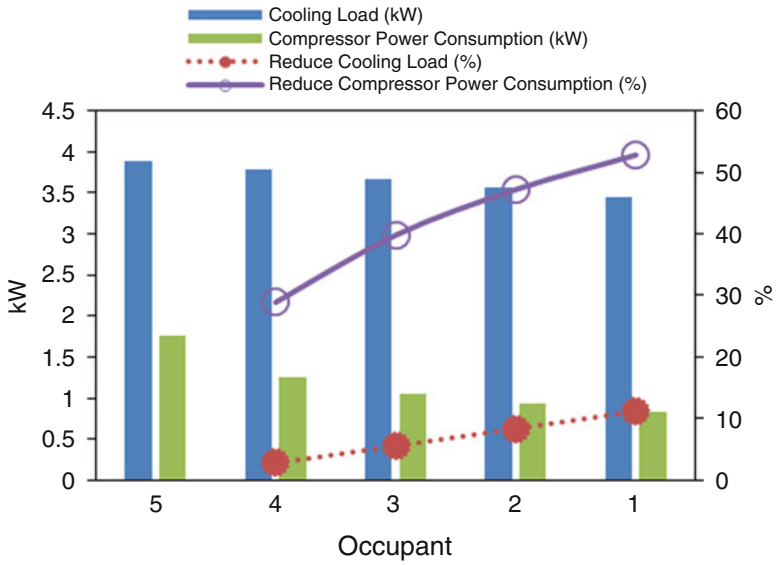

Fig. 6 Compressor energy saving for different numbers of passengers

be seen that the control strategy is key to energy saving for an air-conditioning system for electric vehicles. It is also obvious that the compressor must be kept at a lower speed whenever possible.

4.2 Control Strategy for Passenger Numbers

For vehicles with front and back seat air outlets, air-conditioning can be controlled to meet the actual need. When only the front seats are occupied, only front air outlets are turned on. Moreover, outdoor air supply volume can be controlled according to number of passengers in the car. Figure 6 shows the results of analysis. It can be seen that relative to five passengers, the cooling load can be reduced by about 11.2%. Also compressor power can be reduced by 28.9–52.8% when only one passenger is in the automobile. The high rate of energy saving is feasible, as discussed above, with compressor power being much lower at lower speed and at lower capacity.

4.3 Control Strategy to Meet the Driving Modes

In the course of a day a vehicle will be exposed to different temperature, humidity, and solar radiation conditions. Therefore the air-conditioning load will differ at

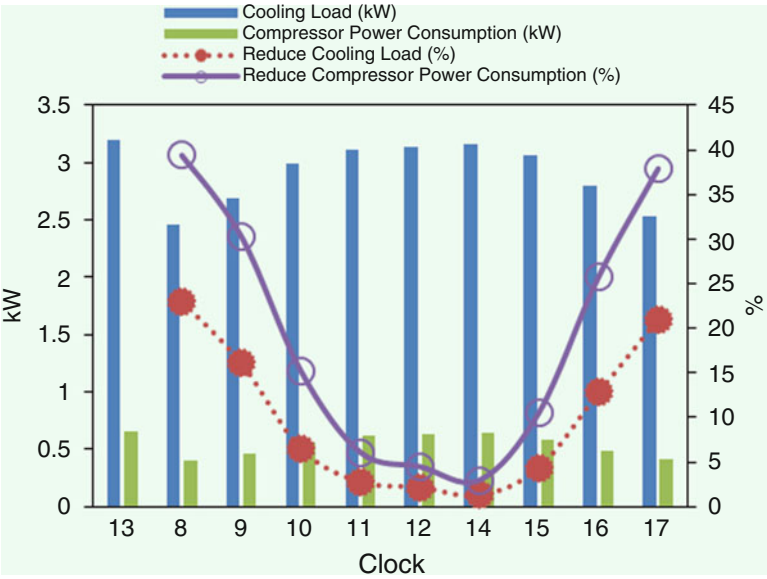

Fig. 7 Compressor power at different times of the day

different times. Figure 7 shows the analysis of the performance at different times of the day. Relative to the peak load that occurs at about 1:00 pm, the compressor power can be reduced by about 3–39% at other times when the compressor speed is controlled according to needs.

4.4 Control Strategy at Different Driving Speeds

The results of the analysis are shown in Fig. 8. It can be seen that cooling is highest when the vehicle is still at 0 km/h. This is due to a higher shell temperature when the car is not moving. A higher driving speed, however, was found to have a smaller cooling load. This is due to convective heat transfer that maintains the shell at a temperature approaching the ambient temperature. The cooling load reduces with speed up to 50 km/h, after that the effects of a lower cooling load are only marginal. It can be seen that the control strategy of compressor speed to meet the cooling load at different car speeds can reduce the compressor power by 44–62% with respect to a speed of 0.0 km/h.

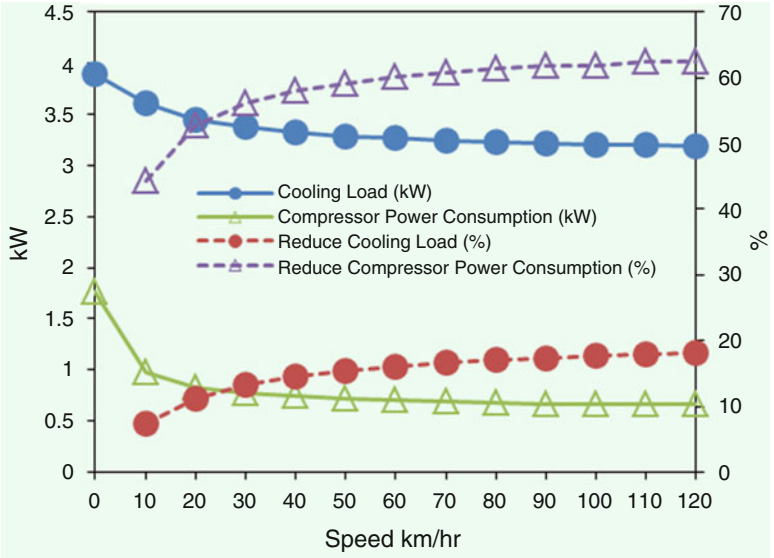

Fig. 8 Compressor at different speeds

4.5 Energy-Saving Analysis for a 1-h Drive

A small size black sedan with five passengers on board was simulated for a ride from 13:00 pm to 14:00 pm in the month of July and with clear skies. The results are shown in Fig. 9. The 1-h drive consists of 10 min of engine idling, 30 min at 30 km/h, and 20 min at 50 km/h. The solar effects were also modelled for each 10-min period. The vehicle was assumed to drive south with an outdoor air temperature and humidity of 33.9 °C and 58% RH, respectively. The temperature and humidity inside the car were set at 23 °C and 55% RH, respectively.

The results of the analysis are also presented in Table 1. It can be seen that for the 1-h driving schedule mentioned above, when the compressor can be controlled to adapt to the air-conditioning needs, energy can be saved by as much as 50.4%.

5 Discussion on Energy Management Adapted to Driving Modes

Energy saving measures for air conditioning are very important for electric- or hybrid-powered vehicles. The driving range of a charged battery can be affected greatly by the air-conditioning needs. In particular, it is necessary to allow air-conditioning control to adapt to different driving modes under different ambient conditions.

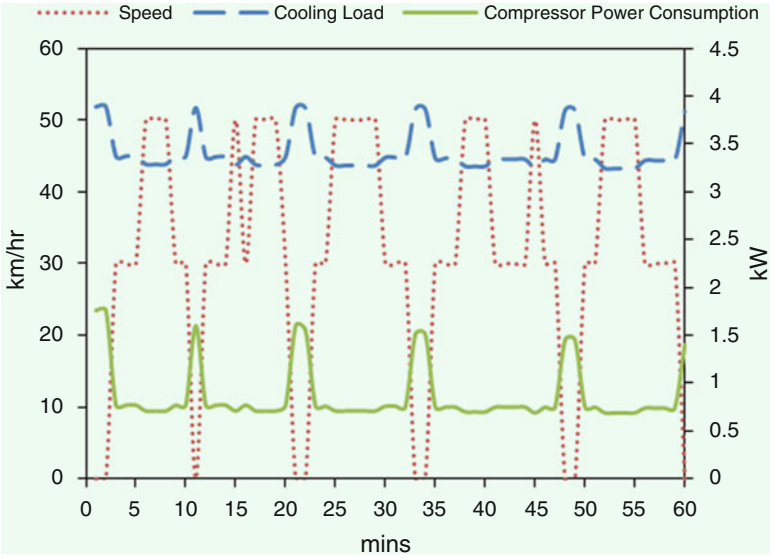

Fig. 9 Analysis of cooling load and compressor power for a 1-h drive

Table 1 Air-conditioning energy analysis for 1 h of driving

Item	Operate at highest load	Control to the cooling need
Driving time (min)	60	60
Cooling need (W)	3887	3243 ~ 3887
Compressor power (kW)	1.76	0.69 ~ 1.76
Energy used (kWh)	1.76	0.87
Energy saving rate relative to operating at highest load (%)	–	50.4

A DC variable speed compressor, electronic expansion valve, and other controls can be used to regulate the power use of automotive air conditioning. The occupants' comfort can be satisfied by multi-air outlets for different seating in a vehicle. It has been shown that compressor power is strongly dependent on compressor speed. Further optimization of the compressor operation matching the cooling capacity could be a control strategy in future research.

6 Conclusion

A cooling-load computation model is proposed in this paper. A comparison of the prediction with the actual measurement has shown the car body's temperatures were predicted to an accuracy of ±1 °C. Optimization of the compressor operation matching the cooling capacity can save compressor power by as much as 52.8%. It was also found that a lighter color car has a lower cooling load. At higher driving speeds convective heat transfer would maintain the car shell at temperatures approaching the ambient temperature and result in lower energy being used. A single drive consists of different driving modes, and when adapting to the air-conditioning needs, energy-saving control can reduce the energy use by 50.4%.

Acknowledgment The support of the National Science Council of Taiwan with project NSC 101-2221-E-027 -047 is gratefully acknowledged.

References

Alkan, A., Hosoz, M.: Comparative performance of an automotive air-conditioning system using fixed and variable capacity compressors. Int. J. Refrig. **33**, 487–495 (2010)

ANSI/ASHRAE Standard 62.1-2004. Ventilation for Acceptable Indoor Air Quality. ASHRAE, Atlanta, USA (2004)

ASHRAE Handbook, Fundamentals, Chapter 4. ASHRAE, Atlanta, USA (2009a)

ASHRAE Handbook, Fundamentals, Chapter 14. ASHRAE, Atlanta, USA (2009b)

Brown, J.: New low global warming potential refrigerants. ASHRAE J. 22–29 (2009)

Hosoz, M., Direk, M.: Performance evaluation of an integrated automotive air conditioning and heat pump system. Energy Convers. Manag. **47**, 545–559 (2006)

Hsiao, P.: A study on refrigerant volume control and energy parameters for electric powered vehicle air-conditioning systems. Master Thesis, National Taipei University of Technology (2011)

IEA. http://iea.org/newsroomandevents/news/2013/february/name,35176,en.html

Lee, Y., Jung, D.: A brief performance comparison of R1234yf and R134a in a bench tester for automobile applications. Appl. Therm. Eng. **35**, 240–242 (2012)

Makino, M., Ogawa, N., Abe, Y., Fujiwara, Y.: Automotive air-conditioning electrically driven dompressor, SAE technical paper series 2003-01-0734 (2003)

Nakane, S., Kadoi, M., Seto, H., Prigain, K.: Air-conditioning system for electric vehicle. JSAE. **64**(4), 35–40 (2010)

Optimization of Energy Cost Seawater Desalinization by Reverse Osmosis: Case of Bousmail Station in Algeria

Souad Bouzid-Lagha and Yacine Matrouh

1 Introduction

The limitation of water resources caused by precipitation shortage and irregularity, to which is added the rapid increase in population's need to drinking water, motivated the Algerian residents to choose seawater desalinization.

The low costs of desalinization, specially reverse osmosis technology, motivated this choice. This decrease is mainly due to progress in energy consumption, which is considered as the main component in the desalinization cost structure.

The aim of this work is the study of a new energy recovery technology in desalinization plants. It relates to a device for transferring the pressure energy of a fluid flow at relatively high pressure to another fluid flow at relatively low pressure, in this case the pressure exchanger (PX).

The main purpose of the study is to explain the method and conditions of the commissioning of this device, the evaluation of its performance in energy gain, and its application in the case of Bousmail desalinization plant using the technology as such as that of El-HAMMA, the first plant used in Algeria.

S. Bouzid-Lagha (✉) • Y. Matrouh
Laboratory of Environment, Water, Geomechanics and Structures (LEEGO), Faculty of Civil Engineering (FGC), University of Sciences and Technologies Houari Boumediene (USTHB) BP. 32, El-Allia, Bab-Ezzouar, 16111 Algiers, Algeria
e-mail: bouzidsouad@yahoo.fr

© Springer International Publishing AG, part of Springer Nature 2018

F. Aloui, I. Dincer (eds.), *Exergy for A Better Environment and Improved Sustainability 2*, Green Energy and Technology,
https://doi.org/10.1007/978-3-319-62575-1_52

2 Seawater Desalination Perspectives

2.1 Water in the World

The saltwater in the world represents 97.5% of the total water volume. This leaves more than 2.5% of freshwater (ice, groundwater, streams, lakes, etc.). Seventy percent of the freshwater glaciers is concentrated in the ice of the polar regions.

It is estimated that 1.4 billion people lack access to safe drinking water and 2.5 billion Others may suffer from lack of water in 2050, caused by the changing demographics and the increase in water consumption in the world .

2.2 Desalination in Algeria

2.2.1 Desalination Advantages in Algeria

Several factors militate in favor of the implementation of this technology in our country, namely:

- A long coastline of 1200 km and a proven availability inexhaustible seawater resource;
- Proximity to the sea of Agricultural and industrial areas large consumer of water.
- A Rapid population growth leading to increased constantly water needs, and along the coast.

2.2.2 Desalination Strategy

To overcome the lack of conventional drinking water resources and meet the domestic needs of over 15 million inhabitants of coastal regions, 43 desalination plants are being finalized. It is expected to reach a total capacity of 2260 million m^3/day, 2.26 billion l/day of desalinated water, from the year 2015 .

3 Desalinization Techniques

All curent installations in use are working with two technologies:

- The évaporation-condensation process based on phase change.
- Membrane processes based on water transport through semi-permeable membranes.

Among the above methods, distillation and reverse osmosis are the most marketed processes in the global market for desalinization. Other techniques have

not experienced significant growth in the area because of the problems usually related energy consumption and/or the amount of investment they require.

Currently, the reverse osmosis (RO) is the process that develops more as compared to other techniques. Its rapid expansion during the past decade is due to:

- The advancement of membrane technology (lower costs, better quality, simple maintenance...).
- The simplified process
- At the Lower energy costs (less than 3 KWh/m^3) which leads to lower cost per m^3 of desalinated water.

4 The Process of Reverse Osmosis

4.1 Definition of the Membrane

The membrane acts as a very specific filter that allows water to pass while retaining suspended solids and other dissolved substances.

4.2 Reverse Osmosis Membrane

In the reverse osmosis membranes are used (Fig. 1):

- Composite polyamide (CAP) spiral (most common)
- Membrane-hollow fiber (triacetate cellulose)

They are characterized by

- Salt rejection: 99.5–99.8%
- The Production by module: 17–32 m^3/day.

4.3 Process of Osmosis

Osmosis is a natural phenomenon that manifests through a semipermeable membrane. Freshwater migrates to the salt one, which is more concentrated. The phenomenon stops upon reaching a pressure (Π), called osmotic pressure (Fig. 2).

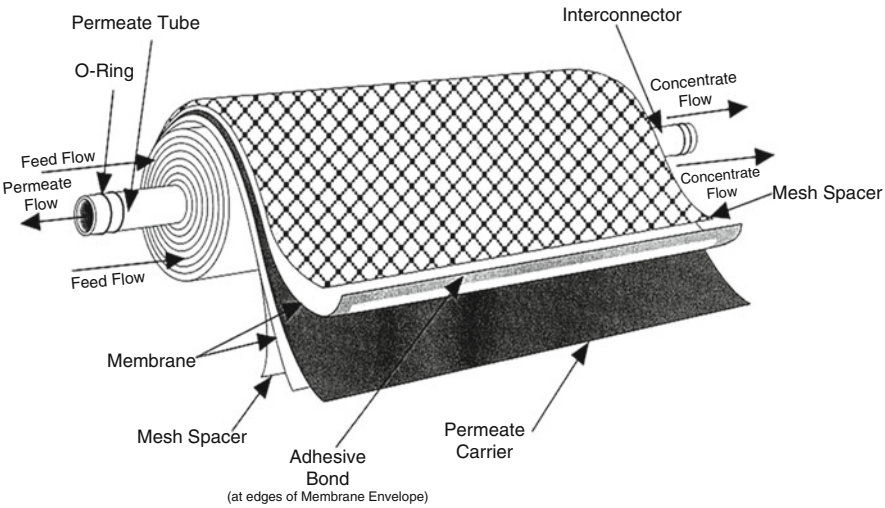

Fig. 1 Spiral membrane module

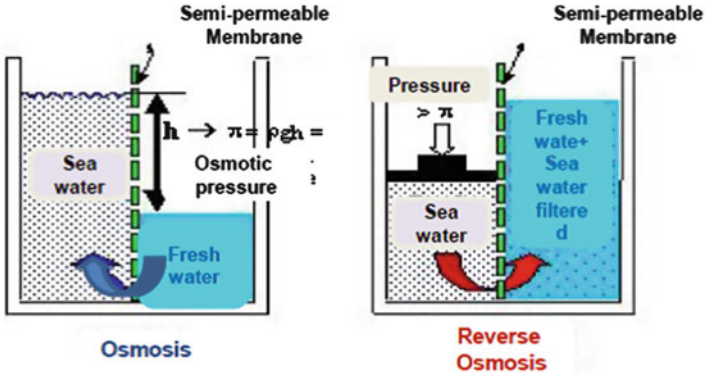

Fig. 2 Process of osmosis and reverse osmosis

4.4 Reverse Osmosis

It is possible to reverse the operation (Fig. 2) by exerting a pressure ($P >> \Pi$) on the saltwater to migrate the water molecules outside from the concentrated environment; this process is known as reverse osmosis (RO).

5 Design of a Desalination Plant by Reverse Osmosis

The pressurizing part is the most important part of the process. It consists of the following items:

- Reverse osmosis block (membranes);
- Pressurizing system (high-pressure (HP) pump group);
- Energy recovery system.

It is noteworthy that 55–60% of the energy injected into the system is in the rejection as high-pressure brine. So, how to recover this energy with maximum efficiency to reinject it into the system?

This energy could be recovered by

- Turbo pumps placed in series with the HP pumps;
- Pelton turbines coupled directly to the HP pump to relieve the electric motors;
- Pressure exchangers (PX).

The method of the pressure exchanger is a system which guarantees a yield exceeding 95% and an energy recovery from 50% to 60%. So, it achieves significantly lower energy consumption of 3 kWh/m^3 of permeate, for the sole purpose of pressurizing the RO.

6 Description of the Pressure Exchanger, PX

The device relates to a pressure exchanger for transferring pressure energy from a relatively high-pressure fluid flow to another fluid flow at relatively low pressure.

It consists of a ceramic rotor positioned on a central axis between two end caps within a vessel under pressure, with a pair of inlet and outlet coaxial in communication with a pair of orifices:

- A low-pressure,
- A pair of high-pressure orifices.

The rotor rotates in the ceramic liner; it is the only moving part during operation (Fig. 3).

7 Introducing the El-Hamma Plant

The desalinization plant EL-HAMMA covers an area of 50,000 m^2. It is the largest resort in Africa. With the daily production capacity of 200,000 m^3/day, it serves a population of 2.7 million for the capital Algiers. Thus, it would cover the needs of the capital's drinking water for 25 years.

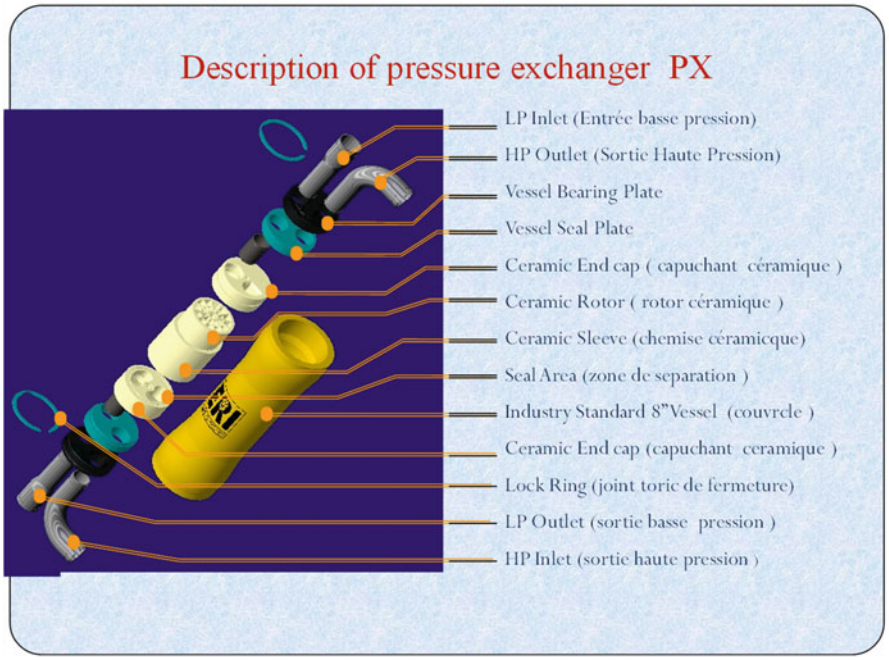

Fig. 3 The pressure exchanger, PX

El-Hamma plant consists of: taking seawater, clarifiers, multilayer filters, cartridge filters, reverse osmosis station, remineralization, reservoir, and production pumps.

8 Introducing the Bousmail Plant

The Bousmail desalinization plant was designed for drinking water production of 5000 m^3/day by the reverse osmosis technology. It is characterized by

- Localization: Bousmail Wilaya of Tipaza
- Flow rate of raw water inlet: 520 m^3/h
- Desalinated water production flow rate: 208 m^3/h
- Total production of desalinated water: 5000 m^3/day.

9 Comparative Study of the Energy Cost of Bousmail Plant

The cost structure based on the various positions is given in Table 1.

Table 1 Summary of the energy cost of desalinization by reverse osmosis

Item	Share in %
Amortization	33–43%
Energy	37–43%, of which 70% consumed by the HP pump
Labor	4–11%
Maintenance	3.5–4.5%
Membrane	2–5%
Reactive	2–6%

9.1 Energy Cost with the Pelton Turbine (Indirect Recovery)

Recovery Pelton turbines are used for more than 20 years. The system recovers energy indirectly from concentrates. The driving of the high-pressure pump is done by the electric motor and the recovery turbine (Fig. 4).

Calculation method

Q_A: flow rate of seawater
Q_C: rejected concentrate flow
Q_p: permeate flow

The conversion rate:

$$Y = \ Q_p/Q_A \times 100$$

The pressure loss in the membranes is

$$\Delta P = P_B \ - P_C$$

The power absorbed by the pump in kW:

$$P_p = Q.d \times P/36.7 \times \eta_p.\eta_m$$

with

d: density of seawater
Q_B: flow rate delivered by the pump
η_p: pump efficiency
η_m: motor pump efficiency

Pressure across the pump motor is

$$P = P_B - P_A$$

The energy consumption per m^3 of water permeate:

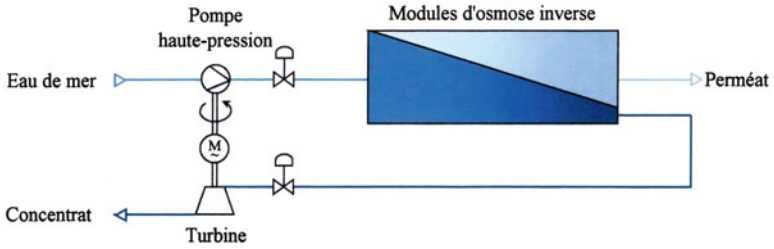

Fig. 4 Indirect recovery energy with the Pelton turbine

$$\text{WkWh/m}^3 = P_\text{p}/Q_\text{p}$$

The energy recovered by the turbine per m^3 of water produced, $WkWh/m^3$:

$$\text{WkWh/m}^3 = (P_\text{C} \times Q_\text{C} \times \eta_\text{tr})/36.7 \times Q_\text{p}$$

So, the total energy consumed by the system is

$$\text{WkWh/m}^3 = W_\text{POMPE} - W_\text{TURBINE}$$

Results of the calculation are given in the Table 2:

9.2 Energy Cost with Pressure Exchanger (Direct Recovery)

The pressure exchanger directly transfers the concentrate hydraulic power in the feed circuit. This is the pressure exchanger, PX, which is the most recent technique. The presence of a booster pump to compensate the pressure losses induced in the pressure exchanger should be noted (Fig. 5).

Calculation method
Power absorbed by the HP pump:

$$P_\text{p} = Q_\text{C}(P_\text{C} - P_\text{A})/\eta_\text{p} \cdot \eta_\text{m} \times 36.7$$

P_P (kW): is the power absorbed across the pump motor.
Power absorbed by the booster pump:

$$P_\text{ps} = Q_\text{D}(P_\text{E} - P_\text{A})/\eta_\text{ps} \cdot \eta_\text{mps} \times 36.7$$

where
P_ps (kW) is the power absorbed by the pump from overpressure; η_ps and η_mps are the performances of the booster pump and its motor.

Table 2 Pelton turbine energy balance (Bousmail)

Pump HP consumption	
Flow rate of the HP pump	231.5 m^3/h
Efficiency of the HP pump	76%
Motor efficiency	96%
Power consumption	520.5 kW
Consumed energy	5 kWh/m^3
Recovered energy by turbine Pelton	
turbine yield	75%
Recovered energy	1.53 kWh/m^3
Consumed energy per m^3 product	3.47 kWh/m^3
Energy gain of the turbine	30.6%

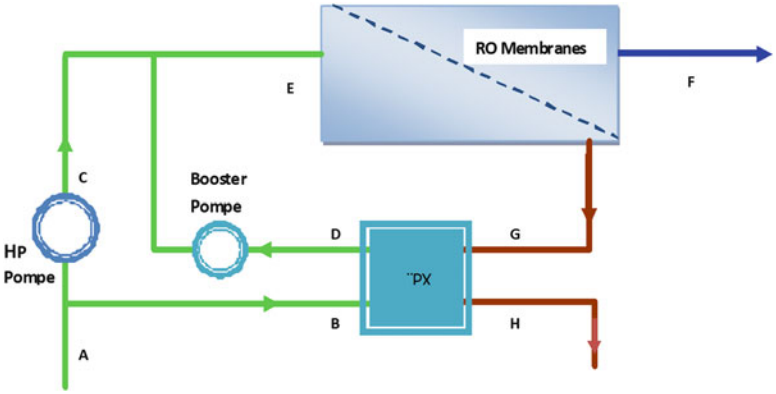

Fig. 5 Schematic of a reverse osmosis desalination system using a pressure exchanger: (*A*) Seawater inflow, (*F*) Freshwater flow, (*G*) Concentrate flow, (*D*) Seawater flow, (*H*) Concentrate (drain), (*C*) HP pump flow, and (*B*) Circulation flow

The osmoser energy consumption reduced to kWh/m^3 product:

$$W_{\mathrm{KWh/m}^3} = P/Q_{\mathrm{F}} = \left(P_{\mathrm{p}} + P_{\mathrm{PS}}\right)/Q_{\mathrm{F}}$$

Q_{F}: permeate flow
$Q_{\mathrm{C}} = Q_{\mathrm{F}} + Q_{\mathrm{L}}$
Q_{L}: lubrication flow

$$P_{\mathrm{D}} = P_{\mathrm{G}} - \Delta P \ \ (\mathrm{hp})$$
$$P_{\mathrm{H}} = P_{\mathrm{B}} - \Delta P \ \ (\mathrm{lp})$$

ΔP(hp): pressure difference in high-pressure PX.
ΔP(lp): pressure difference in low-pressure PX.
Calculation results are given in the Table 3.

Table 3 Energy balance of the osmoser

Consumption of HP pump	
Flow rate of HP pump	41.3 m^3/h
Efficiency of HP pump	0.86%
Motor efficiency	0.96%
Consumed electric energy	79 kW
Consumption of booster pump	
Flow rate	58.7 m^3/h
Efficiency of booster pump	0.85%
Motor efficiency	0.94%
Consumed electric energy	4 kW
Total consumed energy	83 kW
Consumed energy per m^3 product	2.07 kW/m^3
Efficiency of PX	94.7%
Energy gain of PX	56.8%

10 Results Comparison and Conclusion

- The pressure exchanger system (PX) allows an efficiency of 94.7%, while the turbine recovers only 75% of hydraulic energy of the concentrate which reflects the net gain of 17.4% energy compared to the Pelton turbine.
- Using the pressure exchanger system decreases the size of the high-pressure pump at a rate of 108 m^3/h instead of 231.5 m^3/h, and reduces power consumption.
- The pressure exchanger directly recovering the energy of the concentrate operates as an independent HP pump of the primary pump, while the turbine with indirect recovery causes changes in flow and pressure in the reverse osmosis system.
- Note the low efficiency of the HP pump of Bousmail compared to the previous example. Today, there are pumps with only 0.86% yield. So, the choice of the HP pump is important to optimize the energy costs of a reverse osmosis system .
- The electrical energy needs for desalinization of seawater by reverse osmosis are such that they constitute the largest share of operating costs. Of this energy, 70% is absorbed only by the pressurizing device membranes, hence its importance in the price of per m^3 of freshwater produced.
- Therefore, researches in the field of energy recovery from the concentrate were a very important factor in lowering desalination cost.
- From the results obtained by applying the technique of the pressure exchanger on Bousmail station, it was found that with an efficiency of 95%, the pressure exchanger provides an energy gain of 18% relative to the Pelton turbine actually used.
- The pressure exchanger recovers energy directly by reducing the size of the high-pressure pump from the rate of 231.5 m^3/h to a rate of 108 m^3/h. It functions as an independent pump from the main pump, which gives a greater

stability of the system, the fact that working at reduced pressures and higher flows, avoiding the precipitation of salts and reducing, by consequence, the clogging and membrane fouling .

- It is also noted that the compact and small size of PX modules allows its location in smaller premises, thus minimizing the visual impact of the installations, thanks to its optimal integration into its environment.
- The establishment of solutions, more and more innovative to the new seawater desalinization plants as is the case of the pressure exchanger, contributed to the decline in energy consumption, increasing capacity of stations, and reducing the cost of desalinated water.
- All energy balance made in the design of desalinization plants must take account of the energy recovery sector. Components with the best mechanical, hydraulic, and electrical efficiencies and also offering all the guarantees of operation will be called on. We must integrate new technologies addressing the factors that favor the reduction of the cost of desalinization which are as follows:
  - Improving the energy efficiency of the system and the energy recovery system
  - Maintenance of membranes
  - Choice of intake
  - Improved pretreatments
  - Optimization of the size of the installation

To this end, it is important to incorporate desalinization techniques as an option as part of integrated planning and management of water resources and to develop national expertise in this area, with the objective of sustainable development and decision support

References

Agashicheva, S.P., Lootahb, K.N.: Influence of temperature and permeate recovery on energy consumption of a reverse osmosis system. Desalination. **154**(3), 253–266 (2003)

Audinos, R..: Séparations électrochimiques: Électrodialyse, Technique de l'Ingénieur (1997)

Ballif, J.L.P.: L'eau, ressource vitale. Editions JOHANET, Paris (2002)

Barlow, M., Clarke, T.: L'or bleu : l'eau, le grand enjeu du XXIème siècle, Hachette Litteratures, Paris (2002)

Cerci, Y.: Exergy analysis of a reverse osmosis desalination plant in California. Desalination. **142**, 257–266 (2002)

Danis, P.: Techniques de l'Ingénieur, et dessalement d'eau de mer. Paris (2007)

Maurel, A.: Techniques séparatives à membranes – considérations théoriques. In: Techniques de l'Ingénieur. Paris (2003)

Sharif, A.O., Merdaw, A.A., Al Bahadili, H., Al Taee, A., Al Aibi, A., Rahal, Z., Derwish, G.A. W.: A new theoretical approach to estimate the specific energy consumption of reverse osmosis and other pressure driven liquid phase membrane processes. Desalination Water Treat. **3**, 111–119 (2009)

Multi-objective Optimization of Distillation Sequences Using a Genetic-Based Algorithm

Mert Suha Orcun and Özçelik Yavuz

1 Introduction

Distillation is a widely used separation system in chemical processes. Being popular in use but an extensive energy-dependent process, distillation systems have to be carefully handled in the design phase. Not only is the energy usage critical to the system but the initial capital investment and efficient design is also very crucial. Handling the separation process of hydrocarbon mixtures is the main issue in terms of the chemical processes adopted throughout the world. Properly sequencing and deciding the configurations of the columns are common problems during the analysis of topics of relevant studies.

On the other hand, design of this separation system including detailed column configuration and deciding the sequencing of the columns is a complex problem. By nature, it has a complex nonlinear mixed-integer superstructure depending on the component number, type and compositions.

There are various studies presented in the literature about distillation systems and its optimization, where some of them also search a sequencing and multi-objective approach.

The sequencing of a separation system, including a special hierarchical structure, is proposed in the study done by Wang et al. (2008) which is modelled as a multi-hierarchy combinatorial optimization. Moreover, in an earlier work,

M.S. Orcun (✉)
Yuzuncu Yıl University, Faculty of Engineering and Architecture, Department of Chemical Engineering, Kampüs, Van 65080, Turkiye
e-mail: yavuz.ozcelik60@gmail.com

Ö. Yavuz
Ege University, Faculty of Engineering, Department of Chemical Engineering, Bornova, İzmir 35100, Turkiye
e-mail: orcunmert@gmail.com

© Springer International Publishing AG, part of Springer Nature 2018

F. Aloui, I. Dincer (eds.), *Exergy for A Better Environment and Improved Sustainability 2*, Green Energy and Technology,
https://doi.org/10.1007/978-3-319-62575-1_53

sequencing and heat integration were mixed and optimization was based on minimizing the cost of the column (Wang et al. 1998). In the study done by Jain et al. (2012), energetic-efficient of distillation systems was attempted by optimization of distillation sequencing, in which heat integration was included. The solution complex superstructure of sequencing columns for separating azeotropic mixtures was also achieved in the literature (Bauer and Stichlmair 1998; Caballero and Grossmann 2004). Also, in one study, a multi-objective approach was handled for optimization of a compressor-aided distillation system sequencing (Alcántara-Avila et al. 2012).

Various distillation systems including batch columns, solar-driven membrane systems and multi-effect columns are evaluated in the literature from an optimization point of view and most of them use meta-heuristic methods such as simulated annealing and genetic algorithm because of low risk of local optima problem, easy development or commercial availability (Cardoso et al. 2000; Hanke and Li 2000; Burri and Manousiouthakis 2004; Chang et al. 2010; Sayyaadi and Saffari 2010). In some studies, simulation programs like Aspen and MATLAB are used for evaluating the flowchart and physical data for the sake of decreasing the code development (More et al. 2010). In a previous study, exergetic single-objective optimization is applied to a distillation system (Özçelik 2007) considering the sequencing.

Moreover, the design of distillation columns and separation systems are also handled in studies considering reactive distillation (Burri and Manousiouthakis 2004; Amte et al. 2013) and heat integration systems (Gadalla et al. 2003).

Differing from these studies in this chapter, a multi-objective optimization of distillation sequencing for two hydrocarbon mixtures is completed from exergoeconomic profit and exergy destruction points of view. A computer program is developed to solve this complex problem based on a hybrid genetic algorithm that designs each column in detail, including costing, and then tries to optimize the sequencing considering objective functions. Being a unique study with in-house program development and uniting exergy concept with multi-objective optimization, the manuscript greatly contributes to the researchers focused on separation systems, especially distillation trains.

Nomenclature

C	Column
C_{column}	Installed capital cost for a distillation column ($)
C_{Cond}	Capital cost for a condenser ($)
C_{cw}	Annual cost of cooling medium
$C_{p,W}$	Heat capacity of water (kJ/kg °C)
C_{Reb}	Capital cost for a reboiler ($)
C_{tray}	Installed capital cost for trays ($)
c_w	Unit cost of coolant ($/kg)
D_c	The column diameter (m)
D_F	The flow rate of the distillate
Ex_{dest}	Exergy destruction [kW]
H_{bottom}	Enthalpy of bottoms (kJ/kmol)

(continued)

H_c	Height of distillation column (m)
H_{feed}	Enthalpy of feed, (kJ/kmol)
H_{top}	Enthalpy of distillate (kJ/kmol)
N	Molar flow rate
N	Tray number
N_C	Number of components
N_{min}	Minimum number of tray
NS	Number of distillation sequence
P	Exergoeconomic profit [$/kW]
P	Pressure (bar or atm)
QC	Rate of heat flow for condenser
QH	Rate of heat flow for reboiler (kJ/hr)
R	Reflux ratio
TAC	Total annual cost of a distillation sequence
TCC	Total annual cost of a distillation sequence
TD	Distillate temperature
Z	Objective function
Subscript	
B	Bottom product
D	Distillate
Dest	destruction
HK	Heavy Key
in	inlet
LK	Light Key
out	Outlet
Greek	
α	Relative volatility
η	Efficiency
η	Tray efficiency

2 Distillation Sequencing and Design

Hydrocarbon mixtures are widely handled in the industry considering the broad usage areas and energy needs globally. Proper separations of these components are mainly accomplished using distillation trains. In this phase, evaluating and deciding the sequences of a distillation of a multi-component mixture is a complex problem from both mathematical and economic points of view.

The selection of the proper sequencing of a sharp split distillation of multi-component mixtures is a mixed-integer nonlinear programming (MINLP) problem (Andrecovich and Westerberg 1985). Since existence of the columns are present in

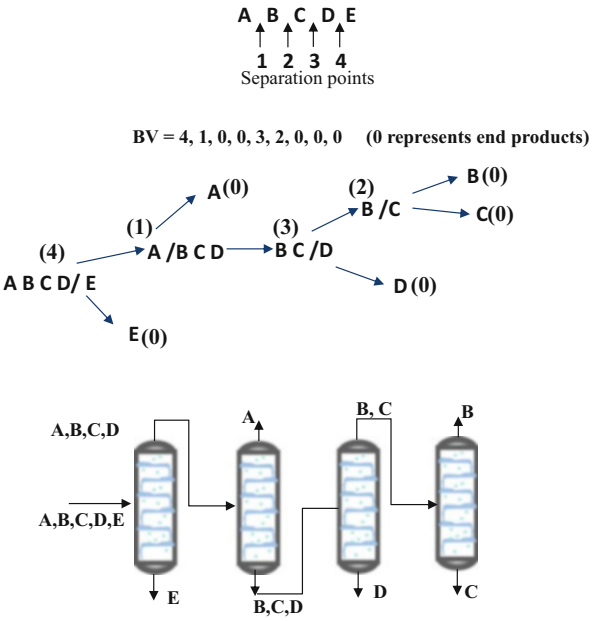

Fig. 1 Binary variable presentation and visualization of an alternative distillation sequence

the model, as well as the detailed design considering reflux rations, vapour/liquid rations and plate design are considered.

The number of possible sharp distillation sequences increases markedly with the number of feed components and can be calculated using the following equation (Wang et al. 1998):

$$\mathrm{NS} = \frac{[2(\mathrm{NC}-1)]!}{\mathrm{NC}!\quad(\mathrm{NC}-1)!} \tag{1}$$

Any alternative distillation sequence for a separation of a mixture can be represented (Özçelik 2011) by a binary vector with 2NC−1 elements (continuous variable vector with NC−1 elements). For example, if a mixture involves five components, such as A, B, C, D and E, it can be represented as given in the Fig. 1 depending on where the determined separation points are, and a sequence number is given according to the developed binary sequencing.

NS and NC are the number of possible distillation sequences and number of compounds, respectively. In a computer-based optimization, many alternatives of sharp distillation sequences may be examined to determine the best sequence, according to a given criterion.

The decision on the sequence of the distillation train completely affects the design of each column in the system and eventually has a considerable effect on the investment and operational cost of the process. As the separation characteristics of the fed mixtures in the columns of the distillation train change, exergetic efficiency

is altered depending on the exergy destruction. Laying onto these phenomena, the exergoeconomic cost of the separation operation changes.

The operating variables in each column such as reflux ratio, 'feed vapour/liquid ratio' and the column pressure are dominant parameters that affect the characteristics of the design. If the feed conditions, design pressures, reflux ratio and the quality of the products are determined, the capital and operating costs of the columns in the sequences can be calculated using sharp distillation column design technique. To calculate the cost of the column, it is necessary to calculate the diameter, height and minimum number of trays in the columns (Pibouleau et al. 1983). The diameter (D_c), minimum number of trays (N_{min}) and the height of the column (H_c) are calculated as follows:

$$D_c = \left\{ \frac{4}{\pi} D_F (R+1) \frac{22.2 T_D}{0.761 (1/P)^{0.5} 273} \frac{1}{3600 P} \right\}^{0.5} \tag{2}$$

$$N_{min} = \frac{\ln \left[\frac{n_{LK,D} n_{HK,B}}{n_{HK,D} n_{LK,B}} \right]}{\ln \propto_{LK-HK}} \tag{3}$$

$$H_c = 0.61 \frac{N}{\eta} + 4.27 \tag{4}$$

The condenser and reboiler duty of each column is calculated and necessary utilities are evaluated for exergy analysis:

$$Q_c = (R+1) D_F \lambda_{top} \tag{5}$$

$$Q_H = H_{bot} + H_{top} + Q_c - H_{feed} \tag{6}$$

Costs of the columns are evaluated depending on the calculated parameters, such as the height, diameter and heat duties. The correlations proposed by Guthrie are used for the evaluation. The general vessels are designed in accordance with American Society of Mechanical Engineering (ASME) codes and thicknesses of the equipment are calculated for resisting 4.5 atm as internal pressure. Trays, tray assemblies, packed beds, lining and other internals are priced and added to the general cost:

$$C_{column} = \left(\frac{M\&S}{280} \right) 101.9 (D_c/0.3048)^{1.066} (H_c/0.3048)^{0.802} (2.18 + F_c) \tag{7}$$

$$C_{tray} = \left(\frac{M\&S}{280} \right) 4.7 (D_c/0.3048)^{1.55} (1.64 NT) F_c \tag{8}$$

The total annual cost of a distillation column in the distillation sequence is calculated in terms of the column, tray and utility costs:

$$\mathrm{TCC} = \left(C_{\mathrm{Column}} + C_{\mathrm{Tray}} + C_{\mathrm{Cond}} + C_{\mathrm{Reb}}\right)/t_{\mathrm{L}} \tag{9}$$

Depending on the cost of each column, the annual cost of the distillation sequence is calculated:

$$\mathrm{TAC} = \sum_{i=1}^{\mathrm{NC}-1} \mathrm{CC}_i \tag{10}$$

3 Exergoeconomic Multi-objective Optimization (ExMOO)

Multi-objective optimization is a mathematical programming technique that considers multiple objectives explicitly and simultaneously in a multi-objective optimization framework. In fact, most of the physical and chemical phenomena are multi-objective in its nature and a complex superstructure. There are many methods available to tackle these kinds of problems.

In this study, a comprehensive exergoeconomic multi-objective optimization (ExMOO) is applied to find out the optimum sequence for distillation of predefined hydrocarbon mixtures from maximization of exergoeconomic profit and minimization of exergy destruction points of view:

$$\begin{aligned}\mathrm{Max}\ P_{\mathrm{Ex}} = {} & \left(\mathrm{Ex}_{\mathrm{Top}}{}^{*}\mathrm{C}_{\mathrm{Top}} + \mathrm{Ex}_{\mathrm{Bot}}{}^{*}\mathrm{C}_{\mathrm{Bot}}\right) \\ & - \left(\mathrm{Ex}_{F}{}^{*}\mathrm{C}_{F} + \mathrm{Ex}_{\mathrm{CU}}{}^{*}\mathrm{C}_{\mathrm{CU}} + \mathrm{Ex}_{\mathrm{HU}}{}^{*}C_{\mathrm{HU}} + Z\right)\end{aligned} \tag{11}$$

$$\mathrm{Min}\ \ \mathrm{Ex}_{\mathrm{D}} = \mathrm{Ex}_{\mathrm{F}} + \mathrm{Ex}_{\mathrm{CU}} + \mathrm{Ex}_{\mathrm{HU}} - \mathrm{Ex}_{\mathrm{Out}} \tag{12}$$

The weighing sum of objectives method is used for dealing the complex superstructure of this multi-objective problem. A weighing factor is given to the objective function parameters which are between 0 and 1 in this method. So the decision of the factors is crucial for the solution. This study offers to the users a chance to select the weighing factors, and besides, the study itself covers a parametric study for different weighing factors with a user-friendly program. The multi-objective problem is separately solved for each case. The results are discussed depending on these broad Pareto solution set:

$$\mathrm{Min}\ Z = \left(w\left(P_{\mathrm{Ex}} - P_{\mathrm{Ex,max}}\right)^2 + (1-w)\left(\mathrm{Ex}_{\mathrm{Dest}} - \mathrm{Ex}_{\mathrm{Dest,Min}}\right)^2\right)^{1/2} \tag{13}$$

Also, in addition to the multi-objective optimization, the parametric investigation of the weighing factors is also implemented to DISMO as well as the exergoeconomic multi-objective optimization, and this behaviour is evaluated.

Exergoeconomic analysis covers the economic concerns with exergy analysis, equipment costs and related thermodynamic irreversibilities through the system (Mert et al. 2007a). Exergy and costs are closely in contact since the exergy analysis seeks for the efficient and effective use of energy through the system. In addition, this situation automatically brings a cost-effective operation.

The exergetic efficiencies of each column and the sequence besides the exergy destruction are calculated according to the exergy balance (Mert et al. 2007b; Dincer and Rosen 2012):

$$\mathrm{Ex}_{\mathrm{dest}} = \mathrm{Ex}_{\mathrm{in}} - \mathrm{Ex}_{\mathrm{out}} \tag{14}$$

For the calculation of the exergy efficiency, exergy recovered (exergy output) to the exergy input is taken into account. Exergy output can be defined as the desired exergy output or useful exergy output (Mert et al. 2012):

$$\eta = \frac{\mathrm{Ex}_{\mathrm{out}}}{\mathrm{Ex}_{\mathrm{in}}} \tag{15}$$

Exergetic cost for separation operation is calculated by exergoeconomic analysis. These calculated costs are generally used for feasibility studies and investment decisions and also for comparing alternative techniques. Besides the choice for the operating conditions and sustaining a cost-effective operation, exergoeconomic analysis should be used (Modesto and Nebra 2009; Mert et al. 2014b).

The aim of the exergoeconomic analysis is defined as follows (Tsatsaronis and Winhold 1985; Mert and Özçelik 2013):

- To identify the location, magnitude and sources of thermodynamic losses
- To calculate the cost associated to exergetic losses and destroyed exergy in any system component
- To analyse the cost formation of each subsystem and product separately

The overall exergetic cost balance is used as follows:

$$\sum \left(\dot{\mathrm{E}}\,\mathrm{x}_{\mathrm{in},i} \cdot C_{\mathrm{in},i}\right) + \dot{Z}_{\mathrm{tot}} = \sum \left(\dot{\mathrm{E}}\,\mathrm{x}_{\mathrm{out},i} \cdot C_{\mathrm{out},i}\right) + P_{\mathrm{net}} \cdot C_{\mathrm{W}} \tag{16}$$

where the $\dot{\mathrm{E}}\,\mathrm{x}_{\mathrm{in},i}$, $\dot{\mathrm{E}}\,\mathrm{x}_{\mathrm{out},i}$, $C_{\mathrm{in},i}$, and $C_{\mathrm{out},i}$ are the exergies and exergy costs. Z_{tot} is the annualized cost of the total system inside the control volume. C_{W} is the cost of the work or the power of the equipment. P_{net} is the net power produced from separation system. The cost balance is applied to the overall system to calculate the cost of the separation system, and depending on these, the exergetic profit is calculated. In order to calculate $Z_{\mathrm{equipment}}$, the annualized (or levelized) cost method (Tsatsaronis and Moran 1997) is used.

4 DISMO Computer Program

This study covers production of a hybrid genetic algorithm-based solver implemented Multi-Objective Optimizer (MOO) program (DISMO) (Fig. 2) in order to solve the complex structure of distillation of the mixtures.

DISMO has a running sub-program (CRANE) which is also developed by our group that governs a database of 650 components for evaluation with all physical and thermodynamic properties defined in the system, including a detailed steam table, and each of these components is suitable for implanting a case study.

The feeds of thermal properties and compositions are dynamically taken by DISMO and related thermodynamic and physical data are calculated by a selection of subroutine depending of CRANE.

In the present study, an algorithm that is a hybrid of Nonlinear Simplex and a Genetic Algorithm (Özçelik 2011) based on the stochastic generation of solution vectors was used to minimize the following multiple objective functions that united with the weighing sum of objectives method (Mert et al. 2014a).

The algorithm of the DISMO is represented in Fig. 3. The calculations begin with the entry of the data and consequently followed by estimation of the physical and thermodynamic properties and initialization of the genetic algorithm. Evaluation of the objective function is dependent on the weighing factors and fitness function produced by the genetic algorithm. The program simultaneously tries to optimize both minimization of the exergy destruction and maximization of the exergetic profit. Termination criteria changes depending on the structure of the solution, that in small number of alternatives, program calculates every alternative solution and decides depending on these latters, where (as in large number of

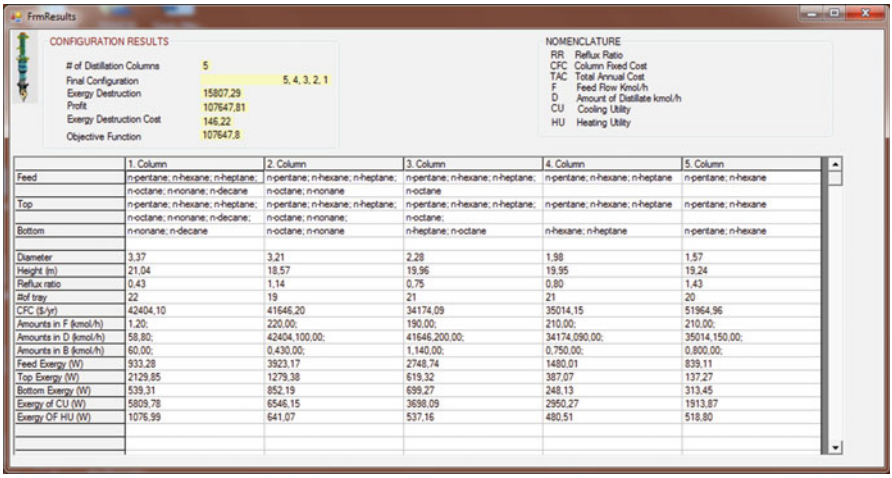

	1. Column	2. Column	3. Column	4. Column	5. Column
Feed	n-pentane; n-hexane; n-heptane; n-octane; n-nonane; n-decane	n-pentane; n-hexane; n-heptane; n-octane; n-nonane	n-pentane; n-hexane; n-heptane; n-octane	n-pentane; n-hexane; n-heptane	n-pentane; n-hexane
Top	n-pentane; n-hexane; n-heptane; n-octane; n-nonane; n-decane;	n-pentane; n-hexane; n-heptane; n-octane; n-nonane;	n-pentane; n-hexane; n-heptane; n-octane;	n-pentane; n-hexane; n-heptane	n-pentane; n-hexane
Bottom	n-nonane; n-decane	n-octane; n-nonane	n-heptane; n-octane	n-hexane; n-heptane	n-pentane; n-hexane
Diameter	3,37	3,21	2,28	1,98	1,57
Height (m)	21,04	18,57	19,96	19,95	19,24
Reflux ratio	0,43	1,14	0,75	0,80	1,43
#of tray	22	19	21	21	20
CFC ($/yr)	42404,10	41646,20	34174,09	35014,15	51964,96
Amounts in F (kmol/h)	1,20;	220,00;	190,00;	210,00;	210,00;
Amounts in D (kmol/h)	58,80;	42404,100,00;	41646,200,00;	34174,090,00;	35014,150,00;
Amounts in B (kmol/h)	60,00;	0,430,00;	1,140,00;	0,750,00;	0,800,00;
Feed Exergy (W)	933,28	3923,17	2748,74	1480,01	839,11
Top Exergy (W)	2129,85	1279,38	619,32	387,07	137,27
Bottom Exergy (W)	539,31	852,19	699,27	248,13	313,45
Exergy of CU (W)	5809,78	6546,15	3698,09	2950,27	1913,87
Exergy OF HU (W)	1076,99	641,07	537,16	480,51	518,80

Fig. 2 A sample results screen of the DISMO computer program

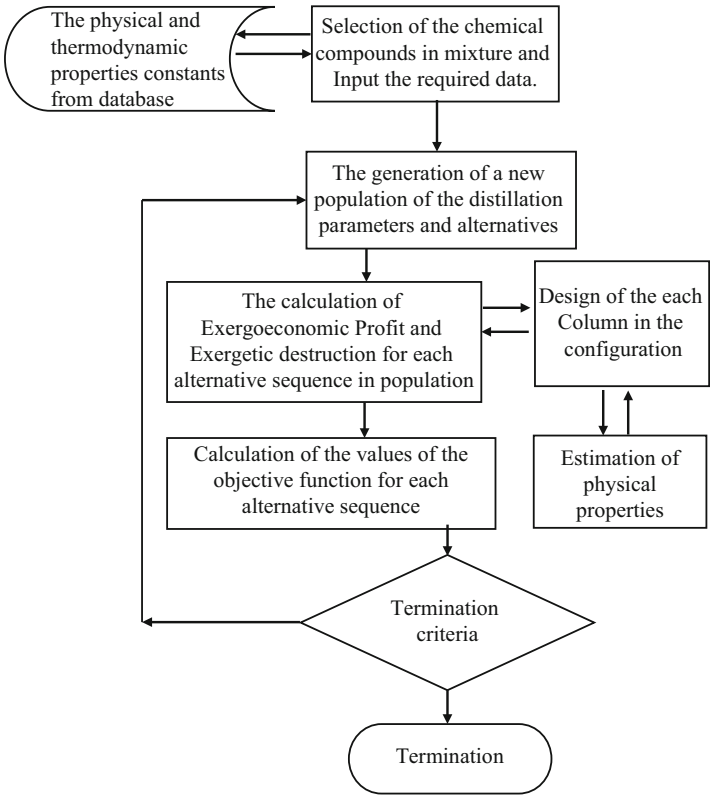

Fig. 3 The algorithm of the DISMO computer program

alternatives) genetic algorithm is strictly applied and convergence of the fitness function is required.

The basic steps of the genetic-based algorithm are given as follows:

- Encoding and generation of initial population depending on the number of variables
- The generation of a new population
  - Reproduction
  - Crossover
  - Mutation
- Generation of new random vectors
- Termination criteria

$$\mathrm{abs}\left(F_{\mathrm{Avg}_i} - F_{\mathrm{Avg}_{i-25}}\right) \leq \in \tag{17}$$

Table 1 Feed compositions and properties of cases

Component/property	Case 1	Case 2
n-Pentane [mol %]	–	20
n-Hexane [mol %]	30	20
n-Heptane [mol %]	–	20
n-Octane [mol %]	28	20
n-Decane [mol %]	42	20
n-Nonane [mol %]	–	–
Pressure [atm]	1	1
Temperature [°C]	40	40
Flow Rate [kmol/h]	600	600

F_{Avg_i} and $F_{\text{Avg}_{i-25}}$ are the average objective function values for 25 consecutive generations.

5 Case Studies

Two hydrocarbon mixtures are selected as case studies for revealing the performance of the derived program and investigated on a complex separation system. Table 1 shows the molar compositions of the cases as well as the temperature, pressure and flow rate of feed to the first column of the system.

The cases are separately investigated covering a range of weighing factors selected depending on the behaviour of the distillation system in a great accordance. Each case has slightly different range of weighing factors depending on the convergence of one of the objective functions to its maximum value which is found by single optimization.

6 Results and Discussion

Each case of the parametric investigation has a different trend depending on the detailed design of each column and costing with an exergetic perspective.

The variation of the exergoeconomic profit is represented in Fig. 4 considering the variation of the weighing factors to the profit objective for Case 1. Considering that Case 1 has three components, the necessary distillation column number is 2, and there are only two alternatives for the separation operation of this mixture. As shown in the figure, increasing the factor of profit objective, the systems stand on a final value with a configuration of 2–1. Any further increase does not change the result as there is no alternative sequencing left. Also Fig. 5 shows the investigation using the other perspective as the importance for the profit increases, the exergetic

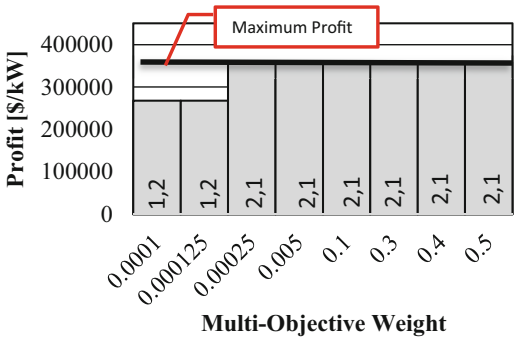

Fig. 4 The variation of exergoeconomic profit depending on weighing factor for Case 1

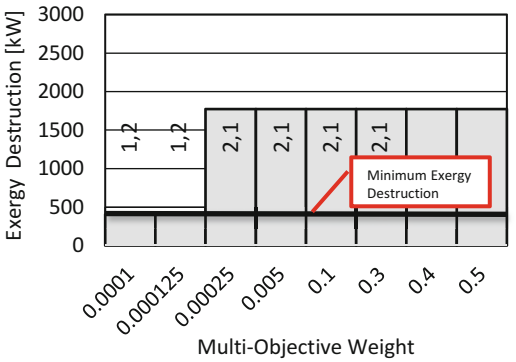

Fig. 5 The variation of exergy destruction depending on weighing factor for Case 1

Table 2 Design results of Case 1

	Maximum profit 358708.3 [$/kW]			
Column	**D_c [m]**	**H[m] [m]**	**N_T [−]**	**R [−]**
1	2.41	23.72	26	0.15
2	1.74	50	60	0.58
	Minimum exergy destruction 403.84 [kW]			
Column	**D_c [m]**	**H[m] [m]**	**N_T [−]**	**R [−]**
1	1.70	15.52	15	0.24
2	1.93	18.70	19	0.77

destruction also increases which proves the conflicting situation between the objectives. The numerical results for the details of the columns of the separation system are tabulated in Table 2. The maximum profit reaches 358707.5 $/kW in the inspection where minimum exergy destruction is 403.84 kW.

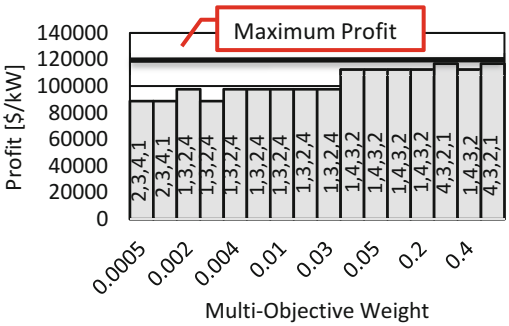

Fig. 6 The variation of exergoeconomic profit depending on weighing factor for Case 2

Table 3 Design results of Case 2

	Maximum profit 116826.9 [$/kW]			
Column	**D_c [m]**	**H[m] [m]**	**N_T [−]**	**R [−]**
1	2.70	20.28	21	0.08
2	2.77	19.43	20	0.96
3	2.14	18.64	19	1.03
4	1.66	16.32	16	1.67
	Minimum exergy destruction 4704.1 [kW]			
Column	**D_c [m]**	**H[m] [m]**	**N_T [−]**	**R [−]**
1	1.85	13.96	13	1.43
2	1.81	20.07	21	1.58
3	1.88	29.55	33	1.76
4	1.53	16.63	16	0.78

The situation is quite different when the number of components increases as Fig. 6 shows the variation of the exergoeconomic profit changes to 30% with respect to weight given to it. The maximum value of profit reaches 116,826$/kW with a sequencing of 4-3-2-1. We can see there are only five sequencing schemes present having better cost and efficiency values, and the difference in the objective functions results mainly from the variation in the reflux besides the other parameters.

The detailed results of each column can be seen in Table 3 where both the limit cases of maximum profit and minimum exergy destruction are given. As it is seen, each column has a different structure depending on the sequence selected since the mixture properties and compositions vary. This complex structure is evaluated from an exergy destruction point of view (Fig. 7). Therefore, the first sequences of 2-3-4-1 have better results when compared with better profit sequences such as 4-3-2-1. The minimum destruction that can be reached is 5132.42 kW which is approximately 10% higher than the global minimum.

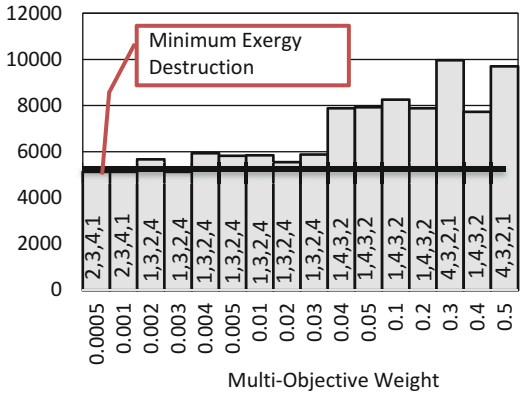

Fig. 7 The variation of Exergy destruction depending on weighing factor for Case 2

7 Conclusion

A comprehensive model development and multi-objective optimization have been applied for determining the proper distillation sequences for two hydrocarbon mixtures in an exergoeconomic perspective using a hybrid genetic algorithm-based solver. The in-house developed computer program DISMO is used for achieving this goal. DISMO has a wide chemical database CRANE with the capability of calculating thermophysical properties of materials.

Distillation sequencing is a crucial step of chemical process modelling and optimization as being an energy and cost-intensive process. In order to reveal the true characteristics of this complex structure, exergoeconomic perspective is used laying on the unavoidable performance of exergy analysis on thermal systems. The multi-objective optimization depending on profit maximization and exergy destruction minimization led us to operate the system using optimum conditions. The weighing sum of objectives method eases the investigation if the decision-maker's choices change from best profit to best exergy destruction.

As a result of the study, a broad PARETO range has been gathered for each weighing factor of each case. Every solution is an optimum one and correct and selected depending on the fitness function of a family of evaluated results in genetic algorithm. The selection of the best optimum is the decision-maker's choice that this study reveals the tendencies of the systems underlines the system dynamics.

This study brings a novel and innovative perspective to the decision-making process in the sequencing of a distillation-based separation system. The results reveal that the best profit is 116826.3 $/kW for five sequences in Case 2 with 4704.1 kW exergy destruction in a sequencing of 4-3-2-1 and 1-2-3-4. On the other hand, for Case 1 where there are only three components and two distillation columns because of low number of alternatives, the model results in a similar

structured results that maximum profit is converged to 358708.3 $/kW with 403.84 kW exergy destruction in a 2-1 sequence.

The small changes in the optimum values are generally the result of reflux ratio and other parameters' effect on the model, whereas the big changes in the results are the consequence of changing in the distillation configuration.

References

Alcántara-Avila, J.R., Kano, M., Hasebe, S.: Multiobjective optimization for synthesizing compressor-aided distillation sequences with heat integration. Ind. Eng. Chem. Res. [Internet]. [cited 2015 Jan 12];**51**(17), 5911–5921 (2012) Available from: http://pubs.acs.org/doi/abs/10.1021/ie2017527

Amte, V., Nistala, S.H., Mahajani, S.M., Malik, R.K.: Optimization based conceptual design of reactive distillation for selectivity engineering. Comput. Chem. Eng. **48**, 209–217 (2013)

Andrecovich, M.J., Westerberg, A.W.: An MILP formulation for heat-integrated distillation sequence synthesis. AIChE J [Internet]. Am. Inst. Chem. Engineers **31**(9), 1461–1474 (1985) Available from: http://dx.doi.org/10.1002/aic.690310908

Bauer, M.H., Stichlmair, J.: Design and economic optimization of azeotropic distillation processes using mixed-integer nonlinear programming. Comput. Chem. Eng. **22**, 1271–1286 (1998)

Burri, J.F., Manousiouthakis, V.I.: Global optimization of reactive distillation networks using IDEAS. Comput. Chem. Eng. **28**, 2509–2521 (2004)

Caballero, J.A., Grossmann, I.E.: Design of distillation sequences: from conventional to fully thermally coupled distillation systems. Comput. Chem. Eng. **28**, 2307–2329 (2004)

Cardoso, M.F., Salcedo, R.L., De Azevedo, S.F., Barbosa, D.: Optimization of reactive distillation processes with simulated annealing. Chem. Eng. Sci. **55**, 5059–5078 (2000)

Chang, H., Wang, G.B., Chen, Y.H., Li, C.C., Chang, C.L.: Modeling and optimization of a solar driven membrane distillation desalination system. Renew. Energy. **35**, 2714–2722 (2010)

Dincer, I., Rosen, M.A.: Exergy: Energy, Environment and Sustainable Development. Newnes, Elsevier (2012)

Gadalla, M., Jobson, M., Smith, R.: Optimization of existing heat-integrated refinery distillation systems. Chem. Eng. Res. Des. IChemE. **81**, 147–152 (2003)

Hanke, M., Li, P.: Simulated annealing for the optimization of batch distillation processes. Comput. Chem. Eng. **24**, 1–8 (2000)

Jain, S., Smith, R., Kim, J.K.: Synthesis of heat-integrated distillation sequence systems. J. Taiwan Inst. Chem. Eng. **43**, 525–534 (2012)

Mert, S.O., Özçelik, Z.: Multi-objective optimization of a direct methanol fuel cell system using a genetic-based algorithm. Int. J. Energy Res. [Internet]. [cited 2015 Jan 2] **37**(10), 1256–1264 (2013). Available from: http://doi.wiley.com/10.1002/er.2963

Mert, S.O., Dincer, I., Ozcelik, Z.: Exergoeconomic analysis of a vehicular PEM fuel cell system. J. Power Sources [Internet]. [cited 2014 May 25] **165**(1), 244–252 (2007a). Available from: http://www.sciencedirect.com/science/article/pii/S0378775306025171

Mert, S.O., Dincer, I., Ozcelik, Z.: Exergoeconomic analysis of a vehicular PEM fuel cell system. J. Power Sources. **165**(1), 244–252 (2007b)

Mert, S.O., Dincer, I., Ozcelik, Z.: Performance investigation of a transportation PEM fuel cell system. Int. J. Hydrog. Energy. **37**(1), 623–633 (2012)

Mert, S.O., Ozcelik, Z., Dincer, I.: Comparative assessment and optimization of fuel cells. Int. J. Hydrogen Energy [Internet]. (2014a.) [cited 2015 Jan 2]; Available from: http://www.sciencedirect.com/science/article/pii/S0360319914031280

Mert, S.O., Özçelik, Z., Dincer, I.: Exergoeconomic based multi–objective optimisation of a solid oxide fuel cell system. Int. J. Exergy. Inderscience Publishers. **14**(4), 413–429 (2014b)

Modesto, M., Nebra, S.A.: Exergoeconomic analysis of the power generation system using blast furnace and coke oven gas in a Brazilian steel mill. Appl. Therm. Eng. Elsevier. **29**(11), 2127–2136 (2009)

More, R.K., Bulasara, V.K., Uppaluri, R., Banjara, V.R.: Optimization of crude distillation system using aspen plus: effect of binary feed selection on grass-root design. Chem. Eng. Res. Des. **88**, 121–134 (2010)

Özçelik, Y.: Exergetic optimization of shell and tube heat exchangers using a genetic based algorithm. Appl. Therm. Eng. [Internet]. [cited 2014 Jul 10] **27**(11–12), 1849–1856 (2007). Available from: http://www.sciencedirect.com/science/article/pii/S1359431107000385

Özçelik, Y.: Exergetic optimization of distillation sequences using a genetic based algorithm. J. Therm. Sci. Technol. **31**(1), 19–25 (2011). Turkish Soc Thermal Sciences Technology TIBTD Makina Muhendisligi Bolumu Odtu, Ankara, 06531, Turkey

Pibouleau, L., Said, A., Domenech, S.: Synthesis of optimal and near-optimal distillation sequences by a bounding strategy. Chem. Eng. J. [Internet]. [cited 2015 Jan 13] **27**(1), 9–19 1983. Available from: http://www.sciencedirect.com/science/article/pii/0300946783800410

Sayyaadi, H., Saffari, A.: Thermoeconomic optimization of multi effect distillation desalination systems. Appl. Energy. **87**, 1122–1133 (2010)

Tsatsaronis, G., Moran, M.J.: Exergy-aided cost minimization. Energy Convers. Manag. Elsevier. **38**(15), 1535–1542 (1997)

Tsatsaronis, G., Winhold, M.: Exergoeconomic analysis and evaluation of energy-conversion plants—II. Analysis of a coal-fired steam power plant. Energy. Elsevier. **10**(1), 81–94 (1985)

Wang, K., Qian, Y., Yuan, Y., Yao, P.: Synthesis and optimization of heat integrated distillation systems using an improved genetic algorithm. Comput. Chem. Eng. **23**, 125–136 (1998)

Wang, X.H., Li, Y.G., Hu, Y.D., Wang, Y.L.: Synthesis of heat-integrated complex distillation systems via Genetic Programming. Comput. Chem. Eng. [Internet]. [cited 2015 Jan 12] **32**(8), 1908–1917 (2008). Available from: http://linkinghub.elsevier.com/retrieve/pii/S009813540700261X

PV Generator Connected to Domestic Three-Phase Electrical Network

Arrouf Mohamed and Almi Med Fayçal

1 Introduction

The most important photovoltaic (PV) application in this century is the PV-grid-connected installations that are proposed to supply the public electrical network.

There are various topologies of management of the PVG connected to a three-phase electrical supply network. Nevertheless, all these approaches based on a PVG connected to electrical network using inverters, which are not only any more limited to convert DC power to AC power but they also ensure a reliable monitoring of the electrical network, to protect this last against the breakdowns and interrupt the connection in the event of problems occurring on either, the electrical network or the installation.

The first difficulty generated by the use of a photovoltaic chain conversion is the coupling between photovoltaic generator and load, either continuous or alternative. Since there are many applications, these problems remain. One of the existing technological barriers in this type of connection is the incorrect dimensioning of the system, because it affects the production and the transfer of power from photovoltaic generator and makes it operate far from its maximum capability. The second difficulty resides at the level of losses generated by the adaptation system during the transfer of the maximum power to the load, as the conversion system output is not always ideally adapted to the application.

A. Mohamed (✉) • A.M. Fayçal
University of Batna, Faculty of Technology, Department of Electrical Engineering, Avenue chahid boukhlouf med El hadi, Batna 05000, Algeria
e-mail: karrouf@hotmail.com

© Springer International Publishing AG, part of Springer Nature 2018

F. Aloui, I. Dincer (eds.), *Exergy for A Better Environment and Improved Sustainability 2*, Green Energy and Technology,
https://doi.org/10.1007/978-3-319-62575-1_54

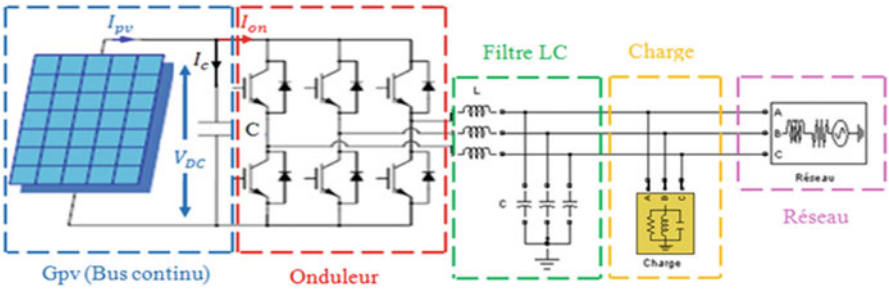

Fig. 1 General scheme of photovoltaic system connected to three-phase electrical network

2 System Layout

The proposed system layout is shown in Fig. 1. This basic structure requires only one inverter. Nevertheless, a number of adaptations are necessary to ensure the right operation of the system.

3 Modeling of Photovoltaic Generator

The modeling of a photovoltaic cell can be carried out according to various levels of complexity of the model. The simplified electrical model of photovoltaic cell is shown in Fig. 2.

This model translates a reference point $(I_{\text{ref}}, V_{\text{ref}})$ to a new point (I, V) according to equations below (Hoque and Wahid 2000):

$$I_{\text{ref}} = I_{\text{sc}}\left[1 - C_1\left[\exp\left(\frac{V_{\text{ref}}}{C_2 V_{\text{co}}}\right) - 1\right]\right] \tag{1}$$

$$C_1 = \left(1 - \frac{I_{\text{mp}}}{I_{\text{sc}}}\right)\exp\left(\frac{-V_{\text{mp}}}{C_2 V_{\text{co}}}\right) \tag{2}$$

$$C_2 = \frac{\left(\frac{V_{\text{mp}}}{V_{\text{co}}} - 1\right)}{\ln\left(1 - \frac{I_{\text{mp}}}{I_{\text{sc}}}\right)} \tag{3}$$

$$\Delta T = T - T_{\text{ref}} \tag{4}$$

$$\Delta I = \alpha\left(\frac{E}{E_{\text{ref}}}\right)\Delta T + \left(\frac{E}{E_{\text{ref}}} - 1\right)I_{\text{sc}} \tag{5}$$

$$\Delta V = -\beta\Delta T - R_{\text{s}}\Delta I \tag{6}$$

$$V = V_{\text{ref}} + \Delta V$$

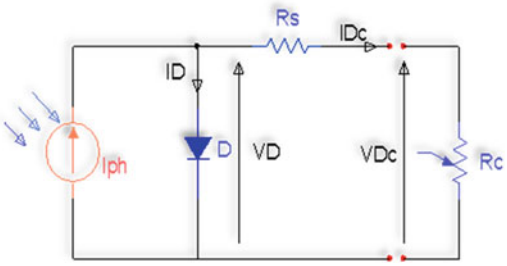

Fig. 2 Simplified electrical model of photovoltaic cell

$$I = I_{\text{ref}} + \Delta I \tag{7}$$

α: Coefficient of current variation according to the temperature.
β: Coefficient of voltage variation according to the temperature.

4 Maximum Power Point Tracking Model

The incremental conductance algorithm (INC) is chosen for its good ratio quality price and ease of implementation (Sera et al. 2000).

The efficiency of maximum power point tracking (MPPT) module is defined as

$$\eta_{\text{MPPT}} = \frac{\int_0^t P_{\text{m}}(t)dt}{\int_0^t P_{\text{MAX}}(t)dt} \tag{8}$$

where P_{m} is the measured output power of panel with MPPT and P_{MAX} is the maximum power that can be delivered by the panel.

The efficiency of the operating point which results from this relation makes it possible to check the validity of the control technique. In fact, it can also be called the control technique efficiency.

Table 1 below shows the efficiency of five MPPT algorithms (Faranda and Leva 2008):

Figures 3 and 4 show the algorithm of incremental conductance technique and its implementation with MATLAB/Simulink.

Table 1 MPPT's efficiency in (%)

MPPT	Efficiency
CV	73%
P&O	81% à 85%
HC	95,52 à 99,13%
INC	88% à89,9%

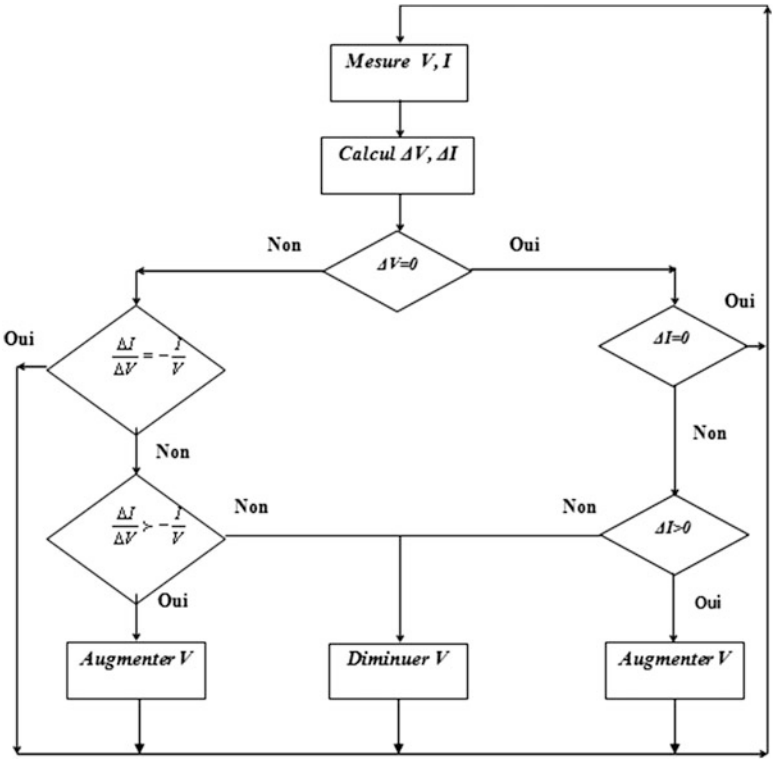

Fig. 3 Algorithm of incremental conductance technique

5 Inverter Model

The three-phase voltage source inverter is used in the system in order to convert DC power to AC power and ensure a reliable monitoring of the electrical network. Figure 5 shows the inverter circuit.

The ratio between the commutation variable vector $[a\ b\ c]^T$ and the phase voltage vector $[V_{ab}\quad V_{bc}\quad V_{ca}]^T$ is given by

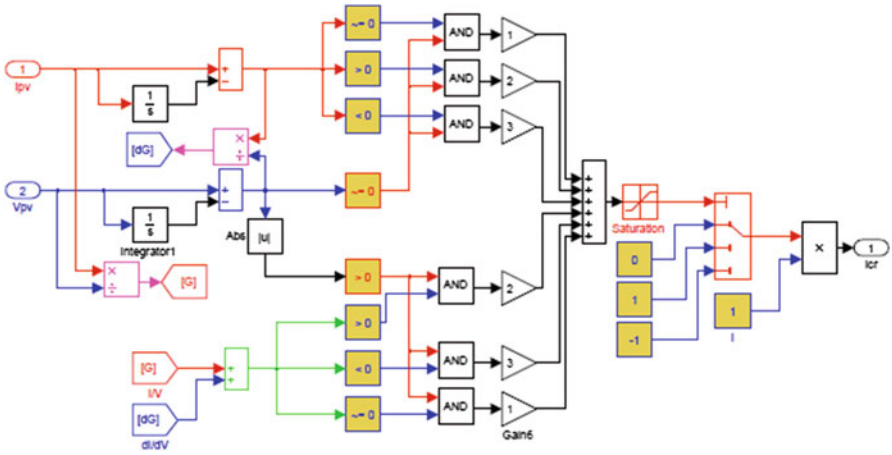

Fig. 4 Implementation of I&C algorithm

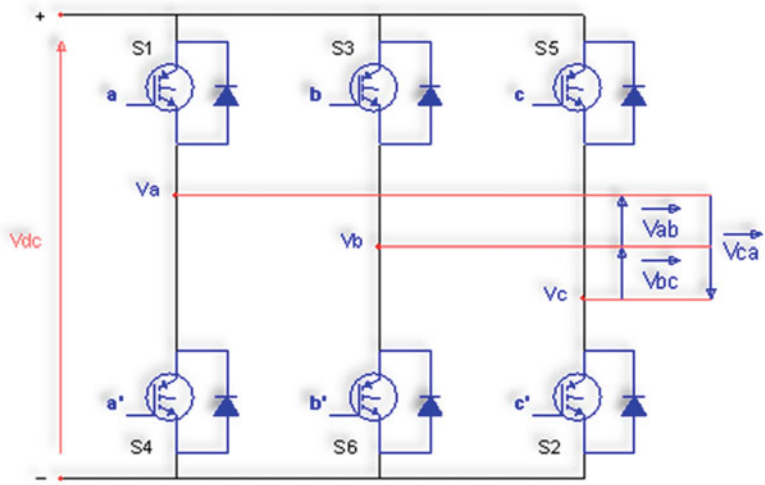

Fig. 5 Three-phase voltage source inverter

$$\begin{bmatrix} V_{ab} \\ V_{bc} \\ V_{ca} \end{bmatrix} = V_{\mathrm{DC}} \begin{bmatrix} 1 & -1 & 0 \\ 0 & 1 & -1 \\ -1 & 0 & 1 \end{bmatrix} \begin{bmatrix} a \\ b \\ c \end{bmatrix} \tag{10}$$

Nevertheless, the ratio between the commutation variable vector $[\,a \quad b \quad c\,]^T$ and the line voltage vector $[\,V_a \quad V_b \quad V_c\,]^T$ can be written as

$$\begin{bmatrix} V_{an} \\ V_{bn} \\ V_{cn} \end{bmatrix} = \frac{V_{DC}}{3} \begin{bmatrix} 2 & -1 & -1 \\ -1 & 2 & -1 \\ -1 & -1 & 2 \end{bmatrix} \begin{bmatrix} a \\ b \\ c \end{bmatrix} \tag{11}$$

6 Dimensioning of Photovoltaic System

In the case of photovoltaic generator connected to electrical network, dimensioning of the system is based on the amounts of power to be developed not according to the need that has to cover, but according to the producible one that a configuration can offer (field/inverter).

6.1 Determination of Continuous Line Voltage $\mathbf{V}_{Bus}$

The inverter connected to three-phase electrical network with line voltage can reach 220 RMS, and the continuous line voltage has to pursue the following relationship (website):

$$V_{\text{Bus}} = 220\sqrt{2}\sqrt{3} + \delta V = 538.89 + \delta V \tag{12}$$

δV: Voltage drops in the inverter semiconductors and the output filter, which can be approximated as

$$\delta V = 2 \cdot V_{\text{CE(IGBT)}} + 2 \cdot L_{\text{filtre}} \cdot \hat{I} + 2 \cdot R_{\text{filtre}} \cdot \hat{I} \tag{13}$$

with

$$V_{\text{CE(IGBT)}} = 3 \text{ V}$$
$$L_{\text{filtre}} = 360 \ \mu H$$
$$R_{\text{filtre}} = 0.5 \ \Omega$$
$$\hat{I} = I_{\text{neff}} \cdot \sqrt{2} \tag{14}$$
$$I_{\text{neff}} = \frac{P_{\text{n}}}{2 \cdot V_{\text{neff}}} \tag{15}$$
$$I_{\text{neff}} = \frac{3000}{660} = 4.545 \text{ A}$$
$$\hat{I} = 6.43 \text{ A}$$

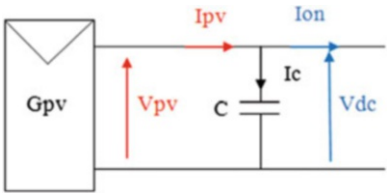

Fig. 6 Continuous line

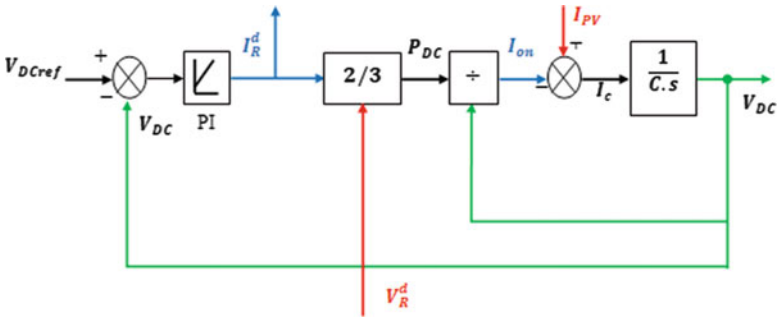

Fig. 7 Continuous line voltage regulation loop

$$\delta V \approx 12.44 \text{ V}$$

Therefore, continuous line voltage is greater than 550 V.
$V_{\text{Bus}} \geq 580$ V is considered in order to obtain the operation in all conditions.

6.2 Continuous Line Voltage Regulation

Continuous line voltage shown in Fig. 6 is regulated with PI corrector parameterized according to the value of the capacitance and the dynamics of the loop as shown in Fig. 7.

$$I_{\text{PV}} = I_{\text{C}} + I_{\text{ON}} \tag{16}$$

$$I_{\text{C}} = C\frac{dV_{\text{DC}}}{dt} \tag{17}$$

$$I_{\text{PV}} = C\frac{dV_{\text{DC}}}{dt} + I_{\text{ON}} \Rightarrow C\frac{dV_{\text{DC}}}{dt} = I_{\text{PV}} - I_{\text{ON}}$$

$$C \cdot S = I_{\text{PV}} - I_{\text{ON}}$$

$$V_{\text{DC}} = \frac{I_{\text{PV}} - I_{\text{ON}}}{C \cdot S}$$

$$P_{\mathrm{DC}} = P_{\mathrm{R}} \tag{18}$$

$$P_{\mathrm{DC}} = I_{\mathrm{ON}} \cdot V_{\mathrm{DC}} \tag{19}$$

$$P_{\mathrm{R}} = 3V_{\mathrm{S}} \cdot I_{\mathrm{S}} = \frac{2}{3} V_{\mathrm{R}}^{\mathrm{d}} \cdot I_{\mathrm{R}}^{\mathrm{d}} \tag{20}$$

$$I_{\mathrm{ON}} = \frac{2}{3V_{\mathrm{DC}}} \cdot V_R^d \cdot I_{\mathrm{R}}^{\mathrm{d}} \tag{21}$$

$$V_{\mathrm{DC}} = \frac{1}{C \cdot S} \left(I_{\mathrm{PV}} - I_{\mathrm{R}}^{\mathrm{d}} \cdot \frac{2 \cdot V_{\mathrm{R}}^{\mathrm{d}}}{3 \cdot V_{\mathrm{DC}}} \right) \tag{22}$$

P_{dc}: Continuous line power of PVG
P_{R}: Power injected into grid
$V_{\mathrm{s:}}$ Inverter RMS output voltage
I_{s}: Inverter RMS output current
$V_{\mathrm{R}}^{\mathrm{d}}$: Projection of V_{s} voltage in Park frame
$I_{\mathrm{R}}^{\mathrm{d}}$: Projection of I_{s} current in Park frame

6.3 *Evaluation of the Capacitance* C *at the Inverter Input*

The purpose of dimensioning the continuous line-side capacity is to limit the ripple of the continuous voltage on the basis of single-phase analysis. The ripple of the voltage is given by the following relationship (Abdeddaim and Betka 2007):

$$\Delta V = \frac{1}{C} \int \frac{P_0(t)}{V_{\mathrm{DCref}}} dt = \frac{V \cdot I}{2 \cdot C \cdot V_{\mathrm{DCref}}} \sin 2\omega t \tag{23}$$

Maximal ripple ΔV_m gives the capacitance value

$$C = \frac{P_0}{\omega \cdot V_{\mathrm{DCref}} \cdot \Delta V_{\mathrm{m}}} \tag{24}$$

For standards conditions ($E = 1000$ W/m^2, $T = 25°$)

$$P_0 = 3 \text{ KW}$$

$$V_{\mathrm{DCref}} = 693 \text{ V}$$

$$\Delta V_{\mathrm{m}} = 2 \text{ V}$$

$$C = 6.95 \cdot 10^{-3} \mathrm{F}$$

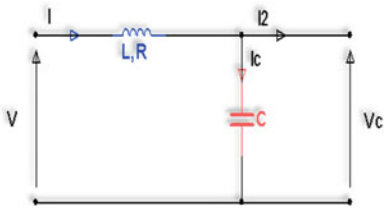

Fig. 8 LC filter circuit

6.4 LC Filter Circuit

A system with forced commutation like PWM (Pulse Midth Modulator) or other control techniques of voltage source inverter generates chopping harmonics. The effect of such harmonics is masked in many works for the fact that the grid to which the inverter is connected is supposed to be ideal. It is obvious that in reality this is not the case, since a direct connection can lead to major dysfunctions. In order to eliminate this harmonics, an LC filter circuit shown in Fig. 8 is inserted between the inverter and the three-phase grid.

6.4.1 Calculation of *L* and *C* Low Band Filter (Qin et al. 2002)

Without load $I_2 = 0$, if the internal resistance of the inductor is neglect ($R = 0$) the filter transfer function becomes

$$F_T(s) = \frac{V_c(s)}{V(s)} = \frac{1}{LCs^2 + 1} \tag{25}$$

$$s = j\omega \tag{26}$$

$$F_T(j\omega) = \frac{V_c(j\omega)}{V(j\omega)} = \frac{1}{LC(j\omega)^2 - 1} \tag{27}$$

$$F_T(j\omega) = \frac{1}{1 - LC\omega^2} \tag{28}$$

In order that the filter operates without diminution of output signal magnitude, it must be that

$$|F_T(j\omega)| = 1 \tag{29}$$

$$1 = LC\omega_c^2$$

$$\omega_c = 2 \cdot \pi f_c \tag{30}$$

where f_c is the cutoff frequency (resonance) of LC filter

$$L = \frac{1}{4\pi^2 f_c^2 \cdot C} \tag{31}$$

The choice of the inductance and the capacity values can be obtained by laying down the simple condition, which consists in eliminating the harmonics of a nature higher than two, this being checked by the fact that they have a frequency equal to twice or higher than that of the fundamental.

In our case, we have chosen

$$f_c = \frac{f_d}{10}$$
$$f_d = 10khz$$
$$f_c = 1khz$$
$$LC = \frac{1}{4\pi^2 \cdot f_c^2} = \frac{1}{4\pi^2 \cdot 10^6}$$
$$LC = 0.0253 \cdot 10^{-6}$$

If we consider $C = 70\ \mu F$, subsequently $L = \frac{0.0253 \cdot 10^{-6}}{70 \cdot 10^{-6}} = 360\ \mu H$.

6.5 *The Three-Phase Electrical Network*

The considered electrical network is shown in Fig. 9 with several significant aspects such as source power short circuit, various loads consumption, and voltage drop due to lines impedances. Thus, its behavior can approach the reality under normal operation, and this furthermore offers the possibility of carrying out certain defects.

6.5.1 Three-Phase PLL (Phase Looked Loop) in Park Domain

The PLL is a system that is intended to control the instantaneous output signal phase $\varphi_s(t)$ on the instantaneous input signal phase $\varphi_e(t)$. Such a system is the base of numerous electronic circuits: synchronous detection and magnitude demodulation

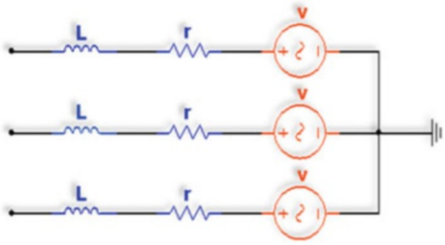

Fig. 9 Three-phase electrical grid 380 V/50 Hz

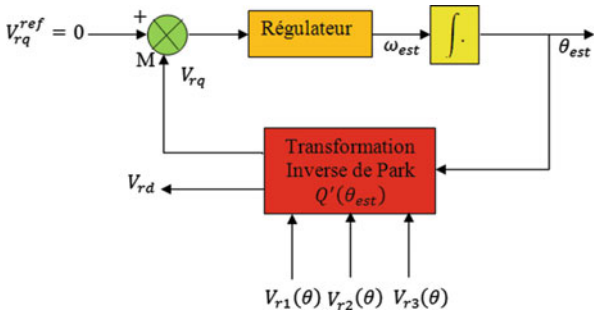

Fig. 10 Principle of PLL in Park domain

of frequency (FM and FSK), frequency synthesis, and digital telecommunications (Best 1987).

In electrical network supply applications, the PLL is primarily used for estimating and filtering the phase and the instantaneous magnitude of the equivalent phasor of a three-phase system. Figure 10 shows the classic structure of three-phase PLL.

6.6 Current-Controlled Voltage Source Inverter

The output array of a voltage source inverter is a voltage. However, this device correctly filtered at the output and with an adequate control can be used for the injection of a controlled current in the grid. The purpose of this control is to obtain an output current which follows its reference with lag and a possible small error, and a sufficient high dynamics.

The simple solution to control the inverter is by hysteresis which gives rapid dynamics, good accuracy, and high rigidity, and there is no compensation in short circuit. However, the major problem of hysteresis control is that the average commutation frequency varies with the load current and therefore irregular and hazardous behavior of switches. The consequence of such behavior is a complementary fatigue of switches, and the dimensioning of the filter becomes difficult.

The control strategy is based on the regulation of current (voltage) in continuous coordinate which is widely used. The closed loops' regulation used in such control provides a rapid response in transient regime and a high performance in a stationary regime. This control strategy allows the inverter to control the voltage in an autonomous way in frequency and magnitude across the load. This strategy contains two regulation loops: internal loop for current regulation and external loop for voltage regulation. The two arrays are controlled in a rotating framework dq. The regulation of i_d current component makes it possible to act on the active power flux, whereas the regulation of i_q current component acts on the reactive power flux.

There are many types of current correctors, and the choice of the corrector type depends again on the characteristics of applications.

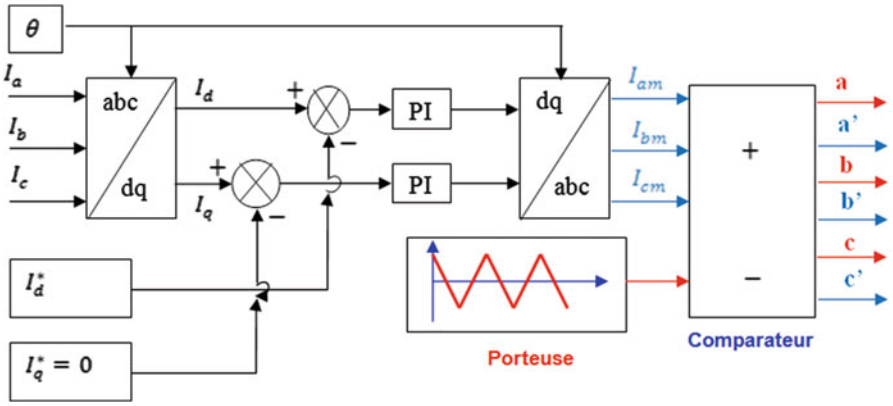

Fig. 11 Scheme of current-controlled photovoltaic system

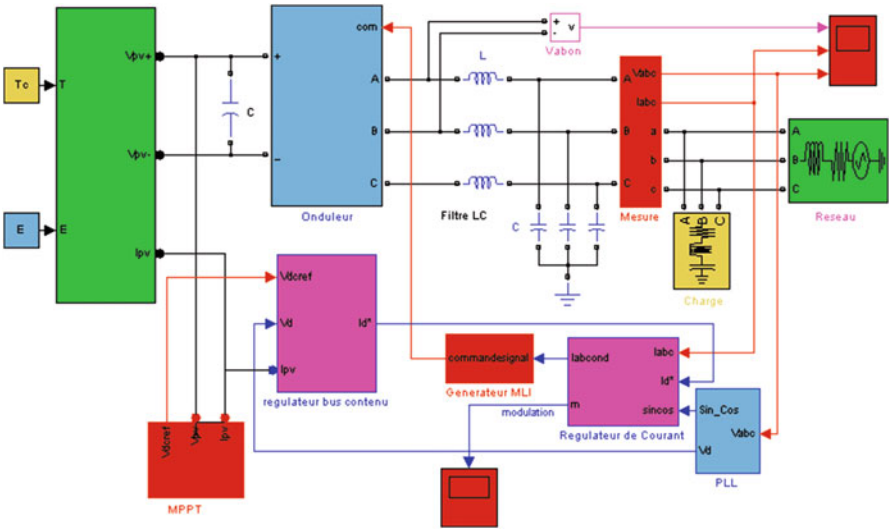

Fig. 12 Scheme of PVG connection to a three-phase electrical network

In this case, the PI regulator has been chosen for its rigidity and good accuracy stability. Figure 11 shows the scheme of current-controlled PV system (Raou and Lamchich 2004).

7 Model of PVG Connected to Three-Phase Electrical Network

Figure 12 shows the photovoltaic system modeled in MATLAB/Simulink environment.

8 Simulation Results

Figure 13 shows the shape of continuous line voltage, which follows its reference without overshooting and static error nearly null in permanent regime. Figure 14 shows the phase voltage between a and b before filtering. Figures 15 and 16 show the line voltage and phase voltage which approximately equals to 220 V and 380 V, respectively, after response time equal to 0.008 s.

Figure 17 shows phase voltage and line current in phase which mean that unit output power factor, whereas Fig. 18 shows the shape of the modulation ratio which stabilizes around 0.86 after a response time of 0.008 s

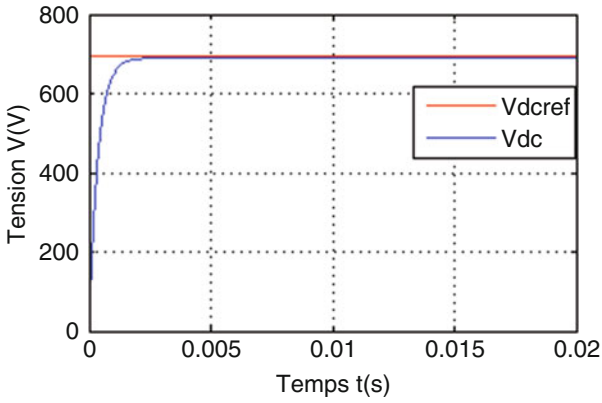

Fig. 13 Regulation characteristics of continuous line voltage

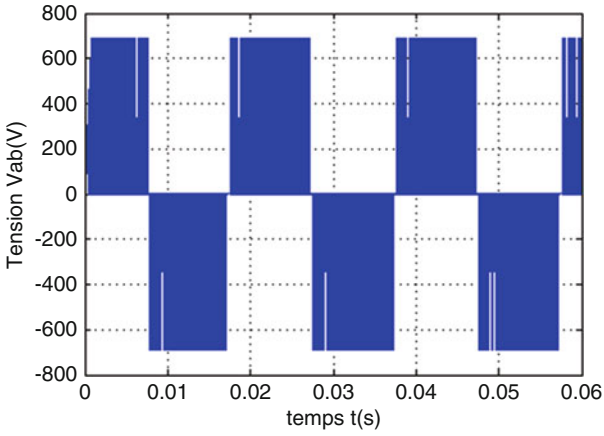

Fig. 14 Inverter output phase voltage V_{ab}

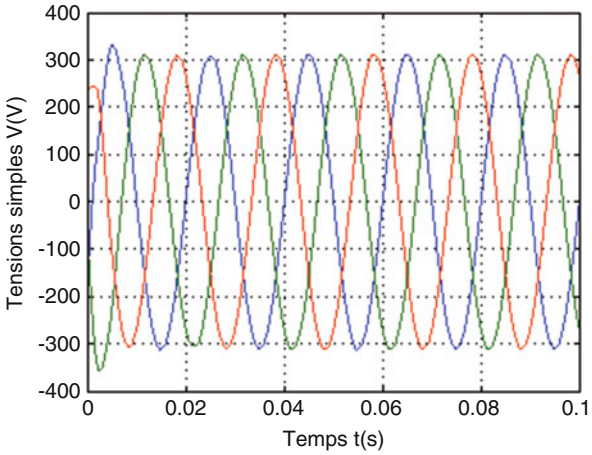

Fig. 15 Line voltage across the load

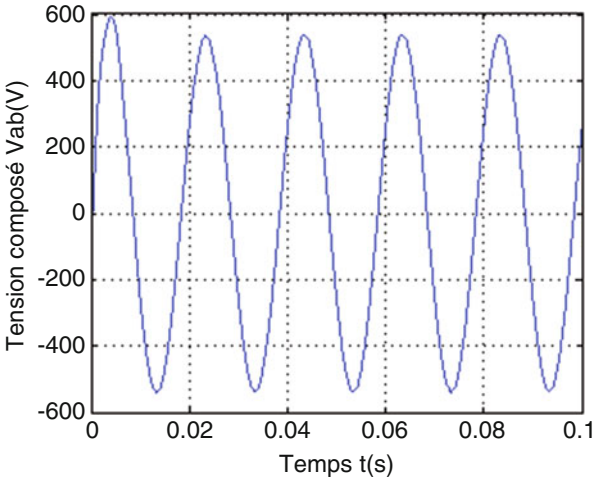

Fig. 16 Phase voltage V_{ab} across the load

9 Conclusions

The system study is focused on the optimization of photovoltaic energy as well as its injection in three-phase electrical network through an inverter with minimum possible losses.

The adopted approach is to improve the operation of different parts of the chain beginning with the selection of photovoltaic panel, the choice of maximum power point (MPPT) strategy, as well as the techniques of connection to the grid.

In order to conceive and make an application, a photovoltaic system connected to three-phase electrical network, a mathematical model of each subsystem is presented.

We have observed a good dynamic behavior of the system. This is due to the control strategy chosen (MLI).

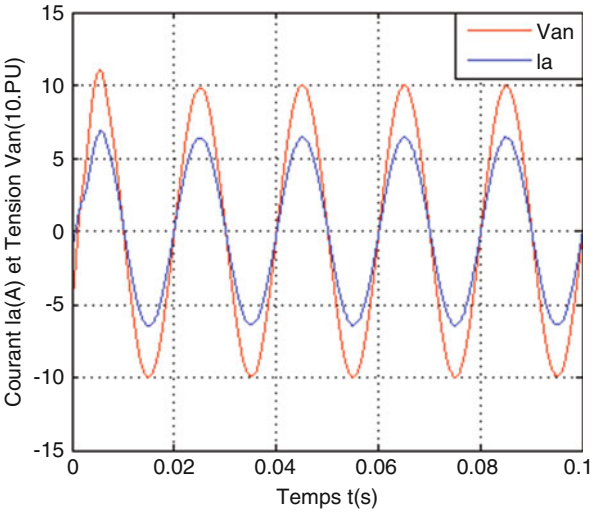

Fig. 17 Line current and voltage across the load

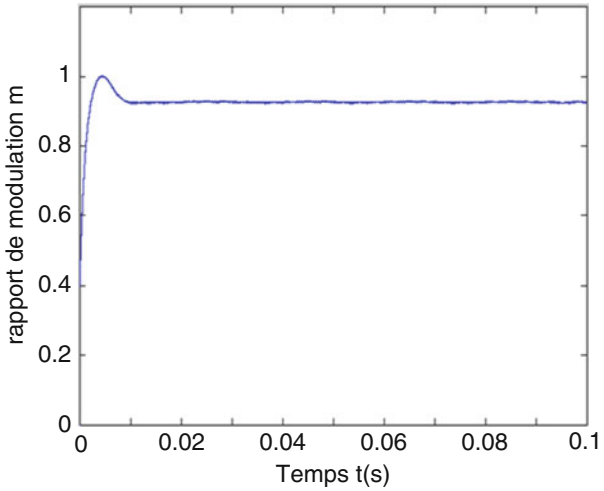

Fig. 18 Modulation ratio *m*

Appendix

Shell SP150-PC panel Characteristics

$$I_{sc} = 4.8 \text{ A}, \ I_{op} = 4.4 \text{ A}, \ V_{co} = 43.4 \text{ V}, V_{op} = 34 \text{ V}$$
$$R_S = 0.529 \ \Omega, \ \alpha = 2 \text{ mA/℃}, \ \beta = -152 \text{ mV/℃}$$
$$N_s = 20, \ N_p = 1$$

Regulator PI parameters: $K_{P1} = 2, K_{i1} = 107.48, K_{P2} = 0.4, K_{i2} = 100$
Inverter input filter parameters:

$$\Delta V_m = 2\text{V}, C = 6.95 \cdot 10^{-2}\text{F}$$

Inverter output filter parameters:

$$C = 70 \ \mu F, L = 360 \ \mu H$$

References

Abdeddaim, S., Betka, A.: Connexion au réseau d'une source photovoltaïque à facteur de puissance unitaire. ICRE'07 Université Bejaia, Algeria (2007)

Best, R.E.: Phase locked loups design, simulation, and applications. Best Engineering, Oberwil (1987)

Faranda, R., Leva, S.: Energy comparison of MPPT techniques for PV systems. WSEAS TRANSACTIONS on POWER SYSTEMS, **3**(6), (2008). ISSN: 1790-5060

Hoque, A.K., Wahid, A.: New mathematical model of a photovoltaic generator (PVG). J. Electrical Eng. The Institute of Engineers, Bangladesh. **EE 28**(1), (2000)

Qin, Y.C., Mohan, N., West, R., Bonn, R.: Status and needs of power electronics for photovoltaic inverters. Sandia National Laboratories, Albuquerque (2002)

Raou, M., Lamchich, M.T.: Average current mode control of a voltage source inverter connected to the grid: application to different filter cells. J. Electrical Eng. **55**(3–4), 77–82 (2004)

Sera, D., Teodorescu, R., Kerekes, T.: Teaching maximum power point trackers using a photovoltaic Array model with graphical user Interface. Photovoltaic specialists conference record of the 28th IEEE 15–22, 1699–1702 (2000). Website: Differentes Archituctures. http://Hmf.Enseeiht.Fr/Travaux/CD0102/Travaux/Optemf/bei_eol/Ge/Archi.Htm

Technical and Economic Prefeasibility Analysis of Residential Solar PV System in South Kazakhstan

Anuar Assamidanov, Nurbol Nogerbek, and Luis Rojas-Solorzano

1 Introduction

Kazakhstan has substantial influence over energy supply of the world since it owns large natural resources (oil, gas, coal, uranium, and other commodities) and a 3% of the raw material available in the planet. According to statistics (EIA 2013), in 2012, the total power generation capacity of Kazakhstan was approximately 19.5 GW, 85% of which was coal-fired power and the remaining 15% was hydropower. Since 2010, the country decided to import electricity from Kyrgyzstan and Uzbekistan to supply its southern regions, since the installed power plants do not reach estimated load and, therefore, the consumption of electricity overcomes its production in the country.

Thus, within this framework, the country is currently devoted to the development of its renewable energy sector. Kazakhstan has important potential in power generation from wind, solar, hydrothermal, and small hydro sources. Indeed, the potential energy generation of Kazakhstan exceeds one trillion kWh per year which is about 10 times the annual energy consumption in the country to date (EIA 2013). By the year 2050, the milestone for renewable energy sources is targeted to reach 50% of total energy consumption (Kazenergy 2014).

At this moment, apart from partial use of hydropower, the potential for renewable energy is not used sufficiently, and a significant generation of electricity may be added by solar power resources according to the economic development targets of the country. For example, 2200–3000 sunny hours per year and 1300–1800 kWh/m^2/year are available due to solar radiation in the country (see Fig. 1 as a reference of the potential in the country) (Kazenergy 2014).

A. Assamidanov (✉) • N. Nogerbek • L. Rojas-Solorzano
Nazarbayev University, Department of Mechanical Engineering, Astana 010000, Kazakhstan
e-mail: aassamidanov@nu.edu.kz

© Springer International Publishing AG, part of Springer Nature 2018

F. Aloui, I. Dincer (eds.), *Exergy for A Better Environment and Improved Sustainability 2*, Green Energy and Technology,
https://doi.org/10.1007/978-3-319-62575-1_55

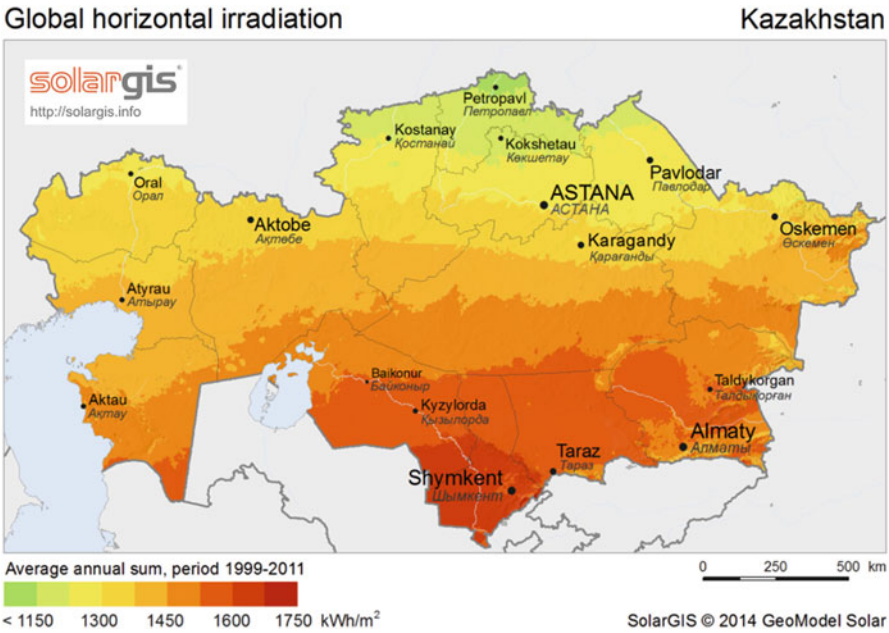

Fig. 1 Horizontal solar radiation on the territory of Kazakhstan (source indicated on the map)

The potential of solar energy in Kazakhstan is estimated at 340 billion tonnes of oil equivalent (toe) annually. However, despite this very attractive scenario for solar power generation this resource is still scarcely used in the country (Energy Charter Secretariat 2013).

Within these favorable conditions, photovoltaics (PV) today attract considerable attention, but on-grid PV market is not a profitable sector by itself (Dornfeldt 2014). It is dependent on the governmental support, which still must stimulate investment with subsidies. In recent years, rapid development in grid-connected building-integrated PV systems around the world, mainly in developed countries, is due to the government-initiated renewable energy programs aiming at the development of renewable energy applications and reduction of greenhouse gas emissions (Erge et al. 2001). For example, in 1990, Germany introduced a "100,000-roof program" (Ramana 2005). Japan came with a 70,000-roof program that started in 1994 and lasted for the rest of that decade (Yang et al. 2004). A PV system dissemination program has been very successful in the USA, and its 1 million solar-roof initiative is gradually advancing (SSE 2009). Grid-connected PV systems, thus, took off in the mid- to late 1990s, and since then, it has been the dominant application in the PV sector.

South Kazakhstan is situated between 42.3° and 44.9° north latitude and 65.5° and 71.4° east longitude with an area of 726 km^2, which is an ideal location for solar energy utilization, as previously shown in Fig. 1. Daily solar radiation varies in the range of 4–4.45 kWh/m^2. Thus, densely populated cities like Shymkent, Taraz, and

Kyzylorda could be electrified by PV on-grid systems using the inexhaustible and pollution-free solar energy with locally available technologies. Extra benefits, such as supporting a weak grid and reducing CO_2 emissions, could be also accounted as potential incomes once the program is in mass scale.

Additionally, Kazakhstan has also established at the end of May 2014 a new feed-in tariff (FIT) law – "On Supporting the Use of Renewable Energy Sources." This policy is expected to further increase the installation of grid-connected photovoltaic (PV) systems. Such policy has been implemented and also has been studied in a number of countries such as the UK, Ukraine, Australia, Spain, Taiwan, Germany, Tanzania, and other countries, with very positive results (Erge et al. 2001). As city-level FIT laws for promoting solar photovoltaic panels are very recent and its suitability has not been thoroughly examined yet (Renewable Market Watch 2014), the fundamental objective of this investigation is to analyze technical and economic prefeasibility of implementing residential photovoltaic system in South Kazakhstan, taking into account the diversity in the southern region and new regulations, as no systematic study has been done to justify the viability of solar power generation in this region to date. As an alternative solution, financial incentives could be obtained if the project is included in the list of priority sectors of the "Business Road Map – 2020" that is one of the "DAMU Entrepreneurship Development Fund" projects. This initiative has as its main goal to provide governmental support for projects of non-primary sectors of the economy (Halyk bank 2013).

2 Solar Energy Resource Potential

2.1 Theoretical Potential

The average sunny hours per day and monthly solar radiation were found, based on an average solar radiation data taken from NASA, for three widespread locations in South Kazakhstan available through RETScreen workbench tool (SSE 2009). According to the climate database from NASA, South Kazakhstan receives approximately 1185 GWh of solar energy every year, which is more than 30 times higher than the current electricity generation in those cities. However, in the course of exploitation, constraints such as land use, geographical area, and climate are encountered. Theoretically, a great potential for developing solar power system is considered when the average daily radiation is above 4 Wh/m^2/day on an average per year (Energy Charter Secretariat 2013).

2.2 Technical Potential

There is a clear market potential for grid-connected PV systems in the densely populated urban and electrified areas, i.e., for solar home systems are central-grid households. Locally available PV system specifications and financial assumptions, according to current conditions and trends in Kazakhstan, were entered in the RETScreen workbench. Then, the expected generation of electricity by the solar power home system was calculated on a yearly basis under different scenarios of feed-in tariff (FIT) in place.

Local company Astana Solar is currently producing Poly-Si photovoltaic modules using Kazakhstani silicon (Astana Solar 2012). The efficiency of the PV array is about 16% and Astana Solar guarantees that its products have a lifetime of at least 25 years. Table 2 shows the detailed technical specifications of the solar panel that was used in this study.

3 Economic Viability of Grid-Connected Solar PV System

3.1 Global Solar Radiation

Due to limited availability of solar radiation data in Kazakhstan, a NASA data set for the period from 1985 to 1995 was used. Ten-year averaged NASA global solar radiation data from three widespread South Kazakhstan locations (Table 1) were used for the technical-economic analysis of grid-connected solar PV systems (SS 2009).

3.2 Proposed 6.6 kW Solar PV System and Financial Assumption

The proposed solar PV grid-connected system is an array with a total power capacity of 6.6 kWp consisting of 30 fixed panels with a total area of 49.2 m^2 (Table 2). The size of the array was chosen such that it fits the estimated roof area of a South Kazakhstani residence. The solar array system costs 2354 US$/kWp (Astana Solar 2012). The PV array is faced toward south and is inclined at a

Table 1 Average daily solar radiation in South Kazakhstan

City name	Elevation (m)	Latitude	Longitude	Radiation (NASA) (kWh/m^2/day)
Kyzylorda	130	44.9°	65.5°	4.21
Taraz	655	42.9°	71.4°	4
Shymkent	604	42.3°	69.7°	4.45

Table 2 Technical specification of solar PV panels used in the analysis

Item	Specification
Manufacturer	Astana solar LLP
PV module type	Multi-Si
Module number	KZ PV 230 M60
Efficiency	16%
Rated power (P_{max})	220 Wp/module
Number of modules	30 (6.6 kWp array)
Voltage at P_{max}	29.4 V
Current at P_{max}	7.5 A
Short circuit current	8.3 A
Open circuit voltage	36.5
Frame area	1.64
Dimension	1.649m × 0.992m × 0.40 m
Weight	19.5 kg

Table 3 Financial assumption and data for the study

Parameter	Value (currency at year 2014 value)
Solar panel	2354 US$/kWp
Inverter cost	220 US$/kWp
Annual O&M	US$168
Inflation rate	5.4%
FIT	191.4 US$/MWh
FIT escalation rate	8%
Debt ratio	80%
Debt interest rate	17%
Debt term	10 years
Project life	25 years

42°angle, equal to the site latitude. Zero azimuth angles were taken for all the studied locations. DC-into-AC string inverters were utilized in the proposed system with a total capacity of 5.94 kW, with an efficiency of 90%. The cost of the inverter is 220 US$/kWp (Astana Solar 2012). The economic feasibility analysis was performed using data on initial costs associated with the implementation of the proposed system, and prevailing loan interest, inflation, and energy escalation rates were prevalent in the country.

In this study, project life is assumed to be 25 years. As this project is in prefeasibility level, calculation of the total cost has been simplified. With respect to total expenses, *development* represents 5%, and *engineering* 15% of the total cost. Annual O&M is about 1% of total initial cost. The cost of the construction phase would be 75% of the total initial expenses. Table 3 provides some details and assumptions considered for the entire financial analysis, based on the current market and financial situation of the country (The National Bank of Kazakhstan 2015). Feed-in tariff (FIT) is specially included according to new government

policies starting on the generation of power from renewable sources, in place since 2014 (Ministry of Energy of Kazakhstan 2014). Therefore in this analysis, the FIT will be assumed as 191.4 $/MWh.

3.3 Results

3.3.1 Electricity Generation

The amount of equivalent DC electrical energy actually generated by the proposed 6.6 kWp solar grid-connected system to the utility was calculated for all three locations in the annual electricity production. The highest electricity annual production was obtained in Shymkent with about 8.9 MWh. The lowest production was obtained in Taraz with an annual electricity generation of 8.1 MWh. For an average city in South Kazakhstan, an estimate of 6.1 MWh/year of electricity can be delivered using the proposed PV system.

3.3.2 Economic Feasibility Indicators

The decision making indicators from the financial analysis throughout the PV system lifetime are presented as follows (see also Table 4):

Internal rate of return (IRR): The maximum IRR of 17.9% was observed in Shymkent, while the minimum IRR of 9.9% was observed in Taraz. Therefore, an IRR of 16% can be obtained from an average city in South Kazakhstan.

Net present value (NPV): The highest NPV was about $14,523 for Shymkent, and the lowest was about $11,366 for Taraz.

Benefit-cost (B-C) ratio: The B-C ratio was found to be highest (9.65) in Shymkent, while the lowest (7.84) was found in Kyzylorda.

Simple payback (SP): It was found that on an average, an SP of about 9.9 years can be obtained from any location of South Kazakhstan.

Table 4 Economic indicators for 6.6 – kWp solar PV system for three locations, South Kazakhstan

Financial results	Shymkent	Kyzylorda	Taraz
IRR on equity	17.9%	17.3%	16%
Net annual income	$1191	$1078	$973
Net present value	$14,523	$13,741	$11,366
Payback period	9.9	10.2	10.8
Benefit-cost ratio	9.65	9.03	7.84

3.4 Sensitivity Analysis

A Monte Carlo analysis, based on a sample of 500 scenarios, allowed finding the probable outcomes under known uncertainty of input parameters. In this study, a ± 10% uncertainty is assumed for the initial cost, O&M, FIT, and debt ratio, while an uncertainty of ±20% was assumed for debt interest rate and debt term, as debt parameters vary widely with current Kazakhstani bank services that depend on project scope.

The impact tornado graph, presented in Fig. 2, shows how much of the variation in the financial parameter can be explained in each input parameter. The impact

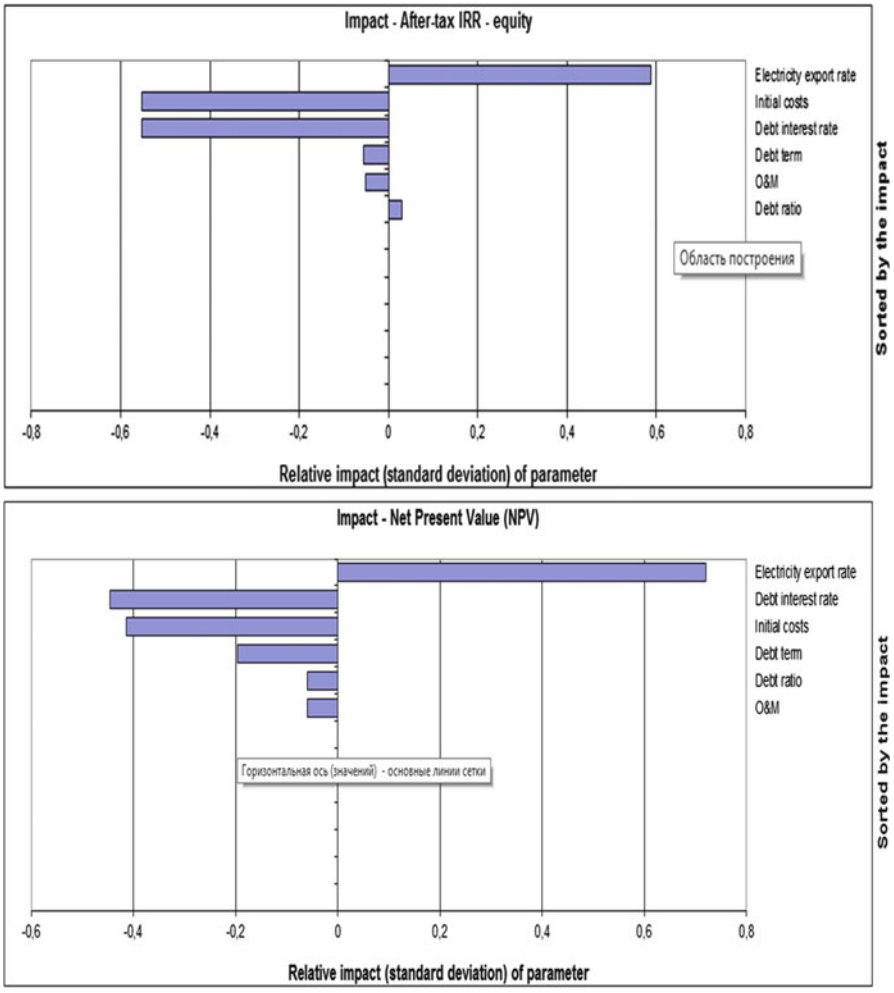

Fig. 2 Impact results of NPV and IRR for Shymkent

Table 5 Comparison of financial viability

Financial results	Residential PV in Shymkent	Residential PV in Shymkent with government subsidy
IRR on equity	17.9	18.1
Net annual income	$1191	$2523
Net present value	$14,523	$26,220
Payback period	9.9	5.5
Benefit-cost ratio	9.65	4.12

analysis demonstrates that the changes in NPV and IRR are largely due to variation of FIT, followed by initial cost and debt interest rate in about the same level of importance, as shown in Fig. 2.

Since residential solar PV has no analogies within the country, this analysis should be used as a support mechanism to stimulate implementation of these types of projects in the country.

According to these results, an even better solution for Shymkent could be obtained if the project is included in the list of priority sectors of the "Business Road Map – 2020" that is one of the "DAMU Entrepreneurship Development Fund" projects. This initiative has, as its main goal, to provide governmental support for projects of non-primary sectors of the economy. In this particular case, if implemented, the government may subsidize 50% of the initial cost of project, and the remainder is taken completely as loan (100% debt ratio, i.e., no equity needed) from the bank by the owner at 7% of debt interest rate (Halyk bank 2013). As it can be observed in Table 5, there are significant differences in financial results when government provides subsidies. All financial parameters indicate that government subsidy is a very beneficial approach to promoting residential solar PV (Fig. 3).

4 Conclusions

This study analyzes the technical and economic potential of solar photovoltaic-grid connected system in South Kazakhstan. The technical assessment considers several locally manufactured PV systems. The study focuses on polycrystalline solar cells (poly-Si) due to its optimal financial and technical specifications for South Kazakhstan climatic conditions.

The analysis determined that with a 6.6 kWp PV array it is possible to generate and export to the grid a minimum of 8.9 MWh in Taraz, and a maximum of 9.1 MWh in Shymkent. Financial indicators from the life cycle cost analysis for all sites showed favorable conditions for the development of the proposed residential solar

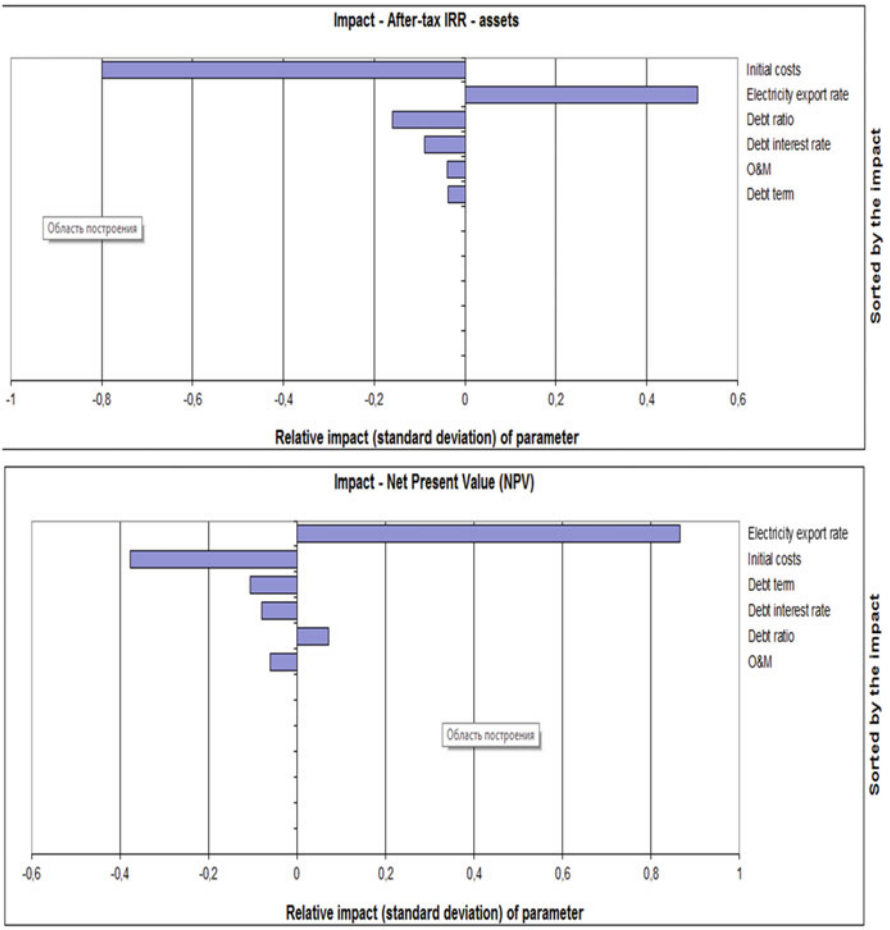

Fig. 3 Impact results of NPV and IRR for Shymkent with government support

PV system in South Kazakhstan, proving that on a lifetime frame of 25 years, the application of solar PV for residential grid-connected systems is quite feasible financially.

A new policy in conjunction with the feed-in tariff (FIT) is envisioned from the study. The economic analysis suggests that a subsidy of 50% of total initial cost should be considered to maximize the advantage for the residential owner of the PV-system in southern regions. This will also help to support the weak grid in the region, under constant threat of breakdown during peak load hours.

References

Astana Solar: About company. Retrieved November 2, 2014, from: http://www.astanasolar.kz/en/about-us (2012)

Dornfeldt, M.: The future of the Kazakh energy sector and the Kazakhstan 2050 strategy. Retrieved November 2, 2014, from 18th REFORM Group Meeting http://www.polsoz.fu-berlin.de/polwiss/forschung/systeme/ffu/veranstaltungen/termine/downloads/13_salzburg/Dornfeldt-Salzburg-2013.pdf (2014)

Energy Charter Secretariat: Investment Climate and Market Structure Review in the Energy Sector of KAZAKHSTAN. Retrieved November 3, 2014, from Energy Charter: http://www.encharter.org/fileadmin/user_upload/Publications/Kazakhstan_ICMS_2013_ENG.pdf (2013)

Erge, T., Hoffmann, U., Kiefer, K.: The German experience with grid-connected PV-systems. Sol. Energy. **704**, 79–87 (2001)

IEA: World Energy Outlook. Retrieved November 3, 2014, from International Energy Statistics: http://www.eia.gov/countries/analysisbriefs/Kazakhstan/kazakhstan.pdf (2013)

Kazenergy: Green Energy of Kazakhstan. Retrieved November 2, 2014, from: http://www.kazenergy.com/ru/5-49-2011/3445-green-energy-of-kazakhstan.html (2014)

Ramana, P.V.: SPV technology dissemination – A global review. In: Solar Photovoltaic Systems in Bangladesh, Experiences and Opportunities, pp. 119–138. The University Press Limited, Dhaka (2005)

Renewable Market Watch: Kazakhstan Solar and Wind Power Markets. New feed-in tariffs and very good opportunities for 2014. Retrieved November 2, 2014., from: http://renewablemarketwatch.com/news-analysis/136-kazakhstan-solar-and-wind-power-market-new-feed-in-tariffs-and-very-good-opportunities-for-2014

SSE: Surface meteorology and Solar Energy, A renewable energy resource web site, sponsored by NASA's Earth Science Enterprise Program. Retrieved October 29, 2014., http://eosweb.larc.nasa.gov/sse

The National Bank of Kazakhstan: Loan market. Retrieved January 24, 2015., from: http://www.nationalbank.kz/?docid=158&switch=english

Yang, H., Zheng, G., Lou, C., An, D., Burnett, J.: Grid-connected building-integrated photovoltaics: a Hong Kong case study. Sol. Energy. **76**, 55–59 (2004)

Contribution of the Cogeneration Systems to Environment and Sustainability

Çomakli Kemal, Çakir Uğur, Çokgez Kuş Ayşegül, and Şahin Erol

1 Introduction

The reserve of energy resources in the world is tending to decrease, while the amount of energy needed by humanity is tending to increase. In addition, the dependence of the humanity on using energy is increasing day by day due to the improving technology and the rise in the life standards of people in the world. This situation is becoming the most important and essential issue of the world. In general, there are two ways to overcome this problem. One of them is to bring out and improve new and renewable energy sources such as solar or wind energy systems. The other way is to improve conventional energy converting systems for using existing energy source more efficiently and for longer time, such as cogeneration systems. In other words, people have to do their best to improve the sustainability of the energy resources. Cogeneration can be explained as the simultaneous production of power and usable heat by using one type of energy source such as oil, coal, natural gas, liquefied gas, biomass, or the sun. This system affords remarkable energy savings and frequently makes it possible to operate with greater efficiency when compared to a system producing heat or power separately. In conventional power plants, a large amount of heat is produced but not used.

Ç. Kemal (✉) • Ç.K. Ayşegül
Atatürk University, Faculty of Engineering Department of Mechanical Engineering, 25000 Erzurum, Turkey
e-mail: ucakir@bayburt.edu.tr

Ç. Uğur
Bayburt University, Faculty of Engineering Department of Mechanical Engineering, 69000 Bayburt, Turkey

Ş. Erol
Ordu University, Technical Vocational High School Machinery and Metal Technology Department, 52000 Ordu, Turkey

© Springer International Publishing AG, part of Springer Nature 2018

F. Aloui, I. Dincer (eds.), *Exergy for A Better Environment and Improved Sustainability 2*, Green Energy and Technology,
https://doi.org/10.1007/978-3-319-62575-1_56

These systems utilize the waste heat produced during electricity generation and allow more efficient fuel consumption. Along with the saving of fossil fuels, cogeneration also allows to reduce the emission of greenhouse gases (GHG) like CO_2 per unit useful energy output. By designing systems that can use the waste heat, the efficiency of energy production can be increased from current levels that range from 35% to 55% in conventional plants to over 90% in cogeneration systems.

Using conventional energy conversion systems and fossil fuels to run them has very negative effect on nature, environment, and ecology. This is known for many years and this issue is on top of the energy politics of the countries. Air pollution and greenhouse problem are the issues that are studied by the scientists to overcome for many years. There is a general thought by nonspecialists in environmental issues renewable energy sources can be used to overcome the negative effects of fossil energy sources and conventional energy conversion systems. But we must analyze this situation as in this millennium, energy is a necessity for us to continue our lives, just like water and air and it is impossible to live without it. In addition to this, in the current situation, all of the existing usable potential of the renewable energy sources is not sufficient to meet the energy demand of humanity. In light of these points, it is apparent we are obliged to use conventional energy sources and fossil fuels; otherwise life will be very hard for us. This means that air pollution and greenhouse effect will keep increasing day by day. Even though it seems impossible to stop air pollution and greenhouse effect, they can be reduced by using more efficient energy conversion systems by using less fuel. One of the energy conversion systems which produce more energy by using less fuel is cogeneration systems. As mentioned before, cogeneration systems produce two or more kinds of energy by using one type of fuel. Generally, heat energy and electrical energy are produced in cogeneration systems. This means that only one type of fuel is required to produce two types of energy. This way, less harmful gases and substances would be emitted to the atmosphere. In this study, environmental benefits and necessity of cogeneration systems are put forward. To achieve this aim, some scientific studies previously made on cogeneration systems are referred and analyzed.

2 Environmental Impact Evaluation of Cogeneration

Although cogeneration is an old and proven energy conversion system, in recent years, a resurgence of interest has come into the world of energetic issue because of the energy crisis that has taken part in dockets of the countries in the world. Cogeneration systems and district heating/cooling applications offer us some proven, reliable, applicable, and cost-effective solutions which make very important contributions to meet global heat and electricity demand. Energy supply efficiency, the use of waste heat, and low carbon renewable energy resources of those systems, they are an important part of greenhouse gas emission reduction strategies of the countries in the world. Cogeneration is the simultaneous

production of power and usable heat by using one type of energy source such as oil, coal, natural gas, liquefied gas, biomass, or the sun. In most of the cogeneration applications, the energy types produced simultaneously are electric and heat energy. Generally, those systems utilize the waste heat energy produced during electricity generation (Çakır et al. 2012; Can et al. 2009; Abuşoğlu and Kanoğlu 2009).

2.1 Emission Balances for Cogeneration and Separate Heat and Electricity

Computing the air quality effects of any technological change is always made difficult by the complexity, expense, and inaccuracy of air quality modeling. In the case of cogeneration, this computation is further complicated by difficulties in determining the emission changes occurring in the central utility system and by substantial variability in the emission factors to be applied to the cogeneration systems. The response of the utility system to an increase in cogenerated power, a critical parameter in determining not only emission impact but also oil savings (or loss), is difficult to predict. The addition of significant levels of cogenerated power to a utility's service area will affect both its current operations and future expansion. If the cogenerated power represents a displacement of current electricity demand in the service area (i.e., with retrofit of an existing facility for cogeneration), the utility will either reduce its own electricity production or power imports, with its decision based on costs, contractual obligations, or, perhaps, politics. It may also move up the retirement date for an older power plant or cancel planned capacity additions in response to cogeneration systems' displacement of either current or anticipated future demand. Because most utility grids draw on a mix of nuclear, coal, and oil-fired steam electric generators for base and intermediate loads, these plants may be scattered over a wide area; and because control systems for the fossil plants may vary drastically in effectiveness, the pollution implications of the response of the utility system to cogeneration are highly variable (Gibbons 1983).

3 Cogeneration Systems' Benefits

Generally, environment-friendly energy sources are thought as a kind of energy which is renewable, meaning that the use of such energy never damages the environmental stability and does not harm nature. Some types of energy can be thought of as renewable and friendly to the environment, and many governments promote the use of such energy and the development of new types of energy generating technology which fits this explanation. Corresponding to the rising

energy demand of people, there is an increase in concerns about that at which the ratio on greenhouse gas emissions and its damages will be realized. There are a lot of factors effective on decreasing the harmful emissions along with some choices that may exist. In connection to this point, energy efficiency is another important consideration. Increasing the energy efficiency is a vital way to make sustainable energy stretch further (Pehnt 2008).

From this point, cogeneration systems may make positive effect to protect the nature in two ways. One of them is to use cogeneration systems together with some renewable energy conversion systems like solar system or heat pumps. This way can be thought as a first-hand application for saving nature. The second one is fuel saving aspect of cogeneration. Less fuel usage brings about less harmful gas emissions.

There are many studies on using cogeneration systems with renewable systems in the open literature. One of the studies conducted was by Martin Pehnt, namely, *Environmental impacts of distributed energy systems: the case of micro cogeneration*. This study investigates environmental impacts of micro cogeneration by carrying out a detailed life cycle assessment and an analysis of local air quality impacts of micro cogeneration systems. Most micro cogeneration systems are superior, as far as the reduction of GHG emissions is concerned, not only to average electricity and heat supply but also to state-of-the art separate production of electricity in gas power plants and heat in condensing boilers. The GHG advantages of micro cogeneration plants are comparable to district heating with combined heat and power (CHP). Under the assumption that gas condensing boilers are the competing heat-supply technology, all technologies are within a very narrow range. Looking at the GHG reduction potential on the level of a supply object (e.g., a single-family house) by modeling the operation with a CHP optimization tool, the achievable mitigation potential is somewhat lower, because the micro cogeneration systems do not supply the whole energy demand. Here, fuel cells offer the advantage of a higher power-to-heat ratio. Environmental impacts other than those related to climate and resource protection relate more specifically to technology. In addition to investigating the emission side, analysis of the air quality situation of a residential area supplied by reciprocating engines was carried out. The analysis shows that for the selected conditions, the additional emission of NO_x due to the engines does not create severe additional environmental impacts. Another study was conducted by Thilak Raj et al. as a review study on renewable energy based on cogeneration technologies. That paper reviews the present-day cogeneration technologies based on renewable sources of energy. In addition, the study of novel methods, existing designs, theoretical and experimental analyses, modeling and simulation, environmental issues, and economic and related energy policies have been discussed in this study. One of the energy conversion applications which is suitable for being used together or as a cogeneration system is solar energy system. Solar energy can be importantly utilized for cogeneration systems and various such technologies have been proposed. Using focusing collectors, solar energy can be converted in a central power plant to electrical energy which can then be utilized to operate a vapor compression refrigerator to produce cooling. At the

same time, the waste heat rejected by the heat engine can be used to drive an absorption refrigerator. This system is simply called a solar powered cogeneration system for air conditioning and refrigeration and can play a dual role by saving energy and reducing the environmental pollution (Thilak Raj et al. 2011). Y. June Wu and Marc A. Rosen conducted a study on assessing and optimizing the economic and environmental impacts of cogeneration/district energy (DE) systems using an energy equilibrium model. In this study, energy equilibrium models can be valuable aids in energy planning and decision making. In such models, supply is represented by a cost-minimizing linear submodel and demand by a smooth vector-valued function of prices. In this paper, we use the energy equilibrium model to study conventional systems and cogeneration-based district energy (DE) systems for providing heating, cooling, and electrical services, not only to assess the potential economic and environmental benefits of cogeneration-based DE systems but also to develop optimal configurations while accounting for such factors as economics and environmental impact. The energy equilibrium model is formulated and solved with the software called WATEMS, which uses sequential nonlinear programming to calculate intertemporal equilibrium of energy supplies and demands. The methods of analysis and evaluation for the economic and environmental impacts are carefully explored. An illustrative energy equilibrium model of conventional and cogeneration-based DE systems is developed within WATEMS to compare quantitatively the economic and environmental impacts of those systems for various scenarios (June Wu and Rosen 1999). Goktun studied the solar power cogeneration system for air conditioning and refrigeration. By employing the energetic optimization technique, the optimal performance of a focusing collector-driven, irreversible Carnot cogeneration system for air conditioning and refrigeration is investigated. A minimum value for the total solar insolation needed to overcome internal irreversibilities for start-up of the system is defined, and the effect of the collector design parameters on this value is investigated (Göktun 1999). Photovoltaic cogeneration in the built environment was investigated and studied by Morgan D Bazilian et al. In this study, it is said that building integrated photovoltaic (BiPV) systems can form a cohesive design, construction, and energy solution for the built environment. The benefits of building integration are well documented and are gaining significant public recognition and government support. PV cells, however, convert only a small portion of the incoming insolation into electricity. The rest is either reflected or lost in the form of sensible heat and light. Various research projects have been conducted on the forms these by-products can take as cogeneration. The term cogeneration is usually associated with utility-scale fossil-fuel electrical generation using combined heat and power production. It is used here in the same sense as in the evaluation of waste heat and by-products in the production of PV electricity. It is important to have a proper synthesis between BiPV cogeneration products, building design, and other HVAC systems in order to avoid overheating or redundancy. Thus, this paper looks at the state of the art in PV cogeneration from a whole building perspective. Both built examples and research will be reviewed. By taking a holistic approach to the research and products already available, the tools for a more effective building

integrated system can be devised. This should increase net system efficiency and lower installed cost per unit area. An evaluation method is also presented that examines the energy and economic performances of PV/T systems. The performed evaluation shows that applications that most efficiently use the low-quality thermal energy produced will be the most suitable niche markets in the short- and mid-term (Bazilian Frederik Leenders et al. 2001). Experimental activity on two tubular solid oxide fuel cell cogeneration plants in a real industrial environment was investigated by M. Gariglio et al. The aim of the mentioned study is the comparison of two similar experimental campaigns performed on the two prototypes with different nominal power, in order to investigate the performance of the two generator designs. The factorial analysis has been applied considering two factors: setup temperature of the generator and fuel utilization factor. First, the obtained data have been analyzed by using the ANOVA of the experimental data of some dependent variables. Then, the regression models have been obtained for every dependent variable considered, and an optimization analysis has been performed. The analysis shows that the stack voltage sensitivity to the fuel utilization of the two systems has nearly the same value; and the stack voltage sensitivity to the generator setup temperature is different for the two systems (Gariglio et al. 2009). In a study on solar cogeneration panels, which investigated the method of combining photovoltaic cells with the transpired solar air heater, constructed prototypes measured the combined electrical and thermal energies produced and compared the results with single function reference panels. The results showed that combining the PV cells with the transpired solar wall panels can produce higher total combined solar efficiencies than either of the PV or thermal panels on their own (Hollick 1998). Lindenberger et al. presented an article on optimization of solar district heating systems, seasonal storage, heat pumps, and cogeneration which focused on to demonstrate the working of deco in a pilot housing project of the Bayerische Forschungsstiftung (Bavarian Research Foundation). The quantitative results, i.e., the percentages of fossil fuels saved and emissions reduced with the help of different technology combinations at different costs, are specific to the pilot project. On the other hand, the qualitative interdependencies between energy conservation, emission mitigation, and cost increases revealed by deco are likely to be the same in all regional energy systems in moderate climates at the present level of energy prices. The use of heat pumps (especially electric driven) has formed a new area of research. Heat pumps can be used together with cogeneration systems in some ways (Lindenberger et al. 2000). Marc A. Rosen conducted a study which is *Allocating carbon dioxide emissions from cogeneration systems: descriptions of selected output-based methods*. In this article, selected methods for allocating emissions for cogeneration systems are described and compared. In addition, exergy values for typical commodities encountered in cogeneration are presented. The reasoning behind the author's view is that the exergy-based method is the most meaningful and accurate of all the methods. Mancarella (2009) proposed a novel approach to energy and CO_2 emission modeling of cogeneration systems coupled to electric heat pumps. The specific objectives were to identify the relevant parameters and variables involved in the analysis of such composite systems and to provide a

synthetic and indicative assessment of the energy and environmental benefits potentially brought with respect to conventional energy systems. The conditions at which energy and emission benefits occur, and their extent with respect to classical generation means, are illustrated through various numerical examples, highlighting the generality and effectiveness of the models introduced (Rosen 2008). A comparative parametric analysis was carried out on a small-scale combined heat and power plant incorporating a heat pump and the conventional system in which heat is produced in a hot water boiler and electrical energy is drawn from the power grid (Soltani et al. 2014).

A study was conducted on multi-objective optimization of a solar-hybrid cogeneration cycle application to CGAM problem. In their study, an exergo-economic multi-objective optimization is reported here of a solar-hybrid cogeneration cycle. Modifications are applied to the well-known CGAM problem through hybridization by appropriate heliostat field design around the power tower to meet the plant's annual demand. The new cycle is optimized via a multi-objective genetic algorithm in Matlab optimization toolbox. Considering exergy efficiency and product cost as objective functions, and principal variables as decision variables, the optimum point is determined according to Pareto frontier graphs. The corresponding optimum decision variables are set as inputs of the system and the technical results are a 48% reduction in fuel consumption which leads to a corresponding decrease in CO2 emissions and a considerable decrease in chemical exergy destruction as the main source of irreversibility. In the analyses, the net power generated is fixed at 30 MW with a marginal deviation in order to compare the results with the conventional cycle. Despite the technical advantages of this scheme, the total product cost rises significantly (by about 87%), which is an expected economic outcome (Malinowska and Malinowski 2003). The researchers conducted a study called cogeneration solar system using thermoelectric module and Fresnel lens. The main purpose of their paper is the experimental investigation of an electricity and preheated water cogeneration system by thermoelectric. In the presented design, Fresnel lens and thermoelectric (TE) module were utilized in order to concentrate solar beam and generate electrical power, respectively. The energy of concentrated sunlight on the heat absorber of TE module is transferred to cold water reservoir. Heat transfer in TE module leads to temperature difference in its both sides and finally electrical power is generated. The main components of this system consist of a mono-axial adjustable structure, a thermoelectric generator (TEG), and a Fresnel lens with an area of 0.09 m^2. Results revealed that matched load output power is 1.08 W with 51.33% efficiency under radiation intensity of 705.9 W/m^2. In order to apply TE module capacity optimally for electrical generation, it is recommended to employ an array of Fresnel lenses which transfer heat to TE module by an intermediate fluid (Hasan Nia et al. 2014).

Rafael Galvao et al. presented the development of an energy model based on a mixed system of renewable energy, with primary energy sources as solar and biomass. It was a hybrid and autonomous system with solar PV panels and gasification cogeneration technology. Also it was an environment-friendly process aiming to reduce the energy demand, costs, and emissions. This energy model is

a new sustainable standard on energy consumption efficiency (electrical and thermal demands) of a small hotel building and a relevant contribution to certify the building in compliance with the laws of the country on the thermal performance of buildings (Rafael Galvão et al. 2011). Some other researchers investigated the socioeconomic drivers of large urban biomass cogeneration sustainable energy supply for Austria's capital, Vienna. They provided a detailed case study on Austria's by far largest biomass cogeneration plant. They described and analyzed the history of the project, putting particular emphasis on the main driving forces and actors behind the entire project development process.

There are some other works in the literature on using cogeneration with different systems to save more energy (Madlener and Bachhiesl 2007).

In the study conducted by Burer et al., *Multi-criteria optimization of a district cogeneration plant integrating a solid oxide fuel cell–gas turbine combined cycle, heat pumps and chillers,* a simultaneous optimization of the design and operation of a district heating, cooling, and power generation plant supplying a small stock of residential buildings has been undertaken with regard to cost and O_2 emissions. The simulation of the plant considers a super structure including a solid oxide fuel cell–gas turbine combined cycle, a compression heat pump, a compression chiller and/or an absorption chiller, and an additional gas boiler. The Pareto-frontier obtained as the global solution of the optimization problem delivers the minimal CO_2 emission rates, achievable with the technology considered for a given accepted investment, or respectively the minimal cost associated with a given emission abatement commitment (Burer et al. 2003).

A study was carried out by Jeff Smithers on the review of sugar cane trash recovery systems for energy cogeneration in South Africa. He says that biomass is a potential sustainable source of energy. Approximately one third of the energy available from sugar cane is contained in the top sand leaves trash, which are generally either burnt prior to harvesting or are not recovered from the field. Based on results reported in the literature and assuming a 50% trash recovery efficiency, it is estimated that 1.353 million ton of soft trash is available annually for cogeneration in South Africa, which could potentially produce 180.1 MW over a 200-day milling season. Studies in Brazil and Australia have shown that, the most efficient way of recovering the top sand leaves for cogeneration of power at sugar mills, is to use a chopper harvester with the separation of canes talk sand trash on the harvester either fully or partially turned off. In South Africa, more than 90% of the sugar cane crop is burnt and manually harvested, and hence new systems are proposed to recover the trash and transport the material to the mill (Smithers 2014). Dario Buoro and his friends conducted a study on Optimization of a Distributed Cogeneration System with solar district heating. The aim of the related study is to identify the optimal energy production system and its optimal operation strategy required to satisfy the energy demand of a set of users in an industrial area. A distributed energy supply system is made up of a district heating network, a solar thermal plant with long-term heat storage, a set of combined heat and power units, and conventional components also, such as boilers and compression chillers. In this way, the required heat can be produced by solar thermal modules, by natural gas cogenerators, or by

conventional boilers. The decision variable set of the optimization procedure includes the sizes of various components, the solar field extension, and the thermal energy recovered in the heat storage, while additional binary decision variables describe the existence/absence of each considered component and its on/off operation status. The optimization algorithm is based on a mixed integer linear programming (MILP) model that minimizes the total annual cost for owning, maintaining, and operating the whole energy supply system. It allows calculating both the economic and the environmental benefits of the solar thermal plant, cooperating with the cogeneration units, as well as the share of the thermal demand covered by renewable energy, in the optimal solutions. The results obtained by analyzing different system configurations show that the minimum value of the average useful heat costs is achieved when cogenerators, district heating network, solar field, and heat storage are all included in the energy supply system and optimized consistently. Thus, the integrated solution turns out to be the best from both the economic and environmental points of view (Buoro et al. 2014). The aim of the study by Marta Serrano Delgado and his friend is to model and simulate the thermal and electrical efficiencies of the cogeneration plant of a paper mill. The final purpose is the benefits optimization by adjusting production to the amount of energy to be sold. It is necessary to know it because the sale price goes down when the actual production of electrical energy does not match the scheduled power (Delgado et al. 2013).

4 Conclusion

Importance of cogeneration systems is well known for many years by the people who are interested in energy conservation. But environmental and ecological aspects of cogeneration are very important too. The systems' less fuel-using specification and efficiency level make them very important to the environment. Due to the primary energy savings with high efficiency levels and decrease in greenhouse gas emissions, these systems make important contributions to the environment and nature. This efficiency also reduces air pollution and greenhouse gas emissions, increases power reliability and quality, reduces grid congestion, and avoids distribution losses. All in all, cogeneration systems make very important contributions to nature in different ways.

References

Abusoglu, A., Kanoglu, M.: Exergetic and thermodynamic analyses of diesel engine powered cogeneration. Part 1. Formulations. Appl. Therm. Eng. **29**, 234–241 (2009)

Bazilian Frederik Leenders, M.D., Van der Ree, B.G.C., Prasad, D.: Photovoltaic cogeneration in the built environment. Sol. Energy. **71**(1), 57–69 (2001)

Buoro, D., Pinamonti, P., Reini, M.: Optimization of a distributed cogeneration system with solar district heating. Appl. Energy. **124**(2014), 298–308 (2014)
Burer, M., Tanaka, K., Favrat, D., Yamada, K.: Multi-criteria optimization of a district cogeneration plant integrating a solid oxide fuel cell–gas turbine combined cycle, heat pumps and chillers. Energy. **28**, 497–518 (2003)
Cakir, U., Comakli, K., Yuksel, F.: The role of cogeneration systems in sustainability of energy. Energy Convers. Manag. **63**, 196–202 (2012)
Can, F.O., Celik, N., Dagtekin, İ.: Energetic and exergetic–economic analyses of a cogeneration ther-mic power plant in Turkey. Int. Commun. Heat Mass Transfer. **36**, 1044–1049 (2009)
Delgado, M.S., Bernad, E.C., Palacín, J.I.G.: Cogeneration process modelling in a paper factory. Procedia Eng. **63**, 966–972 (2013)
Gariglio, M., De Benedictisi, F., Calì, M., Orsello, G.: Experimental activity on two tubular solid oxide fuel cell cogeneration plants in a real industrial environment international. J. Hydrogen Energy. **34**(10), 4661–4668 (2009)
Gibbons: Industrial and commercial cogeneration. http://www.princeton.edu/~ota/disk3/1983/8311/831108.PDF, chapter 6 (1983)
Goktun, S.: Solar powered cogeneration system for air conditioning andrefrigeration. Energy. **24**, 971–977 (1999)
Hasan Nia, M., Abbas Nejad, A., Goudarzi, A.M., Valizadeh, M., Samadian, P.: Cogeneration solar system using thermoelectric module and fresnel lens. Energy Convers. Manag. **84**, 305–310 (2014)
Hollick, J.C.: Solar cogeneration panels. Renew. Energy. **15**, 195–200 (1998)
June Wu, Y., Rosen, M.A.: Assessing and optimizing the economic and environmental impacts of cogeneration/district energy systems using an energy equilibrium model. Appl. Energy. **62**(3), 141–154 (1999)
Lindenberger, D., Bruckner, T., Groscurth, H.-M., Kummel, R.: Optimization of solar district heating systems: seasonal storage heat pumps and cogeneration. Energy. **25**, 591 (2000)
Madlener, R., Bachhiesl, M.: Socio-economic drivers of large urban biomasscogeneration sustainable energy supply for Austria's capital Vienna. Energy Policy. **35**, 1075–1087 (2007)
Malinowska, W., Malinowski, L.: Parametric study of exergetic efficiency of a small-scale cogeneration plant incorporating a heat pump. Appl. Therm. Eng. **23**, 459–472 (2003)
Mancarella, P.: Cogeneration systems with electric heat pumps: energy-shifting properties and equivalent plant modeling. Energy Convers. Manage. **50**, 1991–1999 (2009)
Pehnt, M.: Environmental impacts of distributed energy systems-the case of micro cogeneration. Environ. Sci. Pol. **11**, 25–37 (2008)
Rafael Galvão, J., Leitão Augusto, S., Silva Malheiro, S., Gaio Manuel, T.: Cogeneration supply by bio-energy for a sustainable hotel buildingmanagement system. Fuel Process. Technol. **92**, 284–289 (2011)
Rosen, M.A.: Allocating carbon dioxide emissions from cogeneration systems: descriptions of selected output-based methods. J. Clean. Prod. **16**(2), 171–177 (2008)
Smithers, J.: Review of sugar cane trash recovery systems for energy cogeneration in South Africa. Renew. Sust. Energ. Rev. **32**(2014), 915–925 (2014)
Soltani, R., Mohammadzadeh Keleshtery, P., Vahdati, M., KhoshgoftarManesh, M.H., Rosen, M. A., Amidpour, M.: Multi-objective optimization of a solar-hybrid cogeneration cycle: application to CGAM problem. Energy Convers. Manag. **81**, 60–71 (2014)
Thilak Raj, N., Iniyan, S., Goic, R.: A review of renewable energy based cogeneration technologies. Renew. Sust. Energy. Rev. **15**(8), 3640 (2011)

Solar Calculations of Modified Arch (Semi-spherical)-Type Greenhouse System for Bayburt City

Çakir Uğur, Şahin Erol, Çomakli Kemal, and Çokgez Kuş Ayşegül

1 Introduction

Passive heating and cooling processes can be applied in any object around the world using solar energy. It is necessary to determine primarily the utilisable solar radiation in these structures and the design of the systems where solar energy is used. Parameters such as the design of the collectors, the lighting load in the buildings, calculation of the heating power gained from the sun, the value of the solar ovens and the insolation rate of the greenhouses are established in accordance with the amount of radiation reaching the earth. The oblique rays of the winter sun and the steep-angled rays of the summer sun make the southern face of the northern hemisphere receive more solar radiation in winter and be protected easily in summer. That is why the south-facing fronts are more valued fronts in architecture. Unfortunately, the heat energy gained from the sun is not taken into consideration in the design and construction of many buildings in our country. Especially, this is completely ignored in the buildings designed by small-scale companies or constructed by individuals. As mentioned in the previous section, the south-facing fronts in such buildings are assessed separately from the other parts in quoting and solicitation planning (Kilic and Ozturk 1983).

Ç. Uğur (✉)
Bayburt University, Faculty of Engineering Department of Mechanical Engineering, 69000 Bayburt, Turkey
e-mail: ucakir@bayburt.edu.tr

Ş. Erol
Ordu University, Technical Vocational High School Machinery and Metal Technology Department, 52000 Ordu, Turkey

Ç. Kemal • Ç.K. Ayşegül
Atatürk University, Faculty of Engineering Department of Mechanical Engineering, 25000 Erzurum, Turkey

© Springer International Publishing AG, part of Springer Nature 2018

F. Aloui, I. Dincer (eds.), *Exergy for A Better Environment and Improved Sustainability 2*, Green Energy and Technology,
https://doi.org/10.1007/978-3-319-62575-1_57

Greenhouse is defined as a highly systematic plant-growing process done in various ways in a structural building covered with different types of transparent materials such as glass or plastic to grow various plants, their seeds, seedlings and saplings, and protect or exhibit them throughout the year by controlling the factors such as heat, light, moisture and ventilation without completely or partially depending on the climate-related environmental circumstances (MEGEP 2012). Among the countries around the world, the USA, Japan and the Netherlands do the highest amount of greenhouse plant production. In the USA, California and Florida have the highest amount of production, where 39% of the greenhouses are glass covered. Seventy-eight per cent of the greenhouses produce flowers. In Europe, the Netherlands is the leading greenhouse producer. Bulbed flowers are the main products. Plastic-covered greenhouses are used in countries such as Spain, France and Italy (Anonymous 2012a). There is vast literature on solar energy and greenhouses, some of which are presented in this section. Gupta et al. (2012) demonstrated solar radiations and greenhouses in a virtual environment on AutoCAD. They used the lighting system on AutoCAD as the solar radiation. In the 3D environment they defined, they made comparisons by changing the location and design of the greenhouses. Kilic and Ozturk (1983) analysed the impact of the solar radiations on earth. They determined the angle of the solar radiations and analysed the intensity of the solar radiation reaching the earth at different hours of the day and on different days of the year. Their study of solar energy has become an inspiration for many other forthcoming studies. The terms regarding solar angles have been accepted as in their study. Pucar (2001) studied the calculation of the greenhouse wall and roof angles to receive the highest amount of solar radiation. Pucar (2001) calculated the most ideal roof and wall angles, where she studied how to increase the heat effect of the solar radiation getting in through the roof and walls of the greenhouse and reflecting on the opposite wall. Sethi (2009) worked on the determination of the angle and design of greenhouses that make the highest use of solar radiation. In the study, the walls of various greenhouses were studied separately in terms of their receiving solar radiation. Five types of generally accepted greenhouses were investigated in terms of the solar energy they received at every hour of the day.

In this study, a numerical model was developed that estimates the dimensions and directions for receiving the highest and most direct amount of solar radiation in semi-hemispheric greenhouses suitable for the conditions in the city of Bayburt in the periods when greenhouses were actively used in the city. The estimation process was considered as an optimisation problem, and the numerical model was created on MATLAB accordingly.

2 The City of Bayburt

The city of Bayburt is located on the coordinates of 40°15′35″N 40°13′40″E. Bayburt has a transition climate dominated by continental climate between East Black Sea climate and East Anatolia climate. That is why, it is hot and dry in summer, while it is cold and rainy in winter. However, the climate is milder than that of East Anatolia due to low altitude and the microclimate created by the system of valleys (Anonymous 2012b).

3 Solar Energy Calculations

In order to make good use of solar energy, it is required to know the characteristics and amount of all the solar radiations in the respective area and the time period. To do that, it is necessary to determine the incidence angle of the solar radiation and the sunshine duration of the respective area in accordance with the location and earth's movement around itself and around the sun. Majority of the solar energy calculations used in this study are based on the book *Solar Energy* (Kilic and Ozturk 1983).

3.1 Real Solar Angles

The direction of the straight solar radiation reaching any point on earth can be calculated if the latitude, hour angle and the declination angle of that particular point is known. These angles are known as real solar angles. Latitude angle: It is the angle of a point on the Earth's surface from the Equatorial plane and the radius to that point. Hour angle: The hour angle of a point on the Earth's surface is the angle through which the earth would turn to bring the meridian of the point directly under the sun. Declination angle: The declination of the sun is the angle between the equator and a line drawn from the centre of the Earth to the centre of the sun. It is calculated as follows:

$$d = 23.45 \ \sin\left(360\frac{(n+284)}{365}\right) \tag{1}$$

3.2 Derived Solar Angles

Zenith Angle: It is the angle between the sun and a line that goes straight up (to the zenith). In other words, it is the angle of the solar radiation to the horizontal plane. It is calculated as follows:

$$\cos(z) = \cos(d).\cos(e).\cos(h) + \sin(d).\sin(e) \tag{2}$$

At times of sunrise and sunset, the solar radiations are parallel to the horizontal plane. By using these moments, the sunrise and sunset angles and day length are calculated as follows:

$$\cos(H) = -\frac{\sin(d).\sin(e)}{\cos(d).\cos(e)} = -\tan(d).\tan(e) \tag{3}$$

3.3 Inclined Plane Angles

The solar azimuth angle defines the angle of the inclined plane to a horizontal plane and projection of the normal of the plane to the horizontal plane due West. The projection of the normal inclined plane to the normal of the horizontal plane is cos (s) and to the horizontal plane is sin (s). Solar incidence angle (g) is the angle of the solar radiation to normal of any inclined plane, and it is calculated as follows:

$$\begin{aligned}\cos(g) = &\left[\cos(d).\cos(e)^{*}\cos(h).\cos(s)\right] \\ &+\left[\cos(a).\cos(d).\sin(e).\cos(h).\sin(s)\right] \\ &+\left[\sin(a).\cos(d).\sin(h).\sin(s)\right] + \left[\sin(d).\sin(e).\cos(s)\right] \\ &-\left[\cos(a).\sin(d).\cos(e).\sin(s)\right]\end{aligned} \tag{4}$$

To calculate the amount of solar energy of a plane at a given time, it is necessary to accumulate all the energy the solar radiations give from the very first moment when the solar radiation reaches the plane to the last radiation reaching the plane. For the calculation of the whole day solar radiation, one should do the following: When the solar radiation is parallel to the plane, when $g = 90^{\circ}$

$$C_1 = \sin(a).\cos(d).\left(\sin(s)\right. \tag{5}$$

$$C_2 = \cos(d).\begin{bmatrix}\cos(e).\cos(s) \\ +\cos(a).\sin(e).\sin(s)\end{bmatrix} \tag{6}$$

$$C_2 = \sin(d).\begin{bmatrix}\sin(e).\cos(s) \\ -\cos(\mathrm{a}).\cos(e).\sin(s)\end{bmatrix} \tag{7}$$

$$D^2 = C_1^2 + C_2^2 - C_3^2 \tag{8}$$

This way, for $D^2 > 0$ the hour angles, where solar radiations are parallel to plane are calculated as in Eqs. 9 and 10:

$$H_{1p} = 2 \arctan\left(\frac{C_1 - D}{C_2 - C_3}\right) \tag{9}$$

$$H_{2p} = 2 \arctan\left(\frac{C_1 + D}{C_2 - C_3}\right) \tag{10}$$

The moment the solar radiation is parallel can be before the sunrise or after the sunset. That is why, if the hour angle of the solar radiation's parallel incidence to the inclined plane is bigger than sunrise hour angle in terms of absolute value, then the first incidence hour angle is at sunrise. At solar noon ($h = 0°$) the cosine of solar incidence angle (g_o) can be calculated with the Eq. 11. Then, by using the algorithm in Fig. 1, the sun's first incidence and last declination angles to the inclined plane are determined (Table 1):

$$\cos(g_o) = C_2 + C_3 \tag{11}$$

How many hours the solar radiation reaches the inclined plane is also another important factor. The duration of solar radiation onto the inclined plane is calculated according to the equations presented below:

$$d > 0 \text{ i}\widetilde{\text{c}} \text{ in} : t_{eg} = \frac{2}{15} \arccos[-\tan(d).\tan(e - s)] \tag{12}$$

$$d < 0 \text{ i}\widetilde{\text{c}} \text{ in} : t_{eg} = \frac{2}{15} \arccos[-\tan(e).\tan(d)] \tag{13}$$

The intensity of the solar radiation reaching inclined planes outside atmosphere changes in accordance with the angle of incidence of solar radiation and angle of inclined plane. The amount of radiation reaching the inclined planes outside the atmosphere in a day is calculated with the Eq. 14.

$$Q_{oe} = \frac{12}{\pi} .I_{gs} f. \left[\begin{array}{l} \frac{\pi}{180}(H_2 - H_1).\sin d \\ .(\sin e.\cos s - \cos e.\sin s.\cos a) \\ +(\sin H_2 - \sin H_1).\cos d \\ .(\cos e.\cos s + \sin e.\sin s.\cos a) \\ -(\cos H_2 - \cos H_1).\cos d.\sin s.\sin a \end{array}\right] \tag{14}$$

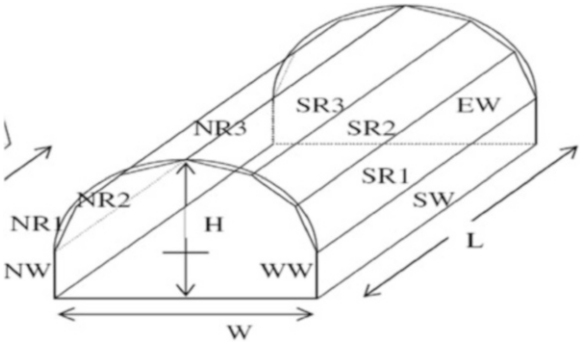

Fig. 1 Hemispherical greenhouse type

Table 1 First and last angles of incidence of solar radiation to inclined plane

		(H_1)	(H_2)
$\cos(g_o) > 0$ ($g_o > 90°$)	$D^2 > 0$	max ($H_{1p,}$ $-H$)	min ($H_{2p,}$ H)
	$D^2 < 0$	$-H$	H
$\cos(g_o) < 0$ ($g_o > 90°$)	$D^2 > 0$	max ($H_{2p,}$ $-H$)	min ($H_{1p,}$ H)
	$D^2 < 0$	No solar radiation	

3.4 Calculations for Arch Greenhouse

A sample design is given in Fig. 1 to visually describe the greenhouse under scrutiny. As a result of this study, it is understood that there are two different seasons to use greenhouses in the city of Bayburt: the optimum greenhouse size and direction to gather the required amount of solar radiation in these seasons (1 April–15 June and 15 August–10 November). For instance, for someone who plans to build a greenhouse of a certain size, the optimum size of that greenhouse and the optimum angle of direction for that size can be determined. Figure 2 shows the schematic review of greenhouses according to different directions and angles.

The accepted dimensions for arch greenhouses are given below. The height of the sidewalls is 2-m flat. The distance between these walls and the highest point of the rooftop of the greenhouse is 1 m flat too (Fig. 3). All the other necessary dimensions are calculated in accordance with the area of the roof. The length of the arch is calculated which is divided into five equal sections for solar energy calculations. The circular roof of the arch greenhouse can be analysed as small rectangular surfaces by dividing it into small linear sections. Figure 4 shows that the roof of the arch greenhouse is formed into five different surfaces with equal dimensions but different inclination angles by dividing it into five equal sections.

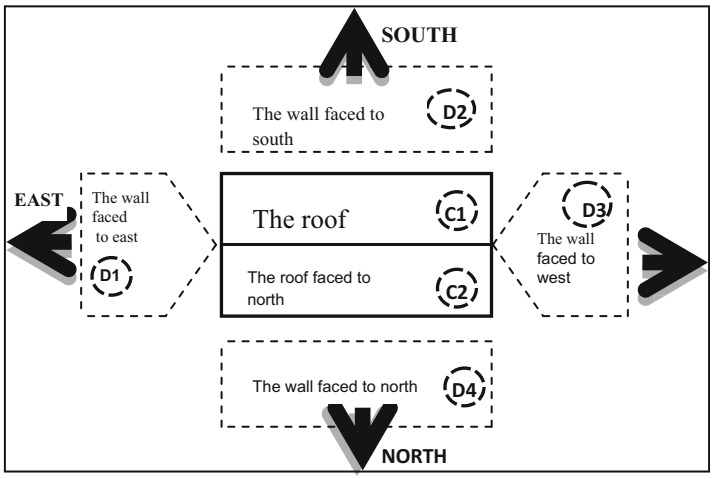

Fig. 2 Schematic review of greenhouses according to various angles

Fig. 3 Dimensions for arch greenhouses

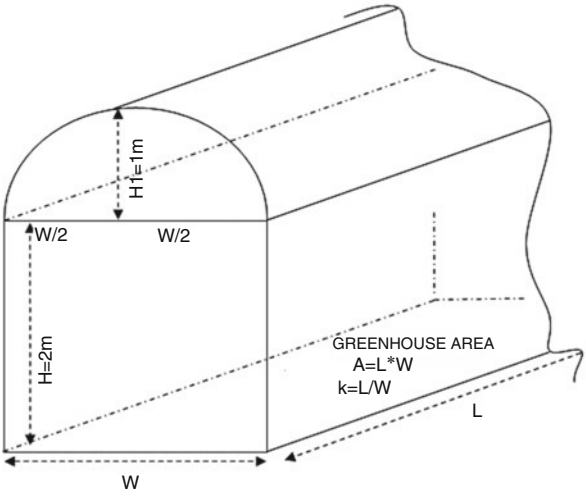

4 Assumptions

The required longitudinal solar measurement for the study in Bayburt does not exist. The study uses direct radiation only. That is why all of the conditions such as distributed radiation, wind, reflection, uncleanliness and datedness of the covering material, cloudiness and the shadowing impact of the greenhouse materials were regarded as the same for all greenhouses. Moreover, the maximum height inside the greenhouses of all types and sizes was regarded as limited to 3 m. Since the study

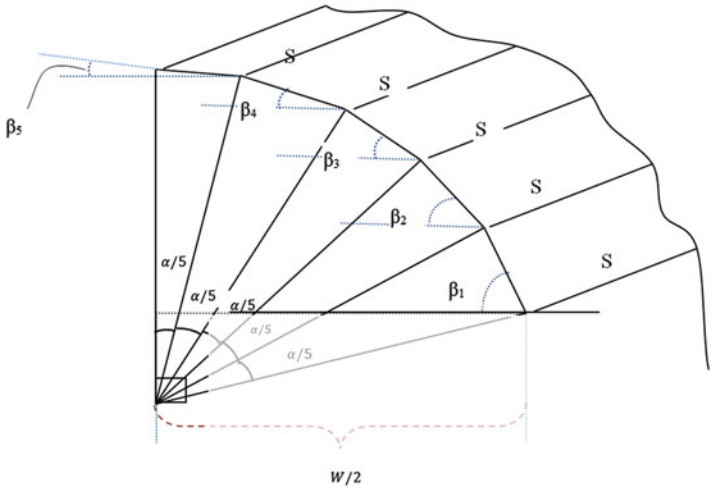

Fig. 4 Sectioning of the circular roof of arch greenhouses

aims to compare different types of greenhouses to each other, these assumptions will not affect the results of the study.

5 Results

5.1 Arch Greenhouses with Surface Area of 400 m^2

Table 2 shows the dimensions of length and width and surface area of a greenhouse with a surface area of 400 m^2. Similar tables for greenhouses of various dimensions were created; however, only 400 m^2 greenhouse is presented.

Figure 5 shows the change in radiation levels received from the sun according to different days of the year and different azimuth angles for different k values. As seen in the figure, the higher the k value (L/W) for a 400-m^2 arch greenhouse, the higher the amount of radiation it receives. This situation changes only when it is around the middle of summer, and the value of azimuth angle is lower than 40 degrees. Figure 6 presents the changes in total solar radiation received in the periods when the greenhouse can be used in Bayburt according to different L/W values for an arch greenhouse of 400 m^2. As seen, for a greenhouse of this type, the optimum azimuth angle is 90° and the optimum k value is 10.

Table 2 400-m^2 arch greenhouse dimension

k	L (m)	W (m)	D1, D3 (m^2)	D2, D4 (m^2)	Roof Part. (m^2)
1	20.00	20.00	53.36	40.00	40.26
2	28.28	14.14	37.75	56.57	40.53
3	34.64	11.55	30.84	69.28	40.79
4	40.00	10.00	26.72	80.00	41.05
5	44.72	8.94	23.91	89.44	41.31
6	49.00	8.166	21.84	97.98	41.57
7	52.92	7.56	20.23	105.83	41.83
8	56.57	7.07	18.93	113.14	42.08
9	60.00	6.67	17.86	120.00	42.33
10	63.25	6.33	16.95	126.49	42.59

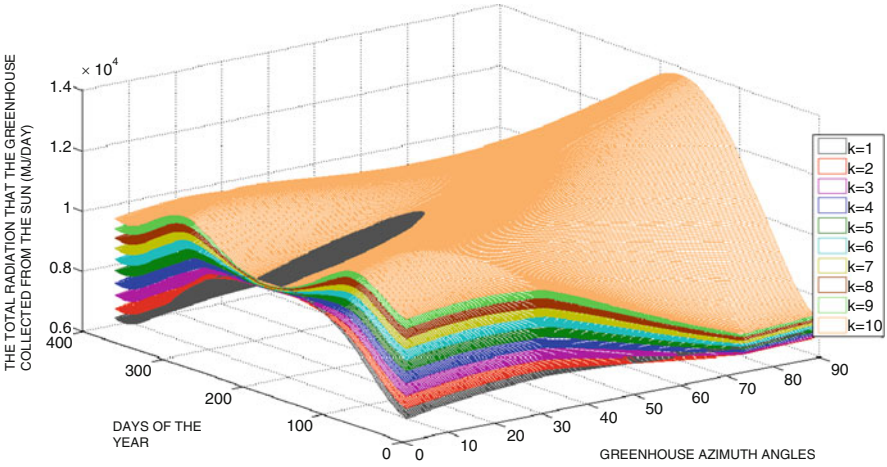

Fig. 5 Changes in solar radiation for 400-m^2 arch greenhouse

5.2 300-m^2 Arch Greenhouse

Figure 7 shows the changes in total solar radiation received in the periods when greenhouse can be used in Bayburt according to different L/W values for an arch greenhouse of 300 m^2. As seen, for a greenhouse of this type, the optimum azimuth angle is 90° and the optimum *k* value is 10. The azimuth angle can also be a value between 30 and 40.

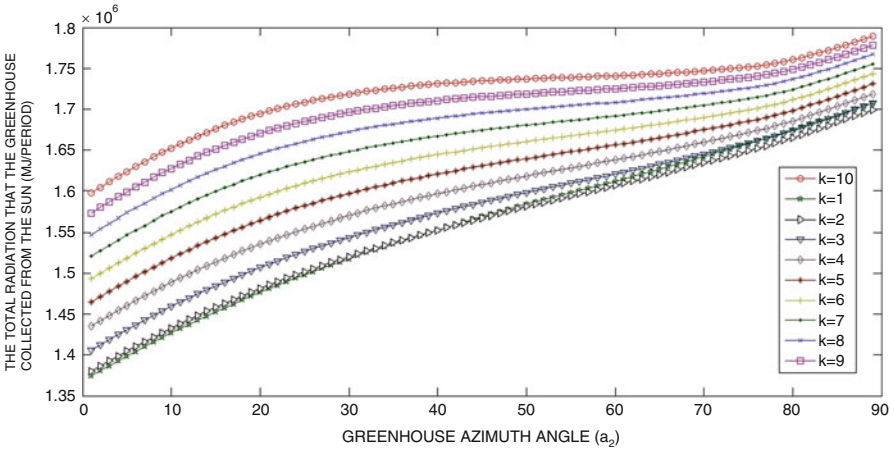

Fig. 6 Changes in solar radiation for 400-m^2 arch greenhouse

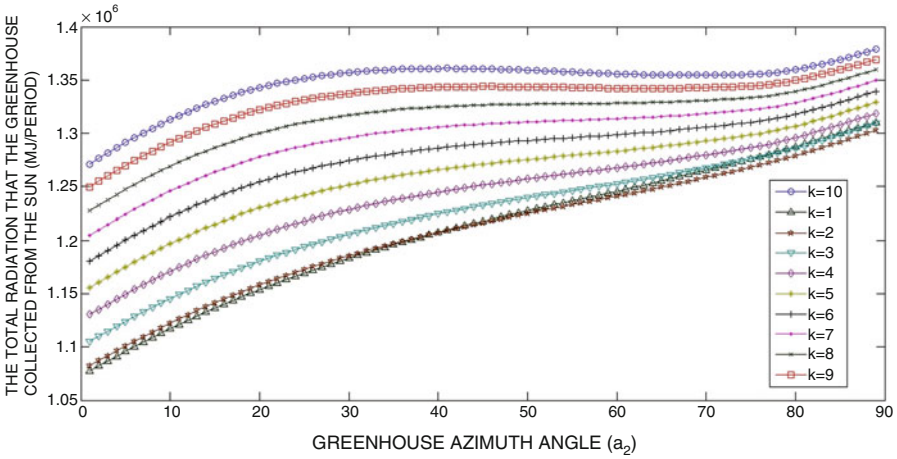

Fig. 7 Changes in solar radiation for 300-m^2 arch greenhouse

5.3 250-m^2 Arch Greenhouse

Figure 8 shows changes in radiation levels for a 250-m^2 arch greenhouse received from the sun according to different days of the year and different azimuth angles for different k values. As seen in the figure, the higher the k value (L/W) for a 250-m^2 arch greenhouse, the higher the amount of radiation it receives. Thus, for a greenhouse of this type, the optimum azimuth angle is 35°, and the optimum k value is 10.

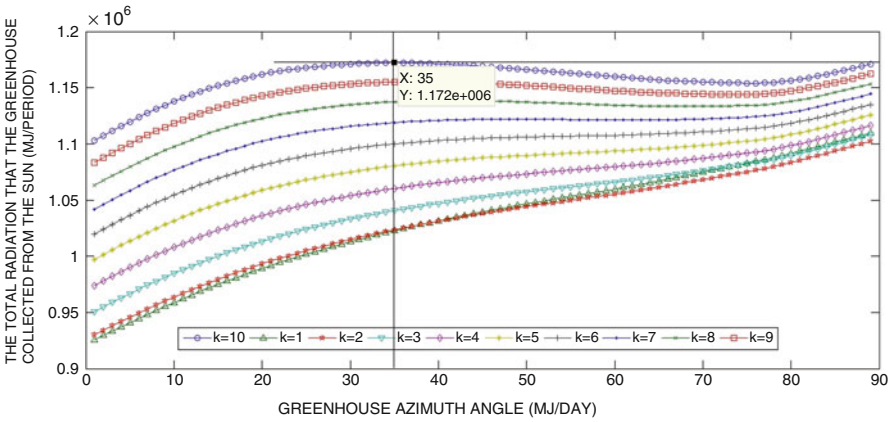

Fig. 8 Changes in solar radiation for 250-m^2 arch greenhouse

5.4 *200-m^2 Arch Greenhouse*

Figure 9 shows changes in total solar radiation received in the periods when greenhouse can be used according to different L/W values for an arch greenhouse of 200 m^2. As understood from the figure, the optimum k value for this greenhouse is 10. However, at this point, one should pay attention to the existing dimensions of the greenhouse and how ergonomically it has been built. It is understood that if k value is 10, then the greenhouse becomes too narrow to be used. Thus, it is considered that under these conditions, the width of the greenhouse should be at least 5 m and k value 8. As seen, for this type of greenhouse, the optimum azimuth angle is 35°, and the optimum k value is 8.

5.5 *150-m^2 Arch Greenhouse*

Due to the condition mentioned above, the width of this greenhouse should be at least 5 m and k value 6. Figure 11 presents changes in total solar radiation received in the periods when greenhouse can be used according to different L/W values for an arch greenhouse of 200 m^2 with a highest k value of 6. As can be seen, the optimum azimuth angle for this type of greenhouse is 34°, and the optimum k value is 6 (Fig. 10).

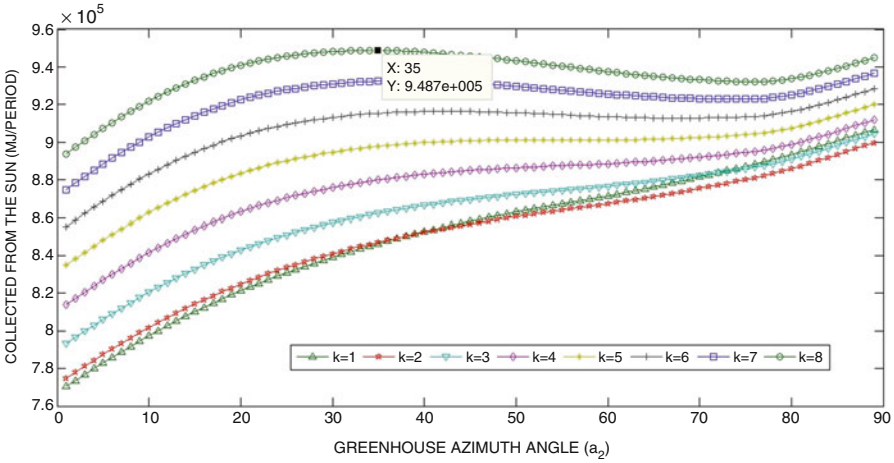

Fig. 9 Changes in solar radiation for 200-m^2 arch greenhouse

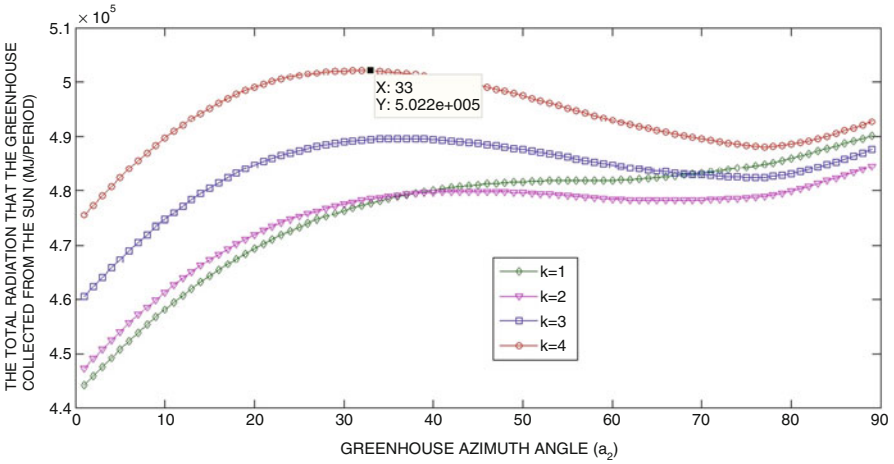

Fig. 11 Changes in solar radiation for 100-m^2 arch greenhouse

5.6 100-m^2 Arch Greenhouse

Figure 11 presents changes in total solar radiation received in the periods when greenhouse can be used according to different L/W values for an arch greenhouse of 100 m^2 with a highest k value of 4. As can be seen, the optimum azimuth angle for this type of greenhouse is 33° and the optimum k value is 4.

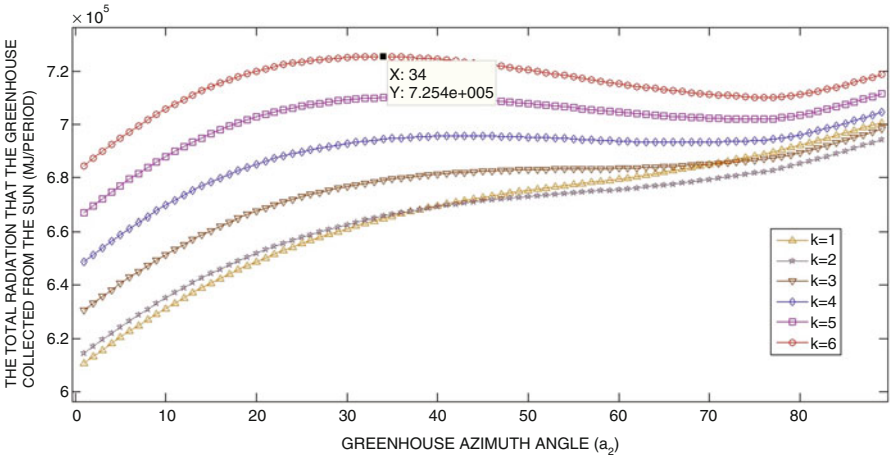

Fig. 10 Changes in solar radiation for 150-m^2 arch greenhouse

5.7 50-m^2 Arch Greenhouse

For these conditions, it is considered that the width of the greenhouse should be at least 5 m and the highest k value 5. As can be seen in Fig. 12, the optimum azimuth angle for this type of greenhouse is 22° and the optimum k value is 4.

As understood above, positioning of the greenhouses varies according to different sizes of greenhouses. This analysis is based only on the months when agricultural activities can be done. Winter season was not taken into account as farming is not possible.

6 Conclusion

Greenhouses are used in temperate climate regions, to make agricultural applications, especially in winter. As it is known, solar radiation energy is captured and kept in greenhouses by the help of greenhouse effect. In this study, we analysed one of the mostly used greenhouse types. Building the best and most useful greenhouses in cold climate regions mean extending the greenhouse season and increasing the productivity.

This script is applicable and suitable for other buildings such as residents and business centres in order to evaluate the incoming solar energy and provide economic benefit by saving energy. Positioning the buildings in order to get more solar heat energy in winter and less in summer brings out energy and money savings and increases the comfort.

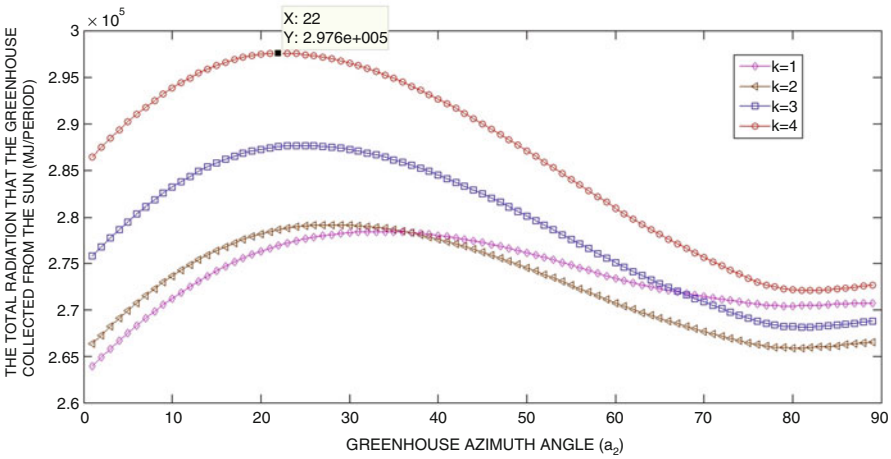

Fig. 12 Changes in solar radiation for 50-m^2 arch greenhouse

References

Anonymous.: www.serabirlik.com (2012a)

Anonymous.: Ministry of Cultur and tourism. Turkey (2012b)

Gupta, R., Tiwari, G.N., Kumar, A., Gupta, Y.: Calculation of total solar fraction for different orientation of greenhouse using 3D-shadow analysis in AutoCAD. Energy Build. **47**, 27–34 (2012)

Kiliç A., Öztürk A.: Güneş Enerjisi, Kipaş Dağıtım ve Yayıncılık (book in Turkish) (1983)

MEGEP.: Bahçecilik ve Sera Yapım Teknikleri, (book in Turkish) (2012)

Pucar, M.D.: Enhancement of ground radiation in greenhouses by reflection of direct unlight. Renew. Energy. **26**(2002), 561–586 (2001)

Sethi, V.P.: On the selection of shape and orientation of a greenhouse, ermal modeling and experimental validation. Sol. Energy. **83**(1), 21–38 (2009)

Estimation of Global Solar Radiation in Arid Climates in Algeria

Malika Fekih and Mohamed Saighi

1 Introduction

In any solar energy conversion system, the knowledge of global solar radiation is extremely important for the optimal design and the prediction of the system performance. The best way of knowing the amount of global solar radiation at a site is to install pyranometers at many locations in the given region and look after their day-to-day maintenance and recording, which is a very costly exercise. The alternative approach is to correlate the global solar radiation with the meteorological parameters at the place where the data are collected. The resultant correlation may then be used for locations of similar meteorological and geographical characteristics at which solar data are not available.

Over the years, many models have been proposed to predict the amount of solar radiation using various parameters Canada (1988a, b). Some works used the sunshine duration (Gueymard 1993). Others used mean daytime cloud cover or relative humidity and maximum and minimum temperature (Supit and Van Kappel 1998), while others used the number of rainy days, sunshine hours and a factor that depends on latitude and altitude (Canada 1988a, b).

Algeria is a high insolation country. The number of sunshine hours amounts almost 3300 h/year. The climate is most favorable for solar energy utilization, but the distribution of the solar radiation is not well known. The importance of this work lies on the fundamental need of knowledge of the global solar radiation data in the country.

M. Fekih (✉) • M. Saighi
Laboratory of Thermodynamics and Energetically Systems/LTSE, Faculty of Physics, University of Science and Technology Houari Boumediene, BP 32 El Alia Bab Ezzouar, 16111 Algiers, Algeria
e-mail: fekih.mali2005@yahoo.fr

© Springer International Publishing AG, part of Springer Nature 2018

F. Aloui, I. Dincer (eds.), *Exergy for A Better Environment and Improved Sustainability 2*, Green Energy and Technology,
https://doi.org/10.1007/978-3-319-62575-1_58

Solar radiation measurements are not easily available for many developing countries for not being able to afford the measurement equipment and techniques involved. Therefore, it is rather important to elaborate methods to estimate the solar radiation on the basis of more readily meteorological data.

Several empirical formulae have been developed to calculate the solar radiation using various parameters.

In the present work, an empirical method originally formulated by Saighi (2002) has been modified to make it fit some Algerian meteorological stations. The model only requires the duration of sunshine and minimum air mass.

2 Calculation Procedure

In the present work, data of monthly mean of daily global solar radiation and sunshine duration from two Algerian meteorological stations (Béchar and Tamanrasset) are used by Capderou (1988). The geographical location of stations are presented in Table 1. The duration of records of sunshine duration is 25 years and of global solar radiation is approximately 10 years. Measurements of global solar radiation were performed with Robitzsh and Kipp-Zonen pyranometers. For the recording of sunshine duration, Campbell-Stokes heliographs are used.

The two meteorological stations are divided into two zones according to the relative duration of sunshine

- Sahara climate for Béchar
- Tamanrasset which is influenced by the African tropical climate

3 Estimation Methods

To estimate the global solar radiation Rg, data consisting of monthly mean temperature, relative humidity, soil temperature, ambient temperature and sunshine duration were taken from the State Meteorology Office of Algiers between 2010 and 2012. Monthly mean daily extraterrestrial radiations Rg, day length N for using the average day of the month, were calculated from Eqs. (1, 2 and 3), respectively (Duffie and Beckman 1991). The clear sky radiation was determined by using methodology related in section estimation of clear sky radiation.

Table 1 Geographical location of stations

Station	Latitude (deg.)(N)	Altitude (m)	Longitude (degree)
Béchar	*31.63*	*806*	*2.40 W*
Tamanrasset	*22.47*	*1378*	*5.31 E*

3.1 Model for Computing Radiation on the Horizontal Surface

The total radiation received on the horizontal is a summation of the direct and diffuse radiation (Parker 1991; Duffie and Beckman 2006).

We estimate the amount of global solar radiation on horizontal surfaces using various climatic parameters, such as sunshine duration, cloud cover, humidity, maximum and minimum ambient temperatures, wind speed, etc. (Chegaar and Chibani 2001; El-Sebaii and Trabea 2005; Gopinathan 1988; Halouani et al. 1993; Jacovides et al. 2006).

In the present work, data of monthly mean of daily global solar radiation from two Algerian meteorological stations (Béchar and Tamanrasset) are used.

Measurements of global solar radiation were performed with Kipp and Zonen pyranometers (Figs. 1 and 2). Fekih (2013).

Fig. 1 Kipp & Zonen pyranometers used

Fig. 2 The solar integrator used

3.2 Radiative Flows (Rn)

The net radiation corresponds to the general balance sheet of the exchanges of radiations of short and big wavelengths on the level of the surface of the ground, it can be written:

$$R_{\mathrm{n}} = (1-\alpha)Rg + \varepsilon\sigma(Ta-6)^4 - \varepsilon\sigma T_S^4$$

3.2.1 Direct Flow

The direct radiation on the presumably horizontal surface of the ground exclaims in the following way and can be written:

$$R_{\mathrm{D}} = I_0\lambda_i A_1 \exp\left(\frac{-A_2}{\sin(h)}\right)\sin(h) \tag{1}$$

with

I_0 = constant solar = 1360 W/m^2
λ_i = coefficient of distance ground sun (Saighi 2002)
h = height of the sun on the horizon (Saighi 2002)
A_1, A_2 = coefficients of disorder

3.2.2 Diffuse Flow

Correlations showed that in clear weather, diffuse flow was a function of the height h of the sun. According to Saighi (2002) and Chouard et al. (1977), suppose that at first approximation diffuse flow is proportional to sin (h) and, basing itself on American statistical studies carried out from raised experimental, propose the following relation for the calculation of diffuse flow:

$$R_{\mathrm{d}} = I_0\lambda_i\left[0.271 - 0.2939A_1\exp\left(\frac{-A_2}{\sin(h)}\right)\right]\sin(h) \tag{2}$$

3.2.3 Global Radiation

The total radiation is composed of the direct radiation and the diffuse radiation. Its expression is given by:

$$\mathrm{Rg} = 0.271\, I_0\, \lambda_i\, A_1 \sin(h) + 0.706\, I_0\, \lambda_i\, A_1 \sin(h) \times \exp\left(\frac{-A_2}{\sin(h)}\right) \tag{3}$$

This formulation of the irradiation is relatively precise and offers the advantage of a great ease of use.

The coefficients A_1 and A_2 depend on the clearness of the sky to the days and place considered; they were identified numerically starting from weather data.

They were identified numerically starting from weather data. The values which we used in this study result from "the solar Atlas of Algeria" of Capderou (1985), the only reference which gives these coefficients in Algeria.

4 Results and Discussions

The Algerian meteorological stations are divided into two zones according to the characteristics of their climate, Mediterranean climate for Algiers and Oran, Sahara climate for Béchar and Tamanrasset which is influenced by the African tropical climate.

Figures 3 and 4 represent an example of curves relating to the global irradiation of the town of Tamanrasset and Béchar calculated starting from the formula established previously.

The global solar radiations are then calculated using Eq. (3).

A comparison with measurements and calculations made by Capderou is also given. The variation of the monthly global irradiation measured and computed is represented in Fig. 3 and in Fig. 4. The best estimates of global irradiation were calculated for Béchar and Tamanrasset.

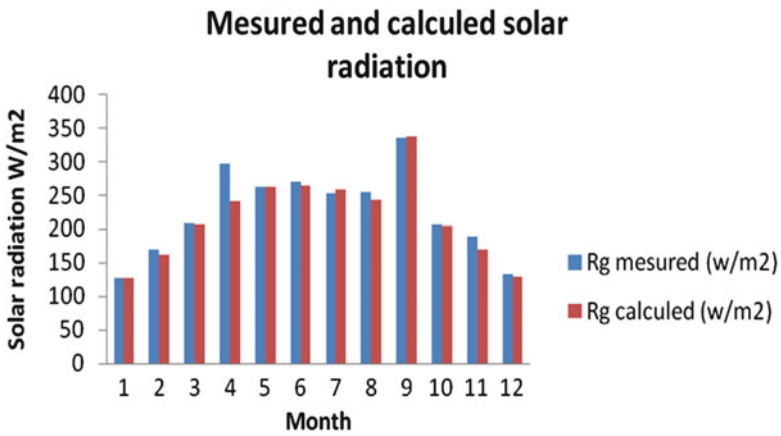

Fig. 3 Monthly average of daily global radiance in Béchar

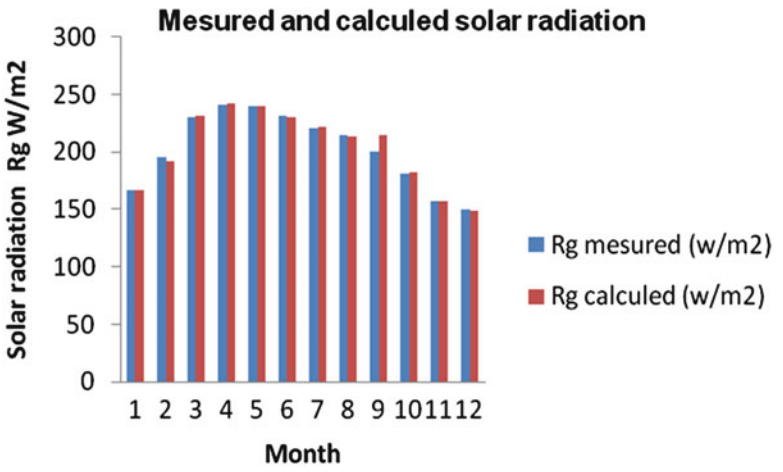

Fig. 4 Monthly average of daily global radiance in Tamanrasset

5 Conclusions

The objective of this study was to evaluate a model for the estimation of the monthly average daily global solar radiation on a horizontal surface for arid climate in Algeria.

The model is tested for two provinces (Béchar and Tamanrasset) of Algeria. Meteorological data were used as the input of the radiation models. Model validation was employed by means of daily solar measurements.

Comparison of the model with the measured data revealed that the model provides predictions in good agreement with the measured data.

References

Canada, J.: Global solar radiation in Pais Valenciano using sunshine hours. International Journal of Ambient Energy. **4**, 197–201 (1988a)

Canada, J.: Global solar radiation in Valencia using sunshine hours and meteorological data'. Solar & Wind Technology. **5**, 597–599 (1988b)

Capderou, M.: Atals Solaire de l'Algérie Tome 2. Edition OPU, Alger (1985)

Capderou, M.: Atlas Solaire de l'Algérie. Office des Publications Universitaires, 'T'. 1–3 (1988)

Chegaar, M., Chibani, A.: Global solar radiation estimation in Algeria. Energy Convers. Manag. **42**, 967–973 (2001)

Chouard, P. et al. - Bilan thermique d'une maison solaire, Ed. Eyrolles Paris, (1977)

Duffle, J.A., Beckman, W.R.: Solar Engineering for Thermal Processes, 3rd edn. Wiley, New York (2006)

Duffie, John.A. and. Beckman, William A : "Solar engineering of thermal processes", Madison: John Wiley & Sons, Inc., pp. 10–23, (1991)

El-Sebaii, A.A., Trabea, A.A.: Estimating global solar radiation on horizontal surfaces over Egypt. Egyptian Journal of Solids. **28**, 163–175 (2005)

Fekih, M.: Etude aérodynamique et aérothermique d'un écoulement de ventautour d'un bac de mesure d'évaporation d'eau. PhD thesis, Université des Sciences et de la Technologie HouariBoumediene USTHB, Alger, Algérie (2013)

Gopinathan, K.K.: A general formula for computing the coefficients of the correlation connecting global solar radiation to sunshine duration. Sol. Energy. **41**, 499–502 (1988)

Gueymard, C.: Analysis of monthly average solar radiation and bright sunshine for different thresholds at Cape Canaveral, Florida. Sol. Energy. **51**, 139145 (1993)

Halouani, N., Nguyen, C.T., Vo-Ngoc, D.: Calculation of monthly average global solar radiation on horizontal surfaces using daily hours of bright sunshine. Sol. Energy. **50**, 247–258 (1993)

Jacovides, C.P., Tymvios, F.S., Assimakopoulos, V.D., Kaltsounides, N.A.: Comparative study of various correlations in estimating hourly diffuse fraction of global solar radiation. Renew. Energy. **31**, 2492–2504 (2006)

Parker, B.F.: Energy in world agriculture, solar energy in agriculture, pp. 1–66. Elsevier Science Publishers, New York (1991)

Saïghi, M.: Nouveau modèle de transfert hydrique dans le système solplante-atmosphère, PhD thesis, Université des Sciences et de laTechnologie Houari Boumediene USTHB, Alger, Algérie (2002)

Supit, I., Van Kappel, R.R.: A simple method to estimate global radiation. Sol. Energy. **63**, 147–160 (1998)

Technical-Economic Assessment of Energy Efficiency Measures in a Midsize Industry

Sara Benavides, Maria Bitosova, Javier De Gregorio, Aubin Welschbillig, and Luis Rojas-Solorzano

1 Introduction

For the realization of this project, the real case of a midsize dairy product manufacturing industry called "CILAM" located in Saint Pierre, South of Reunion Island, was studied. CILAM produces various dairy products such as milk, beverages, desserts, cheese, and ice creams and accounts for about 60% of the dairy market on the island (Agro-oi.com 2015).

The aim is to develop a prefeasibility study in order to evaluate the impact of implementing energy efficiency measures at CILAM. Thus, the outcome will be energy and money savings within a short payback ratio.

Reunion Island is located in the Indian Ocean, east of Madagascar, about 200 km southwest of Mauritius (nearest island). It is an integral part of the French Republic with the same status as those situated on the European mainland. The import of oil products at Reunion Island is primarily intended to cover the energy demand of the transportation and electricity generation sector, as well as industrial and agricultural activities. In 2000, the fuel supply was 886.9 ktoe. Between 2000 and 2011, the fossil fuel supply had increased by 6.1% making the island very dependent on exterior sources. Reunion Island imports as much as 7/8 of its final energy consumption corresponding to fossil fuels, while the remaining 1/8 comes from local resources.

S. Benavides (✉) • M. Bitosova • J. De Gregorio • A. Welschbillig
Ecole des Mines de Nantes, Department of Energy
and Environment Systems, Nantes 44300, France
e-mail: sarabenc@live.com; bitosova@hotmail.com; javierdgpm3e@gmail.com;
aubin.welschbillig@gmail.com

L. Rojas-Solorzano
Nazarbayev University, Department of Mechanical Engineering, Astana 010000, Kazakhstan
e-mail: luis.rojas@nu.edu.kz

© Springer International Publishing AG, part of Springer Nature 2018

F. Aloui, I. Dincer (eds.), *Exergy for A Better Environment and Improved Sustainability 2*, Green Energy and Technology,
https://doi.org/10.1007/978-3-319-62575-1_59

Thus, as part of the effort to accomplish the stipulations and guidelines portrayed in Agenda 21 (Agenda21france.org 2015), the Reunion Island government has adopted a strategy of energy autonomy based on energy efficiency and renewable energy alternatives. One of the main objectives of Agenda 21 is that Energy Self-Sufficiency must be achieved by 2030 (Ricci et al. 2014). In consequence, by the end of 2010, Reunion Island had PV installations which represent approximately an installed capacity of 80 MWp for an electricity production of 60 GWh/year, solar thermal installations that produce near 120 kWh/day, which corresponds to a total of 20.16 MWh of electricity saved during the summer; additionally, the cooling plants have saved 16.5 tons of CO_2 yearly. Wind energy installations produce 15.5 MWh of electricity per year, taking advantage of trade winds on the island's eastern side, while hydropower installations produce 632 GWh and biomass 300 kWh, both on a yearly basis (Praene et al. 2012).

Moreover, the industrial sector is facing many challenges, such as global competition, energy pricing, and environmental impact among others. Consequently, the necessity for energy efficiency measures has become evident, framing the objective of this project so as to assess the technical and economic prefeasibility of implementing energy efficiency measures in a dairy products manufacturing company located at the south of Reunion Island. The scope of the project is focused on one of the nine buildings where the company accomplishes different production processes, specifically in the ultra-high temperature pasteurization facility building (UHT).

Nowadays, dairy industries as well as the majority of other economic sectors are moving toward sustainable production, minimization of energy consumption, and impact on the environment. Application of best energy practices is a field of interest not only to the government and environmental regulators but also to companies' senior management and stakeholders due to their interest in the profitability of the business. In this study, two main sectors of energy use at the UHT building of the dairy production plant are targeted: savings on electrical energy and savings on thermal energy. Savings on electrical energy can be achieved by redesigning the lighting system and improving the processes involved on the cooling system performance. On the other hand, additional savings are foreseen for thermal energy by the reduction of steam losses and the installation of a heat recovery unit for the boiler, which represents economic advantages regarding the consumption of electricity and fossil fuel.

The technical and economic prefeasibility study was carried out in RETScreen®, a Clean Energy Management Software system for energy efficiency, renewable energy and cogeneration project feasibility analysis as well as ongoing energy performance analysis. This Excel-based software is a tool that helps decision makers to determine the technical and financial viability of potential clean-energy projects in a quick and inexpensive way.

The performed study showed that the proposed energy efficiency actions represent benefits for CILAM and are qualified to be implemented in order to reduce operational costs and carbon footprint and augment the quality of the goods produced. The analysis was done from the point of view that the industrial parks

at the Reunion Island are committed to support the strategy conducted by the regional government, with the purpose of achieving energy autonomy based on greater energy efficiency and renewable energy alternatives, as stated in the island's 2030 goals and Reunion Agenda 21.

Nomenclature

CILAM	Compagnie Laitière des Mascareignes
UHT	Ultra High Temperature
HVAC	Heating, Ventilation and Air-Conditioning.
Charcs.	Characteristics
Op. hrs.	Operating Hours
P_{steam}	Steam Pressure
$T_{\text{cond.}}$	Condensation Temperature
T_{Wmakeup}	Temperature Water Makeup
T_{sh}	Super-Heated Temperature
IRR	Internal Rate of Return
NPV	Net Present Value
LED	Light Emitting Diode
kWh	Kilowatt-hour
INRS	Institut National de Recherche et de Securité
GHG	Green House Gases

2 Methodology

The prefeasibility analysis, is done using RETScreen. The inputs concerned or researched for the project were those associated with pasteurization at ultra-high temperature. The technical data are obtained through an energy management data collection system owned by CILAM. Input data implemented in RETscreen were considered for 1 year consumption based on 2013. The tasks to reach the results were carried out by the researchers with the support of two more parties: the academic tutor and the energy manager of the company on site. To manage communication and adjust the schedules, helpful tools such as Dropbox, Google Docs, and Skype calls for online meetings with the international partners were utilized.

3 Prefeasibility Study

3.1 General Description of the Facility

The company consists of nine buildings where different processes are performed; however, for this study, only the UHT Process Building will be considered.

This paper considers the most energy intense processes:

- Steam production and leakages for pasteurization and sterilization
- General refrigeration system for cooling of products and storage purposes
- Lighting in the building

3.2 Data Collection

The consumption for different energy sources was obtained from the annual energy bill of the company in 2013. This data was proportioned by the Energy Manager of CILAM industry. Moreover, reliable and high-quality data was placed as an input in RETScreen, thanks to his direct involvement on the different processes performed in the company.[1]

AutoCAD drawings of the industry were used to determine the area of the UHT building, which has a surface of 2688 m^2. In addition, according to the Energy Manager, the industry uses air conditioning systems only for offices in the social/commercial building. Production buildings such as the UHT building do not have any HVAC system installed and use natural ventilation due to the stable weather of Reunion Island. Consequently, space heating and cooling are not carried into account for this prefeasibility analysis.

3.3 General Considerations

Some assumptions were made to complete the prefeasibility analysis and are presented as follows:

- Steam leakages were estimated at around 20% of the total steam production by the energy manager during an audit in 2013 locating 12 visible leakages in the network. From that audit on, the leakages have been reduced to 5% of the total production. Even though the steam leakage problem has been already solved in the company, the profitability of such energy efficiency improvement will be analyzed in this report.
- Actual lighting data information was not available; hence, the lighting information was estimated with standard values for industries with no energy efficiency measures.

For this study the financial parameters presented in Table 1 will be used for financial analysis.

[1]Energy consumptions of processes, operational parameters, technical drawings, pictures, etc.

Table 1 Financial parameters

Parameter	Value
Inflation rate	1.0%[a]
Discount rate	9.0%[b]
Project lifetime	10 years
Fuel cost escalation rate	5.5%[c]

[a]INSEE (2014)
[b]RETScreen Data Base
[c]CNR (2014)

Table 2 Comparison between RETScreen simulation and real consumptions of the industry

Fuel type	Fuel consumption – unit	Fuel consumption – historical	Fuel consumption	Fuel consumption – variance
			Base case	
Electricity	MWh	5345	5381	1%
Diesel (#2 oil)	L	736,000	726,890	−1%

Since the analysis is based on the 2013 energy consumption data of the company, fuel prices considered for this prefeasibility analysis are based on the price of energy in Reunion Island during the same year:

- Electricity: 0.098 €/kWh
- Diesel: 0.784 €/L

At this moment, there is no defined incentive or subsidy exclusively for the implementation of Energy Efficiency measures in Reunion Island industry.

3.4 Base Case

In the first place, an assessment of the actual conditions of the industry was addressed (base case). Table 2 shows the discrepancy between the simulation in RETscreen and the historical consumption from energy bills of 2013.

The base case energy distribution scheme during 2013 is shown in Fig. 1 (Appendix). The values calculated by RETScreen account for the energy consumption related to the systems and equipment used by UHT building processes, represented in a Sankey diagram.

3.5 Energy Efficiency Improvements

After gathering the data and analyzing the impact of the energy consumption of this industry, four main aspects were identified for improvement: (a) lack of heat recovery from flue gas, (b) sources of significant steam leakages, (c) lighting system, and (d) system refrigeration unit performance.

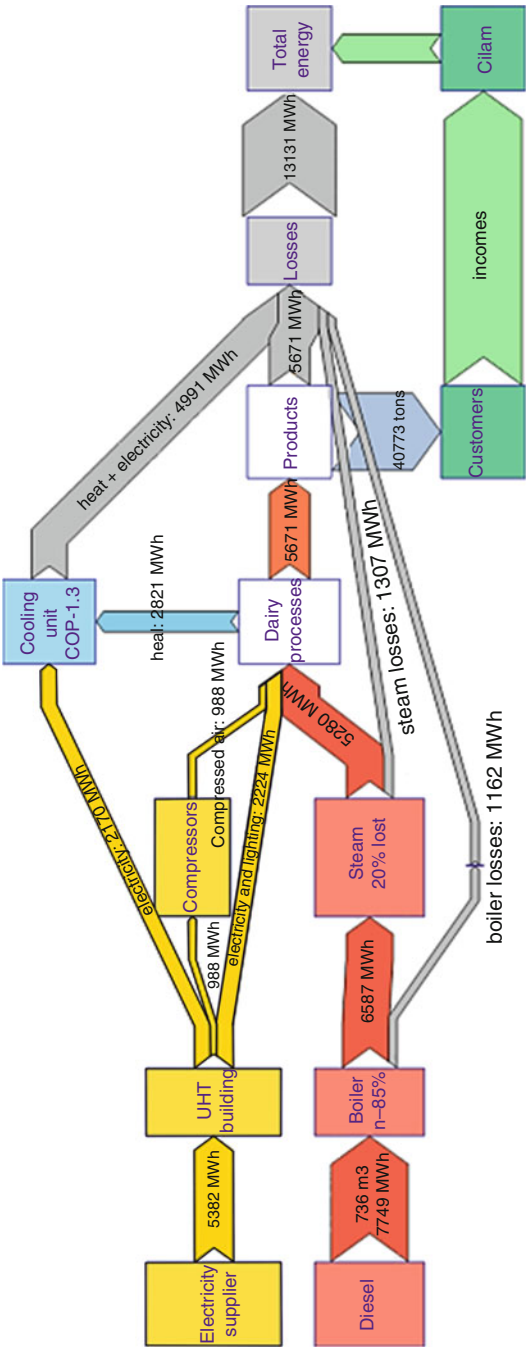

Fig. 1 Energy distribution for base case

Table 3 Boiler characteristic and operating parameters

Charcs.	Operating parameters	Energy consumption: useful steam
465 KW $\eta = 0.85$ Uses diesel	Steam flow: 877 kg/h Op.hrs: 24 h/day P_{steam}: 12 bars T_{sh}: 170 °C Cond. return: 60% $T_{cond.}$: 85 °C $T_{Wmakeup}$: 25 °C	From energy bills and audit: 5473 MWh/year Estimated by RETscreen: 5280 MWh/year Discrepancy: 3.5% Share of total energy consumption: 40.2%

Table 4 Financial impacts of economizer implementation

Costs	Savings	Simple payback time
Investment: 35,000 € the 1st year Maintenance: 2000 €/year	384 MWh/year of diesel (42,393 L of diesel/year) 33,236 €/year	35,000 €/ 33,236 €/year = 1.1 year

3.5.1 Boiler–Steam Production

Table 3 shows the characteristics and operating parameters of the boiler related to the systems and equipment used by the UHT building processes.

In order to improve the current energy consumption of the boiler, it was agreed that an economizer, to recover part of the heat contained in the flue gas, needed to be installed. According to the manufacturer LOOS, now part of BOSH Company, "The heat contained in the flue gases is recovered and the efficiency increased in this way by up to 7% in dry running operation" (Efficiency on a large scale Steam boilers n.d.) for the integration of an economizer in the boiler, but due to possible insulation problems, we account it as 5%. Table 4 shows the financial data for this energy-saving technology.

3.5.2 Steam Leakages

An energy audit was performed in 2013, and it was determined that about 20% of the total steam produced in the boiler was lost due to leakages or to steam traps. During further inspections, twelve steam plumes of about 1 m were identified. Table 5 summarizes characteristics of the leakages identified.

It has been finally considered that the 75% of the leakages (9 units) can be fixed with an immediate action based on professional plumbing service which would cost approximately 5500 € per leakage according to another RETscreen case study (RETScreen International 2012). Financial parameters of this improvement are indicated in Table 6.

Table 7 provides an estimation of diesel and cost reduction after economizer implementation and steam leakage reduction.

Table 5 Leakage characteristics and operational parameters

Characteristics	Operating parameters	Energy consumption: steam leakages
12 Units 1 Leakage/unit 1 m plume	Steam flow/units: 16 kg/h Steam pressure: 12 bar Superheated temperature: 170 °C Operating hours: 24 h/day	1370 MWh/year Estimated by RETscreen: 1307 MWh/year Discrepancy: 4.6% Share of total consumption: 9.9%

Table 6 Financial impacts of steam leakage reduction

Costs	Savings	Simple payback time
Investment: 50,000 € 1st year Maintenance: −4000 €/year	981 MWh/year of diesel (108,302 L of diesel/year) 84,824 €/year	50,000 €/ 84,824 €/year = 0.6 year

Table 7 Estimated diesel and cost reduction after economizer implementation and steam leakage reduction

	Diesel consumption	Costs
Before improvements (based on 2013 data)	726 m^3/year = 7749 MWh/year	569,882 €/year
After improvements	576 m^3/year = 6144 MWh/year	451,822 €/year
Estimated savings	150 m^3/year = 1605 MWh/year 20% reduction	118,060 €/year

Table 8 Estimated electricity and cost reduction after lighting changes

	Lighting power load	Electricity consumption	Costs
Before improvements	10.80 W/m^2	253 MWh/year	24.657 €/year
After improvements	1.07 W/m^2	24 MWh/year	2.339 €/year
Estimated savings	9.73 W/m^2	229 MWh/year 90% reduction	22.318 €/year

3.5.3 Lighting

Since the available information provided by CILAM's energy manager did not include the conditions and the actual electricity consumption of lighting, the estimation of the consumption was made according to the National Institute of Safety and Research of France (INRS), taking into the consideration that currently fluorescent light bulbs are installed in the building.

Table 8 contains data about estimated benefits of replacing old light bulbs with LED, based on the lightning requirements of INRS (120 lum/m^2) representing an investment cost of 3456 € (GE Lighting LED 2012/2013) and savings of 22.318 €/year and simple payback time in 0.15year, according to RETSCreen simulation.

Table 9 Refrigeration system characteristics and operating parameters

Charcs.	Operating parameters	Energy consumption: cooling products and storage
450 kW COP = 1.3	Duty cycle: 70% Operating hours: 24 h/day Drive by electricity	From energy bills: 2209 MWh/year Estimated by RETscreen: 2170 MWh/year Discrepancy: 1.7% Share of total consumption: 16.5%

Table 10 Financial impacts of a new PAC chiller

Costs	Savings	Simple payback time
Investment: 370,000 € the first year[a]	1606 MWh/year 156,711 €/year (Electricity)	370,000 € 156,711 €/year = 2.4 year

[a]Sabroe PAC Chillers (2014)

3.5.4 Refrigeration System

Data for CILAM's current refrigeration system used for cooling and storage purposes are indicated in Table 9.

Energy savings for refrigeration system were proposed by replacing the old cooling system. The aim is to install a new one with higher coefficient of performance (COP = 5) to reduce the electricity consumption from 2170 MWh to 564 MWh per year, according to RETScreen simulation. Financial impacts of this measure are listed in Table 10.

3.6 Proposed Case

After applying the identified possible improvement of energy efficiency, the energy savings are estimated at 3440 MWh/year in total (26.2% of savings). The energy distribution of industrial site after applying the measures proposed would be as shown in Fig. 2.

4 Results and Discussions

From the analysis made using RETScreen software, the results obtained are as follows.

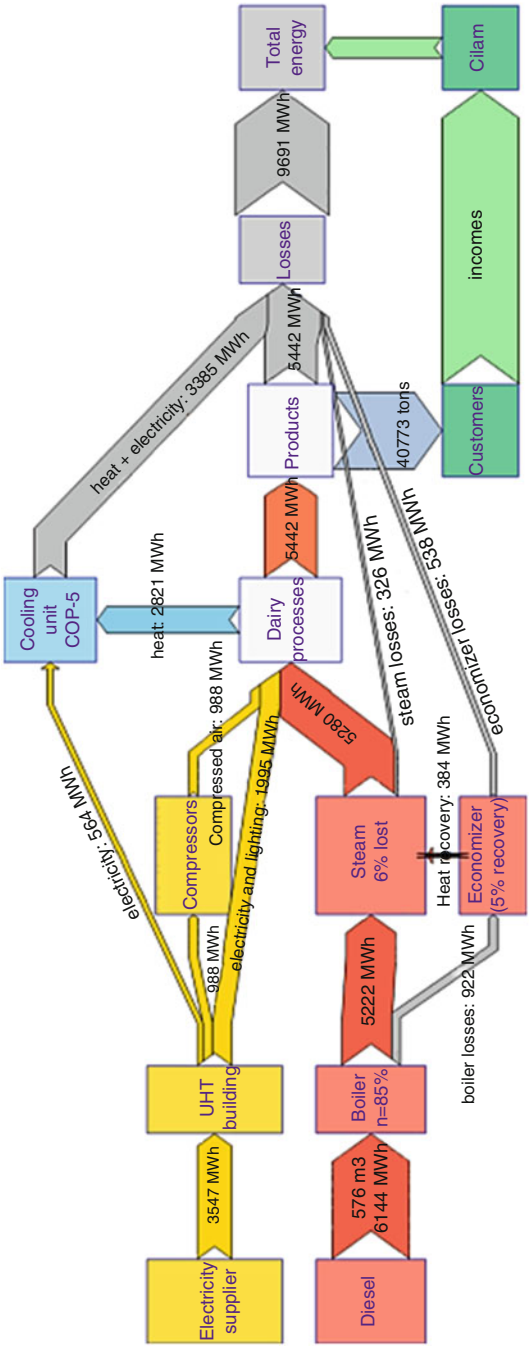

Fig. 2 Energy distribution for proposed case

4.1 Emission Analysis

Reunion Island electricity mix and its associated Green House Gases (GHG) emissions are defined based on data from the annual report of energy production in Reunion Island (Arer.org 2015). The improvement proposed in the industry should lead to a reduction of GHG emission in 1876 tons of CO_2 equivalent per year (equivalent to 800 m^3 of gasoline not consumed).

4.2 Financial Analysis

After implementing the proposed energy efficiency measures, and according to the financial parameter presented above in Table 1, the prefeasibility shows positive NPV of 2,052,109 € with an Annual Life Cycle Savings of 319,760 €/year. The main saving is observed due to the reduction in the fuel consumption, considering Diesel Fuel and Electricity as the inputs to run the UHT process shown in Table 11.

The total savings achieved with the energy efficiency measures proposed is 297,089 € at year 0 value, as it can be also observed in Table 11, regarding the savings in electricity and diesel consumption.

In addition, to complete the financial analysis, it is required to take in consideration the cumulative cash flows graph, shown in appendix Fig. 3; the short payback period of 1.5 years is remarkable. Such a short period of time may encourage rapid implementation of the improvements. Finally, the net benefit–cost (B-C) ratio is 5.5, which indicates the high profitability in this project.

4.3 Risk Analysis

In order to calculate the risks in implementing the proposed efficiency measures in this case study, a set of uncertainties are prescribed, as shown in Table 12.

The range of uncertainty for the fuel cost on the base case is 0% because the current fuel cost value was used throughout the study. For the fuel cost of the

Table 11 Ultra high temperature process energy costs

UHT process energy costs				
		Base	Proposed	Savings
Electricity (+cooling)	kWh Consumed	5,381,600	3,547,200	1,834,400
	Cost (€)	525,240 €	346,211 €	179,029 €
Diesel	Diesel Consumed (L)	726,890	576,304	150,586
	kWh Consumed	7,749,400	6,143,800	1,605,600
	Cost (€)	569,882 €	451,822 €	118,060 €

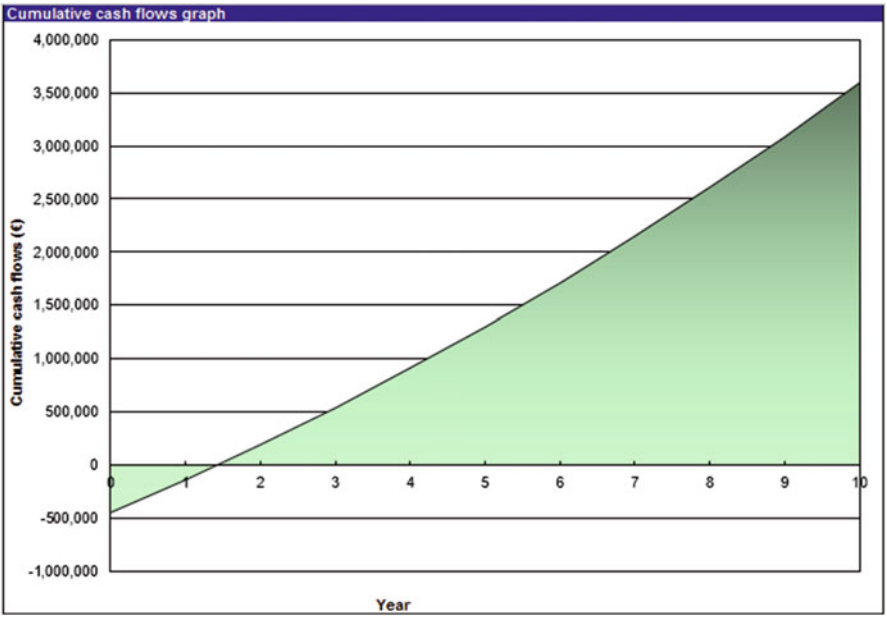

Fig. 3 Cash flow benefits of proposed case over base case

Table 12 The uncertainty range for defined input parameters

Parameter	Unit	Value	Range (+/−)	Minimum	Maximum
Initial costs	€	455,001	10%	409,501	500,501
O&M	€	−1999	10%	−1799	−2199
Fuel cost – proposed	€	798,033	5%	758,131	837,935
Fuel cost – base case	€	1,095,122	0%	1,095,122	1,095,122

proposed case, an uncertainty value of 5% was selected since it is unlikely that the price of the fuel will drastically change within the following year.

As is observed in Fig. 4, RETScreen displays a "Tornado Chart" identifying which parameters have the most influence on the variability of a selected financial parameter, such as the after-tax IRR as it is analyzed in this case. The impact graph shows how much of the variation in the financial parameter can be explained by variation in each input parameter in the risk analysis. This is expressed in relative terms how future changes in fuel cost will impact the feasibility of the proposed energy efficiency measures, as well as any fluctuation on the initial cost will influence the viability of the project. The fuel and initial costs are the most critical input parameters; an increase of one standard deviation in the fuel cost leads to a decrease in the IRR of nearly 0.8 standard deviations, also an increase of one standard deviation in the initial cost leads to a decrease in the IRR of nearly 0.6 standard deviations.

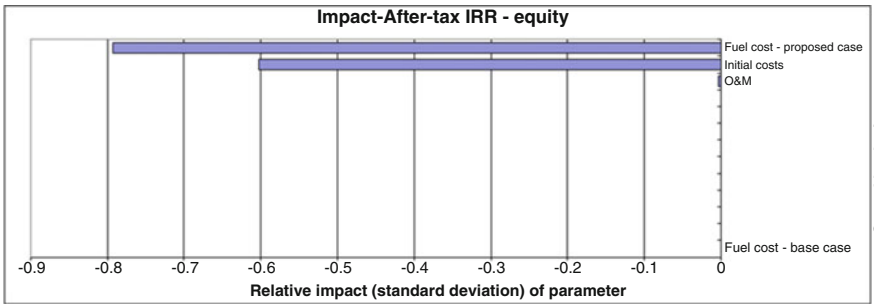

Fig. 4 Tornado chart analysis from RETscreen simulation

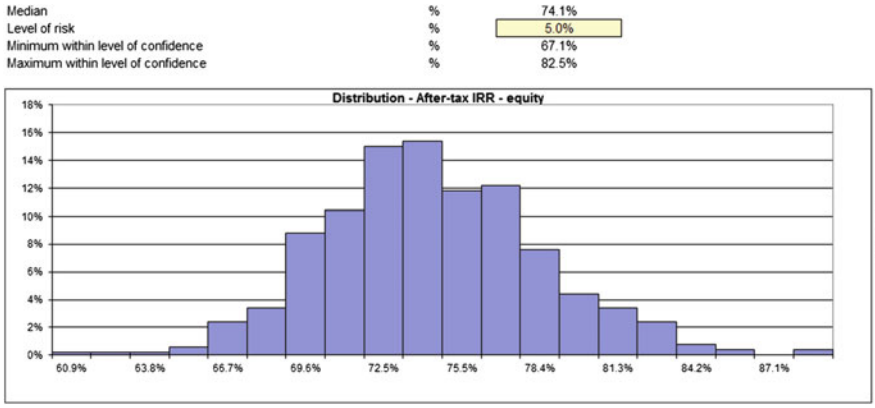

Fig. 5 Monte Carlo analysis from RETscreen simulation

The Monte Carlo analysis, shown in Fig. 5, generates a probability distribution for the financial parameter based on the assumed variations for the input parameters. Specifying a desired level of risk at 5%, RETScreen indicates the range of outcomes for which the after-tax IRR will fall outside the range of 67.1–82.5%. The model calculates the after-tax internal rate of return (IRR) on equity (%), which represents the true interest yield provided by the project equity over its life, after income tax. The yields returned for the project, regarding the proposed case implementation, are gains in the order of 2% and 15% positive values, which measure how much cash flow the company will get for each dollar invested in an equity position.

5 Conclusions

In Reunion Island, as in many other islands around the globe, power generation relies mainly on expensive and high-polluting technologies and methods, like diesel generators (Blechinger et al. 2013). Nowadays, during permanent increase of energy prices and production growth, it is highly important to implement energy-saving technologies as much as possible. However, due to the economic situation worldwide, stakeholders of industrial assets would like to be aware about different aspects of technologies that would allow them to choose the best option for the investment. RETScreen software provides the possibility to perform the analysis of energy-saving procedure and evaluate its attractiveness not only from an environmental but also a financial point of view.

In this paper, an analysis of four different technologies was performed for boosting the energy efficiency at a dairy plant: installation of an economizer for boiler, steam leakage decreasing, improvements in lighting, and the installation of more efficient refrigeration system. It was estimated that the biggest savings of energy were made with improvements in the refrigeration system; however, it got the biggest investment costs and the longest payback. Installation of an economizer and steam leakages made a total diesel savings of 20%, which make these measures financially attractive.

Thanks to the energy-saving technologies that could be implemented, the total savings forecasted are 26.2% of total energy use, 319,760 €/year of life cycle, and 1876 tons of CO_2 in annual savings. These numbers combined with a short payback period of 1.5 years show that the proposed improvements are reasonable and profitable.

In addition, the results here presented are aligned with the initiatives of diesel-free power generation. By using fewer diesels, the power systems are less dependent on the diesel's volatility price which at the same time decreases the risk of the Island's energy supply (Blechinger et al. 2013). For further studies, research about possible introduction of renewable energy sources and the optimization of production equipment can be performed. Moreover, an opportunity of governmental financial support should be taken into account during the decision-making process due to its ability to increase total project profitability.

Acknowledgments We would like to thank Compagnie Laitière des Mascareignes (CILAM) for providing us with the necessary data. Especially, we would like to address our gratitude to CILAM energy manager Mr. Marc Bourhis for his assistance and time. We also would like to thank our academic tutor, Pr. Luis R. Rojas S., for introducing us to RETScreen software and his kind guidance during all stages of the project. Finally, we would like to thank Mrs. Félicie Théron for her administration of the course.

Appendix

References

Agenda21france.org: Agenda 21 de Territoire. [online] Available at: http://www.agenda21france.org/agenda-21-de-territoire/index.html (2015). Retrieved 19 Dec 2014

Agro-oi.com: Agro-oi | CILAM – Compagnie Laitiere Des Mascareignes. [online] Available at: http://www.agro-oi.com/fr/7/1330/cilam-compagnie-laitiere-des-mascareignes.html#.VLzQxkfF-AU (2015). Accessed 1 Oct 2014

Arer.org: Bilan énergétique 2012 de La Réunion. [online] Available at: http://www.arer.org/Bilan-energetique-2012-de-La,736.html?espace=Education (2015). Accessed 1 Nov 2014

Blechinger, P., Howe, E., Cader, C., Pleßmann, G., Hlusiak, M., Seguin, R., Breyer, C.: Assessment of the Global Potential of Renewable Energy Storage Systems on Small Islands in 8th IRES, pp. 294–300, no. (2013)

Efficiency on a large scale Steam boilers. 1st ed. [ebook] Bosch Group, p. 4. Available at: http://www.bosch-industrial.com/files/BR_SteamBoilers_en.pdf (n.d.). Accessed 10 Oct 2014

GE Lighting LED: LED Catalogue. [online] Available at: http://www.gelighting.com/LightingWeb/apac/images/LED-LED-ctlg-EN-052012-PG47-APAC_tcm281-33329.pdf (2012/2013). Accessed 15 Nov 2014

Institut national de la statistique et des études économiques (INSEE): Inflation Rate Database. http://www.insee.fr/fr/. Accessed 3 Nov 2014

Praene, J., David, M., Sinama, F., Morau, D., Marc, O.: Renewable energy: progressing towards a net zero energy island, the case of Reunion Island. Renew. Sust. Energ. Rev. **16**(1), 426–442 (2012)

RETScreen International: Clean Energy Project Analysis: RETScreen Engineering and Cases Textbook (2005)

RETScreen International: Energy efficiency measures – Industrial – Steam losses (2012). [online] Available at: http://www.retscreen.net/ang/templates_steam_losses.php. Accessed 10 Nov 2014

Ricci, O., Selosse, S., Garabedian, S. and Maizi, N.: Réunion Island's energy autonomy objective by 2030. [online] Econpapers.repec.org (2014). Available at: http://econpapers.repec.org/paper/ekd006356/7069.htm. Accessed 11 Nov 2014

Sabroe PAC Chillers: Catalogue. [online] Available at: http://www.sabroe.com/fileadmin/user_upload/Marketing/Brochures/Chillers/PAC_recip_SB-3571_Jan_2015_GB120dpi.pdf (2014). Accessed 20 Oct 2014

Smart Simulator for Tracking the Global Maximum Power Peak of Photovoltaic Arrays Under Partial-Shaded Conditions

Saad Saoud Merwan, Abbassi Hadj Ahmed, Kermiche Saleh, and Ouada Mahdi

1 Introduction

The functioning of a photovoltaic (P-V) array is affected by temperature, solar irradiance, shading, and array configuration. Frequently, the P-V arrays become shadowed, either completely or partially. When the array is operated under partially shaded conditions, the PV characteristics become more complex and the multiple maximum power points tracking (MPPT) can fail to track the absolute MPP. To overcome this problem, complex algorithms have been developed (Kawamura et al. 2003; Nguyen and Low 2010). The effect of shading on the output of the P-V modules and the changes in their I–V characteristics were investigated by Kobayashi et al. (2003).

Because partial shading conditions (PSCs) occur quite commonly due to clouds, trees, or nearby buildings, it is necessary to develop special MPPT schemes that can track the real MPP under PSCs. Although some researchers have worked on real MPP tracking under partial shading conditions, (Carannante et al. 2009; Miyatake et al. 2007, their methods have some drawbacks because of their complexity, tracking failure of the real MPP position, and difficulties involved in their application to the installed power conditioning system.

S.S. Merwan (✉) • A. Hadj Ahmed • K. Saleh
Annaba University, Faculty of Engineering Science,
Electronic Department, Sidi amar, Annaba 23000, Algeria
e-mail: maro34ss@gmail.com; hadj-Ahmed.abbassi@univ-annaba.dz;
salah.kermiche@univ-annaba.dz

O. Mahdi
Annaba University, Faculty of Science of Engineer, Electromechanical
Department, Sidi amar, Annaba 23000, Algeria
e-mail: ouadamehdi@gmail.com

© Springer International Publishing AG, part of Springer Nature 2018

F. Aloui, I. Dincer (eds.), *Exergy for A Better Environment and Improved Sustainability 2*, Green Energy and Technology,
https://doi.org/10.1007/978-3-319-62575-1_60

In general, most of the conventional MPPT algorithms do not have the capability to detect the global peak (the true maximum of the multiple local peaks) effectively, which will lead to considerable power loss (Ramaprabha and Mathur 2009).

Some researchers (Kashif and Salam 2003) have worked on GP-tracking schemes for P-V arrays operating under non-uniform irradiation conditions. Solodovnik et al. (2004) have reported an MPPT scheme that uses a Fibonacci sequence to track the GP under partially shaded conditions. In Bidram et al. (2012), a review on the state-of-the-art MPPT techniques available is presented by Kashif et al. (2011). However, Patel and Agarwal (2008) stated that the "Power Curve Slope" MPPT method is efficient under shading conditions. In this technique, the symbol $\partial P/\partial V$ at different points is used to track the global maximum, and the change in $\partial P/\partial V$ sign from negative to positive indicates the existence of another maximum on the right side of the existing one (Yousra Shaiek et al. 2013). If a local maximum is found, as indicated by a change in $\partial P/\partial V$, it is compared with the stored maximum. If the detected local maximum is greater than the stored maximum, the stored maximum will be updated. Alonso-Gracia et al. (2006) present a comparison between conventional methods and the GA approach for MPPT of shaded solar P-V generators. An experimental study of the effect of partial shading on *I–V* characteristics of the P-V module and the constituent cells was carried out by Hsu (2010).

Recently, one of the best methods for MPPT under partial shade, Particle Swarm Optimization (PSO), has come to light. This is a technique based on the stochastic optimization population developed by Eberhart and Kennedy (1995), inspired by the social behavior of bird flocking or fish schooling. PSO is based on search optimization where the system is initialized with a population of random solutions and searches for optima by updating generations. A special property of PSO is that it can be operated directly in continuous real number space (Ishaque et al. 2012). A significant number of researchers have shown interest in this approach (e.g., Chao et al. 2013). The key advantage of the proposed technique in Miyatake et al. (2011) is the elimination of PI control loops using the direct duty cycle control method. Kashif and Salam (2013) have successfully studied a modified PSO-based MPPT method, and have presented a novel algorithm based on conventional PSO. Mermoud et al. (1998) developed a comprehensive Matlab/Simulink P-V system simulator with partial shading capability based on a two-diode model.

The presence of multiple peaks reduces the effectiveness of the existing MPPT schemes. There is a need to develop a special simulator that can track the GP under these conditions.

The possibility for evaluating the behavior of a system in the presence of shading conditions is to include some commercial programs, P-VSyst, for example [25]. However, these programs give only approximate data, in very limited positions, and are costly.

It is very important to model a simulator for techno-economic purposes having a design and concept of photovoltaic systems, because this will provide a predictive image before the installation, which can considerably reduce the cost of installation and increase the efficiency of P-V generators.

For this reason, the present paper proposes a simplified soft simulator that can achieve this operation. A Matlab/Simulink P-V simulator is used to track the global power peak under partially shaded conditions, using a model of two diodes, based on an extensive study of partially shaded P-V arrays. The simulation results are presented to tested the accuracy and consistency of this simulator; to justify the performance of the proposed model, the results are tested against a comparison method of the simulation and experimental results of PV characteristics under the partially shaded conditions of PSO MPPT proposed in Miyatake et al. (2011).

The paper is organized as follows:

In Section 2 P-V array characteristics under uniform conditions with the impact of various temperatures and irradiations are presented. In Section 3 the study of P-V array characteristics under partially shadied conditions is shown. Finally, the simulation of the outputs for the proposed application is given. The proposed work can be very useful for simulator developers and it is able to validate the effectiveness of existing and new MPPT techniques.

2 P-V Array Characteristics under Uniform Conditions

In the literature there are two possible approaches for extracting solar module parameters: using analytical methods according to Gottschalg et al. (1999), where several parameters of the datasheet are required. However, module datasheets only provide information on standard test conditions (irradiation = 1000 w/m^2 and temperature = 25°). It is known that P-V arrays are impacted by temperature and solar irradiance variations, and numerical methods that are based on a mathematical algorithm to adjust all the points on the I–V curve will provide more accurate results.

The solar cell can be represented by the electrical model with two diodes, as shown in Fig. 1. Its current voltage characteristic is expressed by the following Eq. (1):

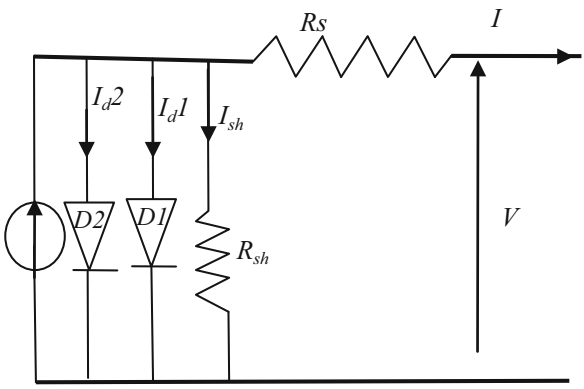

Fig. 1 Equivalent circuit of a solar cell

$$I = I_{\mathrm{Ph}} - I_{\mathrm{d1}} - I_{\mathrm{d2}} - I_{\mathrm{sh}} \tag{1}$$

where I and V are the solar cell output current and voltage respectively, I_{ph} represents the photovoltaic current, q is the charge of an electron, N is the diode quality (ideality) factor, k is the Boltzmann constant, and Rs and Rsh are the series and shunt resistors of the solar cell. I_{d1}, I_{d2}, are the currents of diode 1 and diode 2, I_{sh} is the shunt resistor current. When the photocurrent equal, the following equation is derived:

$$I_{\mathrm{Ph}} = (I_{\mathrm{Ph,n}} + K_I \Delta T)\frac{G}{G_n} \tag{2}$$

$\Delta T = T - T_n$ (being T and T_n the actual and nominal temperatures [K]), G [W/m^2] is the irradiation on the device surface, and G_n is the nominal irradiation. The current diodes are:

$$I_{d1} = I_{01}\left[\exp\left(\frac{V + IR_{\mathrm{s}}}{a_1 V_{T1}}\right) - 1\right] \tag{3}$$

$$I_{d2} = I_{02}\left[\exp\left(\frac{V + IR_s}{a_2 V_{T2}}\right) - 1\right] \tag{4}$$

where I_{01} and I_{02} are the reverse saturation currents of diode 1 and diode 2, V_{T1} and V_{T2} are the thermal voltages of respective diodes, and a_1 and a_2 represent the diode ideality constants.

$$I_{01} = I_{02} = \frac{(I_{sc\text{-}n} + K_I \Delta T)}{\exp[(V_{oc,n} + K_V \Delta T)/V_T] - 1} \tag{5}$$

I_{sc}: short circuit current [A].
K_{i}: cell's short-circuit current temperature coefficient.
V_{oc}: open circuit voltage.
K_{v}: cell's open circuit voltage temperature coefficient.
A: ideal factor.Shunt current equal:

$$I_{\mathrm{sh}} = \frac{V + R_{\mathrm{s}} I}{R_{\mathrm{sh}}} \tag{6}$$

$$Vm = Ns \times V \tag{7}$$

with V_{m} the module voltage and N_{s} number of cell in series.

The P-V array used in this paper is a combination of three series of the Kyocera KC200GT modules. A series combination of modules was chosen to obtain higher output voltage of P-V module. If this chain is under uniform insolation, the MPP value is p = 600 W.

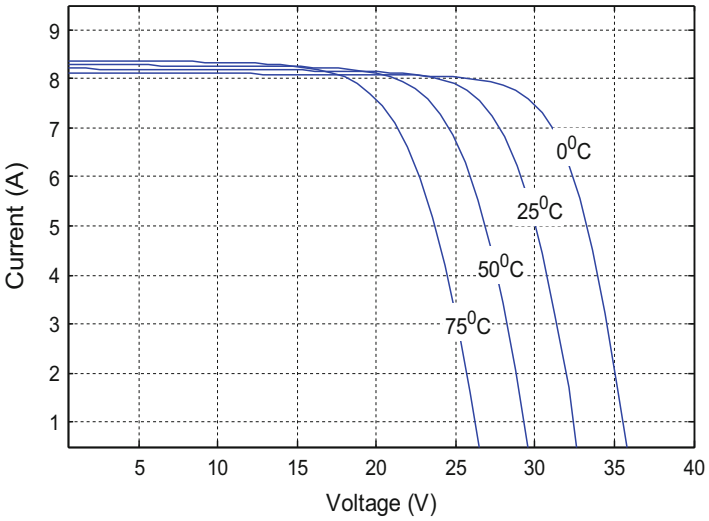

Fig. 2 KC200GT module I-V curve at various temperatures

The KC200GT module itself is composed of 54 silicon cells connected in a series. Each module can generate current up to 8.21 A and a voltage of 32.9 volts. Figure 2 shows the standard condition, and the rise in the maximum power to a 200-W peak at standard testing conditions (25 °C, 1000 W/m^2 and AM = 1.5) (Figs. 3, 4, and 5).

3 Influence of Partial Shading in P-V Array Characteristics

The considerable advantage of the modeling and simulation method in this research is to cover different scales of a P-V system under both normal and partial shading conditions, without analyzing the in-depth semiconductor physics definitions (Carannante et al. 2009).

There are times where some part of the P-V arrays might be shaded (Silvestre et al. 2009).The P-V characteristic of the P-V array exhibits multiple local maxima and only one of them corresponds to the global MPP.

If there is one shaded panel in a series of connected arrays, it can then act as a load on the array. The shaded P-V cells absorb a large amount of the electric power that is generated by other P-V cells that receive high illumination and convert it into heat. This situation is called the hot-spot problem. This is often solved with the inclusion of a bypass diode to a specific number of cells in the series circuit.

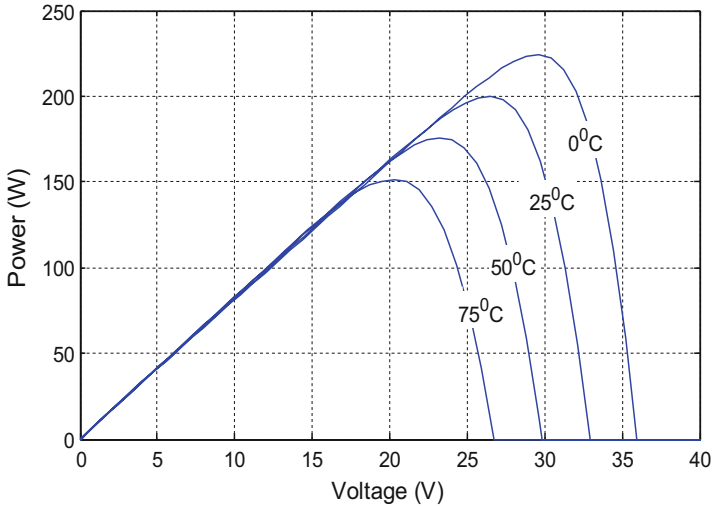

Fig. 3 KC200GT module P-V curve at various temperatures

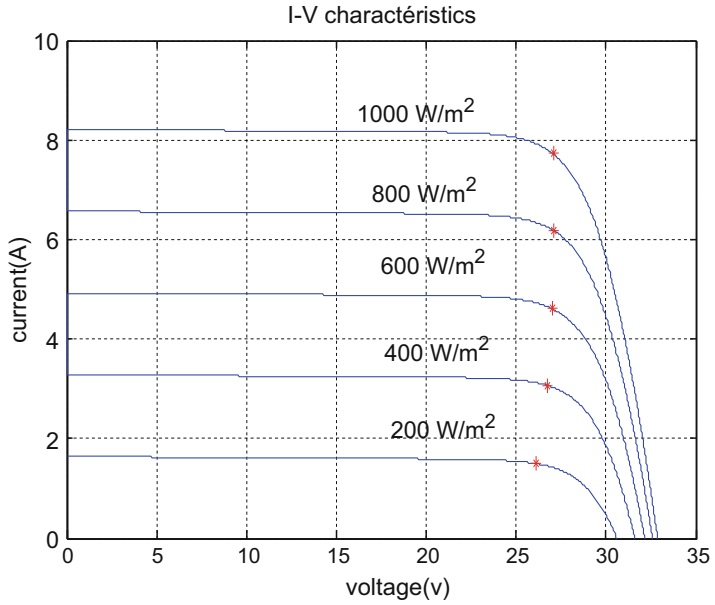

Fig. 4 KC200GT module I-V curve at various insolations

The bypass diodes are connected in an anti-parallel way with each panel, and where the panel is shaded current flows through the bypass diode rather than through the panel (Hsu et al. 2010).

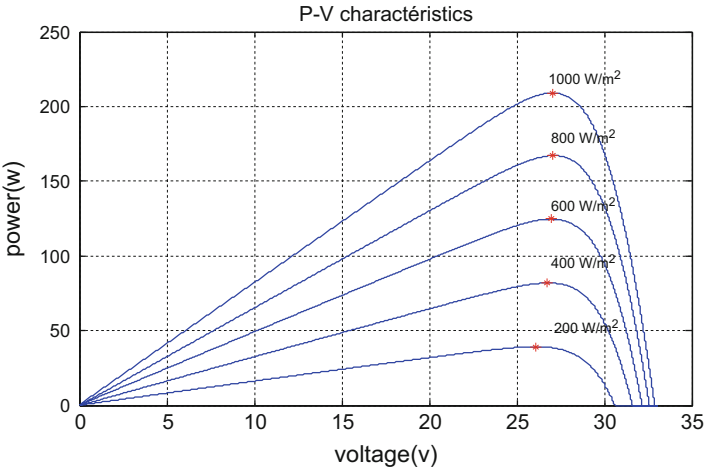

Fig. 5 KC200GT module P-V curve at various irradiations

For this study, three panels connected in a series with non-uniform insulation have been considered. The same concept can be extended to a number of panels connected in series. Figure 6 shows the series connection of three panels with three bypasses diodes.

The inserted bypass diodes that may cause multiple peaks are established in the I-V and P-V characteristic curves under partial-shaded conditions (Villalva et al. 2009), as shown in Figs. 7, 8, and 9

4 The User Interface Simulator

A user can communicate with the proposed simulator through a graphic interface that allows the possibility of loading data sheet parameters of selected P-V modules directly (Voc, Isc, Vmp, Imp, Kv, Ki, and Ns). This step is achieved by calculating Rs and Rsh, a method presented in Villalva et al. (2009), which is used to obtain this operation, as shown in Fig. 10a. In this case the test parameters of irradiation must be equal to modulate these parameters (under uniform conditions),and the user pushes the button "ran" to simulate the adjusting power peak, following which the user pushes the button "next" to then input the different irradiations proposed. For example, authors chose the three panels KC200GT connected in a series under 1000 w/m^2, shown in Fig. 10b.

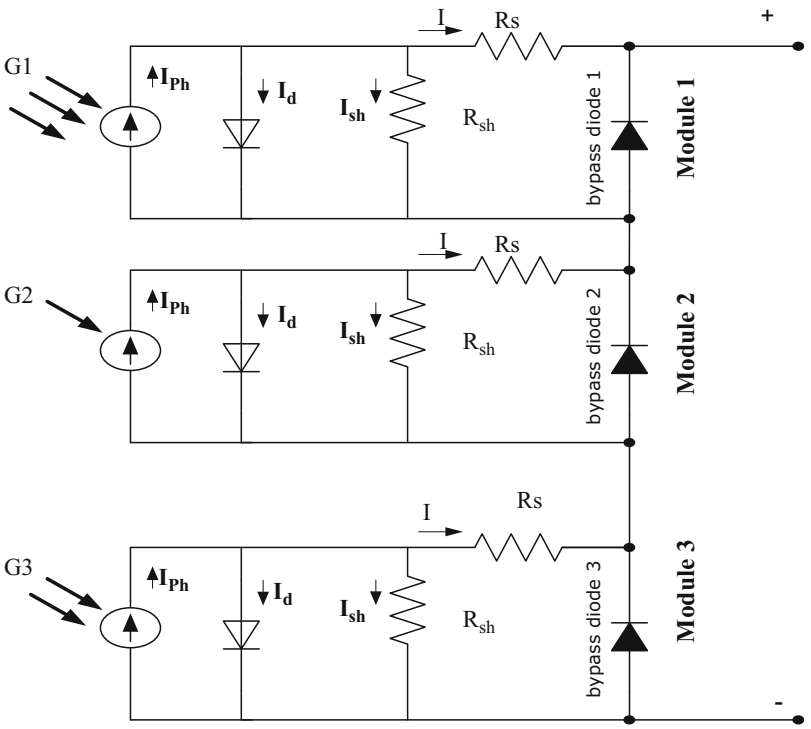

Fig. 6 Schematic representation of three series of panels with bypass diodes

5 Results and Discussion

This section presents the simulation results with the proposed simulator; the first aim of this study was to simulate the characteristics of three panels KC200GT connected in a series response during mismatching conditions, where the author test parameters chosen are:

For first group: The first panel is under uniform irradiation G1 = 1000 w/m^2, the second panel is shaded by G2 = 250 w/m^2, and the third panel is shaded by G3 = 500 w/m^2. When the first panel's current becomes greater than that of the second and third panels, the shaded modules absorb energy. To solve this problem, a bypass diode is connected in parallel to each group.

For the second group all panels are under the same irradiation G = 500 w/m^2, and the purpose of this choice is to validate that the algorithm is able to track the MPP under uniform irradiation too, as shown in Fig. 11.

The second step is tracking the maximum global power where it is based on two phases:

The first is to find the locals peaks: the system scans the power values periodically to find all peaks, than the algorithm searches the maximum power point from

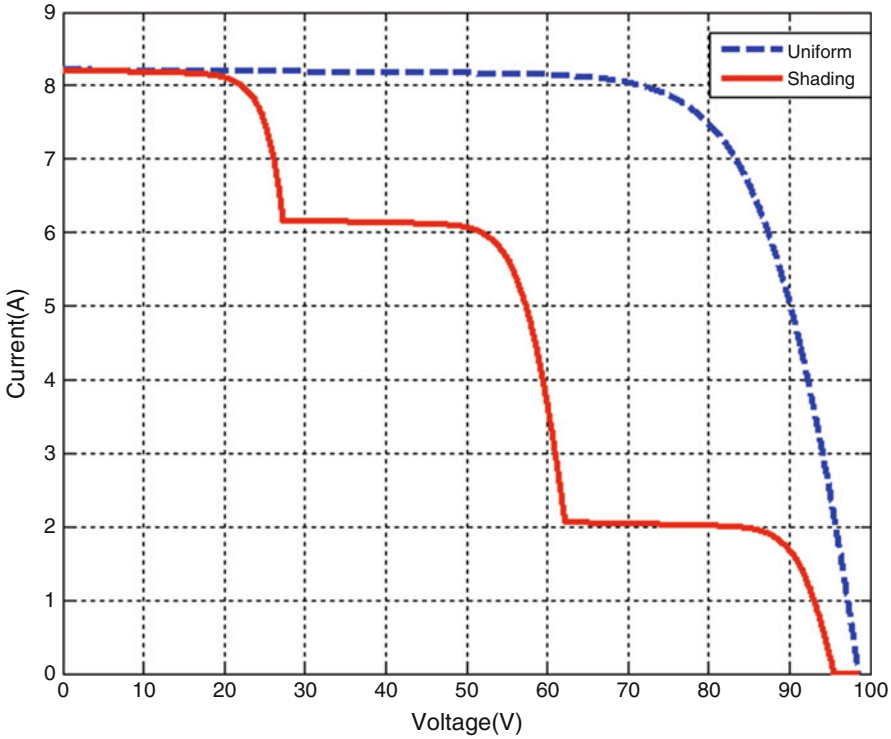

Fig. 7 The resulting simulation I–V curve

the maximum local peaks. The obtained parameter will be called the global peak; the simulation result is shown in Fig. 12.

The biggest advantage of the proposed simulator is that there is the possibility to execute a sequential simulation with only initialization parameters, which allows giving the opportunity to see the different energy levels produced in the function of level shading panels. This clears the impact of partial shading and provides a predictive study before doing the practical installation of solar panels. Figures 13 and 14 explain this advantage, where the following test parameters successively used are:

G1 = [1000 500,250], G2 = [750,600 1000], G3 = [750300800], G4 = [100300800] (w/m^2).

To confirm the efficacy of the simulator we tried using it with mono-crystalline panels e19/425 sunpower, and the results are as follows:

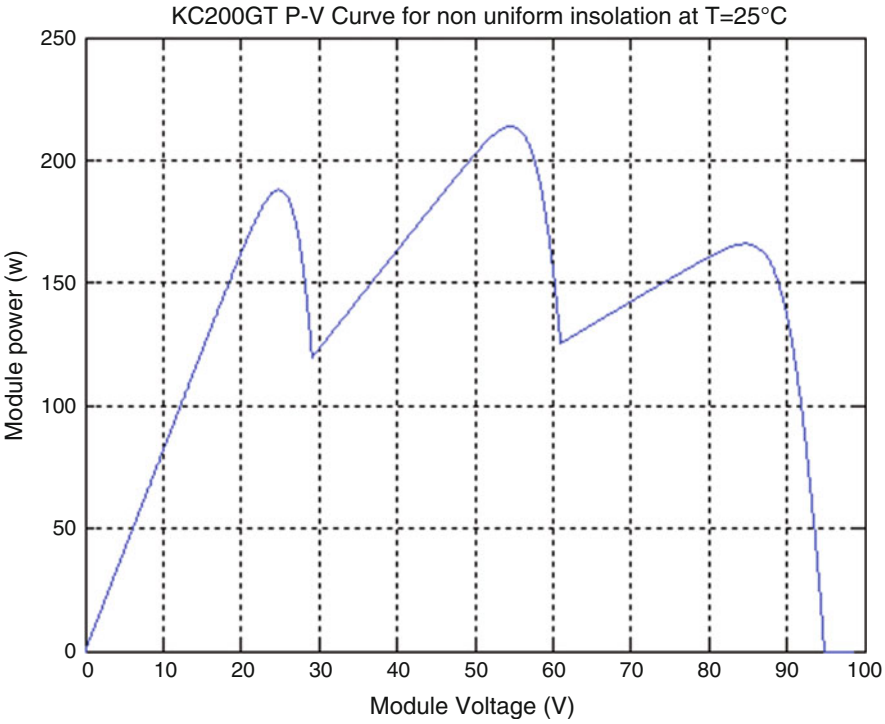

Fig. 8 The simulation results of the P–V curve under shaded conditions

6 Comparative Search for the Maximum Global Peak Power Simulation

To prove that the program is efficient and is accurate in the calculating GP, we compared its responses with the simulation and experimental results of P–V characteristics presented in [20], where the same initialization parameters of P-V systems is carried out.

Here, eight panels KC200GT are connected by the connection method shown in Fig. 15, and the obtained results are shown in Fig. 16.

G1 = 500 w/m^2.

G2 = 800 w/m^2.

The obtained results indicated that the GP is tracked successfully. The results are shown in Fig. 16.

The proposed method does not present any complexity and will be a development platform for researchers in this field. The following conclusions emerge from this study:

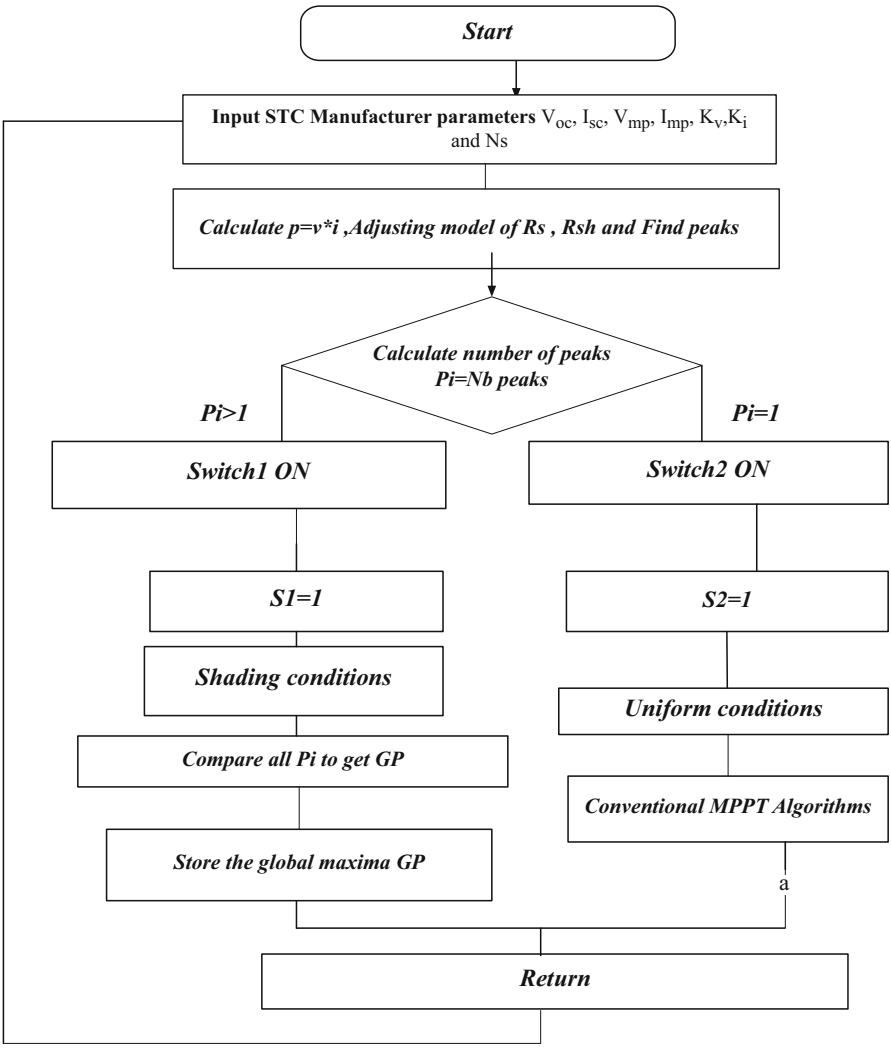

Fig. 9 Flowchart for the proposed algorithm

The hot-spot is a problem that occures where the shaded P-V cells absorb the electric power generated by other P-V cells under uniform irradiation and convert it into heat.

The shaded panels should be bypassed by a diode when they are connected in a series.

The presence of multiple peaks is needed to develop a special algorithm that can track the GP under shaded conditions.

Power provided by P-V cells under partial shading conditions is very low compared to that obtained with P-V cells under standard conditions.

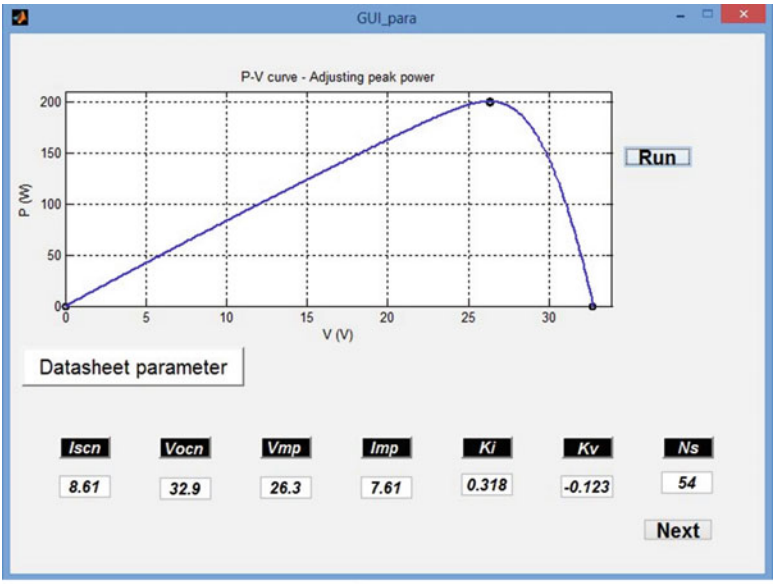

(A)

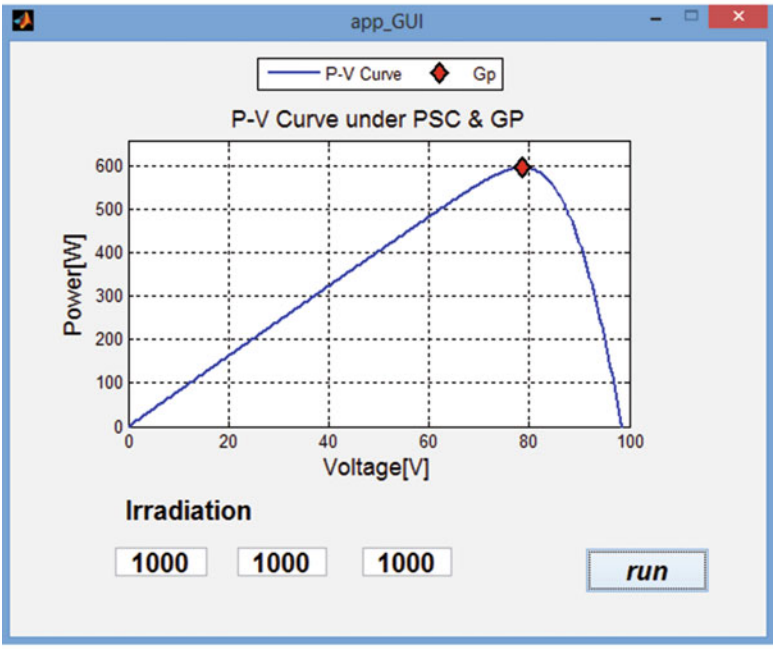

(B)

Fig. 10 Adjusting parameter values

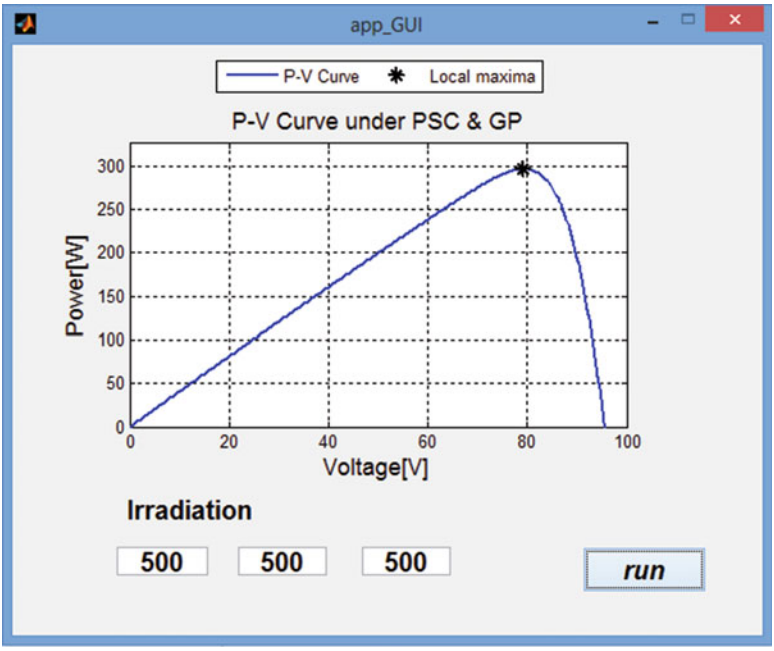

Fig. 11 Searching for the maximum power peak under irradiation G = 500 w/m^2

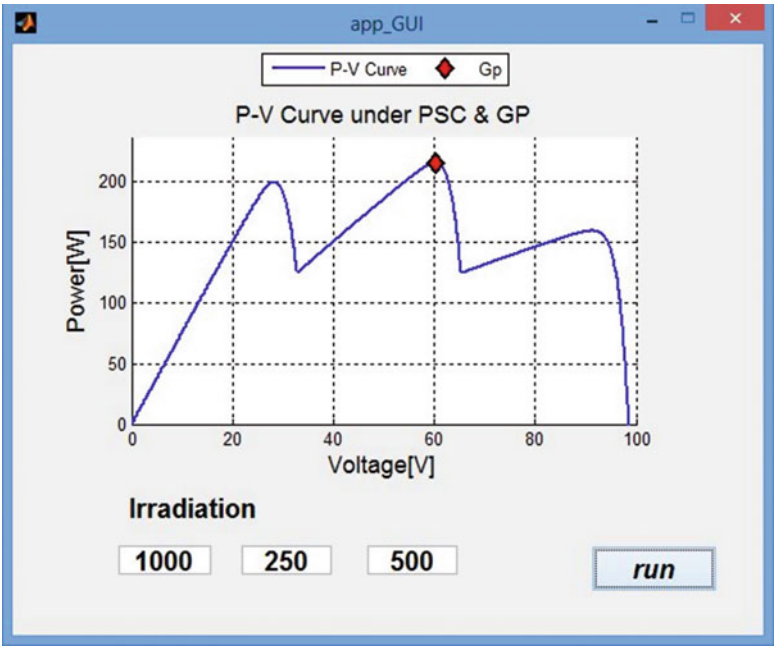

Fig. 12 Searching for the maximum global peak power

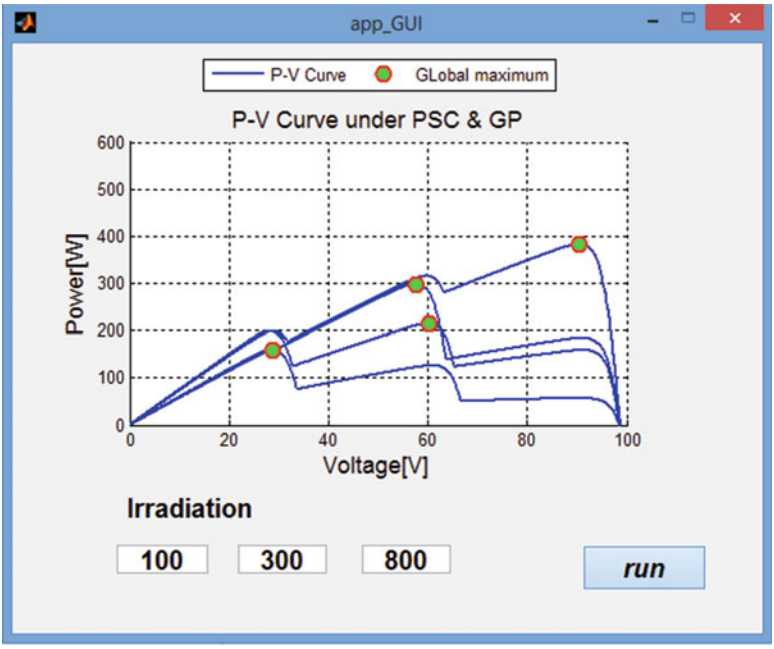

Fig. 13 Searching for the maximum global power peak

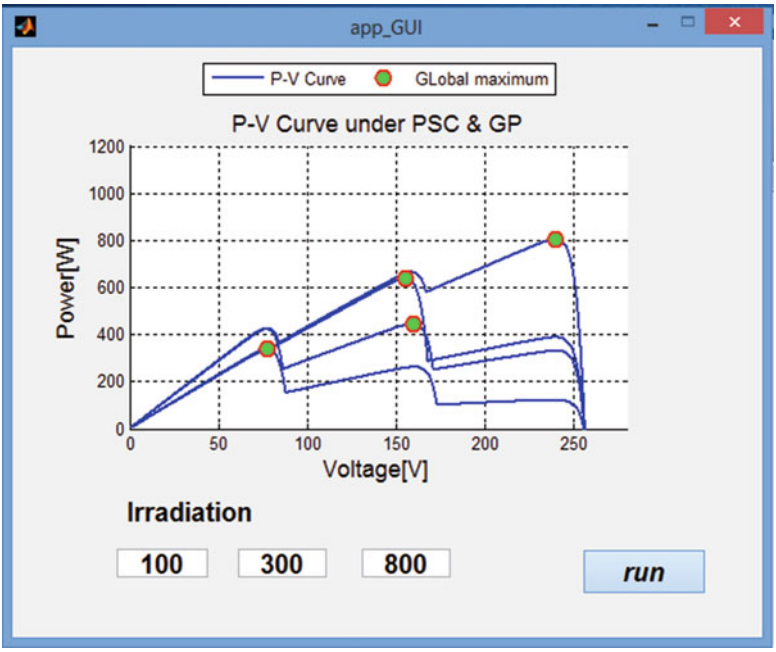

Fig. 14 Search of maximum global power peak of E19/425 panels

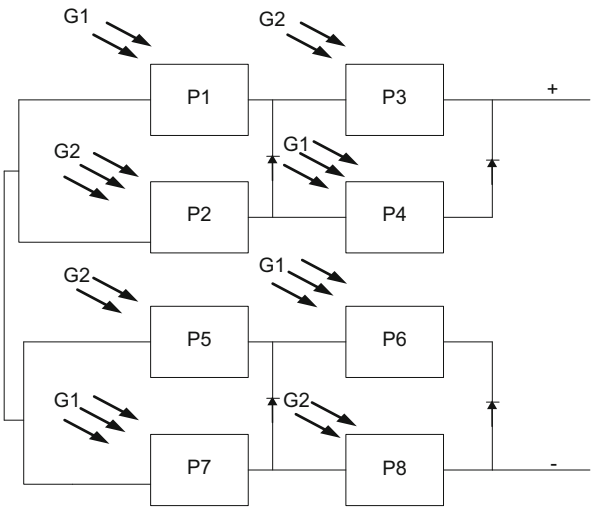

Fig. 15 Schematic representation of eight series of panels with bypass diodes in mismatching conditions

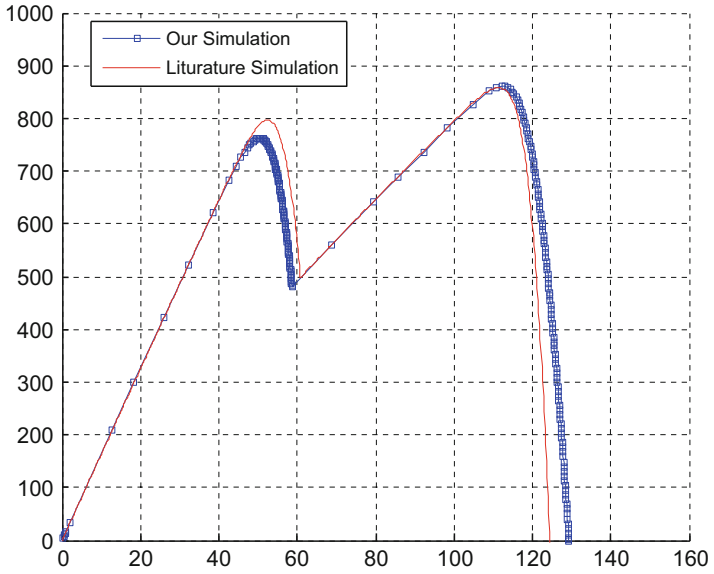

Fig. 16 Simulation results of a P-V curve under shaded conditions

7 Conclusions

Adaptive and flexible simulators with a simple technique for tracking a global maximum power under mismatching conditions based on MATLAB Simulink were developed in this study. The mathematical model and output characteristics of the

P-V panels were analyzed, and the effects of partially shaded phenomena in P-V arrays were examined in detail. The simulation results verify the feasibility and effectiveness of the proposed simulator under the influence of these conditions and proved that the algorithm is capable of tracking the MPP with simplicity, a fast response, and a high level of precision in most cases.

References

Alonso-Gracia, M.C., Ruiz, J.M., Chenlo, F.: Experimental study of mismatch and shading effects in the I–V characteristic of a photovoltaic module. Solar Energy Mater. Solar Cells. **90**(3), 329–340 (2006)

Bidram, A., Davoudi, A., Balog, R.S.: Control and circuit techniques to mitigate partial shading effects in photovoltaic arrays. IEEE J. Photovol. **2**(4), (2012)

Carannante, G., et al.: Experimental performance of MPPT algorithm for photovoltaic sources subject to inhomogeneous insolation. Ind. Electron. IEEE Trans. **56**(11), 4374–4380 (2009)

Chan, D.S.H., Phang, J.C.H.: Analytical methods for the extraction of solar-cell single- and double-diode model parameters from I–V characteristics. Electron. Dev. IEEE Trans. **34**, 286–293 (1987)

Chao, K.-H., et al.: Maximum power point tracking method based on modified particle swarm optimization for photovoltaic systems. Int. J. Photoenergy. **2013**, 583163 (2013.) 6 pages

Eberhart, RC. and Kennedy, J.: A new optimizer using particle swarm theory. In: Proceedings of the 6th International Symposium on Micro Machine and Human Science, pp. 39–43, October 1995

Giraud, F., Salameh, Z.M.: Analysis of the effects of a passing cloud on a grid-interactive photovoltaic system with battery storage using neural networks. Energy Conversion IEEE Trans. **14**(4), 1572–1577 (1999)

Gottschalg, R., et al.: The influence of the measurement environment on the accuracy of the extraction of the physical parameters of solar cells. Meas. Sci. Technol. **10**, 796 (1999)

Hsu, Y.-J.W.P.-C.: Analytical modeling of partial shading and different orientation of photovoltaic module. IET Renew. Power Gener. **4**(3), 272–282 (2010)

Ishaque, K., Salam, Z., Syafaruddin: A comprehensive MATLAB Simulink P-V system simulator with partial shading capability based on two-diode model. Sol. Energy. **85**, 2217–2227 (2011)

Ishaque, K., et al.: A direct control based maximum power point tracking method for photovoltaic system under partial shading conditions using particle swarm optimization algorithm. Appl. Energy. **99**, 414–422 (2012)

Kashif, I., Salam, Z.: A review of maximum power point tracking techniques of P-V system for uniform insolation and partial shading condition. Renew. Sust. Energ. Rev. **19**, 475–48A (2013)

Kashif I., Zainal S., Hamed T.: Accurate MATLAB/Simulink PV systems simulator based on a two-diode model. Journal of power electronics. **11**(2), (2011)

Kawamura, H., Naka, K., et al.: Simulation of I–V characteristics of a P-V module with shaded P-V cells. Sol. Energy Mater. Sol. Cells. **75**(3–4), 613–621 (2003)

Kennedy, J. and Eberhart, R. C.: Particle swarm optimization. In: Proceedings of the IEEE International Conference on Neural Networks, vol. 4, pp.1942–1948, December 1995

Khare, A., Rangnekar, S.: A review of particle swarm optimization and its applications in solar photovoltaic system. Appl. Soft Comput. **13**, 2997–3006 (2013)

Kobayashi, K., Takano, I. and Sawada, Y.: A study on a two stage maximum power point tracking control of a photovoltaic system under partially shaded insolation conditions. In IEEE Power Eng. Soc. Gen. Meet, pp. 2612–2617 (2003)

Mermoud A, Roecker C, Bonvin J, Muller A.: P-VSYSTS 3.0 software: ergonomics & accessibility. In: Proceedings of the second world conference on photovoltaic solar energy conversion 2214–2217 (1998)

Miyatake, M., Inada, T., Hiratsuka, I., Zhao, H., Otsuka, H., Nakano, M.: Control characteristics of a Fibonacci-search-based maximum power point tracker when a photovoltaic array is partially shaded. Proc. IEEE IPEMC. **2**, 816–821 (2004)

Miyatake, M., Toriumi, F., Endo, T., and Fujii, N.: A novel maximum power point tracker controlling several converters connected to photovoltaic arrays with particle swarm optimization technique, In: Power Electronics and Applications, 2007 European Conference on, pp. 1–10.

Miyatake, M., Veerachary, M., Toriumi, F., Fujii, N., Ko, H.: Maximum Power point tracking of multiple photovoltaic arrays: a particle swarm optimization approach. Aerosp. Electron Syst. IEEE Trans. **47**, 367–380 (2011)

Nguyen, L., Low, K.-S.: Global maximum power point tracking scheme employing direct search algorithm for photovoltaic systems. IEEE Trans. Ind. Electron. **57**(10), 3456–3467 (2010)

Patel, H., Agarwal, V.: Maximum power point tracking scheme for P-V systems operating under partially shaded conditions. IEEE Trans. Ind. Electron. **55**(4), 1689–1698 (2008)

Ramaprabha, R., Mathur, B.L.: Impact of partial shading on solar P-V module containing series connected cells. Int. J. Recent Trends Eng. **2**(7), 56–60 (2009)

Ramaprabha R., Mathur B.L.: Matlab based modeling to study the influence of shading on series connected SP-VA. In: Second International Conference on Emerging Trends in Engineering and Technology, ICETET-09.

Roy Chowdhury, S., Saha, H.: Maximum Power point tracking of partially shaded solar photovoltaic arrays. Sol Energy Mater. Sol Cell. **94**, 1441–1447 (2010)

Seyedmahmoudian M., Mekhilef S., Rahmani R., Yusof R., Taslimi Renani E.: Analytical modeling of partially shaded photovoltaic systems. Energies January 2013, 6, 128–144.

Shaiek, Y., Smida, M.B., Sakly, A., Mimouni, M.F.: Comparison between conventional methods and GA approach for maximum power point tracking of shaded solar P-V generators. Sol. Energy. **90**(2013), 107–122 (2013)

Silvestre, S., Boronat, A., Chouder, A.: Study of bypass diodes configuration on P-V modules. Appl. Energy. **86**, 1632–1640 (2009)

Solodovnik, E.V., Liu, S., Dougal, R.A.: Power controller design for maximum power tracking in solar installations. IEEE Trans. Power Electron. **19**(5), 1295–1304 (2004)

Villalva M.G., Gazoli J.R., Ruppert Filho E.: Modeling and Simulation of Photovoltaic Arrays. In: Power Electronics Conference, 2009. COBEP '09. Brazilian (2009)

Study and Analysis on Lighting Energy Management for Highway

Yoomak Suntiti and Ngaopitakkul Atthapol

1 Introduction

In general, most of accidents on the roadway occur at night due to the decreased visual ability with illuminance and age. The principal purpose of roadway and motorway lighting is to improve the visibility for the driver, including accident reduction. Some lighting from roadway lighting will emit onto footpath, which is advantageous for providing sufficient light for pedestrians as well as for drivers. In the past, the high-pressure sodium (HPS) was one of the popular luminaires used in roadway and highway lighting systems. However, the traditional HPS luminaire usage has caused high energy consumption. Nowadays, the trend of employing the light-emitting diode (LED) luminaire for street and roadway lighting has been increased in several capital cities as well as small towns throughout the world owing to its attractive advantages such as long lifetime, low energy consumption, quick turn on, etc. However, the replacement of conventional road lighting, like high-pressure sodium (HPS) luminaire and metal halide (MH) luminaire with LED luminaire, has some disadvantages, for example, high initial cost of LED installation, lighting pollution, and change in the color of the urban sky glow; thus, there are several research papers investigating on the LED component lighting system.

The street lighting regulations and requirements, the thermal management, and the buck-boost power factor control (PFC) stage were considered to the design of LED street lighting system by Nuttall et al. (2008), and Luo et al. (2007) presented that the thermal had an effect to lifetime and efficiency of LED luminaire. Long et al. (2009) proposed the development of 9-LED module (9LEDM) that had been

Y. Suntiti (✉) • N. Atthapol
Faculty of Engineering, King Mongkut's Institute of Technology Ladkrabang, Chalongkrung Road, Bangkok 10520, Thailand
e-mail: knatthap@kmitl.ac.th

© Springer International Publishing AG, part of Springer Nature 2018

F. Aloui, I. Dincer (eds.), *Exergy for A Better Environment and Improved Sustainability 2*, Green Energy and Technology,
https://doi.org/10.1007/978-3-319-62575-1_61

applied to a street lighting system and supported by efficient, intelligent, and reliable electronic drivers. The significant achievement of the 9LEDM was a dramatic reduction in package thermal resistance from the PN junction of the LED chip to fixtures. Moreover, experimental results based on the suggested methodology have been obtained from laboratory measurements and a demonstration project. An intelligent driver based on a quasi-resonant operation flyback topology has been developed by Long and Zhou (2008) for a high performance in terms of the photometric, thermal, and electrical issues. Camponogara et al. (2012) presented a prototype based on a buck-boost discontinuous conduction mode (DCM) and a buck-boost continuous conduction mode (CCM), which was built to increase the efficiency such as high power factor, low total harmonic distortion, and long life span. The experimental results showed a good agreement with the project and a high overall efficiency. A sensor-integrated ultra-long span LED street luminaire was studied by Wang and Liu (2007). The LED street luminaires will automatically adjust their working condition according to the change of environments.

In terms of energy, the comparison of energy efficiency, color of light, control dimmer, and mesopic vision during LED luminaire with HPS luminaire for street lighting system was presented by Fusheng et al. (2009) and Rodrigues et al. (2011). Next paper showed the design of light distribution for LED luminaire, which is a factor for illuminance on road surface, and was proposed by Bender et al. (2013). The results of simulation could calculate the property of lens that gave optimal illuminance and uniformity. Luo et al. (2008) and Yang et al. (2011) designed light distribution lens with optimal performance for street light; their best characteristic was being rectangular. In Taiwan from 2009 to 2011, Huang et al. (2012) proposed the replacement of the mercury luminaires with LED luminaires. The result was shown that LED luminaires could save energy up to 50%; this was beneficial to support the use of LED luminaires. In addition, nowadays, LED luminaires are applied for the solar system that was presented by Ali et al. (2011). The obtained results from LED luminaires applied to the solar system have a high efficiency than the other types and are installed for street lighting to save energy.

As a result of all of the above papers, researchers have mostly focused on developing and designing the driver, PFC, and sensor for LED lamp, in order to attain the low energy consumption, high power factor, low total harmonic distortion, and reduced thermal in fixtures, but not for comparison between LED luminaire and HPS luminaire in terms of the illumination change.

In Thailand, replacement of 250 W HPS with 120 W LED has been studied in roadway lighting system in Bangkok in which MEA (Metropolitan Electricity Authority) is responsible. LED luminaire can save 60% of energy consumption more than traditional luminaire because 250 W HPS luminaire consumes a total energy of 299 W, but 120 W LED luminaire only consumes 130 W. This paper focuses on the energy consumption of 120 W LED luminaire which will replace the 250 W HPS luminaire for roadway lighting system in Thailand. The comparison between HPS luminaire and LED luminaire in terms of illuminance and uniformity is presented with DIALux program in this paper. The three different luminous

intensity distribution curves (or polar curve) of LED luminaire are also considered in order to compare among the characteristics of arrangements of roadway lighting with various polar curves. In addition, this paper proposes the improvement of LED luminaire for roadway lighting system in terms of illuminance and uniformity using the mounting height adjustment method and the pole spacing adjustment method.

2 Illuminance Simulation and Results Between HPS and LED Luminaires

In the case being studied revealed that roadway is simulated using DIALux program. The 250 W HPS luminaire is compared with the 120 W LED luminaire to analyze the illuminance and uniformity with roadway lighting standard of Thailand (by considering illuminance and uniformity). The luminous intensity for both luminaires is illustrated in Fig. 1. By considering Fig. 1, it can be observed that the similarity between both polar curves can be seen. In addition, the luminous flux of HPS luminaire is 31,100 lumens while LED luminaire is 9035 lumens.

The layout or arrangement for the roadway luminaires is one factor to calculate the illuminance; its drawing for DIALux program is illustrated in Fig. 2. By considering Fig. 2a, the width of the road (Y) is 10 m, while the street isle (Z) is 0 m (without street isle). Likewise, in Fig. 2b, the width of the road is also 10 m, while the street isle is 1.5 m. The characteristics of roadway lighting pole parameters such as (1) mounting height of 9 m, (2) overhang of 1.8 m, (3) boom angle of 15°, and (4) boom length of 2.5 m are determined for simulation with DIALux program as shown in Fig. 3. Moreover, the length of roadway is equal to that of the distances between luminaires. Quality or type of road reflective properties on the road surface R3 (u_0Q_0= 0.07) is asphalt road surface.

Before simulation, the mounting height, overhang, road width, and spacing between lighting poles are determined as 9, 1.8, 10, and 40 m, respectively. The maintenance factor (MF) is also determined as 0.8. In addition, there are several arrangements of roadway lighting that can be used such as without isle (single row, double row with opposing, and double row with offset) and with isle (double row with opposing, double row with offset, and twin central), so the arrangement is varied and compared in terms of illuminance with the other arrangements.

After applying the various arrangements and luminaires, the obtained average illuminance on road surface in each case study is illustrated in Figs. 4 and 5, Table 1, and Table 2. By observing Fig. 4, the difference between the illuminance distribution (or it is called as false color rendering) with various arrangements without street isle and luminaire can be clearly seen. By considering the single row arrangement as shown in Fig. 4a, b, the HPS luminaire and LED luminaire are considered as an example; the obtained results can be seen that the difference between the two false color rendering can be visually observed.

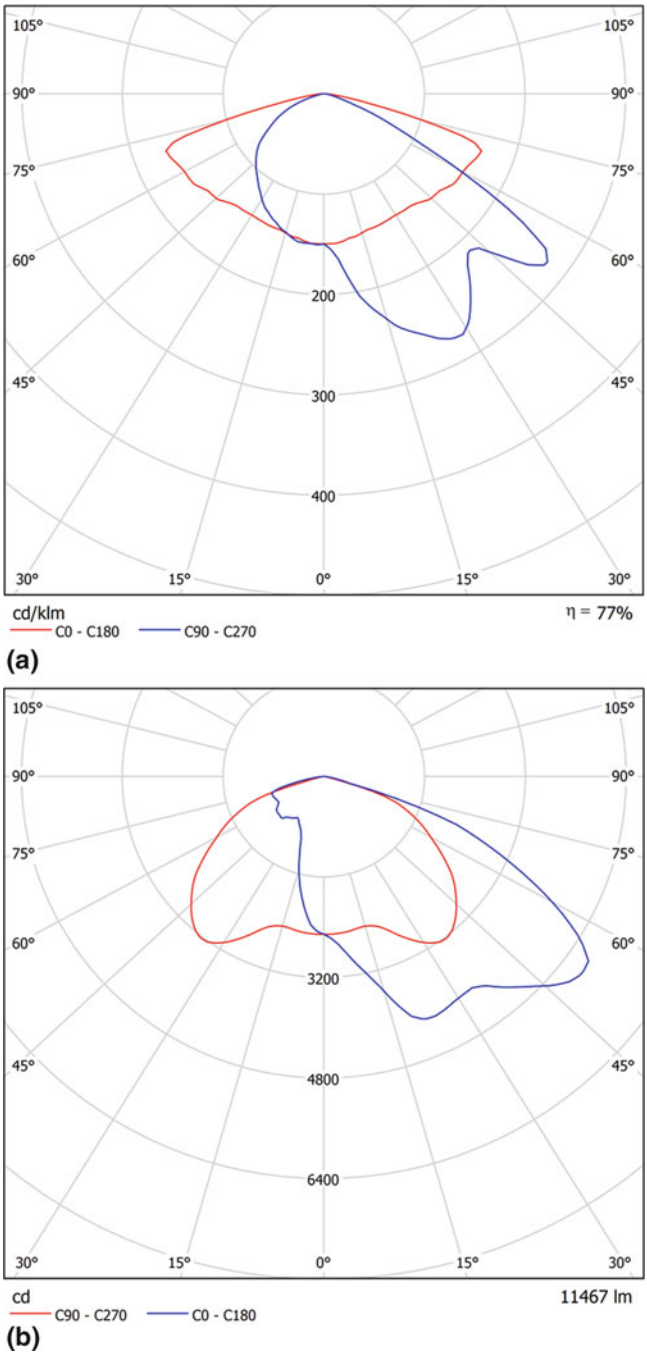

Fig. 1 Luminous intensity distribution curve or polar curve. (**a**) 250 W HPS luminaire. (**b**) 120 W LED luminaire

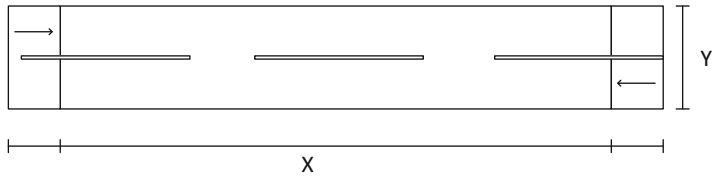

(a) Roadway lighting without street isle

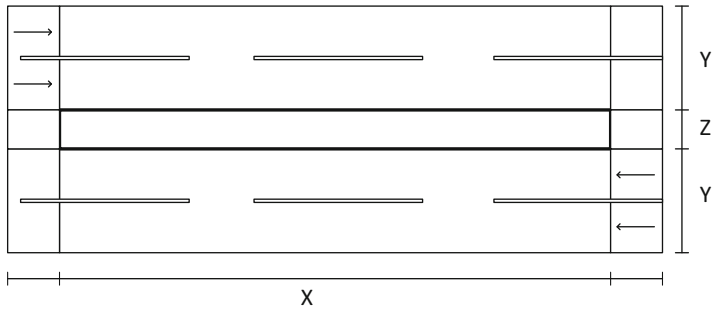

(b) Roadway lighting with street isle

Fig. 2 The layout of roadway for simulation. (**a**) Roadway lighting without street isle. (**b**) Roadway lighting with street isle

Fig. 3 Characteristics of street lighting pole used in simulation

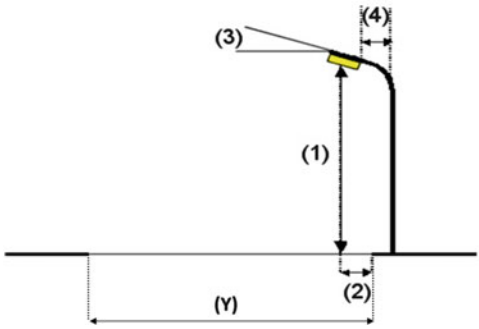

Based on a further analysis of Table 1, by considering the average illuminance (E_{av}), it can be seen that the average illuminance and uniformity (u_0) that are obtained from both cases (HPS luminaire and LED luminaire) are less than the roadway lighting standard of Thailand (standard case). For the next case study, by changing the arrangement of roadway as double row with opposing, the difference between the two false color renderings can be also observed as shown in Fig. 4c, d; it can be seen that the average illuminance of both cases are more than the standard case. By considering the uniformity (u_0), it can be seen that the obtained uniformity (u_0) in case of HPS luminaire is higher than the standard case, while the case of the

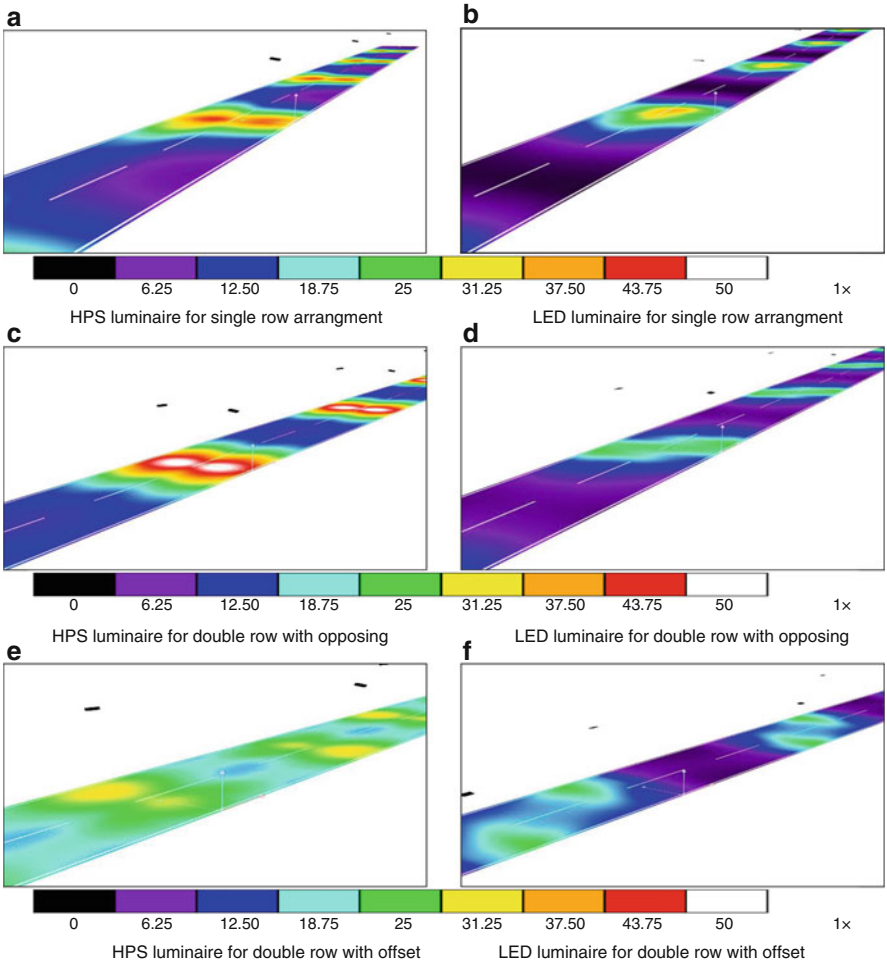

Fig. 4 Simulation results of illuminance distribution (false color rendering) for roadway without isle. (**a**) HPS luminaire for single row arrangement. (**b**) LED luminaire for single row arrangement. (**c**) HPS luminaire for double row with opposing. (**d**) LED luminaire for double row with opposing. (**e**) HPS luminaire for double row with offset. (**f**) LED luminaire for double row with offset

LED luminaire is less than that of the standard case; this indicates that the arrangement of roadway luminaires has impact for decision of the luminaire installation in roadway lighting system as shown in Table 1. To support this assertion, by considering the roadway arrangement constructed as double row with offset, which is shown in Fig. 4e, f, it can be seen that the obtained average illuminance and uniformity (u_0) which are obtained from both cases (HPS luminaire and LED luminaire) have the same characteristics as in the case of the arrangement of roadway as double row with opposing; this indicates that the LED luminaire should be improved.

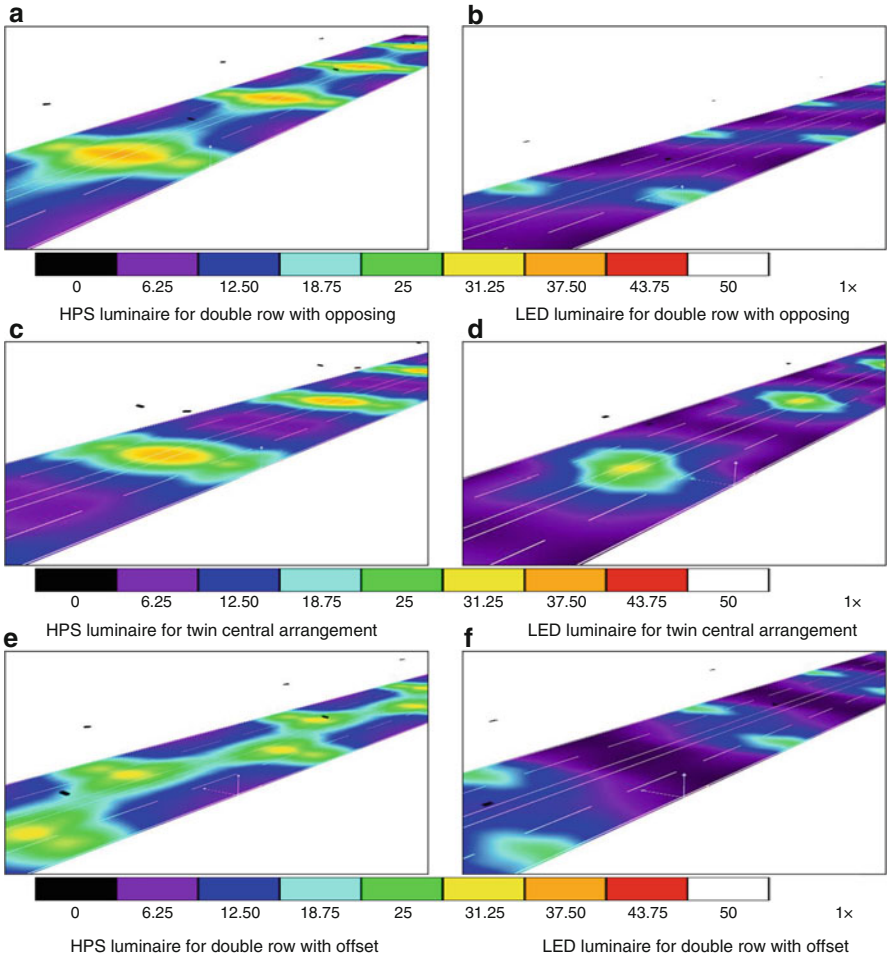

Fig. 5 Simulation results of illuminance distribution (false color rendering) for roadway with 1.5 m width of isle. (**a**) HPS luminaire for double row with opposing. (**b**) LED luminaire for double row with opposing. (**c**) HPS luminaire for twin central arrangement. (**d**) LED luminaire for twin central arrangement. (**e**) HPS luminaire for double row with offset. (**f**) LED luminaire for double row with offset

To evaluate the illuminance and uniformity (u_0) in the case of street isle as shown in Fig. 5 and Table 2, the roadway lighting standard of Thailand (standard case) will be compared with HPS luminaire case and LED luminaire case. Considering the overall results of illuminance for various arrangements of lighting pole, the average illuminance of HPS luminaire is higher than the standard case for all arrangements of lighting pole, while the average illuminance of LED luminaire is less than that of both the standard case and HPS luminaire case for all arrangements of lighting pole. Likewise, by considering the overall results of uniformity for

Table 1 Comparison between HPS and LED luminaires for various arrangements without street isle

Data	Standard	HPS luminaire			LED luminaire		
		Single row	Double row with opposing	Double row with offset	Single row	Double row with opposing	Double row with offset
E_{av} (lux)	21.5	19	37	37	11	22	22
E_{min} (lux)	–	4.89	15	28	1.69	5.52	4.16
E_{max} (lux)	–	39	77	50	34	38	39
u_0	0.4	0.262	0.414	0.761	0.188	0.239	0.242

Table 2 Comparison between HPS and LED luminaires for various arrangements with 1.5 m width of street isle

Data	Standard	HPS luminaire			LED luminaire		
		Double row with opposing	Twin central	Double row with offset	Double row with opposing	Twin central	Double row with offset
E_{av} (lux)	21.5	28	24	28	12	14	12
E_{min} (lux)	–	10	7.93	12	3.84	3.91	3.1
E_{max} (lux)	–	57	56	50	36	44	36
u_0	0.4	0.331	0.337	0.417	0.308	0.273	0.249

various arrangements of lighting pole, the uniformity of HPS luminaire is slightly less than the standard case, except for the arrangement of roadway as double row with offset, whereas the uniformity of LED luminaire is significantly less than the standard case for all arrangements of lighting pole; this also indicates that the installation of LED luminaire should be improved to increase the average illuminance and uniformity (u_0) for roadway lighting.

As a result, the type of luminaire and the arrangement of lighting pole including the luminous flux of luminaire are key factors for the decision of the installation of LED luminaire for roadway lighting.

3 Illuminance Simulation and Results for Polar Curves of LED Luminaire

In the previous section, the simulated result shows that HPS luminaire is replaced with LED luminaire in the case of the nearby polar distribution diagram; in terms of energy usage, the energy consumption of LED luminaire is less than HPS luminaire

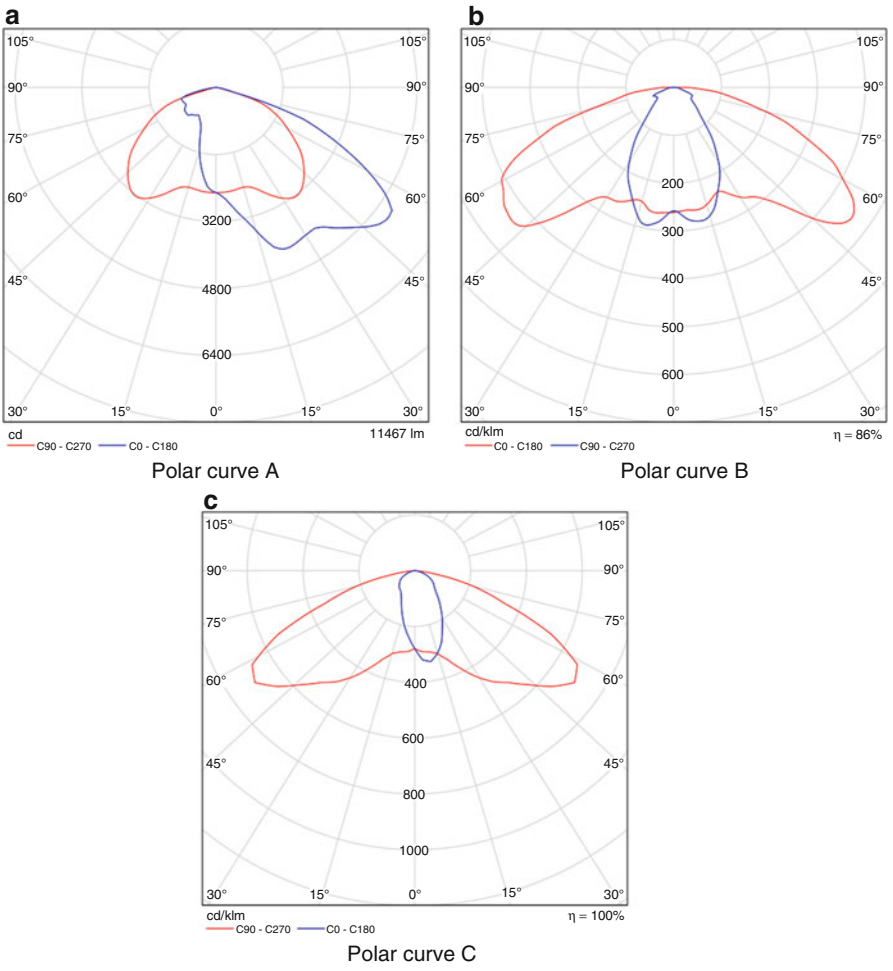

Fig. 6 Luminous intensity distribution curve or polar curve of various LED luminaires. (**a**) Polar curve A. (**b**) Polar curve B. (**c**) Polar curve C

which is the advantage. However, in terms of the average illuminance and uniformity, the LED luminaire is less efficient than HPS luminaire, which is the disadvantage. To overcome this disadvantage, the polar distribution curve of LED luminaire is varied in order to improve the average illuminance and uniformity as shown in Fig. 6. By considering Fig. 6, it can be seen that there are three types of luminous intensity distribution curves which are in comparison with all arrangements of lighting pole, and the results of simulation are shown in Table 3 and Table 4.

By considering the data in Table 3, the arrangements of lighting pole in the case of the roadway without isle (such as single row, double row with offset, and double row with opposing arrangement) are considered as the case study; it can be seen that

Table 3 Comparison among various polar distribution curves of LED luminaire in case of roadway without isle

Data	Standard	Polar curve A			Polar curve B			Polar curve C		
		Single row	Double row with opposing	Double row with offset	Single row	Double row with opposing	Double row with offset	Single row	Double row with opposing	Double row with offset
E_{av} (lux)	21.5	11	22	22	9.16	18	18	12	23	23
E_{min} (lux)	–	1.69	5.52	4.16	2.87	6.83	12	3.55	9.1	13
E_{max} (lux)	–	34	38	39	24	37	28	23	44	31
u_0	0.4	0.188	0.239	0.242	0.313	0.373	0.656	0.305	0.391	0.545

Table 4 Comparison among various polar distribution curves of LED luminaire in case of roadway with 1.5 m width of isle

Data	Standard	Polar curve A			Polar curve B			Polar curve C		
		Double row with offset	Twin central	Double row with opposing	Double row with offset	Twin central	Double row with opposing	Double row with offset	Twin central	Double row with opposing
E_{av} (lux)	21.5	12	14	12	10	11	10	14	13	14
E_{min} (lux)	–	3.84	3.91	3.1	4.45	3.23	4.54	4.37	5.13	4.41
E_{max} (lux)	–	36	44	36	24	30	24	25	26	24
u_0	0.4	0.308	0.273	0.249	0.425	0.294	0.434	0.321	0.385	0.324

the obtained result of polar distribution curve of type A is equal to that of the previous section so that it is decided as the base case. Considering the average illuminance in Table 3, it can be observed that the polar distribution curve of type C is slightly more than both the standard case and the base case, except for the arrangement of roadway as single row, while the polar distribution curve of type B is fairly less than those of all arrangement of roadway.

For the uniformity in Table 3 that is taken into consideration, it can be observed that the polar distribution curve of type C is significantly increased but less than the standard case, except for arrangement of roadway as double row with offset. Likewise, the polar distribution curve of type B is similar to that of type C. This indicates that the luminous intensity distribution curve plays an important role for the uniformity.

To support this assertion, the arrangements of lighting pole in case of the roadway with isle are considered as the case study as shown in Table 4. Considering the average illuminance in Table 4, it can be observed that both polar distribution curves of type B and type C are fairly less than the standard case for the all arrangement of roadway. Considering the uniformity in Table 4, it can be observed that the polar distribution curve of type C is slightly less than that of the all arrangement of roadway in comparison with the standard case, but the uniformity is more than the base case. Considering the polar distribution curve of type B, it can be seen that the obtained uniformity is more than the standard case, except for the arrangement of roadway in Twin central. As a result, although the polar distribution curve of type C gives better results than those of the luminous intensity distribution curve, in terms of the uniformity, it cannot give satisfactory results, especially for the arrangements of lighting pole in case of the roadway with isle. Due to the average illuminance and uniformity which are obtained from the standard of Thailand, it was only specified for HPS luminaire (150–400 W) so that the LED luminaire should be improved by changing the installation of roadway lighting in order for the driver and the pedestrian to benefit.

4 Improvement for LED Luminaire

As in the previous section, the LED luminaire should be improved by changing the installation of roadway lighting. Generally, the installation of roadway luminaire under the responsibility of Department of Highways within the geographical boundary of Thailand is particularly designed for HPS luminance so that the replacement with LED luminaire may be advantageous in terms of energy saving, but in terms of illuminance, it will be disadvantageous for the roadway lighting. This section proposes the methods to improve roadway lighting using mounting height adjustment method and pole spacing adjustment method.

Table 5 The comparison result of various mounting heights for the roadway without isle

Roadway without isle		Mounting height (m)											
LED	Standard	Single row				Double row with opposing				Double row with offset			
		6	7	8	9	6	7	8	9	6	7	8	9
E_{av} E_{av}[lux]	21.5	14	13	12	12	28	26	25	23	28	26	25	23
u_0	0.400	0.110	0.156	0.211	0.280	0.136	0.204	0.287	0.384	0.344	0.420	0.339	0.567

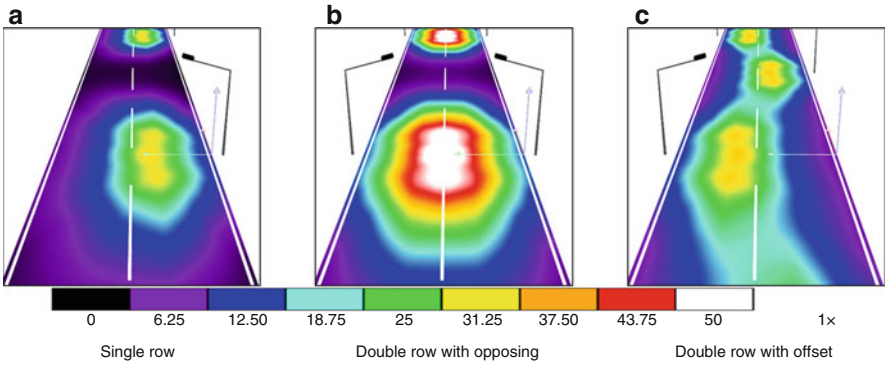

Fig. 7 The false color rendering in case the mounting height is 6 m for the roadway without isle. (**a**) Single row. (**b**) Double row with opposing. (**c**) Double row with offset

4.1 Mounting Height Adjustment Method

Before the simulation process, the 120 W LED luminaire with polar distribution curve of type C is employed in this section because it gives better results than the other polar distribution curves. The arrangements of lighting pole are also considered such as the roadway without isle and roadway with isle 1.5 m. The mounting heights of lighting pole are designated as mounting height range of 6–9 m while the spacing between lighting poles is 40 m.

After adjusting the mounting height, the obtained results for the roadway without isle are shown in Table 5 and Fig. 7, while the results for the roadway with isle are shown in Table 6 and Fig. 8.

By considering the data in Table 5, the arrangements of lighting pole in the case of the street without isle (such as single row, double row with offset, and double row with opposing arrangement) are considered as the case study; it can be seen that, when the mounting height is decreased from 9 to 6 m, the average illuminance tends to increase but the uniformity tends to decrease; this indicates that the reduction of mounting height can slightly improve the average illuminance but not impact on the increase of the uniformity. Considering the false color rendering in Fig. 7, it can be observed that the average illuminance in the case of the arrangement of roadway such as double row with opposing is equal to that of the double row with offset case, but the obtained uniformity has a value of approximately two times smaller.

Similarity, for the arrangements of lighting pole in the case of the street with isle in Table 6 that are taken in consideration, it can be observed that the average illuminance tends to increase with the decrease in the mounting height, while the uniformity tends to decrease; this is the same characteristic as the arrangements of lighting pole in the case of the street without isle. Considering the false color rendering in Fig. 8, it can be observed that both the average illuminance and the uniformity for the all arrangement of roadway with isle have a similar value in comparison with the same mounting height.

Table 6 The comparison result of various mounting heights for the roadway with 1.5 m width of isle

Roadway with isle		Mounting height)m)											
LED	Standard	Double row with opposing				Double row with offset				Twin central			
		6	7	8	9	6	7	8	9	6	7	8	9
E_{av} [lux]	21.5	15	15	14	14	15	15	14	14	15	14	14	13
u_0	0.400	0.129	0.177	0.233	0.299	0.138	0.186	0.239	0.303	0.130	0.188	0.259	0.342

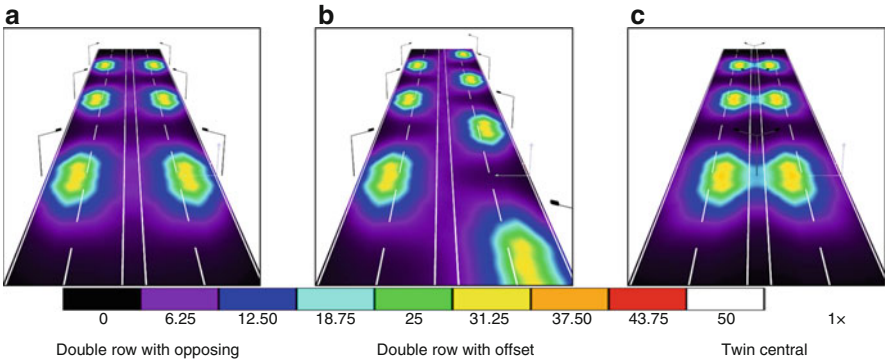

Fig. 8 The false color rendering in case the mounting height is 6 m for the roadway with isle. (**a**) Double row with opposing. (**b**) Double row with offset. (**c**) Twin central

As a result, the adjustment of mounting height has slightly improve the average illuminance but not for the uniformity.

4.2 Pole Spacing Adjustment Method

Before the simulation process, the 120 W LED luminaire with polar distribution curve of type C and the arrangements of lighting pole are also used as same as the previous method. Meanwhile, while the spacing between lighting pole is designated as pole spacing range of 32–40 m, the mounting height of lighting pole is determined as 9 m.

After applying the pole spacing method, the obtained results for the roadway without isle are shown in Table 7 and Fig. 9, while the results for the roadway with isle are shown in Table 8 and Fig. 10.

By considering the data in Table 7, the arrangements of lighting pole in the case of the street without isle (such as single row, double row with offset, and double row with opposing arrangement) are considered as the case study; it can be seen that, when the pole spacing is decreased from 40 to 32 m for all the arrangement of lighting pole without isle, the average illuminance and the uniformity tend to increase; this indicates that the reduction of pole spacing can significantly improve the installation effectiveness of LED luminaire for roadway lighting. Considering the false color rendering in Fig. 9, it can be observed that the average illuminance in the case of the arrangement of roadway as double row with opposing is equal to that of the double row with offset case, but the obtained uniformity has almost the same value in comparison with the same pole spacing.

Similarly, for the arrangements of lighting pole in the case of the street with isle in Table 8 that are taken into consideration, it can be observed that the average

Table 7 The comparison result of various pole spacings for the roadway without isle

Roadway without isle		Pole distance (m)														
LED	Standard	Single row					Double row with opposing					Double row with offset				
		32	34	36	38	40	32	34	36	38	40	32	34	36	38	40
E_{av} E_{av}[lux]	21.5	15	14	13	12	12	29	27	26	25	23	29	27	26	25	23
u_0	0.400	0.422	0.394	0.355	0.311	0.280	0.546	0.514	0.475	0.424	0.384	0.569	0.571	0.569	0.567	0.567

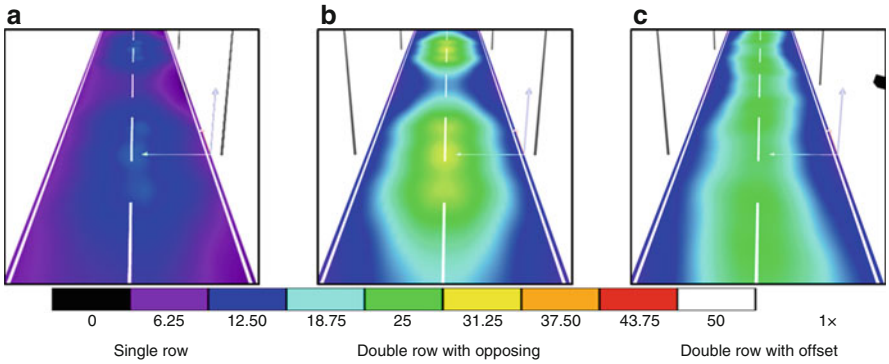

Fig. 9 The false color rendering in case the pole spacing is 32 m for the roadway without isle. (**a**) Single row. (**b**) Double row with opposing. (**c**) Double row with offset

illuminance and the uniformity tend to increase with decreasing pole spacing; this is the same characteristic as the arrangements of lighting pole in the case of the street without isle. Considering the false color rendering in Fig. 10, it can be observed that both the average illuminance and the uniformity for the all arrangement of roadway with isle have almost the same value in comparison with the same pole spacing. As a result, the adjustment of pole spacing of lighting pole can significantly improve the installation effectiveness of LED luminaire for roadway lighting.

5 Conclusion

This paper presented the impact of installation of LED luminaire roadway lighting system in terms of energy consumption and illumination, based on the arrangement of roadway with isle and without isle. In order to evaluate the impact of LED luminaire, the average illuminance and the uniformity were considered and compared with the roadway lighting standard of Thailand and the installation of roadway lighting with HPS luminaire and with LED luminaire. The results can be summarized as follows:

- In terms of energy consumption, LED luminaire uses less energy than the HPS luminaire.
- In terms of illumination, the average illuminance and uniformity of LED luminaire are less than the standard of Thailand as well as the HPS luminaire, especially for the arrangement of roadway with isle.
- Three types of luminous intensity distribution curve is considered and compared in order to improve the average illuminance and uniformity. The obtained results can be concluded that the polar distribution curve can give more illuminance and uniformity.

Table 8 The comparison result of various pole spacings for the roadway with isle

Roadway with isle		Pole distance)*m*)														
LED	Standard	Double row with opposing					Double row with offset					Twin central				
		32	34	36	38	40	32	34	36	38	40	32	34	36	38	40
E_{av} E_{av}[lux]	21.5	17	16	15	14	14	17	16	15	14	14	16	15	15	14	13
u_0	0.400	0.423	0.399	0.365	0.327	0.299	0.417	0.397	0.365	0.332	0.303	0.526	0.488	0.438	0.380	0.342

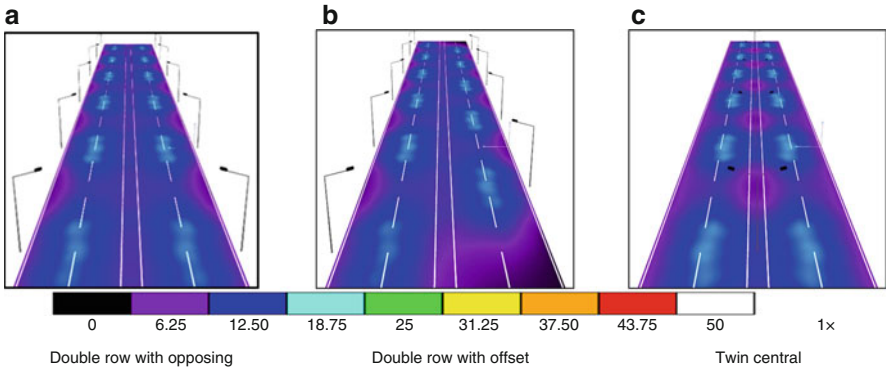

Fig. 10 The false color rendering in case the pole spacing is 32 m for the roadway with isle. (**a**) Double row with opposing. (**b**) Double row with offset. (**c**) Twin central

- The adjustment of mounting height for lighting pole slightly improves the average illuminance but not for the uniformity.
- The adjustment of lighting pole spacing can significantly improve the installation effectiveness of LED luminaire for roadway lighting.

Finally, by considering the overall results, the results can be summarized by focusing on the illumination that is an important factor apart from the energy usage. Further work will be the consideration of the optimal mounting height and pole spacing of lighting pole to attain optimum result for both the energy usage and illumination. In addition, the evaluation of break-even point will be considered to decide worthily the economic investment for LED luminaire, and it will be useful in the installation of LED luminaire for roadway lighting in the future.

Acknowledgments The authors wish to gratefully acknowledge financial support for this research (No. KREF045611) from King Mongkut's Institute of Technology Ladkrabang Research fund, Thailand.

References

Ali, M., Orabi, M., Abdelkarim, E., Qahouq, J.A.A., Aroudi, A.E.: Design and development of energy-free solar street LED light system, IEEE PES Conference on Innovative Smart Grid Technologies - Middle East, 1–7 (2011)

Bender, V.C., Mendes, F.B., Maggi, T., Dalla Costa, M.A., Marchesan, T.B.: Design methodology for street lighting luminaires based on a photometrical analysis, Power Electronics Conference, 1160–1165 (2013)

Camponogara, D., Ferreira, G.F., Campos, A., Dalla Costa, M.A.: Off-line LED driver for street lighting with an optimized cascade structure, IEEE Industry Applications Society Annual Meeting (IAS), 1–6 (2012)

Huang, S., Lee, L., Jeng, M., Hsieh, Y.: Assessment of energy-efficient LED street lighting through large-scale demonstration, International Conference on Renewable Energy Research and Applications, 1–5 (2012)

Li, F., Chen, D., Song, X., Chen, Y.: LEDs: A promising energy-saving light source for road lighting, Power and Energy Engineering Conference, 1–3, (2009)

Long, X., Zhou, J.: An intelligent driver for light emitting diode street lighting, World Automation Congress, 1–5 (2008)

Long, X., Liao, R., Zhou, J.: Development of street lighting system-based novel high-brightness LED modules. IET Optoelectron. **3**, 40–46 (2009)

Luo, X., Cheng, T., Xiong, W., Gan, Z., Liu, S.: Thermal analysis of an 80 W light-emitting diode street lamp. IET Optoelectron. **1**, 191–196 (2007)

Luo, Y., Zhang, X., Liu, J., Zhou, C., Qian, K., Han, Y.: LED street lighting technologies with high human-eye comfortability, International Nano-Optoelectronics Workshop, 84–85 (2008)

Nuttall, D.R., Shuttleworth, R., Routledge, G.: Design of a LED street lighting system, Proc. 4th IET Conference on Power Electronics, Machines and Drives (PEMD 2008), 436–440 (2008)

Rodrigues, C., Almeida, P.S., Soares, G.M., Jorge, J.M., Pinto, D.P., A C Braga, H.: An experimental comparison between different technologies arising for public lighting: LED luminaires replacing high pressure sodium lamps, IEEE International Symposium on Industrial Electronics, 141–146 (2011)

Wang, K., Liu, S.: A sensor integrated ultra-long span LED street lamp system, 8th International Conference on Electronic Packaging Technology, 1–3 (2007).

Yang, K., Song, J., Chen, Y., Lin, B.: Secondary light distribution design for LED street light, International Conference on Electronics and Optoelectronics, 2, 378–381 (2011)

Influence of Wind Farm on Distribution System: Current Characteristics During Fault Occurrence

Santipont Ananwattanaporn, Atthapol Ngaopitakkul, Chaiyan Jettanasen, Chaichan Pothisarn, and Monthon Leelajindakrairerk

1 Introduction

Energy and environmental issue has been giving a huge attention in this past decade. Energy consumption rate has been rapidly increasing proportion to economic growth. Energy from fossil fuel causes an environmental issue due to emission of greenhouse gas causing greenhouse effect. Many countries have been investing alternative energy that has more efficiency and is environmentally friendly. Distributed generator (DG) from renewable energy source has become topic of interest with the increase of environmental issue and cost of transmission. Wind power generation is one of the renewable energy sources that attracts attention in many countries and rapidly increases in their capacity (Mozina 2013). This is because the wind power technology has been currently developed in many aspects, thus providing reduction in investment costs and increasing performance and reliability (IEA 2013). Many utilities are connecting DG to distribution system, and this number is going to get higher in the near future. Several advantages such as improvement in power reliability, reduction of loss in transmission system, and improved efficiency in network can be achieved. However, significant amounts of DG cause several effects on distribution system that need to be considered and solved, such as power flow, grid losses, voltage control, protection scheme, and fault level. Effect of DG strongly depends on type of DG, penetration level, and location of DG (Coster et al. 2011; Sarabia 2011).

S. Ananwattanaporn • A. Ngaopitakkul (✉) • C. Jettanasen • C. Pothisarn
M. Leelajindakrairerk
Department of Electrical Engineering, Faculty of Engineering, King Mongkut's Institute of Technology Ladkrabang, Bangkok 10520, Thailand
e-mail: atthapol.ng@kmitl.ac.th

© Springer International Publishing AG, part of Springer Nature 2018

F. Aloui, I. Dincer (eds.), *Exergy for A Better Environment and Improved Sustainability 2*, Green Energy and Technology,
https://doi.org/10.1007/978-3-319-62575-1_62

From past research, it can be seen that installation of DG has affected many aspects of distribution system. Coster et al. (2010) presented effect of distributed generation on the protection scheme. Another research by Nimpitiwan et al. (2006) also presented that fault current was increased in the presence of DG and proposed optimization method to solve protection device coordination. Ciric et al. (2011) studied and revealed that fault current increased in every type of fault in distribution with the presence of DG.

In the case of wind power generation, many researches have investigated on the effect on distribution system. Research of Mozina (2013) has highlighted technical problem of wind power generation installed into power system that has never been designed for interconnection of DG. Research on different factors that have an effect on short circuit behavior in wind power plant has been done by Muljadi et al. (2013). Many case studies of wind power generation negatively affecting on system performance have been reviewed (Su et al. 2011; Elansari et al. 2012; Kim et al. 2012; Ouyang et al. 2012; Scarlatache and Grigoras 2014).

It can be seen that wind power generation causes negative effect on distribution system when disturbance occurs, but many current researches do not clearly evaluate relation among fault level, fault type, fault location, and wind power generation location. This paper aims to study an effect of wind power generation on distribution system characteristics such as current and voltage during fault occurrence. Many factors able to change system characteristics have been taken into account such as distribution system consisting of multi-wind power generation, size of wind power generation, fault type, and location of fault. The system consisting of single- and multi-wind generation units has been used. Wind power generation has a capacity of 2 MW. Two types of fault have been used for simulation: single line-to-ground fault and three-phase fault. This case selection is based on the fact that about 80% of fault occurrence is single phase-to-ground fault and three-phase fault, which has the highest fault current in the power system (The Electricity Training Association 1995). The analysis on system that consists of wind power generation must be done to ensure safety and reliability of the system when disturbance occurs.

2 Simulation

The simulation is performed using PSCAD/EMTP. Topology of system under this study is from the Provincial Electricity Authority (PEA) part of Thailand's distribution system. Single-line diagram is shown in Fig. 1, and single-line diagram in PSCAD is shown in Fig. 2. From Fig. 1, it can be seen that the substation bus and load bus are connected with 30 km transmission line, and wind power generation bus is connected between the distances of 15 km away from substation. Distribution model used in this simulation consists of three-phase voltage source with base voltage and power, which are 22 kV and 100 MVA, respectively. Overhead line type is space aerial cable (SAC) under PEA's regulation. Load profile is obtained

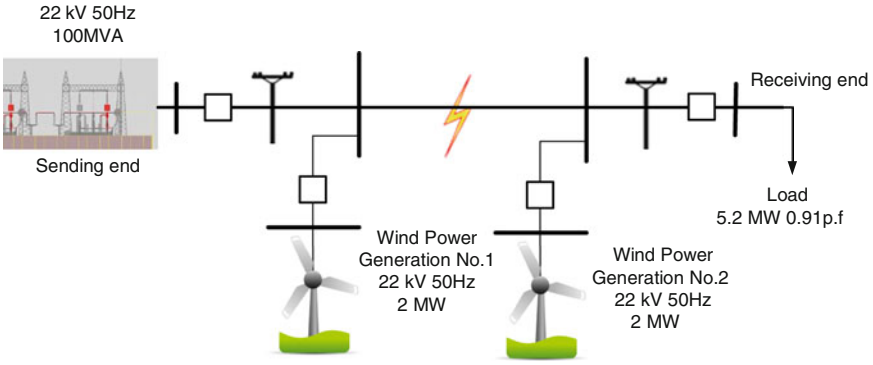

Fig. 1 Single-line diagram of 22 kv distribution network with integration of 2 MW wind generation

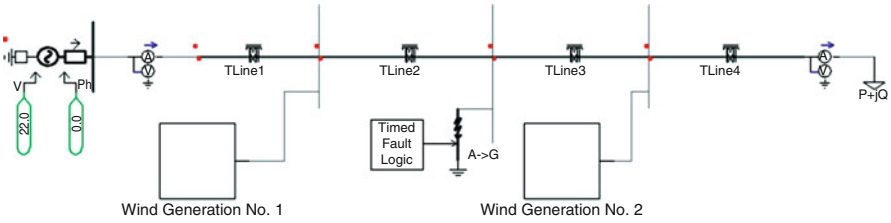

Fig. 2 Single-line diagram of distribution system with installation of two wind generation units using PSCAD

from PEA's Nan province substation. The real power and reactive power of total connected load are 5.2 MW and 2.3 MVar, respectively. Diagram of wind power generation in detail is shown in Fig. 2. From PSCAD model, wind power generation consists of wind source that controls wind speed and is located at point 1, wind turbine governor that controls pitch angle of wind turbine by using speed and real power and is located at point 2, wind turbine module that generates mechanical torque and is located at point 3, and synchronous machine with AC exciters that generates voltage and current to power transformer and is located at point 4. Power generated from wind power generation flows to grid from point A as shown in Figs. 2 and 3. The parameter setting for each device is presented in Table 1. To evaluate the impact of wind power generation, various fault types are used. Data are measured at different fault points: substation bus, wind power generation bus, fault location, and load bus.

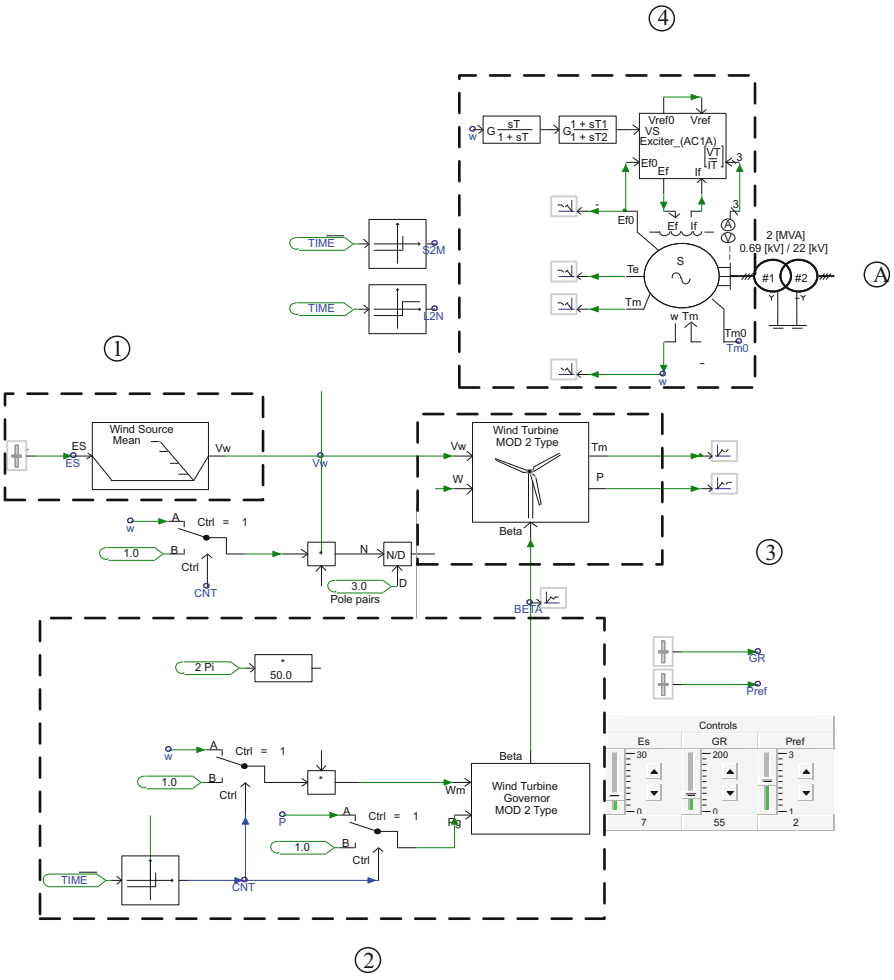

Fig. 3 Diagram of 2 MW wind power generation

3 Single-Wind Generation Simulation

To evaluate effect of wind generation location on system parameters when fault occurs, distribution system consisting of single-wind power generation has been used for simulation. In case studies, parameters taken into account are location of wind power generation, fault location, and fault type as follows:

– Two MW wind power generation units are installed at 3, 15, and 27 km away from substation.
– Location of fault is varied along transmission line at 3, 9, 15, 21, and 27 km away from substation.

Table 1 Parameters of wind power generation unit used in PSCAD simulation

Component	Parameters	Data
Synchronous machine	Rate voltage per phase (kV)	0.398
	Rate current (kA)	1.840
	Frequency (Hz)	50
Wind turbine	Generator rated (MVA)	2
	Rotor radius (m)	43.5
	Rotor area (m^2)	5944
	Air density (kg/m^3)	1.225
Wind source	Average wind speed (m/s)	13
Three-phase transformer	Frequency (Hz)	50
	Apparent power (MVA)	2
	Primary voltage (kV)	0.690
	Secondary voltage (kV)	22

- Type of fault used in simulation is single line-to-ground and three-phase fault.
- System data obtained from measurement point located at substation bus (source), wind power generation bus, fault location, and load bus.

Results from the simulation are shown in Tables 2, 3, 4, 5, 6, and 7. The current waveform when fault occurs in some cases is shown in Fig. 4. For the current waveform when fault occurs in the case of distribution system with wind power generation installed at 15 km away from substation, it can be seen from waveform that in the case of single line-to-ground fault occurrence in Fig. 4a, fault phase in substation bus and wind power generation has the highest fault current level. In load bus, fault phase current level drops down due to current from substation and wind power generation flowing to fault location. The reason is that the impedance in the system is reduced when fault occurs. In the case of three-phase fault in Fig. 4b, current in substation bus is increased about 4–5 times that of normal condition in every phase. Current at wind generation bus also increases, while current at load bus is much lower than single line-to-ground fault case study. Obtained data used for analysis by relation between current at different measured points and fault location are plotted in Figs. 5, 6, 7, 8, 9, and 10.

In Table 2, it shows data obtained from simulation in the case of single line-to-ground fault occurrence and wind power generation installed at 3 km away from substation. Obtained results can be summarized as follows:

- In the case without wind power generation, current in substation bus increases significantly when fault occurs and steadily decreases when fault is located further away from substation bus. On the other hand, voltage is decreased when fault occurs and steadily increased when fault is located further away from substation bus. In load bus, current and voltage are increased when fault moves toward the bus.

Table 2 System voltage and current when single phase-to-ground fault occurs (AG) in the case of distribution system with 2 MW wind generation installed at 3 km away from substation

Data			Without wind power generation				With wind power generation			
				Fault location				Fault location		
			Normal condition	3	15	27	Normal condition	3	15	27
Source	Voltage rms (kV)	A	21.182	16.654	18.361	19.310	21.976	17.351	19.098	20.069
		B	21.182	19.766	20.592	20.762	21.976	20.433	21.334	21.525
		C	21.182	21.104	20.931	21.022	21.977	21.840	21.706	21.806
	Current rms (kA)	A	0.184	1.661	0.852	0.590	0.126	1.616	0.744	0.469
		B	0.184	0.182	0.207	0.218	0.126	0.153	0.130	0.129
		C	0.184	0.189	0.203	0.210	0.126	0.126	0.156	0.173
Wind generation no. 1	Voltage rms (kV)	A	0.000	0.000	0.000	0.000	22.235	14.612	16.913	18.803
		B	0.000	0.000	0.000	0.000	22.236	23.791	22.584	22.167
		C	0.000	0.000	0.000	0.000	22.235	21.307	22.181	22.359
	Current rms (kA)	A	0.000	0.000	0.000	0.000	0.152	0.188	0.172	0.166
		B	0.000	0.000	0.000	0.000	0.152	0.148	0.149	0.150
		C	0.000	0.000	0.000	0.000	0.151	0.142	0.151	0.151
Load	Voltage rms (kV)	A	18.467	11.394	6.087	4.533	19.401	12.123	6.461	4.792
		B	18.467	18.270	20.773	21.916	19.401	19.137	21.767	23.004
		C	18.466	18.948	20.368	21.101	19.401	19.852	21.458	22.203
	Current rms (kA)	A	0.184	0.114	0.061	0.045	0.194	0.121	0.064	0.048
		B	0.184	0.182	0.207	0.219	0.194	0.191	0.217	0.230
		C	0.184	0.189	0.203	0.211	0.194	0.198	0.214	0.222
Fault current rms (kA)		A	0.000	1.555	0.793	0.547	0.000	1.652	0.838	0.578
		B	0.000	0.000	0.000	0.000	0.000	0.000	0.000	0.000
		C	0.000	0.000	0.000	0.000	0.000	0.000	0.000	0.000

Table 3 System voltage and current when three-phase fault occurs (ABC) in the case of distribution system with 2 MW wind generation installed at 3 km away from substation

Data			Without wind power generation				With wind power generation			
				Fault location				Fault location		
			Normal condition	3	15	27	Normal condition	3	15	27
Source	Voltage rms (kV)	A	21.182	10.093	14.772	16.921	21.976	10.356	15.319	17.569
		B	21.182	10.093	14.772	16.921	21.976	10.355	15.319	17.569
		C	21.182	10.093	14.772	16.921	21.977	10.355	15.319	17.569
	Current rms (kA)	A	0.184	2.520	1.379	0.948	0.126	2.520	1.288	0.835
		B	0.184	2.520	1.379	0.948	0.126	2.520	1.288	0.835
		C	0.184	2.520	1.379	0.948	0.126	2.520	1.288	0.835
Wind generation no. 1	Voltage rms (kV)	A	0.000	0.000	0.000	0.000	22.235	7.875	13.410	16.393
		B	0.000	0.000	0.000	0.000	22.236	7.875	13.410	16.393
		C	0.000	0.000	0.000	0.000	22.235	7.875	13.410	16.393
	Current rms (kA)	A	0.000	0.000	0.000	0.000	0.152	0.196	0.179	0.171
		B	0.000	0.000	0.000	0.000	0.152	0.196	0.179	0.171
		C	0.000	0.000	0.000	0.000	0.151	0.196	0.179	0.171
Load	Voltage rms (kV)	A	18.467	6.285	3.625	2.631	19.401	6.670	3.842	2.780
		B	18.467	6.285	3.625	2.631	19.401	6.670	3.842	2.780
		C	18.466	6.285	3.625	2.630	19.401	6.670	3.842	2.780
	Current rms (kA)	A	0.184	0.063	0.036	0.026	0.194	0.067	0.038	0.028
		B	0.184	0.063	0.036	0.026	0.194	0.067	0.038	0.028
		C	0.184	0.063	0.036	0.026	0.194	0.067	0.038	0.028
Fault current rms (kA)		A	0.000	2.465	1.347	0.924	0.000	2.616	1.427	0.977
		B	0.000	2.464	1.347	0.924	0.000	2.616	1.427	0.977
		C	0.000	2.464	1.347	0.924	0.000	2.616	1.427	0.977

Table 4 System voltage and current when single phase-to-ground fault occurs (AG) in the case of distribution system with 2 MW wind generation installed at 15 km away from substation

Data			Without wind power generation				With wind power generation			
				Fault location				Fault location		
			Normal condition	3	15	27	Normal condition	3	15	27
Source	Voltage rms (kV)	A	21.182	16.654	18.361	19.310	21.933	17.294	18.879	19.943
		B	21.182	19.766	20.592	20.762	21.933	20.415	21.157	21.419
		C	21.182	21.104	20.931	21.022	21.933	21.802	21.616	21.736
	Current rms (kA)	A	0.184	1.661	0.852	0.590	0.138	1.628	0.793	0.501
		B	0.184	0.182	0.207	0.218	0.138	0.164	0.147	0.145
		C	0.184	0.189	0.203	0.210	0.138	0.138	0.157	0.178
Wind generation no. 1	Voltage rms (kV)	A	0.000	0.000	0.000	0.000	22.058	14.841	8.074	12.185
		B	0.000	0.000	0.000	0.000	22.055	22.730	26.748	23.849
		C	0.000	0.000	0.000	0.000	22.057	21.628	23.483	23.389
	Current rms (kA)	A	0.000	0.000	0.000	0.000	0.152	0.185	0.192	0.179
		B	0.000	0.000	0.000	0.000	0.152	0.154	0.127	0.143
		C	0.000	0.000	0.000	0.000	0.152	0.143	0.144	0.147
Load	Voltage rms (kV)	A	18.467	11.394	6.087	4.533	20.312	13.291	6.950	5.116
		B	18.467	18.270	20.773	21.916	20.312	20.020	22.535	23.905
		C	18.466	18.948	20.368	21.101	20.313	20.668	22.374	23.279
	Current rms (kA)	A	0.184	0.114	0.061	0.045	0.203	0.133	0.069	0.051
		B	0.184	0.182	0.207	0.219	0.203	0.200	0.225	0.239
		C	0.184	0.189	0.203	0.211	0.203	0.206	0.223	0.232
Fault current rms (kA)		A	0.000	1.555	0.793	0.547	0.000	1.645	0.901	0.616
		B	0.000	0.000	0.000	0.000	0.000	0.000	0.000	0.000
		C	0.000	0.000	0.000	0.000	0.000	0.000	0.000	0.000

Table. 5 System voltage and current when three-phase fault occurs (ABC) in the case of distribution system with 2 MW wind generation installed at 15 km away from substation

Data			Without wind power generation				With wind power generation			
				Fault location				Fault location		
			Normal condition	3	15	27	Normal condition	3	15	27
Source	Voltage rms (kV)	A	21.182	10.093	14.772	16.921	21.933	10.309	14.788	17.322
		B	21.182	10.093	14.772	16.921	21.933	10.309	14.790	17.323
		C	21.182	10.093	14.772	16.921	21.933	10.309	14.789	17.322
	Current rms (kA)	A	0.184	2.520	1.379	0.948	0.138	2.528	1.375	0.877
		B	0.184	2.520	1.379	0.948	0.138	2.528	1.375	0.877
		C	0.184	2.520	1.379	0.948	0.138	2.528	1.375	0.877
Wind generation no. 1	Voltage rms (kV)	A	0.000	0.000	0.000	0.000	22.058	8.702	4.011	9.881
		B	0.000	0.000	0.000	0.000	22.055	8.702	4.011	9.881
		C	0.000	0.000	0.000	0.000	22.057	8.702	4.012	9.881
	Current rms (kA)	A	0.000	0.000	0.000	0.000	0.152	0.193	0.211	0.189
		B	0.000	0.000	0.000	0.000	0.152	0.193	0.211	0.189
		C	0.000	0.000	0.000	0.000	0.152	0.193	0.211	0.189
Load	Voltage rms (kV)	A	18.467	6.285	3.625	2.631	20.312	7.805	3.654	2.960
		B	18.467	6.285	3.625	2.631	20.312	7.805	3.654	2.960
		C	18.466	6.285	3.625	2.630	20.313	7.805	3.654	2.960
	Current rms (kA)	A	0.184	0.063	0.036	0.026	0.203	0.078	0.036	0.030
		B	0.184	0.063	0.036	0.026	0.203	0.078	0.036	0.030
		C	0.184	0.063	0.036	0.026	0.203	0.078	0.036	0.030
Fault current rms (kA)		A	0.000	2.465	1.347	0.924	0.000	2.598	1.358	1.040
		B	0.000	2.464	1.347	0.924	0.000	2.598	1.358	1.040
		C	0.000	2.464	1.347	0.924	0.000	2.598	1.358	1.040

Table 6 System voltage and current when single phase-to-ground fault occurs (AG) in the case of distribution system with 2 MW wind generation installed at 27 km away from substation

Data			Without wind power generation				With wind power generation			
				Fault location				Fault location		
			Normal condition	3	15	27	Normal condition	3	15	27
Source	Voltage rms (kV)	A	21.182	16.654	18.361	19.310	21.888	17.236	18.852	19.769
		B	21.182	19.766	20.592	20.762	21.888	20.379	21.179	21.311
		C	21.182	21.104	20.931	21.022	21.888	21.756	21.573	21.649
	Current rms (kA)	A	0.184	1.661	0.852	0.590	0.150	1.640	0.800	0.535
		B	0.184	0.182	0.207	0.218	0.150	0.174	0.161	0.162
		C	0.184	0.189	0.203	0.210	0.150	0.152	0.170	0.184
Wind generation no. 1	Voltage rms (kV)	A	0.000	0.000	0.000	0.000	21.799	14.937	8.629	6.009
		B	0.000	0.000	0.000	0.000	21.798	21.690	24.536	26.011
		C	0.000	0.000	0.000	0.000	21.801	21.951	23.566	24.572
	Current rms (kA)	A	0.000	0.000	0.000	0.000	0.153	0.183	0.189	0.193
		B	0.000	0.000	0.000	0.000	0.153	0.159	0.141	0.132
		C	0.000	0.000	0.000	0.000	0.153	0.144	0.145	0.140
Load	Voltage rms (kV)	A	18.467	11.394	6.087	4.533	21.223	14.361	8.167	5.468
		B	18.467	18.270	20.773	21.916	21.223	20.929	23.507	24.864
		C	18.466	18.948	20.368	21.101	21.224	21.551	23.171	24.187
	Current rms (kA)	A	0.184	0.114	0.061	0.045	0.212	0.143	0.081	0.054
		B	0.184	0.182	0.207	0.219	0.212	0.209	0.235	0.248
		C	0.184	0.189	0.203	0.211	0.212	0.215	0.231	0.242
Fault current rms (kA)		A	0.000	1.555	0.793	0.000	1.637	0.143	0.887	0.659
		B	0.000	0.000	0.000	0.000	0.000	0.209	0.000	0.000
		C	0.000	0.000	0.000	0.000	0.000	0.215	0.000	0.000

Table 7 System voltage and current when three-phase fault occurs (ABC) in the case of distribution system with 2 MW wind generation installed at 27 km away from substation

Data			Without wind power generation				With wind power generation			
				Fault location				Fault location		
			Normal condition	3	15	27	Normal condition	3	15	27
Source	Voltage rms (kV)	A	21.182	10.093	14.772	16.921	21.888	10.260	14.788	16.930
		B	21.182	10.093	14.772	16.921	21.888	10.259	14.790	16.930
		C	21.182	10.093	14.772	16.921	21.888	10.259	14.789	16.931
	Current rms (kA)	A	0.184	2.520	1.379	0.948	0.150	2.535	1.375	0.946
		B	0.184	2.520	1.379	0.948	0.150	2.535	1.375	0.946
		C	0.184	2.520	1.379	0.948	0.150	2.535	1.375	0.946
Wind generation no. 1	Voltage rms (kV)	A	0.000	0.000	0.000	0.000	21.799	9.435	5.352	2.882
		B	0.000	0.000	0.000	0.000	21.798	9.435	5.350	2.882
		C	0.000	0.000	0.000	0.000	21.801	9.435	5.351	2.882
	Current rms (kA)	A	0.000	0.000	0.000	0.000	0.153	0.191	0.208	0.210
		B	0.000	0.000	0.000	0.000	0.153	0.191	0.208	0.210
		C	0.000	0.000	0.000	0.000	0.153	0.191	0.208	0.210
Load	Voltage rms (kV)	A	18.467	6.285	3.625	2.631	21.223	8.974	4.717	2.687
		B	18.467	6.285	3.625	2.631	21.223	8.974	4.719	2.687
		C	18.466	6.285	3.625	2.630	21.224	8.974	4.717	2.687
	Current rms (kA)	A	0.184	0.063	0.036	0.026	0.212	0.090	0.046	0.027
		B	0.184	0.063	0.036	0.026	0.212	0.090	0.046	0.027
		C	0.184	0.063	0.036	0.026	0.212	0.090	0.046	0.027
Fault current rms (kA)		A	0.000	2.465	1.347	0.924	0.000	2.579	1.357	0.944
		B	0.000	2.464	1.347	0.924	0.000	2.579	1.357	0.944
		C	0.000	2.464	1.347	0.924	0.000	2.579	1.358	0.944

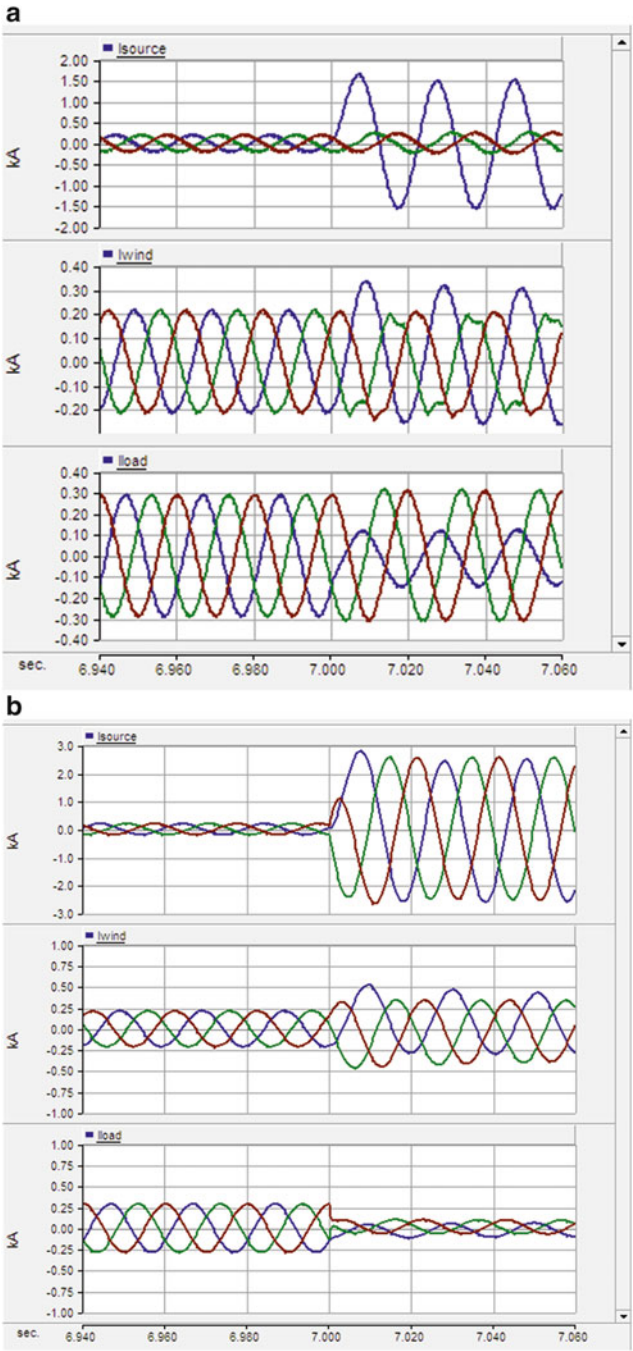

Fig. 4 Current waveform when various fault types occur in distribution system with wind power generation installed at 15 km away from substation. (**a**) Single line-to-ground fault. (**b**) Three-phase fault

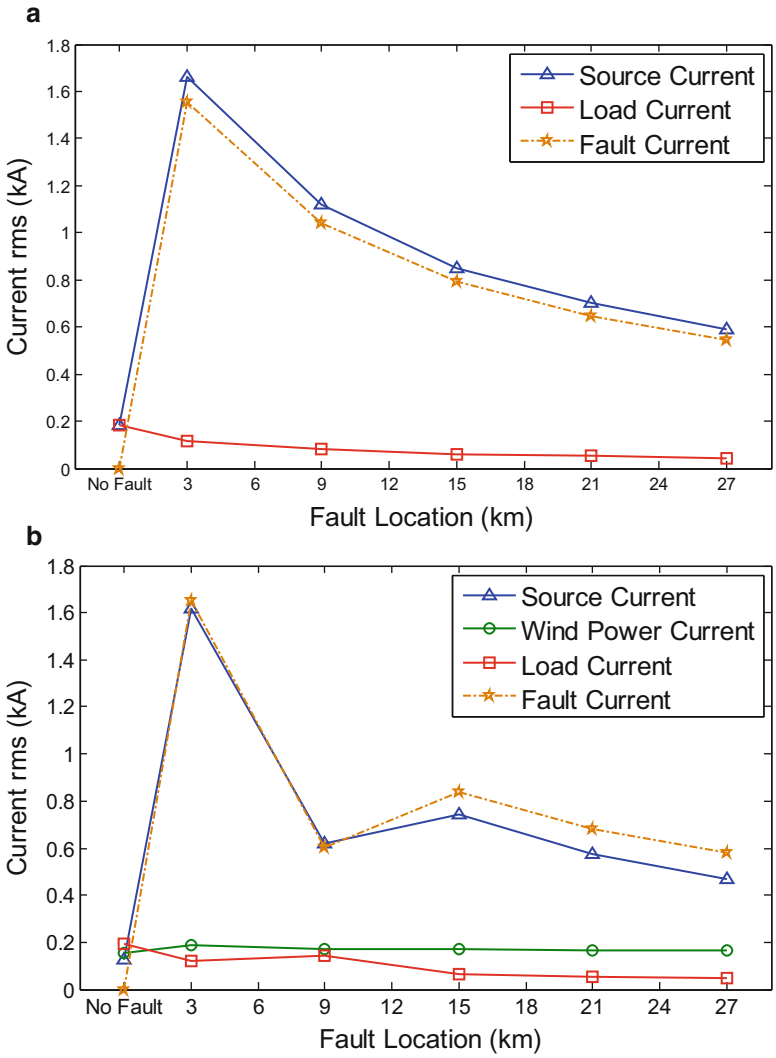

Fig. 5 System current measured from key bus when single phase-to-ground fault occurs in distribution system with 2 MW wind generation installed at 3 km away from substation. (**a**) Without installation of wind power generation unit. (**b**) With installation of wind power generation unit

– In the case with wind power generation, current and voltage are increased in substation bus, fault bus, and load bus because wind power generation generates power to fault location, while wind power generation injects constant current.
– The relation between current and location of fault is shown in Fig. 5. It can be seen that without installation of wind power generation, current measured from fault location is slightly lower than that measured from substation bus. When

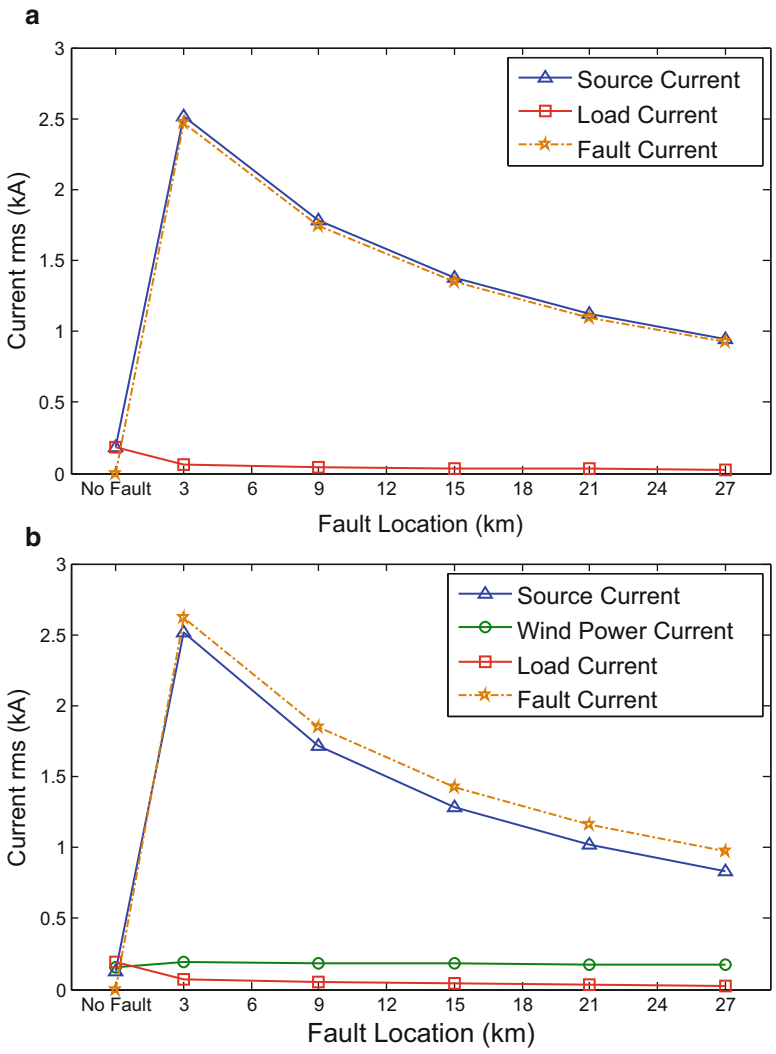

Fig. 6 System current measured from key bus when three-phase fault occurs in distribution system with 2 MW wind generation installed at 3 km away from substation. (**a**) Without installation of wind power generation unit. (**b**) With installation of wind power generation unit

installing wind power generation, current at fault bus is higher than that at substation bus; this is because wind power generation contributes a significant current to fault location.

In Table 3, it shows data obtained from simulation in the case of three-phase fault occurrence and wind power generation installed at 3 km away from substation. The obtained data can be summarized as follows:

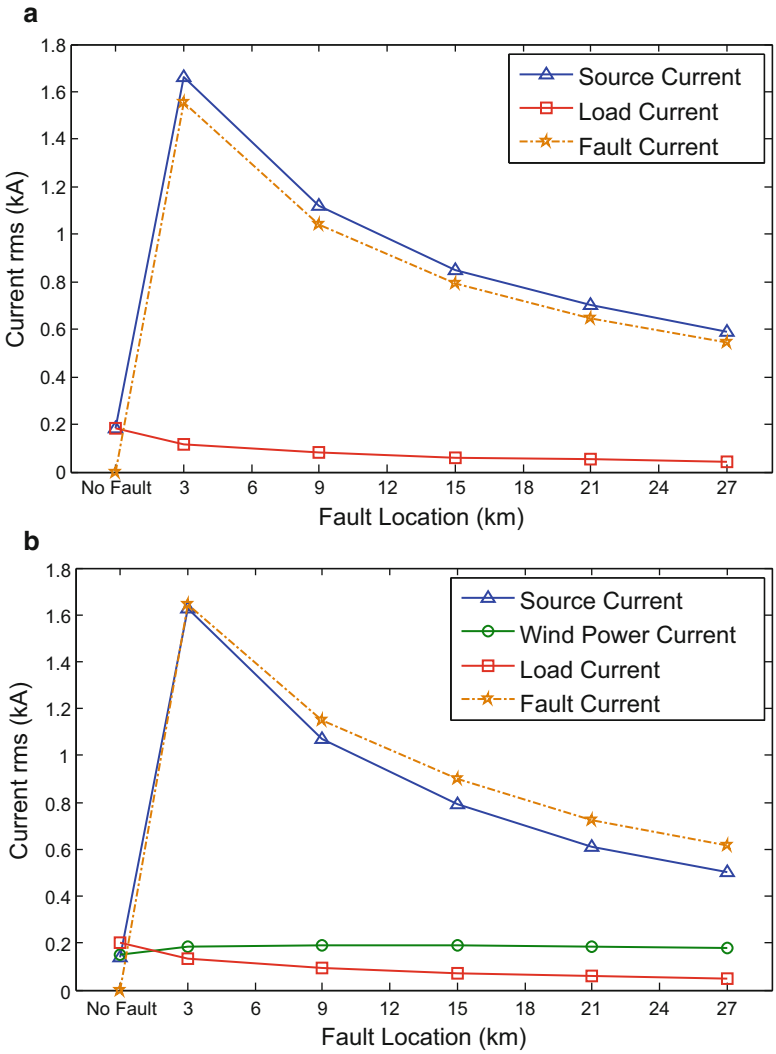

Fig. 7 System current measured from key bus when single phase-to-ground fault occurs in distribution system with 2 MW wind generation installed at 15 km away from substation. (**a**) Without installation of wind power generation unit. (**b**) With installation of wind power generation unit

– In the case without wind power generation, current and voltage behave similarly to the case of single line-to-ground fault, but magnitude of increased current and decreased voltage is much larger owing to the nature of three-phase fault.
– In the case with wind power generation, voltage at substation bus is increased but current is decreased owing to current injection of wind power generation into

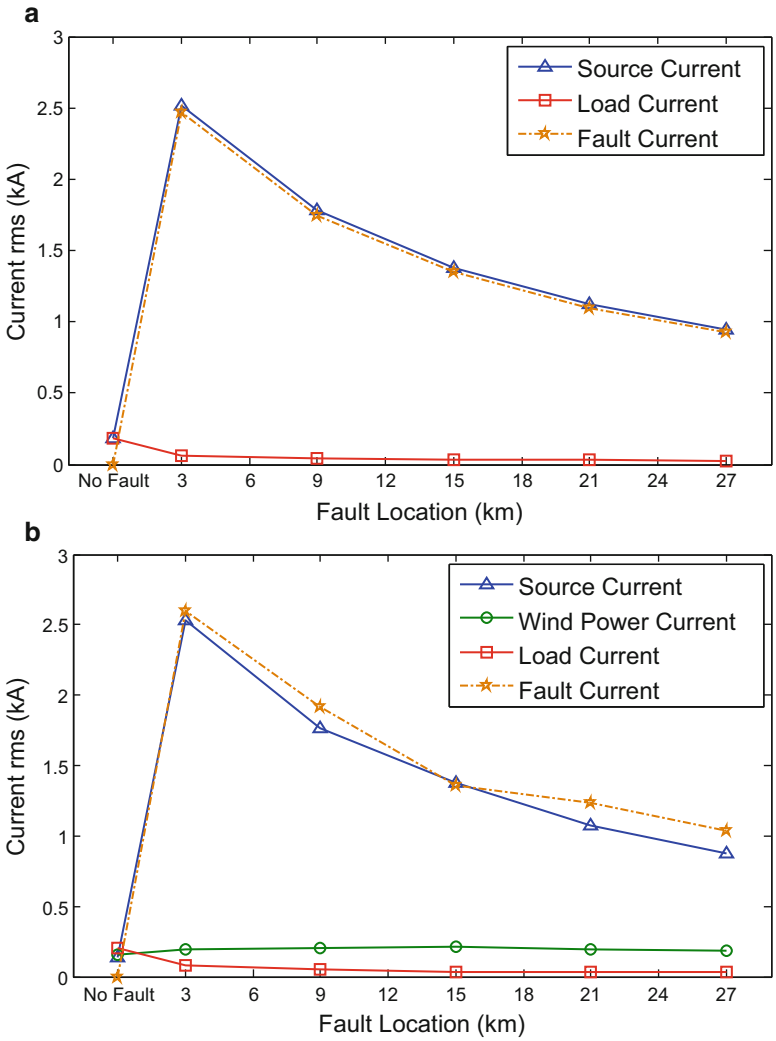

Fig. 8 System current measured from key bus when three-phase fault occurs in distribution system with 2 MW wind generation installed at 15 km away from substation. (**a**) Without installation of wind power generation unit. (**b**) With installation of wind power generation unit

fault location. Voltage and current at load bus are increased as well as current injected to fault location.

– The relation between current and location of fault is shown in Fig. 6. It also shows that installation of wind power generation makes current higher at fault bus and higher than current at substation bus.

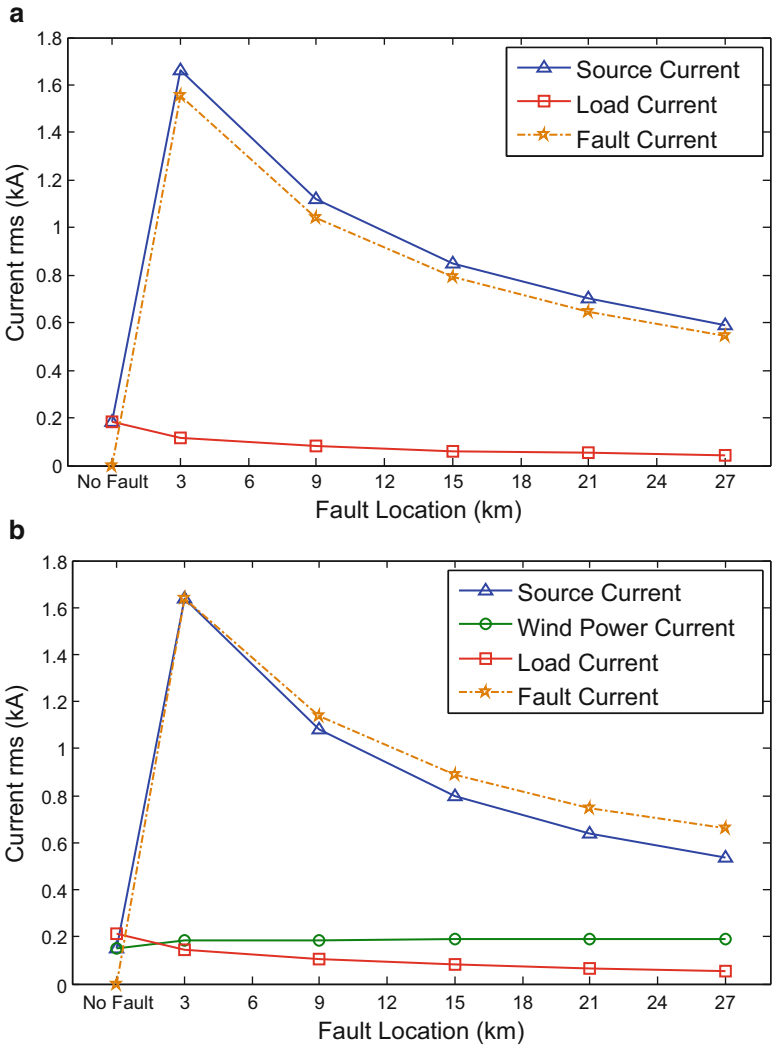

Fig. 9 System current measured from key bus when single phase-to-ground fault occurs in distribution system with 2 MW wind generation installed at 27 km away from substation. (**a**) Without installation of wind power generation unit. (**b**) With installation of wind power generation unit

In Table 4, it shows data obtained from simulation in the case of single line-to-ground fault occurrence and wind power generation installed at 15 km away from substation, and Table 5 shows data in the case of three-phase fault. In these two cases, load current and voltage are higher than the previous case due to the location of wind power generation that can generate more power to load bus. The relation between current and fault location behaves like the previous case as shown in Figs.7 and 8.

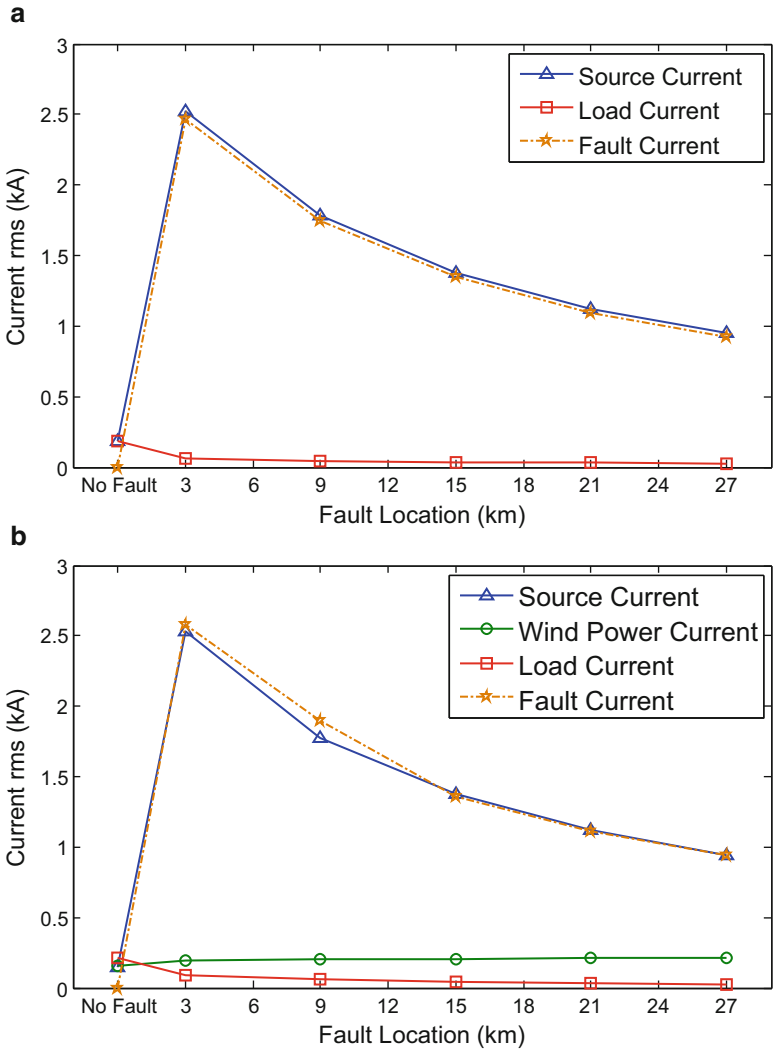

Fig. 10 System current measured from key bus when three-phase fault occurs in distribution system with 2 MW wind generation installed at 27 km away from substation. (**a**) Without installation of wind power generation unit. (**b**) With installation of wind power generation unit

In Table 6, it shows data obtained from simulation in the case of single line-to-ground fault occurrence and wind power generation installed at 27 km away from substation, and in Table 7, it shows data in the case of three-phase fault, In these two cases, load current and voltage are also higher than the previous case, but fault current is equal to substation bus current in three-phase fault because wind power generation generates power to load bus, not to fault location.

4 Multi-wind Generation Simulation

To evaluate the effect of multi-wind generation, distribution system consisting of two wind power generations with capacity of 2 MW has been used. Simulation in these case studies is done by fixing wind generation No. 1 at 3 km away from substation, and wind generation No. 2 is varied along distribution line at 6, 9, 12, 15, 18, 21, 24, and 27 km, respectively. Parameters measured from simulation model are three-phase voltage and three-phase current. Measurement points are located at substation bus (source), wind generation No. 1 bus, wind generation No. 2 bus, fault location, and load bus. Results from the simulation are shown in Tables 8, 9, and 10.

Table 8 shows data in the case of distribution system without fault. In normal condition, current from substation increases when wind power generation unit 2 moves toward load bus. This increases load current and voltage.

In Table 9, it shows data in the case of distribution system when single line-to-ground fault occurs at 15 km away from substation. Current from substation is increased since wind generation unit 2 moves toward load. Substation and wind power generation unit 1 current in phase A are increased significantly.

In Table 10, it shows data in the case of distribution system when three-phase fault occurs at 15 km away from substation. Voltage and current are dropped down near zero because all sources are located before fault location; power cannot flow to load bus until wind power generation unit 2 is located between fault location and load bus.

5 Conclusion

This paper has studied the effect of wind power generation-integrated distribution system in the case of single- and multi-wind power generation units, in terms of voltage and current characteristics. The results indicated that wind power generation injected significant amount of current when fault occurred in distribution system. When fault occurred between substation bus and wind power generation bus, current at load bus was increased when compared to the system without wind power generation due to current from wind power generation unit. Current from substation bus was decreased when fault occurred after wind power generation bus and load bus because wind power injected current to fault location.

Location of DG has impact on source and load current when wind power generation is installed near substation; current at fault location is higher than the case of installing near load. The reason is that current from wind power generation installed near load flows into load side. Current from wind power generation when installing near substation is contributed to fault location, thus, increasing fault current.

Table 8 System current and voltage in the case of distribution system with 3 MW multi-wind generation installation fixed at 3 km and another generation varied along transmission line

Data			Location of wind generation no. 2 (km)							
			6	9	12	15	18	21	24	27
Source	Voltage rms (kV)	A	23.093	23.093	23.093	23.093	23.093	23.093	23.093	23.093
		B	23.093	23.093	23.093	23.093	23.093	23.093	23.093	23.093
		C	23.093	23.093	23.093	23.093	23.093	23.093	23.093	23.093
	Current rms (kA)	A	0.066	0.068	0.071	0.074	0.077	0.080	0.083	0.087
		B	0.066	0.068	0.071	0.074	0.077	0.080	0.083	0.087
		C	0.066	0.068	0.071	0.074	0.077	0.080	0.083	0.087
Wind generation no. 1	Voltage rms (kV)	A	22.878	22.693	22.521	22.359	22.200	22.055	21.911	21.779
		B	22.878	22.693	22.521	22.521	22.200	22.055	21.911	21.779
		C	22.878	22.693	22.521	22.521	22.200	22.055	21.911	21.779
	Current rms (kA)	A	0.100	0.100	0.100	0.1000	0.100	0.100	0.100	0.100
		B	0.100	0.100	0.100	0.1000	0.100	0.100	0.100	0.100
		C	0.100	0.100	0.100	0.1000	0.100	0.100	0.100	0.100
Wind generation no. 2	Voltage rms (kV)	A	23.081	23.087	23.093	23.098	23.103	23.107	23.111	23.114
		B	23.081	23.087	23.093	23.098	23.103	23.107	23.111	23.114
		C	23.081	23.087	23.093	23.098	23.103	23.107	23.111	23.114
	Current rms (kA)	A	0.063	0.066	0.068	0.071	0.073	0.076	0.078	0.080
		B	0.063	0.066	0.068	0.071	0.073	0.076	0.078	0.080
		C	0.063	0.066	0.068	0.071	0.073	0.076	0.078	0.080
Load	Voltage rms (kV)	A	20.465	20.592	20.717	20.850	20.995	21.147	21.308	21.475
		B	20.465	20.592	20.717	20.850	20.995	21.147	21.308	21.475
		C	20.465	20.592	20.717	20.850	20.995	21.147	21.308	21.475
	Current rms (kA)	A	0.194	0.196	0.197	0.198	0.199	0.201	0.202	0.203
		B	0.194	0.196	0.197	0.198	0.199	0.201	0.202	0.203
		C	0.194	0.196	0.197	0.198	0.199	0.201	0.202	0.203

Table 9 System current and voltage when single phase-to-ground fault occurs (AG) in the case of distribution system with 3 MW multi-wind generation installation fixed at 3 km and another generation varied along transmission line

Data			Location of wind generation no. 2 (km)							
			6	9	12	15	18	21	24	27
Source	Voltage rms (kV)	A	23.094	23.094	23.094	23.094	23.094	23.094	23.094	23.094
		B	23,094	23,094	23,094	23,094	23,094	23,094	23,094	23,094
		C	23.094	23.094	23.094	23.094	23.094	23.094	23.094	23.094
	Current rms (kA)	A	1.099	1.092	1.100	1.115	1.112	1.108	1.106	1.102
		B	0.074	0.074	0.072	0.071	0.069	0.066	0.073	0.062
		C	0.121	0.121	0.119	0.123	0.121	0.126	0.135	0.126
Wind generation no. 1	Voltage rms (kV)	A	14.170	9.546	4.837	0.024	0.932	1.846	2.714	3.391
		B	25.401	26.864	28.394	29.910	28.941	28.030	27.116	26.518
		C	25.195	26.597	27.568	28.978	28.664	28.442	28.201	27.819
	Current rms (kA)	A	0.075	0.086	0.102	0.123	0.118	0.117	0.119	0.121
		B	0.059	0.060	0.064	0.069	0.069	0.071	0.077	0.079
		C	0.075	0.082	0.089	0.094	0.095	0.096	0.101	0.103
Wind generation no. 2	Voltage rms (kV)	A	18.738	18.743	18.704	18.64	18.642	18.641	18.641	18.641
		B	24.268	24.265	24.306	24.373	24.367	24.392	24.396	24.429
		C	24.183	24.245	24.216	24.201	24.187	24.212	24.229	24.232
	Current rms (kA)	A	0.105	0.105	0.105	0.105	0.105	0.105	0.106	0.105
		B	0.099	0.100	0.100	0.100	0.100	0.100	0.100	0.100
		C	0.110	0.110	0.110	0.110	0.110	0.110	0.110	0.110

(continued)

Table 9 (continued)

Data			Location of wind generation no. 2 (km)							
			6	9	12	15	18	21	24	27
Load	Voltage rms (kV)	A	3.387	3.427	3.446	3.473	3.640	3.901	4.086	4.648
		B	24.105	24.325	24.382	24.468	24.611	24.713	24.953	24.381
		C	26.219	26.390	26.625	26.844	26.962	27.259	27.491	27.083
	Current rms (kA)	A	0.032	0.032	0.033	0.033	0.035	0.037	0.039	0.044
		B	0.229	0.231	0.232	0.237	0.234	0.235	0.237	0.231
		C	0.249	0.251	0.253	0.255	0.256	0.259	0.261	0.257
Fault current (kA)			1.269	1.277	1.302	1.338	1.329	1.326	1.324	1.316
			0.000	0.000	0.000	0.000	0.000	0.000	0.000	0.000
			0.000	0.000	0.000	0.000	0.000	0.000	0.000	0.000

Table 10 System current and voltage when three-phase fault occurs (ABC) in the case of distribution system with 3 MW multi-wind generation installation fixed at 3 km and another generation varied along transmission line

Data			Location of wind generation no. 2 (km)							
			6	9	12	15	18	21	24	27
Source	Voltage rms (kV)	A	23.094	23.094	23.094	23.094	23.094	23.094	23.094	23.094
		B	23.094	23.094	23.094	23.094	23.094	23.094	23.094	23.094
		C	23.094	23.094	23.094	23.094	23.094	23.094	23.094	23.094
	Current rms (kV)	A	2.262	2.262	2.297	2.319	2.318	2.319	2.319	2.318
		B	2.262	2.261	2.304	2.319	2.318	2.319	2.319	2.318
		C	2.262	2.262	2.300	2.319	2.318	2.319	2.319	2.318
Wind generation no. 1	Voltage rms (kV)	A	14.216	9.584	10.278	10.190	10.236	10.248	10.232	10.271
		B	14.218	9.584	10.278	10.190	10.236	10.248	10.232	10.271
		C	14.217	9.584	10.278	10.190	10.236	10.248	10.232	10.271
	Current rms (kV)	A	0.104	0.103	0.170	0.180	0.173	0.173	0.171	0.172
		B	0.103	0.102	0.172	0.177	0.172	0.170	0.171	0.170
		C	0.103	0.102	0.159	0.165	0.173	0.172	0.176	0.171
Wind generation no. 2	Voltage rms (kV)	A	18.781	18.779	18.710	18.673	18.674	18.674	18.675	18.673
		B	18.780	18.780	18.697	18.673	18.674	18.674	18.675	18.673
		C	18.781	18.779	18.697	18.673	18.674	18.674	18.675	18.673
	Current rms (kV)	A	0.132	0.129	0.131	0.131	0.132	0.130	0.132	0.132
		B	0.132	0.130	0.131	0.131	0.132	0.130	0.132	0.132
		C	0.132	0.130	0.131	0.131	0.132	0.130	0.132	0.132
Load	Voltage rms (kV)	A	0.017	0.017	0.014	0.014	0.418	0.888	1.301	1.745
		B	0.015	0.015	0.014	0.014	0.421	0.909	1.299	1.745
		C	0.015	0.015	0.013	0.014	0.412	0.894	1.288	1.745
	Current rms (kV)	A	0.001	0.001	0.000	0.000	0.005	0.008	0.012	0.016
		B	0.001	0.001	0.000	0.000	0.004	0.008	0.012	0.016
		C	0.001	0.001	0.000	0.000	0.004	0.008	0.012	0.016

(continued)

Table 10 (continued)

Data		Location of wind generation no. 2 (km)							
		6	9	12	15	18	21	24	27
Fault current (kA)	A	2.484	2.484	2.500	2.566	2.371	2.423	2.529	2.565
	B	2.484	2.484	2.500	2.596	2.397	2.400	2.520	2.557
	C	2.484	2.484	2.526	2.564	2.407	2.437	2.554	2.531

In the case of multi-wind power generation unit located near the fault location, it contributed significant amount of current to fault location. When unit was located near load, it generated power to load instead of source or other wind power generation unit. These two case studies revealed that wind power generation injected current to fault location. This has changed current characteristics in distribution system and caused a false operation for protective device. A design for new protection scheme when installing wind power generation to distribution system must be carefully done in order to ensure reliability of the system.

References

Ciric, R., Nouri, H., Terzija, V.: Impact of distributed generators on arcing faults in distribution networks. IET Gener. Transm. Distrib. **5**(5), 596–601 (2011)

Coster, E., Myrzik, J., Kling, W.: In: Gaonkar, D.N. (ed.) Effect of DG on Distribution Grid Protection, Distributed Generation (2010)

Coster, E.J., Myrzik, J.M.A., Kruimer, B., Kling, W.L.: Integration issues of distributed generation in distribution grids. Proc. IEEE. **99**(1), 28–39 (2011)

Elansari, A., Musa, A., Alssnousi, A.: Impact of new wind farms on power distribution networks (Derna Wind project case study), 2012 International Conference on Renewable Energies for Developing Countries (REDEC), pp. 1–6, Beirut, 28–29 Nov. 2012

IEA: Technology Roadmap: Wind Energy – 2013 Edition (2013)

Kim, E.-H., Kim, J.-H., Kim, S.-H., Choi, J., Lee, K.Y., Kim, H.-C.: Impact analysis of wind farms in the Jeju Island power system. IEEE Syst. J. **6**(1), 134–139 (2012)

Mozina, C.J.: Wind-Power Generation. IEEE Trans. Ind. Appl. **49**(3), 1079–1090 (2013)

Muljadi, E., Samaan, N., Gevorgian, V., Li, J., Pasupulati, S.: Different factors affecting short circuit behavior of a wind power plant. IEEE Trans. Ind. Appl. **49**(1), 284–292 (2013)

N. Nimpitiwan et al.: "Consequences of fault currents contributed by distributed generation." Report, Power Systems Engineering Research Center, June (2006)

Ouyang, H., Li, P., Zhu, L., Hao, Y., Xu, C., He, C.: Impact of large-scale wind power integration on power system transient stability, 2012 I.E. Innovative Smart Grid Technologies – Asia (ISGT Asia), pp. 1–6, Tianjin, China, 21–24 May 2012

Sarabia, A.F.: Impact of Distributed Generation on Distribution System. Dissertation, Aalborg University (2011)

Scarlatache, F., Grigoras, G.: Influence of wind power plants on power systems operation. International Conference and Exposition on Electrical and Power Engineering (EPE), 1010–1014, 16–18 Oct. (2014)

Su, S.-Y., Lu, C.-N., Chang, R.-F., Gutiérrez-Alcaraz, G.: Distributed generation interconnection planning: a wind power case study. IEEE Trans. Smart Grid. **2**(1), 181–189 (2011)

The Electricity Training Association: Power System Protection Vol 1–Principles and Components. The Institution of Electrical Engineers, London, United Kingdom (1995)

Operating Oil Refinery Units Under Uncertainty: Thermodynamic and Economic Implications

Eid Al-Mutairi

1 Introduction

Energy conservation is of prime importance in the process industries because of the cost and environmental impact of energy production. The pinch design method (PDM) has been extensively used to achieve energy savings (Linnhoff and Hindmarsh 1983; Linnhoff et al. 1982; Smith 2005). This technique has been studied at length using different approaches, such as genetic algorithms (Allen et al. 2009; Dipama et al. 2008), tree searching methods (Pho and Lapidus 1973), and neural networks (Bittanti and Piroddi 1997). The assumption of constant process stream parameters within the supply and target temperature bounds is common in most of the methodologies proposed for analyzing and solving heat exchanger network (HEN) synthesis problems (Ponce-Ortega et al. 2008).

The physical properties of the process streams depend on the temperature variation along the process streams in the HEN. This temperature dependency could have a significant effect on the design and retrofit of the HEN. Using the concept of the PDM and an evolutionary design, the synthesis of a HEN for maximum energy recovery is guided by the determination of (i) the target utilities and (ii) the pinch point (PP). The outcomes of these design procedures are highly dependent on the number of process streams, their supplied and targeted temperatures, and the heat capacity flow rates.

The assumption of a constant specific heat capacity (C_p) would only be a valid approximation for process streams existing within the temperature bounds in which no phase change occurred. However, for phase-changing process streams, the

E. Al-Mutairi (✉)
King Fahd Universiry of Petroleum & Minerals, Department of Chemical Engineering, Dhahran 31261, Saudi Arabia
e-mail: mutairi@kfupm.edu.sa

© Springer International Publishing AG, part of Springer Nature 2018

F. Aloui, I. Dincer (eds.), *Exergy for A Better Environment and Improved Sustainability 2*, Green Energy and Technology,
https://doi.org/10.1007/978-3-319-62575-1_63

assumption of a constant C_p at the targeting and synthesis stages is no longer valid. Hence, any conclusion drawn based on this assumption may not be accurate. Castier and Queiroz (2002) reported a methodology based on the PP method to solve the energy targeting problem with phase-changing streams. Liporace et al. (2004) and Nejad et al. (2012) presented alternative simplified procedures in which the streams with phase changes were divided into sub-streams. However, they did not provide detailed reports on how the stream properties responded to variations of the process stream temperature.

In the present study, various process stream parameters sensitive to temperature variations were estimated to provide insight on how they can affect the analysis of a HEN. The problem table algorithm (PTA) approach for utility targeting in the PDM was used to compare the energy targets and PPs for (1) the base case, when the process stream properties are constant within temperature intervals defined by the supply and target temperatures, and (2) the phase change case, when the process stream properties are constant within the temperature interval defined by the dew and bubble points.

2 Data Extraction and Process Description

The examined process streams and the data used for this analysis were extracted from simulated data from an existing and functional crude distillation unit. Crude distillation units are mostly similar, with various degrees of design complexity. Generally, the crude feed passes through a group of exchangers, a desalter, followed by another group of exchangers, a preflash column, a heater, and a main column. From the main column, a stream leads to an overhead system with a condenser, a compressor (for gas recovery, stabilization, and liquefied petroleum gas recovery), and a gasoline splitter. Additionally, side streams enter columns that strip side products. From the bottom of the main column, the topping residue passes through a series of exchangers and is sent to storage.

3 Methodology

The simulation model of the process was developed using the data obtained from the plant. The parameters for the process flow diagram were input in the HYSYS (2003) process simulator software. This enabled the validation of simulation data through the comparison with operation data. The simulation was adjusted until a close representation of the real process was obtained. From this model, the stream data were extracted. This data set represented the base case process stream data. To account for the variations of the process stream parameters with the temperature, the supply and target temperature bounds were segmented into new temperature intervals defined by the dew and bubble points. The thermodynamic properties of

the process stream mixture were estimated using an Excel macro-enabled software (ChemSOF), and the analysis was performed using Microsoft Excel spreadsheets. The PPs and the utility demands were estimated using a heat-integration software (Heat-Int 2012).

3.1 Estimation of Heat Load in the Existing Stream

A commonly used heat exchanger in this type of operation is the U-tube shell and tube heat exchanger. The heat capacity flow rate for each stream, which is the product of the mass flow rate (M) and the specific heat capacity (C_p), was estimated from the heat load of the heat exchanger and the supply and target temperatures using Eq. (1) (Sinnott 2005):

$$MC_p = \frac{Q}{\Delta T}. \tag{1}$$

3.2 Determination of Bubble Point, Dew Point, Vaporized Fraction, and Enthalpy

To calculate appropriate temperature intervals with constant process stream properties for a reasonable approximation, the dew and bubble point temperatures were estimated. Subsequently, the existing supply and target temperature bounds in each process stream were segmented into temperature sub-intervals using the estimated bubble and dew points to define the new temperature bounds. Because the components of the mixture were mostly organic compounds (see Table 2), the Peng–Robinson equation of state was used for the estimation of the bubble and dew point temperatures, and the total pressure for the process stream components was assumed constant. The online chemical engineering software ChemSOF was used for the estimation of multicomponent bubble points and dew points, and for flash calculations. The vaporized fractions of the mixture at different temperatures were also generated by the software. The enthalpy of the mixture was estimated by the weighted average of the enthalpy of the individual components at the specified temperature using Eq. (2) (Levine 1997; Singh and Heldman 1993):

$$H_m = H_i w_i + \ldots + H_n w_n, \tag{2}$$

where H_m is the enthalpy of the mixture, H_i is the enthalpy of component i, w_i is the mass fraction of component i, and n is the number of components in the mixture.

3.3 Estimation of Mass Flow Rate and Effective Mean Specific Heat Capacity

For the purpose of energy targeting, the mass flow rate and the effective mean specific heat capacity $\bar{C}_{p_{\text{eff}}}$ for each stream were estimated using Eqs. (3) and (4), respectively:

$$\text{Mass flow rate } (M)\left(\frac{\text{kg}}{\text{s}}\right) = \frac{\text{Heat load } (\Delta H)\ \left(\frac{\text{kJ}}{\text{s}}\right)}{\text{Enthalpy } (H)\ \left(\frac{\text{kJ}}{\text{kg}}\right)}, \tag{3}$$

$$\bar{C}_{p_{\text{eff}}} = \left(\frac{\text{kJ}}{\text{kg}^{\circ}\text{C}}\right) = \frac{\text{Heat capacity flow rate } \left(MC_p\right)\ \left(\frac{\text{kJ}}{\text{s}^{\circ}\text{C}}\right)}{\text{Mass flow rate } (M)\ \left(\frac{\text{kg}}{\text{s}}\right)}. \tag{4}$$

The enthalpy change $\Delta H'$ was estimated using Eq. (5):

$$\text{The enthalpy change } (\Delta H')\left(\frac{\text{kJ}}{\text{kg}}\right) = H'_{\text{S}} - H'_{\text{T}}, \tag{5}$$

where H'_{S} and H'_{T} are the enthalpy values at the supply and target temperatures, respectively.

Depending on the supply and target temperatures of the base case process stream, the interval bounds in the phase change process stream may exist under superheating, phase change, and subcooling conditions. Hence, to account for phase changes in the process stream, the base case process streams were segmented using the temperature interval bounds defined as follows:

For the superheating condition:

$$T_{\text{S}} \leq T \leq T_{\text{DP}}, \tag{6}$$

for the changing phase condition:

$$T_{\text{DP}} \leq T \leq T_{\text{BP}}, \tag{7}$$

and for the subcooling condition:

$$T_{\text{S}} \leq T \leq T_{\text{BP}}. \tag{8}$$

The consideration of the phase change was important because the assumption of a linear distribution of energy during sensible heat transfer due to the superheating, phase change, and subcooling conditions was a more realistic and reasonable approximation than the consideration of sensible heat transfer based on the process stream supply and target temperatures.

3.4 Determination of Thermodynamic Properties of the Process Stream Mixture

The equation of state (EOS) property calculation spreadsheet in ChemSOF was used for the estimation of the enthalpy (H) and density (ρ) of each component of the mixture at specified temperatures. Subsequently, these thermodynamic properties were used with the appropriate mixing rules to obtain the properties of the mixture of the process streams. The following properties of the mixture were estimated: the specific heat capacity of the mixture, the viscosity of the mixture, the thermal conductivity of the mixture, the Nusselt number, the Reynolds number, the Prandtl number, and the heat transfer coefficient. A tube internal diameter (D_e) of 0.01905 m was assumed for the heat exchanger and used in the estimations (Coletti and Macchietto 2011).

3.4.1 Estimation of Prandtl Number

The Prandtl number (P_r) is a function of the specific heat capacity, fluid viscosity, and thermal conductivity. The P_r for the hot stream, z, and the cold stream, j, were estimated using Eqs. (9a) and (9b), respectively (Wilkes et al. 2010):

$$P_{r,z} = \frac{C_{pm,z}\mu_{m,z}}{k_{m,z}} \tag{9a}$$

$$P_{r,j} = \frac{C_{pm,j}\mu_{m,j}}{k_{m,j}} \tag{9b}$$

where $C_{pm,z}$ and $k_{m,z}$ are the respective specific heat capacity and thermal conductivity of the process stream mixture for the hot stream and $C_{pm,j}$ and $k_{m,j}$ are the respective specific heat capacity and thermal conductivity of the process stream mixture for the cold stream.

The specific heat capacities of the individual components of the mixture at each specified temperature were obtained from the literature (Levine 1997). The specific heat capacity of the mixture was estimated by the weighted average of the specific heat capacities of the individual components at the specified temperature using Eq. (10) (Singh and Heldman 1993):

$$C_{p,m} = C_{p,i}w_i + \ldots + C_{p,n}w_n \tag{10}$$

where $C_{p,m}$ is the specific heat capacity of the mixture and $C_{p,i}$ is the specific heat capacity of the individual component i in the mixture.

For the estimation of the thermal conductivity (k_i) of each component of the mixture, the Weber equation (Weber 1980), given as Eq. (11), was used:

$$k_{\mathrm{i}} = 3.56 \times 10^{-5} C_{\mathrm{p}} \left(\frac{\rho_{\mathrm{i}}^4}{M_{\mathrm{wt}}} \right)^{1/3.} \tag{11}$$

Weighted averages are sufficiently accurate for the estimation of the thermal conductivity of the mixtures (k_{m}). Hence, Eq. (12) was used:

$$k_{\mathrm{m}} = \sum_{i=1}^{n} k_i w_i. \tag{12}$$

The heat transfer coefficient is a function of the Nusselt number (N_{u}), the thermal conductivity, and the inner tube diameter of the heat exchanger. It is expressed by Eqs. (13a) and (13b) for the hot stream, z, and the cold stream, j, respectively:

$$h_{\mathrm{z}} = \frac{N_{\mathrm{uz}} k_{\mathrm{z}}}{D_{\mathrm{e}}} \tag{13a}$$

$$h_{\mathrm{j}} = \frac{N_{\mathrm{uj}} k_{\mathrm{j}}}{D_{\mathrm{e}}}, \tag{13b}$$

whereas the Nusselt number is computed as follows.

For gases and for liquids at high or moderate Reynolds numbers, the Nusselt number can be estimated for the hot and cold streams using Eqs. (14a) and (14b), respectively (Donohue 1949):

$$N_{\mathrm{uz}} = 0.023 (N_{\mathrm{Rez}})^{0.8} (P_{\mathrm{rz}})^{0.4} \tag{14a}$$

$$N_{\mathrm{uj}} = 0.023 \left(N_{\mathrm{Rej}}\right)^{0.8} \left(P_{\mathrm{rj}}\right)^{0.3}. \tag{14b}$$

4 Results and Discussion

4.1 Results of Process Stream Data Extraction

The results of the process stream identification and the specification of the base case indicated 24 process streams, of which 16 were hot and eight were cold, as shown in Table 1. The two utility sources were steam and cooling water. Using Eq. (1), the heat capacity flow rates for each process stream were estimated and are presented in Table 1.

Table 1 Base case process streams data

Streams	T_S (°C)	T_T (°C)	Heat capacity flow rate (MC_p; kW/°C)	Heat load (ΔH; kW)
Hot streams				
1	366	188.6	37	6563.8
2	340.6	60	29	8137.4
3	328.8	318	172	1857.6
4	292.2	222.6	324	22,550.4
5	272.9	55	142	30,941.8
6	237	157.7	336	26,644.8
7	222.6	131.1	77	7045.5
8	188.5	40	51	7573.5
9	172.7	145.7	107	2889
10	165.7	75	230	20,861
11	146.1	55	225	20,497.5
12	137.7	40	60	5862
13	135.9	40	33	3164.7
14	118.1	45	291	21,272.1
15	93	40	107	5671
16	56.4	38	207	3808.8
Cold streams				
17	35	223.9	459	86,705.1
18	223.9	239	1257	18,980.7
19	45	118	62	4526
20	55	120.8	72	4737.6
21	127.6	135.9	263	2182.9
22	137.7	145	573	4182.9
23	232.9	264.6	441	13,979.7
24	264.6	365.5	679	68,511.1
Utilities streams				
CU	25	30	–	–
HU	450	440	–	–

4.2 Results of Bubble Point, Dew Point, Vaporized Fraction, and Enthalpy Calculations

The bubble and dew point temperatures for the mixture were 105.37 °C and 159.07 °C, respectively. A comparison of the bubble and dew point temperatures with the supply and target temperatures in Table 1 revealed the possibility of phase changes in the process. This thermodynamic observation showed the true trend of the heat distribution in the shell and tube sides of the heat exchanger. Table 2 presents the condition of the process stream mixture, the vaporized fraction, and their enthalpy at specified temperatures.

The examination of the enthalpy values provided a clear picture of the temperature dependence of the enthalpy. As expected, the enthalpy increased as the

Table 2 Vaporized mass fraction, condition, and calculated enthalpy for the process stream mixture as a function of temperature

Temperature of mixture (°C)	Condition	Vaporized mass fraction	Enthalpy (H') (kJ/kg)
366	Vapor	1.0000	−657.42
365.5	Vapor	1.0000	−658.39
340.6	Vapor	1.0000	−709.32
328.8	Vapor	1.0000	−735.48
318	Vapor	1.0000	−760.7
292.2	Vapor	1.0000	−826.57
272.9	Vapor	1.0000	−881.84
264.6	Vapor	1.0000	−907.45
239	Vapor	1.0000	−994.66
237	Vapor	1.0000	−1002.06
232.9	Vapor	1.0000	−1017.53
223.9	Vapor	1.0000	−1052.97
222.6	Vapor	1.0000	−1058.41
188.6	Vapor	1.0000	−7169.49
188.5	Vapor	1.0000	−7171.01
172.7	Vapor	1.0000	−7407.42
165.7	Vapor	1.0000	−13,932.5
159.07	Vapor	1.0000	−14,101.7
157.7	Liquid + vapor	0.9437	−14,136.2
146.1	Liquid + vapor	0.5805	−14423.3
145.7	Liquid + vapor	0.5709	−14,433
145	Liquid + vapor	0.5545	−14,450.1
137.7	Liquid + vapor	0.4065	−14,626.4
135.9	Liquid + vapor	0.3754	−14,669.5
131.1	Liquid + vapor	0.3	−14,783.9
127.6	Liquid + vapor	0.2507	−14,875.4
120.8	Liquid + vapor	0.165	−15,026.9
118.1	Liquid + vapor	0.1337	−15,090.2
118	Liquid + vapor	0.1326	−15,092.5
105.37	Liquid	0.0000	−18,899.1
93	Liquid	0.0000	−19,280.4
75	Liquid	0.0000	−19,817.2
60	Liquid	0.0000	−22,758
56.4	Liquid	0.0000	−25,176.8
55	Liquid	0.0000	−25,233.1
45	Liquid	0.0000	−25,627.5
40	Liquid	0.0000	−25,820.2
38	Liquid	0.0000	−25,896.5
35	Liquid	0.0000	−26,010.3

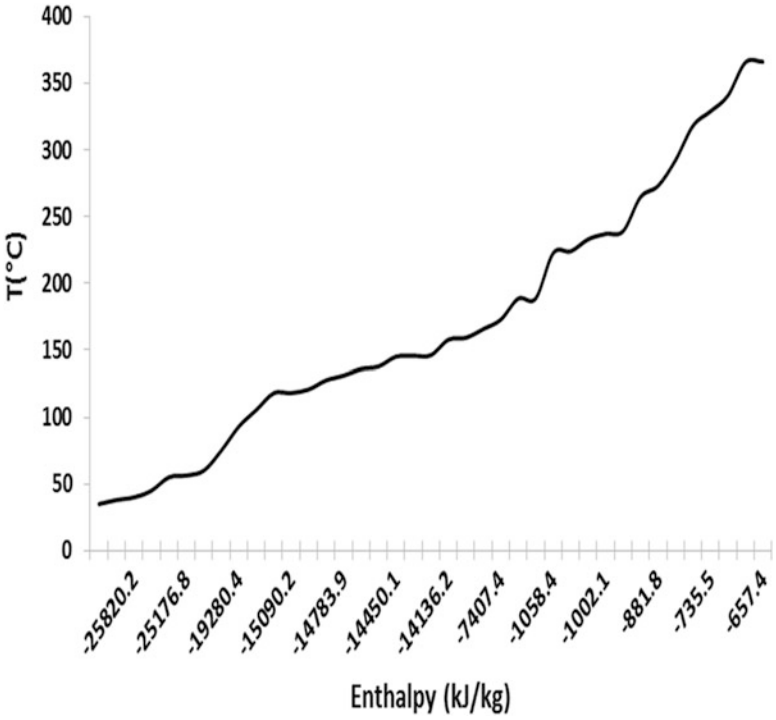

Fig. 1 Dependence of enthalpy on temperature

temperature of the process stream mixture increased as shown in Fig. 1. The dependence of the density of the process stream mixture on the temperature is also shown in Fig. 2. The density of the mixture increased as the temperature of the mixture decreased. At high temperatures, the volume of the unit mass of the mixtures increased and thereby produced a decrease in the density.

4.3 Results of Mass Flow Rate, Enthalpy, and Effective Mean Specific Heat Capacity Calculations

The effective mass flow rate, specific heat capacity, and enthalpy of the base case process streams are presented in Table 3, as estimated using the data from Tables 1 and 3 in Eqs. (3), (4), and (5), respectively. As observed from the heat load and enthalpy change columns in the table, the heat distribution was not a linear function. It depended on the process stream supply and target temperatures and the heat capacity flow rate. Consequently, the wider the difference between the supply and target temperature ranges, the wider the deviation from the exact representation of

Table 3 Process stream properties for the base case

Streams	T_S (°C)	T_T (°C)	Heat capacity flow rate (MC_p) (kW/°C)	Heat load (ΔH) (kW)
Hot stream				
1	366	188.6	37	6563.8
2	340.6	60	29	8137.4
3	328.8	318	172	1857.6
4	292.2	222.6	324	22,550.4
5	272.9	55	142	30,941.8
6	237	157.7	336	26,644.8
7	222.6	131.1	77	7045.5
8	188.5	40	51	7573.5
9	172.7	145.7	107	2889
10	165.7	75	230	20,861
11	146.1	55	225	20,497.5
12	137.7	40	60	5862
13	135.9	40	33	3164.7
14	118.1	45	291	21,272.1
15	93	40	107	5671
16	56.4	38	207	3808.8
Cold stream				
17	35	223.9	459	86,705.1
18	223.9	239	1257	18,980.7
19	45	118	62	4526
20	55	120.8	72	4737.6
21	127.6	135.9	263	2182.9
22	137.7	145	573	4182.9
23	232.9	264.6	441	13,979.7
24	264.6	365.5	679	68511.1

Enthalpy change ($\Delta H'$) (kJ/kg)	Mass flow rate (M) (kg/s)	Effective mean heat capacity (C_p) (kJ/kg°C)
Hot stream		
6512.07	1.0	36.70
22048.68	0.36	78.57
25.22	73.65	2.33
231.84	97.26	3.33
24351.26	1.27	111.75
13134.14	2.02	165.62
13725.49	0.51	150.0
18649.19	0.40	125.58
7025.58	0.41	260.20
5884.7	3.54	64.88
10809.8	1.894	118.65
11193.8	0.52	114.57
11150.7	0.28	116.27

(continued)

Table 3 (continued)

Enthalpy change ($\Delta H'$) (kJ/kg)	Mass flow rate (M) (kg/s)	Effective mean heat capacity (C_p) (kJ/kg°C)
10537.3	2.01	144.14
6539.8	0.86	123.39
719.7	5.295	39.11
Cold stream		
24957.33	3.47	132.11
58.31	325.51	3.86
10,535	0.429	144.31
10206.2	0.46	155.10
205.9	10.60	24.80
176.3	23.72	24.15
110.08	126.99	3.47
249.06	275.07	2.46

the process when the assumption of a constant process parameter was made in the process analysis.

The results for the phase change case are presented in Table 4. The values of $\bar{C}_{p_{\text{eff}}}$ in both Tables 4 and 5 further revealed their dependency on the supply and temperature bounds. The new phase change process streams presented in Table 4 gave a better and more realistic approximation for the heat distribution in the process streams (Figs. 3 and 4).

4.4 Energy Targeting Using Problem Table Algorithms

Energy targeting was performed by inputting the data presented in Table 4 into heat-integration software (Heat-Int 2012). The results for the base and phase change cases and for different values of $\Delta T_{\min}$ are presented in Table 5. The phase changes affected the PPs and utility demands. This influence was more pronounced as the $\Delta T_{\min}$ increased. The crude distillation unit retrofit is often based on a $\Delta T_{\min}$ of 30–40 °C (Linnhoff 1998). The hot and cold pinch temperatures at a $\Delta T_{\min}$ of 30 °C were 253.9 °C and 223.9 °C, respectively, for the constant C_p case, whereas the hot and cold pinch temperatures were 237.0 °C and 207.0 °C, respectively, for the phase change case. The reduction in the pinch points in the phase change case compared with the constant C_p scenario was an indication of a better heat distribution for the former. In the base case, the heating utility demand in the phase change case at a $\Delta T_{\min}$ of 30 °C increased to 80655.1 kW from 77844.7 kW. The cooling utility demand in the phase change case at the same $\Delta T_{\min}$ also increased to 72190.0 kW from 69379.6 kW. This trend was the same for the other values of $\Delta T_{\min}$ except that the percent increase in utility demands increased with increasing $\Delta T_{\min}$.

Table 4 Process stream properties for the phase change original process streams (base case) to generate the case. The first two columns show the segmentation of the new process streams (phase change case)

Original streams	New streams	T_S (°C)	T_T (°C)	$\Delta H'$ (kJ/kg)
1	1	366	188.6	6512.07
2	2	340.6	159.07	13,392.38
	3	159.07	105.37	4797.4
	4	105.37	60	3858.9
3	5	328.8	318	25.22
4	6	292.2	222.6	231.84
5	7	272.9	159.07	13,219.86
	8	159.07	105.37	4797.4
	9	105.37	55	6334
6	10	237	159.07	13,099.64
	11	159.07	157.7	34.5
7	12	222.6	159.07	13,043.29
	13	159.07	131.1	682.2
8	14	188.5	159.07	6930.69
	15	159.07	105.37	4797.4
	16	105.37	40	6921.1
9	17	172.7	159.07	6694.28
	18	159.07	145.7	331.3
10	19	165.7	159.07	169.2
	20	159.07	105.37	4797.4
	21	105.37	75	918.1
11	22	146.1	105.37	4475.8
	23	105.37	55	6334
12	24	137.7	105.37	4272.7
	25	105.37	40	6921.1
13	26	135.9	105.37	4229.6
	27	105.37	40	6921.1
14	28	118.1	105.37	3808.9
	29	105.37	45	6728.4
15	30	93	40	6539.8
16	31	56.4	38	719.7
17	32	35	105.37	7111.2
	33	105.37	159.07	4797.4
	34	159.07	223.9	13,048.73
18	35	223.9	239	58.31
19	36	45	105.37	6728.4
	37	105.37	118	3806.6
20	38	55	105.37	6334
	39	105.37	120.8	3872.2
21	40	127.6	135.9	205.9
22	41	137.7	145	176.3
23	42	232.9	264.6	110.08
24	43	264.6	365.5	249.06

(continued)

Table 4 (continued)

Mass flow rate (M) (kg/s)	Heat duty (ΔH) (kW)	Heat capacity flow rate (MC_p) (kW/°C)	Specific heat capacity (C_p) (kJ/kg°C)
1.0079	6563.80	37.00	36.71
0.3691	4942.66	27.23	73.78
	1770.55	32.97	89.34
	1424.19	31.39	85.05
73.6558	1857.60	172.00	2.34
97.2671	22,550.40	324.00	3.33
1.2706	16,797.75	147.57	116.14
	6095.79	113.52	89.34
	8048.26	159.78	125.75
26574.81	341.01	168.09	
69.99	51.09	25.18	
6695.32	105.39	205.31	
350.18	12.52	24.39	
2814.58	95.64	235.50	
1948.24	36.28	89.34	
2810.68	43.00	105.88	
2752.77	201.96	491.14	
136.23	10.19	24.78	
599.81	90.47	25.52	
17006.57	316.70	89.34	
3254.62	107.17	30.23	
8486.99	208.37	109.89	
12010.51	238.45	125.75	
2237.54	69.21	132.16	
3624.46	55.45	105.88	
1200.41	39.32	138.54	
1964.29	30.05	105.88	
2.0187	7689.19	604.02	299.21
	13,582.91	224.99	111.45
0.8672	5671.00	107.00	123.39
5.2922	3808.80	207.00	39.11
3.4741	24,705.26	351.08	101.05
	16,666.81	310.37	89.34
	45,333.03	699.26	201.28
325.5136	18,980.70	1257.00	3.86
0.4296	2890.63	47.88	111.45
	1635.37	129.48	301.39
0.4642	2940.17	58.37	125.75
	1797.43	116.49	250.95
10.6017	2182.90	263.00	24.81
23.7260	4182.90	573.00	24.15
126.9958	13,979.70	441.00	3.47
275.0787	68,511.10	679.00	2.47

Table 5 Results of energy targeting

$\Delta T_{min} = 20$ (°C)	
$Q_{H,\ \min}$ (kW)	$Q_{C,\ \min}$ (kW)
72,524.7	64,059.6
73,662.5	65,197.4
1.6	1.8
$\mathbf{\Delta} T_{min} = 20$ (°C)	
$Q_{H,\ \min}$ (kW)	$Q_{C,\ \min}$ (kW)
75,184.7	66,719.6
77,158.8	68,693.7
2.6	3.0
$\mathbf{\Delta} T_{min} = 20$ (°C)	
$Q_{H,\ \min}$ (kW)	$Q_{C,\ \min}$ (kW)
77,844.7	69,379.6
80,655.1	72,190
3.6	4.1
$\mathbf{\Delta} T_{min} = 35$ (°C)	
$Q_{H,\ \min}$ (kW)	$Q_{C,\ \min}$ (kW)
80,504.7	72,039.6
84,151.4	75,686.3
4.5	5.1
$\mathbf{\Delta} T_{min} = 40$ (°C)	
$Q_{H,\ \min}$ (kW)	$Q_{C,\ \min}$ (kW)
83,164.7	74,699.6
87,647.7	79,182.6
5.4	6.0
$\mathbf{\Delta} T_{min} = 35$ (°C)	
Case	Pinch temperature (°C)
Original set of process streams	258.9–223.9
New set of process streams	237.0–202.0
Difference in energy target (%)	
$\mathbf{\Delta} T_{min} = 40$ (°C)	
Case	Pinch temperature (oC)
Original set of process streams	263.9–223.9
New set of process streams	237.0–197.0
Difference in energy target (%)	
$\Delta T_{min} = 20$ (°C)	
Case	Pinch temperature (°C)
Original set of process streams	243.9–223.9
New set of process streams	237.0–217.0
Difference in energy target (%)	
$\Delta T_{min} = 25$ (°C)	
Case	Pinch temperature (oC)
Original set of process streams	248.9–223.9

(continued)

Table 5 (continued)

New set of process streams	236.9–211.9
Difference in energy target (%)	
$\Delta T_{min} = 30\ (^{\circ}C)$	
Case	Pinch temperature (°C)
Original set of process streams	253.9–223.9
New set of process streams	237.0–207.0
Difference in energy target (%)	

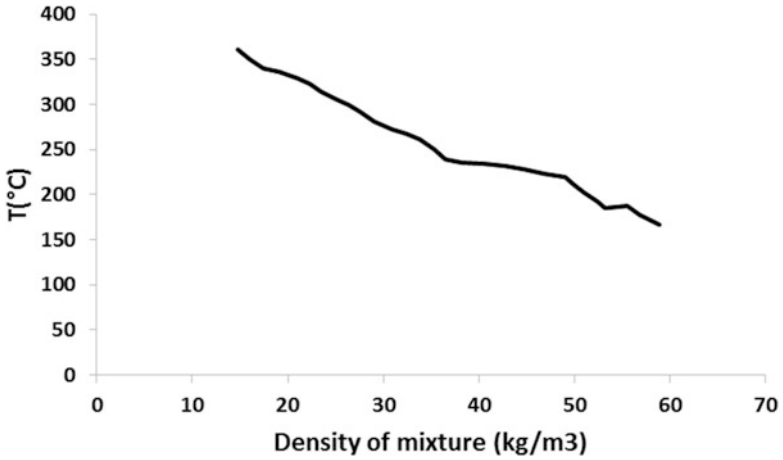

Fig. 2 Dependence of density of process stream mixture on temperature

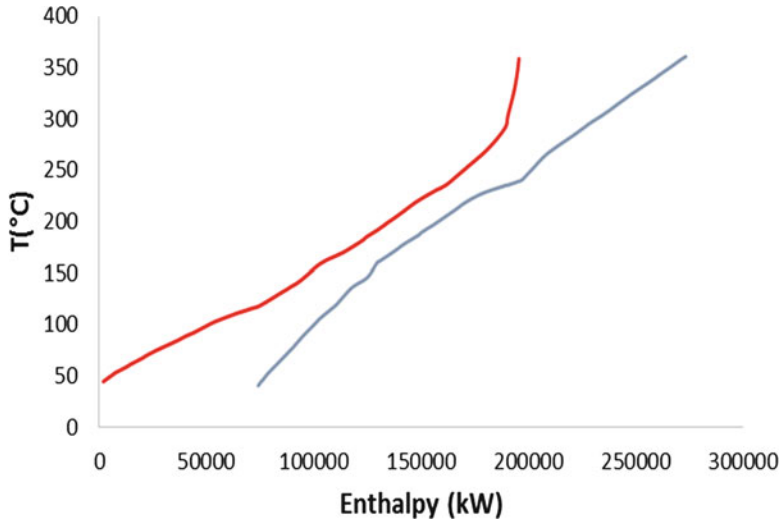

Fig. 3 Composite curves for the phase change process streams at 30 °C

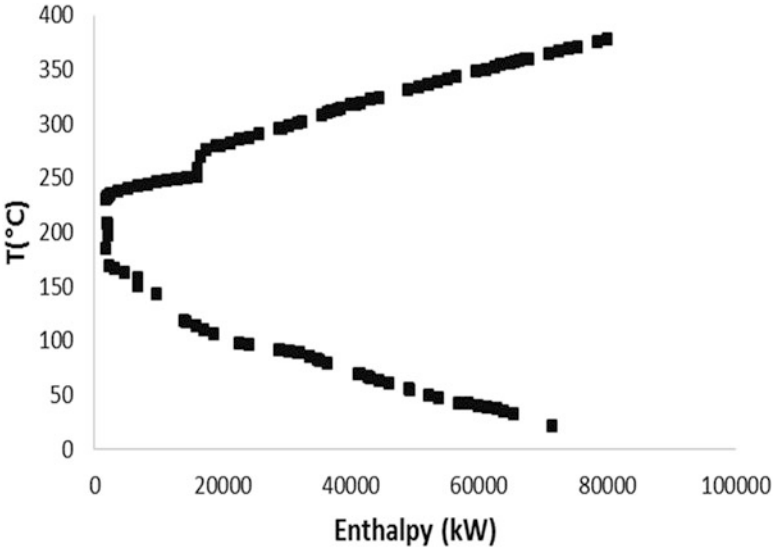

Fig. 4 Grand composite curves for the phase change process streams at 30 °C

5 Conclusions

The dependency of the thermodynamic properties of the process streams on the temperature of a mixture was observed, and the results revealed an influence of phase changes on the process, including a reduced pinch point and increased utility demands and heat transfer area requirements. This could be due to a better heat distribution obtained when the temperature interval was defined by the bubble and dew points rather than the target and supply temperatures. The study concluded that the design of a HEN without a consideration for the phase changes would not provide an accurate representation of the thermal behavior of the heat exchanger.

Acknowledgment The author acknowledges the support provided by King Abdulaziz City for Science and Technology (KACST) through the Science & Technology Unit at King Fahd University of Petroleum & Minerals (KFUPM) for funding this work through project No. 13-ENE-59-04 as part of the National Science, Technology and Innovation Plan.

References

Allen, B., Savard-Goguen, M., Gosselin, L.: Optimizing heat exchanger networks with genetic algorithms for designing each heat exchanger including condensers. Appl. Therm. Eng. **29**(16), 3437–3444 (2009)

Biegler, L., Grossmann, I., Westerberg, A.: Systematic Methods of Chemical Process Design. Prentice-Hall, Upper Saddle River (1997)

Bittanti, S., Piroddi, L.: Nonlinear identification and control of a heat exchanger: A neural network approach. J. Franklin Inst. **334**, 135–153 (1997)
Brooke, A., Kendrick, D., Meeruas, A., Raman, R.: GAMS-Language Guide. GAMS Development Corporation, Washington, D.C. (2006)
Castier, M., Queiroz, E.M.: Energy targeting in heat exchanger network synthesis using rigorous physical property calculations. Ind. Eng. Chem. Res. **41**, 1511–1515 (2002)
ChemSOF.: www.chemsof.com
Coletti, F., Macchietto, S.: A dynamic, distribution model of shell and tube heat exchangers undergoing crude oil fouling. J. Ind. Eng. Chem. Res. **50**, 4515–4533 (2011)
Dipama, J., Teyssedou, A., Mikhaïl, S.: Synthesis of heat exchanger networks using genetic algorithms. Appl. Therm. Eng. **28**(14), 1763–1773 (2008)
Donohue, A.: Ind. Eng. Chem. **41**(11), 2499 (1949)
Heat-Int: Version 1.4.1.335, Built by Process Integration Limited (PIL) (2012)
HYSYS: Integrated simulation environment features advances in steady state and dynamic capabilities critical for optimal design of upstream and refining processes, Aspen Technology Inc. (2003)
Levine, L.: Estimating moisture flash upon discharge from an extrusion die. Cereal Food World. **42**, 144 (1997)
Linnhoff, B.: Introduction to Pinch Technology, pp. 1–63 (1998)
Linnhoff, B., Hindmarsh, E.: The pinch design method for heat exchanger networks. Chem. Eng. Sci. **38**(5), 745 (1983)
Linnhoff, B., Townsend, D.W., Boland, D., Hewitt, G.F., Thomas, B.E.A., Guy, A.R., Marsland, R.H.: A User Guide on Process Integration for Efficient Use of Energy. Warwick Printing Company Ltd, Warks (1982)
Liporace, F.S., Pessoa, F.L.P., Queiroz, E.M.: Heat exchanger network synthesis considering change phase streams. Therm. Eng. **3**(2), 87–95 (2004)
Nejad, S.H.A., Shahraki, F., Birjandi, M.R.S., Kovac Kralj, A., Fazlollahi, F.: Modification of heat exchanger network design by considering physical properties variation. Chem. Biochem. Eng. **26**(2), 79–87 (2012)
Pho, T.K., Lapidus, L.: Topics in computer-aided design. Part II. Synthesis of optimal heat exchanger networks by tree searching algorithms. AICHE J. **19**, 1182–1189 (1973)
Ponce-Ortega, J.M., Jiménez-Gutiérrez, A., Grossmann, I.E.: Optimal synthesis of heat exchanger networks involving isothermal process streams. Comp. and Chem. Engng. **32**, 1918–1942 (2008)
Singh, R.P., Heldman, D.R.: Introduction to Food Engineering. Academic Press Inc., San Diego (1993)
Sinnott, R.K.: Chemical Engineering Design, vol. 6, 4th edn. Elsevier Butter-Worth Heinemann, Oxford (2005)
Smith, R.: Chemical Process Design and Integration. John Wiley and Sons Ltd (2005). isbn:0-471-48680-9
Weber, H.F.: Ann. Phy. Chem. **10**(103) (1980)
Wilkes, J.O., Birmingham, S.G., Kirby, B.J., Cheng, C.: Fluid Mechanics for Chemical Engineers, 2nd edn. Prentice Hall International Series in the Physical and Chemical Engineering Science, Upper Saddle River (2010)

Ecological Analysis of a Wind-Diesel Hybrid Power System in the South Algeria

Khaireddine Allali and El Bahi Azzag

1 Introduction

Energy is one of the major inputs for the economic development of any country. In the case of the developing countries, the energy sector assumes a critical importance in view of the ever-increasing energy needs requiring huge investments to meet them. The growth of the world's human population has created several problems. One of them is global warming caused by the abundance of CO_2 in the atmosphere. Many of these gases are produced from electrical plants burning fossil fuel all over the world. To reduce these emanations out into the atmosphere, alternative sources of energy must be used. In the last two decades, solar energy and wind energy have become an alternative to traditional energy sources. These alternative energy sources are nonpolluting, free in their availability, and renewable De Souza Ribeiro et al. (2011).

In isolated areas such as the Algerian Sahara (Adrar, Bechar, In Salah, Timimoun, Tindouf, Amenas, etc.), electrical energy is often produced with the help of diesel generators. Moreover, the electricity production by the diesel is ineffective, presents significant environmental risks (spilling), contaminates the local air, and largely contributes to GHG emission. In all, we estimate at 16,086 kg/year GHG emission resulting from the use of diesel generators for the subscribers of the autonomous networks in Algeria Basbous et al. (2012), Saheb-Koussa et al. (2010). But numerous isolated areas have significant wind energy potential. It is then interesting to associate diesel with some wind generators as diesel electricity is generally more expensive than wind electricity. To reduce fuel

K. Allali (✉) • E.B. Azzag
Badji Mokhtar University-Annaba, Faculty of Engineering Science, Electrical Engineering Department, P.O. Box 12, Annaba 23000, Algeria
e-mail: allali23000@gmail.com

© Springer International Publishing AG, part of Springer Nature 2018

F. Aloui, I. Dincer (eds.), *Exergy for A Better Environment and Improved Sustainability 2*, Green Energy and Technology,
https://doi.org/10.1007/978-3-319-62575-1_64

consumption and power variations of the diesel, an energy storage system can be associated with the wind-diesel system Leclercq et al. (2003).

The subject of this work is to combine these diesel generators (DG) with wind turbine generators (WTG) plant sized to the needs of consumption, while providing continuous high-quality electric power. The main goal with wind-diesel hybrid system (WDHS) is to reduce fuel consumption and in this way to reduce system operating costs for economic purpose and environmental impact. This system equipped with a control system; a proper control strategy has to be developed to take full advantage of the wind energy during the periods of time.

Nomenclature

WDHS	Wind-diesel hybrid system
DG	Diesel generator
WTG	Wind turbine generator
GHG	Greenhouse gas
DCS	Distributed control system
P	Air density (kg/m^3)
A	Area swept by turbine blades (m^2)
C_p	Rotor power coefficient
v_ω	Wind speed (m/s)

2 Geographical and Meteorological Data of the Studied Site

2.1 Geographical Situation

The studied site is located in Adrar region with geographical coordinates (27°59′N, 0°11′W, 263 m). Adrar state situated in the extreme Algerian South-West extends about over 427,968 km^2 (1/5) of the country.

2.2 Meteorological Data

The climate data of wind speed recorded at Adrar region (Algeria) for the year 2012 were measured at the weather station of the Renewable Energy Research Unit in Saharan Medium (URER-MS) Adrar (see Table 1 below), URER-MS (2012).

Table 1 Wind speed data for a studied site

Months	January	February	March	April	May	June	July	August	September	October	November	December
v (m/s)	6.44	6.22	6.05	5.33	6.27	5.27	7.78	6.41	4.94	4.8	4.86	5.58

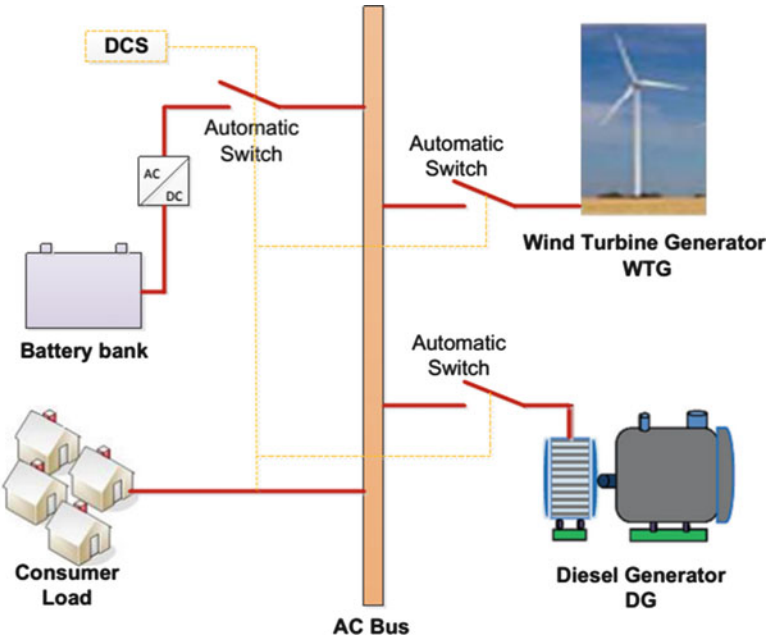

Fig. 1 Schematic diagram of the hybrid wind-diesel generation power system

3 Hybrid System Overview

In this study, Fig. 1 shows the configuration considered in this paper. This configuration consists of wind turbine generator (WTG), diesel generator (DG), battery bank, consumer load, power electronic converters (AC/DC rectifier, DC/AC inverter), monitoring system, distributed control system (DCS), switches and relays, controller and other accessory devices, and cables Kamal et al. (2010), Ibrahim et al. (2011).

4 Operation Modes of Wind-Diesel Hybrid System

The WDHS is classified as being high penetration (HP), Ibrahim et al. (2011). HP-WDHS have three modes as follows:

1. Weak winds ($v_\omega \leq 3$ m/s): diesel only (DO)
2. Moderate winds (3 m/s $< v_\omega \leq 10$ m/s): wind and diesel (WD) in service
3. Strong winds ($v_\omega > 10$ m/s): wind only (WO)

5 The Proposed Control System Strategy

For a multisource energy system, a power flow management strategy is needed according to wind speed values and the power demanded by the consumer load. The power management strategy used in this study is according to the flow chart shown in Fig. 2 (Sedaghat et al. 2012).

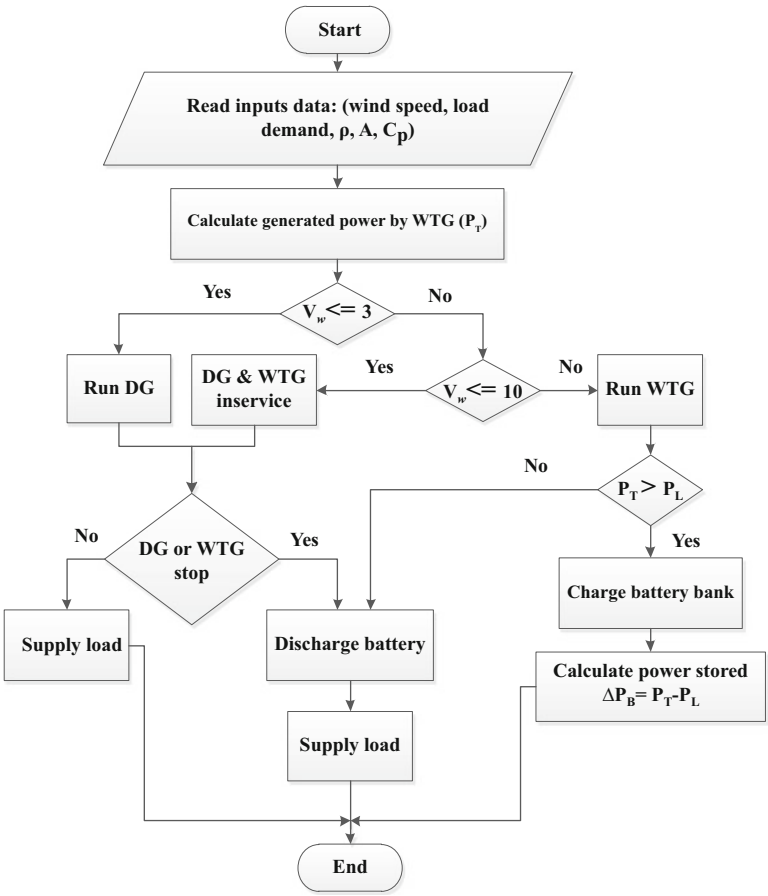

Fig. 2 Main flow chart

6 Simulation Results and Discussions

From Table 1, the highest wind speed was in July (7.78 m/s). Figure 3 shows the average daily wind speed for the considered site in July.

The load detail for the hybrid system shown in Fig. 4 shows the load profile adopted in this study. This profile is considered to be the same for all the days of the year with peak load as 98 kW.

Figure 5 shows electricity produced by wind turbine generator and diesel generator. The wind turbine generator only supplies energy during 12th days; in these cases, the generated power (P_T) is greater than the required power by the consumer load (P_L). So, the surplus wind energy will be stored in a battery bank. But on July 7 and 22, the supply power is ensured by diesel generator only because the wind speed is less than 3 m/s. The battery bank is used only when the renewable source and/or the conventional diesel power system is not able to satisfy the load demand and also when the DG or WTG broke down.

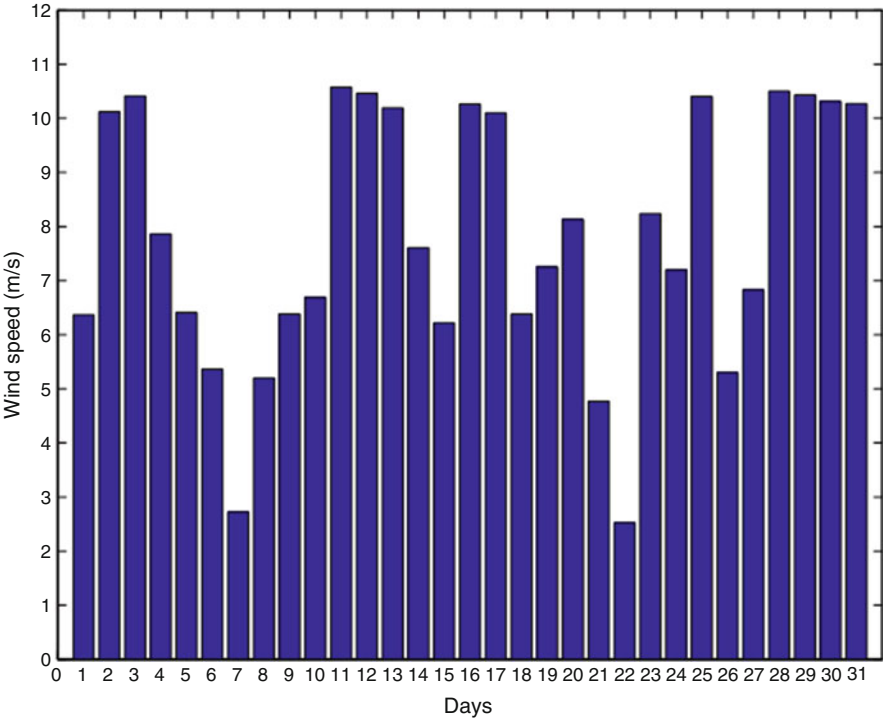

Fig. 3 The average daily wind speed in July

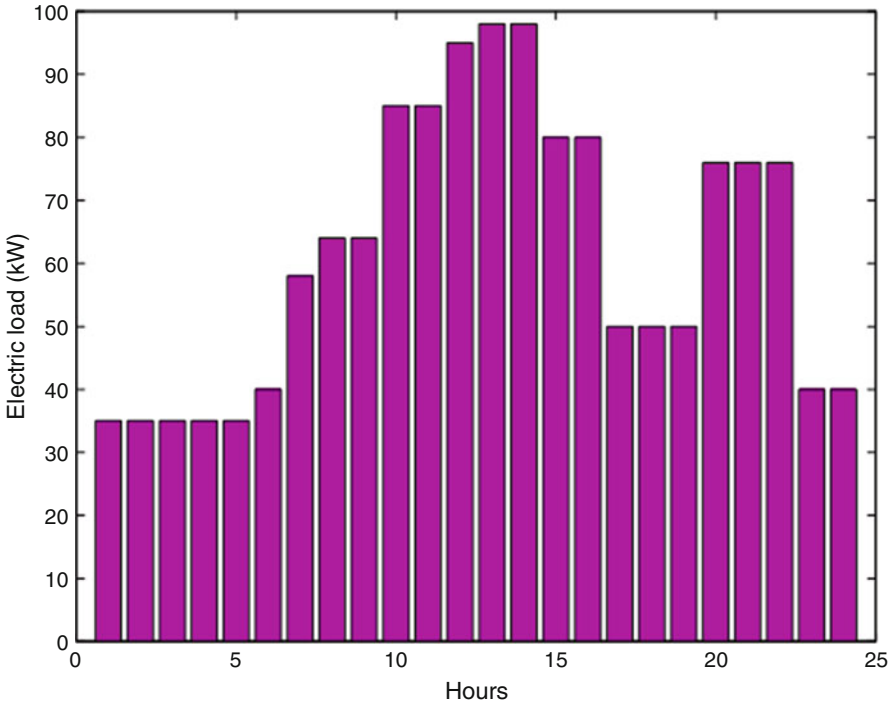

Fig. 4 The daily profile load

The summary of various costs related to the hybrid wind-diesel power system is summarized in Table 2: the energy cost of WTG is greater than DG; this is due to the number of operation of each system, while the latter has the effect of fuel consumption and its impact on CO_2 emissions, moreover cost of fuel consumption.

7 Conclusions

This paper presents a techno-economic analysis and the design of a complete hybrid system, consisting of a wind turbine generator, a diesel generator, and a battery system as a backup power source for a typical isolated area situated in Adrar region. We have demonstrated that the electricity produced with the help of diesel generators is relatively inefficient, very expensive, and responsible for the emission of

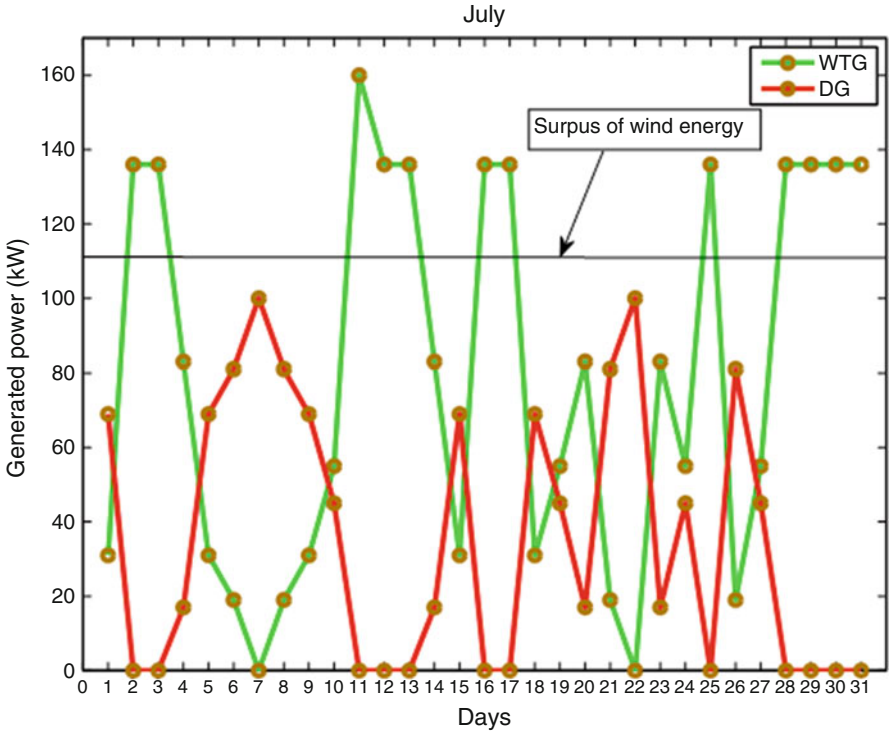

Fig. 5 The daily energy production by wind-diesel hybrid system

greenhouse gas (GHG). The WDHS is a great potential, technical, economical, and ecological promoter and very cost-effective compared with the traditional diesel system. This system has a good control strategy for the management of different power sources (wind, diesel, battery) that allows to optimize the operation of the hybrid system, to take full advantage of the wind energy during the periods of time, and to minimize diesel fuel consumption, in this way to reduce system operating costs and environmental benefits. Therefore, the wind-diesel power system is widely recommended especially for isolated sites that have significant wind energy potential.

Table 2 Summary of various costs related to the hybrid wind-diesel power system

Days	Energy cost WTG (DA) (5.958 DA/kWh)	Energy cost DG (DA) (5.958 DA/kWh)	Fuel consumption (*l*/day)	Fuel cost (DA) (13.7 DA/*l*)	CO_2 emission (kg/day) (2.6 kg/*l*)
1	180.42	411.102	25.119	344.1303	65.3094
2	791.52	0	0	0	0
3	791.52	0	0	0	0
4	483.06	101.286	12.327	168.8799	32.0502
5	180.42	411.102	25.119	344.1303	65.3094
6	110.58	482.598	28.071	384.5727	72.9846
7	0	595.8	32.745	448.6065	85.137
8	110.58	482.598	28.071	384.5727	72.9846
9	180.42	411.102	25.119	344.1303	65.3094
10	320.1	268.11	19.215	263.2455	49.959
11	931.2	0	0	0	0
12	791.52	0	0	0	0
13	791.52	0	0	0	0
14	483.06	101.286	12.327	168.8799	32.0502
15	180.42	411.102	25.119	344.1303	65.3094
16	791.52	0	0	0	0
17	791.52	0	0	0	0
18	180.42	411.102	25.119	344.1303	65.3094
19	320.1	268.11	19.215	263.2455	49.959
20	483.06	101.286	12.327	168.8799	32.0502
21	110.58	482.598	28.071	384.5727	72.9846
22	0	595.8	32.745	448.6065	85.137
23	483.06	101.286	12.327	168.8799	32.0502
24	320.1	268.11	19.215	263.2455	49.959
25	791.52	0	8.145	111.5865	21.177
26	110.58	482.598	28.071	384.5727	72.9846
27	320.1	268.11	19.215	263.2455	49.959
28	791.52	0	0	0	0
29	791.52	0	0	0	0
30	791.52	0	0	0	0
31	791.52	0	0	0	0
Total	**14194.98**	**6655.086**	**429.537**	**5884.6569**	**1116.7962**

References

Basbous, T., Younes, R., Ilinca, A., Perron, J.: A new hybrid pneumatic combustion engine to improve fuel consumption of wind-diesel power system for non-interconnected areas. Appl. Energy. **96**, 459–476 (2012)

De Souza Ribeiro, L.A., Saavedra, O.R., De Lima, S.L., De Matos, J.G.: Isolated micro-grids with renewable hybrid generation: the case of Lençóis Island. IEEE Transactions on Sustainable Energy. **2**(1), 1–11 (2011)

Ibrahim, H., Younès, R., Basbous, T., Ilinca, A., Dimitrova, M.: Optimization of diesel engine performances for a hybrid wind-diesel system with compressed air energy storage. Energy. **36**, 3079–3091 (2011)

Kamal, E., Koutb, M., Sobaih, A.A., Abozalam, B.: An intelligent maximum power extraction algorithm for hybrid wind diesel-storage system. Electrical Power and Energy Systems. **32**, 170–177 (2010)

Leclercq, L., Robyns, B., Grave, J.-M.: Control based on fuzzy logic of a flywheel energy storage system associated with wind and diesel generators. Math. Comput. Simul. **63**, 271–280 (2003)

Saheb-Koussa, D., Haddadi, M., Belhamel, M.: Etude de faisabilité et optimisation d'un système hybride (Eolien-PhotovoltaÏque-Diesel) à fourniture d'énergie électrique totalement autonome. Rev. Sci. Fond. App. **2**(1), 84–95 (2010)

Sedaghat, B., Jalilvand, A., Noroozian, R.: Design of a multilevel control strategy for integration of stand-alone wind/diesel system. Electrical Power and Energy Systems. **35**, 123–137 (2012)

Weather station of the Renewable Energy Research Unit in Saharian Medium (URER-MS) Adrar, Algeria. http://www.urerms.dz/ (2012)

Comparative Study of Two Integrated Solar Collectors with Symmetric and Asymmetric CPC Reflectors Based on a Ray Trace Analysis

Olfa Helal, Raouf Benrejeb, and Béchir Chaouachi

1 Introduction

In order to achieve temperatures in excess of approximately 70 °C from a solar collector, the weak solar radiation has to be concentrated (Helal et al. 2011a). By using internal reflectors, the hot absorber area can be reduced and this minimizes the heat losses. CPCs (Compound parabolic Concentrators) are the optimal choice, since they have the capability of reflecting to the absorber the maximum possible incident radiation (Helal et al. 2011a). The design and performance of different CPC configurations are described in numerous references (Rabl 1976; Souliotis and Tripanagnostopoulos 2008; Colina-Marquez et al. 2010; Helal et al. 2011a; Benrejeb et al. 2015).

Integrated Collector Storage (ICS) systems can satisfactorily cover the need of about 100–200 l per day of hot water in the low temperature range of 40–70 °C (Helal et al. 2011a). These systems consist of one device with dual operation, to collect solar radiation and to preserve the heat of the water storage tank during the night. The main advantages of ICS systems are their lower cost and simpler construction compared to the Flat Plate Thermosiphonic Units (FPTU). On the other hand, their main problem is the greater thermal losses of the stored water tank compared to the corresponding thermal losses of the water tank in the FPTU (Helal et al. 2010). Many researchers have studied the design of several types of ICS systems (Tripanagnostopoulos and Yianoulis 1992; Kessentini and Bouden 2013;

O. Helal (✉) • R. Benrejeb • B. Chaouachi
University of Gabes, National High Engineering School, Research Unit: Environment, Catalyzes and Process Analysis, Omar Ibn Khettab Street, 6029 Gabes, Tunisia
e-mail: helal_olfa@yahoo.fr

© Springer International Publishing AG, part of Springer Nature 2018

F. Aloui, I. Dincer (eds.), *Exergy for A Better Environment and Improved Sustainability 2*, Green Energy and Technology,
https://doi.org/10.1007/978-3-319-62575-1_65

Benrejeb et al. 2015), suggesting improvements for their operation which aim to achieve low cost systems with considerable thermal performance by maximizing solar radiation collection whilst minimizing thermal losses. The modeling of the solar radiation on a CPC can be made by using the ray-tracing technique based on computer programs (Souliotis and Tripanagnostopoulos 2008; Colina-Marquez et al. 2010; Helal et al. 2011b; Benrejeb et al. 2015).

In the present work, a ray trace analysis simulating the reflection of the solar radiation was done on two ICS solar water heater based on asymmetric and symmetric CPC reflectors: ICS_SCPC and ICS_ACPC. The first system was designed, realized, and experimented by (Helal et al. 2011a). It consisted of a compound parabolic concentrating (CPC) reflector composed of two concentrating stages: the first one contains two symmetric parabolic sections and the second one comprises one parabolic part. A cylindrical storage tank of volume equal to 100 l was placed on its focal plane. However, the second model was only designed for comparison. In this new design (ICS_ACPC), which is presented by (Benrejeb et al. 2015), the concentration system is also composed of two concentrating stages. The upper one comprises two symmetric parabolic branches with focal axes tilted by $\pm 48^{\circ}$ from the vertical plane. The lower one is constituted of three involute reflectors. Its cylindrical storage tank covers the triangle formed by the three involute part centers.

The two studied models differ only in the design of the lower stage concentrator and also the placement of their cylindrical storage tanks of same volume. This choice was done for comparison.

Truncation of the upper part of the reflectors was carried out to 50% in order to reduce their sizes, minimize their manufacturing cost, and facilitate their installation.

For this target, a theoretical study based on the ray trace analysis was done on both systems. This technique allows plotting and simulating the reflected rays on the CPC reflectors at any instant using mathematical equations written on a Matlab code. Then, this ray-tracing method was used to produce diagrams corresponding to the spatial distribution of the incoming solar radiation on the absorber surface.

The paper is organized as follows: Section 1 introduces an overview of the ICS systems and the different research studies done in this field. Section 2 provides the design of each studied system. In Section 3, the ray trace analysis is given. Section 4 deals with the energy flux distribution. Section 5 concludes the study.

Nomenclature

A_{app}	Aperture surface area (m^2)
A_{ab}	Absorber (receiver) surface area (m^2)
Al	Aluminum
C	Concentration ratio
D_{ab}	Cylindrical storage tank diameter (m)
D_s	Depth of the system (m)
f	Focal distance of the parabola (m)
F	Focus of the parabola

(continued)

I_b	Beam radiation (kJ = m^2 h)
I_d	Diffuse radiation (kJ = m^2 h)
I_T	Flux on a tilted surface (kJ = m^2 h)
R_i	For (i = 1, 2 and 3) is the radius of the ith involute reactor (m)
T	Translated vector of parameter a and b
V_{ab}	Cylindrical storage tank volume (l)
W	Half system entrance aperture width (m)
W'	Half exit aperture of the system (m)
(x; y)	Cartesian coordinate system
(x_{f1}; y_{f1})	The coordinates of focus F_1 (m)
(u; v)	Cartesian coordinate system rotated counter clockwise from vertical axis
Greek symbols	
α_r	Absorptivity of the absorbing surface
η_o	Optical efficiency
τ_s	Transmissivity of the cover
θ_a	Half acceptance angle of the CPC concentrator (rad)
ρ_r	Reflectivity of the reflector
ρ_e	Effective reflectivity of the concentrator surface for all radiation

2 Design of the ICS Models

2.1 Systems with Full CPC

Two integrated solar collectors with symmetric and asymmetric CPC reflectors (ICS_FSCPC and ICS_FACPC) of half acceptance angles of $\theta_a = 48^\circ$ were designed.

Side section views of the full collectors with their respective cylindrical storage tanks are illustrated in Figs. 1 and 2 and the specifications (physical and geometric characteristics) for each of the collectors are detailed in Table 1.

Both systems are characterized by:

(a) The upper stage concentrator is a symmetrical CPC reflector comprising parabolic reflectors AF_1 and BF_2 between entry aperture AB of width $2W$ and exit aperture F_1F_2 of width $2W'$. It is common to both systems ICS_FACPC and ICS_FSCPC, and it consists of an untruncated CPC of concentration ratio $C_1 = 2W/2W' = 1.34$. Both sections AF_1, BF_2 are parts of parabolas of focuses F_2, F_1 and focal axis parallel to BF_1, AF_2, which are tilted by 48° from the vertical plane.

Considering that the two branches are symmetrical relative to the *y*-axis thus it is enough to determine the equation of one branch and the other is deduced.

(b) The lower stage consists of:

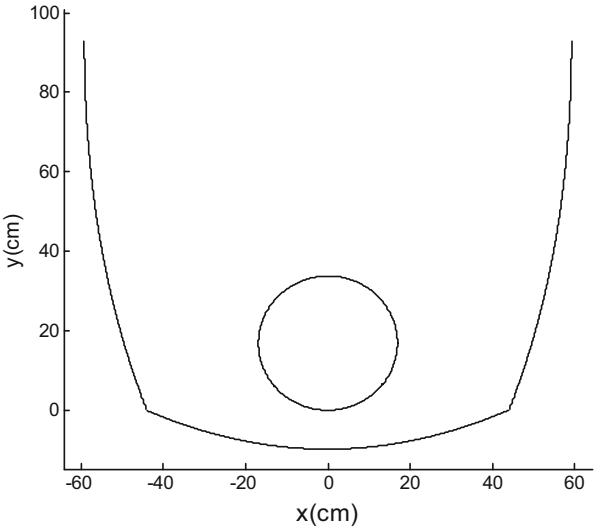

Fig. 1 Side section view of the ICS_FSCPC

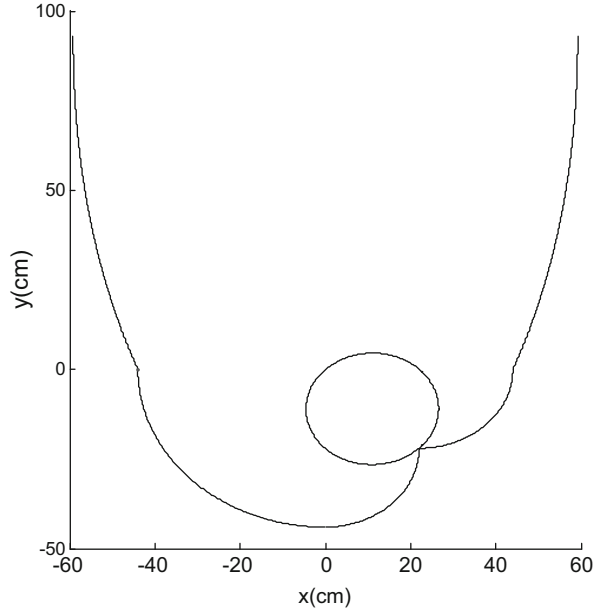

Fig. 2 Side section of the ICS_FACPC

- A parabolic reflector positioned in the exit aperture F_1F_2 of the first stage designed to reflect radiation on a cylindrical absorber of diameter D_{ab} set in the cavity of the system. The focal point of the parabolic reflector, F_3, is at the intersection of QF_1 and PF_2.
- An asymmetric CPC reflector with three involute parts (F_1C), (CD) and (DF_2) of radius $R_1 = W'$, $R_2 = 0.5R_1$ and $R_3 = R_2$.

Table 1 Geometric characteristics of the ICS_FSCPC and ICS_FACPC collectors

Characterization	ICS_SFCPC	ICS_AFCPC
Half acceptance angle	48°	48°
1st stage Concentration ratio	1.34	1.34
System concentration ratio	1.05	1.21
Aperture width(mm)	1180	1180
Aperture length (mm)	1270	1114
Reflector height (mm)	1084	1369
Absorber diameter(mm)	360	311
Absorber length (mm)	990	1114
Reflector material	Aluminum	Aluminum
Reflectivity of reflector	0.85	0.85
Total reflector length (mm)	3430	3282

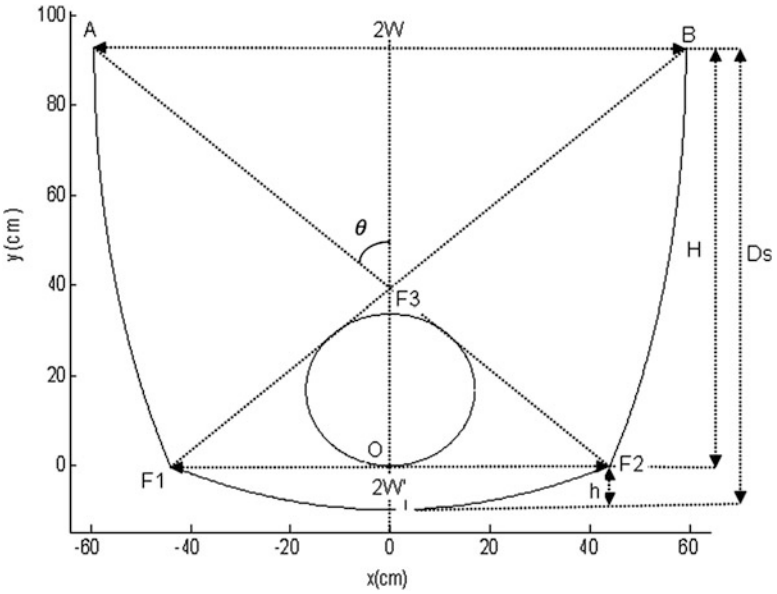

Fig. 3 Geometrical parameters of the ICS_FSCPC

(c) The cylindrical storage tank (absorber) has a volume $V_{ab} = 100$ l.

Figures 3 and 4 represent the different geometrical parameters of both models. Figure 5 gives a photo of the realized ICS_FSCPC.

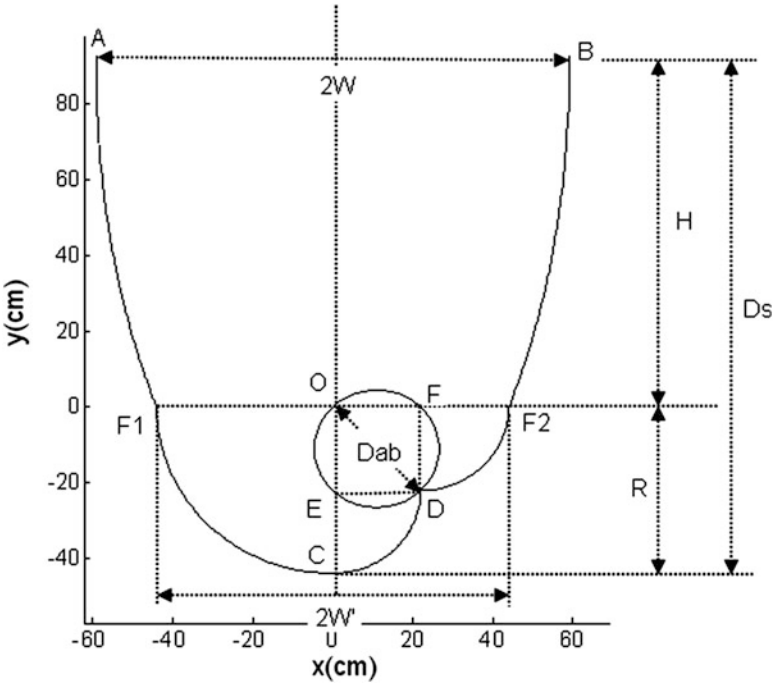

Fig. 4 Geometrical parameters of the ICS_FACPC

2.2 Systems with Truncated CPC

In a second step, truncation of the upper part of the reflectors was carried out to 50% for both collectors (ICS_TSCPC and ICS_TACPC) (Figs. 6 and 7).

Figures 3 and 4 give the side section views of both systems and the specifications (physical and geometric characteristics) are given in Table 2.

3 Ray Trace Analysis

Ray trace technique was employed to evaluate full and truncated CPC designs. Direct solar radiation was only considered.

In Figs. 8, 9, 10, and 11, 50 equally spaced rays across the collector aperture for the incident angles 0° and 30° were traced. It can be seen that:

- At 0° incident angle (case of Figs. 8b, 9, 10, and 11b) it can be observed that almost all the rays perpendicular to the aperture of the ICS systems reach the absorber directly or after being reflected by the reflector surfaces as it was expected and that even the absorber zones which were not exposed to direct

Fig. 5 Photo of the ICS_FSCPC

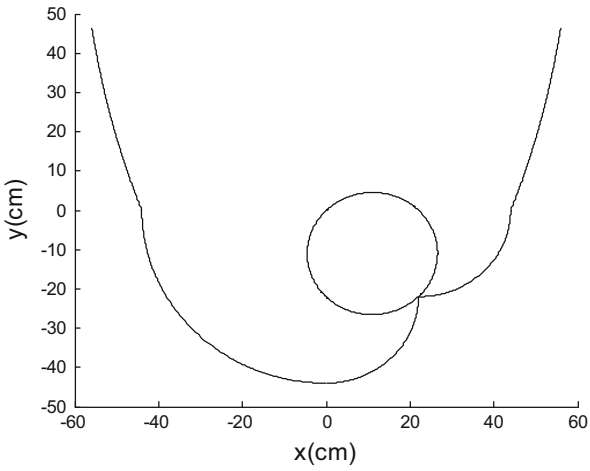

Fig. 6 Side section of the ICS_TACPC

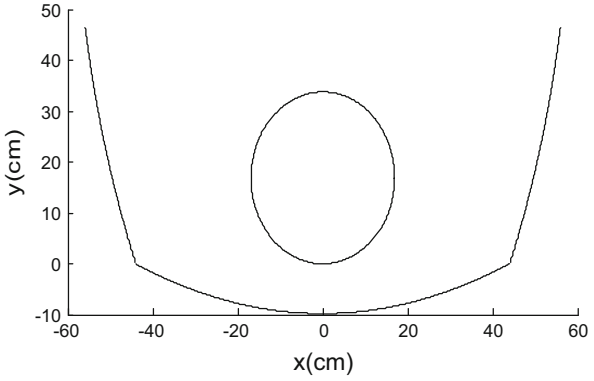

Fig. 7 Side sections of the ICS_TSCPC

Table 2 Geometric characteristics of the ICS_TSCPC and ICS_TACPC collectors

Characterization	ICS_TSCPC	ICS_TACPC
Half acceptance angle	65°	65°
1st stage Concentration ratio	1.27	1.27
System concentration ratio	0.98	1.14
Aperture width (mm)	559	559
Aperture length (mm)	1270	1114
Reflector height (mm)	563	905
Absorber diameter (mm)	360	311
Absorber length (mm)	1114	1114
Reflector material	Aluminium	Aluminium
Reflectivity of reflector	0.85	0.85

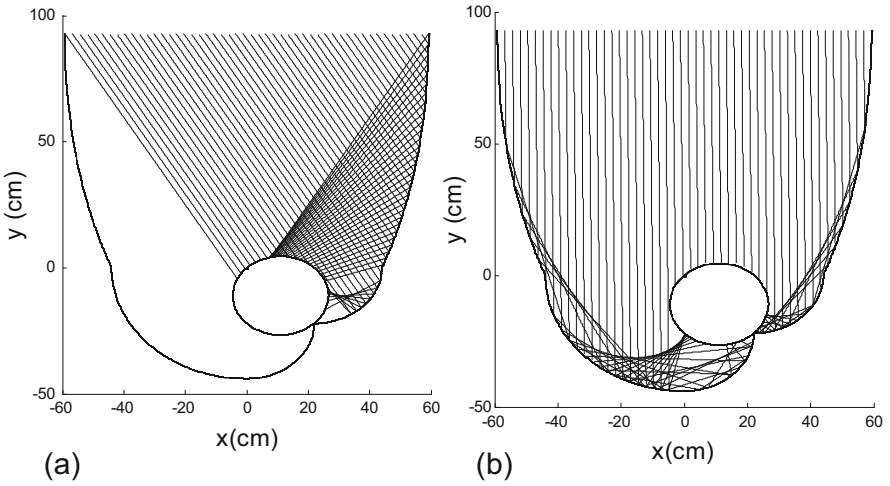

Fig. 8 Ray trace diagram for the ICS_FACPC profile with direct solar radiation at 30° (**a**) and perpendicular (**b**)

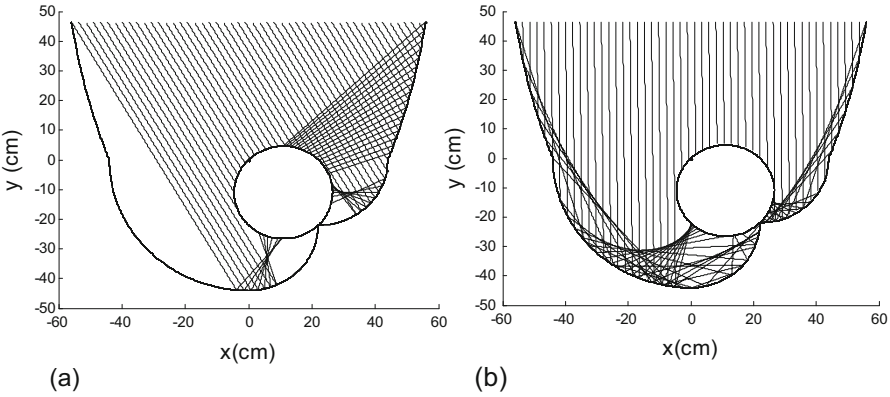

Fig. 9 Ray trace diagram for the ICS_TACPC profile with direct solar radiation at 30° (**a**) and perpendicular (**b**)

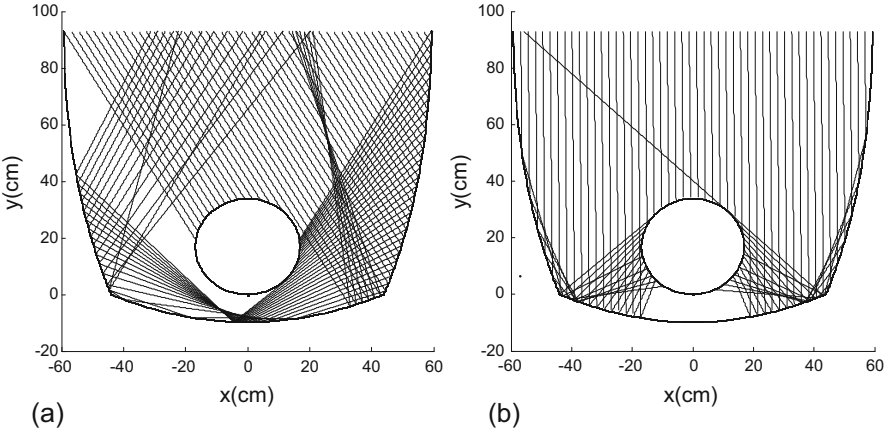

Fig. 10 Ray trace diagram for the ICS_FSCPC profile with direct solar radiation at 30° (**a**) and perpendicular (**b**)

radiation received some energy after successive reflections. This results in creating a mirror symmetry between the left and the right sides of the reflector and the absorber for the case of ICS_FSCPC and ICS_TSCPC. However, it does not create a symmetry for the ICS_FACPC and ICS_TACPC because of the asymmetrical shape of their corresponding reflectors.

- The ray trace diagrams at 30 incident angle (Figs. 8a and 9a) showed that rays are spread across the absorber sections, but not covering the full absorber and are more concentrated to the right side of both the full and truncated CPC collectors. The lower left of the absorber section in the truncated CPC collectors has more rays than that in the full collector. The concentration of the incident rays on the absorber becomes higher with truncation compared to that of full collectors.

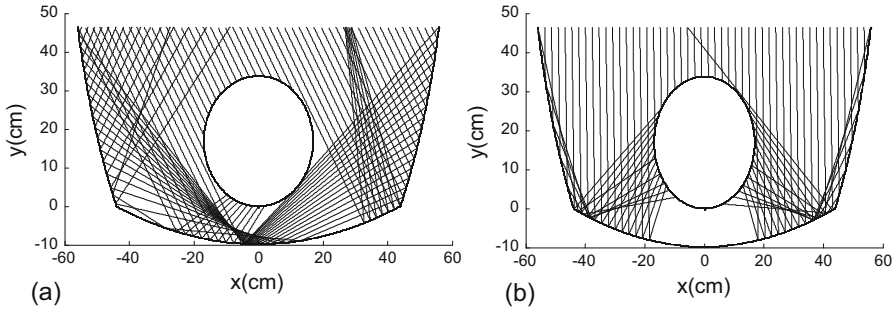

Fig. 11 Ray trace diagram for the ICS_TSCPC profile with direct solar radiation at 30° (**a**) and perpendicular (**b**)

- In Figs. 10a and 11a, it can be seen at 30° incident angle that at least an important proportion of solar rays which strike one or the two branches of the ICS_FSCPC and ICS_TSCPC designs are considered towards outside. This causes a reduction in absorbed energy flux. However, ICS_FACPC and ICS_TACPC designs make it possible to reflect all the rays towards the absorber, even having carried out some reflections.
- The truncation allows a fraction of solar radiation reaching the absorber directly or after being reflected. This fraction increases with the decrease of the height of the upper stage concentrator which improves the system's optical performances.

4 Energy Flux Distribution

The energy flux distribution diagrams showing the absorbed solar radiation distribution on the absorber of the ICS systems were generated and plotted by using the results of the developed ray trace technique. Figures 13, 14, and 15 illustrate at noon (12 h) the distribution patterns of the energy flux on the absorber of each ICS system. For all predictions, the solar radiation intensity assumed was 1000 W/m^2.

Figures 12 and 14 illustrate the distribution patterns of the energy flux distribution on the absorber of each of the full ICS_FSCPC and ICS_FACPC collectors at 0° and 30° incident angles. A variation in energy concentration was realized across the absorber resulting from variation of incidence angles of insolation on the aperture of the collectors. Different distribution patterns resulted from the reflection and refraction of incoming rays at different surfaces. Low energy peaks on the absorber resulted from low flux intensities emerging from either multiple intersecting of the rays with the reflector or rays missing the absorber and exiting to the external environment.

In Tables 1 and 2, several optical and thermal performances are given to compare between the two full ICS systems and then to show the effect of truncation

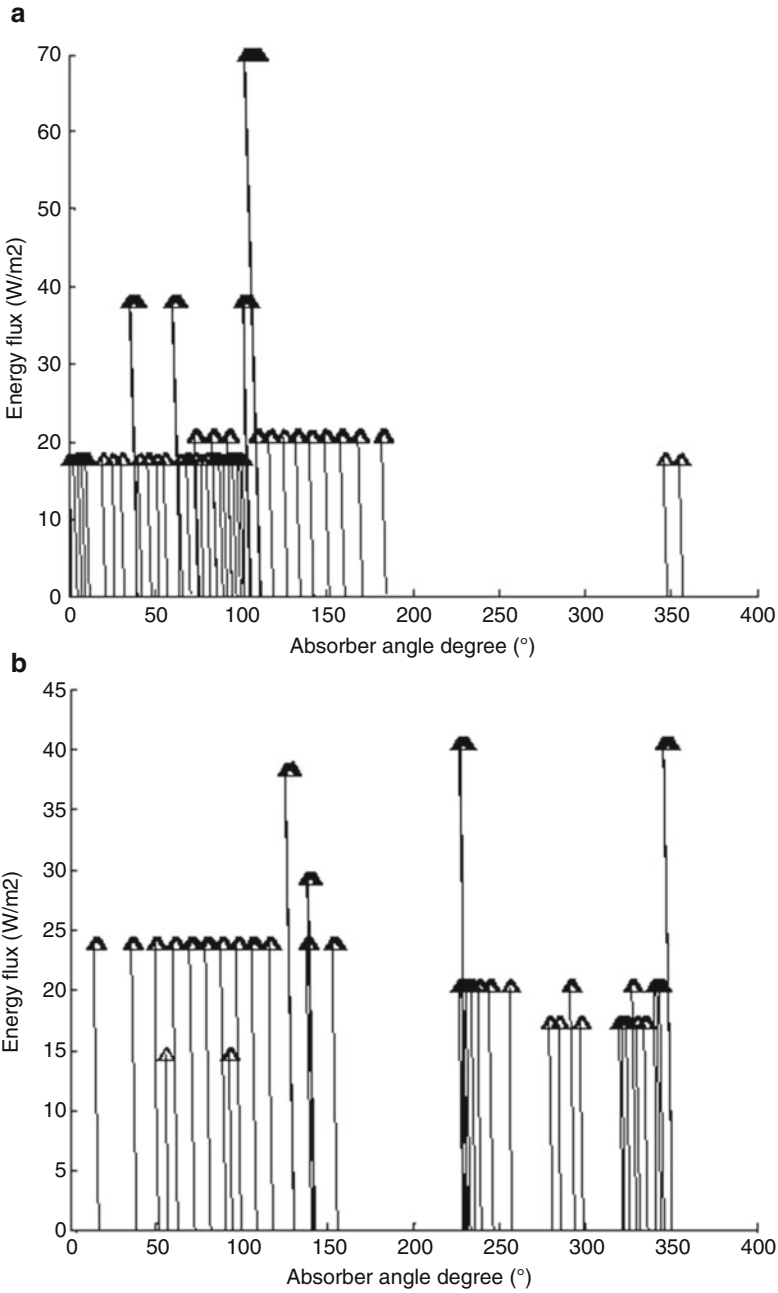

Fig. 12 Energy flux distribution on the absorber of ICS_FACPC at 12 h for incident angles 30 (**a**) and 0° (**b**)

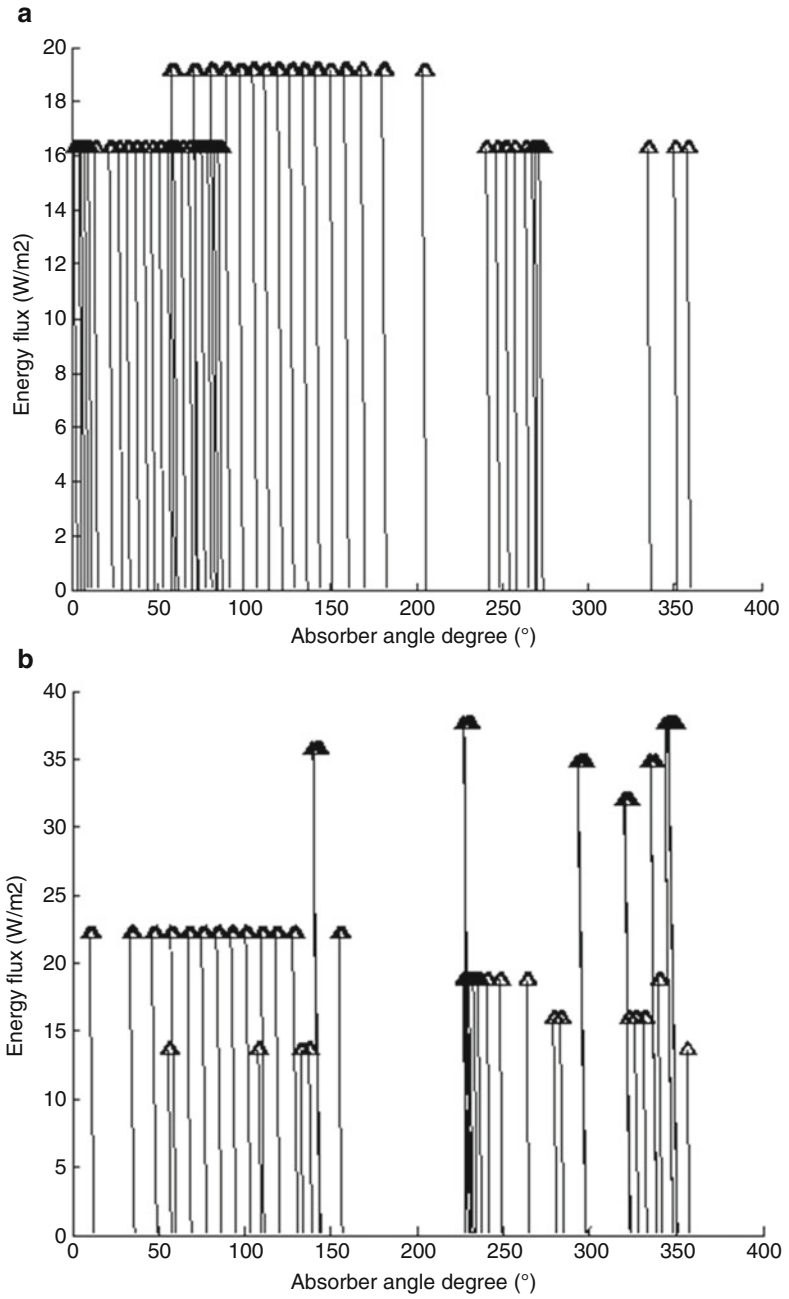

Fig. 13 Energy flux distribution on the absorber of ICS_TACPC at 12 h for incident angles 30 (**a**) and 0° (**b**)

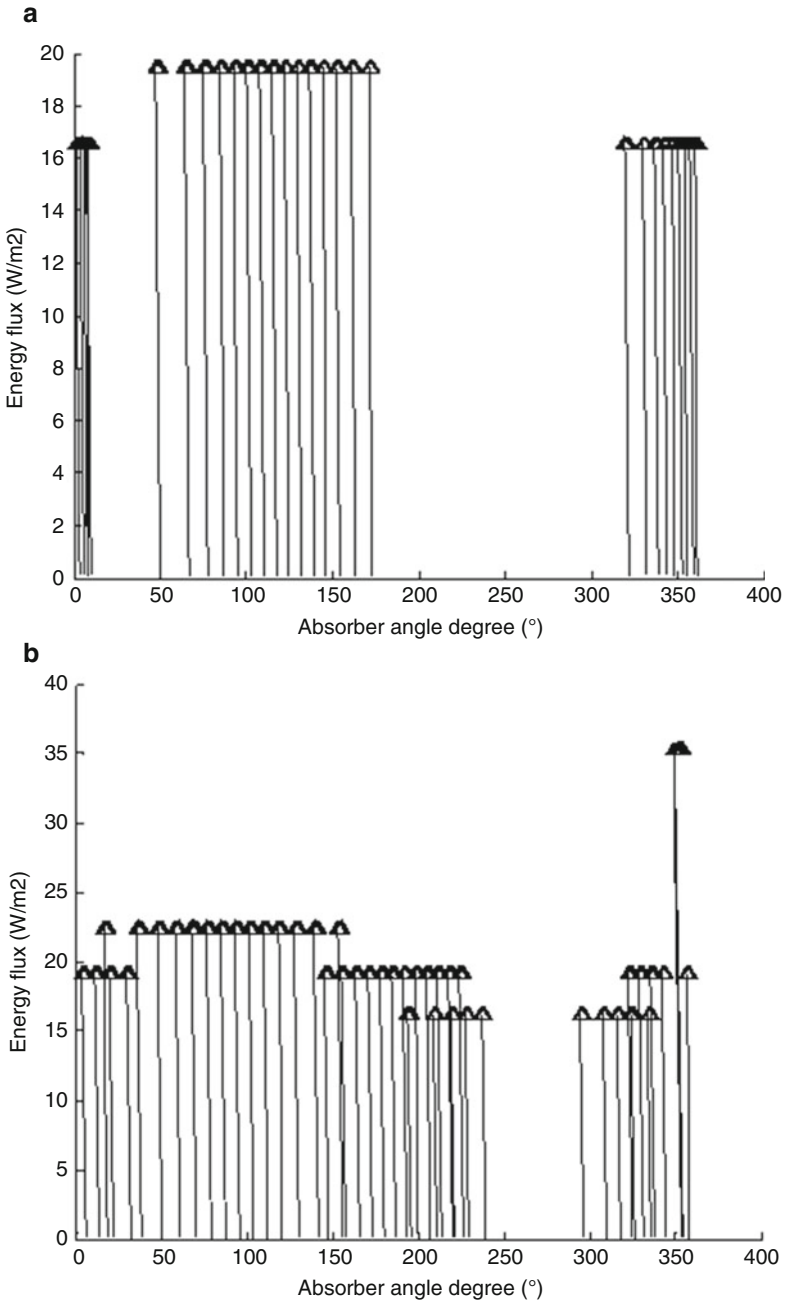

Fig. 14 Energy flux distribution on the absorber of ICS_FSCPC at 12 h for incident angles 30 (**a**) and 0° (**b**)

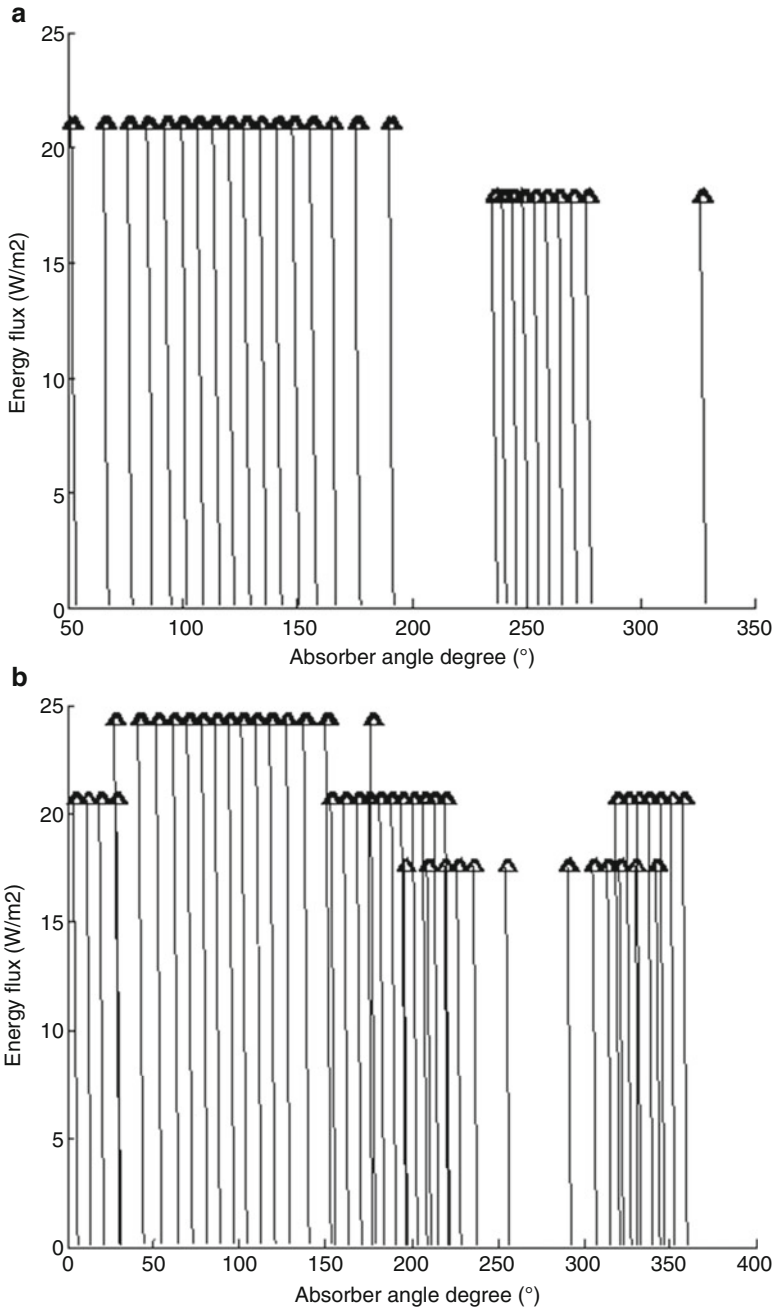

Fig. 15 Energy flux distribution on the absorber of ICS_TSCPC at 12 h for incident angles 30 (**a**) and 0° (**b**)

Table 3 Optical and thermal performances of the ICS_FSCPC and ICS_TSCPC collectors

		ICS_FSCPC	ICS_TSCPC
Average number of reflections	0°	0.94	0.92
	30°	0.38	0.36
Optical efficiency	0°	0.69	0.71
	30°	0.46	0.43
Total energy flux	0°	690	719
	30°	397	376

Table 4 Optical and thermal performances of the ICS_FACPC and ICS_TACPC collectors

		ICS_FACPC	ICS_TACPC
Average number of reflections	0°	1.26	1.22
	30°	0.72	0.7
Optical efficiency	0°	0.6	0.65
	30°	0.74	0.75
Total energy flux	0°	599	659
	30°	645	647

on each system. The average number of reflections, the optical efficiency, and the total energy flux are given at 0° and 30° incident angles.

From Tables 3 and 4, we can see:

- At 0° incident angle, the cylindrical absorber of the ICS_FSCPC receives about 690 W/m^2, and that of the ICS_TCPC obtains the value of 719 W/m^2. However, both absorbers of ICS_FACPC and ICS_TACPC receive only 599 W/m^2 and 659 W/m^2. At this incident angle, the full and truncated ICS_SCPC absorbed more energy flux than the ICS_ACPC collector. The gain is about 13.18% for the full design and 8.34% for the truncated one. If we compare the full with the truncated for both models, we can deduce that truncation has a positive effect on the received energy flux. A gain of 4% is reached for the symmetric design and 9.1% for the asymmetric model.
- An increase in incidence angle from 0° to 30° resulted in a reduction of ICS_SCPC (full and truncated) system total received energy flux. The ICS_FACPC achieves a gain of 38.44% and the ICS_TACPC wins 41.88%.

5 Conclusions

The ICS_SFCPC and ICS_AFCPC systems were modeled, analyzed, and compared using a ray trace technique based on a mathematical code written in Matlab. The investigation studied the behavior of the reflected radiation and the energy flux distribution on the absorber of each system at the incidence angles 0° and 30° for

the full and truncated designs. From the simulation analysis, a number of conclusions were determined:

- With incident solar radiation perpendicular to the aperture of the collector, the full and truncated ICS_SCPC perform better than the ICS_ACPC model (full and truncated).
- At 30° incident angle, the full and truncated ICS_ACPC perform better than the symmetric model.
- Truncation has a positive effect on the optical and thermal performances, especially at 0° incident angle for both designs.

References

Benrejeb, R., Helal, O., Chaouachi, B.: Optical and thermal performances improvement of an ICS solar water heater system. Sol. Energy. **112**, 108–119 (2015)

Colina-Marquez, J.A., Lopez-Vasquez, A.F., Machuca-Martinez, F.: Modeling of direct solar radiation in a compound parabolic collector (CPC) with the ray tracing technique. Dyna. **77** (163), 132–140. Medellin (2010)

Helal, O., Chaouachi, B., Gabsi, S., Bouden, S.: Design modeling and simulation of an integrated collector storage solar water heater. In: Proceedings of the International Conference CICME 10 (2010)

Helal, O., Chaouachi, B., Gabsi, S.: Design and thermal performance on an ICS solar water heater based on three parabolic sections. Sol. Energy. **85**, 2421–2432 (2011a)

Helal, O., Chaouachi, B., Gabsi, S., Colina-Marquez, J.: Ray tracing technique analysis of an integrated collector storage solar water heater. In: The International Conference on Energy systems and Technologies ICEST 2011, Cairo, 14–17 Mar 2011b

Kessentini, H., Bouden, C.: Numerical and experimental study of an integrated solar collector with CPC reectors. Renew. Energy. **57**, 577–586 (2013)

Rabl, A.: Solar concentrators with maximal concentration for cylindrical absorbers. Appl. Opt. **15**, 1871–1873 (1976)

Souliotis, S., Tripanagnostopoulos, Y.: Study of the distribution of the absorbed solar radiation on the performance of a CPC-type ICS water. Renew. Energy. **33**, 846–858 (2008)

Tripanagnostopoulos, Y., Yianoulis, P.: Integrated collector/storage systems with suppressed thermal losses. Sol. Energy. **48**, 31–43 (1992)

Thermoeconomic Optimization of Hydrogen Production and Liquefaction by Geothermal Power

Ceyhun Yilmaz, Mehmet Kanoglu, and Aysegul Abusoglu

1 Introduction

Sustainable energy economy requires sustainable production of energy from renewable energy sources. Hydrogen is a clean energy carrier for renewable energies. Geothermal-based hydrogen production is a potential pathway for a future hydrogen economy. Hydrogen has high energy content by mass but low energy content by volume in gas state. Storage of hydrogen is a challenging task. Hydrogen can be stored as a compressed gas at high pressures, as a liquid which requires a cryogenic temperature of −253 °C, or combined with other compounds in a solid form like being absorbed in a metal hydride. Storage in gas state requires very large tanks; liquefaction requires large work input and super insulated storage tanks; and a metal hydride can only absorb a small amount of hydrogen. Also, hydrogen liquefaction is a low-efficiency process (Scott 2007).

In the last 30 years the development of thermoeconomics has been impressive in more than one direction. The recent developments by Tsatsaronis and Pisa (1994), Lozano and Valero (1993), Frangopoulos (1994), von Spakovsky (1994), and d'Accadia and Rossi (1998) adequately represent the different directions of development. With regard to thermoeconomic optimization methodologies, Tsatsaronis et al. (2002) use an iterative technique of thermoeconomic performance improvement where the analyzer can take part in decision making in the optimization process. Valero et al. (1994) have used the concept of assigning appropriate cost to each and every exergy flow, and thermoeconomic performance improvement of the system is done through local optimization of the subsystems. Frangopoulos (1994) and von Spakovsky (1994) have used the functional decomposition of the

C. Yilmaz (✉) • M. Kanoglu • A. Abusoglu
Department of Mechanical Engineering, University of Gaziantep, 27310 Gaziantep, Turkey
e-mail: ceyhunyilmaz16@gmail.com

© Springer International Publishing AG, part of Springer Nature 2018

F. Aloui, I. Dincer (eds.), *Exergy for A Better Environment and Improved Sustainability 2*, Green Energy and Technology,
https://doi.org/10.1007/978-3-319-62575-1_66

system in the thermoeconomic optimization of the systems. The major fields of application of these developments are the large cogeneration and combined power plants and chemical plants, whereas the domain of refrigeration and air-conditioning is limited. It is because the industrial utilities are probably considered with great interest, as they are capital intensive. However, the performances of refrigeration and air-conditioning have even higher rates of energy consumption and poor performance. These, therefore, deserve greater attention both in the design phase and in everyday handling.

In this study, the thermoeconomic optimization of a hydrogen production and liquefaction by geothermal power system using the thermoeconomic evaluation and optimization method, based on the works of Tsatsaronis et al. (2002), is presented.

The exergoeconomic optimization approach uses an iterative design improvement procedure that does not aim at calculating the global optimum of a predetermined objective function, as the conventional optimization methods do, but tries to find a "good" solution for the overall system design. The basic idea lies in a commonly accepted concept from the cost viewpoint: At constant capacity for a well-designed component, group of components, or total system, a higher investment cost should correspond to a more efficient component and vice versa. With this approach, the cost-optimal exergetic efficiency is obtained for a component isolated from the remaining system components. The iterative exergoeconomic optimization technique consists of the following steps (Abusoglu and Kanoglu, 2009): (i) evaluation of the detailed schematics and inputs of the existing system (including the actual plant data), (ii) a detailed thermoeconomic analysis and evaluations of the system and obtaining the decision variables that affect both the exergetic efficiency and the investment costs, (iii) modification of the cost rates of the components having significantly higher cost rates than the remaining components, to their corresponding cost-optimal exergetic efficiency, and (iv) calculation of the relative deviations of the actual values from the cost-optimal values for the exergetic efficiency and relative cost difference.

In this study, the iterative exergoeconomic optimization method integrated from thermoeconomic isolation method and game theory is applied for the optimization of a hydrogen production and liquefaction by geothermal power system. The use of this optimization approach requires exergetic and exergoeconomic analysis results of the plant, and the exergoeconomic optimization procedure of the system is described. The procedure is used for obtaining cost-optimal exergetic efficiencies and related performance parameters for a component isolated from the remaining system components. The objective functions of the hydrogen production and liquefaction system components are expressed for the optimization criterion as a function of dependent and independent variables.

Nomenclature

C	Cost associated with an exergy stream ($/h)
c	Specific cost of exergy, cost per unit exergy ($/kJ)
Ex	Exergy (kW)
ex	Specific exergy (kJ/kg)

(continued)

f	Exergoeconomic factor
LHV	Lower heating value (kJ/kg)
LC	Levelized cost ($/yr)
PEC	Purchased equipment cost ($)
r	Relative cost difference
W	Power production or power consumption (kW)
y	Exergy destruction ratio over total exergy input
y^*	Component exergy destruction over total exergy destruction
Z	Cost associated with investment expenditure ($/h)
Greek symbols	
ε	Exergetic efficiency
τ	Capacity factor of plant operation
Subscripts	
CC	Carrying charge (for economic calculation)
F	Exergy of fuel
i	ith stream
k	kth component
D	Exergy destruction
OMC	Operation and maintenance
P	Exergy of product
tot	Overall system
Z	Investment costs

2 System Definition and the Assumptions Used in the System

Figure 1 shows the schematic diagram of a hydrogen production and liquefaction by geothermal power system, which uses geothermal water as power source for electrolysis and liquefaction units. The following assumptions are made and expressed below to analyze the system.

The system works in steady state. The temperatures of the condensers, heat exchangers, and electrolysis are constant and uniform throughout the components. The pressure losses in pipes between the components are neglected. The reference environmental state for the system is $T_0 = 25\ ^\circ\text{C}$ (environment temperature) and $P_0 = 1$ atm (atmospheric pressure). The geothermal water temperature at the production well is 200 °C and 100 kg/s (liquid dominated). The cooling water first enters the condenser at 25 °C, then passes through the condenser, and finally is rejected by the system at 35 °C. The air to be cooled enters the evaporator at 25 °C and leaves at 35 °C. The first flash process pressure assumption is 600 kPa at state 2. Binary cycle low and high pressures are between 400 and 2100 kPa, respectively. The flash cycle steam turbine exit proper pressure is 10 kPa for water-cooled

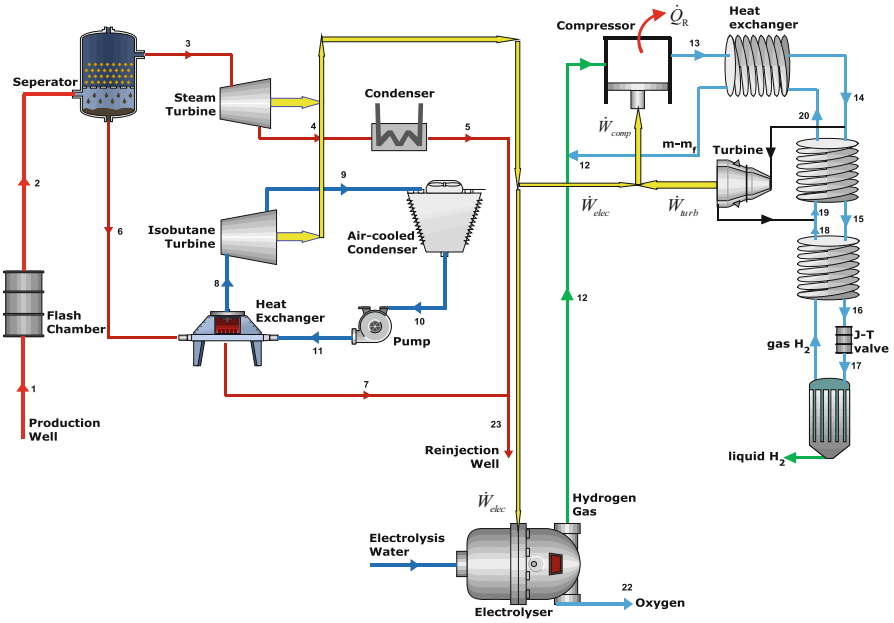

Fig. 1 An integrated system of hydrogen production and liquefaction by geothermal power

condenser. The isotropic efficiencies of all turbines and pumps are assumed to be 85%. The electrolysis operation pressure and the temperature are assumed to be 1 atm and 25 °C, respectively. The liquefaction cycle compressor pressure is assumed to be 4000 kPa at state 13. The cryogenic turbine gas fraction is assumed to be 0.6.

The combined flash binary geothermal power plants incorporate both a binary unit and a flashing unit to exploit the advantages associated with both the systems. The liquid portion of geothermal fluid serves as the heat input for the binary cycle and the steam portion of geothermal fluid drives a steam turbine to produce electrical power. The combined flash binary geothermal power plant operates in a closed loop with no environmental discharge and totally reinjection of geothermal fluid. The geothermal water supplies the energy input for the plant. As the result of the flashes process, the geothermal water properties are 158.8 °C and 600 kPa at the inlet state of the plant. The liquid part of the geothermal water for the binary cycle and the steam portion of geothermal water drives a steam turbine to produce power. In this first cycle, the extracted steam flows through the steam turbine to produce electricity while the geothermal water is reinjected to ground and condensed by water-cooled condenser. Then in the binary cycle of the plant, isobutene working fluid is heated and vaporized in the heat exchanger by the geothermal water. Then the isobutane flows through the turbine to produce electricity, and it is condensed by air-cooled condenser and pumped back to the heat exchanger, completing the binary cycle. Finally, the geothermal water collected from these two cycles is

reinjected back to the ground. The temperature of the isobutane at the inlet state of turbine (or at the exit state of the binary hehat exchanger) is taken to be 150 °C, which is lower than the separated liquid dominated geothermal water temperature at the heat exchanger inlet. About 20% of the power output is used for internal demands of the binary cycle and 5% of the power output is used for internal demand of steam cycle of geothermal plant, such as powering fans in the water and air-cooled condensers. These values closely correspond to those of an actual geothermal power plant.

The electrical power for electrolysis and liquefaction processes is supplied from the geothermal power plant. The geothermal power is used for the electrolysis to produce hydrogen gas and the remaining part of the power is used for the liquefaction of hydrogen gas in the Claude cycle. Alkaline water electrolysis process occurs in the environmental conditions. Hydrogen and oxygen are produced at the environmental conditions. The Claude cycle is shown on the right side of the Fig. 1. Hydrogen gas enters the compressor where its pressure is raised to a high value. The compressed hydrogen gas flows through a series of heat exchangers and eventually through a Joule-Thompson valve. Hydrogen to be liqufied continues through the process and is finally expanded through the expansion valve to the liquid recevier. The cold gas from the liquid recevier is returned through the heat exchangers to cool incoming gas.

A turbine extracts work from high-pressure hydrogen gas in order to reduce work requirement in the cycle.

3 Economic Modeling

The economic analysis takes into account the cost of each component, including operation and maintenance, and the cost of fuel consumption. To define a cost function, which depends on the optimization parameters of interest, component costs have to be expressed as functions of thermodynamic variables. Through an economic analysis, the levelized values of capital investment, fuel costs, and O&M cost for the entire economic life of the analyzed plant are calculated. The total revenue requirement (TRR) method was applied in this paper (Bejan et al. 1996). Table 1 summarizes the main assumptions and parameters used in the economic analysis. The economic life for all components and for the overall system was assumed to be 20 years except for the alkaline water electrolysis unit. The electrolysis unit lifetime was assumed to be approximately 40,000 h, so the stack should be replaced every 5 years (40,000 h with 85% of capacity factor cover nearly 5 years). The future value of the purchased equipment cost of the electrolysis unit is predicted using the nominal escalation rate (e.g., 5.0%) and is discounted to the present value, in 2014, using the average interest rate of return (e.g., 15%).

The purchase and equipment costs (PEC) of the components are estimated to the program of Aspen Plus economic analysis library (Aspen PlusV8.4 2014) and updated to the values for 1 January 2014. Details of the cost model of each component are summarized in Table 2.

Table 1 Aspen Plus assumption for the economic analysis of system (Aspen PlusV8.4 2014)

Parameter	Value
IF (ROR interest factor)	1.2
Nominal escalation rate (%)	5
Construction period (year) (1 January 2014–1 January 2015)	1
Start of commercial operation	January 2016
Economic lifetime for the plant (year)	20
Tax-related plant lifetime (year)	15
Average annual capacity factor (%)	85
Average labor cost ($/yr./person)	482,130
Fixed O&M cost (%)	161,075
Unit cost of isobutane [25]	15.6 $/GJ
Salvage value (percent of initial capital cost, %)	20
Depreciation method	Straight line
Tax rate (%)	40
AF (ROR annuity factor, %)	5
ROR (desired rate of return/interest rate, %)	15
Working capital percentage (%)	5

Table 2 Purchase equipment cost system of each component (Aspen PlusV8.4 2014)

Components	PEC ($10^3$$)	Z_k^{CI} ($/h)	Z_k^{OM} ($/h)	Z_k^{T} ($/h)
Flash valve	20.500	0.5289	0.1063	0.6352
Separator	65.200	1.682	0.3381	2.02
Steam turbine	92.600	24.32	4.889	29.21
Water-cooled condenser	242.900	6.266	1.26	7.526
Binary heat exchanger	348.600	8.993	1.808	10.8
Isobutane turbine	973.400	25.11	5.048	30.16
Air-cooled condenser	229.900	5.931	1.192	7.123
Pump	153.400	3.957	0.7956	4.753
Compressor	7620.000	196.6	39.52	236.1
Heat exchanger 1	69.300	1.788	0.3594	2.147
Heat exchanger 2	21.600	0.5572	0.112	0.6693
Heat exchanger 3	11.800	0.3044	0.0612	0.3656
Turbine	1228.000	3.168	0.6369	3.805
J-T valve	20.500	0.5289	0.1063	0.6352
Receiver	22.700	0.5856	0.1177	0.7033
Electrolysis unit	6.531.300	168.5	33.87	202.4
Other system components	500.00	12.9	2.593	15.49
Purchase and equipment costs (PEC)	17,886.800			
Operating and maintenance costs (OMC)	2962.878			

Through the economic analysis, the levelized cost of carrying charges and the levelized cost of OMC were calculated and the values were distributed to each component, proportionally to the purchased equipment cost. Finally, the values were converted considering the capacity factor of the whole plant operation, as expressed:

$$\dot{Z}_k = \left[\frac{\mathrm{CC_L} + \mathrm{OMC_L}}{\tau}\right] \frac{\mathrm{PEC}_k}{\sum_k \mathrm{PEC}_k} \tag{1}$$

All these levelized capital costs of each component, calculated in economic analysis, were used as inputs for the exergoeconomic analysis.

4 Thermoeconomic Modeling

In an exergoeconomic analysis the exergy costing principle is applied, in which a specific cost c_i is assigned to each exergy stream including material streams and energy streams (Bejan et al. 1996). Through this principle, all cost flows within a system can be analyzed comprehensively in a quantitative manner.

The cost rate associated with the ith stream is calculated by multiplying the specific cost of the ith stream c_i to the exergy rate of the same stream i as shown:

$$\dot{C}_i = c_i \dot{\mathrm{E}}\,\mathrm{x}_i = c_i\left(\dot{m}_i \mathrm{ex}_i\right) \tag{2}$$

To calculate the specific cost of each stream, a cost balance for each component should be stated as shown in Eq. (3), and it can be restated as Eq. (4) based on the concept of fuel exergy and product exergy for the component. Equation (3) implies that the cost of the exergy of fuel and the cost of capital investment for each component are charged to the exergy of product of the same component:

$$\sum_1^m \dot{C}_i + \dot{Z}_k = \sum_1^n \dot{C}_\mathrm{e} \tag{3}$$

$$\dot{C}_\mathrm{F} + \dot{Z}_k = \dot{C}_\mathrm{P} \tag{4}$$

The thermoeconomic costs of all the flows that appear in the system "Fuel·Product" definition are obtained through exergy costing principles. Exergy costing involves formulation of cost balances for each component, which are discussed in the following paragraphs. All cost balance equations and auxiliary equations applied to the system are summarized in Table 3.

When the abovementioned balance equations and auxiliary equations are stated and mathematically solved, the parameters for the exergoeconomic analysis can be calculated (Bejan et al. 1996). The cost of exergy destruction is calculated using Eq. (5):

Table 3 Cost balance equations and auxiliary equations for the exergy costing of the system

Components	Exergetic cost rate balance equations for the components of system	Auxiliary equations
Expansion valve	$\dot{C}_1 + \dot{Z}_{EV} = \dot{C}_2$	c_1 (known) c_2 (variable)
Separator	$\dot{C}_2 + \dot{Z}_{SEP} = \dot{C}_3 + \dot{C}_6$	$c_3 = c_6$
Steam turbine	$\dot{C}_3 + \dot{Z}_{ST} = \dot{C}_{W_{ST}} + \dot{C}_4$	c_{ST} (variable) $c_4 = c_3$
Water-cooled condenser	$(\dot{C}_4 - \dot{C}_5) + \dot{Z}_{WCC} = \dot{C}_b - \dot{C}_a$	$c_5 = c_4$ $c_a = 0$ c_b (variable)
Isobutane turbine	$\dot{C}_8 + \dot{Z}_{IT} = \dot{C}_{W_{IT}} + \dot{C}_9$	c_{IT} (variable) $c_9 = c_8$
Binary heat exchanger	$(\dot{C}_6 - \dot{C}_7) + \dot{Z}_{HE} = (\dot{C}_8 - \dot{C}_{11})$	$c_7 = c_6$ c_8 (variable)
Air-cooled condenser	$(\dot{C}_9 - \dot{C}_{10}) + \dot{Z}_{ACC} = (\dot{C}_d - \dot{C}_c)$	$c_{10} = c_9$ $c_c = 0$ c_d (variable)
Pomp	$\dot{C}_{10} + \dot{Z}_P + \dot{W}_P = \dot{C}_{11}$	c_5 (known) c_6 (variable)
Compressor	$\dot{C}_{12} + \dot{Z}_{COMP} + \dot{W}_{COMP} = \dot{C}_{13}$	c_{12} (known) c_{13} (variable)
Heat exchanger 1	$(\dot{C}_{12} - \dot{C}_{20}) + \dot{Z}_{HE1} = (\dot{C}_{13} - \dot{C}_{14})$	$c_{20} = c_{12}$ c_{14} (variable)
Heat exchanger 2	$(\dot{C}_{20} - \dot{C}_{19}) + \dot{Z}_{HE2} = (\dot{C}_{14} - \dot{C}_{15})$	$c_{19} = c_{20}$ c_{15} (variable)
Heat exchanger 3	$(\dot{C}_{18} - \dot{C}_{gas}) + \dot{Z}_{HE3} = (\dot{C}_{15} - \dot{C}_{16})$	$c_{18} = c_{gas}$ c_{16} (variable)
Rectifier	$\dot{C}_{17} + \dot{Z}_{REC} = \dot{C}_{gas} + \dot{C}_{liquid}$	$c_{liquid} = c_{gas}$
J-T valve	$\dot{C}_{16} + \dot{Z}_{EV3} = \dot{C}_{17}$	
Cryogenic turbine	$\dot{C}_{14'} + \dot{Z}_{TURB} = \dot{C}_{W_{TURB}} + \dot{C}_e$	$c_e = c_{14'}$ c_{TURB} (variable)
Electrolysis unit	$\dot{C}_{22} + \dot{Z}_{Electrolysis} + \dot{W}_{Elecricity} = \dot{C}_{12} + \dot{C}_{23}$	$c_{22} = 0$ c_{12} (variable)

$$\dot{C}_{D,k} = c_{F,k}\dot{E}x_{D,k} \tag{5}$$

where $c_{F,k}$ is the specific cost of the fuel exergy for the kth component, and it can be calculated using Eq. (6)

$$c_{F,k} = \frac{\dot{C}_{F,k}}{\dot{E}x_{F,k}} \tag{6}$$

Similar to the definition of specific cost of the fuel exergy, the specific cost of the exergy of product for the kth component can be calculated using Eq. (7):

$$c_{\mathrm{P},k} = \frac{\dot{C}_{\mathrm{P},k}}{\dot{\mathrm{E}}\,\mathrm{x}_{\mathrm{P},k}} \tag{7}$$

The exergoeconomic factor, which indicates how much the capital investment contributes to the total cost, is calculated using Eq. (8). In components showing a high value of fk the capital investment has a dominant effect on the total cost for the component, so reducing investment cost at the expense of thermodynamic efficiency can be considered for reducing the cost of the product from the overall system. A relatively low value of fk implies that the efficiency of the *k*th component could be improved by increasing the capital investment cost to reduce the exergy destruction, and the consequent exergy destruction cost of the component.

$$f_{\mathrm{k}} = \frac{\dot{Z}_{\mathrm{k}}}{\dot{Z}_k + \dot{C}_{\mathrm{D},k}} \tag{8}$$

Another important variable for the exergoeconomic evaluation is the relative cost difference, rk, which is defined by Eq. (9).

$$r_k = \frac{c_{\mathrm{P},k} - c_{\mathrm{F},k}}{c_{\mathrm{F},k}} = \frac{\dot{C}_{\mathrm{D},k} + \dot{Z}_k}{c_{\mathrm{F},k}\dot{\mathrm{E}}\,\mathrm{x}_{\mathrm{P},k}} \tag{9}$$

5 Thermoeconomic Optimization Modeling

The definition of the two objective functions of the multiobjective optimization problem, which are the exergetic efficiency of the plant (to be maximized) and the total cost rate of operation (to be minimized), are defined as follows (Baghernejad and Yaghoubi 2010):

$$\varepsilon_{\mathrm{overall}} = \frac{\dot{\mathrm{E}}\,\mathrm{x}_{\mathrm{P,\,total}}}{\dot{\mathrm{E}}\,\mathrm{x}_{\mathrm{F,\,total}}} \tag{10}$$

$$\dot{C}_{\mathrm{overall}} = \sum_k \dot{Z}_k \tag{11}$$

The thermodynamic decision variables should be chosen for the system optimization. The following decision variables are selected: the flash pressure of the geothermal water P_2, the compressor pressure ratio of liquefaction compressor P_{r}, the isentropic efficiency of the compressor η_{C}, the temperature of the binary isobutane entering the turbine T_8, the isentropic efficiency of the pump η_{P}, the isobutane inlet pressure of the heat exchanger P_{11}, and the cryogenic turbine mass fraction of liquefaction cycle x. The system is treated as the base case, and the

following nominal values of the decision variables are selected based on the operation program of the constructed site: $P_2 = 600$ kPa, $P_r = 40$, $\eta_C = 0.70$, $T_8 = 148.8$ °C, $\eta_p = 0.85$, $P_{11} = 2100$ kPa, and $x = 0.6$.

Although the decision variables may be varied in optimization procedure, each decision variable is normally required to be within a given practical range of operation as follows [29]: $100 \leq P_2 \leq 1000$ kPa, $10 \leq P_r \leq 50$ kPa, $0.70 \leq \eta_C \leq 0.90$, $130 \leq T_8 \leq 190$ °C, $0.70 \leq \eta_P \leq 0.90$, $1000 \leq P_{11} \leq 3000$ kPa and $0.5 \leq x \leq 0.8$.

6 Results and Discussion

For an objective system such as the geothermal hydrogen production and liquefaction system of the study, performance evaluation and optimization procedure are directly proportional to what may be considered as performance improvement and searching a good solution for the overall system rather than to find a global optimum results by EES subprogram of genetic optimization (application with exergoeconomic analysis) (Klein 2015). In Table 4, the system plant-based assumption results of energy and exergy analysis in the system with respect to Fig. 1 are given. Exergy flow rates, cost flow rates, and unit exergy costs associated with each stream of the system with 7572 kW electricity of geothermal plant, 126.2 kg/h hydrogen production, and 21.62 kg/h liquid hydrogen are given in Table 5.

In Table 6, unit exergetic costs of fuels and products, relative exergetic cost differences, exergy economic factors, cost rate of exergy destructions, and exergy efficiencies for the system components are shown.

The minimum value of the objective function of flash pressure against the number of generations, the fitness curve, is shown in Figs. 2 and 3. It is seen that after about 1000 iterations the objective function stabilizes with EES genetic optimization tool part. The corresponding plots of product cost, fuel cost, exergetic efficiency, cost of exergy destruction, and capital investment cost against the number of generations are shown in Table 7, respectively. The decision variables for the base case and optimum case are given in Table 7.

The comparative results of the base case and the optimum case are given in Tables 7 and 8. The results clearly show decrease in the product cost and the objective function. The exergy destruction, however, is increased by 16.2% with a 4.38% decrease in the exergetic efficiency of the system.

Table 8 compares the fuel exergy, total exergy destruction, fuel cost rate, and the cost rate of exergy destruction in the base case and optimal solution. According to Table 8, the optimization leads to 5.40% reduction in the fuel exergy, 16.2% increase in the total exergy destruction, and also 5.93 and 36.5% reduction in the unit exergetic cost rate of hydrogen production and liquefaction, respectively.

Table 4 System data, thermodynamic properties, mass flow rates, and exergy data in the system with respect to the state points of the ammonia-water absorption refrigeration cycle in Fig. 1

State	Pressure P (kPa)	Temperature T	Mass flow rate $\dot{m}$ (kg/s)	Enthalpy h (kJ/kg)	Entropy s (kJ/kg K)	Specific exergy ex (kJ/kg)
0	100	25	100	104.8	0.3672	0
0′	100	25	60.8	599	2.515	0
0″	100	25	2793	293.6	5.699	0
0‴	100	25	0.03486	3929	53.37	0
1	1555	200	100	352.3	2.331	162.3
2	600	159	100	352.3	2.352	153.6
3	600	159	8.72	2756	6.759	720.1
4	10	45	8.72	2233	7.049	138
5	10	45	8.72	191.8	0.6492	2.351
6	600	159	91.28	670.40	1.931	90.2
7	600	76	91.28	313.6	1.029	17
8	2100	149	60.8	302.7	2.689	145.5
9	400	100	60.8	732.5	2.722	72.99
10	400	30	60.8	270.8	1.245	50.03
11	2100	31	60.8	274.5	1.246	52.97
12	100	25	0.030	3929	53.37	117,113
13	5000	25	0.030	3951	37.24	4562
14	5000	−113	0.030	2015	28.55	5211
14’	5000	−113	0.180	2015	28.55	5211
15	5000	−210	0.012	732.4	16.07	10,128
16	5000	−226	0.012	450.7	10.85	12,889
17	100	−253	0.012	450.7	22.17	12,019
18	100	−208	0.00708	926	34.61	2596
19	100	−201	0.02508	999.7	35.69	3312
20	100	−143	0.02503	1613	25.76	5653
21	100	25	0.3115	104.8	0.3672	900
22	100	25	0.2767	0	0.89	3970
23	36	74	100	307.6	0.9971	15.1

7 Conclusions

Exergoeconomic and thermoeconomic evaluations are conducted for a geothermal-based hydrogen production and liquefaction system. The system and its components are analyzed using the first and second laws of thermodynamics. By combining exergetic analysis and economic calculations, the cost structure of each component and of the entire system are obtained. The electrolysis unit, liquefaction unit, heat exchangers, and turbines appear to be responsible for most of the exergetic costs. By using a geothermal water source at 200 °C at a rate of 100 kg/s, hydrogen gas can be produced to 0.038 kg/s and can be liquefied to −253 °C at a

Table 5 The exergy flow rates, unit exergy costs and the cost flow rates associated with each stream of the plant

State	$\dot{E}$ x (kW)	C ($/GJ)	$\dot{C}$ ($/h)
1	16,227	1.373	80.21
2	15,359	1.459	80.65
3	7247	1.484	38.73
4	1389	1.484	7.421
5	28.69	1.484	0.1533
6	8112	1.484	43.35
7	1529	1.484	8.171
8	8109	2.614	76.32
9	3844	2.614	36.18
10	2789	2.614	26.25
11	2953	3.157	33.56
12	8268	8.577	255.3
13	159.8	4.821	2.773
14	72.99	4.821	1.267
15	180.5	4.821	2.462
16	168.4	4.821	3.133
17	20.78	5.906	3.58
18	96.1	4.821	0.3607
19	164.2	4.821	1.668
20	281.6	0.003916	0.002315
21	1103	0	0
22	1510	0	0
23	16,227	1.531	8.324
e	51.47	4.241	0.7858
g	44.28	11.58	1.847
f	62.96	11.58	2.626
$\dot{W}_{P}$	193	11.11	8.928
$\dot{W}_{IT}$	2828	19.78	304
$\dot{W}_{ST}$	4778	2.14	35.14
$\dot{W}_{COMP}$	19	10.83	8.0315
$\dot{W}_{TURB}$	666.5	4.241	10.175
Produced hydrogen	8268	17.4	255.6
Liquid hydrogen	72.13	14.4	3.71

rate of 0.008 kg/s in the liquefaction cycle. Exergoeconomically optimal values for total product cost flow rate, total cost fuel flow rate, cost of electricity, cost of hydrogen production, and cost of hydrogen liquefaction are calculated to be 1820 $/h, 274.2 $/h, 0.01908 $/kWh, 1.967 $/kg, and 1.095 $/kg, respectively, whereas the corresponding actual base case values are 3031 $/h, 290 $/h, 34.34 $/h, 0.02076 $/kWh, 2.091 $/kg, and 1.725 $/kg, respectively. The use of geothermal energy in

Table 6 Energy, exergy, and exergoeconomic performance results for the subsystems in geothermal hydrogen production and liquefaction cycle

Component	$\dot{E}x_F$(kW)	$\dot{E}x_P$(kW)	$\dot{E}x_D$(kW)	ε (%)	r (%)	f (%)	$C_{F,k}$ ($/GJ)	$C_{P,k}$ ($/GJ)	($/h)
Steam turbine	5859	5029	829.2	85.8	92.8	82.24	1.462	2.95	3.96
Isobutane turbine	4877	4270	606.1	87.6	69.4	79.54	2.497	4.23	5.45
Pomp	223.5	190.2	33.36	85.1	47.4	82.82	5.766	3.036	0.693
Heat exchanger	7575	5978	1598	78.9	70.8	47.42	1.462	2.49	8.41
Air-cooled condenser	1291	433.8	857.6	33.6	69.4	39.36	2.497	4.23	7.71
Water-cooled condenser	1169	330.8	868.7	25.7	45.1	53.62	1.462	0.804	4.57
Separator	15,591	15,591	0	100	103.5	100	1.437	1.46	0
Expansion valve	16,227	15,591	636.6	96.1	4.66	12.42	1.373	1.44	3.15
Electrolysis unit	5484	4117	1367	75.1	201.7	83.36	5.766	17.4	28.4
Compressor	260.3	159	101.3	61.1	72.2	96.32	17.39	4.84	6.34
Heat exchanger 1	163.5	86.37	77.08	52.8	259.2	917.6	4.843	17.4	1.34
Heat exchanger 2	68.57	67.79	0.776	98.9	0	97.2	4.843	0.004	0.014
Heat exchanger 3	75.1	38.5	36.6	51.3	29.6	67.36	4.843	4.84	0.638
J-T valve	179.7	167.6	12.13	93.3	22.5	67.83	4.843	5.93	0.212
Rectifier	167.6	167.6	0	100	141.9	100	5.933	18.09	0
System	58,668	51,721	6947	88.2	945.2	91.85	1.373	14.4	66.9

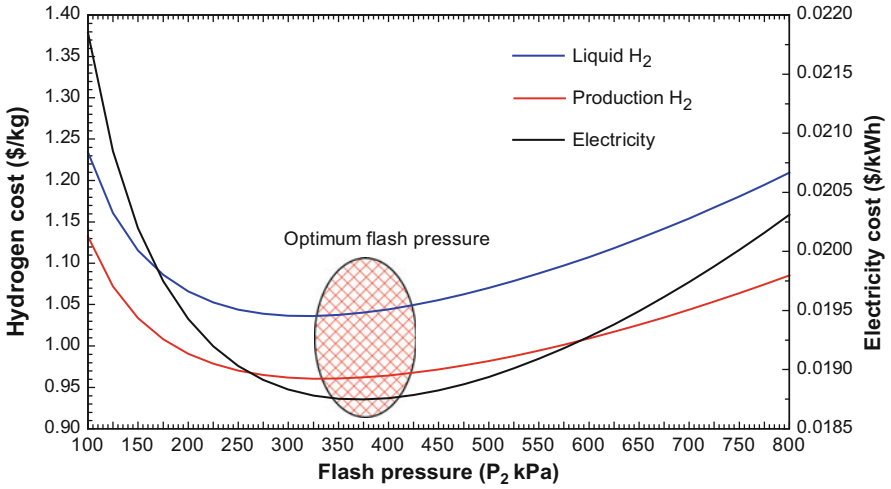

Fig. 2 Optimum unit exergetic cost rate of hydrogen production and liquefaction with respect to the geothermal water flash pressure

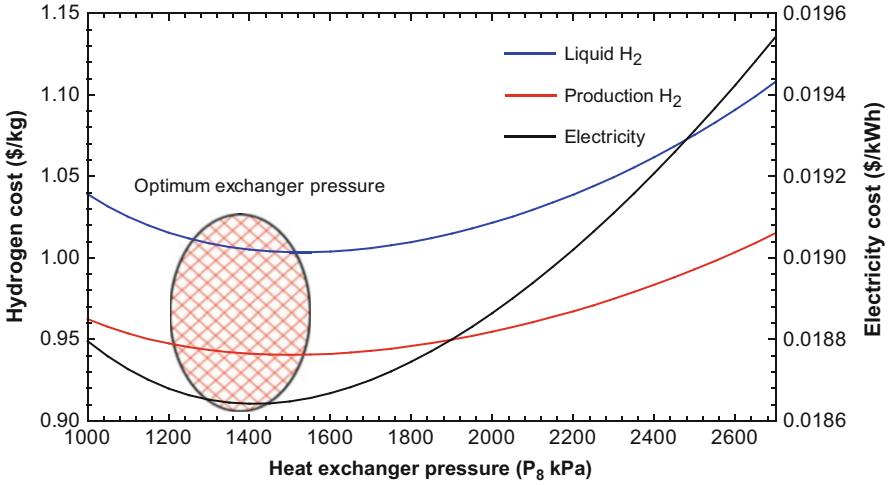

Fig. 3 Optimum unit exergetic cost rate of hydrogen production and liquefaction with respect to the geothermal water flash pressure

Table 7 Comparison of values in base cases design with those obtained at optimum solution of EES genetic optimization (1000 iterations) (Klein 2015)

Properties	Base case	Optimum case
Flash pressure	600 kPa	324.8 kPa
Binary heat exchanger pressure	2100 kPa	1020 kPa
Binary heat exchanger pinch point	5 °C	5 °C
Liquefaction compressor pressure	5000 kPa	4009 kPa
Liquefaction cycle gas fraction (x)	0.6	0.75
Binary heat exchanger temperature	148.8 °C	126.3 °C
Binary heat exchanger pinch point temperature	108.1 °C	72.2 °C
Geothermal electricity production	7572 kW	7611 kW
Electrolysis unit hydrogen production	125.5 kg/h	126.1 kg/h

Table 8 Comparative results between the base case and optimum case of the geothermal hydrogen production and liquefaction system

Properties	Base case	Optimum case	% Variation
Fuel exergy	58,668 kW	55,475 kW	−5.40
Product exergy	51,721 kW	47,188 kW	−8.76
Exergy destruction	6947 kW	8287 kW	+16.2
Fuel cost ($/h)	290 $/h	274.2 $/h	−5.44
Product cost ($/h)	3031 $/h	1820 $/h	−39.9
Exergy destruction cost ($/h)	34.34 $/h	40.96 $/h	+16.2
Exergetic unit cost of electricity	0.02076 $/kWh	0.01908 $/kWh	−8.10
Exergetic cost of hydrogen production	2.091 $/kg	1.967 $/kg	−5.93
Exergetic cost of hydrogen liquefaction	1.725 $/kg	1.095 $/kg	−36.5

hydrogen production and liquefaction can be considered to be a viable pathway in the sustainable hydrogen technology, and the proposed system is an alternative of such an application.

Acknowledgments This study is sponsored by the Scientific and Technological Research Council of Turkey (TUBITAK) with project number 113 M207. This support is greatly appreciated.

References

Abusoglu, A., Kanoglu, M.: Exergoeconomic analysis and optimization of combined heat and power production: a review. Renew. Sustain. Energy Rev. **13**(9), 2295–2308 (2009)

Aspen PlusV8.4. Engineering Economic Analysis Library. Based on 01 January (2014)

Baghernejad, A., Yaghoubi, M.: Genetic algorithm for multi-objective exergetic and economic optimization of parabolic trough collectors integration into combined cycle system (ISCCS). Accepted for presentation in the ASME 2010 Conference (ESDA2010), Istanbul, 12–14 July (2010)

Bejan, A., Tsatsaronis, G., Moran, M.: Thermal Design and Optimization, 1st edn. Wiley & Sons, New York (1996)
d'Accadia, M.D., Rossi, F.: Thermoeconomic optimization of a refrigeration plant. Int. J. Refrig. **21**(1), 42–54 (1998)
Frangopoulos, C.A.: Application of the thermoeconomic functional approach to the CGAM problem. Energy. **19**(3), 323–342 (1994)
Klein, S. A.: Engineering Equation Solver (EES), Academic Professional Version, F-chart Software (2015)
Lozano, M.A., Valero, A.: Theory of the exergetic cost. Energy. **18**(9), 939–960 (1993)
Scott, D. S.: Smelling Land: The Hydrogen Defense Against Climate Catastrophe. Canadian Hydrogen Association (2007)
Spakovsky, M.R.: Application of engineering functional analysis to the analysis and optimization of the CGAM problem. Energy. **19**(3), 343–364 (1994)
Tsatsaronis, G., Pisa, J.: Exergoeconomics evaluation and optimization of energy systems—application to the CGAM problem. Energy. **19**(3), 287–321 (1994)
Tsatsaronis, G., Cziesla, F., Thermoeconomics, R.M.: Encyclopedia of Physical Science and Technology, vol. 16, pp. 659–680. Academic Press, San Diego (2002)
Valero, A., Lozano, M.A., Serra, L., Torres, C.: Application of the exergetic cost theory to the CGAM problem. Energy. **19**(3), 365–381 (1994)

A Case Study of Energy Modeling of a School Building in Astana City (Kazakhstan)

Uyzbayeva Aigerim, Tyo Valeriya, and Sedov Artem

1 Introduction

The growing concern of international community about the rise of energy consumption and production of CO_2 emissions in the construction sector has led to the increased application of energy-efficient measures at the early design stage. The analysis of the State Energy Register of Kazakhstan showed that secondary schools and nurseries are responsible for 36.5% (EPESDI 2014) of buildings consuming more than 500 tons of oil equivalents (Adilet 2017) and are eligible for mandatory energy auditing. This fact directly points at the existing problems in energy balance of these types of buildings. The major concerns are related to high cost of heating and cooling of schools due to possible heat loss through building envelope, use of inefficient technologies, and high energy waste. It should be noted that Astana city is the second coldest capital in the world and energy conservation is an important factor in the city's climatic conditions. According to the Statistics Agency of Kazakhstan, there are around three million students in schools across the country (Statistic Agency of Kazakhstan 2014), and they spend almost 30% of their lives at school and about 60% of their time indoors during the day (Bako-Biro et al. 2012). Consequently, in addition to energy saving, adequate indoor comfort in school buildings must be ensured. Currently, there are no regulations in Kazakhstan's building codes regarding the compulsory tentative energy analysis in computational

U. Aigerim (✉) • T. Valeriya
Nazarbayev University Research and Innovation System, Laboratory of Intelligent Systems and Energy Efficiency, 53, Kabanbay batyr Ave., 9302B, Astana 010000, Kazakhstan
e-mail: aigerim.uyzbayeva@nu.edu.kz; valeriya.tyo@nu.edu.kz

S. Artem
Moscow State University of Civil Engineering (Smart City), Laboratory of intelligent systems in automation, 26, Yaroslavskoye shosse, Moscow 129337, Russia
e-mail: sedov.eit@gmail.com

© Springer International Publishing AG, part of Springer Nature 2018

F. Aloui, I. Dincer (eds.), *Exergy for A Better Environment and Improved Sustainability 2*, Green Energy and Technology,
https://doi.org/10.1007/978-3-319-62575-1_67

programs. Preliminary computer modeling and designing energy-efficient solutions of school buildings lead not only to rational power consumption and development of ecological environment in classrooms but also to improvement of students' academic performance.

There have been many studies carried out toward improving energy performance of buildings (Sartori and Hestnes 2007) including those using computer simulation programs. Most of them are targeted on modeling and assessing residential (Sadeghifam et al. 2015) and office buildings (Andarini 2014). Educational institutions have been evaluated in terms of life cycle cost analysis (Bull et al. 2014), environmental performance (Scheyer et al. 2003), energy consumption (Pereira et al. 2014), and indoor air quality (Elbayoumi et al. 2014). Some research has been done on energy simulation of school buildings (Katafygiotou and Serghides 2014).

This study presents the results of energy modeling of a school building located in Astana city considering its extreme weather conditions and current costs of energy sources. It adopts a holistic approach to evaluate energy consumption, potential of renewable sources, and financial feasibility as well as to make a set of recommendations toward improving energy efficiency and design solutions.

2 Methodology and Approach: Energy Modeling

The approach of estimating the thermal behavior of the school building is given in this section.

2.1 Choice of Materials

The building materials for the envelope is chosen in accordance with local building code – SN RK "2.04.01-2004 Thermal Performance of The Buildings" and are based on the estimation of thermophysical properties of building materials. The building envelope should satisfy the minimum requirements. The normalized heat transfer resistance (minimum required thermal transmittance) of the envelope for the given location is calculated as

$$R_o^{\min} = a \times D_d + b \tag{1}$$

a – coefficients (SNRK 2008)

D_d – degree-days of heating period, C, determined by the formula

$$D_d = (t_{int} - t_{ht}) z_{ht} \tag{2}$$

where

t_{int} – design temperature of indoor air, C, taken according to GOST 30494 depending on the building type (between 16 and 21C)
t_{ht} – average temperature of outdoor air, C
z_{ht} – duration of heating period, days (SNRK 2008)

While designing the building according to the complex index of thermal energy needs, the conventional value of the thermal resistance of each individual element R_o^{con} should be set. In the design of the buildings the condition $\boldsymbol{R_o^{min} \leq R_o^{con}}$ should be satisfied.

For a composite building element made up of a number of layers of different materials, its total resistance without thermally conductive inclusions is conditionally determined by the following formula:

$$R_o^{con} = 1/\alpha_{int} + R_1 + R_2 + \cdots + R_n + 1/\alpha_{ext}, \text{м}^2 \times {}^\circ\text{C/W}, \tag{3}$$

where

R_1, R_2, R_n – thermal resistance of first, second, and other layers of the envelope, $\text{м}^2 \cdot {}^\circ\text{C/W}$
α_{int} – heat transfer coefficient of the inner wall surface, $\text{W/(м}^2 \cdot {}^\circ\text{C)}$
α_{ext} – heat transfer coefficient of external wall surface, $\text{W/(м}^2 \cdot {}^\circ\text{C)}$

Reduced total thermal resistance with heat-conducting inclusions is given as

$$R_o^r = R_o^{con} \cdot \text{r}, \ \text{м}^2 \cdot {}^\circ\text{C/W} \tag{4}$$

where r – heat transfer performance uniformity factor of building envelope that considers heat transfer inclusions (jamb, jamb joints, end lap, fastening elements, concrete studs, etc.).

The materials for the school building envelope including roofs and flooring are chosen according to the results of the abovementioned calculations and to SNRK (2008).

2.2 Selecting a Modeling Tool: Energy Modeling

It is known that the parameters affecting the energy performance of a building should be addressed during early design stages. Energy modeling is a widely used tool for predicting energy use of a building and applying various energy-saving measures. It creates prerequisites for designers, owners, and other stakeholders to implement the design decisions related to the reduction of greenhouse emissions and the overall impact on the environment, as well as to minimize the energy needs for buildings, along with the use of energy-efficient technologies and sources of low-carbon emissions.

Simulation model of the proposed building is consistent with the provision of documentation including the proper accounting of windows and opaque walls, interior lighting, type of control, ventilation and air-conditioning, size, maintenance and management of water supply systems, as well as premises occupation. Analysis of energy consumption includes all energy costs associated with the maintenance of the school building including PC, cooking and other equipment, energy, lightings, hot water supply, and HVAC. Construction materials' thermophysical properties, building orientation, climatic conditions, *R* value, conductivity, glazing, analysis of thermal bridges, and infiltration/exfiltration coefficients are taken into consideration.

For the energy model development, dynamic simulation software TAS, engineered by EDSL, is chosen. The program has been approved by CIBSE ASHRAE as an instrument for thermodynamic analysis and is approved by international standards on ecological certification including LEED and BREAM.

2.3 Systems

For the preliminary analysis of energy consumption, the school building was investigated with three different systems:

1. Heating/ventilation technology-based fan coil units (FCU)
2. Heating/ventilation system on the basis of constant air supply (CAV)
3. Heating/ventilation on the basis of mechanical ventilation system with air preheating and central heating system (water)

It is assumed that the envelope remains the same in all the cases. The parameters of the ventilation system and the efficiency of the main elements are set the same for three systems. All systems contain a heat exchanger with the efficiency of 60%. In addition, the possibilities of introducing renewable energy technologies are observed.

3 Input Data

3.1 Building Characteristics

The selected building represents a traditional standardized design of a two-story secondary school with the capacity of 300 students. The building is assumed to be located in Astana city, Kazakhstan. All design and technical solutions meet the requirements of current building codes and safety standards adopted by the country. The virtual model is drawn in AutoCad software before being transferred into TAS.

The school operates in two shifts with the first group of students starting from 08:00 am to 01:30 pm and the second group of students from 01:30 pm to 07:00 pm.

Floor heights of the first and the second floors are 3 m each, and the height of the basement is 2.7 m.

Building constructions and materials of the proposed model are selected in compliance with the local building codes. The composition of the constructions is given below.

The sloping tiled roof is composed of 220 mm reinforced concrete, 180 mm rock wool insulation, 100 mm keramzit expanded clay, and 5 mm Ruberoid roofing material. In cold season the internal R value is 5503 $m^2 \cdot °C/W$ and the external R value is 5443 $m^2 \cdot °C/W$ for upward heat direction.

The external wall consists of the following layers: 20 mm render, 380 mm brickwork, 132 mm rock wool insulation, and 7 mm of protecting render. When the heat direction is horizontal, R value is 4051 $m^2 \cdot °C/W$ for internal and 3961 $m^2 \cdot °C/W$ for external parameters.

The composition of underground wall is 20 mm render, 300 mm concrete block, 117 mm rock wool insulation, 20 mm render, and 30 mm splitter tile. Internal and external R values are 3501 $m^2 \cdot °C/W$ and 3411 $m^2 \cdot °C/W$ respectively for horizontal heat direction.

For the slab above semiground spaces, we selected 5 mm plastic, 50 mm concrete screed, 125 mm concrete, 175 mm rock wool insulation, and 0.1 mm aluminum. For downward heat direction in cold season, the R values are 4801 $m^2 \cdot °C/W$ for internal and 4671 $m^2 \cdot °C/W$ for external parameters.

The slab on the ground is composed of 5 mm plastic, 50 mm concrete screed, 125 mm concrete, 150 mm crushed brick, and 1000 mm dry sand. This resulted in 3845 $m^2 \cdot °C/W$ and 3715 $m^2 \cdot °C/W$ of internal and external R values, respectively, for downward heat direction in cold season.

Similarly, window parameters meet the requirement of the local building codes. The parameters are represented in Table 1.

The selection of frame and glazing materials is based on the condition that the building is not operating during the summer period.

3.2 Weather Data

The weather data file for energy modeling has been generated from Meteonorm 7.0.20 and Climate Consultant databases to determine average weather parameters of Astana city for 2000–2014 years.

Generally, Astana has a humid continental climate with warm summers and no dry season. As shown in Fig. 1, the temperature typically varies from −22 to 26 °C and is rarely below −32 °C or above 32 °C over the course of a year. The warm season lasts from May to mid-September with an average daily high temperature above 19 °C. The hottest month of the year is July, with an average high of 26 °C and low of 12 °C. The cold season lasts from the end of November to March with an

Table 1 Windows parameters

Elements	Parameters	Baseline model	Proposed model
Glazing	U-value	0.735 W/m^2.°C	0.736 W/m^2.°C
	g-value	0.39	0.39
	Shading devices	Not applied	Not applied
	VLT	59.5	59.5
Frame	U-value	1.3 W/m^2.°C	1.3 W/m^2.°C

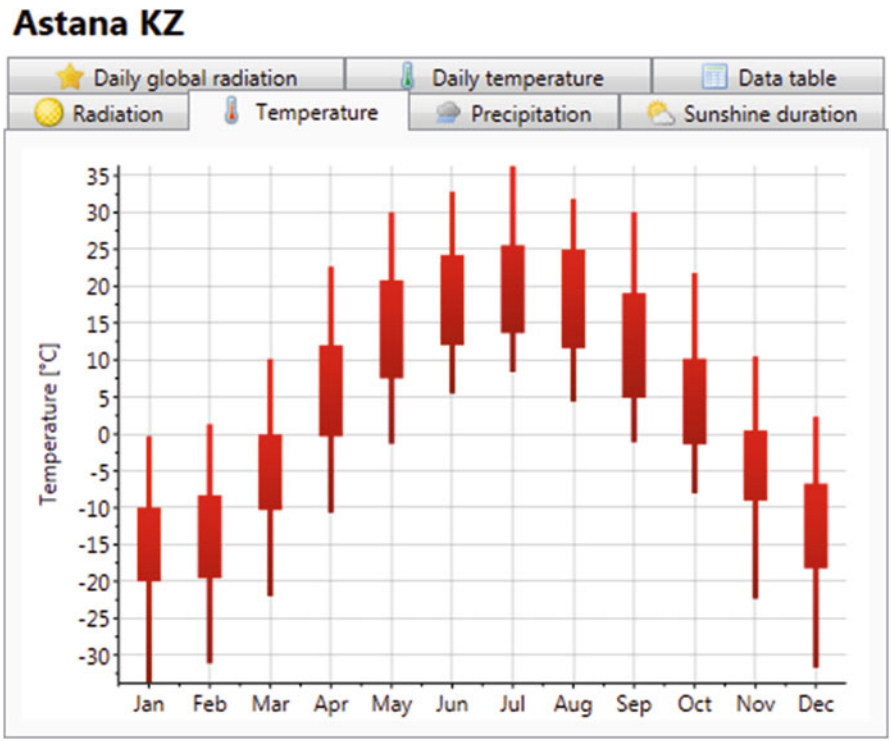

Fig. 1 Temperature, Astana

average daily high temperature below −5 °C. The coldest day of the year is in January, with an average low of −22 °C and high of −13 °C.

The length of the day varies significantly over the course of the year. The shortest days are in December with less than 8 h of daylight; the longest days are in July with 16.5 h of daylight (Fig. 2).

The precipitation in the region varies throughout the year. The most common forms of precipitation are moderate snow, light rain, light snow, and thunderstorms. The most intensive period of precipitation is summer with peak in July, while in February there is less than 30 mm of precipitation observed (Fig. 3).

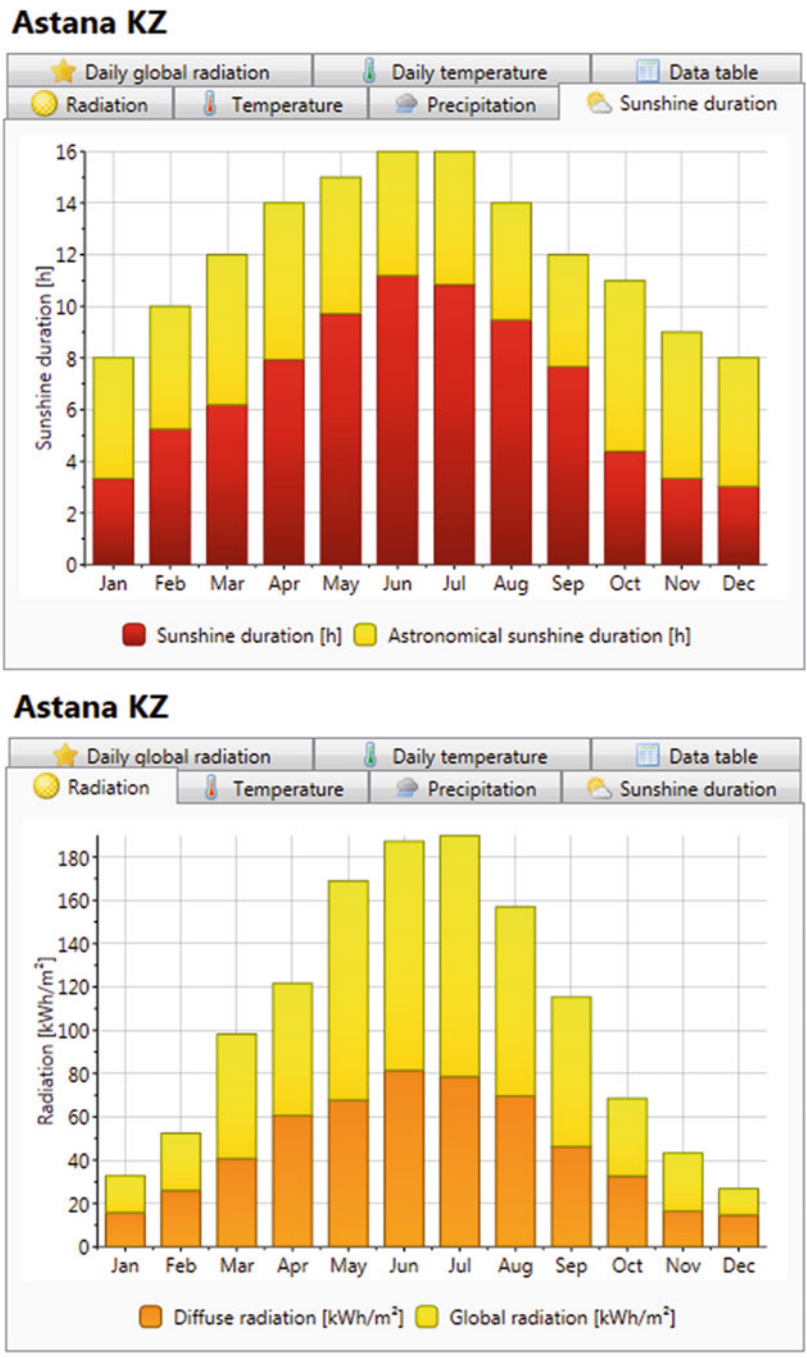

Fig. 2 Sunshine duration and radiation, Astana

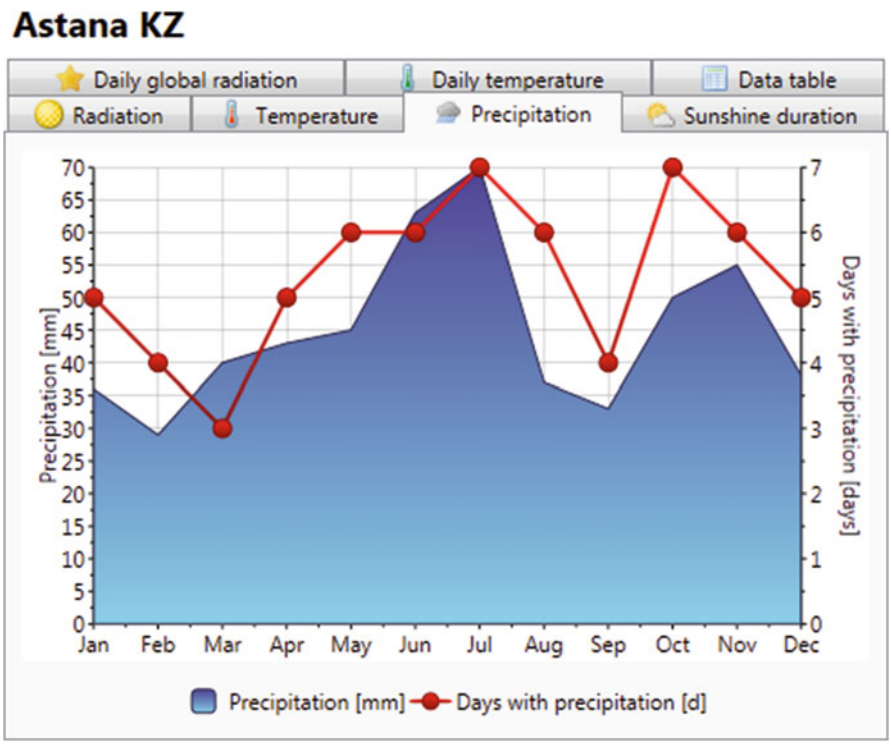

Fig. 3 Precipitation, Astana

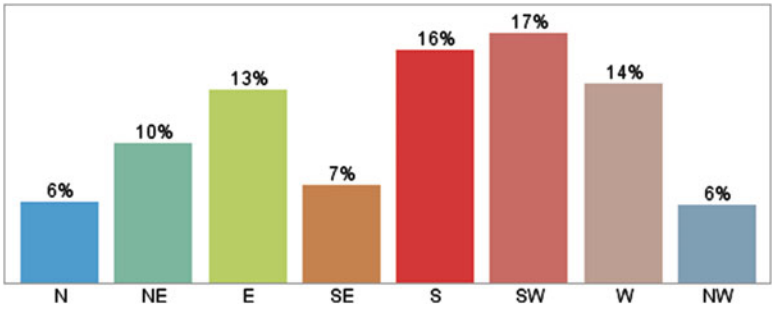

Fig. 4 Wind directions over the year, Astana

Figure 4 shows that the wind most often blows from the southwest and south, while less often is out of north and northwest.

Over the course of the year, typical wind speeds vary from light air and moderate breeze with 1 to 7 m/s to strong breeze rarely exceeding 11 m/s (Fig. 5).

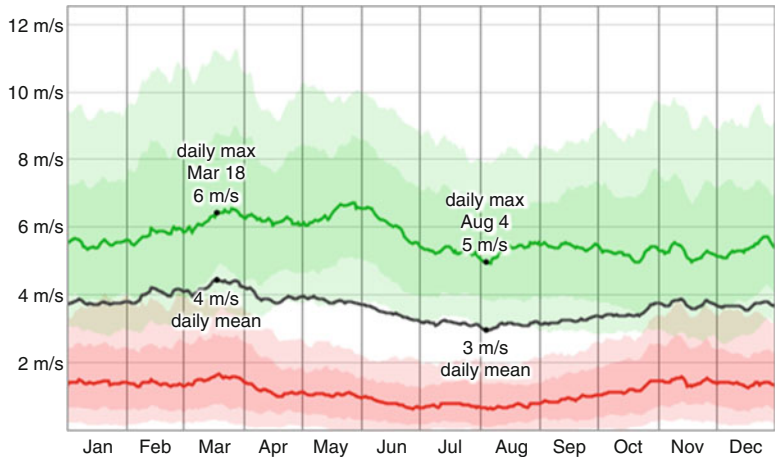

Fig. 5 Wind velocity range, Astana

3.3 Energy Sources Rate

According to the tariffs set by the provider of electricity and heat in Astana "Astanaenergosbyt" LLP in 2014, the average rate for electricity is 0.076 USD per 1 kW/h and 0.011 USD per 1 kW/h for heat energy (Astanaenergosbyt 2015). In this context, considering the given costs integration of any electric heating systems including heat pumps in the building is less preferable compared to the central heating system.

4 Results and Discussion

Based on the energy model, several zones with similar thermal requirements serviced by the same mechanical equipment and controls are identified (Fig. 6) in order to calculate loads for each zone to be able to select optimal building orientation, assess thermal comfort, determine the energy consumption, and conduct financial and life cycle analyses.

4.1 Optimal Building Orientation and Daylight Potential

The loads analysis based on comparison of annual changes in key parameters (heating, cooling, humidity, dehumidification, solar lighting, occupancy, equipment, and internal loads) calculated in four different cardinal directions has been

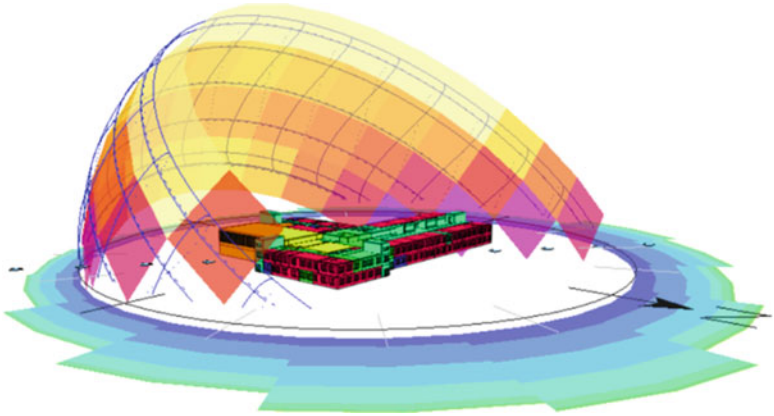

Fig. 6 Thermal zoning of energy model

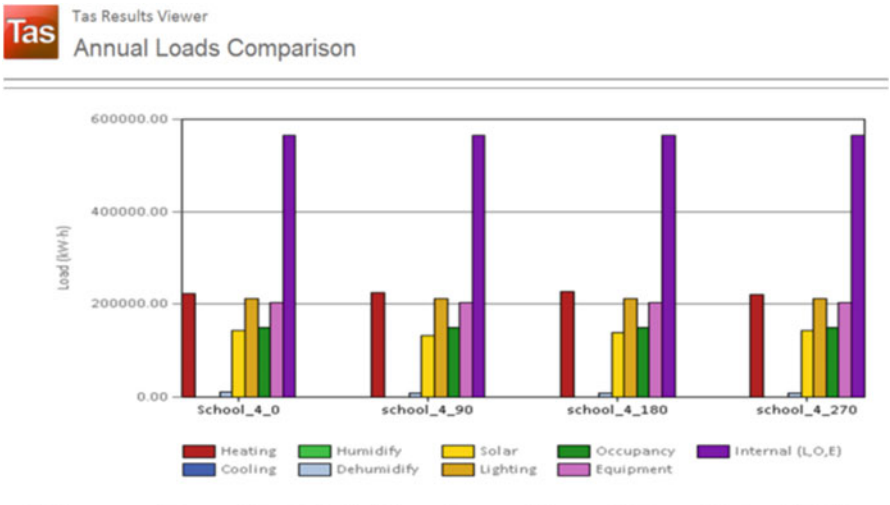

Building	Heating	Cooling	Humidify	Dehumidify	Solar	Lighting	Occupancy	Equipment	Internal (L,O,E)
School_4_0	222999,8	0,0	0,0	10040,4	143502,9	212017,9	151125,5	203358,7	566502,1
school_4_90	225556,4	0,0	0,0	9204,6	133805,9	212017,9	151125,5	203358,7	566502,1
school_4_180	227043,7	0,0	0,0	9496,3	139595,1	212017,9	151125,5	203358,7	566502,1
school_4_270	220391,7	0,0	0,0	8649,6	143867,8	212017,9	151125,5	203358,7	566502,1

Fig. 7 Annual loads comparison

carried out to identify the most optimal orientation of the building. Figure 7 shows that small distinction of the same parameters in different directions is observed. The minimum load on heating and dehumidification is achieved if the building is oriented to the west (270 °C).

To identify daylight potential, two types of glazing are compared. The types are glazing with shading (VLT 0.59) and glazing transparent (VLT 0.80). The results are shown in KEO and Lux units in Fig. 8a for VLT 0.59 and in Fig. 8b for VLT 0.80.

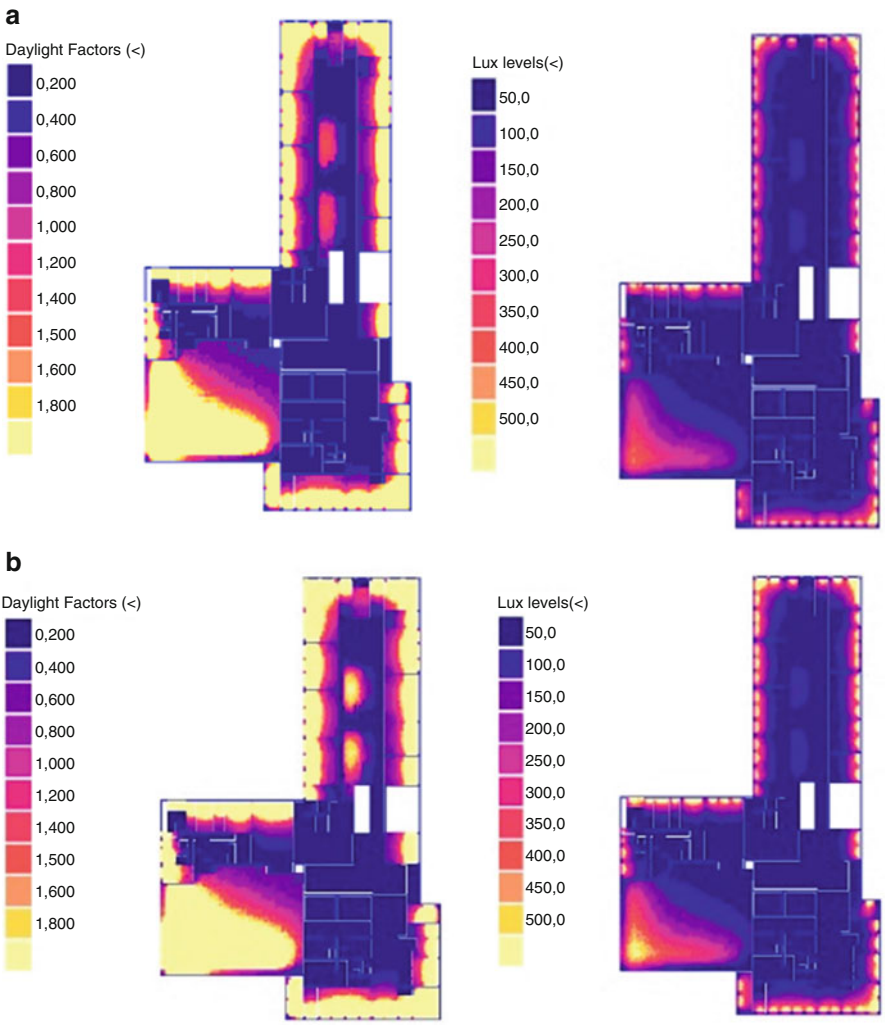

Fig. 8 (**a**) Daylight factor and lux level for VLT 0.59. (**b**) Daylight factor and lux level for VLT 0.80

Obviously, daylight potential is higher with VLT 0.80. Given the fact that the school building is not fully operating in summer period when the sun is strong, it is recommended to select multichamber glazing with no shading or sputtering. In order to reduce energy losses, automatic or manual lighting dimmers should be installed in the classrooms.

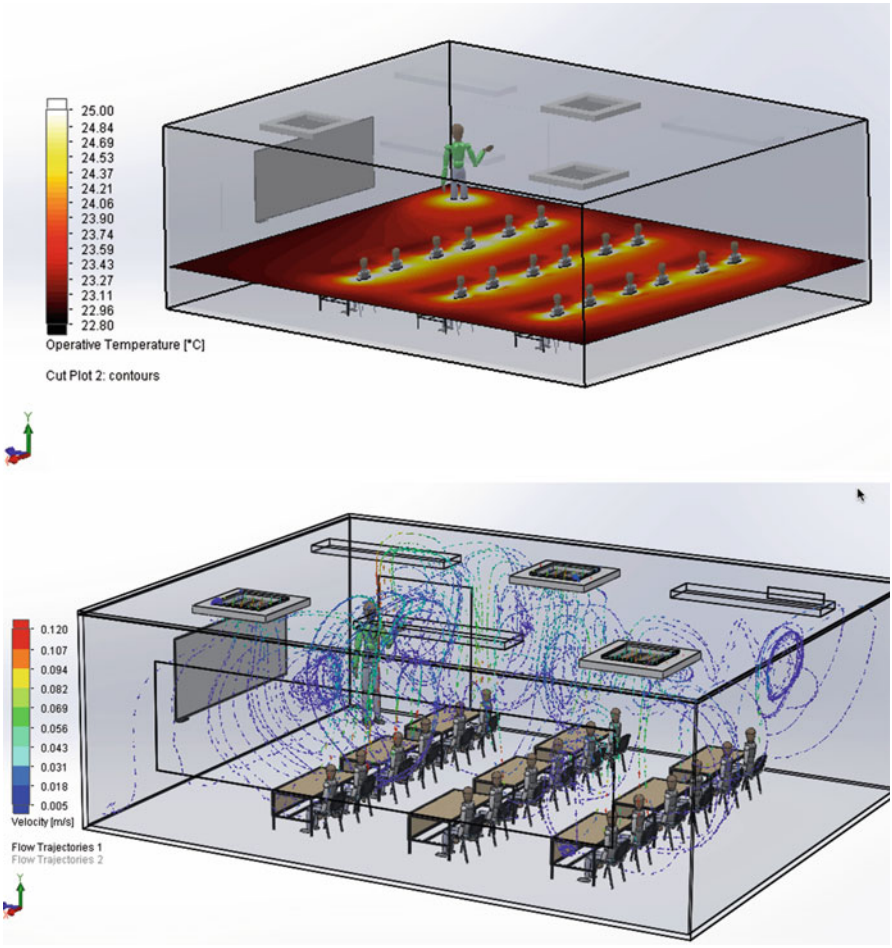

Fig. 9 Temperature range and air velocity in classroom

4.2 Thermal Comfort

The analysis of thermal comfort is based on the simulation of air temperature and air velocity in the classroom (Fig. 9) and the dining room (Fig. 10), where students spend most of their time at school.

As a result, the values of air temperature, predicted mean vote (PMV), and predicted percentage dissatisfied (PPD) are identified as optimal, while air velocity value is found to be lower than required. More specifically, the average air temperature including mean radiant temperature in classroom and dining room are 23.7 and 22.5 °C, respectively. The index of PMV is 0.02 in the classroom

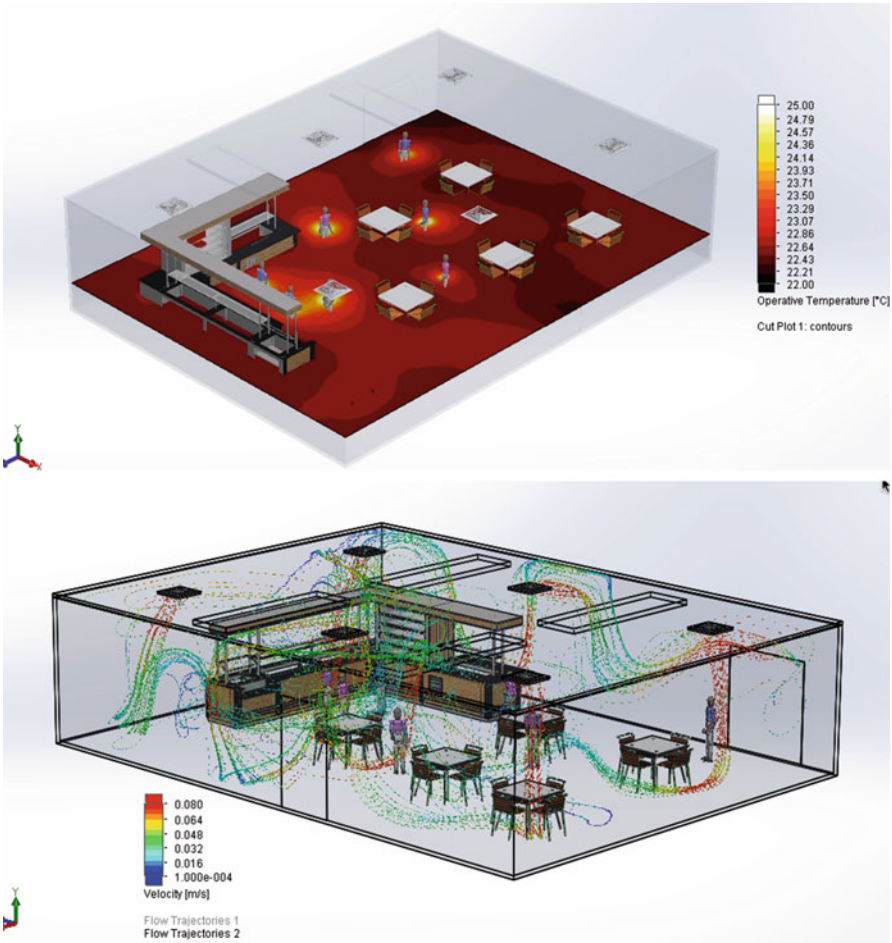

Fig. 10 Temperature range and air velocity in dining room

and −0.22 in the dining room, which is in line with the recommended limits: −0.5 to 0.5 by ASHRAE (2017). The values of PPD are 5.5% in the classroom and 6.2% in the dining room, which is conforming to acceptable PPD range in ASHRAE 55. The largest concern relates to air velocity with only 0.0023–0.042 m/s values, which is not sufficient compared to 0.1 m/s required by the international standards. The low air movement in the room points to inadequate engineering systems in the building.

4.3 Systems and Energy Consumption

The parameters of the ventilation system and the efficiency of the main elements are taken the same as for three systems. All systems contain a heat exchanger with the efficiency of 60%. The water part for all three systems represents a common tank with the capacity of 1000 l (thermoaccumulator) connected with the heat source. The storage tank is also connected with the solar thermal system and DHW consumers. The model accounts for the uniform supply of hot water during working hours (the rate of 2500 l of hot water at a temperature of 55 °C per day). For the purposes of this study, it is assumed that 2000 l of hot water should be consumed by students and school staff. The rest 500 l are used for the needs of the building. Hot water is only consumed during working days of the school.

The graphical representation of the systems is given below (Figs. 11, 12, and 13):

The systems consist of 122 m^2 PV panels with the total installed capacity of 25 kW and 10 small-scale wind turbines (Fig. 14).

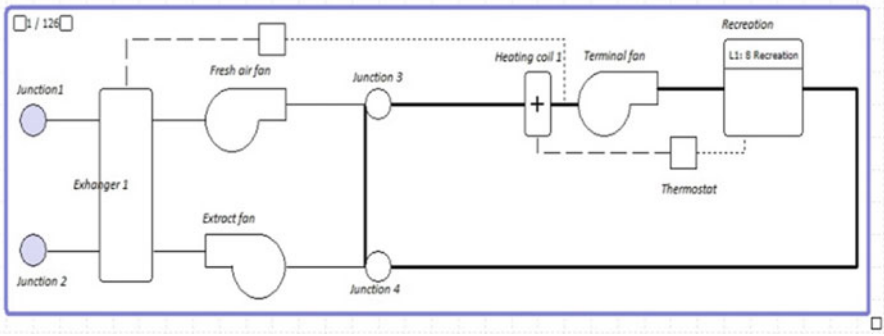

Fig. 11 Schematic representation of the heating/ventilation system based on FCU

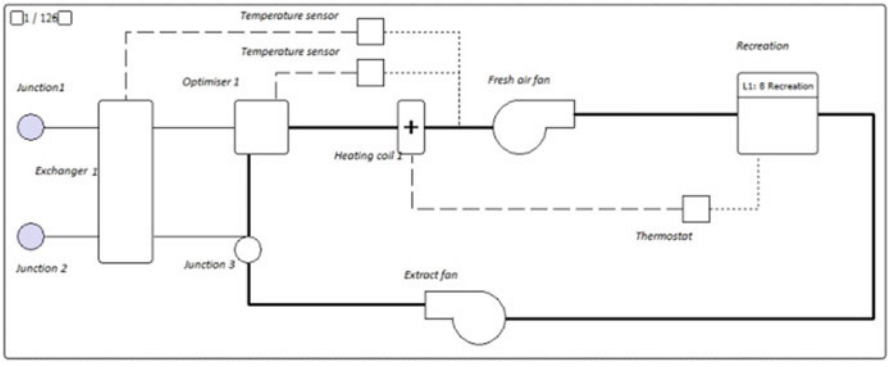

Fig. 12 Schematic representation of the heating/ventilation system based on CAV

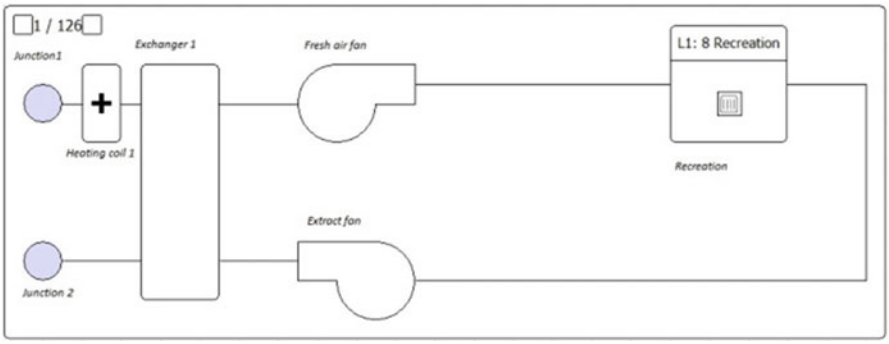

Fig. 13 Schematic representation of the heating/ventilation system based on mechanical ventilation

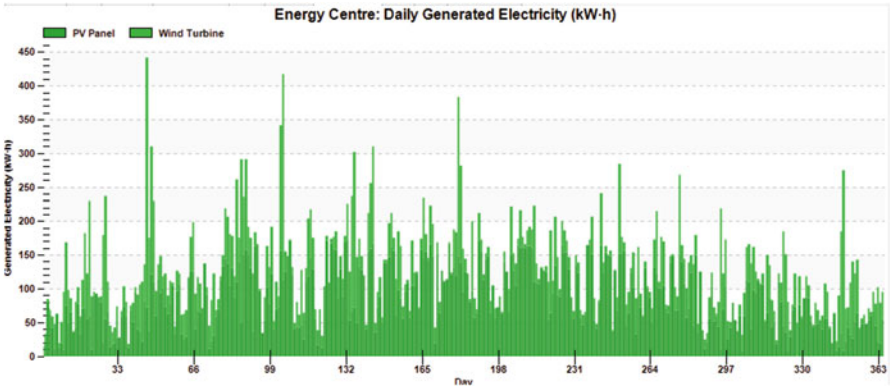

Fig. 14 Dynamics of total generation of electricity from RET

Solar thermal and PV collectors more intensively produce thermal and electrical energies in summer season, when the school is not being exploited in normal regime. Taking into account the high cost of RET, it is necessary to conduct a comprehensive analysis of the feasibility of installing such systems in schools. The following recommendations are given based on the analysis of the energy modeling of the school.

The results of the estimated energy consumption for the assumed three types of HVAC systems are given in Table 2. The values of power consumption and cost are provisional and conditional and may not correspond to the true values.

The calculated values given in Table 2 show the distribution of power consumption parameters depending on the system used. The last column of the table indicates a power value in accordance with tariff and rates in local currency (1 USD = 184 KZT). Energy assessment is based on a simplified and idealized model of the building and may not fully reflect all the details and complexities of the operation of the building as well as all the features of system maintenance and

Table 2 Systems energy consumption and total cost

Analyzed systems	Energy consumption, kWh	Heat, kWh	Electricity, kWh	Cost, KZT
FCU	738,200	423,400	314,800	4,596,780.5
CAV	765,300	394,600	370,700	5,292,402
Mechanical vent/ radiators	811,200	549,300	261,900	4,155,805.8

management. The results are interpreting the potential energy efficiency of the building in the simulation of energy consumption using standard operating file listed in ASHRAE 90.1-2007.

The preliminary life cycle analysis for the three systems has been done in IES software, and 60 years of operation are used in calculations. The inflation rate for the entire period is not used, and the analysis is carried out in the forecast prices without deflation. Initial data in the structure of life cycle cost is the modeled energy consumption of the building, as well as structural features of the building.

After analyzing the energy consumption of three different systems, it is concluded that the use of system No.3 – the system with central heating and ventilation based on mechanical ventilation with the air preheating – for an energy-efficient school in Astana is most optimal and economically feasible. It should be noted that the Government of Kazakhstan has recently approved fixed tariffs for electricity supply from RES. However, the tariffs are not applicable in our case. Therefore, the rates are not taken into account in economic calculations.

5 Recommendations and Conclusion

The following recommendations are given based on the analysis of the energy modeling of the school.

Site selection: in order to reduce environmental impact on the site, it is necessary to conduct environmental site assessment, to develop an action plan on pollution prevention from construction activity and automobile use, as well as to implement a storm water management plan to eliminate pollution from storm water runoff and soil contamination.

Water management: limited or no potable water should be used for landscape irrigation; storm drains water system and water consumption monitoring and rain water harvesting systems should be integrated to ensure efficient water use.

Optimization of energy performance: to be able to reduce economic and environmental impacts associated with excessive energy use, there should be different technologies employed like renewable energy sources such as passive solar heating, geothermal, PV and groundwater cooling as well as optimizing system control strategies by using occupancy sensors CO_2 and air quality monitoring systems.

Building envelope: to ensure durability and high performance of walls, roofs, and other assemblies, the materials should be selected based on long-term insulation and air barrier requirements. It is preferable to use recycled and locally produced materials.

Generally, the proposed model of school building is used to simulate traditional solutions used in older schools previously. From the results of simulation, it could be seen that the air velocity in classrooms is not sufficient. Hence, the design, engineering solutions, and perhaps the legislative base regarding the microclimate in school buildings should also be revised in the future. As the economic feasibility analysis shows, while the cost of electricity and RET is high, the only viable option in Astana weather conditions is central heating system and mechanical ventilation with air preheating.

For the future research, this model could be used and optimized according to different climatic conditions of different regions of Kazakhstan. The life cost and life cycle analysis should also be done.

Acknowledgments This research was supported by the Intelligent Systems and Energy Efficiency Laboratory of the "Nazarbayev University Research and Innovation system" Private Institution.

References

Adilet, Legal information system of Regulatory Legal Acts of the Republic of Kazkahstan, The Law of the Republic of Kazakhstan dated 13 January 2012 No. 541-IV "On Energy Saving and increase of Energy Efficiency". Last retrieved at http://adilet.zan.kz/eng/docs/Z1200000541 (2017)

Agency of Statistics of Republic of Kazakhstan: Basic indicators for 2003–2011. Last retrieved at http://www.stat.gov.kz/faces/wcnav_externalId/homeNumbersEducation?_afrLoop=151545185304555#%40%3F_afrLoop%3D151545185304555%26_adf.ctrl-state%3Dm14xldwga_90 (2014)

American Society of Heating and Air-Conditioning Engineers. Last retrieved at https://www.ashrae.org/standards-research–technology/standards–guidelines (2017)

Andarini, R.: The role of building thermal simulation for energy efficient building design. Energy Procedia. **47**, 217–226 (2014)

Astanaenergosbyt. Last retrieved at http://www.astanaenergosbyt.kz/tarif_ur. (2015)

Bako-Biro, Z., Clements-Croome, D.J., Kochar, N., Awbi, H.B., Williams, M.J.: Ventilation rates in schools and pupils' performance. Build. Environ. **48**, 215–223 (2012)

Building code: SN RK 2.04-21-2004* Energy consumption and thermal protection of civil buildings (2008)

Bull, J., Gupta, A., Mumovic, D., Kimplan, J.: Life cycle cost and carbon footprint of energy efficient refurbishments to 20th century UK school buildings. Int. J. Sustain. Built Environ. **1**, 1–14 (2014)

Elbayoumi, M., Ramli, N.A., Yusol, N.F., Yahaya, A.S., Madhoun, W.A., Ul-Saufie, A.Z.: Multivariate methods for indoor PM10 and PM2.5 modelling in naturally ventilated schools buildings. Atmos. Environ. **94**, 11–21 (2014)

Katafygiotou, M.C., Serghides, D.K.: Analysis of structural elements and energy consumption of school building stock in Cyprus: energy simulations and upgrade scenarios of a typical school. Energ. Buildings. **72**, 8–16 (2014)

Electric Power and Energy Saving Development Institute (EPESDI). Data of Ministry of Industry and New Technologies: A list of objects of State energy register. Last retrieved at http://kazee.kz/gosudarstvennyy-energeticheskiy-reestr/subekty-gosudarstvennogo-energeticheskogo-reestra-/ (2014)

Pereira, L.D., Raimondo, D., Corgnati, S.P., Silva, M.G.: Energy consumption in schools. Renew. Sust. Energ. Rev. **40**, 911–922 (2014)

Sadeghifam, A.N., Zahraee, S.M., Meynagh, M.M., Kiani, I.: Combined use of design of experiment and dynamic building simulation in assessment of energy efficiency in tropical residential buildings. Energy and Building. **86**, 525–533 (2015)

Sartori, I., Hestnes, A.G.: Energy use in the life cycle of conventional and low-energy buildings: a review article. Energy and Building. **39**, 249–257 (2007)

Scheyer, C., Keoleian, G.A., Reppe, P.: Life cycle energy and environmental performance of a new university building: modeling challenges and design implications. Energ. Buildings. **35**, 149–1064 (2003)

SNRK Energy consumption and thermal protection of civil buildings 2.04-21-2004 (2008)

Exergoeconomic and Exergoenvironmental Analysis and Optimization of the Cogeneration Cycle Under Dynamic Solar Radiation Model Using Two Renewable Sources

Kaveh Hanifi, Kourosh Javaherdeh, and Mortaza Yari

1 Introduction

In recent years, availability of new sources of energy is a vital factor for economic development of different countries. According to recent researches, the development of a country is in a direct relationship with the energy consumptions. Soaring regime for energy consumption and access limitation to conventional energy sources such as coal, petroleum, and natural gas, in addition to polluting effects of such energies, have urged the utilization of sustainable and renewable sources such as solar and biomass. Rankine and organic Rankine power cycle, applying solar and biomass energy, are one of the most efficient approaches to produce electricity and hydrogen. In order to make a better use of thermal energy, organic substances have been utilized in power cycle instead of water. Many studies are carried out on selecting the working fluids (Bejan et al. 1996; Delgado-Torres and Garcia-Rodriguez 2010; Chen et al. 2006). Among these working fluids, carbon dioxide has absorbed much attention recently since it has more favorable thermodynamic properties, and it reaches to supercritical state (Beckman 2004). In recent years, Sun et al. (2012), Wang et al. (2013), and Song et al. (2012) introduced the novel power systems driven by solar energy and LNG as their heat sinks. In their

K. Hanifi (✉)
Department of Mechanical Engineering, Lashtenesha-Zibakenar Branch, Islamic Azad University, Lashtenesha, Iran
e-mail: k.hanifi@lziau.ac.ir

K. Javaherdeh
Departments of Mechanical Engineering, Mechanical Engineering Faculty, Guilan University, Rasht, Iran

M. Yari
Department of Mechanical Engineering, Mechanical Engineering Faculty, Tabriz University, Tabriz, Iran

© Springer International Publishing AG, part of Springer Nature 2018

F. Aloui, I. Dincer (eds.), *Exergy for A Better Environment and Improved Sustainability 2*, Green Energy and Technology,
https://doi.org/10.1007/978-3-319-62575-1_68

investigation, they carried out thermodynamic analysis on polygeneration systems with various working fluids.

If thermal systems are optimized by only considering the thermodynamic factor, the total cost of the system increases dramatically. Therefore, a thermal system should be evaluated economically and thermodynamically (Tsatsaronis et al. 1993). Sahoo (2008), by using the exergoeconomic analysis, produced 50 MW of electricity and 15 kg/s of saturated steam at 2.5 bar in the cogeneration system by using evolutionary program optimization. He showed that the cost of electricity and production cost are 9.9% lower in comparison with the base case. Sayyaadi and Sabzaligol (2009) performed an exergoeconomic optimization by using genetic algorithm and demonstrated the fuel cost of the optimized system is greater than the base case. He demonstrated by saving a greater monetary in other economic parts that these lacks are made up. Ahmadi et al. (2001a, b) with using multi-objective optimization presented the cost of the exergy destruction decreases if the gas turbine inlet temperature increases. Carvalho et al. (2011) have considered the trigeneration system to be used in hospital in Spain. The aim of their investigation was to minimize the cost and carbon dioxide emission. Bagdanavicius et al. (2012) took notice to analysis of the four different thermal systems functioned by biomass. However, energy and exergy modeling of a biomass along with gasification combined cycle plant were observed by Bhattacharya et al. (2011). Zare et al. (2012) carried out the exergoeconomic analysis of ammonia-water cycle, by using genetic algorithm optimization; they indicated the total cost of the cycle products is less than by around 18.6% and 25.9% compared to the base case. The thermoeconomic modeling of trigeneration system with steam turbine prime mover using biomass was illustrated by Lian and Chou. (2010). In their analysis, they studied four different configurations through exergy destruction and overall production cost. Ahmadi and Dincer (2010, 2011) considered the primary aim function adding with the cost rate of each equipment and environmental blow. They showed the increasing net power output, the pressure ratio, the compressor and turbine isentropic efficiency, and turbine inlet temperature would preferably be increased. Al-sulaiman et al. (2013) examined three systems: SOFC-trigeneration, biomass-trigeneration, and solar-trigeneration. Their investigation revealed that solar-trigeneration is the best exergoeconomic performance since the cost per exergy unit is the lowest among the three configurations. Sanaye and Shirazi (2013) carried out exergoeconomic optimization of an ice thermal energy storage system. The results of their genetic algorithm optimization indicated that the capital and operational costs in electricity consumption and CO_2 emission were 9% and 9.8% lower than the base case, respectively. Li et al. (2014) practiced the exergoeconomic performance of CO_2 transcritical power cycle and organic Rankine cycle. The results showed the ORC working with R600a presented the highest net power output, while the highest thermal and exergy efficiencies are gained by regenerative ORC working with R601. They showed, with increasing the turbine inlet pressure, the cost per net power output was first reduced to the minimum and then increased finally. Mokheimer et al. (2014) investigated the trigeneration, power/cooling/heating, and system with biomass energy. Their results showed that the optimum

operation of the trigeneration system can be achieved with the lowest ORC evaporator pinch point and the lowest ORC minimum temperatures 20 K and 345 K, respectively. However, they demonstrated that the fuel efficiency from the electrical power to trigeneration increases from 12% to 88% and in trigeneration system, ORC maximum exergy efficiency increases from 13% up to 28%.

As mentioned above, it seems, there is little data on thermoeconomic analysis of CO_2 transcritical cogeneration system. To overcome this shortage, this paper applies the exergoeconomic and exergoenvironmental model to scrutinize hydrogen/refrigeration cogeneration cycle by using two sources of energy. In this study, three configurations of cogeneration system are considered. The cycle is then optimized by means of genetic algorithm from the viewpoints of both thermodynamics and economics by using the EES (Engineering Equation Solver) software. The objectives of this paper are to maximize the hydrogen production rate and refrigeration power and to minimize the sum of the unit costs of the system products, respectively. The objectives of this paper from thermodynamic and exergoeconomic perspective are to maximize the hydrogen production rate and the refrigeration power and to minimize the cost of the system products, respectively.

Nomenclature

$\dot{C}$	Cost rate ($/h)
c	Cost per exergy unit ($/MJ)
e	Specific exergy (kJ/kg)
$\dot{E}x$	Exergy rate (kW)
h	Enthalpy (kJ/Kg)
GA	Genetic algorithm
i_r	Interest rate
K	Constant
$\dot{m}$	Mass flow rate (kg/s)
P	Pressure (bar)
$\dot{Q}$	Heat transfer rate (kW)
s	Specific entropy (kJ/kg·K)
T	Temperature (°C or K)
V	Volume (m^3); volumetric flow rate (lit/s)
Z	Investment cost of components. ($)
$\dot{Z}$	Investment cost rate of components. ($/h)
$\dot{Q}$	Heat transfer rate (kW)
s	Specific entropy (kJ/kg.K)
Greek letters	
α	Absorbpivity
β	Collector tilt factor (°)
δ	Declination (°)
θ	Angle of incidence (°)
φ	Latitude (°)

(continued)

ω	Hour angle (°)
ε	Emissivity
η	Exergy efficiency
τ	Annual plant operation hours
η_p	Isentropic efficiency
ρ	*Reflectivity*
Subscripts and abbreviations	
0	Ambient
boil	Boiler
cond	Condenser
HPROD	Hydrogen production rate optimal design
i	Inlet
e	Exit
CI	Capital investment
0	Ambient
P	Product, pump
PHE	Plate heat exchanger
ref	Refrigeration
RPOD	Refrigeration power optimal design
s	Solar
ST	Storage tank
SUCP	Sum of the unit costs of the products
tur	Turbine

2 System Description

The schematic diagrams of three different cogeneration systems consist of SCTCS, BCTCS, and SBCTCS and are shown in Fig. 1a–c. These systems are composed of three subsystems as the energy source subsystem, the CO_2 transcritical power subsystem, and the hydrogen production subsystem. The liquid flat-plate collector is employed as the source of energy in the system due to its low cost and wide applications, and the thermal storage tank is to bring heat to the power cycles. These cycles are designed to produce hydrogen and refrigeration as the main and the side products, respectively. All of them are composed of three subsystems as the energy source subsystem, the CO_2 transcritical power subsystem, and the hydrogen production subsystem. To simplify the systems, the following assumptions are made Sun et al. (2012):

- The system reaches a steady state; the kinetic and potential energies of fluids are neglected.
- The condenser outlet state is saturated liquid.
- The pressure drops of CO_2 in refrigeration and boiler are assumed to be 2%.

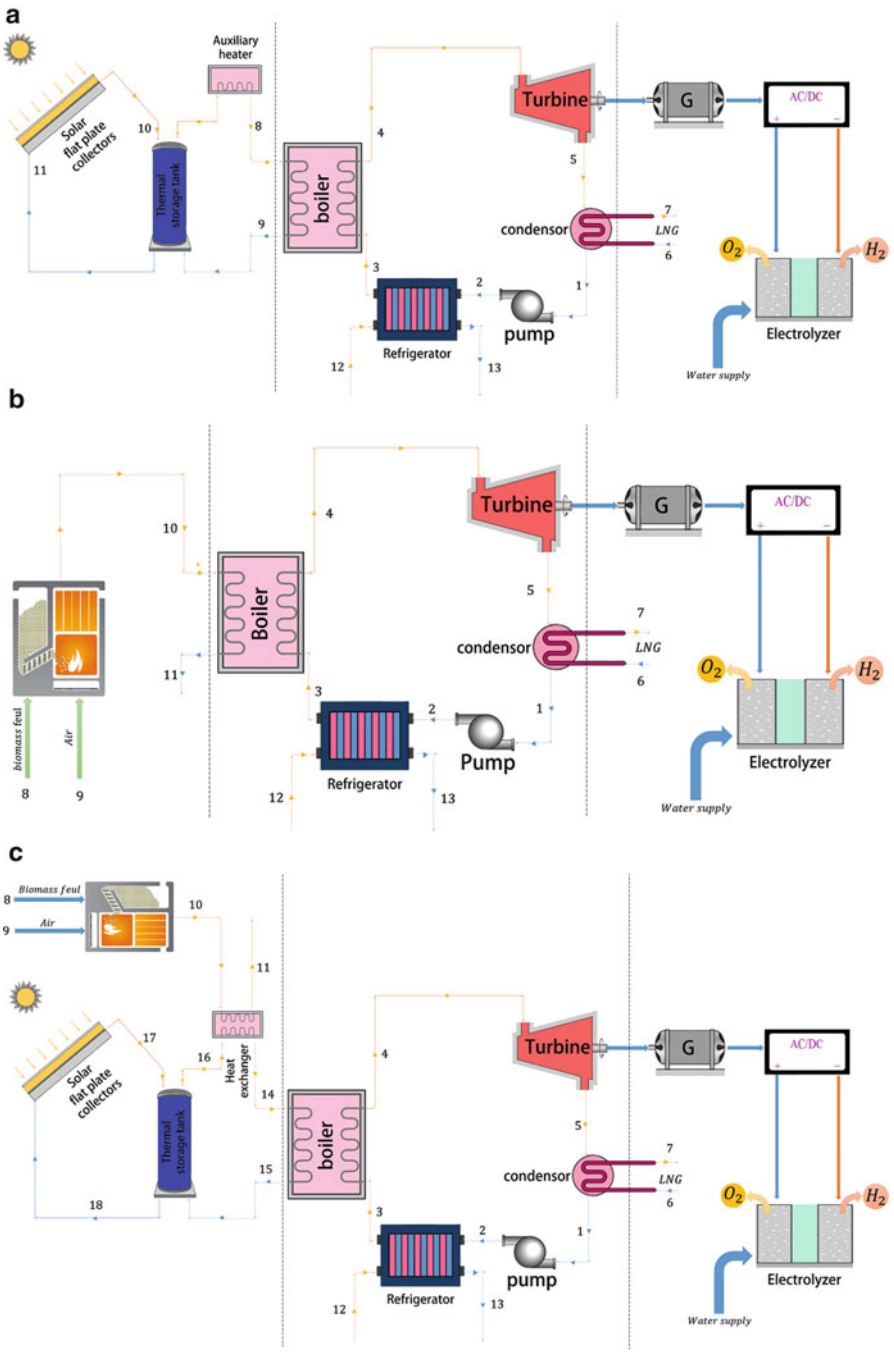

Fig. 1 The schematic of three different configurations of cogeneration system. SCTCS (**a**), BCTCS (**b**), and SBCTCS (**c**)

- The LNG is vaporized at a constant pressure of 0.6 MPa, which equals to the liquefied in LNG filling station.
- All the calculations are based on high heating value (HHV) of hydrogen rather than LHV. Since, HHV accounts for the total amount of energy in the electrolysis process.
- An alkaline electrolyzer with 77% efficiency is chosen to simulation.
- The pressure drops in biomass burner are assumed to be 10% (Al-sulaiman et al. 2012).

2.1 Solar Radiation Dynamic Modeling

The liquid flat-plate collector is employed as the source of energy in the system due to its low cost and wide applications, and the thermal storage tank is to bring heat to the power cycles. The hourly radiation falling on tilted surface is given by:

$$I_T = I_b R_b + I_d R_d + (I_b + I_d) R_r \tag{1}$$

where I_b and I_d are the beam and diffuse radiation, respectively, and R_b, R_d, and R_r as tilt factors for beam, diffuse, and reflected radiations, respectively, are defined by:

$$R_b = \frac{\mathrm{Cos}\,(\theta)}{\mathrm{Cos}\,(\theta_z)} = \frac{\mathrm{Sin}\,\delta\,\mathrm{Sin}\,(\varphi - \beta) + \mathrm{Cos}\,\delta\,\mathrm{Cos}\,\omega\,\mathrm{Cos}\,(\varphi - \beta)}{\mathrm{Sin}\,\varphi\,\mathrm{Sin}\,\delta + \mathrm{Cos}\,\varphi\,\mathrm{Cos}\,\delta\,\mathrm{Cos}\,\omega} \tag{2}$$

$$\delta = 23.45\mathrm{Sin}\left[\frac{360}{365}(284 + n)\right] \tag{3}$$

$$R_r = \frac{1 + \mathrm{Cos}\,\beta}{2} \tag{4}$$

$$R_r = \rho\left(\frac{1 - \mathrm{Cos}\,\beta}{2}\right) \tag{5}$$

The incident solar flux absorbed in the absorber plate is given by:

$$S = I_b R_b (\tau\alpha)_b + [I_d R_d + (I_b + I_d) R_r](\tau\alpha)_d \tag{6}$$

where $(\tau\alpha)_b$ and $(\tau\alpha)_d$ are transmissivity-absorptivity product for beam and diffuse radiation falling on the collector, respectively. The overall loss coefficient U_L is introduced to express the heat lost from the collector

$$q_{\mathrm{L}} = U_{\mathrm{L}} A_{\mathrm{P}} \left(T_{pm} - T_{\mathrm{a}}\right) \tag{7}$$

where A_{P} represents the area of the absorber plate, T_{pm} is the average temperature of the absorber plate, and T_{a} is the environment temperature. Since the heat lost from the collector consists of three parts, namely, top loss, side loss, and bottom loss, the overall loss coefficient is a sum of the three components:

$$U_{\mathrm{L}} = U_{\mathrm{b}} + U_{\mathrm{t}} + U_{\mathrm{s}} \tag{8}$$

$$U_{\mathrm{b}} = \frac{K_{\mathrm{i}}}{\delta_{\mathrm{b}}} \text{ and } U_{\mathrm{s}} = \frac{(L_1 + L_2) L_3 K_{\mathrm{i}}}{L_1 L_2 \delta_{\mathrm{s}}} \tag{9}$$

Where K_{i} is the thermal conductivity of the insulation and δ_{b} the thickness of the insulation.

$$U_{\mathrm{t}} = \left[\frac{M}{\left(\frac{C}{T_{\mathrm{pm}}}\right)\left(\frac{T_{\mathrm{pm}} - T_{\mathrm{a}}}{M+f}\right)^{0.33}} + \frac{1}{h_{\mathrm{w}}} \right]^{-1} + \left[\frac{\sigma\left(T_{\mathrm{pm}}^2 + T_{\mathrm{a}}^2\right)\left(T_{\mathrm{pm}} + T_{\mathrm{a}}\right)}{\frac{1}{\varepsilon + 0.05M\left(1 - \varepsilon_{\mathrm{p}}\right)} + \frac{(2M + f - 1)}{\varepsilon_{\mathrm{c}}}} - M \right] \tag{10}$$

where

$$f = \left(1 - 0.04 h_{\mathrm{w}} + 0.0005 h_{\mathrm{w}}^2\right)(1 + 0.091M) \tag{11}$$

$$C = 365.9\left(1 - 0.00883\beta + 0.0001298\beta^2\right) \tag{12}$$

The collector efficiency factor, $F^{'}$, which represents the ratio of actual useful gain rate to the gain which would occur when the collector absorber plate is at the temperature T_{fi} ,is defined as:

$$F' = \frac{1}{W U_{\mathrm{L}} \left(\frac{1}{U_{\mathrm{L}}((W - D_{\mathrm{o}})\ \phi + D_{\mathrm{o}})} + \frac{1}{\pi D_{\mathrm{i}} h_{\mathrm{f}}} \right)} \tag{13}$$

$$Q_{\mathrm{u}} = F_{\mathrm{R}} A_{\mathrm{P}} [S - U_{\mathrm{L}}(T_{\mathrm{fi}} - T_{\mathrm{a}})] \tag{14}$$

where

$$F_{\mathrm{R}} = \frac{m_{\mathrm{water}} C_{\mathrm{P}}}{U_{\mathrm{L}} A_{\mathrm{P}}} \left[1 - \exp\left(- \frac{F' U_{\mathrm{L}} A_{\mathrm{P}}}{m_{\mathrm{water}} C_{\mathrm{P}}} \right) \right] \tag{15}$$

Figure 2 shows that the incident solar flux, useful and load heat gain, and water temperature at storage tank outlet change deeply with the radiation intensity, rise to

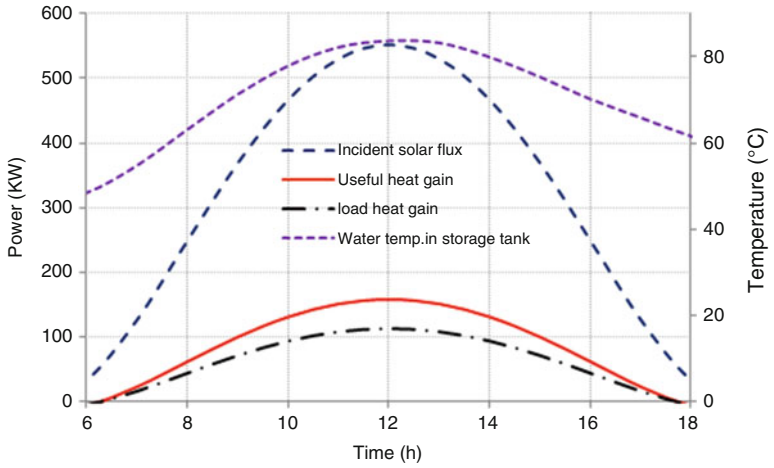

Fig. 2 Variations of S, Q_u, Q_{load}, and T_{st} with time over a day

its peak in midday, and dramatically drop approaching zero when the sun falls (Duffie and Beckman 2006). The system could be operated normally after sunset thanks to the thermal storage tank.

2.2 *Mathematical Model and Thermodynamic Analysis*

Each term of exergy involves four distinctive components. They are physical, chemical, kinetic, and potential exergies. In this research, two of the items, the kinetic and potential, are counted as negligible as the elevation and speed have so little changes (Bejan et al. 1996; Ameri and Ahmadi 2007; Dincer and Al-Muslim 2001). The chemical exergy is an important part of exergy in combustion process. Therefore, the chemical exergy used in two systems consists of biomass burner. The physical exergy is described as a maximum theoretical work gained of a system in a reversible procedure to reach to a dead state (Dincer and Rosen 2007). The required equations (energy and exergy) for modeling of the SCTCS, thermal storage tank, and the CO_2 transcritical system are shown by Sun et al. (2012), Wang et al. (2013), and Song et al. (2012). However, the biomass burner is one of the main components in the BCTCS considered the required details modeling. Further details of the biomass combustion, factors like moisture content factor, low heating value, and the relation governments, are discussed by Al-sulaiman et al. (2012). The exergy destruction rate and the exergy efficiency for each component for whole system in the cycle are shown in Table 1.

For the validity of thermodynamic purpose, the mass flow rate of the CO_2, net power output, the turbine power, and S-H_2 exergy efficiency of the cycle are compared with the available data in the literatures reported by Song et al. (2012)

Table 1 The exergy destruction rate and exergy efficiency equation for cycle components

Components	Exergy destruction	Exergy efficiency
Boiler	$\dot{E}x_{D,B} = (\dot{E}x_3 + \dot{E}x_8) - (\dot{E}x_4 + \dot{E}x_9)$	$\eta_{Ex,B} = \frac{\dot{E}x_4 - \dot{E}x_3}{\dot{E}x_8 - \dot{E}x_9}$
Turbine	$\dot{E}x_{D,TUR} = \dot{E}x_4 - \dot{E}x_5 - \dot{W}_{TUR}$	$\eta_{Ex,TUR} = \frac{\dot{W}_{TUR}}{\dot{E}x_4 - \dot{E}x_5}$
Condenser	$\dot{E}x_{D,CON} = (\dot{E}x_5 + \dot{E}x_6) - (\dot{E}x_1 + \dot{E}x_7)$	$\eta_{Ex,CON} = \left(1 - \frac{\dot{E}x_{D,CON}}{\dot{E}x_5 + \dot{E}x_6}\right)$
Pump	$\dot{E}x_{D,P} = \dot{E}x_1 - \dot{E}x_2 + \dot{W}_P$	$\eta_{Ex,PUMP} = \frac{\dot{E}x_2 - \dot{E}x_1}{\dot{W}_P}$
Refrigeration	$\dot{E}x_{D,REF} = (\dot{E}x_2 + \dot{E}x_{12}) - (\dot{E}x_3 + \dot{E}x_{13})$	$\eta_{Ex,REF} = \left(1 - \frac{\dot{E}x_{D,REF}}{\dot{E}x_2 + \dot{E}x_{12}}\right)$
Storage tank	$\dot{E}x_{D,TSt} = (\dot{E}x_9 + \dot{E}x_{10}) - (\dot{E}x_8 + \dot{E}x_{11})$	$\eta_{Ex,B} = \frac{\dot{E}x_8 - \dot{E}x_9}{\dot{E}x_{11} - \dot{E}x_{10}}$
Burner	$\dot{E}x_{D,bb} = \dot{E}x_8 + \dot{E}x_{cc} - \dot{E}x_9$	$\eta_{Ex,bb} = \frac{\dot{E}x_9}{\dot{E}x_8 + \dot{E}x_{cc}}$

and Sun et al. (2012), respectively. Figures 3 and 4 indicate the comparison between the results. However, Table 2 shows the comparison of the values of modeling in the base and optimum cases in present work via Sun et al. (2012) reference.

These differences are due to the different sources of thermodynamic properties for CO_2 and LNG used in two works. The thermodynamic properties in reference are calculated using the REFPROP, while the properties of the present work are taken from EES software (Sun et al. 2012).

3 Exergoeconomic Analysis

Numerical correlations are applied to evaluate the heat transfer coefficients in the heat exchangers. To evaluate the heat transfer coefficients, the types of exchangers are determined. As for its high efficiency and intensive form, the plate heat exchanger (PHE) type is used in this system (Li et al. 2014). It is supposed in boiler and refrigeration; the single-phase flow regimes and condenser are assumed to have two-phase flow regime. The governing equations for calculation of convection heat transfer coefficient and heat transfer area are explained in Reference Li et al. (2014).

The exergoeconomic model is the latest method to evaluate the cost of system processes based on exergy and economic analysis. By using this method, the cost per exergy unit of the product can be calculated (Bejan et al. 1996; Zare et al. 2012). As in order to define a cost function, component cost can obligatory be expressed as a function of thermodynamic design parameters. The cost balance equations with the required auxiliary equations are applied to estimate each component of the cycle. The cost balance equations may be written as (Bejan et al. 1996):

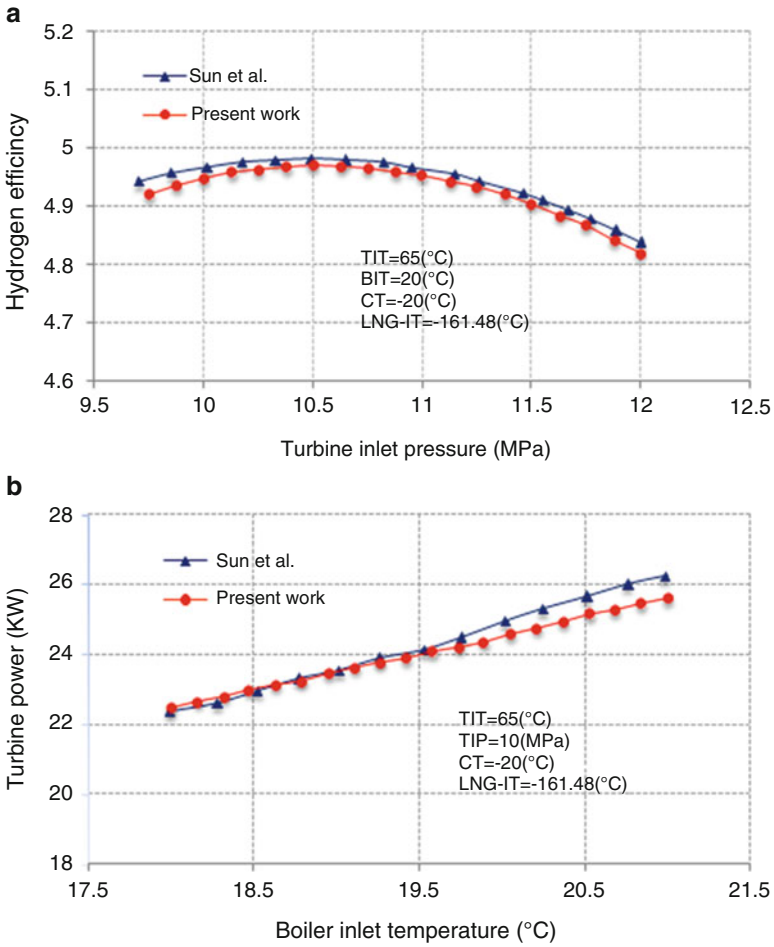

Fig. 3 Validation of hydrogen efficiency (**a**) and turbine power (**b**) of the model developed in the present work by that of the Sun et al. (2012)

$$\sum_{e} \dot{C}_{e,k} + \dot{C}_{\mathrm{w},k} = \sum_{i} \dot{C}_{i,k} + \dot{C}_{\mathrm{q},k} + \dot{Z}_{k} \tag{16}$$

$$\dot{C}_{\mathrm{j}} = c_{\mathrm{j}} \dot{\mathrm{E}}_{\mathrm{xj}} \tag{17}$$

The term $\dot{C}$ is the cost rate, and w and q are the subscripts associated with the output power from the component and input thermal energy to the component, respectively. The balance equations for all components of the system involve a set of nonlinear equations, which were solved for $\dot{C}_{\mathrm{j}}$ and c_{j}. In the cost balance formulation Eq. (16), the cost of the exergy destruction rate is unclear. Thus, if one combines the exergy balance and exergoeconomic balance together, one can obtain the following equations (Bejan et al. 1996; Ahmadi et al. 2001a, b):

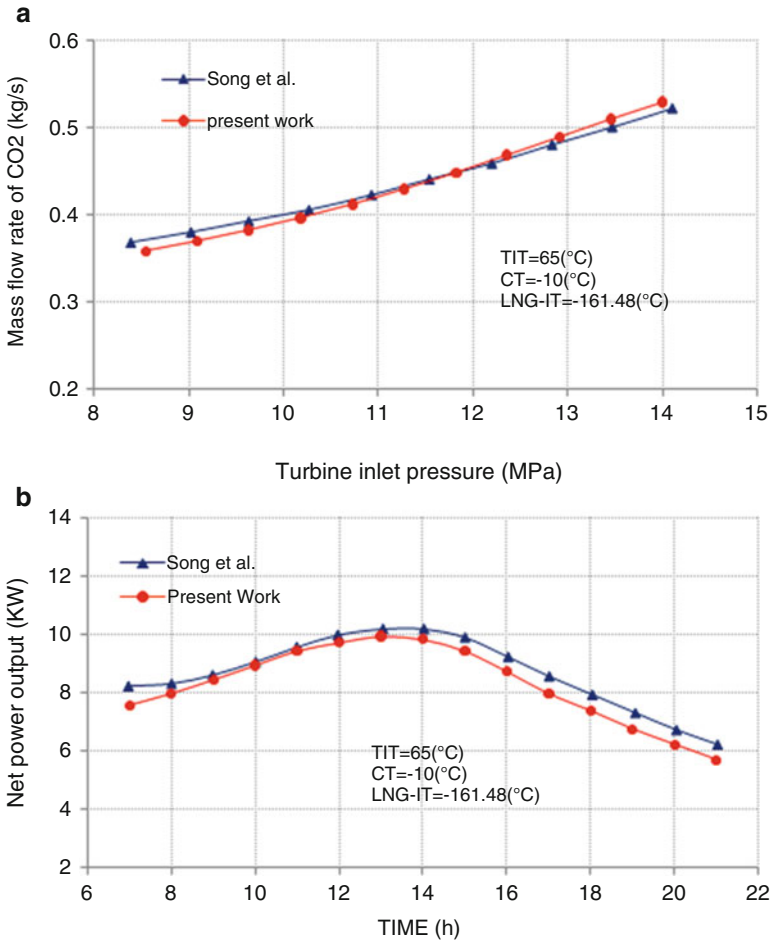

Fig. 4 Validation of mass flow rate (**a**) and net power output (**b**) of the model developed in the present work by that of the Song et al. (2012)

$$\dot{E}\,x_{F,K} = \dot{E}\,x_{P,K} + \dot{E}\,x_{D,K} \tag{18}$$

$$\dot{C}_{F,K} = c_{F,K}\dot{E}\,x_{D,K} \tag{19}$$

$$\dot{C}_{P,K} = c_{P,K}\dot{E}\,x_{D,K} \tag{20}$$

Further details on exergoeconomic analysis, cost balance equation, and exergoeconomic factor are discussed in Refs. Tsatsaronis (1987), Balli and Aras (2007), and Rosen and Dincer (2003). However, the cost functions as suggested by Ahmadi and Sanaye (2008) and Roosen et al. (2003) are referred. The term $\dot{Z}_k$ in Eq. (16) is the total cost rate which is related with capital investment, operation, and maintenance for kth component:

Table 2 Base and optimum values of the present work and Sun et al. (2012)

Terms	Base values		Optimum values	
	Sun et al.	Present work	Sun et al.	Present work
Collector exergy gain (kW)	145.6	146.1	-------	------
Turbine work (kW)	24.22	24.28	41.66	42.56
Pump work (kW)	5.77	5.782	7.16	7.898
Net power output (kW)	18.45	18.5	34.50	34.67
Refrigeration output (kW)	3.66	3.691	11.52	11.498
Hydrogen production rate (L/s)	1.12	1.236	2.1	2.315
S-H_2 exergy efficiency (%)	4.98	4.333	12.38	10.95
CO_2- H_2 exergy efficiency (%)	9.26	9.27	32.05	34.67
Exergy destruction rate (kW)	115.27	115.6	22.25	19.543

$$\dot{Z}_k = \dot{Z}_k^{CI} + \dot{Z}_k^{OM} \tag{21}$$

The annual levelized capital investment for the kth component can be calculated as (Misra et al. 2006):

$$\dot{Z}_k^{CI} = \left(\frac{\text{CRF} \times \varphi}{\tau}\right) Z_k \tag{22}$$

where CRF, τ, and φ are the capital recovery factor, the annual plant operation hours, and maintenance factor, which is often 1.06, respectively. The required equations for achieving the investment cost of the system equipment ($\dot{Z}_k$) such as heat exchangers, pump, and turbine are explained in Ref. Li and Dai (2014), and thermal storage tank is explained in Ref. Bejan (1997). The capital recovery factor is a function of the interest rate, i_r, and the number of useful years of the plant operation, n:

$$\text{CRF} = \frac{i_r(1+i_r)^n}{(1+i_r)^n - 1} \tag{23}$$

$$\dot{Z}_k^{OM} = \gamma_k Z_k + \omega_k \dot{\text{E}}\,\text{x}_{p,k} + R_k \tag{24}$$

where γ_k, ω_k, and R_k are the fixed and variable operation and maintenance costs and all the other operation and maintenance costs, respectively. The last two terms on the right side of the equation are smaller compared with the first one and may also be ignored (Vieira et al. 2009; Misra et al. 2003).

For thermoeconomic validation, the simple cycle of CO_2 transcritical system is considered. The thermal efficiency, the net power output, the total areas of the heat exchangers, and the cost per net power output (CPP) of this cycle are simulated. The results are compared with the available data in the literature reported by Li et al. (2012). According to Figs. 5 and 6, this comparison shows a descent flow within the results. However, Table 3 indicates the comparison between the modeling and optimum values in the present work and the reference given above.

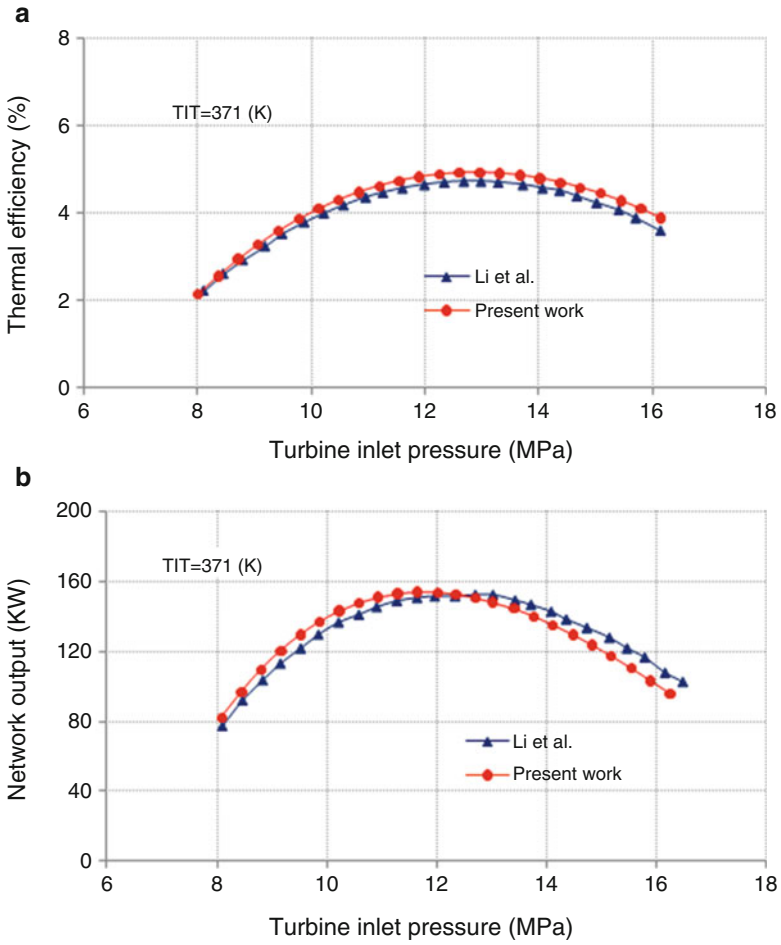

Fig. 5 Validation of thermal efficiency (**a**) and net power output (**b**) of the model developed in the present work by that of the Li et al. (2012)

3.1 Cost Balance Equations

There are two parts in three configurations which are similar: the CO_2 transcritical power and the hydrogen production subsystems. The major difference of these systems is in their sources of energy. Therefore, the formulation of cost balance and required auxiliary equations for main parts conform to one another. These equations are as follows:

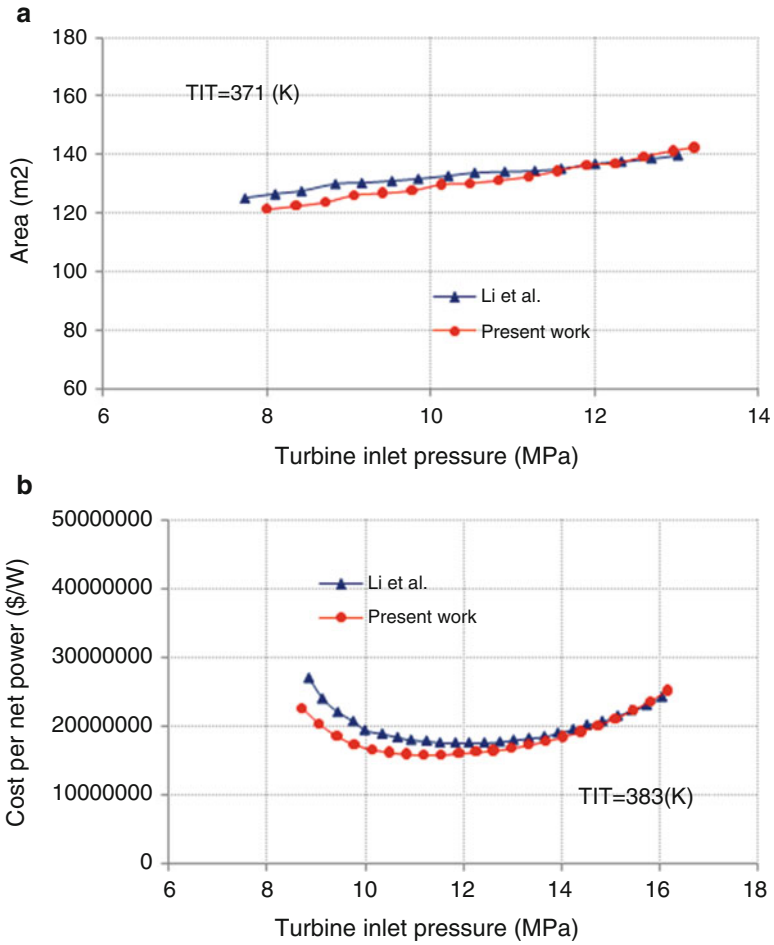

Fig. 6 Validation of area (**a**) and cost per net power (**b**) of the model developed in the present work by that of the Li et al. (2012)

Table 3 Base and optimum values of the present work and Li et al. (2014)

	Base values		Optimum values	
Terms	Li et al.	Present work	Li et al.	Present work
CPP ($/W)	1.88E7	1.568E7	1.750E7	1.349E7
Net power output (KW)	153.635	153.72	173.57	187.4
Thermal efficiency (%)	4.7368	4.846	5.50	5.707
Exergy efficiency (%)	47.235	48.026	54.40	56.451

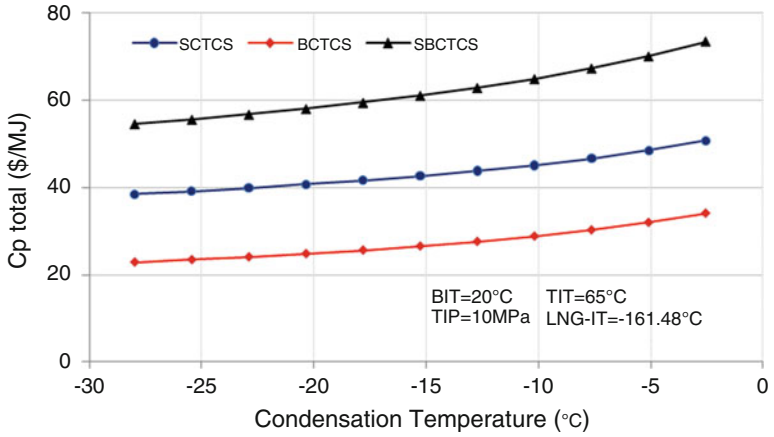

Fig. 6 Effect of condensation temperature on the SUCP of three configurations

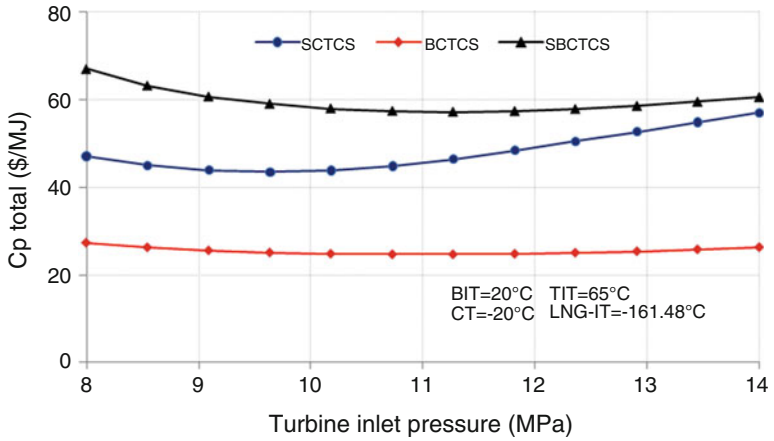

Fig. 7 Effect of turbine inlet pressure on the SUCP of the three configurations

Pump:

$$\dot{C}_2 = \dot{C}_1 + \dot{C}_{W_P} + \dot{Z}_P \tag{25}$$

Refrigeration:

$$\dot{C}_3 + \dot{C}_{13} = \dot{C}_2 + \dot{C}_{12} + \dot{Z}_{ref} \tag{26}$$

$$\frac{\dot{C}_2}{\dot{E}x_2} = \frac{\dot{C}_3}{\dot{E}x_3} \quad \text{or} \quad c_2 = c_3 \tag{27}$$

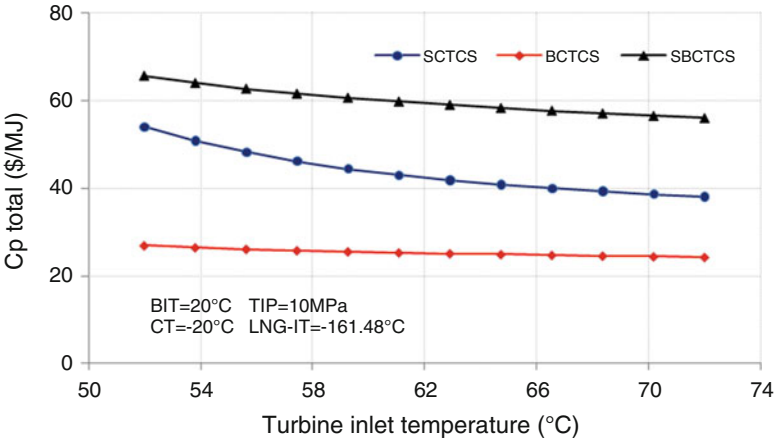

Fig. 8 Effect of vapor supercritical temperature of CO_2 on the SUCP in three configurations

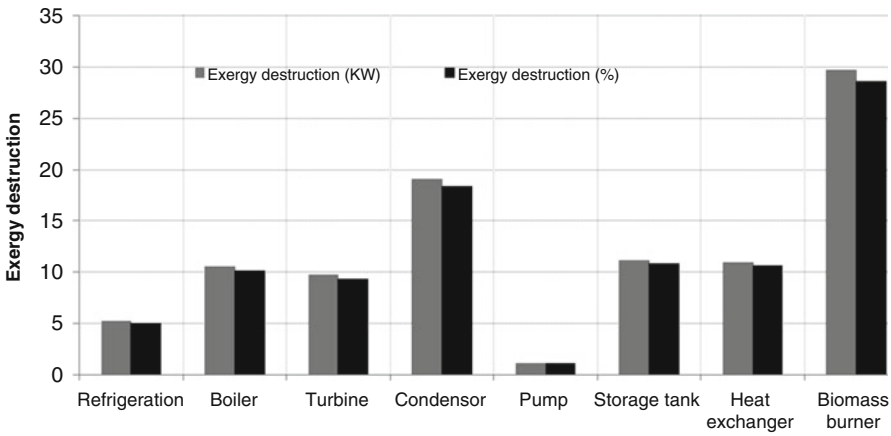

Fig. 9 Exergy destruction of each component of the systems

Turbine:

$$\dot{C}_5 + \dot{C}_{W_T} = \dot{C}_4 + \dot{Z}_{tur} \tag{28}$$

$$\frac{\dot{C}_4}{\dot{E}x_4} = \frac{\dot{C}_5}{\dot{E}x_5} \quad \text{or} \quad c_4 = c_5 \tag{29}$$

Condenser:

$$\dot{C}_1 + \dot{C}_7 = \dot{C}_5 + \dot{C}_6 + \dot{Z}_{Cond} \tag{30}$$

$$\frac{\dot{C}_6}{\dot{E}x_6} = \frac{\dot{C}_7}{\dot{E}x_7} \quad \text{or} \quad c_6 = c_7 \tag{31}$$

Electrolyzer:

$$\dot{C}_{H_2} = \dot{C}_{W_T} + \dot{Z}_{elec} \tag{32}$$

On the contrary, the energy source of three configurations differs from each other. Thus, the cost balance and required auxiliary equations are formulated separately.

3.1.1 Solar Energy Source

Boiler:

$$\dot{C}_4 + \dot{C}_9 = \dot{C}_3 + \dot{C}_8 + \dot{Z}_{boil} \tag{33}$$

$$\frac{\dot{C}_8}{\dot{E}x_8} = \frac{\dot{C}_9}{\dot{E}x_9} \quad \text{or} \quad c_8 = c_9 \tag{34}$$

Thermal storage tank:

$$\dot{C}_8 + \dot{C}_{11} = \dot{C}_9 + \dot{C}_{10} - \dot{C}_{Q_{lhst}} + \dot{Z}_{st} \tag{35}$$

$$\frac{\dot{C}_{10}}{\dot{E}x_{10}} = \frac{\dot{C}_{11}}{\dot{E}x_{11}} \quad \text{or} \quad c_{10} = c_{11} \tag{36}$$

Flat-plate solar collector:

$$\dot{C}_{10} = \dot{C}_{11} + \dot{C}_{fpsc} + \dot{Z}_{fpsc} \tag{37}$$

3.1.2 Biomass Energy Source

Biomass burner:

$$\dot{C}_{10} = \dot{C}_8 + \dot{C}_9 + \dot{C}_{env} + \dot{Z}_{bb} \tag{38}$$

Boiler:

$$\dot{C}_4 + \dot{C}_{11} = \dot{C}_3 + \dot{C}_{10} + \dot{Z}_{evap} \tag{35}$$

$$\frac{\dot{C}_{10}}{\dot{\mathrm{E}}\mathrm{x}_{10}} = \frac{\dot{C}_{11}}{\dot{\mathrm{E}}\mathrm{x}_{11}} \quad \text{or} \quad c_{10} = c_{11} \tag{36}$$

3.1.3 Solar-Biomass Energy Source

Biomass burner:

$$\dot{C}_{10} = \dot{C}_{8} + \dot{C}_{9} + \dot{C}_{\mathrm{env}} + \dot{Z}_{\mathrm{bb}} \tag{38}$$

Heat exchanger:

$$\dot{C}_{11} + \dot{C}_{14} = \dot{C}_{10} + \dot{C}_{16} + \dot{Z}_{\mathrm{hex}} \tag{39}$$

$$\frac{\dot{C}_{10}}{\dot{\mathrm{E}}\mathrm{x}_{10}} = \frac{\dot{C}_{11}}{\dot{\mathrm{E}}\mathrm{x}_{11}} \quad \text{or} \quad c_{10} = c_{11} \tag{40}$$

Boiler:

$$\dot{C}_{4} + \dot{C}_{15} = \dot{C}_{4} + \dot{C}_{14} + \dot{Z}_{\mathrm{boil}} \tag{41}$$

$$\frac{\dot{C}_{14}}{\dot{\mathrm{E}}\mathrm{x}_{14}} = \frac{\dot{C}_{15}}{\dot{\mathrm{E}}\mathrm{x}_{15}} \quad \text{or} \quad c_{14} = c_{15} \tag{42}$$

Thermal storage tank:

$$\dot{C}_{16} + \dot{C}_{18} = \dot{C}_{15} + \dot{C}_{17} - \dot{C}_{\mathrm{Q_{lhst}}} + \dot{Z}_{\mathrm{st}} \tag{43}$$

$$\frac{\dot{C}_{17}}{\dot{\mathrm{E}}\mathrm{x}_{17}} = \frac{\dot{C}_{18}}{\dot{\mathrm{E}}\mathrm{x}_{18}} \quad \text{or} \quad c_{17} = c_{18} \tag{44}$$

Flat-plate collector:

$$\dot{C}_{17} = \dot{C}_{18} + \dot{C}_{\mathrm{fpsc}} + \dot{Z}_{\mathrm{fpsc}} \tag{45}$$

The following supplementary equation:

$$\frac{\dot{C}_{\mathrm{W_T}}}{\dot{W}_{\mathrm{T}}} = \frac{\dot{C}_{\mathrm{W_P}}}{\dot{W}_{\mathrm{P}}} \quad c_{\mathrm{W_T}} = c_{\mathrm{W_P}} \tag{46}$$

4 Exergoenvironmental Analysis

Recently, a decline of carbon dioxide emission such as main greenhouse gas and optimization of cogeneration systems based on environmental blows is paid much attention to. At present work, special attention on emissions of pollutants (e.g., CO and NO_x) is considered, and environmental blows are ignored just as much research reported. Adiabatic flame temperature in primary zone of the biomass burner can be expressed as follows (Ahmadi et al. 2001a, b; Toffolo and Lazzaretto 2004):

$$T_{PZ} = A\sigma^{\alpha}\exp\left(\beta(\sigma+\lambda)^2\right)\pi^{x^*}\theta^{y^*}\psi^{z^*} \tag{47}$$

where π is dimensionless pressure (P/P_{ref}), θ is dimensionless temperature (T/T_{ref}), ψ is the H/C atomic ratio, $\sigma = \varphi$ for $\varphi \leq 1$ (where φ is mass or molar ratio), and $\sigma = \varphi - 0.7$ for $\varphi \geq 1$. Values for these parameters and further details on the methodology are presented by Ahmadi et al. (2001a, b) and Toffolo and Lazzaretto (2004). The pollutant emissions (in gram per kilogram of fuel) can be determined as follows:

$$m_{CO} = \frac{0.179\,E\,9\exp\left(7800/T_{PZ}\right)}{P_{bb}^2\,\tau\left(\Delta P_{bb}/P_{bb}\right)^{0.5}} \tag{48}$$

$$m_{NO_x} = \frac{0.15\,E\,16\,\tau\exp\left(-71100/T_{PZ}\right)}{P_{bb}^{0.05}\left(\Delta P_{bb}/P_{bb}\right)^{0.5}} \tag{49}$$

where τ is the residence time in the combustion zone (assumed constant and equal to 0.002 s) (Rizk and Mongia 1993). T_{PZ} is the primary zone combustion temperature, P_{bb} is the biomass burner inlet pressure, and $\Delta P_{bb}/P_{bb}$ is the non-dimensional pressure drop in the biomass burner.

5 Result and Discussion

In this simulation, the boiler inlet temperature (BIT), turbine inlet temperature (TIT), turbine inlet pressure (TIP), LNG inlet temperature (LNG-IT), and condensation temperature (CT), such as decision variables, affect on the value of the objective, the sum of the unit cost of the products (SUCP), which is carried out. The basic assumption and input parameters are used in simulation and are given in Table 4. The pine trees is found broadly throughout the world and support different climates. One of the common waste wood products is pine sawdust (Al-Sulaiman et al. 2013). Therefore, in this study, the pine sawdust is selected as a biomass type in biomass burner, and its characteristics are listed in Table 5.

An important factor in determining the cost of the products, the unit cost of refrigeration may vary in an extended range. However, the value of 0.09 US$/kWh

Table 4 The input data assumed in the simulation

Parameters	Value
Ambient temperature (°C)	25
Ambient pressure (MPa)	0.1
Time	14:00
Collector tilt angle	8°
Inner diameter of the absorber tube (m)	0.014
Outer diameter of the absorber tube (m)	0.018
Total surface area of absorber plate (m^2)	450
Volume of the storage tank (m^3)	86
Boiler inlet temperature (°C)	20
Turbine inlet temperature (°C)	65
Condensation inlet temperature (°C)	−20
LNG inlet temperature (°C)	−161.48
Turbine inlet pressure (MPa)	10
LNG inlet pressure (MPa)	0.6
Declination	20.4415
Area of the collector (m^2)	1.6 * 1.1
Emissivity of plate	0.92
Emissivity of cover	0.88
Incident flux absorbed by the plate	547.799
Turbine efficiency (%)	80
Pump efficiency (%)	80
Number of collector	256
τ (h/year)	7000
i_r (%)	12
n (year)	20

Table 5 Characteristics of pine sawdust (Al-Sulaiman et al. (2013))

Biomass type	Pine sawdust
Moisture content in the fuel (% wt)	10%
Ultimate analysis (% wt dry basis)	
wc	50.54%
wh	7.08%
wo	41.11%
ws	0.57%

is considered for the base case and parametric study (Sanaye and Shirazi 2013). Here, $\dot{C}_f = c_f.\dot{m}\,\mathrm{LHV}_f$. Also c_f is biomass wood cost, which is taken to be 0.01$/kWh (LHV) [18]. The cost of the pollutant emission is considered such as term in biomass burner $\dot{C}_{env} = \dot{m_{CO}} C_{CO} + \dot{m_{NO_x}} C_{NO_x}$ where $\dot{m}_{CO}$ and $\dot{m}_{NO_x}$ are the pollutant emissions and $C_{CO} = 0.02086$ $/kg and $C_{NO_x} = 6.853$ $/kg are unit damage cost of CO and NO_x, respectively. Considering a known value for the unit exergetic cost of cooling (c_6), the unit exergetic cost of the cooling water can be neglected $c_{12} = 0$ (Gebreslassie et al. 2009a, b), and the unit exergetic cost of the

Table 6 Thermodynamic properties and costs of the SCTCS for the base case

Streams	Temp. (°C)	Pressure (MPa)	Mass flow (kg/s)	Exergy rate (kW)	Costs	
					$\dot{C}$ ($/h)	c ($/MJ)
1	−20	1.97	0.5696	123.6	853.3	1.918
2	−14.69	10.41	0.5696	128.1	917.6	1.99
3	20	10.2	0.5696	124.4	891.3	1.99
4	65	10	0.5696	130.6	1091	2.322
5	−20	1.97	0.5696	99.13	828.6	2.322
6	−161.5	0.6	0.176	190.8	17.17	0.025
7	−30	0.6	0.176	50.74	4.567	0.025
8	83.41	0.11	0.8	16.99	232.4	3.8
9	50	0.11	0.8	3.33	45.56	3.8
10	89.83	0.11	5.799	149.9	1009	1.869
11	83.41	0.11	5.799	123.1	828.4	1.869
12	25	0.1	1.059	0	0	0
13	15	0.1	1.059	0.7599	39.16	14.32

heat loss is assumed zero $c_{Q_{hlst}} = 0$ (Bejan 1997). The linear system of equations for SCTCS, BCTCS, and SBCTCS is included with 18, 17, and 24 unknown variables, respectively. Tables 6, 7, and 8 show the calculated thermoeconomic properties along with the cost flow rates and unit costs at different state points of the SCTCS, BCTCS, and SBCTCS for the base case operating condition, respectively.

Figure 6 shows the variation of sum of the unit cost of products with condensation temperature. The figure illustrates a decrease in condensation temperature leading to an increase in the C_p total. This is due to the decrease in condensation temperature which causes to increase the pump power and heat transfer in condenser; as a result, the SUCP increases.

The effect of turbine inlet pressure on the C_p total of cycle is presented in Fig. 7. The figure demonstrates the SUCP of the three systems which can be minimized at specific value of turbine inlet pressure.

The effect of turbine inlet temperature on SUCP of cycle is shown in Fig. 8. The figure shows with an increase in turbine temperature, the SUCP decreases. In fact, by increasing the turbine temperature, the net power output increases. When the turbine temperature increases by 22°, the C_p of three configurations is decreased by 29.6%, 9%, and 14.7%, respectively.

6 Exergoeconomic Optimization

There are four optimization methods, direct search, variable metric, and genetic algorithm, which are available in EES software. Also, unlike the direct search and variable metric methods, the genetic method is not affected by the assumed values

Table 7 Thermodynamic properties and costs of the BCTCS for the base case

Streams	Temp. (°C)	Pressure (MPa)	Mass flow (kg/s)	Exergy rate (kW)	Costs	
					$\dot{C}$ ($/h)	c ($/MJ)
1	−20	1.97	0.5696	123.6	529.8	1.191
2	−14.69	10.41	0.5696	128.1	569.6	1.236
3	20	10.2	0.5696	124.4	553.3	1.236
4	65	10	0.5696	130.6	663.2	1.411
5	−20	1.97	0.5696	99.13	503.5	1.411
6	−161.5	0.6	0.176	190.8	17.17	0.025
7	−30	0.6	0.176	50.74	4.567	0.025
8	25	0.1	0.1798	39.7	71.84	0.5026
9	25	0.09	0.62	1.26	0	0
10	1809	0.09	0.7998	15.07	88.99	1.641
11	60	0.09	0.7998	−0.7729	−4.565	1.641
12	25	0.1	1.059	0	0	0
13	15	0.1	1.059	0.7599	28.71	10.49

Table 8 Thermodynamic properties and costs of the SBCTCS for the base case

Streams	Temp. (°C)	Pressure (MPa)	Mass flow (kg/s)	Exergy rate (kW)	Costs	
					$\dot{C}$ ($/h)	c ($/MJ)
1	−20	1.97	0.5696	123.6	985.1	2.214
2	−14.69	10.41	0.5696	128.1	1059	2.298
3	20	10.2	0.5696	124.4	1029	2.298
4	65	10	0.5696	130.6	1263	2.687
5	−20	1.97	0.5696	99.13	958.8	2.687
6	−161.5	0.6	0.176	190.8	17.17	0.025
7	−30	0.6	0.176	50.74	4.563	0.025
8	25	0.1	0.1093	24.14	43.68	0.5026
9	25	0.09	0.377	0.7663	0	0
10	1809	0.09	0.4863	9.161	60.84	1.845
11	103.5	0.09	0.4863	−0.4444	−2.951	1.845
12	25	0.1	1.059	0	0	0
13	15	0.1	1.059	0.7599	42.73	15.62
14	83.41	0.11	0.8	16.98	275.9	4.512
15	50	0.11	0.8	3.33	54.09	4.512
16	63.53	0.11	0.8	7.683	199.8	7.223
17	69.09	0.11	5.799	72.1	619.3	2.386
18	63.53	0.11	5.799	55.69	478.4	2.386

Table 9 GA parameters and the range of decision variables for optimization

Parameters	Value
Number of individual in the population	34
Number of generation	72
Maximum mutation rate	0.25
Initial mutation rate	0.005
Minimum mutation rate	0.0005
Crossover probability	0.85
The range of BIT (°C)	18–23
The range of CT (°C)	−50 to 0
The range of TIT (°C)	50–75
The range of TIP (°C)	8–14
The range of LNG-IT (°C)	−161.48 to −70

of the independent variables. The genetic algorithm is one of the best stochastic global search method based on the Darwinian survival of natural principle.

In present work, the genetic algorithm and direct search method are applied for optimization aim. Both of them yield the same optimization results. The parameter optimization conditions are indicated in Table 9. The optimum value of the decision variables in three cases of hydrogen production rate optimal design (HPROD), refrigeration power optimal design (RPOD), and cost optimal design (COD) is given in Tables 10, 11, and 12. To compare, the value of the base case is also presented in these tables. The first three parameters in Table 9 can be illustrated by the EES user. Other parameters of the genetic algorithm are set to default values suggested in the PIKAIA program and are unchangeable within the EES. In this simulation, the number of generation is considered to be 72 after some test.

Tables 10 and 11 show that, in both configurations, the hydrogen production rate in HPROD rises from 1.235 up to 1.81 and refrigeration power in PROD rises 4.429 kW up to 6.515 kW.

In the same condition, the SUCP of the BCTCS is lower than the SCTCS (about 9 $/MJ). The comparison in results shows that more percentage of reduction in costs has happened in SCTCS (about 32.8%). It's about 19% and 23% in BCTCS and SBCTCS, respectively.

Table 12 demonstrates the hydrogen production rate in HPROD and COD cases rises from 1.235 up to 1.656 and 1.533, respectively; however, the SUCP for those cases is 1.92% and 23.6% lower than base case, respectively.

The results indicate the maximum cost of products happened in PROD case. In addition, in three configurations, the reduction of SUCP is more when the optimization is based on refrigeration power instead of hydrogen production rate.

It can be seen from comparisons between three tables that the refrigeration power and hydrogen production rate are equal in SCTCS and BCTCS and they are more than the SBCTCS. However, the SUCP of BCTCS is considerably lower than two other systems. The COD case is the most important reference in designing energy conversion systems, as economic effective system. The results of Table 11 indicated the considered cycle is a cost-effective option, if the required hydrogen

Table 10 SCTCS optimum values of decision variables and objective functions

Decision variable/objective function	Base case	Optimal case		
		HPROD 1	RPOD	COD
Boiler inlet temp. (°C)	20	22.64	23	*23*
Turbine inlet temp. (°C)	65	75	75	*75*
Turbine inlet pres (MPa)	10	8	8	*9.152*
Condensation temp. (°C)	−20	−30	−30	*−30*
LNG inlet temp. (°C)	−161.48	−70	−134.5	*−70*
Net power output (kW)	18.5	27.12	27	*26.32*
CO_2-H_2 exergy efficiency (%)	9.27	28.33	27.68	*28.84*
H_2 production rate (L/s)	1.235	1.811	1.71	*1.757*
Ref. output (KW)	4.429	6.36	6.515	*6.164*
Sum of unit cost of product ($/MJ)	43.54	33.01	35.69	*29.23*

Table 11 BCTCS optimum values of decision variables and objective functions

Decision variable/objective function	Base case	Optimal case		
		HPROD	RPOD	COD
Boiler inlet temp. (°C)	20	23	23	23
Turbine inlet temp. (°C)	65	75	72.76	75
Turbine inlet pres (MPa)	10	8	8	9.395
Condensation temp. (°C)	−20	−30	−30	−30
LNG inlet temp. (°C)	−161.48	−78.71	−72.39	−70
Net power output (kW)	18.5	27.2	26.7	26.09
CO_2-H_2 exergy efficiency (%)	9.27	26.02	27.05	28.16
H_2 production rate (L/s)	1.235	1.817	1.78	1.754
Ref. output (KW)	4.429	6.425	6.515	6.103
Sum of unit cost of product ($/MJ)	24.92	22.24	22.68	20.16

Table 12 SBCTCS optimum values of decision variables and objective functions

Decision variable/objective function	Base case	Optimal case		
		HPROD	RPOD	COD
Boiler inlet temp. (°C)	20	22	23	23
Turbine inlet temp. (°C)	65	75	50	75
Turbine inlet pres (MPa)	10	9.104	8.693	10.2
Condensation temp. (°C)	−20	−22.54	−30	−30
LNG inlet temp. (°C)	−161.48	−161.48	−161.48	−161.48
Net power output (kW)	18.5	21.81	19.91	22.96
CO_2-H_2 exergy efficiency (%)	9.27	10.98	10.15	11.57
H_2 production rate (L/s)	1.235	1.656	1.329	1.533
Ref. output (KW)	4.429	4.987	6.284	5.387
Sum of unit cost of product ($/MJ)	58.3	57.18	72.73	44.51

Table 13 SCTCS exergoeconomic items of components for optimal cases

	HPROD case		RPOD case		COD case	
Components	$\dot{E}x_{D,K}$ (kW)	$\dot{Z}_K$ ($/h)	$\dot{E}x_{D,K}$ (kW)	$\dot{Z}_K$ ($/h)	$\dot{E}x_{D,K}$ (kW)	$\dot{Z}_K$ ($/h)
Refrigeration	5.113	12.44	5.124	12.48	4.779	12.41
Boiler	10.5	12.12	10.46	12.12	8.347	11.53
Turbine	9.7	2.754	9.667	2.745	9.671	2.751
Condenser	19.02	22.158	23.9	22.33	18.55	21.73
Pump	1.094	1.066	1.097	1.067	1.276	1.148
Storage tank	11.16	6.52	11.25	6.555	11.81	6.555
Electrolyzer	6.238	2.145	6.21	2.13	6.053	2.1
Overall system	62.825	59.203	67.708	59.427	60.486	58.224

Table 14 BCTCS exergoeconomic items of components for optimal cases

	HPROD case		RPOD case		COD case	
Components	$\dot{E}x_{D,K}$ (kW)	$\dot{Z}_K$ ($/h)	$\dot{E}x_{D,K}$ (kW)	$\dot{Z}_K$ ($/h)	$\dot{E}x_{D,K}$ (kW)	$\dot{Z}_K$ ($/h)
Refrigeration	5.055	12.32	4.665	12.4	4.715	12.46
Boiler	11.69	25.15	6.176	28.04	9.906	25.42
Turbine	9.782	2.775	9.633	2.722	9.641	2.746
Condenser	24.54	33.54	16.99	32.38	18.62	22.16
Pump	1.183	1.105	1.536	1.068	1.319	1.166
Biomass burner	30.29	13.07	12.78	13.28	28.62	12.84
Electrolyzer	6.213	2.832	5.746	2.832	5.995	2.832
Overall system	88.753	90.792	57.526	92.722	78.816	79.624

production power and refrigeration output are about 1.754 lit/s and 6.103 kW, respectively.

The exergoeconomic items of each component of the system are shown in Tables 13, 14, and 15. The results shown in tables indicate that for all three optimal cases, the biomass burner and condenser have the larger contribution on exergy destruction, respectively. For all three optimal cases, in the three configurations, the investment cost related with the pump is the lowest.

For the overall system, results indicate the lowest total exergy destruction and investment cost rates are associated with HPROD and COD cases, respectively, as expected. For all three optimal cases, the total exergy rate and investment cost of BCTSC are the lowest among three configurations. These parameters are the highest in the SBCTCS as there are many components in this configuration.

Figure 9 shows that the condenser has the largest exergy destruction rate. The second source of the exergy destruction rate is storage tank. This is due to a large temperature difference in these components. On the other hand, the pump has the lowest exergy destruction rate.

Table 15 SCBTCS exergoeconomic items of components for optimal cases

	HPROD case		RPOD case		COD case	
Components	$\dot{E}x_{D,K}$ (kW)	$\dot{Z}_K$ ($/h)	$\dot{E}x_{D,K}$ (kW)	$\dot{Z}_K$ ($/h)	$\dot{E}x_{D,K}$ (kW)	$\dot{Z}_K$ ($/h)
Refrigeration	5.182	12.43	5.203	12.51	4.779	12.862
Boiler	10.49	12.12	10.57	12.16	8.448	12.620
Turbine	9.7	2.756	9.663	2.736	9.706	2.823
Condenser	19.02	37.21	25.012	29.8	19.04	21.036
Pump	1.094	1.067	1.536	1.256	1.076	1.147
Storage tank	11.17	6.55	12.78	6.645	10.759	6.55
Heat exchanger	10.98	25.264	6.052	72.394	10.884	25.13
Biomass burner	29.68	14.23	11.98	55.239	30.247	13.052
Electrolyzer	6.235	2.13	5.746	2.13	6.053	2.13
Overall system	103.569	113.757	88.542	194.87	100.991	97.35

7 Conclusions

Exergoeconomic and exergoenvironmental analysis and optimization of the three configurations for production of hydrogen and refrigeration are carried out in this paper. In SCTCS and SBCTCS, the dynamic model would be registered to search the system behavior during a day (Fig. 2). The effect of key parameters on the hydrogen production, refrigeration power, and costs of products is examined. The optimal values of parameters are examined utilizing genetic algorithm optimization. The achieved results are as follows:

1. In all three cycles, the biomass burner and condenser have the highest exergy destruction rate. Their destruction rate in the RPOD case is the lowest among three cases.
2. The results of the exergoeconomic items of components indicate that the total exergy destruction rate of the overall system, in the HPROD case, is the highest; however, the total investment cost rate of the overall system, in the COD case, is lower than two other cases.
3. As result cogeneration using biomass is the most economic effective system among the three alternative processes.
4. The simulation results show there is an optimum turbine inlet pressure for minimum SUCP. The SUCP decreases as turbine inlet temperature increases and condensation temperature decreases.
5. As the obtained results, in the SCTCS, BCTCS, and SBCTCS, the SUCP in COD case decreases by 32.8%, 19.1%, and 23.6%, regarding the base case, respectively. However, the SUCP value of base case in BCTCS is the lowest among the three cycles.
6. The results of optimization in cogeneration cycle using biomass show that the SUCP is reduced by 9% when the hydrogen production rate and refrigeration power are decreased from 1.811 to 1.754 lit/s and 6.425 to 6.103 kW from HPROD case to COD case, respectively.

7. For all three optimal cases, the total exergy rate and investment cost of BCTCS are the lowest among three cases; however, these parameters are the highest in the SBCTCS as there are many components in this system.

References

Ahmadi, P., Dincer, I.: Exergoenvironmental analysis and optimization of a cogeneration plant system using Multimodel Genetic Algorithm (MGA). Energy. **35**, 5161–5172 (2010)

Ahmadi, P., Dincer, I.: Thermodynamic and exergoenvironmental analyses, and multi-objective optimization of a gas turbine power plant. Appl. Therm. Eng. **31**, 2529–2540 (2011)

Ahmadi, P., Sanaye, S.: Optimization of combined cycle power plant using sequential quadratic programming. In: Procedure of ASME summer heat transfer conference, HT2008–56129, Florida (2008)

Ahmadi, P., Dincer, I., Rosen, M.A.: Exergy, exergoeconomic and environmental analysis and evolutionary algorithm based multi-objective optimization of combined cycle power plants. Energy. **36**, 5886–5898 (2001a)

Ahmadi, P., Rosen, M.A., Dincer, I.: Greenhouse gas emission and exergo-environmental analyses of a trigeneration energy system. Int. J. Greenhouse Gas Control. **5**, 1540–1549 (2001b)

Al-Sulaiman, F.A., Dincer, I., Hamdullahpur, F.: Thermoeconomic optimization of three trigeneration systems using organic Rankine cycle: part II-applications. Energy Convers. Manag. (2013)

Al-Sulaiman, F.A., Dincer, I., Hamdullahpur, F.: Energy and exergy analyses of a biomass trigeneration system using an organic Rankine cycle. Energy. **45**(1), 975–985 (2012)

Ameri, M., Ahmadi, P.: The study of ambient temperature effects on exergy losses of a heat recovery steam generator. In: Proceeding of the international conference on power eng. (2007)

Bagdanavicius, A., Jenkins, N., Hammond, G.P.: Assessment of community energy supply systems using energy, exergy and exergoeconomic analysis. Energy. **45**(1), 247–255 (2012)

Balli, O., Aras, H.: Energetic and exergetic performance evolution of a combined heat and power system with the micro gas turbine (MGTCHP). Int. J. Energy Res. **31**(14), 1425–1440 (2007)

Beckman, E.J.: Supercritical and near-critical CO_2 in green chemical synthesis and processing. J. Supercrit. Fluids. **28**(2), 121–191 (2004)

Bejan, A., Tsatsaronis, G., Moran, M.: Thermal Design and Optimization. Wiley, New York (1996)

Bejan A., Advanced Engineering Thermodynamics, Wiley - Interscience; 2 Edition (1997)

Bhattacharya, A., Manna, D., Paul, B., Datta, A.: Biomass integrated gasification combined cycle power generation with supplementary biomass firing; energy and exergy based performance analysis. Energy. **36**(5), 2599–2610 (2011)

Carvalho, M., Serra, L.M., Lozano, M.A.: Optimal synthesis of trigeneration systems subject to environmental constraints. Energy. **36**(6), 3779–3790 (2011)

Chen, Y., Lundqvist, P., Johnsson, A., Platell, P.A.: Comparative study of the carbon dioxide to transcritical power cycle compared with an organic Rankine cycle with R123 as a working fluid in waste heat recovery. Appl. Therm. Eng. **26**(17), 2142–2147 (2006)

Delgado-Torres, A.M., Garcia-Rodriguez, L.: Analysis and optimization of the low-temperature solar organic Rankine cycle (ORC). Energy Convers. Manag. **51**(12), 2846–2856 (2010)

Dincer, I., Al-Muslim, H.: Thermodynamic analysis of reheats cycle steam power plants. Int. J. Energy Res. **25**, 727–739 (2001)

Dincer, I., Rosen, M.A.: Exegy: Energy, Environment and Sustainable Development. Amsterdam, Elsevier (2007)

Duffie, J.A., Beckman, W.A.: Solar Engineering and Thermal Processes, 3rd edn. Wiley, New York (2006)

Gebreslassie, B.H., Guillen-Gosalbez, G., Jimenez, L., Boer, D.: Design of environmentally conscious absorption cooling systems via multi-objective optimization and life cycle assessment. Appl. Energy. **86**, 1712–1722 (2009a)

Gebreslassie, B.H., Guillen-Gosalbez, G., Jimenez, L., Boer, D.: Design of environmentally conscious absorption cooling systems via multi-objective optimization and life cycle assessment. Appl. Energy. **86**, 1712–1722 (2009b)

Li, S., Dai, Y.: Thermo-economic comparison of kalian and CO_2 transcritical power cycle for law temperature geothermal sources in china. Appl. Therm. Eng. **70**, 139–152 (2014)

Li, M., Wang, J., Li, S., Wang, X., He, W., Dai, Y.: Thermo-economic analysis and comparison of a CO_2 transcritical power cycle and an organic Rankine cycle. Geothermics. **50**, 101–111 (2014)

Li, Y.-R., Wang, J.-N., Du, M.-T.: Influence of coupled pinch point temperature difference and evaporation temperature on performance of organic Rankine cycle. Energy. **42**(1), 503–509 (2012)

Lian, Z., Chou, S.: A thermoeconomic analysis of biomass energy for trigeneration. Appl. Energy. **87**(1), 84–95 (2010)

Misra, R.D., Sahoo, P.K., Gupta, A.: Thermoeconomic optimization of a single effect water/LiBr vapor absorption refrigeration system. Int. J. Refrig. **26**, 158–169 (2003)

Misra, R.D., Sahoo, P.K., Gupta, A.: Thermoeconomic evaluation and optimization of an aqua-ammonia vapor-absorption refrigeration system. Int. J. Refrig. **29**, 47–59 (2006)

Mokheimer, E.M.A., Dabwan, Y.N. Habib, M.A., Said, S.A.M., Al-Sulaiman, F.A.: Techno-economic performance analysis of parabolic trough collector in Dhahran, Saudi Arabia. Energy Convers. Manag. **86**, 622–633 (2014)

Rizk, N.K., Mongia, H.C.: Semi analytical correlations for NOx, CO and UHC emissions. J. Eng. Gas Turbines Power. **115**(3), 612–619 (1993)

Roosen, P., Uhlenbruck, S., Lucas, K.: Pareto optimization of a combined cycle power system as a decision support tool for trading off investment vs. operating costs. Int. J. Therm. Sci. **42**, 553–560 (2003)

Rosen, M.A., Dincer, I.: Exergy-cost energy-mass analysis of thermal systems and processes. Energy Convers. Manag. **44**(10), 1633–1651 (2003)

Sahoo, P.K.: Exergoeconomic analysis and optimization of a cogeneration system using evolutionary programming. Appl. Therm. Eng. **28**(13), 1580–1588 (2008)

Sanaye, S., Shirazi, A.: Thermo-economic optimization of an ice thermal storage system for air-conditioning applications. Energy and. Building. **60**, 100–109 (2013)

Sayyaadi, H., Sabzaligol, T.: Exergoeconomic optimization of a 1000MW light water reactor power generation system. Int. J. Energy Res. **33**(4), 378–395 (2009)

Song, Y., Wang, J., Dai, Y., Zhoa, E.: Thermodynamic analysis of a transcritical CO_2 power cycle driven by solar energy with liquefied natural gas as its heat sink. Appl. Energy. **92**, 194–203 (2012)

Sun, Z., Wang, J., Dai, Y., Wang, J.: Exergy analysis and optimization of a hydrogen production process by solar-liquefied natural gas hybrid driven transcritical CO_2 power cycle. Int. J. Hydrogen. **37**, 18731–18739 (2012)

Toffolo, A., Lazzaretto, A.: Energy, economy and environment as objectives in multi criteria optimization of thermal system design. Energy. **29**, 1139–1157 (2004)

Tsatsaronis, G.: A review of exergoeconomic methodologies. In: Moran, M.J., Sciubba, E. (eds.) Second Law of Analysis of Thermal Systems, pp. 81–87. American Society of Mechanical Engineering, New York (1987)

Tsatsaronis, G., Lin, I., Pisa, J.: Exergy costing in exergoeconomics. J. Energy Resour. Technol. **115**, 9–16 (1993)

Vieira, L.S., Donatelli, J.L., Cruz, M.E.: Exergoeconomic improvement of a complex cogeneration system integrated with a professional process simulator. Energy Convers. Manag. **50**, 1955–1967 (2009)

Wang, M., Wang, J., Zhoa, Y., Zhoa, P., Dai, Y.: Thermodynamic analysis and optimization of a solar-driven regenerative organic Rankine cycle (ORC) based on flat-plate solar collectors. Appl. Therm. Eng. **50**, 816–825 (2013)

Zare, V., Mahmoudi, S.M.S., Yari, M., Amidpour, M.: Thermoeconomic analysis and optimization of an ammonia-water power/cooling cogeneration cycle. Energy. **47**, 271–283 (2012)

Indicators of Sustainability Energy Management Based on Energy Audit for Hotels

M.E.U. Oz, M.Z. Sogut, and T.H. Karakoç

1 Introduction

Hotels within the building sector are commercial structures that consume intensive energy with around 6% of the total energy consumption of the sector. It is predicted that the tourism sector, which has got the capacity exceeding 980 million people in 2011, will exceed about 1.5 million people in 2020 with an increase reaching 55%. This situation, which directly affects the lodging sector, has rendered energy efficiency obligatory especially depending on the development of environmental consciousness of people in the last years together with the cost effects created by the competition among hotels (Karatas and Babur 2013).

In the study made for 610 hotels in Europe including Turkey, energy consumption varies between 200–400 kWh/m^2 per year depending on their dimensions. This is an important consumption potential depending on the occupancy rate of hotels and defined as one of high emission resources in the building sector. So the determination of energy efficiency and energy-saving potential is important, especially for the reduction of the waste and lost energy sources and accordingly for the reduction of CO_2 emissions (Unwto 2011).

M.E.U. Oz (✉)
Vocational School of Technical Sciences, Energy Department, Uludag University, Bursa, Turkey
e-mail: meuguroz@uludag.edu.tr

M.Z. Sogut
Mechanical Engineering, Engineering Faculty, Orhangazi University, Bursa, Turkey
e-mail: mzsogut@gmail.com

T.H. Karakoç
School of Graduate Sciences, Anadolu University, Airframe and Powerplant Maintenance Department, Eskisehir, Turkey
e-mail: hikmetkarakoc@gmail.com

© Springer International Publishing AG, part of Springer Nature 2018

F. Aloui, I. Dincer (eds.), *Exergy for A Better Environment and Improved Sustainability 2*, Green Energy and Technology,
https://doi.org/10.1007/978-3-319-62575-1_69

All these evaluations render the development of sustainable energy management and management strategies obligatory. Hotels have defined the customer-centred comfort conditions as a primary goal. In this process energy consumption and effects of consumption cost are defined as important items in the customer costs. However, energy management in structural analyses is generally evaluated for m^2 areas. When considered as an enterprise, cost loads according to the occupancy rate must be taken into account in terms of management strategies.

The effective use of energy resources and energy efficiency in structures essentially depend on the management of energy and the effectiveness of the management chains. The use of energy directly concerns with the management ability of the system. That an energy management can develop and manage strategies is possible especially when they know the consumption structure, efficiency potential and saving rates. Pre-studies essentially based on energy audits must be made for energy efficiency and management in the whole structure. This study comprises the pre-studies made by taking the occupancy rate and m^2 loads of a sample hotel into account. In the study, two separate studies were made for the hotel's insulated and uninsulated state, and in both states changes, the saving loads were evaluated in terms of management.

2 Energy Management and Energy Audit in Hotels

Hotels having about 360 MToe energy consumption in the world energy consumption have also important effect on the environment due to their activities and energy-based substructures. In the hotel sector having about 7% share within the building sector, European hotels cover about 42% rate with about 5.45 million bed capacity. According to a study including these hotels, mean use of energy is between 305 and 330 $kWh/m^2/yr$. This value suggests around 160–200 $kgCO_2/m^2$ emission per unit energy as CO_2 emission potential for a typical hotel. Energy consumption in hotels is essentially fossil fuels. While about 39% of the total energy for a typical hotel is natural gas and fossil fuels, about 61% is electricity. When the activity structures of hotels are examined, it is seen that energy is used to lighten as well as to heat, cool, air condition and ventilate. The use of the heating requirements comes to the forefront in operations like the swimming pool, cooking and preparing hot meal as well as heating the building (Unwto 2011). Energy use distribution in a typical hotel is seen in Fig. 1 according to the intended use.

According to the energy-saving studies, when the capacity and use rates in hotels are taken into account, it is seen that the energy-saving potentials reach 30%. In European hotels, energy-saving potentials based on used areas are between 15% and 20% in heating, 5% and 30% in cooling, 40% and 70% in preparing hot water, and 7% and 60% in lighting (Unwto 2011). Depending on all these evaluations, establishing an effective and sustainable energy management gains importance when attention is paid to the operating cost effects of yearly energy consumption and energy costs in hotels. For hotels, energy management, with its shortest state, is

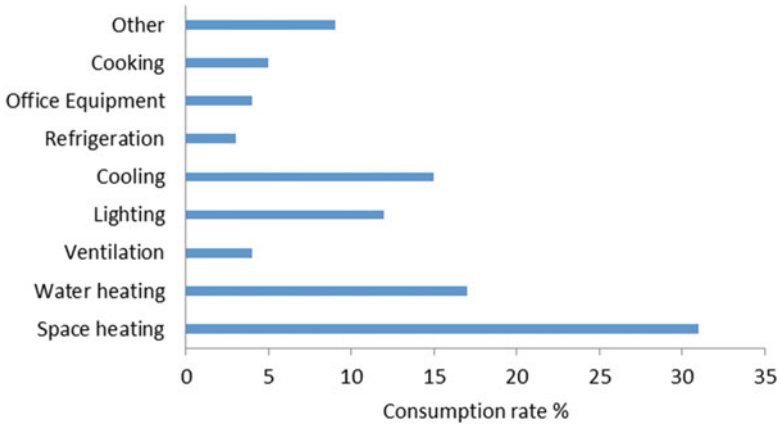

Fig. 1 Distributions of energy consumption rates in a typical hotel

a disciplined study that has been structured and organized without making concessions from the service quality, comfort, security or all environmental conditions and to use energy effectively. Energy management is an important acquirement for structures having multipurpose use and wide-ranging energy consumption like hotels. A short information concerning the energy management concept and organization is given below.

2.1 Energy Management

From the nineteenth century to the present, the developing market economies have planned their social development strategies by paying attention to their abilities in meeting the future generations' requirements. This structure has incited the mass consumption goal in social development perspective depending on economic expectations. This impact has firstly created economic imbalances in societies and also many problems such as uncontrolled consumptions of fossil fuels, water resources, and raw materials which directly destroy ecological balance. However, at the beginning of the twentieth century, the sustainable development concept has changed depending on the development in environmental consciousness in societies, and this concept has been developed as providing development by protecting the quality of life and the natural systems supporting life in the environment (Harris 2000). By this aim, healthy operating of the economy, society, and environment components being elements of sustainable development first depends on true and effective use or management of energy.

Today, it is seen that actualizing a sustainable environment concept seems quite hard especially due to socioeconomic reasons. Therefore, many scenarios have been developed with international associations with respect to limiting CO_2

emission, being one of the most important reasons of global temperature increase. Among these scenarios, this value has been limited as 450 ppm in the fourth evaluation report of the Intergovernmental Panel on Climate Change (IPCC) established by the United Nations Environment Programme (UNEP) and World Meteorology Organization (WMO), and it is predicted that this will increase the world temperature (280 ppm) 2°C compared to the value before industrialization. However, scientific studies of the last years have revealed that the safety limit must be withdrawn to 350 ppm in terms of important ecological transformations like not living climatic ruin this value will create. In spite of all these goals, depending on increased demand of energy, the fossil fuel consumption leads to uncontrolled increases in CO_2 emission (Algedik 2013; IEA 2012).

In the light of all these evaluations, energy is the most important element of social development, and the energy audit comes across us as a primary topic for sustainable development. By this aim, energy should be managed accurately in a sustainable structure from the resource to the use and to environmental effects it leads. However, that energy becomes sustainable in every point from international share and supply security to its management in national base, and its consumption in sectoral points gains value if energy policies, strategies, and formed energy managements happen in a holistic understanding. In this state, a sustainable energy depends on developing national politics and strategies by taking basic components of management into account. By this aim, a model has firstly been developed to define sustainable energy management components, and the distribution scheme of this model has been given in Fig. 2.

The success of energy managements in a country primarily depends on the road maps and strategies developed connected to national goals. And then, it takes shape with an effective management system of energy which each consumer in each sub-sector forms depending on these concepts. In Turkey, this effect has been shaped with the ISO 50001 Energy Management System. The ISO 50001 takes efficiency and productivity of energy as basis in each energy consumption point from the raw material and service to the product or service output for an enterprise. Energy management system is a system which plans commercial and industrial buildings or standard organizations to continuously develop energy performances, optimize consumptions and so reduce operational costs. This system also indirectly contributes to reduction of greenhouse gas emissions (Pekacar 2014; ISO 2011). Energy management system has a flow plan given in Fig. 3.

This circle defined as the circle Plan—Implement—Check—Correct actually shows parallelism with the ISO 14001 environment management system. Effective management of energy is a structure accommodating many concepts from individuals to system, investment costs to sourcing. However, before forming strategies and policies in this topic, if effects of these concepts on each other are not defined and national strategies are not internalized by the society individuals, the success effect of managements becomes low. Therefore, holistic management of energy and defining what kind of interaction the directly related concepts have are firstly important. In Turkey this structure has been shaped with the ISO 50001 Energy Management System. Energy management system is a system which plans

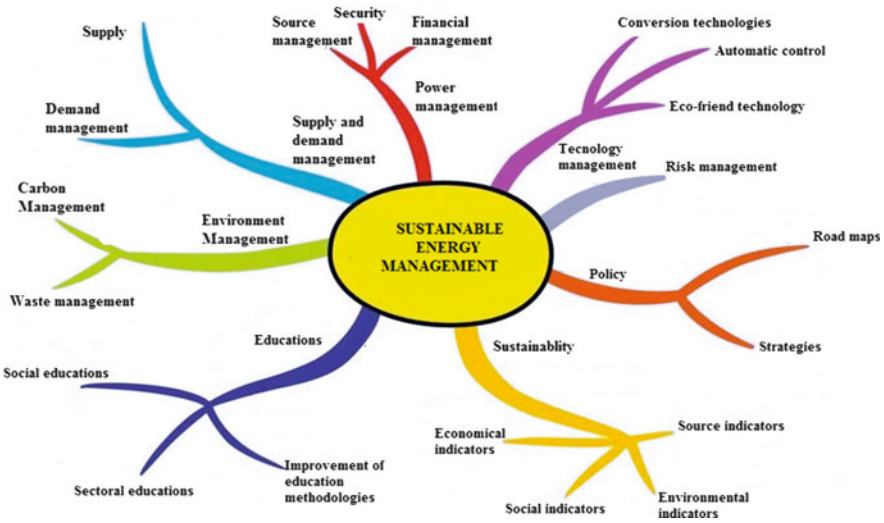

Fig. 2 Sustainable energy management

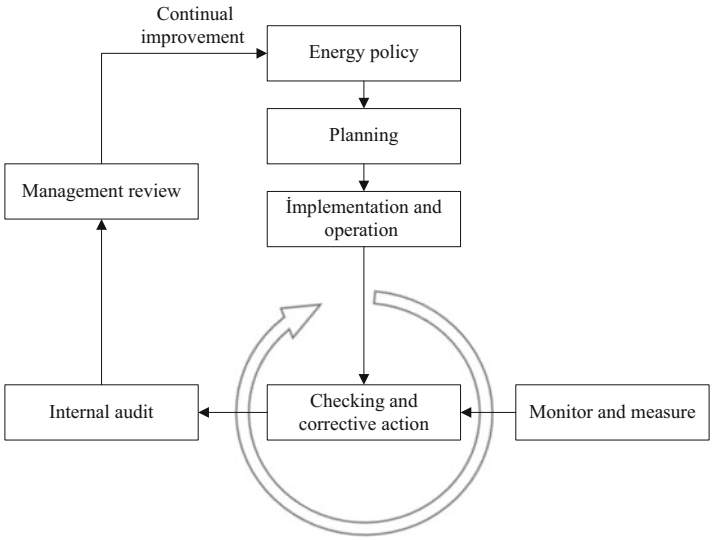

Fig. 3 Cycle of energy management system

commercial and industrial buildings or standard organizations to continuously develop energy performances, optimize consumptions and so reduce operational costs. This system also indirectly contributes to reduce greenhouse gas emissions (Pekacar 2014; ISO 2011). In this scope, an effective energy management is a dynamic structure that acts within the circle of planning, implementation, control, and taking measure. The primary duty of energy management based on an effective

organization is to determine all energy processes and determine the saving potentials with energy audits.

2.2 Energy Audit

Energy audit is the most important phase in determining energy-saving potential and developing productivity. Depending on properties of energy management processes, in the industry sector, the studies for determining the energy-saving potential are widely used. However, in commercial building applications like hotels, the energy management and applications haven't got corporate structure. So there isn't any standard method that has been developed for hotels. Energy consumption in hotels is based on fossil fuel or electricity for needs of electricity, heating, and cooling. In service buildings like hotels, additional energy types used by service sections depending on the type of the enterprise must be taken into account as well as the use of the electricity, heating, and cooling energies in daily needs. Depending on these evaluations, energy audit has been formed depending on an algorithm formed in the study. In Fig. 4, energy audit flow scheme is given.

The first and significant phase of energy audit that will be made in hotels is the data collection process depending on energy consumption types. The data collection process necessitates a strategic approach for energy managements. The type and structure of the data collection have a different structure for every hotel, where the data are collected. According to this, the data collection strategy for a hotel comprises the detection of the data of the cost concerning energy consumption types, measurement types and periods, measurement points, measurement times, data collection places and energy types. In healthy being of the data collection during energy audit, accurate working of the energy measurement devices, with which measurement and taking data are realized, making calibrations and accurate setting of the data records are obligatory. Although measurement periods are important in determining the saving potential based on energy audit, measurement periods are made according to the specialties of the structure and the type of energy will provide the results to be realistic. At least 10–20 sets of data must be taken in periods which will be chosen in energy audit. One of the most important processes in the data collection process is the determination of the data collection type and measurement times. It will be suitable that for collection time, at least 10 weeks interval should be in weekly measurements and at least 1 year interval in monthly measurements.

An approach must be formed by energy managements for the collected data in energy audit to be processed regularly. By this aim, the collected data first must be transformed into a standard structure, and their unit transformations must be provided by doing unit analyses. In this study, for the data to be processed, the energy-saving potential determination was realized with the two-method energy consumption standard and cumulative sum values (CUSUM) approach. Both methods are actively used in the determination of energy-saving potential in the

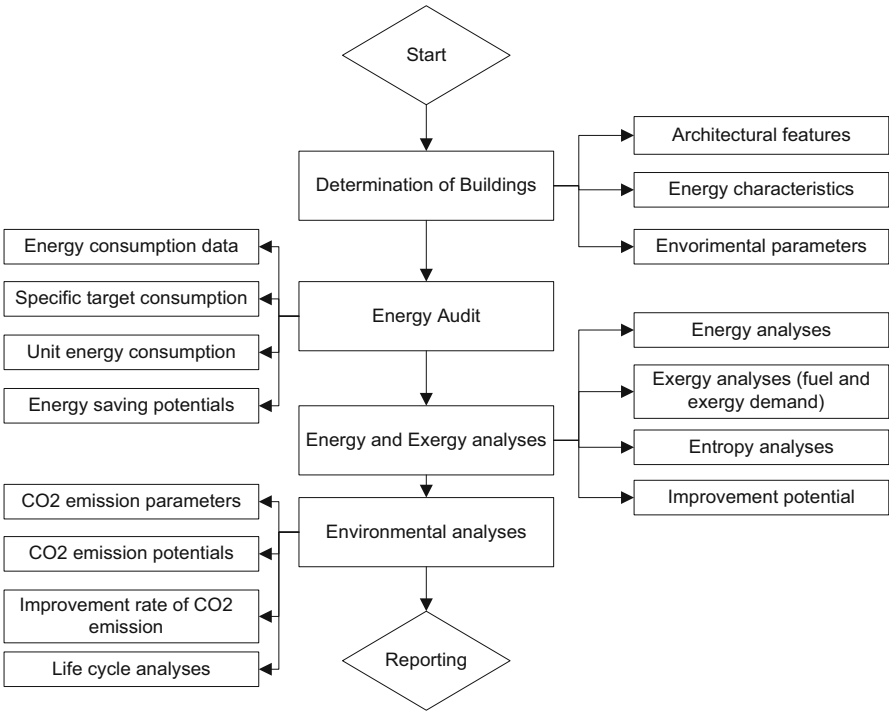

Fig. 4 Flow scheme of energy audit

industry sector. In this study, the applicability of these methods in hotel applications has been examined.

Energy consumption standard is essentially composed of phases of energy consumptions, target energy consumptions, and energy-saving potential determination. Energy consumption in buildings, depending on many factors, can vary day to day, week to week or month to month. These factors are separated into the two as specific variables and controllable variables (Kedici 1993). Specific variables are variables that determine energy demand according to the need demanded by the structure. These variables are used in the standard equations used in order to calculate energy demand. The controllable variables are variables such as the energy systems operating applications, system control and maintenance standard that are planned by the management in order to lower energy consumption to the least. In general, standard equation is a linear equation showing that energy requirement depends on specific variables. This equation

$$E = a + b(P) \tag{1}$$

Here, a and b are constants, and P is a specific variable. Even if three separate linear equations are generally used in applications, in the industrial applications the above

linear equation showing energy requirement depends on specific variables is preferred (Söğüt and Oktay 2006).

After the standard equation is formed depending on energy consumption data, goals are determined paying attention to consumption processes. According to the specialty of the structure, this process can be calculated separately as partial or within the whole of the structure. And the target equation calculated based on energy consumption processes is a linear equation being in the same form with the standard. The data formed for the target equation are classified as the data remaining under the standard line, and a target line is formed again. The equation of this line is the target equation defining the target consumption. For performance to be evaluated after determining the target in the structure, regular comparison of the expected energy use with real energy consumption values must be made. Specific energy consumption values are used to do this. It is possible to define specific energy consumption as the value of energy, which is used depending on the unit need value, in the unit time. For example, specific variable of a building is defined with energy needed in the unit of time. Specific Energy Consumption is stated as

$$\text{SEC} = E_c/\text{Hour} \tag{2}$$

Here, E_c is energy consumption. SEC value is important especially for monitoring the effect of the enterprise's operating conditions on energy consumption performance. The rise in the SEC value refers to poor performance and unnecessary increase of energy consumption (Kedici 1993).

Another method in determining energy-saving potential is the cumulative sum values (CUSUM) method. This method is essentially the cumulative sum of potentials of energy data with the least squares method. This sum value provides a structure to be seen by the help of a graphic. In the CUSUM method, the saving potentials based on the target consumptions are determined in the system examined with graphical study. In order to draw the CUSUM chart, an evaluation is made between the energy data based on the established power and the real energy data (Kedici 1993). The target consumptions based on the data obtained are calculated and energy saving in cumulative sum is calculated. The CUSUM chart is drawn in accordance with the data. When this chart is examined, it is seen that values whose slope is negative and areas staying in the negative region show times when the enterprise has had a good performance, and positive areas show times when deterioration occurs (Söğüt 2005). In order to form the CUSUM chart in the building sector, first, the difference between energy consumption costs and target energy consumption costs is calculated with the cumulative sum. The sum-saving potential depending on the data collection method is

$$\sum_{i=n}^{i} C_{\text{total}} = \sum_{i=n}^{i} C_{\text{cons.}} - \sum_{i=n}^{i} C_{\text{target}} \tag{3}$$

Here, $\sum C_{\text{sum}}$ is cumulative sum-saving potential, $\sum C_{\text{con}}$ is the sum energy consumption cost, and $\sum C_{\text{target}}$ is the target energy consumption cost. In determining cumulative sum-saving potential, the determination of the target consumptions and costs is very important. The target energy consumption potential is

$$\sum_{i=n}^{i} E_{\text{target}} = \sum_{i=n}^{i} E_{\text{cons.}} - \left(1 - \alpha_s\right) \tag{4}$$

Here, $\sum E_{\text{target}}$ is the target energy consumption, $\sum E_{\text{con}}$ is the consumed energy, and α_{s} is energy-saving rate. Here, α_{s} is the proportion of energy-saving rate to the unit energy consumption. The unit energy-saving rate is the difference between the unit energy consumption and the unit target energy consumption. According to this, the target energy cost being important for CUSUM is

$$\sum_{i=n}^{i} C_{\text{target}} = \sum_{i=n}^{i} C_{\text{cons}} - \left(1 - \alpha_s\right) \tag{5}$$

Here, $\sum C_{\text{target}}$ is the target energy consumption cost. The CUSUM chart is an important chart which can provide each collected datum to be examined in terms of both the target energy saving and also energy-saving costs.

3 Result and Discussions

Insulation applications cover significant place in efficient use of energy and energy-saving studies in buildings. A hotel, where pre-study has been made, has realized its external wall insulation in 2011 and formed a saving potential of almost 43% in the building load values. However, it is seen that this hasn't been so useful when energy consumptions have been evaluated for insulated and uninsulated conditions in terms of unit consumptions. In the study, pre-study analyses have been handled two sided as insulated and uninsulated and the effects of the insulation application on consumption have also been questioned. The study, from this aspect, comprises two different pre-study analyses by taking consumption loads of the years 2008 and 2013 as references.

The structure components for the building energy need values have been evaluated separately. The floor areas are 2152 m^2 for the earth touch, balcony area is 32.29 m^2, the total window area is 1442.42 m^2, and the total door area is 13.57 m^2. In the project, the total fill and concrete wall area is 6693.45 m^2, and the total

Table 1 Distribution of energy consumptions 2008 and 2013

Years	Energy	Distribution rate	Unit cost	Total cost	Distribution rate
2008	(kWh)	%	TL	TL	%
Electricity	1,389,970,4	56	0.2	277,994.07	28
Natural gas	1,092,611,5	44	0.65	710,197.45	72
Total	2,482,581,8			988,191.52	
2013					
Electricity	1,406,277,3	60	0.36	506,259.84	37
Natural gas	949,498,5	40	0.9	854,548.65	63
Total	2,355,775,8			1,360,808.5	

penthouse and roof area is 2092.97 m^2. The hotel's closed area's total m^2 measurement is 13,253.04 m^2.

In the pre-studies, energy consumption and cost distributions of both two 2 years have firstly been examined, and the unit consumption and costs and distribution rates have been calculated. In Table 1, energy consumption distributions of the years 2008 and 2013 are seen.

In these analyses, it is seen that 987.40 TEP/year energy consumption comes true for 2008, while the unit energy yearly cost is 0.398 TL/kWh for 2008 in the hotel consuming 875.12 TEP/year energy, in 2013; it is 0.578 TL/kWh in 2013. It can be seen that the investment hasn't got the expected effect even in these two parameters. However, the evaluation should not be made with such simple criteria in commercial enterprises where priority is comfort as in hotels. Pre-study energy evaluations are generally made taking m^2 as a reference in the pre-studies like hotels. This structure is important for energy consumption identity. However, occupancy rate in hotels having commercial identity affects directly the cost-effectiveness. In this study, the pre-audit of energy and, depending on this, energy-saving potentials in hotels have been made taking both m^2 and occupancy rate as references. In the pre-study, the data evaluations have been dealt monthly. The hotel's 2008 and 2003 electricity and natural gas consumptions are given in Fig. 5.

The hotel's increased costs of electricity in the summer months are conspicuous. Especially, the effect of central air-conditioning application is seen. However, even if a parallelism is seen between both these data, the increase rate in electricity consumption between the 9th and 12th months for 2013 disturbs the general flow. That the building has insulation for 2013 hasn't created positivity especially in electricity consumptions; in contrast, that consumption has increased for the 9th and 12th months is seen. Especially in the winter months in natural gas consumption, a 26.51% decrease is seen in the 2008 consumption. This positive effect can be fully evaluated as the effect of insulation if the operating cost is ignored. However, energy consumption has a decreasing graphic also for the next months (this need is for hot water and kitchen use). The unit consumption analyses of the hotel for both 2 months have been made, and firstly its standard and then target consumptions have been found and its saving potentials have been examined. This examination

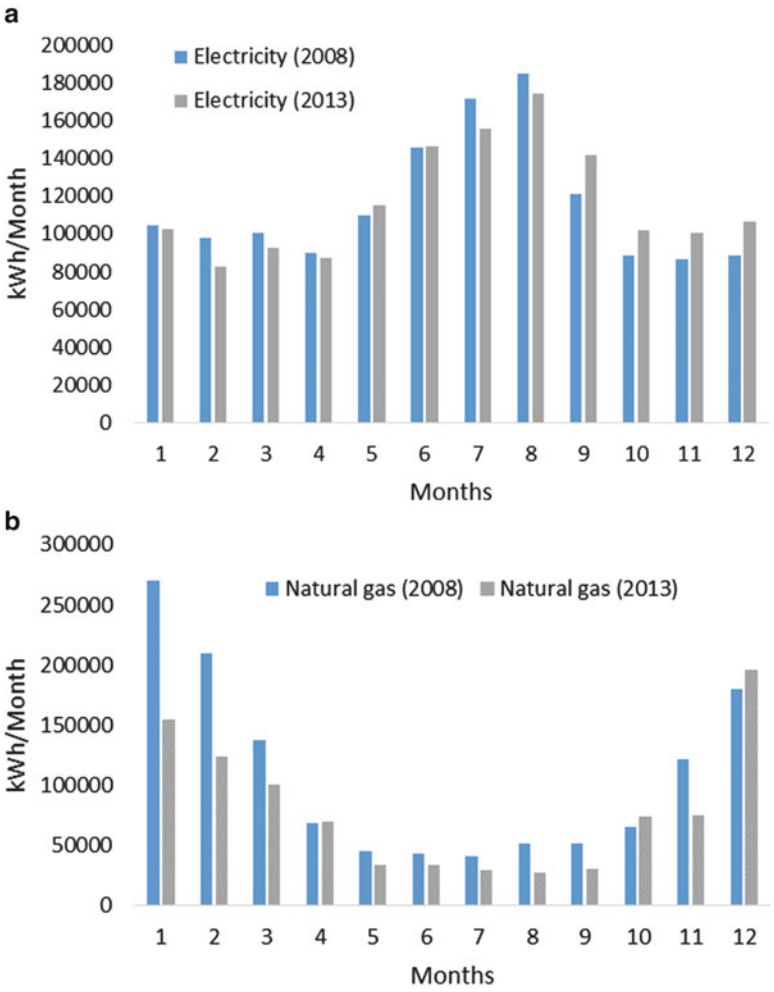

Fig. 5 Distributions of energy consumption of 2008 and 2013. (**a**) Electricity, (**b**) distributions

has been made taking both occupancy rate and also unit m^2 consumptions as references, first in Fig. 6. The hotel's 2008 and 2013 years occupancy rates are given.

While the hotel's 2008 year occupancy mean is 74.64%; this rate has become 51.77% in 2013. This value is important in terms of energy consumption and the hotel's operating efficiency. So while 30.64% decrease has occurred in the occupancy rate, the decrease in energy consumption has been 11.92%. The hotel's unit standard energy consumptions together with the target consumptions and energy potentials have been examined separately, and the data for the unit m^2 are given in Fig. 7.

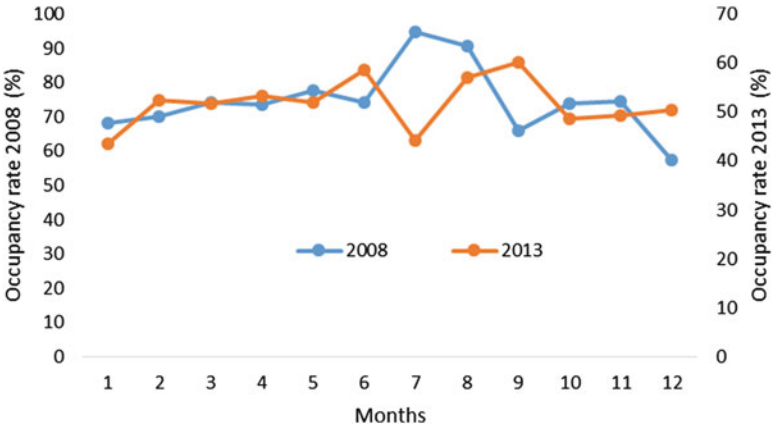

Fig. 6 Occupancy rate of hotel for 2008 and 2013

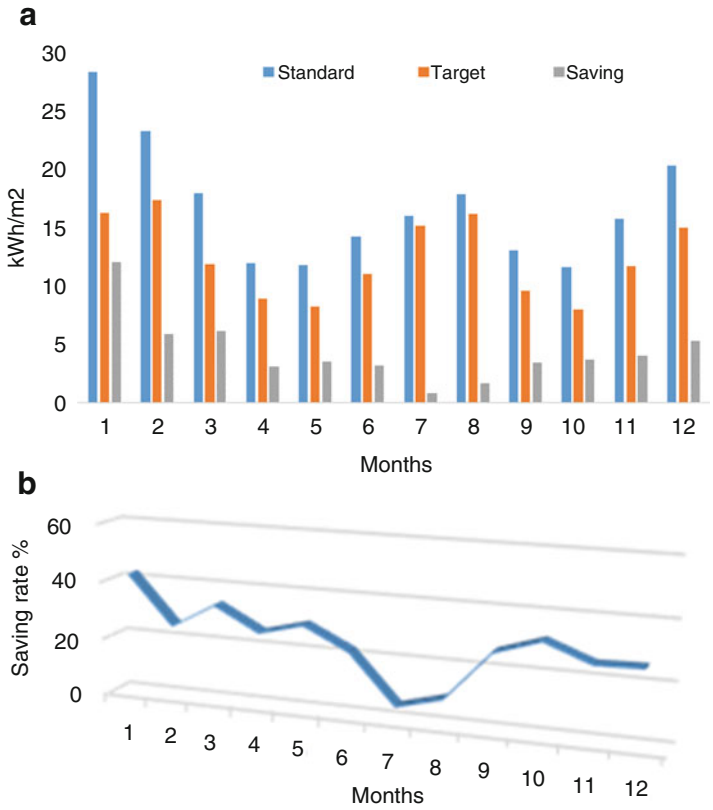

Fig. 7 Specific energy consumption analyses of 2008 for m^2. (**a**) Amounts of standard, (**b**) Distributions of saving rate for m^2 target and saving potential for m^2

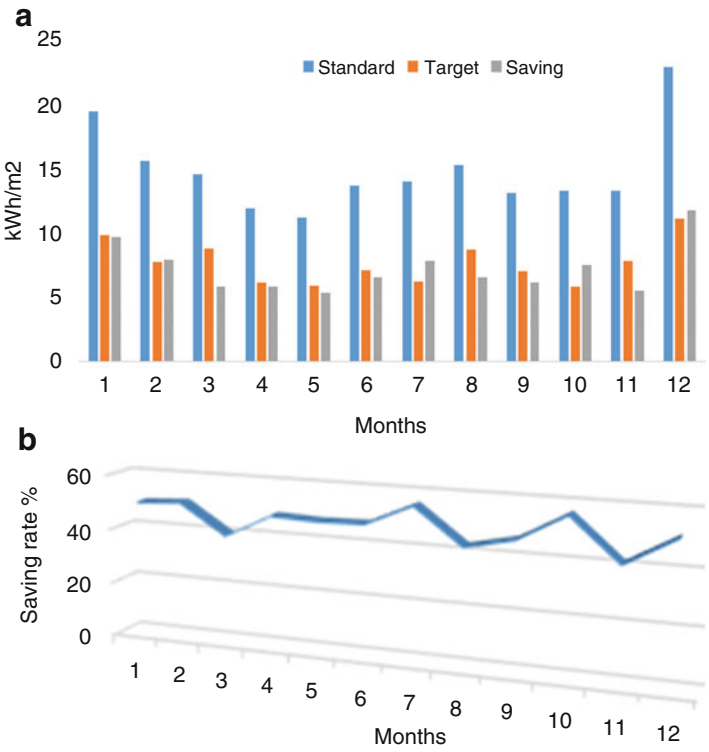

Fig. 8 Specific energy consumption analyses of 2013 for m^2. (**a**) Amounts of standard, (**b**) Distributions of saving rate for m^2 target and saving potential for m^2

While the hotel's unit m^2 standard consumption has turned out to be 16.83 kWh/m^2 for 2008, the peak values for these consumptions has been at a minimum of 11.64 kWh/m^2 and maximum of 28.27 kWh/m^2. The hotel's consumption potential has been found at 12.43 kWh/m^2 in the target consumption analyses made based on Eq. (1), and the peak values for this potential have been calculated at minimum of 7.96 kWh/m^2 and maximum of 17.34 kWh/m^2. In all these analyses for the year 2008, the yearly unit-saving quantity has been found at 4.4 kWh/m^2 and the saving rate at 36.6% in yearly mean. The saving rates according to months have been calculated at a maximum of 42.5% and 5.2%, respectively. Similar analyses have been realized for 2013, and the results are given in Fig. 8.

The 2013 data have given higher results for the unit m^2. While standard unit consumption has turned out to be 14.81 kWh/m^2 yearly mean of 2013, the target consumption potential in yearly mean has been found at 7.64 kWh/m^2, and this shows a 59.7% saving potential in yearly mean. This consumption refers to negative effects of specific variables on consumption when Eq. (1) is paid attention. The m^2 consumption in hotels should also be taken into account in terms of the building components and seasonal effects. However, in enterprises there are controllable

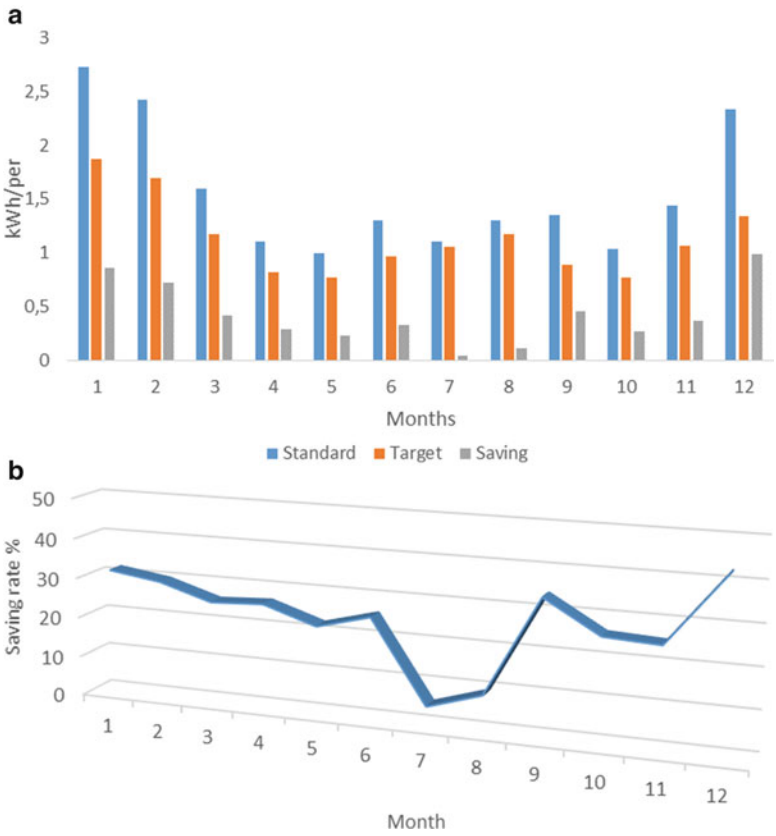

Fig. 9 Specific energy consumption analyses of 2008 for per. (**a**) Amounts of standard, (**b**) Distributions of saving rate for per target and saving potential for person

effects that become effective on consumptions based on the comfort conditions of energy resources.

Hotels are structures having commercial aspects, and operational costs or consumption costs per bed are parameters they pay attention in the pricing processes. In pricing this is identified depending on experience or may not be paid attention much in the market competition. However, this is directly related to the occupancy rate of the hotel, and the consumption costs lived in the name of not making concessions from the comfort conditions can lead to important impacts. In this study, the pre-studies based on occupancy rate have been made for each year separately, and the saving potentials have been identified separately. In Fig. 9, the specific energy consumption analyses according to the year 2008 occupancy rate have been given.

For 74.64% occupancy rate of the year 2008, the hotel's yearly mean standard consumption per unit bed has turned out to be 1.56 kWh/per. The consumption distribution per year is between 1 kWh/per and 2.73 kWh/per. To these values, the

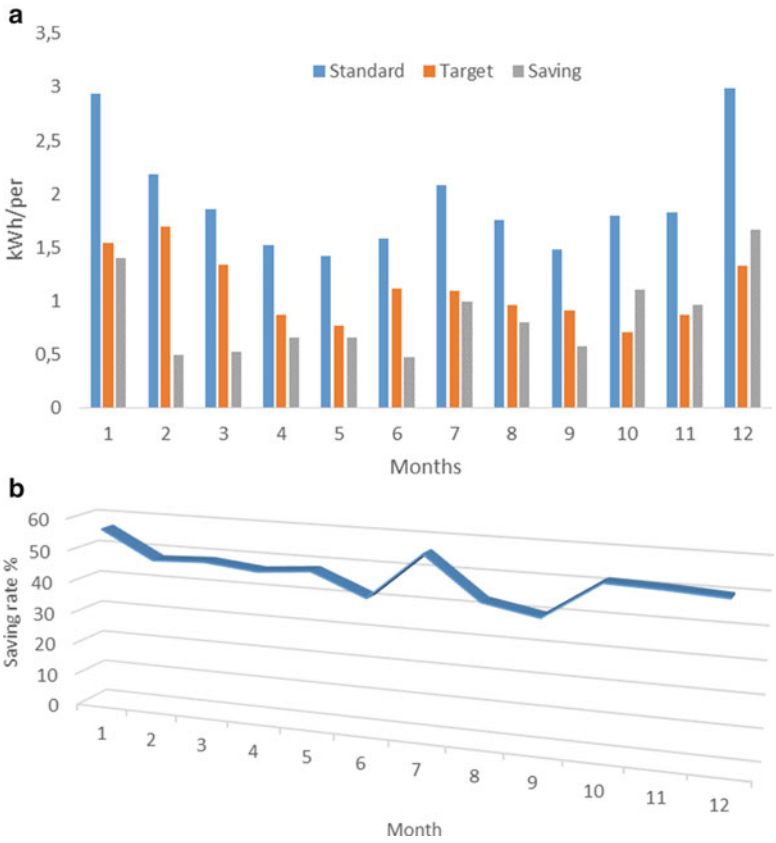

Fig. 10 Specific energy consumption analyses of 2013 for per. (**a**) Amounts of standard, (**b**) Distributions of saving rate for per target and saving potential for person

hotel's target consumption potential is 1.13 kWh/per in yearly mean, and this value states a 27.3% saving in yearly mean. It is seen that consumption surpluses especially in the winter months are significant potential for energy management in the hotel. In this state, how thermal controls and occupancy management are performed in the enterprise must be questioned. Similar analyses have been handled for the year 2013, and specific consumption data is given in Fig. 10.

The yearly mean standard consumption has turned out to be 1.95 kWh/per bed in the hotel having an occupancy rate of 30.64% lower than the year 2008. It's seen that the peak standard consumption interval in the year is maximum at 2.99 kWh/per and minimum of 1.42 kWh/per. About 25% increase is observed in standard mean consumption when compared to the year 2008. According to these consumptions, while yearly mean target consumption potential is found at 1.1 kWh/per, this value identifies a 43.8% saving in yearly mean for 2013. Hotels must drive the energy management organization via the target consumptions, especially in terms of occupancy rates.

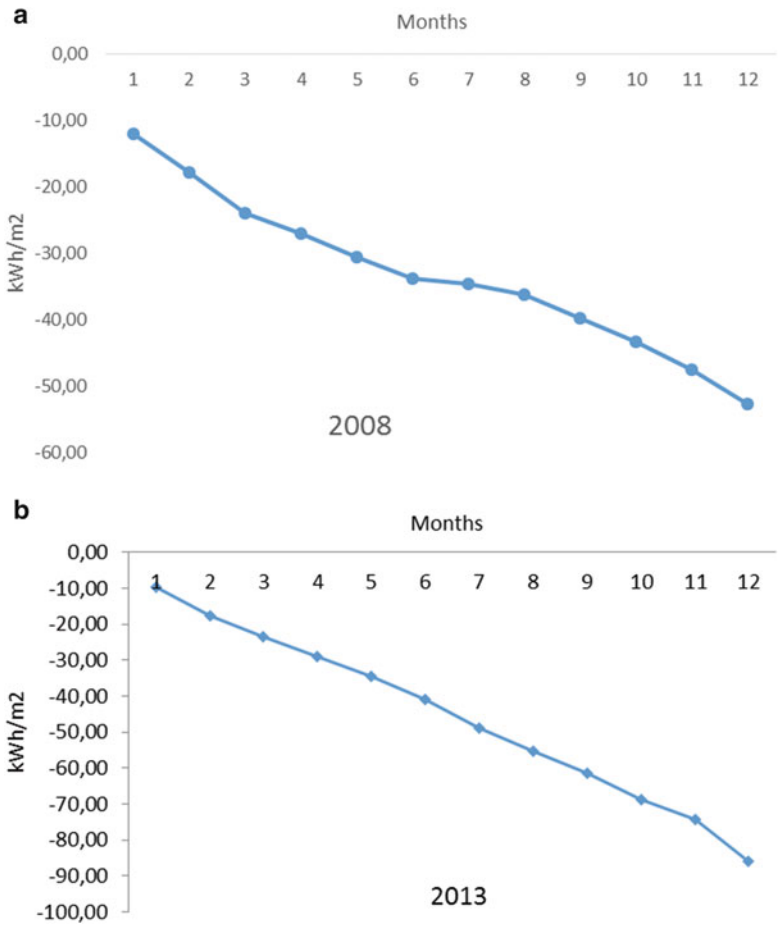

Fig. 11 CUSUM charts for unit area

Another approach different from the saving approach provided with specific analyses made in pre-studies is the formation of cumulative sum values chart (CUSUM). This approach identifying the total saving per the referenced year is an important indication for the hotel. The cumulative sum values chart (CUSUM) depending on the building's pre-audits of energy has only been made for 2013. By this aim, the CUSUM chart formed with the least squares' method depending on the sum consumption data of the year 2013 is given in Fig. 11.

While approximate saving potential for the unit area in cumulative sum is 26.11% for 2008, this value has been found 48.4 % approximately when paid attention to consumptions in 2013. For the hotel the 2013 year energy consumption data have given results which have to be scrutinized greatly. Results of similar analyses that have been made according to the occupancy rate are given in Fig. 12.

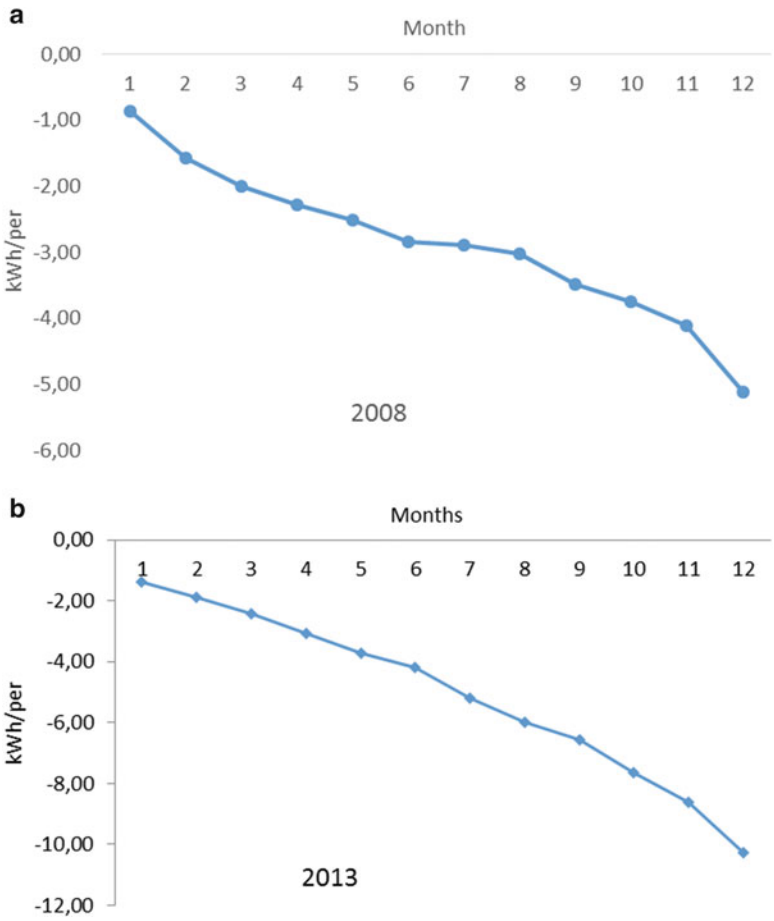

Fig. 12 Cumulative saving potential (kWh/per)

While cumulative sum-saving potential depending on specific energy consumption analyses according to occupancy rate has turned out to be 27.28% for 2008, this value for 2013 has been found to be at 43.82%. Values for both criteria have given quite close results to each other. This state emphasizes significant problems in terms of energy-saving potential in the hotel.

4 Conclusions

This study covers pre-studies executed by considering occupancy rate and loads per m^2 of a hotel taken as a sample. Pre-studies should be treated as an engineering study leading to energy management for strategy and applications. As a matter of

fact, a hotel-unemployed energy manager must establish first energy management system for ISO-50001 utility works. All facilities consuming 500 TEP/year energy in Turkey must certainly establish statutory energy management system. Some results obtained from the study are submitted below:

(a) For uninsulated situation according to scanning in year 2008, yearly mean standard consumption per m^2 is 16.83 kWh/m^2, target consumption 12.43 kWh/m^2 with a decreasing rate of 36.6%.
(b) For insulated hotel building (in 2013), yearly mean standard consumption per m^2 is 14.81 kWh/m^2, target consumption 7.64 kWh/m^2 decreasing rate 59.7%.
(c) Occupancy rate in year 2013 of an insulated hotel building is 51.77% and 74.64% in year 2008. Yearly mean standard consumption in year 2008 is 1.56 kWh/person and 1.95 kWh/person in year 2013.
(d) Target consumption by considering capacity is 1.13 kWh/person in year 2008 and 1.10 kWh/person in 2013 respectively.
(e) Yearly mean energy saving in cumulative sum for year 2013 is 48.4% per m^2, 43.8% per person, 26.11%, and 27.3%, respectively, for 2008.

According to this pre-study, advantage of building insulation in energy consumption has not been utilized sufficiently, any structure on energy requirement control is not present and applications based on efficiency in system choice have not been chosen. It is a big defectiveness to not use renewable energy resource like solar energy system in spite of sunny local of hotel. Real potential in the projects to increase energy efficiency is needed first in detailed studies for energy and exergy analysis.

References

Algedik, Ö.: Role of local government in combating climate change, civil climate summit report, civil climate summit project, Turkey, October (TR). www.iklimzirvesi.org/wp.../11/Yerel-Yonetimlerin-ID-Mucadelede-Rolu.pdf (2013)

Harris, J.M.: Basic principles of sustainable development. Global Development and Environment Institute Working Paper:00–04, Tufts University, Medford. http://www.sdergi.hacettepe.edu.tr/makaleler/EmineOzmet2eviri.pdf (2000)

IEA.: World energy outlook. http://www.worldenergyoutlook.org/publications/weo-2012/ (2012)

ISO (International Organization for Standardization): ISO 50001:2011(en). https://www.iso.org/obp/ui/#iso:std:iso:50001:ed-1:v1:en (2011)

Karataş, M., Babür, S.: Place of tourism sector in the developing world. KMU J. Soc. Econ. Res. **15** (25), 15–24 (2013) (TR)

Kedici Ö.: Energy management, general directorate of electrical power resources survey and development administration energy resources studies department, Ankara (TR) (1993)

Pekacar M.: ISO 50001 energy management system, EVD energy management system, EVD energy management and advisory İzmir. (19.02.2014) (TR). www.emo.org.tr/ekler/1e9a35c8a1d9357_ek.pdf (2014)

Söğüt, Z., Oktay, Z.: Effect energy efficiency of energy audit in industrial sector and an application, dumlupınar university. J. Sci. Inst. **10**, 151–162 (2006) (TR)

SÖĞÜT, Z.: "Energy audit and energy and exergy analyses in production line of heat processes in cement plant", Master Thessis, Balıkesir Üniversity Science Enstitute, Balıkesir, May 2005 (TR) (2005)

Unwto: Hotel energy solutions, analysis on energy use by European hotels: online survey and desk research, hotel energy solutions project publications, Revised version, Madrid, July 2011. www.unwto.org (2011)

Using a Porous Environment In Catalytic Gas Heaters to Optimize Energy Consumption and Reduce Pollution in Heating the Furnaces

Hossein Afshar, Esmaeil Khosroabadi, and Mehdi Tajdari

1 Introduction

Furnaces are the main energy consumption sources in petrochemical and refining processes in most of which the consumption share of furnaces is about 25% (Berman 1978).

Studying flame quality and optimum consumption systems, analyzing the problems of industrial furnaces and boilers, providing appropriate laboratory facilities to evaluate the performance of industrial torches, and carrying out researches on related subjects are of crucial importance which directly lead to optimization of fuel consumption, decrement of emitting gases from chimneys, and increment of efficiency of torches (Jamali 2004).

There are various methods to optimize energy consumption in furnaces from which the method of decreasing the excess air and preheating of combustion air has absorbed more attention. There are different techniques for execution of energy optimization methods in furnaces. These methods can be classified into two groups. The first group acts upon Pinch technology, and the second group was obtained by experimental methods (Jegla et al. 2000).

H. Afshar
Faculty of Mechanical Engineering, East Tehran Branch, Islamic Azad University, Tehran, Iran

E. Khosroabadi (✉)
Faculty of Engineering and New Technologies, Iran Industrial and Mining University, Pakdasht 3397149346, Iran
e-mail: ho_afshar@yahoo.com; afshar@iauet.ac.ir

M. Tajdari
Faculty of Mechanical Engineering, Arak Branch, Islamic Azad University, Tehran 1483796111, Iran

© Springer International Publishing AG, part of Springer Nature 2018

F. Aloui, I. Dincer (eds.), *Exergy for A Better Environment and Improved Sustainability 2*, Green Energy and Technology,
https://doi.org/10.1007/978-3-319-62575-1_70

The emitted gases due to the combustion of fuel in furnaces are often regarded as environmental pollutants. Although in a simple combustion process H2O, CO, and CO_2 are usually observed, in relation to combustion analysis and the interactions with the air in the furnaces, SOx and NOx are the two main pollutants emitted in the furnaces which are also among the main causes of acid rain. This, however, is noteworthy that other polluting gases with a very low percentage are also emitted in this process.

There are generally three main processes in the production of NOx. The main mechanism of its production in natural gas is Thermal NOx which occurs as a result of molecule separation of $\boldsymbol{O}_2$ and $\boldsymbol{N}_2$ due to heat and their joining together. The most amount of NOx are released somewhere near the flame which has the highest level of heat. The influential parameters in heating NOx include the amount of oxygen, high temperature, and length of time spent in high temperature. Any increment in these factors will increase the NOx production. The second mechanism is Prompt NOx which is produced through the interaction of nitrogen molecules in the air with free hydrocarbon radicals of fuel. The amount of the produced Prompt NOx in the flame is low compared to Thermal NOx. The third mechanism is fuel NOx which is the result of the interaction between the nitrogen present in fuel with oxygen. Basically, if gases with low nitrogen were used, the amount of released NOx would be low (Kaviani and Mesgarpor 2009).

Figure 1 indicates the amount of gases, especially NOx, emitted in combustion spaces with different ranges of temperature.

NOx in combustion spaces is produced through fuel NOx and heating NOx. Heating NOx is emitted when the nitrogen present in fuel interacts with oxygen. Fuel NOx, however, can be controlled by decreasing the amount of nitrogen in fuel (by using low-nitrogen fuels such as natural gas) or by lowering the oxygen available around the combustion zone. Heating NOx is also produced when the nitrogen in the air interacts with oxygen (in high temperature) which can be reduced

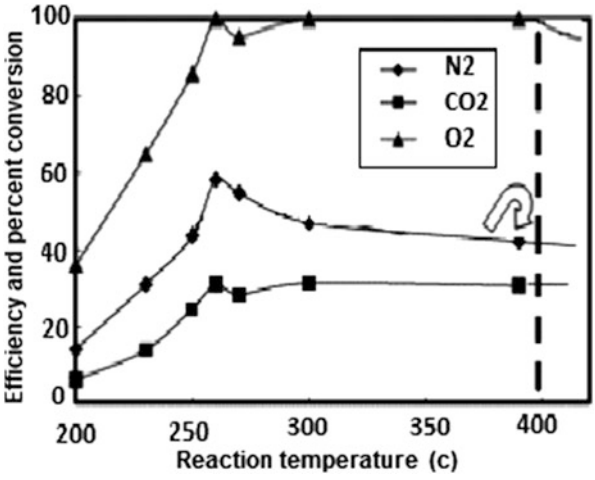

Fig. 1 Showing percent conversion of gases produced in and the range of temperatures in the combustion chamber

by decreasing the available oxygen around the combustion zone or lowering the temperature of the combustion zone. If water or water steam is poured into the combustion space, it can act like a heating well and decrease the temperature by absorbing the heat in the interaction zone. The decrement in temperature can lead into the decrement in NOx emission.

The conducted researches to improve the current technology have led into the creation of a new combustion system called non-flame combustion. And in creating a uniform combustion throughout the furnace and improving the efficiency of combustion, the new system significantly decreases the emission of the pollutants. Two main conditions which must be met for non-flame combustion are too much thinning and increasing the temperature of the interactors. If the emitting gases from the interaction zone are reversed, both of these conditions will be met.

Today, many efforts have been made to decrease the nitrogen pollutant gases. The volume of nitrogen pollutant gases depends on the flame temperature. Injection of water vapor or water decreases the peak temperature and, in turn, decreases the production of nitrogen pollutant gases. There are many papers, including Liever (Mehdizadeh et al. 2005), about decrement of NOx by CFD using spray of water. He showed that by increment of water or steam spray, NOx is decreased by 94%, but this increases the emission of CO significantly (Kaviani and Mesgarpor 2009). It must be noticed that the way of injection of fuel at the entrance of combustion chamber is very important for complete combustion and emissions (Study of hydraulic behavior 2001).

A study by Jodeiri et al., investigating the effect of debit changes of natural gas on the efficiency of the interaction, indicated that any increment in feeding rate, due to the lack of the required oxygen, causes a decrement in the rate of interaction. Moreover, by increasing the density of other hydrocarbons along with natural gas in the process of feeding fuel, the efficiency of the interaction decreases, and if the required oxygen is added to the surface, the level of efficiency can be controlled (Jodeiri et al. 2010).

The present study has used the porous environment to produce non-flame heat for the heating process of the furnaces which eventually will lead into the simultaneous optimization of energy and environmental factors in furnaces. Decrement in fuel consumption, increment in optimization, complete removal of NOx, and lowering of other harmful gases are among other advantages of using this heat-supplying system. A catalytic pad with distinctive porous surface to supply heat is used for this purpose.

De Soete (1966) was one of the pioneers to work on the field of combustion in a porous environment. He analyzed the resistance and dispersal of the flame in a sandy environment with different measures and offered a semi-experimental model to measure the speed of flame and the effect of preheating through solid heat direction.

In 2007, Lari (Hosseinpour and Haddadi 2008) conducted a research on thermal analysis of porous torches in transient state by exploiting two flux models and investigated the effects of various parameters on the performance of the system. The results suggested that the torches with more optical depth have lower

Fig. 2 An example of a porous radiant burner bed

temperature peak. An increment in emissions can be observed, and as a result, the efficiency of the torch is increased as well.

Hosseinpour and Moallemi (2009) investigated the effects of some different multilevel chemical kinetics on temperature graphs, mini bodies, and emission of pollutants and found concordance between the results obtained from different kinetics (Hussein et al. n.d.). A flat radiant porous torch is shown below (Fig. 2).

Gas torches, according to the type of mixing fuel and air, can be divided into two types: (1) premixed torches and (2) torches with crude gas or without premixing. In torches with no premixing, fuel and oxidant are kept away from each other till the condition is ready for the combustion. This is usually applied in torches in which the possibility of flame reversing and explosion is an imminent danger (such as oxygen and fuel torches). Generally, however, radiant torches are of the first type (Baukal 2003).

Nowadays, considering the necessity of designing and building heat-generating systems with high efficiency and eco-friendliness, porous radiating heaters, in which noble metals such as platinum and palladium are used to decrease the activation energy of interaction, have absorbed a lot of attention. Therefore, due to applying radiation panels to generate heat, as well as elimination of flame and its associated dangers, fewer pollutants are released into the environment. Moreover, by using radiation heat in low temperature, the heating of nitrogen of the air which is common in most systems as they produce a great deal of heat and, therefore, cause a decrease in efficiency is lowered, and a higher level of efficiency can be expected.

Combustion in catalytic porous environment was first introduced by Davy. His experiments showed that platinum threads can act as catalyst and ignite the mixture of fuel air without any flame and only by a radiant flux (Pfefferle and Pfefferle 1987).

The process of combustion in this method starts with a very short preheating period to heat the porous environment in order to prepare the conditions for the interaction. In temperature about 100 degrees celsius, (flammable) gas flows through the preheated porous environment and passing through the preheated catalytic pad, oxidation starts (fuel enters from the back of the panel, and the required oxygen comes from the front surface, and the combustion happens on the surface of the panel in the presence of catalytic pad and keeps on spontaneously). The catalytic pad used in these panels is made of noble metals such as platinum and palladium on a base of alumina fiber.

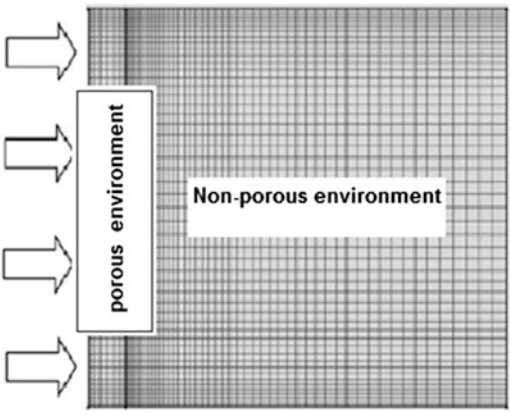

Fig. 3 Geometry and network model

A porous catalytic torch with 300 mm and stable temperature of 800 K was modeled in a study. According to the momentum conservation principle, and considering the fuel requirements of the torch, the stable velocity condition is taken as the boundary condition for the entering nozzle, and all other boundaries are assumed to be faultless except the external boundary (catalyst surface) for which the stable pressure (101,325 Pascal) is assumed. The geometry and network of this torch are shown in Fig. 3. To analyze the effects of exiting combustion products from the porous surface of torch on the Nusselt number on the partition, the modeling is made in two forms of with and without considering the feeding speed behind the porous environment. Figure 4 shows the speed profile in 250 mm height, with and without considering the speed of feeding gas in the temperature of 800 K. As is shown, the two speed profiles are very akin to each other; therefore, the feeding speed in porous environment, due to its low debit, has no significant effect on speed distribution in front part of the panel. Figure 5 shows the temperature profiles for two states of with and without considering the feeding speed. As it is shown, since no significant modification can be observed in speed profiles (it can be concluded that) after applying the feeding with speed and if other equations and physical properties are kept the same, no significant change can be observed (Nield and Bejan 2006, Kreith and Bohn 1993, Incropera and DeWitt 2002).

If all the combustible elements in the fuel are burnt or reach the last level of oxidation, the combustion is completed; if, however, the combustion product contains carbon, the combustion is not completed which results in energy loss and the emission of pollutant gases. Using the proposed system, a complete combustion can be guaranteed.

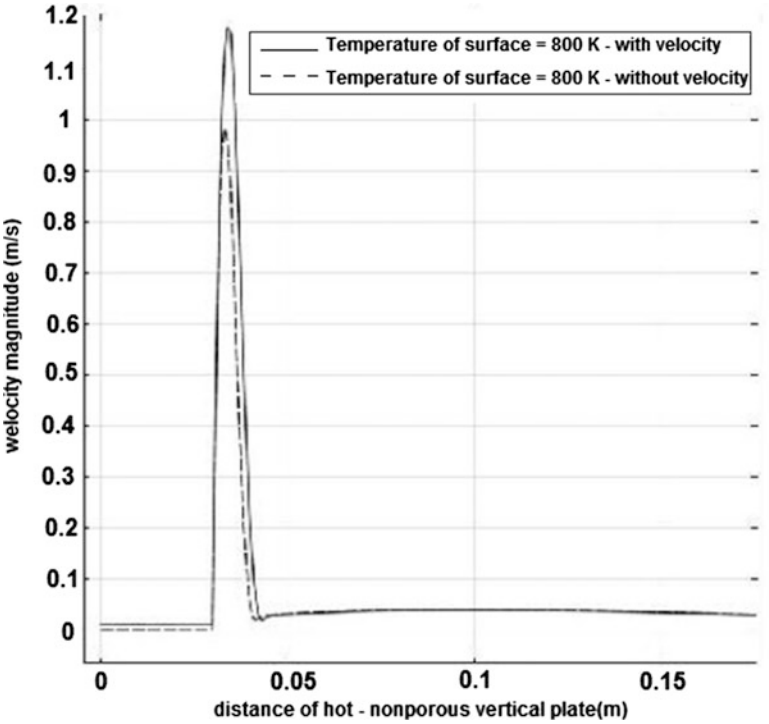

Fig. 4 The speed for two states of with and without considering the feeding speed

2 The Procedures of the Manufactured Porous Pad Operation

The proposed system is proportional to industrial application. In this system, instead of using high-temperature furnaces (with torches) or using electric furnaces, which are not usually economical, a porous environment can be used to provide non-flame radiant heat.

In these panels, a porous environment with a special porous surface is exploited. The results of BET[1] test for this pad is shown in Fig. 6. The first step in order to produce heat is a very short preheating period to prepare the catalyst for the interaction. As soon as it reaches the proper temperature, the condition is ready to feed the gas in order to activate the catalytic combustion. The combustible gas is flown in the preheated porous environment and passes through the preheated catalytic pad; it causes the oxidation of gas and releases heating energy.

[1] Brunauer Emmett Teller

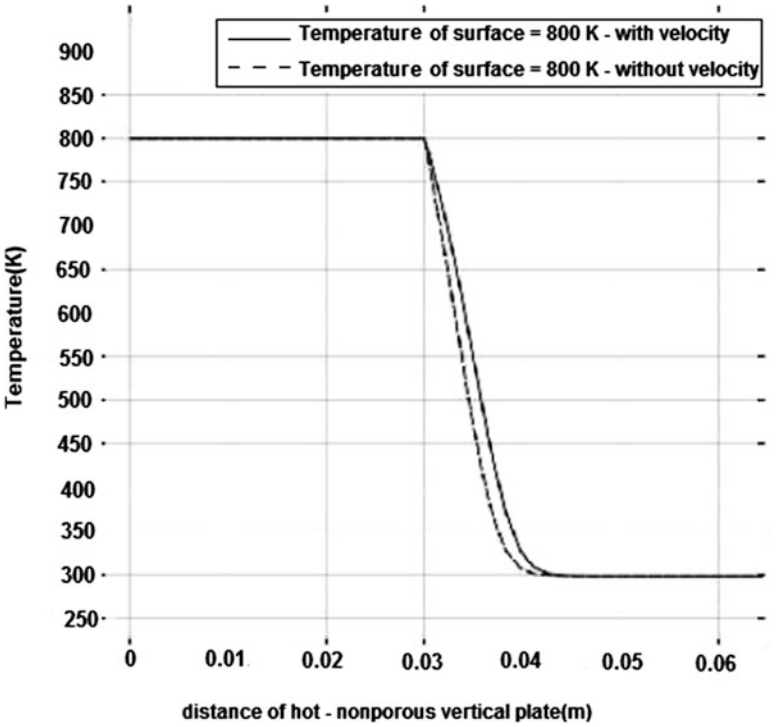

Fig. 5 The temperature profiles for two states of with and without considering the feeding speed

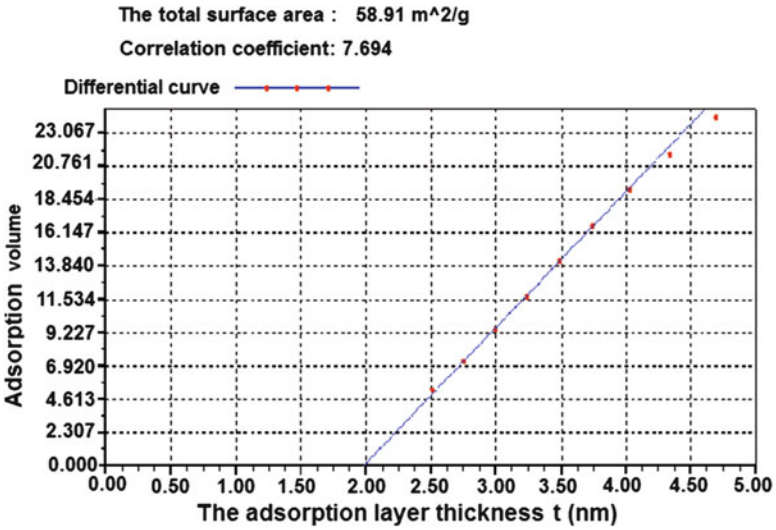

Fig. 6 The graph of porous surface of the catalyst

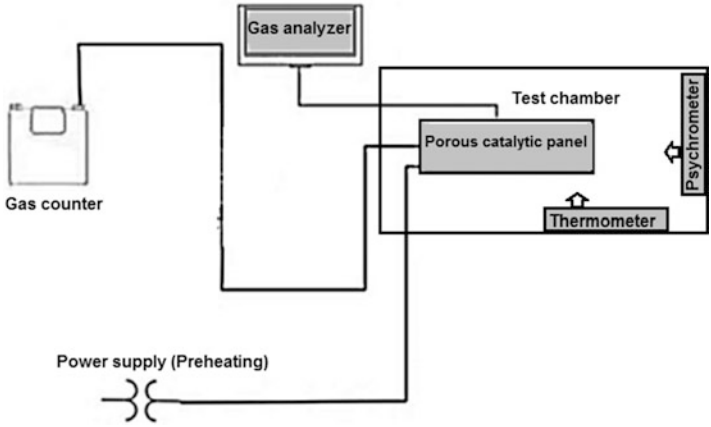

Fig. 7 Schematic of the test collection of the operation of catalytic porous pad

Fig. 8 The gas-analyzing machine implemented in the test

Due to the complete combustion of gas in this system of providing heat, the pollutant gases such as NOx and CO are decreased to the lowest possible level which is a vitally important environmental factor.

To analyze the performance of the proposed system, a machine equipped with measuring tools was designed (Fig. 7). The foregoing machines are capable of measuring parameters such as the temperature of panel surface, debit of consumed fuel, pollutant gases, and wetness.

To measure the temperature of panel surface, a thermometer with the exactitude of 0.1 °c was applied that measured the temperature by using infrared rays. To register the consumption debit, a G4 counter was exploited. To measure the combustion output, an analyzing machine (Fig. 8) made in AiRREX was used which was capable of measuring the released CO, HC, and CO_2 using infrared spectrometry method with exactitude of %0.001 ppm and %0.01, respectively, as well as NOx and O_2 using electrochemical method with the exactitude of %

0.01 ppm1. This machine is equipped with some filters to absorb the dust and moist as well as an automatic calibration.

3 Experimental Facility

In an experimental study, electrostatic powder paint dryer furnace was studied with two different methods of providing heat, and its parameters were analyzed via the aforementioned machine manufactured in the previous stage which was equipped with measuring devices. In the first method, direct flame was used to provide heat, and the furnace needed 1 h of combustion and consumed 0.9 m^3 of natural gas in order to dry the powder paint. Considering the 20-min time of baking paint (time of baking paint: the time in which the painted pieces are placed in preheated furnace to dry their paint during which the flame of the furnace is turned off to avoid burning the paint), the whole process takes 80 min. In the second test, the new proposed system was used. This system has a high starting speed of heating, and considering the radiant mechanism of heat transfer, the whole process takes less than 25 min, and gas consumption can be economized up to 22.23%, and the required time is also optimized as much as 68.75%.

Figure 9 indicates the gas consumption over time for the furnaces with two foregoing methods to provide heat for the same heating power, which confirms the optimized gas consumption in non-flame combustion and waste of energy in the other method.

Table 1 indicates the released gases after the combustion in two systems of providing heat over the same conditions (same time and heating power) which confirms the eco-friendlier conditions in non-flame combustion.

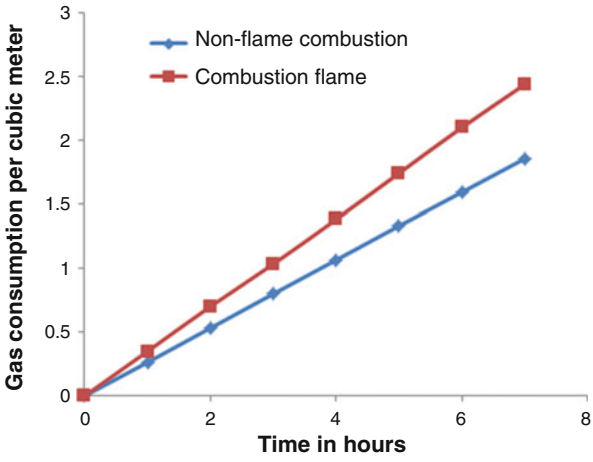

Fig. 9 Gas consumption diagram $\left(\frac{m^3}{h}\right)$

Table 1 Gas emissions from combustion

Emitted gas	Initial	Non-flame combustion	Flame combustion
HC (ppm)	0	282	40
CO (%)	0	.0022	3.67
CO_2 (%)	0	1.43	5.88
NOX (ppm)	0	0	30
O_2 (%)	20.79	20.59	20.69

4 Conclusions

In the present study, a catalytic porous pad is constructed to produce radiant heat. Related laboratory equipment was designed and manufactured to test and analyze the heat transfer in a powder paint dryer furnace in two different methods: (1) using direct torch and (2) applying porous system.

Using the proposed system of providing heat results in the complete removal of NOx release and a significant decrease in CO which are among the most dangerous environmental pollutants. Moreover, the procedure of heat transfer in this method is radiation which offers the possibility of concentrating the heat on the surface of the intended product. Therefore, through this concentration, the surrounding space is not affected by heat, and it takes less time for the product to cool, when the system is turned off. Exploiting this method of heating due to radiant heat transfer, high speed in reaching the intended temperature and requiring less space for installation in furnaces (radiant systems take one third space compared to traditional systems with the same power) results in higher efficiency in furnaces and economizing the fuel consumption.

Acknowledgments We feel obliged to thank the chairman of Tehran Pooshesh Company (Alborz province, Iran) for his cordial support to the research team.

References

Baukal Jr., C.E.: Industrial Burners Handbook. CRC Press, Boca Raton, London, New York, Washington, DC (2003)

Berman, H.L.: Fired heater. Chem. Eng. **85**, 129–140 (1978.) MC Graw-Hill

Hosseinpour, S., Haddadi, B.: Numerical study of the effects of porous burner parameters on combustion and pollutants formation. pp. 1505–1509, WCE, (2008)

Hosseinpour, S., Moallemi, N.: 2D Numerical simulation of combustion in porous media using four different multilevel chemical processes, Iranian Combustion Association, Persian, (2009)

Incropera, F.P., DeWitt, D.P.: Fundamentals of Heat and Mass Transfer, 5th edn. Wiley (2002)

Jamali, A.: Experimental and numerical studies in preheating of heat transformers in oil industry and present a procedure for improving their efficiency, Monthly magazine of oil and energy, 1st year of publish, March (2004)

Jegla, Z., Kohoutek, J., Zachoval, J., Stehlık, P.: Software supporting efficient retrofit design of furnaces and connected pipes as one integrated system, 14th International Congress of Chemical and Process Engineering CHISA (2000)

Jodeiri, N., Wu, L., Mmbaga, J., Hayes, R.E., Wanke, S.E.: Catalytic combustion of VOC in a counter-diffusive reactor. Catal. Today. **155**(1–2), 147–153 (2010)

Kaviani, H., Mesgarpor.: Optimized decrement of Nox pollution caused by gas combustion by adding catalysts. The Third Conference of Fuel and Combustion in Iran. Isfand 1388 (2009)

Kreith, F., Manglik, R.M., Bohn, M.S.: Principles of heat transfer. 5th edn. pp. 80–121. Pacific grove Brooks, USA. http://bcs.wiley.com/he-bcs/Books?action=index&itemId=0471386502&itemTypeId=BKS&bcsId=1737. https://www.amazon.com/Principles-Heat-Transfer-Frank-Kreith/dp/0495667706 (1993)

Mehdizadeh N.S. Tabejamaat, S. Yashini, M.: NOx reduction analysis in fuel gas combustion chamber using Water Injection,Aerospace Eng. Department, Amirkabir Univ. of Technology, MAEJ (2005)

Nield, D.A., Bejan, A.: Convection in Porous Media, 3rd edn, pp. 110–154. Springer, New York (2006)

Pfefferle, L.D., Pfefferle, W.C.: Catalysis in combustion. Catal. Rev. Sci. Eng. **29**, 219–267 (1987)

Soete G.D.: "Stability and Propagation of Combustion Wave in Porous Media" On combustion, pp. 959–966 (1966)

Study of hydraulic behavior of gas in liquid basement reactors, Governmental investigation plan, oil industry investigation center, years of performance (2001–2002)

Sn/Graphene Binary Nanocomposite Anode Electrodes for High-Performance Li-Ion Battery Applications

Guler Mehmet Oguz, Erdas Aslihan, Nalci Deniz, Ozcan Seyma, and Akbulut Hatem

1 Introduction

Li-ion batteries are the most suitable power supplies for many portable electronic devices, such as cellular phones, digital cameras, and notebooks, because of their high energy and power density. The first commercial Li-ion battery was developed by Sony in 1991, and since then a variety of efforts have been undertaken to improve the electrochemical performance of battery materials. Current Li-ion batteries use graphite anodes in which one unit (six carbon atoms for graphite) can store one or less lithium ion, leading to a limited theoretical capacity of 372 mAh g^{-1}. To circumvent the low energy and power density of graphite, alternative materials are highly desired.

Tin anodes have attracted much attention because it delivers a capacity up to three times higher than that of graphite. Theoretically, one tin atom can maximally react with 4.4 lithium atoms to form $Li_{4.4}Sn$ alloy, reaching a capacity of 993 mAh g^{-1}. However, the large amount of lithium insertion/extraction into/from Sn causes a large volume change (about 300%), which causes pulverization of tin particles and loss of contact with current collector, resulting in poor electrochemical performance. Various approaches have been carried out to overcome this issue, including the use of nanosized active materials by Adpakpang et al. (2014) and Tang et al. (2014), active/inactive composite materials by Yi et al. (2014) and Wang et al. (2008), and tin–carbon composites by Park et al. (2007) and Zhang et al. (2005, 2009). These studies have resulted in improvements of the electrochemical performance of Sn-based anodes but only to a limited extent. Recently it has been

G.M. Oguz (✉) • E. Aslihan • N. Deniz • O. Seyma • A. Hatem
Sakarya University, Department of Metallurgical & Materials Engineering, Esentepe Campus, Adapazarı, Sakarya 54187, Turkey
e-mail: guler@sakarya.edu.tr

© Springer International Publishing AG, part of Springer Nature 2018

F. Aloui, I. Dincer (eds.), *Exergy for A Better Environment and Improved Sustainability 2*, Green Energy and Technology,
https://doi.org/10.1007/978-3-319-62575-1_71

reported by Zhang et al. (2004) and Liu et al. (2005) that silicon nanowires directly grown on a current collector can greatly improve the performance of the Si anode due to the excellent electrical connection between Si nanowires and the current collector and the nature of one-dimensionality to effectively release the strain. Zhang et al. (2007) and Mao et al. (1999) also reported great anode performance using carbon-coated, very small (≈10 nm) silicon nanoparticles (SiNPs) or silicon nanotubes. However, in these nanosilicon electrodes, the heavy current collector is larger in weight than Si-active material. In a commercial lithium-ion cell, the anode material is usually coated on a copper foil current collector to form an anode electrode in thin sheet form. The metal current collector on the anode side is usually a 10 μm thick copper sheet with an areal density ≈10 mg/cm^2. This copper sheet is a relatively heavy component in a lithium-ion cell, which is comparable in weight to the anode-active material and accounts for ≈10% of the total weight of the cell.

Graphene nanosheets could be a promising candidate to serve as both the conductive network and the buffer to alleviate the stress from volume expansion, owing to its advantages of a unique network structure with low electrical resistivity and good mechanical properties, such as strength, stiffness, and resilience. All of the previous reports used different dedicated chemical or physical methods to prepare composite materials, which would also increase the cost of the materials. In this study, firstly Sn nanoparticles were synthesized by chemical reduction method. This method is more suitable for the Sn nanoparticle synthesis because the chemical reduction can use a low temperature, resulting in a better control of thermal oxidation of Sn nanoparticles. During the synthesis process, surfactants were used to protect the Sn nanoparticle from oxidation. Multilayer graphene was obtained from graphite flakes using the method described by Hummers. Free-standing and flexible tin/graphene nanocomposite paper was produced by a vacuum filtration technique for use as an anode electrode without using any binder or additives. The unique feature of the sheet-to-sheet assembly (2D–2D) is that each tin and graphene nanosheet will have maximum electrical contact with graphene, which could result in high conductivity of the hybrids. Moreover, strong interfacial interactions between tin and graphene contribute to a robust linking between the two components, which further promoted interfacial electron and lithium-ion transport. Benefitting from the morphological compatibility and intimate integration between tin and graphene, the binder-free and free-standing hybrid electrode exhibited significantly enhanced lithium storage properties in terms of higher specific capacities, better cyclic stability, and rate capability compared to traditional binder-containing electrodes and pure tin electrodes. To the best of our knowledge, this is the first demonstration of a self-supporting binder-free anode prototype with a lamellar hierarchical structure and strong interfacial interaction, which is totally different from previously reported graphene-based hybrid films.

2 Experimental Details

2.1 Synthesis of Sn Nanoparticles

A 4.76 g of Tin(II) chloride dehydrate, $SnCl_2.H_2O$ (Sigma-Aldrich, 98%), was added to a suspension of 2.5 g of polyethylene glycol, PEG 6000 (Sigma-Aldrich), 5 ml of acetic acid, CH_3COOH (Merck), and 100 ml bidistilled water. A clear solution was obtained after mechanically stirring for a few minutes. A 2.5 g of sodium borohydride, $NaBH_4$ (Merck), was dissolved in 100 ml bidistilled water solution that was then introduced dropwise. The mixture turned to red, indicating the formation of a sol of PEG-capped Sn nanoparticles. The hydrosol was further stirred for 2 h before the Sn nanoparticles were spun down in an ultracentrifuge (15,000 rpm for 1 h). The solid product recovered as such was washed with water and methanol, and vacuum dried at 50 °C for 12°h.

2.2 Microwave-Assisted Hydrothermal Carbonization of Sn Nanoparticles

Glucose (≥99.5%, Sigma-Aldrich) was used as the starting precursors for the microwave-assisted hydrothermal carbonization of as-synthesized Sn nanoparticles. Aqueous suspensions of the Sn nanoparticles were prepared using glucose as a catalyst reagent. A 1.5 mol L^{-1} catalyst stock solution was prepared in bidistilled water. About 500 mg of Sn nanoparticles were poured in a reaction container filled with 50 mL of stock solution. The suspensions were placed in a 100 mL polytetrafluoroethylene (PTFE)-sealed reactor for microwave processing. The materials were hydrothermally carbonized using a microwave lab station (Milestone RotoSYNTH) with a magnetron frequency of 2.45 GHz, 1000 W at maximum power and 10 W pulse-controlled power fractions. The system was heated from 20 °C to 85 °C at 22 °C min^{-1}, then from 85 °C to 145 °C at 7 °C min^{-1}, and from 145 °C to 180 °C at 14 °C min^{-1}; finally an isotherm was held at 180 °C for 5 min. The temperature during microwave irradiation was controlled by a thermocouple installed in a reference container. After the carbonization process, the reactor was cooled at room temperature, and the carbonized materials were filtered with PVDF filter (0.45 μm, Millipore) using a mechanical vacuum pump and subsequently washed with bidistilled water until reaching a neutral pH. The solid products were dried under vaccum at 40 °C for 12 h.

2.3 Synthesis of Graphene Oxide

Graphite oxide was synthesized from natural flake graphite by using modified Hummers method. The exfoliation of graphite oxide into graphene oxide was obtained by ultrasonication. For preparation of graphene oxide paper, 30 mg of as-synthesized graphitic oxide was dispersed in 100 mL of distilled water and sonicated for 2 h, and then the solution was filtered on polyvinylidene fluoride, PVDF (0.45 μm, Millipore), membrane by vacuum filtration technique.

2.4 Synthesis of Sn/Graphene Free-Standing Electrodes

A schematic illustration for the preparation process of Sn/graphene nanocomposite is given in Fig. 1. A 30 mg as-synthesized graphene oxide and carbon-coated Sn was dispersed in 50 mL bidistilled water by the aid of 80 mg of SDS (sodium dodecyl sulfate, Merck, Calbiochem, >97%) surfactant and sonicated to form a well-dispersed suspension. In order to produce Sn/graphene paper, the as-synthesized graphene oxide paper was chemically reduced immediately after filtration by hydrazine solution. A 2.0 M, 50 mL hydrazine (anhydrous, 98%, Sigma-Aldrich) solution was slowly poured onto the membrane-supported graphene oxide paper and filtered via vacuum technique. All production steps were performed under open atmospheric conditions. Then the resulting solid was washed up, and the sample dried in vacuum at 40 °C overnight, and the Sn–C/Graphene films were peeled off from the membrane.

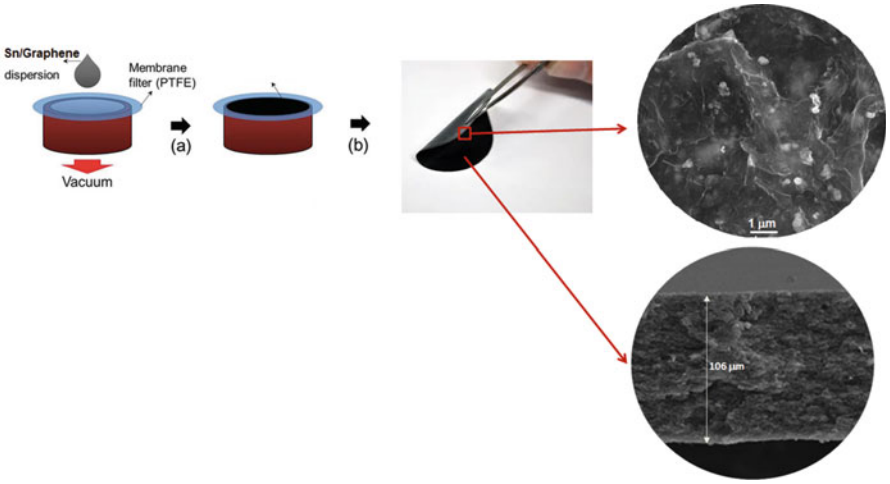

Fig. 1 A schematic illustration for the preparation process of Sn/graphene nanocomposites

2.5 Characterization

The surface and cross-sectional morphologies of the produced sample electrodes were observed by scanning electron microscopy (SEM, Jeol 6060 LV). The phase structures of the samples were investigated by X-ray diffraction (XRD) (Rigaku D/MAX 2000 with thin film attachment) with CuKα radiation.

2.6 Electrochemical Characterization

Coin-type CR2016 cells were assembled in an argon-filled glove box. The electrolyte solution was 1 M $LiPF_6$ (Sigma-Aldrich, ≥99.99%) in EC/DMC (Sigma-Aldrich, 99%/Sigma-Aldrich, ≥99%) (1/1 by volume). The electrochemical performance of the Sn/graphene nanocomposites was evaluated by galvanostatic discharge–charge measurement using a computer-controlled battery tester between 0.02 and 2.5 V using metallic lithium as the counter electrode. The cells were cyclically tested on a MTI Model BST8-MA electrochemical analyzer using 1C (18 mA/dm^2) current density over a voltage range of 0.02–2.5 V. After being cycled for 50 cycles, electrochemical impedance spectroscopy (EIS) was conducted on coin cells using an electrochemical workstation (Gamry Instruments Reference 3000) over a frequency range from 100 kHz to 0.001 Hz with an AC amplitude of 5 mV. The measured voltage was about 0.2 V after the cells were relaxed for 1 h. The data has been normalized and referred per unit of mass for the purpose of comparison. Cyclic voltammograms (CVs) were recorded on an electrochemical workstation (Gamry Instruments Reference 3000) at a scan rate of $0.5 mVs^{-1}$ between 0.02 and 2.5 V. All the potentials indicated here were referred to the Li/Li^+ electrode potential. All electrochemistry tests were carried out at room temperature (25 °C).

3 Results and Discussions

Figure 2 shows the XRD patterns of the as-synthesized Sn nanoparticles. XRD patterns could be readily indexed to the tetragonal phase of Sn (space group I41/and (141)), lattice constants a = 0.583 1 nm and c = 0.318 2 nm (JCPDS 04–0673)). The relative intensity of the peaks was consistent with that of the Sn nanoparticles reported by Jiang et al. (2006). From the XRD patterns, no obvious oxidation or impurity peaks were found. The XRD pattern of the samples produced by microwave-assisted hydrothermal process; carbon with characteristic (002) peak is also displayed in Fig. 2.

The characteristic (002) plane of the carbon also demonstrate that the crystalline nature of carbon. The characteristic peak at 24.5° corresponds to the planes of graphene, indicating that the interplanar spacing of d_{002} had been expanded to

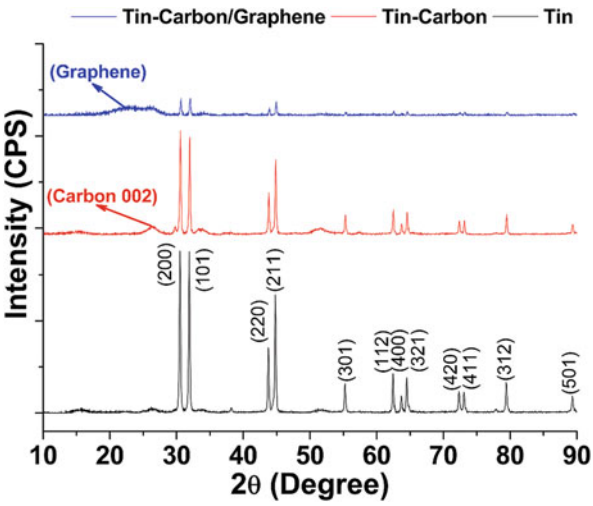

Fig. 2 XRD patterns of Sn, Sn–C, and Sn–C/graphene nanoparticles

0.769 nm after reduction. This is ascribed to the oxygen-containing functional groups that were attached, which has been previously confirmed by Zhang et al. (2007).

The SEM results examined indicate that the sizes and size distributions of Sn nanoparticles synthesized via chemical reduction differ between 10 and 50 nm in size. The extremely polydisperse nanoparticles obtained using tin (II) chloride precursors can be interpreted as the results of multiple nucleation events during extended nucleation periods. The reduction process of Sn ions supplied from the precursor could be represented by the reaction:

$$BH_4^- + 8OH^- + 4Sn^{+2} \rightarrow B(OH)_4^- + 4H_2O\,(g) + 4Sn \quad (1)$$

Reaction (1) will be divided into next two reactions:

$$BH_4^- + 8OH^- \rightarrow B(OH)_4^- + 4H_2O\,(g) + 8e^- \quad (2)$$

$$4Sn^{+2} + 8e^- \rightarrow 4Sn \quad (3)$$

The SEM images of the samples produced by microwave-assisted hydrothermal carbonization of Sn nanoparticles are also shown in Fig. 3.

As can be concluded from the figure, the surfaces of Sn nanoparticles are surrounded with carbon as a conductive network which will buffer to alleviate the stress from volume expansion, owing to its advantages of a unique network structure with low electrical resistivity and good mechanical properties, such as strength, stiffness, and resilience as also reported by Hsu et al. (2006) and Yang et al. (2000).

The morphology of the Sn/graphene nanocomposite was observed by SEM. Figure 4 shows a SEM image of the Sn/graphene nanocomposite. In general as

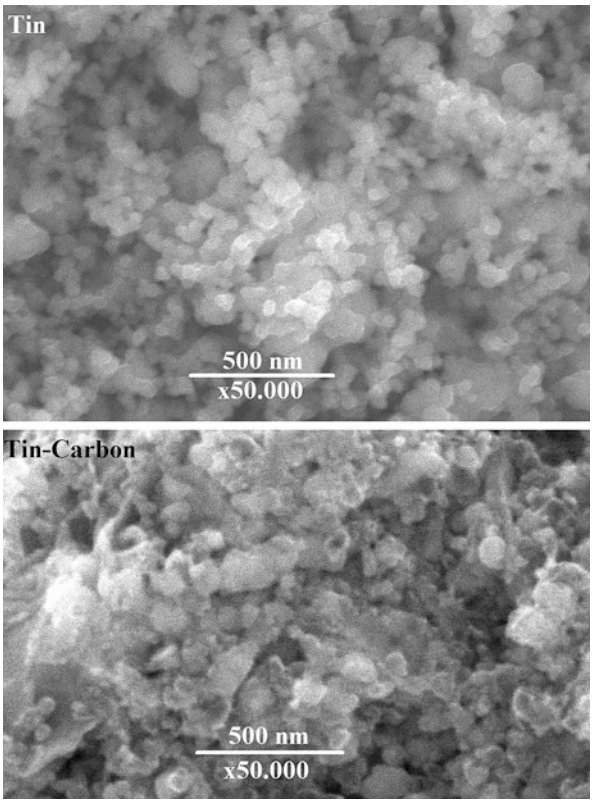

Fig. 3 XRD patterns of Sn and Sn–C nanoparticles

shown in Fig. 4a, graphene nanosheets were crumpled to a curly and wavy shape, resembling flower pedals. The energy-dispersive X-ray spectroscopy (EDS) analysis in Fig. 4a also shows that tiny Sn nanoparticles are homogeneously distributed on the curly graphene nanosheets. Due to the corrugated nature of the graphene nanosheets, substantial voids exist between individual nanosheets. The anchored Sn nanoparticles could act as a spacer to prevent the re-stacking of individual graphene nanosheets. Figure 4b also shows that the graphene paper appears as a porous entangled mat; the film is self-standing due to inter-bundle van der Waals forces and mechanical interlocking within the sheet. Tin nanoparticles are also tiny Sn nanoparticles that are homogeneously distributed over the film as shown in the energy-dispersive X-ray spectroscopy (EDS) analysis.

Cyclic voltammetry (CV) is initially carried out to investigate the electrochemical reactivity of Sn–C/graphene, with the results shown in Fig. 5. Two cathodic current peaks for the Sn–C/graphene electrodes could be observed in the first cycle. The peak around 1.0 V could be assigned to the formation of a solid electrolyte interface on Sn–C/graphene composites, while the peak between 0.01 and 0.5 V is related to the alloying of lithium ions with Sn and the intercalation of lithium ions into graphene as also stated by Duan et al. (2012) and Huang et al. (2010) In the

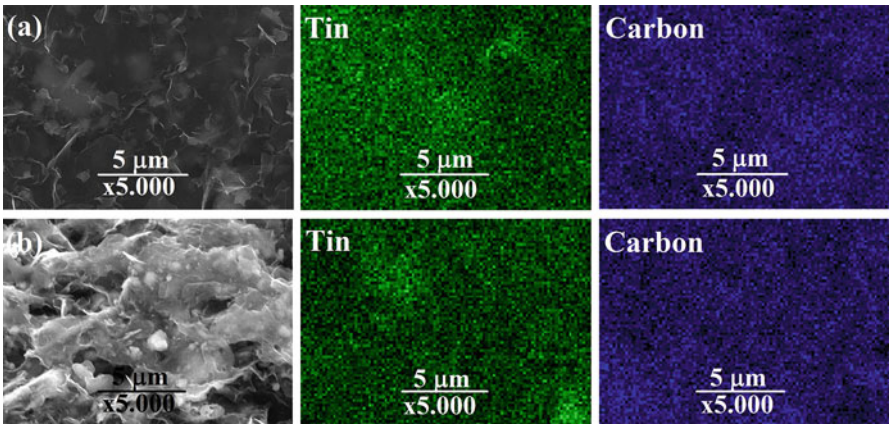

Fig. 4 SEM images of (**a**) surface and (**b**) cross-sectional area of the Sn–C/graphene electrodes

Fig. 5 SEM images of (**a**) surface and (**b**) cross-sectional area of the Sn–C/graphene electrodes

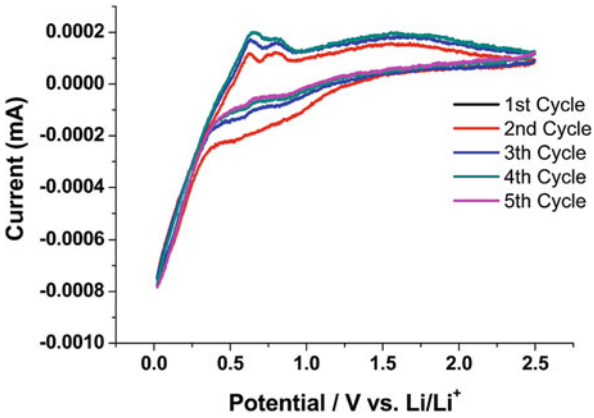

subsequent anodic polarization process of the first cycle, five peaks could be observed at 0.15 V, 0.52 V, 0.62 V, 0.72 V, and 0.79 V, respectively, and are associated with lithium ion extraction from graphene and de-alloying from Li–Sn alloys. In the following second to fifth cycles, the CV curves are nearly overlapped, which suggests good stability of the Sn–C/graphene electrode from the second cycle.

The galvanostatic discharge–charge curves at current density 18 mA dm^{-2} (1C) of Sn–C/graphene anode electrodes between 0.2 and 2.5 V vs. Li^+/Li is presented in Fig. 6. The discharge capacity of the Sn–C/graphene decreases to 818 mAh g^{-1} in the second cycle and 812 mAh g^{-1}, respectively. The capacity fade is slower in subsequent cycles and a stable capacity of 670 mAh g^{-1} after 100 cycles. It is known that cycling performance of metal oxide-based anodes is significantly affected by the volume change of active particles during lithium insertion–extraction process. If active particles could not tolerate the volume

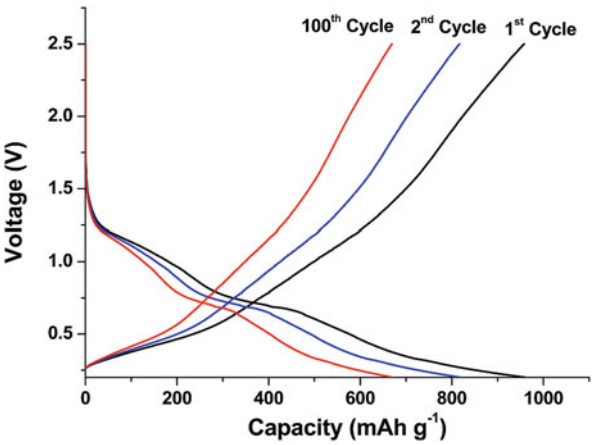

Fig. 6 Galvanostatic charge/discharge potential profiles of Sn–C/graphene electrodes

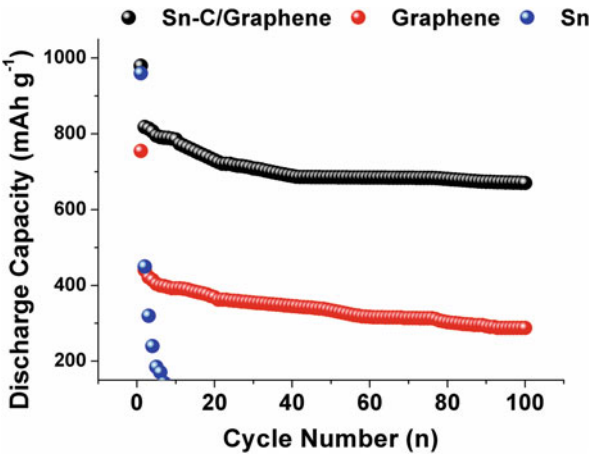

Fig. 7 Cyclic performances of bare Sn, graphene, and Sn–C/graphene electrodes

change, they will pulverize into smaller particles, and electrode is strongly polarized as a result. The nanocomposite electrode's strong performance was due to its unique structure, the synergy of combining Sn and graphene nanosheets, the suppression of side reactions between the nanocomposite, and the electrolyte and an optimization of the SEI film. It is also reasonable to suggest that the smaller crystalline size of Sn in the nanocomposite than when as pure nanoparticles also likely improved capacity because of shorter conduction paths for electrons and lithium ions.

The lithium insertion capacity (discharge) of Sn/graphene nanocomposite electrodes vs. cycle number is shown in Fig. 7. In the first cycle, the Sn/graphene electrode delivered a discharge capacity of 976 mAh g^{-1} and a reversible charging capacity of 960 mAh g^{-1}. The irreversible capacity could be mainly ascribed to the formation of the solid electrolyte interphase (SEI) layers on the surface of the

electrode. From the second cycle, the reversibility of the electrode was gradually improved on cycling, with an average columbic efficiency of 98.4% up to 100 cycles. The electrode maintained a capacity of 670 mAh g^{-1} after 100 cycles. As a comparison, the cycling data of bare graphene electrode and microcrystalline Sn powder electrode are also presented in Fig. 7. The bare graphene electrode delivered a lithium storage capacity of 255 mAh g^{-1} after 100 cycles. The cycling performance of the bare Sn electrode is very poor. After 10 cycles, the bare Sn electrode failed. Therefore, Sn/graphene nanocomposite exhibited an optimized electrochemical performance compared to bare graphene and bare Sn powders.

4 Conclusions

In this study, Sn nanoparticles were synthesized via chemical reduction techniques using tin (II) chloride as the precursor. The as-synthesized Sn nanoparticles were subjected to microwave-assisted hydrothermal carbonization process in order to increase the electrochemical efficiencies during the lithiuation and delithiuation processes. Sn–C/graphene free-standing electrodes were then prepared by vacuum filtration techniques. The resulting Sn–C/graphene hybrid anode thus exhibited superior Li-ion performance with high reversible capacity, excellent cycle ability, and good rate capability. This improved performance could be attributed to the formation of 2D graphene framework decorated with well-dispersed Sn–C nanocrystals, thus inducing fast diffusion of Li ions.

Acknowledgments This research was supported by the Scientific and Technological Research Council of Turkey (TUBITAK), under the contract number 214 M125. These supports are gratefully acknowledged by authors.

References

Adpakpang, K., Park, J., Oh, S.M., Kim, S.J., Hwang, S.J.: A magnesiothermic route to multicomponent nanocomposites of FeSi2@Si@graphene and FeSi2@Si with promising anode performance. Electrochim. Acta. **136**, 483–492 (2014)

Duan, B., Wang, W., Zhao, H., Xu, B., Yuan, K., Yang, Y.: Nano-Sn/mesoporous carbon parasitic composite as advanced anode material for lithium-ion battery. J. Electrochem. Soc. **159**, A2092–A2095 (2012)

Hsu, Y.J., Lu, S.-Y., Lin, Y.-F.: Nanostructures of Sn and their enhanced, shape-dependent superconducting properties. Small. **2**, 268–273 (2006)

Huang, T., Yao, Y., Wei, Z., Liu, Z., Yu, A.: Sn–Co–artificial graphite composite as anode material for rechargeable lithium batteries. Electrochim. Acta. **56**, 476–482 (2010)

Jiang, H., Moon, K.S., Dong, H., Hua, F., Wong, C.P.: Size-dependent melting properties of tin nanoparticles [J]. Chem. Phys. Lett. **429**, 492–496 (2006)

Liu, W.R., Guo, Z.Z., Young, W.S., Shieh, D.T., Wu, H.C., Yang, M.H., Wu, N.L.: Effect of electrode structure on performance of Si anode in li-ion batteries: Si particle size and conductive additive. J. Power Sources. **140**, 139–144 (2005)

Mao, O., Turner, R.L., Courtney, I.A., Fredericksen, B.D., Buckett, M.I., Krause, L.J., Dahn, J.R.: Active/inactive nanocomposites as anodes for Li-ion batteries. Electrochem. Solid-State Lett. **2**, 3–5 (1999)

Park, M.-S., Needham, S.A., Wang, G.-X., Kang, Y.-M., Park, J.-S., Dou, S.-.X.: Nanostructured SnSb/carbon nanotube composites synthesized by reductive precipitation for lithium-ion batteries. Chem. Mater. **19**, 2406–2410 (2007)

Tang, T., Liu, Z., Dai, X., Yang, Z., Chen, W., Ma, D., Lu, Z.: Theoretical study on the Si-doped graphene as an efficient metal-free catalyst for CO oxidation. Appl. Surf. Sci. **308**, 402–407 (2014)

Wang, J.C., Chou, S.L., Chen, J.C., Chew, S.Y., Wang, G.X., Konstantinov, K., Wu, J., Dou, S.X., Liu, H.K.: Paper-like free-standing polypyrrole and polypyrrole–LiFePO4 composite films for flexible and bendable rechargeable battery. Electrochem. Commun. **10**, 1781–1784 (2008)

Yang, C.-S., Liu, Y.Q., Kauzlarich, S.M.: Synthesis and characterization of Sn/R, Sn/Si−R, and Sn/SiO2 Core/Shell nanoparticles. Chem. Mater. **12**, 983–988 (2000)

Yi, R., Zai, J., Dai, F., Gordin, M.L., Wang, D.: Dual conductive network-enabled graphene/Si–C composite anode with high areal capacity for lithium-ion batteries. Nano Energy. **6**, 211–218 (2014)

Zhang, H.X., Feng, C., Zhai, Y.C., Jiang, K.L., Li, Q.Q., Fan, S.S.: Cross-stacked carbon nanotube sheets uniformly loaded with SnO2 nanoparticles: A novel binder-free and high-capacity anode material for lithium-ion batteries. Adv. Mater. **21**, 2299–2304 (2009)

Zhang, T., Gao, J., Zhang, H.P., Yang, L.C., Wu, Y.P., Wu, H.Q.: Preparation and electrochemical properties of Core-Shell Si/SiO nanocomposite as anode material for lithium ion batteries. Electrochem. Commun. **9**, 886–890 (2007)

Zhang, Y., Tan, Y.-W., Stormer, H.L., Kim, P.: Experimental observation of the quantum hall effect and Berry's phase in graphene. Nature. **438**, 201–205 (2005)

Zhang, X.W., Patil, P.K., Wang, C.S., Appleby, A.J., Little, F.E., Cocke, D.L.: Electrochemical performance of lithium ion battery, Nano-silicon-based, disordered carbon composite anodes with different microstructures. J. Power Sources. **125**, 206–213 (2004)

Data-Driven Modeling for Energy Consumption Estimation

Chunsheng Yang, Qiangqiang Cheng, Pinhua Lai, Jie Liu, and Hongyu Guo

1 Introduction

Today it is estimated that building industry contributes over 40% of total energy consumption. The owners of building aim at reducing the cost of energy consumption by developing efficient technologies to optimize or reduce the energy consumptions. With the quick increase of the energy price, developing new technology for building energy management systems (BEMS) or applying new philosophy of operating the systems is becoming more and more important and necessary. In utility industry, one of philosophy to change the existing operation policy is called demand response (D/R) program. It is defined as the incentive program to promote the lower electricity use at times of high wholesale market prices (Albadi and EI-Saadany 2008). To avoid the high prices or the peak time of electricity consumption, BEMS must be able to adjust the use of electricity by changing the usage of energy from their normal consumption pattern or routine operation temporally. To achieve the response, the operators can just reduce the electricity usage during peak hours when the price is high without changing their consumption pattern during other periods. However, this will temporally lose the comfort. It is not expected from the customers. It is desirable that the BEMS can change the energy consumption pattern to avoid the peak hour without any loss of the comfort. For instance, the BEMS can use ice bank for air conditioning (A/C) during peak hours

C. Yang (✉) • H. Guo
National Research Council Canada, 1200 Montreal Road, Ottawa, ON K1A 0R6, Canada
e-mail: Chunsheng.Yang@nrc.gc.ca

Q. Cheng • P. Lai
Nanchang University, 999 Xuefu Dadao, New Honggutan District, Nanchang, China

J. Liu
Careleton University, 1125 Colonel By Drive, Ottawa, ON, Canada, K1S 5B6

© Springer International Publishing AG, part of Springer Nature 2018

F. Aloui, I. Dincer (eds.), *Exergy for A Better Environment and Improved Sustainability 2*, Green Energy and Technology,
https://doi.org/10.1007/978-3-319-62575-1_72

and make and store ice during the idle hours such as midnight. To address this issue, it is necessary and urgent to develop a novel technology which allows BEMS automatically to modify the building operation pattern/condition or change control policy to respond to D/R signal (Online 2000). To this end, one of the fundamental issues is how we can estimate the short-term /long-term energy consumption and the energy consumption of each subsystem to provide the solution for changing the policy or control the energy usage of BEMS.

Recently, many research efforts have been invested on the development of data-driven models for long-/short-term energy consumption prediction by applying machine learning algorithms such as neural network, decision tree, and regression analysis (He et al. 2005; Yalcintas and Akkurt 2005; Catalina et al. 2008; Olofsson et al. 1998; Tso and Yau 2007). There have been some research focusing on development of advanced AHU control methods (Bi et al. 2000) or accessing the building occupancy for energy load prediction (Kwok et al. 2011). There are, however, few works in developing the models for estimating energy consumption of each subsystem or optimizing the usage of energy consumption using data-driven approach rather than traditional modeling which faces a challenge to model energy consumption. To address the issues in developing predictive models for energy consumption estimation and to provide an alternative for modeling energy consumption, we propose a data mining-based modeling technique for developing data-driven predictive models from historic building operation data. This work focused on the development of energy consumption estimation for BEMS subsystems. In this paper we first introduce the data mining-based methodology. Then we present the development of data-driven models for estimating energy consumption of subsystems. In particular, the modeling results for a chiller subsystem and a supply fan in AHU will be presented and discussed as a case study.

The rest of this paper is organized as follows. Section 2 briefly introduces the BEMS and its modeling requirement in general. Section 3 briefly describes the methodology. Section 4 presents the development of data-driven models to estimate energy consumption for a chiller and a supply fan subsystem. Section 5 provides some preliminary experimental results. Section 6 discusses the results and limitation. The final Section concludes the paper.

2 Building Energy Management Systems and Modeling

BEMS mainly consists of heating, ventilation, and air-conditioning (HVAC) systems and lighting systems. HVAC contains many subsystems such as AHU (air handling units), chiller, ice bank, etc. To automatically respond to the D/R signal from smart grid, these subsystems must be integrated as a smart energy consumption system (Online 2000) to perform optimized operation by changing control policies or energy usage pattern. Such a smart system is capable of making decision on when to change the operation pattern, where to optimize the usage of energy for each subsystem, and how to set up the control policy without losing the comfort

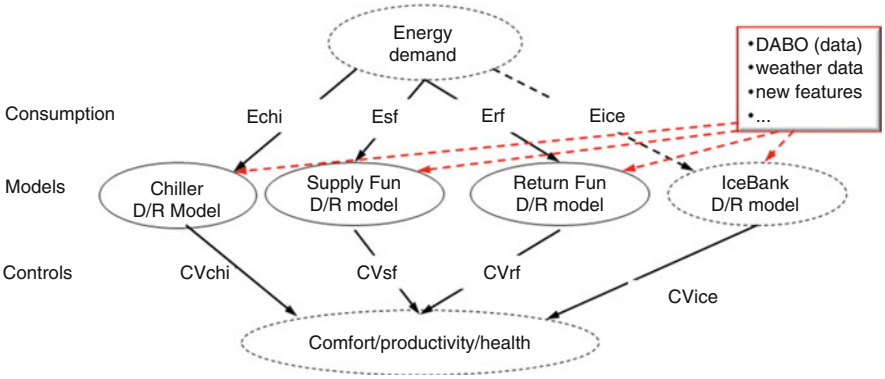

Fig. 1 An example of energy consumption modeling for BEMS subsystems

based on D/R signal and weather forecast. To this end, one of the fundamental issues is how we can predict the peak usage of energy consumption, the short-term / long-term energy consumption, and the energy consumption of each subsystem. In general, four kinds of models are required:

1. To predict the expected total building energy consumption
2. To estimate energy consumption for each subsystems such as chiller, AHU, ice bank, lighting etc.
3. To express control policy by exploiting the relationship between consumption of a given subsystem and its variables such as speed, water temperature, and valves
4. To optimize the energy usage to respond to D/R single from grid or to avoid the peak hours based on the prediction results from former models, weather forecast information, and constrains of comfort settings

Shown in Fig. 1 is an example of BEMS that we have to model the energy consumption for these subsystems. Here two types of models are requested to perform D/R optimization. One is the model for estimating energy consumption given the energy demanding from D/R single; another one is for energy estimation given the comfort setting or health requirement from control policy. In case that energy demanding comes from D/R smart grid, the system decides energy consumption for each subsystem (E_{chi}, E_{sf}, E_{rf}, *and* E_{ice}). So we have to build a model to decide the control policy or control variables for each subsystem. With the help of energy consumption models in the mid-layer, each model corresponding the subsystem will determine the control policy or variables (CV_{chi}, CV_{sf}, CV_{rf}, and CV_{ice}) to control the system to meet the comfort and health requirement in the building.

Unfortunately due to time-varying characteristic and nonlinearity in existing BEMS, it is difficult to build traditional mathematical/physical models to meet those needs. To our best knowledge, there do not exist publicly available models that could predict the complete performance and energy consumption for subsystems (Bendapudi et al. 2002). To address this issue, we proposed to develop energy

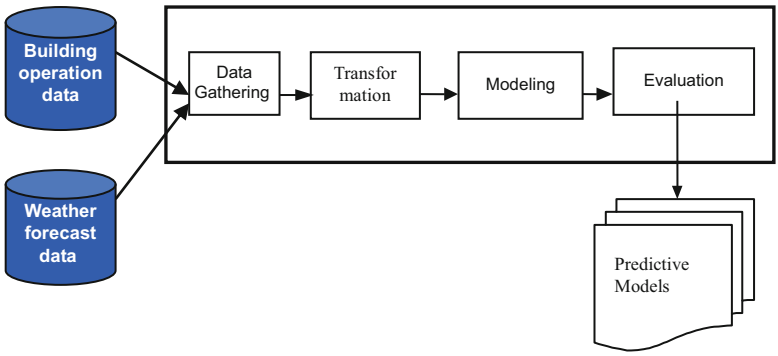

Fig. 2 The data-driven methodology for modeling energy consumption

consumption models for these subsystems using data mining-based approach. The models are able to be built from historic database using techniques from machine learning. As an example, Fig. 1 depicts the so-called DABO (Roche n.d.) database, which is often used to collect building operation data by domain experts. In our case, this database contains over 1600 variables which represent the data collection points for building control, room temperature setting, responding variables, and so on. In this work, we use this DABO database to conduct modeling and model evaluation.

3 Data Mining-Based Methodology

Modern building operation has generated massive data from BEMS, including energy consumption history, building characteristics, operating condition, occupancy, and control records for subsystems, among others. These data are a valuable resource for developing data-driven predictive models. To build the models from these historic operation data, we develop a data-driven methodology by using machine learning and data mining techniques. Figure 2 illustrates the methodology which consists of four steps: data gathering, data transformation, modeling, and model evaluation. The following is a brief description of each step.

3.1 Data Gathering

Most data mining algorithms require as input a dataset, which contains instances consisting of vectors of attribute values. Modern building operation often generates many such datasets. The first problem is to select the best dataset(s) to use to build models for a particular subsystem. Advice from subject matter experts and reliable

documentation can simplify this choice and help avoid a lengthy trial and error process. Not only must a dataset be selected, but a subset of instances must be selected to use in the analysis. The datasets are typically very large so it is inefficient to build models using all instances. Simple solutions, such as random sampling, are also inappropriate. To build the desired predictive models, a much more focused approach was required. In this work, four types of data are used, including energy consumption history, control variables, weather forecast, building parameters, and ambient conditions. Data gathering is to obtain a dataset for subsystems from a big building operation database. This dataset will combine all types of operation data into a set of vectors.

3.2 Data Transformation

In modeling energy consumption, the target variable is numeric. Therefore, this methodology focuses on numeric modeling by applying machine algorithms. In other words, the main goal is to develop repressors by using regression algorithms. To improve the initial, as measured, representation and remove outliers from the original data, data transformation is necessary. The main task is to generate some new features such as moving average, standard deviation, pattern expressions by using methods from process physics, signal processing, time series analysis, etc. The generated new features will enhance model performance significantly.

3.3 Modeling

After updating the initial dataset incorporating data representation enhancements, machine learning algorithms were used to build the predictive models. Dataset is separated into training and testing datasets. The training dataset was used for developing the models, and the remaining data were kept for testing to evaluate the built model. Any regression learning algorithm can be used. In early experiments, simple algorithms such as regression decision trees (Quinlan 1993; Mitchell 1996) and support vector machine were preferred over more complex ones such as ANN (Dzeroski and Zenko 2002) because of their efficiency and comprehensibility. The same algorithm was applied several times with varying attribute subsets and a range of cost functions. Therefore, feature selection was also applied on the augmented data representation to automatically remove redundant or irrelevant features.

In order to build high-performance energy prediction models, another method is to perform the model fusion. Model fusion can be used for two reasons. First, when more than one dataset is relevant for a given component, we can build a model for each dataset and then use model fusion to combine predictions from the various models. Second, we can apply model fusion for performance optimization

regardless of the number of datasets selected. In this case, we learn various models using various techniques or parameter settings and combine them to obtain better performance than using any single model. Bagging and boosting (Dietterich 2000) are two popular techniques to combine models, but they are only applicable when there is a single dataset and one kind of model (a single learning algorithm). For heterogeneous models or multiple datasets, we apply methods based on voting or stacking strategy (Tsoumakas and Blahavas 2004; Zhang et al. 1998). These techniques are globally referred to as multiple model systems (Opitz and Maclin 1999).

3.4 Model Evaluation

To evaluate the performance of the data-driven models, the most important measure of performance is the estimation accuracy achieved by the models after development. The accuracy is often defined using the forecast error which is the difference between the actual and predicted values (Dietterich 2000). Several criteria are available from statistics. The most widely used ones are the mean absolute error (MAE), the sum of squared error (SSE), the mean squared error (MSE), the root mean squared error (RMSE), and the mean absolute percentage error (MAPE). They are defined as follows:

$$\mathrm{MAE} = \frac{1}{N}\sum_{i=1}^{N} \mid e_{\mathrm{i}} \mid \tag{1}$$

$$\mathrm{SSE} = \sum_{i=1}^{N} e_{\mathrm{i}}^2 \tag{2}$$

$$\mathrm{MSE} = \sum_{i=1}^{N} \sqrt{e_{\mathrm{i}}} \tag{3}$$

$$\mathrm{RMSE} = \sqrt{\mathrm{MSE}} \tag{4}$$

$$\mathrm{MAPE} = \frac{1}{N}\sum_{i=1}^{N} \mid \frac{e_{\mathrm{i}}}{y_i}{}_i \mid \times 100 \tag{5}$$

where e_{i} is the individual prediction error, y_i is the actual value, and N is the number of examples in the test data.

The general method is to apply the testing dataset (unseen data) to the models by computing the error terms mentioned above. Each measure metric has its advantages and limitations. It is not necessary to compute all accuracy measures. In this work we focused on three widely used error criteria, namely, MAE, MSE, and MAPE.

4 Energy Consumption Modeling for BEMS

In this section, we demonstrate the development of models for predicting the energy consumption of BEMS subsystems by using the data-driven methodology. We focus on two main subsystems: the chiller and supply fun in an HVAC system. Chiller is a key subsystem in the HAVC system, which provides the chilled water or cooled air to the coil of the AHU for air-conditioning the building. For this work, the chiller is used together with ice bank to provide A/C for the building. It is possible to increase the water temperature of chiller to reduce energy consumption by using ice bank to provide the cooled air for substituting chiller function during the peak hour. On the other hand, chiller can be used to charge ice bank during valley time such as midnight.

Another main subsystem is supply fan which provide fan for ventilation of heating and cooling air. It is also one of the main sources of energy consumer in HAVC. There is a great potential for optimizing the energy consumption to avoid peak time or to respond the D/R signal if we can accurately predict the energy consumption of chiller and set up an optimized control policy.

4.1 Model Development for Chiller and Supply Fan

In the development of chiller and supply fan energy consumption models, we use building operation data from a modern building which uses chiller and ice bank for A/C in the summer. The data were collected from 2009 to 2010. The database contains over 1000 variables for all sensors or control points on the building. There is only one chiller in the building and one supply fan in the AHU in the selected building zone. The first task is to get data related to the chiller and supply fan from this database over thousand of variables. After analyzing the signals of chiller control system and consulting with building operator, the four groups of data are identified, and their variables are extracted from the database. These data are energy consumption (output of chiller), building occupancy, water temperatures at different points, and variables related to ice bank. In order to build high-performance models, we also collected weather forecast data from a local weather station. The weather data consists of temperature, wind speed, wind direction, and humidity. In the end, we can describe the chiller diagram as shown in Fig. 3, and supply fan diagram as shown in Fig. 4. Supply fan provides cooled air to 37 offices on a given building zone, each having their own temperature set point and duct outlet with a programmable damper position. All temperature settings will be input in the models.

After gathering data relevant to chiller and supply fan from the database and combining with weather forecast data, data transformation was performed to generate some new features following the developed methodology. The new features mainly include time series features such as weekday, seasons, moving

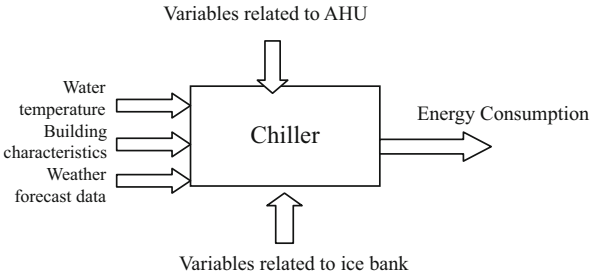

Fig. 3 The diagram of chiller energy consumption

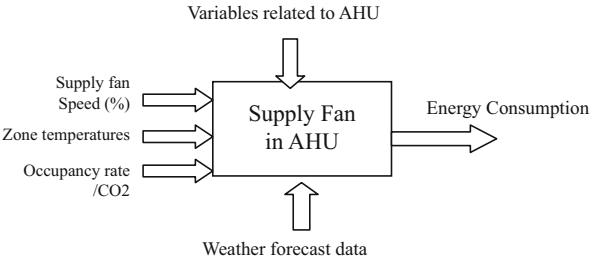

Fig. 4 The diagram of supply fan energy consumption

averages, and the energy consumption for selected past days. These new features enhance the prediction accuracy for the models.

Using dataset with the new features, the modeling experiments were conducted by carefully choosing machine learning algorithms. As mentioned in (Mitchell 1996), many regression-based algorithms were first evaluated by trial–error approach. Then we decide to use two algorithms, i.e., DecisionRegTree and SVM, to model energy consumption for chiller and supply fan. The next subsection presents the experimental results for these selected algorithms.

4.2 Experiment Results

Using the dataset with new features, we conducted modeling experiments. The dataset contains 12,734 instances. We separated the dataset into training and testing sets. Training dataset contains 8000 instances and testing dataset has 4734 instances. Against the training dataset, the predicted models are built with two selected learning algorithms. Then we run the trained models on the testing dataset. Using evaluation criteria, we computed the performance for each model. In building operation, the chill has two working modes: chilling only mode and chill and charging mode. Therefore, we conducted two kinds of modeling experiments corresponding two chiller working modes. Figure 5 shows the modeling result of chilling only mode. The x-axis is the estimate and y-axis is the actual value of energy consumption. The performance of models, as measured by the MAE, MSE, and MAPE, are shown in Table 1.

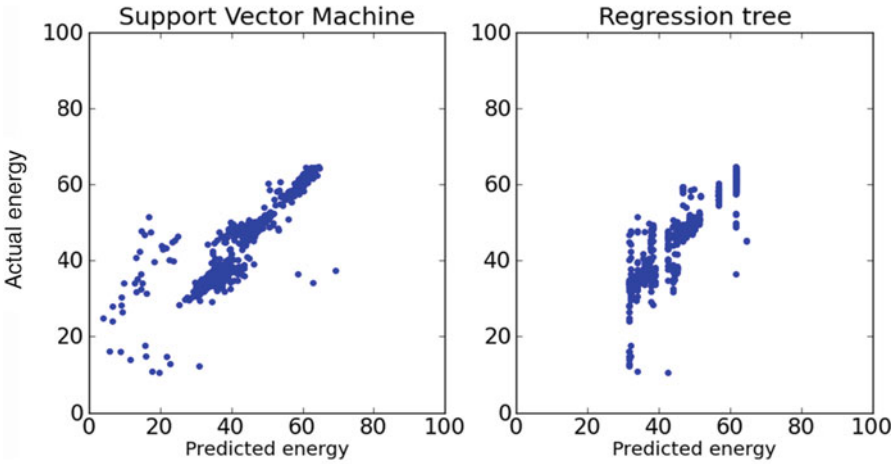

Fig. 5 The results of estimated values vs. actual values (chilling only mode)

Table 1 The performance of the built models (chilling only mode)

	SVM	DecisionRegTree
MAE	1.72	1.28
MSE	13.25	8.15
MAPE (%)	5	4

Figure 6 shows modeling results of chilling and charging mode, and the performance of the model is shown in Table 2.

Figure 7 shows modeling results of supply fan, and the performance of the model is shown in Table 3.

5 Discussion

The experimental results above demonstrated that the data-driven modeling is useful and effective for developing predictive models to estimate the energy consumption for BEMS subsystems such as chiller and AHU. From Tables 1 and 2, it is obvious that nonlinear models show high accuracy results for estimating energy consumptions. In many building operations, it is difficult to build traditional math models to estimate energy consumption because of operation complexity and mutual interaction and constrains among subsystems. The proposed data-driven modeling method provides a feasible alternative for modeling BEMS energy consumption.

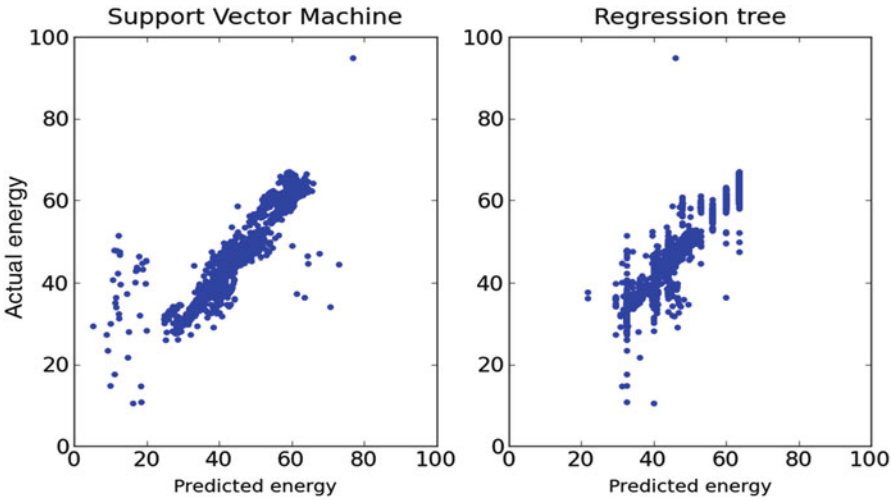

Fig. 6 The results of estimated values vs. actual values (chilling and charging mode)

Table 2 The performance of the built models (chilling and charging mode)

	SVM	DecisionRegTree
MAE	1.40	1.36
MSE	9.64	6.63
MAPE (%)	3	3

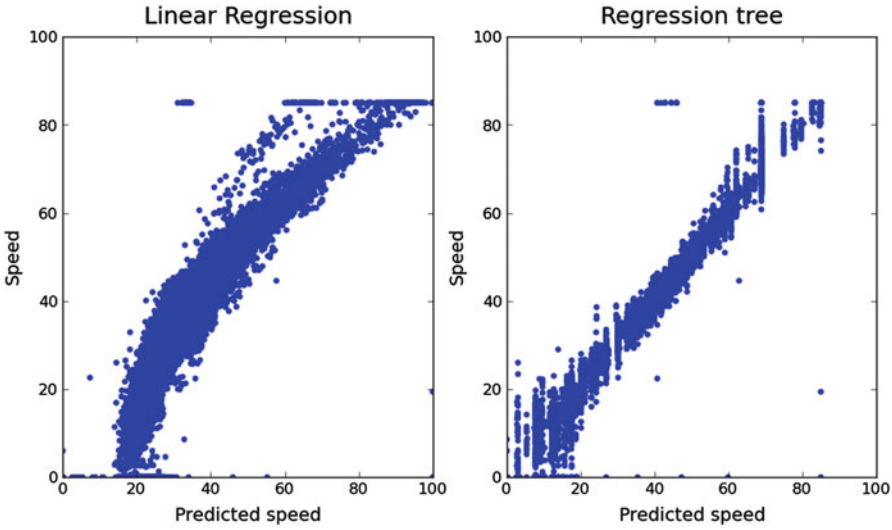

Fig. 7 The results of estimated values vs. actual values for supply fan subsystem

Table 3 The performance of supply fan energy consumption models

	SVM	DecisionRegTree
MAE	7.58	2.39
MSE	108.74	21.61
MAPE (%)	0.28	0.10

It is worth to noting that the energy estimations for two chiller modes are very similar. This suggested that the developed models are very robust and transferable for different chiller working modes.

It is also worth to pointing out that the estimate accuracy for low energy consumption is not as good as that for high energy consumption. The reasons need to be further investigated. But it also suggested that there is a possibility to improve the model performance by focusing on low energy consumption of the BEMS subsystems.

One limitation for the proposed method is the lack of ability of dealing with noisy sensor data. In this work, we found that some data is not accurate under some operation condition. For example, when chiller is operated at low energy consumption, the sensor readings are incorrect; we removed those data based on domain experts' input. Another problem, some data were missing in the database. Therefore, it is better to investigate an effective mechanism to deal with noisy and missing values in the data.

The proposed modeling techniques mainly focused on energy consumption estimation for reactive building operation. For proactive or long-term building operation, it is more important to predict energy consumption ahead in a period of time, say 24 h beyond. To meet such a requirement, we have to develop a predictive model which is able to predict energy load for the whole building or all BEMS 24 h ahead or longer period of time. This will be more challenging. We are working on this issue. The results will be reported in other papers.

6 Conclusion and Future Work

In this paper, we proposed a data-driven methodology for developing data-driven models to estimate energy consumption for BEMS subsystems such as chiller and supply fan in AHU. To attain this goal, we deployed some state-of-the-art machine learning and data mining techniques. We applied the proposed method to build predictive models for chiller in a given commercial building and supply fan in an AHU. The developed models were evaluated using real data from the building owner. The experimental results show that the data-driven method is a useful and effective alternative for modeling BEMS energy consumptions.

As presented in this paper, we have only developed the data-driven models for chiller and one supply fan subsystem. For our future work, we will continue working on modeling other subsystems such as return fan in AHU. In order to perform optimized energy consumption management, we have to also develop data-

driven models for tailoring control policies based on the energy consumption information for specified subsystems and for projecting short-term energy loads for the whole building. Consequently, such predictive models can be used to make decision on energy consumption for each subsystem, resulting in reaching the final goal of energy saving for building operations.

Acknowledgment Many people at the National Research Council Canada have contributed to this work. Special thanks go to Elizabeth Scarlett for the technical support. Thanks are also given to the National Resource of Canada for providing the building data to conduct the modeling experiments and domain knowledge to exploit the database.

References

Albadi, M.H., EI-Saadany, E.F.: A summary of demand response in electricity markets. Electr. Power Syst. Res. **78**, 1989–1996 (2008)

Bendapudi, S., Braun, J.E., Groll, E.A.: A Dynamic model of a vapor compression liquid chiller. In: The Proceedings of International Refrigeration and Air Conditioning Conference (2002)

Bi, Q., et al.: Advanced controller auto-tuning and its application in HAVC systems. Control Eng. Pract. **8**, 633–644 (2000)

Catalina, T., Virgone, J., Blanco, E.: Development and validation of regression models to predict monthly heating demand for residential buildings. Energ. Buildings. **40**, 1825–1832 (2008)

Dietterich, T.: An experimental comparison of three methods for constructing ensembles of decision trees: bagging, boosting and randomization. IEEE Intel. Syst. Appl. **40**, 139–158 (2000)

Dzeroski S., Zenko B.: Stacking with multi-response model trees. In: The Proceeding of International Workshop in Multiple Classifier Systems (MCS2002), pp. 201–211 (2002)

He, M., Cai, W.J., Li, S.Y.: Multiple fuzzy model-based temperature predictive control for HVAC systems. Inform. Sci. **169**, 155–174 (2005)

Kwok, S.K., Yuen, R.K.K., Lee, E.W.M.: An intelligent approach to assessing the effect of building occupancy on building cooling load prediction. Build. Environ. **46**, 1681–1169 (2011)

Mitchell, M.T.: Machine Learning. McGraw Hill, New York (1996)

Olofsson, T., Andersson, S., Ostin, R.A.: Energy load prediction for buildings based on a total demand perspective. Energ. Buildings. **28**, 109–116 (1998)

Online. U.S Department of Energy, Building Technology Program. Energy Solution for Your Building, http://www.eere.energy.gov/buildings/info/office/index.html (2000)

Opitz, D., Maclin, R.: Popular ensemble methods: an empirical study. J. Artif. Intell. Res. **11**, 169–198 (1999)

Quinlan, J.R.: C4.5: Programs for Machine Learning. Machine Learning. **16**(3), 235–240 (1993)

Roche, T.: Introduction to Dabo. http://www.tedtoche.com

Tso, G.K.F., Yau, K.K.W.: Predicting electricity energy consumption: a comparison of regression analysis, decision tree and neural networks. Energy. **32**, 1761–1768 (2007)

Tsoumakas, I.K.G., Blahavas, I.: Effective voting of heterogeneous classifiers. In: Proceedings of the 15th European Conference on Machine Learning (MCML2004), pp. 465–476 (2004)

Yalcintas, M., Akkurt, S.: Artificial neural networks applications in building energy predictions and a case study for tropical climates. Int. J. Energy Res. **29**, 891–901 (2005)

Zhang, G., Patuwo, B.E., Hu, M.Y.: Forecasting with artificial neural networks: the state of the art. Int. J. Forecast. **14**, 35–62 (1998)

A Simple Model of Finite Resource Exploitation: Application to the Case of Oil

A. Heitor Reis

1 Introduction

Most resources of economic value are finite, and the "window of opportunity" for its exploitation is also a finite period in history. Though they cannot fully predict the future, models of resource exploitation can help to put up prospective scenarios of resource availability. The most paradigmatic of such models is due to the pioneering work of M. K. Hubert in the 1950s (see Hubbert 1962) who proposed that oil production would follow a "bell-shaped" symmetric curve. Based on oil data exploitation, Hubbert was able to successfully predict 1970 as the peak year for oil production in the USA. Hubbert's curve is now applied to prospective studies on world's oil production (e.g., Campbell and Laherrère 1998; Rui 2003, 2006; Bardi and Lavacchi 2009), as well as to exploitation of coal and minerals (Bardi 2007; Bardi and Lavacchi 2009). Attempts have been made to establish the theoretical grounds of Hubert's curve by using either system dynamics (Naill 1973), stochastic modeling (Bardi 2005), or else economics (Holland 2008). In a recent paper, Bardi and Lavacchi (2009) develop an explanation of Hubert's curve based on a "predator and prey" model.

In this paper we try a different approach based on two main drivers of the rate at which resources are exploited: the level of economic demand and the level of the technology available for resource exploitation.

A.H. Reis (✉)
Physics Department, and Institute of Earth Sciences, University of Évora,
R. Romão Ramalho, 59, 7000-671 Évora, Portugal
e-mail: ahr@uevora.pt

© Springer International Publishing AG, part of Springer Nature 2018

F. Aloui, I. Dincer (eds.), *Exergy for A Better Environment and Improved Sustainability 2*, Green Energy and Technology,
https://doi.org/10.1007/978-3-319-62575-1_73

Nomenclature

m	Technologic and management index(nondimensional)
N	Number of activities that use oil
t	Time (*years*)
X	Resource amount *(*kg)
A, B, D, b, x	Ratio X/X_o Constants
Greek letters	
ϕ	Cost ratio (*exergy lost in crudeexploitation/exergy content of crude*)
ε	Avidity of market (nondimensional)
Subscripts	
0	Global reserve
u	Useful (commodity)
i, a	Ordinals

2 The Model

Differently from renewable resources, the global amount of finite resources is either constant or continuous; it decreases due to irreversible degradation as they are used in human and economic activities. Common examples of the first case are minerals, while oil, gas, and coal stand for the second one. In this way, a characteristic common to every finite resource is that historically there is a window of opportunity to explore them. Some of them, such as minerals, remain relatively stable as they are used, while others suffer irreversible transformations (e.g., coal, gas, oil) and once they become depleted will never be used in the global economy.

No resource is exploited without a cost associated to its exploitation. The simplest measure of this cost is the fraction of a resource unit whose market value equals the cost of exploitation of a unit of resource. We will call this nondimensional measure, the cost ratio. If we speak of oil, the cost ratio is the ratio of the exergy spent in the extraction of some oil amount to the useful exergy that it is able to deliver in the average conditions of its use in society. With respect to measuring exploitation cost of oil, gas, and coal, a measure commonly used is EROI which means energy return on investment (Hall and Cleveland 1981). Though EROI has various definitions (Bardi and Lavacchi 2009), the most suitable to the present case is societal EROI, which is defined as the ratio of the energy content of some amount of fuel to the energy lost in its exploitation. EROI does not take into account the quality of energy, i.e., it does not differentiate between heat and power, a fact that assigns it some ambiguity as a measure of exploitation cost. Such ambiguity would vanish if EROI was defined as the ratio of the exergy content of some amount of fuel to the exergy lost in its exploitation. In this case, EROI would come close to the inverse of cost ratio, because it may be shown that exergy can be taken as an appropriate measure of market value (Reis 2006).

2.1 Cost Ratio

Let us analyze first the case of fossil fuels and consider that at a time t, some fossil fuel (finite), whose known global (planetary) magnitude amounts to X_0, is exploited at the rate $\dot{X}$ with a cost ratio ϕ. Therefore, the "net fuel" (i.e., the part that is available for the other economic sectors) is put into the market at a rate $\dot{X}_u$ that is given by:

$$\dot{X}_u = \dot{X}(1 - \phi) \tag{1}$$

We assume that the cost ratio increases in time as the reservoirs become depleted of the resource, or new reservoirs are discovered at a greater depth. In this way, we also assume that such increase may be modeled as a power law of the degree of global shortage of that fossil fuel in the natural reservoirs, i.e.:

$$\phi = A(1 - X/X_0)^{-m} \tag{2}$$

where X is total amount exploited up to time t, A stands for the cost ratio at the beginning of the exploitation (X~0), and m is an exponent accounting for the degree of efficiency of the exploitation process. When $m > 1$, relatively high m means low efficiency, while low m means high efficiency (high developed exploitation technologies together with good management of exploitation). If $m < 1$ the cost ratio decreases in time, which means that the degree of exploitation efficiency is high enough to overshadow the negative effect of reservoir shortage.

By integrating Eq. (1) with the help of Eq. (2), one obtains:

$$x_u = x + \frac{A}{1 - m}(1 - x)^{1-m} \tag{3}$$

where x_u and x stand for X_u/X_0 and X/X_0, respectively. Equation (3) describes the total (historic) amount of "net fuel" put into the market in relation to total fuel extracted from the natural reservoirs.

2.2 Market Demand

The exploitation of finite natural resources is driven by the market demand. Demand in the case of fossil fuels is driven by all sectors in society that use energy, the most of it with origin in fossil fuel consumption. In a mental picture, we can imagine the growth of the use of fossil fuels in economy and in society as a diffusive process in which energy of fossil origin is used in an increasingly higher number of activities. Every simple diffusive process scales with $t^{1/2}$(where t stands for time),

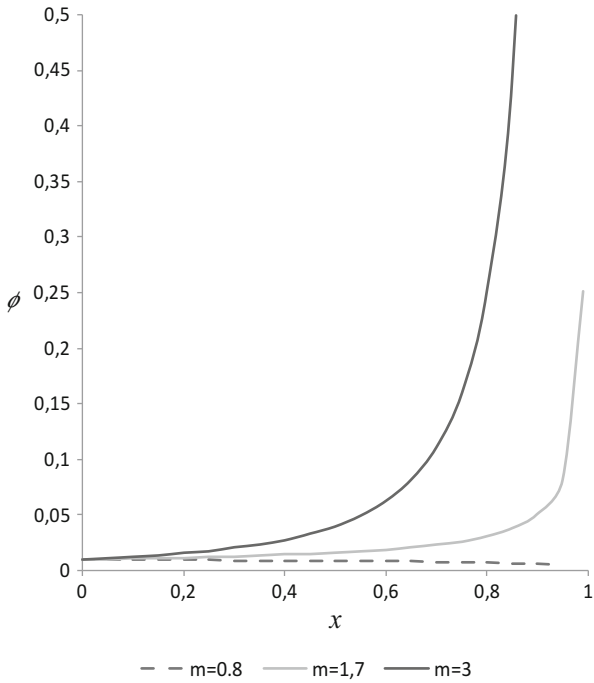

Fig. 1 Cost ratio as a function of fraction of resource extracted in various technologic scenarios

and therefore the number N of activities that use fossil fuel energy scales accordingly with

$$N \sim Dt^{1/2} \tag{4}$$

where D is a constant that accounts for the diffusibility of fossil fuel energy in society. Additionally, we assume that the number n of units in each activity a (industrial unit, house, vehicle, etc.) grows in time according to a power law

$$\sum_{i,a} n_i \sim b_i t^{\varepsilon} \tag{5}$$

where b_i is a constant, and the exponent ε accounts for the growth of sector i powered by the economic development, and namely, by the availability of energy of fossil fuel origin. Therefore, the total fossil fuel energy consumption rate in each activity (sector) is given by:

$$\dot{X}_a = \sum_i n_i \dot{X}_{i,a} \sim \sum_i b_i \dot{X}_{i,a} t^{\varepsilon} = B_a t^{\varepsilon} \tag{6}$$

where $\dot{X}_{i,a}$ is the consumption rate of unit i in sector a. In this way, by using Eq. (6) and summing for all activities (sectors), we find an estimate of the rate of global energy demand as:

$$\dot{X}_{\mathrm{u}} \sim Bt^{1/2+\varepsilon} \tag{7}$$

In Eq. (7) $\varepsilon = 0$ corresponds to pure physical driven diffusion of resource X and means indifference of the market with respect to resource X, while $\varepsilon > 0$ represents avidity for that resource, and $\varepsilon < 0$ stands for the cases when X is combated by the society (e.g., pollution, hallucinogenic drugs).

2.3 Exploitation Curve

By combining Eqs. (1) and (7) and integrating the resulting equation, one obtains:

$$x + \frac{A}{1-m}(1-x)^{1-m} - \hat{t}^{3/2+\varepsilon} = 0 \tag{8}$$

In Eq. (8) the constant B has been eliminated through an appropriate choice of the time scale. Therefore, here $\hat{t}$ represents a time scale in which $\hat{t} = 1$ corresponds to the period at the end of which resource X is completely depleted ($x = 1$).

The exploitation curve represented by eq. (8) is parameterized by:

(i) A, the cost ratio at the beginning of the exploitation (X~0)
(ii) m, the exponent accounting for the degree of efficiency of the exploitation process (technology and management)
(iii) ε, the exponent that accounts for the market avidity for energy of fossil fuel origin

These parameters may be estimated through the data available from resource exploitation, therefore enabling us to construct prospective scenarios of resource availability.

3 Analysis of Finite Resource Exploitation Curve

3.1 The Case of Oil Production

For the case of world oil exploitation, the relation of $\dot{x} \sim t^{\alpha}$ with the exponent $\alpha = 3.1$ fits pretty well the curve of annual production in the period 1930–1980 (see Fig. 2). On the other hand, the average value of A would be close to 0.01 (Gagnon et al. 2009). These basic data enable us to draw some future scenarios for oil production. These scenarios will not include production from shale oil reservoirs

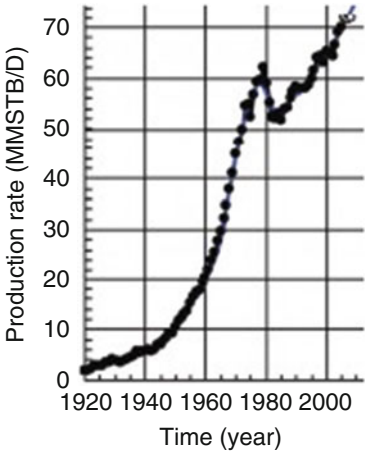

Fig. 2 Evolution of crude oil production rate

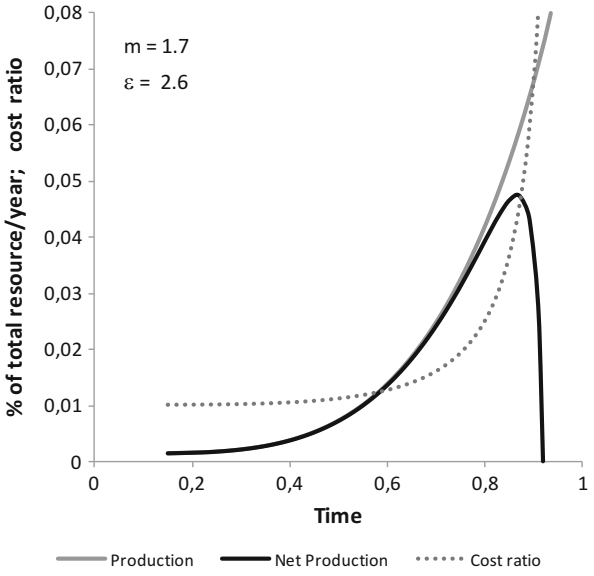

Fig. 3 Scenario for evolution crude oil production rate together with associated *cost ratio* with parameters estimated from actual data

because the parameters were estimated from data of oil production from normal crude oil reservoirs. With this purpose, we assume that α must be close to $1/2+\varepsilon$ (see Eq. 7), because for low values of x, both the curves $\dot{x}(t)$ and $\dot{x}_u(t)$ practically coincide (see Figs. 3, 4, and 5). Therefore, by taking $\varepsilon = 2.6$ and $A = 0.01$, we use Eq. (8) to find out the production curve that in its first part is described by the same exponent $\alpha = 3.1$. Such curve, which is represented in Fig. 3, is parameterized by $m = 1.7$. In this way, the curve in Fig. 3 is likely to stand for a liable scenario of future oil production. On the other hand, as discussed above, the exponent $m = 1.7$ indicates a moderate level of exploitation technology and exploitation

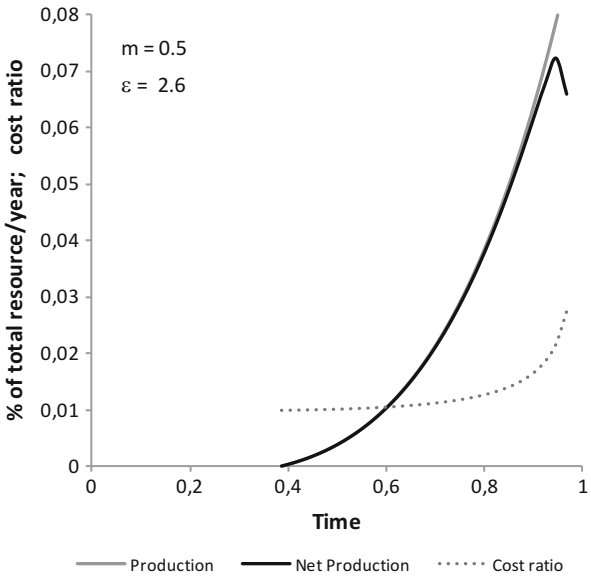

Fig. 4 Scenario for evolution of crude oil production rate together with associated *cost ratio* with parameters corresponding to extremely developed exploitation technology

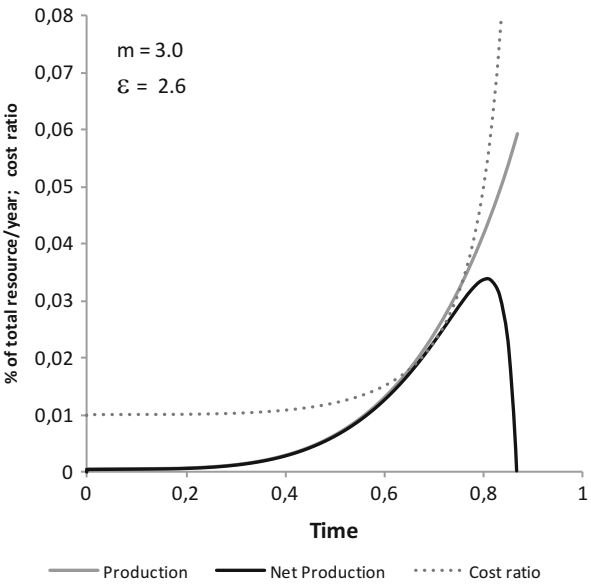

Fig. 5 Scenario for evolution of crude oil production rate together with associated *cost ratio* with parameters corresponding to underdeveloped exploitation technology

management. Several interesting comments can be drawn from Fig. 3. One first comment respects to cost ratio. Though it is not usual to find estimates of this variable in the literature, it can be estimated indirectly because its value is very close to the inverse of the EROI. In a recent paper, Gagnon et al. (2009) have

published recent estimates of EROI for crude oil in the period 1950–2005, which indicate that EROI in the period 1992–1999 was relatively stable close to 38 and has decreased to about 20 from 1999 to 2005. A very recent estimate indicates that EROI might be close to 11 in 2009 (Hall et al. 2009). By coming back to Fig. 3, this kind of evolution fits the steepest part of the cost ratio curve, while the cost ratio = 1/EROI = 0.05 roughly corresponds to the peak of net production. Beyond this point, the rate at which oil is delivered to the market decreases sharply.

If the curve somehow represents a realistic scenario for world oil production, we must conclude that the peak of global net oil production is occurring at the present time. The claim that global oil production is reaching its peak is assumed by many people and international groups, namely, the Association for the Study of Peak Oil (ASPO).

In the scenario depicted on Fig. 3, the peak would occur late in the period corresponding to the "window of opportunity" for oil exploitation, more precisely at time $\hat{t} \sim 0.91$. Based on Eq. (8), we conclude that at $\hat{t} \sim 0.91$ about 79% of the initial oil amount should have been extracted from reservoirs.

The remaining 21% would not be extracted due either to technologic reasons or to lack of economic interest. Moreover, Fig. 3 indicates that the period mediating between the peak of production and the end of economic interest of oil exploitation is of order $\hat{t} \sim 0.09$.

Considering 200 years as the "window of opportunity" for oil extraction, it means that between the peak and the end of exploitation, oil extraction will mediate a period of 18 years. This result must be viewed with some caution because the exponent for oil demand $\alpha = 3.1$ in the period of globalization of the use of oil (1930–1980) was also used for establishing the scenario for the period after the peak production has occurred. Modeling of oil demand in this period must not be described by a single exponent only due to the fact that energy demand will move toward other energy sources, namely, coal and the renewables.

By contrast with Hubert's, the present model does not predict a symmetric curve for oil production.

The reason is that not only oil extraction technology is much more developed but also demand is global, and therefore huge tensions must be at stage by the end of oil production. A scenario in which oil extraction technology is pushed to its limits by achieving reduction of cost ratio ($m = 0.5$) in the context of increasing complexity of oil production is represented in Fig. 4. Here we can see that more oil would be extracted: however, the post-peak period would be shorter than in the more realistic case of Fig. 3.

The scenario in which technology and extraction management would perform worse than that of Fig. 3 is represented in Fig. 5. In this case, not only much more oil would remain unexplored but also the cost ratio would start to increase earlier.

3.2 *Some Limiting Cases for Generic Finite Resources*

The previous analysis may be extended to other finite resources with the appropriate adaptations.

The scenario represented in Fig. 6 corresponds to both poor demand ($\varepsilon = 0.5$) and poor exploitation technology ($m = 3.0$). In this scenario the cost ratio stands high and rises significantly since the beginning of the exploitation. Only about 59% of the resource would be extracted at the end of exploitation (see Eq. 8).

The scenario in Fig. 7 is intended to represent average conditions: moderate demand ($\varepsilon = 1$) together with average technology development ($m = 2.0$). The resource will be exploited up to 72%, while the cost ratio will rise moderately.

Finally, the scenario in Fig. 8 stands for a finite resource whose trade is combated by the society (e.g., uranium), the case in which $\varepsilon < 0$.

For the case of uranium, the exponent m must be high due to the many technologic problems with its exploitation. In such a case, the resource would be explored for economic reasons only up to 66% of the global reservoir, while the cost ratio would rise significantly since the beginning of the exploration.

As a general comment, one must stress that the model presented above is very simple and may be improved to better describe real cases, namely, by allowing the exponents m and ε to be corrected for accommodating either the technologic breakthroughs or sudden discovery of new reservoirs, or else unexpected changes in global policies.

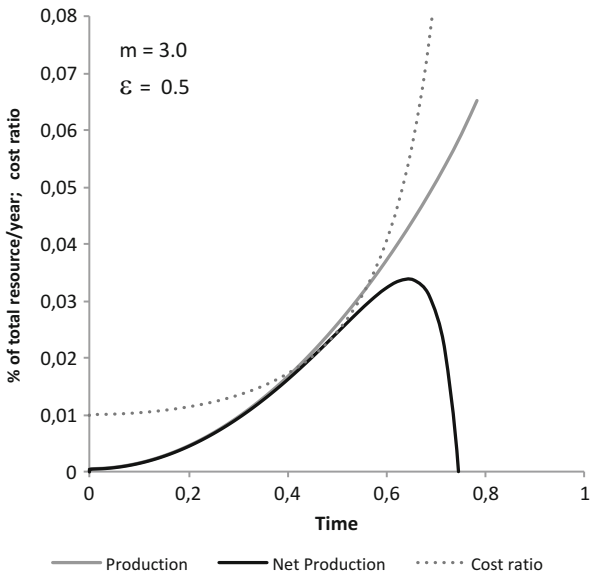

Fig. 6 Scenario for evolution of generic resource exploitation rate together with associated *cost ratio* with parameters corresponding to low market demand together with underdeveloped exploitation technology

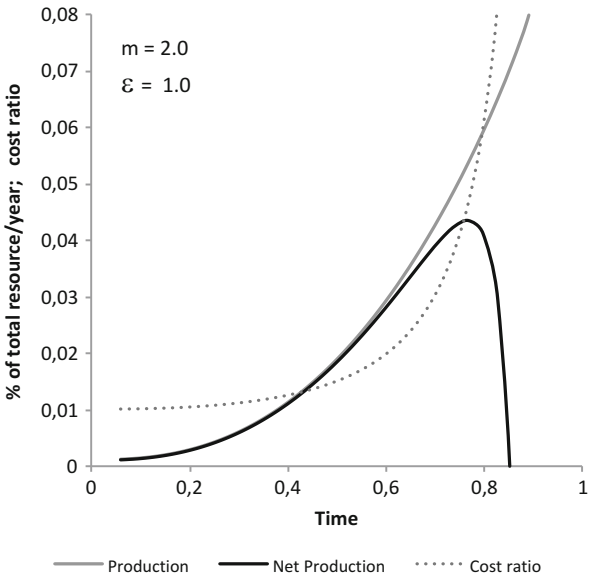

Fig. 7 Scenario for evolution of generic resource exploitation rate together with associated *cost ratio* with parameters corresponding to average market demand together with average exploitation technology

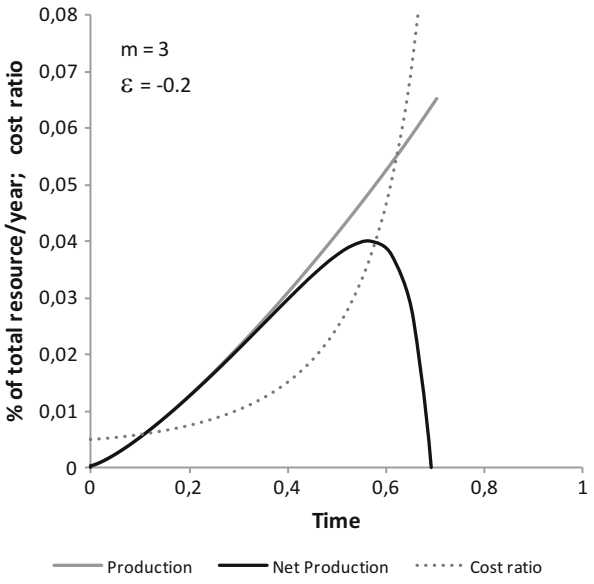

Fig. 8 Scenario for evolution of resource exploitation rate together with associated *cost ratio* and $A = 0.05$ in negative market demand conditions (restrained exploitation)

4 Conclusions

Despite its simplicity, the model developed in this paper enables capture of basic features of resource exploitation. The inputs to the model, namely, resource market demand index and initial cost ratio of exploitation, may be estimated from historical

data, while the technologic index, which is a parameter associated to the level of exploitation technology, may be also inferred from the application of the model to historical data. The case of oil production was considered in the analysis, and a possible future scenario of oil production rate was put up on the basis of the historical production rate. Some scenarios for generic resource exploitation were also considered and analyzed. The model allows future improvements, namely, by considering either unexpected discovery of new reservoirs or market demand transition for new energy sources.

Acknowledgments This research was supported by the Institute of Earth Sciences (ICT), under contract with FCT (Portugal). This support is gratefully acknowledged by the author.

References

Bardi, U.: The mineral economy: a model for the shape of oil production curves. Energ Policy. **33**, 53–61 (2005)

Bardi, U.: Peak oil's Ancestor: The Peak of British Coal Production in the 1920s. ASPO, Uppsala (2007)

Bardi, U., Lavacchi, A.: A simple interpretation of Hubbert's model of resource exploitation. Energies. **2**, 646–661 (2009)

Campbell, C.J., Laherrère, J.H.: The end of cheap oil. Sci. Am. **278**, 78–83 (1998)

Gagnon, N., Hall, C.A.S., Brinker, L.: A preliminary investigation of energy return on energy investment for global oil and gas production. Energies. **2**, 490–503 (2009)

Hall, C.A.S., Cleveland, C.J.: Petroleum drilling and production in the U.S.: yield per effort and net energy analysis. Science. **211**, 576–579 (1981)

Hall, C.A.S., Balogh, S., Murphy, D.J.R.: What is the minimum EROI that a sustainable society must have? Energies. **2**, 25–47 (2009)

Holland, S.P.: Modeling peak oil. Energy J. **29**, 61–80 (2008)

Hubbert, M.K.: Energy Resources. A Report to the Committee on Natural Resources, p. 54. National Academy of Sciences, National Research Council, Washington, DC (1962)

Naill, R.F.: The discovery life cycle of a finite resource. In: Meadows, D.H. (ed.) Towards Global Equilibrium: Collected Papers. Business & Economics, Geneva (1973)

Reis, A.H.: Exergy based analysis of economic sustainability in Perspectives on Econophysics, 147–159, Ed. Un. of Evora. (2006)

Rosa, R.N.: Economic growth in a closed finite world. In Perspectives on Econophysics, 127–146, Ed. Un. of Evora (2006)

Rui R.: Climate Change and Oil Depletion. Energy Exploration & Exploitation **21**(1), 11–28 (2003)

Development and Application of a Simple and Reliable Power Regulator for a Small-Scale Island Wind Turbine

Yongjun Dong, Yang Zhao, Jianmei Chen, Mingqi Xu, Xueming Zhang, and Jingfu Guo

1 Introduction

Islands, which occupy an important place in marine economics, are increasingly concerned. Due to lack of electricity and fresh water, it is very inconvenient for the daily life of the people living on islands. Even if they can depend on the diesel generation, during the onset of severe weather, it is impossible to supply fuel oil, especially to the remote islands. In addition, diesel generation not only has high cost but also easily causes environmental pollution. Thanks to rich wind resources in the islands, electricity generation from wind power is considered as one of the most effective ways to solve the electric power supply on islands.

For wind power generation on islands, because of its high maintenance costs, the reliability of the machine has a higher priority than its efficiency (Whale 2009). Therefore, the most worrisome property in the application of island wind power machine is its operational reliability, especially in strong winds or gusts. For a small-scale horizontal-axis wind power machine, its protection in high wind speeds usually depends on some version of yawing mechanism which tends to turn the rotor out of the wind direction so as to limit the captured energy of the rotor. Some of these yawing devices adopt the method of furling a tail vane to control the rotor speed and output power of the WTG (Bialasiewicz 2003; Bowen et al. 2003; Wright and Wood 2007; Arifujjaman et al. 2008; Audierne et al. 2010). Others achieve the function of yawing by using the combination of a DC motor, a reducer, roller

Y. Dong • Y. Zhao • J. Chen • M. Xu • X. Zhang • J. Guo (✉)
School of Physics, Northeast Normal University, 5268 Renmin Street, Changchun 130024, Jilin Province, China

Key Laboratory of Advanced Energy Development and Application Innovation under Jilin province, 5268 Renmin Street, Changchun 130024, Jilin Province, China
e-mail: renewableerlab@163.com

© Springer International Publishing AG, part of Springer Nature 2018

F. Aloui, I. Dincer (eds.), *Exergy for A Better Environment and Improved Sustainability 2*, Green Energy and Technology,
https://doi.org/10.1007/978-3-319-62575-1_74

bearings, a worm, and so on, which act on the yaw axis (Wu and Wang 2012). Besides, some small-scale horizontal-axis wind turbines have a variable pitch control system (Nagai et al. 2009; Whale 2009; Narayana et al. 2012), just like large wind turbines that limit the captured energy of the rotor by feathering the blades, and some wind turbines adopt passive stall blades. The mechanical furling principle easily leads to frequent swing of the tail vane when the wind changes rapidly, resulting in the vibration of the wind turbine. Meanwhile, because the hinge structures are more fragile under the effect of corrosion in oceanic environments, this impact on the hinge is worse for the frequent swing of the tail vane. Power control by the yawing mechanism acting on the yaw axis or variable pitch mechanism will increase the complexity of wind turbine structure and lead to a cost increase of wind turbines. Controlling the increase of power by passive stall blades mainly depends on the airfoil profile of the blade. It is hard to control the dynamic behavior of stall airfoil blade, especially in continuously increasing wind speed. Because of wrongly estimating for the power grade and blade loads, the captured energy of the turbine will increase uncontrollably with increasing wind speed (Munteanu et al. 2008).

To solve overspeed protection and output power limitation of small-scale wind turbine in strong winds, it is very necessary to develop a simple, reliable, and effective power regulating method. In this paper, we design a power regulator based on electric linear actuator (ELA) and aerodynamic vane. The regulator consists of a rigid tail with an electrical control rotating aerodynamic vane (it is used to yaw the rotor edgewise to the wind direction in high wind speeds), an electric linear actuator, and a controller. It has several advantages including a simple structure that is easy to be manufactured and installed, high controllability, and increased reliability compared to the conventional mechanical vane applied in small-scale wind turbines. The implementation of rotating the vane actively only depends on the generator speed by measuring AC electrical frequency and the output electric power by measuring two DC electrical quantities (i.e., voltage and current), and no mechanical sensors are needed. The regulator has been applied to a 15 kW wind turbine prototype operating on an island for more than 3 years. Field test results as well as simulations will be provided and discussed.

Nomenclature

A	Area of the wind rotor
B	Intensity of magnetic field
C_E	Electromotive force constant
C_P	Power coefficient of the wind rotor
C_T	Torque constant
D	Equivalent viscous damping coefficient of the ELA
D_m	Viscous damping coefficient of the DC motor
D_2	Equivalent viscous damping coefficient of the transmission
$E_a(t)$	Induced electromotive force of the DC motor
f_e	AC frequency of the PMSG
$I_a(t)$	Armature current of the DC motor

(continued)

I_{dc}	DC bus current of the WTG after rectification
J	Equivalent moment of inertia of the ELA
J_m	Moment of inertia of the DC motor
J_2	Equivalent moment of inertia of the transmission
K_E	Proportional constant of the back electromotive force
K_T	Proportional constant of the torque
L_a	Armature inductance of the DC motor
p	Pole pairs of the PMSG
P_a	Aerodynamic power captured by the wind rotor
P_c	Reference power given by the controller PI_1
P_m	Measured power of the WTG
P_{rated}	Rated power of the WTG
R	Rotor radius
R_a	Armature resistance of the DC motor
$T_{em}(t)$	Electromagnetic torque of the DC motor
$U_a(t)$	Power supply voltage of the DC motor
U_{dc}	DC bus voltage of the WTG after rectification
v	Speed of the incident wind
$v_{c\text{-}in}$	Cut-in wind speed of the wind turbine
$v_{c\text{-}out}$	Cut-out wind speed of the wind turbine
$v_{\omega\text{-}rated}$	Wind speed of the turbine speed achieving its rated value
v_{rated}	Wind speed of the generation power achieving its rated value
Greek letters	
ρ	Air density
λ	Tip speed ratio
α	Furling angle of the tail vane
β	Blade pitch angle
γ	Yawing angle
$\theta_m(t)$	Rotation angle of the DC motor rotor
ω	Angular speed of the generator rotor
$\omega_m(t)$	Angular speed of the DC motor rotor
ω_m	Measured rotational speed of the turbine
ω_{rated}	Rated rotational speed of the turbine
Φ	Main magnetic flux of the DC motor
Abbreviation	
AC	Alternating current
DC	Direct current
ELA	Electric linear actuator
HCS	Hill-climb searching
MPPT	Maximum power point track
PMSG	Permanent magnet synchronous generator
WTG	Wind turbine generation

2 Power Control by Electric-Driven Furling

2.1 Principle of Power Control by Yawing

For direct-driven wind energy generation system, the wind turbine captures the power from the kinetic energy contained in the wind and transfers it directly to the rotor shaft of the electric generator. The mechanical energy captured by the wind rotor is estimated by (Burton et al. 2001)

$$P_{\mathrm{a}} = \frac{1}{2}\rho A v^3 C_{\mathrm{P}} \tag{1}$$

where, ρ is the air density (kg/m^3), A is the area of the rotor (m^2) and v is the speed of the incident wind (m/s) that flows through the turbine. The power coefficient C_{P} is usually given as a function of the tip speed ratio and the blade pitch angle. The tip speed ratio λ of a turbine is defined as

$$\lambda = \frac{\omega R}{v} \tag{2}$$

where ω is the angular speed of the rotor and R is the rotor radius. For the fixed-pitch wind turbine, C_{P} only depends on the tip speed ratio λ. In fact, when the turbine is yawed, the value of yawing angle γ, shown in Fig. 1, has a significant effect on the power coefficient. It is verified that the peak power output in yawing condition closely follows the theoretical value given as (Adaramola and Krogstad 2011)

$$C_{\mathrm{P}}(\gamma) = C_{\mathrm{P}}(\gamma = 0)\cos^3(\gamma) \tag{3}$$

According to Eq. (3), the relation between the power coefficient and the yawing angle is illustrated in Fig. 2. By adjusting the yawing angle of the wind turbine, the angle of attack on rotor blades would also change, leading to variation in the aerodynamic characteristics of the blade. In addition, when the turbine is in a

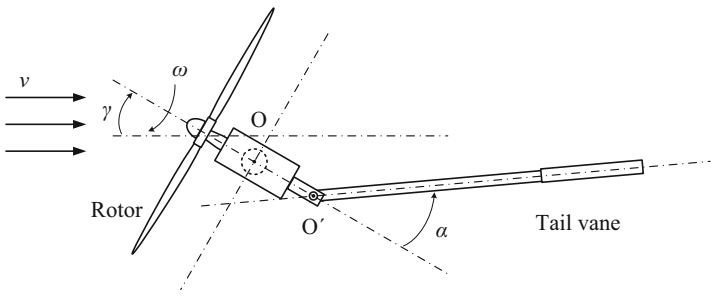

Fig. 1 Horizontal-axis wind turbine in yawing condition by furling the tail vane

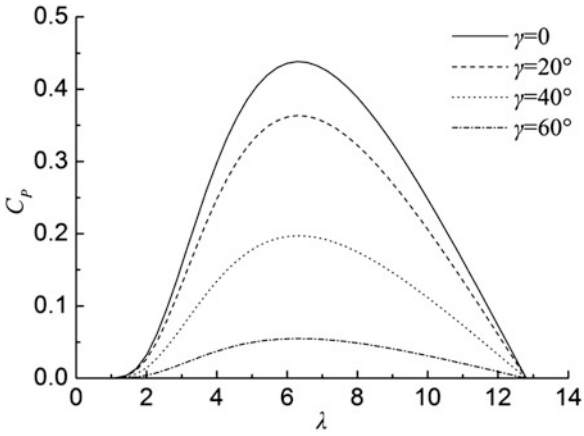

Fig. 2 Power coefficient with the change of the yaw angle

yawing position, it can affect both the effective wind speed and the rotor swept area. The blades operate in a deep stall regime at very low tip speed ratios, therefore the power curves are not significantly affected by the yawing angle. Figure 2 shows that the output power of the turbine will be controlled by adjusting the yawing angle above the rated wind velocity.

For a small-scale horizontal-axis wind turbine, it usually has a tail vane (shown in Fig. 1.) that tends to stay aligned with the wind direction so as to regulate the turbine to properly orient wind direction in low and medium wind speeds. At higher wind speeds, in order to yaw the rotor for overspeed protection and output power limitation, it is an attractive method to furl the tail vane, as shown in Fig. 1. When the tail vane folds at a certain angle α, the wind acting on the tail vane will cause a yawing moment that tends to turn the rotor out of the wind, and the tail vane remains approximately aligned with the wind direction. At a constant wind speed, a new stop position is reached and a yawing angle γ of the rotor is generated. Then, the captured energy of the rotor will be reduced because of the yaw angle. Once the wind speed has fallen below a critical value, recovery from this position and therefore realignment with the wind direction is enabled by a restoring moment that is generally provided by an external force.

2.2 Electric-Driven Furling

Compared to the conventional mechanical furling structure by simply depending on the aerodynamic principles, the method of utilizing electric driver to furl the tail vane actively has high controllability in yawing the rotor edgewise to the wind direction. Such a novel device consists of a rigid tail with an electrical control rotating aerodynamic vane, an electric linear actuator, and a controller, as shown in Fig. 3a.

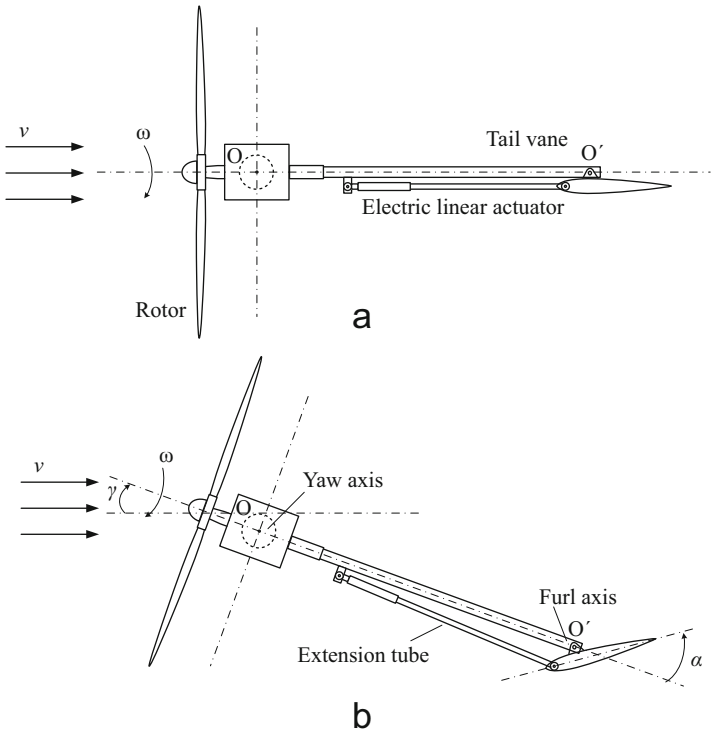

Fig. 3 (**a**) Structure and operation principle (**b**) of electric-driven furling

The ELA is an actuator that creates linear motion by converting rotational movement. It depends on the motor's bidirectional rotation to complete the motion of the extension tube along a straight line, and it has a lot of advantages compared to traditional mechanical and hydraulic systems. Once the tube suffers overloads or moves to the end of the stroke, the motion will be forced to stop by an overload clutch or electronic load monitoring. Besides, the actuator will hold its loads with power removed and no maintenance is required. The rotating tail vane adopts the airfoil structures, which has excellent aerodynamic characteristics compared to the traditional flat tail. By applying the airfoil tail vane, the steering mechanism of small-scale WTG could yaw the turbine more easily.

When the rotation speed of the rotor or the output power is below the corresponding rated value, the tube of the actuator will be in its initial position and the aerodynamic force on the tail of the wind machine keeps it aligned with the wind direction, shown in Fig. 3a, as a common vane does. Once the measured value reaches its rated value, the tube of the electric linear actuator will be stretched out to push the vane to rotate through an angle α around the furl axis O′, shown in Fig. 3b. Then, the drag force on the vane makes the rotor rotate through an angle γ around its

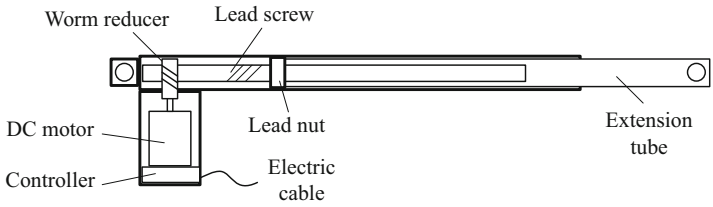

Fig. 4 Typical structure of a DC ELA based on the worm gear and the ball screw

hinge axis O, causing the whole machine to yaw gradually through γ as the wind speed increases, shown in Fig. 3b. Referring to Fig. 2, the captured power will be dramatically reduced by increasing the yawing angle γ.

3 Model of the Electric Furling System

3.1 Structure of the ELA

Figure 4 shows the typical structure of a DC ELA based on the worm gear and the ball screw. It mainly consists of a DC motor, a worm-gear reducer, a ball screw, an extension tube, and a control unit. When powering the electric linear actuator, the DC motor rotor rotates and then drives the lead screw to rotate through the worm-gear reducer. The lead nut, which is connected to the extension tube, is driven by the lead screw to move along the screw. Thus, the rotation of the motor is converted to the linear movement of the extension tube.

3.2 Model of the ELA

As an electromechanical system, the ELA can be modeled by combining several subsystem models, such as the model of the DC motor, the model of transmission, and the model of control unit, as shown in Fig. 5. Figures 6, 7, and 8 show the typical equivalent circuit of the DC motor, the kinetic model of the DC motor, and the model of the transmission system, respectively. By mathematical modeling, the parameters of the electrical drive system can be shown as the linear motion parameters of the mechanical load.

Based on the principles of electrical machinery and mechanical transmission, the transfer function of the electric linear actuator by Laplace transform can be represented as (Ruiz-Rojas et al. 2008)

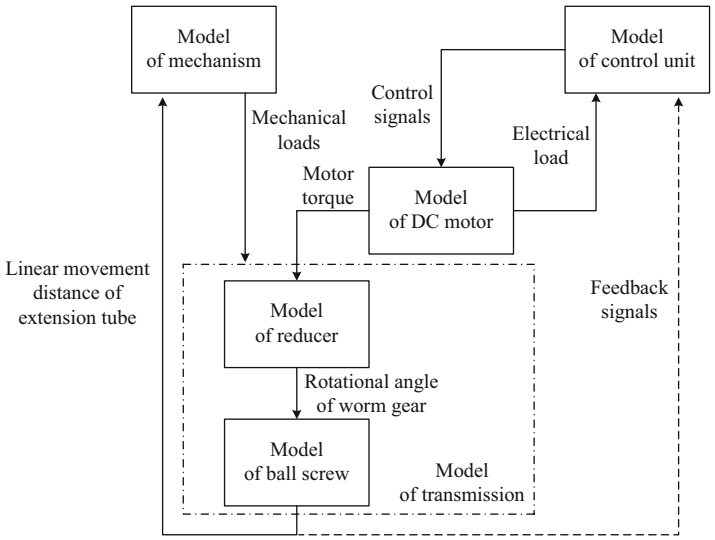

Fig. 5 Diagram of mathematical modeling of linear actuator powered by electricity

Fig. 6 Equivalent circuit of the DC motor

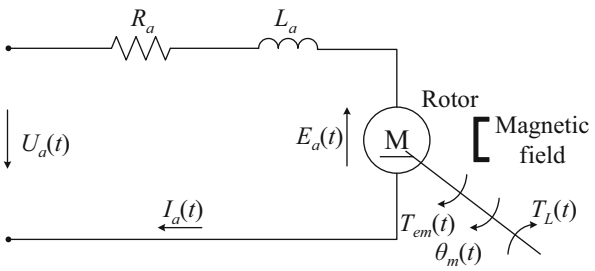

Fig. 7 The kinetic model of the motor and the transmission

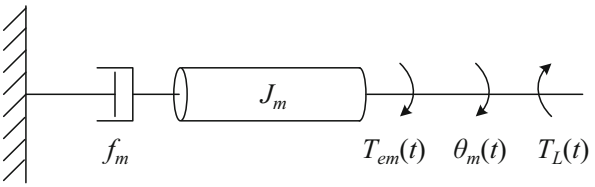

$$\frac{X(s)}{U_{\mathrm{a}}(s)} = \frac{K_T}{P(Js^2 + Ds)(R_{\mathrm{a}} + L_{\mathrm{a}}s) + K_{\mathrm{T}}K_{\mathrm{E}}s} \tag{4}$$

where, $X(s)$ is the Laplace transform of the linear advance $x(t)$ of the ball-screw lead; $U_{\mathrm{a}}(s)$ is the Laplace transform of the DC power supply voltage $U_{\mathrm{a}}(t)$ of the motor; J and D are the equivalent moment of inertia and the equivalent viscous damping coefficient including the motor and the transmission, respectively; R_{a} and

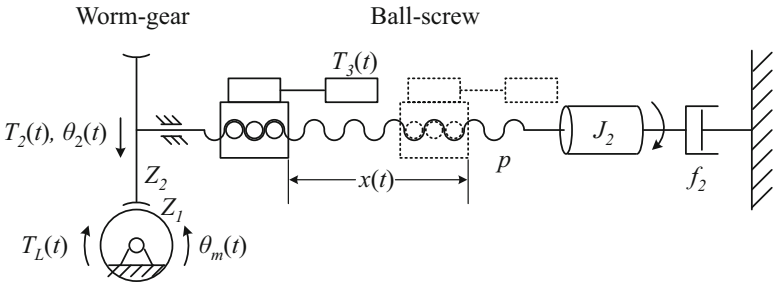

Fig. 8 The model of the transmission

L_a are the armature resistance and inductance of the motor, respectively; K_T and K_E denote the proportional constant of the torque and the back electromotive force in a constant magnetic field, respectively; P is a constant defined as the ratio of 2π and the screw pitch l.

Corresponding state space equations of Eq. (4) can be expressed as follows (Ruiz-Rojas et al. 2008)

$$\begin{bmatrix} \dot{x}_1(t) \\ \dot{x}_2(t) \\ \dot{x}_3(t) \end{bmatrix} = \begin{bmatrix} 0 & 1 & 0 \\ 0 & -\frac{D}{J} & P\frac{K_T}{J} \\ 0 & -\frac{K_E}{PL_a} & -\frac{R_a}{L_a} \end{bmatrix} \begin{bmatrix} x_1(t) \\ x_2(t) \\ x_3(t) \end{bmatrix} + \begin{bmatrix} 0 \\ 0 \\ \frac{1}{L_a} \end{bmatrix} U_a(t)$$

$$y = [1 \ 0 \ 0] \begin{bmatrix} x_1(t) \\ x_2(t) \\ x_3(t) \end{bmatrix} \tag{5}$$

3.3 Model of the Electric Furling Device

Figure 9 shows the structural diagram of the furling device when the measured rotational speed ω_m of the rotor is larger than the rated value ω_{rated}. Based on the output signal that compared ω_m with ω_{rated}, the extension tube of the ELA is elongated to push the tail vane to rotate around the furl axis O′, shown in Fig. 9. For a certain furl angle α, it can be addressed as

$$\alpha = \beta' - \beta \tag{6}$$

where,

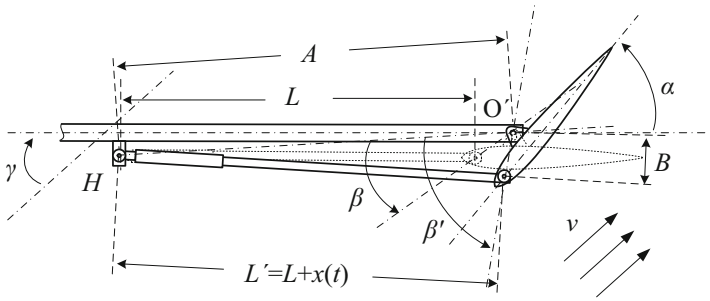

Fig. 9 The structural diagram of the furling device when furling behavior occurs

$$\beta' = cos^{-1}\frac{A^2 + B^2 - L'^2}{2AB} = cos^{-1}\frac{A^2 + B^2 - [L + x(t)]^2}{2AB} \tag{7}$$

$$\beta = cos^{-1}\frac{A^2 + B^2 - L^2}{2AB} \tag{8}$$

Thus, according to Eqs. (5) and (6), we can obtain the furling angle of this electric furling device under steady wind velocity. By adjusting the furling angle, the power captured by the turbine would be limited effectively.

4 Control Method

4.1 Standalone WTG Configuration

Figure 10 shows the block diagram of the standalone WTG with electric furling device. In our design of the WTG prototype, the mechanical torque to the multi-polar three-phase PMSG is directly provided by a horizontal-axis, fixed-pitch, four-blade wind turbine, which is suitable for the application in low wind speeds. A three-phase diode rectifier bridge is used for rectifying the alternating current of the generator to direct current. The high-capacity capacitor C_1 filters out the output voltage oscillations of the rectifier and creates a stable DC-link for the following subsystem. The DC-DC converter converts the output voltage U_{dc} of the rectifier to the voltage U_{bat} for the charge of the batteries under the control of the power regulator. At high wind speeds, according to the measured output electric power and AC frequency, the furling controller provides control instructions to the electric furling device to furl the tail vane. Under the effect of aerodynamic force, the turbine will yaw and then its captured power will be reduced. The MPPT control of the wind turbine depends on the variable-step hill-climb searching (HCS) method

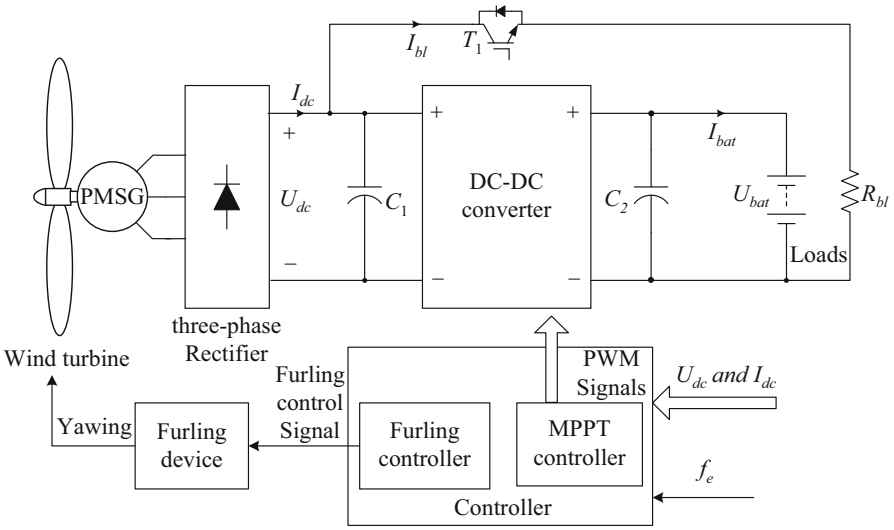

Fig. 10 Standalone WTG configuration with electric furling device

(Kesraoui et al. 2011; Abdullah et al. 2012). The furling controller aims to limit the rotational speed and the captured power of the turbine, and to protect the WTG device against damage during strong winds, and this is also the main issue of this part.

4.2 Control Strategy Analysis

For variable-speed fixed-pitch wind turbine in its operating regimes of the entire wind speed domain from cut-in $v_{\text{c-in}}$ to cut-out $v_{\text{c-out}}$, as depicted in Fig. 11, its ideal operation could be divided into three regimes (Şerban and Marinescu 2012). In the regime between $v_{\text{c-in}}$ and $v_{\omega\text{-rated}}$, the control aims to maintain an optimal power-speed characteristic of the wind turbine, which is also called the MPPT control. In the regime between $v_{\omega\text{-rated}}$ and v_{rated}, the wind turbine operates in a quasi-constant rotor speed regime. In the regime between v_{rated} and $v_{\text{c-out}}$, the wind turbine is controlled to maintain the constant output power no higher than the rated power so that the turbine and generator are not overloaded and dynamic loads do not result in mechanical failure (Bianchi et al. 2007; Behjat and Hamrahi 2014). When the wind speed is above $v_{\text{c-out}}$, the wind turbine must be shut down to avoid being damaged (Abdullah et al. 2012).

Considering the reliable operation of small-scale horizontal-axis fixed-pitch WTG, enough importance should be attached not only during strong wind and gusts but also at low wind speed. When the wind speed exceeds the rated threshold (usually around 9–12 m/s) (Şerban and Marinescu 2012), the tail vane must be furled timely so as to limit the rotational speed and the captured power. When the

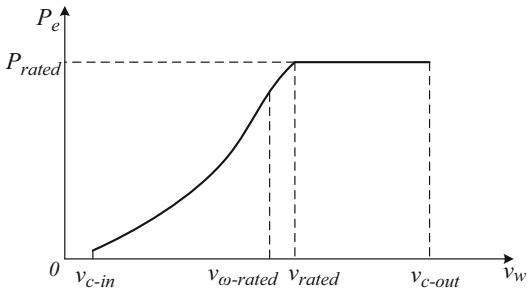

Fig. 11 The ideal operation curve of variable-speed fixed-pitch wind turbine

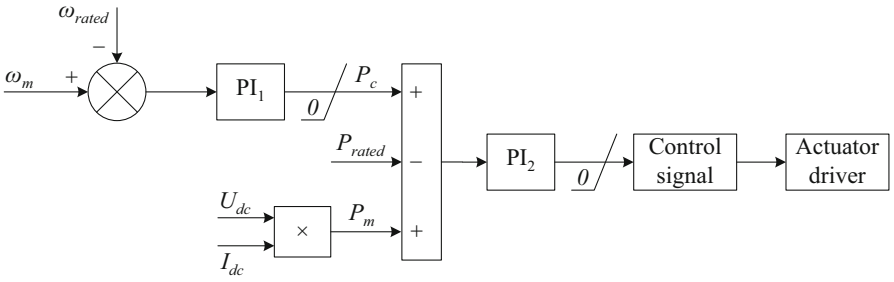

Fig. 12 The control block diagram of the electric furling device

wind speed is below its rated value, although the output power couldn't exceed its rated value, if partial loads or full loads are removed unexpectedly, the rotational speed of the rotor would increase remarkably and would exceed the rated rotor speed. Thus, continuous running under the condition of a rotor speed much higher than the rated value is very harmful to the structure of the WTG. It is necessary to limit the rotational speed of the rotor when the loads are removed during low wind speed.

Based on the above analysis, the electric furling control strategy is proposed, as illustrated in Fig. 12. In this figure, P_c is a reference power, P_m denotes the measured output electric power which is the product of the measured DC voltage U_{dc} and the measured DC current I_{dc}, and P_{rated} is the corresponding rated value. For the direct-driven permanent magnet synchronous generator that is generally adopted in small-scale wind turbine, the rotational speed ω_m of the turbine can be obtained by

$$\omega_m = \frac{2\pi f_e}{p} \tag{9}$$

where, f_e and p denotes the AC frequency and the pole pairs of the PMSG, respectively. The control method aims to maintain one of the output power and the rotor speed to be quasi-constant, while the other is no larger than the corresponding rated value. As one can see in Fig. 12, the regulator PI$_1$ acts on the

error between the measured rotor speed ω_m and its rated value ω_{rated}, providing a reference value P_c. Then, the difference value obtained by the rated power P_{rated} subtracting the measured output power P_m and the reference power P_c is provided for the regulator PI_2 to generate the control signal of the furling system.

When the wind speed varies between $v_{c\text{-}in}$ and v_{rated}, P_m is less than P_{rated}, while ω_m may exceed ω_{rated}. If $\omega_m \leq \omega_{rated}$, the regulator PI_1 is in a state of reverse saturation and its output is identically equal to zero by limiting. Meanwhile, because P_m is less than P_{rated}, the regulator PI_2 is also in reverse saturation and its output is also equal to zero by limiting. Thus, the actuator of the furling system stays in its initial state. In this regime, if $\omega_m > \omega_{rated}$ for some reason, the regulator PI_1 outputs the reference power P_c. Although P_m is still less than P_{rated}, the sum of P_c and P_m will be larger than P_{rated}, and the regulator PI_2 acts on the error between the sum and P_{rated}, providing the control signal for the furling system. When the wind speed is between v_{rated} and $v_{c\text{-}out}$, the output power will exceed its rated value, while ω_m may be below ω_{rated} because of the increase in the loads. Regardless of whether ω_m exceeds ω_{rated}, the sum of P_c and P_m will be greater than P_{rated}. Then the regulator PI_2 acts on the error between the sum and P_{rated}, providing the control signal for the furling system.

5 Simulation Results

In this section, the performance of the proposed furling control method is evaluated by means of simulation. All the simulation models are constructed and implemented in MATLAB/Simulink. According to different furling conditions, such as suffering high wind speed and removing loads in low wind speed, the simulation results are divided into two parts for discussion.

5.1 Suffering High Wind Speed

For a step in wind speed between 8 and 12 m/s illustrated in Fig. 13a, the corresponding characteristics of the different parameters based on simulation are shown in Fig. 13b–f. In the Fig. 13b–d, the dotted red lines denote the output characteristic curves of the WTG without any measures of overspeed protection and power limitation, such as furling the tail vane. After the wind speed steps to 12 m/s, the corresponding rotational speed and output power of the generator begin to increase. Supposing that the WTG is still controlled by MPPT, its rotational speed would almost achieve 18 rad/s and corresponding output power will achieve 26 kW, as shown in Fig. 13b, c, respectively. They have far exceeded their rated value for rated speed 13.6 rad/s and rated power 15 kW. Continuous overspeed operation will intensify the structural vibrations of the wind turbine (Guimarães et al. 2015), which is harmful to the stability of the wind turbine. For overload

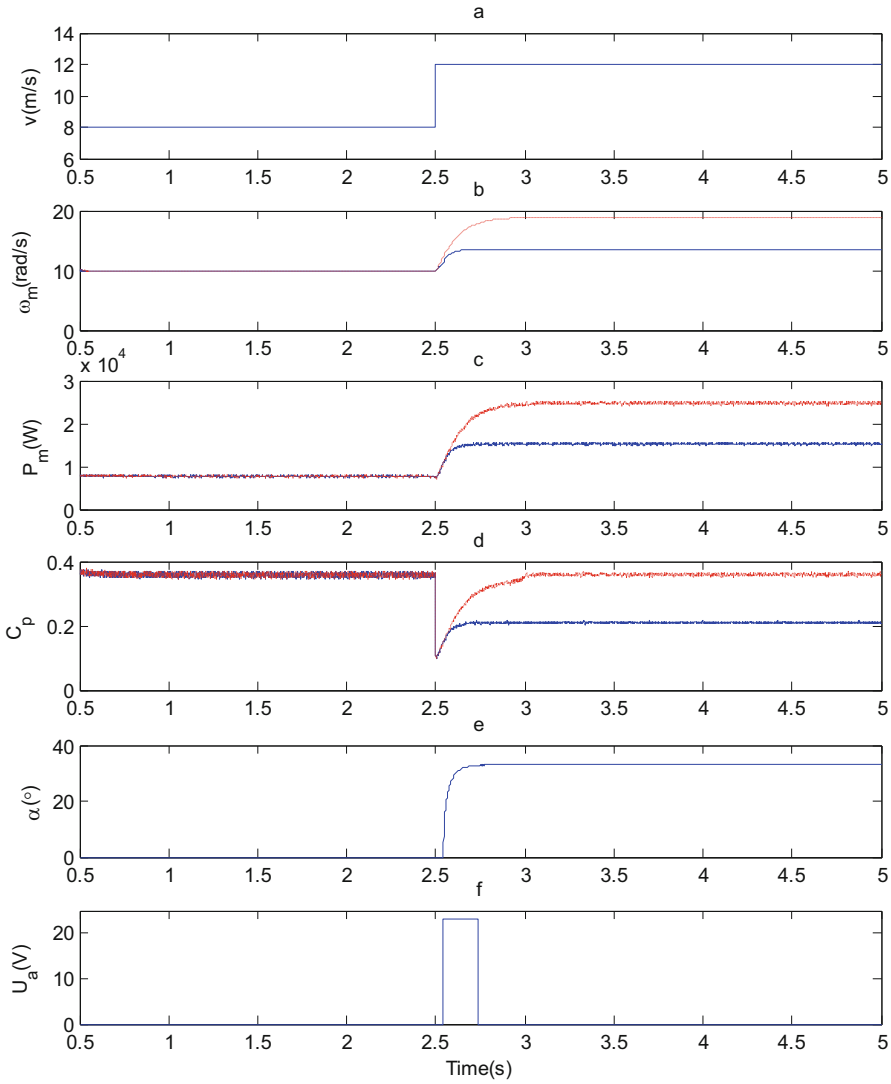

Fig. 13 Output characteristics function of the WTG when suffering high wind speed

protection of electric power, it makes more rigorous demands for the selection of the generator and the power electronic devices, which would cause significant increase in the cost of the wind turbine. The solid blue lines, illustrated in Fig. 13b–f, represent the characteristics by the furling system proposed in this paper. According to the furling model stated in Section 3 and the control algorithm proposed in Section 4, the controller outputs the furling control signal U_a and then the furling angle α of the vane gradually increases to about 33°, as shown in Fig. 13f, e, respectively. Under the ideal condition, the turning of the small-scale

wind turbine completely depends on its tail vane. Finally, the rotational speed and the output electric power are limited to the corresponding rated value, as illustrated in Fig. 13b, c, respectively. Thus, the furling system realizes the overspeed protection and the output power limitation of the WTG at high wind speed.

5.2 Removing Loads

Figure 14 illustrates the characteristics of the different parameters under the condition of partial loads removing when the wind speed is 8 m/s (rated value 10 m/s).

The dotted red lines, as shown in Fig. 14b–d, denote the output characteristics of the WTG without any protections, and the solid blue lines in Fig. 14b–f represent the characteristics after furling the tail vane. When partial loads are removed for some reasons, the rotational speed of the rotor gradually increases. Although the output power becomes less than before (shown in Fig. 14c) and still below the rated power, the final rotor speed will achieve 15.5 rad/s (shown in Fig. 14b), which is higher than the rated rotor speed 13.6 rad/s. As is mentioned above, continuous high rotor speed will bring unforeseen dangers to the wind turbine structures. By taking the measure of actively furling the tail vane, the vane rotates nearly 26°, as shown in Fig. 14e. Finally, the rotor speed is limited in its safe range (below 13.6 rad/s here), as illustrated in Fig. 14b.

6 Field Test

To assess the performance and to verify the functionality of the electric furling system, a device prototype was manufactured and installed on a specially designed wind turbine prototype, which was funded by State Oceanic Administration of China and installed in Dachen Island, Zhejiang Province, as shown in Fig. 15.

The structure of the electric furling actuator and the airfoil tail are illustrated in Fig. 16. The aerodynamic vane consists of an aluminum alloy skeleton and aluminum skin filled with polyurethane foam, and uses the symmetric airfoil of NACA0012 to get better aerodynamic performance. The actuator is installed on the rigid tail stock next to the generator, and its extension tube is connected to the leading edge of the airfoil vane (shown in Fig. 16). The rotation axis of the vane lies on the focus of the airfoil (28% of the chord length), which will make the turbine yaw smoothly out of the wind during high wind speed depending on the aerodynamic compensation ability of the airfoil tail.

The reducer of the ELA is based on worm and gear, which have several advantages, including high reduction ratio, large output torque, low noise level, and self-locking. The ELA could output maximum push force by 7500 N, and its speed control depends on a PWM signal.

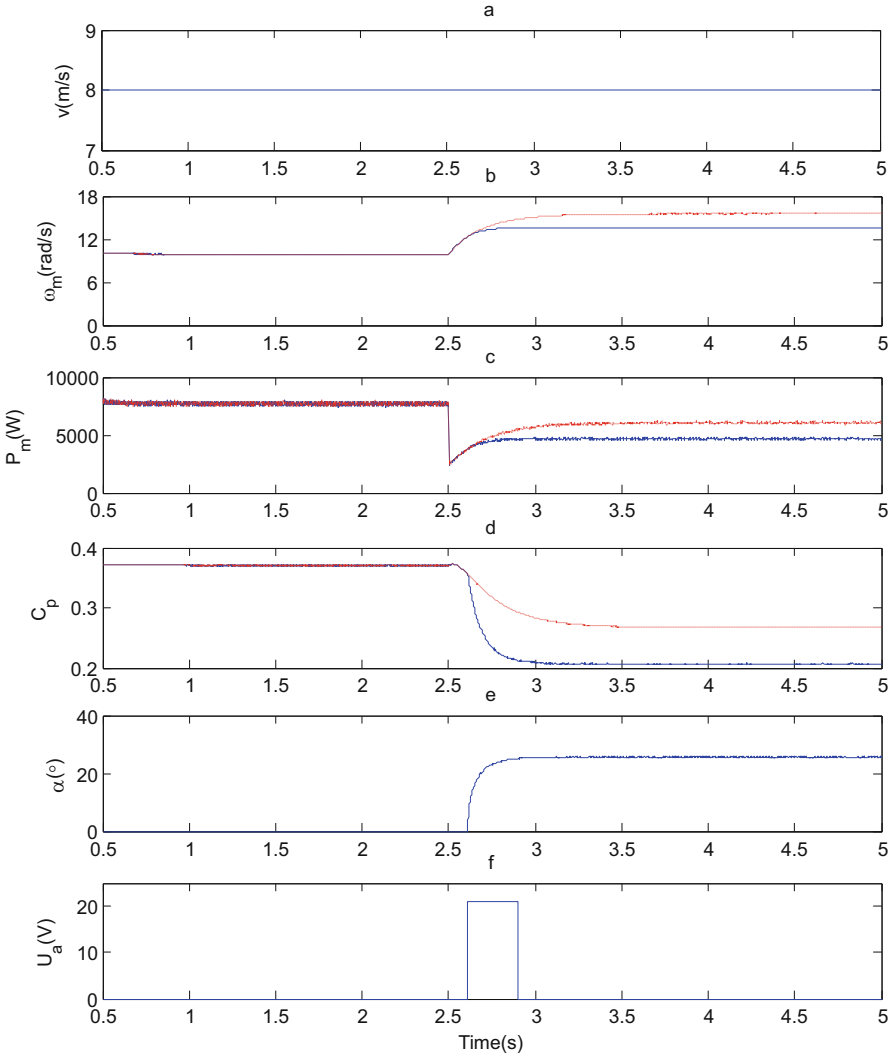

Fig. 14 Output characteristics function of the WTG when removing partial loads at low wind speed

Figure 17 shows the furling controller of the wind turbine prototype, which is separate with the generator controller. The DC output parameters of the generator are obtained from the generator controller through the 485 bus, and the AC frequency is collected from the AC voltage signal by the AD converter. The DC power of the controller is supplied by 24 V lead-acid batteries which are charged directly from the electricity of the generator controlled by a transformer and a DC-DC converter. The control algorithm is realized by a microprocessor.

Fig. 15 Operating wind turbine equipped with electric furling system

Fig. 16 Structure of the electric furling actuator and the airfoil tail

Fig. 17 Furling controller of the wind turbine prototype

By monitoring the operation of the WTG, the output characteristics of the WTG are analyzed based on the method of bins, illustrated in Fig. 18. As one can see in Fig. 18a, when the output electric power exceeds its rated value, it will be limited around the rated value under the control of the furling system. Figure 18b shows the power coefficient of the prototype.

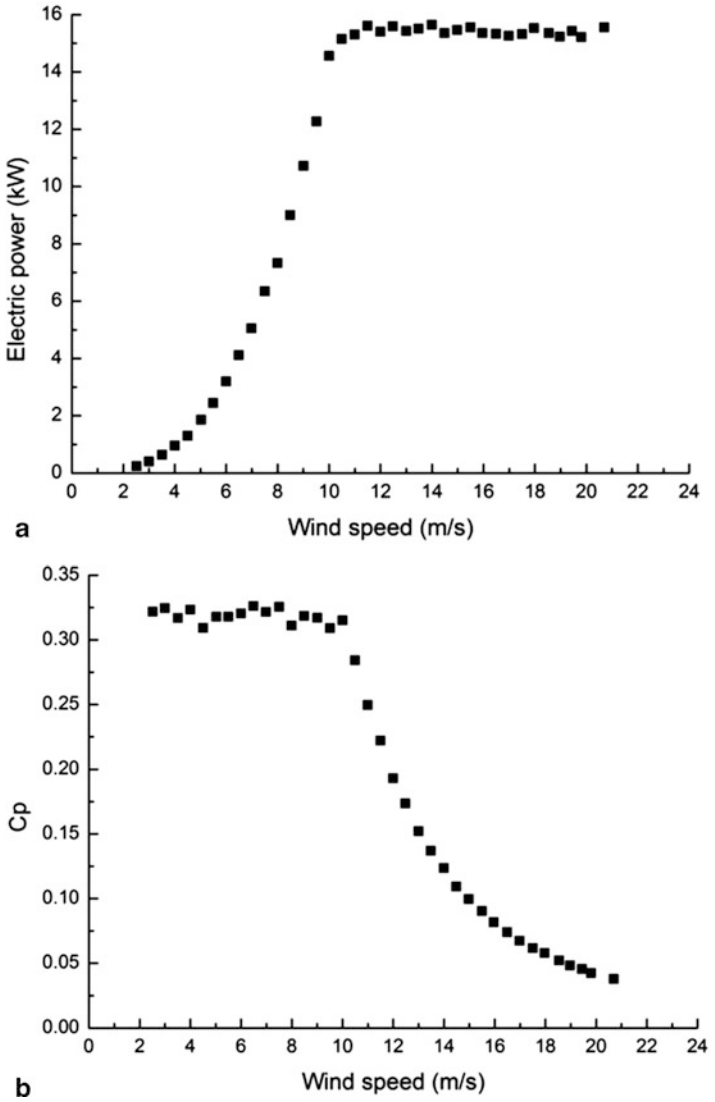

Fig. 18 Characteristics of the wind turbine prototype: the output electric power (**a**); the power coefficient (**b**)

Obviously, when the wind speed is below its rated value, the prototype almost maintains its maximum power coefficient. In the high wind region, the coefficient decreases because of the limitation of the output power.

7 Conclusion

In this paper, a new method for overspeed protection and power limitation of small-scale, horizontal-axis, fixed-pitch wind turbine generation system has been described. The electric furling system based on an electric linear actuator and an airfoil tail was developed and a corresponding structure was modeled. The simulation results of the regulator indicated that the control method can easily prevent the turbine from exceeding the rated values of rotational speed and output power. Meanwhile, the field test of a wind turbine prototype equipped with a furling device verified that this electric furling method could effectively limit the rotational speed and the output power of the turbine. For further optimization, this method can be widely applied for overspeed protection and power limitation of standalone wind energy conversion system.

Acknowledgments This work is sponsored by Science Foundation for Young Teachers of Northeast Normal University (No.14QNJJ009) and Special funds of Marine Renewable Energy of State Oceanic Administration of China (No.GHME2011CL02, No.ZJME2013ZB02).

Appendix

WTG parameters: radius of turbine $r = 4.9$ m, stator resistance $R_a = 0.55\Omega$, stator inductances $L_d = L_q = 0.15$ mH, moment of inertia $J = 19.2$ kg m, pole pairs $p = 22$.

References

Abdullah, M.A., Yatim, A.H.M., Tan, C.W., et al.: A review of maximum power point tracking algorithms for wind energy systems. Renew. Sust. Energ. Rev. **16**(5), 3220–3227 (2012)

Adaramola, M.S., Krogstad, P.Å.: Experimental investigation of wake effects on wind turbine performance. Renew. Energy. **36**(8), 2078–2086 (2011)

Arifujjaman, M., Iqbal, M.T., Quaicoe, J.E.: Energy capture by a small wind-energy conversion system. Appl. Energy. **85**(1), 41–51 (2008)

Audierne, E., Elizondo, J., Bergami, L., et al.: Analysis of the furling behavior of small wind turbines. Appl. Energy. **87**(7), 2278–2292 (2010)

Behjat, V., Hamrahi, M.: Dynamic modeling and performance evaluation of axial flux PMSG based wind turbine system with MPPT control. Ain Shams Eng. J. **5**(4), 1157–1166 (2014)

Bialasiewicz, J.T.: Furling control for small wind turbine power regulation. IEEE Int. Symp. Indus. Elect. **2**, 804–809 (2003)

Bianchi, F.D., Battista, H.D., Mantz, R.J.: Wind Turbine Control Systems – Principle, Modelling and Gain Scheduling Design. Springer, London (2007)

Bowen, A.J., Zakay, N., Ives, R.L.: The field performance of a remote 10 kW wind turbine. Renew. Energy. **28**(1), 13–33 (2003)

Burton, T., Sharpe, D., Jenkins, N., et al.: Wind Energy Handbook. Wiley, West Sussex (2001)

Guimarães, P.V.B., de Morais, M.V.G., Avila, S.M.: Tuned mass damper inverted pendulum to reduce offshore wind turbine vibrations. In: Vibration Engineering and Technology of Machinery, Part of the Mechanisms and Machine Science book series, vol. 23, pp. 379–388. Mechan. Machine Science (2015)

Kesraoui, M., Korichi, N., Belkadi, A.: Maximum power point tracker of wind energy conversion system. Renew. Energy. **36**(10), 2655–2662 (2011)

Munteanu, I., Bratcu, A.I., Cutululis, N.A., et al.: Optimal Control of Wind Energy Systems: Towards a Global Approach. Springer, New York (2008)

Nagai, B.M., Ameku, K., Roy, J.N.: Performance of a 3kW wind turbine generator with variable pitch control system. Appl. Energy. **86**(9), 1774–1782 (2009)

Narayana, M., Putrus, G.A., Jovanovic, M., et al.: Generic maximum power point tracking controller for small-scale wind turbines. Renew. Energy. **44**, 72–79 (2012)

Ruiz-Rojas, E.D., Vazquez-Gonzalez, J.L., Alejos-Palomares, R., et al.: Mathematical model of a linear electric actuator with prosthesis applications. In: 18th International Conference on Electronics, Communications and Computers, pp. 182–186 (2008)

Şerban, I., Marinescu, C.: A sensorless control method for variable-speed small wind turbines. Renew. Energy. **43**(0), 256–266 (2012)

Whale, J.: Design and construction of a simple blade pitch measurement system for small wind turbines. Renew. Energy. **34**(2), 425–429 (2009)

Wright, A.K., Wood, D.H.: Yaw rate, rotor speed and gyroscopic loads on a small horizontal axis wind turbine. Wind Eng. **31**(3), 197–209 (2007)

Wu, Z., Wang, H.: Research on active yaw mechanism of small wind turbines. Energy Procedia. **16**(Part A(0)), 53–57 (2012)

Design and Economic Analysis of Photovoltaic Systems in Different Cities of Turkey

Suphi Anıl Sekuçoğlu and Tülin Bali

1 Introduction

The need for energy is increasing day by day. The conventional fossil fuels are limited. Therefore, research is focused on renewable energy sources. The share of use of renewable energy sources in electricity generation is expected to rise to 22% in 2030.

Turkey is very rich in renewables potential. But few of these potentials have been utilized so far. Renewable energy has become one of the increasingly important topics in Turkey since renewables are considered not only as a way of mitigating import dependency in energy resources but also as a part of finding solutions to environmental problems.

Biomass and hydropower are the two major types of renewable sources commonly used in Turkey, in addition to the rarer uses of other types, such as geothermal, wind, and solar. The expected electric power capacity development in Turkey is summarized in Table 1 for 2010 and 2020. The total installed photovoltaic power capacity in Turkey is estimated at around 300 kW, which should be increased in the near future, together with other renewable energy systems. The currently installed photovoltaic power is relatively small considering the high solar energy resource in Turkey, as summarized in Table 2, regionally.

Photovoltaic conversion is the direct conversion of sunlight into electricity with no intervening heat engine. Photovoltaic devices are simple in design and require very little maintenance. Solar photovoltaic devices can be constructed as stand-alone systems to give outputs from microwatts to megawatts. Therefore, they can be

S.A. Sekuçoğlu • T. Bali (✉)
Karadeniz Technical University, Engineering Faculty, Mechanical Engineering Department, Karadeniz Technical University, Mechanical Engineering Department, Trabzon 61080, Turkey
e-mail: bali@ktu.edu.tr

© Springer International Publishing AG, part of Springer Nature 2018

F. Aloui, I. Dincer (eds.), *Exergy for A Better Environment and Improved Sustainability 2*, Green Energy and Technology,
https://doi.org/10.1007/978-3-319-62575-1_75

Table 1 Renewable energy potential of Turkey

Type	Potential	In operation
Hydro	45.000 MW	17,359.3 MW
Wind	48.000 MW	1,792.7 MW
Solar	300 TWh/year	–
Geothermal	600 MW	114.2 MW
Biomass	17 Mtoe	117.4 MW

Source: Turkish Energy Market: An Investor's Guide 2012, Energy Market Regulatory Authority (EMRA)

Table 2 Annual average solar energy potential by regions of Turkey

	Solar radiation (kWh/m^2)	Sunshine duration (h)
Marmara	1168	2409
Southeast Anatolia	1460	2993
Aegean	1304	2738
Mediterranean	1390	2956
Black Sea	1120	1971
Central Anatolia	1314	2628
East Anatolia	1365	2664
Average	1303	2623

used as power sources for calculators, watches, water pumps, remote buildings, communications, satellites, and space vehicles, and even multimegawatt scale power plants. With such a vast array of applications, the demand for photovoltaics is increasing every year. In 2012, over 31,000 MWp of photovoltaic panels were sold for terrestrial use and the worldwide market has been growing at a phenomenal rate since 2000.

Photovoltaics have been one of the fastest growing energy technologies in the world. The countries with most installed photovoltaic power currently are Germany, Japan, Italy, and the USA, which are the biggest photovoltaic module-producing countries as well. As a result of the high growth rate of stand-alone photovoltaic applications throughout the world, many articles have been published to calculate their performance by Siegel et al.(1981), Bucciarelli (1984), Klein and Beckman (1987), and Clark et al.(1984).

The grid-connected photovoltaic systems have experienced a rapid growth in recent years. This was achieved mostly through the government-induced energy policies of especially the developed countries. Nowadays, more and more articles appear in the literature reporting on the grid-connected photovoltaic systems. These articles include as financial incentives, a reduction in the investment costs, increase in reliability, and distribution of information and enhancement of environmental awareness. Life cycle techno-economic analysis of a grid-connected photovoltaic house in Turkey was investigated by Celik (2006).

Table 3 Solar energy purchase prices (state support)

Austria	0.30–0.46 €/kWh + investment support
Belgium	0.45 €/kWh + for 20 years[a]
France	0.30–0.40 € /kWh + for 20 years[a]
Germany	0.3769–0.4921€/kWh + for 20 years[a]
Italy	0.36–0.49 € /kWh + for 20 years[a]
Portugal	0.28–0.45 € /kWh + for 15 years[a]
Spain	0.23–0.44 € /kWh + for 25 years[a]
Turkey	0.133 $/kWh + for 10 years[a]

[a]Guaranteed government purchases

Solar power purchase price in Europe and state grants are as Table 3.

This paper presents a parametric study examining PV systems that can meet the average energy needs of a single house in Turkey. This study was carried out for six cities that came on more or less solar radiation according to the average annual solar radiation of Turkey. There isn't a comprehensive parametric study about off-grid and on-grid PV systems in selected cities. At the same time, investigation with PV system types, on-grid, off-grid, and on-grid feed-in tariff systems, allows for comparative cost analysis. This study also investigates the effects of a capacity shortage fraction on cost-sizing.

In this paper, the current status of photovoltaic energy in Turkey was studied and the lifetime techno-economic analysis of stand-alone and grid-connected photovoltaic systems was carried out.

This paper presents a comparative study about on-grid (grid-connected) and off-grid (stand-alone) photovoltaic (PV) systems for a single house (2500 kWh annually) in different cities of Turkey.

Nomenclature

i	Annual real interest rest
N	Project lifetime
Abbreviations	
COE	Levelized cost of energy
CRF	Capital recovery factor
CSF	Capacity shortage fraction
NPC	Net present cost
PV	Photovoltaic
PVS	Photovoltaic system
REF	Renewable energy fraction
TAC	Total annualized cost of the system

Belen (36°29′N, 36°13′E), Gelibolu (40°28′N, 26°43′E), Konya (31.42°N, 37.08°E), Sinop (42 01°N, 35 09°E), Kırklareli (41.44°N, 27.12°E), and Karaman (37.11°N, 33.14°E) cities were selected as the design areas in Turkey. The objective of this study is to predict the system costs, the cost of energy generated by the PVS, and to compare costs of stand-alone and grid-connected systems. In order to carry

out system designs and determine the technical and economical parameters of PVS, the HOMER program developed by the National Renewable Energy Laboratory (NREL) was used.

2 HOMER Analysis

In this study, to carry out system designs and determine the technical and economical parameters of each system, the HOMER program was used. HOMER "Hybrid Optimization Model for Electric Renewables" ensures the following (NREL 2012):

- A computer software is developed by United States National Renewable Energy Laboratory (NREL).
- It makes the simulation of the work of the systems throughout the year using the data of hourly time.
- Total net present cost is used for the calculation of the life cycle cost of the system.
- HOMER searches the configuration of the system with the lowest total net present cost and sorts appropriate systems according to this value.
- Assumes that all price increases will take effect at the same rate throughout the life of the project.

The load profile of the system is expressed as the amount of energy per hour arising from the energy requirement of the system. Installation status was determined based on an average annual energy need of a house in Turkey, which was 2500 kWh. In this study, it was assumed that the same daily program is implemented all year round but randomness factors were also taken into consideration in order to ensure flexibility. Randomness values from day to day and hourly time steps were taken at 5%. At the same time, it is assumed that the amount of daylight is enough and is not done lighting during the day. As can be seen in Table 4, the schedule of a daily electricity usage of a house is prepared under these assumptions by Sekucoğlu (2012).

The daily load profile can be seen in Fig. 1. These load profiles were obtained with HOMER program according to the time intervals and the default operation of devices.

PV module and battery characteristics are shown in Table 5. The cost of module is taken as $ 2.84 (2.69 €/W_p) per Watt. To take into account the setup fee and the cost of other system components, total investment cost is considered to be twice the price of the module. The PV life is taken as 25 years. PV panels are placed at an angle of about 30° to the horizontal direction of the south. Tracking system is not used in this study. The cost of battery is taken as $ 0.213 per 1 Wh. Of the total capital cost and cost of replacement, it is assumed the same. Maintenance and repair costs are considered to be $ 0.

Inverter costs for stand-alone systems and grid-connected systems were $ 1 and $ 0.714 per 1 Watt, respectively. The unit energy cost of electricity purchased from the grid was $ 0.12/kWh.

Table 4 Electricity usage chart for the load profile of a house (2500 kWh)

Device	Power (kW)	Daily working time (h)	Daily consumption (kWh)
Refrigerator	–	24	1.54
Washing machine	1.03	1	1.03
Dishwasher	0.90	1	0.9
Vacuum cleaner	0.60	1	0.6
Iron	0.60	1	0.6
Lamp (40 W) 3	0.12	8	0.96
Kitchen devices	0.075	2	0.15
Television	0.075	6	0.45
Satellite receiver	0.036	6	0.216
Computer	0.065	6	0.39

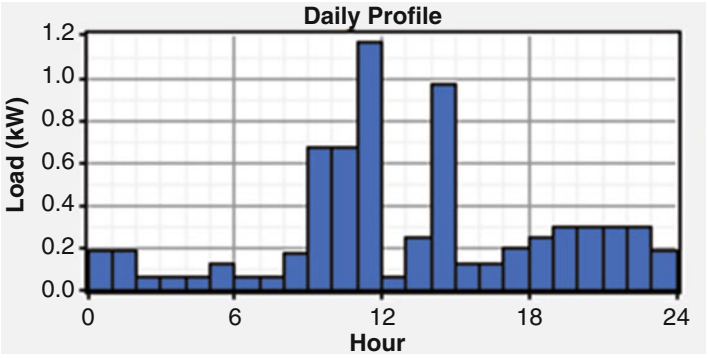

Fig. 1 Daily load profile (*for annually 2500 kWh energy-consuming house*)

Table 5 PV module and battery characteristics (stand-alone system)

PV module	Battery
BP Solar BP4175T	Vision 6FM200D
1.587 m * 0.790 m	V, 12 Volt
$\mathbf{V_{oc}}$ 43.6 V	200 Ah
I 5.45 A	
η(STC) % 14	
Cost per Watt, $ 2.84 (2.69 €/W_p)	$ 0.213

The software HOMER finds the optimum system based on the net present cost, renewable factor, and payback period. The net present cost is the present value of all setup and maintenance costs over the life of the project. It is calculated by using the following equation:

$$\mathrm{NPC}(\$) = \frac{\mathrm{TAC}}{\mathrm{CRF}}$$

In this equation, TAC and CRF are the total annualized cost of the system and the capital recovery factor, respectively. CRF is defined as follows:

$$\mathrm{CRF} = \frac{i(1+i)^N}{(1+i)^N - 1}$$

Here, N is the number of years that the project is expected to last and i is the annual real interest rate. The annual real interest rate is taken as 6%. The project lifetime is taken as 20 years.

The renewable factor is the amount of energy consumed that comes from a renewable source. It is calculated simply by dividing the amount of electricity produced by renewable sources by the total energy consumption of the property. The value of renewable factor is 1 for stand-alone systems.

Capacity shortage is simply a measure of how much of the load is not met. HOMER will add up all of the load that is not supplied in a year to determine the unmet load. The capacity shortage is the ratio between the unmet load and the total load (whether supplied or not). The capacity shortage fraction in the system design was less than 0.5%. In addition, the effects of 10% reduction in the capacity shortage fraction on the system costs are investigated for stand-alone systems.

3 Results and Discussions

The system and levelized costs of energy were investigated for a load of 2500 kWh case annually and the effect of capacity shortage fraction on the system was examined. The systems were designed as grid-connected and stand-alone systems. A stand-alone PVS system and a grid-connected PVS system can be seen in Fig. 2a, b. Batteries were not needed in the grid-connected system because power could be sold back onto the grid at a better rate than it would cost to store it for later use in a battery.

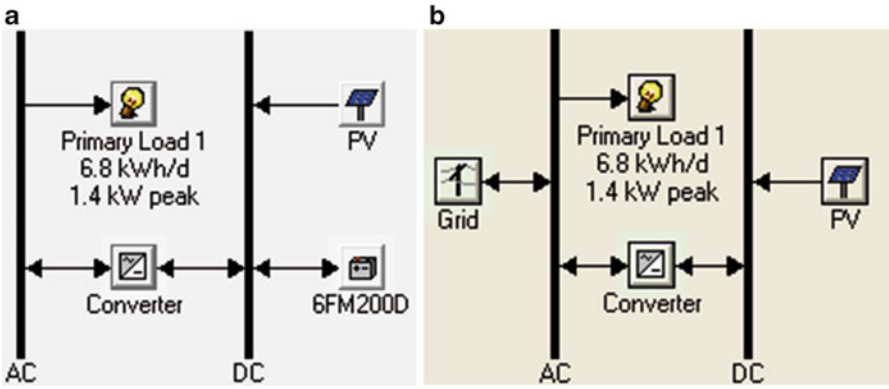

Fig. 2 (**a**) Stand-alone PVS model. (**b**) Grid-connected PVS model

Table 6 Stand-alone PVS optimization results

City	Belen	Gelibolu	Konya	Sinop	Kırklareli	Karaman
PV array [kW]	3.850	5.250	3.675	5.425	5.600	3.675
Capacity of battery [Ah]	200	200	200	200	200	200
Number	20	22	18	22	22	16
Inverter [kW]	3.1	4.2	3.0	4.4	4.5	3.0
NPC [$]	40,180	50,559	37,535	51,733	52,786	35,942
COE [$/kWh]	1.412	1.778	1.318	1.819	1.856	1.263

Table 7 Optimization results for $CSF_{max} = 10$

City	Belen	Gelibolu	Konya	Sinop	Kırklareli	Karaman
PV array [kW]	2.625	3.150	2.450	3.150	3.325	2.275
Capacity of battery [Ah]	200	200	200	200	200	200
Number	10	12	8	14	12	8
Inverter [kW]	2.1	2.6	2.0	2.6	2.7	1.9
NPC [$]	26,276	30,013	24,538	31,069	31,165	23,513
COE [$/kWh]	1.004	1.153	0.937	1.188	1.192	0.897
CSF [%]	10	10	10	10	10	10

Stand-alone system optimization results are shown in Table 6. PV module numbers in Marmara and Black Sea coastal cities (Gelibolu, Kırklareli, and Sinop) are higher than inner Anatolian cities (Konya, Karaman). The net present cost and the levelized cost of energy are obtained at least in Karaman, 35,942 $ and 1.263 $/kWh, respectively.

The network cost element of prices also increased, due to both rising maintenance and grid expansion costs, as well as other costs sometimes incorporated into network costs and tariffs. The cost of energy is high for stand-alone systems under today's conditions. The support provided by the state based on solar energy for electricity generation is 13.3 cents per 1 kWh.

In this study, the effects on the optimum system design and the energy production costs of CSF were investigated. Grid-connected system optimization results for CSF 10% are shown in Table 7. The levelized costs of energy vary between 0.283 and 0.361 $/kWh for PVS in the case of CSF 10%. Program didn't simulate according to peak load in the case of CSF 10%. In this result, the system doesn't include expensive equipment. CSF can be selected between 5% and 10% for optimum system. With a decrease of 10% in the CSF, there exist a decrease between 35% and 41% in the total net present costs and a decrease between 29% and 36% in the levelized costs.

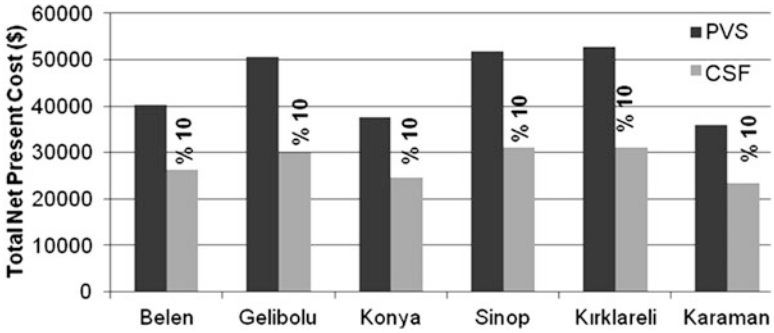

Fig. 3 Total net present cost values for PVS2500 according to CSF

Table 8 Simulation results of grid-connected PVS

	PVS2500		
City	NPC [$]	COE [$/kWh]	REF
Belen	19,953	0.313	0.81
Gelibolu	26,678	0.350	0.84
Konya	18,661	0.285	0.82
Sinop	27,611	0.355	0.84
Kırklareli	28,441	0.361	0.85
Karaman	18,965	0.283	0.83

Total net present cost values are shown in Fig. 3. With a decrease of 10% in the CSF, more decreases in the total net present costs and in the levelized costs existed in Gelibolu, Sinop, and Kırklareli than other cities examined. Thus, the system costs are said to have approached each other in all the regions.

The effect of feed-in tariff on the system and levelized costs of energy is investigated for grid-connected PVS. Simulation results of grid-connected PVS are shown in Table 8. The levelized costs of energy vary between 0.283 and 0.361 $/kWh for PVS in the case of feed-in tariff. According to the obtained results, it is determined that the grid-connected systems are more cost effective than stand-alone systems.

4 Conclusions

In this study, stand-alone and grid-connected PV systems are investigated for six cities in coastal and inner regions of Turkey. According to the results, while the levelized costs of energy vary between 0.283 and 0.361 $/kWh for the case of feed-in tariff, they vary between 0.897 and 1.192 $/kWh for the stand-alone systems. The least levelized cost of energy values is observed in Karaman for all situations. The

utilization rate of renewable energy also varies between 83% and 85% in the case of feed-in tariff. The grid-connected systems are found to be the most suitable solutions for present conditions.

Nowadays, despite the PV systems being expensive, their prices are decreasing with advancing technology. While a PV module price was $ 3.38 per watt in January 2011, it decreased to $ 2.42 per watt in January 2012 (World Energy Resources 2013). Furthermore, these systems are expected to be widely used in the near future due to their characteristics of being maintenance-free, environmentally friendly, noiseless operation, and long life.

References

Celik, A.N.: Present status of photovoltaic energy in Turkey and life cycle techno-economic analysis of a grid-connected photovoltaic-house. Renew. Sust. Energ. Rev. **10**(4), 370–387 (2006)

Bucciarelli, L.L.: Estimating loss-of-power probabilities of stand-alone photovoltaic solar energy systems. Solar Energy. **32**, 205–209 (1984)

Clark, D.R., Klein, S.A., Beckman, W.A.: A method for estimating the performance of photovoltaic system. Solar Energy. **33**, 551–555 (1984)

Klein, S.A., Beckman, W.A.: Loss of load probabilities for stand-alone photovoltaic systems. Solar Energy. **39**, 499–512 (1987)

National Renewable Energy Laboratory (NREL).: http://www.nrel.gov (2012)

Sekuçoğlu, S.A.: Design and economic analysis of PV, Wind and PV-Wind Hybrid systems. MS Thesis, Karadeniz Technical University (2012)

Siegel, M.D., Klein, S.A., Beckman, W.A.: A simplified method for estimating the monthly-average performance of photovoltaic systems. Solar Energy. **26**, 413–418 (1981)

Turkish Energy Market: An Investor's Guide: Energy Market Regulatory Authority (EMRA) (2012)

World Energy Resources: Survey, World Energy Council, ISBN: 978 0 946121 29 8 (2013)

Contribution to the Control Power of a Wind System with a Storage System

Ihssen Hamzaoui, Farid Bouchafaa, and Abdel Aziz Talha

1 Introduction

The development and use of renewable energy have experienced strong growth in recent years (Fernandez et al. 2008). Wind turbines that have their operation based on a double-fed induction generator are widely recognized in the industry as one of the most promising wind turbine configurations (Zhi and Xu 2007). Indeed, this action allows the functioning of a variable-speed wind turbine, which enables production of the maximum possible power with a wide range of variation in wind speed. Furthermore, static converters used to control the machine can be designed to pass only a fraction of the total power (which represents the power of sliding) (Yong et al. 2011). The penetration rate of wind power is limited to less than 30%.

To overcome this drawback, distributed generation must contribute to system services such as that of frequency adjustment, voltage, reactive power, the ability to self-start, and islanding operation. Due to the highly fluctuating and unpredictable nature of the wind, wind alone cannot be relied on in services systems (Robyns et al. 2006). It is necessary to add generation systems or energy storage allowing the possibility of having reserves. To ensure the generation/consumption balance, an inertial storage system has been considered. There are several reasons for this

I. Hamzaoui (✉)
University of Khemis Miliana, Faculty of Sciences and Technology, Ain Defla, Algeria
e-mail: hamzaoui_ihssen2000@yahoo.fr

F. Bouchafaa • A.A. Talha
Laboratory of Instrumentation, Faculty of Electronics and Computer, University of Sciences and Technology Houari Boumediene, BP 32 El- Alia, 16111 Bab-Ezzouar, Algeria
e-mail: fbouchafa@gmail.com; abtalha@gmail.com

© Springer International Publishing AG, part of Springer Nature 2018

F. Aloui, I. Dincer (eds.), *Exergy for A Better Environment and Improved Sustainability 2*, Green Energy and Technology,
https://doi.org/10.1007/978-3-319-62575-1_76

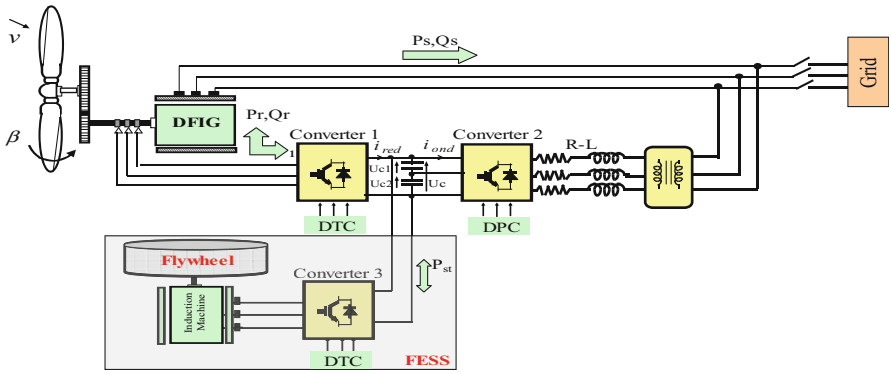

Fig. 1 The system under study

choice, for example: good momentum, good performance, and long lasting, similar to wind (Cimuca et al. 2006).

However, the ongoing development in the field of power electronics allows us the possibility of developing different systems to improve power quality and reduce harmonics generated by the power electronics converters.

Today, in addition to their main function, existing regulations impose an additional condition of good 'quality' power. Several techniques have been employed in the control of these converters (Belfedal et al. 2008; Casadei et al. 2002). In this paper, we present two different command techniques, DTC (direct torque control) and DPC (direct power control), that are applied to the system for converting wind energy with storage. Figure 1 shows the configuration of the generation system retained. The wind turbine is coupled directly to the double-fed induction generator (DFIG) with the inverter connected to the rotor controlled by DTC. The Flywheel Energy Storage System (FESS) is linked with the wind generator via a DC bus controlled by the DTC. The network side converter has three levels that feed and provide constant DC bus voltage, and is controlled by the DPC. The conversion system is connected to the grid.

2 Wind Tubine Model

The aerodynamic torque produced by the wind turbine is given as:

$$T_{\text{aer}} = \frac{P_{\text{aero}}}{\Omega_{\text{t}}} = \frac{1}{2\Omega_{\text{t}}} C_{\text{p}}(\lambda, \beta).\rho\pi R_{\text{t}}^2 v^3 \tag{1}$$

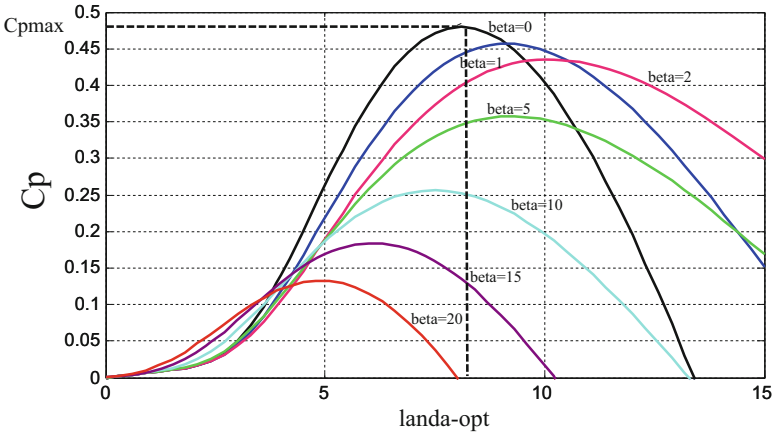

Fig. 2 Representation of C_p as a function of λ for different values of β

Where ρ is the air density, v is the wind speed, R_t is the turbine radius, and Ω_t is the angular velocity of the wind turbine. The power coefficient C_p is a function of the speed ratio λ and the pitch angle of the blades β (Fig. 2). Here, it is given by the expression:

$$C_p(\lambda,\beta) = 0.5176\left(\frac{116}{\lambda_i} - 0.4 - 5\right).\exp\left(\frac{21}{\lambda_i}\right) + 0.0068\lambda \tag{2}$$

with: $\frac{1}{\lambda_i} = \frac{1}{\lambda+0.08.\beta} - \frac{0.035}{\beta^3+1}$.

The speed ratio λ is expressed by the following relationship:

$$\lambda = \frac{\Omega_t R_t}{v} \tag{3}$$

To maximize the power converted, the turbine speed must be adjusted in relation to the wind speed. This is obtained if the relative velocity λ is equal to its optimal value ($\lambda_{opt} = 8.1$, $C_{pmax} = 0.48$, $\beta = 0°$), as shown in Fig. 2.

The purpose of this control is the ongoing search for the Maximum Power Point Tracking (MPPT). To achieve this, the value of the electromagnetic torque reference is set at the maximum value given (Hamzaoui et al. 2011):

$$T_{em-ref} = \frac{1}{2}\frac{\rho\pi {R_t}^5 C_{pmax}}{\lambda_{opt}^3 G^3}\Omega_{mec}^2 \tag{4}$$

3 Direct Torque Control of the Double-fed Induction Generator (DFIG)

A three-phase inverter at two levels of voltage has six switching cells giving eight possible switching states. Among these eight vectors that can be applied to the bounds of the DFIG, the vector $\boldsymbol{\nu 0}$ and $\boldsymbol{\nu 7}$ drive at zero voltage, others give, in the reference α–β, the six directions that the voltage vector can take (Hamzaoui et al. 2013). The direct torque control (DTC) aims to direct torque control of the DFIG, by applying different voltages to vectors of the inverter.

The controlled variables are the rotor flux and the electromagnetic torque, which are controlled by regulator hysteresis. This is to maintain both the instantaneous magnitudes within a band around the desired value. The output of these regulators determines the optimal voltage vector of the inverter to be applied to each switching time (Casadei et al. 2002).

The structure of the direct control of torque is illustrated in Fig. 3.

In the $\alpha\beta$ reference, the rotor flux components of the DFIG are determined as follows (Cárdenas et al. 2013):

$$\begin{cases} \Phi_{r\alpha,\beta} = \int_0^t \left(v_{r\alpha,\beta} - R_r i_{r\alpha,\beta}\right) \mathrm{d}t \\ \Phi_r = \sqrt{\Phi_{r\alpha}^2 + \Phi_{r\beta}^2} \\ \theta_r = \mathrm{arctg}\left(\dfrac{\Phi_{r\beta}}{\Phi_{r\alpha}}\right) \end{cases} \tag{5}$$

The electromagnetic torque is estimated as:

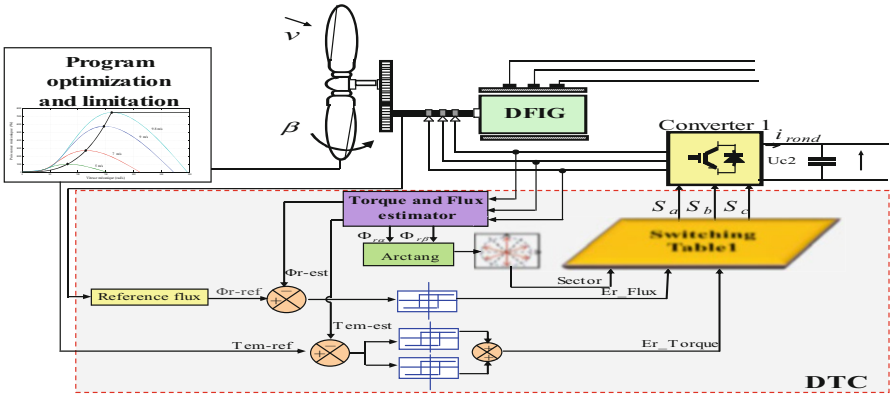

Fig. 3 Structure of the direct torque control applied to a double-fed induction generator (DFIG)

Table 1 Table switching

		1	2	3	4	5	6	Comparator
$C_{\text{Flu}} = 1$	$C_{\text{T}} = 1$	V_2	V_3	V_4	V_5	V_6	V_1	2 level
	$C_{\text{T}} = 1$	V_0	V_7	V_0	V_7	V_0	V_7	
	$C_{\text{T}} = 1$	V_6	V_1	V_2	V_3	V_4	V_5	3 level
$C_{\text{Flu}} = 1$	$C_{\text{T}} = 1$	V_3	V_4	V_5	V_6	V_1	V_2	2 level
	$C_{\text{T}} = 1$	V_0	V_7	V_0	V_7	V_0	V_7	
	$C_{\text{T}} = 1$	V_5	V_6	V_1	V_2	V_3	V_4	3 level

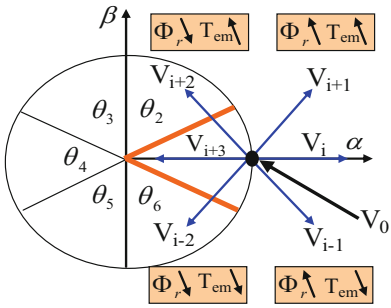

Fig. 4 Selection voltage vector

$$T_{\text{em-DFIG}} = p\left(\Phi_{r\alpha} i_{r\beta} - \Phi_{r\beta} i_{r\alpha}\right) \tag{6}$$

The reference torque is obtained from the wind MPPT technique (see Eq. (5)). The reference flow is obtained by blocking defluxing (Idjdarene et al. 2011).

$$\Phi_{\text{ref}} = \begin{cases} \Phi_n \text{ if } & |\Omega| \leq |\Omega_n| \\ \Phi_n \dfrac{\Omega_n}{|\Omega|} & \text{if } |\Omega| > |\Omega_n| \end{cases} \tag{7}$$

A decision table (Table 1) allows determination of the switching states in the function of the output of each hysteresis controller and the number of the sector θ_i in which the rotor flux vector is found.

Figure 4 shows an example of a rotor flux vector that is located in sector $\boldsymbol{\theta_1}$.

4 Flywheel Energy Storage System (FESS)

With the aim of involving a variable wind speed services system, energy storage of the inertial type is considered with a flywheel mechanically coupled to an asynchronous machine and driven by a power converter, as shown in Fig. 1. E_{v} energy stored in the flywheel J_{v} is shown by the expression:

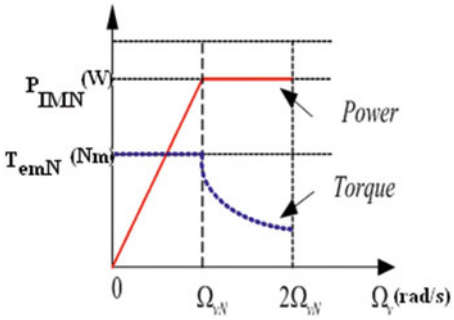

Fig. 5 Allure power and torque versus speed

$$E_{\mathrm{v}} = \frac{1}{2} J_{\mathrm{v}} \Omega_{\mathrm{v}}{}^{2} \tag{8}$$

To calculate the inertia of the wheel, it is based on a power supply for a time Δt: we want the storage to provide the inertial rated P_{IMn} during a time Δt when energy is needed $E_{\mathrm{v}} = P_{\mathrm{IMn}}$. Δt is given by: $\Delta E_{\mathrm{v}} = 1/2 J_{\mathrm{v}} \cdot \Delta \Omega_{\mathrm{v}}{}^{2}$ and $\Delta \Omega_{\mathrm{v}}^{2} = \Delta \Omega_{\mathrm{vMAX}}^{2} - \Delta \Omega_{\mathrm{vMIN}}^{2}$, so we get:

$$J_{\mathrm{v}} = \frac{2 P_{\mathrm{IMn}} \Delta t}{\left(\Omega_{\mathrm{vMAX}}^{2} - \Omega_{\mathrm{vMIN}}^{2} \right)} \tag{9}$$

Two areas of operation for the electrical machine are shown in Fig. 5 (Kairous et al. 2010).

For $0 \leq \Omega_{\mathrm{v}} \leq \Omega_{\mathrm{vN}}$, the nominal torque of the machine is available, but the maximum power is variable, depending on the speed ($P_{\mathrm{IM}} = k\, \Omega_{\mathrm{v}}$), and smaller than the nominal power. This area does not have much interest for FESS.

For $\Omega_{\mathrm{v}} > \Omega_{\mathrm{vN}}$ the power is at a maximum and corresponds to the nominal power of the machine; the electromagnetic torque is inversely proportional to the speed of rotation ($T_{\mathrm{em}} = k/\Omega_{\mathrm{v}}$). This is the area of operation used in FESS because here the power of the machine is available for any speed.

The induction machine with inertial storage will be used in the speed range below $\Omega_{\mathrm{vN}} \leq \Omega_{\mathrm{v}} \leq 2\Omega_{\mathrm{vN}}$, thus allowing operation at a rated power constant.

From a reference power, $P_{\mathrm{v\text{-}ref}}$, one can deduce the torque electromagnetic reference of the machine, $T_{\mathrm{em\text{-}ref}}$, causing the flywheel to measure the speed by the number of rotations, $\Omega_{\mathrm{v\text{-}mes}}$.

$$T_{\mathrm{em-ref}} = \frac{P_{\mathrm{v-ref}}}{\Omega_{\mathrm{v-mes}}} \tag{10}$$

The electromagnetic torque reference is limited to nominal torque for the speed range including between 0 and the nominal speed; beyond the rated speed, the

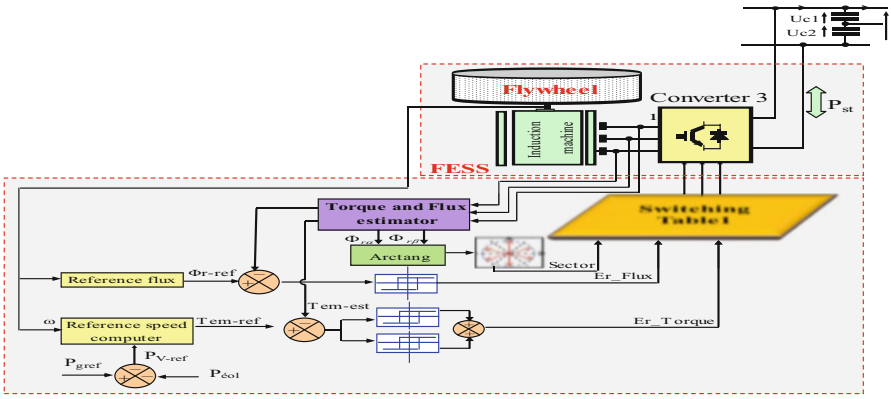

Fig. 6 Block diagram of direct torque control of inertial storage

torque will decrease in order to keep the product $T_{\text{em-ref}} \cdot \Omega_{\text{v}}$ constant. The torque reduction is carried out by defluxing of the machine beyond the synchronous speed; see Eq. (7).

4.1 Direct Torque Control of the FESS

This functions on the same principle of DTC applied to the rotor of the DFIG. The estimated torque values Tem and stator flux Φ_{s} are compared, respectively, at their reference values $T_{\text{em-ref}}$ and $\Phi_{\text{s-ref}}$, using two non-linear elements of a kind of hysteresis in order to ascertain information of the trends in the flux and torque. A decision table (Table 1) allows determination of the switching states in the function of the output of each hysteresis controller and the number of sector θ_i wherein the stator flux vector is found (Idjdarene et al. 2011).

Figure 6 shows the general diagram of the DTC applied to a FESS. Figures 7 and 8 llustrate the operation of the inertial storage system with direct torque control. The value of the inertia coefficient was calculated for a speed range of between 157 and 314 rad/s, and a rated power of 1.5 kW during a time corresponding to 2.5 s.

The initial velocity of the steering wheel is fixed at 157 rad/s. When the storage reference power, $P_{\text{v-ref}}$, is set at 1.5 kW, the speed increases to 157–314 rad/s, and the system stores energy. When the power is fixed to −1.5 kW, the speed decreases to 314–157 rad/s, and the system provides energy.

The main function of the FESS is to smooth the power output of the wind generator, which can cause several problems in the network. To reduce to a

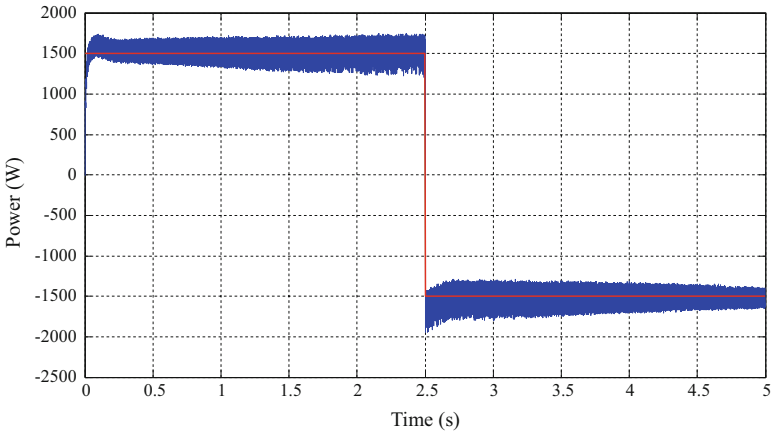

Fig. 7 The power delivered or absorbed by the IM

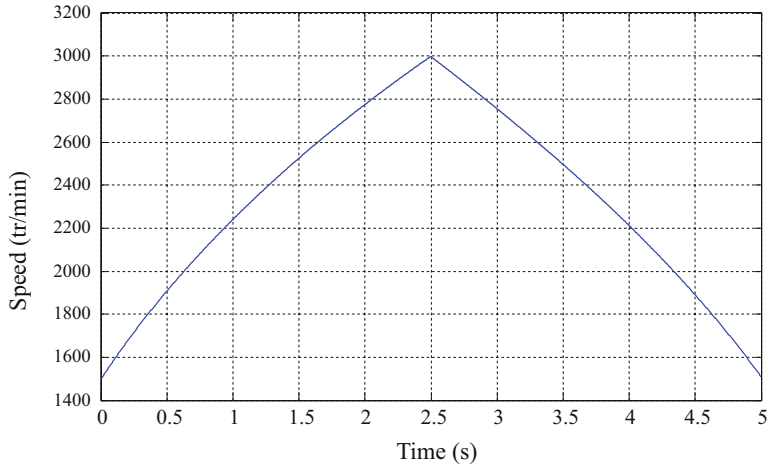

Fig. 8 Speed of the flywheel

minimum the fluctuations of this power, the FESS must ensure compensation for variations in wind power.

The reference power of the FESS is determined by the difference between the power generated by the wind generator, P_{wind} **,** and the power it takes to deliver to a network or on isolated loads, P_{regl}, according to the principle illustrated in Fig. 9.

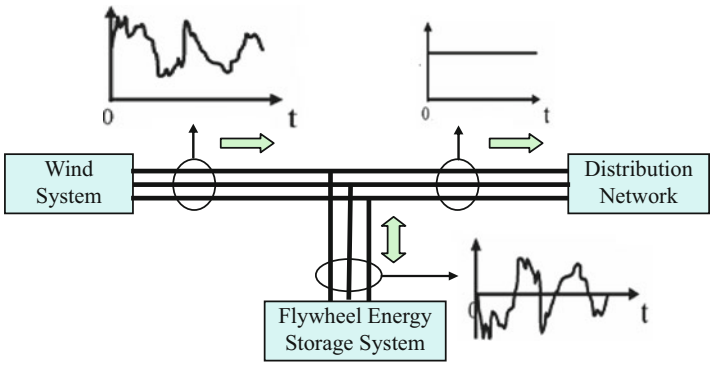

Fig. 9 Smoothing power using the Flywheel Energy Storage System (FESS)

Fig. 10 Space vector diagram of a three-level inverter

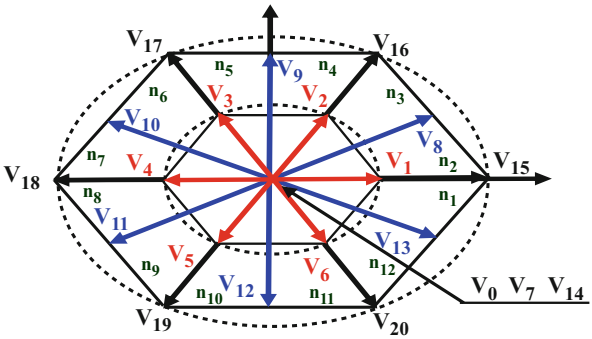

4.2 *Direct Control of Power for the Grid Side Converter*

The three-level NPC converter to which a connected source of wind energy is associated with the flywheel energy storage system can be represented by 27 possible states of switching, 18 active vectors, and three inactive vectors (see Fig. 10). These vectors are expressed by the following equation (Chen et al. 2008; Kulikowskli and Sikorski, 2010):

$$V_{\mathrm{m}} = \frac{1}{3}\begin{cases} \mathrm{Uc}.e^{j(m-1)\frac{\pi}{3}}, \text{for} \quad m = \{1, 2, \ldots 6\} \\ \sqrt{3}.\mathrm{Uc}.e^{j(m-8)\frac{\pi}{3}}, \text{for} \quad m = \{8, 9, \ldots 13\} \\ 2.\mathrm{Uc}.e^{j(m-15)}, \text{for} \quad m = \{15, 16, \ldots 20\} \end{cases} \tag{11}$$

Where: Uc is DC link voltage, $m \in 0,1,2..$,"0" is azero vector, and *m is the* vector number.

The DPC consists of a selective control vector, using a switching table. This is based on the digital error, S_{p}, S_{q} of the instantaneous active and reactive power, as well as on the estimated angular position of the voltage determined by:

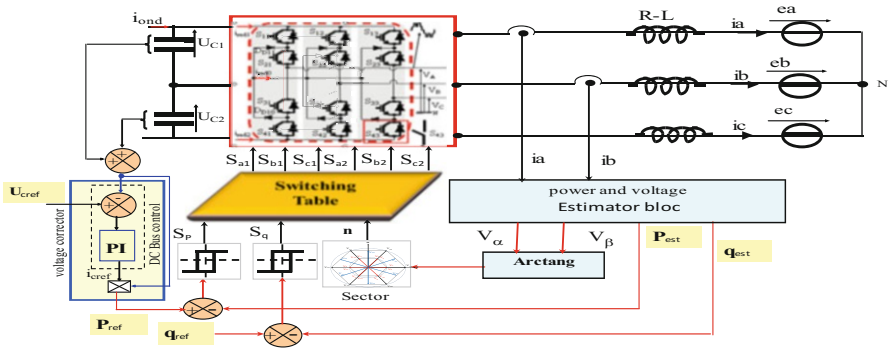

Fig. 11 Diagram of extended direct power control system

$$\theta = \text{Arctg}\left(\frac{v_\alpha}{v_\beta}\right) \tag{12}$$

With $V_{\alpha\text{-}\beta}$ being the grid voltage in the stationary (α, β) coordinate.

The stationary coordinates (α, β) are divided into 12 sectors expressed as (Bouafia et al. 2009):

$$(n-2)\frac{\pi}{6} < \sec t_n < (n-1)\frac{\pi}{6} n \in \{1, .., 12\} \tag{13}$$

The active power reference is given by the regulation of the DC bus, and the reactive power reference depends on the reactive power desired by the grid. The reactive power reference is set to zero to control the unity power factor (Hamzaoui et al. 2011).

Figure 11 shows the overall configuration of the direct power control of three-level converter.

Direct power control (DPC) is developed by analogy with the direct torque control (DTC) of electrical machines, instead of the torque and flux, the instantaneous active and reactive power are control variables. This ensures the PWM rectifier has a sinusoidal current absorption with a decoupled control of active and reactive power.

$$\begin{aligned} \hat{P} = L\left(\frac{di_a}{dt}i_a \frac{di_b}{dt}i_b \frac{di_c}{dt}i_c\right) + \\ V_{dc1}(S_{a1}i_a + S_{b1}i_b + S_{c1}i_c) + \\ \vdots \quad V_{dc2}(S_{a2}i_a + S_{b2}i_b + S_{c2}i_c) \end{aligned} \tag{14}$$

$$\hat{q} = \frac{1}{\sqrt{3}}\left[3L\left(\frac{di_a}{dt}i_c - \frac{di_c}{dt}i_a\right) - v_{dc1}\left(S_{a1}(i_b - i_c) + S_{b1}(i_c - i_a)\right.\right.$$
$$\left.\left. + S_{c1}(i_a - i_b)\right) - v_{dc2}\left(S_{a2}(i_b - i_c) + S_{b2}(i_c - i_a) + S_{c2}(i_a - i_b)\right)\right] \quad (15)$$

With: e_a, e_b, e_c three-phase power-source voltages; V_A, V_B, and V_C are terminal voltages of the PWM rectifier; i_a, i_b, and i_c are the line currents of three-phase grid. L and R represent inductance and resistance of interconnecting reactors, respectively. S_{a1}, S_{b1}, S_{c1}, S_{a2}, S_{b2}, and S_{c2} are switching states of the converter.

The value of capacitors connected in series in the DC side is C, the voltages of which are U_{c1} and U_{c2}.

The active and reactive powers are estimated using the switching state of the converter, the three-phase line currents, the DC bus voltage, and the inductance of the reactors. This can be derived as:

Errors between the commands and the estimated feedback power are input to the hysteresis comparators and digitized to the signals S_p and S_q, where:

$$\begin{cases} S_p = 1 \quad \text{if} \quad P_{ref} - P_{est} > h_p \\ S_p = 0 \quad \text{if} \quad -h_p < P_{ref} - P_{est} < h_p \\ S_p = -1 \quad \text{if} \quad P_{ref} - P_{est} < -h_p \end{cases}$$
$$\begin{cases} S_q = 1 \quad \text{if} \quad q_{ref} - q_{est} > h_q \\ S_q = 0 \quad \text{if} \quad -h_q < q_{ref} - q_{est} < h_q \\ S_q = -1 \quad \text{if} \quad q_{ref} - q_{est} < -h_q \end{cases} \quad (16)$$

Once the logic outputs of the hysteresis comparators are established, and following the sector number of the estimated voltage vector, the vector of voltages to be applied to the input of the rectifier is selected from the switching table, as shown in Table 2.

The synthesis of the switching table (Table 2) based on the signs is derived from active and reactive power in each sector, given by the Eq. (17), and presented in Figs. 12 and 13.

Table 2 Table switching

Sect$_n$		1	2	3	4	5	6	7	8	9	10	11	12
1	1	V_8	V_{15}	V_9	V_{16}	V_{10}	V_{17}	V_{11}	V_{18}	V_{12}	V_{19}	V_{13}	V_{20}
	0	V_{15}	V_9	V_{16}	V_{10}	V_{11}	V_{17}	V_{12}	V_{18}	V_{13}	V_{19}	V_8	V_{20}
	−1	V_5	V_5	V_6	V_6	V_1	V_1	V_2	V_2	V_3	V_3	V_4	V_4
0	1	V_3	V_3	V_4	V_4	V_5	V_5	V_6	V_6	V_1	V_1	V_2	V_2
	0	V_{25}	V_{26}	V_{26}	V_{21}	V_{21}	V_{22}	V_{22}	V_{23}	V_{23}	V_{24}	V_{24}	V_{25}
	−1	V_{23}	V_{24}	V_{24}	V_{25}	V_{25}	V_{26}	V_{26}	V_{21}	V_{21}	V_{22}	V_{22}	V_{23}

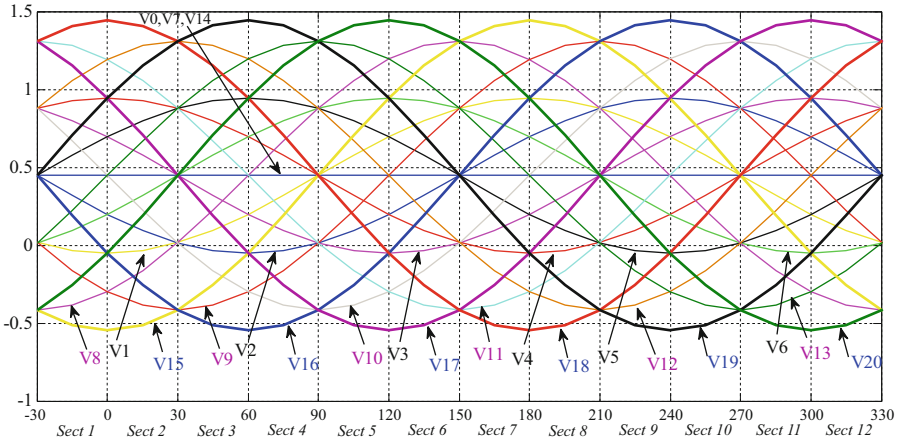

Fig. 12 Change in active power

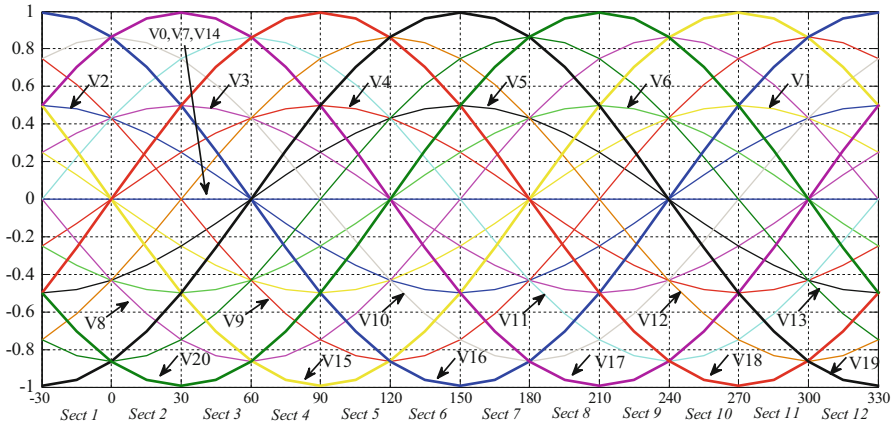

Fig. 13 Change in reactive power

$$\overline{\Delta P}_i = \frac{\Delta P_i}{\frac{1}{L}E.\sqrt{\frac{2}{3}}U_C} = \frac{E}{\sqrt{\frac{2}{3}}U_C} - \left(\cos(\theta).\bar{v}_{\alpha i} + \sin(\theta).\bar{v}_{\beta i}\right) \qquad \overline{\Delta q_i} = \frac{\Delta q_i}{\frac{1}{L}E.\sqrt{\frac{2}{3}}U_C}$$

$$= \left(\cos(\theta).\bar{v}_{\beta i} - \sin(\theta).\bar{v}_{\alpha i}\right) \tag{17}$$

$$\text{with } \bar{v}_{\alpha i} = \frac{v_{\alpha i}}{\sqrt{\frac{2}{3}U_C} \cdot \bar{v}_{\beta i} = \frac{v_{\beta i}}{\sqrt{\frac{2}{3}U_C}}}$$

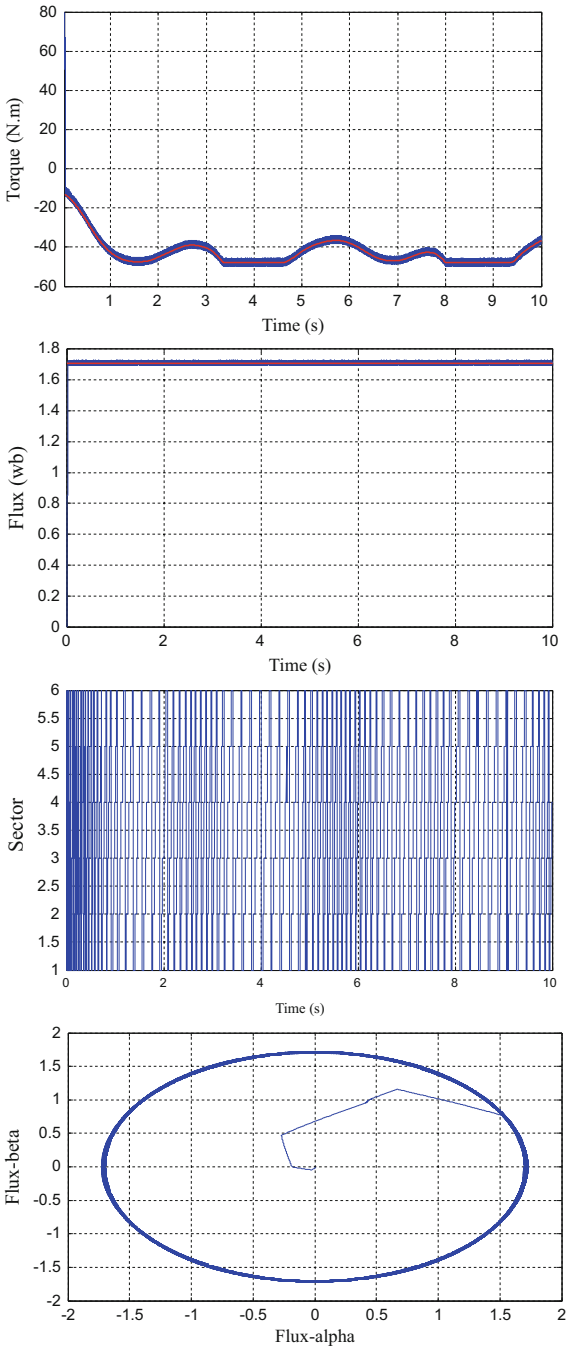

Fig. 14 Torque and rotor flux of the double-fed induction generator (DFIG)

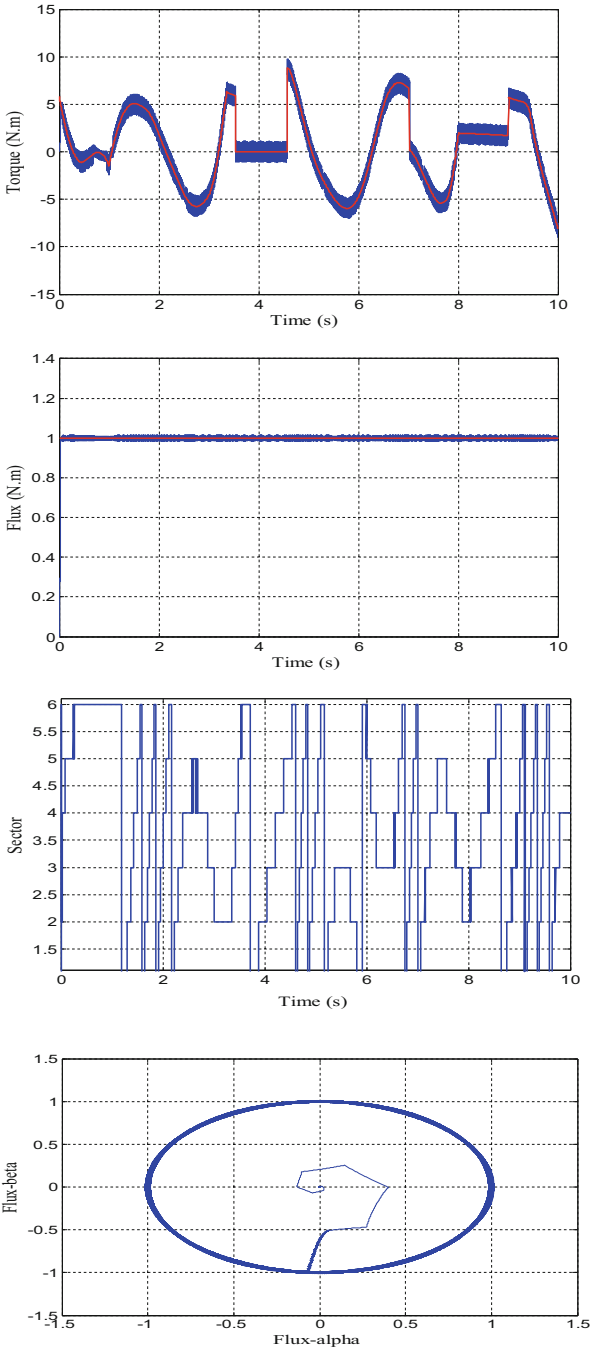

Fig. 15 Torque and stotor flux of the induction machine (IM)

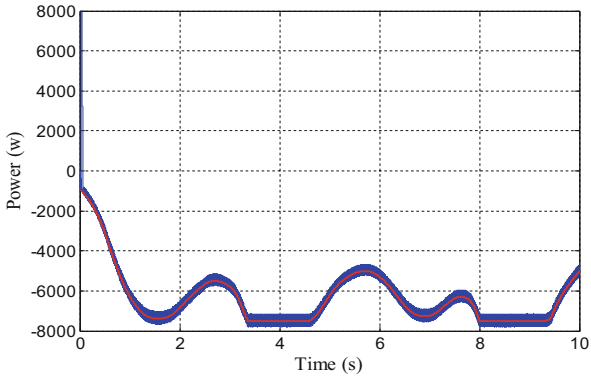

Fig. 16 Power delivered by the wind

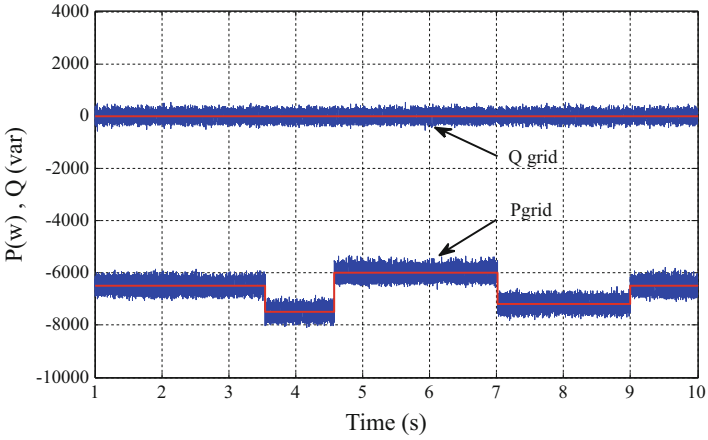

Fig. 17 Power delivered to the network

We have shown the simulation results with the two control techniques, DTC (direct torque control) and DPC (direct power control), applied to the system for converting wind energy with storage, as presented in Fig. 1. FESS with an IM of 1.5 kW is associated with a wind generator of 7.5 kW.

A good dynamic torque has an estimated value that is acceptable for the setpoint value, for DFIG and IM (Figs. 14a and 15a). The module rotor flux of DFIG, and the module of the stator flux IM are shown in Figs. 14b and 15b, following their reference values determined by a defluxing block. The evolution of these flows (α,β), present a circular trajectory with an amplitude fixed at its nominal value (Figs. 14d and 15d). The power delivered by wind as present in Figs. 16. and 17 shows the active and reactive power passed to the network, and their references.

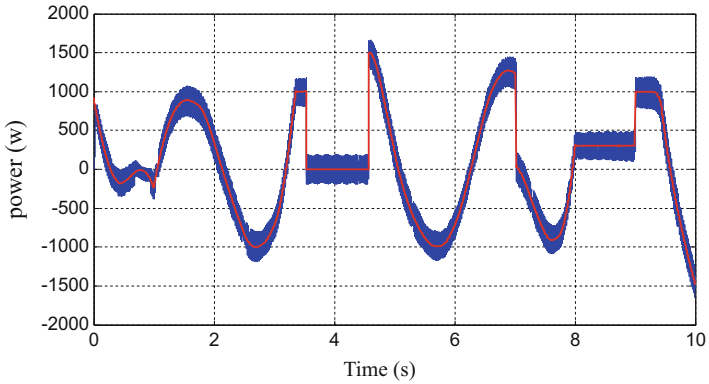

Fig. 18 Electric power of the Flywheel Energy Storage System (FESS)

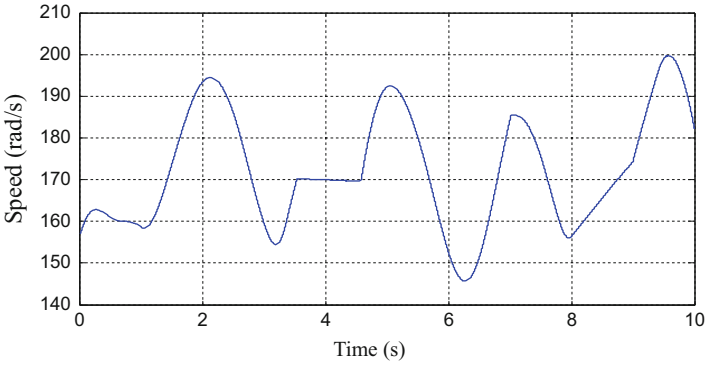

Fig. 19 Speed of the flywheel

Figure 18 shows the power storage unit. This power can be positive or negative depending on wind conditions that allow either charging or discharging, and is limited to1.5 kW. When the reference power is positive, FESS stores electric energy as the speed of the flywheel increases. FESS captures the electrical energy, and when the reference power becomes negative the flywheel speed decreases (Fig. 19). The setting of the DC bus is ensured by the three-level converter side grid, which is kept constant (Fig. 20), and the trajectory of the end of the voltage vector (estimated) is circular (Fig. 21).

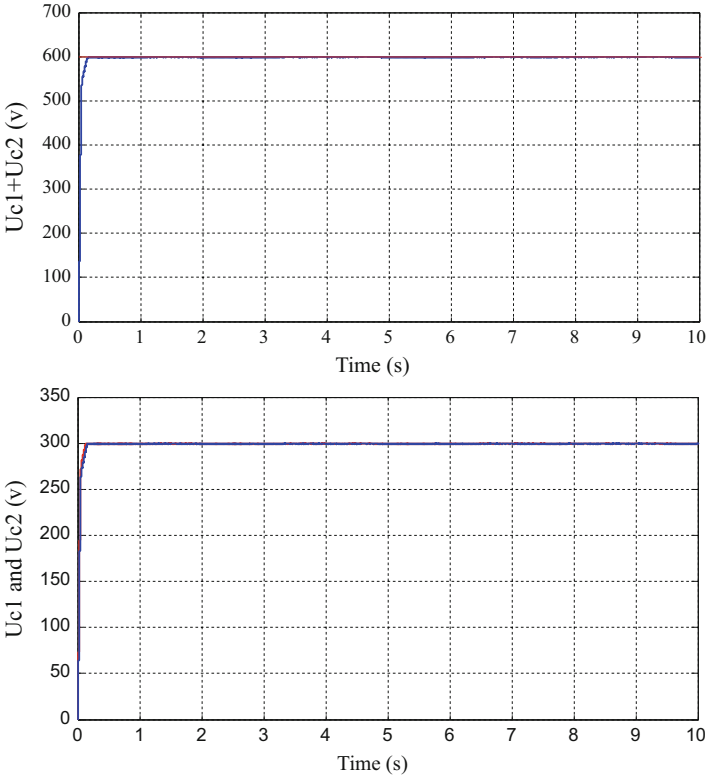

Fig. 20 DC bus voltage

5 Conclusion

This article presents two control techniques: DTC (direct torque control) and DPC (direct power control), which are dedicated to a wind turbine with a variable speed based in DFIG with storage, in order to achieve better performance. Mathematical models of the studied system are presented. DTC applied in DFIG control and IM used in FESS present a torque control of high performance and dynamics of high importance while keeping good accuracy in control. This precision is based on the right choice of the voltage vector, which plays a primordial role in the regulation of the flux vector, and therefore torque. The IM used in FESS very frequently changes its operating mode (motor or generator).The FESS is controlled by a reference power calculated according to the generated power and the power we want to send to the network. The NPC three-level converter control by the DPC is only used to

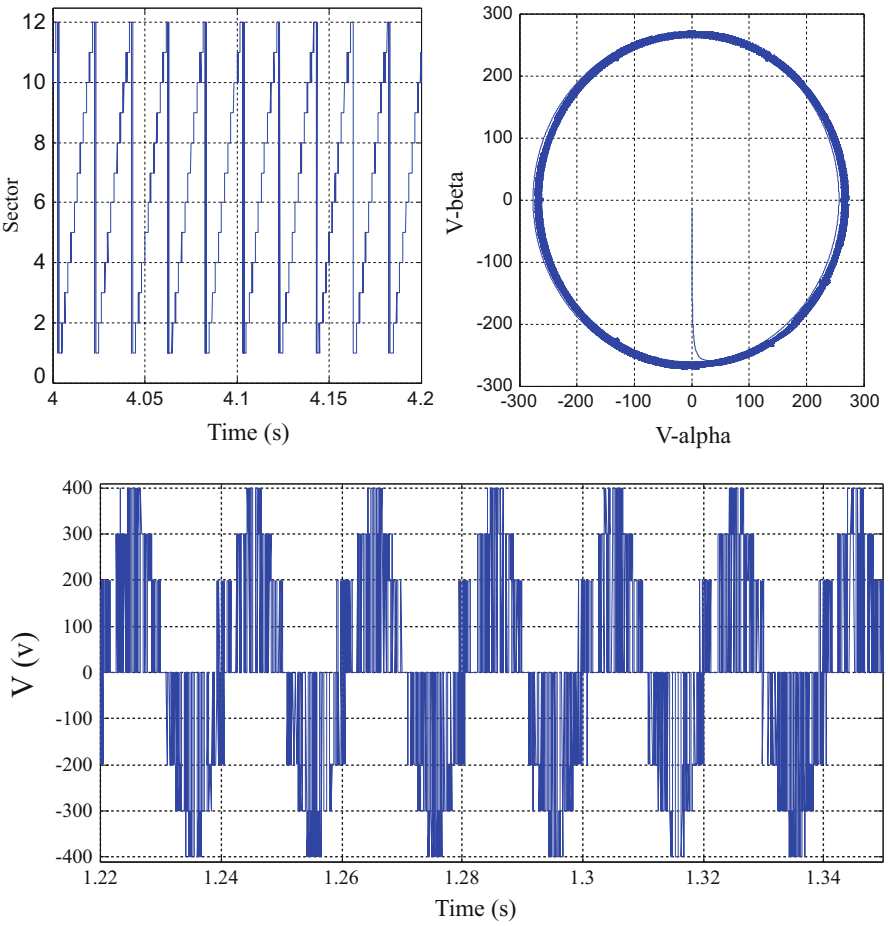

Fig. 21 Output voltage and sector

implant control strategies, allowing the wind generator + FESS to provide system services (control the mains voltage, control the frequency, and control the reactive power). The effectiveness of these techniques is verified by simulation with Matlab/Simulink.

References

Belfedal, C., Moreau, S., Champenois, G., Allaoui, T., Denai, M.: Comparison of PI and direct power control with SVM of doubly fed induction generator. J. Electron. Electr. Eng. **8**(2), 633–641 (2008)

Bouafia, A., Krim, F., Gaubert, J.P.: Design and implementation of high performance direct power control of three-phase PWM rectifier, via fuzzy and PI controller for utput voltage regulation. Energ. Conv. Manag. **50**, 6–13 (2009)

Cárdenas, R., Peña, R., Alepuz, S., Asher, G.: Overview of control systems for the operation of DFIGs in wind energy applications. IEEE Trans. Indust. Electron. **60**(7), 2776–2798 (2013)

Casadei, D., Profumo, F., Serra, G., Tani, A.: FOC and DTC:two viable schemes for induction motors torque control. IEEE Trans. Power Electron. **17**(5), 779–787 (2002)

Chen, W., Zou, Y., Xu, L.: Direct power control for Neutral -point-clamped three-level PWM rectifier. IEEE international conference on industrial technology (IEEE ICIT 2008), Chengdu, China, DOI: 10.1109/ICIT.2008.4608487 (2008)

Cimuca, G.O., Saudemont, C., Robyns, B.: Control and performance evaluation of a flywheel energy-storage system associated to a variable-speed wind generator. IEEE Trans. Indust. Electron. **53**(4), 1074–1085 (2006)

Fernandez, L.M., Garcia, C.A., Jurado, F.: Comparative study on the performance of control systems for doubly fed induction generator (DFIG) wind turbines operating with power regulation. Energy. **33**(9), 1438–1452., Elsevier (2008)

Hamzaoui, I., Bouchafaa, F., Talha, A.: Improvement of the performances MPPT system of wind generation. In: Saudi International Electronics, Communications and Photonics Conference (CIECPC' 11), 23–26 Apr 2011

Hamzaoui, I., Bouchafaa, F., Talha, A.: Comparative study between direct torque control and field-oriented control for induction machine used in flywheel energy storage system. J. Elect. Eng. **13**(7), ISSN 1582–4594, (2013)

Idjdarene, K., Rekioua, D., Rekioua, T., Tounzi, A.: Wind energy conversion system associated to a flywheel energy storage system. Analog Integr. Circuits Signal Process. **69**(1), 67–73 (2011)

Kairous, D., Wamkeue, R., Belmadani, B.: Sliding mode control of DFIG based variable speed WECS with flywheel energy storage. In: International Conference on Electrical Machines – ICEM . IEEE, Rome (2010)

Kulikowskli, K., Sikorski, A.: Comparison of new DPC methods for two- and three-level AC/DC converters. IEEE (2010)

Robyns, B., Davigny, A., Saudemont, C., Ansel, A., Courtecuisse, V.: Impact de l'éolien sur le réseau de transport et la qualité de l'énergie. J3eA-Vol.5 (2006)

Yong, L., Li, H., Yao, J., Zhuang, K.: Operation and control of a grid connected DFIG-based wind turbine with series grid-side converter during network unbalance. Elect. Power Syst. Res. **81**, 228–236 (2011)

Zhi, D., Xu, L.: Direct power control of DFIG with constant switching frequency and improved transient performance. IEEE Trans. Energ. Conv. **22**(1), 110–118 (2007)

Performance Evaluation of SWRO Desalination Plant at Skikda (Algeria)

F. Ammour, R. Chekroud, S. Houli, and A. Kettab

1 Introduction

During the last decades, water resources have been intensively used in Algeria, added to a period of intense drought occurring in the zone, leading to water scarcity (Metiche et al. 2010).

Seawater and brackish water desalination is a strategic option for Algeria which has implemented an ambitious program of desalination of seawater with a production capacity of 2260 million M3 (Metiche et al. 2010; Kehal 2001).

Due to recent developments in membrane technology, the trend in the desalination industry is to use reverse osmosis (RO) for desalting seawater.

One of these plants is investigated in this study. It is an SWRO desalination plant of Skikda, located in the east of Algeria, commissioned in 2009, with a capacity of 100,000 m^3/day.

The most serious problem in BWRO and SWRO plants' operation is the complexity to control membrane fouling and scaling mainly due to frequent variation of quantity/quality of raw water (Arras et al. 2009).

The objective of this paper is to study the performance of the plant and identify the different shortcomings. The plant performance was established from the operation and maintenance data as well as from visits made to the plant.

F. Ammour (✉) • R. Chekroud • S. Houli
Laboratoire de Mobilisation et Valorisation des Ressources en Eau (M.V.R.E.), Ecole Nationale Supérieure de l'Hydraulique (ENSH), Soumaâ, Algeria
e-mail: fasonidz@yahoo.fr

A. Kettab
Laboratoire des Sciences de l'eau, Ecole Nationale polytechnique d'Alger, El Harrach, Algeria

© Springer International Publishing AG, part of Springer Nature 2018

F. Aloui, I. Dincer (eds.), *Exergy for A Better Environment and Improved Sustainability 2*, Green Energy and Technology,
https://doi.org/10.1007/978-3-319-62575-1_77

Fig. 1 Location of Skikda SWRO plant

2 Plant Description

2.1 Study Site

Skikda SWRO plant is located in the Sonatrach company industrial complex in the east of Algeria (Fig. 1).

2.2 Seawater Intake

The choice of the point of collection was decided after various studies to obtain a good quality of water all year round.

An SWRO desalination plant studied includes an open seawater intake. The water captured at a distance of 1431 m is conveyed gravitationally by canal of 2 m of diameter and collected in a tank.

The intake inlet point is located at a depth of 9 m.

2.3 Raw Water Characteristics

Raw water analysis is presented in Table 1:

Table 1 Raw water composition

Physicochemical analysis	
Ca^{2+} (mg/l)	464.21
Mg^{2+} (mg/l)	1278.94
Na^{+} (mg/l)	12301.65
K^{+} (mg/l)	487.89
Al^{3+} (mg/l)	1
Sr^{2+} (mg/l)	5.12
SiO2 (mg/l)	25.42
Cl^{-} (mg/l)	21611.96
SO_4^{2-} (mg/l)	3087.03
HCO_3^{-} (mg/l)	133.45
F^{-} (mg/l)	1.37
CO_3^{2-} (mg/l)	0.39
Alkalinity (mg/l $CaCO_3$)	110.08
Turbidity (NTU)	1.3
T (°C)	27
PH	6.49
Conductivity (μS/cm)	54463.21
STD (mg/l)	39377.53

2.4 Operating Conditions

Operating conditions at Skikda SWRO desalination plant are shown in Table 2.

2.5 Pretreatment and Posttreatment

The pretreatment has a prevalent importance as well on physicochemical and microbiological qualities of permeate as on the longevity of the membrane.

On arrival at the station, the raw water must undergo disinfection. NaOCl is used at the concentration of 5 ppm. The residual chlorine is then removed by dosing of an average of 1.8 ppm of sodium bisulfite.

Sulfuric acid is dosed as carbonate antiscalant to destroy carbonate/bicarbonate in the feed at the concentration of 37.7 ppm.

Ferric chloride is employed in the coagulation step at the concentration of 6 ppm.

The seawater is filtered through 25 pressure sand filters (the first filtration) to remove suspended solids. Then it passes through 15 anthracite filters (second filtration).

Ten cartridge filters of 5 micron are installed just before the high pressure pumps to protect RO membranes from fouling. This pretreated seawater feed has an $SD1 < 3$.

The quality of the produced permeate does not meet all end-use requirements, hence the need for its additional treatments. The water stabilization and alkalinity

Table 2 Operating conditions

Design capacity (m^3/day)	100,000
Hours of operation per day (h)	24
Hours of operation per year (day)	355
Seawater intake capacity (m^3/h)	8.998
Seawater salinity (ppm)	39.381
Seawater temperature (°C)	24
Volume of rejected water (m^3/h)	4831.56
Recovery (%)	47
The quality of the permeate (ppm)	<400
Pressure OI (bars)	67.8

adjustment is done by the passage of permeate on a bed of dolomite, to increase the pH from 5.03 to 8.08.

Product chlorination is done as a final step to prevent growth of microorganism during water distribution or storage.

2.6 RO Units

Filtered water is aspired by high pressure pumps and is driven back with a pressure of 67.8 bars, before being sent toward the tubes of pressure for the separation of salt and water. Each module contains seven spiral wound polyamide membranes. The minimum salt rejection is 99.45%.

The brine is discharged into the sea, at a distance of 714 m, with insufficient dilution.

The technical characteristics of the high pressure system are shown in Table 3.

3 Plant Performance Evaluation and Improvements

Quality parameters of permeate are grouped in the following table. The product water from this plant is within Algerian potable water standards (Table 4).

As mentioned earlier, the Skikda plant is built with polyamide membranes and utilizes seven elements, per pressure vessel.

Membrane cleaning was carried out four times per year. Chemicals used in cleaning membrane are limited to three: citric acid, soda, and biocide.

Cleaning products must be neutralized before their discharge at sea.

Since Skikda plant commissioning, the membranes have been changed only once. Indeed, the chlorine and bisulfite dosing errors caused serious membrane damages during the first year of the Skikda plant operation. Membranes used in the Skikda plant are very sensitive to chlorine, which should be completely removed, to zero chlorine level, from the feed; otherwise the membranes will be damaged.

Table 3 Technical characteristics of high pressure system

Total pumped water flow	4.317 m^3/h
Number of pumps in operation	5
Minimum temperature of raw water	18 °C
maximum temperature of raw water	27 °C
Seawater density	1.0257
Seawater viscosity	0.9266
Pressure losses in pipings and valves	1.4
Pressure at the inlet of the membranes	66.1 bars
Pressure of aspiration of the pump	2.00 bars
Total pump output pressure	67.8 bars
Pump efficiency	84.5%
Number of membranes by module	7
Type of membrane	Arrollamiento en espirale
Material of membrane	Polyamide aromatique
Maximum specific feed	13.96 l/m^2/h

Table 4 Quality parameters of permeate

TDS (mg/L)	<400
Alcalinity (mg/l $CaCO_3$)	65
Hardness (mg/l $CaCO_3$)	50–65
pH	8–8.5
LSI	0–0.4

The Major problem at the Skikda plant is biological fouling of the cartridge filter and the desalination unit. One of these reasons is the reduction of the chlorine dosing due to the incident mentioned above.

The second possible reason for the biological fouling is that the chlorine residence time is insufficient to cause 100% kill of microorganisms, allowing for the passage of some live microorganisms to the cartridge filter and the desalination part of the plant (Ata et al. 1989; Fernandez-Torquemada 2005; Kamel and Chheibi 2001).

This problem can be solved by optimizing the chlorination-dechlorination stage or by replacing chlorine with copper sulphate (CuSO4).

Scaling phenomena, fouling, and chemical degradation affect the performance of the desalination System (Maurel 2001; Ammour 2014):

- Decrease in flow.
- Increase in salinity.
- Increase in pressure losses.
- Reduction of the lifetime of membranes.

The second major problem at the Skikda plant is in the treatment plant, which, in times of flooding, failed to produce the proper SDI, i.e., SD1<3. This deterioration of water quality is due to an increase in turbidity and to the haulage of suspended

Fig. 2 Corrosion in the cartridge filters

sediment and the colloidal matters by the Wadi Safsaf, whose mouth is located near the station. The SDI at the entrance of the membrane increases up to 5, which requires the complete stop of the station in winter.

This problem can be solved by increasing the dose of coagulant and injecting a flocculant.

Another problem encountered in the Skikda plant is material corrosion in pretreatment, especially in the cartridge filters and sand filters, as shown in Figs. 2 and 3.

This corrosion is due to the washing of sand and anthracite filters by the brine and the quality of the material chosen for the joints, fittings, and valves.

4 Conclusions

The pretreatment has a prevalent importance as well on physicochemical and microbiological qualities of permeate as on the longevity of the membrane and equipment. This needs a good operation and maintenance program.

In this paper the performance evaluation of SWRO desalination plant was carried out, and recommendations are suggested to resolve these problems. The plant performance was established from the operation and maintenance data as well as from visits made to the plant.

Fig. 3 Corrosion in sand filters

The SWRO plant supplies a good quality drinking water to Skikda town and Sonatrach company industrial complex. The product water is within Algerian potable water standards.

The first major problem at the Skikda plant is biological fouling of the cartridge filter and the desalination unit. This problem can be solved by optimizing the chlorination-dechlorination stage or by replacing chlorine with copper sulphate (CuSO4).

The second major problem is the deterioration of water quality and the SDI increase up to 5 at the entrance of the membrane, which requires the complete stoppage of the station in winter.

This problem can be solved by increasing the dose of coagulant and injecting a flocculant.

Another problem encountered at the Skikda plant is material corrosion in pretreatment, especially in the cartridge filters and sand filters. This corrosion is due to washing of sand and anthracite filters by the brine and the quality of the material chosen for the joints, fittings, and valves. Also, the plant performance is rated well without serious consequences on equipment and material over the 5 years of operation.

Acknowledgments This research was supported by this project and has been made possible through the cooperation of the National High School for Hydraulic (ENSH) and ADE-ALGERIA, which is gratefully acknowledged.

The authors wish to thank also the industrial complex of Sonatrach Company, for providing their laboratory facilities.

References

Ammour, F., Lounes, S., Houli, S., Kettab, A.: Environmental impact of desalination plant of Bou Smail (Algeria). 13th International Conference on Clean Energy, Istanbul – Turkey (2014)

Arras, W., Ghaffour, N., Hamou, A.: Performance evaluation of BWRO desalination plant-a case study. Desalination. **235**, 170–178 (2009)

Ata, H., Al jarah, S., Al -lohib, T.: Performance evaluation of SWCC and SWRO plants. Desalination. **74**, 37–50 (1989)

Fernandez-Torquemada, Y., Sanchez-Lizaso, J.L., Gonzalez-Correa, J.M.: Preliminary results of the monitoring of the brine discharge produced by the SWRO desalination plant of Alicante (SE Spain). Desalination. **182**, 395–402 (2005)

Kamel, F., Chheibi, H.: Performances de la Station de Dessalement de Gabes (22,500 mVj) apres cinq ans de fonctionnement. Desalination. **136**, 263–272 (2001)

Kehal, S.: Rétrospective et perspectives du dessalement en Algé¬rie. Desalination. **42**, 135–136 (2001)

Maurel, A.: Dessalement de l'eau de mer et des eaux saumâtres, éditions Technique & Documentation Lavoisier, France (2001)

Mitiche, R., Metaiche, M., Kettab, A., Ammour, F.: Desalination in Algeria: current situation and development programs. Desalin. Water Treat. **14**, 259–264 (2010)

Study of a PV-Electrolyzer-Fuel Cell Hybrid System

Amina Gueridi, Abdallah Khellaf, Djaffar Semmar, and Larbi Loukarfi

1 Introduction

The use of renewable energies, with hydrogen as a means of storage, offers autonomy of electric power production (Ipsakisa et al. 2008).

There are several types of hybrid electric systems of autonomous productions like the photovoltaic-fuel cells (PV-FC) (Ganguly et al. 2010), wind energy-fuel cells (W-FC) (Khan et al. 2005), or photovoltaic-wind energy-fuel cells (PV-W-FC) (Hatti et al. 2011).

In the PV-FC hybrid systems, the electrical energy produced by the photovoltaic generators is used directly to feed the load, whereas the excess energy is converted by electrolysis system to hydrogen. The produced hydrogen can be converted into electricity via fuel cells during the period when electrical energy produced from solar PV is not sufficient.

Several softwares are used to size and model the hybrid systems (Vechiu 2005). Among these softwares, we can name HOMER, SOMES, RAPSIM, SOLSIM, and INSEL. All these softwares are used to optimize the hybrid systems. However, the optimization method differs from one software to the other.

A. Gueridi (✉)
University of Blida, Faculty of Science, Department of Physics, Blida, Algeria
e-mail: amina.gueridi@yahoo.com

A. Khellaf
Center of Development of Renewable Energies, Algiers, Algiers, Algeria

D. Semmar
University of Blida, Faculty of Technologie, Department of Mechanics, Blida, Algeria

L. Loukarfi
University of Chlef, Faculty of Technologie, Department of Mechanics, Chlef, Algeria

© Springer International Publishing AG, part of Springer Nature 2018

F. Aloui, I. Dincer (eds.), *Exergy for A Better Environment and Improved Sustainability 2*, Green Energy and Technology,
https://doi.org/10.1007/978-3-319-62575-1_78

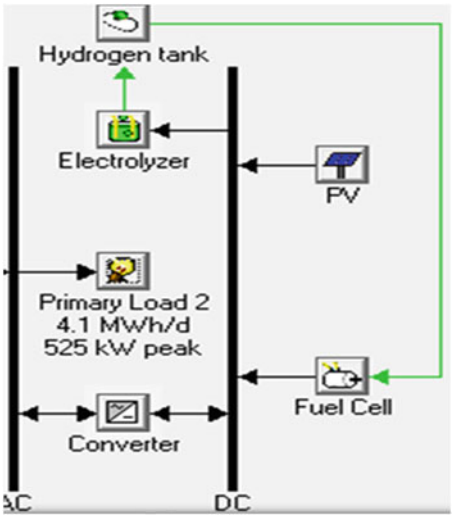

Fig. 1 PV-FC hybrid system model used in the study

The object of this work concerns the sizing of an autonomous PV-FC energy system capable of meeting the electric needs of the University of Chlef using the software of sizing HOMER (Givler and Lilienthal 2005).

2 PV-FC System

A schematic representation of the system under consideration is shown in Fig. 1. In this system, the photovoltaic field feeds directly the user. The excess of energy is stored under chemical form and used when needed. An electrolyzer is used to split water into hydrogen and oxygen. The hydrogen is stored. When the photovoltaic field cannot supply the totality of the requisite electricity, the fuel cell is connected. It generates the needed electricity by recombining the hydrogen and the oxygen directly from the air. The fuel cell produces some pure water, which is stored to furnish the electrolyzer.

3 Characteristics of the Region of Chlef

For this study, we used the ONM data. These data are measured at Chlef airport, situated a few kilometers northeast from downtown Chlef. These data cover a period of 10 years, extending from 1999 to 2008. Table 1 shows the various geographical characteristics of Chlef measurement station.

Table 1 Geographical characteristics of the meteorological station of Chlef

Latitude	Longitude	Roughness	Albedo
36°12′ N	1°20′ E	0.05	20%

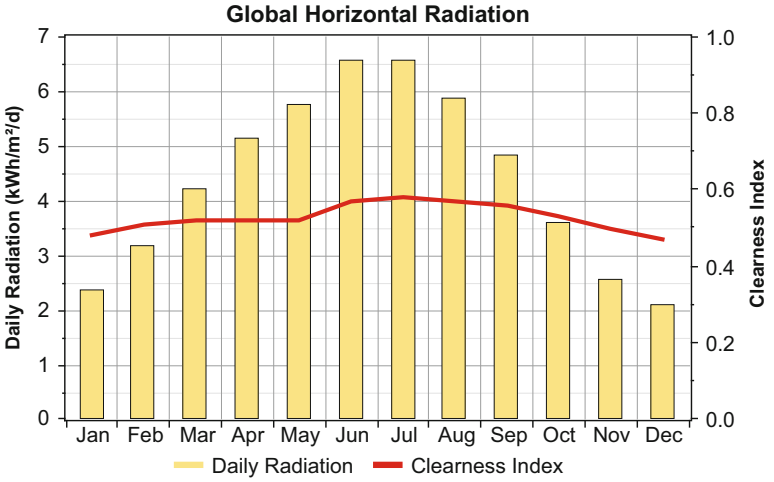

Fig. 2 Chlef solar resource graph

Concerning sunshine duration, the data have also been acquired from ONM. These data under the form of monthly average daily sunshine duration cover a 10-year period from 1999 to 2008. By means of HOMER, the values of the clearness index, and the characteristics of the measurement site, as reported in Table 1, the daily average irradiation for each month of the year is determined. In Fig. 2, the monthly evaluation of the irradiation (in yellow) and that of the clearness index (in red) are represented.

For the temperature of the region of Chlef, as for the cases of meteorological data and the sunshine duration data, the average monthly values of the measured temperature for 15 years (from 1993 till 2007) are acquired from ONM. Figure 3 represents the variation in the average monthly temperature over a 15-year period (from 1993 till 2007).

4 Electrical Load Variation of the University

For the profile of consumption, we used data supplied by the company SONELGAZ. They correspond to the monthly electric power consumed by the University of Chlef during the year 2008. We can see, in Fig. 4, the monthly evolution of the power over 1 year.

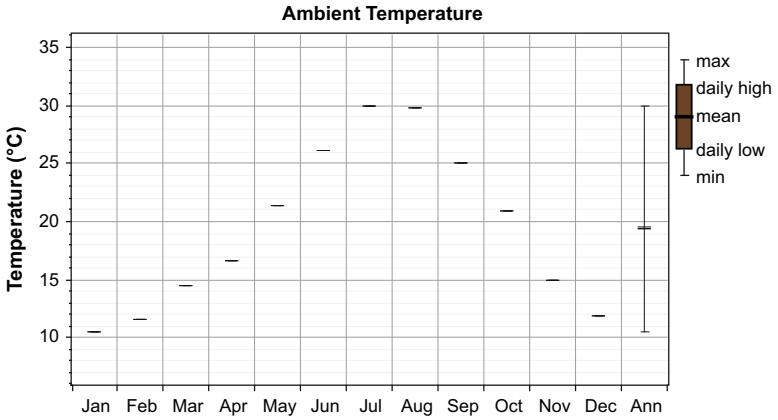

Fig. 3 Monthly evolution of the temperature

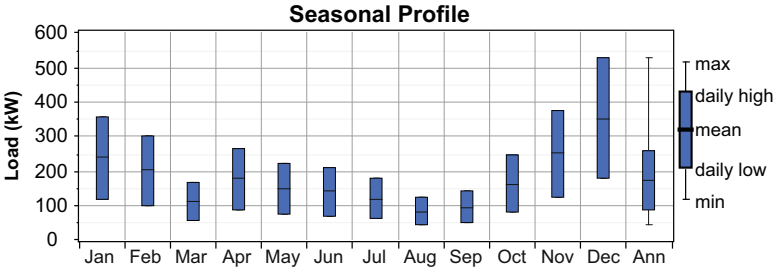

Fig. 4 Monthly average load variation at the university for the year 2008

5 Technical Characteristics of Components

The position of the photovoltaic modules in relation to the sun influences directly their energy production. It is very important to optimize their orientation (Labouret and Villoz 2005). Two parameters define the position of the photovoltaic modules:

- The *orientation* (azimuth): the cardinal point to which the active face of the panel is turned (the South, the North, Southwest)
- The *tilt*: the angle between the photovoltaic panel and the horizontal plan

For our system, we have considered several values of tilt. However, we have chosen only the orientation due south, that is in an azimuth of 0°.

The temperature influences directly the PV panels.

The characteristics of PV panels are presented in Table 2.

Electrolyzers are used to produce the necessary hydrogen to feed the fuel cells for the generation of electricity required to meet the maximum loads of the University of Chlef. Table 3 shows the technical characteristics of the used electrolyzer.

Table 2 PV panel's technical data (Accord Eco vert)

Technology	Thermal coefficient of the cell	NOCT	Return in the standard conditions
Multicrystalline silicon	−0.5%/°C	47 °C	13%

Table 3 Electrolyzer technical data

Characteristic	Type	Return	Cycle
Value	Alkaline/PEM	75%	25 years

Table 4 Converters technical data

Characteristic	Cycle	Return (DC/AC)	Return (AC/DC)
Value	15 ans	90%	90%

In the PV-FC systems, converters are used to transform DC into AC. Table 4 shows the technical characteristics of the used converter.

The stored hydrogen must be sufficient to meet the needs of fuel cells. Tank must be sufficient to store the hydrogen by matching the characteristics quoted in Table 5.

Fuel cells have to be of a sufficient power to feed the load's maximum energy demand by matching the characteristics of Table 6.

6 Economic Parameters

In order to carry out an economic study of our system, we have reported the most important parameters we have used in Table 7. Among these parameters, we have the average of the costs of initial investment, replacement, and operation and maintenance of the various components of the PV-FC system. All the costs are expressed in US dollars. We have also included in this table the technical characteristics such as the cycle lifespan, the return, and the availability of these components.

7 Results and Discussion

The simulation by HOMER software gives a list of the various possibilities of installation of the system cross PV-FC, with the optimum possibilities sorted out according to economic criteria. All these systems are capable of meeting the University of Chlef's needs in a continuous way.

Table 5 Hydrogen tank technical data

Characteristic	Value
Cycle	20 years
Reserved volume	95%

Table 6 Fuel cells technical data

Characteristic	Value
Cycle	43,800 h
Specific consumption	0.03 kgH_2/kWh
Way of functioning	DC

Table 7 Components cost data (Kashefi Kaviani et al. 2009)

Component	PV panel	Electrolyzer	Hydrogen tank	Fuel cells	Converters
Initial capital cost [US$ / unit]	6500	2000	1300	3000	800
Cost of replacement [US$ / unit]	5500	1500	1200	2500	750
O&M [US$/unit-year]	65	25	15	175	8
Cycle [years]	20	20	20	5	15
Return [%]	13	75	95	50	90
Unit	1 kW	1 kW	1 kg	1 kW	1 kW

PV Slope (deg)	PV (kW)	FC (kW)	Conv. (kW)	Elec. (kW)	H2 Tank (kg)	Disp. Strgy	Initial Capital	Operating Cost ($/yr)	Total NPC	COE ($/kWh)	Ren. Frac.	FC (hrs)
20.0	5300	600	600	2700	5000	CC	$ 48,630,000	1,317,344	$ 81,563,600	2.163	1.00	5,171
25.0	5000	600	600	2800	5200	CC	$ 47,140,000	1,307,586	$ 79,829,648	2.117	1.00	5,195
30.0	4800	600	600	2800	5300	CC	$ 45,970,000	1,297,096	$ 78,397,408	2.079	1.00	5,208
36.0	4700	600	600	2700	5500	CC	$ 45,380,000	1,292,667	$ 77,696,680	2.061	1.00	5,220
40.0	4600	600	600	2800	5600	CC	$ 45,060,000	1,294,095	$ 77,412,376	2.053	1.00	5,236
45.0	4500	600	600	2900	5700	CC	$ 44,740,000	1,295,802	$ 77,135,040	2.046	1.00	5,254
50.0	4500	600	600	2800	5800	CC	$ 44,670,000	1,301,882	$ 77,217,040	2.048	1.00	5,307
55.0	4500	600	600	2800	5800	CC	$ 44,670,000	1,307,869	$ 77,366,736	2.052	1.00	5,350
60.0	4400	600	600	3000	6000	CC	$ 44,680,000	1,321,985	$ 77,729,624	2.061	1.00	5,409

Fig. 5 The optimization results with the optimum systems ranked

Table 8 Composition of the PV-FC system

Power crest of the PV field [kW]	Rated output of the converter [kW]	Rated output of the electrolyzer [kW]	Size of the reservoir of H_2 [kg]	Rated output of the FC [kW]
4500	600	2900	5700	600

The optimal position of PV panels is found to be at a tilt of 45°, as we reported in Fig. 5. This unit consists of a solar PV field, an electrolyzer, and a fuel cell system. Table 8 shows the characteristics of the different components of this unit.

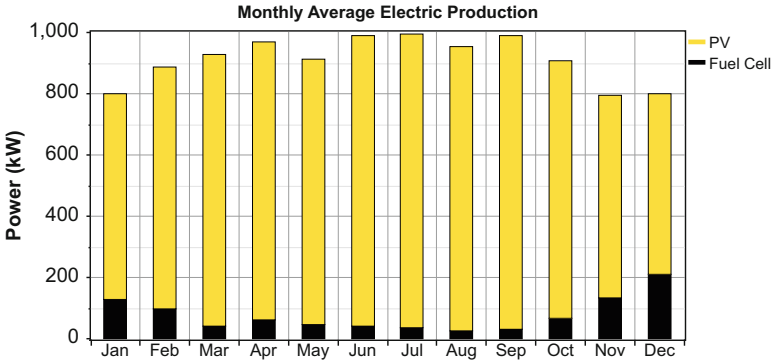

Fig. 6 Monthly energy yield from PV-FC system

The results of the optimization of the system are reported in Fig. 6. This figure shows the energy production of the PV-FC hybrid system.

We can see that 92% of the annual energy produced by the system is photovoltaic energy. Only 8% of this energy is produced by fuel cells. The load consumes 59% of the total consumed energy and 41% is consumed by the electrolyzer to produce the necessary hydrogen to feed the fuel cell during the night and in case of overcast conditions. Table 9 shows the energy balance of the autonomous PV-FC system.

The results of the economic study of this system are detailed in Table 10. The costs of every element of the system as well as the cost of kWh are reported.

Emissions

Greenhouse gas emissions by our hybrid PV-FC system is very low and can be said to be negligible. This is because of the used fuel, which is hydrogen. This hydrogen is produced through water electrolysis and using solar energy. The greenhouse gases produced by the PV-FC system under consideration are reported in Table 11.

8 Conclusion

In this study, we have investigated the use of renewable energy to meet the energy needs of the University of Chlef. We have determined the most suitable system using HOMER software and the costs of the actual system components. The results of the dimensioning models were used to determine the optimal sizing of the configurations. PV panels and the electrolyzer are the major cost factors of the proposed system after optimization.

Moreover, we have found an important excess in energy. This energy could be used to produce more hydrogen. This hydrogen can be used at another energy requirement, such as fuel for transport.

Table 9 Energy contribution of different energy sources

	Production		consumption		
Component	PV	FC	Elec	Load	Excess
Energy [kWh/year]	7,303,934	674,588	1,064,448	1,508,294	5,238,289
[%]	92	8	41	59	65.7

Table 10 Energy contribution of different energy sources

			Hydrogen			
Component	PV	Conv	Elec	Res H_2	FC	System
Cost [$]	35,100,000	726,000	7,250,000	9,120,000	14,932,030	67,127,992
Elementary cost	0.240 $/kWh	–	166 $/kg H_2		139 $/h	2.225 $/kWh

Table 11 Greenhouse gases emitted by PV-FC hybrid system

Emissions [kg/year]	CO_2	CO	SO_2	NO_x
PV-FC	0	0	0	243

References

Accord Eco Vert., www.accord-ev.com

Ganguly, A., Misra, D., Ghosh, S.: Modeling and analysis of solar photovoltaic-electrolyzer-fuel cell hybrid power system integrated with a floriculture greenhouse. Energ. Buildings. **42**, 2036–2043 (2010)

Givler, T., Lilienthal, P.: Using HOMER Software, NREL's Micro Power optimization model, to Explore the role of gen-Sets in small solar power systems; case study: Sri Lanka technical report. National Renewable Energy Laboratory, USA (2005)

Hatti, M., Meharrar, A., Tioursi, M.: Power management strategy in the alternative energy photovoltaic/PEM fuel cell hybrid system. Renew. Sust. Energ. Rev. **15**, 5104–5110 (2011)

Ipsakisa, D., Voutetakisa, S., Seferlisa, P., Stergiopoulos, F., Papadopoulou, S., Elmasides, C., Keivanidis, C.: Energy management in a stand-alone power system for the production of electrical energy with long term hydrogen storage. Comput. Aided Chemical Eng. **25**, 1125–1130 (2008)

Kashefi Kaviani, A., Riahy, G.H., Kouhsari, S.H.M.: Optimal design of a reliable hydrogen-based stand-alone wind/PV generating system, considering component outages. Renew. Energy. **34**, 2380–2390 (2009)

Khan, F.I., Hawboldt, K., Iqbal, M.T.: Life cycle analysis of wind–fuel cell integrated system. Renew. Energy. **30**, 157–177 (2005)

Labouret, A., Villoz, M.: Energie solaire photovoltaïque, Dunod Edit., 2nd Edition, Collection "Technique et Ingénierie", Paris, France (2005)

Vechiu, I.: Modélisation et analyse de l'integration des energies renouvelables dans un réseau autonome. Doctorat thesis, University of HAVER (2005)

Experimental and Numerical Investigations of a Compressed Air Energy Storage (CAES) System as a Wind Energy Storage Option

Abdul Hai Alami, Camilia Aokal, and Monadhel Jabar Alchadirchy

1 Introduction

Energy supply has always been plagued with demand inconsistencies that fluctuate around an ever-growing base load. Energy storage became a necessity to normalize the supply/demand deficit, but the problem recently has been more pronounced with the increased dependence on renewable resources that has an inherent unpredictable supply (Huggins 2010). The challenge remains in capturing sufficient amounts of energy at peak times for later use and pass them through as little conversion steps as possible from their intended end use. This involves the invention of new technologies that would maintain the energy quality and provide power with high efficiencies.

To classify energy storage options, power density and energy density are two key concepts to take into consideration (Abbaspour et al. 2013). The latter is used when a moderate supply of energy needs to be consumed over a long period of time, whereas the former is used when very high amounts of energy is needed for a short period of time. An ideal method of storage would incorporate high amounts of both energy densities and power densities. This, however, may not always be possible. Figure 1 shows the attractive position where compressed air energy storage systems rank, since discharge rates can be mitigated to supply a certain level of energy over an extended period of time depending on air containers which can range from small air bottles capable of holding a few liters under 2–3 bar up to underground caverns occupying volumes of up to 150,000 m^3 with storage pressures reaching up to 70 bar (Brown et al. 2014; Xia et al. 2015; Marano et al. 2012; Safaei et al. 2013).

A.H. Alami (✉) • C. Aokal • M.J. Alchadirchy
Sustainable and Renewable Energy Department, University of Sharjah, PO Box 27272, Sharjah, United Arab Emirates
e-mail: aalalami@sharjah.ac.ae

© Springer International Publishing AG, part of Springer Nature 2018

F. Aloui, I. Dincer (eds.), *Exergy for A Better Environment and Improved Sustainability 2*, Green Energy and Technology,
https://doi.org/10.1007/978-3-319-62575-1_79

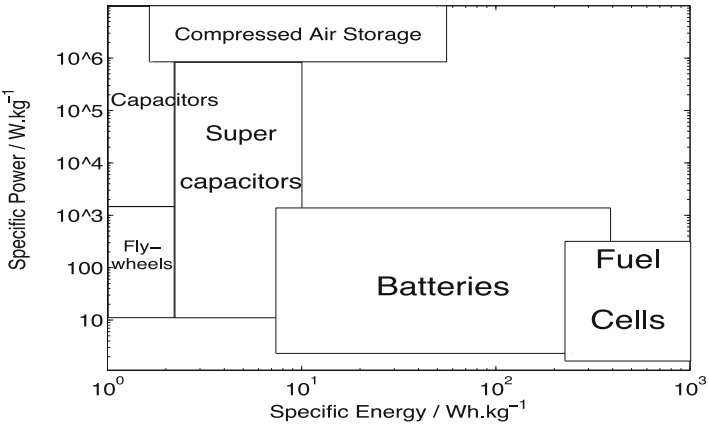

Fig. 1 Energy storage options classification

The main challenge of CAES is the significant temperature rise in the air as compression work is supplied to the system (Xia et al. 2015; Madlener and Latz 2013), requiring cooling before proceeding with the discharge part of the cycle as investigated by many authors (Safaei et al. 2013; Fertig and Apt 2011).

Modeling of CAES systems involved many assumptions depending on the size and discharge rate (power density) of the setup. Smaller systems suffer insignificant temperature change and thus can be modeled as isothermal (Sun et al. 2015) large insulated systems can be modeled as adiabatic (Robb 2011; Wolf and Budt 2014). Other systems utilize intercoolers to approach isothermal compression (Kushnir et al. 2012) and such a system is called diabatic (Zhang et al. 2014a).

Modern CAES systems overlap with the energy density of batteries, as seen in Fig. 1, but offer a higher power density depending on storage tank material and capacity and on discharge rate from the nozzle. Such systems have advantages over batteries by being nontoxic as they utilize no dangerous chemicals and have longer lives (Zhang et al. 2014b).

The main objective of this work is to investigate and identify the important parameters pertinent to compressed air energy storage (CAES) systems. A simplified approach to theoretical modeling based on the ideal gas law is used with the small-scale experimental setup that helps verify the model and provide a quantitative system characterization. The system is upscalable and best suited for coupling with existing wind energy installations as it is economical and easy to implement.

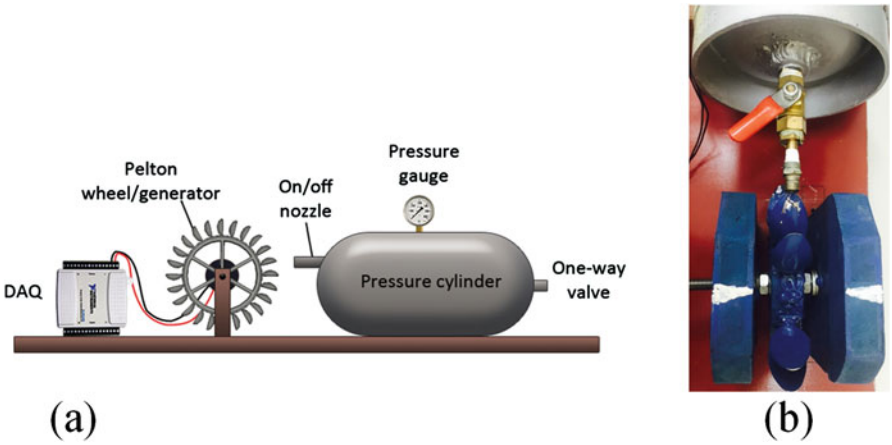

Fig. 2 (**a**) Experimental setup and (**b**) close up to nozzle section

2 Experimental Facility

2.1 Setup

The experimental setup consists of a steel thin-walled pressure vessel with a rating of 8 bar (gauge), fitted with a one-way valve for pressurization and a two-position (close/open) nozzle for discharge. A pressure gauge reads the internal pressure of the cylinder, while a manual reciprocating pump provides the required pressurization. The nozzle discharges into a 12-bucket, 10-cm diameter Pelton wheel weighing 300 g. The wheel is mechanically coupled to a 3 W generator ($V_{\max} = 6$ V) with lead wires connected to an NI USB-6009 data acquisition (DAQ) device set at 1 kHz for 5000 samples, since initial tests on the system revealed that the discharge is complete in $t \approx 4.5$ s. The pressure within the cylinder is varied at two values, 2 and 3 bar (gauge), while the DAQ system measures the voltage and current output (through a 0.01 Ω current conditioner) from the generator with the goal of approximating the efficiency of energy conversion compared with theoretical calculations. A tachometer is also used to measure the rotational velocity of the Pelton wheel during discharge.

A schematic of the experimental setup is shown in Fig. 2.

3 Numerical Scheme

There are three main techniques found in literature used to model CAES systems, based on how to treat the significant amount of heat energy generated during air compression. First there is the isothermal process approximation, second the

adiabatic (isentropic) process, and finally the large system thermodynamics approximation for large storage systems in underground caverns. For the current analysis and considering the small size of the experimental setup that will be introduced in the next section, the system can be considered to be isothermal, as the pressures involved are relatively small and will not exceed 3 bar. This assumption allows the utilization of the ideal gas law ($PV = nRT$) to represent the air compression process. Since the absolute temperature between initial state A and final state B is assumed to be constant ($T_A = T_B = T$), the work done on a control volume of air taken within the compression cylinder between these two states is given to be:

$$W_{A\to B} = \int_{V_A}^{V_B} PdV = \int_{V_A}^{V_B} \frac{nRT}{V} dV = nRT \int_{V_A}^{V_B} \frac{1}{V} dV \tag{1}$$

This can be expanded by carrying out the integration to be:

$$W_{A\to B} = nRT(\ln V_B - \ln V_A) = nRT \ln \frac{V_B}{V_A} \tag{2}$$

which can also be written more conveniently in terms of pressures P_A and P_B:

$$W_{A\to B} = P_A V_A \ln \frac{P_A}{P_B} \tag{3}$$

Since isothermal conditions are assumed to hold, a simplified form of the energy equations is applied between points A and B to estimate the maximum exit velocity of air from the nozzle to be:

$$v_{max} = \sqrt{2\frac{P_A}{\rho_{ave}}} \tag{4}$$

where ρ_{ave} is the average air density between states A and B, assuming a linear pressure drop during system discharge (Cengel and Boles 2001). The angular velocity, ω in rad/s, can be estimated from the basic torque eq. $T = I \times \alpha$, where I is the moment of inertia of the Pelton wheel and α is the uniform angular acceleration in rad/s^2. Starting from rest, the angular acceleration of the wheel is estimated to be the rate of change of the angular velocity over rotation time. The torque that the air jet exerts on the wheel is the thrust force, dm/dt.v_{max}, times the radius of the wheel.

For pressure values of 2 and 3 bar, the air density at 303 K is found to be 3.46 and 4.61 kg/m^3, respectively; the theoretical values of jet velocity, thrust, torque and angular velocity are given in Table 1.

Table 1 Theoretical estimation of kinetic and kinematic quantities

	v_{max} m/s	F_{thrust}, N	T, N.m	ω, rad/s
2 bar	385.7	0.47	0.047	78.2
3 bar	445.3	0.54	0.054	90.3

4 Results and Discussions

Assuming that charging the system with air (compression) will come externally from available excess energy at periods of low demand, only the expansion portion will be of interest for system analysis. Thus, the pressure drop within the cylinder at the onset of discharge (nozzle on) is assumed to drop linearly, converting the stored potential energy of air as static pressure into kinetic energy manifesting as air velocity at the nozzle and angular rotation in the Pelton wheel.

The output voltage, V_{out}, with time is shown in Fig. 3 for the two pressure settings of 2 and 3 bar within the cylinder. Figure 3a shows the time needed to reach a steady-state voltage at around 2 s compared to the case of 3 bar cylinder pressure that required 2.7 s. This result is expected due to the higher potential energy stored as static pressure in the latter case. The fluctuation seen is also due to the binary options for the discharge nozzle (either on or off) and the transient instability caused by the sudden valve opening. It can also be seen from the figure that the average output voltage in the 3 bar setting is around 1.55 V, which is 13% higher than that at 2 bar as is expected given the higher stored potential.

From Table 1, the theoretical exit velocities from the nozzle are 385.6 m/s for the 2 bar case, while it is calculated to be 445.3 m/s for the 3 bar case. From these values, the corresponding expected rotational velocity, ω, for the Pelton wheel can be calculated to be 78.2 rad/s and 90.3 rad/s, respectively. The value at low pressure can be compared with the tachometer reading of 741 rpm (77.6 rad/s), which is lower than predicted most probably due to fluidic losses (expansion, skin friction) and mechanical (coupling friction, windage). At the higher pressures of 3 bar, however, the theoretical model underestimates the angular velocity by around 15% which is measured by the tachometer to be around 1000 rpm (104.7 rad/s). The discrepancy between the 2 and 3 bar settings can be attributed to the air jet convergence into the Pelton wheel blades. The nonlinear response of the jet is better accounted for if an isentropic model of air compression is used instead of the simplified ideal gas law that is used for the theoretical calculation, the latter being a more convenient and straightforward approach (Zukcer and Biblarz 2002).

The experimental power density is shown in Fig. 4 for the two pressure settings, represented by the area under the generated IV curve. It can be seen that the fluctuations in the curve for the 3 bar setting is less than the one for 2 bar, indicating a smoother supply of current as the voltage varies. The area under the curve is around 2.31 W, which is within the rating of the generator. Higher values of pressure were not attempted, as this may cause higher electrical power that can damage the generator, along with being a major safety concern.

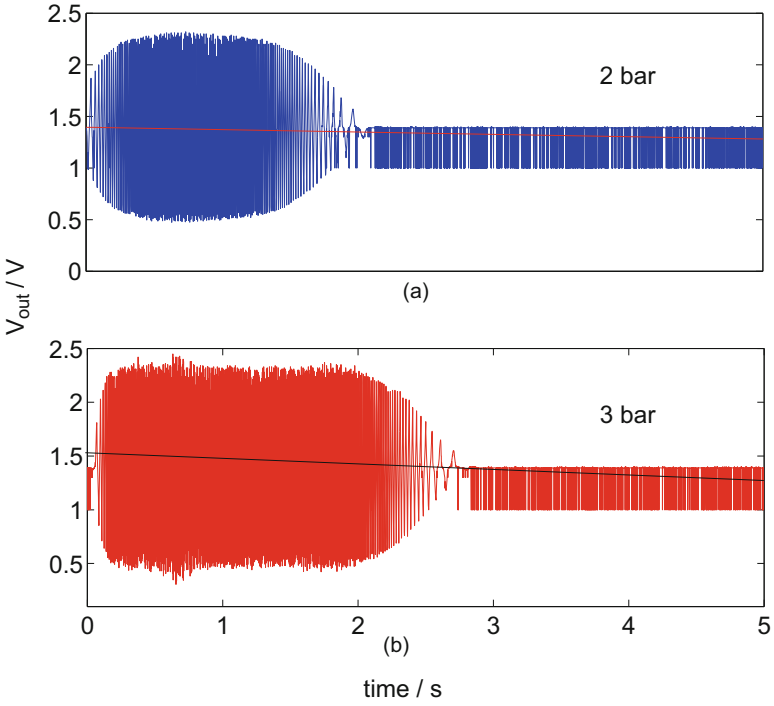

Fig. 3 Voltage variation vs. discharge duration at (**a**) 2 bar and (**b**) 3 bar cylinder pressure

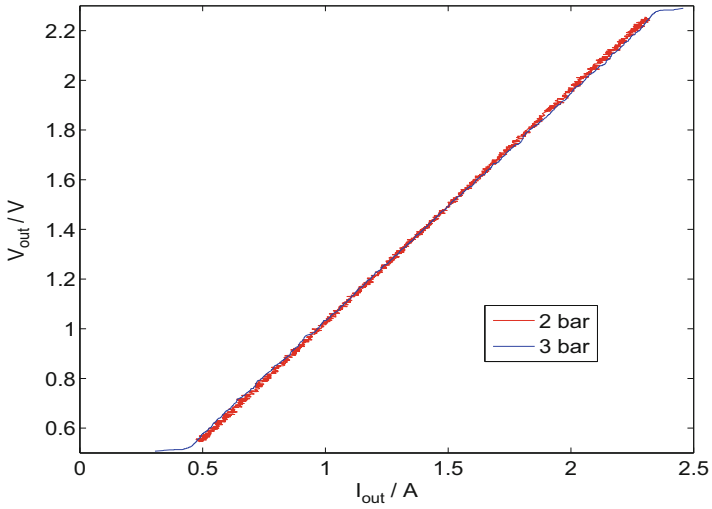

Fig. 4 Voltage change with output current for 2 and 3 bar cylinder pressure

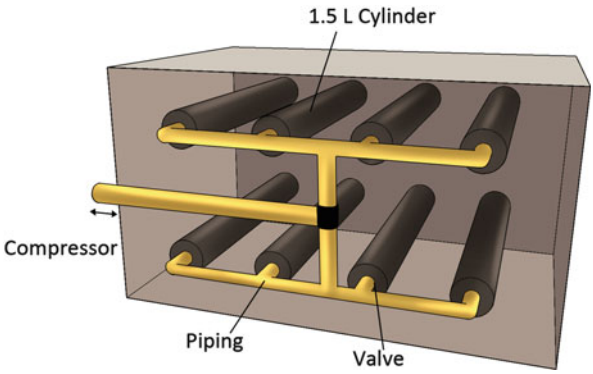

Fig. 5 Modular system depiction as applied in (Alami et al. 2017)

The efficiency of the system is a function of the pressure and can be calculated by considering the potential energy stored within the cylinder at the two values of cylinder pressure (2 and 3 bar) as has been reported in literature for an isothermal process (Zhang et al. 2014a, b). Performing the simple calculation at respective pressure value, the system efficiency is calculated to be 64.8% and 84.8% for 2 and 3 bar internal pressure cases, respectively.

Finally, to help with the varying discharge demand while keeping the isothermal assumption valid, a modular array of multiple pressure cylinders can be connected through valves, as shown in Fig. 5, with the valve operation being controlled via a programmable logic controller (PLC).

This setup helps to control the discharge from the cylinders by either opening all the valves at the same time for high power density requirements or opening them sequentially if longer periods of times are needed, hence fulfilling the overlap with the battery storage that is seen in Fig. 1.

5 Conclusions

Energy storage by virtue of a compressed air system was evaluated. An isothermal compression of air was assumed to accurately model the system since negligible temperature rise is expected in the small cylinder used for the experiment. A fast data acquisition system monitored the voltage generated during discharge and found that the selected electric generator matched the rate of energy generation. The overall system efficiency is a function of cylinder pressure and had a maximum value of 84.8%. The system is amenable for energy storage in wind energy farms and can easily be upscalable.

References

Abbaspour, M., Satkin, M., Mohammadi-Ivatloo, B., Hoseinzadeh, L.F., Noorollahi, Y.: Optimal operation scheduling of wind power integrated with compressed air energy storage (CAES). Renew. Energy. **51**, 53–59 (2013)

Alami, A.H., Aokal, K., Abed, J., Alhemyari, M.: Low pressure, modular compressed air energy storage (CAES) system for wind energy storage applications. Renew. Energy. **106**, 201–211 (2017)

Brown, T.L., Atluri, V.P., Schmiedeler, J.P.: A low-cost hybrid drivetrain concept based on compressed air energy storage. Appl. Energy. **134**(1), 477–489 (2014)

Cengel, Y., Boles, M.: Thermodynamics: An Engineering Approach, 4th edn. Mcgraw-Hill College, London (2001)

Fertig, E., Apt, J.: Economics of compressed air energy storage to integrate wind power: A case study in ERCOT. Energy Policy. **39**(5), 2330–2342 (2011)

Huggins, R.A.: Energy Storage, 2nd edn. Springer, New York (2010)

Kushnir, R., Dayan, A., Ullmann, A.: Temperature and pressure variations within compressed air energy storage caverns. Int. J. Heat Mass Transfer. **55**(21–22), 5616–5630 (2012)

Madlener, R., Latz, J.: Economics of centralized and decentralized compressed air energy storage for enhanced grid integration of wind power. Appl. Energy. **101**, 299–309 (2013)

Marano, V., Rizzo, G., Tiano, F.A.: Application of dynamic programming to the optimal management of a hybrid power plant with wind turbines, photovoltaic panels and compressed air energy storage. Appl. Energy. **97**, 849–859 (2012)

Robb, D.: The CAES for wind. Renew. Energy Focus. **12**(1), 18–19 (2011)

Safaei, H., Keith, D.W., Hugo, R.J.: Compressed air energy storage (CAES) with compressors distributed at heat loads to enable waste heat utilization. Appl. Energy. **103**, 165–179 (2013)

Sun, H., Luo, X., Wang, J.: Feasibility study of a hybrid wind turbine system – Integration with compressed air energy storage. Appl. Energy. **137**, 617–628 (2015.) http://dx.doi.org/10.1016/j.apenergy.2014.06.083

Wolf, D., Budt, M.: LTA-CAES – A low-temperature approach to Adiabatic Compressed Air Energy Storage. Appl. Energy. **125**(15), 158–164 (2014)

Xia, C., Yu, Z., Zhou, S., Zhang, P., Wang, F.: A simplified and unified analytical solution for temperature and pressure variations in compressed air energy storage caverns. Renew. Energy. **74**, 718–726 (2015)

Zhang C., Yan B., Wieberdink J., Li P.Y., Van de Ven J.D., Loth E., Simon T.W.: Thermal analysis of a compressor for application to Compressed Air Energy Storage, Appl. Therm. Eng. (2014a) http://dx.doi.org/10.1016/j.applthermaleng.2014.08.014

Zhang Y., Yang K., Li X., Xu J.: Thermodynamic analysis of energy conversion and transfer in hybrid system consisting of wind turbine and advanced adiabatic compressed air energy storage. Energy. (2014b) http://dx.doi.org/10.1016/j.energy.2014.09.030

Zukcer, R., Biblarz, O.: Fundamentals of gas dynamics, 3rd edn. Wiley, New Jersey (2002)

Feasibility Study of a Novel One-Axis Sun Tracking System with Reflector Displacement in a Parabolic Trough Concentrator

A. Gama, C. Larbes, A. Malek, and F. Yettou

1 Introduction

After the growth of oil prices at the time of the petroleum crisis in 1974, and the facing of disastrous effects caused by hydrocarbon combustion without forgetting the exhaustion of fossils fuels, there is a conscious effort engaged in favoring the renewable energies. South Algeria has an important amount of solar energy of more than 2200 kWh/m^2/year (Boudghene Stambouli 2010), and also a big surface which favors investment in this field. Concentration systems were the best in solar energy conversion, especially the parabolic trough concentrator (PTC). The PTC systems have an important impact in solar energy field, this field motivate researchers to work on, in order to improve its performances, especially sun tracking systems, this system which is essential for the best performance and best PTC efficiency during the day and the year.

The size and the placement of concentrators limit the choices of a sun tracking system; generally, the PTC uses one rotation axis sun tracking system. The sun elevation causes many optical losses, named the cosine effect. It's clear that the cosine effect is negligible in PTC power plants, but in a medium or small installation of parabolic trough concentrator (Fernandez-Garcıa et al. 2010), these losses

A. Gama (✉) • F. Yettou
Unité de Recherche Appliquée en Energies Renouvelables, URAER, Centre de Développement des Energies Renouvelables, CDER, 47133 Ghardaïa, Algeria
e-mail: gama_amor@yahoo.fr

C. Larbes
National Polytechnic School, 10 Hassen Badi Avenue, P.O. Box 182, El Harrach Algiers, Algeria

A. Malek
Centre de Développement des Energies Renouvelables, CDER, 16340 Algiers, Algeria

© Springer International Publishing AG, part of Springer Nature 2018

F. Aloui, I. Dincer (eds.), *Exergy for A Better Environment and Improved Sustainability 2*, Green Energy and Technology,
https://doi.org/10.1007/978-3-319-62575-1_80

are very important and a solution must be found. In this work, we choose to move the reflector in order to recover these losses. In this study, we analyze this idea where we propose a mechanical system as a solution. To verify the efficiency of the proposed system, we have simulated the functionality of two identical parabolic trough concentrators where the first has a regular sun tracking system and the second is equipped with the new proposed system. The optical behavior was simulated by calculating the displacement distance and the concentrated irradiance; for the thermal behavior we use the TRNSYS software in order to calculate the useful energies and the efficiency of the two concentrators.

2 Cosine Effect

If the incident direct irradiance (E_d) forms an angle (θ) with the normal of the aperture plane (Fig. 1), and if concentration ratio is (C), then the irradiance in the absorber is (Chausseriau 1984)

$$E_c = E_d \cdot Cos(\theta) \cdot C \tag{1}$$

To have the best concentration efficiency in parabolic trough concentrators, the solar ray must be perpendicular to the aperture area; the cosine effect has a relation with the focal distance:

$$L = F \cdot Cos(\theta) \tag{2}$$

For different focal distances, we have calculated the distance L of the cosine effect in South Algeria, precisely in the Ghardaïa region (Fig. 2).

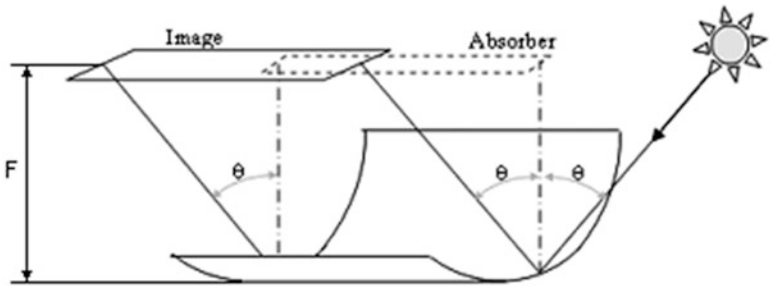

Fig. 1 Cosine effect in the parabolic trough concentrator

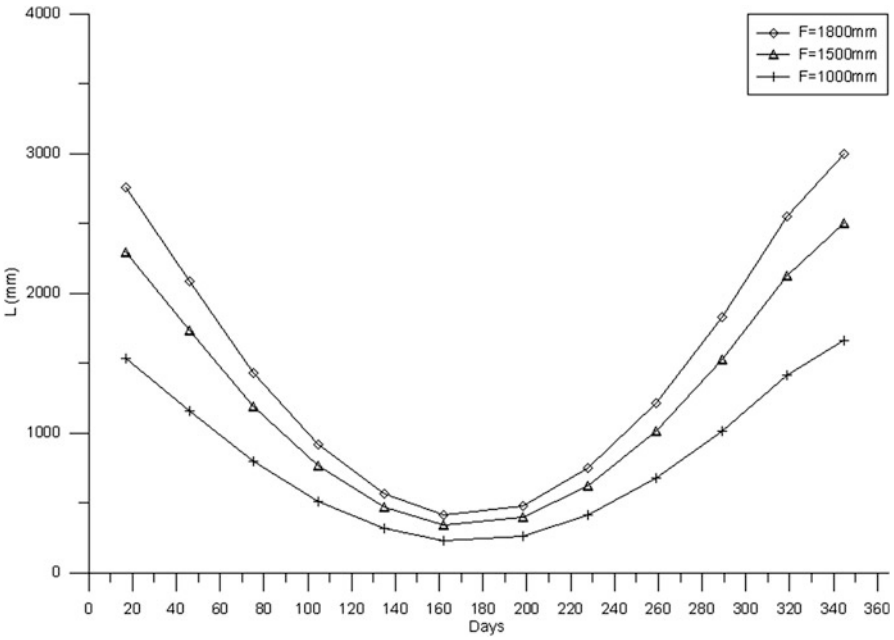

Fig. 2 The distance "*L*" of cosine effect (in millimeters) as a function of the day of year for different focal distances in Ghardaïa (arid region south of Algeria)

3 Mechanical Solution Proposed

The tracking mechanism must be reliable and able to follow the sun with accuracy whatever the weather (Kalogirou 1996). We find two types of sun tracking mechanisms with one-axis and two-axis.

Generally, the two-axis tracker follows the sun's movement from the East to the West and changes the incline angle according to the sun's elevation angle, while the one-axis tracking follows the sun's movement only from the East to the West, and in this case, the energy collected by the solar collector during winter is less due to the sun's changing elevation (Bakos 2006). In PTC, we use the second type of sun tracking system. To minimize the optical losses due to the sun's changing elevation (cosine effect), we propose two solutions (Gama et al. 2013). The first consists of the displacement of the absorber, and the second the displacement of the reflector. We prefer to adopt the last solution for technical reasons.

In this study, we consider a parabolic trough concentrator that is "14.4 m" long, "4 m" wide, and "1.8 m" of focal distance; the concentrator is equipped with one-axis sun tracking oriented N-S.

The mechanical solution that we propose allows us to make sure that the rotation and the displacement of the reflector occur at the same time. For the rotation of the reflector we use a mechanical jack, and for the translation movement we use a CC

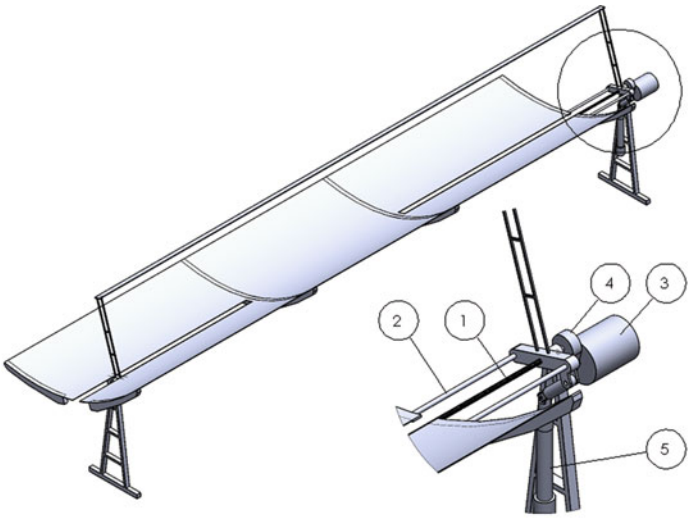

Fig. 3 The proposed parabolic trough concentrator with reflector displacement

motor (3) connected to a speed reducer (4), which rotates a threaded rod (1) that translates the reflector (see Fig. 3). The displacement distance (L) is calculated at any time by the conversion of solar elevation angle, this parameter must be added to the one-axis sun tracking strategy, and we deduce that the displacement distance for South Algeria is between "2.82 m" in winter and "0.41 m" in summer.

4 Thermal Simulation

In order to calculate the thermal performances, we use the TRNSYS software, where the Linear Parabolic Concentrator model is based on equations taken from Duffie and Beckman's "Solar Engineering of Thermal Processes" (Duffie and Beckman 1991). We compare two parabolic trough concentrators with regular sun tracking system and with displacement reflector.

The TRNSYS model of installation (Fig. 4) contains the parabolic trough concentrator linked to a pump of "20 kg/h" flow rate and a storage tank of "1 m^3" equipped with a heat exchanger; the concentrator is simulated for a region in the south of Algeria (GHARDAÏA, Lat = 32.23°, long = 3.66°, Alt = 450 m) for a short and a long day of the year. First, we calculate the useful energy gain and the efficiency of the first concentrator; then for the second concentrator, we use the same installation by adding to the length of the concentrator the distance of the displacement (L) for any day without changing the concentration ratio.

The results obtained after the TRNSYS simulation prove that the new proposed system is efficient, the useful energy gain in the case of concentrator with reflector

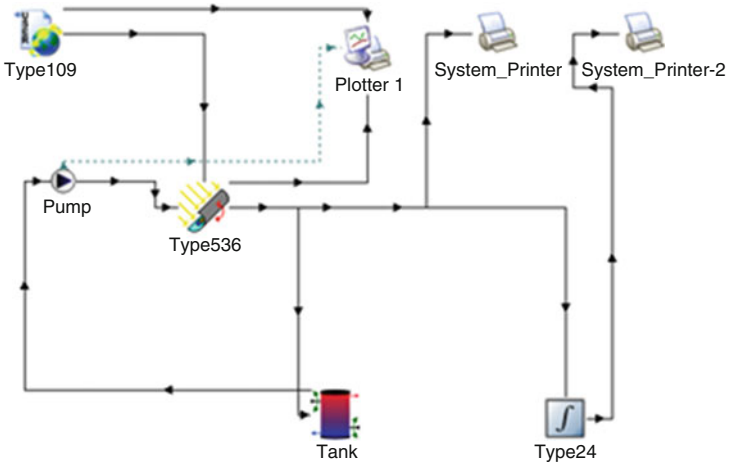

Fig. 4 TRNSYS model of simulation facility

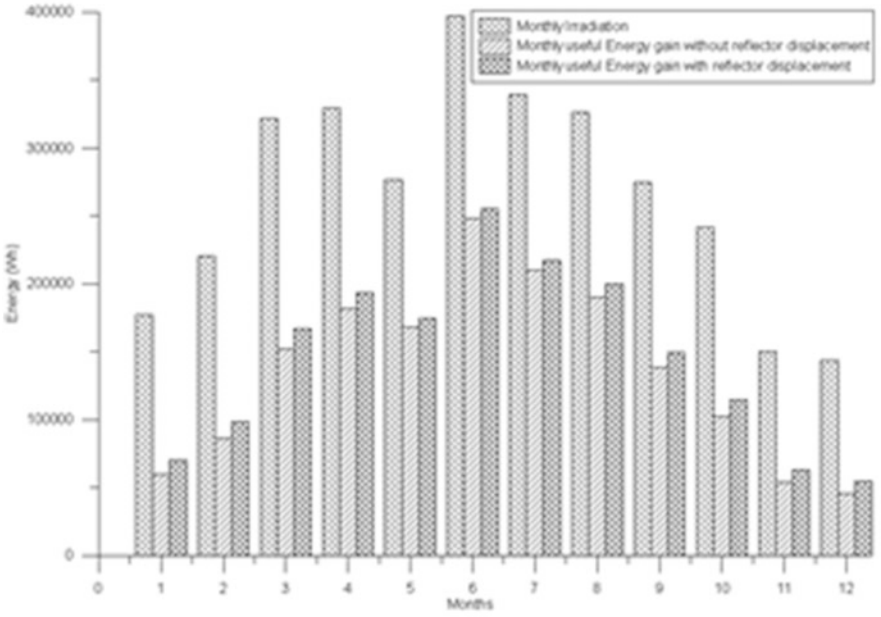

Fig. 5 Irradiation and useful energy gain of a PTC with regular sun tracking system and with reflector displacement

displacement has increased considerably compared with the case of ordinary sun tracking systems (Fig. 5), and the efficiency of the system increases from "31.8%" to "37.98%" during the shortest day of the year and from "62.57%" to "64.3%" during the longest day of the year (Fig. 6).

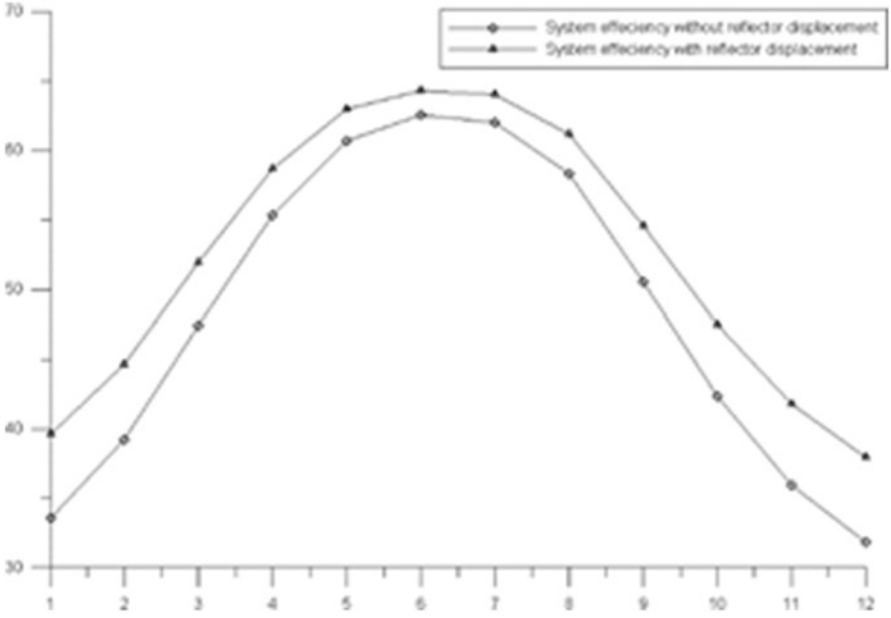

Fig. 6 Efficiency of system in two simulation cases

5 Optical Simulation

According to optical simulation, we can observe that the displacement of the reflector induces the displacement of the concentration line, and therefore we have eliminated the optical losses (cosine effect). In South Algeria, for the shortest day of the year, the cosine effect is very high. We have displaced the reflector by a distance of "2.8 m" (Fig. 7), and the efficiency of the system increases considerably by the recovery of these optical losses.

In South Algeria, the cosine effect is very small in the summer because the solar elevation was at the maximum (Fig. 8), we have displaced the reflector by "0.41 m" (Fig. 9), and the efficiency of the system increases by a small value because the optical losses are very small.

6 Conclusions

Optical loss is the primary disadvantage in the parabolic trough concentrator. The minimization of optical losses increase the optical efficiency of this systems. In this work, we proposed a new sun tracking system based on reflector displacement

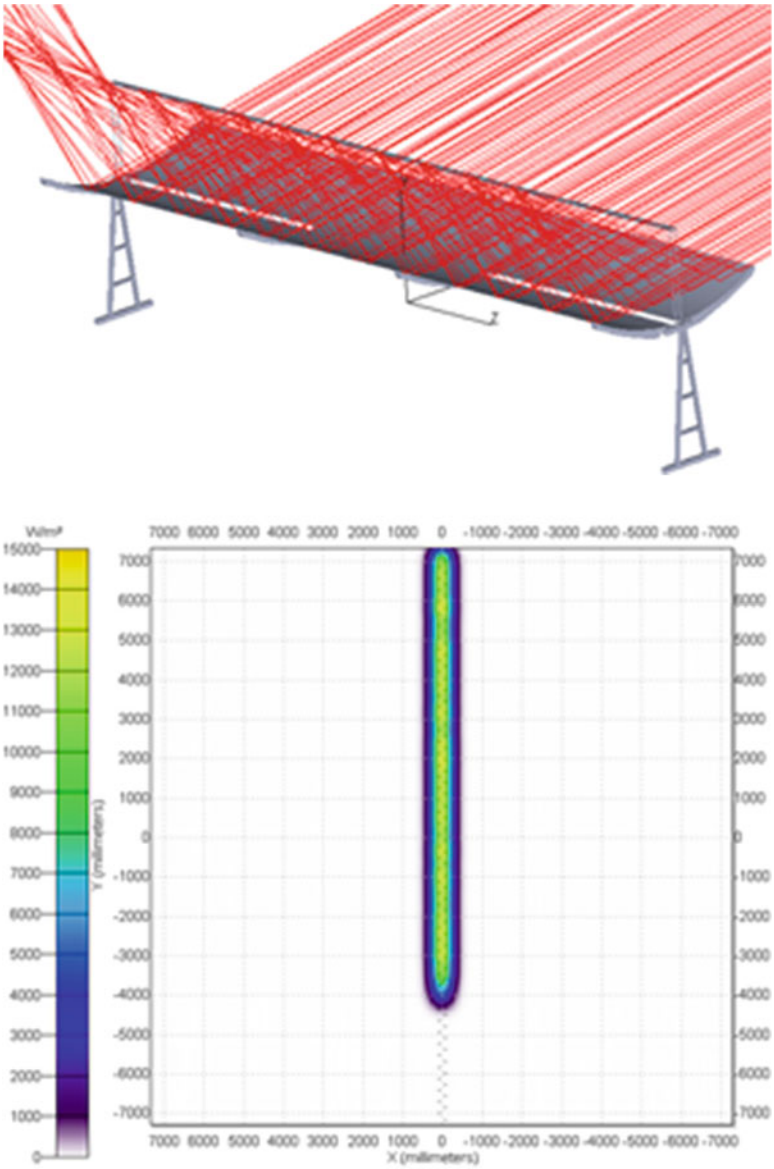

Fig. 7 Presentation of concentrated irradiance beam for the shortest day of the year, system with regular sun tracking

intended to be used in small and medium installations where the optical losses are minimized. To prove this idea we have simulated two systems: the first system with a displaced reflector and the second with an ordinary sun tracking system. The results were very interesting: the efficiency increased considerably with a simple

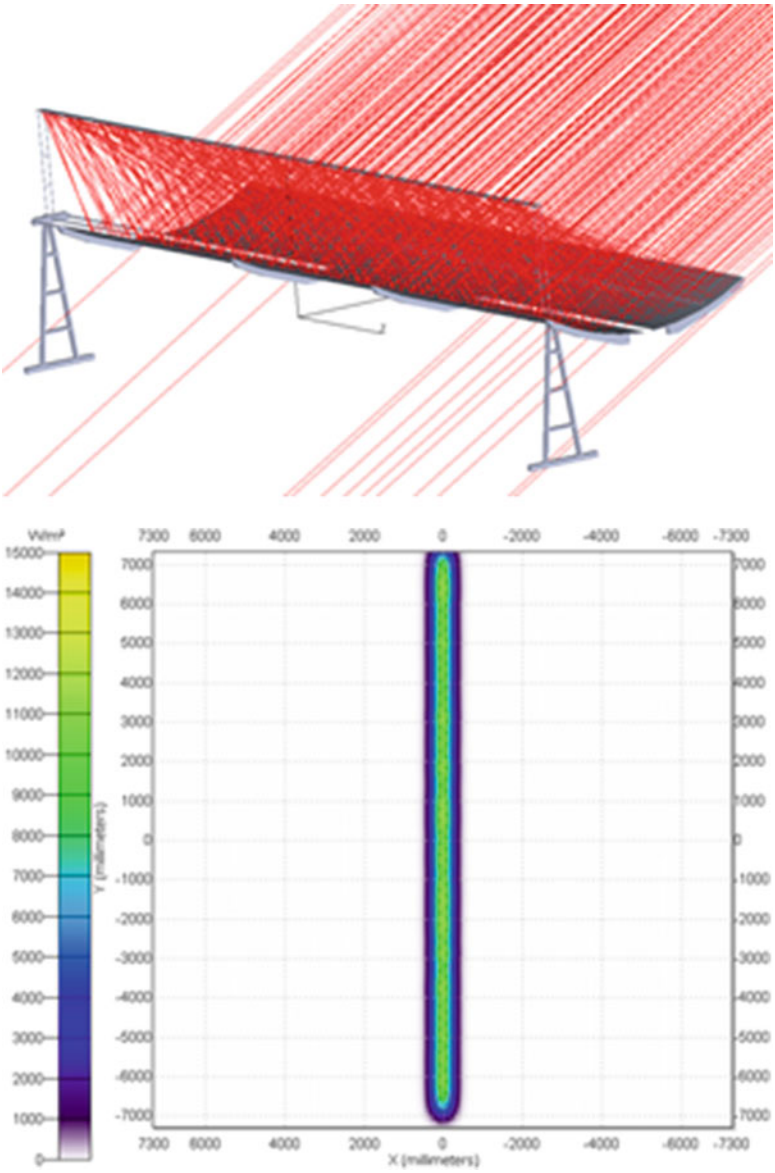

Fig. 8 Presentation of concentrated irradiance beam for the shortest day of the year, system with reflector translation

mechanical solution and a few modifications in the sun tracking strategy. Currently, we are working to prove the new sun tracking system experimentally through a new prototype installed in the south of Algeria.

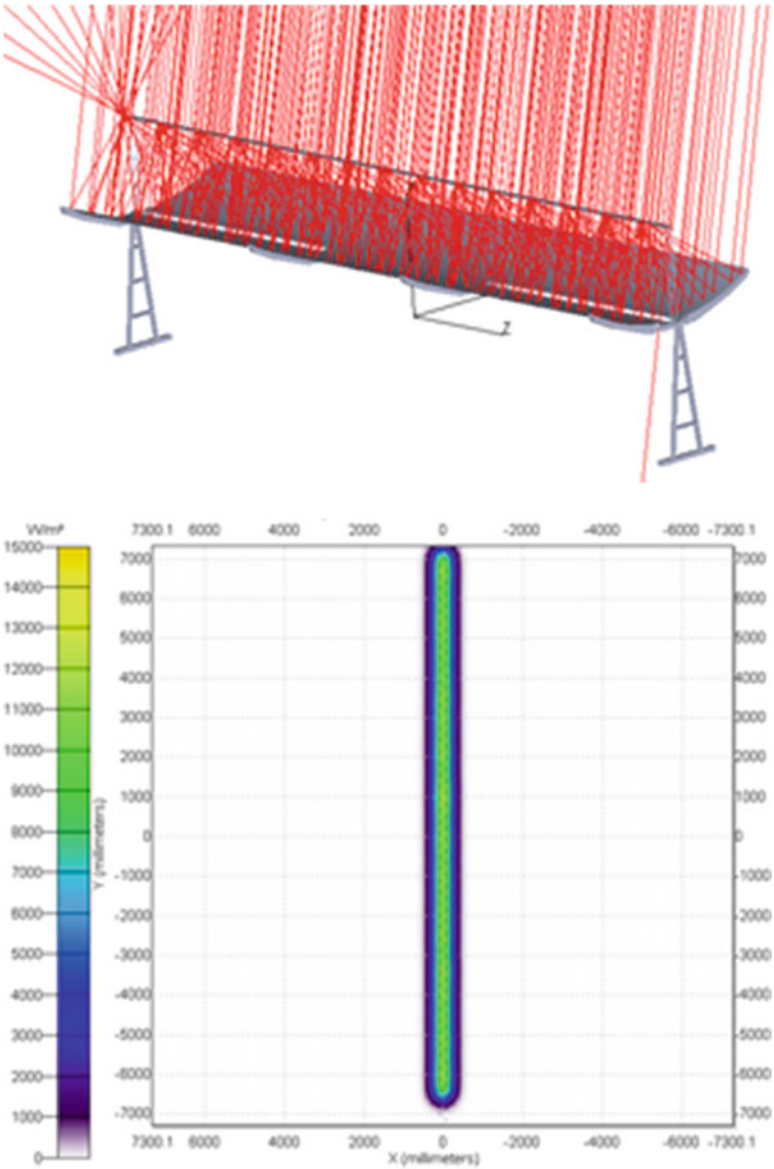

Fig. 9 Presentation of concentrated irradiance beam for the longest day of the year, system with regular sun tracking

References

Bakos, G.C.: Design and construction of a two-axis sun tracking system for parabolic trough collector (PTC) efficiency improvement [Revue]. Renew. Energy. **31**, 2411–2421 (2006)

Boudghene Stambouli, A.: Algerian renewable energy assessment: the challenge of sustainability [Revue]. Energy Policy. (2010). doi:10.1016/j.enpol.2010.10.005

Chausseriau, J.-M.: Conversion thermique du rayonnement solaire [Ouvrage]. Dunod, Paris (1984)

Duffie, J., Beckman, W.: Solar Engineering of Thermal Processes [Ouvrage]. Wiley, Hoboken (1991)

Fernandez-Garcıa, A., Zarza, E., Valenzuela, L., Perez, M.: Parabolic-trough solar collectors and their applications [Revue]. Renew. Sust. Energ. Rev. **14**, 1695–1721 (2010)

Gama, A., Larbes, C., Malek, A., Yettou, F., Adouane, B.: Design and realization of a novel sun tracking system with absorber displacement for parabolic trough collectors [Revue]. J. Renewable Sustainable Energy. **5**, 033108 (2013). doi:10.1063/1.4807476

Kalogirou, S.A.: Design and construction of a one-axis sun-tracking system [Revue]. Sol. Energy. **57**, 465–469 (1996)

Crystal Growth Analysis of R134a Clathrate with Additives for Cooling Applications

Sayem Zafar, Ibrahim Dincer, and Mohamed Gadalla

1 Introduction

The recent global trend has changed from rudimentary energy production or rejection to precisely manage and absorb energy. The energy management is a challenge that needs to be dealt with in order to achieve the goal of sustainable growth. In order to improve the performance of energy systems, more effective tools need to be utilized (Rosen and Dincer 1997). Thermal energy storage (TES) is one such tool that can be applied to manage the energy. TES refers to the storage of heat by increasing or decreasing the temperature of a substance or by changing its phase (Dincer and Rosen 2002).

The most common phase change material in use today for cooling is water. Water changes its phase at 273 K at atmospheric pressure, which means that water has to be taken to 273 K, from ambient temperature, to make it change its phase. However, it would be beneficial to have a material that can change its phase above that temperature so the amount of work to be done gets reduced. Research has shown that refrigerant clathrates can be used for cooling applications where phase change is desired above freezing (Mori and Isobe 1991). Clathrates tend to form when gas molecules get trapped in the water molecule cage under low temperature and high pressure (George 1989; Sloan 1990). Refrigerant clathrates can be used for active as well as passive cooling applications and hence are considered more

S. Zafar (✉) • I. Dincer
Faculty of Engineering and Applied Science, University of Ontario Institute of Technology, 2000 Simcoe Street North, Oshawa, ON L1H 7K4, Canada
e-mail: sayem.zafar@uoit.ca; ibrahim.dincer@uoit.ca

M. Gadalla
Department of Mechanical Engineering, American University of Sharjah, Sharjah, UAE
e-mail: mgadalla@aus.edu

© Springer International Publishing AG, part of Springer Nature 2018

F. Aloui, I. Dincer (eds.), *Exergy for A Better Environment and Improved Sustainability 2*, Green Energy and Technology,
https://doi.org/10.1007/978-3-319-62575-1_81

effective compared with other types of PCMs (Bi et al. 2004; Inaba 2000). Refrigerant clathrates have high heat of fusion and high density which allows them to store more energy per unit volume. Refrigerant clathrates are no more toxic than the base refrigerant, so the existing systems can be utilized to contain them.

Many refrigerants form clathrates, but only a handful are in commercial use. Several chlorofluorocarbons (CFCs), hydrochlorofluorocarbons (HCFCs), and hydrofluorocarbons (HFCs) can form clathrates of refrigerant (Eslamimanesh et al. 2011). For use in cold thermal energy storage system, the refrigerant clathrate should form between temperature ranges from 278 to 285 K (Guo et al. 1996). CFCs are forbidden due to stratospheric ozone layer depletion concerns which leave the hydrochlorofluorocarbon and hydrofluorocarbons to be used for PCM. Refrigerant clathrates of R134a show they can be effective in their role as cold thermal energy storage through phase change (Guo et al. 1996).

PCMs based on refrigerant clathrates have poor thermal transport properties. To make refrigerant clathrates as effective PCMs, additives of different materials have been studied. For instance, adding calcium hypochlorite or benzenesulfonic acid sodium salt improved the cold energy storage capacity and the cold energy transfer rate of R141b based clathrate (Bi et al. 2006). Adding alcohol in R134a-based clathrate has also been studied, which shows it accelerates the cool storage rate and eliminates the floating clathrate during the hydration process (Wua and Wangb 2012).

Metallic nanoparticles have also been added to study the improvement in thermal transport properties. Studies show that even a small fraction of nanoparticles of low thermal conductivity metallic oxides can favorably increase the thermal conductivity of pure a substances, such as water (Murshed et al. 2009; Duangthongsuk and Wongwises 2009). Even for organic compounds such as monoethylene glycol and paraffin fluids, copper oxide nanoparticles can improve the thermal conductivity (Moghadassi et al. 2010). Addition of pure copper nanoparticles in ethylene glycol increases the thermal conductivity by 40% (Eastman et al. 2001). For the refrigerant hydrate, nanoparticles of copper are studied which shows that the heat transfer increases with the addition of nanoparticles of copper (Lia et al. 2006).

This paper describes the experimental investigation that is conducted to test the thermal behavior of R134a clathrates with and without additives. The refrigerant clathrate and additives are studied as phase change materials (PCMs) for cooling applications. The study is focused on the charging capabilities of the PCM while its behavior is analyzed and evaluated. The paper discusses the crystal growth time of R134a clathrate with different proportions of refrigerant. It also studies the effect on crystal growth time when selected additives are added in the R134a clathrate.

2 Analysis

The general energy and exergy balance equations for the PCM charging is described in this section. Charging is described as the process of solidification where the PCM gives away the heat during this process.

For charging the PCM, mass balance for the charging fluid can be described as follows:

$$(m_{\mathrm{PCM}})_{\mathrm{i}} = (m_{\mathrm{PCM}})_{\mathrm{f}} \tag{1}$$

where subscripts "i" for initial and "f" for final.

For water, the mass balance becomes

$$(m_{\mathrm{water}})_{\mathrm{i}} = (m_{\mathrm{water}})_{\mathrm{f}} \tag{2}$$

Energy balance can be described as follows:

$$\begin{aligned}(m\Delta h)_{\mathrm{bath}} &= Q_{\mathrm{sur}} + Q_{\mathrm{heater}} - Q_{\mathrm{coil}} \\ (m\Delta h)_{\mathrm{PCM}} &= Q_{\mathrm{bath}}\end{aligned} \tag{3}$$

where "sur" is referring to heat loss to the surrounding and "coil" for refrigeration coil.

The entropy balance is written as follows:

$$(m\Delta s)_{\mathrm{bath}} = \frac{Q_{\mathrm{sur}}}{T_0} + \frac{Q_{\mathrm{heater}}}{T_0} - \frac{Q_{\mathrm{coil}}}{T_0} \tag{4}$$

$$(m\Delta s)_{\mathrm{PCM}} = \frac{Q_{\mathrm{bath}}}{T_0} \tag{5}$$

Also, the exergy balance can be written as

$$(m\Delta ex)_{\mathrm{bath}} = (m\Delta h)_{\mathrm{bath}} - T_0(m\Delta s)_{\mathrm{bath}} \tag{6}$$

$$(m\Delta ex)_{\mathrm{PCM}} = (m\Delta h)_{\mathrm{PCM}} - T_0(m\Delta s)_{\mathrm{PCM}} \tag{7}$$

3 Experimental Setup and Procedure

For the experiments, a cold constant temperature bath is used as a constant temperature source. Refrigerant, water, and the desired additive are mixed in a pressurized glass tube. The glass tube, that can sustain high pressure, is used with a mounted pressure gauge and an access valve to fill the refrigerant. The tube is comprehensively tested for leaks and measures are taken to make sure there are no

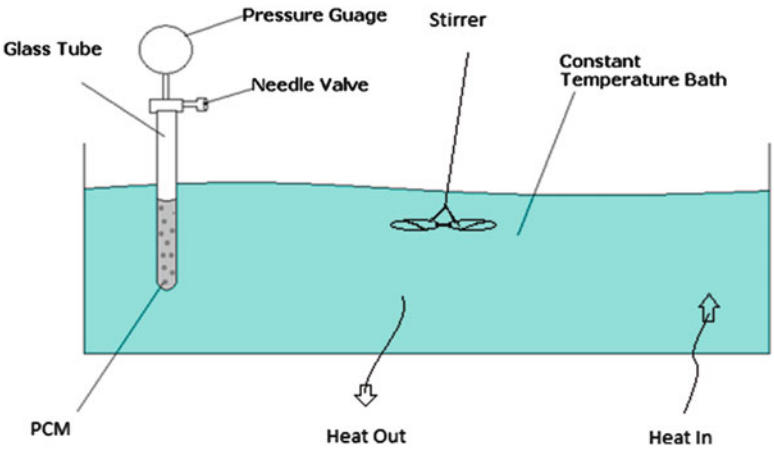

Fig. 1 Schematic diagram of the proposed PCM testing system

leaks. It is important to use a glass tube since the onset of phase change needs to be observed visually. The refrigerant clathrate with additive, named PCM, are formed in glass tubes. The tubes are submerged in the constant temperature water bath for which the temperature is set at 3°. The schematic diagram of the experimental layout is shown in Fig. 1.

The constant temperature bath works by providing cold energy and heat simultaneously to the distilled water to maintain its temperature at 3°. A refrigeration system with cooling coils around the water bath pumps out the heat. A controller constantly monitors the water temperature in the bath while it continues to provide the desired heat to maintain the temperature at 3°. A stirrer is also used which circulates the water in the bath to keep a homogeneous temperature distribution within the water bath. With it, the water near the hot or cold source would change its temperature, while the water away from the source would see its effect later.

4 Results and Discussion

Experiments are conducted to measure the onset and end-set time for R134a clathrate at different proportions. Crystal growth time is important to determine as it yields the total energy used to form the PCM. Low crystal growth time means low energy while increased time means large amount of energy required to form the PCM. Experiments are conducted to determine the onset and end-set time when additives are used with the R134a clathrate. Refrigerant R134a is mixed with distilled water at 25%, 30%, 35%, and 40%. After figuring out the most appropriate percent composition for refrigerant clathrate, additives are included to see the improvement in the crystal growth time. For the additives, ethanol, sodium

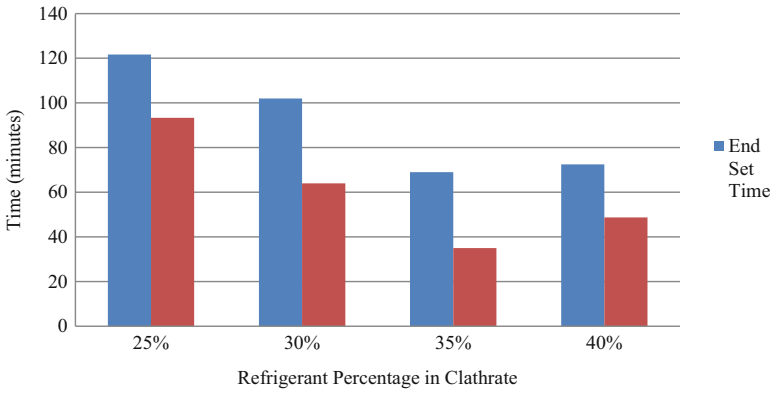

Fig. 2 R134a clathrate crystal growth time for onset and end set at different refrigerant mass proportions

chloride, magnesium nitrate hexahydrate, copper, and aluminum are used. Additives are added from 1% by mass to 5% by mass to see their effect on crystal growth time.

Figure 2 shows the R134a clathrate crystal growth time formation for different refrigerant mass proportions. Onset time is the time clathrate takes to start freezing, while end set is when the process of freezing is complete. It is to be noted that complete freezing does not necessarily mean everything in the tube is frozen. For some percentages, either the water or the refrigerant remains liquid and does not freeze at 3 °C. Refrigerant proportions of 25–40% are shown in the figure. Below 25%, a large proportion of the water remains unmixed while above 40%, the refrigerant does not have enough water to mix with. The graph shows that the crystal growth time reduces until 35% refrigerant mass ratio and then it starts to increase. From the tests, it is concluded that 35% is the most optimal mass percentage for refrigerant since it takes the least amount of time.

Figure 3 shows the results of the tests conducted on R134a clathrate with copper particles as additives. Copper mass percentage is varied from 1% to 5% while their onset and end-set time of the crystal growth is recorded. The onset time with copper particles is found to be the same for all five cases at 10 min. The end-set time varied from 60 min for 1% additive to 90 min for 5% additive. The onset time remains the same since the same amount to additive interacts to initiate the solidification process. The end-set time increases with the increase in additive percentage. Copper particles settle at the bottom of the tube and the ones that are present in the clathrate are not evenly distributed. This causes clathrate to remain liquid in some sections while frozen in the other. The heat transfer process is slow in the frozen region; hence the time to completely solidify the mixture increases. It is important to note that end-set time, unlike onset time where the freezing is obvious, is difficult to note as the change may not be visible.

Figure 4 shows the test results for R134a clathrate crystal growth formation time with magnesium nitrate hexahydrate as additive. The average onset time with

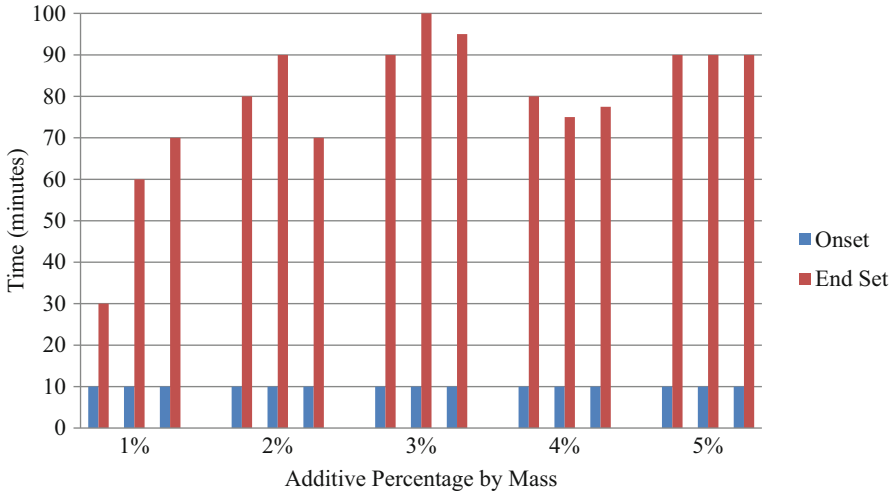

Fig. 3 Crystal growth time for clathrate formation at 3 °C with copper additive at different additive proportions

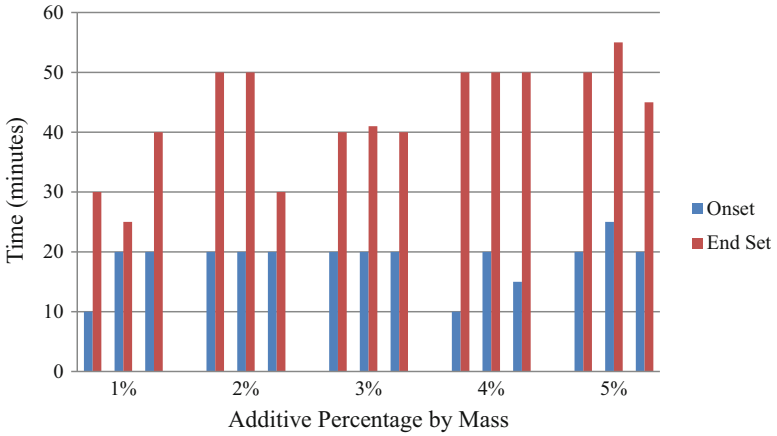

Fig. 4 Crystal growth time for clathrate formation at 3 °C with $MgNO_3$ at different mass proportions

magnesium nitrate hexahydrate is found to be 20 min. The end-set time varied from 30 min for 1% additive to 50 min for 5% additive. The onset and end-set times increase slightly with the increase in additives. At low additive ratios and for onset, magnesium nitrate hexahydrate improves the clathrate formation time because of its slightly better thermal conductivity compared to water. However, end-set time for high additive proportions tends to increase due to the nature of salts to resist clathrate formation.

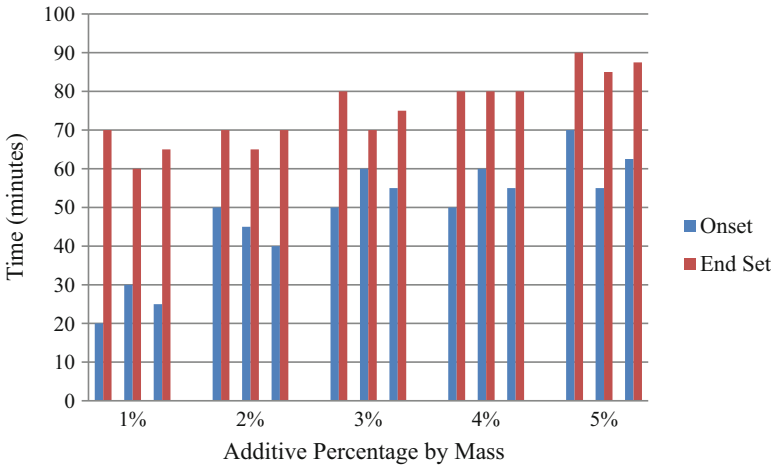

Fig. 5 Crystal growth time for clathrate formation at 3 °C with ethanol for different mass proportions

Figure 5 shows results for R134a clathrate-crystal growth time with ethanol. The onset time with ethanol increased from 25 to 60 min. The end-set time varied from 65 min for 1% additive to 85 min for 5% additive. The onset and end-set time increases with the increase in additives. Although the onset time for ethanol is high, the end set is achieved rather fast once the solidification begins. Since ethanol is liquid, it mixes well with the clathrate; hence the heat transfer is fairly uniform.

Figure 6 shows the results of the tests conducted on R134a clathrate with aluminum particles as additives. The onset time with aluminum particles is found to be 11 min for all five cases. The end-set time varied from 65 min for 1% additive to 90 min for 5% additive. Aluminum, like copper particles, settles at the bottom of the tube and the ones that are present in the clathrate are not evenly distributed. The clathrate remains liquid in some sections while frozen in the other. In the frozen section, the heat transfer process is slow which increases the solidification time.

Figure 7 shows the test results of the crystal growth formation time for sodium chloride as additive in R134a clathrate. The average onset time varied at 40 min for 1% additive to 65 min for 3% additive. The end-set time varied from 80 min for 1% additive to 110 min for 3% additive. For sodium chloride, the R134a clathrate did not form for higher additive percentages. The onset and end-set times increase with the increase in additive proportion. Sodium chloride increased the onset and end-set time for all the tested proportions. Sodium chloride has lower thermal conductivity than the water. It also slows the clathrate formation since salt particles interact with the water molecules preventing it to form the inclusion compound with the refrigerant (clathrate). Sodium chloride at 4% and 5% as additive does not form R134a clathrate.

Figure 8 shows the average onset time of the crystal growth for the five tested additives. The graph shows that copper and aluminum have the lowest onset time

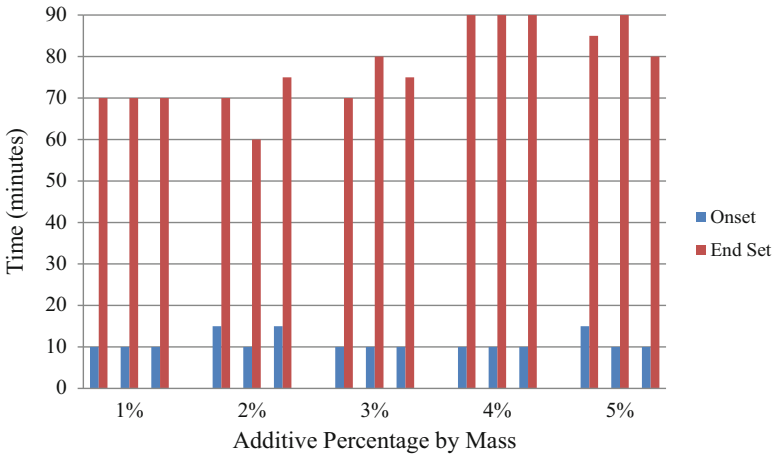

Fig. 6 Crystal growth time for clathrate formation at 3 °C with aluminum for different mass proportions

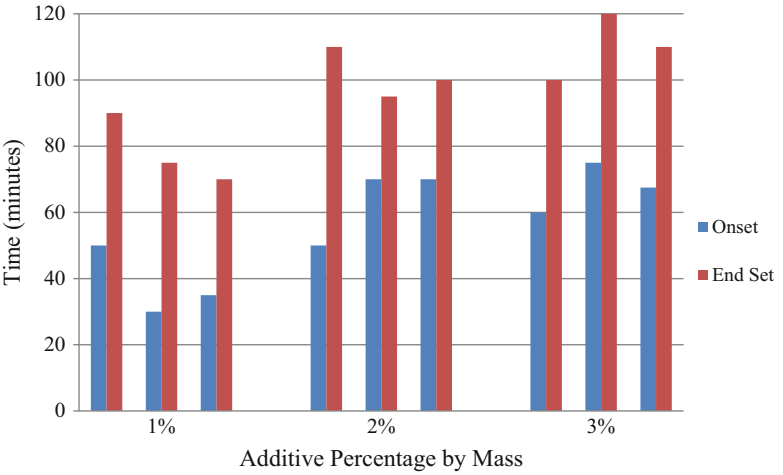

Fig. 7 Crystal growth time clathrate formation at 3 °C with NaCl for different mass proportions

followed by magnesium nitrate hexahydrate, ethanol, and then sodium chloride. For 1% additive by mass, the onset time decreased by 25 min for copper and aluminum when compared to refrigerant clathrate without additive. Magnesium nitrate hexahydrate decreased the time by 20 min, while ethanol reduced it by 10 min. Sodium chloride maintained the onset time. At high additive concentrations, onset time decreased by 25 min for copper and aluminum. For magnesium nitrate hexahydrate, the improvement is of 15 min. For ethanol, the clathrate formation time increased to above 25 min, while for sodium chloride, the increase is of 30 min.

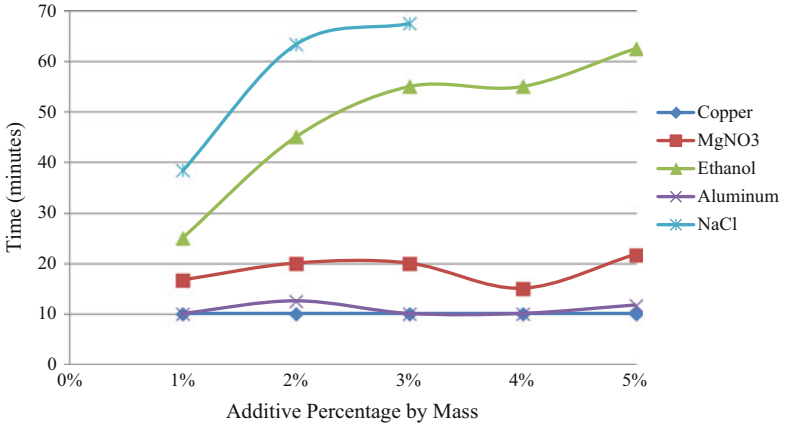

Fig. 8 Clathrate crystal growth onset time comparison for different used additives

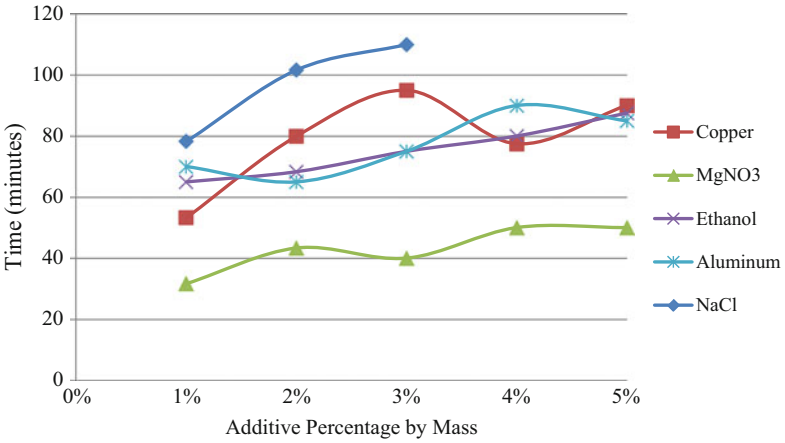

Fig. 9 Clathrate crystal growth end-set time comparison for different used additives

Figure 9 shows the average end-set time for R134a clathrate crystal growth for five tested additives. The graph shows that magnesium nitrate hexahydrate has the lowest end-set time followed by copper, ethanol, aluminum, and then sodium chloride. For 1% additive by mass, the end-set time decreased by 35 min for magnesium nitrate hexahydrate and 15 min for copper. Ethanol and aluminum maintained the end-set time relatively the same as the base R134a clathrate. Sodium chloride increased the end-set time by 10 min. At high additive concentrations, the end-set time decreased by 20 min for magnesium nitrate hexahydrate. All the other additives either maintained the end-set time or increased it.

5 Conclusions

The paper looks at the crystal growth time for R134a clathrate at different mass proportions and with five different additives. Formation of R134a clathrate is tested due to their possible use in active as well as passive cooling applications. First set of tests are conducted to figure out the best refrigerant proportion in the R134a and water mixture. Further tests are conducted with mixing five different additives in the base R134a clathrate. The additive mass proportion is varied from 1% to 5% at 1% interval. Test results are analyzed for onset and end-set time of the crystal growth durations to determine when the solidification starts and when it ends at the prescribed water bath temperatures. The current experimental results for chosen sets of additives and operating conditions confirm the following closing remarks:

- A 35% refrigerant requires the lowest time to form the clathrate.
- Copper, aluminum, magnesium nitrate hexahydrate, and ethanol decrease the onset time. Sodium chloride increases the onset time when used as an additive.
- Magnesium nitrate hexahydrate forms the clathrate fastest, followed by copper, ethanol, aluminum, and then sodium chloride.
- Magnesium nitrate hexahydrate and copper accelerate the clathrate formation, while aluminum and ethanol do not affect the crystal growth time much.
- Sodium chloride delays the clathrate formation time while at 4% and 5% sodium chloride mass percentage, it does not allow clathrate formation.
- Increasing the additive proportion does not help accelerate the process, while in some cases, it decelerates the crystal growth.

Nomenclature

CFC	Chlorofluorocarbons
ex	Specific exergy (J/kg)
HCFC	Hydrochlorofluorocarbons
HFC	Hydrofluorocarbons
m	Mass (kg)
PCM	Phase change material
Q	Heat (J)
s	Specific entropy (J/kg)
T	Temperature (K)
t	Time (s)
TES	Thermal energy storage
Subscripts	
0	Ambient
c	Charging
f	Final
i	Initial
sur	Surrounding

References

Bi, Y.H., Guo, T.W., Zhu, T.Y., Fan, S.S., Liang, D.Q., Zhang, L.: Influence of volumetric-flow rate in the crystallizer on the gas-hydrate cool-storage process in a new gas-hydrate cool-storage system. Appl. Energy. **78**, 111–112 (2004)

Bi, Y.H., Guo, T.W., Zhu, T.Y., Zhang, L., Chen, L.: Influences of additives on the gas hydrate cool storage process in a new gas hydrate cool storage system. Energ. Conver. Manage. **47**, 2974–2982 (2006)

Dincer, I., Rosen, M.A.: Thermal Energy Storage – Systems and Applications. Wiley, Chichester (2002)

Duangthongsuk, W., Wongwises, S.: Measurement of temperature dependent thermal conductivity and viscosity of TiO2-water nanofluids. Exp. Thermal Fluid Sci. **33**, 706–714 (2009)

Eastman, J.A., Choi, S.U.S., Li, S., Yu, W., Thompson, L.J.: Anomalously increased effective thermal conductivities of ethylene glycol-based nanofluids containing copper nanoparticles. Appl. Phys. Lett. **78**, 718–720 (2001)

Eslamimanesh, A., Mohammadi, A.H., Richon, D.: Thermodynamic model for predicting phase equilibria of simple clathrate hydrates of refrigerants. Chem. Eng. Sci. **66**, 5439–5445 (2011)

George, A.: Chapter 1. Phase change thermal storage materials. In: Guyer, C. (ed.) Hand Book of Thermal Design. McGraw Hill Book Co., US (1989)

Guo, K.H., Shu, B.F., Zhang, Y.: Transient behavior of energy charge– discharge and solid–liquid phase change in mixed gas-hydrate formation. In: Wang, B.X. (ed.) Heat Transfer Science and Technology, pp. 728–733. Higher Education Press, Beijing (1996)

Inaba, H.: New challenge in advanced thermal energy transportation using functionally thermal fluids. Int. J. Thermal Sci. **39**, 991–1003 (2000)

Lia, J., Liangb, D., Guob, K., Wangc, R., Fanb, S.: Formation and dissociation of HFC134a gas hydrate in nano-copper suspension. Energ. Conver. Manage. **47**, 201–210 (2006)

Moghadassi, A.R., Hosseini, S.M., Henneke, D.E.: Effect of CuO nanoparticles in enhancing the thermal conductivities of monoethylene glycol and paraffin fluids. Ind. Eng. Chem. Res. **49**, 1900–1904 (2010)

Mori, Y.H., Isobe, F.: A model for gas hydrate formation accompanying direct-contact evaporation of refrigerant drops in water. Int. Commun. Heat Mass Transfer. **18**, 599–608 (1991)

Murshed, S.M.S., Leong, K.C., Yang, C.: A combined model for the effective thermal conductivity of nanofluids. Appl. Therm. Eng. **29**, 2477–2483 (2009)

Rosen, M.A., Dincer, I.: On exergy and environmental impact. Int. J. Energy Res. **21**, 643–654 (1997)

Sloan, E.D.: Clathrate Hydrates of Natural Gases. Marcel, New York (1990)

Wua, J., Wangb, S.: Research on cool storage and release characteristics of R134a gas hydrate with additive. Energ. Buildings. **45**, 99–105 (2012)

Modeling, Simulation, and Optimization of an Irrerversible Solar Absorption Cooling Plant in Transient Regime

Boukhchana Yasmina, Fellah Ali, and Ben Brahim Ammar

1 Introduction

Heat-absorption cooling systems have been the subject of considerable research during the last two decades (Stolk 1980; Suri and Ayyash 1982; Wijeysundera 1996; Ayyash et al. 1985; Charia et al. 1991; Gordon and Choon 1995; Bejan et al. 1995; Vargas et al. 1996). The new interest in this class of refrigeration systems is due to the development of new technologies in renewable energy sources such as solar and waste heat. On the other hand, the improvement and optimization in the design of heat-driven refrigerators has become crucial. They need to compete with conventional refrigeration systems in modern cooling installations. Additionally, the utilization of low-grade heat sources is stressed by economic considerations and by the need for low-environmental-impact refrigeration systems.

From the thermodynamics point of view, a large amount of fundamental research has been carried out (Bejan et al. 1995; Vargas et al. 1996; Bejan 1988a, b; 1989) to optimize thermal systems. In these studies, the method of entropy-generation minimization, also known as the method of finite-time thermodynamics, was used. The method consists of the simultaneous application of heat transfer and thermodynamic principles in order to pursue realistic models that take into account the inherent irreversibility of heat, mass, and fluid flow. The method has been

B. Yasmina (✉) • B.B. Ammar
Research Unit of Applied Thermodynamics, Department of Chemical and Processes Engineering, National School of Engineers of Gabes, University of Gabes, St Omar Ibn El-Khattab, 6029 Gabes, Tunisia
e-mail: boukhchana.yasmina@gmail.com

F. Ali
Research Unit of Applied Thermodynamics, Technology Department, High Institute of Applied Sciences and Technology, University of Gabes, 6029 Gabes, Tunisia

© Springer International Publishing AG, part of Springer Nature 2018

F. Aloui, I. Dincer (eds.), *Exergy for A Better Environment and Improved Sustainability 2*, Green Energy and Technology,
https://doi.org/10.1007/978-3-319-62575-1_82

gaining more importance in the context of shape and structure in engineering and nature.

The objective functions in finite time thermodynamics are often pure thermodynamic parameters including efficiency, entropy production, cooling load, heating load, and coefficient of performance. The results obtained for various thermodynamic cycle analyses using FTT are closer to real device performance than those using classical thermodynamics (Van and Chen 1989; Chen and Yan 1989; Denton 2002; Feidt 2010). Many studies for the performance optimization of refrigerators based on endoreversible and irreversible models have been performed by considering various objective functions.

An extensive study on the theory of irreversible heat transfer refrigeration systems has been done recently (Bejan 1989). Other works give formulae for the coefficient of performance (COP) and cooling rate of an endoreversible refrigeration machine (Agrawal and Menon 1993) and also when maximum specific cooling load is required (Wu 1995). An analytical model for predicting general performance characteristics of an irreversible Carnot cycle machine has been achieved recently (Feidt et al. 2005, 2007). It may be applied to direct or reverse cycle machines. The optimization procedure focused on several objectives, namely, maximum useful effect, minimum consumption, or minimum total dissipation. Several operational and dimensional constraints were introduced in the model. Internal and external irreversibilities of the cycle are also taken into account by two terms that correspond to internal and, respectively, total entropy generation. The internal entropy generation term has been introduced as a parameter in the model so that a more general approach than the irreversibility ratio used in other papers (Sieniutycz and Salamon 1990; Calvo Hernández et al. 2004; El Haj Assad 2000) has been accomplished. The approach concerning the entropic analysis of machines and processes (Bejan 1988a, b; Petrescu et al. 2002; Feidt 1996) becomes an important tool for the design of real-operating machines.

Nevertheless, all those studies focus on the systems' steady-state properties and ignore completely their dynamic behavior.

Steady-state models are useful under many conditions although under strongly dynamic conditions that are often seen in real-life operation, these models can become unacceptably inaccurate (Browne and Bansal 2002). However, steady-state models do not provide time-dependent information on the thermal behavior of absorption refrigerators and are therefore not suitable for transient system simulations.

Research on dynamic system behavior was carried out for absorption refrigerators. Although, Vargas et al. (1998, 2000) studied a transient endoreversible model of a heat-driven refrigeration plant driven by a fuel burning heater. Their optimization is done from the point of view of the heat that drives the cycle. Recently, Hamed et al. (2012) conducted a thermodynamic transient regime simulation of an endoreversible solar-driven absorption refrigerator to find the optimal conditions of a solar-driven absorption refrigerator. In contrast, the model presented in this work allows the simulation of the dynamic absorption refrigerator behavior. It extends the range of applicable models for transient system simulations, where the time

constants of the refrigerator significantly influence the system performance. The dynamic model of an irreversible absorption refrigerator allows the simulations of its transient behavior for changing input conditions or design parameters. This is important because absorption refrigerators usually have a high thermal mass, consisting of their internal heat exchangers, the absorbing solution and the externally supplied heat transfer media.

In the present article, we propose to carry out the optimization of an irreversible absorption refrigeration system that uses a solar collector as the high-temperature heat source. The optimization is done from the point of view of the heat that drives the cycle – in other words, the heat transfer rate received from the solar collector to the generator. The challenge is to minimize the time required to reach a certain operation temperature in the refrigerated space, finding an optimum heat rate and investigating the effect of time in solar collector stagnation temperature and collector temperature. This issue becomes more important in large-scale cooling applications, in which the thermal inertia of the refrigerated space becomes very large.

Nomenclature

A	Area, (m^2)
a, b	Constant in Eq. (5)
B	Dimensionless collector size parameter, Eq. (17)
C	Specific heat, (kJ/kg K)
G	Irradiance on collector surface, (W/m^2)
M	Mass of air in the refrigerated space, (kg)
Q	Heat transfer rate, (W)
S	Entropy generation rate, (kJ/K)
t	Time, (s)
T	Temperature, K
U	Global heat transfer coefficient, (W/m^2 K)
Greek letters	
τ	Dimensionless temperature
θ	Dimensionless time
γ	Dimensionless thermal conductance
η	Efficiency of a flat-plate collector
Subscripts	
0	Ambient
air	Air
C	Reversible compartment
H	Heat source
L	Refrigerated space
load	Cold space thermal load
opt	Optimum
SC	Solar collector
set	Set point
st	Collector stagnation temperature

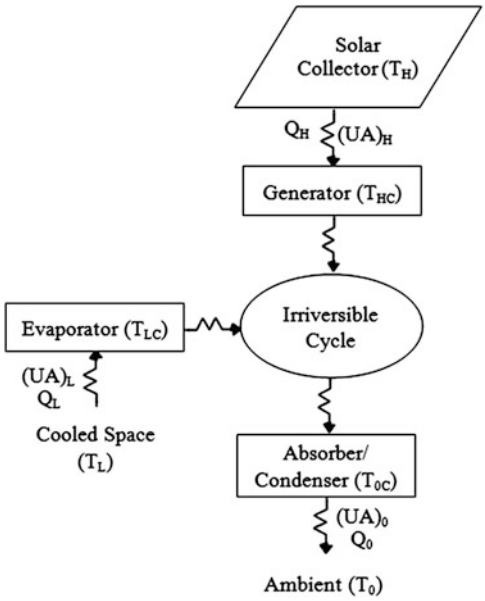

Fig. 1 The heat transfer irreversible model of a solar-driven absorption refrigeration system

2 Solar System and Mathematical Model

2.1 Solar System

A solar-operated absorption refrigeration system is made of a solar collector and a refrigeration cycle as shown in Fig. 1. The system differs from a customary fossil-fuel-fired unit in that the energy supplied to the generator is directly from the solar collector. This arrangement has the advantage of making high-temperature thermal energy available to the generator.

In this analysis, the collector adopted is a flat-plate collector. Flat-plate solar collectors are commonly used in solar space heating. It is economically adopted when the same collector is used for both heating and cooling spaces. However, and regarding the relatively low temperatures attainable, only a few practical applications are available in flat-plate solar-operated cooling processes. One of the most promising schemes is the utilization of an absorption refrigeration cycle with solar energy serving as the source of heat to operate the generator.

The primary components of an absorption refrigeration system are a generator, an absorber, a condenser, and an evaporator. The cycle has negligible work input. The cycle is driven by the heat transfer rate Q_H received from the source temperature T_H, which is determined by the operation temperature of the generator. The refrigeration load Q_L is removed from the refrigerated space, at T_L, and the heat transfer rate Q_0 is rejected to the ambient, T_0.

In this analysis, it is assumed that there is no heat loss between the solar collector and the generator and no work exchange occurs between the refrigerator and its environment. The work input required by the solution pump also is negligible relative to the energy input to the generator and, consequently, it is often neglected for the purposes of analysis.

2.2 The Transient Model

A mathematical model is developed that combines empirical correlations, classical thermodynamics principles, and heat transfer law. The proposed model is then utilized to simulate numerically the system transient and steady-state responses under different operating conditions. The irreversible model takes into account the external and internal irreversibilities, which are fundamental features that will be present in the design of actual absorption refrigerators, no matter how complicated these designs may be.

The instantaneous heat transfer interactions obey the linear heat-transfer law, "Newton's heat transfer law," and are given by

$$Q_{\mathrm{H}} = (UA)_{\mathrm{H}}(T_{\mathrm{H}} - T_{\mathrm{HC}}) \tag{1}$$

$$Q_{\mathrm{L}} = (UA)_{\mathrm{L}}(T_{\mathrm{L}} - T_{\mathrm{LC}}) \tag{2}$$

$$Q_0 = (UA)_0(T_{0C} - T_0) \tag{3}$$

The generator heat input Q_{H} could be estimated by the following expression:

$$Q_{\mathrm{H}} = \eta_{\mathrm{SC}} A_{\mathrm{SC}} G \tag{4}$$

where $A_{\mathrm{S.C}}$ represents the collector area, G is the irradiance at the collector surface, and η_{SC} stands for the collector efficiency.

The efficiency of a flat-plate collector can be calculated as (Bejan et al. 1995; Sokolov and Hershgal 1993a, b)

$$\eta_{\mathrm{SC}} = a - b(T_{\mathrm{H}} - T_0) \tag{5}$$

where a and b are two constants that can be calculated, as discussed by Sokolov and Hershgal (Bejan et al. 1995; Sokolov and Hershgal 1993). Equation (5) can be rewritten by introducing the collector stagnation temperature T_{st} as follows:

$$\eta_{\mathrm{SC}} = b(T_{\mathrm{St}} - T_{\mathrm{H}}) \tag{6}$$

where T_{st} (for which $\eta_{\mathrm{S.C}} = 0$) is given by

$$T_{St} = T_0 + a/b \tag{7}$$

The equation for heat input Q_H can be rewritten by combining Eqs. (4) and (6) as follows:

$$Q_H = A_{SC} G b (T_{st} - T_H) \tag{8}$$

From the first law of thermodynamics

$$Q_H + Q_L - Q_0 = 0 \tag{9}$$

The refrigerator is considered to be irreversible (include external and internal irreversibilities). Internal irreversibilities due to heat transfer, throttling, mixing, and internal dissipation of the working fluid, which are responsible for the entropy generation, are always present in a real heat-driven refrigerator. According to the second law of thermodynamic and the irreversible property of the cycle, we have

$$\frac{dS_{in}}{dt} = \frac{Q_0}{T_{0C}} - \frac{Q_H}{T_{HC}} - \frac{Q_L}{T_{LC}} \tag{10}$$

Generally, it is difficult to model all internal entropy generation sources in order to get an analytical variation law. We have chosen to consider the following approaches (Wijeysundera 1997; Gordon and Ng 2000).

The entropy of the working fluid is represented by using linear variation law with temperature:

$$\frac{dS_{in}}{dt} = \beta_1 (T_{HC} - T_{0C}) + \beta_2 (T_{0C} - T_{LC}) \tag{11}$$

where the parameters β_1 , β_2 are to be estimated by fitting detailed simulation data to predictions.To obtain the best estimates of the parameters β_1 and β_2 from simulated performance data (Boukhchana et al. 2013, 2014), the following least-square procedure is used.

We account for the transient cooling of the refrigerated space by writing the first law:

$$M_{air} C_{v.air} \frac{dT_L}{dt} = (UA)_W (T_0 - T_L) + Q_{load} - Q_L \tag{12}$$

where $(UA)_W (T_0 - T_L)$ accounts for the rate of heat gain from the ambient through the walls of the refrigerated space and Qload is the thermal load or rate of heat generated inside the refrigerated space. By writing the set of Eqs. (1), (2), (3), (4), (5), (6), (7), (8), (9), and (10) for the absorption refrigerator and (12) for the refrigerated room, we take into account the fact that the thermal inertia of the refrigerated space is large enough such that the transient operation of the

refrigerator can be neglected when compared to the time evolution of the temperature inside the refrigerated space.

According to the cycle model mentioned earlier, the rate of entropy generated by the cycle is described quantitatively by the second law as

$$\frac{dS_{\mathrm{Tot}}}{dt} = \frac{Q_0}{T_0} - \frac{Q_{\mathrm{H}}}{T_{\mathrm{H}}} - \frac{Q_{\mathrm{L}}}{T_{\mathrm{L}}} \tag{13}$$

In order to present general results for the system configuration proposed in Fig. 1, dimensionless variables are needed. First, since the thermal conductances (UA)i present in all subsystems i shown in Fig. 1 are commodities in short supply, it makes sense to recognize the thermal conductance inventory (hardware) as a constraint. For example, by selecting the absorption refrigerator system, one may define the total external conductance inventory, UA (hardware), as a design constraint:

$$UA = (UA)_{\mathrm{H}} + (UA)_{\mathrm{L}} + (UA)_0 \tag{14}$$

As a result, for the whole system, dimensionless thermal conductances are defined by

$$\gamma_i = \frac{(UA)_i}{UA} \tag{15}$$

Dimensionless heat transfer and work rates, temperatures, time, and mass are defined by

$$\bar{Q}_{\mathrm{i}} = \frac{Q_{\mathrm{i}}}{UAT_0}, \tau_{\mathrm{i}} = \frac{T_{\mathrm{i}}}{T_0}, \theta = \frac{tUA}{M_{\mathrm{air}}C_{\mathrm{v,air}}} \tag{16}$$

Dimensionless collector size parameter and the rate of entropy generated are defined by

$$B = \frac{A_{\mathrm{SC}}Gb}{UA}, \bar{S} = \frac{S}{M_{\mathrm{air}}C_{\mathrm{v,air}}} \tag{17}$$

In Eqs. (15), (16), and (17), subscripts i refers to a particular location or subsystem in the system shown in Fig. 1.

In a dimensionless model, all variables are directly proportional to the actual dimensional ones, as Eqs. (15), (16), and (17) demonstrate. Therefore, this allows for scaling up or down any system with similar characteristics to the system analyzed by the model. Another important aspect is that any dimensionless variable value used in the simulations could represent an entire and numerous set of dimensional values by varying appropriately the parameters in the dimensionless variables definition, which by itself stresses the generality of the dimensionless

model. Physically, the set of results of a dimensionless model actually represent the expected system response to numerous combinations of system parameters (geometry, architecture) and operating conditions (e.g., ambient conditions, mass flow rates), without having to simulate each of them individually, as a dimensional model would require.

The complete set of nondimensional equations for the model, including the absorption refrigerator steady-state equations is as follows:

$$\bar{Q}_{\mathrm{H}} = \gamma_{\mathrm{H}}(\tau_{\mathrm{H}} - \tau_{\mathrm{HC}}) \tag{18}$$

$$\bar{Q}_{\mathrm{L}} = \gamma_{\mathrm{L}}(\tau_{\mathrm{L}} - \tau_{\mathrm{LC}}) \tag{19}$$

$$\bar{Q}_0 = (1 - \gamma_{\mathrm{H}} - \gamma_{\mathrm{L}})(\tau_{0C} - 1) \tag{20}$$

$$\bar{Q}_{\mathrm{H}} = B(\tau_{\mathrm{st}} - \tau_{\mathrm{H}}) \tag{21}$$

$$\bar{Q}_{\mathrm{H}} + \bar{Q}_{\mathrm{L}} - \bar{Q}_0 = 0 \tag{22}$$

$$\frac{d\bar{S}_{\mathrm{in}}}{d\theta} = \frac{\bar{Q}_0}{\tau_{0\mathrm{C}}} - \frac{\bar{Q}_{\mathrm{H}}}{\tau_{\mathrm{HC}}} - \frac{\bar{Q}_{\mathrm{L}}}{\tau_{\mathrm{LC}}} \tag{23}$$

$$\frac{d\bar{S}_{\mathrm{in}}}{d\theta} = \overline{\beta}_1(\tau_{\mathrm{HC}} - \tau_{0\mathrm{C}}) + \overline{\beta}_2(\tau_{0\mathrm{C}} - \tau_{\mathrm{LC}}) \tag{24}$$

$$\frac{d\bar{S}_{\mathrm{tot}}}{d\theta} = \bar{Q}_0 - \frac{\bar{Q}_{\mathrm{H}}}{\tau_{\mathrm{H}}} - \frac{\bar{Q}_{\mathrm{L}}}{\tau_{\mathrm{L}}} \tag{25}$$

$$\frac{d\tau_{\mathrm{L}}}{d\theta} = \gamma_{\mathrm{w}}(1 - \tau_{\mathrm{L}}) + \bar{Q}_{\mathrm{load}} - \bar{Q}_{\mathrm{L}} \tag{26}$$

3 Thermodynamic Optimization

The problem consists of integrating Eqs. (25) and (26) in time and solving the nonlinear system (18), (19), (20), (21), (22), (23), and (24) at each time step. The objective is to minimize the time θ_{set} to reach a specified refrigerated space temperature, τ_{Lset}, in transient operation. To generate the results shown in Figs. 2, 3, 4, 5, 6, and 7, some selected parameters were held constant and others were varied. The numerical method calculates the transient behavior of the system, starting from a set of initial conditions, then the solution is marched in time and checked for accuracy until a desired condition is achieved (temperature set points or steady state). The equations are integrated in time explicitly using an adaptive time step, 4th–5th order Runge–Kutta method (Yang et al. 2005). Newton–Raphson's method with appropriate initial guesses was employed for solving the above set of nonlinear equations.

During the integration of the ordinary differential equations, once the set of fixed parameters $\tau_{\mathrm{H}}, \tau_{\mathrm{st}}, B, \gamma_{\mathrm{H}}, \gamma_{\mathrm{L}}, \gamma_{\mathrm{W}}$ and $\bar{Q}_{\mathrm{load}}$ is defined Eqs. (18) and (18) give τ_{HC}. The system of Eqs. (18), (19), (20), (21), (22), (23), and (24), at each time step of integration of Eqs. (25) and (26), delivers $\bar{Q}_0, \bar{Q}_{\mathrm{L}}, \tau_{0\mathrm{C}}$, and τ_{LC}.

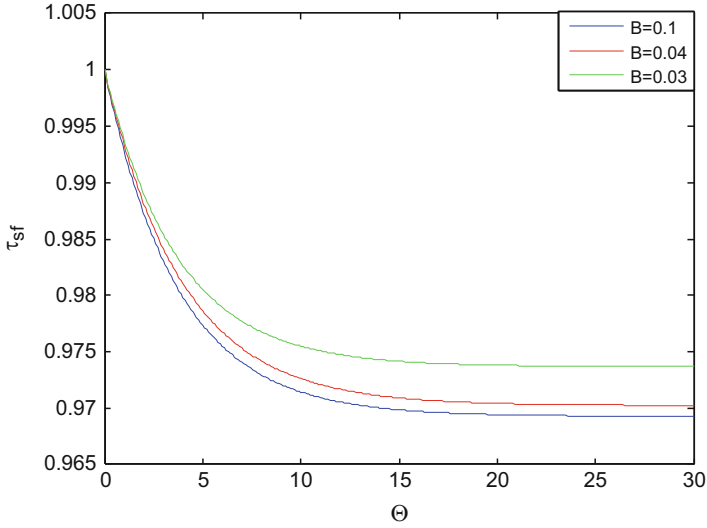

Fig. 2 The behavior refrigeration space temperature, τ_L in time ($\tau_H = 1.3$, $\tau_{st} = 1.6$)

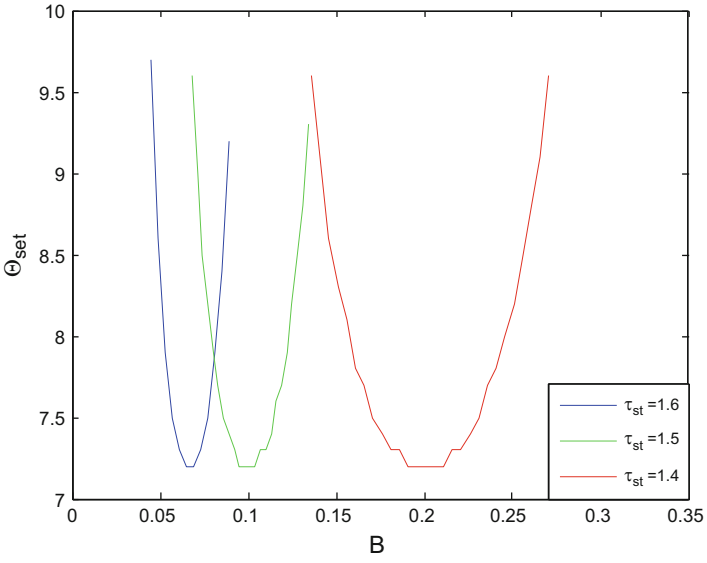

Fig. 3 The effect of dimensionless collector size, B on time set point temperature

To test the model and for conducting the analysis presented in this section, assuming a small absorption refrigeration unit with a low total thermal conductance ($UA = 400$ W/K), we considered a total heat exchanger area $A = 4$ m^2 and an average global heat transfer coefficient $U = 0.1$ kW/m^2 K in the heat exchangers and $U_w = 1.472$ kW/m^2 K across the walls, which have a total surface area

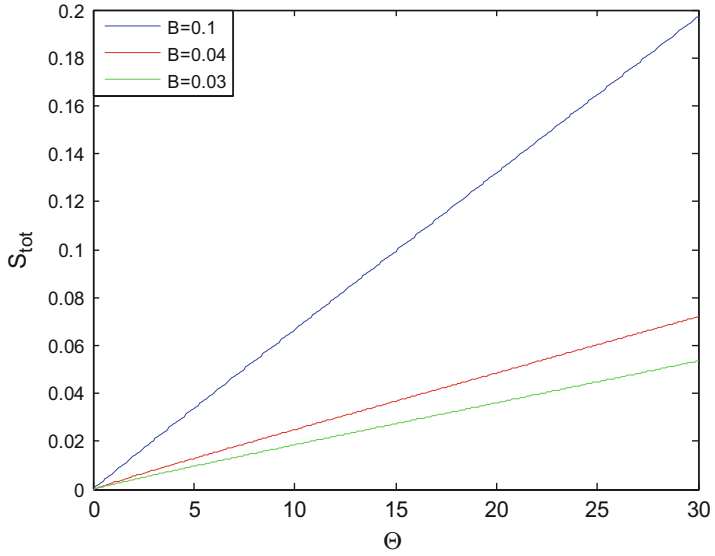

Fig. 4 Transient behavior of total entropy generated during the time ($\tau_H = 1.3$, $\tau_{st} = 1.6$)

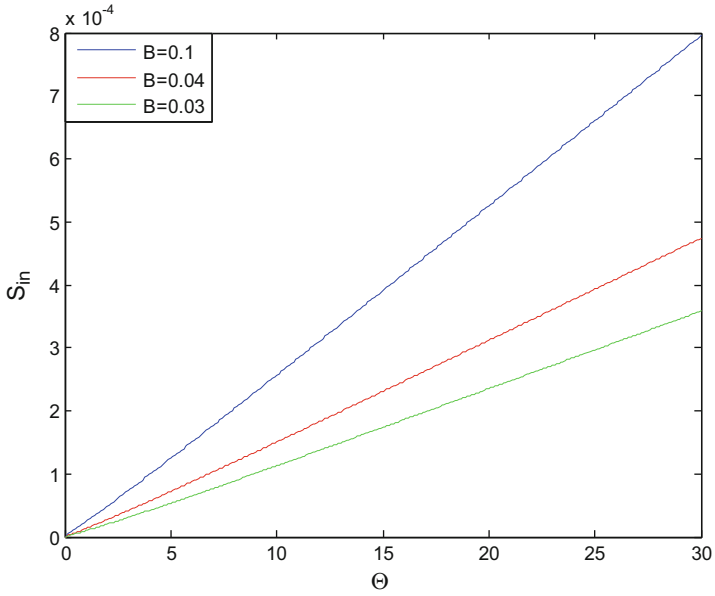

Fig. 5 Transient behavior of internal entropy generated during the time ($\tau_H = 1.3$, $\tau_{st} = 1.6$)

$A_w = 54$ m^2, $T_0 = 25$ °C, and $Q_{load} = 0.8$ kW. Considering a typical air-conditioning application, the refrigerated space temperature to be achieved was established at $T_{L,set} = 16$ °C.

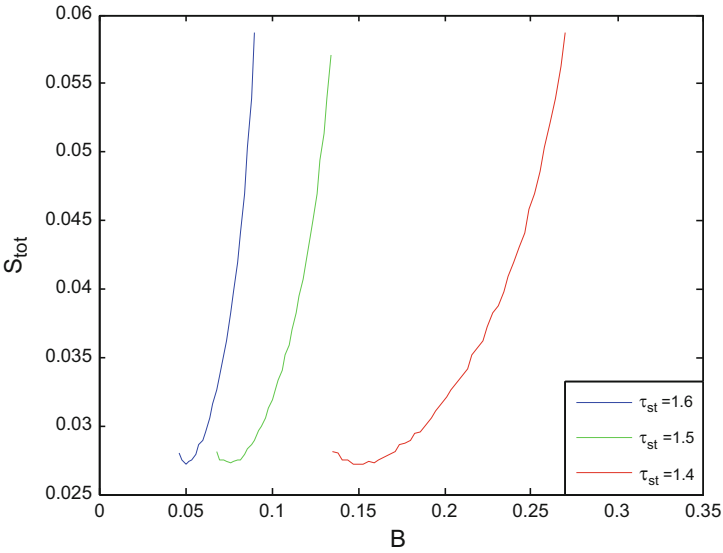

Fig. 6 Total entropy generated to reach a refrigerated space temperature set point temperature

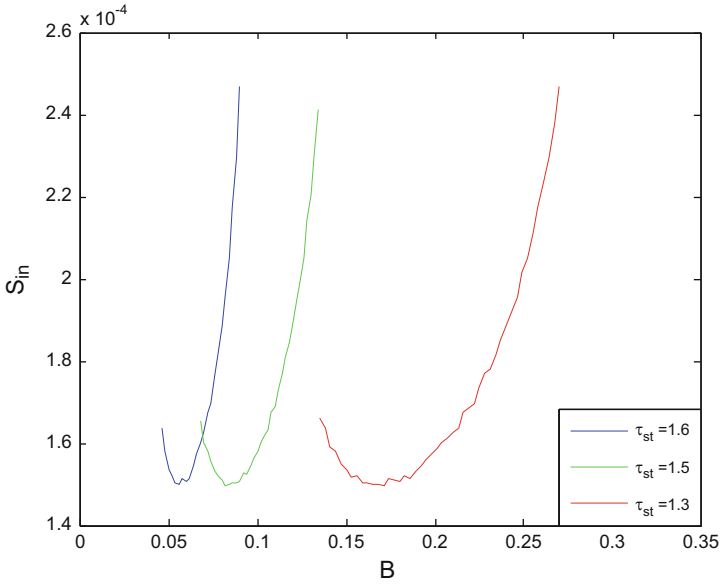

Fig. 7 Internal Total entropy generated to reach a refrigerated space temperature set point temperature

4 Results and Discussion

The search for system thermodynamic optimization opportunities starts by monitoring the behavior of refrigeration space temperature τ_L in time, for three dimensionless collector size parameter B, while holding the other constants, that is, dimensionless collector temperature $\tau_H = 1.5$ and dimensionless collector stagnation temperature $\tau_{st} = 1.8$.

Figure 2 shows that during the heat-up period, the temperature of the evaporator starts to decrease linearly, and then it decreases very slowly. Here, the reaction of the evaporator is seen strongly affected by the generator behavior. This temperature starts rising linearly and then it becomes stable. As the temperature of the generator is higher, more heat is absorbed in the evaporator. While, the temperature of the evaporator is decreasing very slowly the temperature of the generator still maintained quite constantly, indicating that the equilibrium state has reached (Abdullah and Hien 2010). Also, there is an intermediate value of the collector size parameter B, between 0.063 and 0.175, such that the temporal temperature gradient is maximum, minimizing the time to achieve prescribed set point temperature ($\tau_{L,set} = 0.97$).

The optimization with respect to the collector size B is pursued in Fig. 3 for time set point temperature for three different values of the collector stagnation temperature τ_{st} and heat source temperatures $\tau_H = 1.3$. The time θ_{set} decreases gradually according to the collector size parameter M until reaching a minimum time $\theta_{set,min}$ and then it increases. This confirms the results found previously (Fig. 2). The existence of an optimum for the thermal energy input $\bar{Q}_H$ is not due to the irreversible model aspects. However, an optimal thermal energy input $\bar{Q}_H$ results when the irreversible equations are constrained by the recognized total external conductance inventory, UA in Eq. (14), which is finite, and the generator operating temperature T_H. These constraints are the physical reasons for the existence of the optimum point. The minimum time to achieve prescribed temperature is the same for different values of the stagnation temperature τ_{st}.

During the transient operation and to reach the desired set point temperature, there are an internal generated by the working fluid and a total entropy generated by the cycle, which is obtained by integrating Eqs. (23) and (25) in time. Figures 4 and 5 show the behavior of internal and total entropy generated during the simulation time for three different collector size parameters ($B = 0.03, 0.04, 0.1$), holding τ_H, and τ_{st} constant ($\tau_H = 1.3$ and $\tau_{st} = 1.6$). From these figures, it is observed that the entropy rises with the increase of time and it is clear on the basis of the second law of thermodynamics that the entropy production is always positive for an irreversible cycle.

Figures 6 and 7 display the effect of the collector size on the internal and total entropy up to θ_{set}. It can be inferred that there is minimum entropy generated for a certain collector size B.

The variation of evaporator heat transfer with size collector parameters is predicted and shown in Fig. 8. It can be identified from the simulation results that

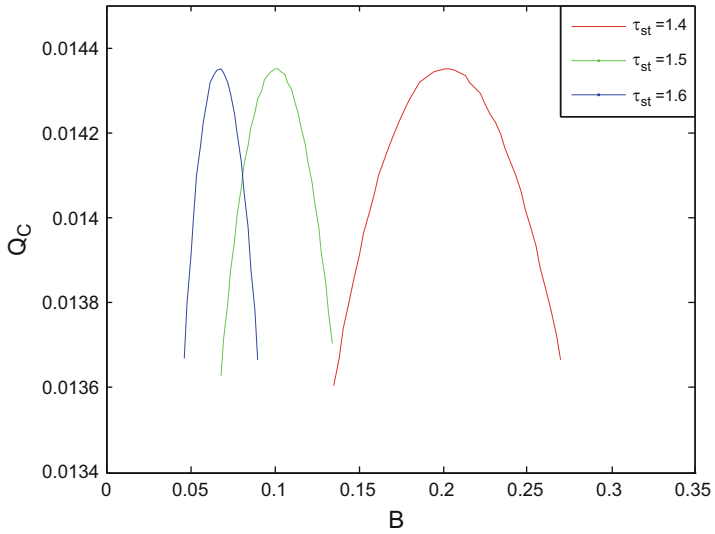

Fig. 8 The effect of dimensionless collector size, *B* on heat absorbed by the evaporator

the cooling capacity increases from the beginning of the refrigeration system start-up. This phenomenon is typical of the system start-up working regime when there is a refrigerant hot flow inside the evaporator that would heat the interior of the refrigerator while the refrigeration system cooling capacity increases. Afterward, evaporator heat transfer reaches a maximum when the steady-state condition is attained in the refrigerator interior. The maximum cooling capacity obtained for the tested refrigerator was 0.0143, for the different values of the stagnation temperature. Maximum cooling capacity does not mean minimum entropy generation by the cycle.

5 Conclusions

A thermodynamic transient regime simulation of a solar-driven absorption refrigerator has been presented in this study. An irreversible model has been analyzed numerically to find the optimal conditions of a solar-driven absorption refrigerator. The existence of an optimal size collector for minimum time to reach a specified temperature in the refrigerated space and minimum entropy generation inside the cycle is demonstrated. The model accounts for the irreversibilities of the three heat exchangers and the finiteness of the heat exchanger inventory (total thermal conductance). Appropriate dimensionless groups were identified and the generalized results reported in charts using dimensionless variables.

From the experiment analysis that had been carried out, the following conclusions can be drawn:

1. The optimum collector size Bopt and minimum time set point temperature $\theta_{set,min}$ depend strongly on the collector temperature τ_H.
2. Optimal size collector identified for minimum time to reach set point temperature in the refrigerated space does not coincide with Bopt, where minimum internal and total entropy occurs.

References

Abdullah, M.O., Hien, T.C.: Comparative analysis of performance and technoeconomics for a H_2O–NH_3–H_2 absorption refrigerator driven by different energy sources. Appl. Energy. **87**, 1535–1545 (2010)

Agrawal, D.C., Menon, V.J.: Finite-time Carnot refrigerators with wall gain and product loads. J. Appl. Phys. **74**(4), 2153–2158 (1993)

Ayyash, S., Suri, R.K., Al, S.H.: Performance results of solar absorption cooling installation. Int. J. Refrig. **8**, 177–183 (1985)

Bejan, A.: Advanced Engineering Thermodynamics. Wiley, New York (1988a)

Bejan, A.: Theory of heat transfer—irreversible power plants. International Journal of Heat Mass and Transfer. **31**, 1211–1219 (1988b)

Bejan, A.: Theory of heat transfer—irreversible refrigeration plants. Int. J. Heat Mass Transf. **32**, 1631–1639 (1989)

Bejan, A., Vargas, J.V.C., Sokolov, M.: Optimal allocation of a heat exchanger inventory in heat driven refrigerators. Int. J. Heat Mass Transf. **38**, 2997–3005 (1995)

Boukhchana, Y., Fellah, A., Ben Brahim, A.: Dynamic model for small-capacity ammonia-water absorption chiller, VIIth International Congress on Renewable Energy and the Environment, Sousse-Tunisia, March 19–21 (2013)

Boukhchana, Y., Fellah, A., Ben Brahim, A.: Numerical study of entropy generation in an irreversible solar-powered absorption cooling systems, 9ème Congrès Francophone de Génie des Procédés, Agadir, Maroc, April 28–30 (2014)

Browne, M.W., Bansal, P.K.: Transient simulation of vapor-compression packaged liquid chiller. Int. J. Refrig. **25**, 597–610 (2002)

Calvo Hernández, A., Medina, A., Roco, J.M.M., Velasco, S.: Comparison of Optimum Thermal Conductance Distribution for an Irreversible Carnot Cycle under Different Optimization Criteria, Advances in Finite Time Thermodynamics, Analysis and Optimization. Nova Science Publishers, New York (2004)

Charia, M., Pilatte, A., Bouidida, M.: Absorption refrigerating machine (water-ammonia) operating with plate solar collectors, located in rabat. International Journal of Refrigeratio. **14**, 297–303 (1991)

Chen, J., Yan, Z.: Unified description of endoreversible cycles. Phys. Rev. A. **39**, 4140–4147 (1989)

Denton, J.C.: Thermal cycles in classical thermodynamics and nonequilibrium thermodynamics in contrast with finite time thermodynamics. Energy Convers. Manag. **43**, 1583–1617 (2002)

El Haj Assad M., Performance characteristics of an irreversible refrigerator Recent Advanced in Finite Time Thermodynamics, Nova Science Publishers: New York, (2000).

Feidt, M.: Thermodynamique et optimisation énergétique des systèmes et procédés. Tech & Doc, Paris (1996)

Feidt, M.: Thermodynamics applied to reverse cycle machines, a review. International Journal of Refrige. **33**, 327–342 (2010)

Feidt, M., Petre, C., Costea, M., Petrescu, S.: General model of reversed cycle Carnot machine with constraints and nonlinear heat transfer laws, Proceedings of ECOS 2005, Trondheim, Norway, 2, pp. 529–536 (2005)

Feidt, M., Costea, M., Petre, C., Petrescu, S.: Optimization of the direct Carnot cycle. Appl. Therm. Eng. **27**, 829–839 (2007)

Gordon, J.M., Choon, K.A.: A general thermodynamic model for absorption chillers: theory and experiment. J. Heat Recovery Syst. CHP. **15**(1), 73–83 (1995)

Gordon, J.M., Ng, K.C.: Cool Thermodynamics. Cambridge Int. Science Publishers, Cambridge (2000)

Hamed, M., Fellah, A., Ben Brahim, A.: Optimization of a solar driven absorption refrigerator in the transient regime. Appl. Energy. **92**, 714–724 (2012)

Petrescu, S., Feidt, M., Harman, C., Costea, M.: Optimization of the irreversible Carnot cycle engine for maximum efficiency and maximum power through use of finite speed thermodynamic analysis. Proceedings of the ECOS 2002 International Conference, Berlin, 2, pp 1361–1368 (2002)

Sieniutycz, S., Salamon, P.: Finite-Time Thermodynamics and Thermo-Economics. Taylor & Francis, New York (1990)

Sokolov, M., Hershgal, D.: Optimal coupling and feasibility of a solar powered year-round ejector air conditioner. Sol. Energy. **50**(6), 507–516 (1993a)

Sokolov, M., Hershgal, D.: Solar-powered compression-enhanced ejector air conditioner. Sol. Energy. **51**, 183–194 (1993b)

Stolk, A.L.: New possibilities for absorption refrigeration Machines for Energy Saving. Int. J. Refrig. **3**, 78–82 (1980)

Suri, R.K., Ayyash, S.: Solar absorption cooling effect on operational parameters on power saving. Int. J. Refrig. **5**, 274–279 (1982)

Van, Z., Chen, J.: An optimal endoreversible three-heat -source refrigerator. J. Appl. Phys. **65**, 1–4 (1989)

Vargas, J.V.C., Sokolov, M., Bejan, A.: Thermodynamic optimization of solar-driven refrigerators. J. Solar Energy Eng. **118**, 130–135 (1996)

Vargas, J.V.C., Horuz, I., Callander, T.M.S., Fleming, J.S., Parise, J.A.R.: Simulation of the transient response of heat driven refrigerators with continuous temperature control. Int. J. Refrig. **21**, 648–660 (1998)

Vargas, J.V.C., Parise, J.A.R., Ledezma, G.A., Bianchi, M.V.A.: Thermodynamic optimization of heat driven refrigerators in the transient regime. Heat Transfer Engineering. **21**, 35–45 (2000)

Wijeysundera, N.E.: Performance limits of absorption cycles with external heat-transfer Irreversibilities. Appl. Therm. Eng. **16**(2), 175–181 (1996)

Wijeysundera, N.E.: Performance of three-heat-reservoir absorption cycles with external and internal irreversibilities. Appl. Therm. Eng. **17**(12), 1151–1161 (1997)

Wu, C.: Maximum obtainable specific cooling load of a refrigerator. Energy Convers. Manag. **36** (1), 7–10 (1995)

Yang, W.Y., Cao, W., Chung, T.S., Morris, J.: Applied Numerical Methods Using MATLAB. Wiley-Interscience/Wiley, Hoboken (2005)

Technical-Economic Prefeasibility Assessment of an Off-Grid Mini-hydropower Plant for an Agribusiness Resort in Kaduna Nigeria

Victor H. ADAMU, Ampofo Nana, Ario Panggi Pramono Jati, Ryan Tulabing, and Rojas-Solórzano Luis

1 Introduction

Per capita consumption of electricity in Nigeria is currently estimated to be 149 kWh/year, which is considered very low compared to 13,246 kWh/year per capita electricity consumption in the USA (World Bank Data 2015). This demonstrates low access to electricity, which is a consequence of poor electricity generation and supply. While a large hydropower potential exists in Nigeria, even above the total electricity demand of the country, by 2013 this technology only accounted for about 32% of the total installed generation capacity connected to the grid. This has led to an extensive use of diesel- or gasoline-operated generating sets for electricity generation for industrial and commercial activities. These emissions are associated to the wide use of small-scale fossil fuel-powered generators by about 55% of its 180 million people, yet to be connected to the grid (Nnaji 2011) (BPE 2011) (Energy Commission 2013) (SEC, 2014). Tuwan Agribusiness Resort (TAR) in Kaduna State, Nigeria, developed by Premier Agricultural Development (PAD) Ltd. is an agricultural service provision centre offering agricultural value chain development services to rural farmers. TAR has demonstration facilities that show various technologies in production and processing of crops and fish. The demonstration facility sits on a 15 hectare plot of land with a stream of water flowing across it. Requirements for electricity are lighting and powering equipment in offices, animal feed production and storage warehouse, recreation spots, lodging

V.H. ADAMU • A. Nana • A.P.P. Jati • R. Tulabing
Ecole des Mines de Nantes, Graduate School of Engineering, PM3E/ME3, La Chantrerie - 4, rue Alfred Kastler – BP 20722, Nantes 44307, France

R.-S. Luis (✉)
Nazarbayev University, Department of Mechanical Engineering, Astana 010000, Kazakhstan
e-mail: luis.rojas@nu.edu.kz

© Springer International Publishing AG, part of Springer Nature 2018

F. Aloui, I. Dincer (eds.), *Exergy for A Better Environment and Improved Sustainability 2*, Green Energy and Technology,
https://doi.org/10.1007/978-3-319-62575-1_83

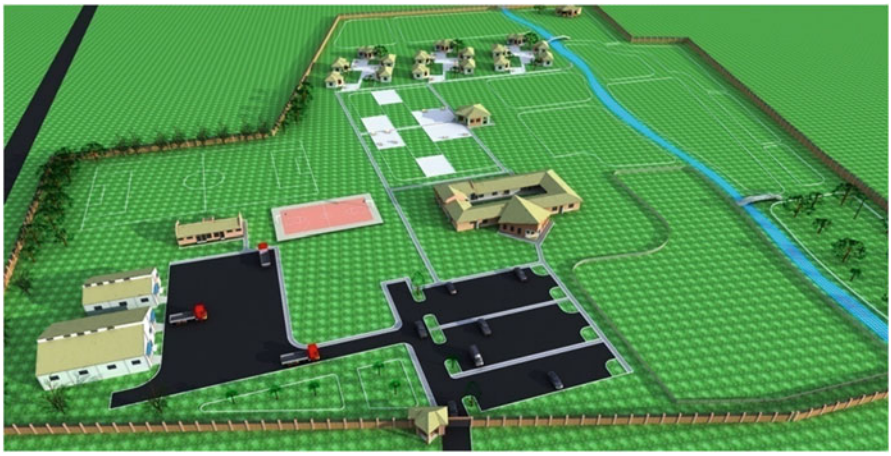

Fig. 1 Tuwan Agribusiness Resort conceptual design Source: Premier Agricultural Development (Nig.) Limited, 2012

facility and the fish fingerling production hatchery. This is currently being met by two 25 kW diesel generators, which increases the operational cost of running TAR beyond what is expected when electricity is accessed from the grid and makes the venture unprofitable in the long run in addition to the considerable negative environmental effects of associated high greenhouse gas (GHG) emissions.

Initiatives similar to TAR are fundamental in Nigeria, where there is a need to support food production activities to enable reduction of hunger and poverty in the country, with about 70% of the population depending on agriculture for income (Osugiri et al. 2012) Fig. 1.

With booming energy demands from a growing population, one major household or business decision is the source of their energy supply, by either renewable sources, fossil fuels or a combination of both.

This study analyses, at prefeasibility level, the technical, economic and environmental advantages of a proposed run-off river, mini-hydro power plant on the Tuwan River supplying part of the energy demand of TAR in comparison with supplying the full demand with two 25 kW diesel generators. This is a relevant project to the community since TAR, an agribusiness service provision outfit, is a social enterprise with a potential to stimulate the creation of over 1000 jobs when fully operational. The expected medium-term outcome is the provision of a viable sustainable alternative to electricity supply for TAR, development of local capacity and community awareness on clean energy and sustainable development, while motivating research by local communities and tertiary institutions. In addition, it will serve as guide for other development agencies and small business owners investing in local communities on meeting their electricity needs beyond the classic choice of purchasing a diesel generating set (The Economist 2010).

2 Methodology

The technical and financial analysis is mainly performed using the RETScreen software supported by extensive bibliographic review of relevant technology and financial information. Required technical input data are obtained through direct field measurements and from existing environmental and technical information databases online, as well as previously developed papers on the subject. Google Earth was also used for the topography study of the target site and to determine the gross head of the river with respect to the position of the hydropower turbine. It was fundamental to maintain close communication between the authors and international partners in Nigeria to obtain reliable onsite data.

3 Results and Discussions

3.1 Field Assessment

The dimensioning of the hydropower plant is based on the net head and the water flow duration curve (Nasir 2014). These are determined specifically from the physiographical and hydrological analysis, respectively, of data measured for at least 1 year. This is usually available from databases of the government or other private agencies.

Climate and geological conditions are also needed to have a comprehensive perspective of the location. In the absence of data, in situ measurements can be made as in this case; for which flow measurements were made in collaboration with workers at the project site. The float method was used to measure the average volumetric flow rate of the river (Froend 2012) as shown in Fig. 2. This measurement was made in November 2014, during the dry season in Nigeria.

Hence, the flow rate measured can safely be taken as the firm flow available at 95–100% of the time since flow is expected to increase during the rainy season. A 20 m length of relatively uniform stretch of the river was marked with three points: start, middle and end points. A float was made to travel between the two extreme points, and the travel time was measured in order to determine the surface velocity (V_{surface}). To estimate the average cross-sectional area (A_{ave}) of the river, the depth was measured at sections 0.5 m apart along the width of the river at the points marked as shown in Fig. 3.

The results of the measurement and the data used for the calculations are shown in Table 1.

From this method, A_{ave} and V_{surface} were determined to be 2.81 m^2 and 0.62 m/s, respectively, and used in Eq. (1):

$$Q = A_{\text{ave}} \times V_{\text{surface}} \times \text{Correction factor} \tag{1}$$

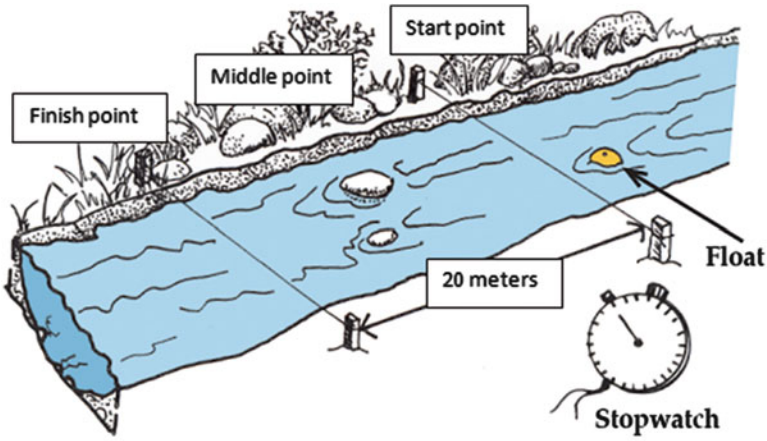

Fig. 2 Flow measurement by float method (Joy et al. 2005)

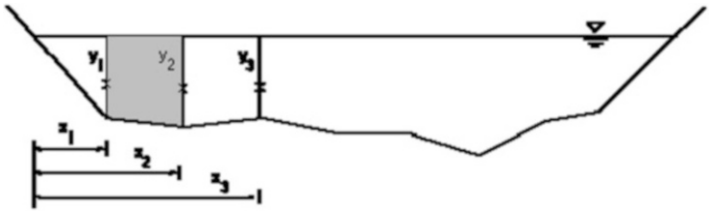

Fig. 3 Cross-sectional area measurement (Reckhow et al. 2010)

Table 1 River flow measurement results

Point		Start	Mid	End
Width (m)		*4.0*	*3.9*	**4.6**
Depth across stream width (m)	**y1**	*0.58*	*0.63*	**0.25**
	y2	*0.67*	*0.68*	**0.25**
	y3	*0.74*	*0.74*	**0.50**
	y4	*0.80*	*0.72*	**0.63**
	y5	*0.83*	*0.62*	**0.59**
	y6	*0.83*	*0.48*	**0.45**
	y7	*0.55*	*0.76*	**0.50**
	y8	*0.76*	*0.34*	**0.23**
Time of travel (s)	**Track 1**	**33.10**		
	Track 2	**30.98**		
	Track 3	**32.15**		

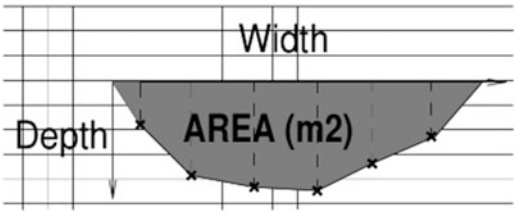

Fig. 4 Cross-sectional area calculation (Joy et al. 2005)

The cross-sectional area was calculated as shown in Fig. 4 above using measured data from the field.

Subsequently, the average flow (Q) of the river has been calculated as 1.2 m^3 /s. The correction factor of 0.85 was used based on the characteristics of the river channel and bed (Hydromatch 2014). This flow is considerably high in comparison to other similar small streams with flow rates in the range of 0.1–1 m^3/s for widths in the range of 1–8 m (WHO 1996). The flow rate was measured in November, a month characterized by draught based on the climatic and rainfall patterns of Nigeria. It is therefore sufficiently accurate at pre-feasibility phase to use this measured flow as the firm flow available at 95–100% of the time in order to evaluate the power potential of the river. The residual flow has been assumed to be nil at this phase.

The land formation of the site is generally of gentle slopes. The approximate head available was determined via topographical applications of Google Earth to be 3 m over a distance of 321 m. Although this value will generally be considered low head (Adhau et al. 2012), the relatively high flow compensates it in order to improve the general potential of the site.

The environmental impact of the project has been considered in terms of civil works. As a run-off river of low-power capacity, there is a need for the construction of a shallow reservoir, for water accumulation and channelling through a penstock. This will have minimum ecological modification impacts to the natural ambience. Nevertheless, an in-depth and compressive environmental impact assessment is mandatory as part of the feasibility study in the advanced stages of such a project.

3.2 Technical Assessment

With a 50 kW peak load from the Tuwan agribusiness off grid system, this hydropower plant is designed to supply half of the load that is currently fully supplied with two 25-kW diesel generators. It is assumed that the small hydropower plant runs all year round alongside one of the diesel generators to accommodate the entire electrical load at TAR, while the second diesel generator is dropped as standby and only activated to take care of peak load conditions or emergencies.

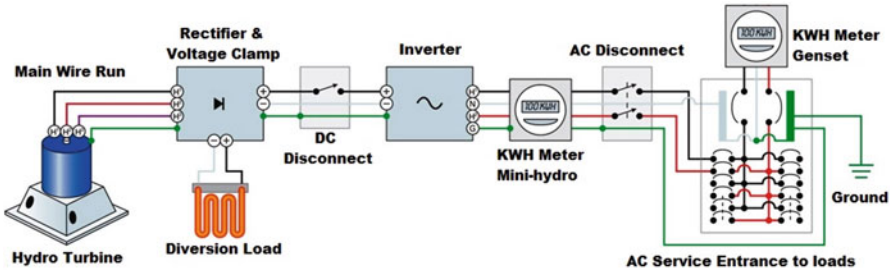

Fig. 5 Typical arrangement of electrical system in mini hydropower plant (Home power 2008)

This project is a run-off river type considering a year-round flow and the low initial cost since there is no need to construct a dam. With a low head, a Kaplan type turbine is selected for this system with the assumption that the flow will be at least 1.2 m^3/s all year round. Power generated from this system is predicted based on Eq. 2 (RETScreen 2004):

$$\text{Power(kW)} \approx 7 \times \text{Head (m)} \times \text{Flow } \left(\text{m}^3/\text{s}\right) \tag{2}$$

$$\text{Power(kW)} \approx 7 \times 3\,\text{m} \times 1.2\,\text{m}^3/\text{s} \approx 25.2\,\text{kW} \tag{3}$$

By conducting a detailed Retscreen simulation, considering the hydraulic losses and generator efficiency, the power output from the generator is about 21 kW. An AC direct electricity system is chosen for this project. An asynchronous generator is used due to the consideration that this type of generator is suitable for isolated small hydropower of less than 100 kW installed capacity. It has several advantages, such as cheaper price compared to synchronous generators and ease of maintenance (Azhumakan et al. 2013). The electrical diagram for the system layout is presented in Fig. 5.

As shown in the system layout, the output generator is connected to a rectifier and diversion load. This diversion load is used to consume any excess energy generated. It also protects the generator and inverter from over speed and overvoltage, respectively. The DC system is then connected to the Inverter to provide the energy to the load with 220 VAC, 50 Hz.

3.3 Cost and Financial Analysis

The entire 20-year lifespan of the project is considered in the cost analysis. This comprises the initial cost, annual cost and periodic cost. Table 2 provides the cost breakdown of the project.

The total initial cost prior to the operation phase of the project amounts to 132,887 USD which is based on the plant capacity and pricing of materials and labour in local and international standards. This breaks down to feasibility study

Table 2 Project cost breakdown

Project cost summary		
Initial cost		**100%**
Feasibility study	*5049.71 USD*	**4%**
Development	*7441.67 USD*	**6%**
Engineering	*15,016.23 USD*	**11%**
Power systems	*70,430.11 USD*	**53%**
Balance of systems & misc	*34,949.28 USD*	**26%**
Annual cost		
Operation & maintenance	*29,260.00 USD*	
Debt payment	*7191.00 USD*	
Periodic cost		
Inverter and parts replacement every 5 years	**25,000.00 USD**	

(3.8%), development (5.6%), engineering (11.3%), power system (53%) and balance of system and miscellaneous costs (26.3%). The bulk of the initial cost is taken by the civil works, turbine, generator and electrical system.

On the other hand, the annual cost in terms of operation, maintenance and payment of debt terms (up to 5 years) sums up to 36,451 USD per year. Meanwhile, a periodic cost of 2500 USD every 5 years is allotted for the replacement of inverters and other parts.

Fortunately, a projected grant of 50,000 USD that can be accessed from development funding partners of PAD Ltd. should reduce the share of loan required to fund the project. Thus, the debt ratio is only 20%, which means only 26,577 USD is to be borrowed from the bank to be paid in 5 years with 11% interest rate. Inflation is assumed to be 8.5%, while the fuel escalation is 10% from its present value of 0.54 USD per litre at year 2014. This project has a positive cash flow of 65,723 USD per year and a steadily increasing positive cash flows in the long run as seen in Fig. 6.

The income elements are mainly the amount of fuel savings and 15,000 USD salvage value of the system at the end of the project lifespan as shown in Table 3.

Aside from the grant, another positive factor is the tax holiday of 5 years (i.e. exception from 15% tax on income during the first 5 years of the project) granted by the government to agricultural organizations and rural infrastructural development (KPMG 2012).

In summary, as indicated in Table 4, the project is viable with net present value (NPV) of 568,178 USD (11% discount rate), internal rate of return (IRR) of 68.1% and benefit-cost ratio of 6.34.

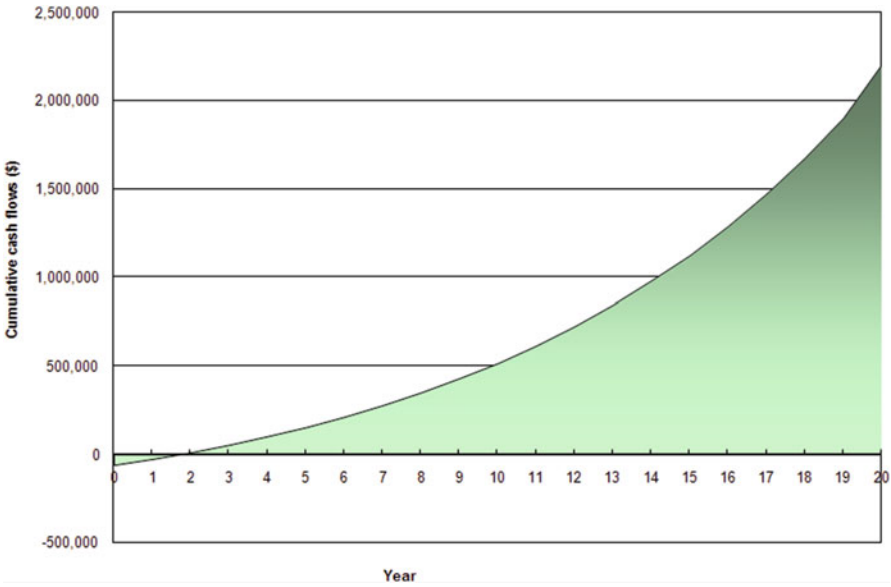

Fig. 6 Cumulative cash flow of the project in 20-year lifespan (RETScreen 2004)

Table 3 Summary of project income and savings

Project income summary	
Annual income	
Fuel savings	*65,723.00 USD*
Periodic income	
System salvage value after 20 years	*15,000.00 USD*

Table 4 Summary of financial viability of the project

Financial viability	
Pre-tax IRR – equity	*72.7%*
Pre-tax IRR – assets	*53.6%*
After-tax IRR – equity	*68.1%*
After-tax IRR – assets	*54.1%*
Simple payback	*2.3 yr*
Equity payback	*1.7 yr*
Net present value (NPV)	*568,178 USD*
Annual life cycle savings	*71,349 USD*
Benefit-cost (B-C) ratio	*6.34*
Debt service coverage	*5.64*

3.4 Green House Gas (GHG) Emission

According to UNIPCC (United Nations Intergovernmental Panel on Climate Change) compounds considered as GHG are carbon di-oxide (CO_2), methane

(CH_4), nitrous oxide (N_2O), ozone (O_3) and water vapour measured in units of tCO_2 equivalent. The Kyoto protocol defines additional compounds of sulphur hexafluoride (SF_6), hydroflourocarbons (HFCs) and perflourocarbons (PFCs) as greenhouse gases. Diesel generators emit a number of these gases, mainly CO_2 and water vapour. Considering the emission factor of diesel fuel of 0.2520 tCO_2 per MWh and estimated energy of 1221 MWh/year produced by the hydro power plant in place of the second diesel generator, the GHG emission avoided is a total of 307.4 tCO_2 equivalent per year. The hydropower plant has no GHG emission as it does not make use of fossil fuel. This GHG emission savings translate to 56 cars and light trucks off the road per year.

3.5 Sensitivity and Risk Analysis

The sensitivity analysis was performed on the net present value (NPV), which is favourable to such a capital-intensive project with long-term profitability. A threshold of 200,000 USD and a sensitivity range of 20% show that varying the fuel cost and the debt interest rate against the initial project cost results in values all above the threshold. This means that the sensitive factors of fuel cost, initial cost, operation and maintenance cost and debt interest rate cannot make the project unviable in the case that they change over the provided range. An increase in the fuel price and a reduction of initial cost, operating and maintenance costs and debt interest rate are favourable to the project analysis. The tornado diagram in Fig. 7 shows that an increase in the fuel cost (base case) and debt ratio will affect the project positively. On the other hand, an increase in the operating and maintenance cost of the mini-hydropower plant, the initial costs of the project, debt term and debt interest rate will affect the project negatively.

At a conservative risk level of 10% (90% of confidence range), the project has a median NPV of 569,451 USD. The minimum and maximum confidence NPV values of 516,324 USD and 625,649 USD, respectively, confirm that the project has 90% of likelihood to succeed in that range, which are indeed still very attractive

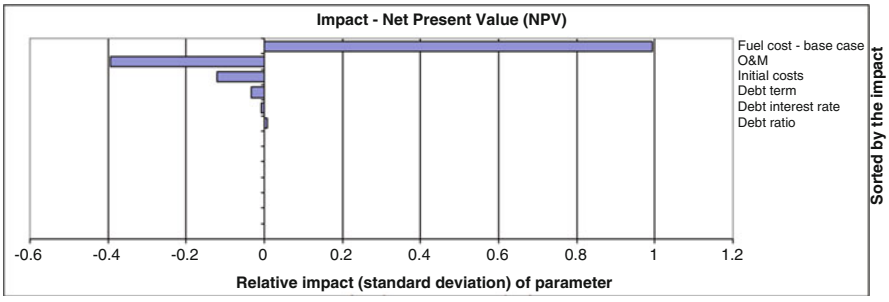

Fig. 7 Project sensitivity analysis (RETScreen 2004)

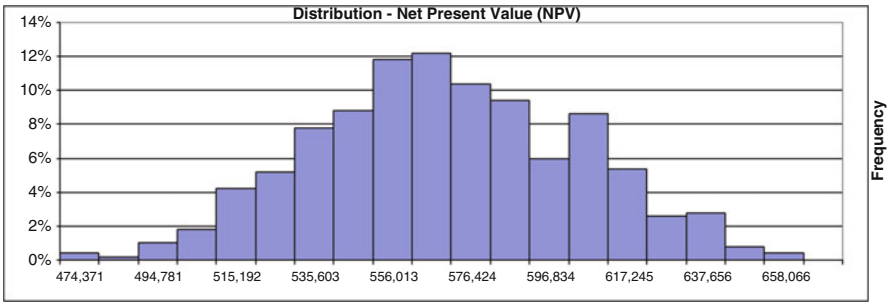

Fig. 8 Project risk analysis (RETScreen 2004)

values for the NPV. The histogram in Fig. 8 shows that the 90% confidence region is much higher than the 10% risk region.

4 Conclusions

The potential of electricity generation by a small hydropower plant on Tuwan River, which flows across TAR (Tuwan Agribusiness Resort) is presented by this project. In particular, the financial and GHG savings of the proposed case are compared to the full power supply using diesel generator sets. The following conclusions are drawn from the analysis:

- According to local measurements, Tuwan River may provide to this project an estimate of at least 21 kW power generation potential with a Kaplan turbine throughout the year.
- The hydropower project provides GHG emissions reduction of 307.4 tCO_2 equivalent.
- A net present value (NPV of 568,178 USD (11% discount rate), internal rate of return (IRR) of 68.1% and benefit-cost ratio of 6.34 with incentives of a 50,000 USD grant and a tax holiday are obtained in favour of the mini-hydropower plant.

The analysis shows that it is economically and environmentally attractive to pursue a mini-hydro project in this location. Thus, it is safe to invest more funds to conduct an extensive feasibility study with the aim of convincing fund (grant and loan) providers to invest in the project.

Acknowledgements This research was made possible with the support of THERON Felicie of Ecole Nationale Superieure des Mines de Nantes. Premier Agricultural Development Ltd. provided the site and corresponding data and their staff carried out required field measurements.

References

Adhau, S.P., Moharil, R.M., Adhau, P.G.: Mini-hydropower generation on existing irrigation projects: cases study of Indian cities [Journal]. Nagpur, India: Renew. Sust. Energ. Rev. **16**, 4785–4795 (2012)

Azhumakan, Z.Z.: Murat Merkebekovich Kunelbayev Ruslan Isaev and Balzhan Abylkanovna Chakenova, Selection of Generator for the Micro Hydro Power Plant [Report] – [s.l.]. American-Eurasian J. Sci. Res. ISSN 1818-6785 (2013)

Bureau of Public Enterprises: Power Generation Status and Outlook, Abuja, Presidential Task Force on Power (2011)

Energy Commission of Nigeria: The Presidency, National Energy Policy, p. 23. Energy Commission of Nigeria, Abuja (2013)

Froend, Oliver: Assessment of hydropower resources – ECOWAS Regional Centre for Renewable Energy and Energy Efficiency [Conference]. Regional Workshop on Small Scale Hydropower, p. 39 (2012)

Home power: [Online] – September 2008 – October 2014 http://www.homepower.com/articles/microhydro-power/design-installation/electric-side-hydro-power

Hydromatch: Flow estimation for streams and small rivers [Online] Hydromatch, October 16, 2014. http://www.hydromatch.com/sites/default/files/downloads/DIY-flow-measurement-guide.pdf

Joy, P.: Michaud and Marlies Wierenga Estimating Discharge and Stream Flows A Guide for Sand and Gravel Operators [Report], pp. 8, 14, 15. Ecology Publication, Washington (2005). 05-10-070

KPMG Nigeria Fiscal Guide: 2012/2013 [Report] – [s.l.]: KPMG (2012)

Nasir Bilal Abdullah: Design considerations of a MIcr-Hydro-Electric Power plant [Conference] – [s.l.]: The International Conference on Technologies and Materials for Renewable Energy, Environment and Sustainability (2014)

Nnaji, B.: Power sector outlook in Nigeria [Report]. Securities and Exchange Commission, Abuja (2011)

Osugiri, I.I., et al.: Population Dynamics, Labour and Small-Holder Farmers' Productivity in Southeast Nigeria [Journal]. J. Econ. Sustain. Dev. **3**, 96 (2012), ISSN 2222–1700 (Paper) ISSN 2222–2855 (Online) [s.l.]: www.iiste.org

Power Sector Outlook in Nigeria: Abuja Securities and Exchange Commission (2011)

Reckhow, D.A., Liu, B., Sheppard, D.: CEE 370 Lab Fall 2010, Lab Exercise #1: Stream flow [Online]. 2010. 20 Nov 2014. http://www.ecs.umass.edu/cee/reckhow/courses/370/Lab1/Stream%20flow%20lab.pdf

Retscreen: Small Hydro Project Analysis [Report]. [s.l.]: Retscreen – ISBN: 0–662–37497-5 (2004)

The Economist, Electricity in Nigeria: Let there be light [Online]. The Economist. – The Economist Newspaper Ltd., 21 October 2010. – 12 Nov 2014. http://www.economist.com/node/17312103

The World Bank Data: The World Bank Group. http://data.worldbank.org/indicator/EG.ELC.ACCS.ZS/countries/1W-NG?display=default (2015)

WHO: Water Quality Assessments – A Guide to Use of Biota, Sediments and Water in Environmental Monitoring – Second Edition [Report] – [s.l.]: WHO, 1996 – ISBN 0 419 21590 5 (HB) 0 419 21600 6 (PB)